Project No. 24-41

DEFINING THE BOUNDARY CONDITIONS FOR COMPOSITE BEHAVIOR OF GEOSYNTHETIC-REINFORCED SOIL STRUCTURES

FINAL REPORT

Prepared for
National Cooperative Highway Research Program
Transportation Research Board

of

The National Academies of Sciences, Engineering, and Medicine

Jorge G. Zornberg
Amr M. Morsy
Behdad Mofarraj Kouchaki
The University of Texas at Austin, Austin, Texas

Barry Christopher
Independent Consultant, St. Augustine, Florida

Dov Leshchinsky
ADAMA Engineering, Inc., Portland, Oregon

Jie Han
University of Kansas, Lawrence, Kansas

Burak F. Tanyu
Fitsum T. Gebremariam
George Mason University, Fairfax, Virginia

Panpan Shen
Tongji University, Shanghai, China

Yan Jiang
Terracon, Savannah, Georgia

October 31, 2018

ACKNOWLEDGMENT OF SPONSORSHIP

This work was sponsored by one or more of the following as noted:

■ American Association of State Highway and Transportation Officials, in cooperation with the Federal Highway Administration, and was conducted in the **National Cooperative Highway Research Program,**

☐ Federal Transit Administration and was conducted in the **Transit Cooperative Research Program**,

☐ Federal Aviation Administration and was conducted in the **Airport Cooperative Research Program,**

☐ The National Highway Safety Administration and was conducted in the **Behavioral Traffic Safety Cooperative Research Program,**

which is administered by the Transportation Research Board of the National Academies of Sciences, Engineering, and Medicine.

DISCLAIMER

TABLE OF CONTENTS

EXECUTIVE SUMMARY
NCHRP PROJECT 24-41

DEFINING THE BOUNDARY CONDITIONS FOR COMPOSITE BEHAVIOR OF GEOSYNTHETIC-REINFORCED SOIL STRUCTURES

The overall objective of this report is to quantify the effect of adopting a closely-spaced reinforcement layout in geosynthetic-reinforced soil structures. While research since the early 1980s has identified the beneficial effect of closely-spaced reinforcement in reinforced soil structures, such improvement in performance is not accounted for in the simplified methodologies established by AASHTO. Considering the effect of closely-spaced reinforcement may be particularly relevant in critical structures, such as load-carrying geosynthetic-reinforced MSE (GMSE) bridge abutments, which eliminate the use of deep foundations to support the bridge loads. In fact, the adoption of closely-spaced reinforcement was identified as being particularly relevant for these type of structures, leading to specific design guidelines developed by FHWA for structures that became identified as Geosynthetic Reinforced Soil Integrated Bridge System, or GRS-IBS.

The terms "GRS," "MSE," and "GMSE" have been used since the 1980s, often indistinctly in the technical literature, to refer to mechanically stabilized earth structures that are reinforced with geosynthetics. For consistency with AASHTO, the term "GMSE" is adopted herein to refer to geosynthetic-reinforced soil structures, irrespective of the magnitude of its reinforcement vertical spacing. An expression that also requires clarification within the context of this report is the term "composite behavior." Accordingly, a GMSE structure is identified as showing a composite behavior when loading of a given geosynthetic reinforcement affects the deformation response and load magnitude of adjacent reinforcement layers. An important objective of this study is to unequivocally define the boundaries for such behavior. In addition, this study aims at proposing changes into AASHTO LRFD Bridge Design Specifications to account for such behavior.

An evaluation of the state-of-the-art on the different components of this study was conducted. The information was grouped into experimental, field monitoring, numerical, and design-related literature. The focus of this review was to summarize pertinent information published in technical venues that was deemed relevant to assess (1) the different components of the research and (2) the composite behavior of GRS structures.

A comprehensive summary of the state-of-the-practice was compiled to document the characteristics of the various components of geosynthetic-reinforced soil bridge abutments constructed worldwide. This is a type of structure for which closely-spaced reinforcement has often been adopted.Data on the characteristics of the geosynthetic-reinforced soil abutments used nationally and internationally was collected via a survey that targeted researchers, practitioners, wall system providers and geosynthetic reinforcement manufacturers. The wide range of characteristics of load-carrying GMSE bridge abutments, as obtained from the survey, is

noteworthy, particularly considering the reasonably prescriptive nature of this type of structure as constructed in the US. Specifically, the majority of geosynthetic-reinforced soil bridge abutments in the US were constructed with smaller reinforcement vertical spacings than those adopted in most other abutments constructed worldwide. While the most common geosynthetic type is geogrids, the majority of US structures were constructed using woven geotextiles. Additionally, while the facing types utilized in geosynthetic-reinforced soil abutments varies widely around the world, the use of masonry block facing systems has prevailed in the US. A characteristic common to structures designed in the US and those designed abroad are the stringent requirements regarding the selection of backfill material.

Reinterpretation of data from FHWA's large-scale experimental structures was among the various sources of experimental and field data that, while collected as part of previous studies, was relevant to the objectives of the study. Since the 1970s, the FHWA has conducted extensive research to evaluate the behavior of reinforced soil structures, which led to the development of design guidelines first included in AASHTO in the early 1980s. These guidelines have continued evolving as additional research has been conducted and the number of reinforced soil structures built has increased. The current practice in the US relies largely on the latest design specifications developed by the FHWA in 2009 and also adopted by AASHTO. Recently, the FHWA developed a set of empirical and analytical design models for geosynthetic-reinforced soil structures constructed with small reinforcement spacings. These models were developed assuming that a geosynthetic-reinforced soil mass with close reinforcements behaves as a composite. The FHWA calibrated these models experimentally through a number of physical experimentation and field monitoring studies. To assess the reliability of the new approach, this study presents a reevaluation of a number of FHWA experimental structures and included models for bearing capacity, vertical and lateral displacements, and lateral earth pressures. This reevaluation indicated that the FHWA models provide reasonable predictions of the behavior of geosynthetic-reinforced soil structures. However, the scatter associated with these predictions was found to be reasonably high, especially at working stress ranges.

Reinterpretation of data generated as part of a KDOT field investigation involving the use of secondary reinforcements was also useful to assess the effect of closely-spaced reinforcement. Specifically, three MSE wall sections reinforced with geogrids were constructed and monitored by KDOT: (1) an MSE wall section with uniaxial geogrids as primary and secondary reinforcements; (2) an MSE wall section with uniaxial geogrids as primary reinforcements, with biaxial geogrids as secondary reinforcements; and (3) an MSE wall section with uniaxial geogrids as primary reinforcements only (i.e., the control section). Earth pressure cells, inclinometers, and foil-type strain gauges were used in test wall sections to measure the vertical and lateral earth pressures, lateral wall facing deflections, and strains of primary and secondary geogrids, respectively. A reevaluation was conducted of the collected data with focus on the effect of vertical spacing. Based on an analysis of the field test results, the following conclusions were drawn: (1) the secondary reinforcements reduced the wall facing deflections as compared with those in the control section; (2) the measured vertical earth pressures were consistent with the computed trapezoid stresses and increased with construction of the wall; (3) the distribution of measured lateral earth pressures in the control section increased linearly with depth, while the

distribution of the measured lateral earth pressures in the sections with secondary reinforcements were approximately uniform with depth; (4) the measured tensile strains at the connection in all sections were comparatively small; and (5) the use of secondary reinforcements was found to reduce the maximum tensile strains in the primary geogrids.

Research conducted at the University of Delaware in the 1990s and 2000s was also reinterpreted, as it focused directly on the effect of reinforcement vertical spacing on the behavior of geosynthetic-reinforced soil structures. Data from that research was synthesized as part of this study and the relevant findings from that study were integrated with recent ones related to the effect of reinforcement vertical spacing. Specifically, an experimental testing program conducted in the 1990s on geosynthetic-reinforced soil unit cells was reevaluated to gain insight of the effect of reinforcement vertical spacing with focus on the soil arching phenomenon. In this testing program, a pullout testing device was developed to evaluate the displacement and strain fields within a reinforced soil unit cell. Two testing series were carried out: pullout of single reinforcement layers, and pullout of two reinforcement layers connected to a rigid facing panel. The tests conducted to assess the influence of a single reinforcement layer indicated that if the vertical spacing is less than twice the arching zone, contiguous reinforcement layers interact with each other and tend to behave as a single composite material. A field evaluation was also conducted as part of that study, which included field pullout tests on two geosynthetic-reinforced soil walls. Results showed that wall displacements, reinforcement strains and lateral pressure on the facing were small and the soil confined between reinforcements acted as a monolithic block, which was consistent with observations from the experimental program. Lastly, a numerical simulation was conducted to assess the effect of reinforcement spacing. The effect of closely-spaced reinforcements was observed to increase with increasing backfill shear strength. The results indicated that interaction of the various wall components may affect wall performance. Overall, even though it is not considered in common design methodologies, soil arching was found to affect the behavior of geosynthetic-reinforced soil.

A substantial number of centrifuge models involving geosynthetic-reinforced soil structures, previously tested to assess different performance aspects were also reevaluated as part of this study. An advantage of centrifuge modeling is that the stress state of reduced-scale models corresponds to that of prototypes because of the increased gravitational field. Consequently, centrifuge tests are suitable to validate several design aspects experimentally, including the effect of reinforcement vertical spacing. While the centrifuge experimental studies conducted in the past were tailored to address specific aspects of geosynthetic-reinforced soil design, they were collectively found to provide a relevant source of experimental data that was mined as part of this study to assess additional aspects of geosynthetic-reinforced soil behavior. Accordingly, this study included the compilation of a large volume of data generated by testing geosynthetic-reinforced soil models in geotechnical centrifuges, from which a portfolio was created of centrifuge data on geosynthetic-reinforced soil structures, with an emphasis on data in which reinforcement vertical spacing was varied. Overall, the results from these studies collectively indicate that the impact of reinforcement vertical spacing on the behavior of geosynthetic-reinforced soil structures is not strictly proportional to the impact of reinforcement mechanical

properties (e.g. stiffness, ultimate tensile strength), but that it outweighs the relevance of the mechanical properties for particularly small values of vertical spacing.

Field monitoring data from the Founders/Meadows bridge, constructed in Castle Rock, Colorado in 1999, was also reassessed as part of this study. This structure is the first load-carrying GMSE abutment constructed on a major highway in the US. The abutments were extensively instrumented and monitored during construction and for approximately 5 years following opening to traffic. Because these abutments are the largest and among the oldest geosynthetic-reinforced soil structures in service, they have been used in several numerical studies to extend the range of parameters beyond those strictly collected from field monitoring performance of geosynthetic-reinforced soil abutments. The field monitoring data collected for the Founders/Meadows abutments were compiled and reevaluated in this study considering the current understanding of the behavior of geosynthetic-reinforced soil under bridge loads. This reevaluation examined the data collected on the outward movements of the abutment, settlement of the abutment, reinforcement strains, differential settlement between the abutment and approaching roadway, temperature and moisture changes, and vertical and lateral stresses within the geosynthetic-reinforced soil mass. The monitored vertical stress distribution revealed the pattern of stress propagation within the geosynthetic-reinforced soil mass. It was determined that temperature variations, construction sequence and construction season may have significant effect on the behavior of load-carrying GMSE bridge abutments.

Field monitoring data from five additional load-carrying GMSE bridge abutments was also reevaluated in order to synthesize information relevant to the impact on behavior of reinforcement vertical spacing. The five load-carrying GMSE abutments included three structures designed following GRS-IBS guidelines. Particular attention was paid to the response of these structures (constructed in Colorado, Delaware, Minnesota, and Louisiana) in relation that specifically monitored as part of this study in Virginia. Overall, the field monitoring data revealed that the profile of maximum reinforcement tension showed a relatively uniform distribution with depth, particularly for the case of closely-spaced reinforcement vertical spacings. Also, the profile of connection loads was found to also show a reasonably uniform distribution with depth for different reinforcement vertical spacings. The connection load values in the observed uniform distribution were found to fall within the range of the values that would be obtained using a triangular distribution considering the maximum unit tension in the reinforcements. Also, field monitoring data revealed that the vertical stress distribution shows similar trends and magnitude consistent with those predicted by conventional stress distribution methods (AASHTO 2:1 and Boussinesq). As expected, settlements in the structures were observed to increase with an increase in abutment height.

The experimental component of this study included the development of a new device to comprehensively assess the soil-reinforcement composite interaction under both working stress and failure conditions. This new equipment was able to assess the mechanical behavior of a geosynthetic-reinforced soil mass considering varying reinforcement vertical spacings. It also facilitated investigating interface shear stress transfer mechanisms. The device provided suitable measurements of the strains developed in both actively tensioned and adjacent reinforcement

layers. It allowed direct visualization of the kinematic response of soil particles adjacent to the geosynthetic reinforcement layers, which facilitated evaluation of the soil displacement field via digital image analysis. Evaluation of the soil displacement field allowed quantification of the extent of the zone of shear influence around a tensioned reinforcement layer. Finally, the device allowed monitoring of dilatancy within the reinforced soil mass, providing additional insight into the effect of reinforcement vertical spacing on the reinforced soil mass.

A newly developed experimental device was used to conduct a comprehensive testing program. The experimental plan was tailored to evaluate the effects on the interaction among neighboring reinforcements in relation to: (1) the normal stress at the soil-reinforcement interface; (2) the vertical spacing between reinforcements; (3) the reinforcement properties; and (4) the fill type. Analysis of the experimental results revealed that the existence of the zone of shear influence and its extent can be directly related to the interaction between contiguous reinforcement layers. The interaction between adjacent reinforcement layers was found to increase with decreasing reinforcement vertical spacing. A minimum reinforcement vertical spacing threshold was identified below which the interaction between adjacent reinforcements develops fully. In addition, a maximum reinforcement vertical spacing threshold was identified beyond which the interaction between adjacent reinforcements becomes negligible. For the testing program implemented in this study, the minimum and maximum threshold vertical spacings were identified as 0.10 and 0.20 m (4 and 8 in.), respectively. Therefore, according to these experimental results, the zone of shear influence extends an average distance of 0.15 m (6 in.) from the soil-geosynthetic interface. That is, interaction between adjacent reinforcements could be observed for a vertical spacing value corresponding to 0.30 m (12 in.), or twice the average distance from the reinforcement for which interaction occurs.

The field monitoring component of this study involved a GRS-IBS structure constructed by the Virginia Department of Transportation's (VDOT), Staunton District in an area primarily characterized as a dry stream bed. The dimensions of the structure (2.4 m [8 ft.] high and 9 m [30 ft.] wide) were consistent with mini-pier tests constructed by FHWA as part of the development of the GRS-IBS system. The main focus of the field monitoring evaluation was on understanding the stress and strain distributions within the structure, as well as the lateral movements of the facing, as they relate to both sections of the structure constructed using reinforcement vertical spacings of 0.2 m (8 in.) in the primary reinforcement zone and 0.1 m (4 in.) in the bearing bed zone. The structure was designed and constructed by VDOT in accordance with FHWA guidelines. This included the use of woven geotextiles, AASHTO No. 8 aggregate and facing blocks. The two abutments were instrumented, with one of them constructed with a beam seat of 0.6 m (2ft.) and the other with a beam seat of 1.2 m (4 ft.). The instrumentation program aimed at understanding: (1) the stress and strains distribution behind the facing blocks; (2) the differences between the stress and strain distributions anticipated within the primary and bearing bed zones (i.e. zones with different vertical reinforcement spacing); and (3) the effect of the beam seat width (or contact stresses) on the stress distribution within the abutment. Instrumentation included vertical and horizontal earth pressure cells, strain gages, extensometers (placed in geotextiles and soil), settlement cells and survey targets. Field monitoring results also aimed at

providing information suitable for calibration of the numerical model conducted as part of the numerical component of the project.

Data generated at different construction stages was evaluated as part of the field performance: self-weight of the backfill material, placement of the bridge slab, and loading of the slab with a truck after construction. Additionally, loading tests were conducted in stages during construction by placing Jersey barriers 0.3 m (1 ft.) away from the facing blocks of select layers. The results showed that the presence of secondary reinforcements (with comparatively small vertical spacing) led to a reduction in vertical and lateral stresses, reinforcement strains and backfill deformation. The vertical stress distribution due to the slab load was observed to agree with the theoretical AASHTO 2:1 and Boussinesq stress distribution methods. Overall, the profile of lateral earth pressures was found to be relatively uniform, with magnitudes of stresses comparatively higher those estimated using GRS-IBS design guidelines. The maximum measured strains in the geotextile were below 0.5% and connection load values ranging from 0.8 to 1.2 kN/m (4.6 to 6.9 lb/in). The reinforcement strain and connection load distribution with depth were also found to be reasonably uniform. Foundation settlement and lateral facing displacements were comparatively small and below the maximum vertical and lateral deformations allowed per GRS-IBS design guidelines. As expected, the abutment constructed with a wider beam seat exhibited a comparatively smaller magnitude of vertical stresses and facing displacements.

Numerical simulations were carried out under both serviceability and limit strength states to broaden the range of parameters adopted in the experimental and field components of this project. Numerical models were initially calibrated and validated against laboratory and field test data to provide reliable and accurate simulations of the behavior of GMSE structures in general and load-carrying GMSE bridge abutments in particular. After model calibration, three series of numerical parametric studies were conducted to investigate the effects of key parameters (e.g. wall height, reinforcement spacing, backfill and reinforcement properties, facing rigidity, foundation conditions, and loading conditions) on the behavior of GRS structures. The parametric studies included numerical investigations: (1) of soil-geosynthetic interaction tests; (2) of GRS piers; and (3) of GRS-IBS structures. In addition, this study investigated the effect of boundary conditions on the behavior of GRS structures and the stability of GRS structures under the strength limit state.

A numerical analysis of GRS mini-pier tests indicated that the impact of decreasing the reinforcement spacing was more significant than that increasing the reinforcement stiffness while maintaining a stiffness/spacing ratio constant. However, a numerical evaluation of GRS-IBS structures revealed similar behavior between two structures simulated with the same stiffness/spacing ratio. The main difference between the GRS mini-pier and GRS-IBS was their boundary conditions. A numerical investigation on the effect of boundary conditions showed that the impact of the stiffness/spacing ratio depends on the dominant internal stability mechanism (i.e. reinforcement pullout or breakage). When reinforcement pullout controls the performance, a structure with small reinforcement spacing and low reinforcement stiffness showed better performance than a structure with large reinforcement spacing and high reinforcement stiffness (for a constant stiffness/spacing ratio). However, when reinforcement pullout does not control

performance, the two structures required essentially the same reinforcement tension capacity for different reinforcement spacings and stiffness values selected using a constant stiffness/spacing ratio.

The results of stability analyses showed that the shape of the critical slip surface was different for structures simulated with reinforcement spacing of 0.2 m (8 in.) and 0.6 m (16 in.). in the first case, the critical slip surface initiated from the wall toe and followed a Rankine slip plane up to approximately 2/3 of the wall height, then extending vertically to the edge of the bridge bearing seat. The tensile strength of the reinforcements was mobilized in both primary reinforcement zone and the bearing reinforcement zone (with smaller reinforcement vertical spacing). The maximum tension in the reinforcements showed an essentially uniformly distributed trend with depth. For the case with a vertical spacing of 0.6 m (24 in.), the slip surface was found to initiate at the wall toe and extend to the end of the bearing reinforcement zone. The required tensile strength of the reinforcement was not uniform and was only mobilized in the primary reinforcements.

Recommendations to modify the existing design procedures were finally compiled based on the wealth of experimental, field monitoring and numerical data generated in this study. Focus was on implementation of the recommendations into Section 11.10 AASHTO LRFD Bridge Design Specifications (AASHTO 2017). The proposed design procedure accounts for the boundaries identified for the composite behavior of GMSE structures established in the experimental research component of the study. Specifically, a zone of influence ranging from 0.1 to 0.2 m (4 to 8 in.) on each side of the geosynthetic is recommended for cases where the coefficient of interaction exceeds 0.8 and free draining fill materials are adopted in construction. The results from the field monitoring component and numerical component of this study were used to reassess current approaches, including correlations established by the FHWA regarding the effect of vertical spacing. This information allows proper integration of the findings of this project into the current AASHTO LRFD framework. With this background in mind,

A total of five design aspects were identified for possible revision into current guidelines to facilitate incorporation of the effect of reinforcement vertical spacing into the design of GMSE structures in general and load-carrying GMSE abutments in particular. The identified design aspects that deserve reevaluation and specific revisions to current design methods regarding these aspects are as follows:

1 **Effect of the vertical reinforcement spacing on the magnitude and distribution of maximum reinforcement tension**: A uniform distribution of maximum reinforcement tension with depth is recommended for GMSE structures with closely-spaced vertical reinforcement spacing. This recommended distribution has cost-effectiveness implications for the case of structures designed using the same vertical reinforcement spacing and reinforcement design strength in the entire height of the GMSE structure.
2 **Effect of vertical spacing on the magnitude and distribution of connection loads**: A uniform distribution of reinforcement connection load with depth is recommended for GMSE structures with closely-spaced vertical reinforcement. This recommended distribution also

has cost-effectiveness implications for the case of structures designed using the same vertical reinforcement spacing and reinforcement design strength.

3 **Effect of vertical spacing on stress distribution and the design of the bearing seat**: Increased density of reinforcement is recommended in this under the bearing seat of load-carrying GMSE abutments (including GRS-IBS structures). In particular, a reinforcement vertical spacing of 0.1 m (4 in.) was shown to result in improved performance

4 **Effect of vertical spacing on the structure's vertical and lateral deformation**: Improvement of structural stiffness is observed in structures with closely-spaced reinforcement, as it relates to comparatively decreased lateral displacements of the overall structure. A model is proposed for preliminary prediction of maximum lateral displacements.

5 **Effect of vertical spacing on the "bump at the end of the bridge:"** The use of closely-spaced reinforcement is recommended as it was verified to lead to a decreased bump at the end of the bridge for the case of load-carrying GMSE bridge abutments (including GRS-IBS structures).

Specific revisions to appropriate articles in AASHTO's Section 11 are provided for incorporation of each of these structural advantages into the specific design aspects. Additionally, modifications to the current Article 11.10.10.1, Concentrated Load Conditions, are also proposed for the case of load-carrying GMSE bridge abutments in general and for the case of GRS-IBS structures in particular, due to the uniqueness of the approach and documented performance. The research basis supporting the proposed revisions to incorporate the vertical spacing as an additional variable in design procedures are summarized. In reviewing the acceptance of the design advances proposed for use with closely-spaced reinforcements, consideration should also be given to several inherent benefits that improve the overall conservatism of the structure, which should offset any uncertainties resulting from the proposed modifications. These include increased redundancy in the system, comparatively better control of lift thickness and overall better backfill compaction control.

1 INTRODUCTION

1.1 MOTIVATION AND GENERAL CONTEXT

Geosynthetic reinforcements have been successfully used for retaining wall support since the early 1970s. These systems were extensively evaluated in the 1980s, particularly by comparing their performance with that of other reinforced soil systems available at the time (e.g. metallic grid and strip reinforced soil systems). Perhaps the most notable of these studies are the National Cooperative Highway Research Program (NCHRP) and the Federal Highway Administration (FHWA) subsequent studies conducted on the Behavior of Reinforced Soil, which resulted in NCHRP Report 290 (Mitchell and Villet 1987) and FHWA-RD-89-043 (Christopher et al. 1989a, b). The FHWA study was specifically performed to evaluate the various design methods available at that time and to unify them into a consistent design approach. These landmark studies concluded that the performance of geosynthetic-reinforced soil structures could be as viable as that of other reinforced soil systems. Achieving a unified design framework allowed designers to systematically evaluate reinforced wall alternatives based on performance and cost, ultimately leading to a significant increase in the number of constructed reinforced soil structures relative to conventional systems. It was recognized early in the development of the unified design framework for soil reinforcement that important considerations should be made to account for specific attributes of different systems. For example, the early studies cited previously (Mitchell and Villet 1987, Christopher et al. 1989a, b) revealed the importance of accounting for the effect of reinforcement stiffness on the stresses within the reinforced soil mass, thereby incorporating appropriate relations into the design framework. The studies also established that wall face deformation, an important performance criterion, may be significantly affected by design factors not accounted for at that time, while noting that face deformation is highly sensitive to variations in the reinforcement vertical spacing. While a maximum reinforcement vertical spacing value was established to control face deformation, methods capitalizing on the additional advantages of closely spaced reinforcements were not identified at that time. Furthermore, most efforts at the time were devoted to the design of roadway walls, with only limited focus on bridge loads, where the use of closely-spaced reinforcement has recently been reported by FHWA (2012, 2018) to result in significant performance advantages.

Based on the 1980s studies, FHWA worked with AASHTO in the 1990s to simplify the design approach and develop specifications that resulted in grouping all reinforced soil structures under Mechanically Stabilized Earth (MSE) walls using the Simplified Method as a unifying design framework (Allen et al. 2001). Accordingly, any reinforced soil system could be considered for design of grade separation structures (FHWA Demo-82 and AASHTO 1998 Interims). A positive outcome of this approach was that it now allowed geosynthetic-reinforced soil walls to be considered for projects in which only metallic reinforcements had previously been used. However, no clear advantages were established at that time for closely-spaced geosynthetic reinforced soil (GRS) structures over those that involve wider reinforcement spacings.

While research since the early 1980s has identified the beneficial effect of closely-spaced reinforcement (e.g. Leshchinsky et al. 1994, Leshchinsky and Vulova 2001), such improvement in performance was not accounted for by the Simplified Method. Largely neglected advantages of closely-spaced geosynthetic reinforcement include increased confinement, reduced lateral deformation, suppressed dilation, and a reduction in connection stress (e.g. Nicks *et al.* 2013a). While the use of a unified framework for reinforced soil wall design in AASHTO and FHWA has served the transportation industry well, additional advantages can be realized by incorporating the benefits of closely-spaced reinforcement.

Acceptability of load-carrying geosynthetic-reinforced MSE (GMSE) bridge abutments, which eliminate the use of deep foundations to support the bridge loads, improved in the US in the late 1990's (e.g. Zornberg et al. 2001, Abu-Hejleh et al. 2002). The adoption of closely-spaced reinforcement was subsequently identified as being particularly relevant for these type of structures, leading to specific design guidelines developed by FHWA for structures that became identified as Geosynthetic Reinforced Soil Integrated Bridge System, or GRS-IBS (FHWA 2012, 2018). FHWA also calibrated the reliability of these models using performance test data, which have been correlated against results from laboratory and field monitoring programs (Nicks *et al.* 2013b). The results from these comprehensive studies, which included loading of large-scale laboratory GRS test piers, have clearly demonstrated the improved load bearing capacity when closely-spaced reinforcements are used. However, the results of those studies are deemed valid only for the conditions specifically simulated in that research, as the studies did not define the boundaries for which improved performance occurs due to closely-spaced reinforcement. Moreover, direct comparison with other aspects of field performance (e.g. Nicks *et al.* 2013b) and identification of design parameters from GRS test pier results may be compromised by the differences in boundary conditions between the test piers and actual GRS structures. For example, the surcharge in GRS field applications is not applied uniformly across the entire top surface, as is the case when loading GRS test piers.

While FHWA has already accepted a GRS wall design methodology for closely-spaced reinforcements, AASHTO has shown interest in obtaining additional information on GRS structures because the available studies have not defined a clear boundary beyond which the additional benefits of closely-spaced reinforcements should be considered. This project includes an objective and unique experimental procedure specifically aimed at answering this fundamental question. After having addressed the key question of what constitutes closely-spaced reinforcement, this project embarked on implementing robust field monitoring and numerical components. Unequivocally defining the boundaries for composite behavior, along with the results from field and numerical research formed the basis for introducing the corresponding changes into the AASHTO LRFD Bridge Design Specifications.

1.2 TERMINOLOGY

To facilitate reading this report, the definition of some key terms that are consistently used throughout is provided in this section. The intent is not to provide a comprehensive glossary of terms adopted in this document, but to clarify the definitions adopted in this report for those terms that have been used with multiple connotations in the technical literature.

The terms "GRS," "MSE," and "GMSE" have been used since the 1980s, often indistinctly in the technical literature, to refer to mechanically stabilized earth structures that are reinforced with geosynthetics. For consistency with AASHTO, the term "GMSE" is adopted throughout this report to refer to geosynthetic-reinforced soil structures, irrespective of the magnitude of its reinforcement vertical spacing. The qualifiers "closely-spaced" or "widely-spaced" reinforcement are explicitly used as appropriate. This terminology will also be consistent with the revisions to AASHTO as proposed in Chapter 8 of this report. While the terms "GRS" and "GMSE" have been used generically and irrespective of their reinforcement vertical spacing in most of the technical literature, it is recognized that the term "GRS" has been associated with small reinforcement vertical spacing as per FHWA (2012, 2018). Accordingly, no additional clarification is provided in this report when referring to structures designed following these FHWA guidelines regarding the closely-spaced nature of their reinforcement. In summary, the term GMSE is used throughout this report when referring to a geosynthetic-reinforced soil structure (e.g. a wall or an abutment), unless it was designed following FHWA (2012, 2018) guidelines.

GMSE walls constructed as part of a bridge system are identified in this report as "GMSE bridge abutments," irrespective of whether they carry only the load of the approaching road (i.e. the most common case) or the loads of both the approaching road and the bridge superstructure. The more specific term "load-carrying GMSE bridge abutment" is used throughout this report to identify GMSE bridge abutments whose reinforced fill receive the full load of the bridge girders, rather than transferring such load directly to the foundation soils via pile systems. Other terms (e.g. "true abutments") that have been used in practice are avoided herein to describe this type of system. As previously mentioned, the term "GMSE" is adopted in this report for all ranges of reinforcement vertical spacing to be consistent with current AASHTO specifications. Accordingly, GRS-IBS structures designed following FHWA (2012, 2018) are identified as a subset of "load-carrying GMSE bridge abutment" systems.

The term "integral" abutment is used throughout this report to identify those abutments that have: (1) no thermal expansion joints between the bridge superstructure and approach road; and (2) no bearings or elastomeric pads isolating the superstructure from the substructure. Some GMSE bridge abutments, including most GRS-IBS structures, would classify as "integral" bridges according to this definition.

Figure 1.2.1 summarizes the interrelationship among the terms "GMSE walls," "GMSE bridge abutments," "load-carrying GMSE bridge abutments," "integral GMSE bridge abutments," and "GRS-IBS" as adopted in this NCHRP report.

An additional relevant expression that requires careful definition within the context of this report is the term "composite behavior." This term has been described in FHWA (2018) as a more effective behavior of geosynthetic-reinforced structures that results from adopting close reinforcement spacing (less than 0.30 m (12 in.)) as compared to that of walls with comparatively larger reinforcement spacing. Building on this description, a somewhat more quantifiable definition is adopted in this report to characterize "composite behavior." Specifically, the definition of "composite behavior" adopted herein is the response of GMSE structures that results when loading of a geosynthetic reinforcement affects the deformation response and load magnitude of adjacent reinforcement layers. The term "closely-spaced" reinforcement is adopted in this report to identify the reinforcement vertical spacing below which such interaction, or composite behavior, occurs.

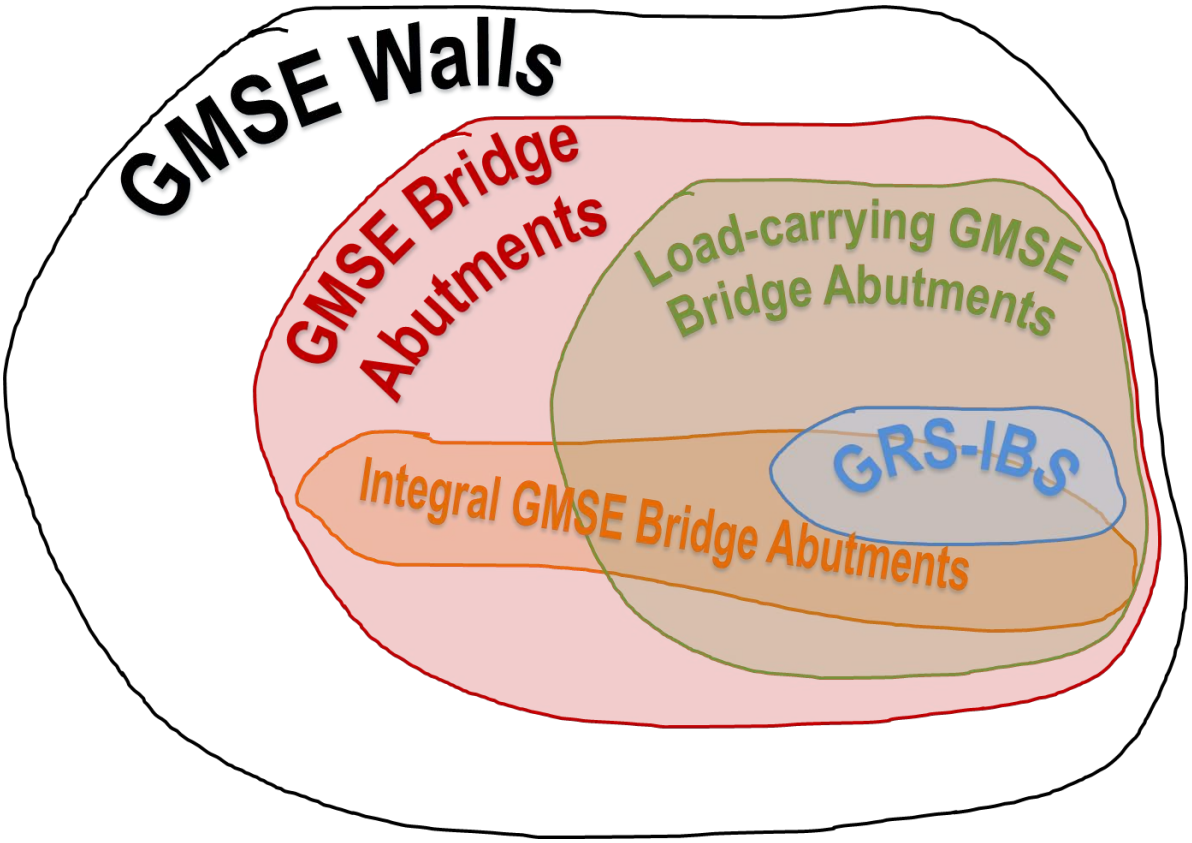

Figure 1.2.1: Interrelation of different GMSE structures, as defined in this report.

1.3 ORGANIZATION OF THIS REPORT

This report has been structured in eight chapters. Each chapter presents components of the overall research conducted as part of this project in a self-contained format. Accordingly, the objectives, scope and lessons learned from each research component are explicitly stated in each

chapter or sub-chapter, as appropriate. References are also provided for each chapter or research component.

This first chapter provides the general motivation and key terminology adopted for the entire document. Significant effort was made on not overlooking the lessons learned by the volume of research already available. Accordingly, Chapters 2 through 4 in this study focus on mining as much information as possible from the state-of-the-art, as gathered from published literature (Chapter 2), from the state-of-the-practice as gathered from identifying load-carrying GMSE bridge abutments worldwide (Chapter 3) and from reinterpretation of research data collected by others but with source data available to members of the Research Team (Chapter 4). More specifically, Chapter 2 includes the results of a comprehensive literature review conducted as part of this research. The information gathered on previous research has been grouped into experimental, field monitoring, numerical, and design-related literature. The focus of this review was to summarize pertinent information published in technical venues that was deemed relevant to assess the composite behavior of GRS structures. In order to gain insight on the state-of-the-practice regarding load-carrying GMSE bridge abutments (the main type of structure where closely spaced reinforcement has been proposed), Chapter 3 presents an international perspective of load-carrying GMSE abutments, which encompass a group of geosynthetic-reinforced soil bridge abutments that have been designed using reasonably different philosophies worldwide. Among the types of load-carrying GMSE abutments designed and constructed in the US, those identified as GRS-IBS constitute a significant majority.

The overall objective of the information documented in Chapter 4 was to complement that presented in Chapter 2 by capitalizing on the availability of published and unpublished experimental and field monitoring data available to the Research Team compiling this report. The focus is consequently on the detailed evaluation of actual data sources (both published and unpublished) considered particularly valuable for this study. The sources involved the reevaluation of six sets of actual experimental and field monitoring data, as follows: (1) FHWA data compiled to assess the composite behavior of geosynthetic-reinforced structures with closely-spaced reinforcement; (2) published and unpublished field monitoring data collected from a series of GMSE walls constructed by KDOT, characterized by their use of primary and secondary reinforcements at various vertical spacings; (3) published and unpublished data from experimental and field work conducted in the early 1990s that had focused on understanding the composite nature of GRS walls with closely-spaced reinforcement; (4) a significant volume of centrifuge experimental data on geosynthetic-reinforced soil models; (5) published and unpublished data on the performance of the Founders/Meadows GMSE abutment that was constructed and heavily instrumented in 1998; and (6) data from field monitoring investigations of recently constructed GRS-IBS structures, including those constructed by MnDOT, DOTD, DelDOT, and CDOT.

Chapter 5 of this report summarizes the results of a comprehensive experimental component conducted at the University of Texas at Austin (UT-Austin) to generate experimental data suitable to: (1) identify the geosynthetic spacing that constitutes ‘closely-spaced reinforcement’ leading to a ‘composite behavior’; (2) quantify the effect of reinforcement and backfill properties on this

spacing; and (3) provide input on material properties for subsequent numerical modeling. This chapter documents the design of a multi-layer, large-scale, highly instrumented soil-geosynthetic interaction device, results from a comprehensive testing program, and interpretation of the results of the previously mentioned comprehensive testing program, facilitating determination of the vertical spacing to be adopted as the limit of the composite behavior of geosynthetic-reinforced soil structures.

An extensive and carefully designed field implementation component is detailed in Chapter 6. The field effort was led by George Mason University (GMU) and involved conceiving a monitoring system, installation of the instrumentation and data collection for a GRS-IBS abutment structure constructed by the Virginia Department of Transportation (VDOT). The objectives of this field monitoring component included: (1) obtaining performance data from a GRS-IBS structure that would supplement, rather than duplicate, previous monitoring efforts; and (2) compiling field monitoring data to facilitate calibration of the subsequent parametric evaluation conducted as part of the numerical component of the research.

With key material properties obtained from the experimental component and performance data obtained from the field component of this project, Chapter 7 documents the results of an extensive numerical component conducted at the University of Kansas (KU). The numerical simulations were conducted to extend the available hard data to a wide range of additional configurations and material properties suitable for the refinement of design recommendation development. Evaluations included numerical simulations of UT-Austin's soil-geosynthetic interaction tests, FHWA's geosynthetic-reinforced soil systems, GMU's GRS-IBS structure, as well as a numerical parametric evaluation and limit equilibrium analyses.

Finally, the wealth of experimental, field monitoring and numerical data was organized as a compilation of relevant revisions and refinements to design methodologies for geosynthetic-reinforced soil structures. This comprises Chapter 8, in which the research findings were synthesized into recommendations on a group of five relevant design aspects. This included recommendations to account for the effect of reinforcement vertical spacing on: (1) the reinforcement maximum tension; (2) facing connection loads; (3) stress distribution within the reinforced soil mass; (4) vertical and lateral deformations; and (5) development of a bump at the end of a bridge. The recommendations are presented in a manner consistent with AASHTO design of foundations and retaining walls.

The report also includes Appendix A with unit conversion factors between SI and US customary units and Appendix B with complementary information on the field data collected as part of the Virginia GRS-IBS.

1.4 REFERENCES

Abu-Hejleh, N., Zornberg, J.G., Wang, T., and Watcharamonthein, J. (2002). “Monitored Displacements of Unique Geosynthetic-Reinforced Soil Bridge Abutment.” Geosynthetics International, Vol. 9, No. 1, pp. 71-95.

Adams, M., Nicks, J., Stabile, T., Wu, J., Schlatter, W., and Hartmann, J. (2012). *Geosynthetic-reinforced Soil Integrated Bridge System, Interim Implementation Guide*. Report No. FHWA-HRT-11-026, Federal Highway Administration, McLean, VA.

Adams, M., and Nicks, J. (2018). *Design and Construction Guidelines for Geosynthetic Reinforced Abutments and Integrated Bridge Systems*. Report No. FHWA-HRT-17-080, Federal Highway Administration, McLean, VA.

Allen, T., Christopher, B., Elias, V., and DeMaggio, J. (2001). Development of the Simplified Method for Internal Stability Design of Mechanically Stabilized Earth Walls, Report WA-RD 513.1, Washington State Department of Transportation, Olympia, Wash.

Christopher, B.R., Gill, S., Giroud, J., Juran, I., Mitchell, J.K., Schlosser, F., and Dunnicliff, J. (1989a). Reinforced Soil Structures. Volume I, Design and Construction Guidelines, Federal Highway Administration, Washington, D.C. Report FHWA-RD-89-043.

Christopher, B.R., Gill, S., Giroud, J., Juran, I., Mitchell, J.K., Schlosser, F., and Dunnicliff, J. (1989b). Reinforced Soil Structures. Volume II, Design and Construction Guidelines, Federal Highway Administration, Washington, D.C. Report FHWA-RD-89-043.

Leshchinsky, D., Kaliakin, V., Bose, P., and Collin, J. (1994). “Failure Mechanism in Geogrid-Reinforced Segmental walls: Experimental Implications.” Soils & Foundations, Journal of the Japanese Society of Soil Mechanics & Foundation Engineering, 34(4):33-41.

Leshchinsky, D. & Vulova, C. (2001). “Numerical investigation of the effects of geosynthetic spacing on failure mechanisms in MSE block walls.” Geosynthetics Int., 8(4):343-365Mitchell, J.K., and Villet, W.C. (1987). "Reinforcement of earth slopes and embankments." NCHRP Report, (290), Transp. Res. Board, Washington, D.C.

Zornberg, J.G., Abu-Hejleh, N., and Wang, T. (2001). “Geosynthetic-Reinforced Soil Bridge Abutments.” Geotechnical Fabrics Report, Vol. 19, No. 2, March, pp. 52-55.

2 INFORMATION GATHERING: STATE-OF-THE-ART

2.1 OVERVIEW OF THE INFORMATION GATHERED

The primary objective of this chapter is to provide a state-of-the-art on the experimental, numerical, field monitoring, and design aspects that constitute a relevant background for the study conducted as part of this project. This state-of-the-art compilation was prepared considered the available published literature. As indicated in Chapter 1, this information will be complemented with the state-of-the-practice in load-carrying GMSE bridge abutments compiled as part of Chapter 3, and ultimately with a series of evaluations of the actual data sources compiled in Chapter 4 using information available to the members of the research team.

The pertinent information summarized in this chapter has been gathered through an extensive literature review of published articles, reports, communications with professionals in the field and reevaluation of data gathered in past projects.The purpose is to establish a comprehensive background that will benefit the new data to be generated in this study, which will not repeat the already existing information but that rather determines what is further needed to confirm, modify, or develop a design procedure that could be presented to AASHTO.

The information on previous research gathered as part of this effort has been grouped into experimental, field monitoring, numerical, and design-related literature. Each group of relevant references also includes research from international sources. A summary of the characteristics and relevance of the multiple identified publications is provided in the following sub-sections of this chapter.

2.2 GATHERING OF EXPERIMENTAL INFORMATION

This section summarizes the information gathered from previous research that focuses on experimental work. This information has been grouped, in turn, into previous experimental research: (i) focusing on GMSE and GRS-IBS structures, and (ii) involving soil-geosynthetic interaction tests. The first group of experimental literature is relevant to the overall objectives of this project, independent of the experimental techniques used by previous researchers. The second group of experimental literature is relevant to the specific soil-geosynthetic tests which is documented in chapter 5, independent of the specific objectives investigated by the researchers.

2.2.1 PREVIOUS EXPERIMENTAL RESEARCH FOCUSING ON GMSE AND GRS-IBS STRUCTURES

A summary of previous experimental research conducted by FHWA to provide support to the design of GMSE and GRS-IBS structures is provided first. Additional studies conducted by other agencies are summarized next, which involve large-scale tests and provide insight into the soil-geosynthetic composite behavior.

2.2.1.1 PREVIOUS EXPERIMENTAL RESEARCH BY FEDERAL HIGHWAY ADMINISTRATION (FHWA)

The Federal Highway Administration (FHWA) has conducted research on the GRS-IBS technology. Recently, FHWA has identified GRS-IBS as a market-ready technology, and has promoted this technology through its Every Day Counts (EDC) initiative. A number of publications document the research conducted by FHWA or with the use of FHWA facilities. These publications were identified and are summarized in this section. Note that even though the term GRS is adopted in this report in association with GRS-IBS structures designed following FHWA (2012,2018), this term is used when describing the research presented in this section as it involved study of the technology that eventually led to the GRS-IBS system.

Ketchart and Wu (1996) developed a testing apparatus and procedure to assess the performance of GRS composite behavior. They utilized reinforced granular and cohesive soils in addition to unreinforced soils in their tests. The authors concluded that GRS composites do not experience creep with granular soils. In addition, loads in geosynthetics may decrease with time for the case of typical field constructions involving granular soils.

Ketchart and Wu (FHWA-RD-01-018, 2001) investigated the behavior of GRS masses under various loading conditions. The study aimed at developing a simplified analytical model for predicting deformation characteristics of a generic GRS mass. Specifically, the researchers developed Soil-Geosynthetic Performance (SGP) laboratory test with the objective of mimicking field placement conditions of GRS structures. This test aimed at capturing the effect of the interaction between the backfill soil and the geosynthetic reinforcement. Ketchart and Wu (2001) conducted a set of SGP tests using various soil types, geosynthetic reinforcements, and loading sequences. In addition, the study evaluated the effect of preloading on the GRS behavior. The authors correlated the results of SGP tests to full-scale GRS structures in order to assess the degree of accuracy of the SGP test to predict the reduction in settlement due to preloading. Specifically, two preloaded reinforced soil structures and their corresponding SGP test were examined: (1) FHWA pier (Adams 1997) and the second generation SGP test, and (2) Black Hawk abutments reported by Wu *et al.* (FHWA-RD-00-038, 2001) and the modified SGP test. The correlations were generated in terms of normalized values of loads and displacements.

Wu *et al.* (FHWA-RD-038, 2001) describe in detail three projects involving load testing of GRS abutments and piers. The first project is a full-scale bridge pier load test conducted at the Turner-Fairbank Highway Research Center (TFHRC). This pier is referred to as the Turner-Fairbank pier. The second project involves a full-scale, long-term load test of a bridge abutment and a bridge pier conducted by the Colorado Department of Transportation (CDOT) and the University of Colorado at Denver. These piers and abutment are referred to as the Havana Yard piers and abutment. The third project involves the load test of a production bridge abutment performed by Yenter Companies in Black Hawk, Colorado. This abutment is referred to as the Black Hawk abutment. The abutments evaluated as part of these studies were instrumented to assess behavior under load testing. Wu *et al.* (2001) provide a comprehensive description to the projects along with testing results and analysis. Recommendations to GRS applications are incorporated in the report.

Ketchart and Wu (2002) developed a modified Soil-Geosynthetic Interactive Performance (SGIP) testing apparatus to assess the deformation behavior of GRS composites. The test consists of applying a vertical load on a GRS composite under plane strain condition. The applied load is transferred from soil to geosynthetic allowing both to deform in an interactive manner. Lateral and vertical displacements of the GRS mass are measured along with the reinforcement strains. Ketchart and Wu (2002) conducted a set of tests to investigate repeatability, failure mode, and deformation behavior of different GRS composites. The behavior of tested GRS was compared to that of a GRS pier to verify the test applicability.

Wu *et al.* (2006a) developed a design methodology and construction guidelines for GRS bridge abutments with flexible facing. They depended on the findings reported in the literature along with findings of full-scale experiments and analytical study performed. Wu *et al.* (2006a) constructed full-scale GRS abutments and piers. The tested GRS structures showed good performance and high load-carrying capacity. In addition, the authors compiled a design methodology and construction procedure for GRS abutments with flexible facing. Detailed design examples were also provided. Adams *et al.* (2007) conducted five large-scale GRS Mini Pier tests to assess the effect of reinforcement spacing and reinforcement strength on the behavior of GRS masses. The authors reported that the bearing capacity for closely-spaced GRS was significantly improved and that the contribution of the reinforcement spacing was more relevant to the performance of a GRS mass than the reinforcement strength.

Wu and Adams (2007) investigated the long-term creep behavior of GRS systems and proposed revisions to the current design methods. The authors recommended a cumulative long-term reduction factor for geosynthetic reinforcement. This reduction factor is a function of the backfill gradation and index properties, reinforcement spacing, and geosynthetic polymer type. The authors presented a procedure to account for soil-geosynthetic interactive creep behavior based on SGIP test.

Adams *et al.* (FHWA-HRT-11-026, 2012) provide a design methodology and construction procedure for GRS-IBS structures. This manual aims at providing background knowledge of GRS-IBS technology as well as of its fundamental characteristics as an alternative to other construction methods. In addition to providing detailed guidance on the design of GRS-IBS, the manual includes analytical and empirical design methodologies involving both the Allowable Stress Design (ASD) and Load and Resistance Factor Design (LRFD) approaches. Background knowledge in support of the design methodology is summarized by Adams *et al.* (FHWA-HRT-11-027, 2011), which documents the fundamental characteristics of GRS-IBS technology as an alternative construction method. This document supplements the interim implementation manual (FHWA-HRT-11-026) by Adams *et al.* (2012) and provides a generic design methodology and construction outline of the GRS-IBS. In addition, it includes the results of research conducted to provide the basis for the design method. Finally, case histories are summarized to document the performance of in-service GRS-IBS.

Nicks *et al.* (FHWA-HRT-13-066, 2013a) reported the results of a series of experimental GRS performance tests, also identified as mini-pier experiments. The tests were conducted by axially

loading a GRS mass while measuring the resulting deformations and, thus, documenting the mini-piers' performance. The mini-piers included alternating layers of compacted granular fill and geosynthetic reinforcement connected frictionally to facing elements. This report documents the testing procedure and provides the axial load-deformation results for the performance tests conducted in this study. In addition, this research aimed at establishing a database of GRS material properties for the purposes of construction of GRS-IBS structures. The results are used to: (i) establish a relationship between reinforcement strength and spacing, (ii) quantify the contribution of the frictionally connected facing elements at the service limit and strength limit states, (iii) assess the internal stability design method proposed by Adams *et al.* (2011) for GRS, and (iv) provide the basis for a reliability analysis of the soil-geosynthetic capacity equation for LRFD calibration. In addition, Nicks *et al.* (2013b) determined the material strength properties of particular GRS composites based on GRS performance test results. The effects of backfill type and compaction on the GRS composites were also investigated. Nicks *et al.* (2013b) outlined the performance test methodology along with resulting load-deformation characteristics.

Wu *et al.* (FHWA-HRT-10-077, 2013) investigated the composite behavior of a GRS mass by conducting a series of large-scale generic soil geosynthetic composite (GSGC) tests. These tests were designed to assess the behavior of a GRS mass under well-controlled conditions. The experimental results showed that reinforcement spacing influences the GRS behavior more significantly than reinforcement strength. Wu *et al.* (2013) developed analytical model that allowed description to the relative contribution of reinforcement strength and reinforcement spacing. In addition, equations were developed based on the analytical model. These equations were developed to calculate the apparent cohesion of a GRS composite, the ultimate load-carrying capacity of a GRS mass, and the required tensile strength of reinforcement for a given reinforcement spacing. The suitability of the developed equations was evaluated by comparing the predictions against the results of GSGC tests, large-size experiments performed by other researchers, and finite element (FE) simulations. Moreover, an analytical procedure was developed to predict the lateral wall movement and the required tensile strength of reinforcement. In addition, an analytical model for estimating compaction-induced stresses in a GRS mass was proposed. The model predictions were compared against the results of GSGC tests and FE simulations. Wu *et al.* (2013) also investigated the dilatant behavior of GRS composites. They reported that reinforcements tend to suppress dilation of the surrounding soil and reduce its angle of dilation.

Table 2.2.1a provides a summary of the characteristics of the parameters adopted in multiple studies conducted by FHWA.

2.2.1.2 ADDITIONAL PREVIOUS EXPERIMENTAL RESEARCH INVOLVING LARGE-SCALE LABORATORY TESTS

Wichter *et al.* (1986) conducted large-scale loading tests on a geotextile-reinforced soil wall. Weathered clay marl was used as backfill material. The wall displacements and reinforcement strains were measured. The wall did not reach failure even under relatively high applied loads. The authors had predicted the capacity of the wall before testing based on rigid-body-failure

assumption. Yet, they showed that their assumptions lead to a significant underestimation of the reinforced wall capacity under surcharge loads.

Wu and Helwany (1996) developed a laboratory performance test to evaluate the creep behavior of geosynthetic reinforcement due to soil-geosynthetic interaction. The geosynthetic reinforcement and the confining soil were loaded for a long period of time and allowed to deform in an interactive manner. Clean sand and kaolin clay were used as backfills for two different tests. The results showed that the geotextile creep deformation is significantly affected by the time-dependent deformation characteristics of soils under confinement. The authors concluded that evaluating the soil-geosynthetic composite creep potential could be misleading if it is based on the results of geosynthetic element creep tests only.

Pötzl (2007) presents results of a testing program aimed at evaluating the effect of temperature changes and shrinkage of concrete bridges that lead to cracking and restraint stresses. These stresses were reported to be significantly reduced for the case of newly developed flexible abutments that involved geogrid-reinforced soil systems. The testing program involved large-scale tests to monitor the deformations in a geogrid-reinforced soil mass. The results aim at providing insight into the reduction of restrained stresses.

Ruiken and Ziegler (2009) performed a series of large-scale triaxial tests to investigate the reinforcing effect of geogrids. The authors considered a mechanical model to identify the stress paths that developed in the reinforced test specimens. The shear parameters representing a composite material were determined based on the experimental results. In addition, this research evaluated approaches by which the increase in soil strength could be incorporated into design.

Ruiken *et al.* (2011) conducted large-scale laboratory tests to explore the composite behavior of geosynthetic-reinforced systems. They focused on the earth pressures and the mechanical behavior of the resulting composite material. The testing apparatus used in this study allowed evaluation of geogrid-reinforced soil systems under plane strain conditions. The heavily instrumented testing apparatus allowed identifying the effect of displacements on the development and distribution of stresses within the reinforced mass. The results also provide insight on the facing connection loads for various geogrid reinforced specimens. In addition, the kinematic behavior of the geosynthetic-reinforced system was assessed by monitoring particle displacements and their rotation.

Ziegler (2011) summarizes research conducted to provide understanding of the load-bearing characteristics of geosynthetic-reinforced soil masses. The experimental component of the study included large-scale biaxial tests on geosynthetic-reinforced systems to investigate the effect of the presence of reinforcements on the soil state of stresses. In turn, the state of stresses effect on the soil-geosynthetic composite strength and deformation was also investigated. Digital Image Correlation (DIC) methods were used to collect several of the experimental results. In this study, the researcher concluded that interlocking mechanisms and the resultign confining effect of geosynthetics leads to a different stress path compared to that of unreinforced cases, which are

comparatiavely more isotropic and not necessarily consistent with results predicted by limit state theorems.

Jacobs *et al.* (2012a, 2012b, and 2013) utilized a laboratory apparatus at RWTH Aachen University to investigate the behavior of soil-geosynthetic composites. This apparatus allows large-scale biaxial compression testing of soil-geosynthetic systems under constant confining pressure. The testing program aimed at investigating the mechanisms of the geosynthetic-soil composite behavior. In addition, the apparatus allowed evaluation of the composite stress-strain behavior and of the interaction mechanisms between soil and geogrids. The apparatus also includes a transparent side wall that allows identifying the reinforcing effect on the kinematic behavior during compression as it allows capturing the particle deformation and rotations. Jacobs *et al.* (2012a) conducted tests under plane strain conditions with constant confining pressure applied by vacuum. In addition, Jacobs *et al.* (2012b) investigated the stress-strain behavior of the geosynthetic-soil composites accounting for the large size geogrid apertures. Finally, Jacobs *et al.* (2013) investigated the load transfer between soil and geogrid based on experimental results. The development of the shear zone was captured for various reinforced specimens, which allowed evaluation of different reinforcing mechanisms in specimens reinforced with strips or geogrids. Jacobs et al. (2013) concluded that little displacements are needed for transfer of bearing-type loads. They also concluded that the tensile stiffness of geogrid do not affect the magnitude of the frictional load transfer. They also observed that the presence of transverse ribs had a significant effect on load transfer between soil and geosynthetics. Finally, , they reported a comparatively more isotropic stress with a broader shear zone (with a decline near reinforcement layers) was achieved as load transfer increased.

2.2.1.3 *Additional previous experimental research involving small-scale laboratory tests*

Lees (2014) proposed a new measurement method for soil-geogrid interaction which can be simulated by numerical models and conventional limit equilibrium design methods. Instead of measuring soil and geogrid properties separately, the enhanced strength of composite mass was measured in a direct shear test. A geogrid was placed horizontally within the soil mass at various spacings ranging between 0.01 to 0.4 m (0.4 to 15.7 in) above the shear plane. The confining effect was measured as an increased cohesion in the soil. The paper provided the methodology of modelling the effect of reinforcing soil in design calculations and numerical simulations.

.

Table 2.2.1a. Testing parameters adopted in research conducted under FHWA

Reference	Test Dimensions (L x W x H)	Reinforcement Spacing	Backfill	Geosynthetic Type	Geosynthetic Strength	Applied Loading
Wu and Helwany (1996) A Performance Test for Assessment of Long-Term Creep Behavior of Soil-Geosynthetic Composites	SGP Tests Sand backfill test: 0.813 x 0.45 x 0.61 m Clay backfill test: 0.457 x 0.45 x 0.508 m	Sand backfill test: 0.305 m Clay backfill test: 0.254 m	Sand: Subrounded Ottawa Sand, D_{10} = 0.35 mm, C_u = 1.43, C_c = 1.16, G_s = 2.65, γ_{dmax} = 17.7 kN/m^3, γ_{dmin} = 15.3 kN/m^3 Clay: Dover White cohesive soil, LL = 28%, PL = 22%, γ_{dmax} = 16 kN/m^3, w_{opt} = 21%	Nonwoven geotextile	Grab tensile: 534 N	Plane strain condition Surcharge applied on the top surface Sand backfill test: 109 kN/m^2 Clay backfill test: 45 kN/m^2
Ketchart and Wu (1996) Long-Term Performance Tests of Soil-Geosynthetic Composites	SGP Tests Sand backfill test: 0.61 x 0.61 x 0.305 m Clay backfill test: 0.305 x 0.61 x 0.305 m (modified after Wu (1994) and Wu and Helwany (1996))	Sand backfill test: 0.1525 m Clay backfill test: 0.1525 m	Road base: A-1-B(0), 76% passing sieve #4, 19% passing sieve #200, G_s = 2.67, γ_{dmax} = 134 pcf, w_{opt} = 7.2% Clayey soil: A-6, 100% passing sieve #4, 43% passing sieve #200, PI = 11%, LL = 26% γ_{dmax} = 120 pcf, w_{opt} = 11%	Amoco 2044 woven geotextile Amoco 2002 woven geotextile (not manufactured primarily for reinforcement) Typar 3301 nonwoven geotextile (used primarily for easiness for strain	Amoco 2044 – Wide width strength: 400 lb/in, grab tensile: 600 lb Amoco 2002 – Wide width strength: 120 lb/in, grab tensile: 200 lb Typar 3301 – Wide width strength: 35 lb/in, grab tensile: 120 lb	Surcharge applied on the top surface Movable walls controlled by air cylinders which allow lateral deformation in the longitudinal direction in an unconfined condition

				gauge installation and accuracy of measurement)		
Ketchart and Wu (2001) Performance Test for Geosynthetic Reinforced Soil Including Effects of Preloading	SGP Tests 0.254 x 0.565 x 0.61 m (modified after Wu and Helwany (1996) and Ketchart and Wu (1996))	0.305 m	Ottawa sand: Subrounded uniform sand, G_s = 2.65, γ_{dmax} = 17.65 kN/m^3, γ_{dmax} = = 15.34 kN/m^3 Road base: Silty sand, SM-SC, 12% fines, PI = 6%, LL = 27%, γ_{dmax} = 18.75 kN/m^3 – w_{opt} = 14.2%, used in Black Hawk abutments	Amoco 2044 woven geotextile (used in Black Hawk abutments) Typar 3301 nonwoven geotextile (used primarily for filtration and drainage applications)	Amoco 2044 – Wide width strength: 70 kN/m, grab tensile: 2.22 kN (fill direction)/2.67 kN/m (wrap direction) Typar 3301 – Wide width strength: 6 kN/m, grab tensile: 0.53 kN	Surcharge applied on the top surface Unrestrained longitudinal direction During testing, plastic sheets replace the rigid side walls of the longitudinal direction
Ketchart and Wu (2002) A Modified Soil-Geosynthetic Interactive Performance Test for Evaluating Deformation Behavior of GRS Structures	SGP Tests 0.305 x 0.61 x 0.305 m	0.152 m	Road base: A-1-B(0), γ_{dmax} = 21 kN/m^3 - w_{opt} = 7.2% Clayey soil: A-6, PI = 11%, LL = 26 - γ_{dmax} = 18.8 kN/m^3 – w_{opt} = 11%	2 woven and 1 nonwoven geotextiles	Geotextile 1 – Woven, wide width strength: 70 kN/m, grab tensile: 2.22 kN (fill direction)/2.67 kN/m (wrap direction) Geotextile 2 – Woven, wide width strength: 21 kN/m, gran tensile: 0.89 kN (fill and wrap directions) Geotextile 3 – Nonwoven, wide width strength: 6 kN/m, grab tensile: 0.53 kN	Surcharge applied on the top surface Unrestrained longitudinal direction During testing, side walls of the longitudinal direction are removed to provide free deformation

Table 2.2.1a. Testing parameters adopted in research conducted under FHWA (Continued)

Reference	Test Dimensions (L x W x H)	Reinforcement Spacing	Backfill	Geosynthetic Type	Geosynthetic Strength	Applied Loading
Wu et al. (2006) Design and Construction Guidelines for Geosynthetic-Reinforced Soil Bridge Abutments with a Flexible Facing	2 back to back full scale bridge abutments (each has 1 abutment, 2 wing walls, geosynthetic reinforced soil mass, and top sill) 4.65 m high	Amoco section: 0.2 m Mirafi section: 0.2 m	Non-plastic silty sand: SP-SM, 8.5% fines, γ_{dmax} = 18.3 kN/m^3 – w_{opt} = 11.5%	Amoco 2044 woven geotextile (selected to represent a "lower bound" high strength Reinforcement) Mirafi 500x woven geotextile (selected to represent a low- to medium-strength reinforcement).	Amoco 2044 – Wide width tensile strength: 70 kN/m Mirafi 500x – Wide width tensile strength: 21 kN/m	Bridge sill was loaded along its longitudinal centerline in equal increments of 50 kPa average vertical pressure (loading terminated at 814 kPa on Amoco section, and 414 kPa on Mirafi section)
Adams et al. (2007) Mini Pier Experiments – Geosynthetic Reinforcement Spacing and Strength as Related to Performance	5 Mini Piers (NR, A, B, C, D)	Spacing: NR: none A: 0.4 – 0.6 m B: 0.4 m C: 0.2 m D: 0.2 m	Well graded gravel: GW-GM, γ_{dmax} = 24 kN/m^3, w_{opt} = 6%	NR: Unreinforced A: A2044 woven geotextile B: A2044 woven geotextile C: A2000 woven geotextile D: A2044 woven geotextile	A2044 – Strength: 70 kN/m A2000 – Strength: 21 kN/m	Load is applied vertically on a concrete pad on the top surface CMU facing which is removed the load test and the geotextiles were trimmed to the edge of the compacted soil

Nicks et al. (2013) Performance Testing For Geosynthetic Reinforced Soil Composites	5 Mini Piers External: 1.37 x 1.37 x 1.94 m Internal: 0.98 x 0.98 x 1.94 m	0.2 m	DC-1: D_{max} = 12.7 mm, ϕ = 54 deg, γ_{dmax} = 15.9 kN/m^3 DC-2: D_{max} = 19.0 mm, ϕ = 46 deg, γ_{dmax} = 15.9 kN/m^3 DC-3: D_{max} = 25.4 mm, ϕ = 52 deg, γ_{dmax} = 15.9 kN/m^3 DC-4: D_{max} = 9.5 mm, ϕ = 49 deg, γ_{dmax} = 15.9 kN/m^3 DC-5: D_{max} = 12.7 mm, ϕ = 54 deg, γ_{dmax} = 15.9 kN/m^3	Geotextile	70 kN/m	Load is applied vertically by four jacks on bolted beams supported on a concrete footing on the top surface

Table 2.2.1a. Testing parameters adopted in research conducted under FHWA (Continued)

Reference	Test Dimensions (L x W x H)	Reinforcement Spacing	Backfill	Geosynthetic Type	Geosynthetic Strength	Applied Loading
Nicks et al. (2013, FHWA-HRT-13-066) Geosynthetic Reinforced Soil Performance Testing – Axial Load Deformation Relationships	15 Mini Piers 76.25 in. tall and 2 Mini Piers 78.75 in. tall.	7.625 in. for 13 tests, 15.25 in. for 2 tests, 3.8125 in. for 2 tests, and 11.25 in. for 2 tests. 6 tests had two courses of bearing bed reinforcement placed at the top	AASHTO No. 8 (OH): A-1-a, GP, γ_{dmax} = 101.27 pcf, ϕ = 54 deg, c = 0, D_{max} = 0.50 in., C_c = 1.19, C_u = 2.36 AASHTO No. 8 PG (OH): A-1-a, GP, γ_{dmax} = 115.75 pcf, ϕ = 46 deg, c = 0, D_{max} = 0.75 in., C_c = 1.30, C_u = 2.23 AASHTO No. 57 (OH): A-1-a, GP, γ_{dmax} = 108.69 pcf, ϕ = 52 deg, c = 0, D_{max} = 1.00 in., C_c = 1.18, C_u = 2.05 AASHTO No. 9 (OH): A-1-a, SP, γ_{dmax} = 110.66 pcf, ϕ = 53 deg, c = 0, D_{max} = 0.38 in., C_c = 1.35, C_u = 2.78 AASHTO No. 8 (VA): A-1-a, GP, γ_{dmax} = 112.82 pcf, ϕ = 55 deg, c = 0, D_{max} = 1.00 in., C_c = 0.96, C_u = 1.78 VDOT 21A: A-1-a, GW-GM, γ_{dmax} = 148.90 pcf, w_{opt} = 7.7%, ϕ = 54 deg, c = 115 pcf, D_{max} = 1.00 in., C_c = 2.67, C_u = 46.67	Woven geotextile	Wide width strength: 1400, 2400, 3600, and 4800 lb/ft (wrap and fill directions)	Load is applied vertically by four jacks on bolted beams supported on a concrete footing on the top surface 11 tests conducted with CMU facing and 6 tests without any facing

Zhou *et al.* (2012) performed a set of pullout tests in an attempt to study the soil-geosynthetic interaction. They used one type of geogrid and one sand material in their tests. High-resolution digital camera and charge couple device (CCD) camera were utilized to capture the motion of soil particles around the ribs. This allowed identifying the macro behavior of the sand-rib interaction. The paper showed the necessity of considering the effect of the size and shape of the bearing members on the bearing resistance of geogrids.

Ahmed and Meguid (2009) conducted a review on the devices and techniques commonly used to measure contact pressure in different soil-structure interaction cases. The authors compared between the different measuring techniques in regards to their applicability and limitations. This study is relevant as it provides information about measuring the contact pressure between a structure and the surrounding ground which is essential for the analysis and design of different geotechnical engineering disciplines.

Munoz *et al.* (2012) and Tatsuoka *et al.* (2012) have conducted research to evaluate the dynamic stability of GMSE structures under seismic loading. These studies are relevant as they enhance the understanding of the geosynthetic reinforced soil behavior not only under static loads but also dynamic loads.

2.2.2 PREVIOUS EXPERIMENTAL RESEARCH INVOLVING SOIL-GEOSYNTHETIC INTERACTION TESTS

2.2.2.1 LARGE-SCALE SOIL-GEOSYNTHETIC INTERACTION EQUIPMENT

A large-scale soil-geosynthetic interaction equipment was constructed at The University of Texas at Austin in support to the experimental component (Chapter 5) of this NCHRP project. Accordingly, this section includes a detailed literature review on pullout testing equipment, which corresponds to the device that serves as basis for the development of the new equipment. This review focuses on the reported limitations of soil-geosynthetic interaction equipment (e.g. dimensions, materials, instrumentation) in order to benefit from the experience of other studies.

While much of the focus of the testing program conducted in Chapter 5 corresponds to pre-failure conditions, the setup of pullout tests is a good basis to investigate the soil-reinforcement interaction behavior. Pullout tests have been proven to be suitable for different types of geosynthetics and soil types (ASTM D6706). The pullout resistance was found to be function of variables such as soil gradation, plasticity, relative compaction, moisture content, and geosynthetic characteristics (ASTM D6706). Pullout tests involve embedding a geosynthetic within soil mass and imposing axial loads to mobilize soil-geosynthetic interaction mechanisms. The soil mass is subjected to a normal pressure to reproduce a representative state of stresses on the soil-reinforcement interface. Much of the previous research has been on different boundary effects, testing procedures, preparation methods, and compaction techniques (Juran *et al.* 1988; Farrag *et al.* 1993). The test was recently standardized in latest revision of ASTM D6706 in a way to mimic the as-built conditions as closely as possible. The characteristics and limitations of pullout testing equipment, as reported in the technical literature, are summarized next.

Box dimensions: According to ASTM D6706 the length of the box should exceed 0.6 m (24 in.) while also exceeding 5 times the maximum geosynthetic aperture size. The width of the box should be greater than 0.75 m (30 in.) in devices with rough side walls and 0.45 m (18 in.) in devices with smooth side walls. Also, the width should exceed 20 times the D_{85} of the soil, as well as 6 times the maximum soil particle size. The box depth should accommodate soil thickness above and below the geosynthetic greater than 0.15 m (6 in.), greater than 6 times the D_{85} of the soil, and greater than 3 times the maximum particle size of the soil. Ladeira (1995) developed a box 1.53 m long by 1.00 m wide by 0.80 m high box. The author showed that these dimensions resulted in minimal lateral and horizontal boundary effects.

Specimen length: According to ASTM D6706, the specimen length in pullout tests should exceed 0.6 m (24 in.) beyond the sleeve and it should be at least twice the sample width (i.e. length to width ratio should exceed 2.0). Lopes and Ladeira (1996) investigated the effect of the length of a geogrid specimen on the pullout resistance and failure displacement. They reported that the effect of specimen length depends on the soil density. For dense sands, they reported that pullout resistance decreases with increasing the specimen length; whereas in loose sands, it increases with increasing the specimen length. Lopes and Ladeira (1996) explain that the decrease in pullout resistance encountered in dense sands could be due to the increase in the strain. This increase in strain results in increasing the void ratio of the dense sand and thus increasing the total reaction of the geogrid transverse ribs (Dyer 1985; Palmeira and Milligan 1989). Lopes and Ladeira (1996) defined the adherence factor as the ratio between the tangential stress at the soil-reinforcement interface to the product of normal stress at the interface and the tangent of the soil friction angle at the testing stress level. The authors reported decrease in the adherence factor with increasing the specimen length. However, they mentioned that the adherence factor should have been greater than the reported values as the specimens failed due to the increase of tensile stresses beyond the capacity not due to deficiency in adherence. Lopes (1992) showed that the influence of specimen length on the interface shear resistance is minimal beyond a certain length value. However, Moraci and Recalcati (2006) reported that the pullout behavior depends on the specimen length. They indicated that pullout interaction mechanism develops progressively along the specimen length with a progressive increase in the pullout resistance with an increase in the displacement.

Specimen width/side boundaries: According to ASTM D6706 there should be a clearance between the edge of the specimen and the side wall in both sides. This clearance should exceed 0.075 m (3 in.) in devices with smooth side walls and 0.15 m (6 in.) in devices with rough walls (ASTM D6706; Farrag *et al.* 1993). Also, the specimen width should be greater than 0.3 m (12 in.) and includes at least five tensile elements. The friction of the side walls was found to reduce the amount of normal stresses applied at the soil-reinforcement interface (Farrag *et al.* 1993). Jewell (1980) recommended lining the side walls by lubricated membranes to minimize the friction of the side walls. Lopes and Ladeira (1996) studied the effect of the specimen width on the pullout resistance. The authors did not notice a significant influence for the specimen width on the pullout resistance. However, the results showed a slight increase in the pullout resistance and slight decrease in the adherence factor when decreasing the specimen width.

Soil thickness/upper and lower boundaries: ASTM D6706 requires that the box depth accommodate a soil thickness above and below the geosynthetic greater than 0.15 m (6 in.), greater than 6 times the D_{85} of the soil, and greater than 3 times the maximum particle size of the soil. Interaction may develop between the upper and lower boundaries and the soil-reinforcement interface. This interaction has been reported to increase with decreasing soil thickness, and thus influencing the test results (Farrag *et al.* 1993). Farrag *et al.* (1993) reported the development of shear forces between the soil and the horizontal boundaries, particularly the bottom boundary. Brand and Duffy (1987) studied the effect of the soil thickness on the pullout resistance. Based on a limited number of tests, the authors observed that the pullout resistance decreased with increasing the soil thickness until reaching a value beyond which there was no further changes due to the soil thickness. Lopes and Ladeira (1996) showed that the predicted friction angle of the soil may increase beyond the friction angle measured using conventional techniques. This was reported to be due to an increased confining pressure due to repressing soil dilatancy (Lopes and Ladeira 1996; Farrag *et al.* 1993). Lopes and Ladeira (1996) reported that the specimen length affects significantly the impact of the upper and lower boundaries on the results. Palmeira and Miligan (1989) reported that an increasing specimen length to soil thickness ratio leads to increasing influence of the upper and lower boundaries of the pullout box. Farrag *et al.* (1993) reported that the soil thickness should exceed 0.3 m (12 in.) above and 0.3 m (12 in.) below the reinforcement to eliminate the effect of the horizontal boundaries. Farrag *et al.* (1993), Ladeira (1995), and Lopes and Ladeira (1996) used a modular structured box to facilitate changes in the soil thickness during testing.

Sleeve length: According to ASTM D6706 the box should have a metal sleeve involving two thin plates less than 12.5 mm (0.5 in.) thick. The sleeve should extend inside the box to a distance greater than 0.15 m (6 in.) and preferably equivalent to the soil thickness above the geosynthetic. The interior sleeve end should be tapered to reach a maximum contact thickness of 3 mm (0.12 in.) Palmeira and Milligan (1989) reported that interaction develops between the reinforced soil mass and the rigid front wall of the pullout box. The authors showed that this interaction increases with increasing friction along the front wall. During pullout tests, the lateral earth pressure developed on the front wall of the box increases, resulting in increases in the pullout resistance results (Farrag *et al.* 1993). The sleeve allows transferring the pullout force application line away from the soil adjacent to the front wall to the inner soil mass (Christopher 1993; Farrag *et al.* 1993). Williams and Houlihan (1987) used front flexible walls in an attempt to reduce the effect of rigid walls. Lopes and Ladeira (1996) investigated the effect of sleeve on the pullout resistance. They observed increase of approximately 10% in the apparent pullout resistance in the absence of the sleeve. They reported that the frictional stresses developed on the front wall of the box resulted in increases in the vertical stress acting on the reinforcement. Lopes and Ladeira (1996) measured the lateral pressure in their study and observed a higher pressure on the front wall in the absence of the sleeve during testing. This increased lateral pressure resulted in increasing shear stresses developed at the soil-reinforcement interface at the front section of the specimen and in decreasing shear stresses developed at the back sections. Lopes and Ladeira (1996) recommended using a sleeve 0.2 m (8 in.) long inside the box to reduce the frictional effects of the front wall boundary. Farrag *et al.* (1993) reported that a sleeve of at least 0.3 m (12 in.) length should be used to eliminate the front wall effect.

Axial loading system: The axial force must be at the same level of the geosynthetic plane so as not to interfere with the soil-reinforcement shear surface (ASTM D6706). According to ASTM D6706 the pullout force should be applied at a constant displacement rate of 1 mm/min (0.04 in/min) +/- 10%. However, constant stress loading approach can also be adopted. This approach may be achieved by three different methods. The first approach involves controlled stress rate, which simulates a short-term condition. In this method a uniform rate of loading is applied to a maximum value of 2 kN/m/min (11.4 lb/in/min). The second approach involves incremental stress, which is suitable also for short-term condition. In this method a stepped increase in the pullout load is conducted every period of time. The third approach involves constant stress (creep), which is suitable for long-term conditions. In this method one of the two previous methods is adopted until reaching the desired loading level, and then maintaining a constant stress for a period of time.

The pullout force has been reported using displacement rates ranging from 0.1 to 20 mm/min (4 mil/min to 0.8 in/min). The pullout force is typically applied at a controlled displacement rate (Farrag *et al.* 1993). However, some researchers have carried out pullout tests using load controlled systems (e.g. Tzong and Cheng-Kuang 1987). Myles (1982) reported that test results involving a direct shear box are not significantly affected when varying the displacement rate from 10 to 75 mm/min (0.4 to 3 in/min). On contrary, Rowe and Ho (1986) reported that geogrid tensile capacity was significantly affected by the applied displacement rate. Farrag *et al.* (1993) also studied the effect of displacement rate on the pullout resistance. They conducted tests using displacement rates of 2, 6, 10, and 20 mm/min (0.1, 0.2, 0.4 and 0.8 in/min). The authors reported that high displacement rates affect the pullout force and the displacement distribution. Specifically, they reported that at high displacement rates, the strains along the reinforcement is minimally mobilized which results in higher contribution to the interface resistance than the passive resistance of the transverse ribs. They recommended displacement rates below 6 mm/min (0.2 in/min) to minimize the displacement rate effects. Fannin and Raju (1993) studied the influence of the pullout displacement rate on the pullout resistance at low rate levels. They adopted displacement rates of 0.25, 0.50, and 1.00 mm/min (0.01, 0.02 and 0.04 in/min). The authors reported that the pullout resistance is independent of the pullout displacement rate at low rate values. Yet, their data showed a slight increase in the pullout resistance upon increasing the displacement rate.

Unconfined portion: Some studies reported the clamping of reinforcement outside the box, and thus leaving a portion of the reinforcement unconfined outside the box (Koerner 1986; Brand and Duffy 1987; Stadler 2001; Zornberg *et al.* 2009). Other researchers used clamps inside the sleeve to avoid having unconfined zones (Farrag *et al.* 1993; Ladeira 1995; Lopes and Ladeira 1996).

Clamping system: A clamp is used to attach the geosynthetic to the pulling system. The design should be such that the specimen is held without any slipping, breaking, or weakening. The clamp should ensure uniform pullout stress distribution along the width of the specimen and horizontally so as not to interfere with the shear stress on the soil-reinforcement interface (ASTM D6706). The clamping system typically consists of two steel plates sandwiching the geosynthetic

(e.g. Farrag *et al.*; Stadler 2001). Roller grips have also been used mechanism to clamp the geosynthetic specimen to the pullout box. Zornberg *et al.* (2009) used roller grip consists of a steel cylinder with a slit where the specimen could be attached and bolted. Zornberg *et al.* (2009) reported that the roller grip design helps to prevent the stress concentration at a single plane throughout the specimen by distributing it uniformly over a wider area.

Normal stress loading: Normal stress is applied to the top of the soil such that the soil-reinforcement interface reaches the desired level of confinement. The applied normal stress should be uniform and remain constant throughout the test. In order to maintain constant normal stress, ASTM D6706 recommends using a flexible pneumatic or hydraulic diaphragm-loading device that covers the entire area of the box. Normal stress has been commonly applied by an air-bag fixed to the inner side of the top side of the box and covers the entire area to ensure a constant uniform stress on the top of the soil (Ingold 1983; Palmeira and Milligan 1989; Farrag *et al.* 1993). Lopes and Ladeira (1996) used a thick neoprene rubber layer and wooden plates to achieve uniform stress distribution on the top of the soil. They applied confining stress to the wooden plates using ten pressure cylinders. Zornberg *et al.* (2009) and Hanumasagar *et al.* (2014) used six air pressure cylinders jacking against a steel lid. Jayawickrama *et al.* (2014) utilized nine pressure plates hydraulically jacked against three wide flange cross beams.

Displacement measurements: To measure the internal displacements and assess the reinforcement elongation along the specimen, inextensible wires are typically attached to the reinforcement at different locations. These inextensible wires are in turn attached from their other sides to linear potentiometers (Lopes and Ladeira 1996) or LVDTs (ASTM D6706; Farrag *et al.* 1993; Zornberg *et al.* 2009) that are fixed outside the pullout box. The wires are protected from the confining pressure applied to the soil mass by tubes (ASTM D6706; Farrag *et al.* 1993). The movements that develop at different locations along extensible reinforcement specimens during a pullout test have been reported to involve two components. The first component corresponds to the displacement due to the shear strain of the soil-reinforcement interface. The second component corresponds to the reinforcement elongation.

Compaction and specimen preparation: During the preparation of a pullout test. Soil layers are placed and compacted in the box to its mid-height and then the reinforcement specimen is placed and then the rest of the soil layers are compacted on its top to the full height of the box. The required number of lifts and compaction effort depend upon the type of the soil and the desired compaction moisture content (ASTM D6706). Farrag *et al.* (1993) and Lopes and Ladeira (1996) placed and compacted soil layers 0.15 m (6 in.) thick. Sand has been placed in the box by pouring it from a constant height (Jewell 1980; Palmeira and Milligan 1989; Farrag *et al.* 1993; Lopes and Ladeira 1996). Compaction has also been performed using electric vibratory hammers (Lopes and Ladeira 1996), electric jack hammers, standard proctor hammers (Saxena and Budiman 1985), mechanical compaction (Chang *et al.* 1977; Farrag *et al.* 1993; Alfaro *et al.* 1995a; Stadler 2001), hand tamping (Elias 1979; Hanumasagar *et al.* 2014), and pluviation (Palmeira and Milligan 1989; Farrag *et al.* 1993; Min *et al.* 1995; Ochiai *et al.* 1996). Relative density of the compacted layer can be verified by using density gauges (Farrag *et al.* 1993; Lopes and Ladeira 1996), conducting

sand cone tests (Stadler 2001), or weighing the box before and after soil placement (Alfaro *et al.* 1995a; Cuelho 1998).

Table 2.2.2a shows the characteristics of pullout equipment used in several studies along with the requirements of GRI GT6 (1991) and EN 13798 (2004).

2.2.2.2 TRANSPARENT SOIL-GEOSYNTHETIC INTERACTION EQUIPMENT

Transparent soil technology was used as part of the experimental component (Chapter 5) of this NCHRP project in order to provide additional insight on the shear band that develops due to the soil-geosynthetic interaction. Accordingly, this section includes a detailed literature review on previous studies that are relevant to this component of the testing program. Transparent soils have been used in geotechnical engineering to evaluate a variety of foundation engineering problems (Wakabayashi 1950, Gill and Lehane 2001, Sadek *et al.* 2003, McKelvey *et al.* 2004, Song *et al.* 2009, Iskander and Liu 2010). The principle of transparent soils is based on submerging a translucent material into a liquid with the same refractive index. This approach makes the translucent material become transparent under saturation. The characteristics of previous research involving transparent soil techniques are summarized next.

Use of glass beads: Crushed glass or glass beads were used in the past with a fluid having the same refractive index (Wakabayashi 1950, Drescher 1976, Allersma 1982). However, these glass beads were more translucent than transparent, which did not provide adequate transparency through the particulate medium. Also, the medium was deemed not to represent well the properties of natural soils (Mannheimer and Oswald 1993, Sadek *et al.* 2002). Wakabayashi (1950) applied this principle using crushed glass and a solution of carbon-disulphide and benzene to conduct photo-elastic studies of stress distribution generated by a loaded footing on the soil surface. Dyer (1985) produced a transparent soil with crushed Pyrex glass and a colorless liquid paraffin to conduct photo-elastic experiments with direct shear and pullout tests. However, transparent soils obtained from crushed glass have been reported not to have similar geotechnical properties to sands (Sadek *et al.* 2002).

Table 2.2.2a. Reinforcement pullout test devices (Modified after Minažek and Mulabdić 2013)

Reference	Dimensions L (m) x W (m) x H (m)	Pullout force generation, with increase D – deformation (mm/min), N – stress (description)	Sleeve: exist (yes/no, description, width (m))/clamping system (description)	Soil thickness bellow/above reinforcement (m)	Force and displacement sensors	Compaction and density
Chang et al. (1977)	1.30 x 0.91 x 0.51	D	-	-	-	Mechanical compaction
Yuan and Chua (1991)	0.76 x 0.71 x 0.61	D (hydraulic)	-	0.30/0.30	Load cell, displacement transducers	-
Palmeira and Milligan (1989)	0.25 x 0.15 x 0.15 1.10 x 1.10 x 1.10	D (0.5 mm/min, hydraulic)	No (just opening in front box side) // clamps (connected with bolts and aluminum alloy to reinforcement)	-	Photo measurement of wires out of the box, 8 load cells on the front box side, LVDT – on the piston, load cell	Pluviation, vibrocompactor, cylinders in the box
Farrag et al. (1993)	1.52 x 0.90 x 0.76	D, N (max 6 mm/min, hydraulic)	Yes (width 0.3 m) // clamps (plates inside sleeve and soil)	Min. 0.30/0.30	LVDT, velocity transducers and load cells, pressure cell on front box side	Pluviation, mechanical compaction, nuclear densimeter
Alfaro et al. (1995b)	1.60 x 0.70 x 0.50	D (1 mm/min)	Yes (width 0.2 m) // clamps (plates inside sleeve)	0.25/0.15	LVDT, load cells	-
Fannin and Raju (1993)	1.30 x 0.64 x 0.60	D	No // clamps (there is upper and lower clamps)	-	Load cell, 2 displacement transducers, piezometers, 5 extensometers	-
Kharchafi and Dysli (1993)	-	-	-	-	x-ray records	-
Bergado et al. (1994)	1.30 x 0.80 x 0.50	D (1 mm/min, hydraulic)	-	-	Load cell, LVDT	-
Koerner (2005)	1.90 x 0.91 x 1.10	D, N (1 mm/min, hydraulic)	Yes // clamps (no)	Min. 0.30/0.30	Load and displacement transducers	-
Min et al. (1995)	0.60 x 0.60 x 0.20	N (hydraulic, electric, cyclic load, force increments for 24 h)	No // clamps (grid glues on metal plates which extend 0.1 m in the box)	-	Load cells, LVDT at front, 4 extensometers on grid	Pluviation

Alfaro et al. (1995a)	1.60 x 0.50 x 0.60	D	Yes // clamps (inside the box)	0.25/0.15	Load cell, LVDT	Mechanical compaction, weighing
Lopes and Ladeira (1996)	1.53 x 0.80 x 1.00	D (hydraulic)	No or yes (width 0.2 m) // clamps (exist)	0.30/0.30	Load cell. LVDT, vertical pressure cell LVDT on grid	Nuclear densimeter
Ochiai et al. (1996)	0.60 x 0.40 x 0.40	D (1 mm/min, reducer, cyclic)	Yes // -	-	Load cell, displacement transducers	Pluviation
Bernal et al. (1997)	1.22 x 0.50 x 1.22	D (1 mm/min, 2 hydraulic cylinders)	Yes (width 0.15 m) // clamps (reinforcement sample in resin, bolted to two plates)	0.205/0.205	Load cell, LVDT, 3 displacement transducers on sample, total cell on box bottom	Hand compaction
Cuelho (1998)	1.25 x 1.10 x 0.90	D, N (0-2 mm/min, electrical-reducer, 2 air cylinders)	Yes (width 0.26 m) // clamps (plates with reinforcement samples glued)	-	Load cell, extensometers (5), glued deflectometers	Vibro-compactor, weighing
Teixeira (2003)	1.50 x 0.48 x 0.70	D (4,6 mm/min, electrical, reducer)	Yes (width 0.2 m) // clamps (bolted to the reinforcement samples, passing through sleeve)	-	Load cell, 3 total cells, 6 extensometers on the sample, deflectometers	-
Alagiyawanna et al. (2001)	0.68 x 0.625 x 0.30	D (1 mm/min)	No, sponge to prevent soil loss, // -	-	Displacement transducer, laser sensors for grid displacements, load cell for vertical and horizontal direction	-
Bergado and Teerawattanasuk (2001)	1.27 x 0.76 x 0.51	D (1 mm/min, hydraulic)	-	-	-	Pluviation

Table 2.2.2a. Reinforcement pullout test devices (Modified after Minažek and Mulabdić 2013) (continued)

Reference	Dimensions L (m) x W (m) x H (m)	Pullout force generation, with increase D – deformation (mm/min), N – stress (description)	Sleeve: exist (yes/no, description, width (m))/clamping system (description)	Soil thickness bellow/above reinforcement (m)	Force and displacement sensors	Compaction and density
Meyer et al. (2003)	1.50 x 0.70 x 0.60	D (2 mm/min, hydraulic, cyclic load up to 4 Hz)	Yes (width 0.2 m) // clamps (reinforcement is rolled or pulled with two rods)	-	3 load cells on bottom, LVDT	Weighing, nondestructive methods
Marques (2005)	1.53 x 1.00 x 0.80	(hydraulic)	Yes (width 0.2 m) // -	0.40/0.40	Different measuring instruments	Mechanical compaction, weighing system on the box bottom
Moraci and Gioffrè (2006)	1.70 x 0.60 x 0.68	(electrical)	Yes (width 0.25 m) // clamps (inside soil)	-	RVDT (6 on grid sample), load cell	-
Abdel-rahman et al. (2007)	1.20 x 1.16 x 0.70	(hydraulic, hand)	No // clamps (two steel plates with thickness of 6 mm)	-	2 sensors: 1 vertical, 1 horizontal, 2 LVDT on sample	Mechanical compaction
Aydogmus and Klapperich (2008)	0.60 x 0.50 x 0.20	D (0.000001-12 mm/min)	No // clamps (outside the box)	0.10/0.10	Load cell, pressure measurement at box bottom and in airbags	Pluviation, mechanical
Abdelouhab et al. (2010)	2.00 x 1.10 x 1.10	-	-	-	Load cell and total cell (front and bottom box side)	-
Requirements of EN 13798 (2004)	1.50 x 0.60 x 0.30	D, N (2+/-0.2 mm/min, hydraulic)	Yes (width 0.20 m), clamps (articularly connected)	6Dmax/6Dmax	LVDT, load cells	-
Requirements of GRI GT6 (1991)	1.20 x 0.75 x 0.60 or > 20D85	D (1 mm/min)	Yes (width 0.15 m) // clamps (2 plates width 0.20 m)	Min. 0.30/0.30	LVDT, measuring ring, load cells	-
Stadler (2001)	0.95-1.50 x 1.20 x 0.60 (adjustable length)	D (1 mm/min, hydraulic)	Yes (width 0.15 m) // clamps (outside the box)	0.18/0.18	3 LVDTs for confined geosynthetic, 2 LVDT for pullout bar, 1 LVDT for unconfined geosynthetic, 2 pressure transducers for pullout actuators	Mechanical and hand compaction, sand cone test

Jayawickrama et al. (2014)	3.60 x 3.60 x 1.20	(hydraulic)	-	-	5 vertical pressure cells, pressure transducer for normal stress jacks, load cell for pullout jack, optical and digital measures for geosynthetic displacement	-
Hanumasagar et al. (2014)	1.50 x 0.60 x 0.30	D (1 mm/min, hydraulic)	Yes (width 0.75 m) // clamps (roller grips outside the box)	0.15/0.15	-	Hand tamping and jack hammer
Zornberg et al. (2009)	1.50 x 0.60 x 0.30	D (1 mm/min, hudraulic)	Yes (width 0.75 m) // clamps (roller grips outside the box)	0.15/0.15	Load cell for pullout force and LVDTs for geosynthetic displacement	Hand tamping and jack hammer

Use of silica gel beads: Silica powder or silica gel was used with colorless pore fluids having the same refractive index. Iskander *et al.* (1994, 2002a, 2002b), Gill and Lehane (2001), Sadek *et al.* (2002), Liu *et al.* (2003), Zhao and Ge (2007), and Hird and Stanier (2010) used precipitated and flumed silica powder and silica gel beads as soil simulants. Sadek *et al.* (2002) used transparent soil obtained from silica gel beads saturated with a blend of white mineral oil and paraffinic solvent. The authors reported geotechnical properties of this transparent soil to be comparable to those of sands. However, the use of the silica gel particles was also found to have important drawbacks. Specifically, they were found to deform plastically even under low confining pressures (Iskander 1998, Iskander *et al.* 2003, Zhao and Ge 2007). Also, silica gel particles were found to be difficult to de-air (Iskander *et al.* 2002b, 2003) and to be affected by high humidity and water (hydroscopic). This was reported to affect the particles color and stability. In addition, silica gel particles may undergo chemical reactions with time that cause changes in color and reduce their transparency (Iskander 2010). Sadek *et al.* (2002) reported using a paraffinic solvent with some mineral oil as a pore-fluid. This solvent is volatile, thus classified as hazardous material.

Use of crushed fused quartz: Ezzein and Bathurst (2011a, 2011b) have recently proposed using crushed quartz submerged in a mixture of mineral oil. The transparent soil was reported to have a geotechnical behavior comparable to that of sands, and a matching refractive index fluid that is composed of non-volatile, non-hazardous liquids. Also, the transparent soil is non-porous and incompressible, with transparency that does not degrade over time. Surveys of reported combinations of transparent granular materials with matching transparent fluids by Iskander (2010) and Ezzein and Bathurst (2011a) indicate that the combination of fused quartz and mineral oil material has the greatest viewing depth.

Digital image analysis: Although digital image analysis techniques have found widespread application in disciplines such as medicine, biology, and geography, applications within civil engineering are more incipient (Mora *et al.* 1998). However, recent advances in hardware and software for digital image processing and analysis have opened the way for major breakthroughs in areas relevant to geotechnical engineering. In fact, promising advances involving image-processing techniques have recently been made for the purposes of granular soil characterization, including evaluation of porosity, fabric, structure, and uniformity of cohesionless soils (Kemeny *et al.* 1993, Thomas *et al.* 1994, Kuo and Frost 1996, Frost and Kuo 1996, Obaidat *et al.* 1998, Jang and Frost 1998, Jang *et al.* 1999). Progress has also been made in the use of digital image analysis for assessment of deformation of granular soils and shear band development (Gustafsson *et al.* 1994, Raschke *et al.* 1996, Liang *et al.* 1997) as well as for measurement of geomembrane surface roughness (Dove and Frost 1996, 1999). In addition, the use of digital image analysis techniques has been adopted for evaluation of the pore opening size distribution of geotextiles (Aydilek *et al.* 2002) and for measurement of strain distribution under tensile testing (Kutay *et al.* 2006).

Particle Image Velocimetry (PIV) is a technique used to obtain velocity measurements through digital image correlations. It has been traditionally used in studies of fluid mechanics. In these studies, seeding particles are added to the fluid and worked as tracers since these seeding particles are chosen such that they create a significant contrast against the fluid. Images are

obtained at a specific rate and are later processed and compared to determine the velocity vectors at each time step. This technique has also been used in geotechnical applications, and has become the technique of choice in studies involving tracking the movement of soil. White *et al.* (2003), Raffel *et al.* (2007), and Pan *et al.* (2009) provided detailed description of this technique.

While the use of transparent soil and digital image analysis was adopted in this study, other techniques (e.g. photo-elastic methods, X-ray tomography) have also been used in previous studies. These techniques are not practical for evaluation of soil-geosynthetic interaction but these studies provide further insight into transfer mechanisms. Wakabayashi (1950) determined the stress distribution in a powdered mass using photo-elastic methods. Specifically, by placing phenolite in locations where determination of stresses was desired, Wakabayashi (1950) was able to define the direction of the principal stresses within the soil mass. Dyer (1985) subsequently used photo-elastic methods to observe stress concentrations in reinforced soil systems. Computerized X-ray tomography (CT) has more recently been used in geology, geosciences, and rock mechanics. It was used to study soil and rock properties such as density, porosity, water content, solute concentration, macroscopic size, and fracture size (Shi *et al.* 1999). CT is based on the attenuation of X-rays after penetrating objects and on their collection by detectors behind the object. The resulting images have been used to define properties that depend on the material density and atomic number (Colletta *et al.* 1991). CT has been used in geotechnical research to quantify shear strains and fracture features (e.g. Leung *et al.* 1995, Walters 1995, Desrues *et al.* 1996, Wibowo 1996). Shi *et al.* (1999) utilized CT to monitor the evolution of the internal failure in soil masses and visualize shear bands, while Wong (1999) used CT to visualize shear fractures. Otani *et al.* (2001) used similar CT techniques to observe the soil displacement field in sand confined geogrids.

2.3 GATHERING OF FIELD INSTRUMENTATION INFORMATION ON GRS-IBS AND GMSE STRUCTURES

The information gathered for this section was obtained from available reports written by State and Federal government agencies, journal publications, conference presentations and papers, doctoral dissertations, magazine articles, and verbal communications with individuals. Lists of the documents gathered to compile the information presented in this section are provided in Sections 2.3.1 and 2.3.2.

2.3.1 OVERVIEW OF INSTRUMENTED GRS-IBS

Table 2.3.1a summarizes the list and source of the available information gathered for documenting the instrumented GRS-IBS constructed to-date. There are twenty-six references identified in Table 2.3.1a, which overall describe twenty-four field instrumented GRS-IBS structures and one non-instrumented site in Montana. All of the structures listed in Table 2.2.2 were constructed in U.S. as no published case histories that fit the specific description to be called GRS-IBS structure were noted from international sources. However, there are closely-spaced GMSE structures from foreign studies, which are summarized in Section 2.3.2.

The GRS-IBS structures in U.S. were constructed over a 30-year time-period (Adams *et al*. 2011) and were primarily owned by state, federal, and county agencies. However, most of these structures were not instrumented nor documented in the literature. The instrumented structures summarized herein were distributed within eleven States and one State territory, including five in Ohio, three in Virginia and Louisiana, two in California and Colorado, and one each in Minnesota, Hawaii, Pennsylvania, Iowa, Utah, Delaware, Massachusetts, and Puerto Rico. In addition to the above listed structures, an investigation was performed to document the GRS-IBS sites in Rhode Island, Maine, Oregon, West Virginia, and Missouri. No available literature could be found related to these structures; however, based on phone conversations with FHWA, it was determined that these structures were not instrumented. Additionally, two instrumented GRS-IBS sites were identified, which are located in Wisconsin and New York but there was no available literature associated with these sites to document the instrumentation plan and the associated data. However, a memorandum that shows a summary of site visits of seven GRS-IBS structures built in St. Lawrence County, New York is available (Christopher 2013). This memorandum provides surface profile data for bridge joints for one of the bridges. It states that the surface profile data were used to calculate International Roughness Index (IRI) for the roadway section. It also states that all of the examined bridges were in excellent condition and the pavement surfaces at the bridge joints for all sites were very smooth.

Relevant characteristics (including height of each structure, length of the bridge span, foundation type, type of backfill, and maximum vertical spacing in between reinforcements) of the twenty-four structures identified in Table 2.3.1a are summarized in Table 2.3.1b. Most of the structures constructed with instrumentation to-date have been reinforced with woven geotextiles with the exception of the structure constructed in Minnesota, which was reinforced with geogrids. In all of the structures, the primary reinforcements were placed with 0.2 m (8 in.) of vertical spacing. The height of the structures ranged approximately from 1.8 m (6 ft.) to 9.0 m (30 ft.) with bridge spans ranging approximately from 7.5 m (25 ft.) to 42 m (140 ft.). The majority of the structures were founded on reinforced soil foundations (RSF). The backfill used at these sites ranged from base course materials with up to 12 percent fines to open graded gravel with no fines.

Table 2.3.1c summarizes the type of field instrumentation adopted in these twenty-four structures as well as the collected data mentioned in the associated literature. Figure 2.3.1 and 2.3.2 provide a summary of the generic and typical instrumentation layout schemes that were tabulated in Table 2.3.1c to provide an overview of all of the instruments used to-date at instrumented GRS-IBS field sites as determined from the available literature. As can be seen from Figure 2.3.1, some of the instrumentation focuses more on observing the behavior of the superstructure with data being collected: (1) within the contact of bridge span and integrated approach, (2) specifically within bearing bed, and (3) through the facing. There have been also attempts to understand the horizontal loads against the facing of the structure by placing earth pressure cells vertically up against the facing blocks. However, due to the size of the pressure cells and the frequency of their installation along the facing, provides challenges for interpreting the data reliably. In summary, the field instrumentation to-date is missing reliable data to capture the stresses on the reinforced blocks as well as behind the blocks, along the face of the structure. Also estimation of stress via strain measurements in the reinforcement at the reinforced fill has

not been evaluated. The boundary conditions related to these stress distributions as it relates to variation within vertical spacing of reinforcements have not been documented in the field studies to-date.

This literature review showed that majority of the field instrumentation has been designed to monitor the performance of the structure but not necessarily to confirm specific design components. Furthermore, the existing GRS-IBS design methodology is primarily based on empirical observations from the mini pier performance tests. The boundary conditions in the field in terms of GRS-IBS being implemented as a bridge abutment is different than the geosynthetic reinforced soil tested as a pier. Furthermore, the pier tests in the laboratory were conducted to test the ultimate capacity. The instrumentation data obtained from the literature on field studies do not provide information regarding the ultimate capacity of the structure and hence a direct comparison is currently not available. The existing field instrumentation data also does not address the boundary conditions related to differences in reinforcement spacing. The impact of boundary conditions on the potential differences in response between geosynthetic reinforced soil piers and GRS-IBS could be evaluated, for example, through systematic numerical simulations. Providing such insight is one of the objectives in the series of numerical simulations to be presented as part of Chapter 7 of this report.

Additional information from instrumented GRS-IBS sites (located in Minnnesoata, Louisiana, and Delaware) and load-carrying GMSE bridge abutment sites (located in Colorado) has been gathered. However, the details of data evaluation and assesement is presented in chapter 4.6.

2.3.2 OVERVIEW OF INSTRUMENTED GMSE

This section summarizes the documented field instrumentation of GMSE structures that were constructed within and outside of the U.S. Identified literature that provides relevant information related to field instrumentation of GMSE structures is summarized in Table 2.3.2a These structures were primarily constructed as retaining walls or full-scale test walls.

Relevant characteristics of the field instrumented GMSE structures that were constructed in the U.S. are tabulated in Table 2.3.2b. The table contains thirteen structures built in nine States, including three in Illinois, two in Colorado and Washington and one each in Virginia, Arizona, Massachusetts, Kansas and Georgia. The height of these structures ranges between 4.5 m (15 ft.) and 12.5 m (41 ft.). The structures were primarily constructed with coarse-grained backfill with reinforcements ranging from geogrids and woven and nonwoven geotextiles. The reinforcements were vertically spaced at a range of 0.38 m (15 in.) to 1 m (39 in.) with the largest spacing used in a wall that was intentionally designed to fail. The field instrumentation program included monitoring the performance of the GMSE structures under loading and different site conditions. Table 2.3.2c summarizes the type of field instrumentation adopted in these structures. The collected data from these instruments were primarily focused on analyzing vertical and horizontal deformations of the structure, deflection of the facing element, earth pressure within the GMSE mass, and induced strains in the whole structure and geosynthetic reinforcements.

Relevant characteristics of the field instrumented GMSE structures that were constructed outside of the U.S. are presented in Table 2.3.2d. These structures were constructed in Canada, Brazil, China, Korea, Japan, Norway, Italy, Germany, and Australia. Most of the structures were built as retaining walls, although some were constructed as abutments or full-scale experimental structures. The height of these structures ranges between 2.7 m (9 ft.) and 21.0 m (69 ft.), where the structures were constructed over a wide range of foundation conditions. The structures were reinforced with geogrids and woven and nonwoven geotextiles and were vertically spaced at a range of 0.23 m (9 in.) to 1.6 m (63 in.). The structures with reinforcement spacing of 0.3 m (12 in.) or less had varying reinforcement spacing within the structure. For example, the site with 0.23 m (9 in.) reinforcement spacing also had 0.36 m (14 in.) reinforcement spacing. Therefore, these structures were synthesized as GMSE and not GRS-IBS. The reinforced fill used in these structures varies anywhere from silty clay to gravel covering wide range of soils.

Among the foreign countries where GMSE structures have been constructed and instrumented, Japan has a unique design that was primarily developed by Prof. Tatsuoka. These structures have been previously cited by Ketchart and Wu (2001) as geosynthetic reinforced soil structures adopting a preloading concept. Some of the references associated with these structures include Tatsuoka *et al.* (1997) and Tatsuoka *et al.* (2009). It should be noted that review of these structures is not covered in full detail in this literature summary because one of the most important elements of these structures is their facing (essentially a structural component of the structure). Unlike the GRS-IBS structures designed in U.S., facing of the structure is considered an important structural element in this design. Also, in structures reported by Prof. Tatsuoka and others, design is based on limit equilibrium and there is no consideration of composite behavior.

Table 2.3.2e summarizes the type of field instrumentation adopted in these structures. The collected data from the majority of these instruments were primarily focusing on analyzing vertical and horizontal deformations of the structure, with some instrumentation programs focusing only on evaluating induced strains in the reinforced structure (global strain) and geosynthetic reinforcements (local strain).

Table 2.3.1a. Field instrumented GRS-IBS structures in the United States

No.	Structure	Location	Authors	Year of Ref.	Title	Document Type
1	Lake Mamie - GRS-IBS	California (CA)	Adams, M.T., Nicks, J.E., Stabile, T., Wu, J.T.H., Schlatter, W., and Hartmann, J.	2011	Geosynthetic Reinforced Soil Integrated Bridge, System Synthesis Report	Report
2	Twin - GRS-IBS	California (CA)	Adams, M.T., Nicks, J.E., Stabile, T., Wu, J.T.H., Schlatter, W., and Hartmann, J.	2011	Geosynthetic Reinforced Soil Integrated Bridge, System Synthesis Report	Report
3	Black Hawk - Geosynthetic-reinforced soil abutment	Colorado (CO)	Wu, J.T.H., Ketchart, K., and Adams, M.T.	2001	GRS Bridge Piers and Abutments	Report
4	Havana Yard - Geosynthetic-reinforced soil abutment	Colorado (CO)	Lee, K.Z.Z. and Wu, J.T.H.	2004	A synthesis of case histories on GRS bridge supporting	Conference paper
			Wu, J.T.H., Ketchart, K., and Adams, M.T.	2001	GRS Bridge Piers and Abutments	Report
5	Delaware - GRS-IBS	Delaware (DE)	Talebi, M., Meehan, C. L, Cacciola, D. V., and Becker M. L.	2014	Design and Construction of a Geosynthetic Reinforced Soil Integrated Bridge System	Technical paper
6	Lahaina Bypass Road - GRS-IBS	Hawaii (HI)	Ooi., P.	2014	Field Instrumentation of GRS-IBS in Hawaii	Conference call
7	Buchanan County - GRS-IBS	Iowa (IA)	Vennapusa, P., White, D. J., Klaiber, F.W., Wang, S., and Gieselman, H.	2012	Geosynthetic Reinforced Soil for Low-Volume Bridge Abutments	Report
8	Cecil Creek - GRS-IBS	Louisiana (LA)	Adams, M., and Saunders, S.A.	2007	Upper Ouachita National Wildlife Refuge GRS Abutments for Replacement Bridges	Presentation
9	Big Lake - GRS-IBS	Louisiana (LA)	Adams, M., and Saunders, S.A.	2007	Upper Ouachita National Wildlife Refuge GRS Abutments for Replacement Bridges	Presentation
10	Cut off Creek - GRS-IBS	Louisiana (LA)	Adams, M., and Saunders, S.A.	2007	Upper Ouachita National Wildlife Refuge GRS Abutments for Replacement Bridges	Presentation
11	Massachusetts - GRS-IBS	Massachusetts (MA)	FHWA - Sent by Daniel Alzamora	2013	Instrumentation & Monitoring Program on GRS-IBS	Presentation
12	Minnesota - GRS-IBS	Minnesota (MN)	Budge, A., Dasenbrock, D., Mattison, D., Bryant, G., Grosser, A., Adams, M., and Nicks, J.	2014	Instrumentation and Early Performance of a Large Grade GRS-IBS Wall	Technical paper

13	Montana - GRS-IBS	Montana (MT)	Abernathy, C.	2014	Montana DOT Rebuilds an Old Bridge with a New System	Magazine article
			Abernathy, C.	2013	Experimental Projects Construction Report - Geosynthetic Reinforced Soil - Integrated Bridge System (GRS-IBS)	Report
14	New York – GRS-IBS	New York (NY)	Christopher, B.R.	2013	Review of June 18, 2013 GRS-IBS Showcase at Clarkson University, Potsdam, New York and St. Lawrence County Wall Visits	Memorandum
15	Yauco Bridges - GRS-IBS	Puerto Rico (PR)	FHWA - Sent by Daniel Alzamora	2014	Puerto Rico PR-2 - Geosynthetic Reinforced Soil Integrated Bridge System Showcase	Presentation

Table 2.3.1a. Field instrumented GRS-IBS structures in the United States (continued)

No.	Structure	Location	Authors	Year of Ref.	Title	Document Type
16	Defiance County (Tiffin River Bridge) -GRS-IBS	Ohio (OH)	Warren, K.A., Whelan, M.J., Hite J., and Adams M. Adams, M.T., Nicks, J.E., Stabile, T., Wu, J.T.H., Schlatter, W., and Hartmann, J.	2014 2011	Three Year Evaluation of Thermally Induced Strain and Corresponding Lateral End Pressures for a GRS IBS in Ohio Geosynthetic Reinforced Soil Integrated Bridge, System Synthesis Report	Technical paper Report
17	Vine Street - GRS-IBS	Ohio (OH)	Adams, M.T., Nicks, J.E., Stabile, T., Wu, J.T.H., Schlatter, W., and Hartmann, J.	2011	Geosynthetic Reinforced Soil Integrated Bridge, System Synthesis Report	Report
18	Glenburg road - GRS-IBS	Ohio (OH)	Adams, M.T., Nicks, J.E., Stabile, T., Wu, J.T.H., Schlatter, W., and Hartmann, J.	2011	Geosynthetic Reinforced Soil Integrated Bridge, System Synthesis Report	Report
19	Huber Road - GRS-IBS	Ohio (OH)	Adams, M.T., Nicks, J.E., Stabile, T., Wu, J.T.H., Schlatter, W., and Hartmann, J.	2011	Geosynthetic Reinforced Soil Integrated Bridge, System Synthesis Report	Report
20	Bowman road - GRS-IBS	Ohio (OH)	Adams, M.T., Nicks, J.E., Stabile, T., Wu, J.T.H., Schlatter, W., and Hartmann, J.	2011	Geosynthetic Reinforced Soil Integrated Bridge, System Synthesis Report	Report
			Adams, M.T., Schlatter, W., and Stabile, T.	2011	Geosynthetic Reinforced Soil Integrated Bridge System	Conference paper
			Adams, M.T., Schlatter, W., and Stabile, T.	2007	Geosynthetic Reinforced Soil Integrated Abutments at the Bowman Road Bridge in Defiance County, Ohio	Conference paper
21	Mount Pleasant Road - Bridge	Pennsylvania (PA)	Bloser, S., Shearer, D., Corradini, K., and Scheetz, B.	2012	Geosynthetically Reinforced Soil-Integrated Bridge Systems (GRS-IBS) Specification Development for PennDOT Publication 447	Report
22	I-84 Echo (Summit County) - GRS-IBS	Utah (UT)	Raghunathan, D., Sadasivam, S., and Mallela, J.	2014	Geosynthetic Reinforced Soil Integrated Bridge System on I-84 near Salt Lake City	Draft Report
23	TFHRC - GRS-IBS abutment with tunnel	Virginia (VA)	Adams, M.T., Nicks, J.E., Stabile, T., Wu, J.T.H., Schlatter, W., and Hartmann, J.	2011	Geosynthetic Reinforced Soil Integrated Bridge, System Synthesis Report	Report
24	TFHRC - NCHRP full-scale-Geosynthetic-	Virginia (VA)	Wu, J.T.H., Lee, K.Z.Z., Helwany, S.B., and Ketchart, K.	2006	Design and Construction Guidelines for Geosynthetic- Reinforced Soil Bridge Abutments with a Flexible Facing	Report

	reinforced soil abutment					
25	TFHRC - Geosynthetic-reinforced soil abutment	Virginia (VA)	Wu, J.T.H., Ketchart, K., and Adams, M.T.	2001	GRS Bridge Piers and Abutments	Report

Note: The complete references for the sources listed in this table are provided in the References section of this chapter.

Table 2.3.1b. Relevant characteristics of instrumented GRS-IBS structures

No.	Structure	Location	Wall Height (ft.)	Bridge Span (ft.)	Foundation Information	Backfill Type	Reinforcement Type	Reinforcement Spacing (in)
1	Lake Mamie - GRS-IBS	California (CA)	N/A	67	Reinforced soil foundation	N/A	N/A	8
2	Twin - GRS-IBS	California (CA)	N/A	71	Reinforced soil foundation	N/A	N/A	8
3	Black Hawk - Geosynthetic-reinforced soil abutment	Colorado (CO)	15 - 25	N/A	Stiff soil and competent rock	Silty Clayey Sand	Woven geotextile	12
4	Havana Yard - Geosynthetic-reinforced soil abutment	Colorado (CO)	24 - 25	N/A	Reinforced soil foundation	Road base material	Woven geotextile	8
5	Delaware - GRS-IBS	Delaware (DE)	16	28	Reinforced soil foundation and Clay, Sand	No. 8 stone	Woven geotextile	8
6	Lahaina Bypass Road - GRS-IBS	Hawaii (HI)	6.7	109	Reinforced soil foundation and incompressible foundation	N/A	Woven geotextile	8
7	Buchanan County - GRS-IBS	Iowa (IA)	N/A	N/A	Reinforced soil foundation	Well graded Gravel with sand	Woven geotextile	8
8	Cecil Creek - GRS-IBS	Louisiana (LA)	N/A	76	Reinforced soil foundation	Base coarse aggregate	Woven geotextile	8
9	Big Lake - GRS-IBS	Louisiana (LA)	N/A	76	Reinforced soil foundation	Base coarse aggregate	Woven geotextile	8
10	Cut off Creek - GRS-IBS	Louisiana (LA)	N/A	76	Reinforced soil foundation	Base coarse aggregate	Woven geotextile	8
11	Massachusetts - GRS-IBS	Massachusetts (MA)	N/A	N/A	Reinforced soil foundation	N/A	N/A	8
12	Minnesota - GRS-IBS	Minnesota (MN)	22.7	77.5	Reinforced soil foundation	Crushed granite material	Geogrid	8

13	Montana – GRS-IBS	Montana (MT)	7	N/A	Reinforced Soil foundation	Granular fill	Woven geotextile	8
14	Yauco Bridges - GRS-IBS	Puerto Rico (PR)	30	42.67	Reinforced Soil foundation	Coarse grained soil	Woven geotextile	8

Note: N/A refers to information not available.

Table 2.3.1b. Relevant characteristics of instrumented GRS-IBS structures (continued)

No.	Structure	Location	Wall Height (ft.)	Bridge Span (ft.)	Foundation Information	Backfill Type	Reinforcement Type	Reinforcement Spacing (in)
15	Defiance County (Tiffin River) - GRS-IBS	Ohio (OH)	19.26	140.1	Reinforced soil foundation	AASHTO No. 89	Woven geotextile	8
16	Vine Street - GRS-IBS	Ohio (OH)	11.36	50	Reinforced soil foundation	N/A	Woven geotextile	8
17	Glenburg road - GRS-IBS	Ohio (OH)	13.01	30.6	Reinforced soil foundation	N/A	Woven geotextile	8
18	Huber Road - GRS-IBS	Ohio (OH)	16.73	28	Reinforced soil foundation	N/A	Woven geotextile	8
19	Bowman road - GRS-IBS	Ohio (OH)	16.69	79	Reinforced soil foundation	Crushed limestone aggregate	Woven geotextile	8
20	Mount Pleasant Road - GRS-IBS	Pennsylvania (PA)	N/A	N/A	Reinforced soil foundation	AASHTO No. 8 coarse aggregate	Geotextile	8
21	I-84 Echo (Summit County) - GRS-IBS	Utah (UT)	N/A	N/A	Unreinforced foundation on dense granular soil	Road base gravel	Woven geotextile	8
22	GRS-IBS abutment with tunnel	Virginia (VA)	N/A	N/A	Reinforced soil foundation	N/A	Woven geotextile	8
23	TFHRC - NCHRP full-scale- GRS abutment	Virginia (VA)	15.25	N/A	Reinforced concrete foundation	Non-plastic Silty Sand (SP-SM)	Woven geotextile	8
24	TFHRC - GRS abutment	Virginia (VA)	17.71	N/A	Reinforced soil foundation	Well Graded Gravel (GW)	Woven geotextile	8

Note: N/A refers to information not available.

Table 2.3.1c. Type of field instrumentation adopted in GRS-IBS projects

No.	Structure	Location	Instrumentation	Available Collected Data
1	Lake Mamie - GRS-IBS	California (CA)	N/A	Short-term settlement
2	Twin - GRS-IBS	California (CA)	N/A	Short-term settlement
3	Black Hawk - Geosynthetic-reinforced soil abutment	Colorado (CO)	Survey targets and strain gauges	Settlement, lateral movement and strain
4	Havana Yard - Geosynthetic-reinforced soil abutment	Colorado (CO)	Leveling rod and strain gauges	Vertical and horizontal deformations
5	Delaware - GRS-IBS	Delaware (DE)	Inclinometer sensor, piezometer, static and dynamic pressure cell, strain gauge, volumetric water content	N/A
6	Lahaina Bypass Road - GRS-IBS	Hawaii (HI)	Inclinometers, strain gauges, lateral and vertical earth pressure cells	N/A
7	Buchanan County - GRS-IBS	Iowa (IA)	Survey targets, earth pressure cells, contact pressure cells and inclinometer	Vertical and horizontal deformations, vertical stresses and lateral earth pressure
8	Cecil Creek - GRS-IBS	Louisiana (LA)	Magnetic extensometer, inclinometer and survey	Lateral movement, settlement and calculated angular distortion
9	Big Lake - GRS-IBS	Louisiana (LA)	Magnetic extensometer, inclinometer and survey	Lateral movement, settlement and calculated angular distortion
10	Cut off Creek - GRS-IBS	Louisiana (LA)	Magnetic extensometer, inclinometer and survey	Lateral movement, settlement and calculated angular distortion
11	Massachusetts - GRS-IBS	Massachusetts (MA)	Survey targets, earth pressure cells, contact pressure cells, inclinometer and inertial profilometer	N/A
12	Minnesota - GRS-IBS	Minnesota (MN)	AccelArray (SAA), array of optical prisms, earth pressure cells and weather station	Vertical and horizontal deformations, earth pressure and thermal cycle effects

13	Yauco Bridges - GRS-IBS	Puerto Rico (PR)	Strain sensors and load cells	N/A

Note: N/A refers to information not available.

Table 2.3.1c. Type of field instrumentation adopted in GRS-IBS projects (continued)

No.	Structure	Location	Instrumentation	Available Collected Data
14	Defiance County (Tiffin River) - GRS-IBS	Ohio (OH)	Strain gauge and earth pressure cells Electronic Distance Measurement (EDM) and vibrating wire earth pressure cells	Thermally induced strains and lateral pressure Settlement, lateral pressures and calculated angular distortion
15	Vine Street - GRS-IBS	Ohio (OH)	Standard Survey level & rod system	Settlement and calculated angular distortion
16	Glenburg road - GRS-IBS	Ohio (OH)	Standard Survey level & rod system or Electronic Distance Measurement (EDM)	Settlement and calculated angular distortion
17	Huber Road - GRS-IBS	Ohio (OH)	Standard Survey level & rod system	Settlement and calculated angular distortion
18	Bowman road - GRS-IBS	Ohio (OH)	Electronic Distance Measurement (EDM), earth pressure cells and strain gauges	Vertical and horizontal deformations and calculated angular distortion
19	Mount Pleasant Road - GRS-IBS	Pennsylvania (PA)	Survey pole	Settlement
20	I-84 Echo (Summit County) - GRS-IBS	Utah (UT)	Horizontal earth pressure cells, one facing inclinometer, and survey targets	Horizontal movement and lateral stresses
21	GRS-IBS abutment with tunnel	Virginia (VA)	Standard Survey level & rod system	Settlement
22	TFHRC - NCHRP full-scale- GRS-IBS	Virginia (VA)	Potentiometer, linear voltage displacement transducers (LVDT), strain gauges and contact pressure cells	Lateral movement, settlement and strains
23	TFHRC – GRS-IBS abutment	Virginia (VA)	Potentiometer, linear voltage displacement transducers (LVDT) and strain gauges	Vertical and horizontal deformations

Note: N/A refers to information not available.

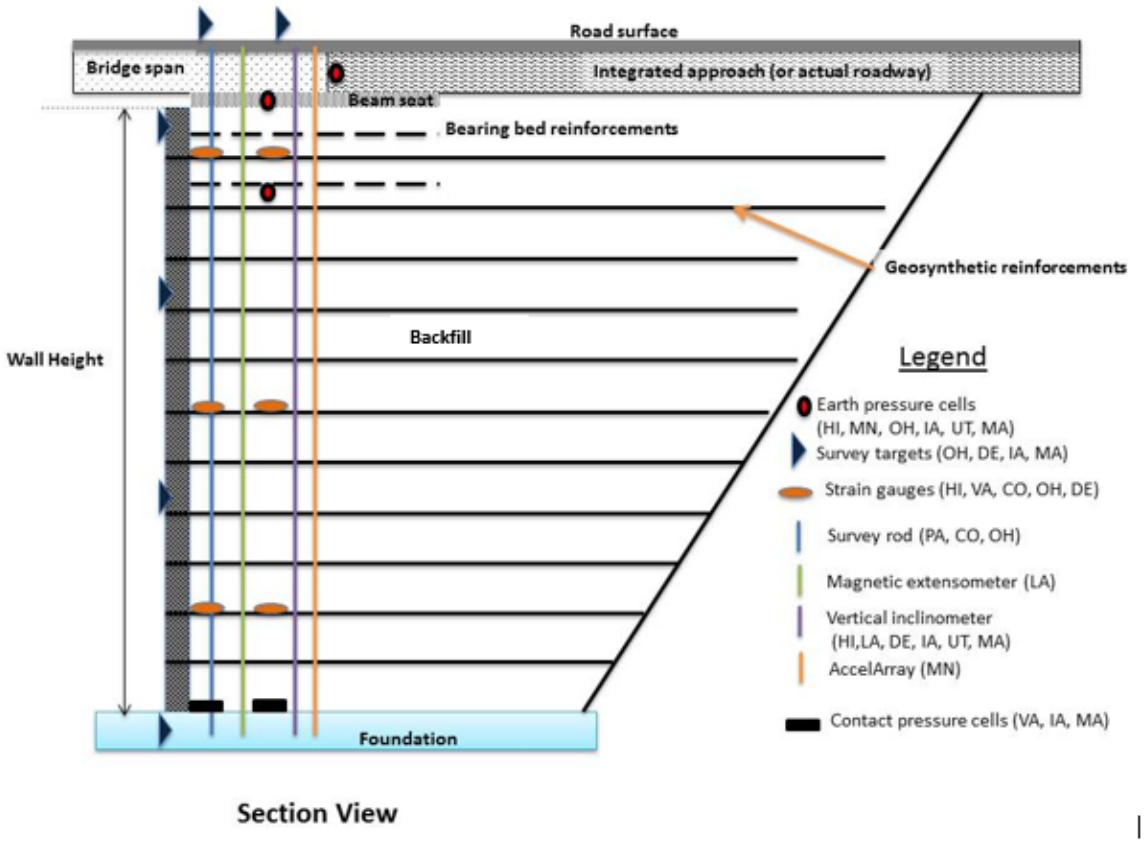

Figure 2.3.1. Generic layout of instrumentation used in GRS-IBS structures

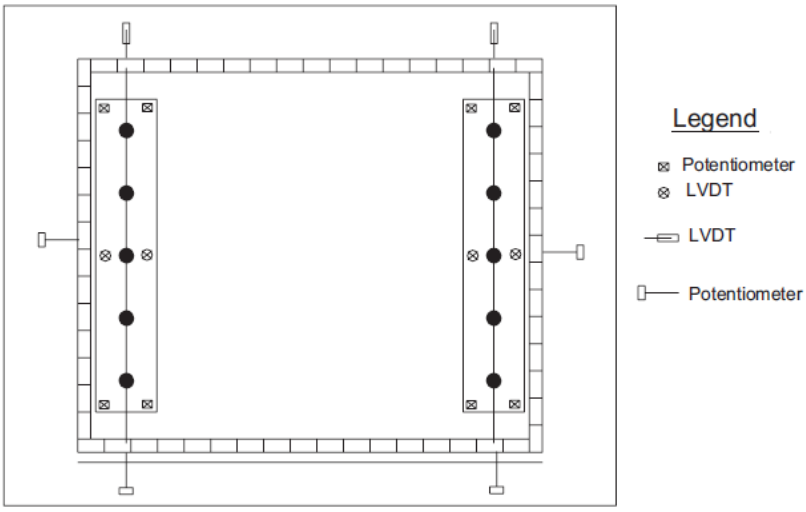

Figure 2.3.2. Plan view of layout out of instrumentation in TFHRC - NCHRP full-scale- GRS abutment Colorado (CO) (Wu et. al. 2006)

Table 2.3.2a. Field instrumented GMSE structures

No.	Structure	Location	Authors	Year of Ref.	Title	Document type
1	Tanque Verde - GMSE wall	Arizona (AZ)	Desai, C.S., and Hoseiny, K.E.E.	2005	Prediction of Field Behavior of Reinforced Soil Wall Using Advanced Constitutive Model	Journal paper
2	Glenwood Canyon - GMSE wall	Colorado (CO)	Wu, J.T.H.	2001	Revising the AASHTO Guidelines for Design and Construction of GRS Walls	Report
3	Founders/Meadow Load-carrying GMSE abutment	Colorado (CO)	Abu-Hejleh, N., Zornberg, J.G., Wang, T., and Watcharamonthein, J.	2002	Monitored Displacements of Unique Geosynthetic-Reinforced Soil Bridge Abutment	Journal paper
			N. Abu-Hejleh, J.G. Zornberg, T. Wang, and J. Watcharamonthein	2001	Monitored Displacements of a Unique Geosynthetic-Reinforced Walls Supporting Bridge and Approaching Roadway Structures	Conference paper
4	Mesa - GMSE wall	Georgia (GA)	Ling, P., and Leshchinsky, D.	1996	Mesa Walls : Field Data Reduction, Finite Element Analysis, and Preliminary Design Recommendations	Report
5	FHWA - Full-scale GMSE test wall 1	Illinois (IL)	Christopher, B. R. (latter reported by Allen, T.M., and Bathurst, R.J.)	1993 2001	Prediction of Soil Reinforcement Loads in Mechanically Stabilized Earth (MSE) Walls	Report
6	FHWA - Full-scale GMSE test wall 2	Illinois (IL)	Christopher, B. R. (latter reported by Allen, T.M., and Bathurst, R.J.)	1993 2001	Prediction of Soil Reinforcement Loads in Mechanically Stabilized Earth (MSE) Walls	Report
7	FHWA - Full-scale GMSE test wall 3	Illinois (IL)	Christopher, B. R. (latter reported by Allen, T.M., and Bathurst, R.J.)	1993 2001	Prediction of Soil Reinforcement Loads in Mechanically Stabilized Earth (MSE) Walls	Report
8	Hybrid GMSE-GRS wall	Kansas (KA)	Han, J., and Jiang Y.	2014	Field Monitoring and Numerical Modeling of Geosynthetic-Reinforced Earth Walls in Kansas	Presentation
9	NCHRP - GMSE wall	Massachusetts (MA)	Stulgis, R.P.	2006	Full-Scale MSE Test Walls	Conference paper
10	TFHRC - Field scale GMSE test wall	Virginia (VA)	Morrison, K. F., Harrison, F. E., Collin J. G., Dodds A., and Arndt B.	2006	Shored Mechanically Stabilized Earth (SMSE) Wall Systems Design Guidelines	Report
11	WSDOT - GMSE wall	Washington (WS)	Allen, T.M., and Bathurst, R.J.	2001	Prediction of Soil Reinforcement Loads in Mechanically Stabilized Earth (MSE) Walls	Report

12	Seattle - GMSE wall	Washington (WS)	Allen, T.M., Christopher, B.R., and Holtz, R.D.	1992	Performance of a 41-Foot High Geotextile Wall	Report
13	New South Wales-GMSE structure	Australia	Wu, J.T.H., Lee, K.Z.Z., Helwany, S.B., and Ketchart, K.	2006	Design and Construction Guidelines for Geosynthetic- Reinforced Soil Bridge Abutments with a Flexible Facing	Report
14	GMSE wall 1	Brazil	Santos, E. C. G., Palmeira, E. M., and Bathurst, R. J.	2014	Performance of Two Geosynthetic Reinforced Walls with Recycled Construction Waste Backfill and Constructed on Collapsible Ground	Journal paper
15	Bairro Novo - GMSE wall	Brazil	Portelinha, F.H.M., Zornberg, J.G., and Pimentel, V.	2014	Field Performance of Retaining Walls Reinforced with Woven and Nonwoven Geotextiles	Journal paper
16	Sao Paulo - GMSE wall	Brazil	Portelinha, F.H.M., Bueno, B.S., and Zornberg, J.G.	2013	Performance of Nonwoven Geotextile-Reinforced Walls Under Wetting Conditions: Laboratory and Field Investigations	Journal paper

Table 2.3.2a. Field instrumented GMSE structures (continued)

No.	Structure	Location	Authors	Year of Ref.	Title	Document type
17	GMSE wall 2	Brazil	Benjamim, C.V.S., Bueno, B.S., and Zornberg, J.G.	2007	Field Monitoring Evaluation of Geotextile-Reinforced Soil-Retaining Walls	Journal paper
18	Full-scale GMSE test wall	Brazil	Bueno, B. S., Benjamim, C.V.S., and Zornberg, J.G	2005	Field Performance of a Full-Scale Retaining Wall Reinforced with Nonwoven Geotextiles	Conference paper
19	London Ontario - GMSE wall	Canada	Allen, T.M., and Bathurst, R.J.	2001	Prediction of Soil Reinforcement Loads in Mechanically Stabilized Earth (MSE) Walls	Report
20	Fredericton New Brunswick - GMSE wall	Canada	Allen, T.M., and Bathurst, R.J.	2001	Prediction of Soil Reinforcement Loads in Mechanically Stabilized Earth (MSE) Walls	Report
21	Full-scale GMSE test wall	Canada	Bathurst, R.J., Walters, D., Vlachopoulos, N., Burgess, P., and Allen, T.M.	2000	Full Scale Testing of Geosynthetic Reinforced Walls	Conference paper
22	Shanghai - GMSE wall	China	Xue, J.F., Chen, J.F., Liu, J.X. a, and Shi, Z.M.	2014	Instability of a Geogrid Reinforced Soil Wall on Thick Soft Shanghai Clay With Prefabricated Vertical Drains: a Case Study	Journal paper
23	Shandong Province - GMSE wall	China	Yang, G., Liu, H., Zhou Y., and Xiong, B.	2014	Post-Construction Performance of a Two-Tiered Geogrid Reinforced Soil Wall Backfilled with Soil-Rock Mixture	Journal paper
24	Bao-Cang - GMSE wall	China	Yang, G., Liu, H.B., Lv, P., and Zhang B.	2012	Geogrid-Reinforced Lime-Treated Cohesive Soil Retaining Wall: Case Study and Implications	Journal paper
25	Ganzhou-Longyan GMSE wall	China	Yang, G., Zhang B., Lv P., and Zhou Q.	2009	Behaviour of Geogrid Reinforced Soil Retaining Wall with Concrete-Rigid Facing	Journal paper
26	Tiroler Ache – GMSE wall	Germany	Brau, G., and Floss, R.	2000	Geotextiles Structures Used for the Reconstruction of the Motorway Munich-Salzburg	Conference paper
27	Ilsenburg- GMSE structure	Germany	Herold, A.	2002	The First Permanent Road-Bridge Abutment in Germany Built of Geosynthetic-Reinforced Earth	Conference paper
28	Vicenza - GMSE wall	Italy	Allen, T.M., and Bathurst, R.J.	2001	Prediction of Soil Reinforcement Loads in Mechanically Stabilized Earth (MSE) Walls	Report

29	Mount Fuji Shizuoka - GMSE wall	Japan	Kongkitkul, W., Tatsuoka, F., Hirakawa, D., Sugimoto, T., Kawahata, S., and Ito, M.	2010	Time Histories of Tensile Force in Geogrid Arranged in Two Full-Scale High Walls	Journal paper
30	Full-scale GMSE test wall	Korea	Yoo, C., and Kim, S.B.	2008	Performance of a Two-Tier Geosynthetic Reinforced Segmental Retaining Wall under a Surcharge Load: Full-Scale Load Test and 3D Finite Element Analysis	Journal paper
31	Segmental GMSE wall	Korea	Yoo, C.	2004	Performance of a 6-Year-Old Geosynthetic Reinforced Segmental Retaining Wall	Journal paper
32	Oslo - GMSE wall	Norway	Allen, T.M., and Bathurst, R.J.	2001	Prediction of Soil Reinforcement Loads in Mechanically Stabilized Earth (MSE) Walls	Report

Note: More detailed citations for the references listed above are provided at the end of this report in the references section.

Table 2.3.2b. Relevant characteristics of field instrumented GMSE structures in the United States

No.	Structure	Location	Wall Height (ft.)	Foundation Information	Backfill Type	Type of Reinforcement	Reinforcement Spacing (in.)
1	Tanque Verde - GMSE wall	Arizona (AZ)	16	Sand	Gravelly-Sand	Geogrid	12 - 35
2	Glenwood Canyon - GMSE wall	Colorado (CO)	15	Weak foundation soil	Well graded Sandy Gravel	Geotextile	9 - 14
3	Founders/Meadow Load carrying GMSE abutment	Colorado (CO)	15	Bedrock	Well graded Gravelly Sand	Geogrid	16
4	Mesa - GMSE wall	Georgia (GA)	23	Sand	Sand	Geogrid	16 - 32
5	FHWA - Full-scale GMSE test wall 1	Illinois (IL)	20	Gravelly-Sand and Sandy-Silt	Gravelly-Sand	Geogrid	30
6	FHWA - Full-scale GMSE test wall 2	Illinois (IL)	20	Gravelly-Sand and Sandy-Silt	Gravelly-Sand	Geogrid	24 - 39
7	FHWA - Full-scale GMSE test wall 3	Illinois (IL)	19	Gravelly-Sand and Sandy-Silt	Gravelly-Sand	Non-woven geotextile	30
8	Hybrid GMSE-GRS wall	Kansas (KA)	45	N/A	Coarse-grained soil	Geogrid	18
9	NCHRP - GMSE wall	Massachusetts (MA)	20	N/A	Silt, Sand and Gravel	Geogrid and geotextile	18
10	WSDOT - GMSE wall	Washington (WS)	39	Gravelly-Sand and Clayey-Silt	Gravelly-Sand	Geogrid	15
11	Seattle - GMSE wall	Washington (WS)	41	Granular materials	Gravelly-Sand	Woven geotextile	15
12	TFHRC - Field scale GMSE test wall	Virginia (VA)	18	Concrete pit	Granular fill	Geogrid	18

Notes: N/A refers to information not available.

If the type of reinforcement is filled as geotextile only, it means that the geotextile is not specified as woven or non-woven in the literature

Table 2.3.2c. Type of field instrumentation in GMSE structures in the United States

No	Structure	Location	Instrumentation	Available Collected Data
1	Tanque Verde - GMSE Wall	Arizona (AZ)	Resistance strain gauge, vertical load cell, inductance coil and resistance thermometer	Vertical and horizontal soil stress, strain and horizontal movement
2	Glenwood Canyon - GMSE wall	Colorado (CO)	Horizontal inclinometer	Settlement
3	Founders/Meadow – Load-carrying GMSE abutment	Colorado (CO)	Survey targets, inclinometer, strain gauges and road profiler	Vertical and horizontal deformations, geosynthetic strain and bridge bump problem
4	Mesa - GMSE wall	Georgia (GA)	Inclinometer and tell-tales (mechanical extensometer)	Horizontal movement and strains
5	FHWA - Full-scale GMSE test wall 1	Illinois (IL)	Strain gauges, inclinometers and magnetic extension gauges, survey targets, earth pressure cells, load cell and thermistors	Vertical and horizontal deformations, local and global strains, stress distribution, vertical force and thermal cycle effects
6	FHWA - Full-scale GMSE test wall 2	Illinois (IL)	Strain gauges, inclinometers and magnetic extension gauges, survey targets, earth pressure cells, load cell and thermistors	Vertical and horizontal deformations, local and global strains, stress distribution, vertical force and thermal cycle effects
7	FHWA - Full-scale GMSE test wall 3	Illinois (IL)	Strain gauges, inclinometers and magnetic extension gauges, survey targets, earth pressure cells, load cell and thermistors	Vertical and horizontal deformations, local and global strains, stress distribution, vertical force and thermal cycle effects
8	Hybrid FMSE-GRS wall	Kansas (KA)	Survey targets, inclinometer and horizontal pressure cells	lateral earth pressure, horizontal movement and strains
9	NCHRP - GMSE wall	Massachusetts (MA)	Piezometer, inclinometer, rod extensometer, strain gauges and settlement rod	Geosynthetic strain
10	WSDOT - GMSE wall	Washington (WS)	Strain gauge and extensometer	Local and global strain
11	Seattle - GMSE wall	Washington (WS)	Bonded resistance strain gauge, mechanical extensometer, earth pressure cell, inclinometer, thermocouple, settlement gauge, inductance coil strain gauge and weather station	Strains, settlement, horizontal movement, deflection and vertical stress
12	TFHRC - Field scale GMSE test wall	Virginia (VA)	Bonded resistance strain gauge, vertical and horizontal earth pressure cells, inclinometer, optical survey, linear variable displacement transducers (LVDT) and potentiometers	Strains, lateral earth pressure, vertical pressure, horizontal displacement, settlement and deflection

Table 2.3.2d. Relevant characteristics of field instrumented GMSE structures outside of the United States

No.	Structure	Location	Wall Height (ft.)	Foundation Information	Backfill Type	Type of Reinforcement	Reinforcement Spacing (in.)
1	New South Wales- GMSE structure	Australia	33	Silty-Sand and Bedrock	Sand	Geogrid	16 - 24
2	GMSE wall 1	Brazil	12	Porous collapsible soil	Recycled construction waste	Geogrid and non-woven geotextile	24
3	Bairro Novo - GMSE wall	Brazil	18	Fine grained soil	Fine-grained soil	Woven and non-woven geotextile	16
4	Sao Paulo - GMSE wall	Brazil	33	N/A	Fine-grained soil	Woven and non-woven geotextile	24
5	GMSE wall 2	Brazil	13	Sand	Sand	Non-woven geotextile	16
6	Full-scale GMSE test wall	Brazil	13	Sand	Sand	Non-woven geotextile	16
7	London Ontario - GMSE wall	Canada	24	Sandy till	Silty-Sand and Gravel	Geogrid	15 - 55
8	Fredericton New Brunswick - GMSE wall	Canada	20	Sandstone	Sand and Gravel	Geogrid	24
9	Full-scale GMSE test wall	Canada	9 - 12	Concrete foundation	Sand with some gravel	Geogrid	24 - 35
10	Shanghai - GMSE wall	China	25	Fill material and Clay	Silty-Clay	Geogrid	20 - 24
11	Shandong Province - GMSE wall	China	56	Rock foundation	Soil-Rock mixture	Geogrid	12 - 24
12	Bao-Cang - GMSE wall	China	20	Stiff foundation	Cohesive soil with 6% lime	Geogrid	16 - 24
13	Ganzhou-Longyan GMSE wall	China	40	Gravel	Rammed Clay and Gravel	Geogrid	16 - 20

14	Tiroler Ache - GMSE wall	Germany	16	Compressible foundation	Sandy-Gravel	Geogrid and non-woven geotextile	N/A
15	Ilsenburg- GMSE structure	Germany	9	Stones and Clay	Recycled concrete	Geogrid	14
16	Vicenza - GMSE wall	Italy	13	Dense foundation	Clayey-Sandy-Gravel	Geogrid	31 - 63
17	Mount Fuji Shizuoka - GMSE wall	Japan	55 - 69	Gravel	Gravel	Geogrid	24 - 47
18	Full-scale GMSE test wall	Korea	18	N/A	Silty Sand	Geogrid	24
19	Segmental GMSE wall	Korea	27 - 32	Granite soil	Poorly graded Sand	Geogrid	15 - 39
20	Oslo - GMSE wall	Norway	26	Gravelly-Sand	Sand	Geogrid	24

Note: N/A refers to information not available.

Table 2.3.2e. Field instrumented GMSE structures outside of the United States

No.	Structure	Location	Instrumentation	Available Collected Data
1	Mount Fuji Shizuoka - GMSE wall	Japan	Settlement gauge, inclinometer, strain gauge, pore water pressure transducer and earth pressure transducer	Settlement, lateral displacement, tensile strain
2	GMSE wall 1	Brazil	Tell-tales, earth pressure cells and inclinometer	Horizontal displacements, vertical and horizontal stresses and strain
3	Bairro Novo - GMSE wall	Brazil	Tell-tales, survey targets and tensiometers	Vertical and horizontal displacements and pore water pressures
4	Sao Paulo - GMSE wall	Brazil	Earth pressure cells and horizontal and vertical magnetic extensometers	Vertical and horizontal stresses and internal displacements
5	GMSE wall 2	Brazil	Mechanical extensometers, surveying and magnetic extensometers	Horizontal displacements and vertical settlement
6	Full-scale GMSE test wall	Brazil	Survey target, vertical magnetic extensometer and tell-tails	Strain and vertical and horizontal displacement
7	London Ontario - GMSE wall	Canada	Strain gauge	Local reinforcement strain
8	Fredericton New Brunswick - GMSE wall	Canada	Strain gauge	Local reinforcement strain
9	Full-scale GMSE test wall	Canada	Potentiometer, earth pressure cell, settlement plate, inductance coil, strain gauge, extensometer and load rings	Deflection, horizontal displacement, strain, horizontal and vertical toe load and connection load
10	Shanghai - GMSE wall	China	Settlement plate, magnetic extensometers, pore water pressure meters and displacement markers	Settlement, excess pore water pressure and horizontal movement
11	Shandong Province - GMSE wall	China	Vertical and horizontal earth pressure cells, strain gauges and total station surveying	Horizontal earth pressures, horizontal displacements and strain
12	Bao-Cang - GMSE wall	China	Flexible displacement sensor, vertical and horizontal earth pressure cells	Strains and vertical and horizontal earth pressures
13	Ganzhou-Longyan GMSE wall	China	Survey target, load cell, inclinometer and flexible sensor	Verttical stress, horizontal earth pressure, strain and horizontal deformation

14	Tiroler Ache - GMSE walls	Germany	Vertical and horizontal extensometers, Bowden cable displacement gauges and earth and pore water pressure transducers	Vertical and horizontal deformations
15	Ilsenburg- GMSE structure	Germany	Earth pressure cells, inclinometer, extensometer and bonded resistance strain gauge	Vertical and horizontal deformations, strain and Vertical and horizontal stresses
16	Vicenza - GMSE wall	Italy	Strain gauge	Local reinforcement strain
17	Mount Fuji Shizuoka - GMSE wall	Japan	Settlement gauge, inclinometer, strain gauge, pore water pressure transducer and earth pressure transducer	Settlement, lateral displacement, tensile strain
18	Full-scale GMSE test wall	Korea	Survey target and strain gauge	Lateral displacement and strains
19	Segmental GMSE wall	Korea	Survey targets	Lateral displacement
20	Oslo - GMSE wall	Norway	Inductance coils	Global strain

2.4 GATHERING OF INFORMATION ON NUMERICAL SIMULATION OF GRS-IBS AND GMSE

Numerical methods, finite element and finite difference methods, have been successfully used to simulate GMSE structures (e.g. Leshchinsky and Vulova 2001; Hatami and Bathurst 2005; and Huang *et al.* 2011 and 2013) and GRS-IBS (e.g. Wu *et al.* 2006b; Pham 2009). Compared with laboratory experiments and field instrumentation, numerical methods have the following two major advantages: (1) obtaining more comprehensive results than laboratory and field tests; (2) investigating the effects of influence factors which are difficult and/or costly to achieve in laboratory and field tests. Literature review of experimental studies and field instrumentation of GRS-IBS and GMSE structures has been presented in the preceding two sections (Sections 2.1 and 2.2). This section will present a review on numerical simulation of GRS-IBS and GMSE structures. The literature associated with the numerical study has been collected from various sources, including journal papers, doctoral dissertations, and research reports published by the industry, states, and the federal government agencies. A list of references for the numerical simulation of GRS-IBS and GMSE structures is provided in Table 2.4.1a.

2.4.1 OVERVIEW OF THE NUMERICAL SIMULATION OF GRS-IBS

Limited numerical studies have been done so far on GRS-IBS. All these studies used the finite element method. Most of the numerical analyses were done in 2D under working or ultimate strength conditions. The GRS-IBS structures analyzed had the following parameters: (1) wall height ranging from 1.9 m (6.2 ft.) to 6.7 m (22.0 ft.), (2) reinforcement length ranging from 1.4 m (4.6 ft.) to 5.0 m (16.7 ft.), (3) reinforcement spacing ranging from 0.2 m (0.7 ft.) to 0.4 m (1.3 ft.), (4) geologic cap or hardening soil model, (5) mostly linearly elastic geosynthetic elements, (6) fully-bonded interface between geosynthetic and soil, (7) use of interface between backfill soil and facing block, and interface between facing blocks, and (8) compressible or incompressible foundation. In all the reviewed GRS-IBS studies, no seismic condition was considered. A brief description of each study is presented below.

The early numerical simulation of GRS-IBS was conducted by Wu *et al.* (2006b). In their study, a finite element code DYNA3D/LS-DYNA was employed to estimate the allowable bearing pressure a bridge can convey to GRS-IBS with flexible facing under static conditions. The numerical analysis used a geologic cap model to capture the dilation and time dependency of the backfill material. The geosynthetic reinforcement was modeled as an elastic material. The bearing capacities based on two criteria were compared and discussed. Moreover, Wu *et al.* (2006b) recommended a bearing capacity for preliminary design.

Helwany *et al.* (2007) used the same finite element code and the same geologic cap soil model as Wu *et al.* (2006b) did to study the performance of load-carrying GMSE bridge abutments. Helwany *et al.* (2007) used an isotropic elastic-plastic model to describe the response of the geosynthetic reinforcement. The vertical and horizontal displacements under different surcharge loading from the numerical modeling were compared with those from the two experimental tests. Additionally, a parametric study was conducted to evaluate the effects of the geosynthetic

spacing, the backfill friction angle, and the geosynthetic stiffness on the performance of the GRS-IBS including the vertical displacement and horizontal displacements at the beam seat, the maximum facing displacement, and the footing distortion. The parametric results showed that the geosynthetic stiffness at 2% strain had a significant effect on the performance of the GRS-IBS, the geosynthetic spacing had a moderate effect, and the fill friction angle had the least effect.

Pham (2009) utilized a 2D finite element software, Plaxis2D, to study the composite behavior of GRS-IBS structures considering the effect of compaction induced stress. In his analysis, the backfill soil was modeled by a hardening soil model that is a hyperbolic model considering elastic-plastic and dilative behavior of soil. A special tension element provided by Plaxis2D was used to simulate the geotextile reinforcement. The interface between geotextile reinforcement and backfill material was assumed fully bonded. Pham's study reached the following key conclusions: (1) the numerical method can simulate the behavior of soil-geosynthetic composites; (2) the soil-geosynthetic composites become strong when the dilation of backfill is restrained by geosynthetic reinforcement; and (3) the numerical model verified the derived analytical solution for the compaction induced stress.

2.4.2 OVERVIEW OF THE NUMERICAL SIMULATION OF GMSE WALLS

More numerical studies have been conducted on GMSE walls than on GRS-IBS. Both the finite element method and the finite difference method have been used. For the finite element method, various programs have been used to model GMSE walls, including CANDE, GEOFEM, AFENA, SSCOMP, M-CANDE, DACSAR, DSC-SST-2D, DYNA3D/LS-DYNA, and Plaxis. However, FLAC is the only finite difference software used to model GMSE walls. Among 22 numerical studies reviewed, 19 studies used 2D models (i.e. plane strain) to simulate GMSE walls, whereas only 3 studies (Huang *et al.* 2011, 2013, and 2014) adopted 3D models to simulate GMSE walls. In the Huang *et al.* (2011, 2013, and 2014) studies, the 3D modeling was necessary because the lateral deformation of the wall resulted from a laterally-loaded pile. The GMSE structures analyzed had the following parameters: (1) wall height ranging from 2.6 m (8.5 ft.) to 12.6 m (42 ft.), (2) reinforcement length ranging from 0.6 m (2 ft.) to 12.0 m (40 ft.), (3) reinforcement spacing ranging from 0.2 m (0.7 ft.) to 1.5 m (5.0 ft.), (4) linearly elastic-perfectly plastic soil model with the Mohr-Coulomb failure criterion, or stress-dependent nonlinear soil model (Duncan-Chang hyperbolic soil model, hardening soil model, or cap-yield soil model), (5) mostly linearly elastic cable, bar, or geosynthetic elements, (6) sliding or fully-bonded interface between geosynthetic and soil, (7) use of interface between facing blocks in most studies, and (8) compressible or incompressible foundation. Further discussion on these parameters is provided below.

Christopher *et al.* (1989a, 1989b), Ling *et al.* (1994), Ho and Rowe (1996), Holtz and Lee (2002), Helwany *et al.* (2003), Ling and Leshchinsky (2003), and Fakharian and Attar (2007) studied the effect of reinforcement length on the performance of GMSE walls. Seven numerical studies (Ho and Rowe 1996, Ling and Leshchinsky 1996, Leshchinsky and Vulova 2001, Rowe and Skinner 2001, Holtz and Lee 2002, Ling and Leshchinsky 2003, and Guler *et al.* 2007) investigated the effect of reinforcement spacing on the performance of GMSE walls and only Leshchinsky and Vulova (2001) reduced the reinforcement spacing to less than 0.3 m (1.0 ft.).

Most GMSE walls have been considered having modular blocks as facing. The facing modular blocks have been mostly modeled as elastic discrete bricks. Retained soil and foundation soil have been modeled as elastic materials or linearly elastic-perfectly plastic materials with the Mohr-Coulomb failure criterion. All researchers recognized the importance of properly modeling the backfill material, the reinforcement, and the interface between backfill soil and reinforcement. The linearly elastic-perfectly plastic soil model with the Mohr-Coulomb failure criterion (commonly referred to as the Mohr-Coulomb model) or the stress dependent nonlinear soil model has been commonly adopted for the backfill. The stress-dependent nonlinear soil models include the Duncan-Chang hyperbolic soil model, the hardening soil model, and the cap yield model. Huang *et al.* (2013 and 2014) found that the cap yield model not only could well describe the nonlinear elastic behavior but also could well capture the plasticity resulting from shear stress and compressive stress. Both the hardening soil model and the cap yield model can consider the dilation of soil between reinforcements. In the numerical modeling of GMSE structures, Hatami and Bathurst (2005) and Guler *et al.* (2007) modeled the compaction-induced stresses by applying a 1.2 psi (8 kPa) distribution pressure on the top of each lift. Mirmoradi and Ehrlich (2014) modeled the compaction-induced stresses by applying a 1.2 psi (8-kPa) distribution stress at the top and bottom of each soil layer. Huang *et al.* (2013 and 2014) simulated the effect of compaction-induced stress by applying additional lateral stress of 1.5 psi (10 kPa) to each lift if a heavy compactor is used or 1.2 psi (8 kPa) if a light compactor is used. The reinforcement has been modeled as linearly elastic structural elements (cable, bar, or geosynthetic elements) in most studies. Nonlinear structural elements were used for reinforcement in few studies. The interface between backfill and reinforcement has been modeled as fully bonded with a tensile rupture strength, rigid plastic with the Mohr-Coulomb failure criterion, and linearly elastic-perfectly plastic with the Mohr-Coulomb failure criterion. Most numerical studies assumed incompressible foundations under GMSE walls but few studies (Christopher *et al.* 1989, Ling and Leshchinsky 1996, Rowe and Skinner 2001, Ling and Leshchinsky 2003, Skinner and Rowe 2005, Fakharian and Attar 2007) simulated compressible foundations under the GMSE walls. Among all the numerical studies on GMSE walls, two studies modeled real spread footings buried in the GMSE walls to support bridge girders while three studies modeled simple spread footings seated on the GMSE walls without any embedment to support simplified vertical and/or horizontal loads.

Table 2.4.1a. Summary of numerical modeling of GRS-IBS and GMSE structures

No.	1	2	3	4	5	6	7
Authors	Christopher et al.	Adib et al.	Ling et al.	Karpurapu and Bathurst	Ho and Rowe	Ling and Leshchinsky	Leshchinsky and Vulova
Year	1989b	1990	1994	1995	1996	1996	2001
Type of structure	GMSE	GMSE	GMSE	GMSE	GMSE	GMSE	GMSE
NM	FEM	FEM	FEM	FEM	FEM	FEM	FDM
Software	SSCOMP	SSCOMP	CANDE	GEOFEM	AFENA	SSCOMP; M-CANDE	FLAC
2D or 3D	2D	2D	2D	2D	2D	2D	2D
H (ft.)	20-40	20.0	16.7	10.0	20.0	22.8	8.5-28.6
L (ft.)	5.5-20.0	14.0	2.0-11.7	10.0	6.0-25	6.7	5.0
S (ft.)	2.5	2.5	1.0	2.5	1.7-5	1.3-2.7	0.7-3.3
Load on wall top	Footing to support bridge	No load	Footing load	Uniform vertical load	No load	Uniform vertical load	No load
Backfill constitutive model	Stress dependent hyperbolic model with MC failure criterion	Stress dependent hyperbolic model with MC failure criterion	Stress dependent hyperbolic model with MC failure criterion	Stress dependent hyperbolic model with MC failure criterion	Nonlinearly elastic and perfectly plastic granular material with MC failure criterion	Stress dependent hyperbolic model with MC failure criterion	MC
RCM	Linearly elastic; bar element	Hyperbolic model	Linearly elastic; bar element	A nonlinear elastic material considering the creep effect	Linearly elastic; bar element	Non linearly elastic; fully bonded	Linearly elastic; cable element
BRI	Hyperbolic model	Hyperbolic model	Fully bonded with tensile rupture strength	Linearly elastic and perfectly plastic with MC failure criterion	Rigid plastic with MC failure criterion	Hyperbolic model with MC failure criterion	Sliding interface with MC failure criterion
BBI	Yes	Not described	No	Yes	Yes	Yes	Yes
BI	No	Not described	Yes	Yes	No	Yes	Yes
CIS	Yes	No	No	No	No	No	No

Foundation type	Incompressible and compressible	Compressible	Incompressible	Incompressible	Incompressible	Compressible	Incompressible
Stress conditions	Working stress	Working stress	Working stress and ultimate strength	Working stress and ultimate strength	Working stress	Working stress	Ultimate strength

Note: NM: Numerical method; FEM: finite element method; FDM: finite difference method; H: wall height; L: reinforcement length; S: reinforcement spacing; BCM: backfill constitutive model; RCM: reinforcement constitutive model; BRI: backfill/reinforcement interface; BBI: Backfill/Block interface; BI: block interface; CIS: compaction-induced stress; LR: long reinforcement; SR: short reinforcement; MC: Mohr-Coulomb.

Table 2.4.1a Summary of numerical modeling of GRS-IBS and GMSE structures (continued)

No.	8	9	10	11	12	13
Authors	Rowe and Skinner	Holtz and Lee	Helwany et al.	Ling and Leshchinsky	Desai and Hoseiny	Skinner and Rowe
Year	2001	2002	2003	2003	2005	2005
Type of structure	GMSE	GMSE	GMSE	GMSE	GMSE	GMSE
NM	FEM	FDM	FEM	FEM	FEM	FEM
Software	AFENA	FLAC	DACSAR	CANDE	DSC-SST-2D	AFENA
2D or 3D	2D	2D	2D	2D	2D	2D
H (ft.)	26.7	12.0-42	21.5	19.0	15.3	20.0
L (ft.)	20 (LR) and 3 (SR)	9.7-33.0	25-40	3.3-16	12.7	13.3
S (ft.)	1.7-3.3	1.3-2.5	1.3	0.5-3.4	1.0-2.0	2.0
Load on wall top	No load	No load	Footing to support bridge	No load	No load	Footing to support bridge
BCM	Nonlinearly elastic and perfectly plastic granular material with MC failure criterion	Stress dependent hyperbolic model with MC failure criterion	Stress dependent hyperbolic model with MC failure criterion	Stress dependent hyperbolic model with MC failure criterion	Disturbed state concept model	Nonlinearly elastic and perfectly plastic model with MC failure criterion
RCM	Linearly elastic; bar element	Linearly elastic; geogrid element	Linearly elastic	Linearly elastic; bar element	Linearly elastic	Linearly elastic; bar element
BRI	Rigid plastic with MC failure criterion	Sliding interface with MC failure criterion	Fully bonded	Fully bonded with tensile rupture strength	Not described	Rigid plastic with MC failure criterion
BBI	Yes	Yes	Yes	Yes	No	Yes
BI	Yes	Yes	Yes	Yes	No	Yes
CIS	No	Yes	No	No	No	No
Foundation type	Compressible	Incompressible	Incompressible	Compressible to incompressible	Incompressible	Compressible

Stress conditions	Working stress and ultimate strength	Working stress	Working stress	Working stress	Working stress	Working stress and ultimate strength

Table 2.4.1a. Summary of numerical modeling of GRS-IBS and GMSE structures (continued)

No.	14	15	16	17	18	19
Authors	Hatami and Bathurst	Hatami and Bathurst	Wu et al.	Helwany et al.	Fakharian and Attar	Guler et al.
Year	2005	2006	2006	2007	2007	2007
Type of structure	GMSE	GMSE	GRS-IBS	GRS-IBS	GMSE	GMSE
NM	FDM	FDM	FEM	FEM	FDM	FEM
Software	FLAC	FLAC	DYNA3D/LS-DYNA	DYNA3D/LS-DYNA	FLAC	Plaxis
2D or 3D	2D	2D	2D	2D and 3D	2D	2D
H (ft.)	12.0	12.0	15.6	15.5	19.3	12.0
L (ft.)	8.4	8.4	16.7	10.5	24.0-40.0	8.4
S (ft.)	2.0	2.0	0.7	0.7	1.3	2.0-3.0
Load on wall top	No load	Uniform vertical load	Footing to support bridge	Footing to support bridge	Footing to support bridge	No load
BCM	Stress dependent hyperbolic model with MC failure criterion	Stress dependent hyperbolic model with MC failure criterion	Geologic cap model	Geologic cap model	Stress dependent hyperbolic model with MC failure criterion	Hardening soil model
RCM	Hyperbolic model considering load-strain-time for PP geogrids; cable element	Hyperbolic model with load-strain-time for PP geogrids; and linearly elastic-perfectly plastic for PET geogrids cable element	Linearly elastic	Isotropic elastic-plastic considering linear strain hardening and material failure	Elasto-plastic; cable elements	Linearly elastic; geosynthetic element
BRI	Fully bonded	Fully bonded	Not described	Fully bonded	Not described	Not described
BBI	Yes	Yes	Not described	Yes	Yes	Yes
BI	Yes	Yes	Not described	Yes	Yes	Yes
CIS	Yes	Yes	No	No	No	Yes
Foundation type	Incompressible	Incompressible	Compressible	Compressible	Compressible	Incompressible

Stress conditions	Working stress	Working stress	Working stress and ultimate strength	Working stress and ultimate strength	Working stress	Working stress

Table 2.4.1a. Summary of numerical modeling of GRS-IBS and GMSE structures (continued)

No.	20	21	22	23	24	25	26
Authors	Pham	Huang et al.	Huang et al.	Huang et al.	Wu et al.	Mirmoradi and Ehrlich	Huang et al.
Year	2009	2009	2011	2013	2013	2014	2014
Type of structure	GRS-IBS	GMSE	GMSE	GMSE	GRS-IBS	GMSE	GMSE
NM	FEM	FDM	FDM	FDM	FEM	FEM	FDM
Software	Plaxis	FLAC	FLAC	FLAC	Plaxis	Plaxis	FLAC
2D or 3D	2D	2D	3D	3D	2D	2D	3D
H (ft.)	6.5	12.0	20.0	20.0	6.5	13.3	20.0
L (ft.)	4.6	8.4	14.0	14.0	4.6	9.3	14.0
S (ft.)	0.7-1.3	2.0	2.0	2.0	0.7-1.3	1.3	2.0
Load on wall top	Uniform vertical load (Pier)	Uniform vertical load	Lateral load	Lateral load	Uniform vertical load (Pier)	No load	Lateral load
BCM	Hardening soil model	MC, Modified Duncan-Chang hyperbolic model, and Lade's Model	MC	Cap yield model	Hardening soil model	Hardening soil model	Cap yield soil model
RCM	Linearly elastic; geosynthetic element	Hyperbolic model with load-strain-time for PP geogrids; cable element	Linearly elastic; geogrid element	Linearly elastic; geogrid element	Linearly elastic; geosynthetic element	Linearly elastic; geosynthetic element	Linearly elastic; geogrid element
BRI	Fully bonded	Sliding interface with MC failure criterion	Sliding interface with MC failure criterion	Sliding interface with MC failure criterion	Fully bonded	Fully bonded	Sliding interface with MC failure criterion
BBI	Not described	Yes	No	No	Not described	Yes	No
BI	Yes	Yes	No	Yes	Yes	Yes	Yes
CIS	Yes	Yes	No	Yes	Yes	Yes	Yes

Foundation type	Incompressible	Incompressible	Incompressible	Incompressible	Incompressible	Incompressible	Incompressible
Stress conditions	Working stress	Working stress	Working stress	Working stress	Working stress	Working stress	Working stress

2.5 GATHERING OF INFORMATION ON DESIGN METHODOLOGIES

This section of the Final Report provides the philosophy for the design procedure and implementation of GMSE and GRS-IBS structures. In doing so, background is provided on previous design guidelines and procedures.

Wu (2001) proposed four revisions to the AASHTO guidelines regarding the design and construction of GMSE structures (AASHTO, 1996). The proposed revisions included: (1) lateral earth pressure on wall facing was proposed to be simulated by a "bin pressure" diagram on the wall facing of segmental GMSE structures instead of the Rankine active earth pressure, (2) cumulated long-term reduction factor was proposed, which depends on backfill type and placement conditions, reinforcement spacing, and polymer type of the reinforcement, (3) truncated reinforcement length at wall base was proposed where excavation is needed as it is impractical to have full design length reinforcement. Yet, the external stability has to be checked when truncated base is adopted, and (4) embedment depth (measured from the leveling pad to the grade in front of the wall) is not necessary for GMSE structures. A large number of GMSE structures was reported to show good performance with zero to 0.20 m (8 in.) embedment. A leveling pad of compacted gravel or road base material is proposed to be used under the first facing blocks course to facilitate construction. Wu (2001) summarized the noted issues associated with each of the four aspects in the AASHTO guidelines along with the proposed revision for every aspect. In addition, the limitations and practical implications concerned with the proposed revisions were included and discussed.

Allen *et al.* (2005) included description of methodologies to determine load and resistance factors for geotechnical and structural design. This reference comprehensively documents: (1) the basic reliability concepts, (2) detailed procedures used to characterize data and develop the statistics and functions needed for reliability analysis, (3) detailed step-by-step examples, (4) practical considerations when statistical data are limited, and (5) description on how load and resistance factors are developed along with cases where new load and resistance factors must be developed, or not directly applicable. Allen *et al.* (2005) included closed-form solutions for estimating load and resistance factors used for simple cases, as well as more rigorous probabilistic analysis methods (e.g. Monte Carlo method). In addition, they provided procedures for situations where either single or multiple loads must be considered.

Bathurst *et al.* (2012a) reviewed the conventional approach of the limit state determination for geosynthetic reinforcement tensile rupture. They proposed a reliability-based analysis framework suitable for LRFD calibration using bias statistics. A significant database was compiled to examine the results of in-air tensile tests and creep-rupture data points along with results of creep tests from 21 different sources. This data was used to compute virgin and creep-reduced strength bias statistics for different geosynthetic product categories. The results of analysis showed that the variability in the creep-reduced strength prediction is very low. In addition, the results implied that that creep strength reduction factors could be taken as deterministic in the LRFD design. The study also provided a summary of computed creep-reduction factors to help estimating this factor from laboratory creep testing and for preliminary design purposes. As a follow up to this study, Bathurst *et al.* (2012b) and Huang *et al.* (2012) reported the results of LRFD calibration for the pullout limit state in geogrid reinforced soil walls. Bathurst *et al.* (2012b) showed that the current AASHTO simplified method is overly conservative in reinforcement load determination under operational conditions. This, in turn,

was reported to lead to poor prediction accuracy of the underlying deterministic model used in LRFD calibration. Bathurst *et al.* (2012b) and Huang *et al.* (2012) proposed refinements to the load and pullout capacity models and design charts in the AASHTO and FHWA guidance documents for load predictions and estimation of the pullout resistance factor. In addition, a comparison between LRFD and ASD (AASHTO simplified method) showed that the operational factors of safety using a reliability-based LRFD approach give the same or higher factors of safety and lower probabilities of failure. Bathurst *et al.* (2012b) showed that the current empirical minimum reinforcement length criteria will likely control the design for pullout.

While some relevant projects have been constructed involving GRS-IBS approaches outside the U.S., the design has not been formalized in the form of design guidelines. Some literature has been identified that addresses the design practice in other countries. For example, Martins (2000) provided an evaluation of the conceptual design and construction methods adopted in three highway projects in the state of Minas Gerais, Brazil. These projects include bridge abutments in one project and reinforced embankments in the other two projects. The author analyzed the projects according to the original design premises. The author then repeated the analysis based on more realistic design criteria considering adopted soil strength parameters, reinforcement strength, soil-reinforcement interaction, design methodology, and construction process.

2.6 REFERENCES

American Association of State Highway and Transportation Officials (AASHTO). (1996). Standard specifications for highway bridges, 16th Ed., Washington, D.C.

Abdelouhab, A., Dias, D., and Freitag, N. (2010). "Physical and Analytical Modelling of Geosynthetic Strip Pull-Out Behaviour." Geotextiles and Geomembranes, Vol. 28, No. 1, pp. 44–53.

Abdel-Rahman, A.H., Ibrahim, M.A., and Ashmawy, A.K. (2007). "Utilization of a Large-Scale Testing Apparatus in Investigating and Formulating the Soil/Geogrid Interface Characteristics in Reinforced Soils." Australian Journal of Basic and Applied Sciences, Vol. 1, No. 4, pp. 415-430.

Abernathy, C. (2013). "Experimental Projects Construction Report - Geosynthetic Reinforced Soil - Integrated Bridge System (GRS-IBS)." Report No. MT-12-04, Montana Department of Transportation, Montana, November 2013, 26 p.

Abernathy, C. (2014). "Montana DOT Rebuilds an Old Bridge with a New System." Geosynthetics, Vol. 32, No. 2.

Abu-Hejleh, N., Outcalt, S., Wang, T., and Zornberg, J.G. (2000a). "Performance of Geosynthetic-Reinforced Structures Supporting the Founders/Meadows Bridge and Approaching Roadway Structure. Report 1: Design, Materials, Construction, Instrumentation, and Preliminary Results." Report No. CDOT-DTD-R-00-5, Colorado Department of Transportation, Denver, Colorado, June 2000, 97 p.

Abu-Hejleh, N., Wang, T., and Zornberg, J.G. (2000b). "Performance of Geosynthetic-Reinforced Walls Supporting Bridge and Approaching Roadway Structures." Advances in Transportation and Geoenvironmental Systems using Geosynthetics, Denver, Colorado, August, ASCE Geotechnical Special Publication No. 103, Zornberg, J.G. and Christopher, B.R. (Editors), pp. 218-243.

Abu-Hejleh, N., Zornberg, J.G., and Wang, T. (2001a). "Monitored Displacements of a Unique Geosynthetic-Reinforced Walls Supporting Bridge and Approaching Roadway Structures."

Proceedings of the 80th Annual Meeting, Transportation Research Board, 07-11 January, Washington, D.C. (CD-ROM).

Abu-Hejleh, N., Zornberg, J.G., Wang, T., and Watcharamonthein, J. (2002). "Monitored Displacements of Unique Geosynthetic-Reinforced Soil Bridge Abutment." Geosynthetics International, Vol. 9, No. 1, pp. 71-95.

Abu-Hejleh, N., Zornberg, J.G., Wang, T., McMullen, M., and Outcalt, W. (2001b). "Performance of Geosynthetic-Reinforced Walls Supporting the Founders/Meadows Bridge and Approaching Roadway Structures. Report 2: Assessment of the Performance and Design of the Front GRS Walls and Recommendations for Future GRS Abutments." Report No. CDOT-DTD-R-2001-12, Colorado Department of Transportation, Colorado, October, 145 p.

Adams, M.T., and Saunders, S.A. (2007). "Upper Ouachita National Wildlife Refuge GRS Abutments for Replacement Bridges." Presentation by Adams, M., and Saunders, S.A., FHWA.

Adams, M.T. (1997). "Performance of a Prestrained Geosynthetic-Reinforced Soil Bridge Pier." International Symposium on Mechanically Stabilized Backfill, Wu, J.T.H. (ed), Denver, USA, Balkema, pp. 35-53.

Adams, M.T., Nicks, J.E., Stabile, T., Wu, J.T.H., Schlatter, W., and Hartmann, J. (2012). "Geosynthetic Reinforced Soil Integrated Bridge System Interim Implementation Guide." Report No. FHWA-HRT-11-026, Federal Highway Administration, McLean, VA.

Adams, M.T., Nicks, J.E., Stabile, T., Wu, J.T.H., Schlatter, W., and Hartmann, J. (2011). "Geosynthetic Reinforced Soil Integrated Bridge System, Synthesis Report." Report No. FHWA-HRT-11-027, Federal Highway Administration, McLean, VA.

Adams, M.T., Schlatter, W., and Stabile, T. (2011). "Geosynthetic Reinforced Soil Integrated Bridge System." EuroGeo4 Paper number 271.

Adams, M.T., Schlatter, W., and Stabile, T. (2007). "Geosynthetic Reinforced Soil Integrated Abutments at the Bowman Road Bridge in Defiance County, Ohio." Proceedings of Geo-Denver, 2007, pp. 01-11.

Adib, M., Mitchell, J.K., and Christopher, B. (1990). "Finite Element Modeling of Reinforced Soil Walls and Embankments." Geotechnical Special Publication (GSP), No. 25, pp. 409-423.

Ahmed, M.R. and Meguid, M.A. (2009). "Patents and Techniques of Contact Pressure Measurement in Geotechnical Engineering." Recent Patents on Engineering, Vol. 3, pp. 210-219.

Alagiyawanna, A.M.N., Sugimoto, M., Sato, S., and Toyota, H. (2001). "Influence of Longitudinal and Transverse Members on Geogrid Pullout Behavior during Deformation." Geotextiles and Geomembranes, Vol. 19, No. 8, pp. 483–507.

Alfaro, M.C., Hayashi, S., Miura, N., and Watanabe, K. (1995a). "Pullout Interaction Mechanism of Geogrid Strip Reinforcement." Geosynthetics International, Vol. 2, No. 4, pp. 679-698.

Alfaro, M.C., Miura, N., and Bergado, D.T. (1995b). "SoiI-Geogrid Reinforcement Interaction by Pullout and Direct Shear Tests." Geotechnical Testing Journal, GTJODJ, Vol. 18, No. 2, pp. 157-167.

Allen, T. M., Nowak, A. S., and Bathurst, R. J. (2005). "Transportation Research Circular E-C079: Calibration to Determine Load and Resistance Factors for Geotechnical and Structural Design." Transportation Research Board of the National Academies, Washington, D.C., 83 p.

Allen, T.M., and Bathurst, R.J. (2001). "Prediction of Soil Reinforcement Loads in Mechanically Stabilized Earth (MSE) Walls." Report No. WA-RD 522.1, Washington Department of Transportation, Washington, 2001.

Allen, T.M., Christopher, B.R., and Holtz, R.D. (1992). "Performance of a 41-Foot High Geotextile Wall." Report No. WA-RD 257.1, Washington Department of Transportation, Washington, 1992.

Allersma, H. (1982). "Photoelastic Investigation of the Stress Distribution During Penetration." Proceedings of the 2nd European Symposium on Penetration Testing, Amsterdam, May 24–27, ESOPT-II, Netherlands, pp. 79–83.

ASTM D6706-01 (2013). "Standard Test Method for Measuring Geosynthetic Pullout Resistance in Soil." ASTM Standards, American Society for Testing and Materials (ASTM), West Conshohocken, Pennsylvania.

Aydilek, A.H., Oguz, A.H., and Edil, T.B. (2002). "Digital Image Analysis to Determine Pore Opening Size Distribution of Nonwoven Geotextiles." Journal of Computing in Civil Engineering, Vol. 16, No. 4, pp. 280-290.

Aydogmus, T. and Klapperich, H. (2008). "Design and Evaluation of an Enhanced Shear and Pull-Out Testing Device." Proceedings of the 4th European Geosynthetics Conference, paper 170.

Baecher, G.B. and Christian, J.T. (2003). "Reliability and Statistics in Geotechnical Engineering." John Wiley and Sons.

Bathurst, R.J., Huang, B. and Allen, T.M. (2012a). "LRFD calibration of the ultimate pullout limit state for geogrid reinforced soil retaining walls." ASCE International Journal of Geomechanics, Special Issue on Geosynthetics, Vol. 12, No. 4, pp. 399-413.

Bathurst, R.J., Huang, B., and Allen, T.M. (2012b). "Interpretation of laboratory creep testing for reliability-based analysis and load and resistance factor design (LRFD) calibration." Geosynthetics International, Vol. 19, No. 1, pp. 39-53.

Bathurst, R.J., Walters, D., Vlachopoulos, N., Burgess, P., and Allen, T.M. (2000). "Full Scale Testing of Geosynthetic Reinforced Walls." ASCE Special Publication, Proceedings of GeoDenver 2000.

Benjamim, C.V.S., Bueno, B.S., and Zornberg, J.G. (2007). "Field Monitoring Evaluation of Geotextile-Reinforced Soil-Retaining Walls." Geosynthetics International, April, Vol. 14, No. 2, pp. 100-118.

Berg, R.R., Christopher, B.R. and Samtani, N.C. (2009). "Design and Construction of Mechanically Stabilized Earth Walls and Reinforced Soil Slopes." FHWA NHI-10-024 Vol I and NHI-10-025 Vol II, U.S. DOTFHWA-NHI-09-083 and FHWA GEC-011, Federal Highway Administration, Washington, D.C., 2009, pp 306 (Vol I) and pp. 378 (Vol II).

Bergado, D.T. and Chai, J.-C. (1994). "Pullout Force/Displacement Relationship of Extensible Grid Reinforcements." Geotextiles and Geomembranes, Vol.13, No.5, pp. 295-316.

Bergado, D.T. and Teerawattanasuk, C. (2001). "Analytical Models for Predicting the Pullout Capacity and Interaction Between Hexagonal Wire Mesh and Silty Sand Backfill." Tamakang Journal of Science and Engineering, Vol. 4, No. 4, pp. 227-238.

Bernal, A., Salgado, R., Swan Jr., R.H., and Lovell C.W. (1997). "Interaction between Tire Shreds, Rubber-Sand and Geosynthetics." Geosynthetics International, Vol. 4, No. 6, pp. 623-643.

Bloser, S., Shearer, D., Corradini, K., and Scheetz, B. (2012). "Geosynthetically Reinforced Soil-Integrated Bridge Systems (GRS-IBS) Specification Development for PennDOT Publication 447." Publication No. 447 (10-14), Pennsylvania Department of Transportation.

Bose, P. (1993). "Experimental Study of Strain Field Around a Geogrid Under Tension." MS. Thesis, University of Delaware, Newark, DE.

Brand, S.R. and Duffy, D.M. (1987). "Strength of Pull-Out Testing of Geogrids." Proceedings of Geosynthetics 1987, Vol. 1, New Orleans, LA, pp. 226-236.

Brau, G. and Floss, R. (2000). "Geotextile Structures used for the Reconstruction of the Motorway Munich-Salzburg." Proceedings of Second European Geosynthetics Conference, Bologna, Italy, Vol. 1, pp. 373-377.

Budge, A., Dasenbrock, D., Mattison, D., Bryant, G., Grosser, A., Adams, M., and Nicks, J. (2014). "Instrumentation and Early Performance of a Large Grade GRS-IBS Wall." Geo-Congress 2014, Geo-characterization and Modeling for Sustainability, ASCE.

Bueno, B. S., Benjamim, C.V.S., and Zornberg, J.G (2005). "Field Performance of a Full-Scale Retaining Wall Reinforced with Nonwoven Geotextiles." Slopes and Retaining Structures Under Seismic and Static Conditions, 2005, pp. 1-9.

Chang, J.C., Hannon, J.B., and Forsyth, R.A. (1977). "Pullout Resistance and Interaction of Earthwork Reinforcement and Soil." Transportation Research Record 640, National Research Council, Washington, DC, pp. 1-7.

Christopher, B.R. (1993). "Deformation Response and Wall Stiffness in Relation to Reinforced Soil Wall Design." Ph.D. Dissertation, Department of Civil Engineering, Purdue University, West Lafayette, IN, 354 p.

Christopher, B.R. (2013). "Review of June 18, 2013 GRS-IBS Showcase at Clarkson University, Potsdam, New York and St. Lawrence County Wall Visits." Memorandum by Christopher, B.R.

Christopher, B.R., Gill, S.A., Giroud, J.P., Juran, I. Scholsser, F., Mitchell, J.K., and Dunnicliff, J. (1989a). "Reinforced Soil Structures, Volume I. Design and Construction Guidelines and Volume II. Summary of Research and Systems Information." Report No. FHWA-RD-89-043, Federal Highway Administration, Washington DC, November 1989, 287 p.

Christopher, B.R., Gill, S.A., Giroud, J.P., Juran, I., Mitchell, J.K., Schlossser, F., and Dunnicliff, J. (1989b). "Reinforced Soil Structures Volume II. Summary of Research and Systems Information." Report No. FHWA-RD-89-043, Federal Highway Administration, Washington DC, November 1989, 158 p.

Colletta, B., Letouzey, J., Pinedo, R., Ballard, J.F., and Bale, P. (1991). "Computerized X-ray Tomography Analysis of Sandbox Models: Examples of Thin-Skinned Thrust Systems." Geology, Vol. 19, pp. 1063–1067.

Costa, C.M.L., Zornberg, J.G., and Costa, Y.D.J. (2014). "Failure of Geotextile-Reinforced Walls under Sustained Loading using Centrifuge Modeling." Advanced Materials Research, Vol. 831, pp. 3121-325.

Cuelho, E.V. (1998). "Determination of Geosynthetic Constitutive Parameters and Soil/Geosynthetic Interactions by In-Air and In-Soil Experiments." MS Thesis, Montana State University, MT.

D'Appolonia Consulting Engineers (2007). "LRFD Calibration of Coherent Gravity Method for Metallically Stabilized Earth Walls." Association for Metallically Stabilized Earth, http://www.amsewalls.org.

Desai, C.S., and Hoseiny, K.E.E. (2005). "Prediction of Field Behavior of Reinforced Soil Wall Using Advanced Constitutive Model." Journal of Geotechnical and Geoenvironmental Engineering, ASCE, Vol. 131, No. 6, pp. 729-739.

Desrues, J., Chambon, R., Mokni, M., and Mazerolle, F. (1996). "Void Ratio Evolution Inside Shear Bands in Triaxial Sand Specimens Studied by Computed Tomography." Géotechnique, Vol. 46, No. 3, pp. 529–546.

Dove, J.E. and Frost, J.D. (1996). "A Method for Measuring Geomembrane Surface Roughness." Geosynthetics International, Vol. 3, No. 3, pp. 369–392.

Dove, J.E., and Frost, J.D. (1999). "Peak Friction Behavior of Smooth Geomembrane-Particle Interfaces." Journal of Geotechnical and Geoenvironmental Engineering, ASCE, Vol. 125, No. 7, pp. 544–555.

Drescher, A. (1976). "An Experimental Investigation of Flow Rules for Granular Materials using Optically Sensitive Glass Particles." Geotechnique, Vol. 26, No. 4, pp. 591–601.

Dyer, M.R. (1985). "Observation of the Stress Distribution in Crushed Glass with Applications to Soil Reinforcement." Ph.D. Thesis, The University of Oxford, UK.

Edil, T.B., Benson, C.H., Bin-Shafique, M.S., Tanyu, B.F., Kim, W.H., and Senol, A. (2002). "Field Evaluation of Construction Alternatives for Roadway Over Soft Subgrade." Transportation Research Record, Vol. 1786, pp. 36-48.

Elias, V. (1979). "Friction in Reinforced Earth Utilizing Fine Grained Backfills." International Conference on Soil Reinforcement, Paris, France, pp. 435-8.

Ezzein, F.M. and Bathurst, R. (2011a). "A Transparent Sand for Geotechnical Laboratory Modeling." Geotechnical Testing Journal, Vol. 34, No. 6, pp. 1–12.

Ezzein, F.M. and Bathurst, R. (2011b). "Development of a Geosynthetic Pullout Test Apparatus with Transparent Granular Soil." Proceedings 2011 Pan-American Canadian Geotechnical Society Geotechnical Conference, Toronto, Canada, 6p.

Fakharian, K. and Attar, I.H. (2007). "Static and seismic numerical modeling of geosynthetic-reinforced soil segmental bridge abutments." Geosynthetics International, Vol. 14, No. 4, pp. 228-243.

Fannin, R.J. and Raju, D.M. (1993). "On the Pullout Resistance of Geosynthetics." Canadian Geotechnical Journal, Vol. 30, No. 3, pp. 409-417.

Farrag, K., Acar, Y.B., and Juran, I. (1993). "Pull-Out Resistance of Geogrid Reinforcements." Geotextiles and Geomembranes, Vol. 12, No. 2, pp. 133-159.

FHWA (2014). "Yauco Bridges PR-2 Km 20.5 Instrumentation." FHWA Presentation, Sent by Alzamora, D., Federal Highway Administration.

Frost, J.D. and Kuo, C.-Y. (1996). "Automated Determination of the Distribution of Local Void Ratio from Digital Images." ASTM Geotechnical Testing Journal, Vol. 19, No. 2, pp. 107–117.

Gill, D.R. and Lehane, B.M. (2001). "An Optical Technique for Investigating Soil Displacement Patterns." Geotechnical Testing Journal, Vol. 24, No. 3, pp. 324–329.

GRI Test Methods (1991). "GRI GT6 Geotextile Pullout." GRI.

Guler, E. and Selek, O. (2014). "Reduced-Scale Shaking Table Tests on Geosynthetic-Reinforced Soil Walls with Modular Facing." Journal of Geotechnical and Geoenvironmental Engineering, Vol. 140, No. 6.

Guler, E., Hamderi, M., and Demirkan, M. M. (2007). "Numerical Analysis of Reinforced Soil-Retaining Wall Structures with Cohesive and Granular Backfills." Geosynthetics International, Vol. 14, No. 6, pp. 330-345.

Gustafsson, L. and Knutsson, S. (1994). "An Image Analysis Method for Studying Movement in Granular and Solid Bodies." ASTM Geotechnical Testing Journal, Vol. 17, No. 1, pp. 95–100.

Han, J. and Jiang Y. (2014). "Field Monitoring and Numerical Modeling of Geosynthetic-Reinforced Earth Walls in Kansas." Presentation by Han, J., and Jiang Y.

Hanumasagar, S.S., Roodi, G.H., and Zornberg, J.G. (2014). "Pullout Characterization of Geogrids Embedded in Blends of Dredged Material and Steel Slag Fines." 10th ICG Conference, Berlin, Germany.

Hatami, K. and Bathurst, R.J. (2006). "Numerical Model for Reinforced Soil Segmental Walls under Surcharge Loading." Journal of Geotechnical and Geoenvironmental Engineering, ASCE, Vol. 132, No. 6, pp. 673-684.

Hatami, K. and Bathurst, R.J. (2005). "Development and Verification of a Numerical Model for the Analysis of Geosynthetic-Reinforced Soil Segmental Walls under Working Stress Conditions." Canadian Geotechnical Journal,Vol. 42, No. 4, pp. 1066-1085.

Helwany, S.M.B., Wu, J.T.H., and Froessl, B. (2003). "GRS Bridge Abutments-an Effective Means to Alleviate Bridge Approach Settlement." Geotextiles and Geomembranes, Vol. 21, pp. 177-196.

Helwany, S.M.B., Wu, J.T.H., and Kitsabunnarat, A. (2007). "Simulating the Behavior of GRS Bridge Abutments." Journal of Geotechnical and Geoenvironmental Engineering, ASCE, Vol. 133, No. 10, pp. 1229-1240.

Helwany, S.M.B., Wu, J.T.H. et al. (2012). “Seismic Design of Geosynthetic Reinforced Soil Abutments”. Web document Report 187, National Cooperative Highway Research Program, Washington D.C. (January 2012).

Herold, A. (2002). "The First Permanent Road-Bridge Abutment in Germany Built of Geosynthetic-Reinforced Earth." 7th International Conference on Geosynthetics, Nice, France.

Hird, C.C. and Stanier, S.A. (2010). "Modelling Helical Screw Piles in Clay using a Transparent Soil." Proceedings of the 7th International Conference on Physical Modelling in Geotechnics, Zurich, International Society for Soil Mechanics and Geotechnical Engineering, Jun 28–July 1, Switzerland, p. 6.

Ho, S.K. and Rowe, R.K. (1996). "Effect of Wall Geometry on the Behaviour of Reinforced Soil Walls." Geotextiles and Geomembranes, Vol. 14, pp. 521-541.

Holtz, R.D. and Lee, W.F. (2002). "Internal Stability Analyses of Geosynthetic Reinforced Retaining Walls." Report No. WA-RD 532.1, Washington State Department of Transportation, January, 379 p.

Huang, B.Q., Bathurst, R.J., and Allen, T.M. (2012). "Load and resistance factor design (LRFD) Calibration for Steel Strip Reinforced Soil Salls." ASCE Journal of Geotechnical and Geoenvironmental Engineering, Vol. 138, No. 8, pp. 922-933.

Huang, B.Q., Bathurst, R.J., and Hatami, K. (2009). "Numerical Study of Reinforced Soil Segmental Walls Using Three Different Constitutive Soil Models." Journal of Geotechnical and Geoenvironmental Engineering, ASCE, Vol. 135, No. 10, pp. 1486-1498.

Huang, J., Bin-Shafique, S., Han, J., and Rahman, M.S. (2014). "Modelling of Laterally Loaded Drilled Shaft Group in Mechanically Stabilised Earth Wall." Proceedings of the ICE-Geotechnical Engineering, Vol. 167, No. 4, pp. 402-414.

Huang, J., Han, J., Parsons, R.L., and Pierson, M. (2013). "Refined Numerical Mmodeling of a Laterally-loaded Drilled Shaft in an MSE Wall." Geotextiles and Geomembranes, Vol. 37, pp. 61-73.

Huang, J., Parsons, R.L., Han, J., and Pierson, M.C. (2011). "Numerical Analysis of a Laterally Loaded Shaft Constructed Within an MSE Wall." Geotextiles and Geomembranes, Vol. 29, pp. 233-241.

Ingold, T.S. (1983). "A Laboratory Investigation of Grid Reinforcements in Clay." Geotechnical Testing Journal, Vol. 6, No. 3, pp. 112-119.

Iskander, M. (1998). "Transparent Soils to Image 3D Flow and Deformation." Proceedings of the 2nd International Conference on Imaging Technologies: Techniques and Applications in Civil Engineering, Davos, Switzerland, May 25–30, 1997, ASCE, New York, pp. 255–264.

Iskander, M. and Liu, J. (2010). "Spatial Deformation Measurement Using Transparent Soil." Geotechnical Testing Journal, Vol. 33, No. 4, pp.1–8.

Iskander, M., Lai, J., Oswald, C., and Mannheimer, R. (1994). "Development of a Transparent Material to Model the Geotechnical Properties of Soils." Geotechnical Testing Journal, Vol. 17, No. 4, pp. 425–433.

Iskander, M., Liu, J., and Sadek, S. (2002a). "Transparent Amorphous Silica to Model Clay." Journal of Geotechnical and Geoenvironmental Engineering, Vol. 128, No. 3, pp. 262–273.

Iskander, M., Liu, J., and Sadek, S. (2003). "Modeling 3D Flow and Soil Structure Interaction using Optical Tomography." Final Report, NSF Project No. CMS 9733064, p. 280.

Iskander, M., Sadek, S., and Liu, J. (2002b). "Optical Measurement of Deformation using Transparent Silica Gel to Model Sand." International Journal of Physical Modelling in Geotechnics, Vol. 2, No. 4, pp. 13–26.

Iskander, M.G. (2010). "Modelling with Transparent Soils: Visualizing Soil Structure Interaction and Multi Phase Flow, Non-Intrusively." Springer.

Iwamoto, M.K., Ooi, P.S.K., Adams, M.T., and Nicks, J.E. (2013). "Composite Properties from Instrumented Load Tests on Soil Columns Reinforced with Geotextiles." Transportation Research Broad, TRB 2014 Annual Meeting.

Jaber, M.B. (1989). "Behavior of Reinforced Soil Walls in Centrifuge Model Tests." Doctoral Thesis submitted to University of California, Berkeley, California, 303 p.

Jacobs, F., Ruiken, A., and Ziegler, M. (2012a). "Experimental Investigation of Geogrid Reinforced Soil Under Plane Strain Conditions." Geosynthetics Asia 2012, 5th Asian Regional Conference on Geosynthetics, 10 to 14 December 2012, Bangkok, Thailand.

Jacobs, F., Ruiken, A., and Ziegler, M. (2012b). "Investigation of Geogrid Reinforced Soil with Large Scale “Element” Testing." GeoAmericas 2012, Lima, Perú, May 2012.

Jacobs, F., Ziegler, M., and Ruiken, A. (2013). "Experimental Investigation of the Stress-Strain Behaviour of Geogrid Reinforced Soil." GeoAfrica 2013, Accra, Ghana, 18–20 November 2013.

Jang, D.J. and Frost, D.J. (1998). "Sand Structure Differences Resulting from Specimen Preparation Procedures." ASCE Geotechnichal Special Publication no. 75, Geotechnical Earthquake Engineering and Soil Dynamics III, Dakuolas, Yegian, and Holtz (eds.), Seattle, Vol.1, pp. 234–245.

Jang, D.J., Frost, J.D., and Park, J.K. (1999). "Preparation of Epoxy Impregnated Sand Coupons for Image Analysis." ASTM Geotechnical Testing Journal, Vol. 22, No. 2, pp. 147–158.

Jayawickrama, P.W., Lawson, W.D., Wood, T.A., and Surles, J.G. (2014). "Pullout Behavior of Welded Grid Reinforcements Embedded in Coarse Granular Backfill." Geo-Congress, Atlanta, GA, February 2014.

Jewell, R.A. (1980). "Some Effects of Reinforcement on the Mechanical Behavior of Soils." Dissertation, Cambridge University, Cambridge, UK.

Juran, I., Guermazi, A., Chen, C.L., and Ider, M.H. (1988). "Modelling and Simulation of Load Transfer in Reinforced Soil: Part 1." International Journal for Numerical and Analytical Methods in Geomechanics, Vol. 12, No. 2, pp. 141-155.

Karpurapu, R. and Bathurst, R.J. (1995). "Behaviour of Geosynthetic Reinforced Soil Retaining Walls Using the Finite Element Method." Computers and Geotechnics, Vol. 17, pp. 279-299.

Kemeny, J.M., Devgan, A., Hagaman, R.M., and Wu, X. (1993). "Analysis of Rock Fragmentation Using Digital Image Processing." Journal of Geotechnical Engineering, Vol. 119, No. 7, pp. 1144–1160.

Ketchart, K. and Wu, J.T.H. (1996). "Long-Term Performance Tests of Soil-Geosynthetic Composites." Report No. CDOT-CTI-96-1, Colorado Department of Transportation, Denver, CO.

Ketchart, K. and Wu, J.T.H. (2002). "A Modified Soil-Geosynthetic Interactive Performance Test for Evaluating Deformation Behavior of GRS Structures." ASTM International, Vol. 25, No. 4, pp. 405-413.

Ketchart, K., and Wu, J.T.H. (2001). "Performance Test for Geosynthetic-Reinforced Soil Including Effects of Preloading." Report No. FHWA-RD-01-118, Federal Highway Administration, McLean, VA.

Kharchafi, M. and Dysli, M. (1993). "Study of Soil-Geotextile Interaction by an X-Ray Method." Geotextiles and Geomembranes, Vol. 12, No. 4, pp. 307-325.

Kim, W.H., Edil, T.B., Benson, C.H, and Tanyu, B.F. (2005). "Structural Contribution of Geosynthetic-Reinforced Working Platforms in Flexible Pavement." Transportation Research Record, Vol. 1936, pp. 43-50.

Kim, W.H., Edil, T.B., Benson, C.H, and Tanyu, B.F. (2006). "Deflection of Prototype Geosynthetic-Reinforced Working Platforms Over Soft Subgrade." Transportation Research Record, Vol. 1975, pp. 137-145.

Kniss, K.T., Wright, S.G., Zornberg, J.G., and Yang, K.H. (2007). "Design Considerations for MSE Retaining Walls Constructed in Confined Spaces." Report No. 0-5506-1, Center for Transportation Research (CTR), Austin, Texas, October 2007.

Koerner, R.M. (2005). "Designing with Geosynthetics, Fifth Edition." Pearson Prentice Hall.

Koerner, R.M. (1986). "Direct Shear/Pull-Out Tests on Geogrids." Report No. 1, Departement of Civil Engineering, Drexel University, Philadelphia, PA.

Kongkitkul, W., Tatsuoka, F., Hirakawa, D., Sugimoto, T., Kawahata, S., and Ito, M. (2010). "Time Histories of Tensile Force in Geogrid Arranged in Two Full-Scale High Walls." Geosynthetics International, Vol. 17, No. 1, pp. 12-32.

Kuo, C.-Y. and Frost, J.D. (1996). "Uniformity Evaluation of Cohesionless Specimens Using Digital Image Analysis." Journal of Geotechnical Engineering, Vol. 122, No. 5, pp. 390–396.

Kutay, M.E., Guler, M., and Aydilek, A.H. (2006). "Analysis of Factors Affecting Strain Distribution in Geosynthetics." Journal of Geotechnical and Geoenvironmental Engineering, Vol. 132, No. 1, pp. 1-11.

Ladeira, M.A.S.A. (1995). "Estudo dos Fenômenos de Interação Solo-Geossintetico Através de Ensaios de Arranque." (In Portuguese) MS Thesis, University of Porto, Portugal.

Lee, K.Z.Z., and Wu, J.T.H. (2004). "A Synthesis of Case Histories on GRS Bridge Supporting Structures with Flexible Facing." Geotextiles and Geomembranes, Vol. 22, No. 4, pp. 181-204.

Lees, A. (2014). "Measurement of the Geogrid Confining Effect." 10th International Conference on Geosynthetics (10th ICG), Berlin, Germany.

Leshchinsky, D. and Vulova, C. (2001). "Numerical Investigation of the Effects of Geosynthetic Spacing on Failure Mechanisms of MSE Block Walls." Geosynthetics International, Vol. 8, No. 4, pp. 343-365.

Leshchinsky, D., Kaliakin, V., Bose, P., and Collin, J. (1994). "Failure Mechanism in Geogrid-Reinforced Segmental Walls: Experimental Implications." Soils and Foundations, Vol. 34, No. 4, pp. 33-41.

Leung, S.K., Kry, P.R., and Wong, R.C.K. (1995). "Visualization of Deformation in Unconsolidated Athabasca Oil Sand." Proceedings of the International Heavy Oil Symposium, Calgary, Alberta, Canada.

Liang, L., Saada, A., Figueroa, J.L., and Cope, C.T. (1997). "The Use of Digital Image Processing in Monitoring Shear Band Development." ASTM Geotechnical Testing Journal, GTJODJ, Vol. 20, No. 3, September, pp. 324–339.

Ling, H.I. and Leshchinsky, D. (2003). "Finite Element Parametric Study of the Behavior of Segmental Block Reinforced-Soil Retaining Walls." Geosynthetics International, Vol. 10, No. 3, pp. 77-94.

Ling, H.I., Tatsuoka, F., and Tateyama, M. (1994). "Simulating Performance of GRS-RW by Finite-Element Procedure." Journal of Geotechnical Engineering, ASCE, Vol. 121, No. 4, pp. 330-340.

Ling, P. and Leshchinsky, D. (1996). "Mesa Walls: Field Data Reduction, Finite Element Analysis, and Preliminary Design Recommendations." Report to Tensar Earth Technologies, Inc., Atlanta, GA, February 1.

Liu, J., Iskander, M., and Sadek, S. (2003). "Consolidation and Permeability of Transparent Amorphous Silica." Geotechnical Testing Journal, Vol. 26, No. 4, pp. 390–401.

Lopes, M.L. (1992). "Walls Reinforced with Geosynthetics." (In Portuguese) Ph.D. Thesis, University of Porto, Portugal, 335 p.

Lopes, M.L. and Ladeira, M. (1996). "Role of Specimen Geometry, Soil Height and Sleeve Length on the Pull-Out Behaviour of Geogrids." Geosynthetic International, Vol. 3, No. 6, pp. 701-719.

Mannheimer, R. and Oswald, C. (1993). "Development of Transparent Porous Media with Permeabilities and Porosities Comparable to Soils, Aquifers, and Petroleum Reservoirs." Ground Water, Vol. 31, No. 5, pp. 781–788.

Marques, J.M.M.C. (2005). "Finite Element Modelling of the Pull-Out Test of Geosynthetics." VIII International Conference on Computation Plasticity, E. Onate and D.R. Owen (eds.).

Martins, C.C. (2000). "Análise e Reavaliação de Estruturas em Solos Reforcados com Geotexteis." Dissertação, Universidade Federal de Ouro Preto, Escola de Minas, Departamento de Engenharia Civil.

McKelvey, D., Sivakumar, V., Bell, A., and Graham, J. (2004). "Modeling Vibrated Stone Columns in Soft Clay." Proceedings of the Institution of Civil Engineers: Geotechnical Engineering 157, Issue GE3, pp. 137–149.

Meyer, N., Nernheim, A., and Emersleben, A. (2003). "Influence of Confining Pressure, Soil Density and Types of Geogrids on Soil-Geogrid Interaction Coefficient." E-Conference "Modern Trends in Foundation Engineering: Geotechnical Challenges and Solutions", IITM, India.

Min, Y., Leshchinsky, D., Ling, H.I., and Kaliakin, V.N. (1995). "Effects of Sustained and Repeated Tensile Loads on Geogrid Embedded in Sand." Geotechnical Testing Journal, Vol. 18, No. 2, pp. 204-225.

Minažek, K. and Mulabdić, M. (2013). "A Review of Soil and Reinforcement Interaction Testing in Reinforced Soil by Pullout Test." Građevinar 2013, Vol. 65, No. 3, pp. 235-250.

Mirmoradi, S.H., and Ehrlich, M. (2014). "Numerical Evaluation of the Behavior of GRS Walls with Segmental Block Facing under Working Stress Conditions." Journal of Geotechnical Engineering, ASCE.

Mora, C.F., Kwan, A.K.H., and Chan, H.C. (1998). "Particle Size Distribution Analysis of Coarse Aggregate Using Digital Image Processing." Cement and Concrete Research, Vol. 28, No. 6, pp. 921–932.

Moraci, N. and Gioffre, D. (2006). "A Simple Method to Evaluate the Pullout Resistance of Embedded in a Compacted Granular Soil Extruded Geogrids." Geotextiles and Geomembranes, Vol. 24, No. 2, pp. 116–128.

Moraci, N. and Recalcati, P. (2006). "Factors Affecting the Pullout Behaviour of Extruded Geogrids Embedded in a Compacted Granular Soil." Geotextiles and Geomembranes, Vol. 24, No. 4, pp. 220–242.

Morrison, K. F., Harrison, F. E., Collin J. G., Dodds A., and Arndt B. (2006). "Shored Mechanically Stabilized Earth (SMSE) Wall Systems Design Guidelines." Report No. FHWA-CFL/TD-06-001, Federal Highway Administration.

Munoz, H., Tatsuoka, F., Hirakawa, D., Nishikiori, H., Soma, R., Tateyama, M., and Watanabe, K. (2012). "Dynamic Stability of Geosynthetic-Reinforced Soil Integral Bridge." Geosynthetics International, Vol. 19, No. 1, pp. 11–38.

Myles, B. (1982). "Assessment of Soil Fabric Friction by Means of Shear Evaluation." Proceedings of 2nd International Conference, Las Vegas, Nevada, Vol. 3, pp. 787-791.

Nicks, J.E., Adams, M.T., and Stabile, T. (2013a). "Performance Testing for Geosynthetic Reinforced Soil Composites." Proceedings of the 5th International Young Geotechnical Engineers' Conference.

Nicks, J.E., Adams, M.T., Ooi, P.S.K., and Stabile, T. (2013b). "Geosynthetic Reinforced Soil Performance Testing—Axial Load Deformation Relationships." Report No. FHWA-HRT-13-066, Federal Highway Administration, McLean, VA.

Obaidat, M.T., Al-Masaeid, H.R., Gharaybeh, F., and Khedaywi, T.S. (1998). "An Innovative Digital Image Analysis Approach to Quantify the Percentage of Voids in Mineral Aggregates of Bituminous Mixtures." Canadian Journal of Civil Engineering, Vol. 25, pp. 1041-1049.

Ochiai, H., Otani, J., Hayashic, S., and Hirai, T. (1996). "The Pull-Out Resistance of Geogrids in Reinforced Soil." Geotextiles and Geomembranes, Vol. 14, No. 1, pp. 19-42.

Ooi., P. (2014). "Field Instrumentation of GRS-IBS in Hawaii." Conference Call with Ooi., P.

Otani, J., Miyamoto, K., and Mukunoki, T. (2001). "Visualization of Interaction Behavior Between Soil and Reinforcement Using X-ray CT." Proceedings of Landmarks in Earth Reinforcement, Ochiai, H., Otani, J., Yasufuku, N., Omine, K (editors), A.A. Balkema, Tokyo, Japan, Vol. 1, pp. 117–120.

Palmeira, E.M. (1987). "The Study of Soil-Reinforcement Interaction by Means of Large Scale Laboratory Tests." Ph.D. Thesis, The University of Oxford, UK.

Palmeira, E.M. (2009). "Soil-Geosynthetic Interaction: Modelling and Analysis." Geotextiles and Geomembranes, Vol. 27, No. 5, pp. 368–390.

Palmeira, E.M. and Milligan, G.W.E. (1989). "Scale and Other Factors Affecting the Results of Pull-Out Tests of Grids Buried in Sand." Geotechnique, Vol. 39, No. 3, pp. 511-524.

Pan, B., Qian, K., Xie, H., and Asundi, A. (2009). "Two-Dimensional Digital Image Correlation for In-plane Displacement and Strain Measurement: A Review." Measurement Science and Technology, Vol. 20, No. 6, 17 p.

Pham, T.Q. (2009). "Investigating Composite Behavior of Geosynthetic reinforced Soil (GRS) Mass." Ph.D. Thesis, The University of Colorado at Denver, 358 p.

Pierson, M.C., Parsons, R.L., Han, J., and Brennan, J.J. (2011). "Laterally Loaded Shaft Group Capacities and Deflections behind an MSE Wall." Journal of Geotechnical and Geoenvironmental Engineering, ASCE. Reston, Virginia, Vol. 137, No. 10, pp. 882-889.

Portelinha, F.H.M., Bueno, B.S., and Zornberg, J.G. (2013). "Performance of Nonwoven Geotextile-Reinforced Walls Under Wetting Conditions: Laboratory and Field Investigations." Geosynthetics International, Vol. 20, No. 2, pp. 90-104.

Portelinha, F.H.M., Zornberg, J.G., and Pimentel, V. (2014). "Field Performance of Retaining Walls Reinforced with Woven and Nonwoven Geotextiles." Geosynthetics International, Vol. 21, No. 4, pp. 270-284.

Pötzl, M. (2007). "Jointless Concrete Bridges – Development of a Flexible Abutment." IABSE Symposium Report, IABSE Symposium, Weimar, Germany 2007, pp. 40-46(7).

Raffel M., Willert, C., and Kompenhans, J. (2007). "Particle Image Velocimetry: A Practical Guide." Springer, Berlin.

Raghunathan, D., Sadasivam, S., and Mallela, J. (2014). "Geosynthetic Reinforced Soil Integrated Bridge System on I-84 near Salt Lake City." Draft Report, Federal Highway Adminstration.

Raschke, S.A., Hryciw, R.D., and Donohoe, G.W. (1996). "Micro-Deformations in Sands by Digital Image Processing and Analysis." Transportation Research Record 1548, pp. 31–37.

Rowe, R.K. and Ho, S.K. (1986). "Determination of Geotextile Stress-Strain Characteristics Using a Wide Strip Test." Proceedings of the 3rd International Conference on Geotextiles, Vol. 3, Vienna, Austria, April 1986, pp. 885-890.

Rowe, R.K., and Skinner, G.D. (2001). "Numerical Analysis of Geosynthetic Reinforced Retaining Wall Constructed on a Layered Soil Foundation." Geotextiles and Geomembranes, Vol. 19, No. 7, pp. 387-412.

Ruiken, A. and Ziegler, M. (2009). "Large Scale Laboratory Element Testing of Geogrid Reinforced Soil." GIGSA GeoAfrica 2009 Conference, 2 - 5 September 2009, Cape Town, South Africa.

Ruiken, A., Jacobs, F., and Ziegler, M. (2012). "Large Scale Biaxial Compression Testing of Geogrid Reinforced Soil." 5th European Geosynthetics Congress, Valencia, 2012.

Ruiken, A., Ziegler, M., Vollmert, L., and Höhny, S. (2011). "Investigation of the Compound Behavior of Geogrid Reinforced Soil." XV. ECSMGE, Athens, Greece.

Sadek, S., Iskander, M., and Liu, J. (2002). "Geotechnical Properties of Transparent Silica." Canadian Geotechnical Journal, Vol. 39, No. 1, pp. 111–124.

Sadek, S., Iskander, M.G., and Liu, J. (2003). "Accuracy of Digital Image Correlation for Measuring Deformations in Transparent Media." Journal of Computing in Civil Engineering, Vol. 17, No. 2, pp. 88-96.

Santos, E.C.G., Palmeira, E.M., and Bathurst, R.J. (2014). "Performance of Two Geosynthetic Reinforced Walls with Recycled Construction Waste Backfill and Constructed on Collapsible Ground." Geosynthetics International, Vol. 21, No. 4, pp. 256-269.

Saxena, S.K. and Budiman, J.S. (1985). "Interface Response of Geotextiles." Proceedings of the 11th International Conference on Soil Mechanics and Foundation Engineering.

Shi, B., Murakami, Y., Wu, Z., Chen, J., and Inyang, H. (1999). "Monitoring of Internal Failure Evolution in Soils Using Computerization X-ray Tomography." Eng. Geol. (Amsterdam), Vol. 54, No. 3-4, pp. 321-328.

Skinner, G.D., and Rowe, R.K. (2005). "Design and Behaviour of a Geosynthetic Reinforced Retaining Wall and Bridge Abutment on a Yielding Foundation." Geotextiles and Geomembranes, Vol. 23, pp. 234-260.

Song, Z., Hu, Y., O'Loughlin, C., and Randolph, M.F. (2009). "Loss in Anchor Embedment During Plate Anchor Keying in Clay." Journal of Geotechnical and Geoenvironmental Engineering, Vol. 135, No. 10, pp. 1475–1485.

Stadler, A.T. (2001). "Geogrid Reinforcement of Piedmont Residual Soil." Report No. HWY-2001-02, North Carolina Department of Transportation, Raleigh, NC.

Stulgis, R.P. (2006). "Full-Scale MSE Test Walls." Proceedings of the 19th Geosynthetic Research Institute Conference, 2005.

Talebi, M., Meehan, C.L., Cacciola, D.V., and Becker, M.L. (2014). "Design and Construction of a Geosynthetic Reinforced Soil Integrated Bridge System." Geo-Congress 2014, Geo-characterization and Modeling for Sustainability, ASCE.

Tatsuoka, F., Uchimura, T., and Tateyama, M. (1997) "Preloaded and Presetressed Reinforced Soil," Soils and Foundations, Vol. 37, No. 3, pp. 79-94.

Tatsuoka, F., Hirakawa, D., Nojiri, M., Aizawa, H., Nizhikioro, H., Soma, R., Tateyama, M., and Watanabe, K. (2009) "A New Type of Integral Bridge Comprising Geosynthetic-Reinforced Soil Walls," Geosynthetics International, Vol. 16, No. 4, pp. 301-326.

Tatsuoka, F., Munoz, H., Kuroda, T., Nishikiori, H., Soma, R., Kiyota, T., Tateyama, M., and Watanabe, K. (2012). "Stability of Existing Bridges Improved by Structural Integration and Nailing." Soils and Foundations, Vol. 52, No. 3, pp. 430-448.

Technical Committee CEN/TC 189 (2004). "EN 13738 Geotextiles and Geotextile-Related Products - Determination of Pullout Resistance in Soil." European Committee for Standardization, Technical Committee CEN/TC 189, Brussels, Beligum.

Teixeira, S.H.C. (2003). "Estudo da Interação Solo-Geogrelha em Testes de Arrancamento e a sua Aplicação na Análise e Dimensionamento de Maciços Reforçados." Tese apresentada a Escola de Engenharia de São Carlos, da Universidade de São Paulo, São Carlos.

TFHRC (2013). "Instrumentation and Monitoring Program on GRS-IBS." FHWA Presentation, Sent by Alzamora, D., Federal Highway Administration.

The American Association of State Highway and Transportation Officials (2014). "AASHTO LRFD Bridge Design Specifications." Seventh Edition, 2014.

Thomas, T.W., White, T.D., and Kuczek, T. (1994). "Siliceous Content Determination of Sands Using Automatic Image Analysis." Transportation Research Record 1437, pp. 51-58.

Tzong, W.H. and Cheng-Kuang, S. (1987). "Soil-Geotextile Interaction Mechanism in Pullout Test." Proceedings of Geosynthetics 1987, Vol. 1, New Orleans, LA, pp. 250-259.

Vennapusa, P., White, D. J., Klaiber, F.W., Wang, S., and Gieselman, H. (2012). "Geosynthetic Reinforced Soil for Low-Volume Bridge Abutments." Report No. IHRB Project TR-621, Iowa Department of Transportation, Ames, IA, January 2012.

Vulova, C. (2000). "Effects of Geosynthetic Reinforcement Spacing on the Performance of MSE Walls." MS Thesis, University of Delaware, Newark, DE.

Vulova, C. and Leshchinsky, D. (2003). "Effects of Geosynthetic Reinforcement Spacing on The Behavior of Mechanically Stabilized Earth Walls." Report No. FHWA-RD-03-048, Federal Highway Administration, McLean, VA.

Wakabayashi, T. (1950). "Photo-Elastic Method for Determination of Stress in Powdered Mass." Journal of the Physical Society of Japan, Vol. 5, No. 5, pp. 383-385.

Walters, D.A. (1995). "Fracturing in Oil Sands." M.Sc. thesis, Department of Civil Engineering, The University of Calgary, Calgary, Alberta, Canada.

Warren, K.A., Whelan, M.J., Hite J., and Adams M. (2014). "Three Year Evaluation of Thermally Induced Strain and Corresponding Lateral End Pressures for a GRS IBS in Ohio." Geo-Congress 2014, Geo-characterization and Modeling for Sustainability, ASCE.

White, D.J., Take, W.A., and Bolton, M.D. (2003). "Soil Deformation Measurement Using Particle Image Velocimetry (PIV) and Photogrammetry." Geotechnique, Vol. 53, No. 7, pp. 619–631.

Wibowo, R. (1996). "Bioremediation and Fracturing in Soil." M.Sc. thesis, Department of Civil Engineering, The University of Calgary, Calgary, Alberta, Canada.

Wichter, L., Risseeuw, P., and Gay, G. (1986). "Large-Scale Test on the Bearing Behaviour of a Woven-Reinforced Earth Wall." 3rd International Conference on Geotextiles, Vienna, Austria.

Williams, N.D. and Houlihan, M.F. (1987). "Evaluation of Interface Friction Properties between Geosynthetics and Soils." Proceedings of Geosynthetics 1987, Vol. 2, New Orleans, LA, pp. 616-627.

Wong, R. (1999). "Mobilized Strength Components of Athabasca Oil Sand in Triaxial Compression." Canadian Geotechnical Journal, Vol. 36, No. 4, pp. 718-735.

Woodruff, R., and Zornberg, J.G. (2003). "Centrifuge Modeling for MSE-Shoring Composite Walls." Geotechnical Research Report, December, 109 p.

Wu, J. T. H. (1994). “Design and Construction of Low Cost Retaining Walls: The Next Generation in Technology.” Rep. CTI-UCD-1-94, Colorado Transportation Institute, Denver.

Wu, J., Pham, T.Q., and Adams, M. (2010). "Composite Behavior of Geosynthetic-Reinforced Soil (GRS) Mass." Report No. FHWA-HRT-10-077, Federal Highway Administration, McLean, VA.

Wu, J.T.H. (2001). "Revising the AASHTO Guidelines for Design and Construction of GRS Walls." Report No. CDOT-DTD-R-2001-16, Colorado Department of Transportation, 148 p.

Wu, J.T.H. and Adams, M.T. (2007). "Myth and Fact on Long-Term Creep of GRS Structures." GSP 165 Geosynthetics in Reinforcement and Hydraulic Applications, pp. 1-12.

Wu, J.T.H. and Helwany, S.M.B. (1996). "A Performance Test for Assessment of Long-Term Creep Behavior of Soil-Geosynthetic Composites." Geosynthetic International, Vol. 3, No. 1, pp. 107-124.

Wu, J.T.H. and Pham, T.Q. (2013). "Load-Carrying Capacity and Required Reinforcement Strength of Closely Spaced Soil-Geosynthetic Composites." Journal of Geotechnical and Geoenvironmental Engineering, Vol. 139, No. 9, pp. 1468–1476.

Wu, J.T.H. and Pham, T.Q. (2014). "Closure to “Load-Carrying Capacity and Required Reinforcement Strength of Closely Spaced Soil Geosynthetic Composites”." Journal of Geotechnical and Geoenvironmental Engineering.

Wu, J.T.H., Ketchart, K., and Adams, M.T. (2001). "GRS Bridge Piers and Abutments." Report No. FHWA-RD-00-038, Federal Highway Administration, McLean, VA.

Wu, J.T.H., Ketchart, K., and Adams, M.T. (2001). "GRS Piers and Abutments." Report No. FHWA-RD-00-038, Federal Highway Administration, McLean, VA.

Wu, J.T.H., Lee, K.Z.Z., Helwany, S.B., and Ketchart, K. (2006a). "Design and Construction Guidelines for Geosynthetic-Reinforced Soil Bridge Abutments with a Flexible Facing." Report No. 556, National Cooperative Highway Research Program, Washington, DC..

Wu, J.T.H., Lee, K.Z.Z., and Pham, T. (2006b). "Allowable Bearing Pressures of Bridge Sills on GRS Abutments with Flexible Facing." Journal of Geotechnical and Geoenvironmental Engineering, ASCE, Vol. 132, No. 7, pp. 830-841.

Wu, J.T.H., Pham, T.Q., and Adams, M.T. (2013). "Composite Behavior of Geosynthetic Reinforced Soil Mass." Report No. FHWA-HRT-10-077, Federal Highway Administration, McLean, VA.

Xue, J.F., Chen, J.F., Liu, J.X., and Shi, Z.M. (2014). "Instability of a Geogrid Reinforced Soil Wall on Thick Soft Shanghai Clay with Prefabricated Vertical Drains: a Case Study." Geotextiles and Geomembranes, Vol. 42, pp. 302-311.

Yang, G., Liu, H., Lv P., and Zhang, B. (2012). "Geogrid-Reinforced Lime-Treated Cohesive Soil Retaining Wall: Case Study and Implications." Geotextiles and Geomembranes, Vol. 35, pp. 112-118.

Yang, G., Liu, H., Zhou Y., and Xiong, B. (2014). "Post-Construction Performance of a Two-Tiered Geogrid Reinforced Soil Wall Backfilled with Soil-Rock Mixture." Geotextiles and Geomembranes, Vol.42, No. 2, pp. 91-97.

Yang, K.H., Ching, J-Y., and Zornberg, J.G. (2011). "Reliability-Based Design for External Stability of Narrow Mechanically Stabilized Walls: Calibration from Centrifuge Tests." Journal of Geotechnical and Geoenvironmental Engineering, ASCE, Vol. 137, No.3, March, pp. 239-253.

Yang, K.-H., Zornberg, J.G., and Wright, S.G. (2008). "Numerical Modeling of Narrow MSE Walls with Extensible Reinforcements." Center for Transportation Research (CTR), Report No. 0-5506-2, Austin, Texas, February 2008.

Yang, G., Zhang B., Lv P., and Zhou, Q. (2009). "Behaviour of Geogrid Reinforced Soil Retaining Wall with Concrete-Rigid Facing." Journal of Geotextiles and Geomembranes, Vol. 27, Issue 5, pp. 350-356.

Yang, X., Han, J., Leshchinsky, D., and Parsons, R.L. (2013). "A three-dimensional mechanistic-empirical model for geocell-reinforced unpaved roads." Acta Geotechnica, Vol. 8, No. 2, pp. 201-213.

Yoo, C. (2004). "Performance of a 6-Year-Old Geosynthetic Reinforced Segmental Retaining Wall." Geotextiles and Geomembranes, Vol. 22, pp. 377-397.

Yoo, C., and Kim, S.B. (2008). "Performance of a Two-Tier Geosynthetic Reinforced Segmental Retaining Wall under a Surcharge Load: Full-Scale Load Test and 3D Finite Element Analysis." Geotextiles and Geomembranes, Vol. 26, pp. 460-472.

Yuan, Z. and Chua, K.M. (1991). "Numerical Evaluation of the Pullout Box Method for Studying Soil-Reinforcement Interaction." Transportation Research Record 1278, Transportation Research Board, Washington, D.C., pp. 116-124.

Zhao, H. and Ge, L. (2007). "Camera Calibration Using Neural Networks for Image-Based Soil Deformation Measurement Systems." Geotechnical Testing Journal, Vol. 31, No. 2, pp. 1-6.

Zhou, J., Chen, Chen, J.-F., Xue, J.-F., and Wang, J.-Q. (2012). "Micro-Mechanism of the Interaction between Sand and Geogrid Transverse Ribs." Geosynthetics International, 2012, Vol. 19, No. 6, pp. 1072-6349.

Ziegler, M. (2011). "Interaction of Soil Reinforcement as Key Issue for Ground Reinforcement." Invited Lecture. XV. ECSMGE, Athens, Greece.

Zornberg, J.G. and Arriaga, F. (2003). "Strain Distribution within Geosynthetic-Reinforced Slopes." Journal of Geotechnical and Geoenvironmental Engineering, ASCE, Vol. 129, No. 1, pp. 32-45.

Zornberg, J.G., Abu-Hejleh, N., and Wang, T. (2001). "Geosynthetic-Reinforced Soil Bridge Abutments." Geotechnical Fabrics Report, Vol. 19, No. 2, March, pp. 52-55.

Zornberg, J.G., Barrows, R.J., Christopher, B.R., and Wayne, M.H. (1995). "Construction and Instrumentation of a Highway Slope Reinforced with High Strength Geotextiles." Proceedings of the Geosynthetics '95 Conference, Nashville, Tennessee, February, Vol. 1, pp. 13-27.

Zornberg, J.G., Ferreira, J.A.Z., Gupta, R.V., Joshi, R.V., and Roodi, G.H. (2009). "Geosynthetic-Reinforced Unbound Base Courses: Quantification of the Reinforcement Benefits." Center for Transportation Research (CTR), Report No. FHWA/TX-10/5-4829-1, Austin, Texas, December 2009, Revised February 2012, 170 p.

Zornberg, J.G., Mitchell, J.K., and Sitar, N. (1997). "Testing of Reinforced Soil Slopes in a Geotechnical Centrifuge." ASTM Geotechnical Testing Journal, Vol. 20, No. 4, December, pp. 470-480.

Zornberg, J.G., Sitar, N., and Mitchell, J.K. (1998a). "Performance of Geosynthetic Reinforced Slopes at Failure." Journal of Geotechnical and Geoenvironmental Engineering, ASCE, Vol. 124, No. 8, pp. 670-683.

Zornberg, J.G., Sitar, N., and Mitchell, J.K. (1998b). "Limit Equilibrium as Basis for Design of Geosynthetic Reinforced Slopes." Journal of Geotechnical and Geoenvironmental Engineering, ASCE, Vol. 124, No. 8, pp. 684-698.

3 INFORMATION GATHERING: STATE-OF-THE-PRACTICE

3.1 INTRODUCTION

A comprehensive literature review was provided in Chapter 2, which provided background to the different components conducted as part of this NCHRP project. This involved background relevant to the experimental, field monitoring, and numerical components of the study. The literature review compiled as part of Chapter 2 is complemented with two additional evaluations as part of this NCHRP project. One of these additional evaluations is provided in this chapter, and includes the results of a comprehensive survey of load-carrying GMSE bridge abutments. Complementing the information available in the US regarding this type of structures (e.g. Abu Hejleh et al. 2001, Adams et al. 2012, Adams and Nicks 2018), the focus of this survey and evaluation is on structures constructed overseas. Much of the collected information has been gathered from archives of geosynthetic manufacturers and geotechnical designers. The overall objective is to gain insight on the trends regarding the design of these structures in relation to the approaches adopted in the US. This information is deemed relevant to the objectives of this study, which aims at evaluating the effect of closely-spaced reinforcements, as the use of small vertical spacing has been adopted for bridge abutment projects in the US.

As previously discussed, the use of the geosynthetic-reinforced walls has evolved to directly support bridge loads. This technology has shown very promising performance in avoiding piles to transfer bridge loads to foundation soils and in providing the necessary flexibility to alleviate the "bump at the end of bridge". Implementation of this alternative has also led to improvements in bridge construction. Herold (2006) reported that approximately 60 to 80% of the concrete volume is reduced when employing reinforced soil abutments instead of conventional reinforced concrete abutments. GMSE bridge abutments are favored for being cost-effective alternatives to traditional abutment types. Herold (2005, 2006) stated that GMSE abutments cost approximately 20 to 30% less than alternative reinforced concrete abutments. Adams *et al.* (2011) reported that bridges constructed using GMSE abutments cost 25 to 60% less than those constructed using traditional methods. Furthermore, utilization of GMSE abutments minimizes construction time when compared to other abutment alternatives. Adams *et al.* (2011) reported that the construction time of an abutment can be reduced from months to weeks , thus reducing traffic disruptions and shutdowns. Herold (2005, 2006) noted that the simplicity of dismantling the system entirely allows recycling of both the geosynthetics and soil for applications requiring construction of a temporary abutment, resulting in a highly sustainable alternative in multiple construction projects.

Many studies have been conducted to provide a design methodology for GMSE abutments (e.g. Allen and Bathurst 2003; Herold 2005, 2006; Wu et al. 2007; Berg et al. 2009; Adams et al. 2011, 2012; RTRI 2012; AASHTO 2014; Lenart 2014). However, a full understanding of the load transfer mechanisms has not yet been achieved. Consequently, comparatively few bridges have been constructed using this technology worldwide. This chapter synthesizes information on the structures identified worldwide to date. More specifically, information is presented on the

various structures' components gathered from several published and unpublished sources. A few case histories from different states-of-the-practice are also reported. Finally, this chapter provides insight into the major components and aspects that have been the design focus for GMSE bridge abutments in worldwide practice. The significance of these design aspects will prove useful when identifying design aspects in US practice that are worth revisiting when synthesizing design recommendations in Chapter 8 of this report.

3.2 GEOGRAPHIC DISTRIBUTION OF LOAD-CARRYING GMSE BRIDGE ABUTMENTS

A relatively small number of GMSE bridge abutments have been built worldwide, possibly due to a lack of confidence and limited understanding of the behavior of these structures. Figure 3.2.1 shows a world map with the distribution by country of bridges supported by GMSE abutments. Note that the number of bridges in each country may not necessarily represent the total number of bridges that have been constructed so far. Instead, it represents the number of bridges identified by the authors following an extensive search of published and unpublished sources. In fact, additional information is expected to continue to be gathered after publication of this report, and the database plans to be synthesized elsewhere. In North America, the United States tops the world's list, with 174 identified bridges. Many experimental GMSE abutments have been constructed in the continental U.S. as part of various research studies to understand their behavior. However, this chapter did not take into account these experimental structures and focused on operational bridges only. At the time of the initial compilation of this database, four bridges each were identified in Puerto Rico, Canada and Panama, and one bridge in Jamaica. In South America, five bridges were identified in Brazil, three bridges in Peru, and one bridge each in Bolivia and Chile. In Europe, 72 bridges were identified in the Netherlands, seven bridges in Germany, 13 bridges in the United Kingdom and one bridge each in Denmark, Italy, Slovenia, and France . While full-scale experimental abutments were identified in Austria and Latvia, no bridges in these countries were identified as having implemented load-carrying GMSE technology. Other experimental abutments were identified in Germany, Italy, Turkey and France as well. In Asia, Tatsuoka *et al.* (1997) reported that 17 bridges were constructed in Japan through April 1997, after which the design of load-carrying GMSE abutments was modified so that the bridge superstructure would rest on the facing rather than on the reinforced soil mass; 34 bridges were identified as having adopted this design. In spite of its particular load transfer approach, these structures are also considered in this chapter since the bridge load is still transferred primarily to the reinforced soil mass (through a rigid facing rather than through a footing), and makes no use of deep foundations. In addition to Japan, five bridges were identified in the United Arab Emirates, and one bridge each in China, Hong Kong and Iran. Lastly, in Oceania, one structure was identified in Australia. In the following subsections, several of the identified structures are detailed using the descriptive information and performance data gathered.

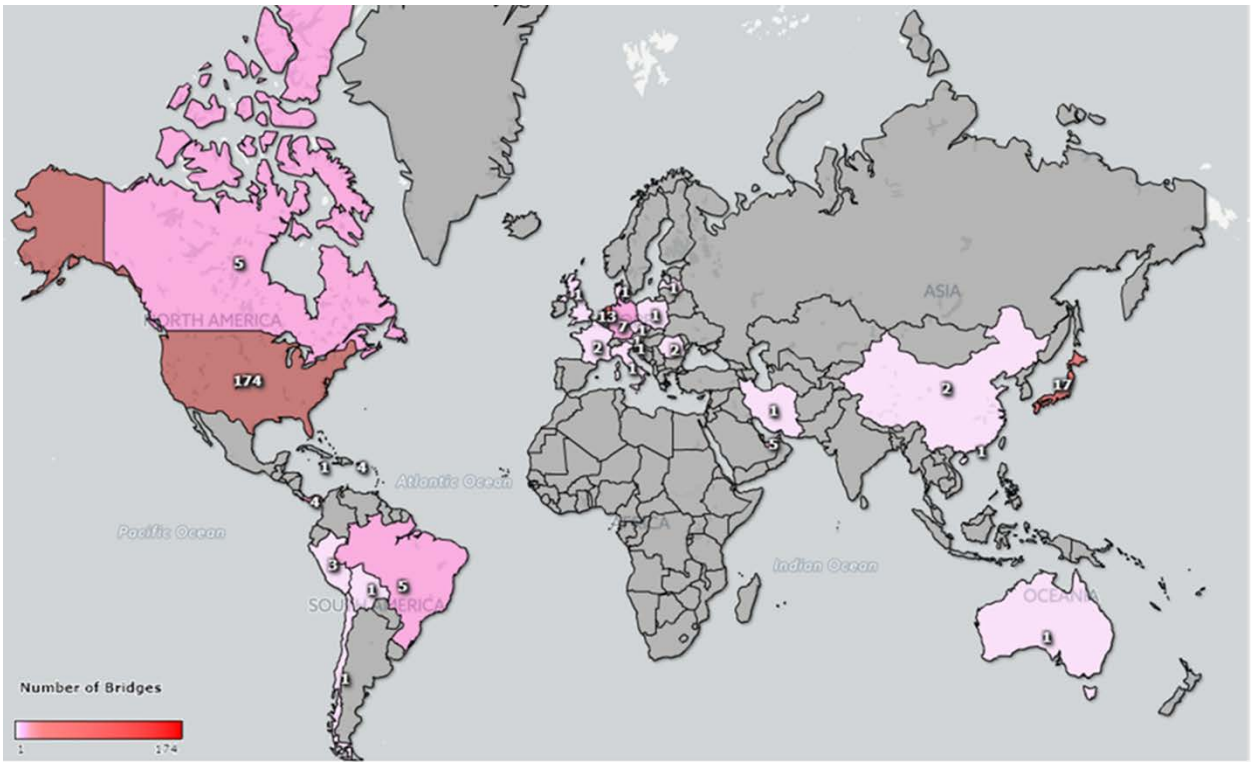

Figure 3.2.1. Global geographic distribution of load-carrying GMSE bridge abutments by country

A list of representative load-carrying GMSE bridge abutments identified worldwide is provided in Table 3.2.1. Seven of these structures are reported in more detail in Section 3.3, in order to illustrate the different characteristics in terms of structure layout, which is characterized by a significantly wide range of geosynthetic types, reinforcement vertical spacing, and facing characteristics. Finally, a synthesis of different metrics regarding the information gathered in this component of this study is provided in Section 3.4.

Table 3.3.1: Characteristics of representative load-carrying GMSE bridge abutments identified as part of the survey conducted in this study

No.	Structure(s)	Location	Year	Maximum Abutment Height	Bridge Span	Reinforcement Type	Reinforcement Strength	Reinforcement Spacing	Facing Type	Bearing Seat Width (m)	Setback Distance (m)	Reference
1	New South Wales	Australia	1994	10.0 m		Geogrids	80, 110 kN/m	0.6 m (0.4 m at the bottom)	Segmental blocks	2.5 m	2.5 m	Won et al. (1996)
2	Carretera Uyuni – Condo K, Potosí	Bolivia	2015	5.9 m		Geogrids			Concrete panels			Personal communication
3	BR 101-SC Hwy	Brazil				Geogrids	200 kN/m	0.4 m				Ortiago et al. (2001); Fahel et al. (2000)
4	Maringa Railway Line (4 bridges)	Brazil	2011	7.6 m	19 m	Geogrids	110 kN/m (upper half), 200 kN/m (lower half)	0.4 m (upper half), 0.6 m (lower half)	Segmental blocks	2.0 m	1.5 m	DaSilva & Brugger (2012)
5	Nadahini Creek	Canada	2013	6.9 m	15.3 m	Geotextiles	70 kN/m	0.2 m (lower), 0.275 m (upper), 0.1375 m (bed)	Aluminum sheeting	0.9 m	0.38 m	Wadey & Idrees (2014)
6	Fullerton	Canada				Geogrids			Segmental blocks			Tensar®
7	San Francisco, Mostazal	Chile	2001	8.5 m	30 m	Geogrids	70 kN/m (top), 114 kN/m (middle), 144 kN/m (bottom)	0.4 m (0.2 m near top), 0.6 m (0.4 m near top and bottom)	Segmental blocks	3.0 m	1, 1.5 m	Mendez (2016)
8	Chu Xiangyun Highway	China		6.35 m	16, 30, 16 m	Geogrids	80, 110 kN/m	0.4 m	Segmental blocks	2.5 m		Zhou et al. (2000)
9	Ullerslev	Denmark	1992	8.0 m	15.5 m	Geogrids	110 kN/m	0.5 m	Full-height wall	1.0 m	1.1 m	Kirschner & Hermansen (1994)

10	The Lagoons (5 bridges)	United Arab Emirates	2008	8.4, 13.3 m	33, 45 m	Geogrids	110, 80, 55, 30 kN/m		Steel mesh			Huesker®
11	RN 38 at Saint Saturnin	France	2005	9.5 m		Geotextiles	150 kN/m	0.39 m	Segmental blocks	1.5 m	0.33 m	Nancey et al. (2006)
12	Arnstadt	Germany	1996	4.0 m	26 m							Herold (2005, 2006, 2007)
13	Ilsenburg	Germany	2000	4.0 m	22 m	Geogrids	140 kN/m	0.35 m	Gabions	1.5 m	1.6 m	Herold (2002, 2005, 2006, 2007)
14	Magdeburg	Germany	2001	9.0 m	6 m	Geogrids	110 kN/m	0.3 m		2.5 m	0.5 m	Herold (2005, 2006, 2007)
15	Mainzer	Germany	2003									Herold (2005, 2006, 2007)
16	Weimar	Germany	2003			Geogrids		0.25 m	Gabions			Herold (2005)
17	Mandelholz	Germany	2006	3.0 m	15 m			0.5 m	Segmental blocks	1.75 m	0.75 m	Herold (2007, 2008)
18	Lust	Germany	2007	3.3 m		Geogrids		0.25 m	Segmental blocks	2.5 m	1.0 m	Herold (2005, 2006)
19	Tuen Mun	Hong Kong		14.0 m		Geogrids	30 kN//m	0.4 m (middle), 0.35 m (top and bottom)	Full-height wall	3.5 m	0.5 m	Ng and Mak (1988)
20	Tehran, Iran	Iran	2009	7.5 m	114 m	Geogrids	80 kN/m	0.4 m	Gabions	3.5 m	1.85 m	Mirlatifi (2012)
21	State Road NR 28	Italy	2000s	30.4 m		Geogrids	80 kN/m	0.6 m	Vegetation			Rimoldi & Intra (2009)
22	Queens River	Jamaica				Geotextiles	70, 31.5 kN/m	0.3 m	Segmental blocks			Barrett & Ruckman (1996)
23	Nagoya	Japan		6.0 m		Geogrids	60 kN/m	0.3 m	Full-height wall	2.0 m	1.0 m	Kasugai & Tateyama (1992)
24	Seibu Railway (2 bridges)	Japan		4.0, 5.0 m	13.2 m	Geogrids	60 kN/m	0.3 m	Full-height wall	2.5 m	1.0 m	Tatsuoka et al. (1997)
25	Venlo (2 bridges)	Netherlands	2011	7.4, 10.0 m	31 m	Geogrids	200 kN/m (400 kN/m at the top)	0.5 m	Gabions			Duijnen et al. (2012); Deret & Thomson (2013)

26	N242 Road KW-B	Netherlands				Geogrids	110 kN/m	0.5 m	Clay over fly ash and sand	3.5 m	0.6 m	Snijders & Brok (2007)
27	N242 Road KW-O	Netherlands			5.6 m	Geogrids	300 kN/m (150 kN/m at the top)	0.5 m	Clay over fly ash and sand	3.5 m	0.85 m	Snijders & Brok (2007)
28	A2, Gleen	Netherlands			27, 34.5 m	Geogrids	150 kN/m	0.5 m				Huesker®
29	N302 Fietsburg Harderwijk	Netherlands		6.0 m		Geogrids	110 kN/m	0.5 m				Huesker®
30	S-27	Peru	2008	10.5 m		Geogrids		0.5 m (0.25 m at the bottom)	Vegetation	2.5 m	2.5 m	Tecnologia de Materilas
31	(2 bridges)	Peru				Geogrids			Segmental blocks			Tecnologia de Materilas
32	PR-2, Yauco	Puerto Rico		10.0 m	13 m	Geotextiles		0.2 m				
33	Barceloneta	Puerto Rico										
34	Utuado	Puerto Rico										
35	Pavlovski potok Stream in Zerovinci	Slovenia				Geogrids	80 kN/m	0.3 m (0.1 m at the top)	Full-height wall	0.85 m	0.45 m	Lenart et al. (2016)
36	Naadestraat, Laarderhoogt, Laren	Netherlands				Geogrids			Segmental Blocks			Pauls et al. (2016)
37	A1, Laarderhoogt, Laren	Netherlands				Geogrids			Full-height wall			Pauls et al. (2016)
38	N417 National Road, Zwaluwerberg, North Holland	Netherlands				Geogrids			Full-height wall			Pauls et al. (2016)
39	Utrecht-Hilversum Railway,	Netherlands				Geogrids			Steel mesh			Pauls et al. (2016)

	Zwaluwerberg, North Holland											
40	A27 Motorway, Zwaluwerberg, North Holland	Netherlands				Geogrids			Segmental blocks			Pauls et al. (2016)
41	Boele Staal, Soesterberg, Utrecht	Netherlands		4.5 m		Geogrids			Full-height wall			Pauls et al. (2016)
42	Smit Vest, Boerenverdriet	Netherlands	2016									Wurck
43	River Aire, Kirkstall, Leeds	United Kingdom	2015		30 m	Geogrids	35, 55 kN/m	0.4 m	Segmental blocks			Scotland et al. (2016)

3.3 CASE HISTORIES

3.3.1 FOUNDERS/MEADOWS BRIDGE IN THE UNITED STATES

The Founders/Meadows Bridge, pictured in Figure 3.3.1, was the first bridge in the United States constructed on a major highway with its superstructure supported directly by GMSE abutments. The bridge was constructed in Castle Rock, Colorado in 1999 (Zornberg et al. 2001, Abu-Hejleh et al. 2002). The abutments support not only the bridge superstructure, but also the approaching roadway structures. The bridge replaced an old two-span bridge with a new superstructure and abutments, while reusing the middle pier in the new bridge. The superstructure of the new bridge spans 34.5 m (113.2 ft) and consists of 20 precast pre-stressed concrete girders. The heights of the GMSE abutments were 4.5 and 5.9 m (14.8 and 19.4 ft) from the base of the reinforced soil to the bearing seats. Figure 3.3.2 presents a schematic of a GMSE abutment cross-section. The bridge loads are transferred to the reinforced soil mass through reinforced concrete bearing seats that rest directly on the reinforced soil mass. The bearing seats consist of U-shaped concrete walls on shallow strip footings measuring 3.81 m (12.5 ft) wide and placed with a setback of 1.55 m (5.1 ft) from the outer edge of the facing. The abutments were constructed directly on the native bedrock with a minimum embedment depth of 0.45 m (1.5 ft) in front of the abutment.

Figure 3.3.1. View of the Founders/Meadows Bridge

Three different reinforcement types were employed: (1) a uniaxial geogrid reinforcement with a tensile strength of 157.3 kN/m (898 lb/in), used to reinforce the backfill material beneath the bridge footings; (2) a uniaxial geogrid reinforcement with a tensile strength of 64.2 kN/m (367 lb/in); and (3) a uniaxial geogrid with a tensile strength of 39.3 kN/m (224.4 lb/in). The latter two reinforcement types were used to reinforce the backfill material behind the bearing seats and beneath the roadway approach structures, as seen in Figure 3.3.2. The reinforcement layers were placed at a vertical spacing of 0.4 m (16 in). The backfill material used was angular crushed stone, which classifies as SW-SM according to the Unified Soil Classification System (USCS). The backfill was characterized by a maximum grain size of 18 mm (0.7 in), a friction angle of 40 degrees and cohesion of 70 kPa (10.2 psi). A drainage system was used that includes: (1) a drainage blanket with pipe drains, installed at the bottom of the reinforced soil mass; and (2) a geomembrane with a collector pipe, installed underneath the approaching roadway structures. Expanded polystyrene layers 75 mm (3 in) thick were used behind the bearing seats to reduce the

magnitude of the lateral earth pressure exerted on the backwalls. The facing system included segmental blocks that are mechanically connected to the reinforcement layers. The facing blocks are backed with 0.3 m (1 Ft) thick zone of crushed stone.

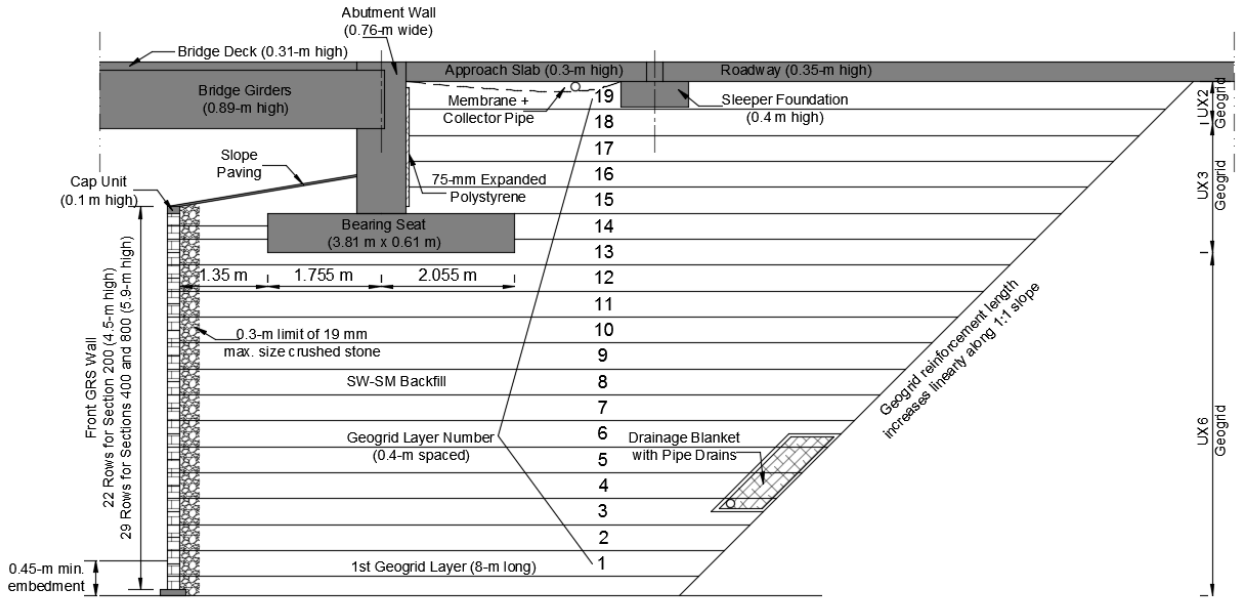

Figure 3.3.2. Cross-section of the Founders/Meadows load-carrying GMSE bridge abutment (redrawn after Abu-Hejleh et al. 2002).

3.3.2 MARINGA RAILWAY LINE BRIDGES IN BRAZIL

A trench was excavated to downgrade the railroad tracks of a railway line passing through approximately three kilometers in Maringa City in Paraná, Brazil. This project involved the use of GMSE retaining structures on the sides of the excavated trench, as pictured in Figure 3.3.3 (Da Silva *et al.* 2012; Brugger *et al.* 2012). Four bridges were constructed across the railway line using GMSE abutments designed in accordance with Ehrlich and Mitchell (1994). Each bridge had a 19 m long single-span superstructure that crossed a three-track railway line. The abutments ranged from 8.0 to 9.0 m (26.2 to 29.5 ft) in height and were constructed directly on the local soil. Bearing seats, used to rest the superstructures on the GMSE abutments, ranged from 1.8 to 2.0 m (5.9 to 6.6 ft) in width and were placed at a setback distance ranging from 0.5 to 1.5 m (1.6 to 4.9 ft) from the outer edge of the facing.

Da Silva *et al.* (2012) and Brugger *et al.* (2012) reported that the backfill material used in the abutments was local red clays ("Argilas Vemelhas") from northern Paraná, Brazil. The backfill was characterized by a friction angle of 27 degrees and cohesion of 8 kPa (1.2 psi). The backfill was compacted at its optimum moisture content. The facing system consisted of hollow segmental blocks, frictionally connected to the reinforcement layers, and filled with gravel to enhance this frictional connection. Furthermore, the reinforcement layers were folded at 1.0 m (3.3 ft) to provide a double-layer connection. Polyvinyl alcohol geogrid reinforcements were utilized, which

provided a tensile strength of 110 kN/m (7.5 kips/ft) and 200 kN/m (13.7 kips/ft) for the upper and lower layers, respectively, as depicted in Figure 3.3.4. The reinforcement vertical spacing was 0.4 m (1.3 ft) and 0.6 m (2 ft) for the upper and lower layers, respectively.

Figure 3.3.3. Load-carrying GMSE bridge abutments over the Maringa Railway Line (Brugger et al. 2012).

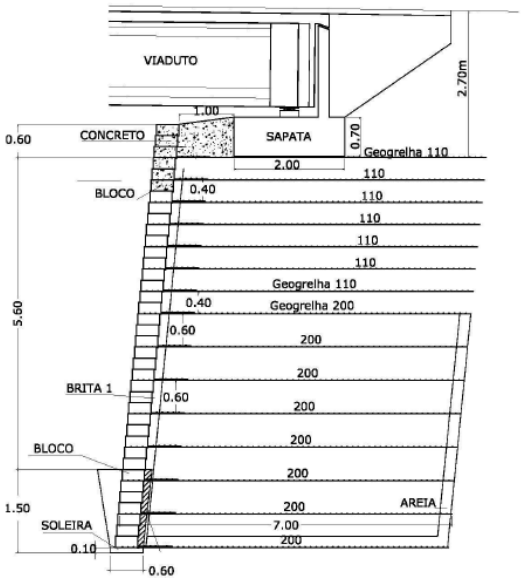

Figure 3.3.4. Cross-section for the Maringa Railway Line load-carrying GMSE bridges abutment (Da Silva et al. 2012).

3.3.3 ILSENBURG BRIDGE IN GERMANY

Figure 3.3.5 presents a picture of Ilsenburg Bridge, constructed in 2000 in Ilsenburg, Saxony-Anhalt, Germany. This bridge is regarded as the first permanent load-carrying GMSE bridge

abutments in Germany. The bridge was constructed over the River Ilse as part of the K1355 district road rehabilitation project (Herold 2002). The superstructure spans 22 m (72.2 ft), rests on GMSE abutments 2.7 m (8.9 ft) in height, and transfers the bridge load to the abutments through 1.5 m (4.9 ft) wide bearing seats placed at a setback distance of 1.6 m (5.2 ft), as shown in Figure 3.3.6.

The backfill material used was recycled, crushed concrete fill with a friction angle of 35 degrees and no apparent cohesion. The backfill was compacted to 100% of its Proctor density, which was verified for each layer on-site. A polyvinyl alcohol geogrid layer was used as the reinforcement, with a tensile strength of 140 kN/m (800 lb/in). The facing consisted of galvanized gabion baskets filled with riprap stones and stiffened by diagonal metal rods. The reinforcement layers were placed at a vertical spacing of 0.35 m (1.1 ft) and mechanically connected to the facing by wrapping the ends around the gabion baskets for 1.0 m (3.3 ft) in length (Herold 2002).

Horizontal deformation of the abutments was monitored by vertical inclinometers installed in each abutment. The maximum horizontal deformation recorded three months after the bridge was inaugurated to traffic was around 0.08 mm (3 mil), whereas the deformation recorded five years after construction was 0.2 mm (8 mil). Maximum lateral deformation was observed to occur near the top surface of the abutment. However, the maximum deformation became more uniform over the upper segment of the abutment as deformation progressed. Vertical deformation was monitored by six settlement gauges placed in each abutment in the superstructure, bearing seat and abutment wings. The settlement recorded at the top surface of the abutments five years after construction ranged from 3.0 to 4.5 mm (0.12 to 0.18 in). The soil pressure was also monitored under static and rolling (dynamic) load testing. Rolling tests were conducted for two years after construction by running a four-axle HGV (heavy goods vehicle) weighing 40 tons at speeds of 20, 40 and 60 km/h (12.4, 24.8 and 37.3 mph). An earth pressure sensor was installed under the superstructure at the elevation of the uppermost reinforcement layer to measure any tensile stresses that might develop beneath the superstructure in its static condition or during rolling tests (Herold 2002).

Figure 3.3.5. Ilsenburg load-carrying GMSE bridge abutment (Herold 2006).

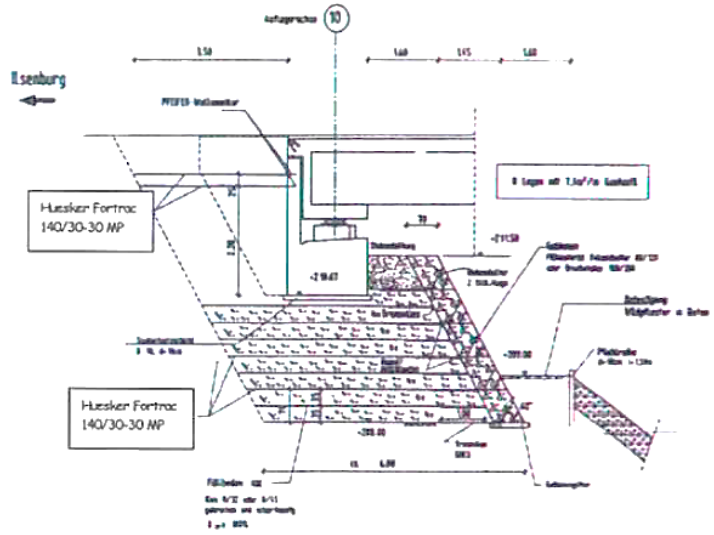

Figure 3.3.6. Cross-section of Ilsenburg Bridge abutment (Herold 2002).

3.3.4 VENLO BRIDGES IN THE NETHERLANDS

Two bridges were constructed in tandem, as shown in Figure 3.3.7, in 2011 near Venlo, Netherlands to provide a direct connection, A74, between the Dutch A73 and the German BAB61. The superstructures of the bridges spans approximately 31 m (101.7 ft) and are supported

directly by load-carrying GMSE abutments. The heights of the abutments are 10 m (32.8 ft) for one bridge and 7.4 m (24.3 ft) for the other. Polyvinyl Alcohol reinforcement geogrid layers were employed at a vertical spacing of 0.5 m (1.6 ft). The reinforcement tensile strength is 400 kN/m (2.3 kips/in) for the top four layers and 200 kN/m (1.1 kips/in) for the rest of the layers. The backfill material used was compacted crushed recycled material. The abutments were preloaded with 100 kPa (0.6 kips/in) surcharge for two months after their construction. The preloading aimed to mobilize the initial deformation of the abutments before the placement of the bearing seat and the bridge superstructure. The facing system used resembled the gabion facing to provide protection and aesthetic appearance (van Duijnen *et al.* 2012).

Two sections were instrumented in each abutment (van Duijnen et al. 2012). The instrumentation included 26 markers with 8 markers for each section of the 10-m (32.8 ft) high abutment and 5 markers for each section of the 7.4-m (24.3 ft) high abutment as shown in Figure 3.3.8. Monitoring started after construction and before preloading. The vertical deformation measured at the top of the abutments was approximately 11 mm (0.4 in) for the 10-m (32.8 ft) high abutment and 6 mm (0.24 in) for the 7.4-m (24.3 ft) high abutment; whereas, the vertical deformation measured at the base of the abutments was approximately 8 mm (0.3 in) for the 10-m (32.8 ft) high abutment and 6 mm (0.24 in) for the 7.4-m (24.3 ft) high abutment. The vertical deformation measured at the base of the abutments was in the same order of the deformation measured at the top of the abutments, which implied that the settlement is mainly due to subsoil compression (Van Duijnen *et al.* 2012; Detert and Thomson 2013). The deformation remained relatively constant during the 2-month application of the preload. After the preload removal and decks installation, the vertical deformation at the top of the abutments increased to approximately 26 mm (1.02 in) for the 10-m (32.8 in) high abutment and 23 mm (0.91 in) for the 7.4-m (24.3 ft) abutment. However, the bridge deck weight was almost the same as the preload applied. The vertical deformation at the base of the abutments after the placement of the decks was approximately 22 mm (0.87 in) for both abutments. This does not, however, agree with the experimental observations reported by Gourc et al. (1995), Gotteland et al. (1997), Alexiew (2007, 2008), Alexiew and Detert (2008), and Detert and Thomson (2013) in which the load-reload cycles of reinforced-soil mass does not increase its deformation. The maximum horizontal deformation measured after preloading was approximately 13 mm (0.51 in) for the 10-m (32.8 ft) high abutment and occurred approximately 2.5 m (8.2 ft) below the bearing seat; whereas, the maximum deformation was 8 mm (0.31 in) for the 7.4-m (24.3 ft) high abutment and occurred approximately 1.5 m (59 in) below. On the other hand, the maximum deformation after the deck placement was approximately 20 mm (0.8 in) for the 10-m (32.8 ft) high abutment and occurred at approximately 1 m (3.3 ft) below the bearing seat; whereas, the maximum deformation was 9 mm (0.35 in) for the 7.4-m (24.3 ft) high abutment and occurred approximately 2 m (6.6 ft) below the bearing seat.

Figure 3.3.7. View of the load-carrying GMSE bridge abutments at Venlo (van Duijnen et al. 2012)

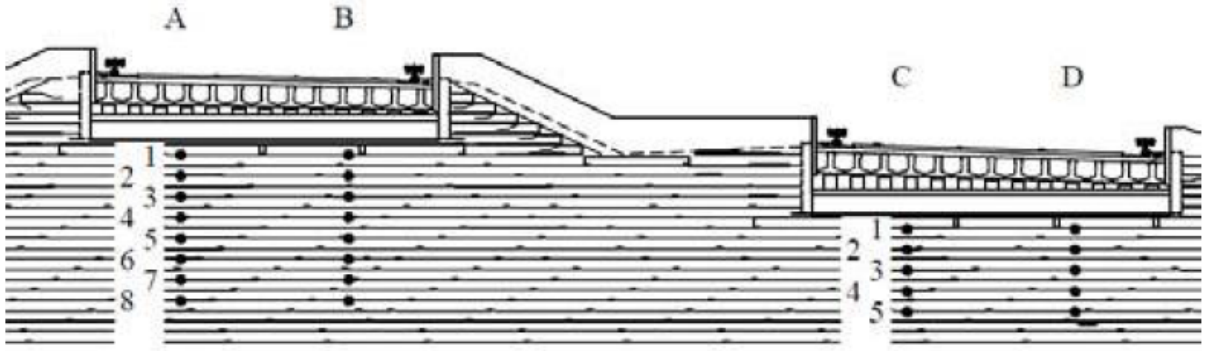

Figure 3.3.8. Venlo Bridges instrumented abutment sections (van Duijnen et al. 2012)

3.3.5 NAGOYA BRIDGE IN JAPAN

A railway bridge was constructed at Nagoya Station on the Tokaido Shinkansen (the Japanese Bullet Train) rail line in Nagoya, Japan. The bridge superstructure was supported by GMSE abutments 6 m in height, as d depicted in Figure 3.3.9. The reinforcement used in the abutments involved geogrid layers made of vinylon covered with vinyl chloride. The reinforcement had a tensile strength of 60 kN/m (342 lb/in) and were placed at a vertical spacing of 0.3 m (1 ft). The backfill material was a high-quality well-graded gravel compacted to a dry density of 2200 kg/m^3 (139 pcf). To resist the seismic lateral loads exerted by the bridge superstructure during extreme events, both abutments had a full-height rigid facing installed over gabions, which were wrapped by the reinforcement layers. Gabions were adopted to mitigate possible connection failure upon differential settlements between the rigid facing walls and the backfill. Anchor elements were

used to secure the facing walls to the reinforced soil, as displayed in Figure 3.3.9. A drainage system was used to prevent the accumulation of water behind the facing walls (Kasugai and Tateyama 1992).

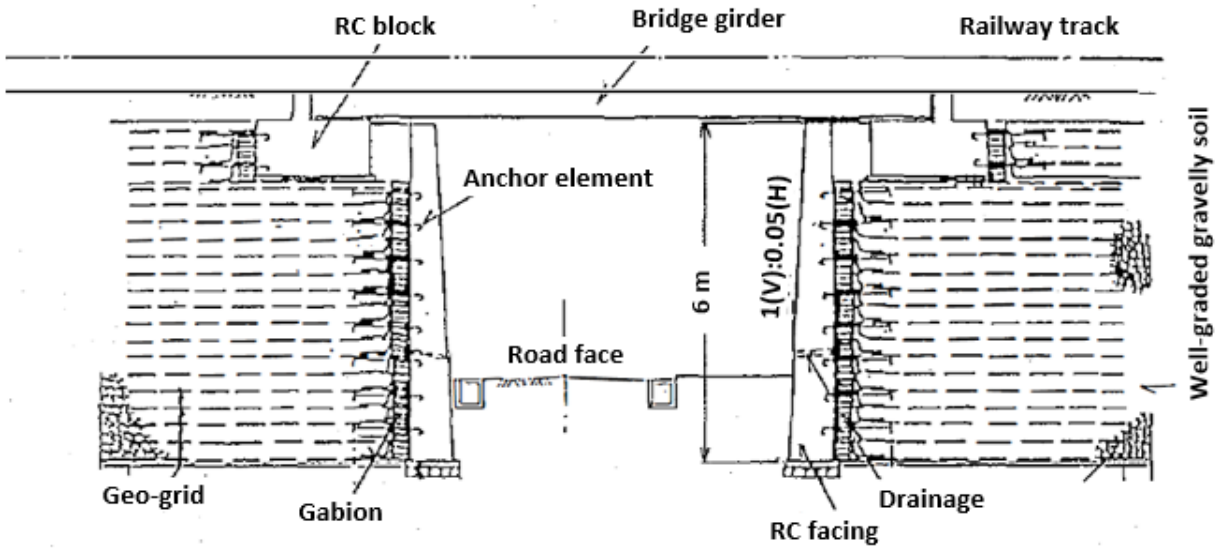

Figure 3.3.9. Cross-section of Nagoya Bridge (Kasugai and Tateyama 1992).

3.3.6 NEW SOUTH WALES BRIDGE IN AUSTRALIA

The New South Wales Bridge was constructed in 1994 and is considered a major bridge on the Pacific Highway at its intersection over the Tweed River. The bridge is located 104 km (64 mi) south of Brisbane, Australia and regarded as the first large-scale use of GMSE structures in supporting bridges. The bridge consisted of a nine-span superstructure whose ends rest on bearing seats supported directly by GMSE abutments. The bearing seats were 2.5 m (8.2 ft) wide and placed at a 2.5 m (8.2 ft) setback distance, with polystyrene layers installed behind the bearing seats. The abutments were tiered as Figure 3.3.10 shows. One abutment consisted of three tiers that totaled 6.5 m (21.3 ft) in height, while the other abutment involved four tiers that totaled 9.5 m in height. The reinforcement vertical spacing was 0.4 m (1.3 ft) for the lower layers and 0.6 mm (0.02 in) for the upper layers. (Won *et al.* 1994).

Uniaxial geogrid layers were used as reinforcement, with a tensile strength of 80-kN/m (457 lb/in)for the upper layers and 110-kN/m (628 lb/in) for the lower layers, as seen in Figure 3.3.11. Sand was used as the backfill material, which was placed at a relative compaction of 95% (in relation to Standard Proctor). The facing consisted of masonry segmental blocks, chosen instead of gabion for their durability and aesthetics. The blocks were stacked and connected by fiberglass dowels, the shear strength of which factored into the strength of the connection between the facing units and the reinforcement layers. The blocks were hollow and filled with aggregate during construction (Won *et al.* 1994).

The maximum vertical displacement measured at the foundation level of the abutment was 80 mm (3.2 in), observed toward the rear of the abutment (Won *et al.* 1994). This value remained the same for about 40 months after bridge construction (Lo 2004).

Figure 3.3.10. New South Wales load-carrying GMSE bridge abutment (Lo 2004)

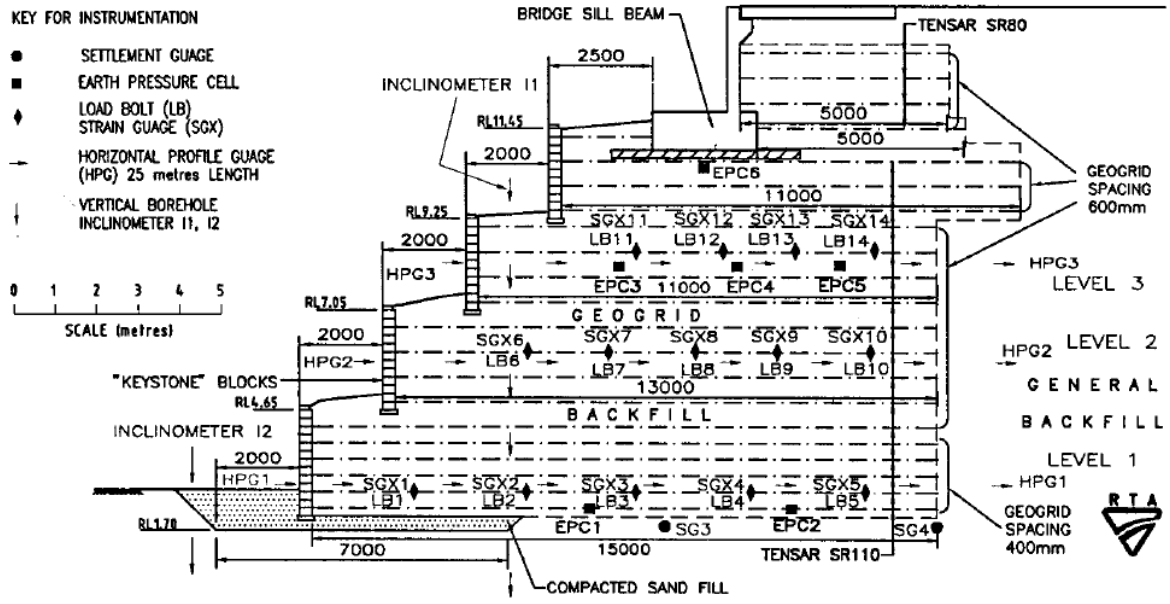

Figure 3.3.11. New South Wales Bridge abutment cross-section (Won et al. 1994)

3.3.7 SAN FRANCISCO BRIDGE IN CHILE

Figure 3.3.12 shows a picture of the San Francisco Bridge, constructed in 2001 along Route H-10 overpassing a railway line in Mostazal, O'Higgins Region, Chile. The superstructure, comprising four precast pre-stressed concrete girders skewed at an angle of 39.53 degrees, spanned over 30 m and rested on bearing seats that rested directly on the reinforced soil mass. The bridge orientation was approximately east-west, with east and west abutments that were 7.72 and 8.49 m (25.3 and 27.9 ft) high, respectively, from the leveling pads (base of the reinforced soil mass) to the foundation level of the bearing seats.

The foundation soils were characterized by a unit weight of 20 kN/m^3 (128 pcf), a friction angle of 32 degrees and a cohesion of 15 kPa (2.2 psi). The backfill material used in the abutments was cohesionless, with a friction angle of 42 degrees. High-density polyethylene (HDPE) uniaxial geogrid layers were employed in the abutments. The vertical spacing in the east abutment was 0.4 m (1.3 ft) near the top and bottom, and 0.6 m (2 ft) near the mid-height of the abutment, while the spacing in the west abutment was 0.4 m (16 in) and 0.2 m (8 in) near the top, all of which are depicted in Figure 3.3.13. Additionally, the reinforcement spacing in the side slopes (sloping reinforced mass of the abutments) was 0.6 m (24 in) throughout the height. Three different reinforcements with three different ultimate tensile strengths were utilized: (1) a 144-kN/m (822 lb/in) reinforcement near the bottom; (2) a 114-kN/m (651 lb/in) near the mid-height; and (3) a 70-kN/m near the top.

Figure 3.3.12. San Francisco load-carrying GMSE bridge abutment (courtesy of Alejandro Mendez)

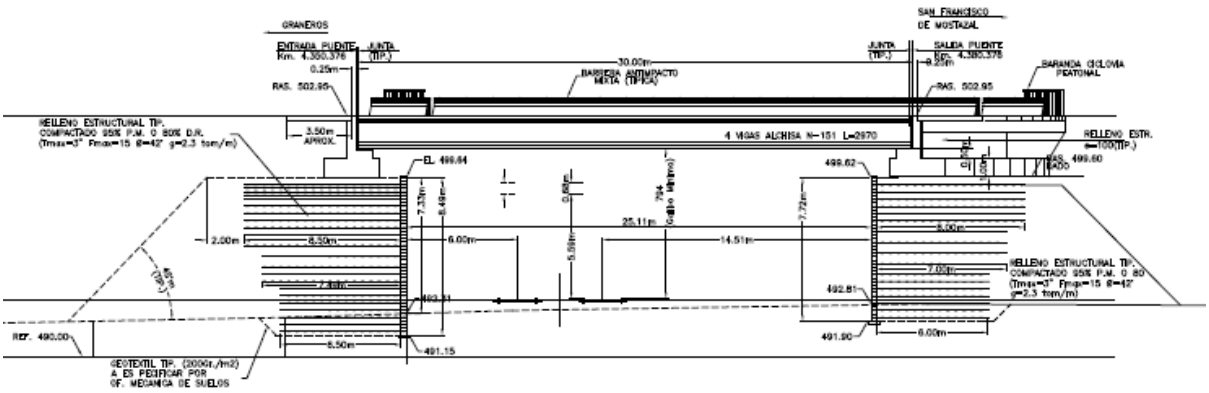

Figure 3.3.13. Cross-sectio nof the San Francisco Bridge abutment (courtesy of Alejandro Mendez)

The San Francisco Bridge was subjected to a major extreme event: the 2010 Maule earthquake in Chile. The 2010 Maule earthquake struck central Chile on 17 February 2010 at 03:34:14 AM local time (06:34:14 UTC). The United States Geological Survey (USGS) estimated the magnitude of the earthquake at Mw 8.8 (moment magnitude scale), with the epicenter located 35.909 degrees S (latitude) and 72.733 degrees W (longitude), and the hypocenter 35 km (22 mi) deep. Note that the geographical coordinates of the San Francisco Bridge are approximately -34.03 degrees S (latitude) and -70.72 degrees W (longitude). The epicenter was located 95 km (59 mi) from Chillán, 105 km (65 mi) from Concepción, 115 km (71 mi) from Talca, and 335 km (208 mi) from Santiago, all of which are the major Chilean cities. The distance between the bridge and epicenter was determined as approximately 300 km (186 mi). The Maule earthquake was deemed the fifth strongest earthquake recorded in worldwide history (Elnashai et al. 2010). In a simulation of the fault rupture, Lay et al. (2010) demonstrated that the duration of the earthquake exceeded 3 minutes. However, the significant energy was released within the first the 2 minutes. It was also concluded that the fault was bilateral, with the rupture propagating away from the epicenter in the north and south directions. Elnashai et al. (2010) reported that the ground uplift movement reached up to 2 m (6.6 ft), whereas the ground settlement reached up to 0.4 m (16 in). Furthermore, the Chilean coast moved westward into the ocean, with movement reaching up to 6 m in some locations.

The earthquake strongly affected a considerably large area, shown in Figure 3.3.14. The figure shows that at some locations the intensity reached IX, according to the Modified Mercalli Intensity Scale. The bridge was located in a region where the intensity had reached VII (denoted by red arrows in Figure 3.3.14). According to the USGS, the number of aftershocks recorded after the main shock exceeded 130 by 6 March (13 of which had magnitudes greater than Mw 6.0), and 304 of magnitude 5 Mw or more by 26 April 2010 (21 of which had magnitudes greater than Mw 6.0). The bridge had an east-west orientation, which is perpendicular to the direction of rupture propagation of the earthquake. Yen et al. (2011) observed ground movement in the San Francisco Bridge area due to weak sensitive clays. In general, the abutments performed very well, exhibiting no signs of lateral or vertical movement due to the earthquake. Yen et al. (2011) reported that the bridge suffered some relatively minor damage, but this was not caused by the abutments. It was also reported that the damage was probably due to the large skew angle of

the superstructure, and similar observations of other skewed bridges investigated in Chile after the same earthquake event were reported as well. Moreover, they suggested that the damage could also have been caused by a tendency for the bridge to slide downhill because of its location on a downhill roadway grade.

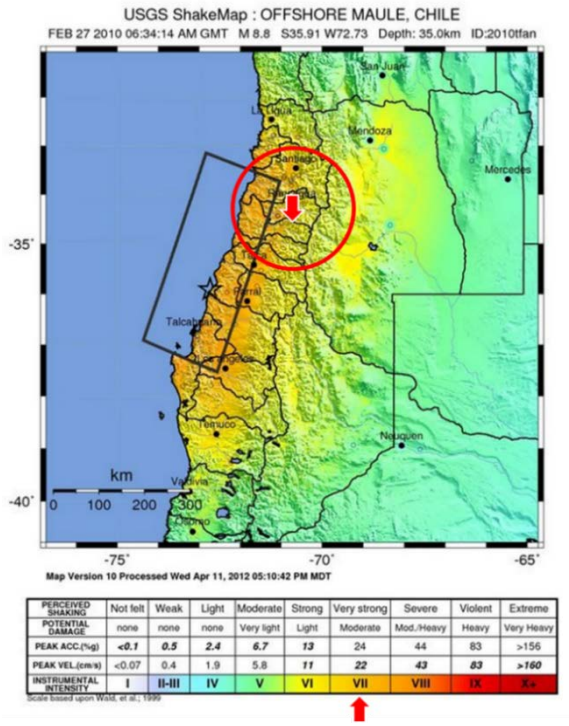

Figure 3.3.14. Instrumental intensity map for the main shock (after USGS 2012).

3.4 DESIGN IMPLICATIONS

This section provides insights into the major components of load-carrying GMSE bridge abutments and the alternatives that have been adopted in practice. A significant effort was undertaken to identify all load-carrying GMSE bridge abutments constructed so far (2018). Whenever possible, the information refers to information that has been documented in technical publications, brochures, design drawings, and web pages. The literature has been collected in multiple languages. The information published through different venues was verified and complemented through personal communications with the wall designers, manufacturers of the geosynthetics adopted in the projects, and representatives of the structure owners. Overall, a total of 421 load-carrying GMSE bridge abutments were identified. The following information was sought out from each identified structure: (1) bridge geometry with regard to the number of spans, span length and abutment height; (2) backfill material with regard to type, strength and compaction level; (3) reinforcement type with regard to geosynthetic type, polymer type and tensile strength; (4) reinforcement vertical spacing with regard to value and variability over the height of the abutment; (5) facing system with regard to type, rigidity and attachment to the geosynthetic reinforced soil mass; and (6) the bearing seat with regard to presence, width and

setback distance. While the construction and existence of all structures was verified by the authors, the details of each structure was not always available for each one of them. While most likely not all existing structures have been identified, it is considered that the characteristics of the structures identified in this evaluation are representative of the worldwide state-of-the-practice regarding load-carrying GMSE bridge abutments.

3.4.1 BRIDGE GEOMETRY

This section includes information on the maximum span length and number of spans per bridge superstructure that has been identified worldwide. In addition, the maximum height of the identified GMSE bridge structures is evaluated. Figure 3.4.1 presents the span of the longest load-carrying GMSE abutment identified for each continent. In North America, the bridges with the longest span are the CR 55 Bridge overpassing Montana Southern Railway in Montana, USA (span = 42.7 m (140.1 ft)) and the Steve Road Bridge overpassing the Tiffin River in Ohio, USA (span = 42.7 m (140.1 ft)). In South America, the San Francisco Bridge in Mostazal, Chile (span = 30 m) was identified as having the longest span . In Europe, the bridge with the longest span was identified to be the A2 Bridge in Gleen, Netherlands (span = 34 m). In Asia, the Milad Bridge in Iran has the maximum span length, at 114 m (374 ft) (cable-stayed bridge), which corresponds to the load-carrying GMSE bridge with the maximum span length among all identified structures.

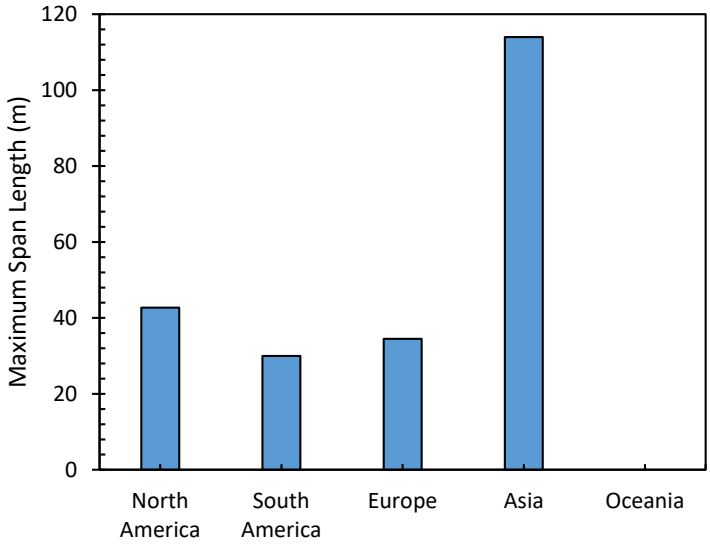

Figure 3.4.1. Span of the longest load-carrying GMSE bridge abutment identified in each continent

Herold (2005, 2006) reported that while single-span bridges with a precast superstructure have been a preferred option, multi-span bridges with shallow or deep foundations and reinforced soil abutments are feasible. Adams et al. (2011) reported that geosynthetic-reinforced soil abutments are suitable to support single-span bridges. Figure 3.4.2 shows the maximum number of spans identified for each continent. In North America, the bridge with the maximum number of spans identified was the I-70 Bridge near Denver, Colorado, USA (three spans). Other bridges identified with more than one span in North America include (1) the Founders/Meadows Bridge

in Castle Rock, Colorado, USA (two spans) and (2) the Knox County Beach Bridge in Maine, USA (two spans). All bridges identified in South America were single-span bridges. In Europe, the bridge identified as having the maximum number of spans was the A2 Bridge in Gleen, Netherlands (two spans measuring 27 m (88.6 ft) and 34 m (111.5 ft) in length). In Asia, the bridge identified as having the maximum number of spans was Chu Xiangyun Highway Bridge in China (three spans, with two measuring 16 m (52.5 ft) and one measuring 30 m (98.4 ft) in length). In Oceania, the bridge with the maximum number of spans identified was New Wales Bridge in Australia (nine spans).

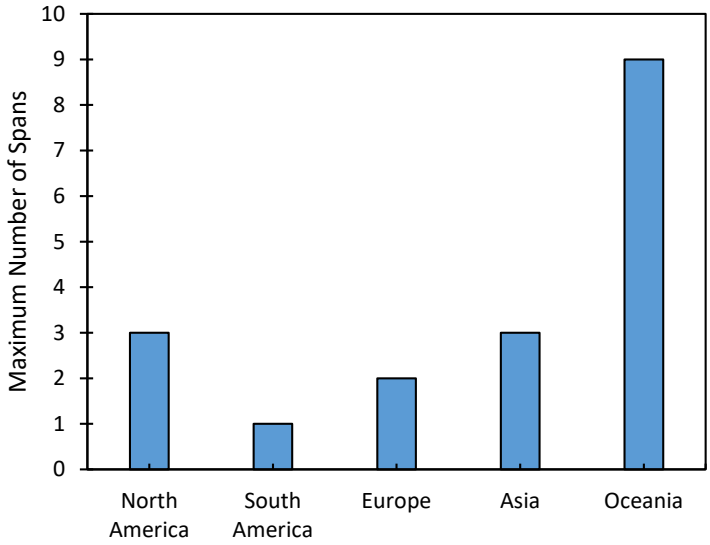

Figure 3.4.2. Maximum number of spans by continent.

Figure 3.4.3 shows the maximum abutment height identified for each continent. In North America, the highest abutment identified is 7.5 m (24.6 ft) high at Black Hawk Bridge in Colorado, USA. In South America, the maximum abutment height identified is 10.5 m (34.4 ft) at S-27 Bridge in Yanacocha, Peru. In Europe, the maximum abutment height identified is 30.4 m (100 ft) at State Road NR 28 Bridge in Imperia, Italy, also deemed the highest among all abutments identified. In Asia, the maximum abutment height identified is 14 m (46 ft) at Tuen Mun Bridge in Hong Kong. In Oceania, the maximum abutment height identified is 10 m (32.8 ft) at New Wales Bridge in Australia .

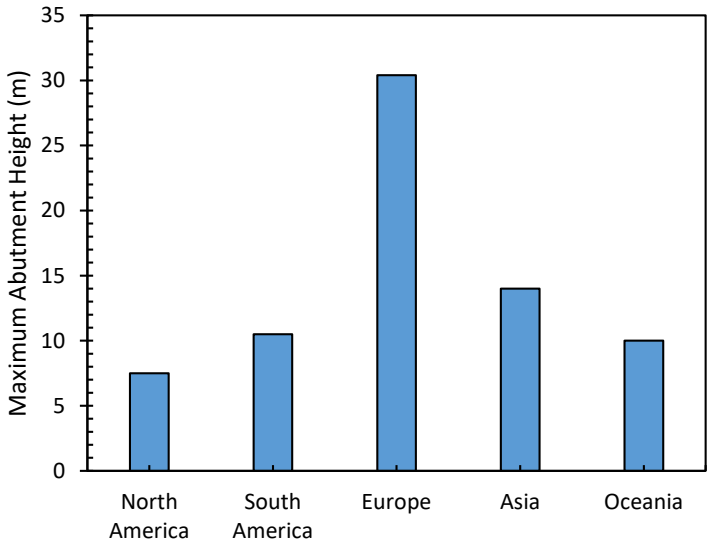

Figure 3.4.3. Height of the tallest load-carrying GMSE bridge abutments height by continent

3.4.2 BACKFILL TYPE

The backfill material used adopted in the project is a key design consideration . Typically, compacted crushed aggregate or gravel has been used to facilitate construction and minimize deformations. Sand backfill material has been employed in many structures, including several constructed in Brazil, the Netherlands, Australia and Japan. Some projects have also utilized sandy gravel backfill material, such as the Milad Bridge in Iran and the Ullerslev Bridge in Denmark. Backfill material with a comparatively low friction angle was employed at New South Wales Bridge, as reported in Won *et al.* (1994), where the selected material was a fine sand with a friction angle of 32 degrees. Based on the relative compaction levels identified for the case studies reported herein, the minimum relative compaction for a backfill was 94% at 250th Street Bridge in Buchanan County, Iowa, USA, as reported in Vennapusa *et al.* (2012, 2014).

The use of comparatively low quality backfill soils has been necessary in cases where quality backfill material is particularly expensive . For instance, nearly saturated clay backfill showed good performance as a backfill material in many geosynthetic-reinforced walls constructed in Japan (Tatsuoka *et al.* 1986, 1987; Tatsuoka and Yamauchi 1987; Yamauchi *et al.* 1987; Tatsuoka 1993; Ling *et al.* 1995; Tatsuoka *et al.* 1997). The bridges constructed over Maringa Railway Line in Brazil utilized clay backfill for the load-carrying GMSE abutments. Ling and Tatsuoka (1994) showed experimentally good performance for saturated clay as a backfill material when reinforced with geotextile composite, which allows consolidation of the clay backfill to occur anisotropically.

3.4.3 REINFORCEMENT TYPE

This section discusses the geosynthetic reinforcement layers used in the reinforced soil mass. The properties of the reinforcement, such as reinforcement type, strength and material, are central

in the design. Reinforcement inclusions in soil has been shown to lead to improved behavior of the composite mass through: (1) increased confinement; (2) enhanced strength; and (3) reduced strains (Yang 1972; Yang and Singh 1974; Schlosser and Long 1974; Hausmann 1976; Bassett and Last 1978; Ingold 1982; Athanasopoulos 1993, 1994; Gray and Ohashi 1983; Maher and Woods 1990; Elton and Patawaran 2004, 2005).

Using information gathered on the reinforcements employed in the case studies reported section, Figure 3.4.4 depicts the percentages of geogrid and geotextile reinforcement usage by continents. It was determined that in Europe, geogrid reinforcements have been preferred over the geotextiles. Eleven out of 15 bridges were supported by geogrid-reinforced abutments, and one on knitted geotextile-reinforced abutments. In contrast, the geotextile reinforcement has been preferred over geogrid reinforcements in North America, with most structures in the United States constructed employing geotextile reinforcement. Two structures identified in the United States, in Colorado and Minnesota, have utilized geogrid reinforcement, as did Fullerton Bridge in Canada. In Japan, geogrid reinforcement has been typically preferred and used with cohesionless backfill material to provide interlock with the aggregate, whereas composites of nonwoven and woven geotextile reinforcements have been preferred for nearly saturated cohesive backfill material (Tatsuoka et al. 1997). Alexiew et al. (2000) reported that a geogrid reinforcement of adequate aperture size has been preferred over other reinforcement types for its high interface and anchorage strengths in the backfill material, and high permeability. In addition, geogrids are less susceptible to installation aggression and have a higher resistance to chemical and biological degradation.

Figure 3.4.4. Percentage of geotextile and geogrid usage per continent (continued)

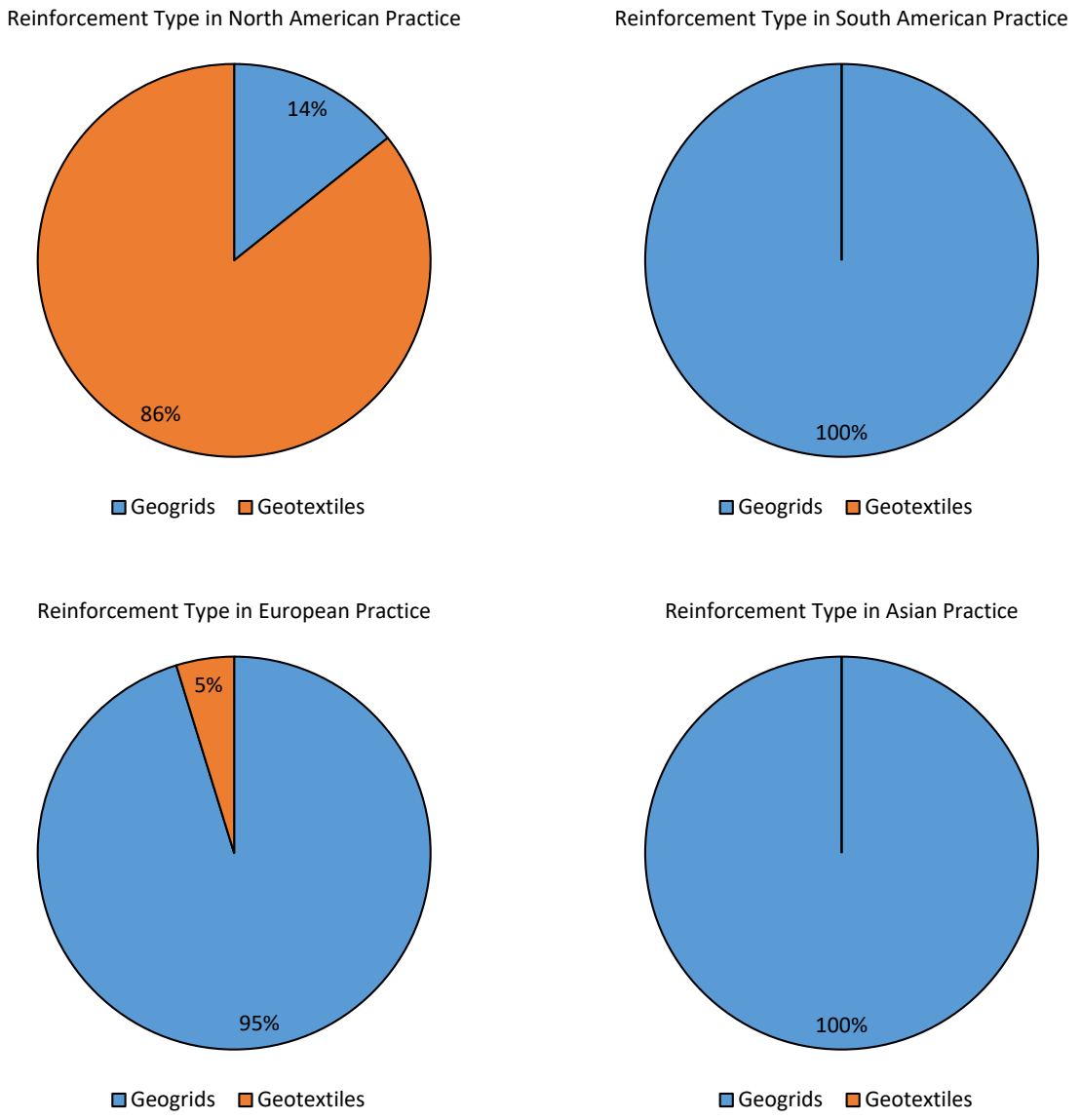

Figure 3.4.4. Type of reinforcement used in load-carrying GMSE bridge abutments per continent (continued)

Geosynthetic reinforcements have been manufactured using polymers that include: (1) polyester (usually coated with polyvinyl chloride); (2) polyethylene; (3) polypropylene; or (4) polyvinyl alcohol. Reinforcements manufactured using the first three polymers have been most commonly used in soil reinforcement applications. However, polyvinyl alcohol reinforcements have been used in several bridge abutments around the world. The selection of the reinforcement material depends on the environmental conditions at the structure location and on long-term degradation characteristics. Alexiew et al. (2000) reported that the ideal polymeric material would have the following features: (1) appropriate tensile strength; (2) low creep; (3) high interface shear strength; (4) high permeability; (5) low susceptibility to installation damage; (6) high resistance against chemical and biological degradation; and (7) low cost.

Guidelines in the US (Adams et al. 2011) require a reinforcement tensile strength that exceeds 70 kN/m (400 lb/in). Figure 3.4.5 shows the range of ultimate reinforcement tensile strengths adopted in the state-of-the-practice for each continent. The load-carrying GMSE bridge abutment constructed with the reinforcement identified as having the lowest tensile strength was identified at 250th Street Bridge in Buchanan County, Iowa, USA (T_{ult} = 21 kN/m (120 lb/in)). The structure that adopted reinforcements with the highest maximum tensile strength was identified at Venlo bridges in the Netherlands.

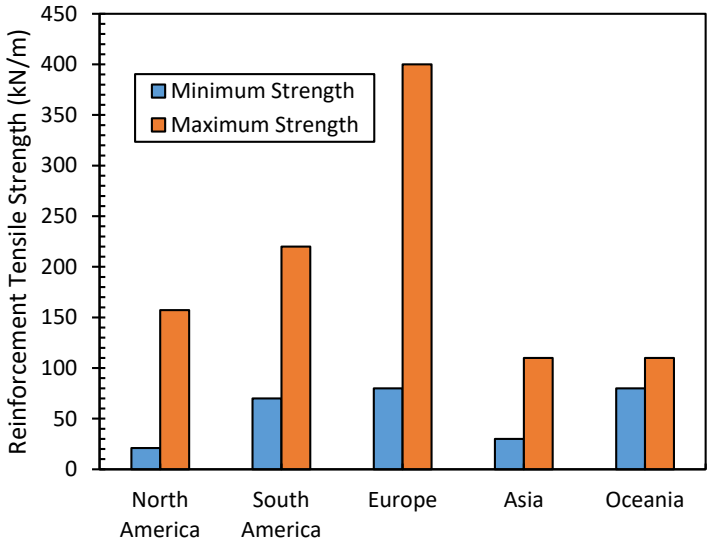

Figure 3.4.5. Range of reinforcement ultimate tensile strength for load-carrying GMSE bridge abutments in the different continents

3.4.4 REINFORCEMENT VERTICAL SPACING

In this section, the importance of reinforcement vertical spacing in the design of load-carrying GMSE bridge abutments is evaluated. As the vertical spacing decreases, the strength of the reinforced soil mass increases. Recent studies (e.g. Adams 1997; Adams *et al.* 2007; Ketchart and Wu 2001; Elton and Patawaran 2005; Ziegler *et al.* 2008) have indicated that reinforcement spacing has more influence than reinforcement tensile strength on closely-spaced reinforced structures. Soil-reinforcement interaction plays an important role in the behavior of the soil-geosynthetic composite. The shear stress generated at the soil-reinforcement interface propagates to the adjacent soil, which affects the interaction behavior of the contiguous reinforcement layers. Wu *et al.* (2006) reported that the default design reinforcement spacing for load-carrying GMSE abutments with flexible facing is 0.2 m (8 in), with a maximum allowable spacing of 0.4 m (16 in). Adams *et al.* (2011) reported that the maximum spacing beyond which the interaction is no longer significant is 0.3 m (1 ft). The range of reinforcement vertical spacing adopted in the state-of-the-practice for each continent is presented in Figure 3.4.6. The vertical spacing considered when secondary reinforcements were adopted in the design. Considering the structures identified, vertical spacing ranged from 0.2 m (8 in) to 0.6 m (2 ft). Many load-carrying GMSE structures in the United States, which correspond to the subgroup identified as GRS-IBS,

implemented a spacing of 0.2 m (8 in), with 0.1 m (4 in) spacing in the upper layers below the bridge bearing seat. The maximum reinforcement spacing identified for a load-carrying GMSE bridge abutment in South America, Europe and Oceania is 0.6 m (2 ft).

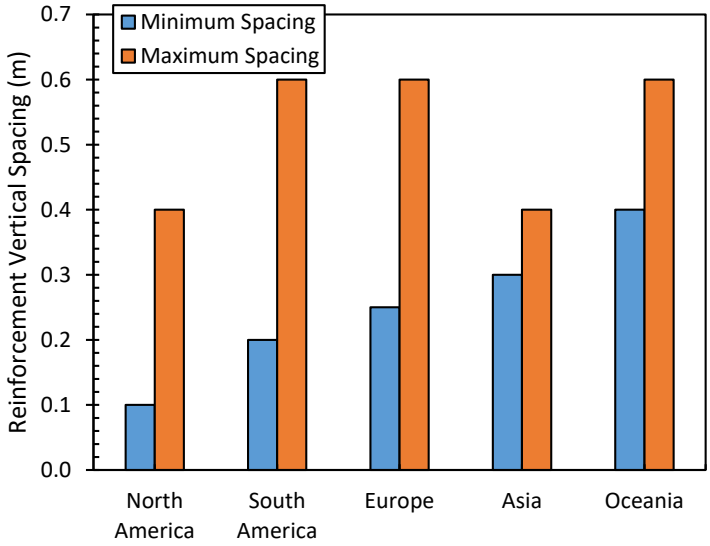

Figure 3.4.6. Range of reinforcement vertical spacing for load-carrying GMSE bridge abutments by continent

The reinforcement pattern adopted beneath the bearing seat has often been tailored to account for the stress concentration anticipated at this location within the reinforced soil mass. Some structures have adopted double reinforcement layers below the bearing seat, such as Mammoth Lakes Bridges in California, USA, as reported by Keller and Devin (2003). Wadey and Idrees (2014) reported that secondary reinforcement was used in the mid-layers below the bearing area at Nadahini Creek Bridge in British Columbia, Canada. This alternative has been adopted recently in many structures in the United States as well (e.g. Adams *et al.* 2012). Ullerslev Bridge, described in Kirschner and Hermansen (1994), used an additional reinforcement layer at a reduced spacing below the bearing seat level. Some structures, including Nadahini Creek Bridge and New Wales Bridge, had reduced vertical spacing at the bottom of the abutments to increase the reinforcement density at greater depths where the lateral earth pressure is predicted to be high. In contrast, Maringa Railway Bridges adopted reduced spacing for the lower layers and denser reinforcement for the upper layers.

3.4.5 FACING SYSTEM

Facing systems retain the soil at the vertical face of the reinforced soil mass. Multiple types of facing were adopted in the load-carrying GMSE abutments identified herein. Generally, the facing systems of reinforced-soil retaining structures include prefabricated modular blocks, segmental precast units, wrapped around reinforcement, steel wire mesh, gabions and vegetation. Some rehabilitated structures utilized old abutments as facing for the new reinforced-soil abutments, such as Lake Mamie Bridge reported in Keller and Devin 2003. Figure 3.4.7 shows the various

facing systems adopted in the state-of-the-practice, grouped by continent. In North and South America, segmental-block systems that can be mechanically or frictionally attached to the reinforcement layers are the leading facing system utilized. Three major types of facing systems were used in the European bridges identified: (1) segmental-block facing; (2) full-height wall facing; and (3) gabion facing. The predominant facing system used in Asia is the full-height wall system, employed extensively in Japan.

In the United States, many recent structures have adopted the modular block facing system with a frictional connection to the reinforcement layers (e.g., Adams *et al.* 2012). The reinforcement layers are sandwiched between modular block rows. Solid modular blocks covered with riprap tend to be used at the bottom of abutments to prevent erosion and scour, whereas hollow blocks tend to be used for upper abutment layers to mitigate the normal pressure on the lower blocks. The upper few rows are connected to one other vertically via dowels to prevent movement.

Wadey and Idrees (2014) reported that 3.175 mm thick corrugated aluminum sheeting was employed at Nadahini Creek Bridge in Canada to speed up construction. Deadman anchors were utilized to sustain the verticality of the sheeting without adding structural support to the reinforced soil mass. This facing system would prevent scour and erosion, and provide a more plumb wall. However, some difficulties were encountered in maintaining the verticality of the wall and placing the reinforcement without wrinkles. Sheet-pile facing has also been used in the United States in (1) Scott County, Iowa, (2) Kaw Nation, Oklahoma, and (3) at I-70 near Denver, Colorado.

In Japan, the full-height rigid facing is the typical system used with geosynthetic-reinforced soil abutments (Tatsuoka *et al.* 1997). This facing consists of cast-in-place lightly-reinforced concrete backed by wrap-around geosynthetic-reinforced layers. Gravel-filled bags are used at each soil layer around which the reinforcement layer is wrapped. To secure the concrete wall to the soil, steel bars are embedded in the concrete wall via semi-circular hooks that are mounted to continuous anchorage plates from the other side. This facing system has been reported to show excellent performance in resisting seismic lateral loads generated by bridge superstructures and limiting lateral deformation. This system has also been implemented in a structure in Slovenia, which is considered the first bridge to be constructed with a full-height rigid facing in Europe (Lenart *et al.* 2016).

In Germany, a concrete block (H+P) facing system was employed in some of the identified structures (Herold 2006). This system couples blocks filled with concrete by vertical tubes with various modular facing configurations. The blocks are reinforced so that edge cracking and chipping is avoided. The reinforcement is delivered to the site with its design length rolled and reinforcement strips are integrated into the facing units.

Facing Type in North American Practice

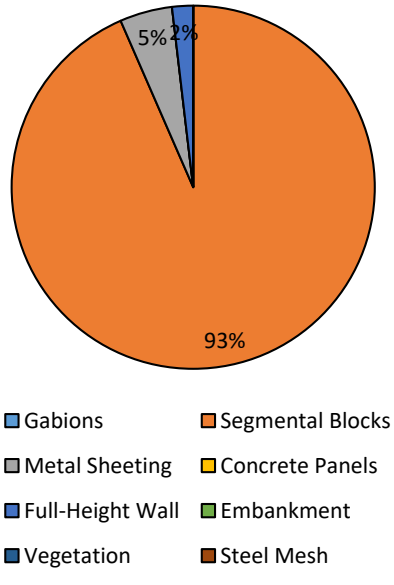

Facing Type in South American Practice

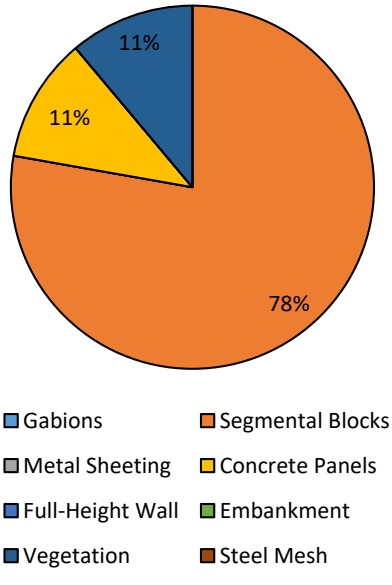

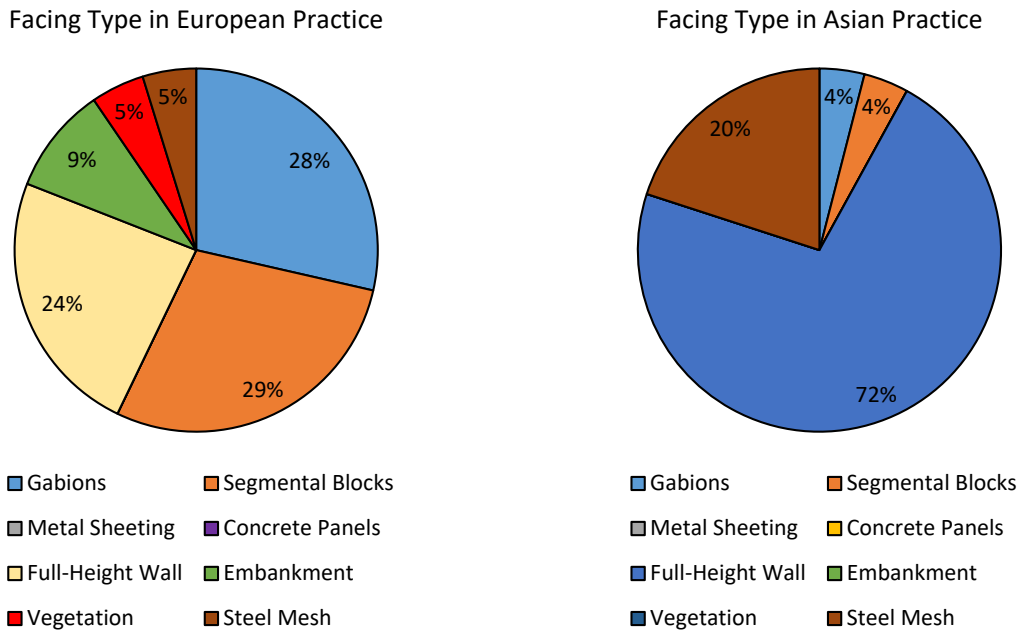

Figure 3.4.7. Type of facing in load-carrying GMSE abutments per continent

3.4.6 BEARING SEAT

Bearing seats are placed on top of the reinforced soil mass, beneath the bridge superstructure. Most of the bridges identified herein have employed bearing seats as an essential component in load-carrying GMSE abutments. In the US, many bridges that have adjacent concrete girder superstructures are constructed without bearing seats and instead use foam boards behind the facing, on top of the geosynthetic reinforced soil mass, to mitigate any pressure that might be conveyed from the bridge superstructure to the facing. Concrete blocks are placed on top of the foam boards, which are then placed on top of the facing, next to the concrete blocks, so that the corners of the foam boards at different levels are touching. In contrast, bridges with different types of superstructures (*e.g.* steel girders) may require bearing seats (Adams *et al.* 2012). Figures 3.4.8 and 3.4.9 illustrate the ranges of bearing seat width and setback distance, respectively, in the state-of-the-practice by geographic continent. Overall, the bearing seat width ranged from 0.2 m (8 in) to 3.8 m (12.5 ft) among the structures identified in this study. The bearing seat setback distance, measured from the front of the facing to the outside edge of the bearing seat, ranged from 0.2 m (8 in) to 2.5 m (8.2 ft). Adams *et al.* (2012) reported that the setback distance in the USA is usually 0.2 m (8 in) and can also be greater.

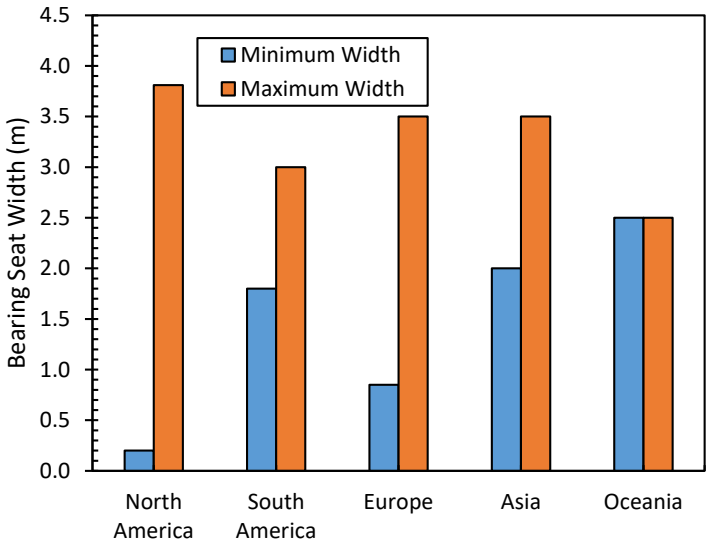

Figure 3.4.8. Range of the width of the bearing seat by continent

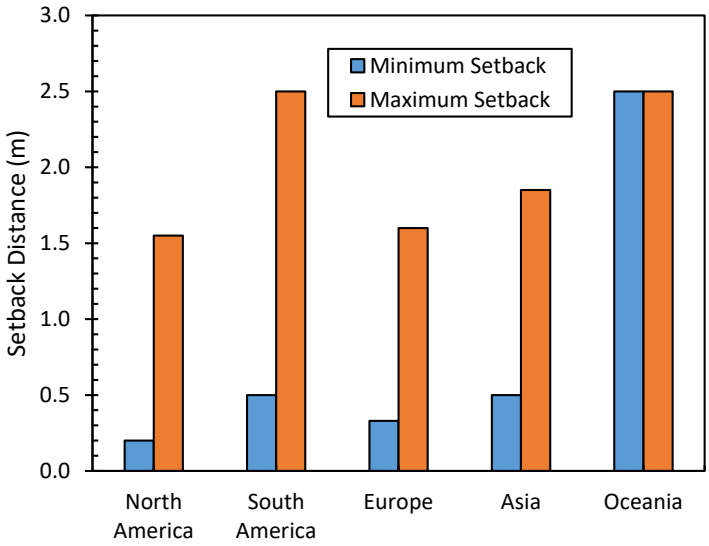

Figure 3.4.9. Range of setback distance of the bearing seat by geographic continent

3.5 SUMMARY

This chapter provides a summary of the state-of-the-practice, documenting the characteristics for the various components of the structures as constructed worldwide. The data was collected through a survey that targeted researchers, practitioners, wall system providers, and geosynthetic reinforcement providers. The survey collected information about the characteristics of GMSE abutments used nationally and internationally. The GMSE abutments included the

abutments of systems referred to GRS-IBS by FHWA (2011, 2018). An important outcome of this survey is that the range of reinforcement vertical spacing, geosynthetic type, facing type and even backfill materials is very wide. Partly because of the success of the Every Day Counts initiative, this wide range is in contrast to the reasonably prescriptive nature of this type of structures as constructed in the US. Specifically, as a conseqeuence of this initiative, the great majority of load-carrying GMSE bridge abutments can be characterized as GRS-IBS (i.e. designed following FHWA 2012, 2018). Accordingly, the reinforcement vertical spacing is significantly smaller than that adopted in most other structures worldwide. Also, while the most common geosynthetic type has been geogrids, the majority of the strucutres in the US have been constructed using woven geotextiles. In addition, while the types of facing in load-carryng GMSE bridge abutments varies widely worldwide, the use of masonry block facing systems has prevailed in the US. A common characteristic between the strucutres designed in the US and designed abroad has been the stringent requireements regarding selection of backfill material.

The motivation for the selection of load-carrying GMSE bridge abutments has been their anticipated good performance in providing adequate bearing capacity to support bridge loads and the flexibility required to reduce the bumps at the ends of bridges while acceptable deformations. Additional common reasons for their selection has been the smaller construction time as compared to conventional abutment alternatives. and their comparatively lower cost in relation to conventional abutments, as they do not require special equipment or a highly-skilled workforce.

Considering the significant number of bridges worldwide, still a comparatively small number of bridges have been constructed using this technology. Many studies have been conducted to provide a design methodology for load-carrying GMSE abutments. Of the bridges identified herein, the maximum number of spans was nine and the maximum span length was 42.7 m (140.1 ft). The maximum abutment height identified was 30.4 m (1 ft). While the types of backfill material employed ranged widely, high-quality, open-graded, coarse-aggregate backfills were favored for their high strength, stiffness and high drainage capacity. Various reinforcement types were implemented in the bridges identified, primarily geogrid and geotextile reinforcements, and the reinforcement spacing ranged from 0.1 m (4 in) to 0.6 m (2 ft). However, it is important to note that these spacings may be applied at different reinforcement densities (reinforcement configurations) within the same abutment. Of the European bridges identified, a variety of facing systems were used, with four predominant types: (1) segmental-block facing with mechanical or frictional connections; (2) full-height wall facing with mechanical connections; (3) gabion facing with mechanical connection; and (4) metallic sheeting (aluminum sheeting or steel sheet-piles).

3.6 REFERENCES

Abernathy, C. (2013). *Geosynthetic-reinforced Soil – Integrated Bridge System (GRS-IBS)*. Experimental Projects Construction Report. Montana Department of Transportation Research Programs. November 2013.

Abernathy, C. (2014). “Montana DOT Rebuilds an Old Bridge with a New System.” *Geosynthetics*, April 2014, Vol. 32, No. 2.

Abernathy, C. (2015). *Geosynthetic-reinforced Soil - Integrated Bridge System (GRS-IBS)*. Experimental Projects Construction and Site Inspection Report. Montana Department of Transportation Research Programs, June 2015.

Abu-Hejleh, N., Wang, T., and Zornberg, J.G. (2000b). "Performance of geosynthetic-reinforced walls supporting bridge and approaching roadway structures." *Geotechnical Special Publication*, pp. 218-243.

Abu-Hejleh, N., Zornberg, J.G., Wang, T., and McMullen, M. (2000a). *Performance of Geosynthetic-Reinforced Walls Supporting the Founders/Meadows Bridge and Approaching Roadway Structures*. Colorado Department of Transportation Report No. CDOT-DTD-R-2000-5.

Abu-Hejleh, N., Zornberg, J.G., Wang, T., and McMullen, M. (2001). *Performance of Geosynthetic-Reinforced Walls Supporting the Founders/Meadows Bridge and Approaching Roadway Structures*. Colorado Department of Transportation Report No. CDOT-DTD-R-2001-12.

Abu-Hejleh, N., Zornberg, J.G., Wang, T., and Watcharamonthein, J. (2002). "Monitored displacements of unique geosynthetic-reinforced soil bridge abutments." *Geosynthetics International*, Vol. 1, pp. 71-95.

Adams, M., Ketchart, K., Ruckman, A., DiMillio, A.F., Wu, J.T.H., and Satyanarayana, R. (1999). "Reinforced Soil for Bridge Support Applications on Low-Volume Roads." *Transportation Research Board*, Washington, D.C.

Adams, M., and Nicks, J. (2012). *Design and Cosntruction Guidelines for Geosynthetic Reinforced Soil Abutments and Integrated Bridge Systems*. Report No. FHWA-HRT-17-080, Federal Highway Administration, McLean, VA.

Adams, M., Nicks, J., Stabile, T., Wu, J., Schlatter, W., and Hartmann, J. (2012). *Geosynthetic-reinforced Soil Integrated Bridge System, Interim Implementation Guide*. Report No. FHWA-HRT-11-026, Federal Highway Administration, McLean, VA.

Adams, M., Nicks, J., Stabile, T., Wu, J., Schlatter, W., and Hartmann, J. (2011). *Geosynthetic-reinforced Soil Integrated Bridge System, Synthesis Report*. Report No. FHWA-HRT-11-027, Federal Highway Administration, McLean, VA.

Adams, M., Schlatter, W., and Stabile, T. (2007b). "Geosynthetic-Reinforced Soil Integrated Abutments at the Bowman Road Bridge in Defiance County, Ohio." *Geosynthetics in Reinforcement and Hydraulic Applications (GSP 165)*, Gabr, and Bowders (Eds.). ASCE, Reston, VA, pp. 119-129.

Adams, M.T. (1997). "Performance of a Prestrained Geosynthetic-reinforced Soil Bridge Pier," *Proceedings of the International Symposium on Mechanically Stabilized Backfill*, J.T.H. Wu (Ed.), Balkema, Rotterdam, Netherlands.

Adams, M.T., Ketchart, K., and Wu, J.T.H. (2007). "Mini Pier Experiments: Geosynthetic Reinforcement Spacing and Strength as Related to Performance," *Proceedings of Geo-Denver 2007*, American Society of Civil Engineers, Denver, CO.

Albert, G.R. (2012). Unpublished monitoring data for the Huston Township, Clearfield 585 County Mount Pleasant Road Bridge.

Alexiew and Detert (2008). "Analytical and Numerical Analyses of a Real Scaled Geogrid Reinforced Bridge Abutment Loading Test." *EuroGeo4 Paper number 257*.

Alexiew, D. (2007) "Belastungsversuch an einem 1:1 Modell eines geogitterbewehrten Bruckenwiderlagers." *Proceedings of KGeo 2007*, Munich, Germany. (In German).

Alexiew, D. (2008). “Ultimate bearing capacity tests on an experimental geogrid-reinforced vertical bridge abutment without stiffening facing.” *New Horizons in Earth Reinforcement, Taylor and Francis Group, London*, pp. 507-511.

Alexiew, D., Sobolewski, J., and Pohlmann, H. (2000). “Projects and Optimized Engineering with Geogrids from 'Non-Usual' Polymers.” *EuroGeo 2000: Proceedings of the 2nd European Geosynthetics Conference.* Volume 1: Mercer Lecture, Keynote Lectures, Geotechnical Applications.

Allen, T. M., Bathurst, R. J., Holtz, R. D., Walters, D., and Lee, W. F. (2003). “A new working stress method for prediction of reinforcement loads in geosynthetic walls.” *Canadian Geotechnical Journal*, Vol. 40, No. 5, pp. 976-994.

Athanasopoulos, G.A. (1993). “Effect of Particle Size on the Mechanical Behavior of Sand-Geotextile Composite.” *Geotextiles and Geomembranes*, Vol. 12, pp. 255-273, International Geosynthetics Society, West Palm Beach, FL.

Athanasopoulos, G.A. (1994). “On the Enhanced Confining Pressure Approach to the Mechanics of Reinforced Soil.” *Geotechnical and Geological Engineering* Vol. 12, pp. 122-132, Springer, Netherlands.

Bassett, A.K. and Last, N.C. (1978). “Reinforcing Earth below Footings and Embankments.” *Proceedings of the ASCE Spring Convention and Exhibit*, Pittsburgh, PA.

Benigni, C., Bosco, G., Cazzuffi, D., Col, R.D., 1996. “Construction, performance of an experimental large-scale wall reinforced with geosynthetics.” In: Ochiai, H., Yasufuku, N., Omine, K. (Eds.), Earth Reinforcement, Vol. 1. A. A. Balkema Publisher, Rotterdam, pp. 315-320.

Berg, R.R., Christopher, B.R., and Samtani, N.C. (2009). *Design of Mechanically Stabilized Earth Walls and Reinforced Soil Slopes–Volume II*. Report No. FHWA-NHI-10-025. National Highway Institute, Federal Highway Administration, Washington, D.C.

Bloser, S., Shearer, D., Corradini, K., and Scheetz, B. (2012). *Geosynthetically Reinforced Soil-Integrated Bridge Systems (GRS-IBS) Specification Development for PennDOT Publication 447.* Pennsylvania Department of Transportation Bureau of Planning and Research.

Brugger, P.J., Gomes, R.D.O.M., and Conte, M. (2012). “Rebaixamento da Linha Férrea de Maringá Utilizando Muros em Solo Reforçado.” *Proceedings of IGS Brasil CURSOS*. (In Portuguese).

Budge, A.S., Dasenbrock, D.D., Mattison, D.J., Bryant, G.K., Grosser, A.T., Adams, M., and Nicks, J. (2014). “Instrumentation and Early Performance of a Large-Grade GRS-IBS Wall.” *Geo-Congress 2014 Technical Papers Geo-characterization and Modeling for Sustainability*, 4213-4227.

Da Silva, A.E.F., Brugger, P.J., and Engenharia, B. (2012). “Análise do Comportamento de Muro de Contenção Portante em Solo Reforçado a partir de Monitoramento de Campo.” *12th Congresso Brasileiro de Mecanica dos Solos e Engenharia Geotechnica (COBRAMSEG).* (In Portuguese).

Detert, O., and Thomson, G. (2013). “Geogrid-Reinforced Bridge Abutments: Report on a Full Scale Test and Executed Projects.” *Advances in Geotechnical Infrastructure*. Edited by C. F. Leung, S.H. Goh and R.F. Shen. 241-246.

Ehrlich, M., Mitchel, J. K. (1994) Working Stress Design Method For Reinforced Soil Walls, *Journal of Geotechnical Engineering,* ASCE, Vol. 120, No. 4, pp. 625-647.

Elias, V.E., Christopher, B.R., and Berg, R.R. (2001). *Mechanically Stabilized Earth Walls and Reinforced Soil Slopes Design and Construction Guidelines*. Technical Report No. FHWA-

NHI-00-043, National Highway Institute, Federal Highway Administration, Washington, D.C.

Elton, D.J., and Patawaran, M.A.B. (2004). "Mechanically stabilized earth reinforcement tensile strength from tests of geotextile-reinforced soil." *Transportation Research Record: Journal of the Transportation Research Board*, Vol. 1868, pp. 81-88.

Elton, D.J., and Patawaran, M.A.B. (2005). *Mechanically stabilized earth (MSE) reinforcement tensile strength from tests of geotextile-reinforced soil*. Alabama Highway Research Center, Auburn University, Aurburn, AL.

Fahel, A.R., Palmeira, E.M., and Ortigao, J.A.R. (2000). "Behaviour of Geogrid Reinforced Abutments on Soft Soil in the BR 101-SC Highway, Brazil." *Geotechnical Special Publication*, 257-270.

Gotteland, Ph., Gourc, J.P., Villard, P., 1997. "Geosynthetics reinforced structures as bridge abutments: full scale experimentation and comparison with modelisations." In: *Wu, J.T.H. (Ed.), Mechanically Stabilized Backfill.* A. A. Balkema Publisher, Rotterdam, pp. 25–34.

Gourc, J.P., Gotteland, P., Haza, E., Perrier, H., and Baraize, E. (1995). "Geotextile reinforced structures as bridge abutments: full-scale experimentation." *Proceedings of Geosynthetics 1995 Conference Proceedings*, Nashville, TN, pp. 79-92.

Gray, D.H. and Ohashi, H. (1983). "Mechanics of Fiber Reinforcement in Sand," *Journal of Geotechnical Engineering*, Vol. 109, pp. 335–353, American Society of Civil Engineers, Reston, VA.

Hausmann, M.R. (1976). "Strength of Reinforced Earth," *ARRB Proceedings*, Vol. 8, ARRB Group, Melbourne, Australia.

Herold, A. (2002). "The first permanent road-bridge abutment in Germany built of geosynthetic-reinforced earth." *Proceedings of the 7th International Conference on Geosynthetics (7ICG), Delmas,* Gourc and Girard (eds).

Herold, A. (2005) "Brückenwiderlager aus KBE-Kunststoffbewehrte Erde, Einsatzgebiete Und Anwendungsgrenzen." *Geotechnik-Kolloquium*, Freiberg, Technische Institut für Geotechnik der Universität Bergakademie Freiberg, Heft 2005-2, pp. 195-217. (In German).

Herold, A. (2006) "Brückenwiderlager aus KBE-Kunststoffbewehrte Erde, Einsatzgebiete Und Anwendungsgrenzen." *Sächsisches Textilforschungsinstitut Bautextilien-Symposium*, Bautex 2006, Institut für Technische Textilien GmbH, Chemnitz, pp. 1-12. (In German).

Herold, A. (2007) "10 Jahre Verformungsbeobachtungen an KBE-Bauwerken – Ist die Dehnsteifigkeit der Geokunststoffe der Schlüssel zur korrekten Prognose des Verformungsverhaltens von KBE Stützbauwerken?" *Geotechnik*, Vol. 29, No. 2, pp. 79-86. (In German).

Herold, A. (2008) "Brückenwiderlager aus KBE-Hinweise fur Entwurf und Ausfuhrung." *Kolloquium "Bauen in Boden und Fels" in* Ostfildern , Technische Akademie Esslingen e.V., Tagungshandbuch 2008, pp. 533-543. (In German).

Herold, A., Aydoğmuş, T., and Sander, H. (2008). "Large Constructions and Bridge Abutments: Solutions with Geosynthetic-reinforced Earth." *Proceedings of Structures Congress 2008 Crossing Borders*, pp. 1-10.

Huesker Synthetic GmbH. *The Lagoons – Dubai*. Huesker Synthetic GmbH, Gescher.

Ingold, T.S. (1982). Reinforced Earth, Thomas Telford Ltd., London, United Kingdom.

Kasugai, A., and Tateyama, M. (1992). "Application of geosynthetic-reinforced soil for bridge abutments." *Earth Reinforcement Practice*, Ochiai, Hayashi & Otani (eds), 1992, Balkema, Rotterdam, pp. 363-368.

Keller, G. and Devin, S. (2003). "Geosynthetic-reinforced soil bridge abutments." *Transportation Research Record: Journal of the Transportation Research Board*, Vol. 1819, pp. 362-368.

Ketchart, K. and Wu, J.T.H. (2001). *Performance Test for Geosynthetic-reinforced Soil Including Effects of Preloading*. Report No. FHWA-RD-01-018, Federal Highway Administration, Washington, DC.

Kirschner, R., and Hermansen, E. (1994). "Abutments in Reinforced Soil for a Road Bridge." *Proceedings of the 5th International Conference on Geotextiles, Geomembranes, and Related Products*. Singapore, September, 1994, pp. 259-260.

Lee, K.Z., and Wu, J.T. (2004). "A synthesis of case histories on GRS bridge-supporting structures with flexible facing." *Geotextiles and Geomembranes*, Vol. 22, No. 4, pp. 181-204.

Lenart, S. (2014). *Final report of development of reinforced soil bridge abutments*. Report No. P 320/13-710-8, Oddelek za geotehniko in prometnice, Zavod za gradbeništvo Slovenije, 2014 (in Slovenian).

Lenart, S., Kralj, M., Medved, S.P., and Šuler, J. (2016). "Design and construction of the first GRS integrated bridge with FHR facings in Europe." *Transportation Geotechnics*, Vol. 8, pp. 26-34.

Ling, H.I. and Tatsuoka, F. (1994). "Performance of Anisotropic Geosynthetic-Reinforced Cohesive Soil Mass", *Journal of Geotechnical Engineering*, ASCE, Vol. 120, No. 7, pp. 1166-1184.

Ling, H.I., Tatsuoka, F., and Tateyama, M. (1995). "Simulating the Performance of GRS-RW by Finite Element Procedure." *Journal of Geotechnical Engineering*, ASCE, Vol. 124, No. 4, pp. 330-340.

Lo, S.R. (2004). Application of Numerical Modelling to the Design of Reinforced Soil Walls for Infrastructure Projects-Some Australian Experiences. In *GeoAsia2004: 3rd Asian Regional Conference on Geosynthetics: Now and Future of Geosynthetics in Civil Engineering*. June 2004.

Maher, M.H. and Woods, R.D. (1990). "Dynamic Response of Sand Reinforced with Randomly Distributed Fibers," *Journal of Geotechnical Engineering*, Vol. 116, pp. 1116–1131, American Society of Civil Engineers, Reston, VA.

Mirlatifi, S., and Fatahi, B. (2012). "Numerical Analysis of Geosynthetic-reinforced Soil Wall as Bridge Abutment." *Proceedings of the 11th Australia - New Zealand (ANZ) Conference on Geomechanics Ground Engineering in a Changing World*. Melbourne, Australia. July 2012, pp.1383-1388.

Mirlatifi, S.A.S. (2012). "Analysis, Design, and Construction Stages of Milad Geosynthetic-reinforced Soil Bridge Abutment in Tehran-Iran." *Australian Geomechanics*, Vol. 47, No. 3, September 2012, pp. 125-132.

Mohamed, K., Abouzakhm, M., and Elias, M. (2011). "Applications and performance of geosynthetic-reinforced soil abutments on soft subsurface soil conditions." *Transportation Research Board*.

Nancey, A., Rossi, D., and Boons, B. (2006). "Survey of a bridge abutment reinforced by geosynthetics, with optic sensors integrated in geotextile strips." *Proceedings of IGC 8th,* September 18-22, Yokohama, Japan, pp. 1071-1074.

Nguyen, Q. (2012). *GRS Abutments for Bridge Replacement National Wildlife Refuge.* A New Era of Partnerships - Investing in America's Treasures, U.S. Department of Transportation, FHWA, EFLHD.

Ortigao, J.A.R., Fahel, A.R., Palmeira, E.M., and Simmonds, A.J. (2001). "Stability and deformation monitoring of geogrid reinforced embankments." *Proceedings of Transportation Research Board Meeting on Geo-Construction Processes, TRB Meeting,* pp. 51-62.

Powell, W., Keller, G.R., and Brunette, B. (1999). "Applications for Geosynthetics on Forest Service Low-Volume Roads." *Transportation Research Record*, Vol. 1652, pp. 113-120.

Rimoldi, P. and Intra, E. (2009). "Design and Construction of Tall Reinforced Embankments in Static and Seismic Conditions." *GIGSA GeoAfrica 2009 Conference*, Cape Town, September 2009.

Railway Technical Research Institute (2012). *Design Standards for Railway Structures and Commentary Earth Retaining Structure*. Edited by Railway Technical Research Institute (RTRI), under supervision of Railway Bureau of Ministry of Land, Infrastructure, Transport and Tourism, (MLIT), Japan.

Schlosser, F. and Long, N.T. (1974). "Recent Results in French Research on Reinforced Earth." *Journal of Construction Division*, Vol. 100, pp. 223–237, American Society of Civil Engineers, Reston, VA.

Snijders, B., and Brok, C. (2007). "N242 Bridge Abutments on geogrid reinforced soil near the city of Alkmaar in the Netherlands." *Proceedings of the 14th European Conference on Soils Mechanics and Geotechnical Engineering (Geotechniek ECSMGE)*. Madrid, Spain, September 2007, pp. 12-14.

Suits, L.D., and Hsuan, Y.G. (2003). "Assessing the photo-degradation of geosynthetics by outdoor exposure and laboratory weatherometer." *Geotextiles and Geomembranes*, Vol. 21, No. 2, pp. 111-122.

Tatsuoka, F. (1993). "Roles of Facing Rigidity in Soil Reinforcing." *Earth Reinforcement Practice*, Keynote Lecture, Ochiai, H.,Hayashi, S. and Otani, J., Editors, Balkema, 1993, Proceedings of the International Symposium on Earth Reinforcement Practice, IS Kyushu 1992, Vol. 2, Kyushu, Fukuoka, Japan, November 1992, pp. 831-870.

Tatsuoka, F., and Yamauchi, H. (1987). "A Reinforcing Method for Steep Clay Slopes Using a Non-Woven Geotextile", *Geotextiles and Geomembranes*, Vol. 4, pp. 241-268.

Tatsuoka, F., Tamura, Y., Nakamura, K., Iwasaki, K., and Yamauchi, H. (1987). "Behavior of Steep Slope Clay Embankments Reinforced With a Non-Woven Geotextile Having Various Face Structures." *Proceedings of the Post Vienna Conference on Geotextiles*, Singapore, pp. 387-403.

Tatsuoka, F., Tateyama, M., Uchimura, T., and Koseki, J. (1997). Geosynthetic-Reinforced Soil Retaining Walls as Important Permanent Structures 1996-1997 Mercer Lecture. *Geosynthetics International*, Vol. 4, No. 2, pp. 81-136.

Tatsuoka, F.,Ando,H., Iwasaki, K. and Nakamura, K. (1986). "Performance of Clay Test Embankments Reinforced With a Non-Woven Geotextile", *Proceedings of the Third International Conference on Geotextiles,* Vol. 3, Vienna, Austria, April 1986, pp. 355-360.

Tecnologia de Materiales. *Muros de Solo Reforçado Como Estribos de Ponte S27 – Yanacocha.* Tecnologia de Materiales (TDM), Peru. (In Portuguese).

Tensar North American Green (2001). *The Mesa Systems Bridge Commerce in North Vancouver, B.C.* Tensar North American Green.

The American Association of State Highway and Transportation Officials (2014). AASHTO LRFD Bridge Design Specifications. Seventh Edition, 2014.

Van Duijnen, P.G., Linthof, T., Brok, C.A.J.M., and Eekelen, S.J.M. (2012). "Measuring deformations of a 10 m high geosynthetic-reinforced earth retaining wall." *Proceedings of the 5th European Geosynthetics Congress*. Valencia, 2012. Proceedings Vol 5. Topic: Soil Improvement and Reinforcement, pp. 157-161.

Vennapusa, P.K., White, D.J., and Keierleber, B. (2014). A Case Study of Geosynthetic-Reinforced Soil in a Low-Volume Bridge Abutment in Iowa. *Geo-Congress 2014 Technical Papers Geo-characterization and Modeling for Sustainability.* February 2014, pp. 4156-4166.

Vennapusa, P., White, D.J., Klaiber, F.W., Wang, S., and Gieselman, H. (2012). *Geosynthetic-reinforced soil for low-volume bridge abutments*. Report No. IHRB Project TR-621, Iowa Highway Research Board and Iowa Department of Transportation. 114p.

Wadey, L., and Idrees, M. (2014). Nadahini Creek Geosynthetic-reinforced Soil Integrated Bridge System. In Transportation 2014: Past, Present, Future-2014 Conference and Exhibition of the Transportation Association of Canada//Transport 2014: Du passé vers l'avenir-2014 Congrès et Exposition de'Association des transports du Canada.

Warren, K. A., Schlatter, W., Adams, M., Stabile, T., and LeGrand, D. (2010). "Preliminary Results for a GRS Integrated Bridge System Supporting a Large Single Span Bridge." *Proceedings of Earth Retention Conference 3*, ASCE, Reston, VA, pp. 612-619.

Warren, K.A., Whelan, M., Adams, M., and Nicks, J. (2013). "Preliminary Evaluation of Thermally Induced Strains and Pressured Developed in GRS Integrated Bridge System." *Geosynthetics Conference*, Long Beach, CA.

Warren, K. A., Whelan, M. J., Hite, J., and Adams, M. (2014). "Three-Year Evaluation of Thermally Induced Strain and Corresponding Lateral End Pressures for a GRS IBS in Ohio." In *Geo-Congress 2014 Technical Papers Geo-characterization and Modeling for Sustainability*. February 2014, pp. 4238-4251.

Werner, G., and Resl, S. (1986). "Stability mechanisms in geotextile reinforced earth-structures." In *III International Conference on Geotextiles, Vienna, Austria*, Vol. 4, pp. 1131-1135.

Won, G.W., Hull, T., De Ambrosis, L. (1996). "Performance of a geosynthetic segmental block wall structure to support bridge abutments." In: Ochiai, H., Yasufuku, N., Omine, K. (Eds.), *Earth Reinforcement*, Vol. 1. A. A. Balkema Publisher, Rotterdam, pp. 543–548.

Wu, J.T.H. (2006). Design and construction guidelines for geosynthetic-reinforced soil bridge abutments with a flexible facing (No. 556). Transportation Research Board.

Wu, J.T.H., Ketchart, K., and Adams, M. (2001). GRS *bridge piers and abutments*. Report No. FHWA-RD-00- 038. Federal Highway Administration, US Department of Transportation, Washington, D.C. 136p.

Yamauchi, H. and Tatsuoka, F., Nakamura, K., Tamura, Y. and Iwasaki, K. (1987). "Stability of Steep Slope Clay Embankments ReinforcedWith a Non-WovenGeotextile," *Proceedings of the Post Vienna Conference on Geotextiles*, Singapore, pp. 370-386.

Yang, Z. (1972). *Strength and Deformation Characteristics of Reinforced Sand*, PhD. Thesis, University of California at Los Angeles, Los Angeles, CA.

Yang, Z. and Singh, A. (1974). *Strength and Deformation Characteristics of Reinforced Sand*, International Meeting on Water Resources Engineering, Los Angeles, CA.

Ziegler, M., Heerten, G., and Ruiken. G. (2008). "Progress in the Understanding of Geosynthetic/Soil Composite Material Behaviour in Geosynthetic-reinforced Earth Structures," Presented at *The First Pan American Geosynthetics Conference and Exhibition*, Cancun, Mexico.

Zornberg, J.G., Abu-Hejleh, N., and Wang, T. (2001). "Geosynthetic-Reinforced Soil Bridge Abutments." Geotechnical Fabrics Report, Vol. 19, No. 2, March, pp. 52-55.

4 REEVALUATION OF PUBLISHED DATA

While the research conducted as part of this project has generated a substantial volume of data, it was also found to be particularly beneficial to capitalize on the availability of important experimental and field monitoring data from previous studies. This includes studies that have been previously conducted by members of the Research Team, information that was available through collaborative efforts, as well as relevant data generated previously by FHWA. The main objective of the review documented in Chapter 2 was to summarize relevant information, as published in technical venues that was relevant to assess the composite behavior of GRS structures. Instead, the emphasis of the information presented in Chapter 4 is on the detailed evaluation of actual data sources (both published and unpublished) that were deemed particularly valuable. This included actual experimental and field monitoring data. Interpretation of the source data proved to be important and useful to support the implementation of the experimental, field and numerical research components subsequently documented in Chapters 5, 6, and 7, respectively.

In this context, Chapter 4.1 provides a reevaluation of FHWA data compiled to assess the composite behavior of geosynthetic-reinforced structures with closely-spaced reinforcement. Chapter 4.2 subsequently evaluates published and unpublished field monitoring data collected from a series of GMSE walls constructed by KDOT, characterized by their use of primary and secondary reinforcements at various vertical spacings. Chapter 4.3 includes an assessment of published and unpublished data from experimental and field work conducted in the early 1990s that had focused on understanding the composite nature of GRS walls with closely-spaced reinforcement. Chapter 4.4 includes evaluation of a significant volume of centrifuge experimental data on geosynthetic-reinforced soil structures conducted at the University of California, Davis and the University of Colorado Boulder. Chapter 5.5 documents a reassessment of published and unpublished data on the performance of the Founders/Meadows GMSE abutment that was constructed and heavily instrumented in 1998. Finally, Chapter 4.6 includes the presentation and evaluation of instrumentation data from field monitoring investigations involving recently constructed GRS-IBS structures, including those constructed by MnDOT, LDOT and CDOT.

4.1 EVALUATION OF THE PERFORMANCE OF LARGE-SCALE EXPERIMENTAL GEOSYNTHETIC-REINFORCED SOIL (GRS) STRUCTURES

4.1.1 INTRODUCTION

Soil reinforcement technology has become a vital alternative for many structures, such as bridge supports. Soil reinforcement has proven to provide economic, time-efficient solutions. Soil-reinforcement technology has been adopted in bridge-supporting structures using (1) metallic reinforcement forming metallically reinforced MSE abutment and (2) geosynthetic reinforcement forming geosynthetically reinforced MSE abutment. Although the FHWA 1980s research program indicated that reduced stresses develop in the reinforcements towards the face of the wall, AASHTO has conservatively required that the connection stress should equal the maximum reinforcement tension. Also, state agencies often rely on manufacturer's design recommendations, which have traditionally placed strong pressure towards using comparatively wider spaced, more economical, higher strength geosynthetic reinforcements. Partly in response to these issues, FHWA has recently developed both empirical and analytical design models for GRS-IBS structures (Adams et al. 2012 – FHWA-HRT-11-026; Adams et al. 2011 – FHWA-HRT-11-027). FHWA has also calibrated the reliability of these models using results from GRS test piers, which have been correlated against monitored field results.

The GRS mini-pier tests were performed both with and without facing elements and with a reinforcement spacing of 0.1 m (4 in.) at the top of the structure. The program included GRS test piers constructed with various reinforcement vertical spacings (i.e. approximately 0.10 m (4 in.), 0.2 m (8 in.), 0.275 m (10.8 in.), and 0.375 m (14.8 in.) as well as with and without facing blocks. The piers were subjected to very large uniform surcharge loading and tested to failure. These tests have been extensively evaluated for vertical and horizontal deformations of the composite system and some of the results from these experiments have been published (e.g. Nicks et al. 2013a, 2013b). Although the tests clearly show the difference in load bearing behavior among the constructed structures, as in all laboratory experiments, the results represent conditions unique to those used in the tests. It should be noted, for example, that the surcharge used in the laboratory is uniform and centered over the reinforced pier, while surcharge in a bridge abutment is not necessarily uniform, being often eccentric. Consequently, in the laboratory simulations surcharge increased simultaneously both the pullout load and the pullout resistance whereas in an actual abutment only the load may increase. Furthermore, while the pier tests are extremely instructive, there is a very significant impact of 3D conditions, mainly since the piers were short relative to its cross section dimensions. Such 3D effects may result in increased inherent stability thus making non-straightforward the correspondence to prevailing 2D conditions in a GRS abutment. Consequently, the full scope of realistic field conditions needs to be addressed before a design may be considered acceptable by AASHTO LRFD. Accordingly, this study presents an independent reassessment of the published and unpublished monitoring data on the GRS mini-pier tests and instrumented field structures was conducted as part of this study to critically evaluate these boundary effects.

Many studies have been conducted to define the service limit states of deformations and stresses of geosynthetic-reinforced soil bridge abutments and piers. Reliable yet simple prediction of the service state of these structures is crucial for their serviceability assessment. The study collects published data for real and experimental structures. It assesses the practical models that were developed recently. Finally, the study proposes recommendations for modifying the assessed models.

4.1.2 BACKGROUND

Reinforced soil walls were introduced in 1966 by the French Engineer Henri Vidal who stated: "if we could put in place one layer of grains in contact with one layer of reinforcement, then one layer of grains, and so on, we should not have any need for facing. The facing retains the grain located near the exterior between two layers of reinforcement; it corresponds to a very local problem." While this statement was controversial with the conventional retaining walls, this technology is still accepted to this day. Later, soil-reinforcement has evolved to employ geosynthetic reinforcement. The first geosynthetically reinforced MSE structure in North America, which was a retaining wall, was constructed in 1974 in the United States of America (Berg et al. 2009a). Since then, the use of geosynthetically reinforced MSE walls has become a considerable alternative for retaining structures. They have become even more popular after the introduction of the geogrid reinforcement in 1982, and the segmental facing units in 1985 (Berg et al. 2009a). The technology has been adopted and advancing globally.

The Federal Highway Administration (FHWA) has conducted a long-term research on the MSE technology that started in the 1980s. The first design and construction guidelines were generated and published in Christopher et al. (1990a). The work that has been conducted by that time was summarized in Christopher et al. (1990b). Continued work has resulted in revised design and construction guidelines (Berg et al. 2009a, 2009b). Recently, FHWA has introduced geosynthetic-reinforced soil (GRS) technology as closely-spaced reinforced MSE structures. FHWA has promoted this technology through its Every Day Counts (EDC) initiative program. A number of publications document the research conducted by FHWA or with the use of FHWA facilities.

Several studies have attempted to study the long-term behavior of GRS structures (e.g. Allen et al. 1992; Wu and Helwany 1996). Wu and Helwany (1996) developed a laboratory performance test (see Figure 4.1.1) to evaluate the creep behavior of geosynthetic reinforcement due to soil-geosynthetic interaction. The geosynthetic reinforcement and the confining soil were loaded for a long period of time and allowed to deform in an interactive manner. Clean sand and kaolin clay were used as backfills for two different tests. The results showed that reinforced soils have higher stiffness and strength than unreinforced soils. Yet, some vertical and horizontal deformations have to take place to mobilize the reinforcing effects. In addition, it was also concluded that the time-dependent deformation of the confining soil plays a very important role in the long-term creep potential of a GRS structure. That is, the reinforcement creep deformation is significantly affected by the time-dependent deformation characteristics of soils under confinement. Time-dependent deformation of sands and clays is very different. Sands have tendency to deform at slower rate than the geotextile. Conversely, clays have tendency to deform at a higher rate than

the geotextile. Wu and Helwany (1996) concluded that evaluating the soil-geosynthetic composite creep potential could be misleading if it is based on the results of geosynthetic element creep tests only. Ketchart and Wu (1996) reported that the creep deformation with time at a decreasing rate. In sands, vertical and lateral deformation are limited and similar. In clays, lateral deformation is negligible; however, the vertical deformation is significant. In addition, higher reinforcement strength further reduces the deformation significantly.

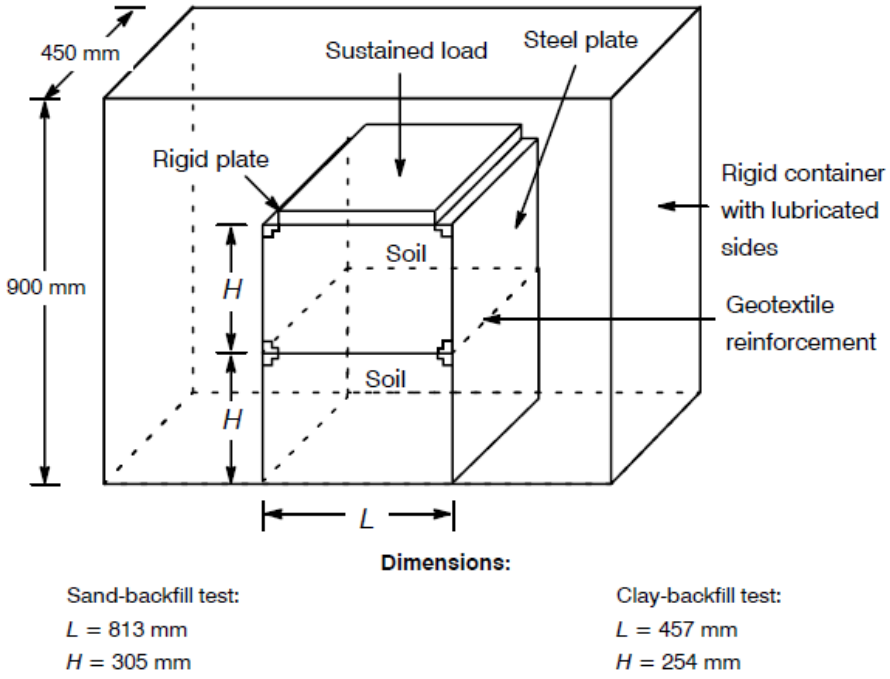

Figure 4.1.1: Soil-Geosynthetic Performance (SGP) testing apparatus developed by Wu and Helwany (1996)

Christopher et al. (1986) developed a test for determining the confined stress-strain behavior characteristics of reinforcement, which provided satisfactory results. Also, Ketchart and Wu (FHWA-RD-01-018, 2001) investigated the behavior of GRS masses under various loading conditions. The study aimed at developing a simplified analytical model for predicting deformation characteristics of a generic GRS mass. Specifically, the researchers developed Soil-Geosynthetic Performance (SGP) laboratory test with the objective of mimicking field placement conditions of GRS structures. This test aimed at capturing the effect of the interaction between the backfill soil and the geosynthetic reinforcement. Ketchart and Wu (2001) conducted a set of SGP tests using various soil types, geosynthetic reinforcements, and loading sequences. The study evaluated the effect of preloading on the GRS behavior. The authors correlated the results of SGP tests to full-scale GRS structures in order to assess the degree of accuracy of the SGP test to predict the reduction in settlement due to preloading. Specifically, two preloaded reinforced soil structures and their corresponding SGP test were examined: (1) FHWA pier (Adams 1997) and the second generation SGP test, and (2) Black Hawk abutments reported by Wu *et al.* (FHWA-RD-00-038, 2001) and the modified SGP test. The correlations were generated in terms of

normalized values of loads and displacements. Ketchart and Wu (2001) concluded that (1) preloading increases soil stiffness, but has no effect on shear strength, while reloading stiffness depends on confining pressure and unloading load level; (2) preloading increases geosynthetic stiffness, very slightly decreases tensile strength, while reloading stiffness reduces with increasing preloading load level; (3) preloading has no effect on shear strength of interface. Reloading stiffness increases with preloading and normal stress applied on the interface; (4) preloading has no effect on the GRS carrying capacity; (5) the creep of geosynthetic reinforcement is negligible when using well-compacted granular fill, and stress relaxation occurs right after construction; and (6) unloading and reloading stress-strain behavior nearly coincides.

Wu *et al.* (FHWA-RD-038, 2001) describe in detail three projects involving load testing of GRS abutments and piers. The first project is a full-scale bridge pier load test conducted at the Turner-Fairbank Highway Research Center (TFHRC). This pier is referred to as the Turner-Fairbank pier. The second project involves a full-scale, long-term load test of a bridge abutment and a bridge pier conducted by the Colorado Department of Transportation (CDOT) and the University of Colorado at Denver. These piers and abutment are referred to as the Havana Yard piers and abutment. The third project involves the load test of a production bridge abutment performed by Yenter Companies in Black Hawk, Colorado. This abutment is referred to as the Black Hawk abutment. The abutments evaluated as part of these studies were instrumented to assess behavior under load testing. Wu *et al.* (2001) provide a comprehensive description to the projects along with testing results and analysis. Recommendations to GRS applications are incorporated in the report.

Ketchart and Wu (2002) developed a Soil-Geosynthetic Interactive Performance (SGIP) testing apparatus (see Figure 4.1.2) to assess the deformation behavior of GRS composites. The test is a modified version of the SGP test developed earlier by Ketchart and Wu (FHWA-RD-01-018, 2001). The test consists of applying a vertical load on a GRS composite under plane strain condition. The applied load is transferred from soil to geosynthetic allowing both to deform in an interactive manner. Lateral and vertical displacements of the GRS mass are measured along with the reinforcement strains. Ketchart and Wu (2002) conducted a set of tests to investigate repeatability, failure mode, and deformation behavior of different GRS composites. The behavior of tested GRS was compared to that of a GRS pier to verify the test applicability. Wu and Adams (2007) investigated the long-term creep behavior of GRS systems and proposed revisions to the current design methods. The authors recommended a cumulative long-term reduction factor for geosynthetic reinforcement. This reduction factor is a function of the backfill gradation and index properties, reinforcement spacing, and geosynthetic polymer type. The authors presented a procedure to account for soil-geosynthetic interactive creep behavior based on SGIP test.

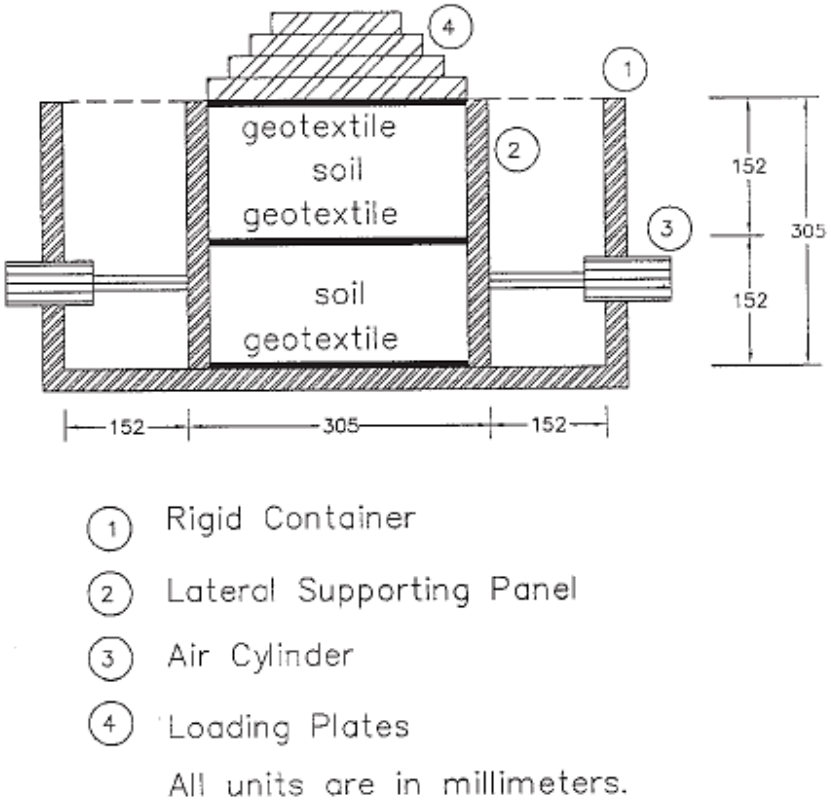

Figure 4.1.2: Modified Soil-Geosynthetic Interactive Performance (SGIP) testing apparatus developed by Ketchart and Wu (1996)

Wu *et al.* (NCHRP 556, 2006) developed a design methodology and construction guidelines for GRS bridge abutments with flexible facing (i.e., geotextile-wrapped, timber, and natural rock facing). They depended on the findings reported in the literature along with findings of full-scale experiments and analytical study performed. Wu *et al.* (NCHRP 556, 2006) constructed full-scale GRS abutments (see Figure 4.1.3). The tested GRS structures showed good performance and high load-carrying capacity. In addition, the authors compiled a design methodology and construction procedure for GRS abutments with flexible facing. Detailed design examples were also provided. Adams *et al.* (2007a) conducted five large-scale GRS Mini Pier tests to assess the effect of reinforcement spacing and reinforcement strength on the behavior of GRS masses. The authors reported that the bearing capacity for closely-spaced GRS was significantly improved and that the contribution of the reinforcement spacing was more relevant to the performance of a GRS mass than the reinforcement strength.

Adams *et al.* (FHWA-HRT-11-026, 2012) provide a design methodology and construction procedure for GRS-IBS structures. This manual aims at providing background knowledge of GRS technology as well as of its fundamental characteristics as an alternative to other construction methods. In addition to providing detailed guidance on the design of GRS-IBS, the manual includes analytical and empirical design methodologies involving both the Allowable Stress Design (ASD) and Load and Resistance Factor Design (LRFD) approaches. Background knowledge

in support of the design methodology is summarized by Adams *et al.* (FHWA-HRT-11-027, 2011), which documents the fundamental characteristics of GRS technology as an alternative construction method. This document supplements the interim implementation manual by Adams *et al.* (FHWA-HRT-11-026, 2012) and provides a generic design methodology and construction outline of the GRS-IBS. In addition, it includes the results of research conducted to provide the basis for the design method. Finally, case histories are summarized to document the performance of in-service GRS-IBS and GRS walls.

Nicks *et al.* (FHWA-HRT-13-066, 2013a) reported the results of a series of experimental GRS performance tests, also identified as mini-pier experiments. The tests were conducted by axially loading a GRS mass while measuring the resulting deformations and, thus, documenting the mini-piers' performance. The mini-piers included alternating layers of compacted granular fill and geosynthetic reinforcement connected frictionally to facing elements. This report documents the testing procedure and provides the axial load-deformation results for the performance tests conducted in this study. In addition, this research aimed at establishing a database of GRS material properties for the purposes of construction of GRS-IBS structures. The results are used to: (1) establish a relationship between reinforcement strength and spacing, (2) quantify the contribution of the frictionally connected facing elements at the service limit and strength limit states, (3) assess the internal stability design method proposed by Adams *et al.* (2011) for GRS, and (4) provide the basis for a reliability analysis of the soil-geosynthetic capacity equation for LRFD calibration. In addition, Nicks *et al.* (2013b) determined the material strength properties of particular GRS composites based on GRS mini-pier performance test results. The effects of backfill type and compaction on the GRS composites were also investigated. Nicks *et al.* (2013b) outlined the performance test methodology along with resulting load-deformation characteristics. Nicks *et al.* (2013a) concluded that (1) particle angularity of the backfill improves the GRS composite ultimate strength; (2) compaction doesn't affect the GRS ultimate strength but provide much stiffer response; (3) bearing bed (secondary reinforcement placed at the upper portion of the GRS mass) improves the vertical capacity but not vertical strain; however, it limits its local lateral deformation; (4) frictional CMU facing provides confinement leading to stiffer GRS composite response (increasing ultimate capacity and decreasing vertical strain; and (5) for the same reinforcement strength-to-spacing ratio (T_f/S_v), reinforcement spacing impacts the behavior more than reinforcement strength, unlike largely-spaced GRS (reinforcement spacing greater than 0.3 m (1 ft.)) where reinforcement spacing is proportional to reinforcement strength.

Wu *et al.* (FHWA-HRT-10-077, 2013) investigated the composite behavior of a GRS mass by conducting a series of large-scale generic soil geosynthetic composite (GSGC) tests. This involved constructing GRS piers with two fixed sides to mimic a plane-strain condition. Similar test has been conducted by Bathurst and Benjamin (1990), which involved constructing GRS abutment with two fixed sides and unreinforced shored fill behind the GRS mass. Wu *et al.* (FHWA-HRT-10-077, 2013) designed their tests to assess the behavior of a GRS mass under well-controlled conditions. The experimental results showed that reinforcement spacing influences the GRS behavior more significantly than reinforcement strength. Wu *et al.* (FHWA-HRT-10-077, 2013) developed analytical model that allowed description to the relative contribution of reinforcement strength and reinforcement spacing. In addition, equations were developed based

on an analytical model. These equations were developed to calculate the apparent cohesion of a GRS composite (acquired cohesion due to the reinforcement inclusion), the ultimate load-carrying capacity of a GRS mass, and the required tensile strength of reinforcement for a given reinforcement spacing. The suitability of the developed equations was evaluated by comparing the predictions against the results of GSGC tests, large-size experiments performed by other researchers, and finite element (FE) simulations. Moreover, an analytical procedure was developed to predict the lateral wall movement and the required tensile strength of reinforcement. In addition, an analytical model for estimating compaction-induced stresses in a GRS mass was proposed. The model predictions were compared against the results of GSGC tests and FE simulations. Wu *et al.* (FHWA-HRT-10-077, 2013) also investigated the dilatant behavior of GRS composites. They reported that reinforcements tend to suppress dilation of the surrounding soil and reduce its angle of dilation.

4.1.3 GRS EXPERIMENTAL STRUCTURES DATABASE

Since soil-reinforcement interaction depends on the normal stresses, laboratory observations alone may not be sufficient to predict field performance. Accordingly, an independent reassessment of the published and unpublished monitoring data on the GRS mini-pier tests and some instrumented field structures was conducted to critically evaluate the feasibility of these tests. In addition, reliable prediction of the service state of these structures is crucial for their serviceability assessment. Accordingly, this study collected a massive amount of published data for experimental structures (Morsy 2017). This section presents the database established in favor of this evaluation.

4.1.3.1 GSGC TESTS BY WU ET AL. (FHWA-HRT-10-077, 2013)

Wu et al. (FHWA-HRT-10-077, 2013) conducted five experiments large-scale GRS columns. The GRS is fixed from two sides by stiffened transparent walls to simulate a plane-strain condition as shown in Figure 4.1.3. The GRS mass was 1.94-m (6.4 ft) high and 1.2 x 1.4 m (3.9x4.6 ft) in plan. The backfill material used was well-graded gravel classified as A-1-a in accordance to AASHTO and GW-GM in accordance to USCS. The friction angle and the cohesion of the soil were 50 degrees and 70 kPa (10.2 psi), respectively, obtained from large-scale triaxial testing. The maximum dry density and optimum moisture content of the backfill were 24.1 kN/m^3 (155 pcf) and 5.2%, respectively. The backfill had approximately 15% fine content. The soil was reinforced by a medium-strength woven geotextile layers employed at 0.2-m (8 in.) vertical spacing. The reinforcement was Geotex® 4×4 polypropylene woven geotextile manufactured by Propex®. The reinforcement spacing varied from 0.2 to 0.4 m (7.9 to 15.7 in.). The ultimate tensile strength of the reinforcement was 70 kN/m (400 lbf/in). The testing program involved using double layer reinforcement so as two different reinforcement types could be used: (1) a single reinforcement layer; and (2) a double reinforcement layer (two glued layers), which showed approximately twice the tensile stiffness and strength of the single layer in uniaxial tension tests. Facing hollow concrete blocks were used for the deformable sides of the GRS mass. The configurations of the five conducted tests are summarized in Table 4.1.1.

(a)

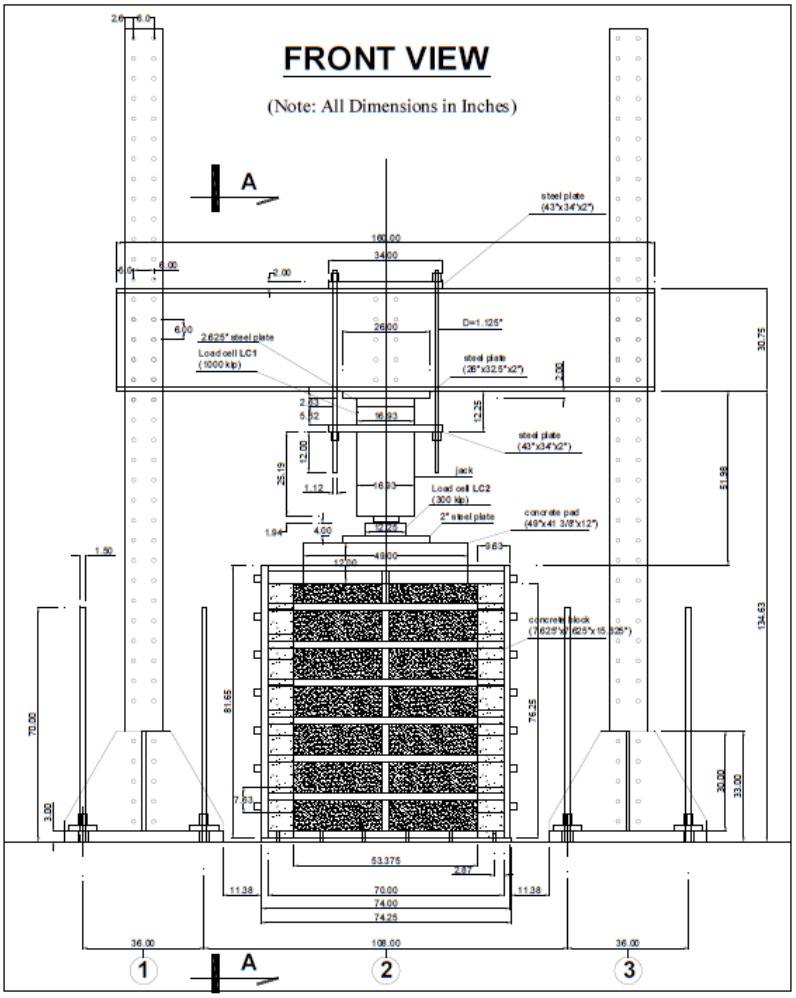

(b)

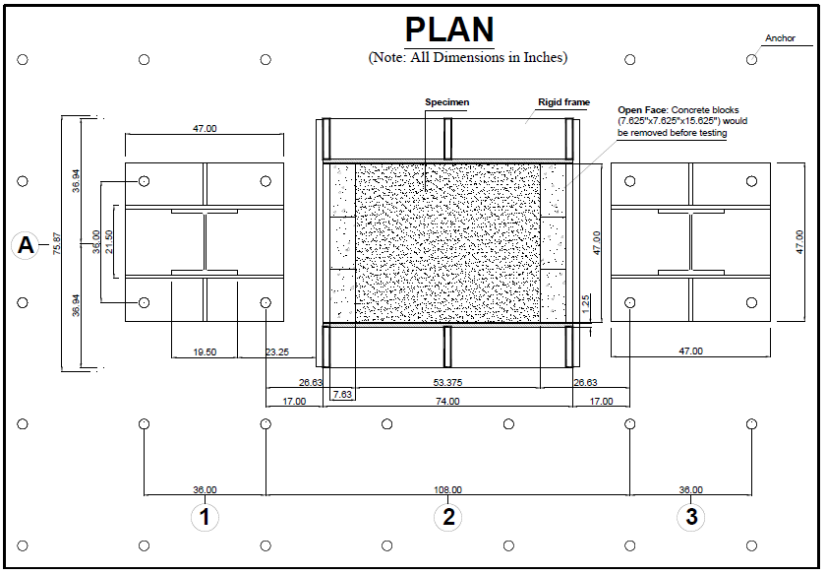

Figure 4.1.3: GSGC test setup: (a) front view; (b) plan view (Wu et al. 2013 – FHWA-HRT-10-077).

Table 4.1.1: Test configurations (Wu et al. 2013)

Test Designation	Geosynthetic Reinforcement	Confining Pressure (kPa)	Wide-width Strength Reinforcement (kN/m)	of Reinforcement Spacing (m)
GSGC1	None	34	None	None
GSGC2	Geotex® 4x4	34	70	0.2
GSGC3	Double-sheet Geotex® 4x4	34	140	0.4
GSGC4	Geotex® 4x4	34	70	0.4
GSGC5	Geotex® 4x4	0 (unconfined)	70	0.2

4.1.3.2 CYLINDRICAL COLUMN TESTS BY ELTON AND PATAWARAN (2004, 2005)

Elton and Patawaran (2004, 2005) tested GRS cylindrical columns (see Figure 4.1.4) 0.76 m (2.5 ft) in diameter and 1.52-m (5 ft) high. The backfill material used was poorly graded sand classified as SP in accordance to USCS. The maximum dry density and the optimum moisture content were 18 kN/m^3 (116 pcf) and 9.3%, respectively. The friction angle and the cohesion of the soil were 40 degrees and 29 kPa (4.2 psi), respectively, obtained from direct shear testing. The reinforcement used was polypropylene nonwoven geotextile layers placed at vertical spacing of 0.15 m (0.5 ft). Different reinforcement types were used with different mass per unit area. The reinforcement tensile strength varied from 9 to 25 kN/m (51 to 143 lb/in.). Note that the tensile strength of the used reinforcement was different in machine and cross-machine directions.

Figure 4.1.4: Cylindrical GRS column (Elton and Patawaran 2005)

4.1.3.3 NCHRP EXPERIMENTAL ABUTMENTS BY WU ET AL. (NCHRP 556, 2006)

Wu et al. (NCHRP 556, 2006) tested two full-scale experimental GRS bridge abutments 4.65-m (15.3 ft) high, as shown in Figure 4.1.5, to assess the behavior of GRS abutments subject to various vertical load levels. These abutments were constructed back-to-back over a rigid floor (reinforced concrete mat). The backfill was a non-plastic silty sand with fines content of 8.5% classified as SP-SM in accordance to USCS. The maximum dry density and the optimum moisture content of the soil were 18.3 kN/m^3 (118 pcf) and 11.5%, respectively. The backfill material was compacted in the abutments at relative density of 99% and 1.7% wet of optimum moisture content. The shear strength parameters were obtained by large-scale triaxial and large-scale direct shear tests on samples prepared at the same relative density and moisture as the backfill placed in constructed abutments. The friction angle and the cohesion obtained from the large-scale triaxial tests were 37.3 degrees and 20 kPa (2.9 psi), respectively; whereas, the friction angle and the cohesion obtained from the large-scale direct shear tests were 36.5 degrees and 0 kPa (0 psi), respectively. Polypropylene woven geotextile reinforcement was used in both abutments, which included Amoco 2044 for one abutment and Mirafi 500x for the other abutment. The tensile strength for Amoco 2044 and Mirafi 500x geotextiles were 70 and 21 kN/m (400 lbf/in and 120 lbf/in), respectively, in their cross-machine direction. The reinforcement was employed at a vertical spacing of 0.2 m (8 in.) for both abutments. Additional reinforcement layers were added near the top of the abutments to form bearing beds as shown in Figure 4.1.5. The facing used for the abutments involved concrete cinder blocks with a split-face.

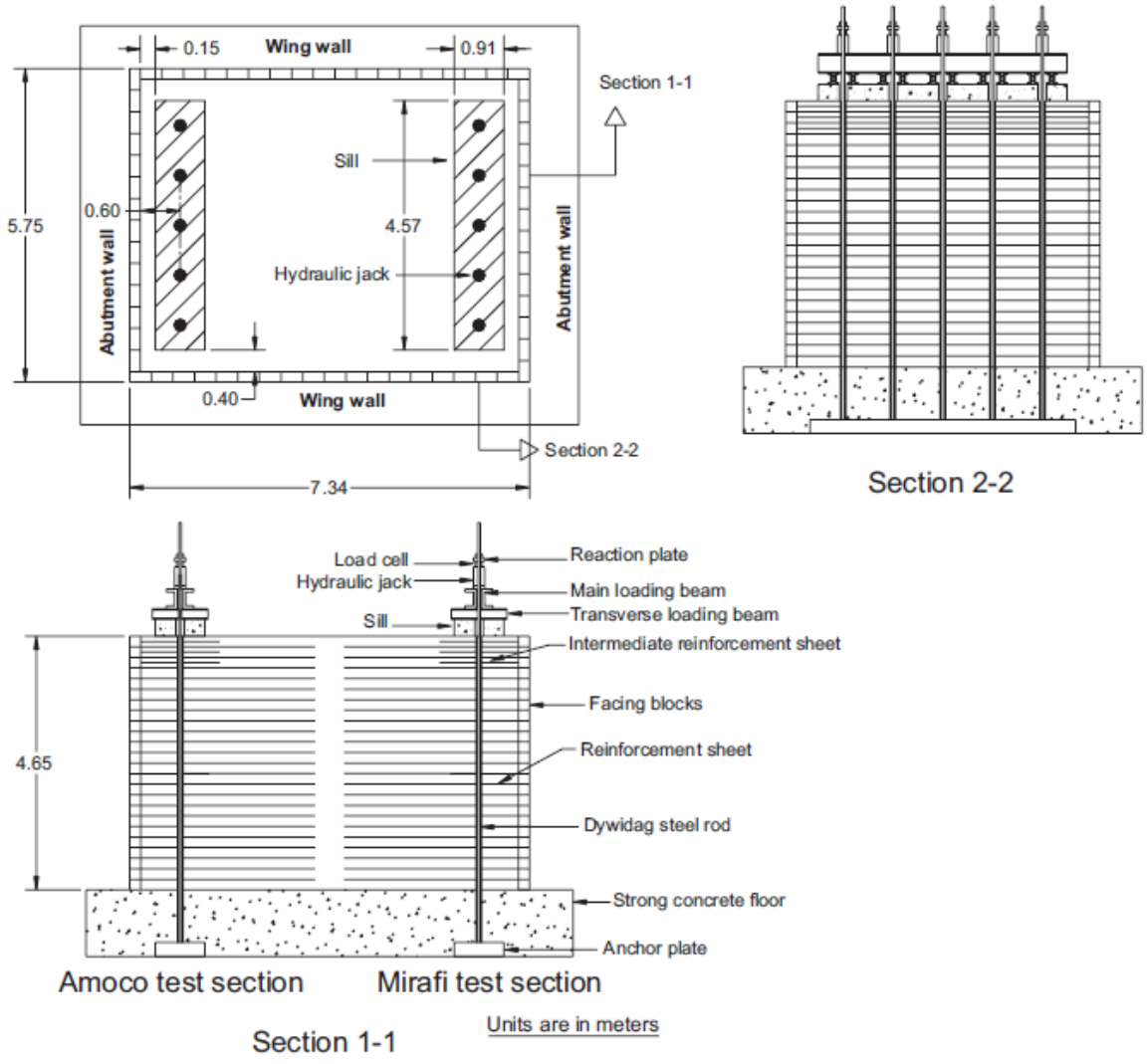

Figure 4.1.5: Configuration of the NCHRP full-scale test abutments (Wu et al. 2006 – NCHRP 556)

4.1.3.4 FHWA PIER TEST BY ADAMS (1997)

Adams (1997) conducted a vertical loading test on a full-scale GRS. The pier was 5.4-m (17.7 ft) high and its base dimensions were 3.6 x 4.8 m (11.8x15.7 ft). The facing of the pier was battered as shown in Figure 4.1.6. The backfill material used in the construction of the pier was compacted road base. The reinforcement employed involved polypropylene woven geotextile with tensile strength of 70 kN/m (400 lbf/in). The reinforcement layers were placed at a vertical spacing of 0.2 m (8 in.). The facing used was dry stacked modular blocks (split face cinder blocks). The pier was constructed on reinforced soil foundation, formed on 1.2-m (4 ft) thick compacted backfill and reinforced with three biaxial geogrid layers placed at a vertical spacing of 0.3 m (12 in.).

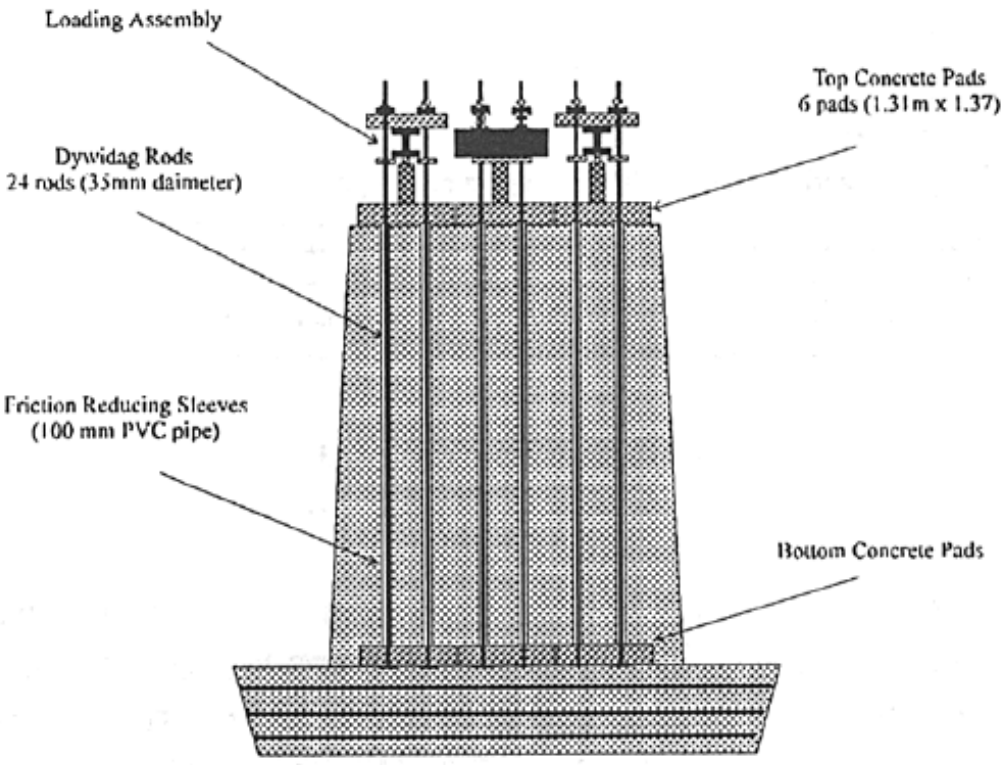

Figure 4.1.6: Schematic of the FHWA pier (Adams 1997)

4.1.3.5 VEGAS MP MINI-PIER TEST BY ADAMS ET AL. (2002)

Adams et al. (2002) tested a GRS mini-pier, which involved a GRS mass of 1.12 x 1.12 m (44x44 in.) cross-sectional area (excluding the facing) and 2.4 m (8 ft) in height as shown in Figure 4.1.7. The backfill material used was gravel classified as GP-GM in accordance to USCS. The facing used was Segemental Retaining Wall (SRW) blocks, which were solid dry cast concrete with split-face. The reinforcement used was polypropylene woven geotextiles with tensile strength of 35 kN/m (200 lbf/in). The reinforcement was placed at a vertical spacing of 0.15 m (0.5 ft) with additional two reinforcement courses at the top of the pier (creating a beading bed).

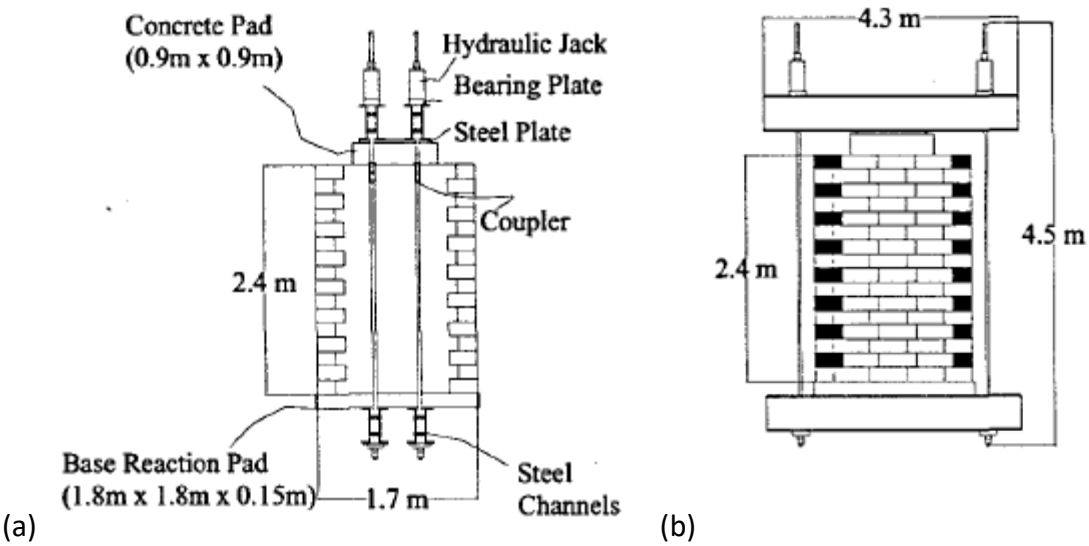

Figure 4.1.7: Schematic of the Vegas mini-pier: (a) side view; (b) front view (Adams 2002).

4.1.3.6 MINI-PIER TESTS BY MITCHELL (200)

Mitchell (2002) conducted four GRS mini-pier performance tests (see Figure 4.1.8). The backfill material used was well-graded gravelly sand with fines content of 11.5%. The maximum dry density and the optimum moisture content of the soil were 23.1 kN/m^3 (148 pcf) and 8.75%, respectively. The shear strength properties of the soil was obtained by direct shear testing. The friction angle and cohesion measured were 36 degrees and 30.5 kPa (4.4 psi), respectively. The reinforcement used was woven geotextile with tensile strength of 30.7 kN/m (175 lbf/in). The facing used was concrete blocks known as split face Keystone.

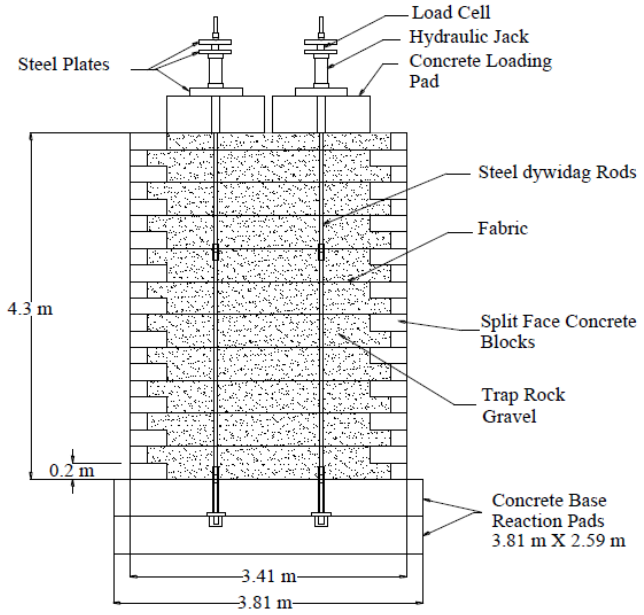

Figure 4.1.8: Schematic of GRS mini-piers (Mitchell 2002).

4.1.3.7 MP MINI-PIER TESTS BY ADAMS ET AL. (2007A)

Adams et al. (2007a) conducted four performance tests on the mini piers with the dimensions shown in Figure 4.1.9. The testing configurations are summarized in Table 4.1.2. The facing used involved Concrete Masonry Units (CMUs), which was removed before the load tests to negate its effect on the GRS behavior. The reinforcement used was polypropylene woven geotextile layers with different tensile strength. MP A, MP B, and MP D were constructed with a strong geotextile reinforcement placed at different vertical spacing; whereas, MP C was constructed with a weak geotextile placed at 0.2-m (8 in.) spacing. The backfill material used was well graded crushed base rock classified as GW-GM in accordance to USCS with a fines content of approximately 10%. The maximum dry density and the optimum moisture content of the backfill were 24 kN/m^3 (154 pcf) and 6%, respectively. The placement density of the backfill material in the various tests is summarized Table 4.1.2.

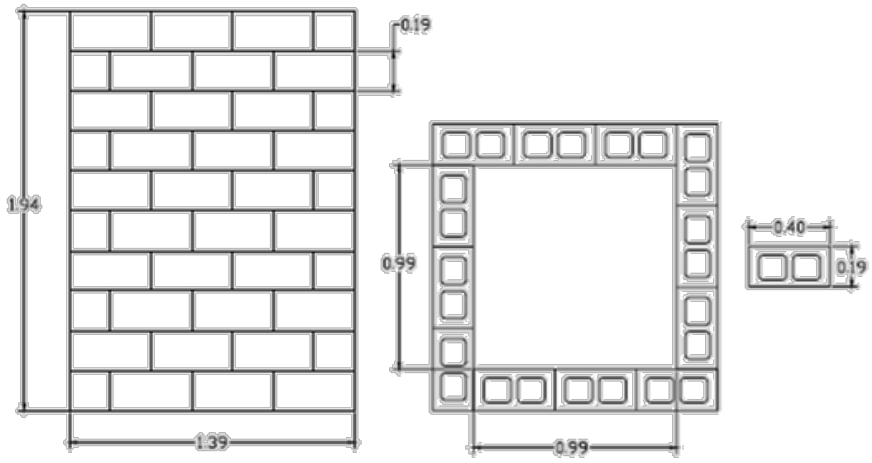

Figure 4.1.9: Schematic for the mini-piers (Adams et al. 2007a).

Table 4.1.2: Summary of the testing configurations (Adams et al. 2007a).

Experiment	Fill Average Density (kN/m^3)	Geotextile Reinforcement Schedule		
		Polypropylene Type	Strength (kN/m)	Spacing (m)
MP NR	22.4	None	None	None
MP A	23.0	A2044	70	0.4-0.6
MP B	22.7	A2044	70	0.4
MP C	Not Available	A2000	21	0.2
MP D	22.8	A2044	70	0.2

4.1.3.8 DC AND TF MINI-PIER TESTS BY NICKS ET AL. (FHWA-HRT-13-066, 2013A)

Nicks et al. (FHWA-HRT-13-066, 2013a) conducted 19 mini-pier performance tests denoted as DC (5 tests) and TF (14 tests) piers. A schematic of the mini-pier test is shown in Figure 4.1.10. The tests conducted with facing and without facing in which after construction facing units were removed. The facing used was split-faced concrete masonry units (CMUs). Several backfill and reinforcement materials were adopted in the testing program as summarized in Table 4.1.3.

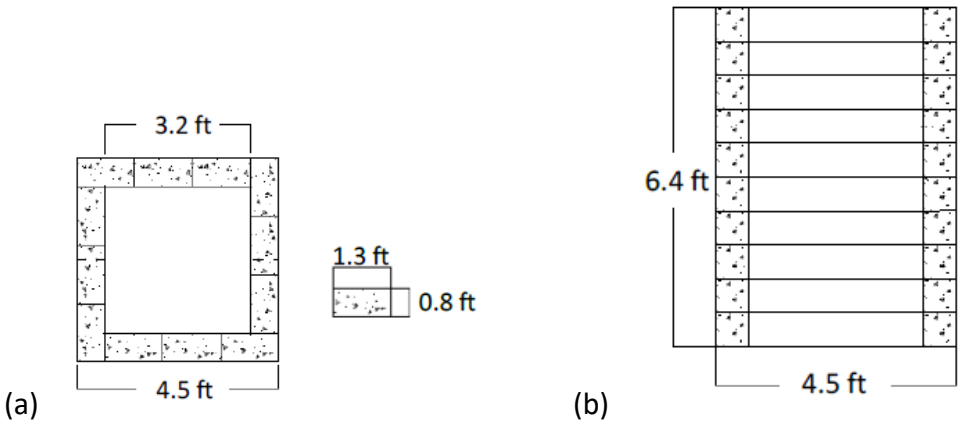

Figure 4.1.10: Schematic for the Defiance County (DC) mini-pier: (a) plan view; (b) elevation view (Nicks et al. 2013 – FHWA-HRT-13-066).

Table 4.1.3: Summary of the testing configurations (Nicks et al. 2013a – FHWA-HRT-13-066).

Test No.	Backfill				Reinforcement			Facing
	Type	ϕ (deg)	c (psf)	dmax (in.)	Tf (lb/ft)	Sv (in.)	Tf/Sv (lb/ft2)	
DC-1	8	54	0	0.5	4,800	7.625**	7,600	CMU
DC-2	8P*	46	0	0.75	4,800	7.625**	7,600	CMU
DC-3	57	52	0	1	4,800	7.625**	7,600	CMU
DC-4	9	49	0	0.375	4,800	7.625**	7,600	CMU
DC-5	8***	54	0	0.5	4,800	7.625**	7,600	CMU
TF-1++	8	55	0	0.5	2,400	7.625	3,800	CMU
TF-2	21A	53	115	1	2,400	7.625	3,800	CMU
TF-3	21A	53	115	1	2,400	7.625	3,800	no CMU
TF-4+	21A	53	115	1	4,800	7.625	7,600	no CMU
TF-5++	21A	53	115	1	4,800	7.625	7,600	no CMU
TF-6++	21A	53	115	1	4,800	7.625	7,600	CMU
TF-7	21A	53	115	1	4,800	7.625	7,600	no CMU
TF-8	21A	53	115	1	4,800	7.625**	7,600	no CMU
TF-9	21A	53	115	1	4,800	15.25	3,800	CMU
TF-10	21A	53	115	1	4,800	15.25	3,800	no CMU
TF-11	21A	53	115	1	1,400	313/16	4,400	no CMU
TF-12	21A	53	115	1	1,400	3.1825	4,400	CMU
TF-13	21A	53	115	1	3,600	11.25	3,800	no CMU
TF-14	21A	53	115	1	3,600	11.25	3,800	CMU

*Rounded pea-gravel angularity.

**Two courses of bearing bed reinforcement placed at the top of the pier.
***Uncompacted sample.
+Technical difficulties required termination during testing.
++Technical difficulties resulted in unloading/reloading of the composite.

4.1.3.9 LARGE-SCALE TRIAXIAL TESTS BY RUIKEN AND ZIEGLER (2009)

Ruiken and Ziegler (2009) conducted 8 large-scale triaxial tests (4 reinforced and 4 unreinforced) on samples 0.5 m (1.6 ft) in diameter and 1.1-m (3.6 ft) high as shown in Figure 4.1.11. The backfill material they used was crushed base course material compacted at a relative density of either 95% or 100%. The reinforcement employed in the samples involved biaxial polypropylene geogrids with tensile strength of 12 kN/m (69 lbf/in) at 2% axial strain and 24 kN/m (137 lbf/in) at 5% strain. The samples were confined laterally by vacuum; the confinement levels adopted were 10, 30, 50, 70 kN/m² (1.5, 4.4, 7.3, 10.2 psi). Three geogrid layers were placed at a vertical reinforcement spacing of approximately 0.3 m (12 in.).

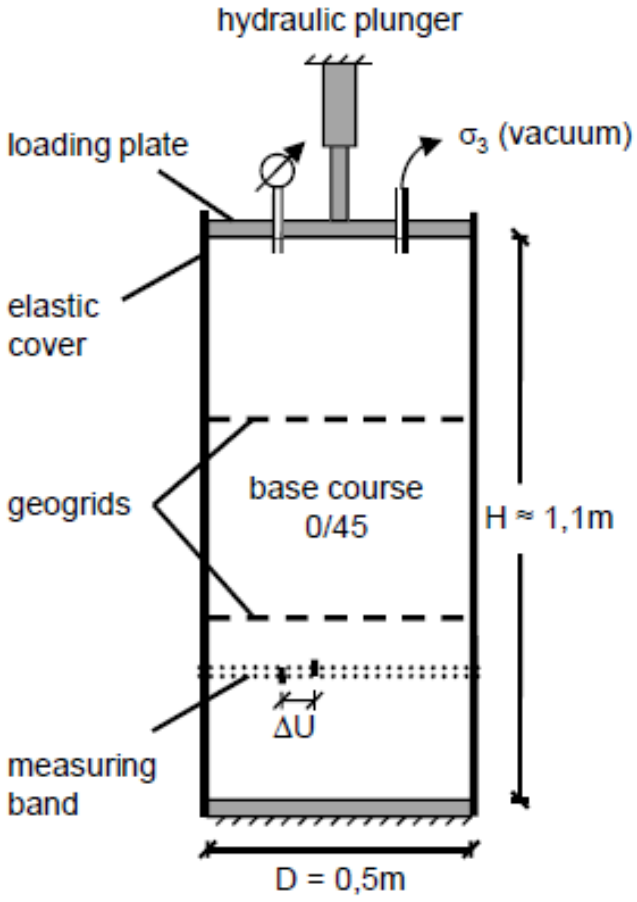

Figure 4.1.11: Schematic for the large-scale triaxial test (Ruiken and Ziegler 2009).

A summary of the consolidated GRS experimental structures database is presented in Table 4.1.4. While the information presented in the table does not exclusively include all the compiled data, it includes the essential information about the materials employed in each of the collected experimental structure to complete the summary given earlier. In addition, more information are presented in the analysis section as needed.

Table 4.1.4: GRS experimental structures database (after Morsy 2017)

Number	Test Name	Facing Type	Sv (m)	Tf (kN/m)	dmax (m)	c (kPa)	Φ (deg)	Φ method	Geometry	Reference
1	GSGC 1	Concrete Blocks/Plexiglas	N/A	N/A	0.033	70	50	TX	Fixed Wall	Pham (2008); Wu et al. (2013)
2	GSGC 2	Concrete Blocks/Plexiglas	0.2	70	0.033	70	50	TX	Fixed Wall	Pham (2008); Wu et al. (2013)
3	GSGC 3	Concrete Blocks/Plexiglas	0.4	140	0.033	70	50	TX	Fixed Wall	Pham (2008); Wu et al. (2013)
4	GSGC 4	Concrete Blocks/Plexiglas	0.4	70	0.033	70	50	TX	Fixed Wall	Pham (2008); Wu et al. (2013)
5	GSGC 5	Concrete Blocks/Plexiglas	0.2	70	0.033	70	50	TX	Fixed Wall	Pham (2008); Wu et al. (2013)
6	Elton and Patawaran 1	None	0.15	9	0.0127	29	40	DS	Cylindrical Column	Elton and Patawaran (2004, 2005)
7	Elton and Patawaran 2	None	0.3	9	0.0127	29	40	DS	Cylindrical Column	Elton and Patawaran (2004, 2005)
8	Elton and Patawaran 3	None	0.15	14	0.0127	29	40	DS	Cylindrical Column	Elton and Patawaran (2004, 2005)
9	Elton and Patawaran 4	None	0.15	15	0.0127	29	40	DS	Cylindrical Column	Elton and Patawaran (2004, 2005)
10	Elton and Patawaran 5	None	0.15	19	0.0127	29	40	DS	Cylindrical Column	Elton and Patawaran (2004, 2005)
11	Elton and Patawaran 6	None	0.15	20	0.0127	29	40	DS	Cylindrical Column	Elton and Patawaran (2004, 2005)
12	Elton and Patawaran 7	None	0.15	25	0.0127	29	40	DS	Cylindrical Column	Elton and Patawaran (2004, 2005)
13	NCHRP 1	CMU	0.2	21	0.0254	0.020	36.5 37.3	LSDS LSTX	Abutment	Wu et al. (2006)
14	NCHRP 2	CMU	0.2	70	0.0254	0.020	36.5 37.3	LSDS LSTX	Abutment	Wu et al. (2006)
15	Defiance 1	CMU	0.2	35	0.0127	0	50.7	LSDS	Square Column	Adams et al. (2007b)
16	Defiance 2	CMU	0.2	70	0.0127	0	50.7	LSDS	Square Column	Adams et al. (2007b)
17	Vegas MP	SRW	0.15	35	0.0254	70	50	TX	Square Column	Adams et al. (2002)

18	MP NR	None	N/A	N/A	0.0254	0	53.5	LSDS	Square Column	Adams et al. (2007a)
19	MP A	None	0.6	70	0.0254	0	53.5	LSDS	Square Column	Adams et al. (2007a)
20	MP B	None	0.4	70	0.0254	0	53.5	LSDS	Square Column	Adams et al. (2007a)
21	MP C	None	0.2	21	0.0254	0	53.5	LSDS	Square Column	Adams et al. (2007a)
22	MP D	None	0.2	70	0.0254	0	53.5	LSDS	Square Column	Adams et al. (2007a)
23	DC-1 (VS-1)	CMU	0.2	70	0.0127	0	54	LSDS	Square Column	Nicks et al. (2013a)
24	DC-2 (VS-2)	CMU	0.2	70	0.01905	0	46	LSDS	Square Column	Nicks et al. (2013a)
25	DC-3 (VS-3)	CMU	0.2	70	0.0254	0	52	LSDS	Square Column	Nicks et al. (2013a)
26	DC-4 (VS-4)	CMU	0.2	70	0.009525	0	49	LSDS	Square Column	Nicks et al. (2013a)
27	DC-5 (VS-5)	CMU	0.2	70	0.0127	0	54	LSDS	Square Column	Nicks et al. (2013a)
28	TF-1	CMU	0.2	35	0.0127	0	55	LSDS	Square Column	Nicks et al. (2013a)
29	TF-2	CMU	0.2	35	0.0254	5.5	53	LSDS	Square Column	Nicks et al. (2013a)
30	TF-3	None	0.2	35	0.0254	5.5	53	LSDS	Square Column	Nicks et al. (2013a)
31	TF-4	None	0.2	70	0.0254	5.5	53	LSDS	Square Column	Nicks et al. (2013a)
32	TF-5	None	0.2	70	0.0254	5.5	53	LSDS	Square Column	Nicks et al. (2013a)
33	TF-6	CMU	0.2	70	0.0254	5.5	53	LSDS	Square Column	Nicks et al. (2013a); Iwamoto (2014)
34	TF-7	None	0.2	70	0.0254	5.5	53	LSDS	Square Column	Nicks et al. (2013a); Iwamoto (2014)
35	TF-8	None	0.2	70	0.0254	5.5	53	LSDS	Square Column	Nicks et al. (2013a)
36	TF-9	CMU	0.4	70	0.0254	5.5	53	LSDS	Square Column	Nicks et al. (2013a); Iwamoto (2014)
37	TF-10	None	0.4	70	0.0254	5.5	53	LSDS	Square Column	Nicks et al. (2013a); Iwamoto (2014)
38	TF-11	None	0.1	20	0.0254	5.5	53	LSDS	Square Column	Nicks et al. (2013a); Iwamoto (2014)
39	TF-12	CMU	0.1	20	0.0254	5.5	53	LSDS	Square Column	Nicks et al. (2013a); Iwamoto (2014)
40	TF-13	None	0.3	56	0.0254	5.5	53	LSDS	Square Column	Nicks et al. (2013a); Iwamoto (2014)
41	TF-14	CMU	0.3	56	0.0254	5.5	53	LSDS	Square Column	Nicks et al. (2013a); Iwamoto (2014)

42	Mitchell 1	CMU	0.6	30.6	0.0254	30.5	36	LSDS	Square Column	Mitchell (2002)
43	Mitchell 2	CMU	0.4	30.6	0.0254	30.5	36	LSDS	Square Column	Mitchell (2002)
44	Mitchell 3	CMU	0.2	30.6	0.0254	30.5	36	LSDS	Square Column	Mitchell (2002)
45	Mitchell 4	CMU	0.8	30.6	0.0254	30.5	36	LSDS	Square Column	Mitchell (2002)
46	FHWA Pier	Cinder Block	0.2	70	N/A	N/A	N/A	N/A	Square Column	Adams (1997)
47	Ruiken and Ziegler 1	Elastic Cover	0.3	24	0.0508	0	46.5	TX	Cylindrical Column	Ruiken and Ziegler (2009)
48	Ruiken and Ziegler 2	Elastic Cover	0.3	24	0.0508	0	46.5	TX	Cylindrical Column	Ruiken and Ziegler (2009)
49	Ruiken and Ziegler 3	Elastic Cover	0.3	24	0.0508	0	46.5	TX	Cylindrical Column	Ruiken and Ziegler (2009)
50	Ruiken and Ziegler 4	Elastic Cover	0.3	24	0.0508	0	46.5	TX	Cylindrical Column	Ruiken and Ziegler (2009)
51	Ruiken and Ziegler 5	Elastic Cover	0.3	24	0.0508	0	46.5	TX	Cylindrical Column	Ruiken and Ziegler (2009)
52	Ruiken and Ziegler 6	Elastic Cover	0.3	24	0.0508	0	46.5	TX	Cylindrical Column	Ruiken and Ziegler (2009)
53	Ruiken and Ziegler 7	Elastic Cover	0.3	24	0.0508	0	46.5	TX	Cylindrical Column	Ruiken and Ziegler (2009)

4.1.4 ANALYSIS

The consolidated database is looked at extensively to account for the differences in the nature of each experimental structure. A thorough reassessment of the monitoring data was conducted to critically evaluate the effects of the several parameters of the GRS structures. In addition, the analysis assesses the practical models that were proposed by Adams et al. (FHWA-HRT-11-027, 2011). This includes the global bearing capacity prediction methods, vertical and horizontal deformation prediction methods, and the lateral earth pressure prediction method.

4.1.4.1 BEARING STRENGTH

The global bearing capacity of a GRS structure (q_{ult}) can be evaluated using an analytical formula proposed by Wu et al. (FHWA-HRT-10-077, 2013a) shown in Equation 4.1.1. This formula is adopted by Adams et al. (FHWA-HRT-11-027, 2011) and reported to be applicable to GRS structures. However, Adams et al. (FHWA-HRT-11-027, 2011) reported that the analytical formula applies to GRS structures that employs when the employed backfill material characteristics conforms to the criteria in Adams et al. (FHWA-HRT-11-026, 2012).

$$\boldsymbol{q_{ult} = \left[\sigma_c + 0.7^{\left(\frac{S_v}{6d_{max}}\right)} \frac{T_f}{S_v}\right] K_{pr} + 2c\sqrt{K_{pr}}} \qquad \textbf{(4.1.1)}$$

where: σ_c: the lateral confining pressure.
S_v: the reinforcement vertical spacing.
d_{max}: the maximum grain size of the backfill material.
T_f: the reinforcement ultimate tensile strength.
K_{pr}: the coefficient of passive earth pressure.

This equation was used with all the identified GRS experimental structures that were brought to failure (i.e., structures that did not reach failure were excluded from the comparison). Figure 4.1.12 shows a comparison between the ultimate capacity values predicted using Equation 4.1.1 and the measured capacity values retrieved from the experimental data. Note that the structures involved in this comparison included different boundary conditions such as square columns, cylindrical columns, fixed-wall columns, and experimental abutments. It should also be noted that no correction factors were applied to account for the structure type of geometry. Adams et al. (FHWA-HRT-11-027, 2011) reported that the ultimate capacity used in design should be modified to neglect lateral confining pressure due to its significantly small value and backfill cohesion to account for long-term conditions. However, the comparison was conducted by using the original equation (i.e., by incorporating the confining pressure and cohesion) since some of the experimental structures were exposed to a considerably high confining pressure. Also, the tests were conducted in a short-term condition in which the strength parameters of the backfill material were short-term parameters.

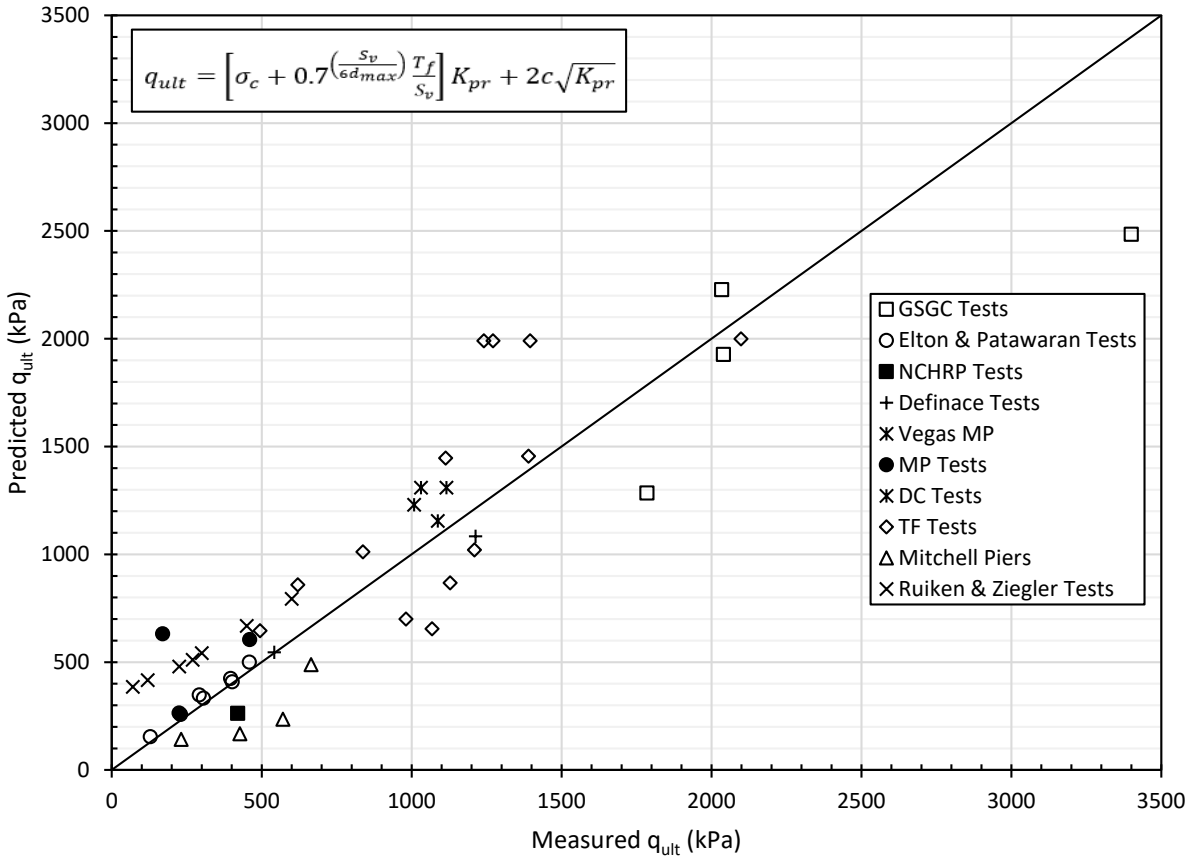

Figure 4.1.12: Measured vs. predicted (using Wu method) GRS bearing strength.

4.1.4.2 VERTICAL STRESS-STRAIN BEHAVIOR

The database was extended to include the vertical stress-strain behavior of the GRS experimental structures. Figure 4.1.13 shows a master presentation of all the data that was compiled for structures that have a wide range of parameters. It can be noticed that the ultimate capacity for the majority of the structures was significantly high. While this observation enhances the fact that the strength of GRS structures is high enough to support bridge loads, the ultimate capacity is not the most vital information to look at. Instead, the structural behavior of under service stress levels up to approximately 200 kPa (29 psi) is more decisive. Whereupon, side-by-side comparisons were made between the behavior of the various structures in the ultimate and service stress levels. A set of figures were prepared and presented in this section to study the effect of the various GRS structural parameters on the behavior of GRS structures in general, in ultimate and service stress conditions. Note that this comparison does not intend to evaluate trends but intends to assess the validity of using the "semi-empirical design" method proposed in the FHWA.

Note that the comparisons were conducted in terms of vertical stress-strain behavior, where the vertical strain is determined globally (i.e., percentage of settlement to total structure height). The reason for this choice is to evaluate the empirical method proposed by Adams et al. (FHWA-HRT-

11-027, 2011) for estimating the ultimate bearing capacity of GRS structures based on representative performance tests, which were conducted by Nicks et al. (FHWA-HRT-13-066, 2013). That is, some structures involved in a single comparison might have different height. However, attention was paid when comparisons were analyzed. It should be noted that global stress or strain are not very meaningful. They represents applied and measured values at the boundary treating the GRS mass as a black box.

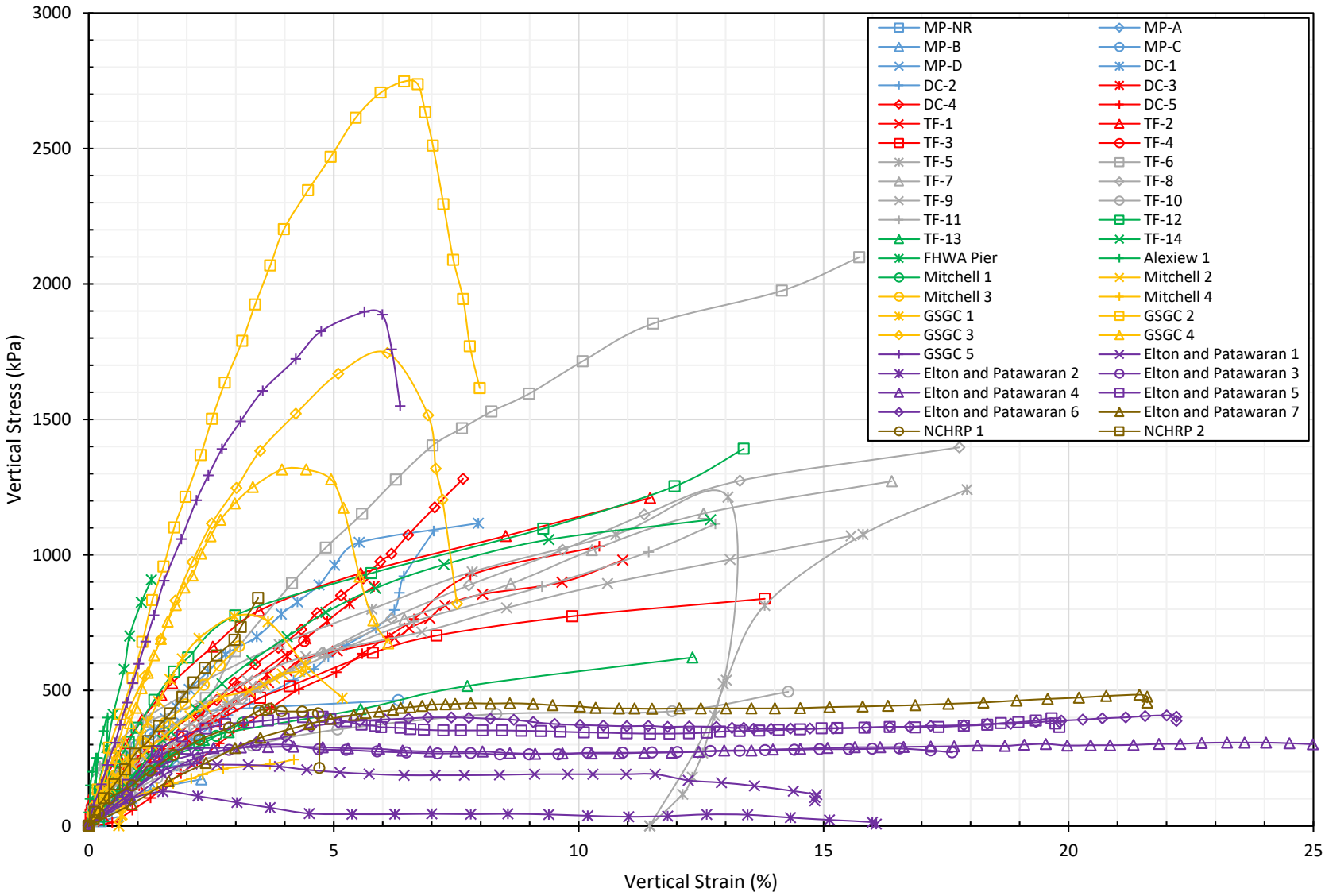

Figure 4.1.13: Vertical stress-strain behavior for the GRS experimental structures database.

Figure 4.1.14 comprises tests that have reinforcement of the same tensile strength of 70-kN/m (400 lbf/in) and placed at the same vertical spacing of 0.2 m (8 in.). All three tests did not involve bearing bed reinforcement. GSGC-2 was tested in plane strain condition, NCHRP-2 was an abutment test, and TF-6 and FHWA Pier were square column tests. The backfill material used in GSGC-2 had 50-degree friction angle, 70-kPa (10.2 psi) cohesion, and 0.033-m (1.25 in.) maximum grain size (strength parameters obtained from triaxial testing). The backfill materials used in the various structures had different characteristics as shown in summary table in Figure 4.1.14. Note that the confining pressure might be set to zero; however, some confinement due to facing is possible. For instance, Nicks et al. (FHWA-HRT-13-066, 2013) has estimated that confinement effect of the CMU facing used in the TF tests approximately 0.97 kPa (20 psf). Figure 4.1.14a shows a comparison between the behaviors exhibited by the various structures upon loading them vertically. Figure 4.1.14b shows a close-up of the behavior in the service stress range. Similarity was observed in the behavior of TF-6 and NCHRP 2 and in the behavior of FHWA pier and GSGC 5. However, the characteristics of TF-6 differs than those of NCHRP 2 mainly in the geometry and the higher friction angle of the backfill material. While stiffer backfill material should result in a stiffer behavior, the height of NCHRP 2 was greater than that of TF-6. That is, for the same vertical strain, NCHRP 2 exhibited a bigger settlement than TF-6. An important conclusion can be drawn from this observation. The empirical design based on the data from a representative performance test (design envelopes) proposed by Adams et al. (FHWA-HRT-11-027, 2011) may require a better definition for vertical strain that can avoid the bias of the use of global vertical strain in structures with various heights.

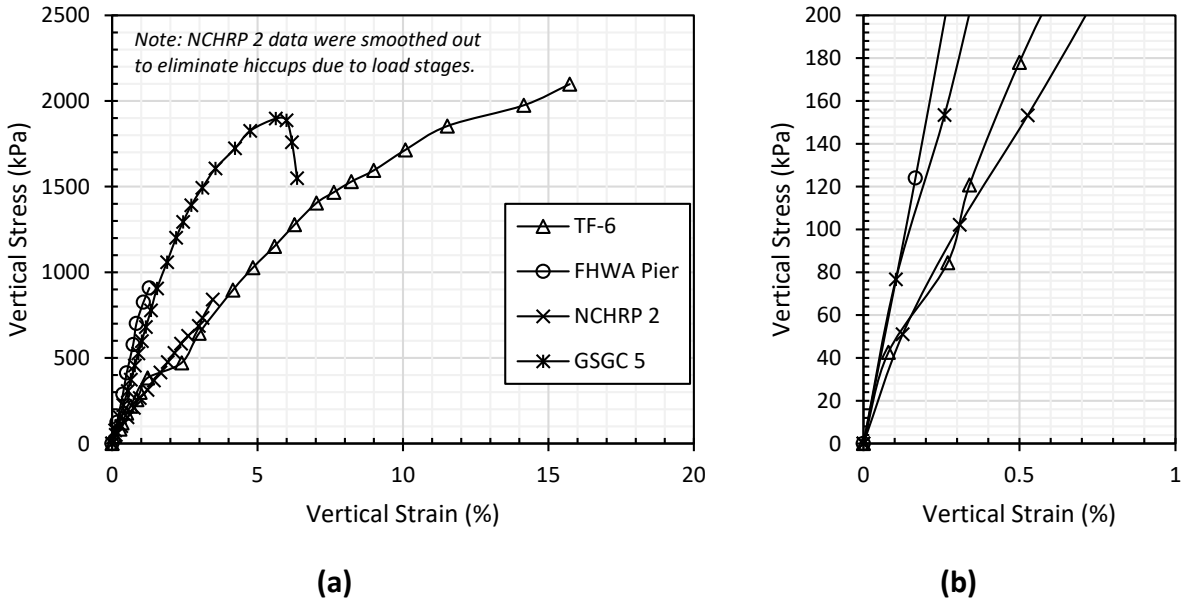

Note:

Test Name	qult,measured (kPa)	Facing Type	σconfining (kPa)	H (m)	Sv (m)	Tf (kN/m)	Tf/Sv (kN/m/m)	dmax (m)	c (kPa)	ϕ (deg)	c,ϕ Method	Geometry	Reference
GSGC 5	2034	CMU/Plexiglas	0.0	2.00	0.20	70	350	0.033	70	50	TX	Fixed Wall Column	Pham (2008); Wu et al. (2013)
NCHRP 2	Didn't reach failure	CMU	0.0	4.65	0.20	70	350	0.025	0.0 20	36.5 37.3	LSDS LSTX	Abutment	Wu et al. (2006)
TF-6	2098	CMU	0.97	1.94	0.20	70	350	0.025	5.5	53	LSDS	Square Column	Nicks et al. (2013a); Iwamoto (2014)
FHWA Pier	Didn't reach failure	Cinder Block	0.0	5.40	0.20	70	350	N/A	N/A	N/A	N/A	Square Column	Adams (1997)

Figure 4.1.14: Stress-strain behavior for similar tests: (a) Available stress range; (b) Service stress range.

Figure 4.1.15 comprises tests that have the same characteristics. These tests were conducted by Nicks et al. (FHWA-HRT-13-066, 2013) to assess the repeatability of the GRS mini-pier performance tests they conducted. The summary table in Figure 4.1.15 shows the characteristics of the various structures. Geotextile reinforcement layers with 70-kN/m (400 lbf/in) tensile strength were employed in all piers and were spaced at 0.2 m (8 in.). Nicks et al. (FHWA-HRT-13-066, 2013) noted that TF-4 test was terminated before reaching failure due to technical difficulties that has caused uneven loading of the pier. In addition, they noted that TF-5 was initially loaded then was unloaded-reloaded up to failure. All test piers did not include bearing bed (extra reinforcement layers near the top). Also, the facing units were removed and the reinforcement tails were trimmed from all piers prior loading. The stress-strain behavior of the three tests may look similar when looked at the entire figure. However, over the service stress range, the discrepancy between the test results is significantly high as shown in Figure 4.1.15b. The vertical strain is approximately ranged from 0.6% to 1.1% (excluding the reloading of TF-5).

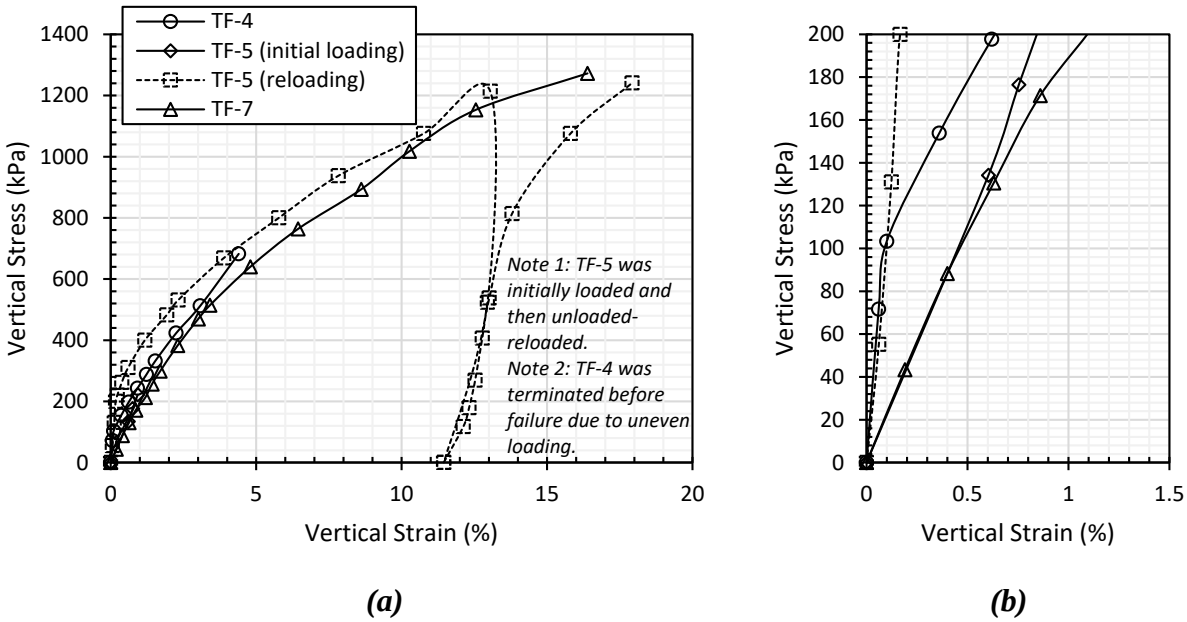

Note:

Test Name	qult,measured (kPa)	Facing Type	σconfining (kPa)	H (m)	Sv (m)	Tf (kN/m)	Tf/Sv (kN/m/m)	dmax (m)	c (kPa)	ϕ (deg)	c,ϕ Method	Geometry	Reference
TF-4	Didn't reach failure	None	0.0	1.94	0.20	70	350	0.025	5.5	53	LSDS	Square Column	Nicks et al. (2013a)
TF-5	1241	None	0.0	1.94	0.20	70	350	0.025	5.5	53	LSDS	Square Column	Nicks et al. (2013a)
TF-7	1271	None	0.0	1.94	0.20	70	350	0.025	5.5	53	LSDS	Square Column	Nicks et al. (2013a); Iwamoto (2014)

Figure 4.1.15: Stress-strain behavior for identical tests: (a) Available stress range; (b) Service stress range.

Figure 4.1.16 shows the vertical stress-strain behavior of two tests that have similar characteristics. However, the geometry is different; GSGC 4 is a column with two fixed walls, whereas, TF-9 is a square column free to deform from all four directions. Also, a relatively high confining pressure was imposed on GSGC 4, whereas TF-9 was only confined by the effect of its facing. A summary of the characteristics of the two structures is shown in the table in Figure 4.1.16. The characteristics of the backfill materials employed were somewhat different in the two structures, yet both materials conform to the backfill properties recommended by Adams et al. (FHWA-HRT-11-026, 2012). Both structures were reinforced with geotextile layers of 70-kN/m (400 lbf/in) tensile strength spaced at 0.2 m (8 in.); no bearing bed reinforcement was involved. A significantly higher strength and stiffness were observed for GSGC 4 compared to TF-9. This can be attributed to the difference in the confinement imposed on the GRS mass. Another possible reason might be the effect of wall fixation in GSGC 4.

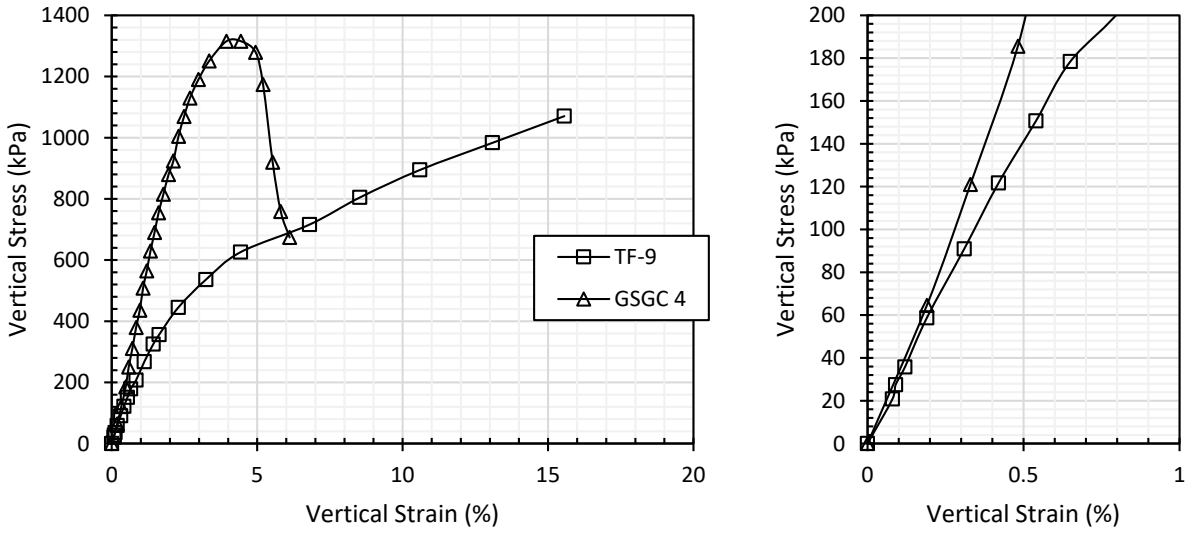

(a) ***(b)***

Note:

Test Name	qult,measured (kPa)	Facing Type	σconfining (kPa)	H (m)	Sv (m)	Tf (kN/m)	Tf/Sv (kN/m/m)	dmax (m)	c (kPa)	ϕ (deg)	c,ϕ Method	Geometry	Reference
GSGC 4	1785	CMU/Plexiglas	34	2.00	0.40	70	175	0.033	70	50	TX	Fixed Wall Column	Pham (2008); Wu et al. (2013)
TF-9	1068	CMU	0.97	1.94	0.40	70	175	0.025	5.5	53	LSDS	Square Column	Nicks et al. (2013a); Iwamoto (2014)

Figure 4.1.16: Stress-strain behavior for similar tests: (a) Available stress range; (b) Service stress range.

Figure 4.1.17 shows the vertical stress-strain behavior for six experimental structures. The summary table in Figure 4.1.17 shows the characteristics of the various structures. The structures had similar characteristics except that the backfill materials had different friction angles and maximum grain sizes. The friction angle of the various backfill ranged from 36.5 to 54 degrees determined by large-scale direct shear testing and the maximum grain size ranged from 0.01 to 0.025 m (0.4-1 in.). All structures employed geotextile reinforcement layers of 70-kN/m (400 lbf/in) tensile strength placed at a vertical spacing of 0.2 m (8 in.). Also, note that NCHRP 2 is an abutment and did not include bearing bed reinforcement, whereas all the other structures are piers and included bearing bed reinforcement. While DC-1 and DC-5 have identical characteristics, Nicks et al. (FHWA-HRT-13-066, 2013a) reported that DC-5 was constructed with uncompacted backfill unlike DC-1. In addition, technical difficulties were reported during loading of DC-5. Also, the backfill of DC-2 was round pea gravel.

The only testing parameter changing from one test to another is the friction angle of the backfill material used, which is a result of the different grain size of these cohesionless materials. Figure 4.1.17a shows unreasonable rank in the ultimate bearing capacity of the structures (excluding DC-3 and DC-4 tests, which were not loaded to failure). In addition, Figure 4.1.17b also does not show a reasonable rank in the stiffness of the reinforced soil. Typically, structures constructed with a higher friction angle backfill would be expected to exhibit a higher bearing capacity and loading stiffness than structures constructed with a lower friction angle backfill. Nicks et al.

(FHWA-HRT-13-066, 2013) attributed this observation to the difference in gradation of the backfill materials used. DC-4 was prepared with a more graded soil, which provided a better performance than that of DC-3 despite the lower friction angle of the backfill of DC-4. While NCHRP 2 had the weakest backfill among all the structures in comparison, and it did not include bearing bed reinforcement unlike all the other tests in comparison, it showed the stiffest behavior as shown in Figure 4.1.17b. This can be explained by the difference in structure height. The height of NCHRP 2 is approximately 2.4 times that of the DC structures.

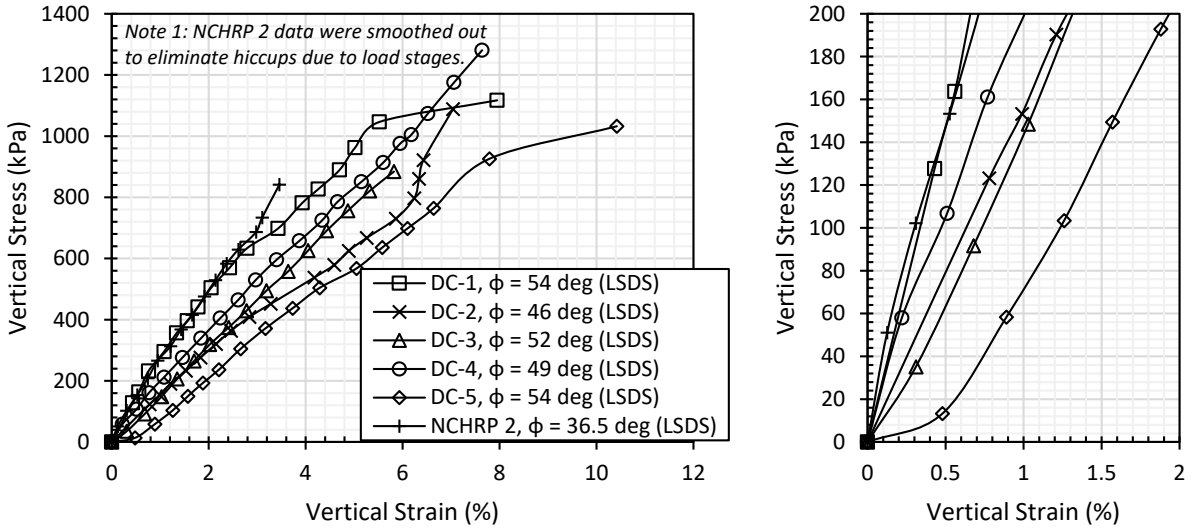

Note:

Test Name	$q_{ult,measured}$ (kPa)	Facing Type	$\sigma_{confining}$ (kPa)	H (m)	Sv (m)	Tf (kN/m)	Tf/Sv (kN/m/m)	D_{max} (m)	c (kPa)	ϕ (deg)	c,ϕ Method	Geometry	Reference
NCHRP 2	Didn't reach failure	CMU	0.0	4.65	0.20	70	350	0.025	0.0 20	36.5 37.3	LSDS LSTX	Abutment	Wu et al. (2006)
DC-1	1116	CMU	0.97	1.94	0.20	70	350	0.013	0.0	54	LSDS	Square Column	Nicks et al. (2013a)
DC-2	1087	CMU	0.97	1.94	0.20	70	350	0.019	0.0	46	LSDS	Square Column	Nicks et al. (2013a)
DC-3	Didn't reach failure	CMU	0.97	1.94	0.20	70	350	0.025	0.0	52	LSDS	Square Column	Nicks et al. (2013a)
DC-4	Didn't reach failure	CMU	0.97	1.94	0.20	70	350	0.010	0.0	49	LSDS	Square Column	Nicks et al. (2013a)
DC-5	1031	CMU	0.97	1.94	0.20	70	350	0.013	0.0	54	LSDS	Square Column	Nicks et al. (2013a)

Figure 4.1.17: Effect of backfill friction angle on the stress-strain behavior: (a) Available stress range; (b) Service stress range.

Figure 4.1.18 presents the global vertical stress-strain behavior of three GRS experimental structures. This includes a square column (TF-1) and the two abutments (NCHRP 1 and NCHRP 2). The characteristics of these structures are summarized in the table in Figure 4.1.18. The structures were constructed with geotextile reinforcement of different tensile strength values. The reinforcement was placed at a vertical spacing of 0.2 m (8 in.) and did not involve bearing bed. Figure 4.1.18a shows that the stiffness of the reinforced soil mass in NCHRP 2 was the highest, which employed the strongest reinforcement, followed by that of the reinforced soil in

TF-1, whereas that of NCHRP 1 exhibited the least stiffness, which had the weakest reinforcement. However, over the service stress range TF-1 and NCHRP 1 showed very similar behavior. This similarity is deemed misleading, since TF-1 had not only stronger reinforcement but also stronger backfill material than NCHRP 1. However, since the height of NCHRP 1 is greater than that of TF-1, similar vertical strains reflects more settlement. A minor effect was observed within the service stress range (up to 200 kPa (29 psi)). This observation strengthens the conclusion made earlier that the empirical design based on the data from representative performance tests proposed by Adams et al. (FHWA-HRT-11-027, 2011) may require a better definition for vertical strain that can avoid the bias of the use of global vertical strain in structures with various heights.

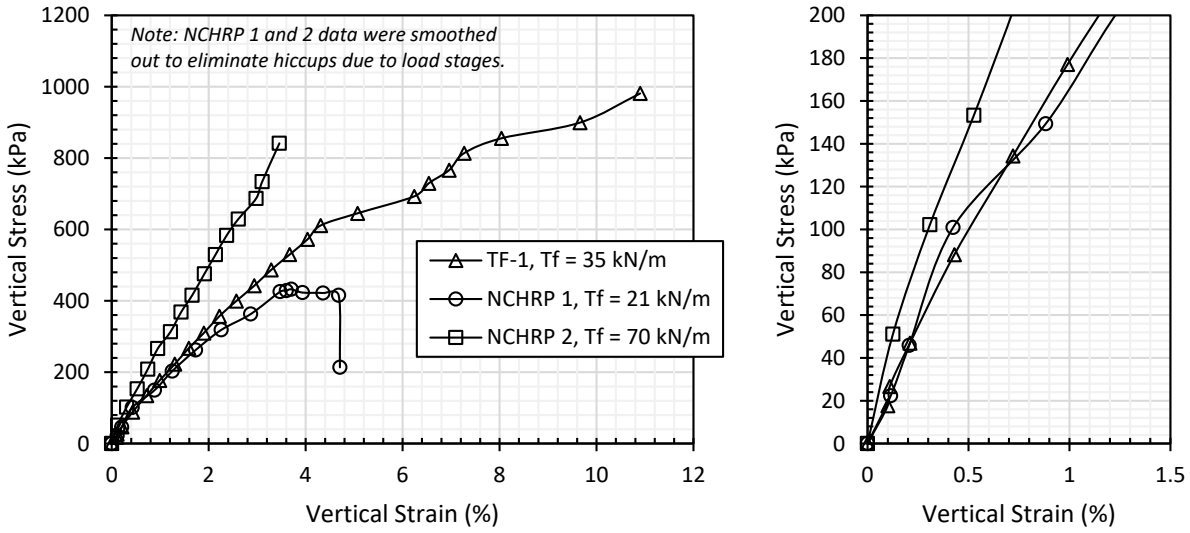

Note:

Test Name	$q_{ult,measured}$ (kPa)	Facing Type	$\sigma_{confining}$ (kPa)	H (m)	S_v (m)	T_f (kN/m)	T_f/S_v (kN/m/m)	D_{max} (m)	c (kPa)	ϕ (deg)	c,ϕ Method	Geometry	Reference
NCHRP 1	Didn't reach failure	CMU	0.0	4.65	0.20	21	105	0.025	0.020	36.5 37.3	LSDS LSTX	Abutment	Wu et al. (2006)
NCHRP 2	Didn't reach failure	CMU	0.0	4.65	0.20	70	350	0.025	0.020	36.5 37.3	LSDS LSTX	Abutment	Wu et al. (2006)
TF-1	981	CMU	0.97	1.94	0.20	35	175	0.013	0.0	55	LSDS	Square Column	Nicks et al. (2013)

Figure 4.1.18: Effect of reinforcement tensile strength on the stress-strain behavior: (a) Available stress range; (b) Service stress range.

Figure 4.1.19 shows the performance of three vertical loading tests on GRS experimental structures. The table in Figure 4.1.19 comprises a summary of the characteristics of the three structures. The reinforcement employed in all tests was geotextile layers of 70-kN/m (400 lbf/in) tensile strength. The reinforcement vertical spacing varied amongst the structures. No bearing bed reinforcement nor facing were included. Note that MP-D was not loaded to failure. As shown in Figure 4.1.19a and 4.1.19b the highest stiffness was exhibited by the structure in which the reinforcement spacing was the smallest (MP-D). However, MP-A showed higher stiffness than MP-B, yet the reinforcement spacing in MP-A was larger than that in MP-B. Adams et al. (2007) explained this unexpected rank that the compaction of the backfill material in MP-A was better than that in MP-B. They referred to the measured average backfill density, which was 23.0 kN/m^3 (148 pcf) for MP-A and 22.7 kN/m^3 (146 pcf) for MP-B. This difference, however, is not significant to cause this big difference in the performance of GRS structures.

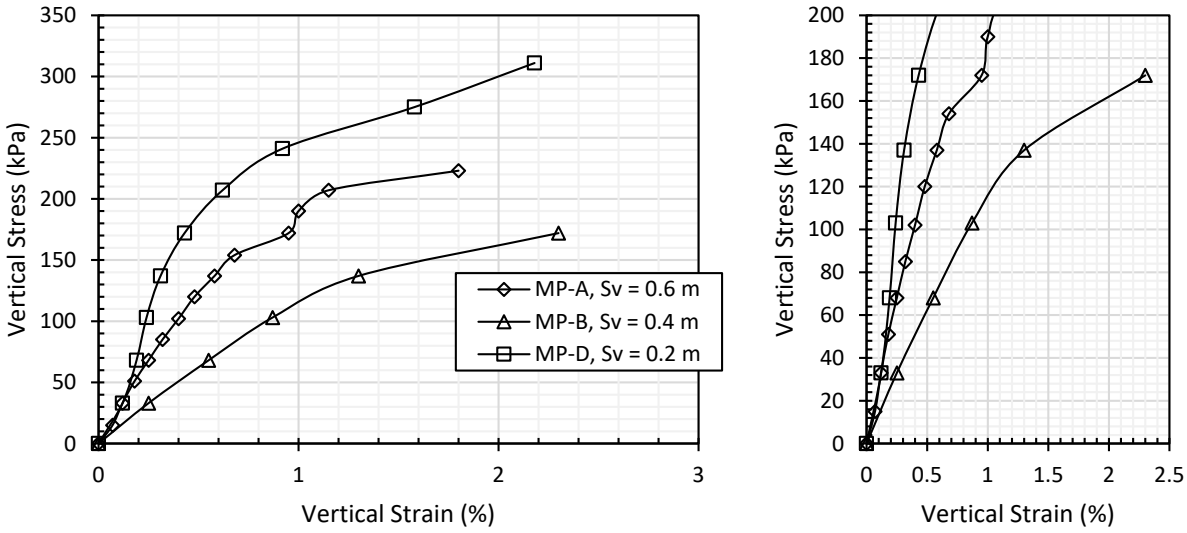

(a) ***(b)***

Note:

Test Name	$q_{ult,measured}$ (kPa)	Facing Type	$\sigma_{confining}$ (kPa)	H (m)	Sv (m)	T_f (kN/m)	T_f/S_v (kN/m/m)	D_{max} (m)	c (kPa)	ϕ (deg)	c,ϕ Method	Geometry	Reference
MP-A	225	None	0.0	1.94	0.60	70	116.7	0.025	0.0	53.5	LSDS	Square Column	Adams et al. (2007a)
MP-B	170	None	0.0	1.94	0.40	70	175	0.025	0.0	53.5	LSDS	Square Column	Adams et al. (2007a)
MP-D	Didn't reach failure	None	0.97	1.94	0.20	70	350	0.025	0.0	53.5	LSDS	Square Column	Adams et al. (2007a)

Figure 4.1.19: Effect of reinforcement vertical spacing on the stress-strain behavior: (a) Available stress range; (b) Service stress range.

Figure 4.1.20 shows the behavior of loading tests conducted on two GRS experimental structures. The table in Figure 4.1.20 summarizes the characteristics of the two structures. Both structures were constructed using the same reinforcement, which was geotextile layers of 70-kN/m (400 lbf/in) tensile strength. The reinforcement vertical spacing was different between the two structures. GSGC 2 showed higher bearing strength and stiffness than GSGC 4 as shown in Figure 4.1.20a and 4.1.20b, respectively, which is due to the difference in the reinforcement spacing.

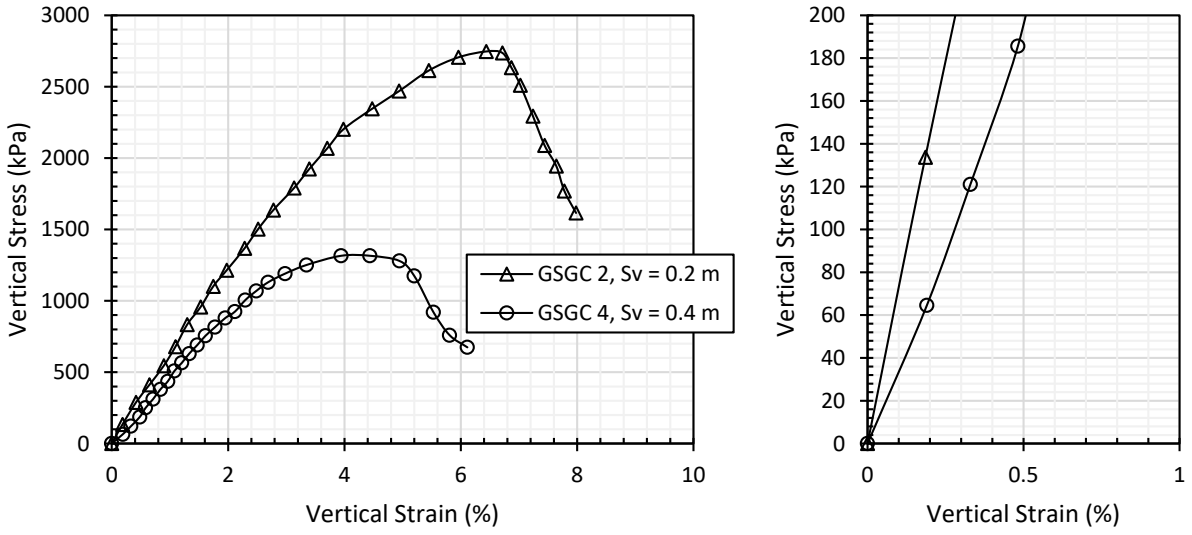

(a) ***(b)***

Note:

Test Name	$q_{ult,measured}$ (kPa)	Facing Type	$\sigma_{confining}$ (kPa)	H (m)	Sv (m)	T_f (kN/m)	T_f/S_v (kN/m/m)	D_{max} (m)	c (kPa)	ϕ (deg)	c,ϕ Method	Geometry	Reference
GSGC 2	3400	CMU/Plexiglas	34	2.00	0.20	70	350	0.033	70	50	TX	Fixed Wall Column	Pham (2008); Wu et al. (2013)
GSGC 4	3400	CMU/Plexiglas	34	2.00	0.40	70	350	0.033	70	50	TX	Fixed Wall Column	Pham (2008); Wu et al. (2013)

Figure 4.1.20: Effect of reinforcement vertical spacing on the stress-strain behavior: (a) Available stress range; (b) Service stress range.

4.1.4.3 LATERAL PRESSURE

Wu (2001) studied the lateral earth pressure on the facing of GRS structures. It was reported that the lateral earth pressure on the facing is quite small compared to the lateral pressure predicted from Rankine earth pressure theory. In addition, it was reported earth pressure near the reinforcement levels approaches zero; however, some pressure may build up upon reinforcement straining. Wu (2001) proposed a method to estimate the lateral earth pressure exerted on the facing of GRS structures. The proposed distribution involves bin pressure diagram shown in Figure 4.1.21a, which depends on the reinforcement spacing, the shear strength parameters of the backfill material, and the facing rigidity. It was indicated that the main function of the facing is to prevent soil sloughing for GRS structures reinforced at small spacing (less than 0.3 m (12 in)).

Wu and Ooi (FHWA-HRT-14-094, 2015) conducted a comparison between some measured lateral earth pressure values and two prediction methods: (1) Wu (2001) method, whose distribution is

shown in Figure 4.1.21a; and (2) Soong and Koerner (1997) method, whose distribution is shown in Figure 4.1.21b. The comparison was not very robust though since it included few measured values, most of which were negative values retrieved from Mitchell (2002). Whereupon, more reliable data was sought and compiled to strengthen the assessment of the prediction models. In addition, lateral pressure using Rankine theory was assessed; however, the effect of the superstructure loading was ignored (i.e., prediction was conducted based on backfill self-weight only). Note that the models by Wu (2001) and Soong and Koerner (1997) also do not basically involve the effect of additional superstructure loading.

Figure 4.1.22 shows a comparison between the measured lateral earth pressure values and the predicted values. A good agreement is shown between the measured values and the predicted values using Rankine Theory. Note that, however, the effect of additional superstructure loading was not accounted for. On the other hand, the other two prediction models significantly underestimated the lateral earth pressure. Rankine theory usually shows good prediction in GRS structures in which no additional loading is imposed. However, adding the lateral earth pressure due to additional vertical pressure predicted by Boussinesq elastic solution results in a significant overestimation to the lateral earth pressure.

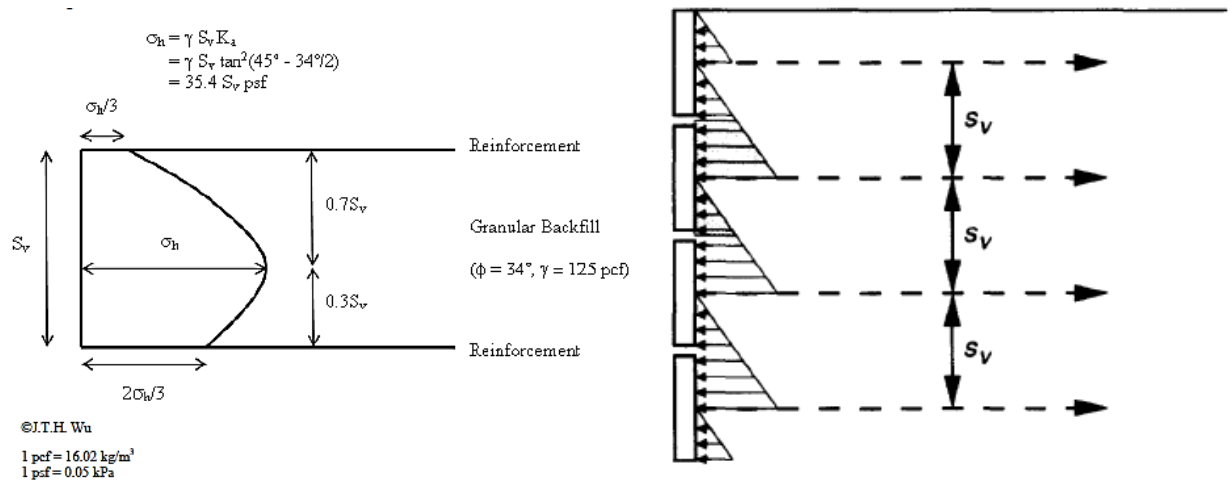

(a) ***(b)***

Figure 4.1.21: Idealized lateral earth pressure distribution: (a) Wu (2001); (b) Soong and Koerner (1997).

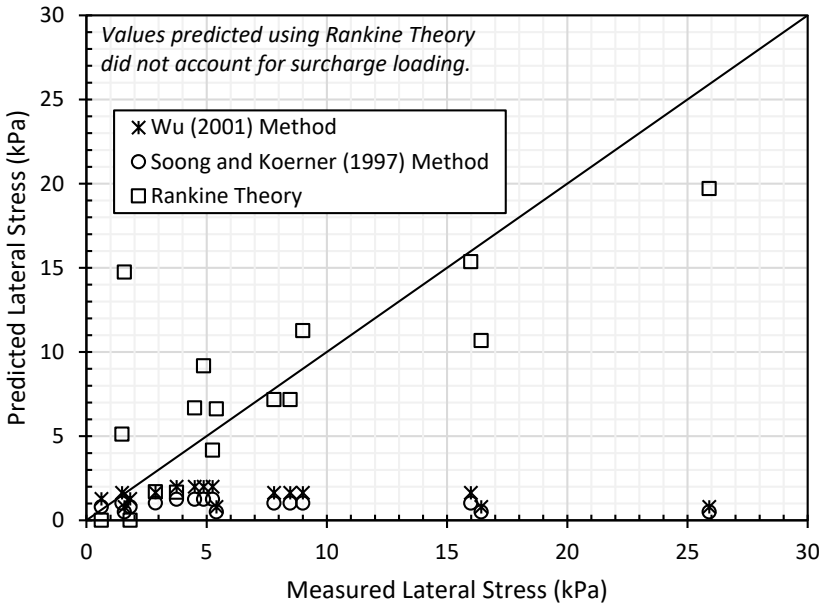

Figure 4.1.22: Measured vs. predicted lateral earth pressure on GRS facing.

4.1.4.4 LATERAL STRAIN

Adams et al. (FHWA-HRT-11-026, 2012) proposed a method for predicting the maximum lateral displacement in GRS abutments. This method has been referred to as "Adams method" in Xiao et al. (FHWA-HRT-15-080, 2016) and Khosrojerdi et al. (2016). This method assumes that there are no volume changes in GRS abutments. That is, the vertical strain is compensated by equivalent lateral strain preserving the same volume of GRS mass. This is deemed a conservative approach (Adams et al. 2012 – FHWA-HRT-11-026). It was reported that the composite behavior of GRS mass ideally results in monolithic deformation of the reinforcement and soil. Adams et al. (FHWA-HRT-11-026, 2012) proposed that the maximum lateral displacement and strain can be estimated using Equations 4.1.2 and 4.1.3, respectively.

$$D_L = 2\ x\ B\ x\ \frac{D_V}{H} \qquad (4.1.2)$$

$$\varepsilon_L = 2\varepsilon_V \qquad (4.1.3)$$

where: D_L: The maximum lateral displacement.
B: The width of the load along the top of the wall including the setback.
D_V: The vertical settlement of the load.
H: The height of the structure.
ε_L: The maximum lateral strain.
ε_V: The vertical strain.

This method is derived based on a simplified geometry of deformation diagram assuming that the vertical deformation under the load will always be uniform and that the lateral deformation

will always take the shape of a triangular prism. Regardless the location of the maximum ordinate, the equation would still give a rough estimate of the magnitude of the maximum lateral displacement (the peak of the triangle). Whereupon, in order to properly assess the performance of this method initially proposed by Adams et al. (FHWA-HRT-11-026, 2012), a modification had to be done to account for the fact that abutments are allowed to deform from only one side; whereas, square piers deform from four sides and fixed-wall piers deform from two side as shown in Figure 4.1.23. This modification allows using this method with structures of different geometry configurations. Equations 4.1.4 and 4.1.5 modify the maximum lateral displacement and strain, respectively.

$$D_L = 2\ x\ B\ x\ \frac{D_V}{H}\ x\ \frac{1}{n} \qquad (4.1.4)$$

$$\varepsilon_L = \frac{2\varepsilon_V}{n} \qquad (4.1.5)$$

where: *n*: The number of deformable sides of the structure (n = 4 for square piers; n = 2 for fixed-wall piers; and n = 1 for abutments).

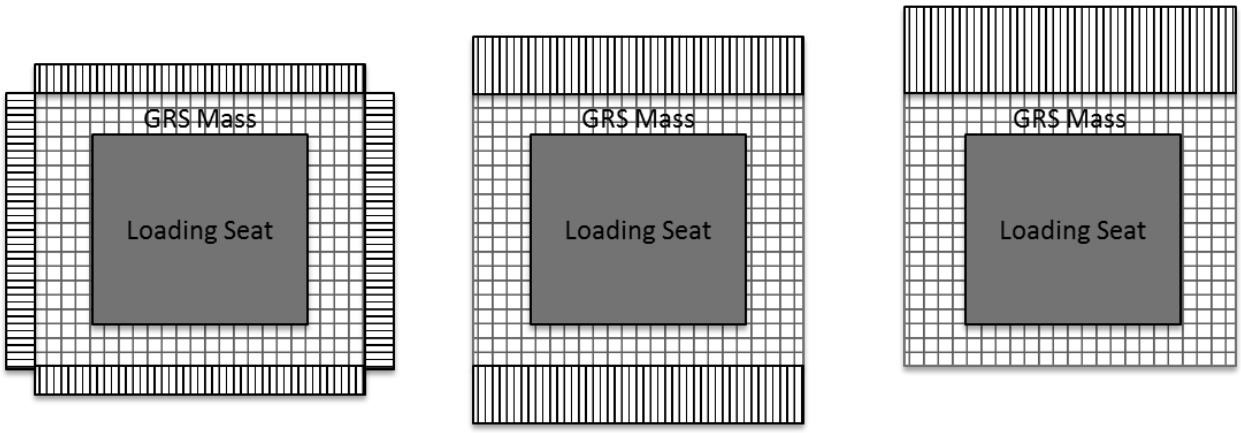

Figure 4.1.23: Typical deformation diagrams in plan: (a) square pier; (b) fixed-wall pier; (c) abutment.

Figure 4.1.24a shows the comparison between the measured and predicted values of the maximum lateral strain (regardless its location). The method seems to overestimate the deformation of the fixed-wall piers and underestimate the deformation of the abutments. It should be noted that GSGC 1 is an unreinforced fixed-wall pier. However, its performance conformed well to the predicted values. That is, the method is deemed a rough estimate that applied to any flexible wall/abutment where triangular lateral deformation is likely.

Adams et al. (FHWA-HRT-11-026, 2012) reported that the maximum lateral strain should be limited to 1.0%. Accordingly, Figure 4.1.24b was constructed to show a close-up of the comparison in Figure 4.1.24a up to lateral strain of 2%. The method does not seem to provide a good prediction of the maximum lateral strain.

(a)

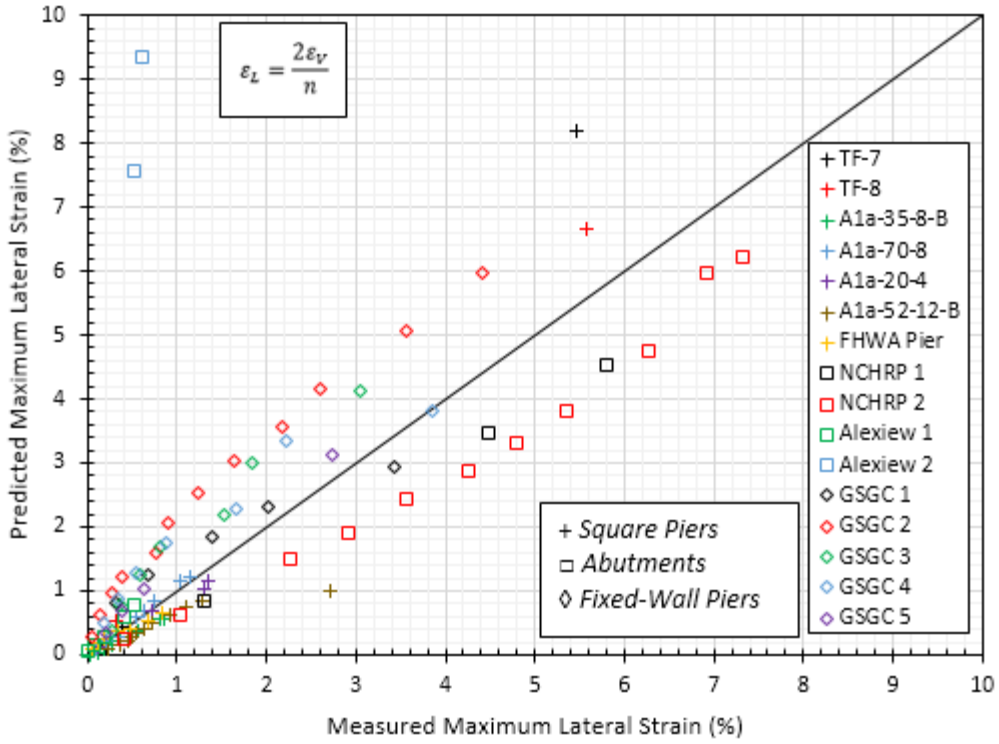

(b)

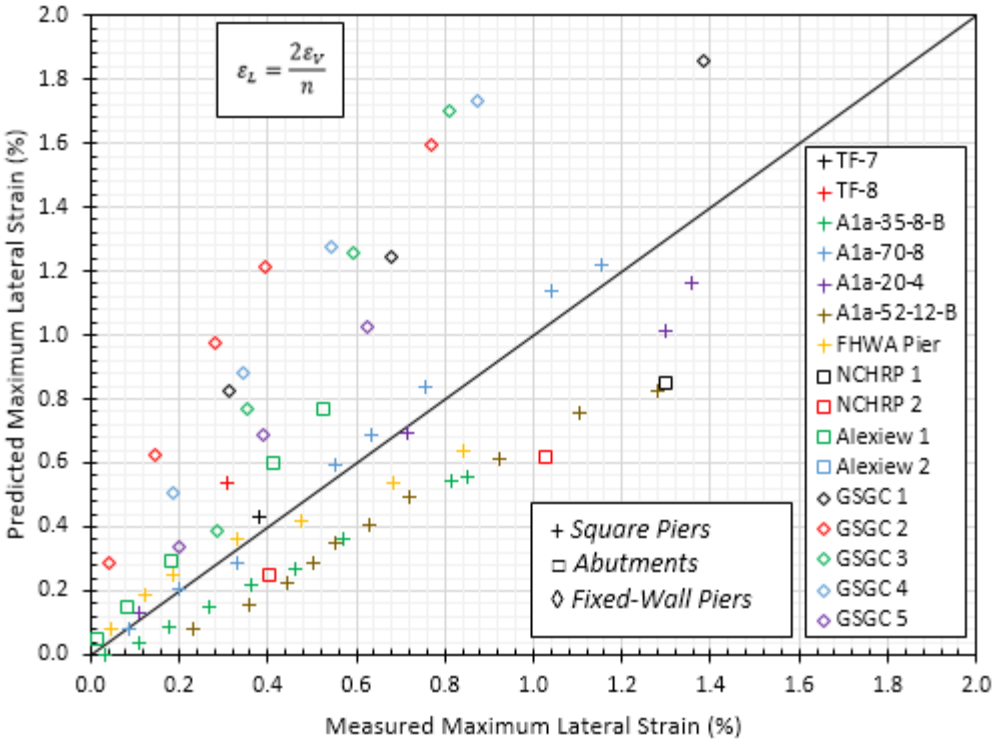

Figure 4.1.24: Measured vs. predicted maximum lateral strain of GRS facing: (a) Available strain range; (b) Service strain range.

4.1.5 FINAL REMARKS

The data collected pointed towards the effect of reinforcement spacing in reducing the lateral deformation and settlement, and increasing the bearing capacity of the reinforced soil mass. However, these conclusions are limited to the configurations tested by Nicks et al. (2013). This study led to the following findings:

This chapter aimed at evaluating the design models used in the FHWA GRS-IBS design guidelines (Adams et al. 2011, 2012). It should be noted that the experimental data reported in the reviewed research studies points towards the effect of reinforcement vertical spacing in reducing the lateral deformation and settlement, and increasing the bearing capacity of the reinforced soil mass. This study led to the following findings:

- The empirical design proposed by FHWA using the vertical stress-strain envelopes from a representative GRS Performance Test (Mini-Pier) was reevaluated at working stress levels (vertical stresses below 200 kPa (29 psi)). While the proposed envelopes were found to provide a very good repeatability on the full range of vertical stress-strain relationship, reassessment of the data was found not to be repeatable at working stress levels. In addition, the comparison conducted on the behavior of GRS structures of comparable materials and different boundary conditions revealed differences in performance (structural vertical and lateral deformation). A relevant outcome of the reassessment is that the difference in the boundary conditions between test piers and actual abutments may need to be taken into consideration to predict the behavior of GRS structures.

- The FHWA design guidelines do not account for the possible failure that can take place at the facing connection because the expected lateral earth pressures are small when the reinforcement layers are placed at comparatively close vertical spacings. However, reassessment of the collected data revealed that the reduction of lateral earth pressure due to the decrease in the reinforcement spacing could still be considered, although as a function in the reinforcement spacing and the type of backfill material used in the GRS structure.

- The FHWA design guidelines ruled out reinforcement pullout as a possible mode of failure. However, the decrease in the reinforcement spacing below a specific limit may decrease the mobilization of pullout resistance at the soil-reinforcement interfaces causing pullout failure in reinforcement groups similar to the group failure in piles (refer to Chapter 4 of this dissertation).

- It was reported that densifying reinforcement near the top of the GRS mass (i.e., bearing bed) can reduce the lateral deformation below the load.

- The GRS piers of closely-spaced reinforcement layers exhibited less lateral deformation and reinforcement strain than GRS piers of largely-spaced reinforcement layers of the same Tf/Sv ratio. However, no information was mentioned about the

reinforcement tensile stiffness or the soil-reinforcement interaction, which are believed to explain the behavior of the GRS mass.

4.1.6 REFERENCES

Adams, M.T. (1997). "Performance of a Prestrained Geosynthetic-Reinforced Soil Bridge Pier." *International Symposium on Mechanically Stabilized Backfill*, Wu, J.T.H. (ed), Denver, USA, Balkema, pp. 35-53.

Adams, M.T., Ketchart, K., and Wu, J.T. (2007a). "Mini pier experiments–geosynthetic reinforcement spacing and strength as related to performance." *Proceedings of Geo-Denver*.

Adams, M.T., Lillis, C.P., Wu, J.T.H., and Ketchart, K. (2002). "Vegas GRS Mini Pier Experiment and the Postulate of Zero Volume Change." *Proceedings of Geosynthetics 7th ICG*, Delmas, Gourc and Girad (eds.), pp. 389-394.

Adams, M.T., Nicks, J.E., Stabile, T., Wu, J.T.H., Schlatter, W., and Hartmann, J. (2012). *Geosynthetic Reinforced Soil Integrated Bridge System Interim Implementation Guide.* Report No. FHWA-HRT-11-026, Federal Highway Administration, McLean, VA.

Adams, M.T., Nicks, J.E., Stabile, T., Wu, J.T.H., Schlatter, W., and Hartmann, J. (2011). *Geosynthetic Reinforced Soil Integrated Bridge System, Synthesis Report.* Report No. FHWA-HRT-11-027, Federal Highway Administration, McLean, VA.

Adams, M.T., Schlatter, W., and Stabile, T. (2007b). "Geosynthetic Reinforced Soil Integrated Abutments at the Bowman Road Bridge in Defiance County, Ohio." *Proceedings of Geo-Denver*, 2007, pp. 01-11.

Allen, T.M., Christopher, B.R., and Holtz, R.D. (1992). "Performance of a 12.6 m High Geotextile Wall in Seattle, Washington." *International Symposium on Geosynthetic-Reinforced Soil Retaining Walls*, Balkema Publishers, Netherlands, pp. 81-100.

Bathurst, R.J. and Benjamin, D.J. (1990). "Failure of a Geogrid-Reinforced Soil Wall." *Transportation Research Record*, Vol. 1288, pp. 109-116.

Berg, R.R., Christopher, B.R., and Samtani, N.C. (2009a). *Design of Mechanically Stabilized Earth Walls and Reinforced Soil Slopes–Volume I*. Report No. FHWA-NHI-10-024, Federal Highway Administration. National Highway Institute.

Berg, R.R., Christopher, B.R., and Samtani, N.C. (2009b). *Design of Mechanically Stabilized Earth Walls and Reinforced Soil Slopes–Volume II*. Report No. FHWA-NHI-10-025, Federal Highway Administration. National Highway Institute.

Christopher, B.R., Gill, S.A., Giroud, J.P., Juran, I., Mitchell, J.K., Schlosser, F., and Dunnicliff, J. (1990a). *Reinforced soil structures Volume I. Design and construction guidelines*. Report No. FHWA-RD-89-043. Federal Highway Administration.

Christopher, B.R., Gill, S.A., Giroud, J.P., Juran, I., Mitchell, J.K., Schlosser, F., and Dunnicliff, J. (1990b). *Reinforced soil structures Volume II. Summary of Research and Systems Information*. Report No. FHWA-RD-89-044. Federal Highway Administration.

Christopher, B.R., Holtz, R.D. and Bell, W.D. (1986). "New Tests for Determining the In-Soil Stress-Strain Properties of Geotextiles." *Proceedings of the Third International Conference on Geotextiles*, Vol. 3, Vienna, Austria, April 1986, pp. 683-686.

Elton, D., and Patawaran, M.A. (2004). "Mechanically Stabilized Earth Reinforcement Tensile Strength from Tests of Geotextile-Reinforced Soil." *Transportation Research Record: Journal of the Transportation Research Board*, Vol. 1868, pp. 81-88.

Elton, D., and Patawaran, M.A. (2005). Mechanically Stabilized Earth (MSE) Reinforcement Tensile Strength from Tests of Geotextile-Reinforced Soil. A report to the Alabama Highway Research Center, June 2005, 77p.

Iwamoto, M.K., Ooi, P.S.K., Adams, M.T., and Nicks, J.E. (2013). "Composite Properties from Instrumented Load Tests on Soil Columns Reinforced with Geotextiles." *Transportation Research Broad*, TRB 2014 Annual Meeting.

Ketchart, K. and Wu, J.T.H. (1996). *Long-Term Performance Tests of Soil-Geosynthetic Composites.* Report No. CDOT-CTI-96-1, Colorado Department of Transportation, Denver, CO.

Ketchart, K. and Wu, J.T.H. (2002). "A Modified Soil-Geosynthetic Interactive Performance Test for Evaluating Deformation Behavior of GRS Structures." *ASTM International*, Vol. 25, No. 4, pp. 405-413.

Ketchart, K., and Wu, J.T.H. (2001). *Performance Test for Geosynthetic-Reinforced Soil Including Effects of Preloading.* Report No. FHWA-RD-01-118, Federal Highway Administration, McLean, VA.

Morsy, A. M. (2017). Evaluation of soil-reinforcement composite interaction in geosynthetic-reinforced soil structures. Doctoral dissertation, The University of Texas at Austin, Austin, Texas, USA.

Nicks, J.E., Adams, M.T., Ooi, P.S.K., and Stabile, T. (2013a). *Geosynthetic Reinforced Soil Performance Testing—Axial Load Deformation Relationships*. Report No. FHWA-HRT-13-066, Federal Highway Administration, McLean, VA.

Nicks, J.E., Adams, M.T., and Stabile, T. (2013b). "Performance Testing for Geosynthetic Reinforced Soil Composites." *Proceedings of the 5th International Young Geotechnical Engineers' Conference*.

Pham, T.Q. (2009). *Investigating Composite Behavior of Geosynthetic-Reinforced Soil (GRS) Mass*. Ph.D. thesis, University of Colorado Denver, Colorado, USA.

Ruiken, A. and Ziegler, M. (2009). "Large Scale Laboratory Element Testing of Geogrid Reinforced Soil." *Proceedings of GIGSA GeoAfrica 2009 Conference*, Cape Town, September.

Soong, T-Y. and Koerner, R.M. (1997). "On the Required Connection Strength of Geosynthetically Reinforced Walls." *Geotextiles and Geomembranes*, Vol. 15, pp. 377-393.

Wu, J.T.H. (2001). *Revising the AASHTO Guidelines for Design and Construction of GRS Walls*. Report No. CDOT-DTD-R-2001-16, Colorado Department of Transportation, 148 p.

Wu, J., Pham, T.Q., and Adams, M. (2013). *Composite Behavior of Geosynthetic-Reinforced Soil (GRS) Mass.* Report No. FHWA-HRT-10-077, Federal Highway Administration, McLean, VA.

Wu, J.T.H. and Helwany, S.M.B. (1996). "A Performance Test for Assessment of Long-Term Creep Behavior of Soil-Geosynthetic Composites." *Geosynthetic International*, Vol. 3, No. 1, pp. 107-124.

Wu, J.T.H., Ketchart, K., and Adams, M.T. (2001). *GRS Bridge Piers and Abutments.* Report No. FHWA-RD-00-038, Federal Highway Administration, McLean, VA.

Wu, J.T.H., Lee, K.Z.Z., Helwany, S.B., and Ketchart, K. (2006). *Design and Construction Guidelines for Geosynthetic-Reinforced Soil Bridge Abutments with a Flexible Facing.* Report No. 556, National Cooperative Highway Research Program, Washington, DC.

4.2 SUMMARY OF KDOT WALLS

4.2.1 INTRODUCTION

Geosynthetic reinforced mechanically stabilized earth (GMSE) walls have been typically constructed using primary reinforcement at large vertical reinforcement spacing (typically 0.6 m). This large reinforcement spacing requires a high connection strength and sometimes results in wall facing bulging, especially when backfill is not well compacted. To mitigate this problem, researchers suggested the use of secondary reinforcement between layers of primary reinforcement (e.g., Leshchinsky, 2000). Theoretical and numerical studies have been carried out to investigate the effect of secondary reinforcement on the improved performance of geosynthetic reinforced mechanically stabilized earth (GMSE) walls, but no field study has been performed to verify the benefits of secondary reinforcement on the improved performance of GMSE walls.

In this study, three MSE wall sections with geogrid reinforcement were constructed and instrumented: (1) an MSE wall section reinforced with uniaxial geogrid layers as primary and secondary reinforcement (i.e., test section 1, referred to as TS1), (2) an MSE wall section reinforced with uniaxial geogrid layers as primary reinforcement and biaxial geogrid layers as secondary reinforcement (referred to as TS2), and (3) an MSE wall section reinforced with uniaxial geogrid layers as primary reinforcement only (i.e., the control section, referred to as TS3). Earth pressure cells, inclinometer casings and probes, and foil-type strain gauges were used in these three test wall sections to measure vertical and lateral earth pressures, accumulated lateral wall facing deflections, and strains of primary and secondary geogrid layers during construction, respectively. The measured results from three MSE wall sections during construction were analyzed and are presented in this report. The effects of secondary reinforcement on the performance of MSE walls are discussed as well. The use of secondary reduced the vertical spacing of reinforcement close to the wall facing. The test results show that the use of secondary reinforcement reduced the lateral deformation of wall facing and the maximum tensile forces in the primary reinforcement layers. Biaxial secondary geogrid was more effective than the uniaxial reinforcement in reducing the tensile strains in the primary geogrid.

4.2.2 TEST WALL SECTIONS

The GMSE wall is located at Bonner Springs, Wyandotte County, Kansas. This GMSE wall was constructed to support a new ramp in the Kansas DOT I-70/K-7 interchange project. The construction of the test wall sections started in October 2013 and was completed by September 2014, lasting about 11 months. In this GMSE wall, three test wall sections were monitored. Figure 4.2.1 presents the front view of these test wall sections. The three test wall sections had a width ranging from 10.2 to 11.3 m (33.5 to 37.1 ft), and had a height ranging from 11.3 to 11.9 m (37.1 to 39 ft).

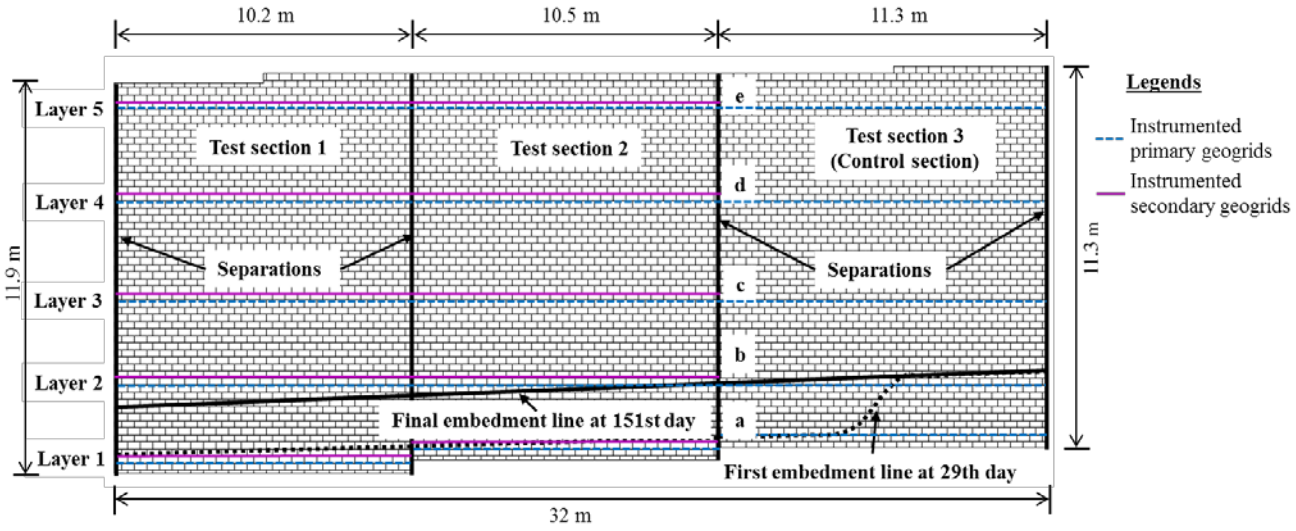

Figure 4.2.1. *Front view of three test wall sections (not to scale)*

Figure 4.2.2 shows the cross sections and the layout of primary and secondary reinforcement of the test wall sections. These wall sections had 3 (H): 1 (V) toe slopes and 4:1 back slopes. The primary reinforcement lengths of TS1, TS2, and TS3 were 18.9, 18.6, and 18 m (62, 61 and 59 ft), respectively. The primary reinforcement was placed every two blocks (i.e., 0.4 m (1.3 ft)) in the lower one-third part of the test wall sections and placed every three blocks (i.e., 0.6 m (2 ft)) in the upper two-third part of the test wall sections. The secondary reinforcement in TS1 was 1.4 m (4.6 ft) long (without including tails) and placed between two layers of primary reinforcement with vertical spacing of 0.2 m (8 in.). Similarly, the secondary reinforcement in TS2 was 1.3 m (4.3 ft) long and placed between two layers of primary reinforcement with vertical spacing of 0.2 m (8 in.). The coverage ratio of both primary and secondary reinforcement in three test wall sections was 100 percent. The main difference among these test sections is the secondary reinforcement and the objective of this study was to investigate the effect of secondary reinforcement. The ratio of the section width to the secondary reinforcement length is about 7 to 8, which is typically required for a plane strain condition.

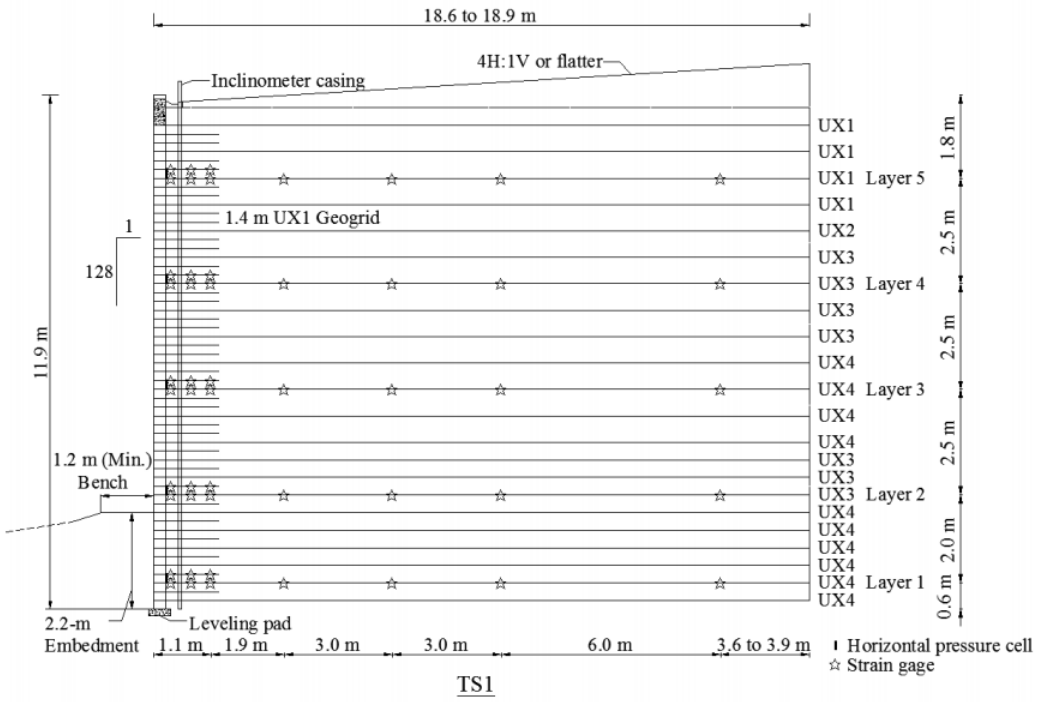

(a)

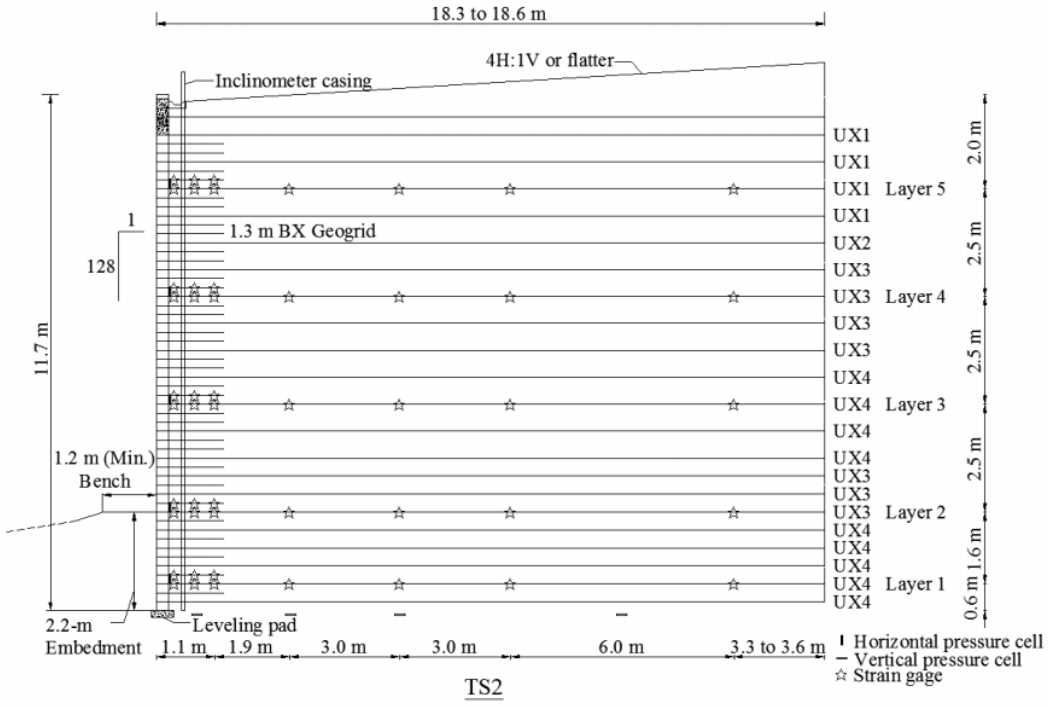

(b)

Figure 4.2.2. *Cross sections of three test wall sections with instrumentation (not to scale): (a) TS1; (b) TS2.*

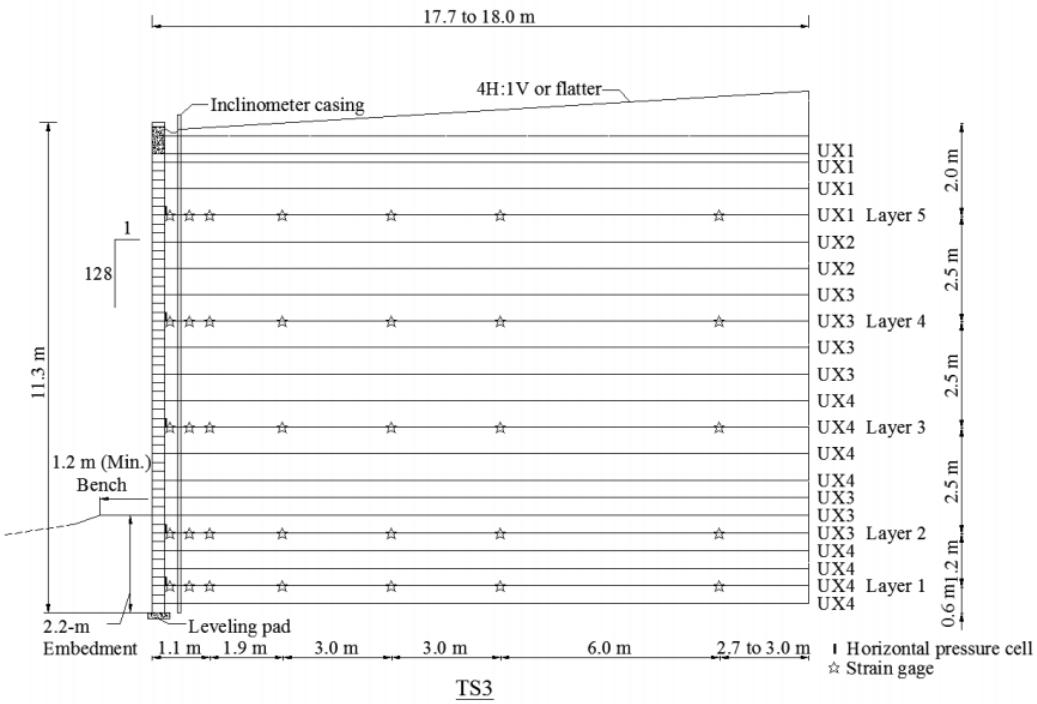

(c)

Figure 4.2.2. *Cross sections of three test wall sections with instrumentation (not to scale) (continued): (c) TS3.*

The heights of the wall test sections ranged from 11.3 to 11.9 m (37.1 to 39 ft). Four types of punched-drawn uniaxial high-density polyethylene (HDPE) uniaxial geogrid layers were used as primary reinforcement, which were referred to as UX1, UX2, UX3, and UX4. UX1 was also used for the secondary reinforcement in TS1. Punched-drawn biaxial polypropylene (PP) geogrid (referred to as BX) was used as the secondary reinforcement in TS2. Table 1 summarizes the properties of these geogrid layers used in the design. Based on the tensile tests conducted by the researchers, the tensile stiffness values of BX, UX1, UX2, UX3, and UX4 at 2% global strain were 400, 550, 625, 1075, and 1250 kN/m (2300, 3144, 3570, 6145, 7145 lbf/in), respectively. The spacing of primary geogrids within the lower 1/3 wall weight was 0.4 m (1.3 ft) while that within the upper 2/3 wall height was 0.6 m (2 ft). The secondary geogrids used between primary geogrids in TS1 and TS2 had vertical spacing of 0.2 m (8 in.). The length of the secondary uniaxial geogrid was 1.4 m (4.6 ft) while that of the secondary biaxial geogrid was 1.3 m (4.3 ft).

Table 1. Properties of Geogrid (provided by manufacturer)

Property	UX1	UX2	UX3	UX4	BX
Ultimate tensile strength (kN/m)	58	70	114	144	-
Maximum allowable (design) strength for 120-year design life (kN/m)	21.2	25.6	41.8	52.7	-
Reduction factor for installation damage RFID	1.1				-
Reduction factor for creep RFCR	2.6				-
Reduction factor for durability RFD	1.1				-

Note: The relevant BX properties are in the cross-machine direction (XMD); the initial modulus of BX in use is 400 kN/m (2284 lbf/in) the tensile strength of BX at 2% strain is 6.6 kN/m (37.7 lbf/in); the junction efficiency of BX is 93%.

The test wall sections were backfilled with aggregate. Sieve tests were conducted to determine the aggregate particle size distribution as shown in Figure 4.2.3. The obtained aggregate particle size distribution met the requirement of AASHTO (2007) and KDOT (2007) for backfill materials of MSE walls. The average moist unit weight and the dry unit weight of the compacted aggregate were approximately 18.1 and 17.5 kN/m^3 (116 and 112 pcf), respectively. The peak friction angle of the aggregate, $\phi_{peak,}$ was 47 degrees.

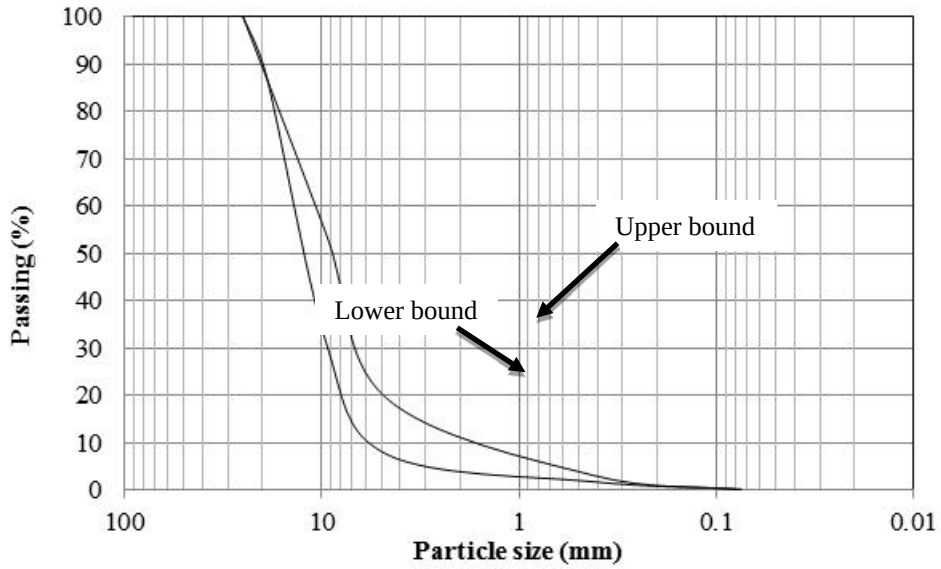

Figure. 4.2.3. *Particle size distribution of the aggregate*

In this study, inclinometer casings, earth pressure cells, and strain gauges were employed to monitor accumulated lateral wall facing deflections, distributions of lateral earth pressures, and distributions of tensile strains in geogrid layers during construction. Figure 4.2.2 presents the layout of instrumentation in the test sections in this study.

4.2.3 RESULTS AND DISCUSSIONS

4.2.3.1WALL FACING DEFLECTIONS

The profiles of measured accumulated wall facing deflections with wall height before and after the construction of the backslope are shown in Figure 4.2.4. Since the inclinometer casing was keyed into the bedrock, the casing portion inside the bedrock was fixed and used as a reference for zero displacement. The accumulated wall facing deflection at each location shown in Figure 4.2.4 was calculated by adding the deflection at the current location since the block was installed after the wall facing had deflected below this location. As shown in Figure 4.2.4, the accumulated facing deflections increased with the construction of the backslope because additional lateral earth pressure due to the weight of the backslope was applied on the wall facing. It should be pointed out that the embedment soil in front of the wall in TS3 was placed earlier than that in other two sections. As a result, the measured accumulated wall facing deflections within the lower portion of TS3 were smaller than those in other two sections. However, the measured accumulated wall facing deflections within the upper 2/3 portion of the wall section in TS1 and TS2 were lower than those in TS3 (i.e. the control section) indicating that the inclusion of secondary reinforcements led to a reduction in the accumulated wall facing deflections. In addition, the accumulated wall facing deflections in the three test wall sections after the construction of the backslope were calculated by integrating the measured strains along the length of the geogrid at each instrumented layer as shown in Figure 4.2.4(b). In this calculation, the end of each geogrid at the interface between the reinforced fill and the retained soil was taken as a reference (zero relative displacement). The displacement was accumulated from the reference position towards the wall facing. The details of the measured strains will be presented in the “Global strains of geogrid” section later. Figure 4.2.4(b) shows that the accumulated wall facing deflections estimated based on the measured strains of the geogrid show similar trends and magnitudes as those obtained from the inclinometers. In addition, the maximum accumulated wall facing deflections calculated from the geogrid strains in TS3 were slightly larger than those in TS1 and TS2. This result is consistent with that measured by the inclinometers. The difference might be caused by the displacement of the reference point at the end of the reinforcement.

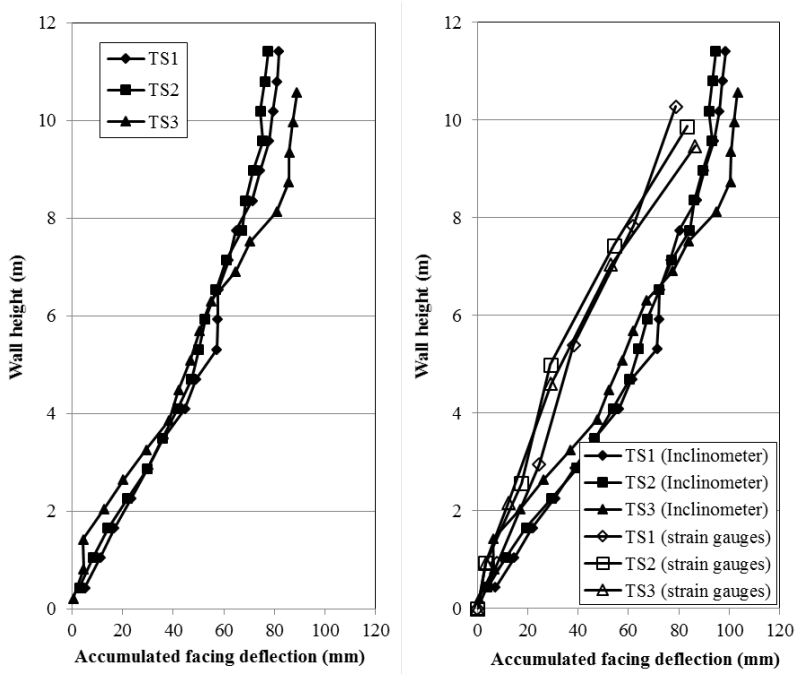

Figure 4.2.4. *Profiles of wall deflections with full wall height: (a) before the construction of the backslope; (b) after the construction of the backslope*

4.2.3.2VERTICAL EARTH PRESSURE

Figure 4.2.5 presents the distributions of the measured vertical earth pressures and the calculated overburden stresses under the TS2 wall before the construction of the backslope and after the construction of the backslope. The pressure cell at the distance of 3 m (9.8 ft) from the wall facing was judged as malfunctioning during the field measurement. Before the construction of the backslope, the measured vertical earth pressures were slightly higher than the calculated overburden stresses and the equivalent trapezoidal stresses considering an external lateral earth pressure, as shown in Figure 4.2.5(a). The measured vertical stress close to the wall facing was higher than that away from the wall facing because the external lateral earth pressure from the retained soil led to an increased eccentricity of the reinforced soil mass towards the toe of the wall facing and to an increased bearing stress close to the wall facing. This trend was well captured by the calculated trapezoidal stresses. However, the distribution of the calculated overburden stresses of the wall was uniform because the calculation of the overburden stress did not consider the lateral earth pressure from the retained soil.

After the construction of the backslope, the measured vertical earth pressures continued to increase due to construction loads. In addition, the measured vertical earth pressures were slightly higher than the calculated overburden stresses. However, the pattern of the distribution of the measured vertical earth pressures after the construction of the backslope changed as compared with that before the construction of the backslope. The measured vertical earth pressures close to the wall facing were lower than those away from the wall facing because the

backslope added more overburden stress and as an eccentric load led to a potential rotation away from the toe of the wall. This pattern was captured by both the calculated overburden stresses and trapezoidal stresses. In addition, the calculated overburden stresses were lower than the calculated trapezoidal stresses at the locations close to the wall facing while the calculated overburden stresses became higher than the calculated trapezoidal stresses at the locations away from the wall facing. This trend can be attributed to the backslope acting as an eccentric load.

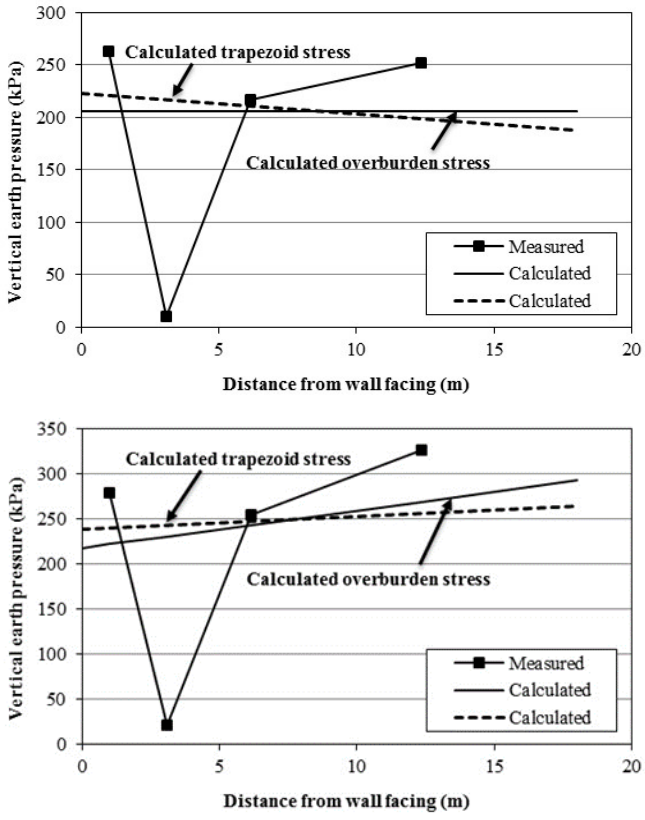

(a) (b)

Figure 4.2.5. Distributions of measured vertical earth pressures under the wall: (a) before the construction of the backslope; and (b) after the construction of the backslope.

4.2.3.3HORIZONTAL EARTH PRESSURE

Figure 4.2.6 presents the profiles of the measured lateral earth pressures against the back of the wall facing for the three test wall sections at the end of the construction. For comparison purposes, the profiles of calculated active earth pressure using two friction angles (34°, a friction angle used in the original design; 47°, a peak friction angle of aggregate obtained from triaxial tests and also used in the updated analysis) and the profile of at-rest earth pressure using the peak friction angle of aggregate from the triaxial tests are plotted as well. The active earth pressures were calculated based on the coefficient of active earth pressure using Rankine's theory considering the backslope on the top of the wall as follows:

$$K_a = \cos\beta\left[\frac{\cos\beta - \sqrt{\cos^2\beta - \cos^2\phi}}{\cos\beta + \sqrt{\cos^2\beta - \cos^2\phi}}\right] \quad (4.2.1)$$

where ϕ is the friction angle of the aggregate and β is the angle of the backslope. The lateral earth pressures at rest were calculated based on the coefficient of earth pressure at rest proposed by Jaky (1948):

$$K_0 = 1 - \sin\phi \quad (4.2.2)$$

Figure 4.2.6 shows that the calculated active earth pressures using the design friction angle of 34° were mostly higher than the measured earth pressures behind the wall facing. In TS3 (i.e. the control section), the measured lateral earth pressures increased approximately linearly with depth and were between the calculated active earth pressures and at-rest earth pressures using the actual friction angle of 47°. The measured earth pressures at the bottom part of the wall were close to the at-rest earth pressure using the actual friction angle of 47° because the existence of the embedment limited the wall deflection at the bottom of the wall. However, the measured earth pressures within the upper portion of the wall were close to the active earth pressure because the wall deflection was sufficient to allow the fill to be in an active state within the upper portion of the wall.

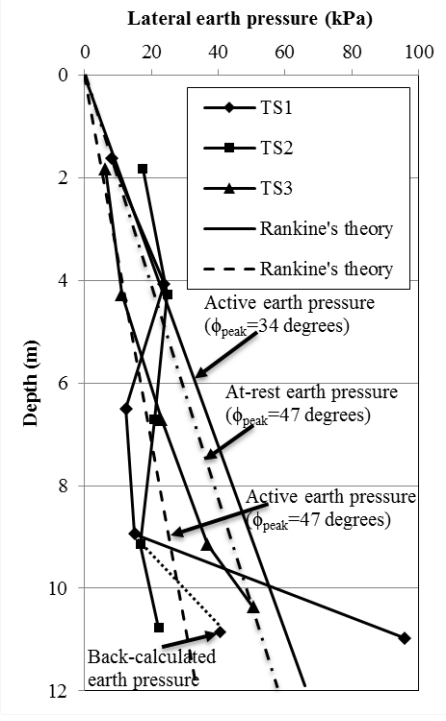

Figure 4.2.6. Profiles of measured lateral earth pressures

Compared with the linear distribution of the measured lateral earth pressures in TS3, the distribution of the measured lateral earth pressures in TS1 and TS2 (i.e. test wall sections

reinforced by secondary geogrid) were approximately uniform. The earth pressures within the upper portion of the wall were close to the at-rest earth pressures while those within the lower portion were close to the active earth pressures. This result is likely because the inclusion of secondary reinforcement reduced the wall deflection within the upper portion of the wall and the total earth pressure was re-distributed due to the construction sequence.

The total lateral thrust forces applied on the back of wall facing for the three test sections at the end of the construction were calculated by integrating the measured lateral earth pressure along the wall height as 324.1, 220.9, and 241.3 kN (35.7, 24.3, 26.5 tons) for TS1, TS2, and TS3, respectively. TS2 and TS3 had similar thrust forces; however, TS1 had a much higher thrust force than TS2 and TS3 because TS1 had a much higher measured lateral earth pressure at the depth of 11.3 m (37.1 ft). Since the three wall sections had similar dimensions, it is expected that they should have similar total lateral thrust forces. Therefore, the much higher lateral earth pressure at the depth of 11.3 m (37.1 ft) was unreasonable. Because TS1 and TS2 had similar geogrid layouts and wall heights, the total lateral thrust forces on the back of wall facing in TS1 and TS2 could be assumed to be equal. Then the lateral earth pressure at the depth of 11.3 m (37.1 ft) in TS1 could be back-calculated as 42.6 kPa (6.2 psi). Figure 4.2.6 shows that the back-calculated lateral earth pressure at the depth of 11.3 m (37.1 ft) fitted the profile well.

Coefficient of lateral earth pressure behind the wall can be estimated in two ways: (1) using the measured lateral earth pressure behind the wall facing as

$$K_h = \frac{\sigma_h}{\sigma_v} \tag{4.2.3}$$

where σ_h = the measured lateral earth pressure behind the wall facing and σ_v = the vertical overburden stress and (2) using the measured maximum tension in the reinforcement as

$$K_r = \frac{T_{max}}{S_v \cdot R_c \cdot \sigma_v} \tag{4.2.4}$$

where T_{max} = the measured maximum tension in the reinforcement (can be estimated using the global strain of a geogrid multiplied by its tensile stiffness, S_v = the vertical spacing of geogrid, and R_c = the coverage ratio of geogrid. A normalized coefficient of lateral earth pressure is defined as K_r / K_a, where $K_a = tan^2\left(45^o - \phi/2\right)$. The method for calculating the coefficient of lateral earth pressure based on the measured maximum tension in the reinforcement was adopted by AASHTO to develop the profile of K_r / K_a with depth included in AASHTO (2007) and AASHTO (2014).

Figure 4.2.7 shows that the profile of the normalized coefficient of lateral earth pressure with the depth when $\phi = 47°$ was used. Figure 4.2.7(a) presents the profile back-calculated based on the measured lateral earth pressures behind the wall facing. It is shown that TS3 had the K_h / K_a

ratio close to 1.0. However, for TS1 and TS2, the K_h / K_a ratio was greater than 1.0 when the depth was less than 6.0 m (19.7 ft), while the ratio was less than 1.0 when the depth was greater than 6.0 m (19.7 ft). Overall, TS1 and TS2 had similar K_h / K_a ratios width depth. This comparison shows that TS3 (control section) had the lowest K_h / K_a ratio within the upper 6 m (19.7 ft) due to its largest wall movement as compared with other two wall sections. Figure 4.2.7(b) presents the profile back-calculated based on the measured maximum tension in the reinforcement, which is the method adopted by AASHTO. It is shown that the K_r / K_a ratios at the top three layers of the instrumented geogrid were between 0.56 and 0.69, 0.41 and 0.63, and 0.89 and 1.27, in TS1, TS2, and TS3, respectively. This comparison shows that TS3 T had the greatest K_r / K_a ratio within the upper 6 m (19.7 ft) due to its highest tension as compared with other two wall sections. Therefore, the K_h / K_a ratio based on the measured earth pressure is different from the K_r / K_a ratio based on the measure maximum tension in the reinforcement and the K_r / K_a ratios calculated by the maximum tension in the reinforcement are close to those used in the practice.

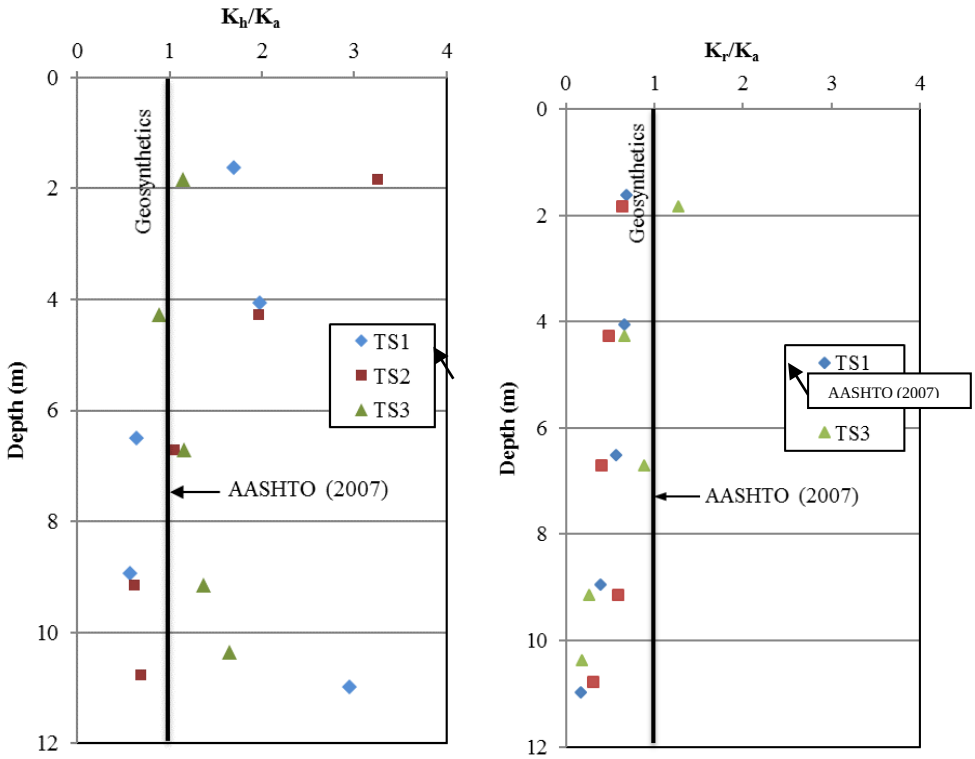

(a) (b)

Figure 4.2.7. *Distribution of coefficient of lateral earth pressure with depth: (a) from measured lateral earth pressures; and (b) from maximum tensile forces.*

Several field instrumentations showed that the measured maximum tension in the reinforcement in an MSE wall under an operational condition was lower than that predicted using $K_r = K_a$ (e.g., Allen and Bathurst, 2015). The average ratio at the top three layers of the instrumented geogrid in TS3 was greater than those in TS1 and TS2. This result can be explained that the secondary reinforcement shared part of the required tension and reduced the maximum tension in the primary reinforcement. The K_r / K_a ratios at the bottom two layers of the instrumented geogrid in TS3 were less than those in TS1 and TS2 due to the effect of the embedment. Figure 4.2.7 also shows that the K_h / K_a ratios back-calculated based on the measured lateral earth pressures are greater than those back-calculated based on the measured maximum tension in the reinforcement. Leshchinsky and Vahedifard (2012) and Leshchinsky et al. (2014) clearly illustrated that the measured maximum tension in the reinforcement was reduced by the toe resistance of the wall due to embedment and shear resistance of block facing. In the practice, however, the toe resistance is often ignored in the design. The back wall friction could also reduce the lateral earth pressure, but its effect happened for all three walls. It should be pointed out that the back-calculated ratio based on the measured maximum tension in the reinforcement has been used by most researchers and included in the AASHTO method. This back-calculated ratio can be used for design if there is no toe resistance in the field or the toe resistance effect is considered in the design.

4.2.3.4 STRAINS IN GEOGRIDS

Figure 4.2.8 presents the profile of the maximum strains with depth for all three test wall sections, respectively. The strain distributions in the primary reinforcement show that the maximum strains for all three test wall sections occurred at the locations close to the wall facing within the reinforced backfill zone. The maximum strains in the primary geogrids were in the range of 0.15%-0.43%, 0.26%-0.5%, and 0.14%-0.69%, for TS1, TS2, and TS3, respectively. Similar magnitudes of strains were obtained by Allen and Bathurst (2014a and 2014b) in their instrumented MSE walls, in which the measured maximum strains of geogrid were less than 1%. The maximum strains of primary geogrid at the instrumented layers above the embedment (instrumented Layers 3, 4, and 5) in TS3 in this study were larger than those in TS1 and TS2. This result can be explained that the secondary reinforcement in TS1 and TS2 carried a portion of the tensile force from lateral earth pressures and reduced the maximum tensile force in the primary geogrid.

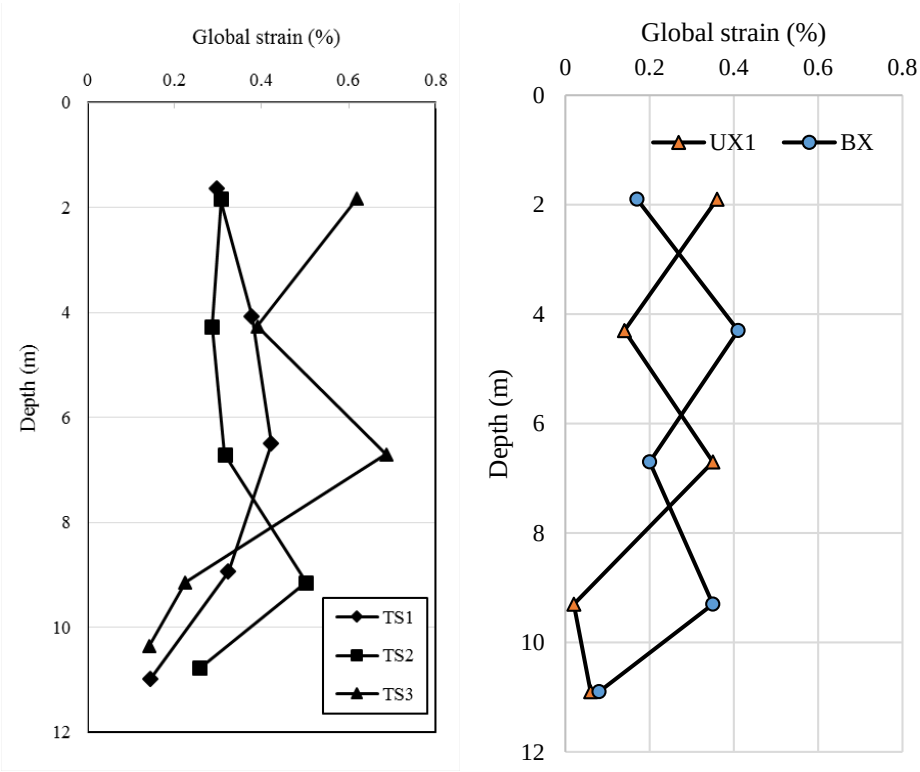

(a) Primary geogrid (b) Secondary geogrid

Figure 4.2.8. Profiles of the maximum global strains of primary and secondary geogrids.

However, the maximum strains of the primary geogrid at the first two instrumented layers (i.e., Layers 1 and 2) in TS3 were smaller than those in TS1 and TS2. This result can be attributed to the influence of the embedment. TS3 had more embedment than TS1 and TS2 at the first embedment level (i.e., the 29th day of the construction as shown in Figure 4.2.1), which resulted in the reduction in the strains of the lower geogrid layers in TS3. At the second embedment level (i.e., the 151st day of the construction), the three test wall sections had the same embedment; therefore, the influence of the toe resistance on the geogrid strains installed after reaching the second embedment level was minimal.

The measured maximum strains in the secondary geogrids in TS1 (UX1) and TS2 (BX) show similar magnitudes of strains as shown in Figure 4.2.8(b).

An analysis was conducted to calculate the total tensions carried by all the reinforcement layers (including primary and secondary geogrids) in all three test sections as follows: 104 (TS1), 100 (TS2), and 89 kN/m (594, 571 and 508.8 lbf/in) (TS3). This analysis shows that the reinforcement in the test sections with secondary reinforcement carried almost the same total tension while the reinforcement in the test section without secondary reinforcement carried less total tension. This result can be explained that the test sections with secondary reinforcement had smaller wall deflections and therefore they were less mobilized towards the active state.

4.2.4 CONCLUSIONS

In this study, three geosynthetic reinforced mechanically stabilized earth (GMSE) wall test sections, consisting of one test section with primary uniaxial geogrid layers and secondary uniaxial geogrid layers (TS1), one test section with primary uniaxial geogrid layers and secondary biaxial geogrid layers (TS2), and one test section with primary geogrid layers only (TS3), were instrumented and monitored during construction with earth pressure cells, inclinometer casings, and strain gauges. The measured vertical earth pressures, lateral earth pressures, accumulated wall facing deflections, and global strains of geogrid from these three MSE wall sections were analyzed. The following conclusions can be drawn:

(1) The maximum accumulated wall facing deflections in TS1 and TS2 were smaller than that in TS3, indicating that the inclusion of secondary geogrid reduced the accumulated wall facing deflections.
(2) The measured vertical stress close to the wall facing was higher than those away from the wall facing before the construction of the backslope because the lateral earth pressure from the retained soil increased the eccentricity of the reinforced soil and increased the bearing stress close to the wall facing. The measured vertical earth pressures close to the wall facing were lower than those away from the wall facing after the construction of the backslope because, as an eccentric load, the backslope led to potential rotation away from the toe of the wall.
(3) In the test wall section without secondary geogrid layers, the measured lateral earth pressure at the back of the wall increased approximately linearly with depth and was between the calculated active earth pressure and the at-rest earth pressure using the actual friction angle of the aggregate. The measured earth pressures within the lower portion of the wall were

close to the at-rest earth pressures because the existence of the embedment limited the wall deflection. However, the measured earth pressures within the upper portion of the wall were close to the active earth pressure because the wall deflection was sufficient to allow the reinforced soil to be in an active state.

(4) The measured lateral earth pressures at the back of the wall in the test wall sections with secondary geogrid layers were approximately uniform with depth. The measured lateral earth pressures within the upper portion of the wall were close to the at-rest earth pressures because the existence of secondary reinforcement reduced the wall deflection.

(5) The average normalized earth pressure coefficient ratio at the top three layers of the instrumented geogrid in TS3 was greater than those in TS1 and TS2. This result can be explained that the secondary reinforcement shared part of the required tension and reduced the maximum tension in the primary reinforcement. The normalized earth pressure coefficient ratios back-calculated using the measured lateral earth pressures behind the wall facing were greater than those back-calculated using the measured maximum tension in the reinforcement because the toe resistance of the wall due to embedment and the shear resistance of block facing reduced the maximum tension in the reinforcement.

(7) The secondary reinforcement carried a portion of the tension force from lateral earth pressures and reduced the tension force in the primary geogrid layers.

(8) The analysis shows that the reinforcement in the test sections with secondary reinforcement carried almost the same total tension while the reinforcement in the test section without secondary reinforcement carried less total tension.

4.2.5 REFERENCES

AASHTO (2007). AASHTO LRFD Bridge Design Specifications. 4th Ed., Washington, DC.

AASHTO (2014). AASHTO LRFD Bridge Design Specifications, 7th Ed., Washington, DC.

Allen, T.M. and Bathurst, R.J. (2014a). Performance of a 11 m high block-faced geogrid wall designed using the K-stiffness Method, Canadian Geotechnical Journal, 51(1): 16-29 (http://dx.doi.org/10.1139/cgj-2013-0261).

Allen, T.M. and Bathurst, R.J. (2014b). Design and performance of a 6.3 m high block-faced geogrid wall designed using the K-stiffness Method, J. Geotech. Geoenviron. Eng., 142(2): 12 p. (http://dx.doi.org/10.1061/(ASCE)GT.1943-5606.0001013).

Allen, T.M. and Bathurst, R.J. (2015). “An improved simplified method for prediction of loads in reinforced soil walls.” ASCE Journal of Geotechnical and Geoenvironmental Engineering, 141(11): 04015049 (http://10.1061/(ASCE)GT.1943-5606.0001355).

Christopher, B.R., Gill, S.A., Giroud, J.P., Juran, I. Scholsser, F., Mitchell, J.K., and Dunnicliff, J. (1989). "Reinforced Soil Structures, Volume I. Design and Construction Guidelines and Volume II. Summary of Research and Systems Information." Report No. FHWA-RD-89-043, Federal Highway Administration, Washington DC, November 1989, 287p.

Elias, V. and Christopher, B.R. (2001). "Mechanically stabilized earth walls and reinforced soil slopes, design and construction guidelines." Federal Highway Administration Demonstration Project 82, Ground Improvement, Report No. FHWA-SA-96-071, U.S. Department of Transportation, Federal Highway Administration, Washington DC, 367p.

Jaky, J. (1948). “Pressure in silos.” 2nd ICSMFE, London, 1, 103-107.

Jiang, Y., Han, J., Parsons, R.L., and Cai, H. (2015). Field Monitoring of MSE Walls to Investigate Secondary Reinforcement Effects. KTran Report, Kansas Department of Transportation.

Kansas Department of Transportation (KDOT) (2007). Standard Specifications for State Road and Bridge Construction, Section 1107 - Aggregates for Backfill.

Leshchinsky, D. (2000). “Alleviating connection load.” Geotechnical Fabrics Report, 34-39

Leshchinsky, D., Zhu, F., and Meehan, C. (2010). “Required unfactored strength of geosynthetic in reinforced earth structures.” J. Geotech. Geoenviron. Eng., 136(2), 281–289.

Leshchinsky, D. and Vahedifard, F. (2012). “Impact of toe resistance in reinforced masonry block walls: design dilemma.” J. Geotech. Geoenviron. Eng., 138(2), 236–240.

Leshchinsky, D., Kang, B.J., Han, J., Ling, H.I., (2014). “Framework for Limit State Design of Geosynthetic-Reinforced Walls and Slopes,” Trans. Infras. Geotech., 1(2), 129-164.

Rowe, R.K., and Ho, S.K. (1998). "Horizontal Deformation in Reinforced Soil Walls." Can. Geotech. J., 35, 312-327.

4.3 STUDY ON THE EFFECT OF REINFORCEMENT SPACING ON THE BEHAVIOR OF GEOSYNTHETIC-REINFORCED SOIL

4.3.1 INTRODUCTION

The interaction between soil backfill and geosynthetic reinforcement may be affected by phenomena that are related to the reinforcement vertical spacing. Such phenomena developing in a reinforced soil mass may be related to soil arching, as described by Terzaghi's classic trap-door theory (Terzaghi 1936). Soil arching develops during soil deformation and can take different arching shapes (e.g. Chen et al. 2008, Costa et al. 2009, Iglesias et al. 2013, Rui et al. 2016). This phenomenon may also take place in reinforced soil, especially in cases involving closely-spaced reinforcement. Such phenomenon is expected to depend on the soil density, grain size distribution, overburden pressure, and interface characteristics. Previous studies have been conducted on GRS to study the impact of closely-spaced reinforcement. Specifically, an experimental testing program was conducted by Leshchinsky et al. (1994) on GRS unit cells to study the impact of reinforcement vertical spacing with focus on the soil arching phenomenon. Specifically, a pullout testing device was developed to evaluate the displacement and strain fields within a reinforced soil unit cell. The testing program included pullout of single reinforcement layers and of two reinforcement layers connected to a rigid facing panel. This study presents a reevaluation of the experimental results obtained by Leshchinsky et al. (1994) and their integration to assess the performance of field monitoring and numerical results, which were also conducted to evaluate the effect of geosynthetic reinforcement vertical spacing. The field research component involves the evaluation of two GRS walls, and was complemented with numerical simulations conducted to extrapolate the findings of the field study with focus on the effect of reinforcement spacing. The integrated experimental, field, and numerical results aim at assessing the interaction of the various wall components that may affect wall performance with varying reinforcement vertical spacing.

4.3.2 EXPERIMENTAL AND ASSOCIATED NUMERICAL COMPONENTS: REEVALUATION OF RESULTS

Leshchinsky et al. (1994) conducted an experimental study to evaluate the effect of vertical reinforcement spacing on the failure mechanism in geosynthetic-reinforced structures. The motivation of their study was to assess failure mechanisms based on limit state analysis, which involve development of a failure slip surface extending from the toe to the crest of the structure. The reinforcement must extend beyond the slip surface to tie back the unstable zone to the stable zone. Limit equilibrium analysis does not account for the interaction occurring in soil and reinforcement layers considering spacing. For instance, the interaction among reinforcement layers may increase with decreasing vertical reinforcement spacing. In this case, the interaction between largely-spaced reinforcement layers would be comparatively minor, making the limit state a practical design approach. However, for closely-spaced reinforcement, the assumption may no longer be valid as the interaction (or load shedding) would increase with decreasing reinforcement spacing.

Two testing series were performed: (1) pullout of single reinforcement layer embedded in a confined soil mass, which assessed the performance of a reinforcement layer in a soil mass in conventional testing conditions; and (2) pullout of two reinforcement layers embedded in a confined soil mass, which assessed the effect of interaction between reinforcement layers. Two devices were used to evaluate the behavior of single and double reinforcement layers embedded in soil mass, respectively. Figure 4.3.1a shows a schematic view of the device where a single reinforcement layer was employed. The device involved a steel frame that accommodates samples that were 0.6 m (2 ft) long, 0.19 m (0.6 ft) wide, and 0.3 m (1 ft) high. The reinforcement layers were of the same width as the box. A normal confining pressure was applied to the top surface of the reinforced soil mass using a pressurized air bag. The second device was similar to the first one except that it was twice as high (i.e., 0.6 m (2 ft) high), as shown in Figure 4.3.1b. The side walls of both devices were made of transparent Plexiglas to enable photogrammetric measurement of soil movements as the pullout load increases. This allowed evaluation of the interaction between the reinforcements and the soil mass. The transparent walls also allowed evaluation of the kinematics of the shear band that developed upon generation of shear stresses at the soil-reinforcement interface. The second device allowed placement of two reinforcement layers, enabling assessment of the interaction between two contiguous reinforcement layers. The vertical spacing of the reinforcement layers was 0.2 m (0.7 ft). A horizontal force was applied to a panel connected to the reinforcement layers. Accordingly, the test was conducted by imposing lateral displacements to a facing unit located between two reinforcement layers (rather than by increasing the overburden pressure on the reinforced soil mass). The test results suggest that the vertical reinforcement spacing influences the stiffness of the reinforced soil mass composite. For closely-spaced reinforcement of typical stiffness and strength, the failure surface was not likely to develop within the reinforced soil mass. Instead, the failure surface developed behind the reinforced soil zone. Closely-spaced reinforcement allowed formation of composite material that behaved as monolithic mass.

The backfill material used in the testing program was Ottawa sand, which is classified as poorly graded sand (SP according to the Unified Soil Classification System). The average and maximum particle sizes were 0.26 and 0.90 mm (10 and 35 mil), respectively. The backfill was compacted dry to a relative density of 70%, which corresponds to an average unit weight of 16.8 kN/m^3 (108 pcf). The backfill was placed in six lifts by pluviation and was densified by slight tapping on the walls of the box. Triaxial tests conducted on specimens prepared at a 70% target relative density resulted in peak and residual friction angles of 38 and 34 degrees, respectively. The reinforcement used in this study was polypropylene biaxial geogrid with a tensile strength of 45.2 kN/m (258 lbf/in) in the testing direction.

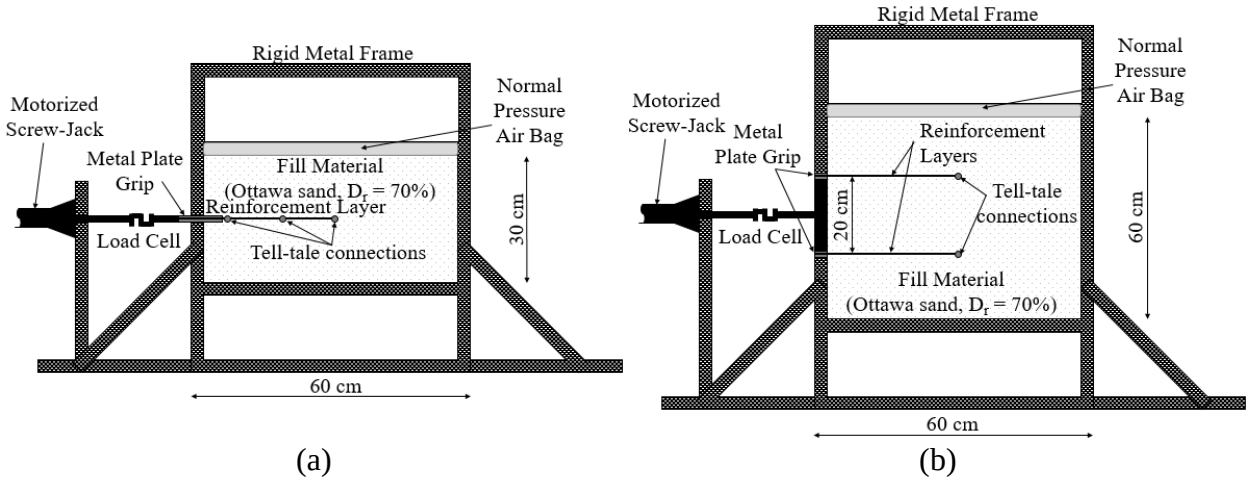

Figure 4.3.1. Pullout equipment: (a) single-reinforcement test; and (b) double-reinforcement test (redrawn after Leshchinsky et al. 1994).

Overall, the pullout process was observed to progressively propagate from the front end of the reinforcement to its rear end. Accordingly, the portions of the reinforcement closer to the line of load application reached pullout resistance capacity prior to the further portions. Accordingly, the soil-reinforcement interface strength in the front zones reached a residual condition before the rear zones to mobilize their strength from pre-peak, peak, to ultimately post-peak shear strength.

The results of single-reinforcement tests showed that the shear stresses generated at soil-reinforcement interface influenced a soil region ranging in thickness from 25 to 50 mm (1 to 2 in.) on each side of the reinforcement. This zone can be referred to as a shear band and is schematically shown in Figure 4.3.2a. This pattern was found to be independent of the confinement. Note that since measurements are those observed on the latex membrane assumed to deform in unison with the adjacent soil. It was concluded that, for the geogrid and sand used in the study, the zone of influence of a single deforming geogrid is about 0.03 m (1.2 in.) on each side. This implies that two deforming geogrids (i.e., two geogrids subjected to tension load) will interact with each other (i.e., behave as a composite soil-geogrid material) if the vertical spacing is at most 0.06 m (2.3 in.). Note that this is valid for the type of backfill employed in the study, for which D_{50} = 0.26 mm (10 mil), ϕ_{peak} = 38° and $\phi_{residual}$ = 34°. Backfill with particles larger than the sand used in these tests are expected to have larger effects. The tests conducted in this study were not intended to simulate pullout performance but rather to identify mechanisms and a response that could be deemed as composite material behavior.

The results of the double-reinforcement tests showed that the pullout resistance was essentially the same as that obtained using a single-reinforcement of the same length and confinement configuration. That is, the soil between the reinforcement layers was found to stiffen, resulting in the soil/reinforcement unit to behave as a monolithic block. This block involves two outer interfaces on which shear stresses develop against the adjacent soil, while no shear displacements (and associated shear stresses) could be identified on the two inner interfaces

adjacent to the stiffened soil block. This resulted in a pullout resistance in the double-reinforcement tests equivalent to that in the single-reinforcement tests. However, this response was found only at comparatively high confining pressures, which is when the soil between the reinforcements is stiff enough to behave as a monolithic block. On the other hand, at low confining pressure the pullout resistance in the double-reinforcement tests was higher than that in the single-reinforcement layer tests. This is probably due to the generation of shear stresses at the inner interface between the reinforcement layers and the soil between the reinforcement layers. In addition, the tensile stiffness in the double-reinforcement test was higher than that in the single-reinforcement test. The observed deformation field is schematically represented in Figure 4.3.2b.

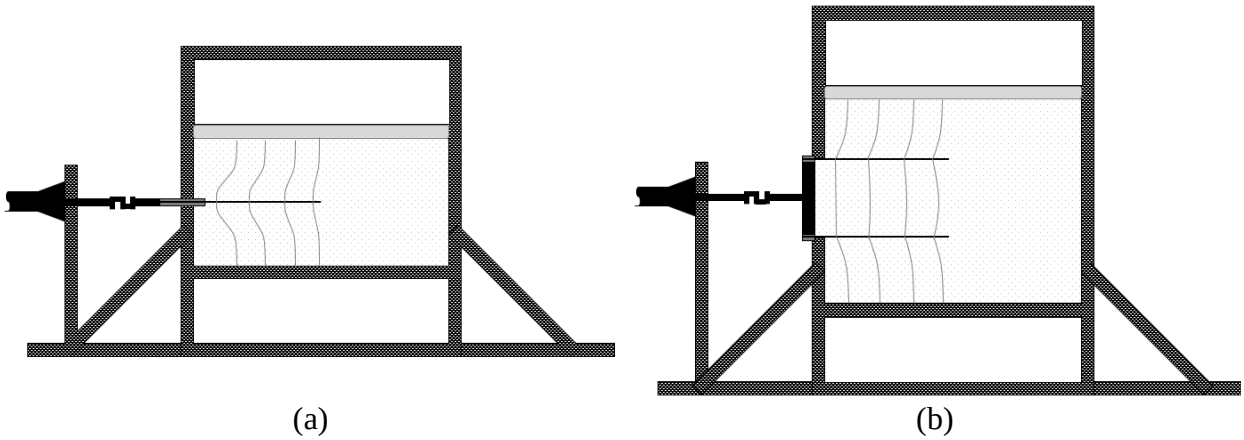

Figure 4.3.2. Schematic representation of shear band: (a) single-reinforcement test; and (b) double-reinforcement test (redrawn after Leshchinsky et al. 1994).

Figure 4.3.3a shows the expected failure mechanism, consistent with current design methodologies, when the active state is reached. However, the active state mechanism depicted in Figure 4.3.3a was not observed in the double-reinforcement tests. In addition, the load measured in the load cell after completion was expected to be compressive consistent with those predicted by active earth pressure theory; instead, they were zero. Accordingly, it appears that some 'silo' or arching effects developed, which resisted the lateral pressures that were expected to act in the block between the two geogrids. Figure 4.3.3b shows the actual failure mechanism observed in the double-reinforcement tests. As shown in Figure 4.3.3b, deformation in the soil mass followed the facing movement. For the spacing and geogrid stiffness used in this experimental program, only an external failure occurred (i.e., in a soil mass outside that bounded by the two layers). The soil between the two geogrids moved 'rigidly' with the geogrids, without developing an active slip surface.

A numerical evaluation was conducted to study the effects of vertical reinforcement spacing (Leshchinsky and Vulova 2001). Extensive parametric studies were conducted using a finite difference software, which employs a finite difference approach. The numerical model adopted "moving reference" algorithm where every new soil layer and block row are placed on top of a

preceding layer that is allowed to deform during construction. This allowed the wall facing to undergo lateral outward deformation cumulatively as construction progresses. Simulated construction continued until a prevailing mode of failure occurred.

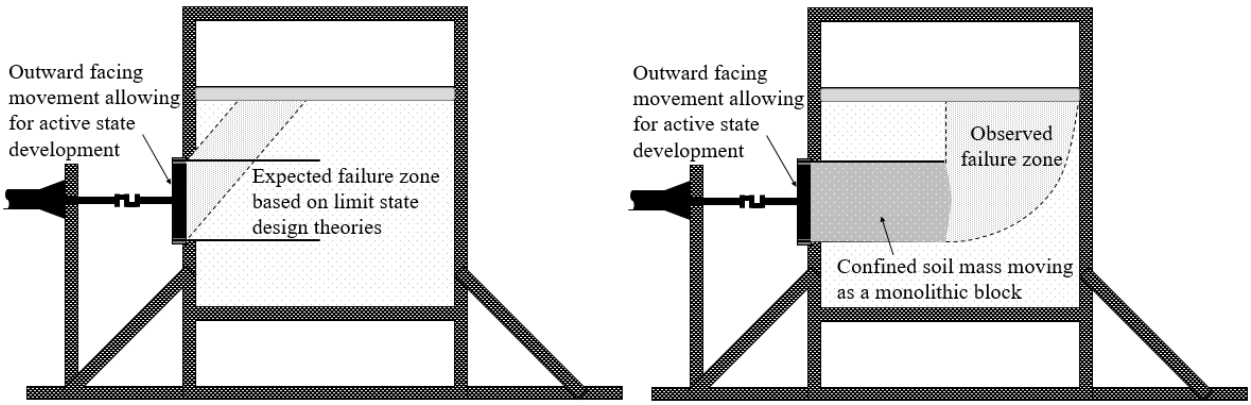

Figure 4.3.3. Failure mechanism: (a) postulated failure mechanism in active-state design; and (b) observed failure (redrawn after Leshchinsky et al. 1994).

The results indicated that the effect of closely-spaced reinforcement increases with increasing backfill shear strength. This trend was found to be more pronounced if the foundation soil is stiff (i.e., competent foundation). For reinforcement spacing values below 200 mm (8 in.), the reinforced soil mass was found to behave as a coherent mass and did not develop internal plastic zones. On the other hand, comparatively large spacing (beyond 600 mm (24 in.)) were found to lead to connection failure. Reinforcement spacing was found to play a major role in wall behavior and it significantly affected the prevailing mode of failure, inconsistent with current design approaches, overlook the effect of spacing on the prevailing mode of failure. Overall, the numerical results indicated that interaction of all wall components (i.e., facing, foundation, retained soil, reinforced soil, and reinforcement properties) may affect wall performance. Also, the numerical results implied that, for high quality backfill, “close spacing” corresponds to values below 400 mm (15.7 in.); although this value was found to be highly dependent on multiple factors. Also, the parametric studies indicated that, for closely spaced reinforcement, commonly used methods for external stability analysis (e.g., direct sliding, toppling, deep-seated failure, and compound) are adequate for design. However, current design guidelines may not be accurate for the case of predicting reinforcement strength requirements.

4.3.3 FIELD AND ASSOCIATED NUMERICAL COMPONENTS

Based on the findings of the experimental component of this research, a field evaluation was conducted, which involved two GRS retaining walls constructed in Stockbridge, Georgia. Construction started in November 1994 and was completed in August 1995. The walls utilized segmental concrete blocks; the walls are referred to herein as WALL 1 and WALL 2. The walls were 6.84 m-high (36 block rows) and were reinforced at vertical spacing values of 0.4 and 0.8 m

(16 and 32 in.) (i.e., every two and four block courses), respectively. The walls were subjected to a surcharge corresponding to a 0.76-m (2.5 ft) thick soil layer. The geosynthetic reinforcement used in the walls involved uniaxial geogrids with an ultimate tensile strength of 70 and 114 kN/m (400 and 651 lbf/in) for WALL 1 and WALL 2, respectively. The reinforced backfill material, which was the same as the retained soil, was a concrete sand characterized by an average grain size, D_{50}, of 0.79 mm (31 mil). The reinforcement length to wall height ratio, L/H, was approximately 0.3, which is significantly lower than the minimum ratio of 0.7 established by the American Association of State Highway and Transportation Officials (AASHTO) requirements and of 0.6 established by the National Concrete Masonry Association (NCMA) requirements. However, an L/H ratio of 0.3 had already been adopted by Tatsuoka (1994) while using rigid facing. Short reinforcement was deemed acceptable, particularly considering that planar reinforcements (i.e. geosynthetic sheets) are used. This reinforcement enhances the stability of the structures due to its large contact area with backfill, unlike strip reinforcements that should be longer in order to transfer similar loads in a smaller contact area (Tatsuoka 1994). The comparatively large contact area results in a comparatively large pullout resistance as long as the tensile capacity is comparatively high. The short reinforcement length adopted in these walls was defined based on external stability calculations assuming factors of safety of 1.5 for sliding and overturning. It should be noted that AASHTO requires a factor of safety of 2.0 for overturning. The foundation soil was competent, so bearing capacity was not a governing design issue. The premise was that the proximity of layers in the walls under investigation was deemed close for the particle size and the friction angle of the well-graded, angular sand in the walls. Consistent with the results of the previous experimental component of this study, a consistent performance of the full-scale walls would be expected to show no development of internal failure surfaces.

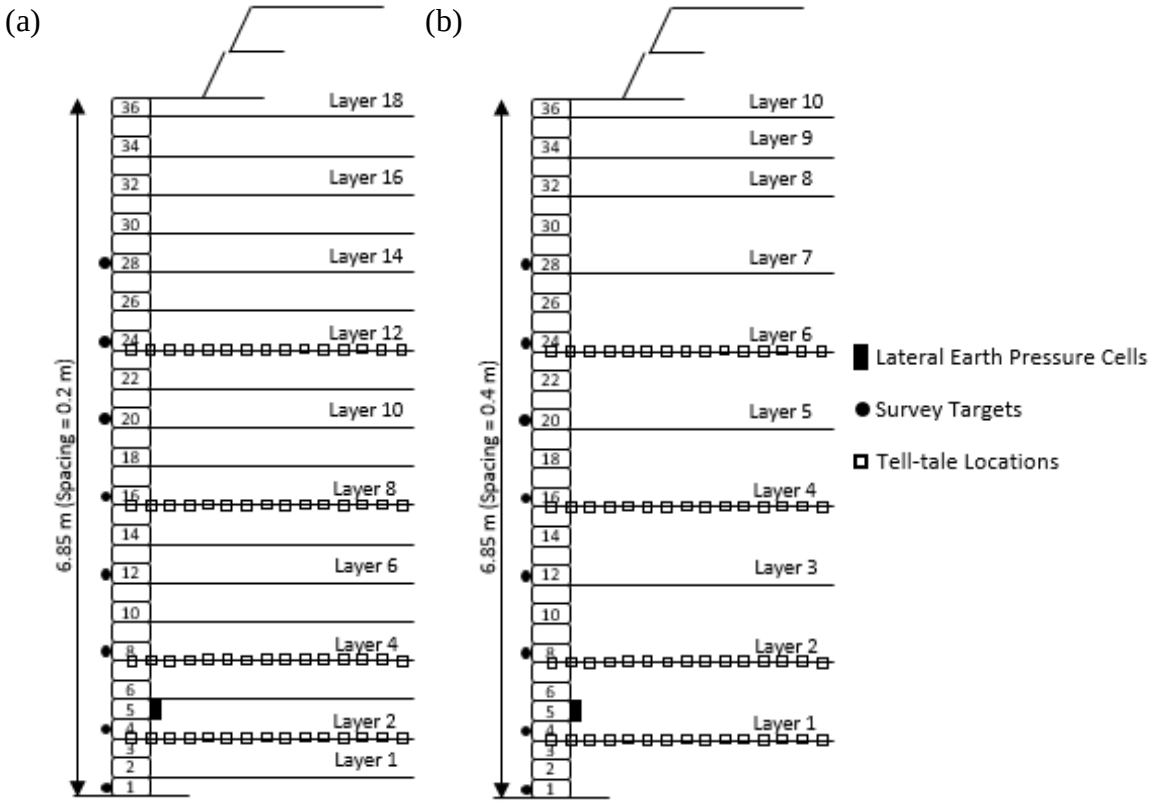

Figure 4.3.4: Instrumented cross-sections of the GRS walls: (a) WALL 1; and (b) WALL 2

Figure 4.3.4 shows the instrumented cross-sections of the constructed walls. Both walls were boosted with eight survey targets on the facing units (rows 1, 4, 8, 12, 16, 20, 24, and 28). Four reinforcement layers were instrumented by 15 displacement sensors attached to the layers along their length using tell-tales. Layers instrumented in WALL 1 were layers 2, 4, 8, and 12; whereas, those instrumented in WALL 2 were layers 1, 2, 4, and 6. Note that the instrumented layers in both walls are placed at the same elevation. In addition, two lateral earth pressure cells were installed at the back of facing block 5 in both walls.

The two walls were modelled using a two-dimensional soil-structure interaction code originally developed by Seed and Duncan (1984), and subsequently modified by Boulanger et al. (1991) and Bray (1995). Backfill and facing blocks were represented by 4-node quadrilateral elements and the geogrid reinforcement layers were represented by 2-node bar elements. Interface elements were assigned at possible slippage surfaces between the various structure components. The model simulated construction to the wall full height using 18 increments for WALL 1 and 10 increments for WALL 2. The foundation soils were represented by a 3-m (9.8 ft) thick soil layer of the same material as the backfill material. A description of the properties adopted in the numerical simulations is described next.

Backfill material and facing blocks properties: A set of drained triaxial compression tests were conducted on the backfill material under confinement levels ranging from 34 to 103 kPa (4.9 to 14.9 psi) , which were deemed representative to those in the field. The obtained failure envelope

was nonlinear, stress-level dependent. The behavior of the backfill material was represented by a hyperbolic model (Duncan and Chang 1970). Since the hyperbolic model does not consider dilation, the bulk modulus (B) was used by specifying Young's modulus (*E*) and Poisson's ratio (*υ*). Soil compaction was not considered in the simulations. The behavior of the facing blocks was also simulated using a linear elastic hyperbolic model. Table 4.3.1 summarizes the hyperbolic model parameters assigned to the backfill and facing block materials.

Table 4.3.1: Hyperbolic model parameters for backfill material and facing blocks.

Parameter	Backfill Material	Facing Blocks
Unit weight, γ (kN/m3)	18	20
Young's modulus number, K	542	2 x107
Young's modulus exponent, n	0.18	0
Failure ratio, Rf	0.78	0
Bulk modulus number, KB	4517	952380
Bulk modulus exponent, m	0	0
Cohesion, c (kN/m2)	0	0
Friction angle at 1 atm, Φ (deg)	46.7	50
Friction angle reduction, ΔΦ (deg)	11	0
At-rest lateral earth pressure coefficient, Ko	0.5	0.1
Unload-reload modulus number, Kur	542	2 x107

Reinforcement properties: While a nonlinear model would be appropriate to simulate the behavior of the reinforcement layers, a linear model was adopted, as the finite element code used in this study could only simulate linear elastic bar elements. The stiffness at 2% axial strain was adopted in analysis to represent the linear stiffness of the reinforcement layers. The various geogrid reinforcement properties adopted in the simulations are summarized in Table 4.3.2.

Table 4.3.2: Geogrid reinforcement properties.

Parameter	WALL 1	WALL 2
Young's modulus, E (kN/m2)	11526	11205
Cross-section area, A (m2/m)	0.0018	0.0028
Axial stiffness, EA (kN/m)	20.7	31.4

Interface and linkage elements properties: Generally, interface elements simulate potential slippage between two different materials. Interface elements were assigned at the possible slippage surfaces: (1) geogrid-backfill interfaces; (2) geogrid-facing block interfaces; and (3) facing block-block interfaces. Standard values for the normal, shear spring, and unloading shear spring coefficients were employed (Boulanger et al. 1991). Interface friction angles adopted considered full-scale block-block and geogrid-facing block shear tests. The interface stress-displacement behaviors were simulated by nonlinear hyperbolic models. The interface element properties adopted in the simulations are summarized in Table 4.3.3. Linkage elements were assigned to reinforcement layers. Linkage elements are springs that allow pullout while enforcing compatible displacements of the bar elements nodes linked. The linkage elements are described by two

parameters: (1) normal stiffness coefficient (K_n), which was assumed as 1 x10^8; and (2) shear stiffness coefficient (K_s), which has a standard value of 1 x10^5.

Table 4.3.3: Interface element properties.

Parameter	Geogrid-Backfill	Geogrid-Facing Block	Facing Block-Block
Adhesion (kN/m2)	0	0	0
Friction angle at 1 atm, Φ (deg)	35	45	45
Friction angle reduction, ΔΦ (deg)	0	0	0
Normal spring coefficient, Kn	1 x108	1 x108	1 x108
Shear spring coefficient, Ks	5 x105	5 x105	5 x105
Unloading shear spring coefficient, Ksu	5 x103	5 x103	5 x103
Modulus exponent, n	0.2	0.2	0.2
Failure ratio, Rf	0.7	0.7	0.7

WALL 1 was represented by 988 nodes, 580 quadrilateral elements, 167 bar elements, 18 link elements, and 324 interface elements. On the other hand, WALL 2 was represented by 868 nodes, 612 quadrilateral elements, 95 bar elements, 10 link elements, and 180 interface elements. It should be noted that the difference between the two walls is the reinforcement vertical spacing, which is 0.4 and 0.8 m (16 and 32 in.) for WALL 1 and WALL 2, respectively. The outward facing displacement profiles, as measured in the field for WALL 1 and WALL 2, are presented in Figures. 4.3.5a and 4.3.5b, respectively. The maximum displacements for both walls were observed at one third of the wall height. The outward displacements for WALL 1 were found to be slightly smaller than those for WALL 2. Numerical predictions of the outward displacement profiles are also presented in Figures. 4.3.5a and 4.3.5b for WALL 1 and WALL 2, respectively. While the predicted displacement values underpredict those measured in the field, the profile shapes are fairly similar. In terms of displacement magnitude, the measured and predicted displacements in both walls were comparatively small (less than 15 mm (0.6 in.) at the facing's mid-height). Overall, the measured and predicted displacement profiles are deemed consistent.

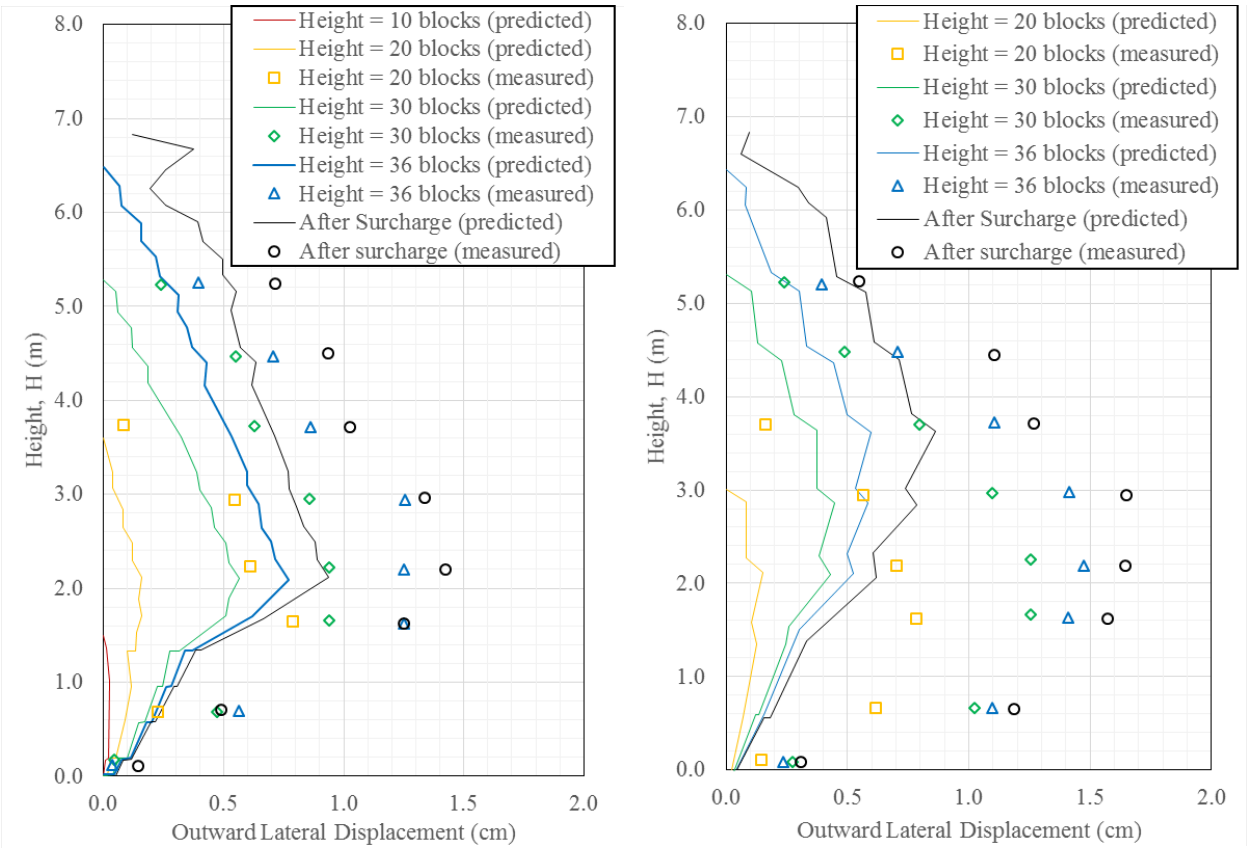

Figure 4.3.5. Outward lateral displacement profile at various construction stages: (a) WALL 1; and (b) WALL 2.

Figures. 4.3.6 and 4.3.7 show the reinforcement strains at various levels for WALL 1 and WALL 2, respectively. Figures. 4.3.6a through 4.3.6d show the reinforcement tensile strains at various construction stages for layers 2, 4, 8, and 12, respectively. On the other hand, Figures. 4.3.7a through 7d show the reinforcement tensile strains at various construction stages for layers 1, 2, 4, and 6, respectively. That is, the elevations where strains were measured in WALL 1 correspond to the same elevations where some of the reinforcements were also measured in WALL 2. The measured strain values fluctuate somewhat between tension and compression. However, as shown in Figures. 4.3.6 and 4.3.7, overall reinforcement strains were below 0.4%. It should be noted that reinforcement strains increased from 0.1% to less than 0.4% after adding the surcharge. The largest value of tensile strain was observed at reinforcement layers close to one third of the wall height. The strains predicted using numerical simulations were found to be smaller than those measured strains.

Lateral pressure transducers showed comparatively small stresses acting against the block facing. Similarly, results from the numerical simulations indicated significantly low pressures against the block facing elements. When the height of the wall was reduced after completion of the field tests, no collapse occurred as the facing units were removed. It was concluded that the soil confined between the geogrids (in both walls) acted as a monolithic block, which is consistent

with the experimental findings of the experimental component of the study. This is in spite of differences in backfill materials and reinforcement vertical spacing. In fact, the D_{50} in the experimental component

(a)

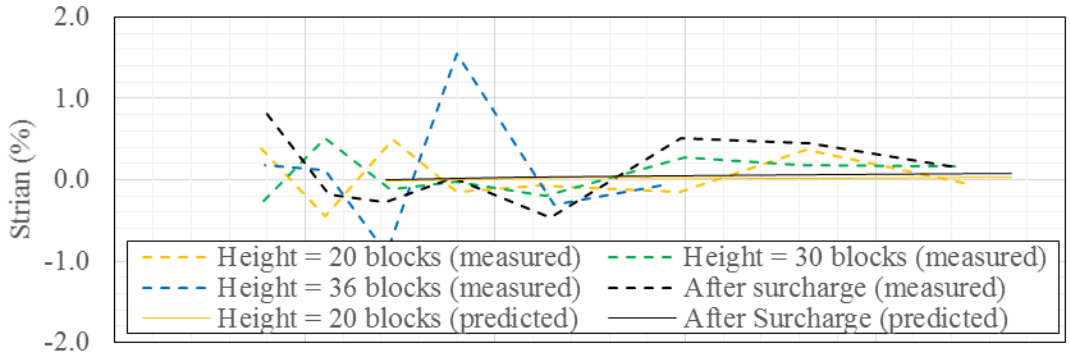

(b)

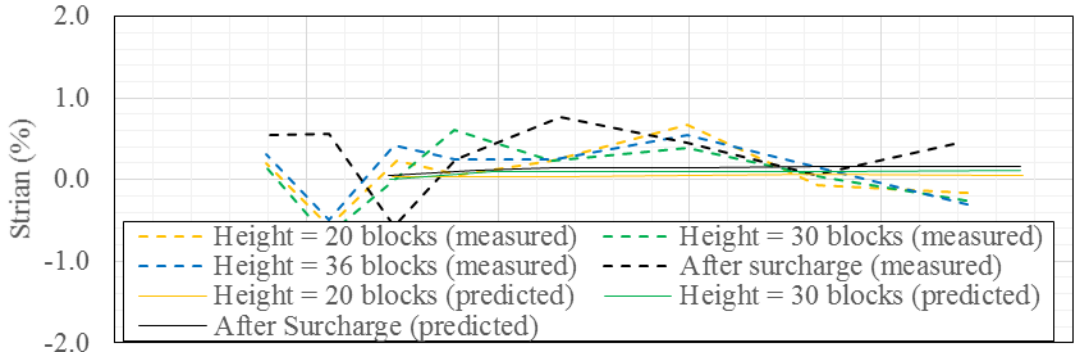

(c)

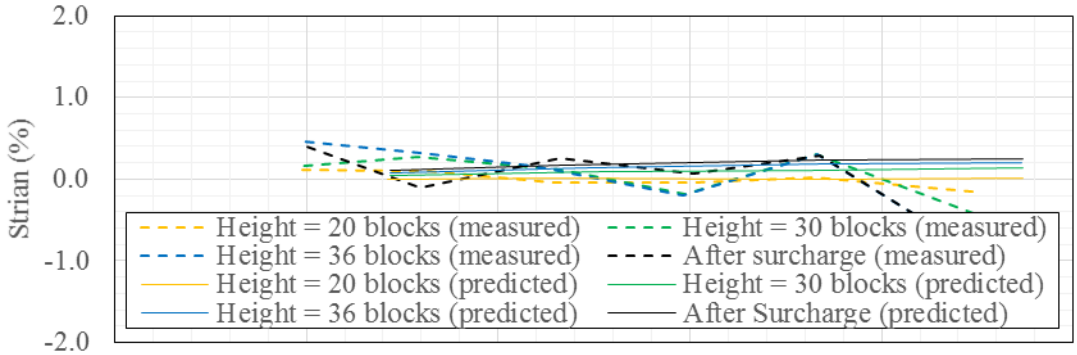

(d)

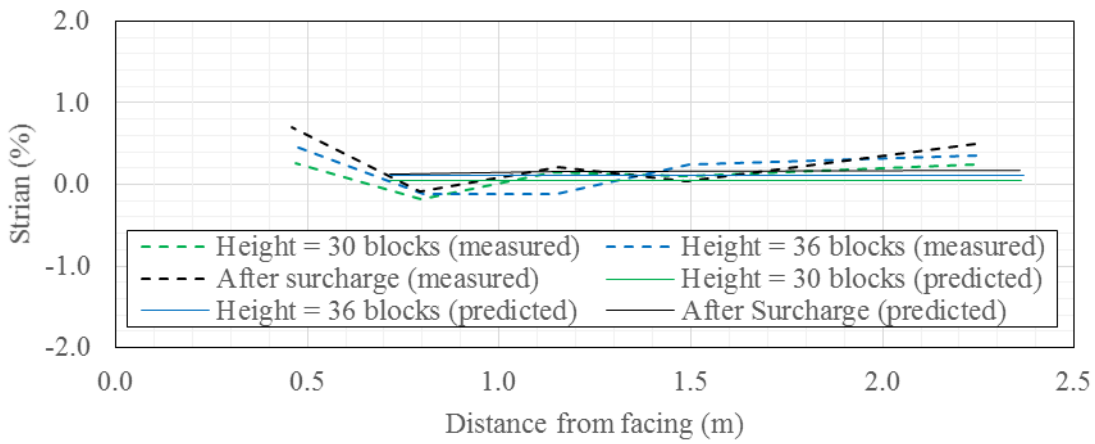

Figure 4.3.6. Measured and predicted reinforcement straining: (a) Layer 2; (b) Layer 4; (c) Layer 8; and (d) Layer 12.

(a)

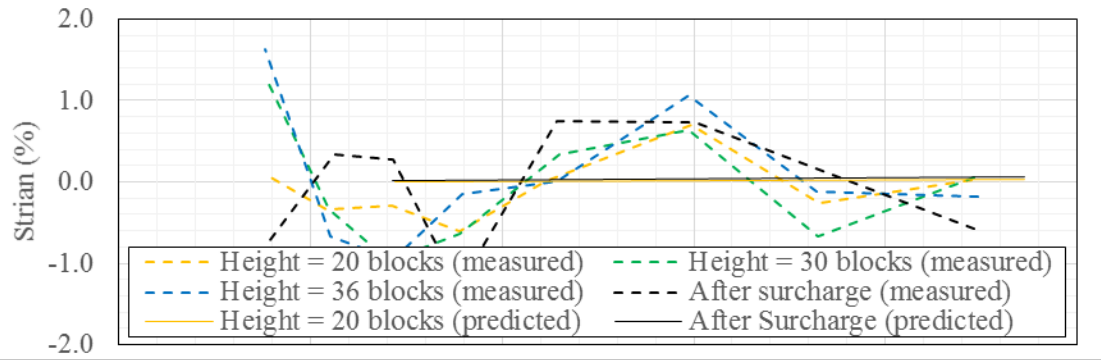

(b)

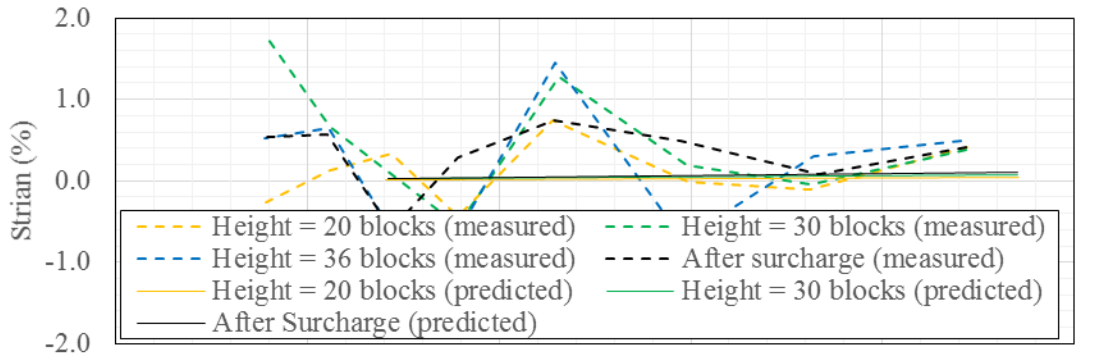

(c)

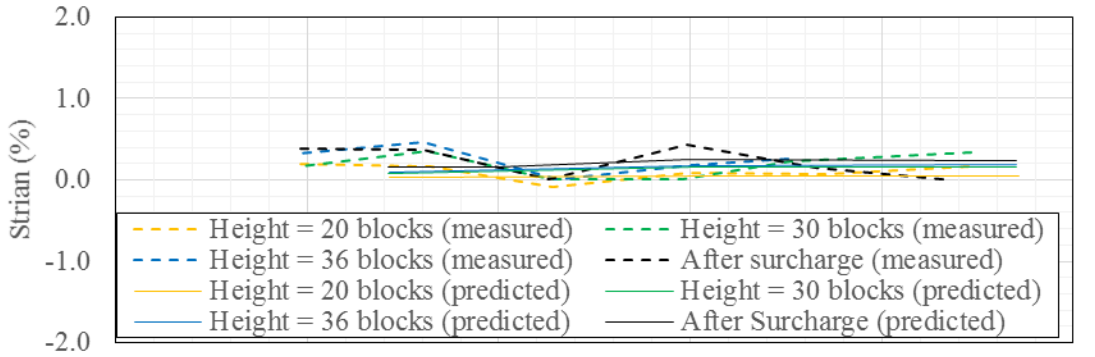

(d)

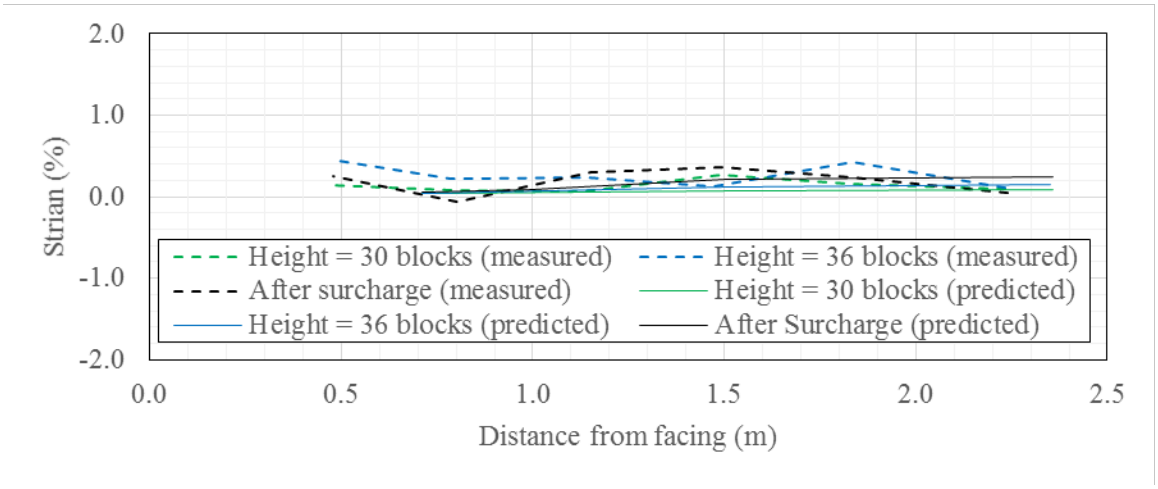

Figure 4.3.7. Measured and predicted reinforcement straining: (a) Layer 1; (b) Layer 2; (c) Layer 4; and (d) Layer 6.

was 0.26 mm (10 mil), or approximately 3 times finer than in the field test. Also, the reinforcement vertical spacing in the experimental component was 0.2 m (8 in.), or approximately half the spacing in WALL 2 and a fourth of the spacing in WALL 1. The effect of closely-spaced reinforcement is expected to be proportional to the D_{50} of the backfill material as shear band is also a function of the median grain size. In this case, it may be concluded that field and experimental observations related to composite behavior of GRS structures are in reasonable agreement. The relationship between the reinforcement vertical spacing and particle size is supported by the work initially conducted in Cambridge in the 1960s showing that, generally, the thickness of a shear band is about 15 to 20 times D_{50}. This response may be construed as the 'arching' influence zone being directly proportional to D_{50}. It was noted that increased reinforcement vertical spacing led to larger lateral displacements as well as to larger loads being carried by the reinforcement. Slight decrease in reinforcement stiffness may result in rapid increase of internal movements thus potentially invalidating the composite wall approach.

4.3.4 CONCLUSIONS

An experimental evaluation was conducted, which indicated that the interaction of reinforcement layers in a geosynthetic-reinforced structure may be significant and could render a composite material behavior. For the conditions evaluated in this experimental component, which used a sand backfill, a mobilization of a single geosynthetic reinforcement indicted that a spacing of 0.06 m (2.4 in.) would render such behavior, although mobilization of a double geosynthetic reinforcement system indicated that 0.2 m (8 in.) may also be adequate to render composite behavior. Results of the double geosynthetic reinforcement system indicated that the soil mass between reinforcements was mobilized as a monolithic system.

A field evaluation, involving monitoring of two geosynthetic-reinforced walls with different vertical reinforcement spacing, was also conducted. The results showed that wall displacements, reinforcement strains, and lateral pressure on facing were comparatively small. This observation implied that the soil confined between reinforcement acted as a monolithic block, which is

consistent with the observations gathered in the experimental program. Field results indicated that the composite behavior occurred but was limited to reinforcement spacings below 0.6 m (2 ft) for the geogrids used in this research component.

Overall, results of the experimental and field components of this investigation, jointly point towards the beneficial impact of closely-spaced reinforcement on the performance of reinforced soil structures and, particularly, on the impact of closely-spaced reinforcement on the stresses acting against the wall facing components. While a value was not established for the reinforcement vertical spacing below which a composite behavior should be expected, the following practical recommendations can be drawn: (1) composite behavior is not expected for reinforcement vertical spacing values beyond 0.6 m (2 ft), although this value is expected to correspond to a minimum value of geosynthetic reinforcement stiffness; (2) the length of geosynthetic reinforcement is expected to be governed by external stability considerations (e.g. direct sliding, overturning/eccentricity); and (3) the impact of closely-spaced reinforcement on decreasing the stresses acting against the wall facing components is significant.

4.3.5 ACKNOWLEDGEMENTS

Support received for this study from Tensar (experimental and field components) and Federal Highway Administration (numerical component) is greatly appreciated.

4.3.6 REFERENCES

Boulanger, R.W., Bray, J.D., Chew, S.H., Seed, R.B., Mitchell, J.K., & Duncan, J.M. (1991). *SSCOMPPC: Finite element analysis program for evaluation of soil-structure interaction and compaction efforts*. Report No. UCB/GT/91-02, Univ of California, Berkeley.

Bray, J.D. (1995). Personal Communications, Univ of California, Berkeley.

Broms, B.B., (1978). "Design of fabric reinforced retaining structures." *Proc. of the Symposium on Earth Reinforcement*, ASCE, Pittsburgh, PA, April 27, 1978, 282-304.

Chen, Y.M., Cao, W.P., & Chen, R.P. (2008). "An experimental investigation of soil arching within basal reinforced and unreinforced piled embankments." *J. G&G*, 26(2):164–74.

Costa, Y.D., Zornberg, J.G., Bueno, B.S., & Costa, C.L. (2009). "Failure Mechanisms in Sand over a Deep Active Trapdoor." *JGGE*, ASCE, 135(11):1741-1753.

Duncan, J.M. & Chang, C-Y. (1970). "Nonlinear analysis of stress and strain in soils." *J. of the Soil Mechanics & Foundations Division*, ASCE, 96(SM5):1629-1653.

Iglesias G.R., Einstein H.H., & Whitman R.V. (2013). "Investigation of soil arching with centrifuge tests." *JGGE*, 140(2):248–56.

Leshchinsky, D., (1997). *Design procedure for geosynthetic reinforced steep slopes*. Technical Report REMR-GT-23, Jan. 1997, WES, Vicksburg, MS.

Leshchinsky, D., Kaliakin, V., Bose, P., & Collin, J. (1994). "Failure Mechanism in Geogrid-Reinforced Segmental walls: Experimental Implications." *Soils & Foundations*, Journal of the Japanese Society of Soil Mechanics & Foundation Engineering, 34(4):33-41.

Leshchinsky, D. & Vulova, C. (2001). "Numerical investigation of the effects of geosynthetic spacing on failure mechanisms in MSE block walls." Ge*osynthetics Int.*, 8(4):343-365

Ling, H.I., Cardany, C.P., Sun, L-X., & Hashimoto, H. (2000). “Finite Element Study of a Geosynthetic-Reinforced Soil Retaining Wall with Concrete-Block Facing.” *Geosynthetics Int.*, 7(2):137-162.

Rui, R., van Tol, F., Xia, X. L., van Eekelen, S., Hu, G., & Xia, Y. Y. (2016). “Evolution of soil arching; 2D DEM simulations.” *Journal of Computers & Geotechnics*, 73, 199-209.

Seed, R.B. & Duncan, J.M. (1984). A finite element analysis program for evaluating soil-structure interaction & compaction efforts. Report No. UCB/GT/84-02, Univ of California, Berkeley.

Tatsuoka, F., Tateyama, M., Murata, O. & Tamura, Y. (1994). “Closure on ‘Geosynthetic-Reinforced Soil Retaining Walls with Short Reinforcement and a Rigid Facing.’” Recent Case Histories of Permanent GRS Retaining Walls, Balkema, Proc. of Seiken Sym. 11, Tokyo, Japan, 323-344.

Terzaghi K. (1936). “Stress distribution in dry and in saturated sand above a yielding trap-door.” *Proc. of 1st int. conference on soil mechanics & foundation engineering*. Cambridge, MA.

Terzaghi, K. & Peck, R.B. (1967). Soil mechanics in engineering practice. 2nd edition, John Wiley & Sons, Inc.

4.4 EFFECT OF REINFORCEMENT SPACING ON THE BEHAVIOR OF GEOSYNTHETIC-REINFORCED SOIL CENTRIFUGE MODELS

4.4.1 INTRODUCTION

A significant volume of data has been generated over the years with the objective of assessing the performance of geosynthetic reinforced soil structures using centrifuge modeling. An advantage of centrifuge modeling is that the stress state of reduced-scale models corresponds to that of prototypes because of the increased gravitational field. Accordingly, centrifuge tests are useful to validate experimentally a number of design aspects. This includes the effect of reinforcement vertical spacing, which is of key relevance to the geosynthetic reinforced soil behavior. A number of centrifuge research projects have been conducted to evaluate the performance of geosynthetic reinforced soil structures (Jaber 1989; Guler and Goodings 1992; Zornberg et al. 1997, 1998a, 1998b; Zornberg and Arriaga 2003; Woodruff 2003; Kniss et al. 2007; Yang et al. 2008, 2011; Lee et al. 2010a, 2010b; Costa et al. 2016). The centrifuge testing programs in these studies were conceived to address specific aspects in geosynthetic reinforced soil design. Collectively, however, they represent a vast source of experimental data that can be mined to assess additional aspects of geosynthetic reinforced soil behavior and provide significant insight into the composite behavior of geosynthetic reinforced soil structures. This study involved implementation of a testing program that aimed at evaluating the effect of the reinforcement spacing and surcharge loading on the behavior of geosynthetic reinforced soil structures. This was rigorously conducted thorough consolidating and reassessing the information generated using the entire portfolio of centrifuge data on geosynthetic reinforced soil structures with an emphasis on data in which vertical reinforcement spacing are varied.

4.4.2 BACKGROUND

Full-scale field studies are deemed time consuming and are costly, which makes them infeasible to generate a good database from which solid conclusions can be drawn. Hence, many research studies have developed small-scale laboratory methods. For instance, the behavior of geosynthetic reinforced soil structures subjected to vertical load has been studied in small-scale models at normal gravity, i.e. 1 g (e.g. Lee et al. 1973, Juran and Christopher 1989, Palmeira and Lanz 1994; Gomes et al. 1994; Vafaeian and Abbaszadeh 2006). However, these reduced-scale models were not subjected to the same stress levels that can mimic real structures. Subsequently, geotechnical centrifuge modeling technique has emerged allowing accurate analysis of the performance of soil structures subjected to representative stress levels (Schofield 1980).

Geotechnical centrifuge modelling has proven a time-saving and efficient way to simulate many of the geotechnical problems. This has significantly facilitated understanding of the mechanical behavior through observation of realistic results. Geotechnical centrifuge creates an environment in which the inertial acceleration is higher than the gravitational acceleration. This replicates as-real environment for the test models, which in turn replicates soil behavior in terms

of stresses, strength, and stiffness. That is, centrifuge modelling enables implementation of parametric studies on small-scale structures, but with generating as-real behavior of prototype structures. Several published research studies were identified in the technical literature in which the reinforcement vertical spacing was varied. Table 4.4.1 presents a summary of the studies that were identified in technical literature. Other references have also been identified that are of relevance such as Santamrina (1984), Goodings (1990), Porbaha and Goodings (1994), and Arriaga (2003). Note that quite limited research has been conducted on vertically loaded geosynthetic reinforced soil structures (e.g., Jabar 1989 on walls constructed with plastic strips) to model load-carrying GMSE bridge abutments.

Vertical reinforcement spacing is deemed to play a crucial role in the behavior of geosynthetic reinforced soil structures. It was reported that reducing the reinforcement spacing improves significantly the behavior of geosynthetic reinforced soil structures: (1) improves the bearing strength of the geosynthetic reinforced soil mass (Vafaeian and Abbaszadeh 2006; Sommers and Viswanadham 2009); (2) curbs significantly the deformation (Sommers and Viswanadham 2009; Lin et al. 2013; Iacorossi et al. 2013; Malinowska 2015); and (3) enhances the overall stability (Woodruff 2003; Iacorossi et al. 2013). Sommers and Viswanadham (2009) observed that the vertical deformation depended greatly on the reinforcement distribution. They reported that the reinforcement vertical spacing significantly affects the vertical loading capacity of the geosynthetic reinforced soil mass. In addition, they concluded that placement of closely-spaced reinforcement layers in the upper half of the reinforced soil mass can enhance the performance of loaded geosynthetic reinforced soil structures.

Palmeira and Lanz (1994) and Gomes et al. (1994) tested 1-g models reinforced with various reinforcement patterns, which included hybrid vertical spacings and reinforcement lengths. It was concluded that reinforcement arrangement has a significant effect on external and internal deformation of the reinforced soil mass (Palmeira and Lanz 1994; Viswanadham and Mahajan 2007). Specifically, they concluded that short secondary reinforcement layers with largely spaced primary reinforcement facilitates the construction but has a limited benefit on curbing deformation (Palmeira and Lanz 1994). Zornberg and Arriaga (2003) and Viswanadham and Mahajan (2007) reported that maximum peak strain in reinforcement layers occurs at mid-height of geosynthetic reinforced soil structures, which contradicts with the conventional triangular distribution of reinforcement tension. Zornberg and Arriaga (2003) added that the maximum peak strain occurs below the structure's crest.

Table 4.4.1. Centrifuge modelling studies for geosynthetic-reinforced soil structures at various reinforcement spacing.

Structure Type	Structure Height (mm)	Backfill Type	Reinforcement Type	Facing Type	Various Spacing	Spacing Range (mm)	Added Surcharge	Year	Reference
GRS slopes	229	Sand	Geotextile	Wrapped around	No	20	No	2016	Costa et al. (2016)
GRS walls	320	Sand	Geogrid	Gabions	Yes	20-40	No	2015	Malinowska (2015)
GRS walls	320	Sand	Geogrid	Gabions	Yes	20-40	No	2013	Lin et al. (2013)
GRS walls	145	Sand	Geogrid	Modular blocks	Yes	22-66	No	2013	Iacorossi et al. (2013)
GRS slopes	270	Sand	Geotextile	Wrapped around	Yes	30-40	Yes	2009	Sommers & Viswanadham (2009)
GRS slopes	270	Sand	Geotextile	Wrapped around	Yes	30-40	No	2007	Viswanadham & Mahajan (2007)
GRS slopes	229	Sand	Geotextile	Wrapped around	Yes	19.05-25.4	No	2004	Costa (2004)
GRS walls	228	Sand	Geotextile	Wrapped around	Yes	10-50	No	2003	Woodruff (2003)
GRS slopes	228	Sand	Geotextile	Wrapped around	Yes	12.7-25.4	No	2003	Zornberg & Arriaga (2003)
GRS walls	240	Sand/Gravel-Sand	Geotextile	Wrapped around	Yes	20-60	No	2002	Zhang et al. (2002)
GRS slopes	228	Sand	Geotextile	Wrapped around	Yes	12.7-38.1	No	1998	Zornberg et al. (1998a)
GRS walls	152	Clay	Geotextile	Wrapped around	Yes	12.7-25.3	No	1996	Porbaha & Goodings (1996)
GRS slopes	228	Sand	Geotextile	Wrapped around	Yes	12.7-38.1	No	1994	Zornberg (1994)
GRS walls	240-440	Sand	Geotextile	Wrapped around	Yes	50-100	Yes	1994	Gomes et al. (1994)

4.4.3 CONCEPT OF CENTRIFUGE MODELLING

Many research studies have been conducted to study the scaling of the centrifuge models to real structures. Principally, virtually increasing the gravitational force in centrifuge models can result in a proportional increase in stresses. This can be done by spinning the structural model in a centrifuge to create large centrifugal acceleration, which acts as an increased virtual gravitational acceleration for the model. The model has to be placed in the centrifuge such that its initial gravity direction aligns with the centrifugal acceleration during its flight in the centrifuge. The increased stresses in centrifuge models are representative to those in real structures. Bucky (1935) concluded that substituting the gravitational force by centrifugal force that is N times higher than the gravitational force produces a model environment that replicates the real environment. This simulated environment has the same stress and strain conditions as that of the real structure.

4.4.3.1 SCALING IN CENTRIFUGE MODELLING

Table 4.4.2 shows the scaling relations for various physical quantities as reported by Ko (1988b). The table was modified to include the dimensions of each quantity, which help identifying the scaling relation for any other physical or engineering quantity. The fundamental dimensions *M*, *L*, and *T* are modeled by scaling factors of *1/N3*, *1/N*, and *1/N*, respectively. The scaling factors for reinforcement tensile strength and stiffness have been investigated extensively in literature (e.g., Springman et al. 1992; Porbaha and Goodings 1996; Zornberg et al. 1997; Viswanadham and König 2004; Mahajan 2007). It was reported that scaling factor of 1/N for both parameters (Springman et al. 1992; Zornberg et al. 1997; Viswanadham and König 2004). This factor also conforms to the scaling factors reported by Ko (1988a) for the stresses and strains. Table 4.4.3 summarizes the scaling relations of the various parameters of reinforced soil structures. Lee (2010) conducted a study on the effect of the geogrid aperture size and observed no influence on the performance of the walls. It was also concluded that the performance of GRS-shoring systems is sensitive to the backfill relative density.

Table 4.4.2. Centrifuge scaling relations (after Ko 1988b)

Quantity	**Prototype**	**Model**
Length [L]	N	1
Area [L^2]	N^2	1
Volume [L^3]	N^3	1
Velocity [LT^{-1}]	1	1
Acceleration [LT^{-2}]	1	N
Mass [M]	N^3	1
Force [MLT^{-2}]	N^2	1
Energy [ML^2T^{-2}]	N^3	1
Stress [$ML^{-1}T^{-2}$]	1	1
Strain [-]	1	1
Mass Density [ML^{-3}]	1	1
Energy Density [$ML^{-1}T^{-2}$]	1	1
Time (Dynamic) [T]	N	1
Time (Diffusion) [L^2]	N^2	1
Time (Creep) [-]	1	1
Frequency [T^{-1}]	1	N

Table 4.4.3. Centrifuge scaling relations of reinforced soil structures (after Zornberg et al. 1998a)

Quantity	**Prototype**	**Model**
Soil parameters		
Friction angle, Φ [-]	1	1
Cohesion, c [$ML^{-1}T^{-2}$]	1	1
Stress-strain behavior [$ML^{-1}T^{-2}$]	1	1
Reinforcement parameters		
Tensile strength, T_{ult} [MT^{-2}]	N	1
Tensile modulus, J [MT^{-2}]	N	1
Interface parameters		
Interface shear strength, tanδ [-]	1	1
Interface stress-strain behavior [$ML^{-1}T^{-2}$]	1	1

4.4.3.2 LIMITATIONS OF CENTRIFUGE MODELLING

Geotechnical centrifuge modeling has some limitations, which may result in sources of error. Zornberg et al. (1997) categorized the mains limitation into four sources: (1) the variability of the acceleration field within the centrifuge model; (2) the discrepancy between stress paths of the prototype and the model, (3) the boundary effects of the model, and (4) scale effects of the model. The acceleration field within the centrifuge model is directly proportional to the radius of the arm. However, the variation in g-level within the model is proportional to the size of the model compared to the arm of the centrifuge. That is, this effect fades in relatively large arm centrifuges. The stress paths in the model are not identical to those in a prototype structure is subjected during construction. For instance, compaction loading exerted in the field during construction cannot be replicated in the model since the model is constructed at acceleration 1g before being brought to a prototype scale in the centrifuge. The boundary effects result from the sidewalls of the container in which the model is placed. These effects can be mitigated by employing a low interface frictional material to line the internal surfaces of the container to ascertain a plane strain testing condition. Scale effects are a concern in centrifuge modeling caused by the relative size of backfill particles between model and prototype. These effects are eliminated by using backfill and reinforcement materials that can still behave as a continuum. In addition, Ovesen (1975) showed that the width of a contact zone must be larger than about 15 particle diameters.

4.4.4 ASSESSMENT OF REINFORCEMENT SPACING EFFECT

To investigate the effect of reinforcement spacing and tensile strength on the behavior of geosynthetic reinforced soil structures. Many studies proved the fact that increasing the reinforcement density (number of layers of the same reinforcement type) should result in enhancing the overall performance and structural stability of geosynthetic reinforced soil structures. Figure 4.4.1 shows the g-level at failure for many centrifuge tests data retrieved from centrifuge models portfolio generated as shown in Table 4.4.4 (Morsy 2017). The figure shows the effect of decreasing the reinforcement spacing while maintaining the same reinforcement tensile strength for each reinforcement layer in geosynthetic reinforced soil models (i.e., increasing the T_f/S_v ratio). Note that Woodruff (2003) data in this figure belong to models with comparatively small *L/H* ratio, which explains why the models failed at a lower g-level compared to the other models in the figure despite their higher reinforcement strength.

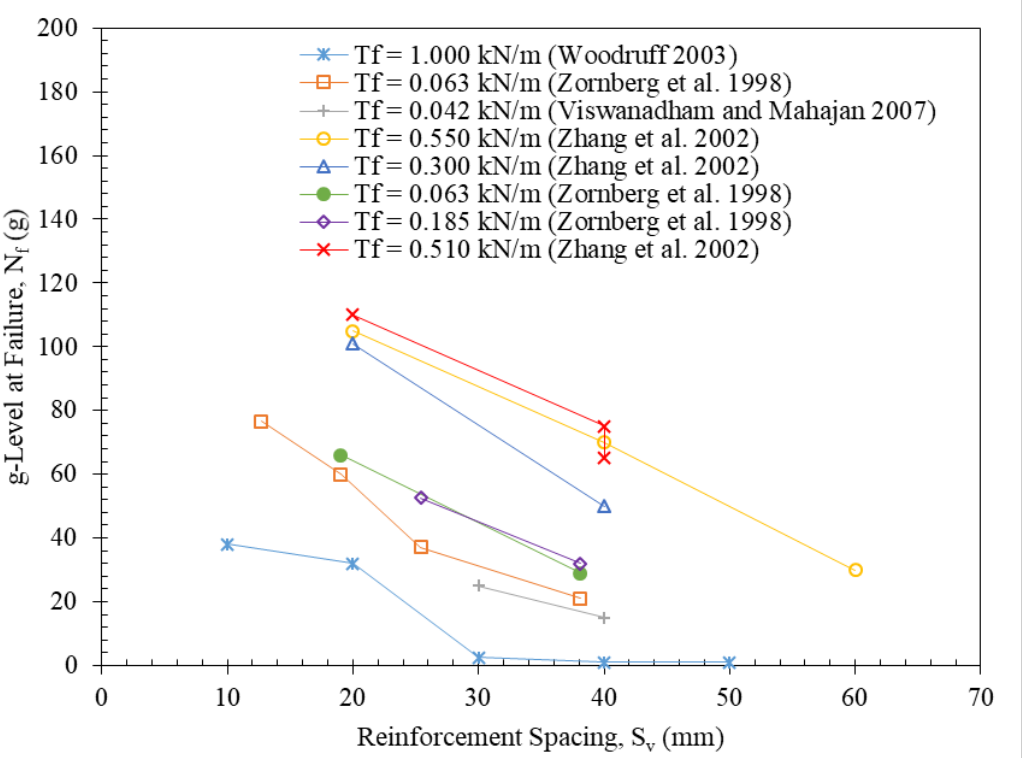

Figure 4.4.1. Effect of reinforcement vertical spacing on the g-level at failure.

Table 4.4.4. Summary of the models used in the assessment of the effect of reinforcement spacing (Morsy 2017).

#	Reference	ID	Type	Facing Type	Reinforcement Type	H (mm)	L/H	S_v (mm)	T_f (kN/m)	T_f/S_v (kN/m/m)	J (kN/m)	J/S_v (kN/m/m)	Backfill Type	φ (deg)	D_{50} (mm)	γ (kN/m^3)	D_r (%)
1	Zornberg et al. (1998a)	B18	Slope	Wrapped Around	Geotextile	228	0.89	12.7	0.063	4.96	0.38	29.92	Sand	35.00	0.400	15.64	55
2	Zornberg et al. (1998a)	B12	Slope	Wrapped Around	Geotextile	228	0.89	19.05	0.063	3.31	0.38	19.95	Sand	35.00	0.400	15.64	55
3	Zornberg et al. (1998a)	B9	Slope	Wrapped Around	Geotextile	228	0.89	25.4	0.063	2.48	0.38	14.96	Sand	35.00	0.400	15.64	55
4	Zornberg et al. (1998a)	B6	Slope	Wrapped Around	Geotextile	228	0.89	38.1	0.063	1.65	0.38	9.97	Sand	35.00	0.400	15.64	55
5	Zornberg et al. (1998a)	D12	Slope	Wrapped Around	Geotextile	228	0.89	19.05	0.063	3.31	0.38	19.95	Sand	37.50	0.400	16.21	75
6	Zornberg et al. (1998a)	D6	Slope	Wrapped Around	Geotextile	228	0.89	38.1	0.063	1.65	0.38	9.97	Sand	37.50	0.400	16.21	75
7	Zornberg et al. (1998a)	S9	Slope	Wrapped Around	Geotextile	228	0.89	25.4	0.185	7.28	0.75	29.53	Sand	35.00	0.400	15.64	55
8	Zornberg et al. (1998a)	S6	Slope	Wrapped Around	Geotextile	228	0.89	38.1	0.185	4.86	0.75	19.69	Sand	35.00	0.400	15.64	55
9	Costa et al. (2016)	F1	Slope	Wrapped Around	Geotextile	229	0.87	20	0.033	1.65	0.30	15.00	Sand	36.40	0.700		70
10	Costa et al. (2016)	F2	Slope	Wrapped Around	Geotextile	229	0.87	20	0.033	1.65	0.30	15.00	Sand	36.40	0.700		70
11	Costa et al. (2016)	F3	Slope	Wrapped Around	Geotextile	229	0.87	20	0.033	1.65	0.30	15.00	Sand	36.40	0.700		70
12	Costa et al. (2016)	F4	Slope	Wrapped Around	Geotextile	229	0.87	20	0.033	1.65	0.30	15.00	Sand	36.40	0.700		70
13	Costa et al. (2016)	F5	Slope	Wrapped Around	Geotextile	229	0.87	20	0.144	7.20	0.60	30.00	Sand	36.40	0.700		70
14	Costa et al. (2016)	F6	Slope	Wrapped Around	Geotextile	229	0.87	20	0.144	7.20	0.60	30.00	Sand	36.40	0.700		70

Table 4.4.4. Summary of the models used in the assessment of the effect of reinforcement spacing (Continued).

#	Reference	ID	Type	Facing Type	Reinforcement Type	H (mm)	L/H	S_v (mm)	T_f (kN/m)	T_f/S_v (kN/m/m)	J (kN/m)	J/S_v (kN/m/m)	Backfill Type	φ (deg)	D_{50} (mm)	γ (kN/m^3)	D_r (%)
15	Woodruff (2003)	5c	Wall	Wrapped Around	Geotextile	229	0.25	20	1.000	50.00	N/A	N/A	Sand	36.70	0.700	16.05	70
16	Woodruff (2003)	7a	Wall	Wrapped Around	Geotextile	229	0.25	10	1.000	100.00	N/A	N/A	Sand	36.70	0.700	16.05	70
17	Woodruff (2003)	7b	Wall	Wrapped Around	Geotextile	229	0.25	30	1.000	33.33	N/A	N/A	Sand	36.70	0.700	16.05	70
18	Woodruff (2003)	7c	Wall	Wrapped Around	Geotextile	229	0.25	40	1.000	25.00	N/A	N/A	Sand	36.70	0.700	16.05	70
19	Woodruff (2003)	7d	Wall	Wrapped Around	Geotextile	229	0.25	50	1.000	20.00	N/A	N/A	Sand	36.70	0.700	16.05	70
20	Viswanadham & Mahajan (2007)	RS4	Slope	Wrapped Around	Geotextile	270	0.85	30	0.042	1.40	N/A	N/A	Sand	34.00	0.021	N/A	55
21	Viswanadham & Mahajan (2007)	RS6a	Slope	Wrapped Around	Geotextile	270	0.85	40	0.216	5.40	N/A	N/A	Sand	34.00	0.021	N/A	55
22	Zhang et al. (2002)	M2	Wall	Wrapped Around	Geotextile	240	0.18	20	0.510	25.50	5080.00	254000.00	Sand	37.50	0.170	15.50	N/A
23	Zhang et al. (2002)	M4	Wall	Wrapped Around	Geotextile	240	0.18	40	0.300	7.50	4520.00	113000.00	Sand	37.50	0.170	15.50	N/A
24	Zhang et al. (2002)	M5	Wall	Wrapped Around	Geotextile	240	0.18	20	0.300	15.00	4520.00	226000.00	Sand	37.50	0.170	15.50	N/A
25	Zhang et al. (2002)	M6	Wall	Wrapped Around	Geotextile	240	0.18	20	0.550	27.50	6520.00	326000.00	Sand	37.50	0.170	15.50	N/A
26	Zhang et al. (2002)	M7	Wall	Wrapped Around	Geotextile	240	0.18	40	0.550	13.75	6520.00	163000.00	Sand	37.50	0.170	15.50	N/A
27	Zhang et al. (2002)	M8	Wall	Wrapped Around	Geotextile	240	0.18	60	0.550	9.17	6520.00	108666.67	Sand	37.50	0.170	15.50	N/A
28	Zhang et al. (2002)	M12	Wall	Wrapped Around	Geotextile	240	0.18	40	0.510	12.75	5080.00	127000.00	Sand	37.50	0.170	15.50	N/A
29	Zhang et al. (2002)	M13	Wall	Wrapped Around	Geotextile	240	0.18	40	0.510	12.75	5080.00	127000.00	Sand	37.50	0.170	15.50	N/A
30	Zhang et al. (2002)	M24	Wall	Wrapped Around	Geotextile	240	0.18	40	0.410	10.25	4460.00	111500.00	Sand	37.50	0.170	15.50	N/A

Table 4.4.4. Summary of the models used in the assessment of the effect of reinforcement spacing (Continued).

#	Reference	ID	Type	Facing Type	Reinforcement Type	H (mm)	L/H	S_v (mm)	T_f (kN/m)	T_f/S_v (kN/m/m)	J (kN/m)	J/S_v (kN/m/m)	Backfill Type	φ (deg)	D_{50} (mm)	γ (kN/m^3)	D_r (%)
31	Iacorossi et al. (2013)	L2S6	Wall	Modular Blocks	Geogrid	145	0.20	66	10.400	157.58	474.50	7189.39	Sand	28.20	0.015	15.75	N/A
32	Iacorossi et al. (2013)	L2S4	Wall	Modular Blocks	Geogrid	145	0.20	44	10.400	236.36	474.50	10784.09	Sand	28.20	0.015	15.75	N/A
33	Iacorossi et al. (2013)	L2S2	Wall	Modular Blocks	Geogrid	145	0.20	22	10.400	472.73	474.50	21568.18	Sand	28.20	0.015	15.75	N/A
34	Iacorossi et al. (2013)	L3S6	Wall	Modular Blocks	Geogrid	145	0.30	66	10.400	157.58	474.50	7189.39	Sand	28.20	0.015	15.75	N/A
35	Iacorossi et al. (2013)	L3S4	Wall	Modular Blocks	Geogrid	145	0.30	44	10.400	236.36	474.50	10784.09	Sand	28.20	0.015	15.75	N/A
36	Iacorossi et al. (2013)	L3S2	Wall	Modular Blocks	Geogrid	145	0.30	22	10.400	472.73	474.50	21568.18	Sand	28.20	0.015	15.75	N/A
37	Iacorossi et al. (2013)	L4S6	Wall	Modular Blocks	Geogrid	145	0.40	66	10.400	157.58	474.50	7189.39	Sand	28.20	0.015	15.75	N/A
38	Iacorossi et al. (2013)	L4S4	Wall	Modular Blocks	Geogrid	145	0.40	44	10.400	236.36	474.50	10784.09	Sand	28.20	0.015	15.75	N/A
39	Iacorossi et al. (2013)	L4S2	Wall	Modular Blocks	Geogrid	145	0.40	22	10.400	472.73	474.50	21568.18	Sand	28.20	0.015	15.75	N/A

Zornberg et al. (1998) investigated the failure mechanisms of geosynthetic-reinforced steep slopes. Their study involved testing 8 centrifuge test models. Their testing program included varying several parameters reinforcement vertical spacing, reinforcement tensile strength, and backfill density reinforcement vertical spacing and reinforcement tensile strength. The characteristics of these test models are summarized in Table 4.4.4. It was observed that the location of the failure surface was not affected by the reinforcement spacing, reinforcement strength, or backfill density. In addition, crest settlement was independent of reinforcement spacing and strength, but was affected by backfill density.

Zhang et al. (2002) conducted a comprehensive study on the behavior of GMSEwalls. They studied the behavior of 24 centrifuge test models with various parameters. This included varying reinforcement tensile strength, reinforcement vertical spacing, reinforcement length, backfill material, foundation material. In their study, they addressed the effect of changing wall parameters on the deformation mechanisms, failure modes, and failure surfaces of GMSE models. Nine test models were used in reinforcement spacing assessment herein are their characteristics are summarized in Table 4.4.4.

A comparison has been conducted from compiled data retrieved from several studies in the technical literature (Zornberg et al. 1998 and Zhang et al. 2002). These studies involved testing structural models in geotechnical centrifuge; these structures included GMSEwalls (steep face batter) and geosynthetic-reinforced steep geosynthetic reinforced soil slopes (mild face batter). The performance of the structural models was compared based on their reinforcement strength to spacing (T_f/S_v) ratio. That is, the models were compared based on their reinforcement tensile capacity per unit height (reinforcement strength density). This parameter is believed to be the key controlling parameter of the behavior of geosynthetic-reinforced soil structures in many design guidelines (e.g. AASHTO, NCMA).

Figures 4.4.2a and 4.4.6b show the g-level at failure versus the T_f/S_v ratio for several models from Zornberg et al. (1998) and Zhang et al. (2002), respectively. Contour lines were established for models having the same reinforcement spacing and varying tensile strength (dashed lines) or the same reinforcement tensile strength and varying spacing (dotted lines) as shown in Figures 4.4.2a and 4.4.6b. These contours show the effect of increasing the reinforcement spacing (while maintaining the same reinforcement strength) or increasing of the reinforcement strength (while maintaining the same reinforcement spacing) on the behavior of geosynthetic reinforced soil models. It was observed that the effect of reinforcement spacing overweighs that of the reinforcement tensile strength on the structural stability of geosynthetic reinforced soil structures by approximately 2.3 times. This observation was found consistent among all the contour lines established for models from the same study and among models from different studies. Similarly, Figures 4.4.3a and 4.4.3b show the g-level at failure versus the J/S_v ratio for several models from Zornberg et al. (1998) and Zhang et al. (2002), respectively. These figures are more representative for the behavior of geosynthetic reinforced soil structures at working stress levels. It was observed that the effect of reinforcement spacing also overweighs that of the reinforcement tensile stiffness on the structural stability of geosynthetic reinforced soil structures.

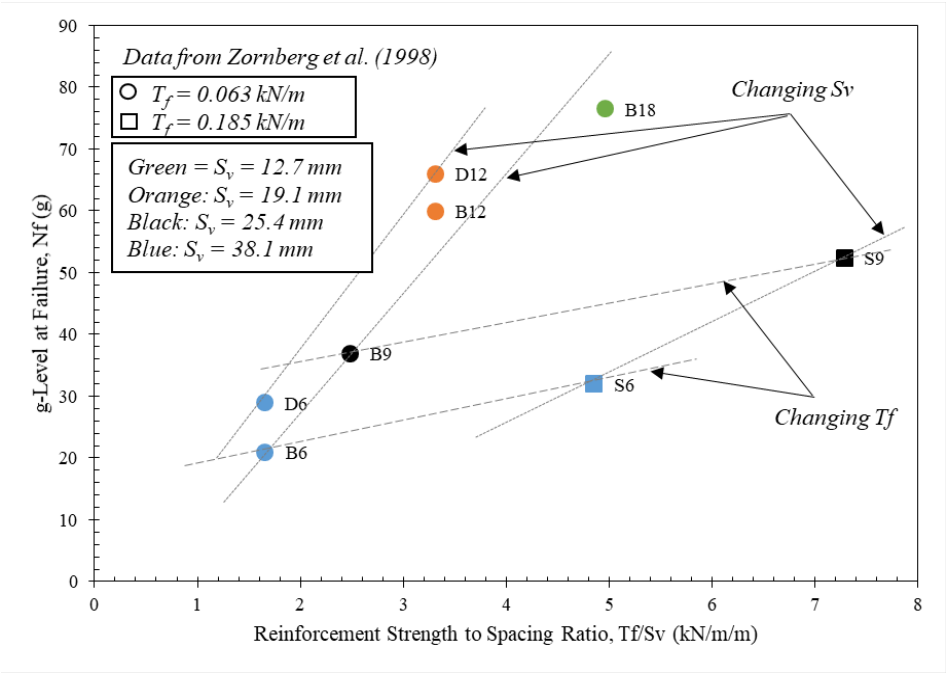

(a)

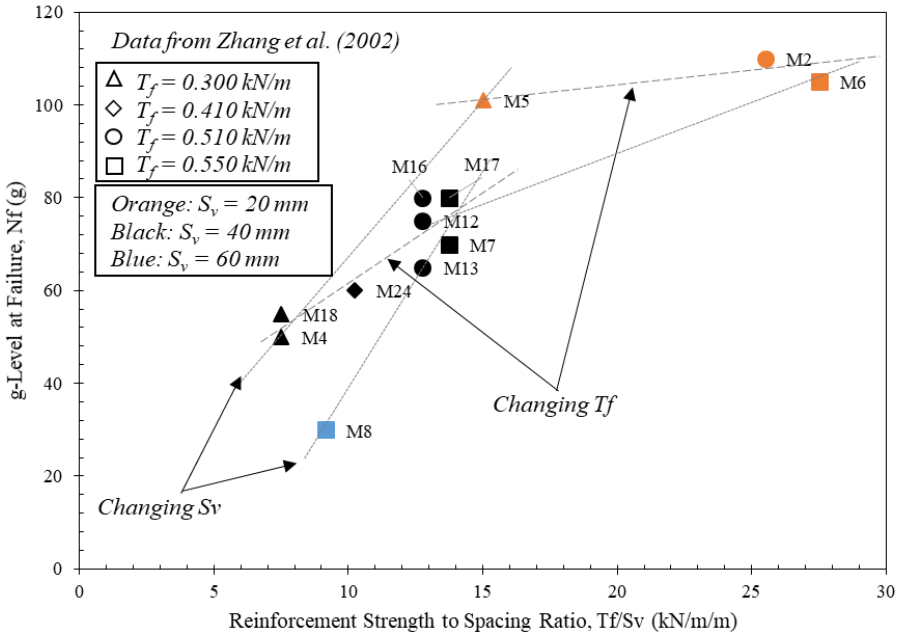

(b)

Figure 4.4.2. Effect of reinforcement spacing and tensile strength on the behavior of geosynthetic reinforced soil structures: (a) geosynthetic reinforced soil slopes; (b)GMSE walls.

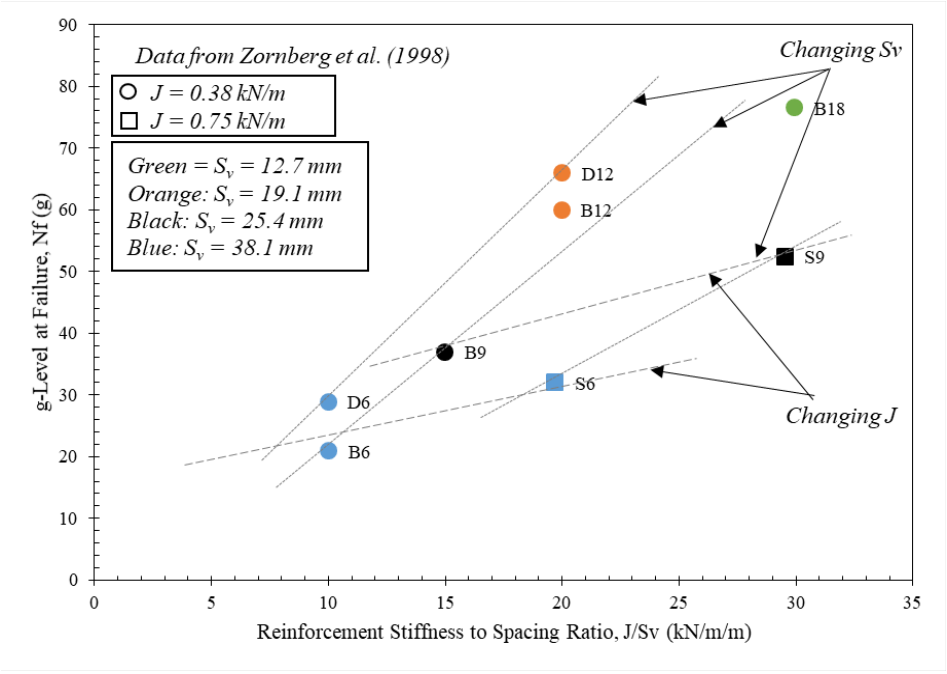

(a)

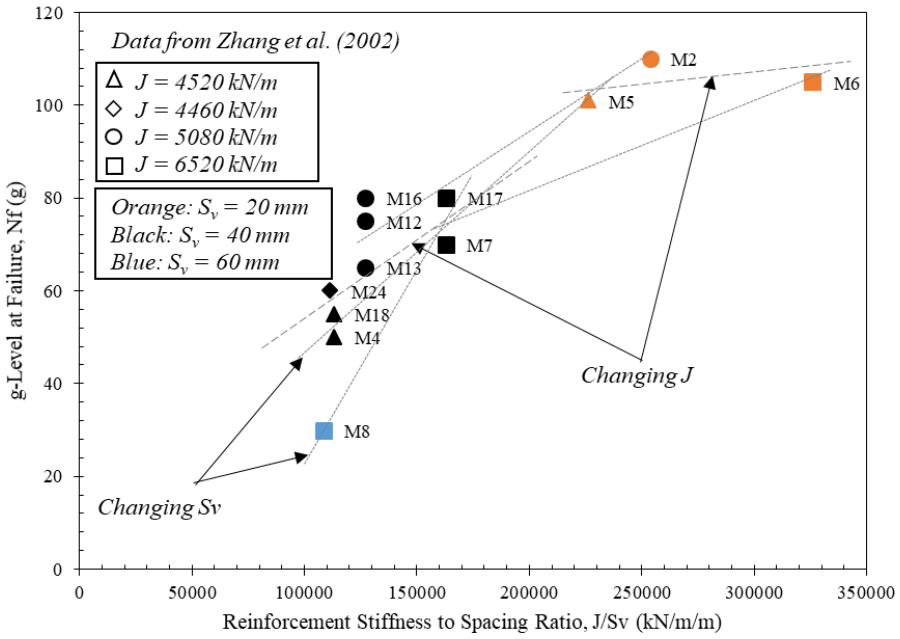

(b)

Figure 4.4.3. Effect of reinforcement spacing and tensile stiffness on the behavior of geosynthetic reinforced soil structures: (a) geosynthetic reinforced soil slopes; (b)GMSE walls.

Models B18 and S6 are two geosynthetic reinforced soil slope models with very close T_f/S_v ratios. The g-level at failure reported by Zornberg et al. (1998) was much higher (90% higher) for Model B18 (the model with one third the reinforcement spacing and one third the reinforcement strength) than that for Model S6 (the model with three times the reinforcement spacing and three times the reinforcement strength) as shown in Figure 4.4.4. That is, the reinforcement spacing has a higher effect on the model stability and strength than the reinforcement strength.

However, the model with the smaller reinforcement spacing and weaker reinforcement exhibited a catastrophic failure unlike the other model which failed progressively. Note that the *J/Sv* ratio in Model B18 (30) was higher than that of Model S6 (20). In addition, the global soil-reinforcement interface (defined as the total number of soil-reinforcement interfaces as defined by the soil-geotextile interface friction, δ_{sg} or $\Sigma(2L \cdot \tan \delta_{sg})$) for Model B18 (18 layers with peak friction angle of 30 deg) was higher than that for Model S6 (6 layers with peak friction angle of 31 deg). This provides more interaction with the reinforced soil mass rendering better performance at working stress conditions.

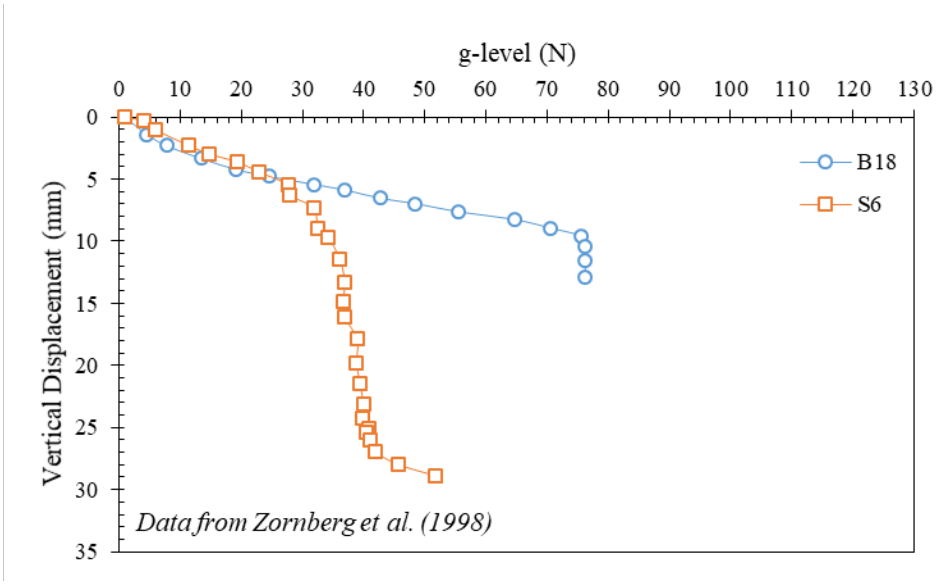

Figure 4.4.4. Vertical displacement on top of GMSE during centrifuge testing for geosynthetic reinforced soil Slope Models with T_f/S_v 4.9-5.0 (S_v = 12.7 mm (0.5 in.) for B18 and 38.1 mm (1.5 in.) for S6)

Models M8 and M24 are two GMSE wall models with very close T_f/S_v and J/S_v ratios. The characteristics of these models are summarized in Table 4.4.4. The models were constructed using the same backfill material, sand with friction angle of 37.5 degrees. The reinforcement length used in both models was 0.18 of the wall height (i.e., L/H = 0.18) and were wrapped around at the facing. Reinforcements with different tensile strength and spacing were adopted. However, both models had similar T_f/S_v ratio, which was 9.17 and 10.25 kN/m/m (1.33 and 1.49 lbs/in/in) for Models M8 and M24, respectively. The g-level at failure reported by Zhang et al. (2002) was 3.2 times higher for Model M24 (the model with smaller reinforcement spacing and weaker reinforcement) than that for Model M8 (the model with larger reinforcement spacing stronger reinforcement) as shown in Figure 4.4.5. The total stiffness of the reinforcement layers used in both models was very close. However, Model M24 has more soil-reinforcement interfaces, and thus a stiffer behavior compared to that of Model M8 at working stress conditions as shown in Figure 4.4.5.

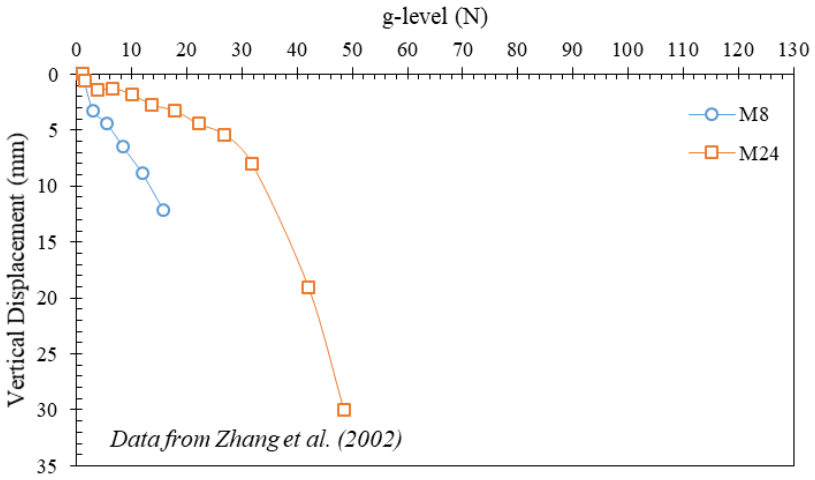

Figure 4.4.5. Vertical displacement on top of GMSE models during centrifuge testing for GMSE Wall Models with T_f/S_v 9.2-10.3 (S_v = 60 mm (2.34 in.) for M8 and 40 mm (1.56 in.) for M24)

Models M5 and M7 also had very close T_f/S_v ratios, which are 15.00 and 13.75 kN/m/m (2.2 and 2 lbs/in/in), respectively. Both models have similar characteristics as summarized in Table 4.4.4. However, the reinforcement in Model M5 was placed at a smaller vertical spacing and had a weaker tensile strength compared to the reinforcement in Model M7. The g-level at failure reported by Zhang et al. (2002) for Model M5 (the model with smaller reinforcement spacing and weaker reinforcement) was 2.2 times that for Model M7 (the model with larger reinforcement spacing stronger reinforcement) as shown in Figure 4.4.6. Both the total stiffness of reinforcement layers and total interface friction in Model M5 were higher than those in Model M7. This resulted in a stiffer behavior for Model M5 in working stress conditions as shown in Figure 4.4.6.

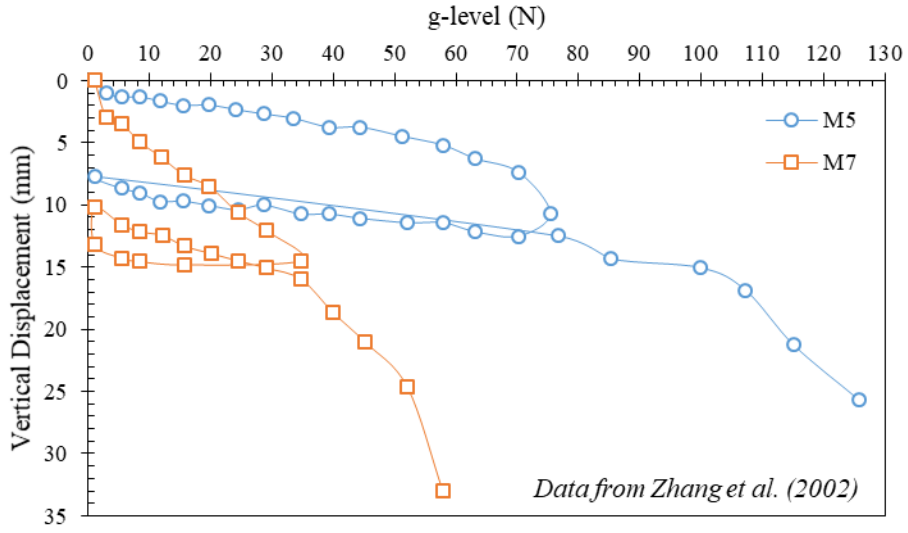

Figure 4.4.6. Vertical displacement on top of GMSE models during centrifuge testing for GMSE Wall Models with T_f/S_v 13.8-15.0 (S_v = 20 mm (0.8 in.) for M5 and 40 mm (1.6 in.) for M7)

4.4.5 GENERAL OBSERVATIONS FROM CENTRIFUGE TEST RESULTS

Based on the observations from the centrifuge test results, the following Figure 4.4.7 demonstrates the effect of changing reinforcement parameters. Figure 4.4.7 shows schematic diagrams for four wall pairs. Each pair represents the effect of changing one reinforcement parameter. Figure 4.4.7a shows two walls with reinforcements placed at different vertical spacing and have the same total reinforcement tensile capacity (ΣT_f), the same total reinforcement tensile stiffness (ΣJ), the same soil-geosynthetic interface friction (δ_{sg}). That is, both walls have the same T_f/S_v and J/S_v; however, the number of interfaces in the wall reinforced at a smaller spacing is higher than that reinforced at a larger spacing. This provides more interaction with the reinforced soil mass rendering observed better performance at working stress conditions.

Figure 4.4.7b shows two walls with reinforcements placed at the same vertical spacing and have the same tensile strength and stiffness; however, the reinforcements of one wall have higher soil-geosynthetic interface friction than the other. Even though the T_f/S_v and J/S_v ratios are the same for both walls, the performance of the wall with higher soil-reinforcement interface friction would render a better performance at working stress conditions. This is apparently due to the higher interaction the reinforcements have with the soil mass.

Figure 4.4.7c shows two walls with reinforcements placed at the same vertical spacing and have the same tensile strength and soil-geosynthetic interface friction; however, the reinforcements of one wall have higher tensile stiffness than the other. That is, the total reinforcement tensile capacity for both walls is the same and the total number of soil-reinforcement interfaces contributing in soil stabilization is the same. However, the performance of the wall with stiffener reinforcements should perform better at working load conditions. The reinforcement stiffness plays a role in controlling the deformation of the reinforced soil mass.

Figure 4.4.7d shows two walls with reinforcements placed at the same vertical spacing and have the same tensile stiffness and soil-geosynthetic interface friction; however, the reinforcements of one wall have higher tensile strength than the other. That is, the parameters that control the reinforcement deformation and soil-reinforcement deformation are the same. Both walls should exhibit the same performance at working stress conditions. However, the wall reinforced with stronger reinforcements can sustain higher stress at failure condition.

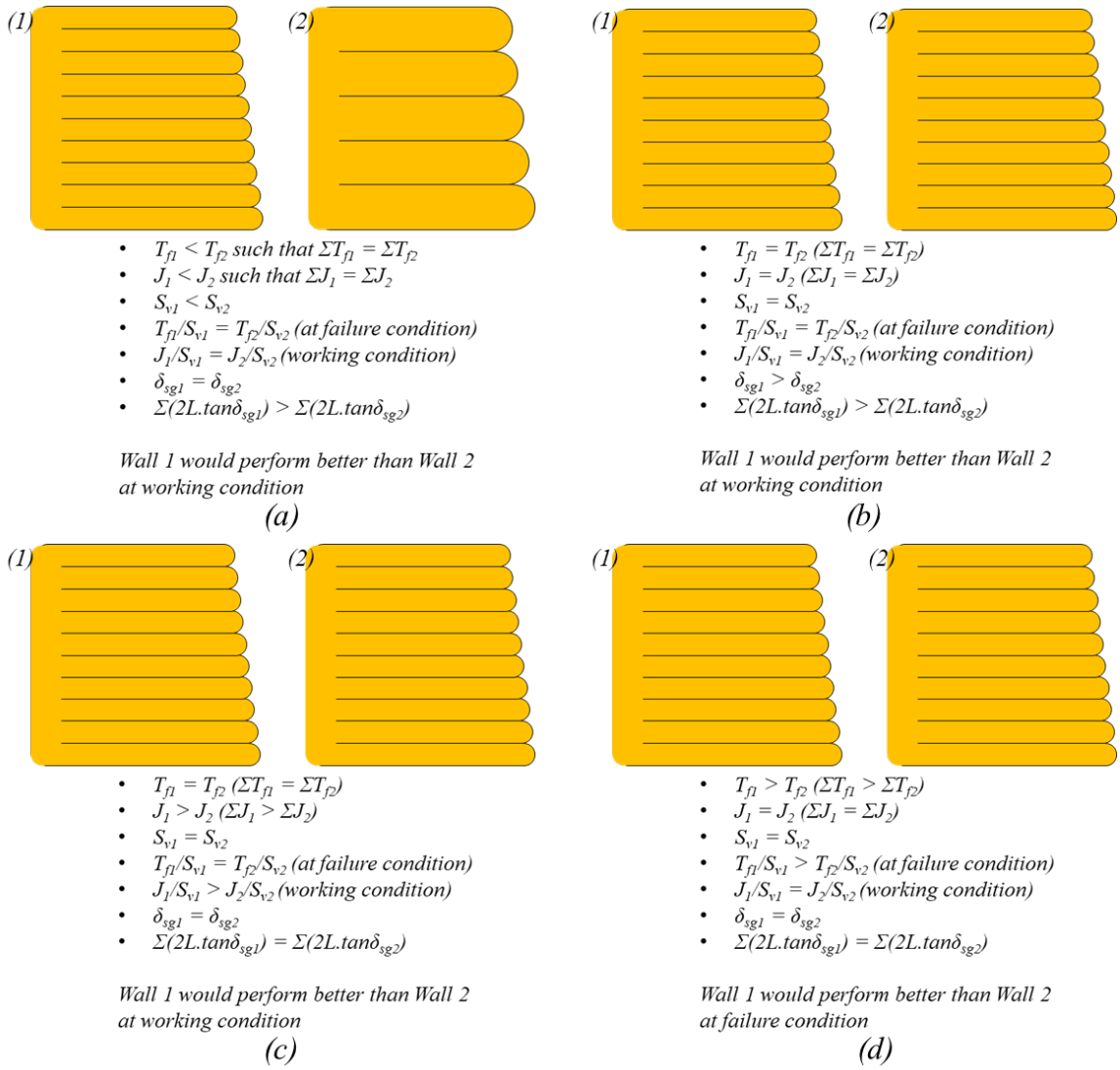

Figure 4.4.7. Parametric evaluation: (a) Effect of reinforcement spacing, S_v; (b) Effect of soil-geotextile interface friction, δ_{sg}; (c) Effect of reinforcement stiffness, J; (d) Effect of reinforcement tensile strength, T_f.

4.4.6 CONCLUSIONS

The geotechnical centrifuge technology is very powerful in modelling geosynthetic-reinforced structures. It allows simulating as-real conditions in reduced-scale models that would allow investigating the strain and stress states scaled to real structures. This provides crucial practical insights into the type of behavior expected from these structures and optimizing design accordingly. This study consolidated and analyzed a large number of geosynthetic reinforced soil centrifuge models reported in literature with focus on models in which the reinforcement vertical spacing was varied. This study resulted in the following insights:

- Reducing the reinforcement vertical spacing increases the structural stability of the walls even with small *L/H* ratios.
- The reassessment of data indicated that decreasing the reinforcement spacing results in significant reduction in lateral deformation and thus less vertical deformation (settlement) within the reinforced soil mass.
- The reassessment of data indicated that geosynthetic reinforced soil structures constructed with the same total reinforcement tensile capacity ($\sum T_f$) and total reinforcement stiffness ($\sum J$) were found to perform better if their reinforcements were placed at closer vertical spacing.
- Using a comparatively large number of reinforcement layers of comparatively low tensile strength and stiffness but placed at a comparatively small vertical spacing can result in a better overall structural performance than a comparable structure with reinforcements of strong tensile strength and stiffness but placed at a large vertical spacing. This difference in performance is attributed to the large number of soil-reinforcement interfaces in structures with closely-spaced reinforcement. The large number of interfaces enhances the compatibility between the soil and the reinforcement layers.
- Soil-reinforcement interaction (a key parameter in resisting the pullout failure) also appears to play a key role in controlling the deformation of the entire reinforced soil mass.
- GRS structural performance at working stress conditions shown by centrifuge data reassessment was found to be controlled by reinforcement vertical spacing, reinforcement stiffness, soil-reinforcement interface stiffness, and soil stiffness (as observed in numerous other studies). All of which are needed to render proper design of geosynthetic reinforced soil structures.

4.4.7 REFERENCES

AASHTO (2016). AASHTO LRFD Bridge Design Specifications. Seventh Edition, American Association of State Highway and Transportation Officials (AASHTO).

Arriaga, F. (2003). Response of Geosynthetic-Reinforced Structures under Working Stress and Failure Conditions. Ph.D. dissertation, Department of Civil Engineering, University of Colorado, Boulder, Colorado.

Bathurst, R.J., Nernheim, A., Walters, D.L., Allen, T.M., Burgess, P., and Saunders, D.D. (2009). "Influence of Reinforcement Stiffness and Compaction on the Performance of Four

Geosynthetic-Reinforced Soil Walls." Geosynthetics International, Vol. 16, No. 1, pp. 43-59.

Bathurst, R.J., Walters, D., Vlachopoulos, N., Burgess, P., and Allen, T.M. (2000). "Full Scale Testing of Geosynthetic Reinforced Walls." Proceedings of GeoDenver Conference, pp. 1-17.

Bathurst, R.J., Vlachopoulos, N., Walters, D.L., Burgess, P.G., and Allen, T.M. (2006). "The Influence of Facing Stiffness of Two Geosynthetics Reinforced Soil Retaining Walls." Canadian Geotechnical Journal, pp. 1225-1237.

Boyle, S.R. and Holtz, R.D. (1994). "Deformation Characteristics of Geosynthetic-Reinforced Soil." Proceedings of the 5th International Conference on Geotextiles, Geomembranes and Related Products, September 1994, Vol. 1, pp. 361-364.

Costa, C.M.L. (2004). "Deformacoes Dependentes do Tempo em Muros de Solo Reforcado Com Geotexteis." Ph.D. Dissertation, Escola de Engenharia de Sao Carlos, da Universidade de Sao Paulo, 330p. (In Portuguese).

Costa, C.M.L., Zornberg, J.G., de Souza Bueno, B., and Costa, Y.D.J. (2016). "Centrifuge Evaluation of the Time-Dependent Behavior of Geotextile-Reinforced Soil Walls." Geotextiles and Geomembranes, Vol. 44, No. 2, pp. 188-200.

Goodings, D.J. (1990). "Research on Geosynthetics in Reinforced Cohesive Soil Retaining Walls at the University of Maryland." Geotechnical News, pp. 23-25.

Gomes, R.C., Palmeira, E.M., and Lanz, D. (1994). "Failure and Deformation Mechanisms in Model Reinforced Walls Subjected to Different Loading Conditions." Geosynthetics International, No. 1, No. 1, pp. 45-65.

Gourc, J.P., Gotteland, Ph., Haza, E., Perrier, H., and Baraize, E. (1995). "Geotextile Reinforced Structures as Bridge Abutments: Fullscale Experimentation." Proceedings of the 5th International Conference on Geosynthetics, Nashville, Tennessee, USA, pp. 79-92.

Güler, E. and Goodings, D.J. (1992). "Centrifuge Models of Clay-Lime Reinforced Soil Walls." Proceedings of Grouting, Soil Improvement and Geosynthetics, ASCE, pp. 1249-1260.

Hatami, K. and Bathurst, R.J. (2005). "Development and Verification of a Numerical Model for the Analysis of Geosynthetic-Reinforced Soil Segmental Walls Under Working Stress Conditions." Canadian Geotechnical Journal, Vol 42, No. 4, pp. 1066-1085.

Hatami, K. and Bathurst, R.J. (2006). "Numerical Model for Reinforced Soil Segmental Walls Under Surcharge Loading." Journal of Geotechnical and Geoenvironmental Engineering, Vol. 132, No. 6, pp. 673-684.

Haza, E., Gotteland, P., and Gourc, J.P. (2000). "Design Method for Local Load on a Geosynthetic Reinforced Soil Structure." Geotechnical & Geological Engineering, Vol. 18, No. 4, pp. 243-267.

Holtz, R.D. and Lee, W.F. (2002). Internal Stability Analyses of Geosynthetic Reinforced Retaining Walls. Washington State Department of Transportation, Report No. WA-RD 532.1, Olympia, Washington, USA.

Iacorossi, M. (2012). Earth Reinforced Retaining Structures. Report, Department of Civil Engineering, Columbia University, NY, USA.

Iacorossi, M., Ling, H.I., Gottardi, G., and Li, L. (2013). "Centrifuge Modeling of Earth-Reinforced Retaining Walls." Proceedings of International Symposium on Design and Practice of Geosynthetic-Reinforced Soil Structures. Bologna, Italy.

Jaber, M.B. (1989). Behavior of Reinforced Soil Walls in Centrifuge Model Tests. Berkeley. Ph.D. Dissertation, University of California, Berkeley, 239p.

Jaber, M., Mitchell, J.K., Christopher, B.R. and Cutter, B.L., "Large Centrifuge Modeling of Full Scale Reinforced Soil Walls", Design and Performance of Earth Retaining Structures, Lambe, P.C. and Hansen, L.A., Editors, Proceedings of a Conference Sponsored by the American Society of Civil Engineers, New York, NY, USA, Jun 1990, pp. 379-393

Jewell, R.A. (1991). "Application of Revised Design Charts for Steep Reinforced Slopes." Geotextiles and Geomembranes, Vol. 10, No. 3, pp. 203-233.

Juran, I. and Christopher, B. (1989). "Laboratory Model Study on Geosynthetic Reinforced Soil Retaining Walls." Journal of Geotechnical Engineering, Vol. 115, No. 7, pp. 905-926.

Kniss, K.T., Yang, K.-H., Wright, S.G., and Zornberg, J.G. (2007). "Earth Pressures and Design Consideration of Narrow MSE Walls." Proceedings of the Conference of Texas Section-ASCE Meeting, Taylor, Texas, April, 2007.

Ko, H.Y. (1988a). "The Colorado Centrifuge Facility." Proceedings of International Conference of Centrifuges in Soil Mechanics, James and Schofield (eds.), pp. 319-324.

Ko, H.Y. (1988b). "Summary of the State-of-the-art in Centrifuge Model Testing." Proceedings of International Conference of Centrifuges in Soil Mechanics, James and Schofield (eds.), pp. 11-18.

Lee, Y.-B. (2010). Deformation behavior of shored mechanically stabilized earth (SMSE) wall systems. PhD thesis, University of Colorado, Boulder, CO, USA.

Lee, K.L., Adams, B.D., and Vagneron, J.M.J. (1973). "Reinforced Earth Retaining Walls." Soil Mechanics and Foundation Engineering, ASCE, Vol. SM10, pp. 745–764.

Lee, Y.-B., McCartney, J.S., and Ko, H.-Y. (2010a). "Centrifuge Modeling of Shored Mechanically Stabilized Earth Walls." Proceedings of International Conference on Physical Modeling in Geotechnics, Zurich, Switzerland, pp. 481-486.

Lee, Y.-B., Ko, H.-Y., and McCartney, J.S. (2010b). "Deformation Response of Shored MSE Walls under Surcharge Loading in the Centrifuge." Geosynthetics International, Vol. 17, No. 6, pp. 389-402.

Leshchinsky, D. and Boedeker, R.H. (1989). "Geosynthetic Reinforced Soil Structures." Journal of Geotechnical Engineering, Vol. 115, No. 10, pp. 1459-1478.

Lin, H., Ling, H.I., Collin, J.G., Leshchinsky, D., and Rimoldi, P. (2013). "Centrifuge Modeling of Gabion Walls Reinforced with Geosynthetics." Proceedings of International Symposium on Design and Practice of Geosynthetic-Reinforced Soil Structures. Bologna, Italy.

Ling, H.I., Wu, J.T., and Tatsuoka, F. (1992). "Short-Term Strength and Deformation Characteristics of Geotextiles Under Typical Operational Conditions." Geotextiles and Geomembranes, Vol. 11, No. 2, pp. 185-219.

Malinowska, E.E. (2015). "Gabion Wall Testing during the Forced Overloading in the Geotechnical Centrifuge." Acta Scientiarum Polonorum. Architectura, Vol. 14, No. 3.

Mahajan, R.R. (2007). Centrifuge Model Studies on Geosynthetic Reinforced Soil Slopes. Ph.D. Dissertation. Indian Institute of Technology Bombay, India.

McGown, A., Andrawes, K.Z., and Kabir, M.H. (1982). "Load Extension Testing of Geotextiles Confined in Soil." Proceedings of the 2nd International Conference on Geotextiles, August 1982, Vol. 3, pp. 793-798. Roseville, Minnesota.

Mitchell, J.K. and Christopher, B.R., "North American Practice in Reinforced Soil Systems", Design and Performance of Earth Retaining Structures, Lambe, P.C. and Hansen, L.A., Editors, Proceedings of a Conference Sponsored by the American Society of Civil Engineers, New York, NY, USA, June 1990, pp. 322-346.

Mitchell, J.K., Jaber, M., Shen, C.K. and Hua, Z.K. (1988), Behavior of Reinforced Soil Walls in Centrifuge Model Tests", Centrifuge 88, Corte, J.F. (ed.), Balkema, Rotterdam, pp. 259-271.

Morsy, A. M. (2017). Evaluation of soil-reinforcement composite interaction in geosynthetic-reinforced soil structures. Doctoral dissertation, The University of Texas at Austin, Austin, Texas, USA.

NCMA (1997). Design Manual for Segmental Retaining Walls. Second Edition, National Concrete Masonry Association (NCMA), Publication Number TR 127A.

Ovesen, N. (1975). "Centrifuge testing applied to bearing capacity problems of footings on sand." Geotechnique, Vol. 25, No. 2, pp. 394-401.

Palmeira, E.M. and Lanz, D. (1994). "Stresses and Deformation in Geotextile Reinforced Model Walls." Geotextiles and Geomembranes, Vol. 12, No. 5, pp. 331-348.

Porbaha, A. and Goodings, D.J. (1994). "Geotextile Reinforced Cohesive Slopes on Weak Foundations." Proceedings of Centrifuge, Vol. 94, pp. 623-628.

Porbaha, A. and Goodings, D.J. (1996). "Centrifuge Modeling of Geotextile-Reinforced Cohesive Soil Retaining Walls." Journal of Geotechnical Engineering, Vol. 122, No. 10, pp. 840-848.

Santamarina, J.C. (1984). Effect of adjacent soils on reinforced soil structures-centrifuge model testing. Ph.D. Dissertation, Purdue University, West Lafayette, Indiana, USA.

Schofield, A. (1980). "Cambridge Geotechnical Centrifuge Operation." Geotechnique, Vol. 30, No. 3, pp. 227-268.

Sommers, A.N. and Viswanadham, B.V.S. (2009). "Centrifuge Model Tests on the Behavior of Strip Footing on Geotextile-reinforced Slopes." Geotextiles and Geomembranes, Vol. 27, No. 6, pp. 497-505.

Springman, S.M., Bolton, M.D., Sharma, J., and Balachandran, S. (1992). "Modelling and Instrumentation of a Geotextile in the Geotechnical Centrifuge." Proceedings of the International Symposium on Earth Reinforcement Practice, Kyushu, September 1992, Vol. 167, p. 172.

Thamm, B.R., Krieger, B., and Krieger, J. (1990). "Fullscale Test on Geotextile Reinforced Retaining Structure." Proceedings of the 4th International Conference on Geotextiles, Geomembranes and Related Products, Hague, The Netherlands, Vol. 1, pp. 3-8.

Vafaeian, M. and Abbaszadeh, R. (2006). "Laboratory Small Scale Tests to Study the Behaviour of Reinforced Soil Wall." Proceedings of 8th International Conference on Geosynthetics, Kuwano, J., Kuseki, J. (eds.), Millpress Science, Rotterdam, Vol. 4, pp. 1409-1412.

Viswanadham, B.V.S. and König, D. (2004). "Studies on Scaling and Instrumentation of a Geogrid." Geotextiles and Geomembranes, Vol. 22, No. 5, pp. 307-328.

Viswanadham, B.V.S. and Mahajan, R.R. (2007). "Centrifuge Model Tests on Geotextile-reinforced Slopes." Geosynthetics International, Vol. 4, No. 6, pp. 365-379.

Wichter, L., Risseeuw, P., and Gay, G. (1986). "Large Scale Test on Bearing Behaviour of a Woven Reinforced Earth." Proceedings of 3rd International Conference on Geotextiles, Vienna, Austria, pp. 1073-1078.

Woodruff, R. (2003). Centrifuge modeling for MSE-shoring composite walls. MS Thesis, University of Colorado, Boulder, CO, USA.

Wright, S.G. and Duncan, J.M. (1991). “Limit Equilibrium Stability Analyses for Reinforced Slopes.” Transportation Research Record, No. 1330, pp. 40–46.

Wu, J.T.H., Lee, K., Helwany, S., and Ketchart, K. (2006). Design and Construction Guidelines for Geosynthetic-Reinforced Soil Bridge Abutments with a Flexible Facing System. NCHRP Report 556, Project 12-59, National Cooperative Highway Research Program, Transportation Research Board, National Research Council, Washington, DC.

Yang, K.-H., Kniss, K.K., Zornberg, J.G., and Wright, S.G. (2008). “Finite-Element Analyses for Centrifuge Modeling of Narrow MSE Walls.” Proceedings of the First Pan American Geosynthetics Conference, GEOAMERICAS-2008 (CD-ROM), International Fabrics Association Int., Rosevile, MN, USA, pp. 1246–1255.

Yang, K.H., Zornberg, J.G., Hung, W.Y., and Lawson, C.R. (2011). “Location of Failure Plane and Design Considerations for Narrow Geosynthetic Reinforced Soil Wall Systems.” Journal of GeoEngineering, Vol. 6, No. 1, pp. 27-40.

Zhang, W., Lai, Z., and Xu, G. (2002). “Centrifuge Model Tests of Geosynthetics Reinforced Retaining Walls.” Proceedings of the International Conference on Physical Modelling in Geomechanics: ICPMG ’02, Philips, Guo, and Popescu (eds.), pp. 999-1004.

Zornberg, J.G. (1994). Performance of Geotextile-reinforced Soil Structures. Ph.D. Dissertation, University of California, Berkeley, CA, USA.

Zornberg, J.G. and Arriaga, F. (2003). “Strain Distribution within Geosynthetic Reinforced Slopes.” Journal of Geotechnical and Geoenvironmental Engineering, Vol. 129, No. 1, pp. 32-45.

Zornberg, J.G. and Mitchell, J.K. (1994). “Reinforced Soil Structures with Poorly Draining Backfills. Part I: Reinforcement Interactions and Functions.” Geosynthetics International, Vol. 1, No. 2, pp. 103-147.

Zornberg, J.G., Mitchell, J.K., and Sitar, N. (1997). “Testing of Reinforced Slopes in a Geotechnical Centrifuge.” Geotechnical Testing Journal, Vol. 20, No. 4, pp. 470-480.

Zornberg, J.G., Sitar, N., and Mitchell, J.K. (1998a). “Performance of Geosynthetic Reinforced Slopes at Failure.” Journal of Geotechnical and Geoenvironmental Engineering, Vol. 124, No. 8, pp. 670-683.

Zornberg, J.G., Sitar, N., and Mitchell, J.K. (1998b). “Limit Equilibrium as Basis for Design of Geosynthetic Reinforced Slopes.” Journal of Geotechnical and Geoenvironmental Engineering, Vol. 124, No. 8, pp. 684-698

4.5 ASSESSMENT OF THE FOUNDERS/MEADOWS LOAD-CARRYING GMSE BRIDGE ABUTMENT PERFORMANCE

4.5.1 INTRODUCTION

The Founders/Meadows Bridge was the first in the United States to use GMSE bridge-supporting abutments on a major highway. The structure is located in Castle Rock, 20 miles south of downtown Denver, Colorado, USA along Founders/Meadows Parkway crossing US Interstate Highway 25 (I-25). The structure replaced an out-of-service two-span bridge in which the abutments were supported by H-piles and the central pier was supported by a spread footing. The old central pier was reemployed in the new bridge. The behavior of the Founders/Meadows reinforced soil structures has been studied repeatedly since its opening to traffic in June 1999. These studies addressed the pressure distribution within the reinforced soil mass and reinforcement straining (e.g. Abu-Hejleh *et al.* 2001a; Helwany *et al.* 2003; Fakharian and Attar 2007; Zheng *et al.* 2015). However, these studies addressed only the short-term response of the bridge. Also, a thorough analysis of the pressure distribution and reinforcement straining has not yet been provided. This chapter evaluates the field monitoring data of the Founder/Meadows bridge abutments during construction and around four service years. Specifically, the evaluation conducted in this study assessed the data collected on: (1) the lateral deformation the bridge abutments; (2) the settlement of the abutments; (3) the reinforcement straining; (3) the differential settlement between the bridge superstructure and the approaching roadway structures, which points towards the formation of the bumps at the ends of the bridge; (4) temperature and moisture changes and their effect on the behavior of the geosynthetic reinforced soil mass; and (5) the vertical and lateral stresses within the geosynthetic reinforced soil mass. The section provides insightful conclusions into the behavior of the structure, which can also be generalized on similar reinforced soil structures.

4.5.2 DESCRIPTION OF THE FOUNDERS/MEADOWS BRIDGE

The Founders/Meadows Bridge is located in Castle Rock, Colorado to separate the two-way traffic of Founders/Meadows Parkway (Colorado State Highway 86) from that of the US Interstate Highway 25 (I-25). This highway is heavily packed with traffic; the total Annual Average Daily Traffic (AADT) recorded on Founder/Meadows Parkway in 2014 by traffic stations located at immediate west and immediate east of the bridge was approximately 39000 and 42000 vehicles/day, respectively (CDOT 2016). According to Highway Performance Monitoring System (HPMS), the AADT level of Founders/Meadows Parkway at this location classifies as Volume Group #7. In addition, CDOT (2016) records show that the AADT for trucks in 2014 at traffic stations west and east the bridge was 2600 and 1390 truck/day, respectively. The total projected AADT for 2023 as per CDOT (2016) is 75894 and 43386 vehicles/day at the west and east sides of the bridge, respectively. Also, the projected AADT for trucks 5060 and 1436 truck/day at the west and east sides of the bridge, respectively.

The bridge has six traffic lanes (three lanes per traffic direction), two sidewalks, and a median. The bridge consists of a two-span superstructure that rests on two GMSE abutments and a central pier as shown in Figure 4.5.1. The bridge superstructure is 69-m (226 ft) long (each span is 34.5-m (113 ft) long) and 34.5-m (113 ft) wide (each direction is 17.25-m (57 ft) wide). The superstructure consists of 20 pre-stressed reinforced concrete box girders. Each of the GMSE abutments consists of a reinforced concrete footing with U-shaped reinforced concrete walls (Figure 4.5.1) resting on a geosynthetic-reinforced soil mass constructed on bedrock. The front walls of the geosynthetic reinforced soil mass extend to the sides at a 90-degree angle forming wing walls on both sides (lower GMSE walls) as shown in Figure 4.5.2. Another tier of side wing walls extends beyond the legs of the U-shaped reinforced concrete footing as shown in Figure 4.5.2. The central pier consists of five columns resting on a spread footing founded on bedrock. The construction was completed over two phases: (1) Phase I, which included the westbound direction of the bridge; and (2) Phase II, which included the eastbound direction of the bridge. Sections 200, 400, and 800 (locations are shown on Figure 4.5.2) were instrumented; Section 800 was heavily instrumented, while Sections 200 and 400 were lightly instrumented for the purpose of behavior verification. In addition, Sections 200, 300, 400, 800 and 900 (locations are shown on Figure 4.5.2) were surveyed to monitor the lateral deformation.

Figure 4.5.1. View of the Founders/Meadows Bridge in 2016.

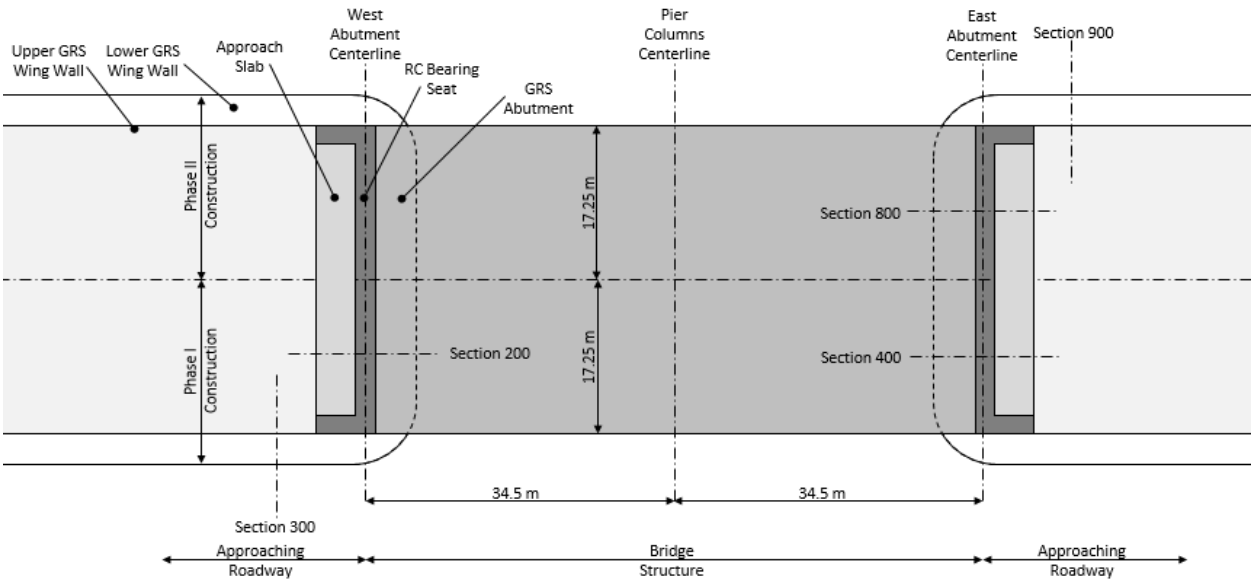

Figure 4.5.2. Top view of the Founders/Meadows Bridge (redrawn after Abu-Hejleh et al. 2002).

The main cause of differential settlements in typical bridge foundation systems is the use of different foundation types. Approaching roadway structures are typically founded on compacted backfill soil while bridge abutments are usually founded on deep foundations that convey the bridge loads to a stronger soil stratum, which are less likely to settle. The Founders/Meadows Bridge rests on geosynthetic-reinforced soil abutments that provide flexible behavior and compatible deformations between the abutments and the approaching roadway structures alleviating any potential differential settlements. Differential settlements can also arise by erosion of the backfill material induced by the surface water runoff. In the Founders/Meadows abutments, precautions were adopted to prevent the surface water and the groundwater from reaching the reinforced soil mass and the bedrock at its base. These precautions included: (1) impervious membranes with collector pipes placed underneath the roadway structures as shown in Figures 4.5.3a and 4.5.3b; and (2) drainage blankets with drainage pipes placed behind the reinforced soil mass to divert groundwater and infiltration as shown in Figure 4.5.3a. In addition, temperature changes can cause the bridge superstructure to expand and contract inducing lateral pressure on the abutments. In the Founders/Meadows abutments, compressible 75 mm-thick (3 in.), low-density, expanded polystyrene sheets were placed vertically between the reinforced backfills and the abutment walls as shown in Figure 4.5.3a. These compressible sheets alleviate the lateral earth pressure on the back of the concrete wall due to thermal-induced movements of the bridge superstructure.

Table 4.5.1 summarizes the construction stages of the Founders/Meadows Bridge. Figure 4.5.4 shows the construction time history of the bridge for construction Phase I (which includes Sections 200 and 400) and construction Phase II (which includes Section 800). The bridge construction was completed in approximately 160 days (Stages I through VI). Note that Stage VII

monitoring extended for up to four years after the bridge was inaugurated to traffic on 30 June 1999.

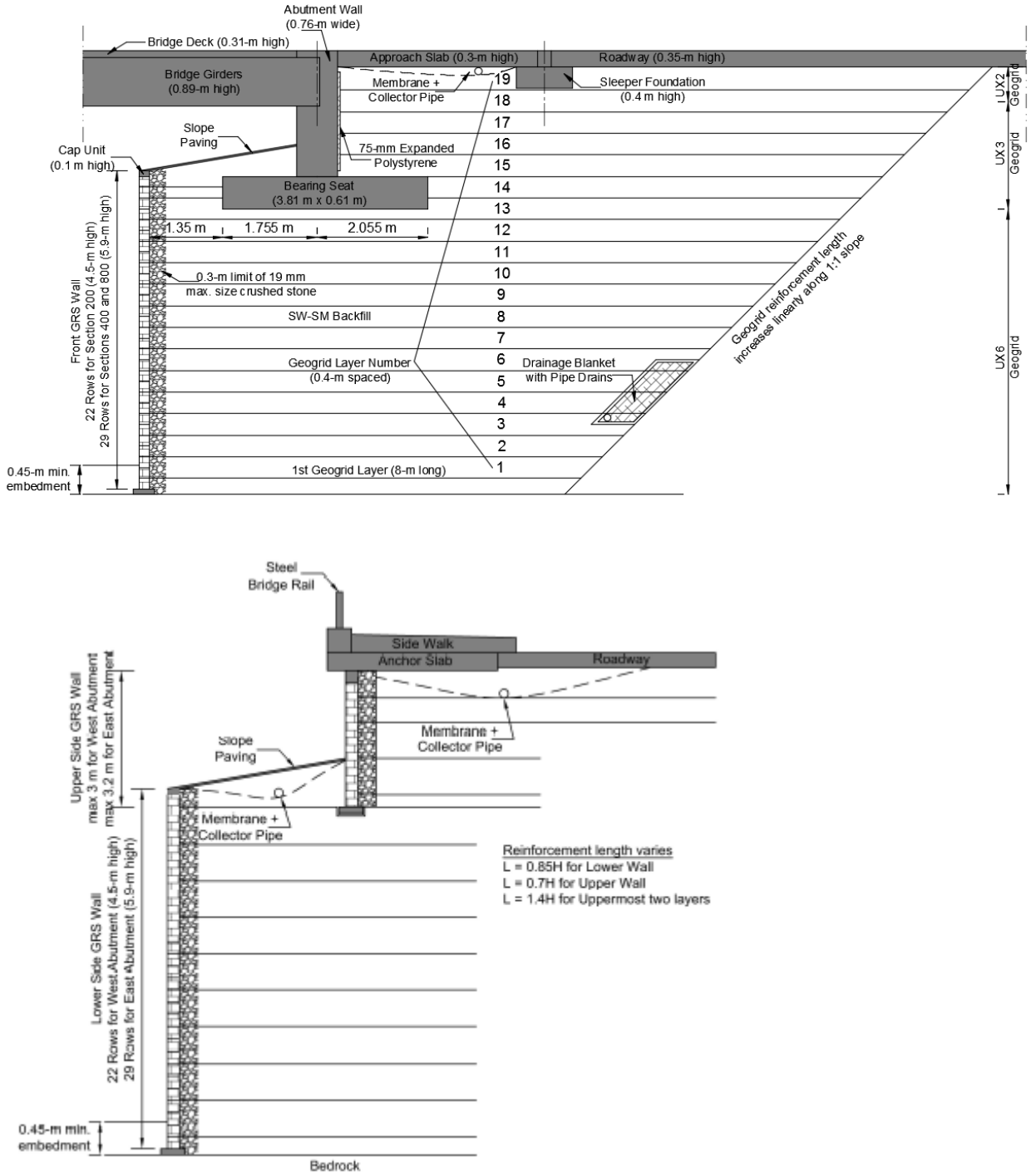

Figure 4.5.3: Typical cross-section of the Founders/Meadows Bridge abutment: (a) Sections 200, 400, and 800 (redrawn after Abu-Hejleh et al. 2002); and (b) Section 300 and 900.

Table 4.5.1. Construction stages.

Stage #	Description
0	Leveling pad placement
I	Construction of the front GMSE wall up to the bridge footing elevation. The Stage I structure provides support for the bridge and approaching roadway structures
II	Placement of bridge footing and girders seats
III	Placement of girders
IV	Placement of the reinforced backfill behind the abutment wall from the bridge footing elevation to the bottom of the sleeper footing
V	Placement of bridge deck
VI	Placement of the approaching roadway structure (including approach slab) and other minor structures
VII	Post-construction after opening the structure to traffic

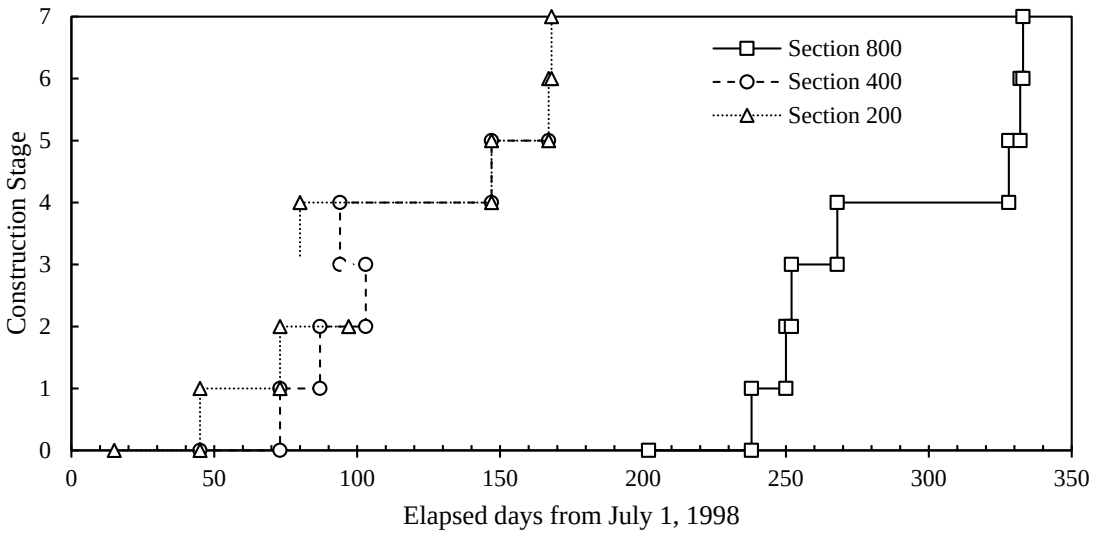

Figure 4.5.4. Time history of construction

4.5.3 MATERIAL CHARACTERISTICS OF THE GMSE ABUTMENTS

The reinforced soil mass of the Founders/Meadows Bridge abutments consist primarily of alternating layers of backfill material and reinforcement. The reinforced soil zone is covered by a facing system. The material characteristics of the abutments are summarized in the following subsections:

4.5.3.1 BACKFILL MATERIAL

The backfill material used in the Founders/Meadows Bridge abutments was a mixture of gravel (35.0%), sand (54.4%), and fines (10.6%). The liquid limit and plasticity index for the fines content were 25 and 4, respectively. The soil classifies as SW-SM in accordance with ASTM 2487 and as A-1-B (0) in accordance with AASHTO M 145. The average unit weight, dry unit weight, and water content of the compacted backfill as measured during compaction were 22.1 kN/m^3 (142 pcf), 21.0 kN/m^3 (135 pcf), and 5.6%, respectively. The backfill was compacted to 95% of the maximum dry unit weight determined in accordance with AASHTO T-180A. A set of conventional direct shear tests were conducted in accordance with AASHTO T-236 on the backfill after excluding the 35% gravel portion. The maximum dry unit weight and optimum moisture content of the backfill without the gravel portion were 19.9 kN/m^3 (128 pcf) and 8.8% as per AASHTO T-99A. The specimens were compacted to 95% of the maximum unit weight and a moisture content of 9.6%. The peak friction angle and the cohesion intercept obtained for the tested specimens were 40.1 degrees and 17.0 kPa (2.5 psi), respectively. Meanwhile, a set of large-scale direct shear and large-scale triaxial tests were conducted on the backfill including the gravel portion to evaluate the suitability of the measured strength parameters obtained from the conventional direct shear tests. The specimens where prepared at similar unit weight and moisture content to those measured in the field. The large-scale direct shear tests were conducted on specimens compacted at dry unit weight of 21.0 kN/m^3 (135 pcf) and moisture content of 5.6% and tested in a large-size direct shear box in accordance with ASTM D3080. Figure 4.5.5a shows the test results for three different confinement levels. The peak friction angle and the cohesion intercept obtained for the tested specimens were 47.7 degrees and 110.5 kPa (16 psi), respectively. The large-scale triaxial tests were conducted on specimens compacted at 20.6 kN/m^3 (132 pcf) dry unit weight and 5.7% moisture content. Figure 4.5.5b shows the test results for three different confinement levels. A peak friction angle of 39.5 degrees and 69.8 kPa (10.1 psi) cohesion intercept were obtained. In addition, Figure 4.5.6 shows the volumetric-axial strain relationship obtained from the three conducted triaxial tests.

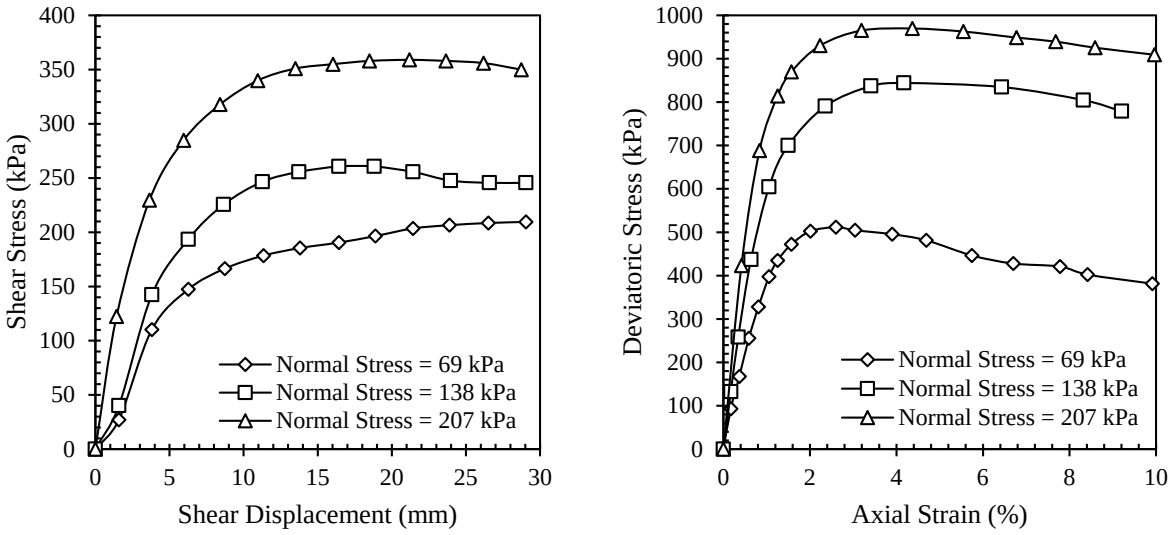

Figure 4.5.5. Shear strength test results: (a) large-scale direct shear; (b) large-scale triaxial.

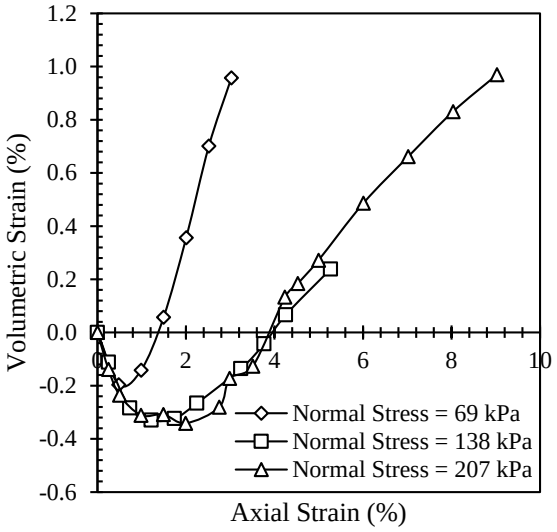

Figure 4.5.6. Volumetric strain versus axial strain relationship obtained from triaxial testing.

4.5.3.2 REINFORCEMENT

The reinforcement used in the Founders/Meadows Bridge abutments was polyethylene geogrids from Tensar Earth Technologies. Tensar® Uniaxial UX6 geogrids were used beneath the bridge footing and Uniaxial UX3 and UX2 geogrids were used behind the abutment wall as shown in Figure 4.5.3. The ultimate tensile strengths of the employed geogrids in accordance with the ASTM D 4595 were 157.3, 64.2, and 39.3 kN/m (898, 367 and 224 lbf/in) for the UX6, UX3, and UX2 geogrids, respectively. The tensile stiffness of the UX6 and UX3 geogrids at the 0-2% tensile strain range were approximately 2000 and 1000 kN/m (11420 and 5710 lbf/in), respectively. The geosynthetic reinforced soil mass was constructed in a trapezoidal shape that had 1:1 back slope

as shown in Figure 4.5.3a. The reinforcement length was made long to support not only the bridge superstructure bearing seats but also the approaching roadway structures to mitigate the possible differential settlement between the bridge deck and the approaching slabs. In addition, the extension of the reinforced soil mass intended to enhance the overall stability of the bridge abutments.

4.5.3.3 CONCRETE FACING BLOCKS

Mesa concrete facing blocks (Figure 4.5.7) were used with positive mechanical connectors between the blocks and the reinforcement layers, and between the blocks themselves (Figure 4.5.8). The Mesa facing blocks had a compressive strength of 28 MPa (4060 psi) and were 0.457 m (1.5 ft) long, 0.279 m (0.9 ft) wide, and 0.203 m (0.7 ft) high. Crushed stone of 19-mm (0.7 in.) maximum size was placed behind the facing blocks for a distance of 0.3 m (1 ft) to facilitate the compaction process. This zone provided an internal drainage system and prevented the migration of fines to the wall facing.

(a)  (b) 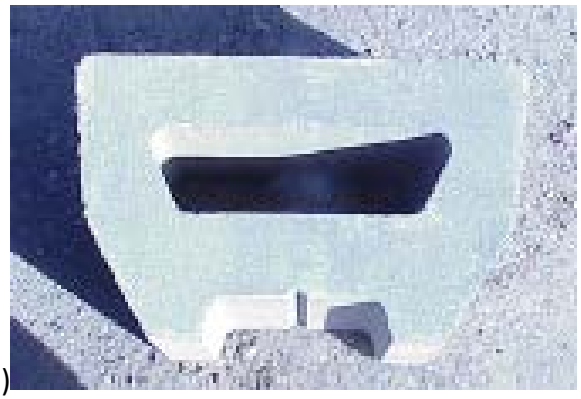

Figure 4.5.7. Mesa concrete facing blocks: (a) top view; and (b) bottom view.

4.5.3.4 FACING CONNECTORS

The mechanical connectors used had a mobilized connection strength of 57.7 kN/m (330 lbf/in) measured in accordance with the National Concrete and Masonry Association (NCMA) Test Method SRWU-1 at a horizontal movement of 19 mm (0.7 in.) (Service state).

(a)  (b) 

Figure 4.5.8. Mechanical connectors: (a) general view; and (b) assembly view.

4.5.4 INSTRUMENTATION PROGRAM

The Founders/Meadows Bridge abutments were heavily instrumented. Figure 4.5.9 shows the instrumentation layout of Section 800. The instrumentation included can be divided into two categories: (1) instrumentation to monitor the external deformation of the structure, which included surveying, a dipstick road profiler, and an inclinometer; and (2) instrumentation to monitor the internal response of the structure, which included vertical earth pressure cells, lateral contact pressure cells, reinforcement strain gages, temperature gages, and water content reflectometers. Information on the various instrumentation employed in the structure are summarized in the following subsections:

4.5.4.1 INSTRUMENTATION TO MONITOR THE EXTERNAL DEFORMATION OF THE STRUCTURE

4.5.4.1.1 Surveying points

Reflective sign sheeting were mounted on the facing of the walls, girders, and abutments. Survey targets marked by nails were flushed into holes in the bridge deck, approaching slab, and roadway slab. The locations of the targets are shown in Figure 4.5.9. The targets were shot by a surveying total station.

4.5.4.1.2 Dipstick road profiler

A dipstick road profiler was utilized to profile the bridge deck and the approaching roadways. The road surface was profiled along the external edges of the bridge and into the roadway surface in both directions. The profiler was used to plot an accurate profile of a roadway surface. The profiler used has a digital level with two pivoting legs that are 0.3-m (1-foot) apart. That is, this profiler can acquire elevation data every 0.3-m (1 ft) increment.

4.5.4.1.3 Inclinometer

One Geokon Model 6000 inclinometer was installed vertically behind the facing to measure the lateral deformation of the reinforced soil mass. The inclinometer is divided into segments and measures the displacement of the junctions between the settlements. Consequently, displacement values from the inclinometer represent average displacement for multiple layers. The inclinometer was placed in Section 400.

4.5.4.2 INSTRUMENTATION TO MONITOR THE INTERNAL RESPONSE OF THE STRUCTURE

4.5.4.2.1 Vertical earth pressure cells

Geokon 4800 earth pressure cells with a range of 345 kPa (50 psi) were used to measure the localized vertical pressure within the reinforced soil mass. The array of the vertical earth pressure cells installed for Section 800 is shown in Figure 4.5.9. This cell is designed to be placed in the soil and was positioned horizontally to measure vertical pressure.

4.5.4.2.2 Lateral earth pressure cells

Geokon 4810 contact pressure cells were used to measure the horizontal pressure exerted by the reinforced soil mass on the facing. The array of the vertical earth pressure cells installed for Section 800 is shown in Figure 4.5.9. These cells were placed vertically against the back of the block facing and the abutment wall to measure the horizontal pressure exerted by the reinforced soil.

4.5.4.2.3 Strain gages

Geokon 4050 strain gages with a gage length of 150 mm (6 in) and range of 0.7% were used to measure the localized reinforcement strain. The array of the strain gages installed for Section 800 is shown in Figure 4.5.9. The strain gages were mounted using two brackets which clamp to the geogrid.

4.5.4.2.4 Resistive temperature probes

Geokon temperature probe was used to monitor the air temperature changes. The probe was placed on the top of front GMSE abutment and below the girders (Figure 4.5.9) to protect it against the direct sunlight and precipitation. Vibrating wire sensors associated with thermistors were buried within the reinforced soil mass to monitor the change in the backfill temperature. One sensor was placed under the girder at the elevation of Layer 16 to monitor the air temperature and two sensors were placed at Layer 10, Locations A and B to measure the difference in the temperature alterations near the facing and under the center of the bearing seat.

4.5.4.2.5 Water content reflectometers

Campbell Scientific CS615 water content reflectometers were used to monitor the change in moisture content within the reinforced soil mass. Two sensors were placed below the sleeper foundation at Section 800 as shown in Figure 4.5.9. Theses sensors determine the change in water content through the change in the dielectric constant of the soil.

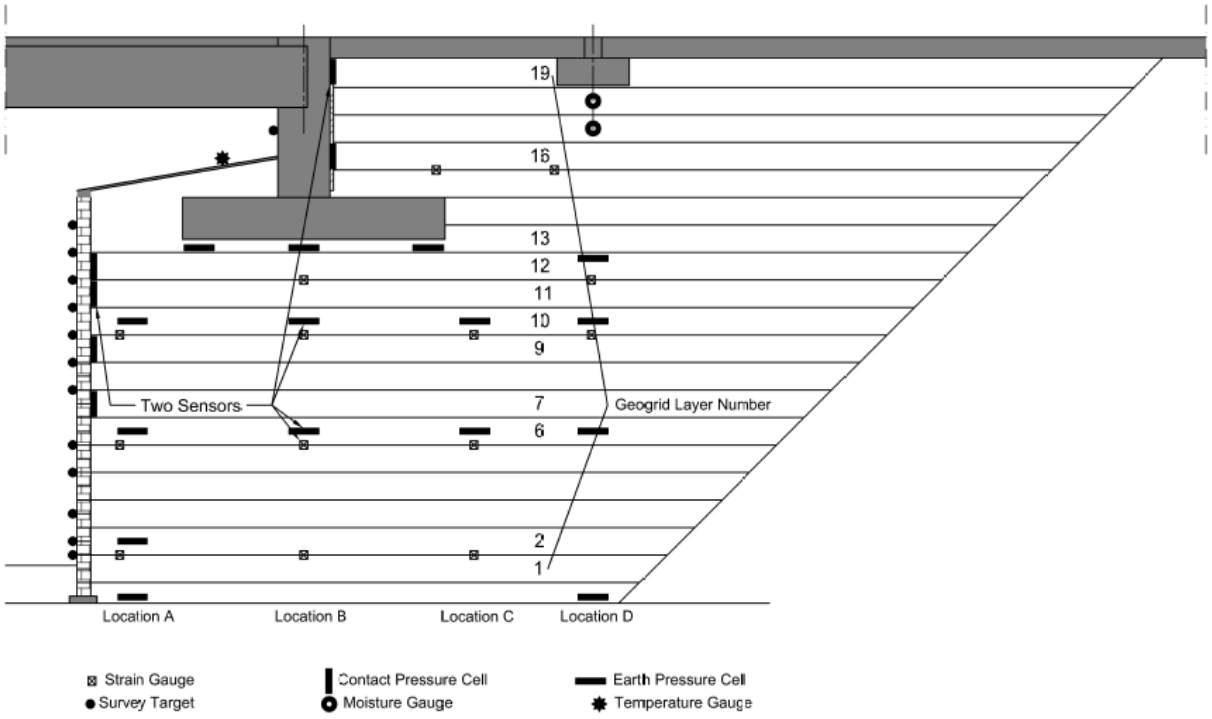

Figure 4.5.9. Layout of Instrumented Section 800 (redrawn after Abu-Hejleh et al. 2002).

4.5.5 ABUTMENT LATERAL DEFORMATION

The lateral deformations of the instrumented sections were measured by surveying occasionally during construction and after the bridge was opened to traffic. Figures 4.5.10a through 10e show the measured lateral deformation since the construction of the GMSE backfill (*i.e.*, since the completion of Stage II) at different dates for Sections 800, 400, 200, 300, and 900, respectively. Note that the bridge construction was completed and the bridge was opened to traffic in June 1999. The lowermost 1 m (3.3 ft) was not surveyed since the embedment depth had been buried by the time the walls were surveyed except for the first reading for Sections 400, 200, and 300. In addition, the second meter was not surveyed for Sections 800, 400, and 200 due to the placement of the right-of-way jersey barriers in front of the abutment front walls.

The lateral deformation was found insignificant where the maximum value observed was 22.6 mm (0.9 in.) and was recorded for Section 400. However, the maximum lateral deformation that was experienced by the structure after its completion is 15.7 mm (0.6 in.) and was observed in Section 400 as well. Sections 400 and 200 showed very similar deformations in their early readings (during construction). However, Section 400 has shown slightly higher lateral deflection in the later readings. This is attributed to the difference in wall height, where Section 400 is 5.9-m (19.4 ft) high. Similarly, the lateral deformation at Section 300 was observed to be less than that at Section 900 due to the difference in wall heights. The difference in lateral deformation between the two sections was pronounced under higher loads. On the other hand, Section 800 exhibited less lateral deflection compared to Section 400, which has the same height as Section 800. This can be attributed to three possible reasons: (1) the construction season of the GMSE

abutments. The construction of the GMSE abutments at Sections 400 and 200 (Phase I) was completed by November 1998 and the subsequent construction of the bridge was completed by December 1998 (*i.e.*, during the warm season), whereas the construction of the GMSE abutments at Section 800 (Phase II) was completed by March 1999 and the subsequent construction of the bridge was completed by June (*i.e.*, during the warm season). This resulted in higher lateral deformation of the front walls. On contrary, the superstructure of Phase II was constructed and experienced possible expansion of the warm season. This resulted in less lateral deformation of the front walls; (2) an additional reason is that construction during the cold season in this district where temperature drops below the freezing temperature of water would have frozen the soil layers as they get covered. Note that as construction advanced layers are buried under their successive layers and reducing the possibility of thawing over short time period; and (3) the construction sequence of Phase I and Phase II had a difference. In Phase I (represented in Section 400) the bridge girders were placed after the placement of the backfill behind the abutment wall. That is, a lateral load was applied on the abutment before it is probed by the bridge girders. On contrary, in Phase II (represented in Section 800) the bridge girders were placed before the placement of the backfill behind the abutment wall. That is, the lateral load applied by the added backfill was after the abutment was probed by the girders. This resulted in a larger lateral deformation at Section 400 compared to that at Section 800. Note that the hypotheses mentioned herein contradicts with the hypotheses made by Abu-Hejleh *et al.* (2002), which was based on surveying data recorded for Stage I only.

An inclinometer was placed right behind the facing at Section 400 to provide redundancy in the lateral deformation measurements. The inclinometer started recording its data after the bridge Phase I construction had completed and the measured lateral deformation is presented in Figure 4.5.11a. The data measured from the inclinometer can be compared to the lateral deformation measured by surveying after the completion of Phase I construction. Subsequently, the lateral deformation measured after construction by surveying was plotted and is presented in Figure 4.5.11b. While, the lateral deformation obtained from both surveying and the inclinometer are in the same order of magnitude, the inclinometer exhibited less deformation. This is because the inclinometer measured deformation based on a fixed reference point at its tail (the first point of its array). However, the surveying data showed that the lowermost point of the abutment has moved. This implies that the reference point of the inclinometer has moved laterally and its data is underestimating the lateral deformation. To correct the data measured by the inclinometer, the average of lowermost lateral deflection value (at elevation 2 m (6.6 ft)) measured from surveying was used to correct for the corresponding average deflection value measured from the inclinometer. The difference between these two values is 2.4 mm (0.1 in.), which was added to all the inclinometer data to adjust its data. Note that average values were used since the data obtained by inclinometer and surveying was not for the same time periods, however it was over a similar time span. The corrected lateral deformation obtained from the inclinometer data was then plotted and is presented in Figure 4.5.11c. The lateral deformation measurement in the early years after construction and the vertical profiles of the wall show that the deformation occurred to the walls is primarily sliding deformation and there is no any overturning potential.

In order to evaluate the long-term performance of the load-carrying GMSE abutments, the walls for all the monitored sections were surveyed in March 2016 (approximately 17 years after construction). The vertical profiles of Sections 800, 400, and 200 are plotted as shown in Figure 4.5.12a, whereas those of Sections 300 and 900 are plotted in 12b. While the absolute lateral deformation could not be determined. The abutment front facing batter angle measured was approximately 4 degrees (14V:1H). This value is deemed very small compared to the maximum batter allowed as per original design, which was 15 degrees.

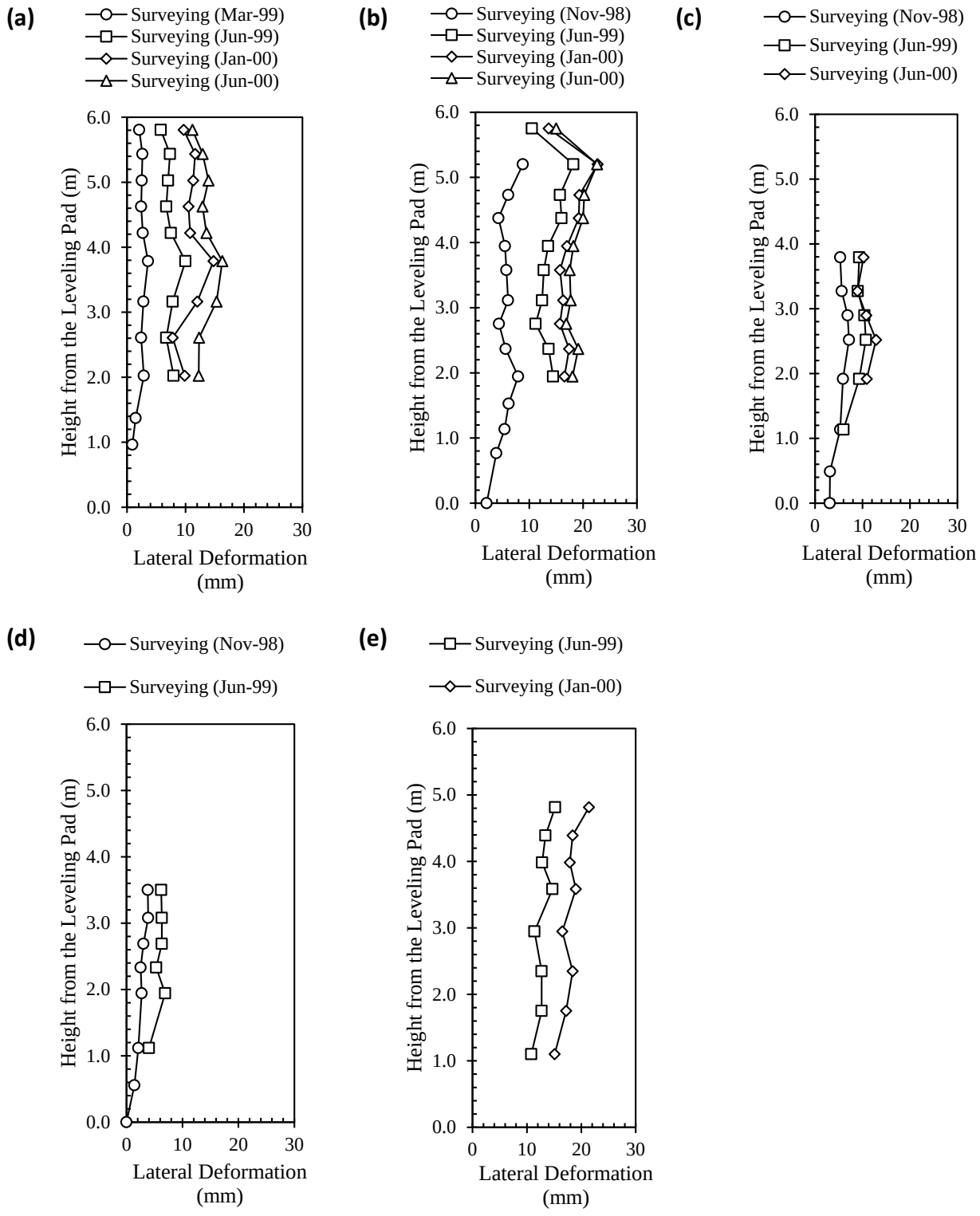

Figure 4.5.10. Lateral deformation measured during and after construction (i.e., Stages II to IV) from surveying for (a) Section 800, (b) Section 400, (c) Section 200, (d) Section 300, and (e) Section 900.

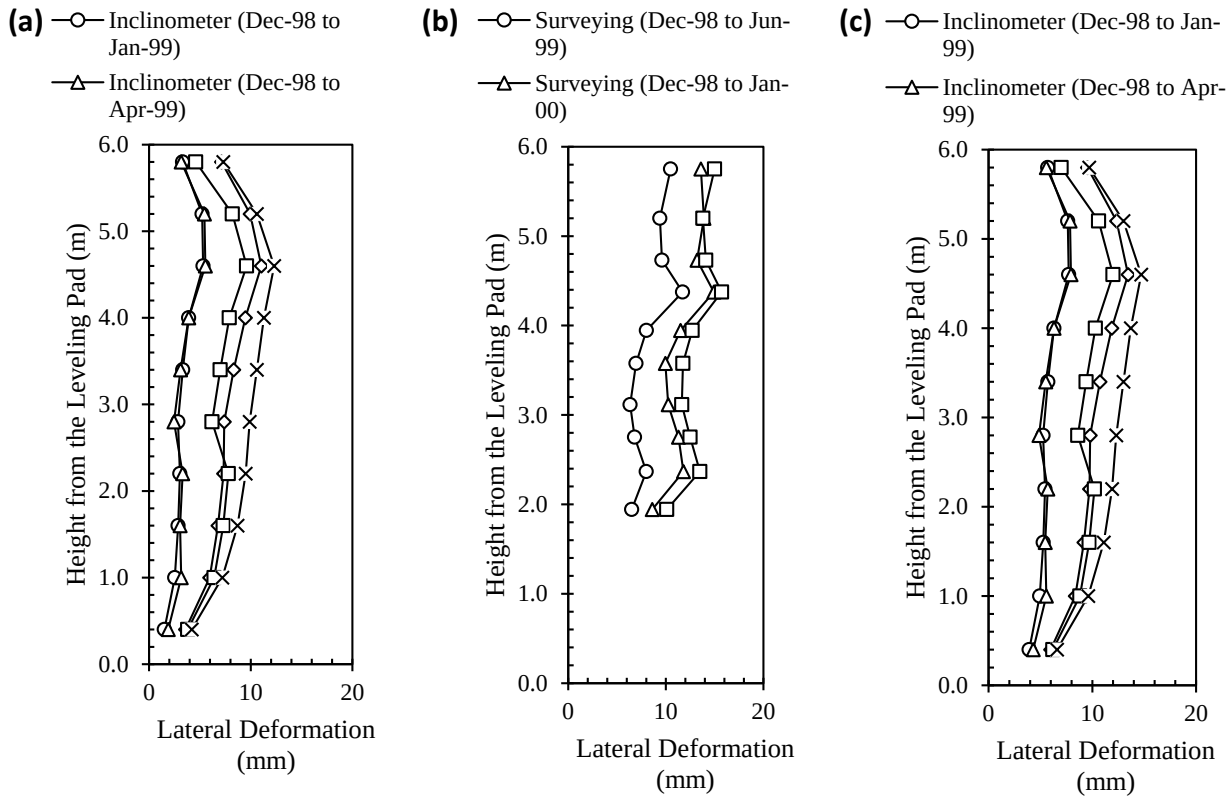

Figure 4.5.11. Lateral deformation measured after construction for Section 400: (a) from inclinometer; (b) from surveying; (c) from inclinometer corrected for surveying.

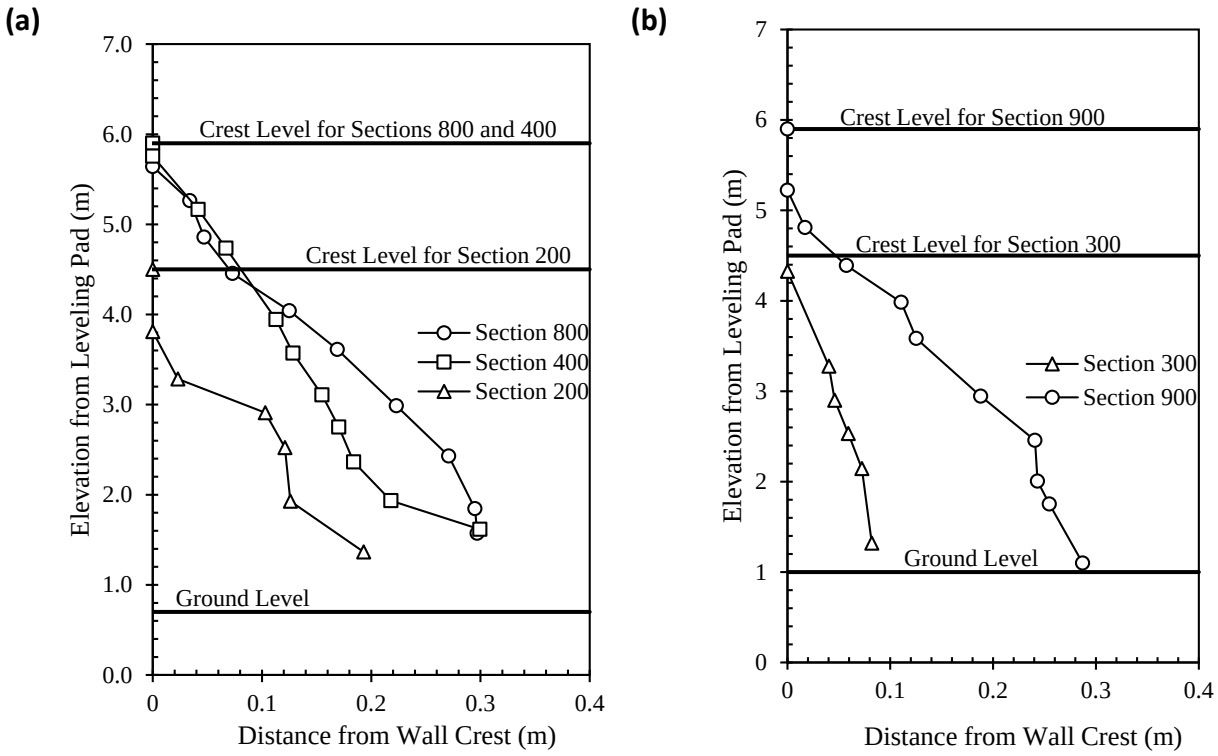

Figure 4.5.12. Vertical wall profiles in March 2016: (a) Sections 800, 400, and 200; and (b) Sections 300 and 900.

4.5.6 ROAD PROFILE

Differential settlements occur across the transition section from bridge deck to approaching roadway in typical bridges. This is due to the different foundation systems used for the bridge deck and the approaching roadway structures. Unlike the conventional bridges, Founders/Meadows was supported directly by the reinforced soil abutments. The reinforced soil extended to support the approaching roadway structures. The bridge elevation profiles along the transition from bridge deck to approaching roadway was monitored along four lines: (1) at the east bridge abutment along eastbound direction; (2) at the east bridge abutment along westbound direction; (c) at the west bridge abutment along eastbound direction; and (d) at the west bridge abutment along westbound direction. Monitoring conducted in February 2000 and November 2001 using a digital road profiler and in March 2016 using a total station. Figures 4.5.13a through 4.5.13d show the elevation profile relative to the abutment crest elevation along the four profiling lines, respectively. The distance is measured from the abutment location such that the positive values denote distances toward the approaching slab and the negative values denote distances towards the bridge deck. Note that the bridge deck is downhill towards the west. The expansion joints are located on the approach slabs around 4 m (13.1 ft) away from the

bridge abutments as shown in Figure 4.5.3. The profiles shown in Figure 4.5.13 indicate the absence of any differential settlements at the transition between the bridge and approaching roadway and the expansion joints. The data collected in March 2016, 17 years after the bridge construction and inaugurated to traffic, proves that the geosynthetic reinforced soil technology perfectly eliminates the bump-at-the-bridge problem. That is, the GMSE provides the required integration between the bridge superstructure and the approach slab to ensure a smooth bridge ride.

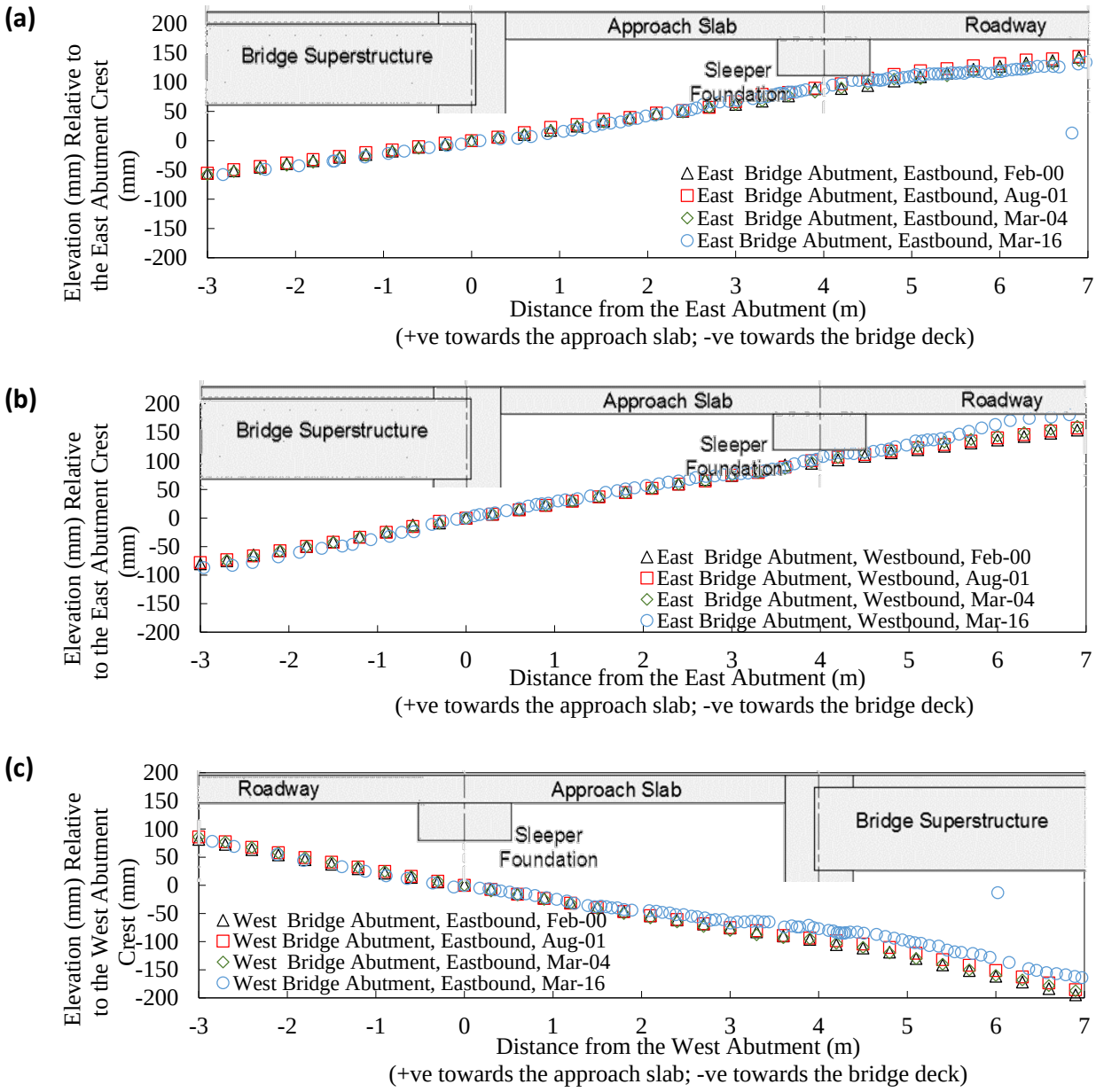

Figure 4.5.13. Elevation profiles along the transition from bridge deck to approaching roadway: (a) at the east bridge abutment, eastbound direction; (b) at the east bridge abutment, westbound

direction; (c) at the west bridge abutment, eastbound direction; and (d) at the west bridge abutment, westbound direction.

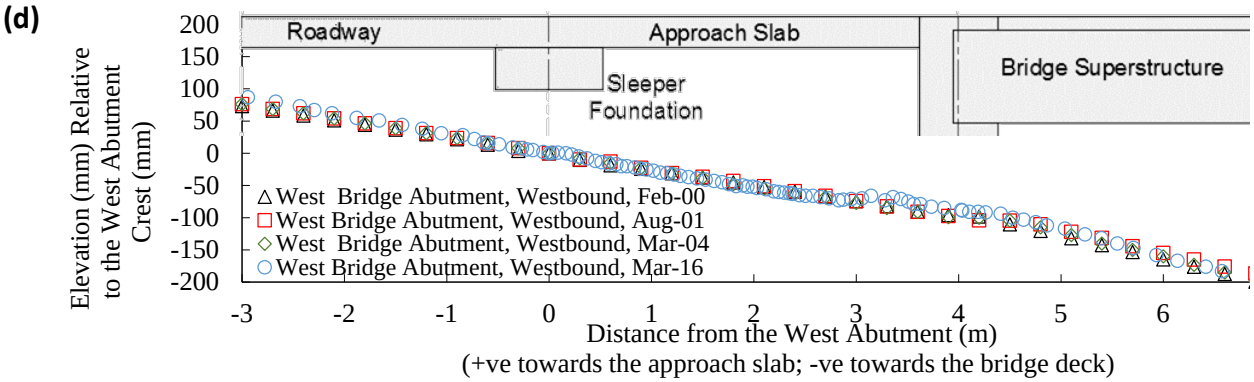

Figure 4.5.13. Elevation profiles along the transition from bridge deck to approaching roadway: (a) at the east bridge abutment, eastbound direction; (b) at the east bridge abutment, westbound direction; (c) at the west bridge abutment, eastbound direction; and (d) at the west bridge abutment, westbound direction. (Continued)

4.5.7 TEMPERATURE MONITORING

Temperature was monitored at three locations during construction and after the construction completion and bridge inauguration to traffic. The temperature was monitored specifically at three different locations: (1) on the top of the GMSE abutment and under the bridge superstructure. This location was selected to monitor the air temperature change while protecting the sensor from the direct sunlight and the environmental events; (2) behind the facing (*i.e.*, at Location A) at Layer 10. This sensor intended to monitor the temperature changes at a shallow region within the geosynthetic reinforced soil mass (*i.e.*, close to the GMSE boundaries); and (3) under the footing (*i.e.*, at Location B) at Layer 10. This sensor intended to monitor the change in temperature at a deep region within the geosynthetic reinforced soil mass (*i.e.*, far from the GMSE boundaries). Figure 4.5.14 shows the time history of the recorded temperature at the three different locations. The sensors embedded within the geosynthetic reinforced soil mass were stopped around 2.7 years after construction, while readings from the air temperature sensor lasted until the fifth years post construction. It is clear from the air temperature time history that the temperature was lowest at the top during the years of peak winter seasons and was highest at the mid during the years of the peak summer seasons. The temperature at the shallow regions followed the air temperature strongly in its time history and magnitude. However, the short-term fluctuations in the temperature was not as high as the air temperature. On the other hand, the temperature at the deep regions did not promptly change with the air temperature changes. This is clear in Figure 4.5.14 where the time history of the temperature recorded at Layer 10, Location B exhibits a phase difference by around 3 months in its seasonal cycles. The air temperature change did not fully alter the temperature at deep regions within the geosynthetic reinforced soil mass. In addition, no short-term temperature

fluctuations (daily temperature changes) were observed at the deep regions as presented in Figure 4.5.14.

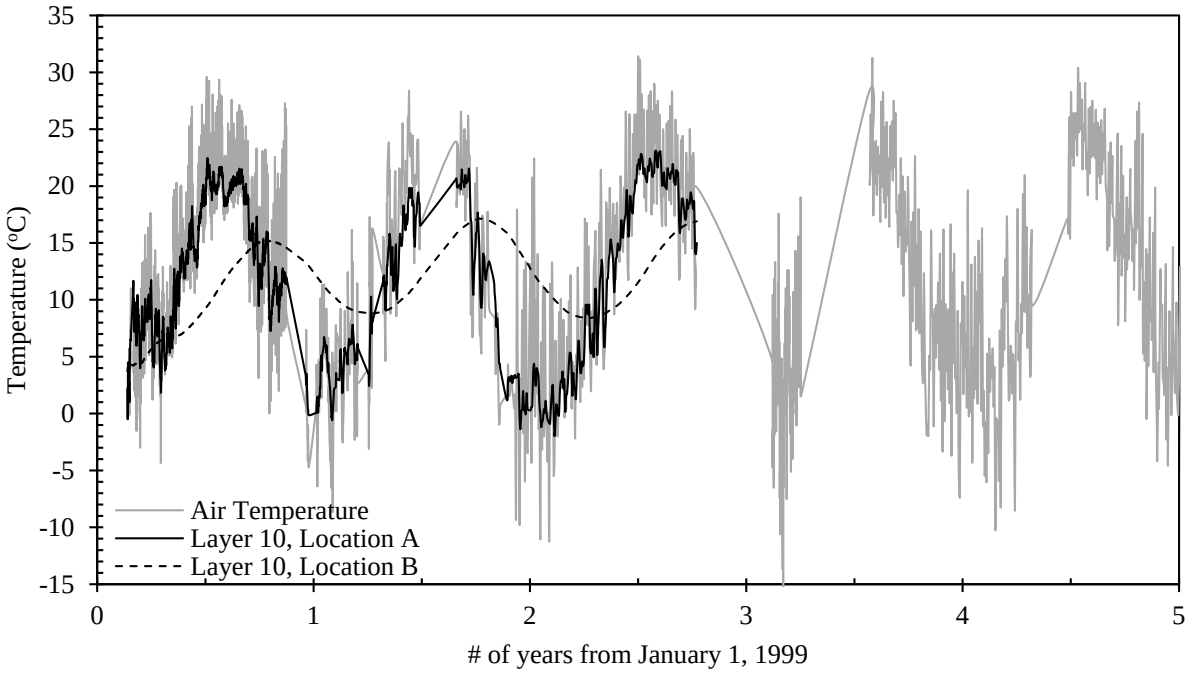

Figure 4.5.14. Temperature time history.

4.5.8 MOISTURE MONITORING

Two water content reflectometers were installed under the sleeper foundation (*i.e.*, Location D), which was placed under the expansion joint between the concrete roadway structure and the concrete approach slab. The sensors were placed at Layer 17 (0.5-m (1.6 ft) deep) and Layer 18 (0.1-m (0.3 ft) deep). Figure 4.5.15 shows the moisture time history (gravitational and volumetric water contents) recorded at the two specified locations over five years after construction. The fluctuation in the moisture content was not very high due to dry environment of the bridge location. However, the fluctuation that was observed in the moisture at depth 0.1 m (0.3 ft) was less pronounced at depth 0.5 m (1.6 ft) as shown in Figure 4.5.15. That is, the drainage system placed underneath the approach slab worked efficiently.

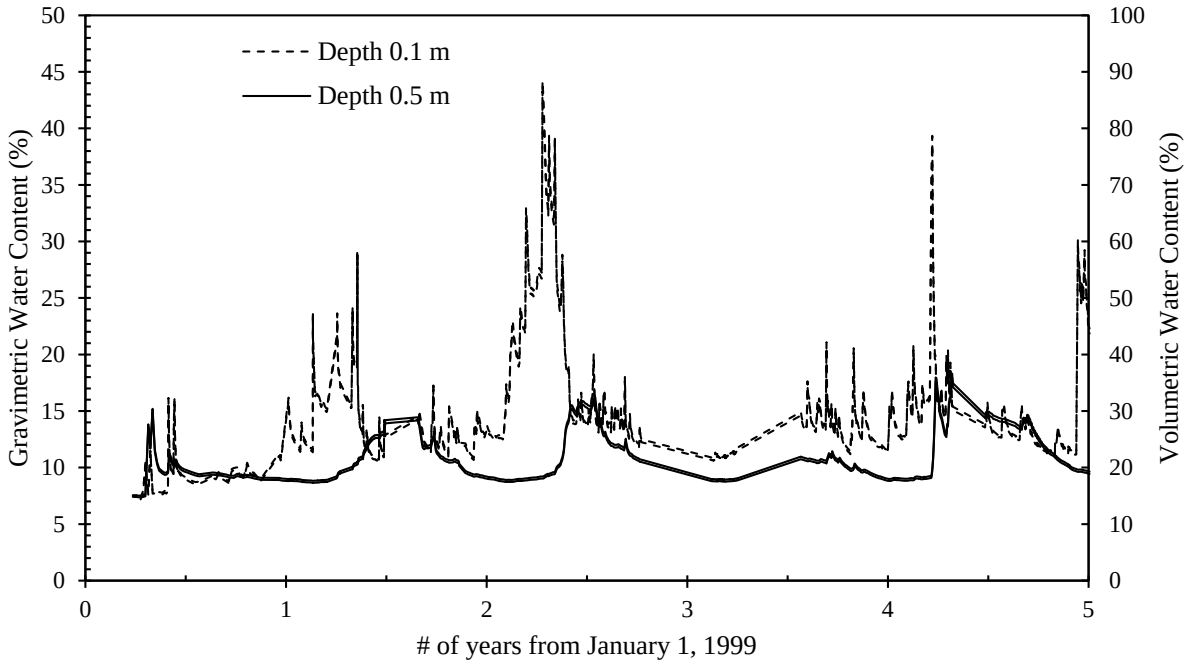

Figure 4.5.15: Moisture time history.

4.5.9 VERTICAL EARTH PRESSURES

Figure 4.5.16 shows average estimated vertical stress increase at the foundation level of the bearing seats and at the base of the geosynthetic reinforced soil mass as the construction progressed. Figure 4.5.17 shows the vertical earth pressure distribution within the geosynthetic reinforced soil mass at Section 800 for different elevations throughout the various bridge construction stages and after the bridge completion and inauguration to traffic. Figure 4.5.17a shows the earth pressure distribution across the base of the geosynthetic reinforced soil mass. At this elevation, only two vertical pressure cells were placed at Locations A and D. The measured stresses showed that the vertical pressure at Location A was higher than that at location D in the early construction stages. This may be attributed to the locked-in compaction induced stresses close to the facing. It was also observed that the rate of increase in the vertical pressure was almost the same at both locations up to construction Stage III. Yet, beyond Stage IV, the vertical pressure at Location A dropped. This can be attributed to the outward lateral movement of the facing after placement of the bridge superstructure. This lateral movement may have released the locked-in stresses behind the facing. The pressure at Location A built up again after Stage V and increased at a similar rate to that at Location D. The vertical pressure measured at Locations A and D maintained constant after the construction completion and until the monitoring has terminated 2.3 years after the traffic was allowed on the bridge. Figure 4.5.17a also shows the estimated earth pressure distribution at layer 0 in accordance to the integration of Boussinesq (1885) solution.

Figures 4.5.17b and 4.5.17c show the vertical earth pressure distribution across the geosynthetic reinforced soil mass at Layers 6 and 10, respectively. It is clear that there was a general increase in the vertical earth pressure across the geosynthetic reinforced soil mass as the construction progressed. The rate of increase in the vertical pressure at location B was observed to be the highest across the geosynthetic reinforced soil mass at both Layers 6 and 10. This observation agrees with the fact that the vertical pressure below the center of the distributed load is the maximum and fades towards the edges. Figures 4.5.17b and 4.5.17c also show the estimated earth pressure distribution at layer 0 in accordance to the integration of Boussinesq (1885) solution. The predicted values consider that the increase in the overburden pressure at Locations C and D upon the construction of the reinforced backfill underneath the roadway approach structure. The figures show a good agreement in regards of the stress values and distribution patterns. Accordingly, the measured vertical earth pressure was extrapolated from Location A to the facing (over a distance of 0.6 m (2 ft)) by subtracting the difference in vertical stress estimated by the integration of Boussinesq (1885) solution. Note that two pressure cells were placed at Location B on both Layers 6 and 10. The pressure cells showed very consistent and similar data for both layers; the data plotted is the average of the data recorded by each couple of sensors for the different layer. The vertical pressure measured beneath the footing was recorded by all sensors maintained constant after the construction completion and until the monitoring has terminated 2.3 years after the bridge inauguration to traffic.

A reverse trend in the vertical earth pressure was observed close to the facing for both Layers 6 and 10. The vertical earth pressure at Location A increased throughout the construction stages up to Stage IV. Then, following Stage IV, a reduction was observed in the vertical pressure. This may be attributed to the increase in the outward movement of the facing, which was clear beyond Stage IV. In addition, the down-drag force on the facing units may have contributed in the initial increase in the earth pressure readings in the early construction stages. Abu-Hejleh et al. (2001a) reported that the high pressure recorded behind the facing for Layers 0 and 6 could be attributed to the down-drag force. This down-drag force is induced by friction between the backfill material and the back surface of the facing units (Buttry *et al.* 1996; Hatami and Bathrust 2006). This down-drag force was mobilized during compaction and caused a higher pressure at Location A than at Location C resulting in some eccentricity at Layers 6 and 10. Hatami and Bathrust (2006) reported that generally there is a local reduction in the vertical earth pressure immediately behind the facing. This observation agrees with the behavior shown by the Founders/Meadows Bridge abutment. Helwany *et al.* (2003) conducted a numerical study on the Founder/Meadows Bridge abutment and reported predicted pressure values similar to the measured pressure at Layers 6 and 10. Fakharian and Attar (2007) argued that the drop in vertical earth pressure behind the facing at Layer 6 was illogical and due to instrumentation and monitoring problems. However, this argument is not valid as the same trend was encountered in all of the instrumented layers. Zheng et al. (2015) reported that the large lateral movement occurring during Stage V caused a drop in the lateral and vertical earth pressures near the facing (*i.e.*, at Location A).

As the construction progressed, settlement and outward facing movement may have relieved the down-drag force, and thus reduced the vertical earth pressure behind the facing. In addition,

Abu-Hejleh *et al.* (2001a) reported that the wall system might be rigid during winter and that deformations occurred mainly during the warm seasons. These deformations reduced the frictional down-drag force (Buttry *et al.* 1996) and also reduced the lateral earth pressure. Based on those studies, it can be concluded that as construction advanced, and the load increased, reinforcement layers started to strain allowing the facing units to move and reducing the pressure behind them. In turn, the pressure could have diffused inwards to the rest of the layer due to soil arching. This happened when the load increased enough to strain the reinforcement where the reinforcement strain rate increased after Stage IV (will be discussed later). Note that the reinforcement strains in Stage I occurred during backfill placement and compaction (before considerable pressure was applied). The load distributed uniformly over the layer with a rise behind the facing units. This can be attributed to soil arching as blocks were more confining than the retained native soil during the early construction stages and until the reinforcement strained. The drop in the readings of the strain gages at location A implies that these gauges were compressed. While this compression implies that the localized reinforcement strain decreased; however, the integration of the strain over the length of the reinforcement confirms that the total outward movement increased. McGown *et al.* (1998) reported that if the lateral boundary of the wall is not allowed to yield, the resulting pressure will equate or exceed that obtained under at-rest conditions (upper limit). On the contrary, if the lateral boundary of the wall is allowed to yield sufficiently to mobilize a large tensile resistance in the reinforcement, and if the required forces and available forces balance, theoretically there should be no lateral earth pressure acting on the wall (lower limit). However, even in the case of the lower limit, the soil masses between the reinforcing layers may have a tendency to produce localized stresses near the facing. These stresses develop because each soil layer acts separately causing the wall to be subjected to active horizontal pressure over the depth of the layer.

Figure 4.5.17d shows the vertical earth pressure across the GMSE below the concrete foundation. The pressure distribution is similar to that observed from the other layers in the early construction stages. Beyond Stage III, a different pressure distribution was observed, where the pressure increased below the edges of the foundation to be more than the pressure below the center. This pressure distribution is typical for rigid foundations on compacted granular soils. Boussinesq (1885) solution was not plotted for this layer since it assumes flexible foundation, which is not the case in this layer. Helwany *et al.* (2003) reported higher predicted pressure values than the measured pressure underneath the bridge footing. However, the predicted pressure values at lower elevations were in a good match with the measured ones. Note that the predicted data they reported showed that the pressure decreases towards the facing, which contradicts the measured data. They attributed that soil arching might be one of the reasons for the difference between predicted and measured soil pressure underneath the bridge footing. Abu-Hejleh *et al.* (2000b) suggested that the vertical pressure distribution had no overturning potential. They attributed this to the flexibility of the reinforced soil structure which redistributed the overturning stresses. The vertical pressure measured beneath the footing was recorded by all sensors maintained constant after the construction completion and until the monitoring has terminated 2.3 years after the bridge was opened to traffic.

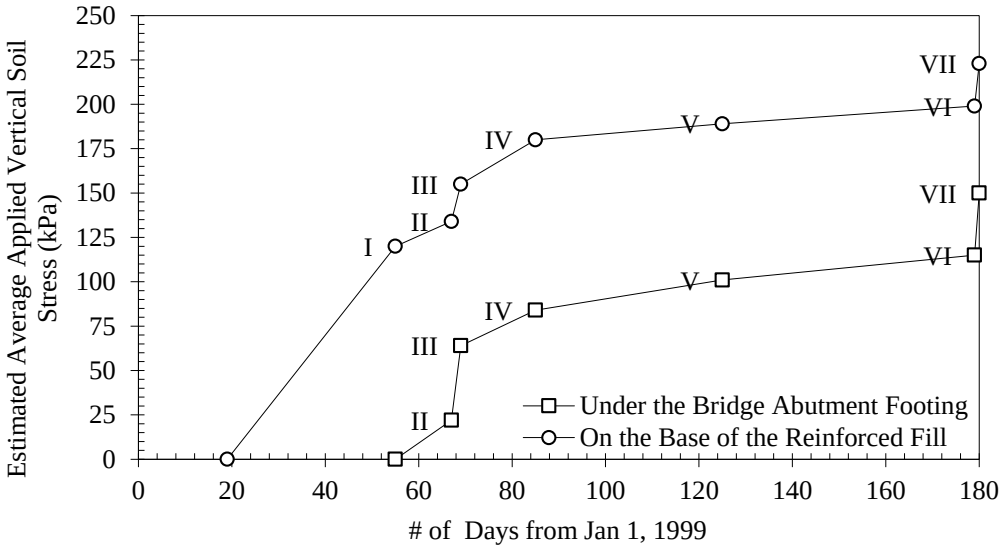

Figure 4.5.16. Estimated vertical stress increase under the bridge footing and at the base of the reinforced fill through the various construction stages

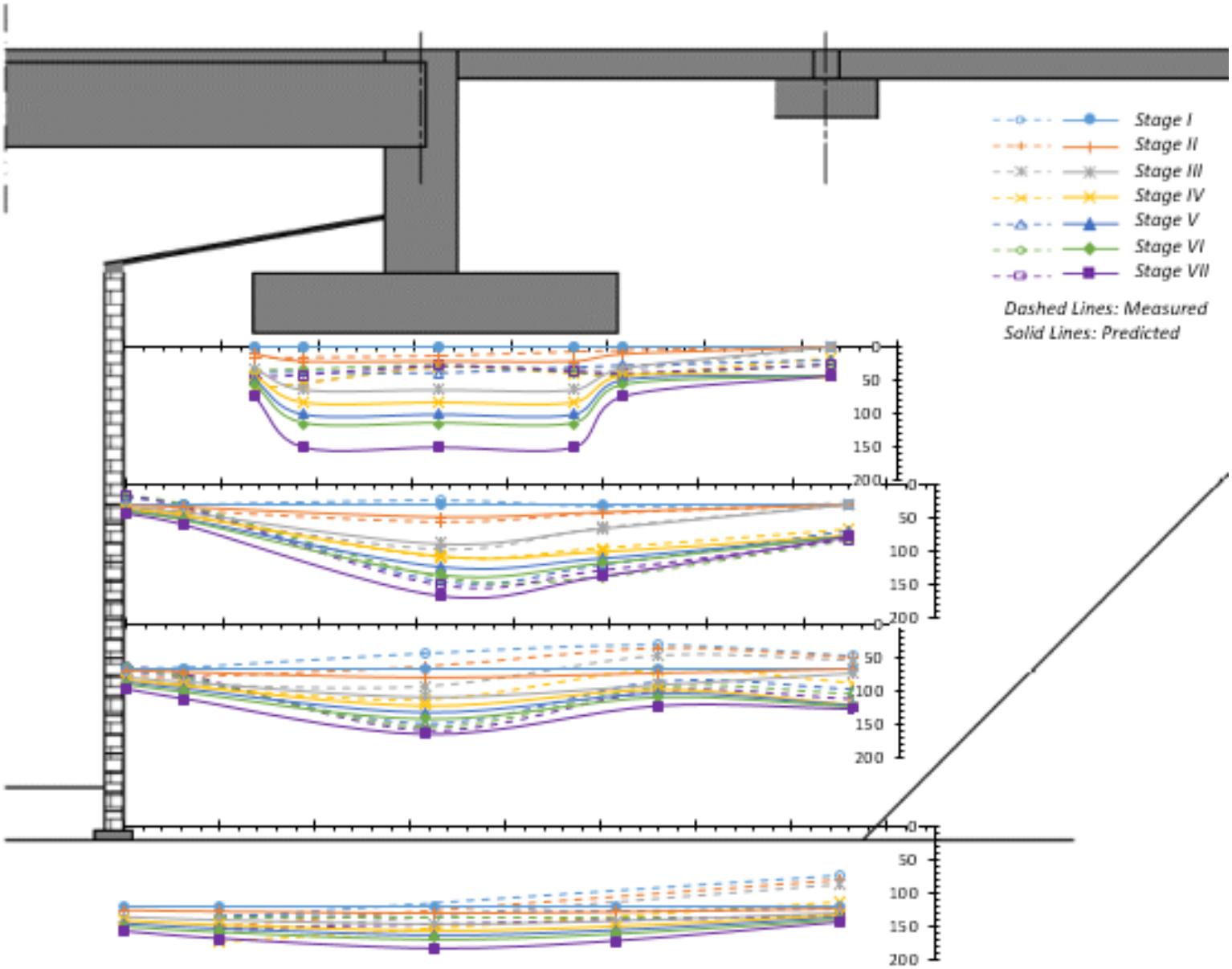
Stage I
Stage II
Stage III
Stage IV
Stage V
Stage VI
Stage VII
Dashed Lines: Measured
Solid Lines: Predicted
0
50
100
150
200

(a)

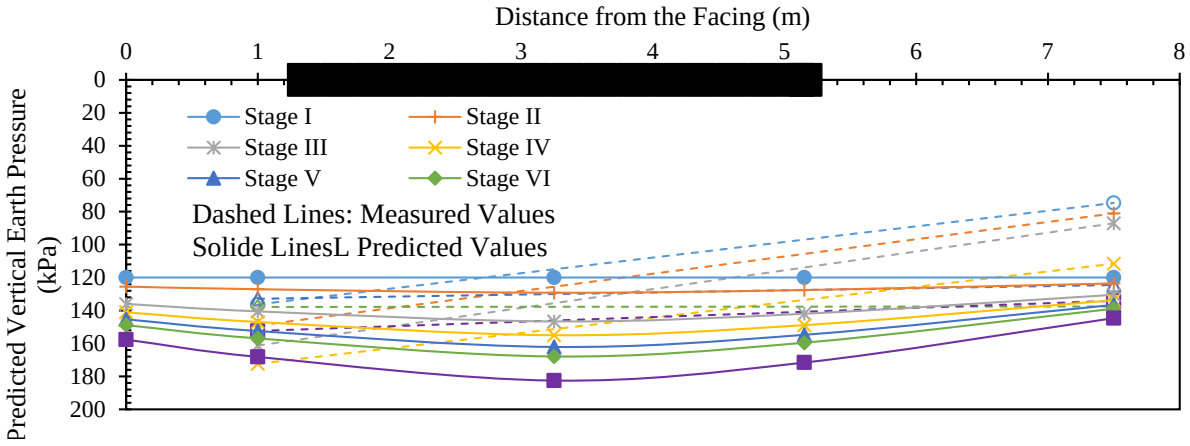
Distance from the Facing (m)
Predicted Vertical Earth Pressure (kPa)
Stage I
Stage II
Stage III
Stage IV
Stage V
Stage VI
Dashed Lines: Measured Values
Solide LinesL Predicted Values

(b)

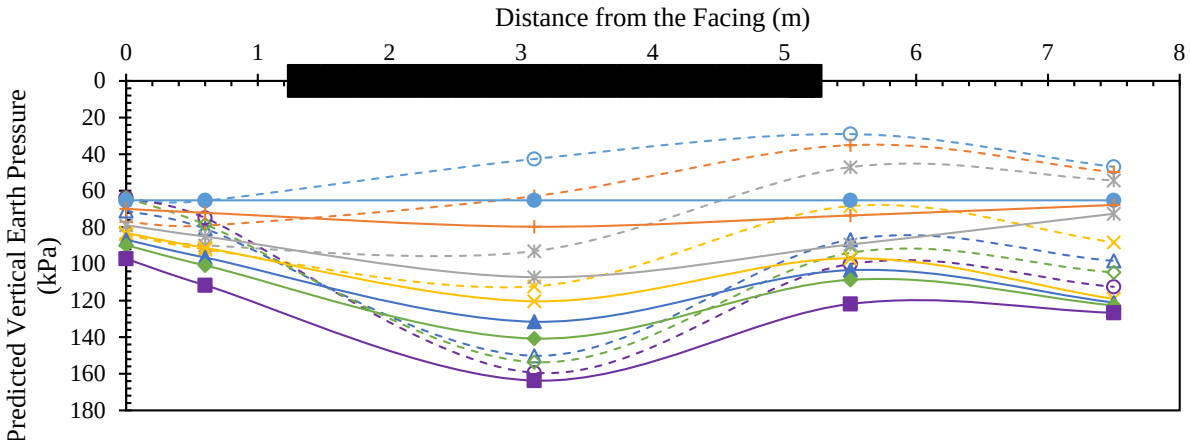
Distance from the Facing (m)
Predicted Vertical Earth Pressure (kPa)

(c)

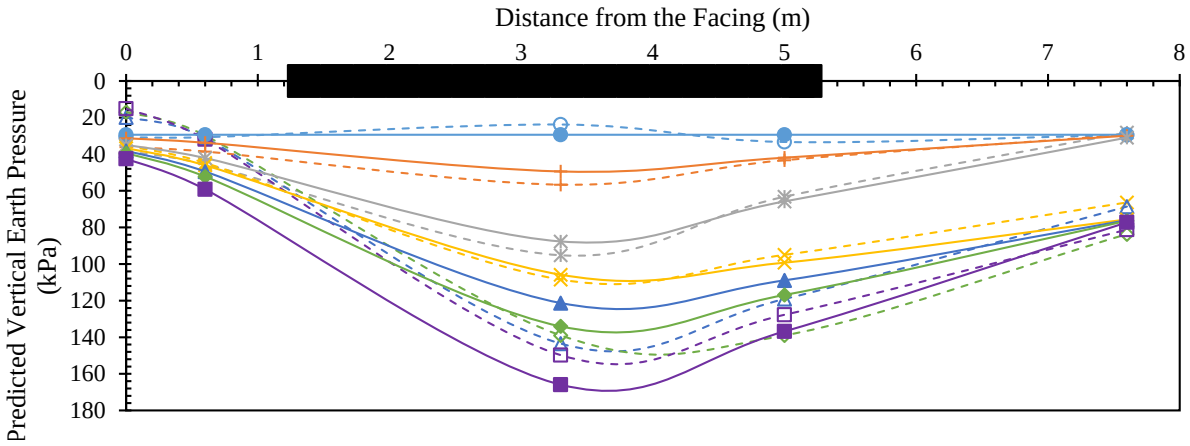
Distance from the Facing (m)
Predicted Vertical Earth Pressure (kPa)

(d)

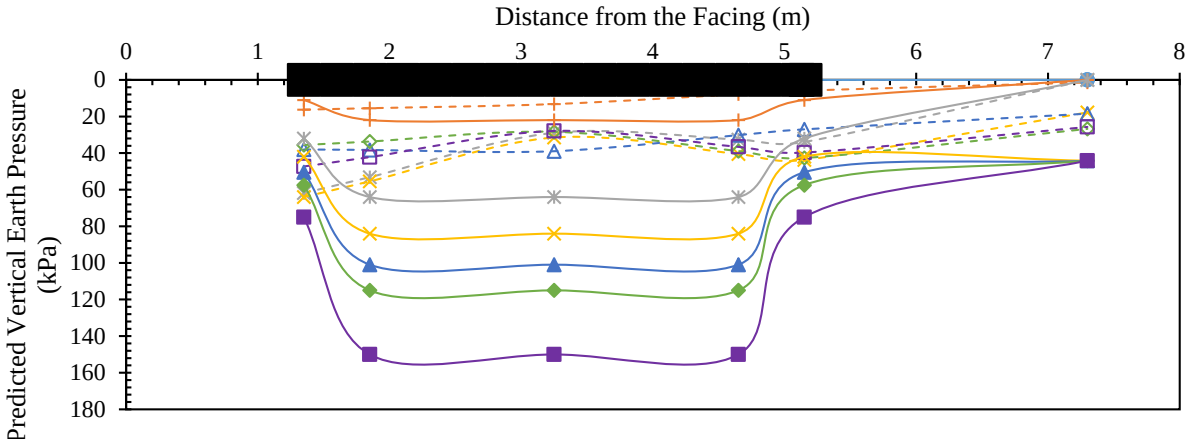

Figure 4.5.17. Vertical earth pressure across the front GMSE structure: (a) at the base of the reinforced soil (layer 0); (b) between reinforcement layers 6 and 7; (c) between reinforcement layers 10 and 11; (d) between reinforcement layers 13 and 14 (at the foundation level of the abutment footing).

4.5.10 LATERAL EARTH PRESSURES

The lateral earth pressure was monitored on the back side of the facing and the backside of the concrete abutment wall throughout the various construction stages and after the bridge was opened to traffic. The lateral pressure was monitored at Section 800 at Layers 7, 9, 11, and 12 (on the facing of the front GMSE abutment), and at Layers 16 and 19 (on the backside of the concrete abutment wall). Note that two pressure cells were placed at Layers 11 and 19; while pressure cells at Layer 11 showed very consistent and similar data, one of the pressure cells at Layer 19 was faulty. Subsequently, the lateral pressure plotted for Layer 11 resulted from the average of data recorded by its both sensors, whereas that plotted for Layer 19 resulted from the data recorded by the proper sensor. Figure 4.5.18 shows the lateral earth pressure on the front GMSE abutment facing during the various construction stages. The lateral earth pressure is much less than the estimated stresses by solutions derived from Rankine (1857), Boussinesq (1885), Scott (1963), or NAVFAC (1986) for conventional retaining structures.

Figures 4.5.19a and 4.5.19b show the long-term lateral earth pressure on the front facing of the GMSE abutment and on the concrete abutment wall, respectively. The figures shows the lateral earth pressure every half a year from 1 January 1999. Note that the construction of the bridge was completed and traffic was allowed to bridge in 30 June 1999 (*i.e.*, after half a year and at the end of Stage VI). The figure shows a significant fluctuation in the lateral earth pressure that is very consistently synchronized with the temperature fluctuation (Figure 4.5.14). During the warm seasons (Stage VI and Stage VII 1.5, 2.5, 3.5, and 4.5 years) the bridge superstructure tended to expand pushing the concrete bearing seats against the backfill. On contrary, during the cold seasons (Stage VII 1, 2, 3, 4, and 5 years) the bridge superstructure tended to contract releasing the pressure exerted by the concrete bearing seats against the backfill. In addition, during the

cold seasons the backfill tended to freeze which resulted less lateral pressure on the facing. Note that the temperature behind the facing can be represented by the sensor placed behind the facing whose recorded time history is presented in Figure 4.5.14. The seasonal fluctuation in temperature is very consistent with the air temperature. In addition, the backfill used in the GMSE abutment had a considerable amount of fines (10.6%) that can hold water until it freezes. Also, Figure 4.5.15 shows a consistent presence of water in the geosynthetic reinforced soil mass. Note that the pressure cells reduced data considered temperature in accordance with the manufacturer datasheet. In addition, no fluctuation was observed for the vertical pressure cells, which were exposed to the same temperature alterations. The fluctuation in the lateral pressure was more pronounced on the abutment concrete wall than the front facing of the GMSE abutment since it is directly connected to the bridge superstructure.

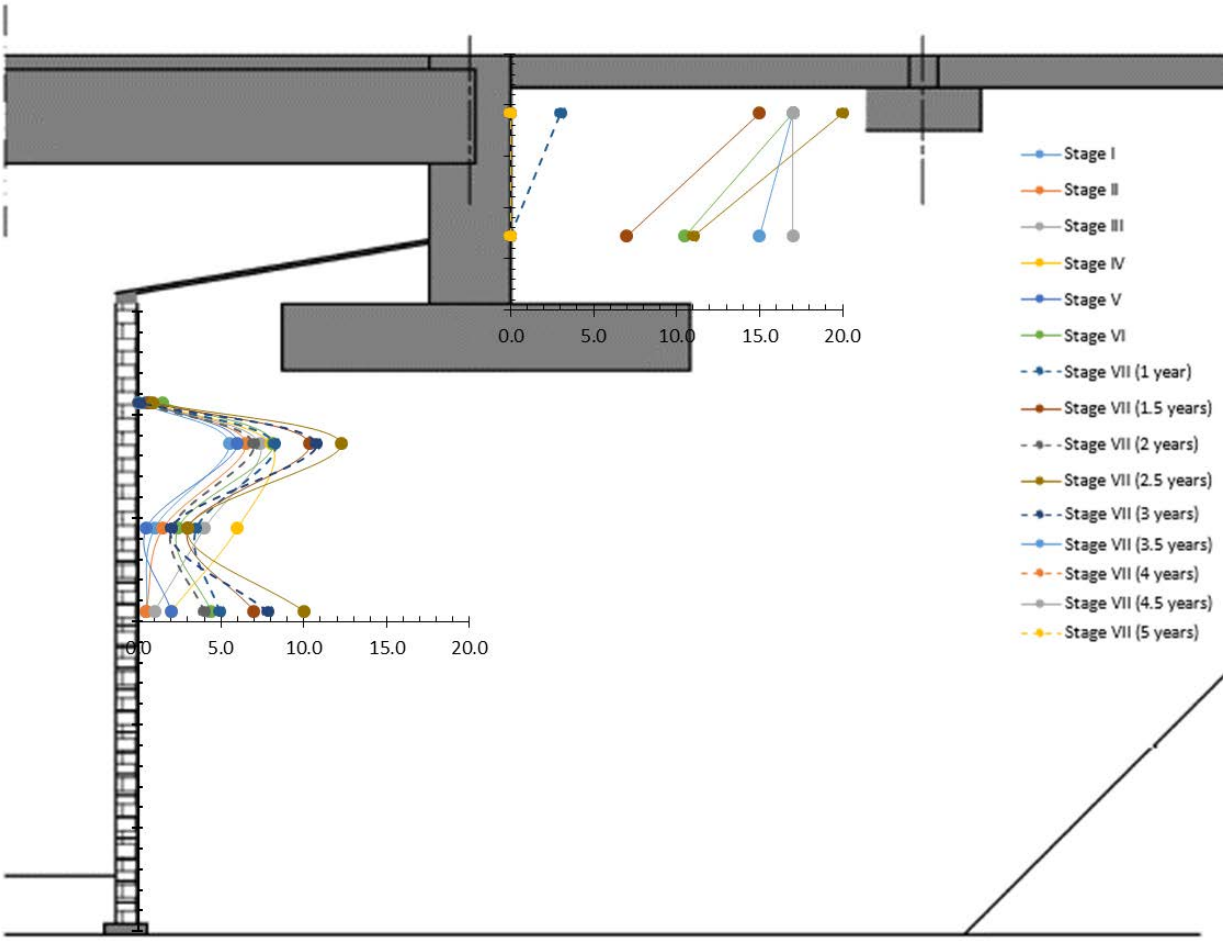

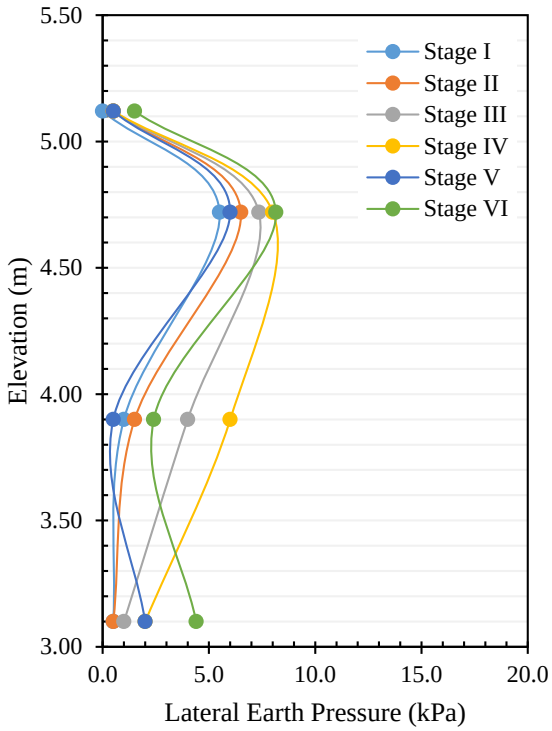

Figure 4.5.18. Measured lateral earth pressure on the front facing of the GMSE abutment during construction.

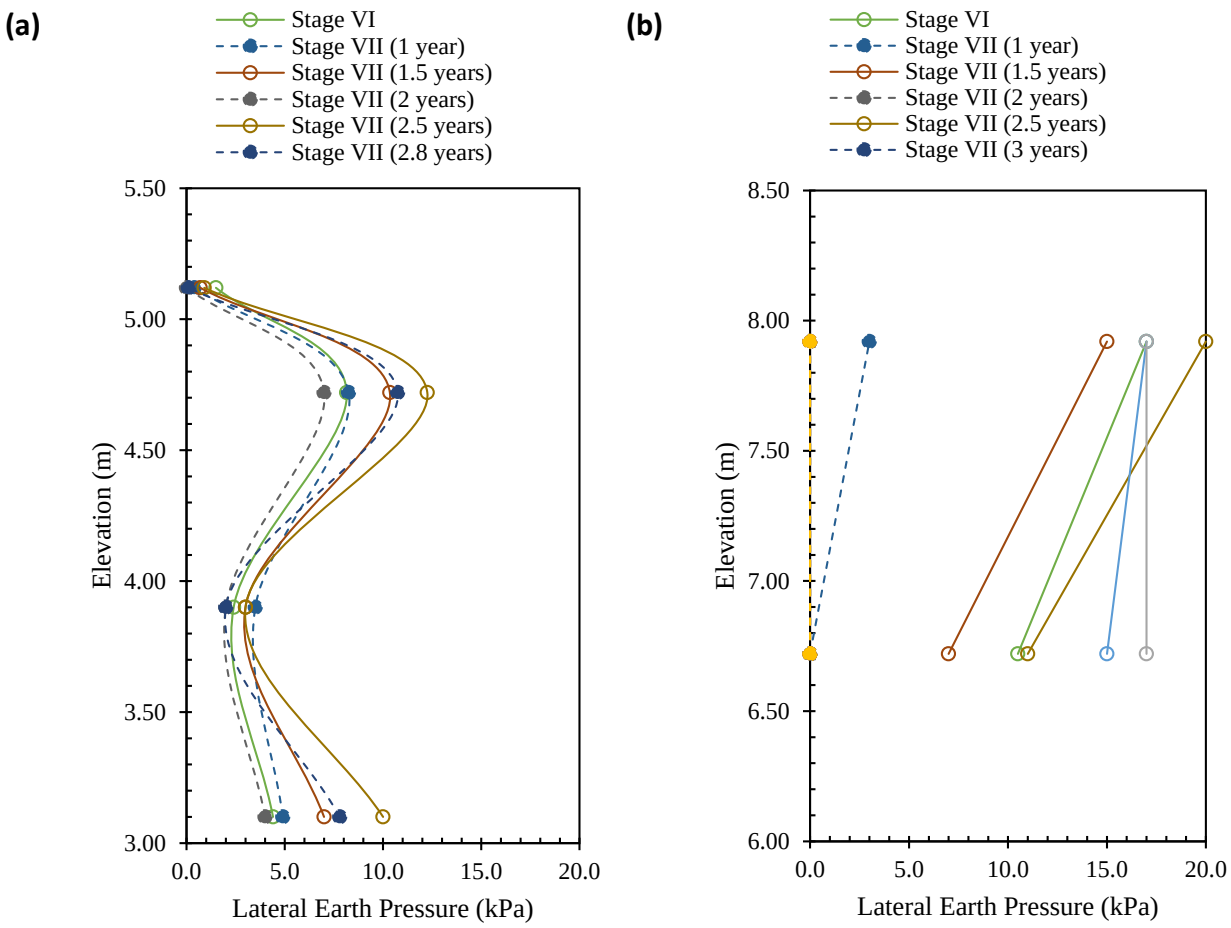

Figure 4.5.19. Measured lateral earth pressure after construction completion: (a) on the front GMSE wall facing; (b) on the concrete abutment wall.

4.5.11 REINFORCEMENT STRAINING

Figure 4.5.20 shows the reinforcement strains measured by the strain gauges along the reinforcement length across the front facing of the GMSE abutment at Section 800 for different reinforcement layers. Large reinforcement strains were recorded at all locations during Stage I. This can be attributed to the compaction effect and the compaction induced stress that might have stretched the reinforcement while the normal pressure on the reinforcement was negligible. Abu-Hejleh *et al.* (2001a) reported that 50% of the reinforcement strains developed during the backfill placement and compaction stage (Stage I). Abu-Hejleh *et al.* (2000b) explained that the sharp increase in the reinforcement strains in Stage I were possibly because of the locked-in strains. McGown *et al.* (1998) reported that locked-in strains can happen during compaction where the soil particles are forced into the reinforcement apertures causing straining that will be locked-in after the compaction ends. Locked-in strains have a similar effect to a confining stress on the soil (i.e. they increase the strength of the soil and reduce lateral earth

pressure). Abu-Hejleh *et al.* (2001a) suggested that the compaction methodology, construction season, and construction sequence may affect the deformations in the structure. Abu-Hejleh *et al.* (2002) reported that these large movements during Stage I were due to (1) soil compaction, (2) low confining pressure, and (3) reinforcement wrinkles.

Figure 4.5.20a shows the reinforcement strains along Layer 2 throughout the various construction stages. Three strain gages were installed at this layer: one at Location A, one at Location B, and one at Location C. The reinforcement strain recorded at Location A was greater than that recorded at Location B while the strains at Location D was the least. The same trend was observed during the construction stages. This might be due to the effect of the side boundary where Location D is close to a lateral confined mass and Location A is closer to a laterally open to displacement mass. The reinforcement strain increased as the construction advanced and the vertical load at the reinforcement layers increased. Note that the reinforcement strain at Location A (*i.e.*, close to facing) dropped at Stage IV. This was due to the drop in the vertical pressure at the same location. Reinforcement strain was measured after construction every half a year and up to 1.5 years after bridge construction completion; however, data is available only at Location D.

Figure 4.5.20b shows the reinforcement strains along Layer 6 throughout the different construction stages. Four strain gages were installed at this layer: one at Location A, two at Location B, and one at Location C. It can be inferred that the strains at Location A are greater than the strains at Location C. This can be attributed to the side boundary, which is confined at Location C (inwards) and open to displacement at Location A (outwards). In addition, the strain accumulates to the open side of the structure which forces the movement outwards. At Location B, the strains increased with loading in which the reinforcement is expected to bow downwards at all times (Figure 4.5.17b) increasing the tensile stresses in the reinforcement. The reinforcement strain at Location C did not show a significant increase throughout the various construction stages except during Stage I. This can be attributed to the confinement of this zone, which has restricted the soil movement unlike Location A. Reinforcement strain was measured every half a year and up to 4 years after bridge construction completion (4.5 years from 1 January 1999). Figure 4.5.20b shows very slow rate of strain increase was observed during the long-term monitoring. Note that Figure 4.5.20b was reported in Abu-Hejleh *et al.* (2002) at an early stage of monitoring. However, after 4.5 years of monitoring it was realized from the time history that the strain data plotted for Location B was for a faulty strain gage. Consequently, the data plotted for Location B herein is from the other strain gage, which worked properly over the entire monitoring program.

Figure 4.5.20c shows the reinforcement strain along Layer 10 throughout the different construction stages. Four strain gages were installed at this layer: one at Location A, one at Location B, one at Location C, and one at Location D. In general, the trend is very similar to that observed for Layers 2 and 6, where the reinforcement strains at Location A are higher than the strains at Location D. This observation is similar to that of Layers 2 and 6, which strengthens the argument mentioned earlier on the lateral confinement effect. The reinforcement strain increased as construction progressed; however, a drop in the strain was observed at Location A

after Stage IV, upon adding the bridge superstructure. This is consistent with the drop in the vertical pressure at the same location and at the same construction stage. A similar trend has been observed in Kongkitkul *et al.* (2008) in which a drop in the reinforcement strain occurred upon construction completion. Abu-Hejleh *et al.* (2002) reported that the outward displacement at Layer 10 was higher than that of Layer 6. They attributed this to the increase in the width of the active zone combined with the elevation from the base of the reinforced mass. The active zone is defined by the locus of maximum tension in the reinforcement layer. They attributed movements during Stage VII to traffic loads, creep under constant applied load, and seasonal changes. Reinforcement strain was monitored every half a year and up to 4 years after bridge construction completion (4.5 years from 1 January 1999) and traffic was allowed on the bridge. It was observed that the strain increased at a very low rate. Note that Figure 4.5.20c was reported in Abu-Hejleh *et al.* (2002) at an early stage of monitoring. By the end of the 4.5-year monitoring program it was realized that the strain gage at Location C was faulty; subsequently, its data was discarded herein.

Figure 4.5.20d shows the reinforcement strain along Layer 12 (close to the concrete bearing seat foundation level) throughout the various construction stages. The reinforcement strains recorded only at Locations B and D; the strains recorded at Location B were greater than those recorded at Location D. This happened during Stages III and IV in which the vertical stresses at Location B was higher than that at Location D. However, after Stage IV the vertical stresses at both Locations B and D were close resulting in similar reinforcement strains. Reinforcement strain was monitored every half a year and up to 4 years after bridge construction completion (4.5 years from 1 January 1999) and traffic was allowed on the bridge.

Figure 4.5.20e shows the reinforcement strain along Layer 16 behind the concrete abutment wall and below the sleeper of the approaching roadway structure (*i.e.*, from Location C to Location D) throughout the various construction stages. Two strain gages were installed at this layer; one gage at each of Location C and Location D. Although a lower vertical pressure was applied on this portion than on the other portions of the geosynthetic reinforced soil mass, the reinforcement experienced some strains. This is due to the reinforcement used in this area (UX3 for Layer 16) was of lower stiffness than the reinforcement used in below the bearing seat foundation level (UX6). In addition, the presence of the flexible polystyrene sheet that was placed behind the concrete abutment wall to alleviate the lateral earth pressure exerted on the abutment wall. This flexible sheet may have allowed movement of the reinforced fill behind the abutment wall. The reinforcement stain was almost uniform over the portion between location C and location D. Yet, as construction advanced the strain at Location D increased after the construction of the sleeper foundation, which is located at Location D.

It was observed from the time history of the strain gauges that the rate of strain increase during the cold seasons was higher than that in the warm seasons. This effect was more pronounced at the top layers (strain gauges placed at Layers 12 and 16), which are close to the surface and more susceptible to temperature changes as discussed earlier. This caused apparent strain fluctuation of approximately 0.05%. The readings from these gauges were corrected to negate the effect of temperature changes on the strain gauges.

Andraws and Yogarajah (1994) compared the stiff and flexible facing connections. They reported that the stiff connection causes a linear tensile strain distribution along the reinforcement with maximum strains close to facing. In contrast, the flexible connection results in a maximum tensile strain far from the facing and results in a larger shear resistance mobilized in soil resulting in reduced lateral pressure on the facing units. This indicates that the behavior of the facing connections of the lower layers was more rigid than that of the upper layers. In addition, this explains why the vertical earth pressure behind the facing is higher at lower layers than that at upper layers. Also, Tatsuoka (1992) showed that the higher the connection strength, the higher the tensile stresses in the reinforcement near the facing. The distribution of the tensile stresses idealized by Tatsuoka (1992) for the no-connection strength showed that the stresses increase from the facing to the boundary of the unstable zone then decays towards the end of the reinforcement. On the other hand, the idealized distribution for the high-strength connection showed that the stresses is high over the entire unstable zone then decays towards the end of the reinforcement. The difference in the reinforcement strain distribution between Layer 10 and Layers 6 and 2 (see Figures 4.5.20a through 4.5.20c) implies that the facing connection near Layer 10 was weaker than that at Layers 6 and 2 with respect to their applied load. This is due to the higher lateral pressure at Layer 10 in comparison to Layer 6 (and most possibly Layer 2) as shown in Figure 4.5.18. It was observed that in maximum strain in Layer 10 was close to the facing during construction stages and then was shifted inwards. Similar observation was made by Bathrust et al. (2006) for segmental walls.

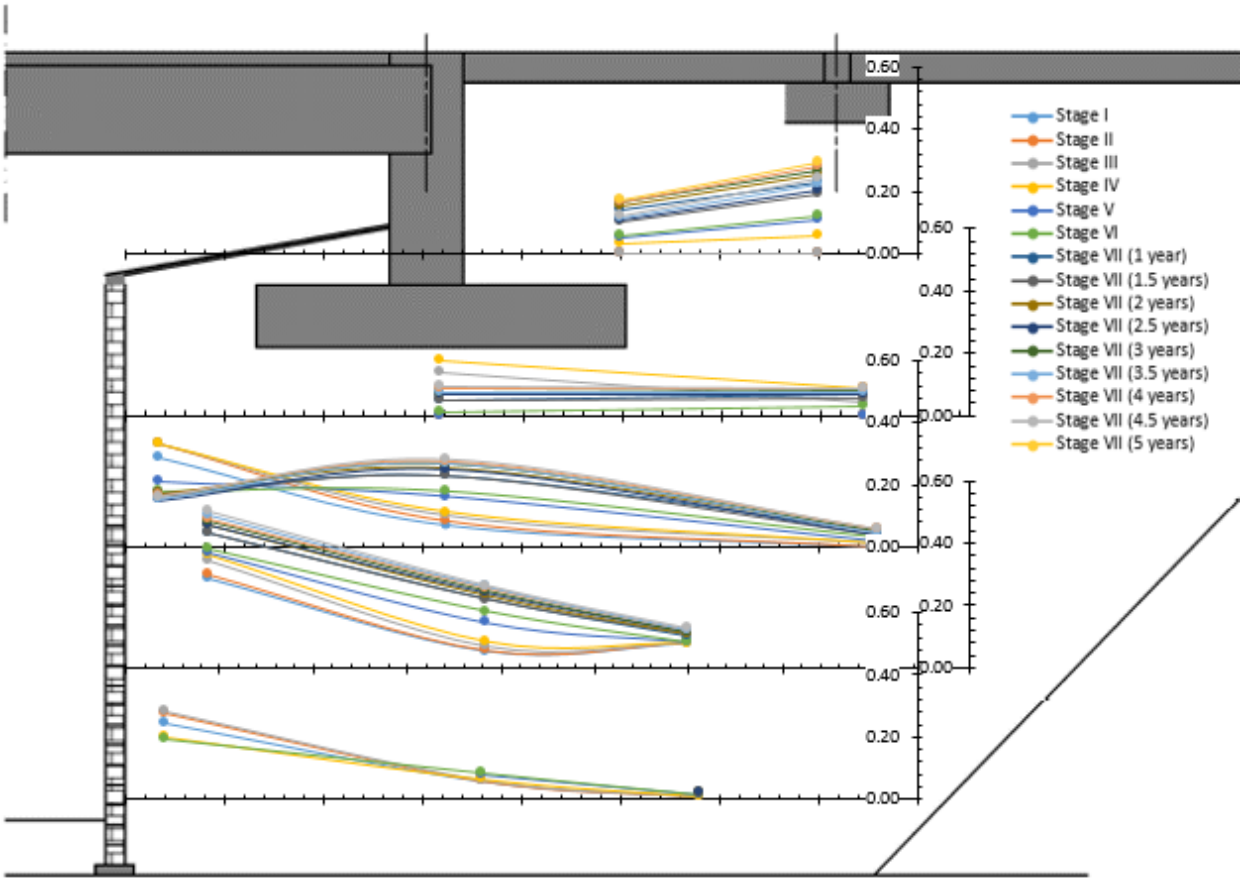
0.60
0.40
0.20
0.00
Stage I
Stage II
Stage III
Stage IV
Stage V
Stage VI
Stage VII (1 year)
Stage VII (1.5 years)
Stage VII (2 years)
Stage VII (2.5 years)
Stage VII (3 years)
Stage VII (3.5 years)
Stage VII (4 years)
Stage VII (4.5 years)
Stage VII (5 years)

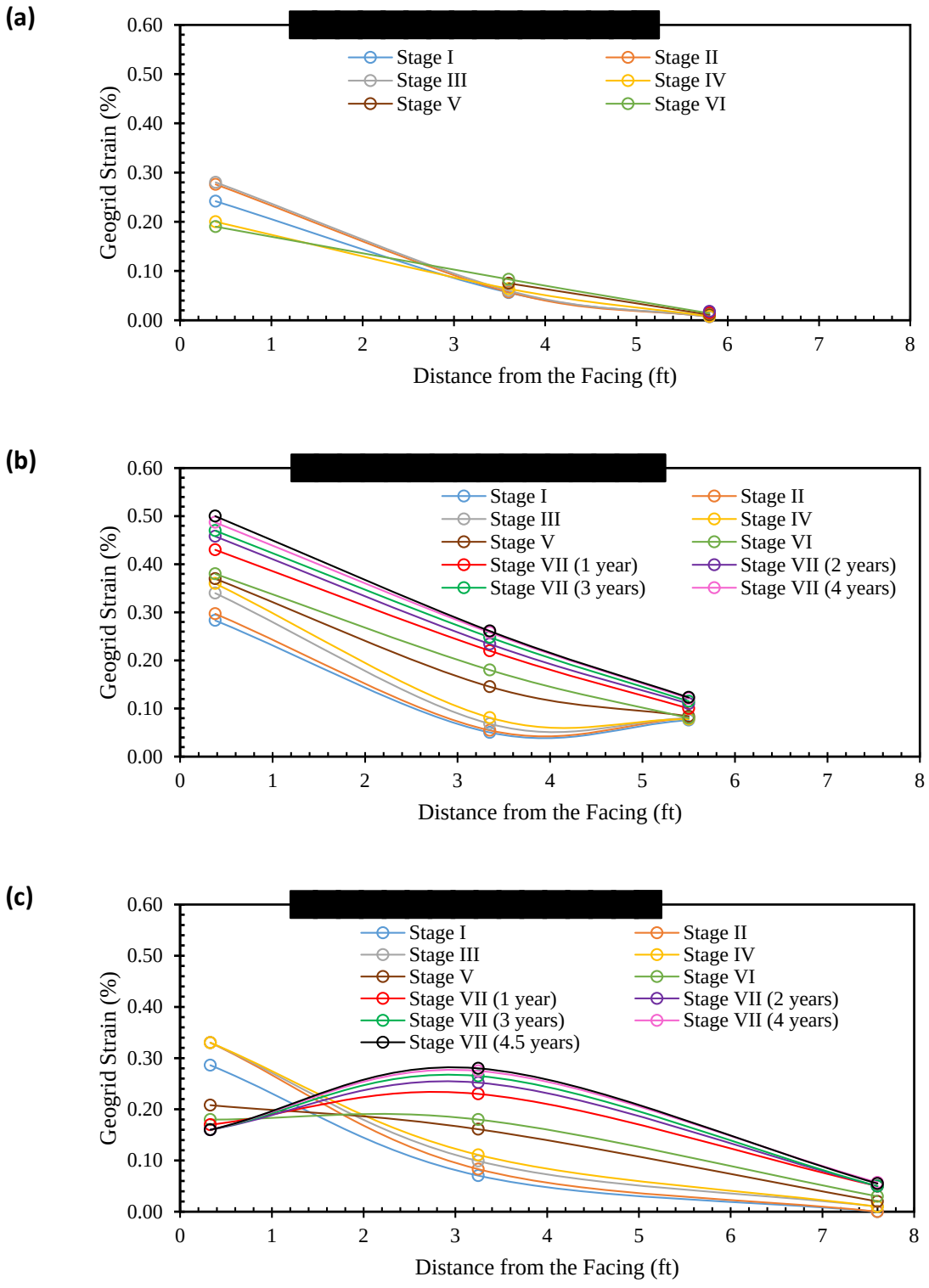

Figure 4.5.20. Measured reinforcement strain across the front facing of the GMSE abutment: (a) at reinforcement layer 2; (b) at reinforcement layer 6; (c) at reinforcement layer 10; (d) at reinforcement layer 13; and (e) at reinforcement layer 16. (continued)

(d)

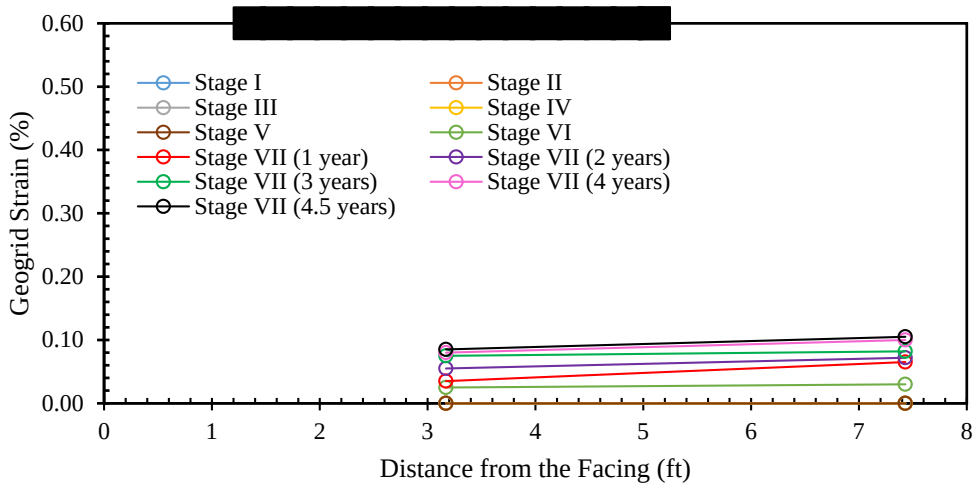

(e)

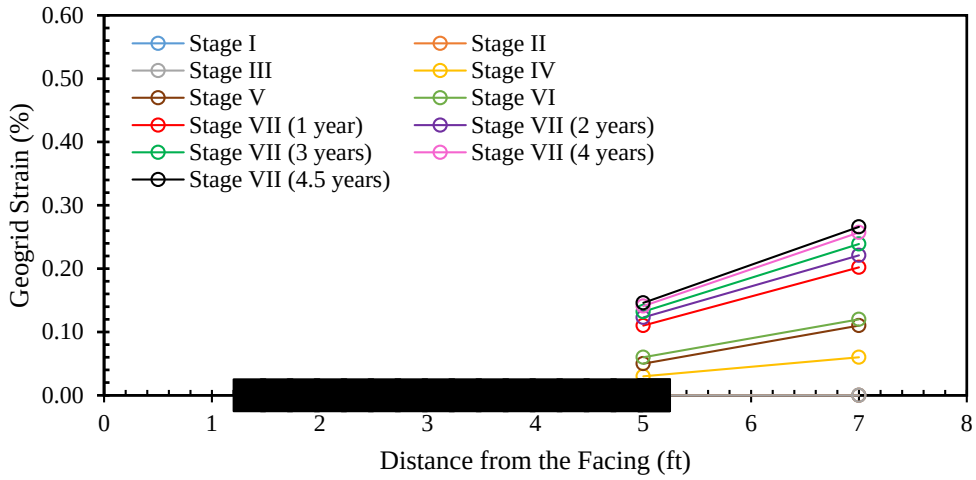

Figure 4.5.20. Measured reinforcement strain across the front facing of the GMSE abutment: (a) at reinforcement layer 2; (b) at reinforcement layer 6; (c) at reinforcement layer 10; (d) at reinforcement layer 13; and (e) at reinforcement layer 16. (continued)

4.5.12 CONCLUSIONS

While the use of load-carrying GMSE abutments in supporting bridges has been recently recognized, their use is limited to the small low-traffic bridges due to the lack of understanding of their behavior. This report revisits the performance data of the Founders/Meadows bridge case study, which is considered a major inspiration for the evolution of this technology in the United States of America. The study aimed to provide better understanding of the behavior of the GMSE abutments. The evaluation of the data led to the following conclusions on the GMSE bridge abutments:

- The GMSE structure might be rigid during cold seasons and subsequent deformations occur mainly during warm seasons.
- The lateral earth pressure on the abutment facing is susceptible to seasonal temperature variation due to superstructure expansion and contraction.
- As construction advances and the load increases reinforcement layers strain allowing the facing to move. This results in a reduction in the vertical earth pressure behind the facing. In turn, the pressure transfers inwards to the rest of the layer due to soil arching.
- The vertical earth pressure distribution showed no overturning potential as the overturning stresses redistribute due to the flexibility of the reinforced soil structure.
- A significant portion of the total reinforcement strains takes place during the backfill placement and compaction. This happens because of the locked-in strains where the soil particles are forced into the reinforcement apertures causing strains. These strains will remain locked-in after the compaction ends. Note that Founders Meadows abutment used geogrid reinforcements.
- The compaction methodology, construction season, and construction sequence may affect the deformations occur to the structure.

4.5.13 REFERENCES

Abu-Hejleh, N., Wang, T., and Zornberg, J.G. (2000b). "Performance of Geosynthetic-reinforced Walls Supporting Bridge and Approaching Roadway Structures." *Geotechnical Special Publication*, pp. 218-243.

Abu-Hejleh, N., Zornberg, J.G., Elias, V., and Watcharamonthein, J. (2003). "Design Assessment of the Founders/Meadows GRS Abutment Structure." In *Proceedings of the 82nd Annual TRB Meeting*.

Abu-Hejleh, N., Zornberg, J.G., Wang, T., and McMullen, M. (2000a). *Performance of Geosynthetic-Reinforced Walls Supporting the Founders/Meadows Bridge and Approaching Roadway Structures*. Colorado Department of Transportation Report No. CDOT-DTD-R-2000-5.

Abu-Hejleh, N., Zornberg, J.G., Wang, T., and McMullen, M. (2001a). *Performance of Geosynthetic-Reinforced Walls Supporting the Founders/Meadows Bridge and Approaching Roadway Structures*. Colorado Department of Transportation Report No. CDOT-DTD-R-2001-13.

Abu-Hejleh, N., Zornberg, J. G., and Wang, T. (2001b). "Monitored Displacements of a Unique Geosynthetic-Reinforced Walls Supporting Bridge and Approaching Roadway Structures." In *TRB annual meeting*.

Abu-Hejleh, N., Zornberg, J.G., Wang, T., and Watcharamonthein, J. (2002). "Monitored Displacements of Unique Geosynthetic-reinforced Soil Bridge Abutments." *Geosynthetics International*, *9*(1), 71-95.

Abu-Hejleh, N., Hanneman, D., White, D. J., Wang, T., and Ksouri, I. (2006). *Flowfill and MSE Bridge Approaches: Performance, Coast, and Recommendations for Improvements*. Colorado Department of Transportation Report No. CDOT-DTD-R-2006-2.

Adams, M. and Nicks, J. (2015). “Comparison of GMSE and GRS Design Methodology.” In *Proceedings of Geosynthetics 2015*, February 15-18, Portland, Oregon.

Andrawes, K.Z., and Yogarajah, I. (1994). “Effects of Reinforcement Connections on the Behaviour of Reinforced Soil Retaining Walls.” *Computer Methods and Advances in Geomechanics*, Vol. 2, pp. 1313-1318.

Bathurst, R.J., Vlachopoulos, N., Walters, D.L., Burgess, P.G., and Allen, T.M. (2006). “The Influence of Facing Stiffness on the Performance of Two Geosynthetic Reinforced Soil Retaining Walls.” *Canadian Geotechnical Journal*, Vol. 43, No. 12, pp. 1225-1237.

Boussinesq, M.J. (1885). “Application des potentiels a l'etude de l'equilibre et du movement des solides elastiques, principalement au calculations des deformations et des pressions que produisent, dans ces solides, des efforts quelconques exerces sur une petite partie de leur surface ou de leur interieur: Memoire suivi de notes etendues sur divers points de physique mathematique et d'analyse,” *GauthierVillars*, Paris, pp. 722. (In French).

Buttry, K., McCullough, E., and Wetzel, R. (1996). “Temperatures and Related Behavior in Segmental Retaining Wall System.” *Transportation Research Record: Journal of the Transportation Research Board*, Vol. 1534, pp. 19-23.

CDOT (2014). Annual Average Daily Traffic. Colorado Department of Transportation.

Fakharian, K. and Attar, I.H. (2007). “Static and seismic numerical modeling of geosynthetic-reinforced soil segmental bridge abutments.” *Geosynthetics International*, *14*(4), 228-243.

Hatami, K., and Bathurst, R.J. (2006). “Numerical Model for Reinforced Soil Segmental Walls under Surcharge Loading.” *Journal of Geotechnical and Geoenvironmental engineering*. Vol. 132, No. 6, pp. 673-684.

Helwany, S. M., Wu, J.T., and Froessl, B. (2003). “GRS Bridge Abutments—An Effective Means to Alleviate Bridge Approach Settlement.” *Geotextiles and Geomembranes*, Vol. 21, No. 3, pp. 177-196.

Ingold, T.S. (1979). “The Effects of Compaction on Retaining Walls.” *Geotechnique*, Vol. 29, No. 3, pp. 265-283.

Kongkitkul, W., Hirakawa, D., Sugimoto, T., Kawahata, S., Yoshida, T., Ito, S., and Tatsuoka, F. (2008). “Post-construction Time History of Tensile Force in the Geogrid Arranged in a Full-Scale High Wall.” *Proceedings of 4th GeoSynthetics* Asia, Shanghai, pp. 64-69.

Lee, K.Z., and Wu, J.T. (2004). “A Synthesis of Case Histories on GRS Bridge-supporting Structures with Flexible Facing.” *Geotextiles and Geomembranes*, Vol. 22, No. 4, pp. 181-204.

McGown, A., Andrawes, K.Z., Pradhan, S., and Khan, A.J. (1998). “Limit State Design of Geosynthetic Reinforced Soil Structures.” *Proceedings of the 6th International Conference on Geosynthetics*, pp. 144-179.

NAVFAC (1986). *Foundations and Earth Structures*. Design Manual DM-7.02. Naval Facilities Engineering Command.

Rankine, W. (1857). “On the Stability of Loose Earth.” Philosophical Transactions of the Royal Society of London, Vol. 147.

Scott, R.F. (1963). “Principles of Soil Mechanics.” *Addison Wesley*, Reading, Mass, 550p.

Tatsuoka, F. (1992). “Roles of facing rigidity in soil reinforcing.” Keynote Lecture, *Proceedings of Earth Reinforcement Practice*, IS-Kyushu ’92, Ochiai *et al.* eds., Vol. 2, pp. 831−870.

Xiao, C., Han, J., and Zhang, Z. (2016). “Experimental Study on Performance of Geosynthetic-reinforced Soil Model Walls on Rigid Foundations Subjected to Static Footing Loading.” *Geotextiles and Geomembranes,* Vol. 44, No. 1, pp. 81-94.

Zheng, Y., Fox, P.J., and Shing, P.B. (2015). “Verification of Numerical Model for Static Analysis of Geosynthetic Reinforced Soil Bridge Abutments.” *Proceedings Conference on Geosynthetics*, pp. 152-160.

Zornberg, J.G., Abu-Hejleh, N., and Wang, T. (2001). “Geosynthetic-reinforced Soil Bridge Abutments.” *Geotechnical Fabrics Report*, Vol. 19, No. 2, pp. 52-55.

Zornberg, J.G. (2015). “Performance of a Geosynthetic-reinforced Bridge Abutment in the US.” *Proceedings of the 2nd International GSI-Asia Geosynthetics Conference (GSI-Asia 2015)*, Seoul, Korea (Rep.), June 24-26, 2015.

4.6 FIELD MONITORING DATA FROM OTHER PROJECTS

This sub-task focuses on data evaluation of field monitored GRS-IBS and load-carrying GMSE bridge abutment projects in the U.S. to obtain information relevant to the objectives of this research. The field instrumented GRS-IBS and GMSE sites are located in Colorado, Minnesota, Louisiana, and Delaware. These specific sites were selected because of the type of instruments used in the field monitoring programs were the same (similar) to the instruments used in the field monitoring of the Virginia GRS-IBS of this research. The research team had access to the instrumentation data to of the Colorado load-carrying GMSE bridge abutment and Minnesota GRS-IBS projects. Evaluation of instrumentation data from these two sites involves interpreting the processed data in the same way the instrumentation data from chapter 6 of this research will be interpreted. The Louisiana and Delaware field instrumentation data were not accessible to the research team and the data evaluation from this project is based on information available on published journal articles (Saghebfar et al. 2016 and Meehan et al. 2016). The details of the field monitoring programs and evaluation and assessment of instrumentation data from the projects is presented below.

4.6.1 COLORADO LOAD-CARRYING GMSE ABUTMENT

The load-carrying GMSE bridge abutment constructed in Colorado is part of project that involves the construction of two multi-span bridges that convey I-70 over Smith Road. The abutment is 4.3 m (14.1 ft.) high. Class I structural backfill reinforced with a geotextile fabric was used to construct the abutment. Based on AASHTO and USCS classifications, the backfill is reported as A-1-b and SM material. The maximum dry density of backfill is 21 kN/m^3 (135 pcf) and the optimum moisture content is 7.1 %. The effective friction angle (φ) of the backfill material is 51.8 degrees. The backfill was placed at 0.1 m (4 in.) reinforcement spacing in part of the abutment that supports the bridge slab and it was placed at 0.3 m (12 in.) reinforcement spacing in part of the abutment that supports the road. The facing element was constructed using sheet pile.

The field monitoring program was implemented on two instrumentation lines of the abutment. Aerial view of the instrumented site and the location of the two instrumentation lines (l1 and l2) are shown in Figure 4.6.1. Instrumentation line 1 and line 2 include the same type and number of instruments. The instruments used in this project include vertically installed earth pressure cells (to measure horizontal pressures), horizontally installed earth pressure cells (to measure vertical pressures), strain gages, ShapeAccellArrays (SAA), and crack-meters. The earth pressure cells and the strain gages were placed horizontally in different locations along the height of the GMSE abutment. An earth pressure cell was installed horizontally on the sheet pile. The strain gages were installed on anchor rod close to the foundation of the structure. The vertical and horizontal stress measurements obtained from the earth pressure cells are discussed below.

Vertical stress distribution profiles for self-weight of backfill material in instrumentation lines 1 and 2 are shown in Figures 4.6.2 and 4.6.3. The profiles are developed for earth pressure cells installed in front (0.3 m (1 ft.) from facing), middle (1.8 m (6 ft.) from facing), and back (3.9 m

(12.8 ft.) from facing) sections of the GMSE abutment. With the exception of stress data at 4.3 m depth from instrumentation line 1 that showed a lower value than the calculated stress, the results show that the stress distributions follow the calculated stress distribution and the magnitude of stresses are within range of calculated stresses. Figures 4.6.4 and 4.6.5 show stress distribution profiles developed for bridge slab loading in instrumentation lines 1 and 2 respectively. Since the earth pressure cells were installed far from the bridge slab loading, only earth pressure cells installed in the front and middle are considered. The total dead load from the slab was around 44.5 kPa (6.5 psi). The results show that there is reduction of stresses with depth and the distribution profile in instrumentation line 1 and 2 was similar. The stress distribution obtained from the field was compared with 2:1 method used for GMSE in AASHTO (2017) and the Boussinesq method used for GRS-IBS in FHWA (2018). Both stress distribution methods provided similar stress distribution trends as obtained from the field. The Boussinesq stress distribution method showed more comparable stress magnitudes to field stress magnitudes when compared to the 2:1 method.

Lateral stress distribution profiles developed from horizontal earth pressure cells installed behind the facing of the structure in instrumentation lines 1 and 2 are shown in Figures 4.6.6 and 4.6.7. The profiles are developed for self-weight of the backfill loading. The profiles are compared with active and at-rest earth lateral earth pressures calculated using a backfill friction angle of 51.8 degrees. The lateral stress distribution profiles obtained from the field were between the active and at-rest lateral earth pressure in top section of the abutment. For lower section of the abutment, the lateral stress distribution profiles obtained from the field are uniform with the magnitude being lower than both the active and at-rest lateral earth pressures. The overall observed lateral stress distribution with depth obtained from instrumentation lines 1 and 2 shows a slightly increasing distribution. After construction, the earth pressure cells did not provide reliable results and the lateral earth stress distribution for combined self-weight of backfill and super-structure loading is not evaluated.

Connection load (T_o) profiles are estimated using lateral stresses obtained from the field and tributary vertical reinforcement spacing. T_o profiles obtained from the field for self-weight of backfill loading in instrumentation lines 1 and 2 is shown in Figure 4.6.8. T_o profiles are plotted together with calculated forces using active and at-rest lateral earth pressures. T_o profile obtained from the field follows the lateral stress distribution with a slightly increasing distribution with depth. The maximum connection force was 1.4 kN/m (8 lb/in.) and higher force magnitudes were observed from earth pressure cells at higher depth. The connection forces were close to calculated forces using at-rest lateral earth pressure in top sections and they were between calculated forces using active and at-rest lateral earth pressure at higher depth.

Fig. 4.6.1: Aerial view of the instrumented GMSE site in Colorado

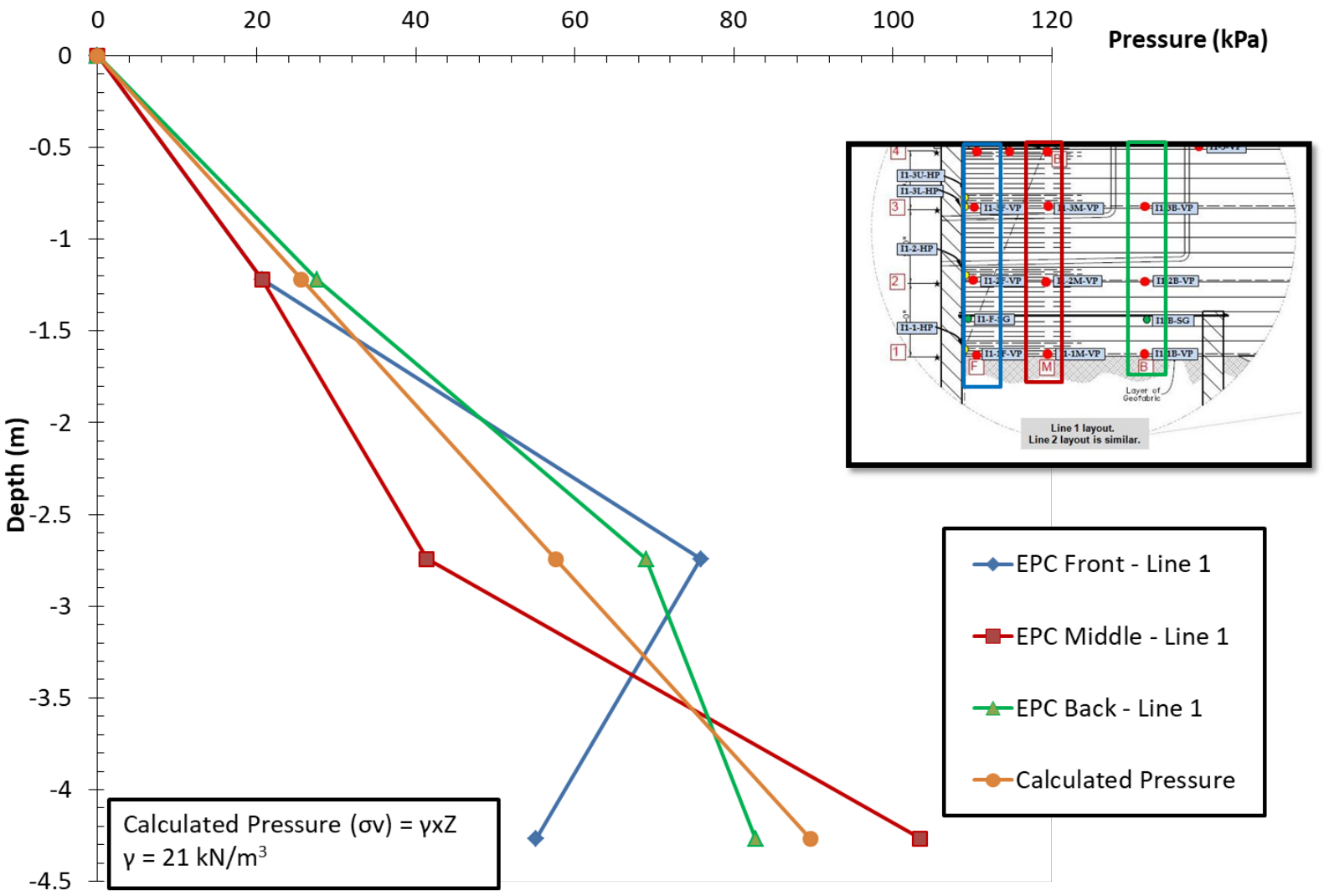

Fig. 4.6.2: Vertical stress distribution due to self-weight of backfill loading in instrumentation line 1

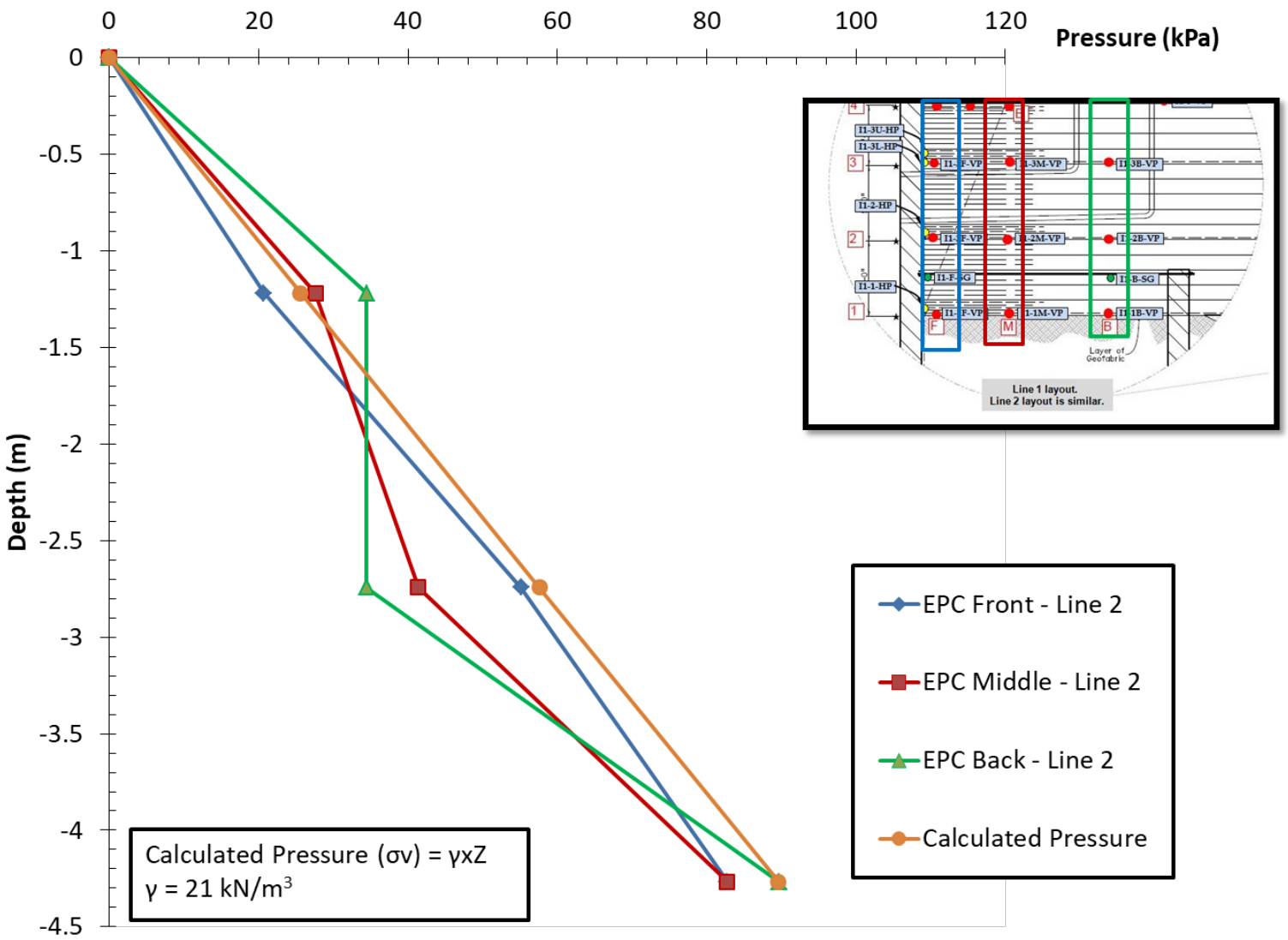

Fig. 4.6.3: Vertical stress distribution due to self-weight of backfill loading in instrumentation line 2

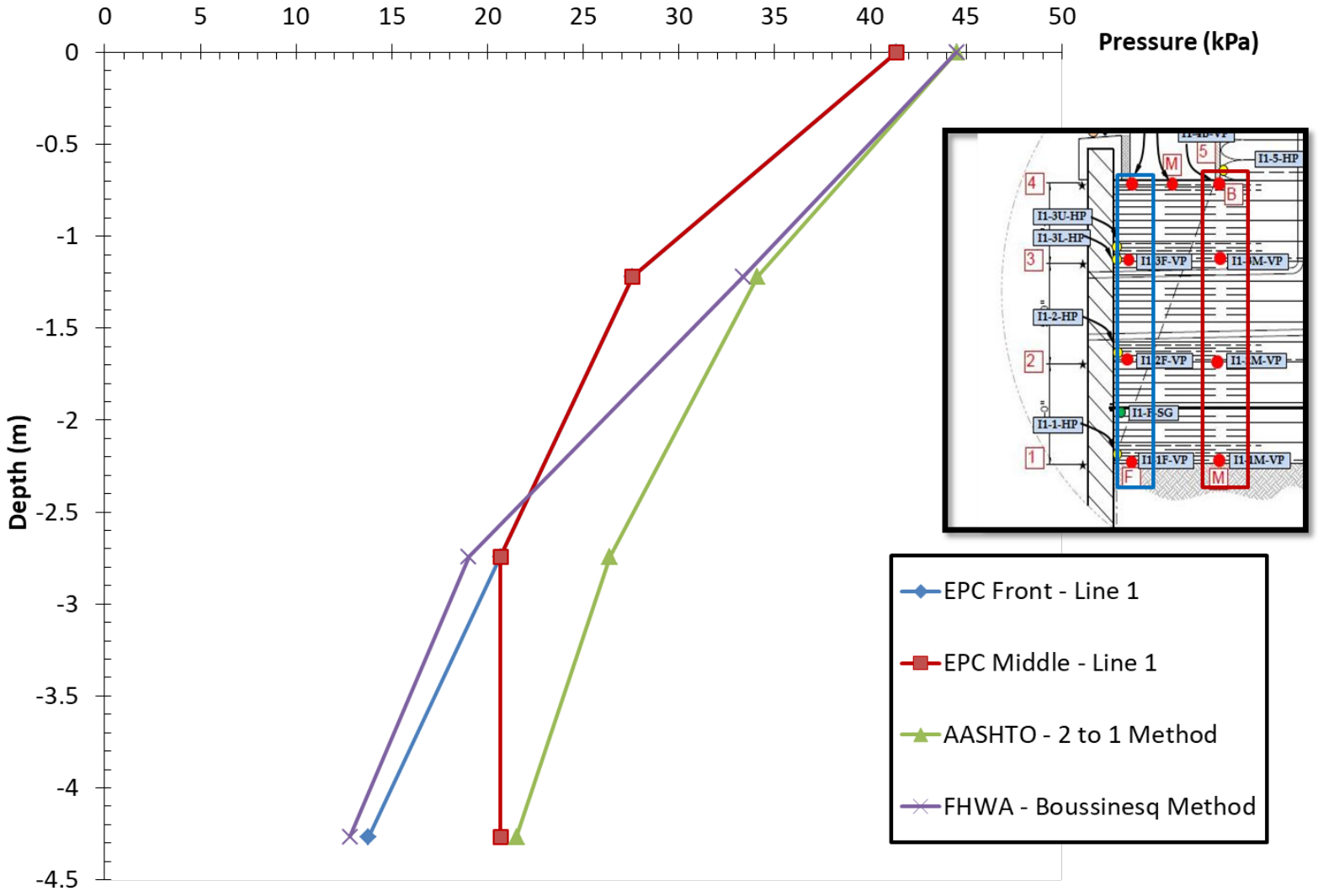

Fig. 4.6.4: Vertical stress distribution due to bridge slab loading (without self-weight loading) in instrumentation line 1

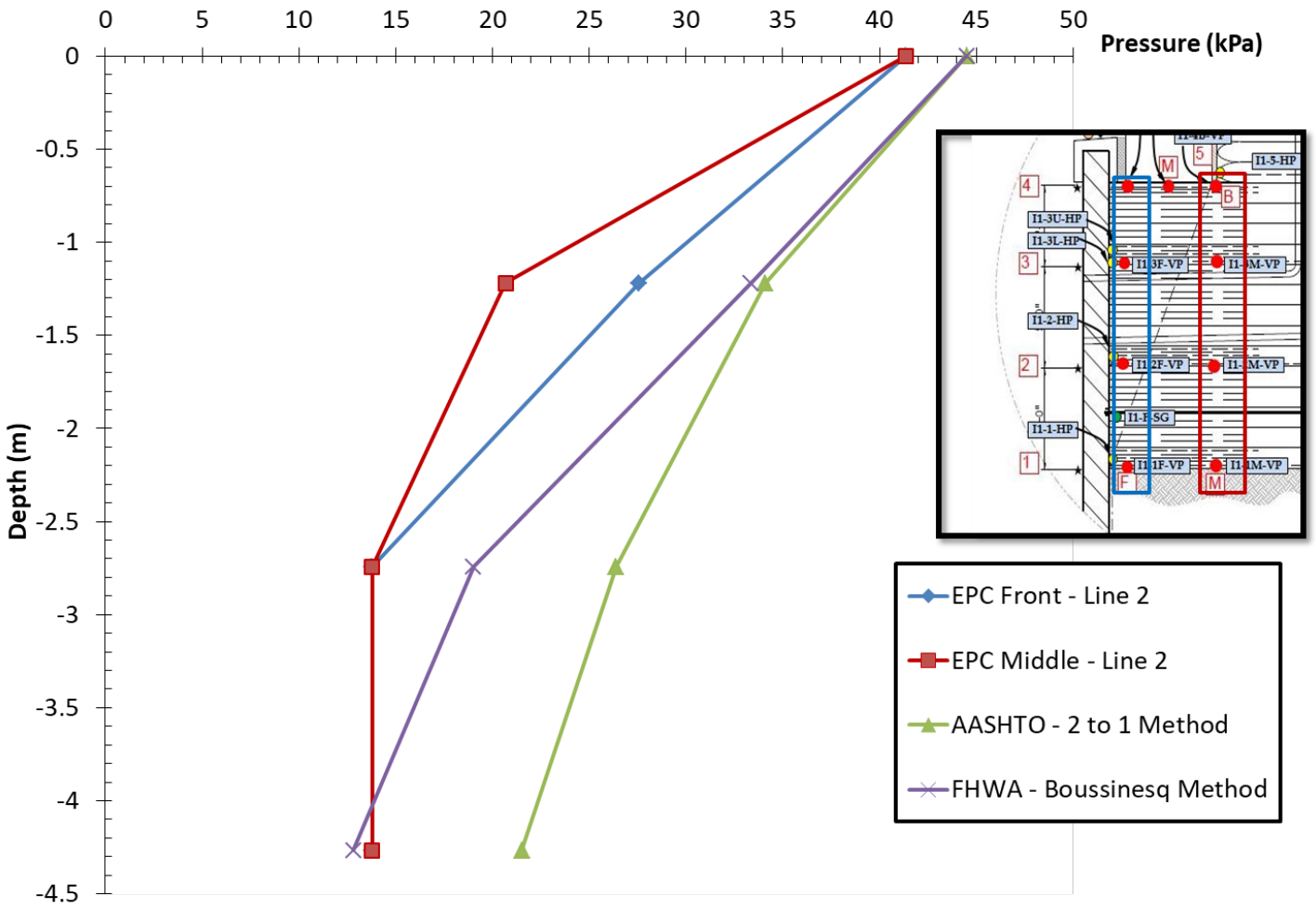

Fig. 4.6.5: Vertical stress distribution due to bridge slab loading (without self-weight loading) in instrumentation line 2

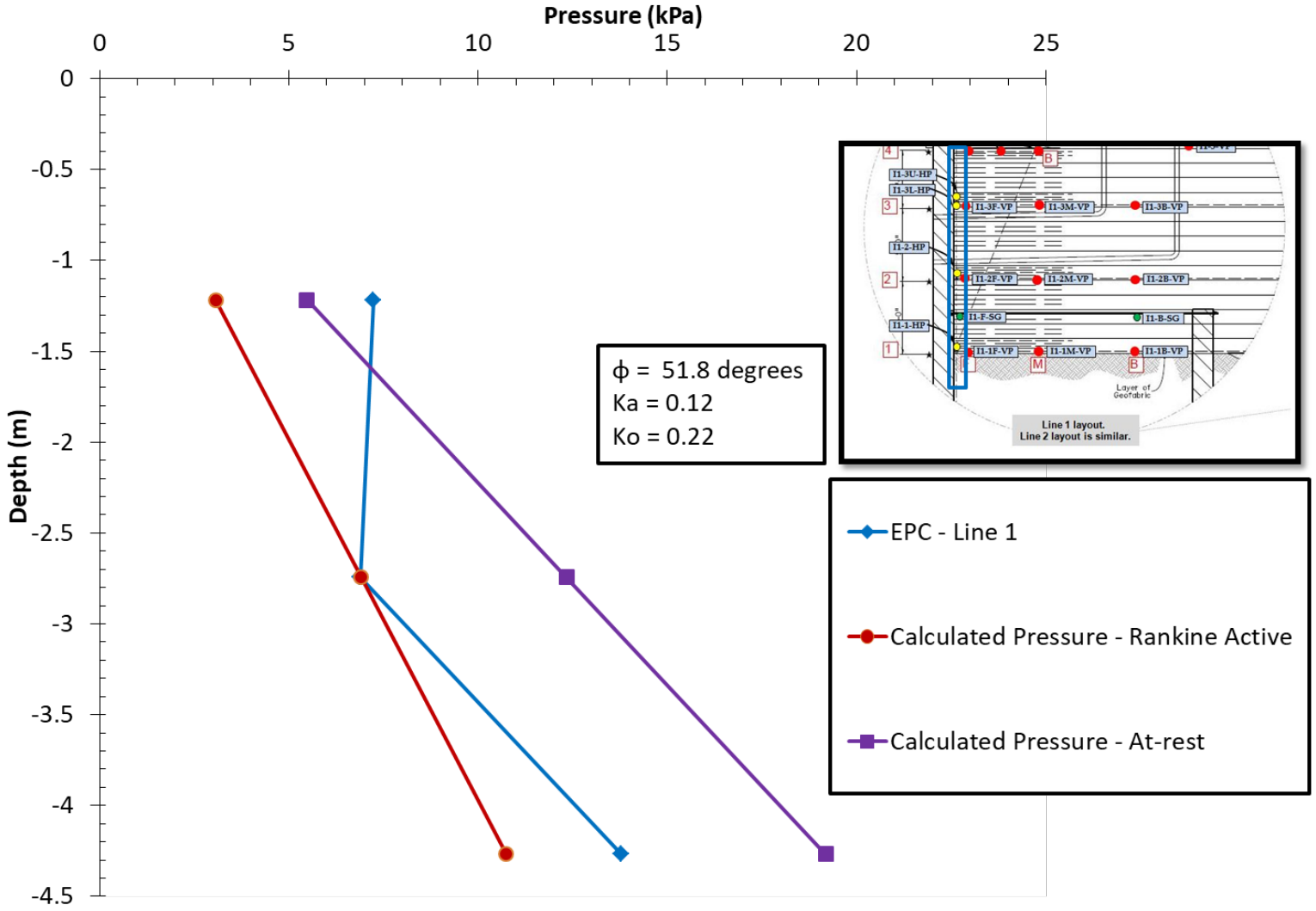

Fig. 4.6.6: Lateral stress distribution due to self-weight of backfill loading in instrumentation line 1

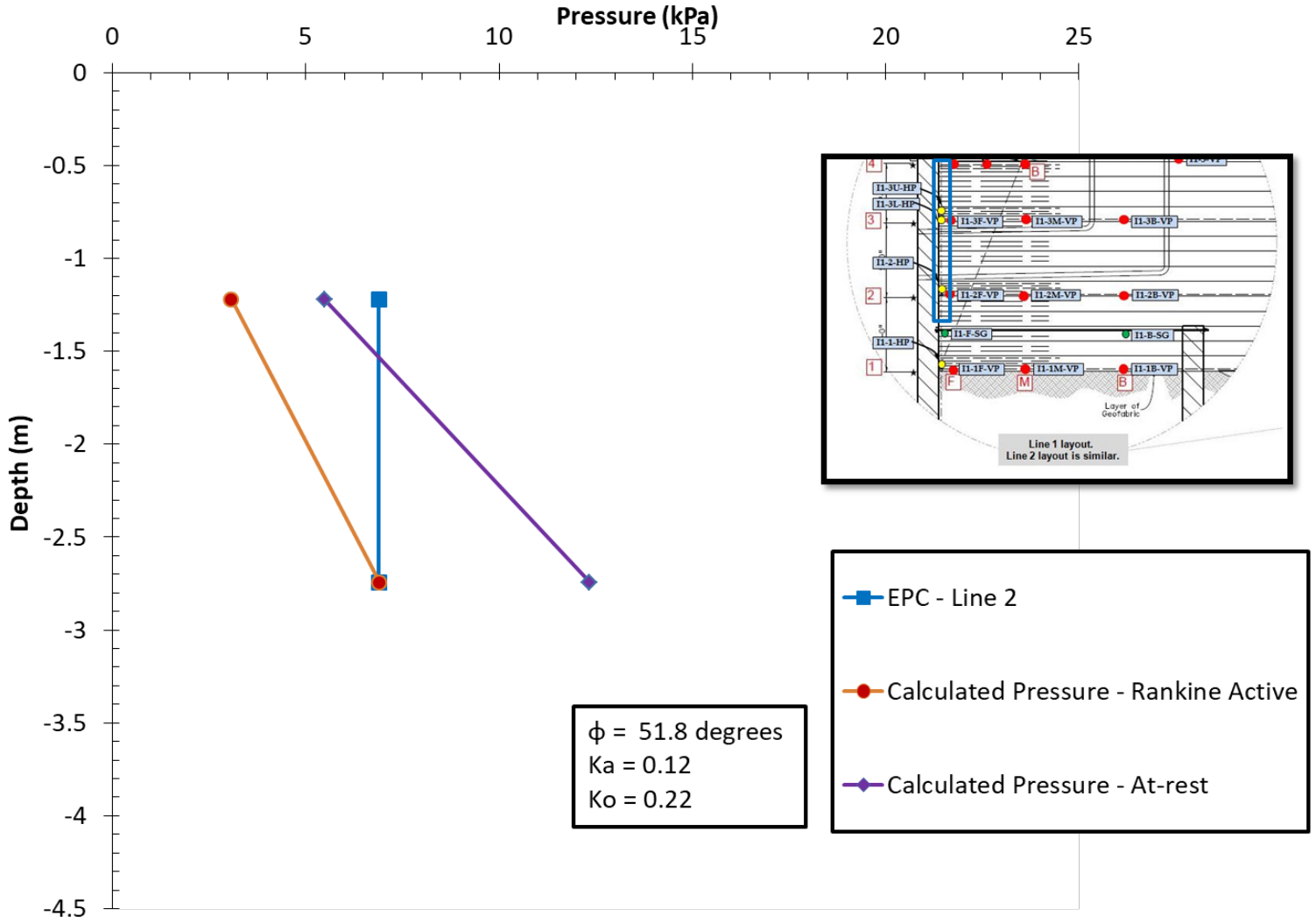

Fig. 4.6.7: Lateral stress distribution due to self-weight of backfill loading in instrumentation line 2

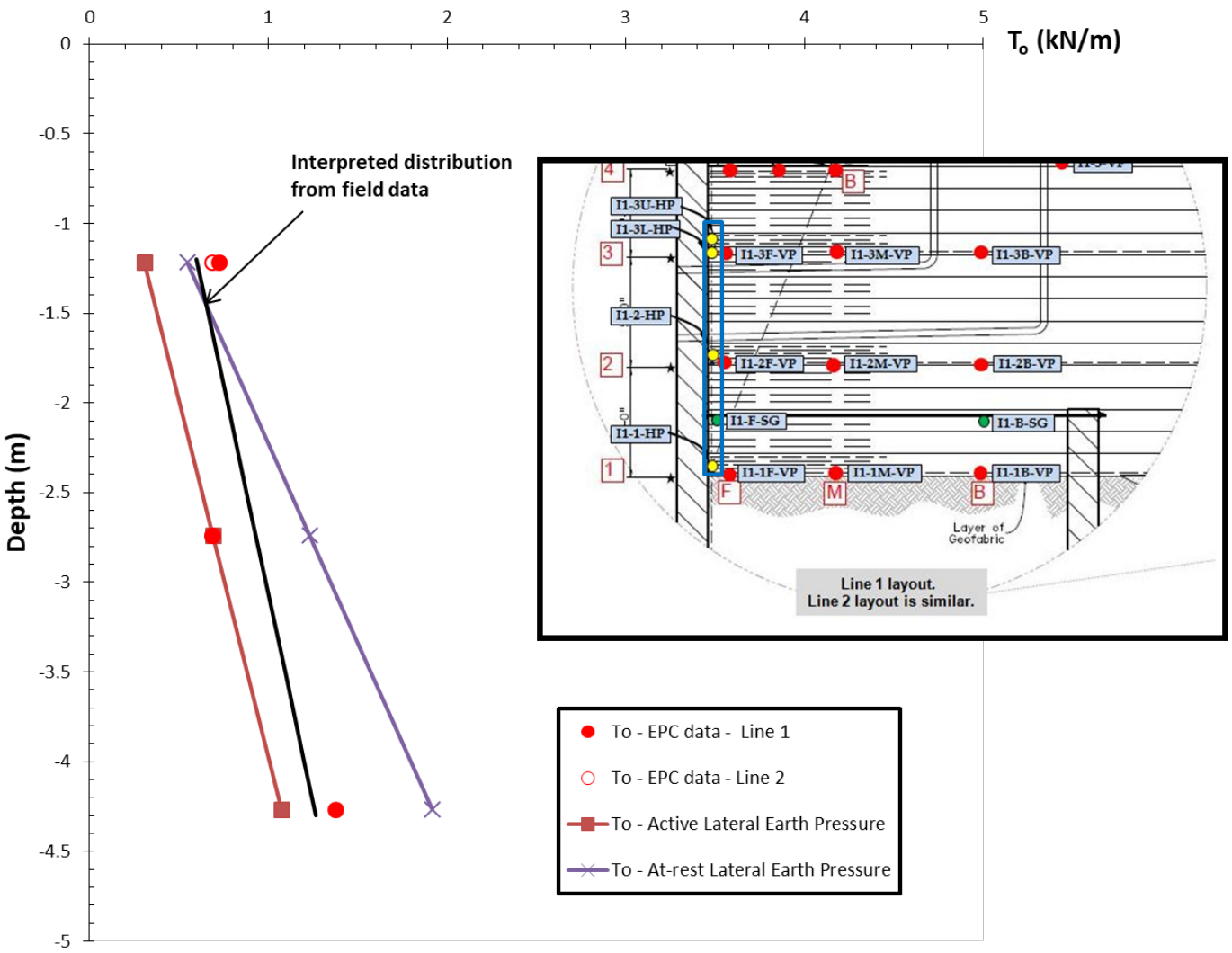

Fig. 4.6.8: To versus depth profiles due to self-weight of backfill loading in instrumentation lines 1 and 2

4.6.2 MINNESOTA GRS-IBS

The field monitored GRS-IBS is located at Rock County Highway 55 in southwestern Minnesota. The bridge has a span length of 24 m (78.7 ft.) and abutment height of 7 m (23 ft.). The backfill material was crushed granite that has a friction angle of 44 degrees. The backfill was reinforced with geogrid reinforcement. The reinforcement spacing in the primary reinforcement zone was 0.2 m (8 in.). The instrumentation program includes mainly embedment and contact earth pressure cells and ShapeAccelArrays (SAA). The embedment earth pressure cells were installed below the reinforced soil foundation to measure vertical stresses on foundation soils. The contact earth pressure cells were installed on concrete box beams of the bridge super-structure to monitor lateral stresses at the beam-soil interface The SAA were used to measure lateral deformations in the GRS-IBS abutment (Budge et al. 2014 and Dasenbrock et al. 2017). For relevancy of this research only data from earth pressures installed to measure vertical stresses and ShapeAccelArrays (SAA) installed to measure vertical deformation (settlement) are evaluated.

Eight earth pressure cells were installed below the reinforced soil foundation to measure the behavior of the foundation pressure with time. Five earth pressure cells were installed on North abutment and three were installed on South abutments. In the North abutment 3 earth pressure cells were installed 1.2 m (4 ft.) from the front edge and 2 earth pressure cells were installed 2.4 m (8 ft.) from the front edge. In the South abutment 3 earth pressure cells were installed 1.2 m (4 ft.) from the front edge. The layout of instrumentation as presented on the data processing website is shown in Figure 4.6.9. Vertical stress distribution profiles developed for self-weight of backfill material in the North and South abutments are shown in Figures 4.6.10 and 4.6.11. The stress distributions obtained from the field were compared with calculated stress distribution. The unit weight of backfill material was assumed to be 20 kN/m^3 (128 pcf). In all cases, the observed vertical stresses from the field were higher than the calculated stresses. This could occur due to usage of inaccurate calibration factors to interpret field data. This observation was also reported by Dasenbrock et al. (2017) and proper calibration of earth pressure cells was recommended by the authors to ensure reasonable measurements are obtained. In the North abutment, the earth pressure cells installed 2.4 m (8 ft.) from the front edge (EPC 4 and 5) provided much higher stresses than earth pressure cells installed 1.2 m (4 ft.) from the front edge. The vertical stresses below the foundation showed increase for backfill and bridge slab loadings. The recorded data from the ShapeAccelArrays (SAA) show that the maximum wall settlement after completion of the GRS-IBS was about 50 mm (2 in.) (Budge et al. 2014 and Dasenbrock et al. 2017).

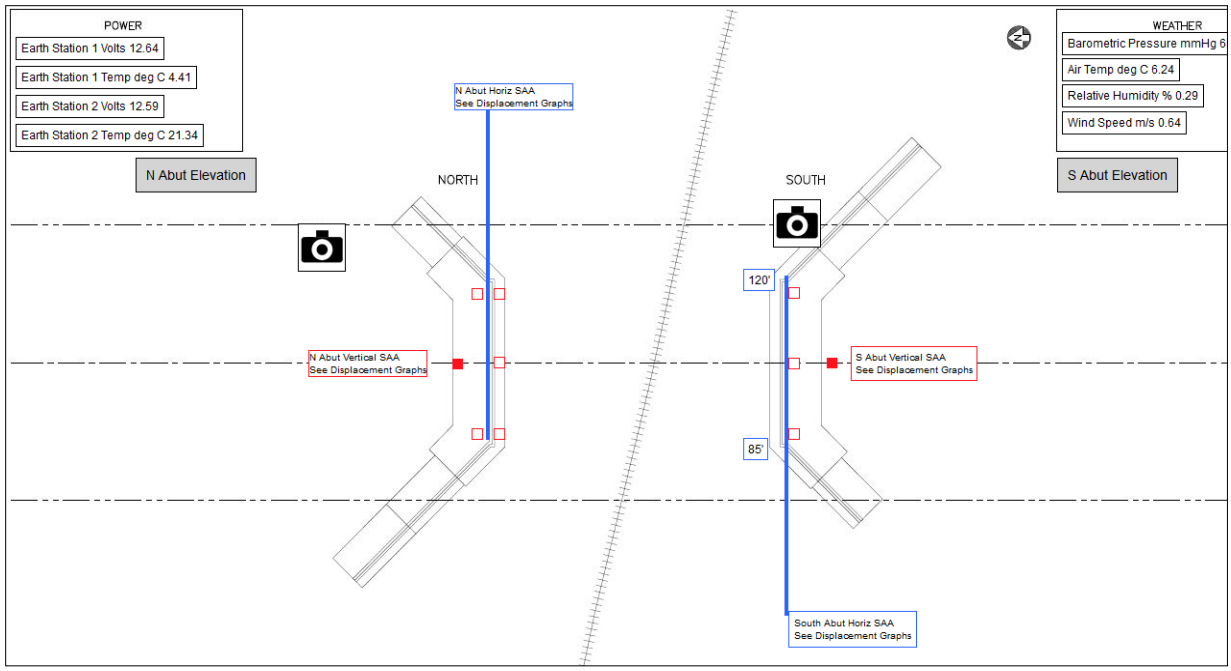

Fig. 4.6.9: Layout of instrumentation in North and South abutment of Minnesota GRS-IBS

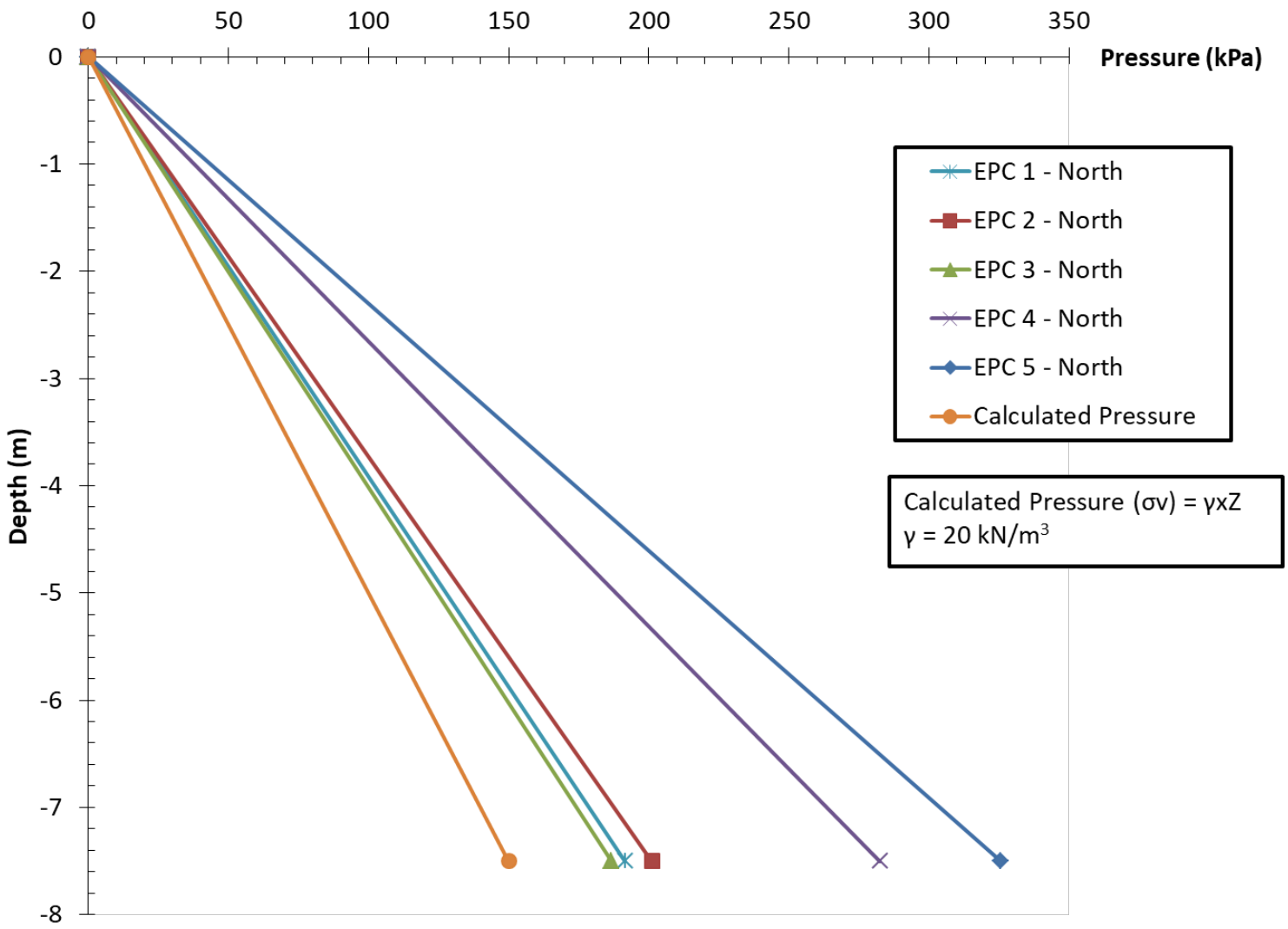

Fig. 4.6.10: Vertical stress distribution for self-weight of backfill loading in North abutment

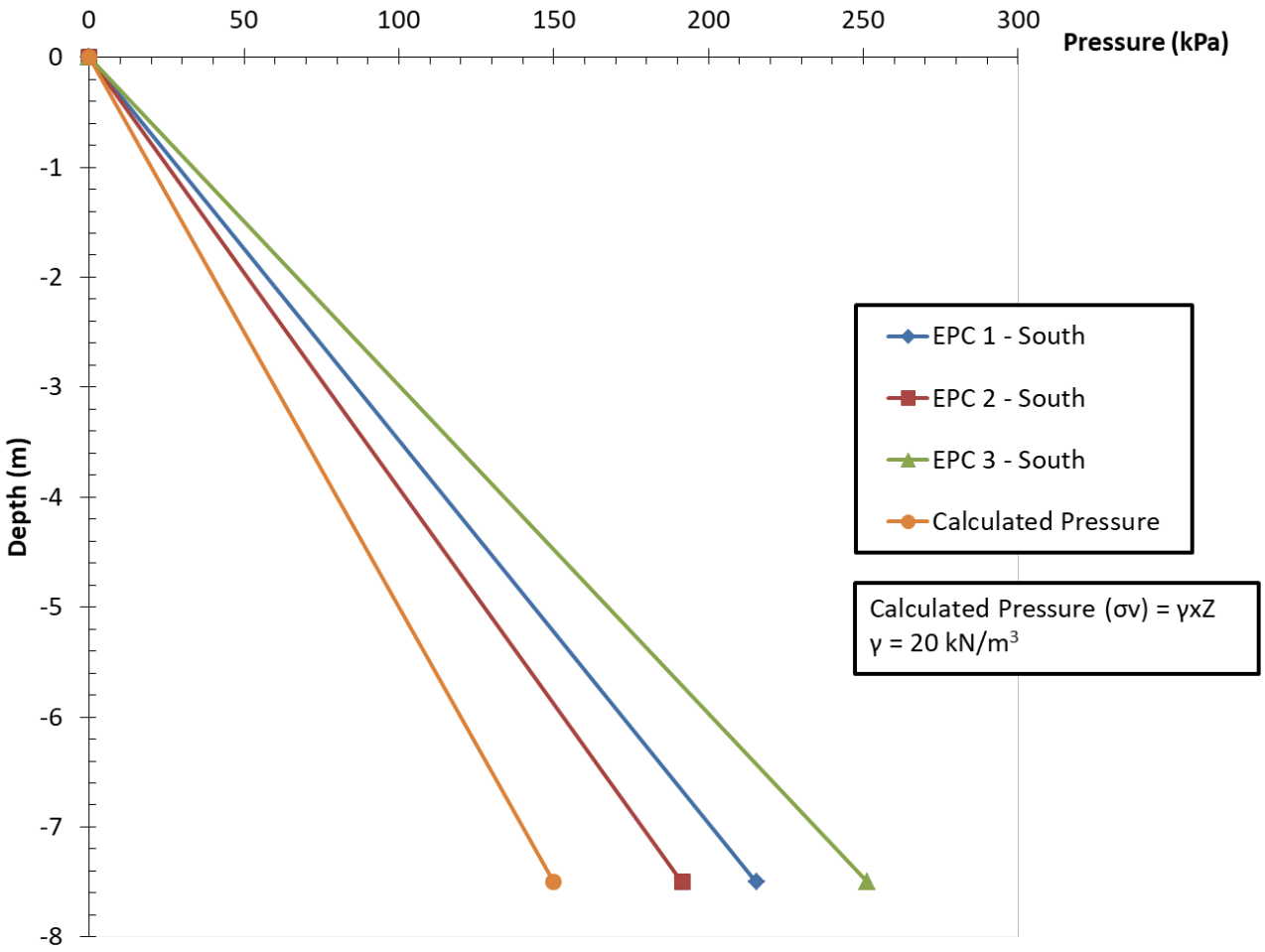

Fig. 4.6.11: Vertical stress distribution for self-weight of backfill loading in South abutment

4.6.3 LOUISIANA GRS-IBS

The field monitored GRS-IBS is located in Route LA 91 Vermilion Parish in Louisiana. The bridge span is 22 m (72.2 ft.) and the abutment height is 4.3 m (14.1 ft.). The backfill material was an open-graded crushed rock with a maximum particle size of 12.7 mm (0.5 in.). The maximum dry density of the aggregate is 2-130 kg/m^3 (134 pcf). Based on large scale direct shear test, the friction angle of the aggregate is 50.9 degrees. A woven geotextile that ultimate tensile strength 80 kN/m (456.8 lbf/in.) was used as reinforcement. The vertical reinforcement spacing in the primary reinforcement zone was 0.2 m (8 in.). The instrumentation program includes instruments such as earth pressure cells, geotextile strain gages, ShapeAccelArrays (SAA), settlement gages, piezometers, and thermocouples. The layout of instrumentation in this project is shown in Figure 4.6.12. In this section, the results obtained from earth pressure cells, geotextile strain gages and settlement gages (as reported in Saghebfar et al. 2016) are discussed.

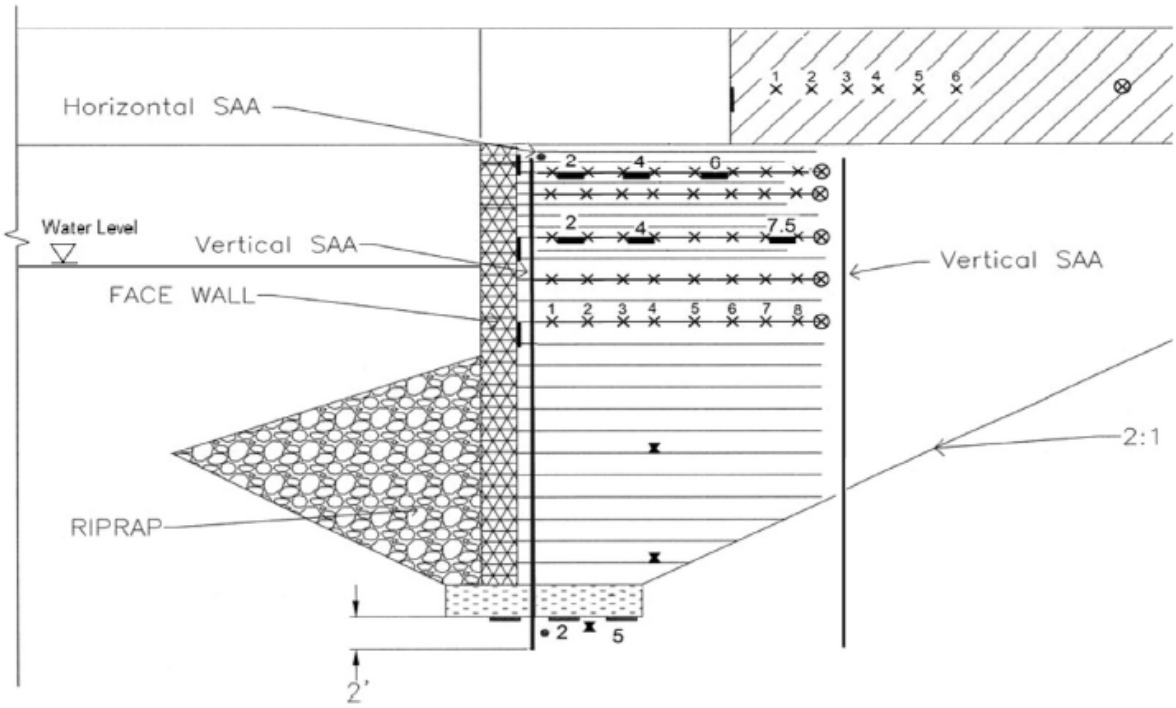

Fig. 4.6.12: Layout of instrumentation in Louisiana GRS-IBS

The earth pressure cells were installed horizontally below the reinforced soil foundation and bearing bed reinforcement zone. The maximum vertical stress was recorded from the earth pressure cells installed below the foundation. Earth pressure cells installed close to the facing and away from the facing showed similar stress levels. Vertical stresses due to self-weight of backfill were within the range of calculated pressures. Stress distribution of the bridge slab loading is shown in Figure 4.6.13. The total dead load from the bridge slab was around 100 kPa (14.5 psi). The earth pressure cells were located 0.6 m (2 ft.) from the facing. They were located at depth of 0.4 m (1.3 ft.), 1 m (3.3 ft.), and 5 m (16.4 ft.) below the bridge super-structure. The

stress distribution obtained from the field was compared with 2:1 method used for GMSE in AASHTO and the Boussinesq method used for GRS-IBS in FHWA. Both stress distribution methods provided proximate stress levels as obtained from earth pressure cells located 0.4 m (1.3 ft.) and 1 m (3.3 ft.) below bridge super-structure. However, the earth pressure cell installed 5 m (16.4 ft.) below the bridge super-structure (below the RSF) provided higher stress than both theoretical stress distribution methods.

The earth pressure cells were installed to measure horizontal stresses in 3 locations behind the facing of the GRS-IBS abutment. They were located at depth of 0.2 m (0.7 ft.), 0.8 m (2.6 ft.), and 1.6 m (5.2 ft.) below the bridge super-structure. Two earth pressure cells were installed in the bearing bed zone (S_v = 0.1 m (4 in.)) and 1 earth pressure cell was installed in the primary reinforcement zone (S_v = 0.2 m (8 in.)). Lateral stress distribution for self-weight of backfill loading is shown in Figure 4.6.14. The lateral stress distribution was compared with active and at-rest lateral earth pressures calculated using a backfill friction angle of 50.9 degrees. The lateral stress distribution profile obtained from the field was smaller than the active and at-rest lateral earth pressures and showed a uniform distribution with depth. Lateral stress levels obtained from the horizontal earth pressure cells did not show much of a change for super-structure loading. Connection load (T_o) profiles are estimated using lateral stresses obtained from the field and tributary vertical reinforcement spacing. T_o profiles obtained from the field for self-weight of backfill loading is shown in Figure 4.6.15. T_o profile is plotted together with calculated forces using active and at-rest lateral earth pressures. T_o profile obtained from this site follows the lateral stress distribution trend with a uniform distribution with depth. A maximum connection force of 0.1 kN/m (0.57 lbf/in.) was observed from earth pressure cell at a higher depth. The connection forces were less than forces calculated using active and at-rest lateral earth pressures. Figure 4.6.15 also shows T_o profile obtained from strain gage installed 0.3 m (1 ft.) from facing blocks. T_o was estimated using the strain data and the modulus of the geotextile at 2% strain. T_o distribution with depth showed a relatively uniform distribution with depth and all T_o values were higher than forces calculated using active and at-rest lateral earth pressures.

The calculated T_0 values from strain gages installed behind the facing blocks are the actual tensile stress that reinforcements are experiencing. The design T_0 values can also be calculated using the lateral earth pressure and the tributary reinforcement spacing in accordance to AASHTOO design guidelines. When compared, the T_o estimates from strain gage data were found to be much higher than the T_o calculated using earth pressure cell data. The discrepancy between strain gage data and earth pressure cell data may occur due to the condition that estimated T_o from lateral stress data may not reflect the actual condition in a frictionally connected system as it is hard to measure the load at the connection between the reinforcement and the facing using earth pressure cells. As a result, theoretical force equilibrium between T_o and lateral earth pressure acting in the reinforcement tributary area may not be fully satisfied. However, the lateral stress data can be used as one approach to estimate the force in the backfill behind the facing within the tributary area, which can potentially designate T_o especially in closely spaced reinforcement where the backfill and the reinforcement are assumed to deform laterally together.

Geotextile strain gages were installed in in 5 layers of the abutment. They were installed in 3 layers of the bearing bed zone (S_v = 0.1 m (4 in.)) and 2 layers of the primary reinforcement zone (S_v = 0.2 m (8 in.)). They were located at depth of 0.2 m (0.7 ft.), 0.4 m (1.3 ft.), 0.8 m (2.6 ft.), 1 m (3.3 ft.), and 1.4 m (4.6 ft.) below the bride super-structure. They were installed in series close to and away from the facing. The maximum strain due to self-weight of backfill loading was observed at lower levels. However, for combined self-weight of backfill and bridge slab loading, maximum strains were recorded from strain gages installed in upper layers. The maximum observed geotextile strain was 1.2 %. The strain levels obtained from the strain gages can be used to estimate the maximum tension in the reinforcement (T_{max}). At 2 % strain, the geotextile has a tensile strength of 17 kN/m (97.1 lbf/in) and a modulus of 850 kN/m (58.2 kips/ft). Reinforcement loads in the geotextile layers can be estimated by multiplying the modulus value with the strains obtained from the strain gages. Reinforcement load profile along the reinforcement layers estimated from strain gages installed 0.3, 0.6, 0.9, 1.2, 1.5, 2.2, and 2.4 m (1, 2, 3, 4, 5, 7.2, and 8 ft.) from the facing blocks are shown in Figure 4.6.16. Strains measured on layer located at 0.2 m (8 in.) depth showed unreasonably high initial strain levels as a response of self-weight loading. However, strain data from this location and the remaining four layers were used to estimate reinforcement loads. The reinforcement load profile showed a small increase with depth under self-weight in most locations. The values of reinforcement loads in the top section of the abutment showed an increase with application of the slab load. However, the values of reinforcement loads in lower section of the abutment did not show a significant increase with application slab load. The maximum reinforcement loads (T_{max}) were observed 1.2 m (4 ft.) from the facing of the structure. T_{max} distribution with depth due to self-weight of backfill loading is shown in Figure 4.6.17**.** The T_{max} profile is plotted with calculated reinforcement loads for active and at-rest earth pressures. With the exception of T_{max} value at 1 m (3.3 ft.) depth, the T_{max} profile showed a relatively uniform distribution with depth and all T_{max} values were higher than forces calculated using active and at-rest lateral earth pressures as shown in Figure 4.6.17.

Settlement gages were installed to monitor settlement of the soil foundation. Settlement monitoring took place during construction and up to four months after construction. The settlement of the foundation increased with increase of placed backfill. More settlement was observed near the center of the abutment that the corners. The rate of settlement was fast during early stage of construction. However, the rate of settlement decreased with time. The maximum observed foundation settlement was less than 6 mm (0.2 in.).

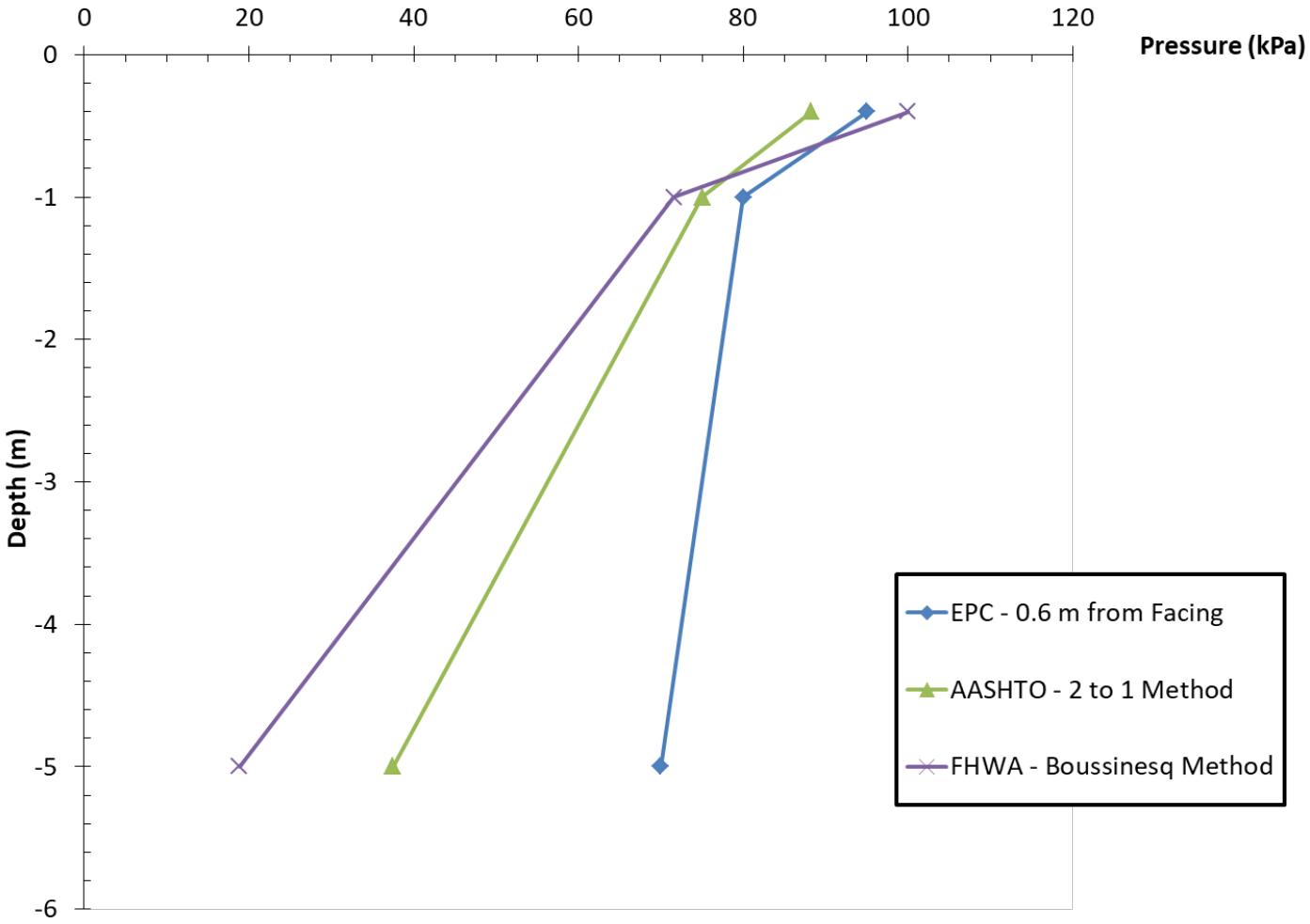

Fig. 4.6.13: Vertical stress distribution due to bridge slab loading (without self-weight loading)

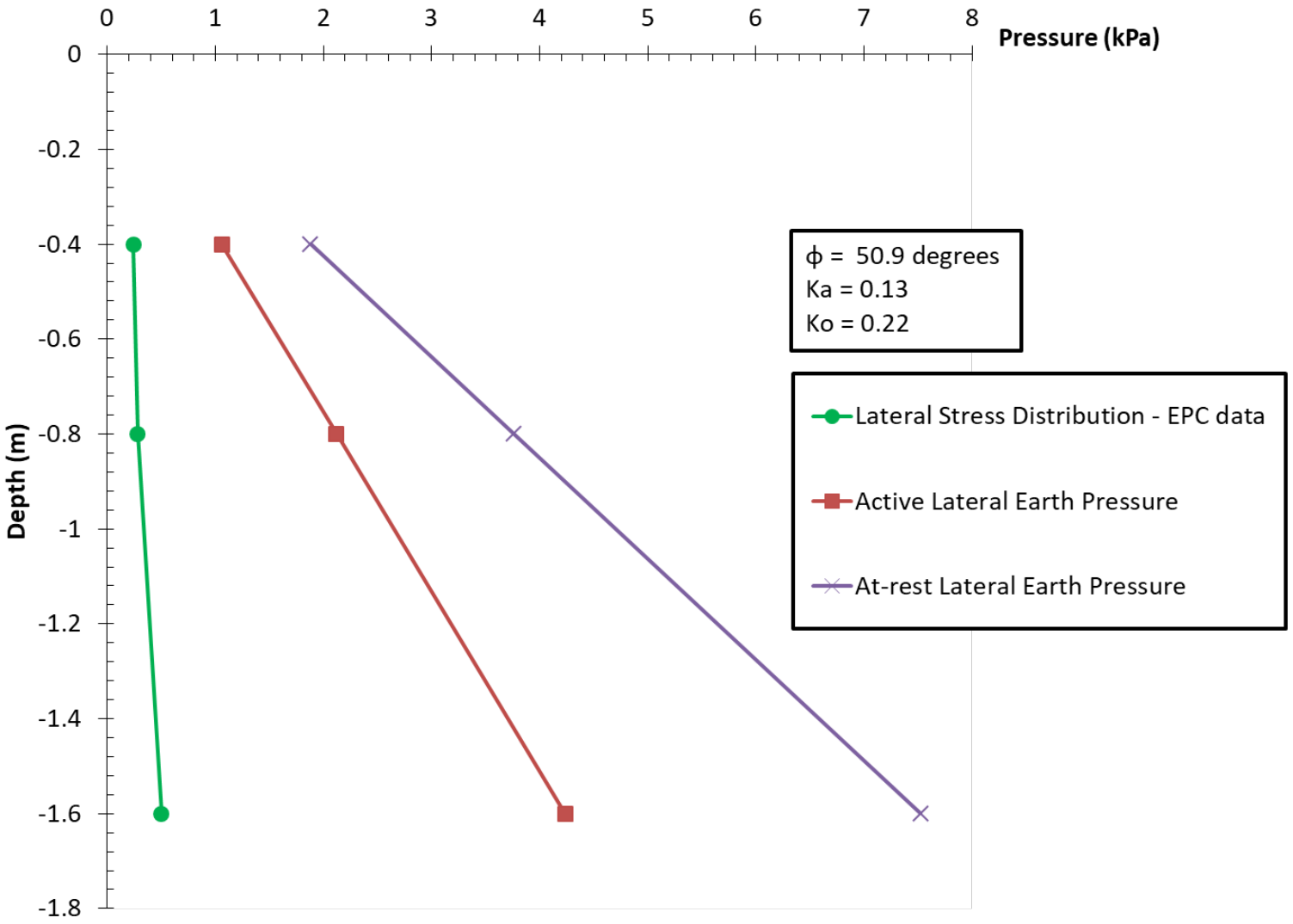

Fig. 4.6.14: Lateral stress distribution for self-weight of backfill loading

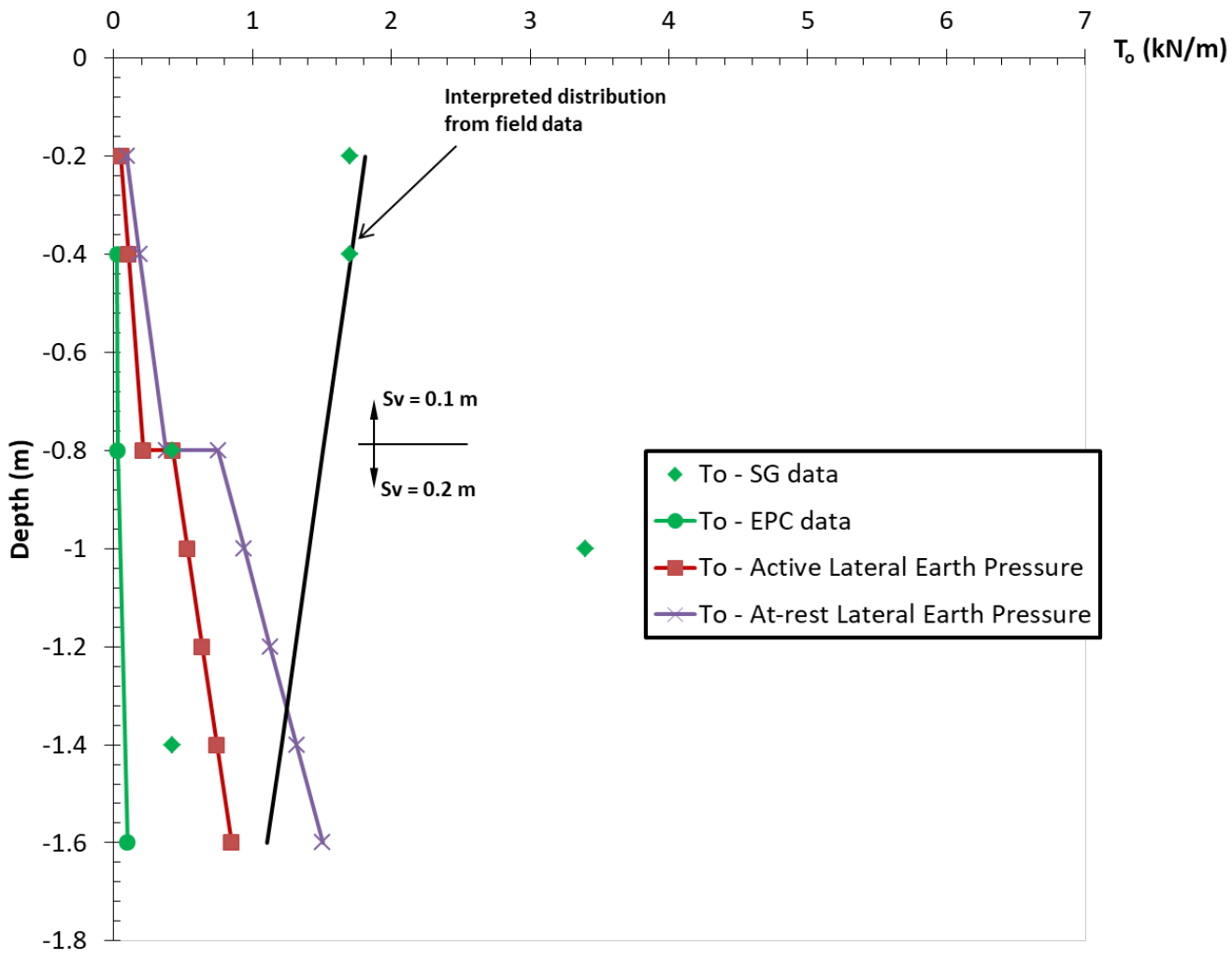

Fig. 4.6.15: T_o versus depth profiles due to self-weight of backfill loading

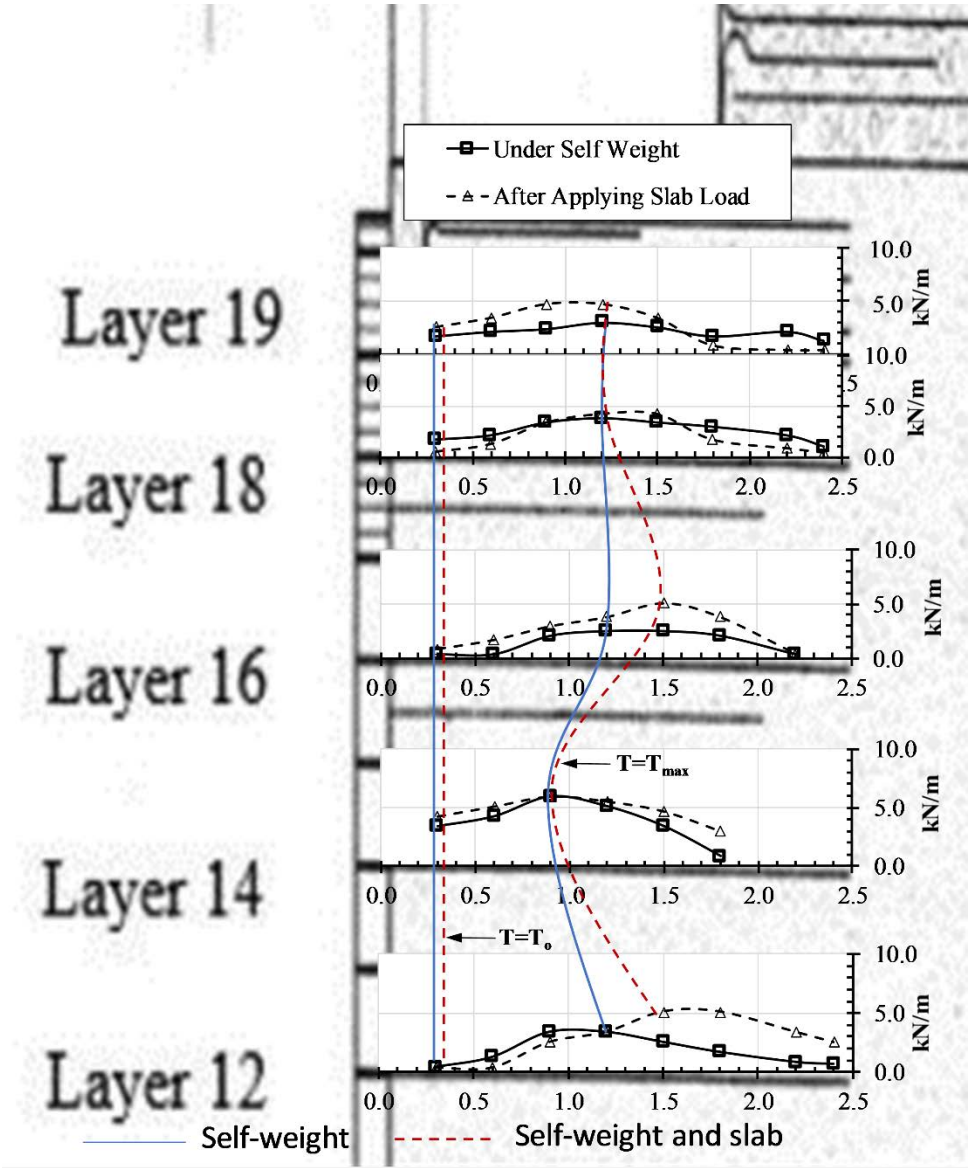

Fig. 4.6.16: Reinforcement load profiles along the reinforcement layers *due to self-weight of backfill and slab loading*

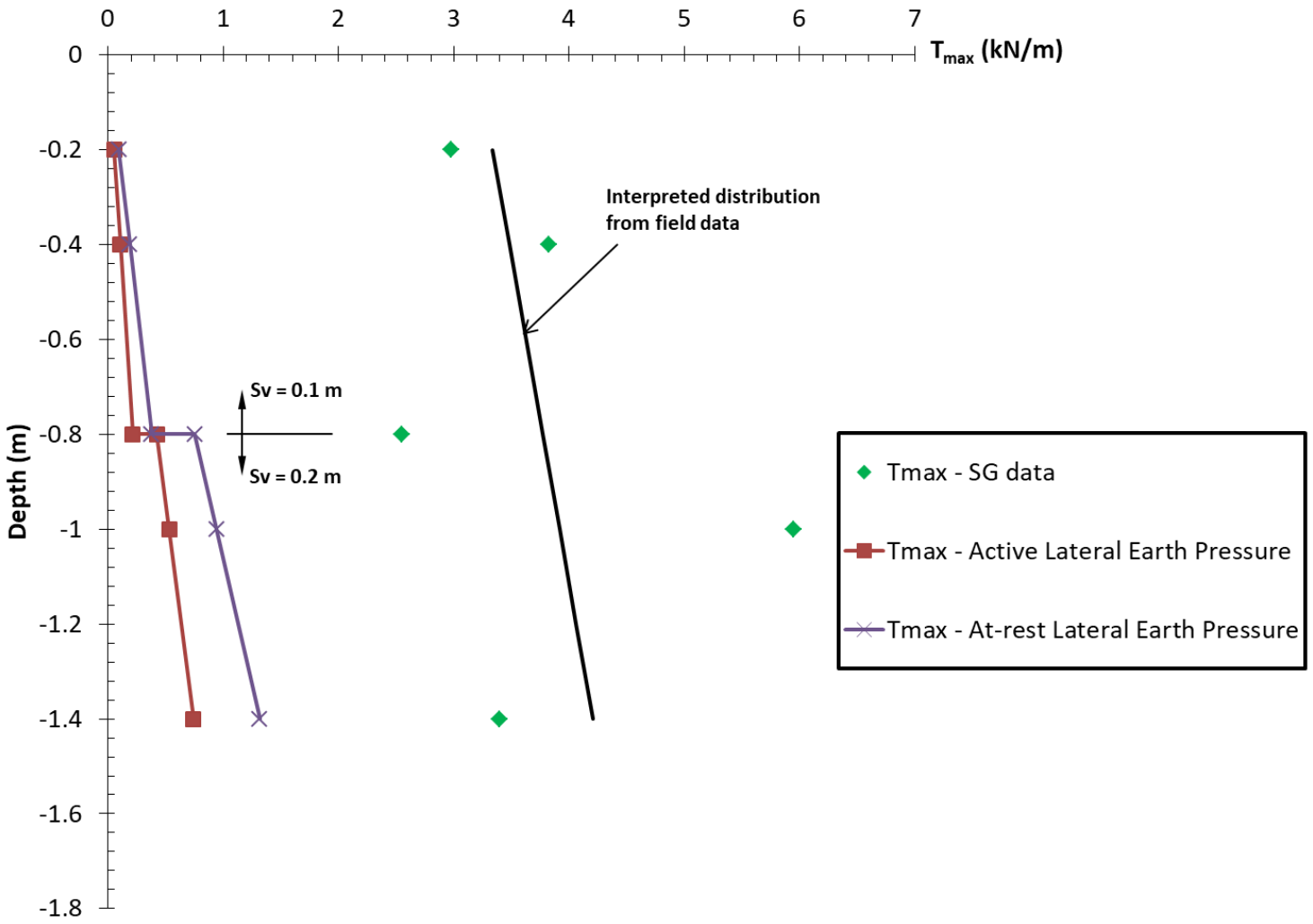

Fig. 4.6.17: T_{max} versus depth profile due to self-weight of backfill loading

4.6.4 DELAWARE GRS-IBS

The field monitored GRS-IBS is located in New Castle County, on Chesapeake City Road over Guthrie Run. The structure was constructed in 2013 to replace for an existing bridge that had reached the end of its design life span. The abutment has a height of 4.8 m (15.7 ft.) with reinforced soil foundation thickness of 0.63 m (2.1 ft.). The bridge has a span of 12.2 m (40 ft.) and 14.6 m (48 ft.) including two shoulders. The width of the bridge is 12.2 m (40 ft.) and 14.6 m (48 ft.) including two shoulders. The structure rests on soil that can be classified as CL material per USCS classification. The soil has a unit weight of 20 kN/m^3 (128 pcf) and cohesion of 100 kPa (14.5 psi). The CL is founded on a stiff sandy clay layer. The backfill material used to construct the abutment is No. 8 stone that has a unit weight of 20 kN/m^3 (128 pcf) and a maximum particle size of 0.013 m (0.5 in.). The backfill has internal friction angle of 40 degrees with no cohesion. The type of geosynthetics used as reinforcement is a biaxial, woven polypropylene (PP) geotextile (HPG-57) with ultimate tensile strength of 70 kN/m (400 lbf/in). The vertical reinforcement spacing is 0.2 m (8 in.). The facing of the structure is made up of split-face concrete masonry unit (CMU) with nominal dimensions of 0.2 m (8 in.) by 0.2 m (8 in.) by 0.4 m (16 in.). The field monitoring program involves selection of various types of instruments. The instruments used in this project include inclinometer sensors, static and dynamic pressure cells, strain gages, survey targets, piezometers, and water content and temperature sensors (Meehan et al. 2016). The instruments were installed on the east and west abutments. The layout of instrumentation on the east and west abutment is shown in Figure 4.6.18**.**

Based on the objectives of this research, the data from geotextile strain gages is only evaluated in this section. Short and long foil strain gages that were glued to the geotextile were used in the instrumentation program. The strain gages were installed in 5 layers of both east and west abutments (0.3 m (1 ft.), 1.3 m (4.3 ft.), 2.1 m (7 ft.), 3.1 m (10.1 ft.), and 4.1 m (13.4 ft.) from the top of the abutment). The strain gages were installed right behind the facing and away from the facing. Strain data obtained from the strain gages is used to estimate the reinforcement loads using the modulus of the geotextile at 2% strain, which was 700 kN/m (48 kips/f.). Figure 4.6.19 shows reinforcement load profiles estimated from strain gages installed 0.25, 1.2, 2.2, 3, 4, 4.8 m (0.8, 4, 7.2, 9.8, 13.1, 15.7 ft.) from the facing due to self-weight and slab loading in east and west abutments. In estimation of reinforcement loads, average of strain data obtained from short and long strain gages was considered. The reinforcement load profiles obtained from both abutments showed a small increase with depth under self-weight. The values of reinforcement loads in the top section of the abutments showed an increase with application of the slab load. However, the values of reinforcement loads in lower section of the abutment did not show a significant increase with application slab load. Figure 4.6.20 shows connection load (T_o) and tension in the reinforcement (T) distribution with depth due to self-weight of backfill loading in east and west abutments. T_o was estimated using strain data obtained from strain gages located 0.25 m (0.8 ft.) from the facing and T was estimated using strain data from strain gages located at varying distances from the facing as shown in Figure 4.6.19. As it can be seen from Figure 4.6.20, T_o and T values were close to each other in west abutment and T_o values were slightly higher than T values in east abutment. Additionally, T_o values were found to be higher than T values after placement of the bridge slab in both east and west abutments (Figure 4.6.19). Based

on the observed behavior from Delaware site, it appears that the T_0 is the governing parameter and may coincide with the locus of T_{max}. In Figure 4.6.20, T_o and T distribution with depth was plotted with theoretically calculated forces in the reinforcements for active and at-rest earth pressures. Overall, the observed reinforcement loads were lower than active condition along the height of the abutment and remained relatively constant with depth.

The results obtained from surveying of the GRS-IBS show that maximum recorded settlement after completion of structure was 5 mm (0.02 in.).

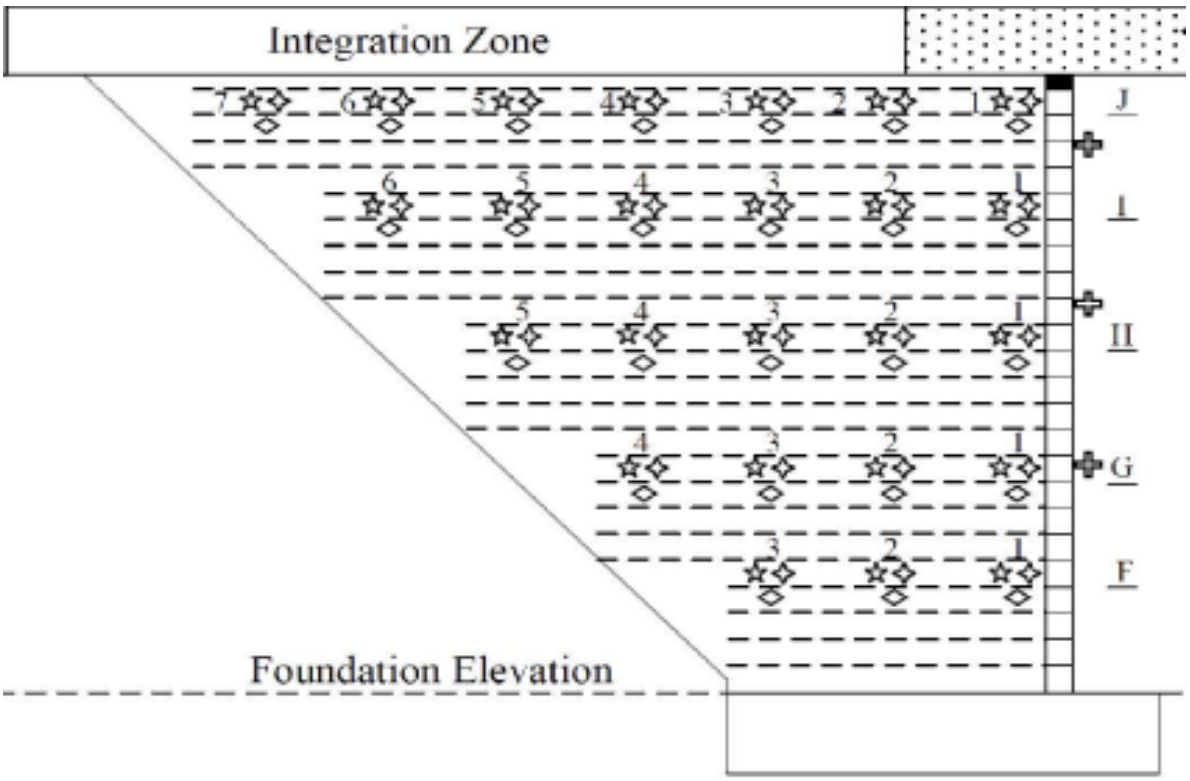

(a)

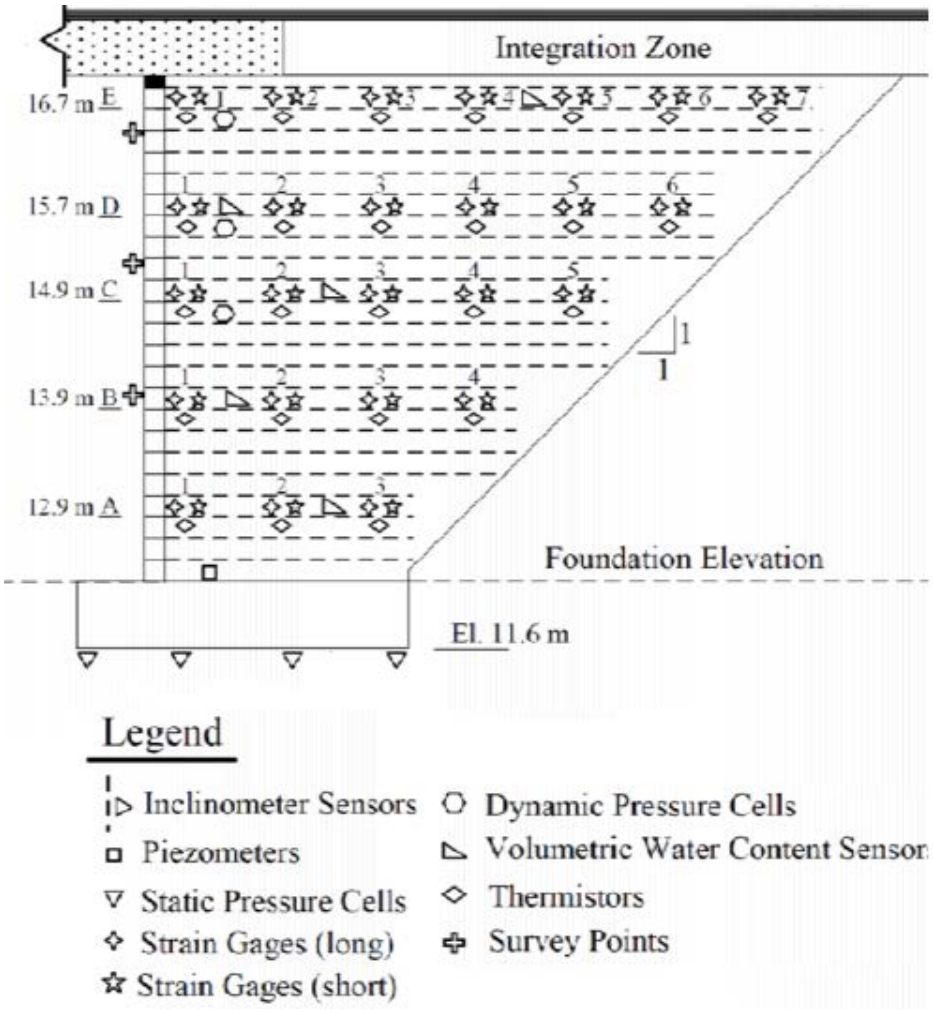

(b)

Fig. 4.6.18: Layout of instrumentation in Delaware GRS-IBS: (a) east abutment; (b) west abutment

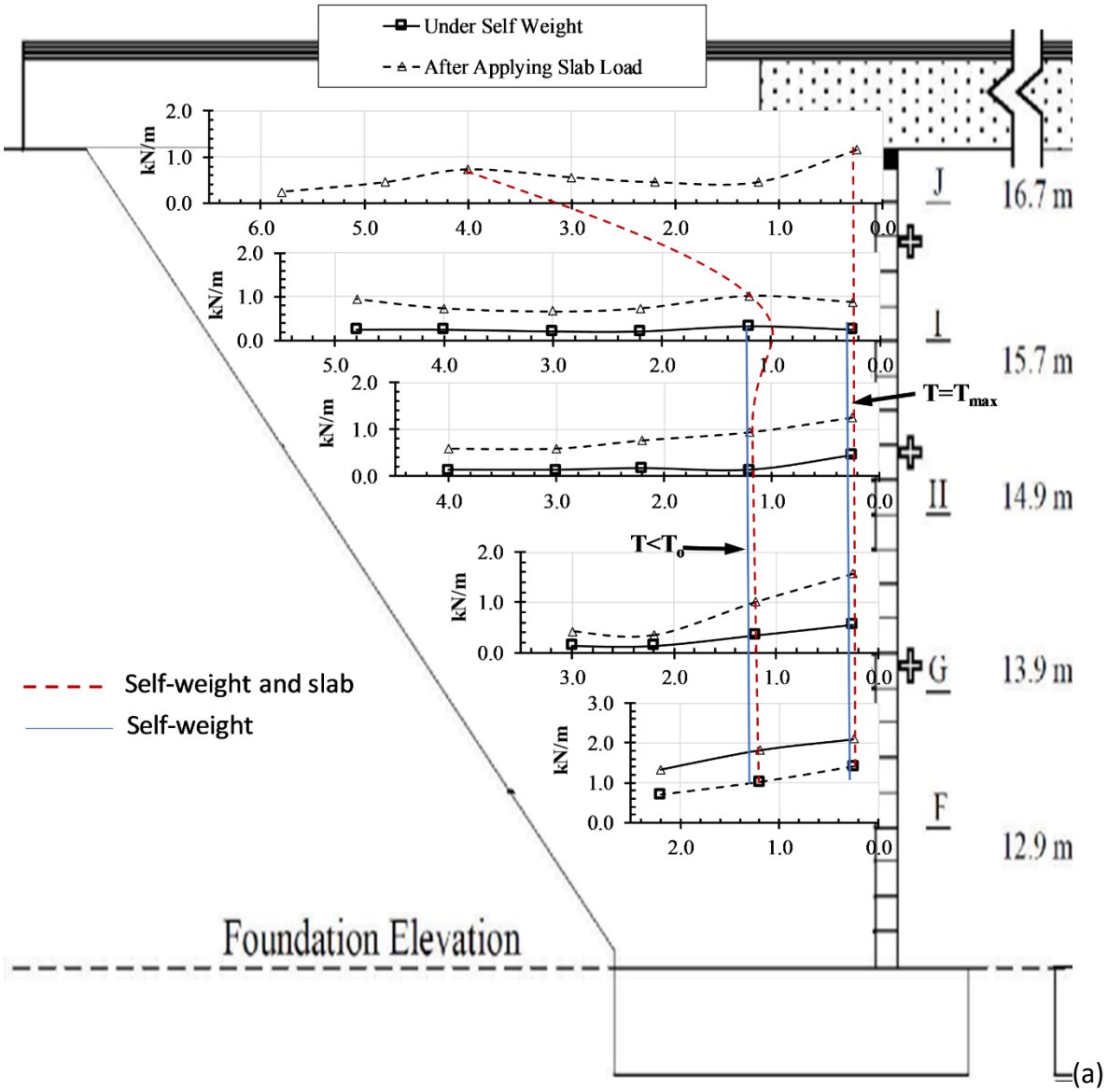
Under Self Weight
After Applying Slab Load
kN/m
J
16.7 m
I
15.7 m
T=T_max
II
14.9 m
T<T_o
G
13.9 m
F
12.9 m
Self-weight and slab
Self-weight
Foundation Elevation
(a)

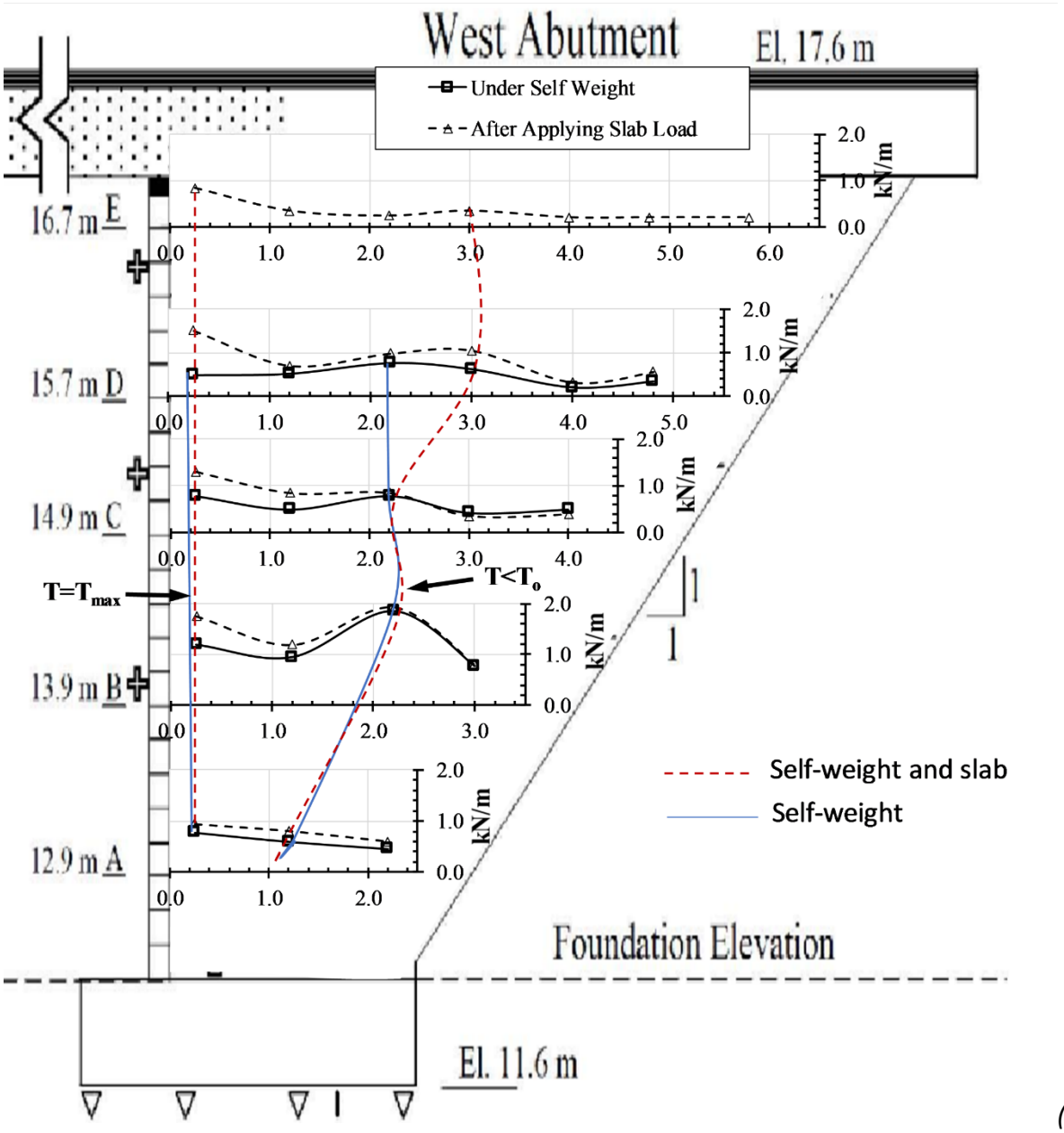

Fig. 4.6.19: Reinforcement load profiles along the reinforcement layers *due to self-weight of backfill and slab loading: (a) east abutment; (b) west abutment*

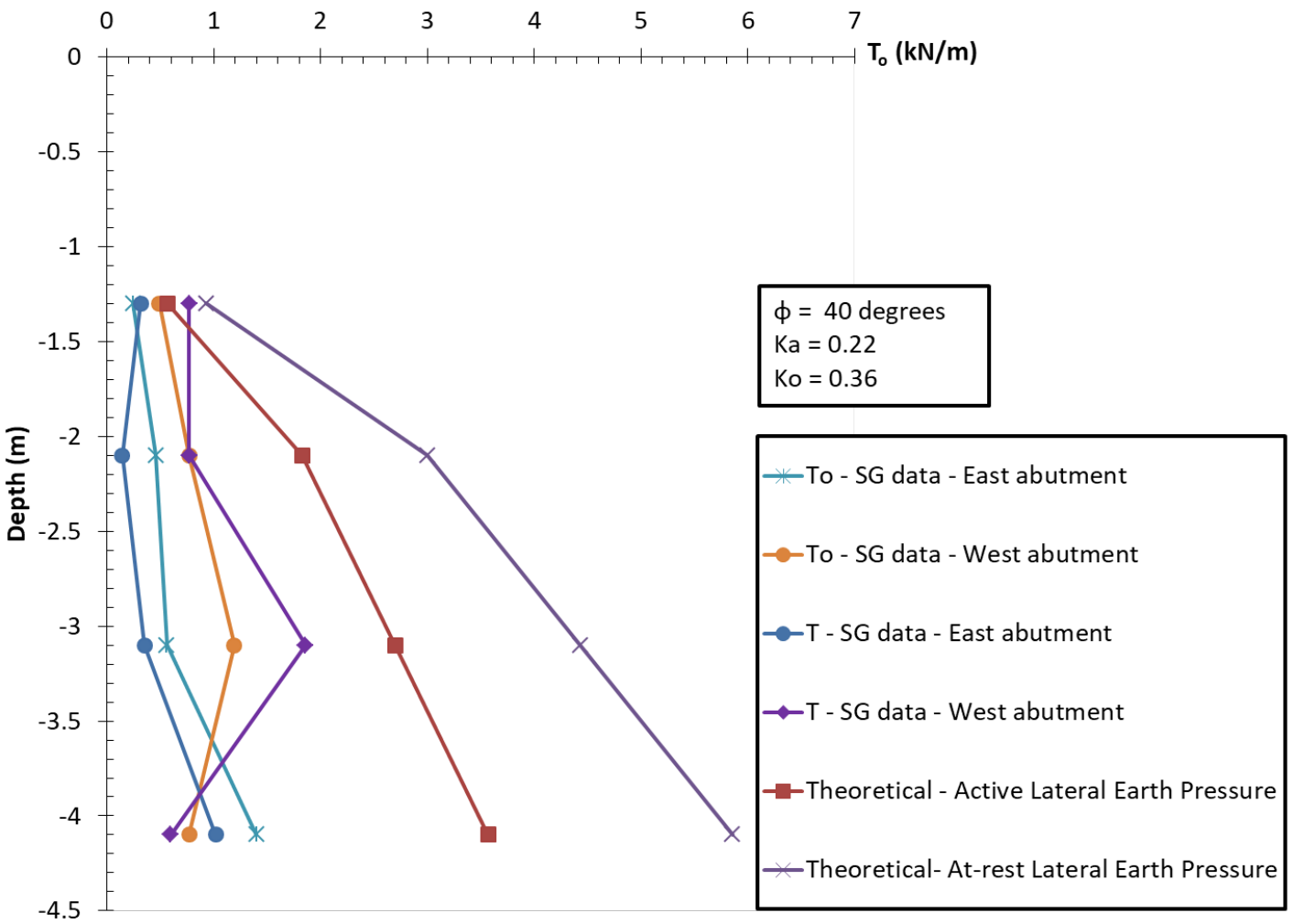

Figure 4.6.20: T_o versus depth profile due to self-weight of backfill loading

4.6.5 FOUNDERS MEADOWS LOAD-CARRYING GMSE ABUTMENT

The project description, characteristics of the structure, material properties, and field monitoring program, and data evaluation of Founders Meadow load-carrying GMSE abutment has already been presented in detail as part of sub-task 4.5. In this section, analyses of maximum tension in the reinforcement (T_{max}), connection load (T_o), and settlement of structure are only discussed. The data from strain gages, earth pressure cells installed at the back of the facing, and surveying work is evaluated. The data obtained from strain gages is used to estimate reinforcement loads using the modulus of the geogrid at 2 % strain. The strain gages were installed 1.2, 2.8, and 4.4 m (4, 9.2 and 14.4 ft.) from the top of the abutment and behind the facing, 3.2 m (10.5 ft.), and 5.2 m (17.06 ft.) from the facing of the structure. Figure 4.6.21 shows reinforcement loads estimated from stain gages data due to self-weight of backfill material and slab loading. In case of self-weight loading, the maximum tension in the reinforcement layers was observed right behind the facing of the structure. Based on this observation T_o appears to be higher than T_{max} and dictates the locus of T_{max}. However, after the bridge footing was placed on the abutment, the maximum tension in the reinforcement layers was observed away from the facing extending up to the backside of the bridge footing as reported in Abu-Hejleh et al. 2003. Figure 4.6.22 shows T_{max} distribution with depth due to self-weight loading. The profile is plotted with calculated reinforcement loads for active and at-rest earth pressures. Overall, the observed T_{max} distribution suggests a reasonably uniform distribution with depth. From the figure it can be observed that reinforcement loads were low at higher depth. This may occur due the embedment of the structure in a stiff foundation resulting in restraining tension in the reinforcement and deflection of the facing. Abu-Hejleh et al. 2003, states that the strain gages at 1.2 m (3.9 ft.) depth showed initial magnitudes that were much higher than the expected range and the estimated reinforcement loads at this location may be unreasonable. If the value of reinforcement loads estimated from this location decreases, then the T_{max} distribution with depth would show a more uniform distribution trend.

The connection load (T_o) was estimated using the lateral stress data from earth pressure cells installed at the back of the facing and the tributary reinforcement spacing. The earth pressure cells were installed 0.2, 0.6, 1.4, and 2.2 m (0.7, 2, 4.6, and 86.6 ft.) from the top of the abutment. T_o profile obtained from the field due to self-weight of backfill loading is plotted in Figure 4.6.23. T_o profile is plotted together with calculated forces using active and at-rest lateral earth pressures. Except from the data point at 0.6 m (2 ft.) depth, the T_o profile was almost uniform with depth and the magnitudes of the connection forces were lower than the active condition. Figure 4.6.23 also shows T_o profile obtained from strain gages installed close to the facing. T_o estimated using strain gages data follows uniform distribution with depth. T_o estimates from strain gage data were higher than earth pressure cell data. This observation is consistent with the results obtained from the Louisiana GRS-IBS. Overall, T_o distribution with depth appears to be uniform.

The results obtained from surveying of the facing of the abutment show that maximum recorded settlement after completion of structure was 20 mm (0.8 in.).

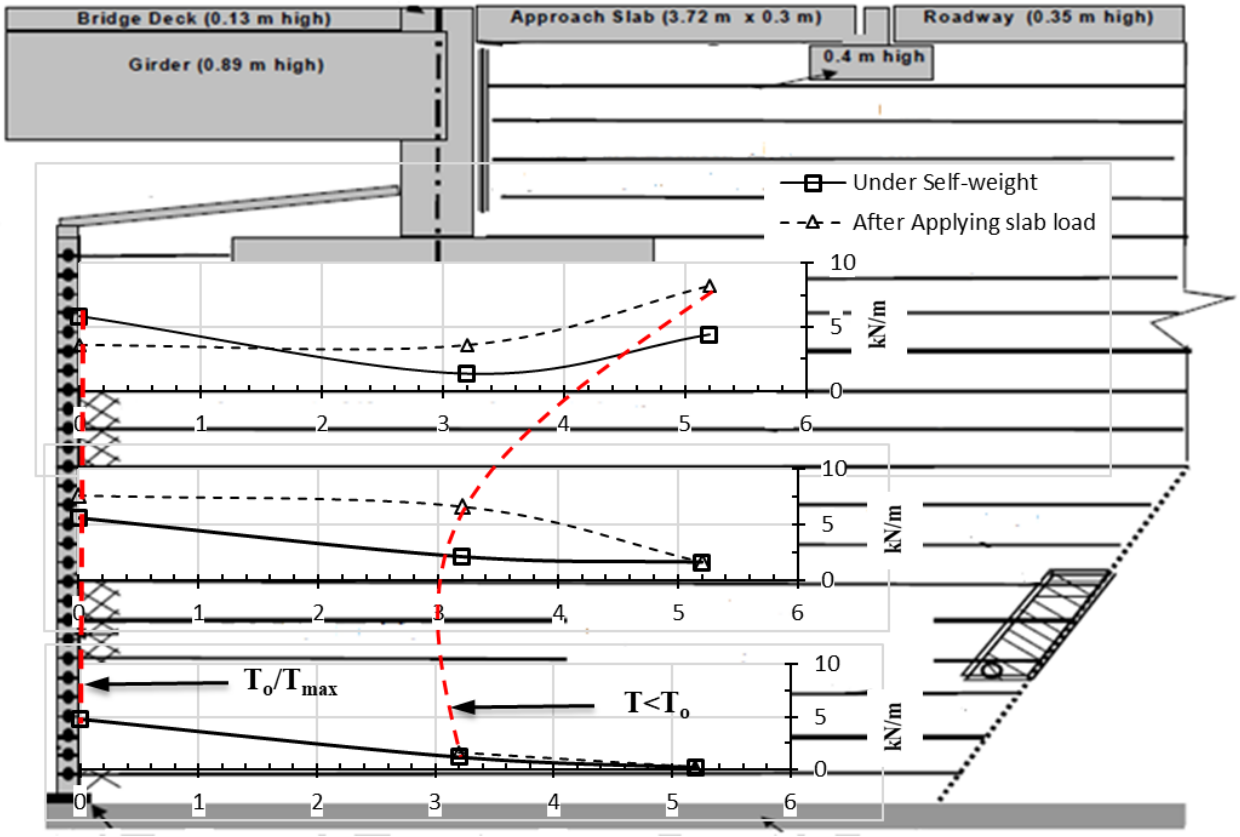

Fig. 4.6.21: Reinforcement load profiles along the reinforcement layers *due to self-weight of backfill and slab loading*

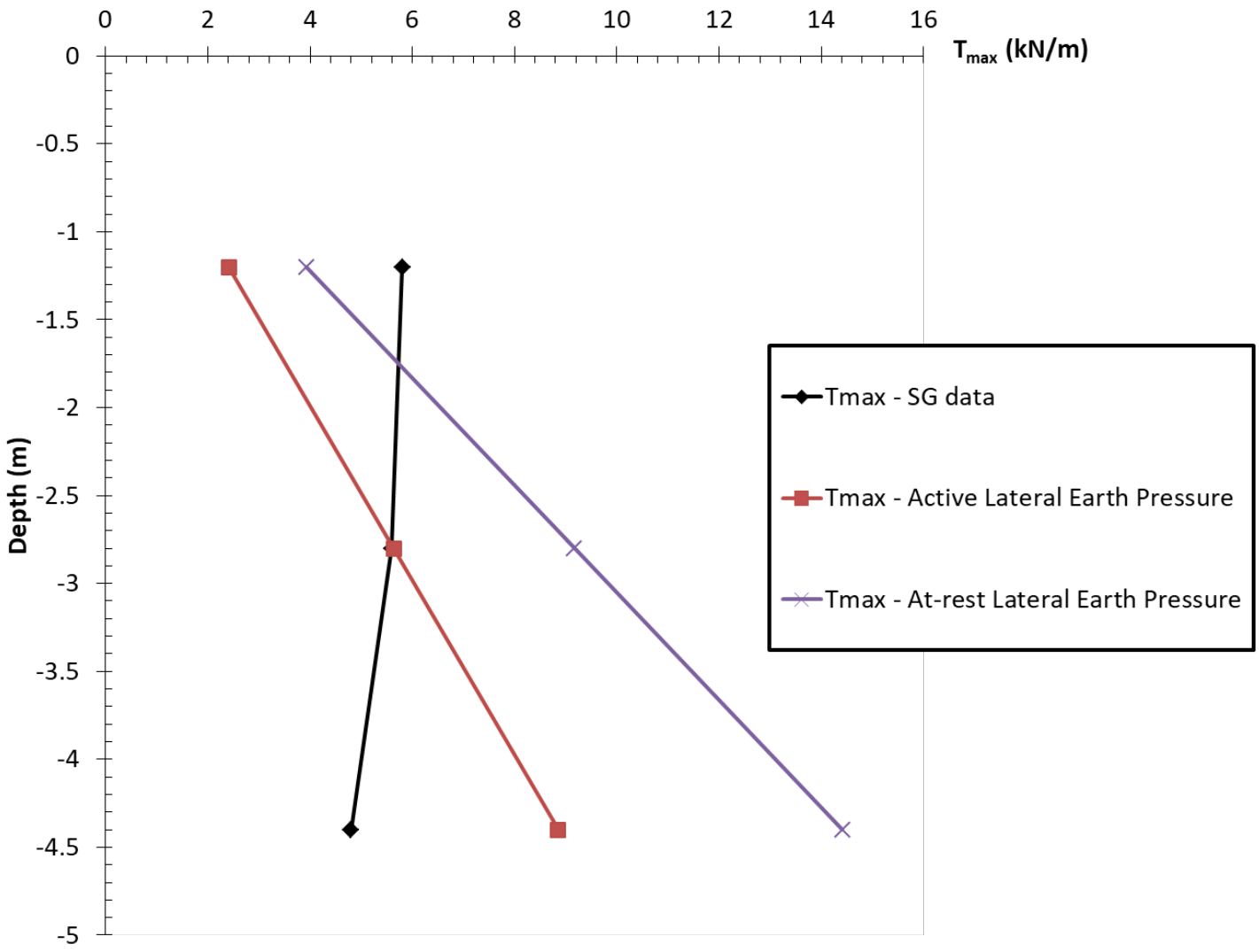

Fig. 4.6.22: T_{max} versus depth profile for self-weight of backfill loading

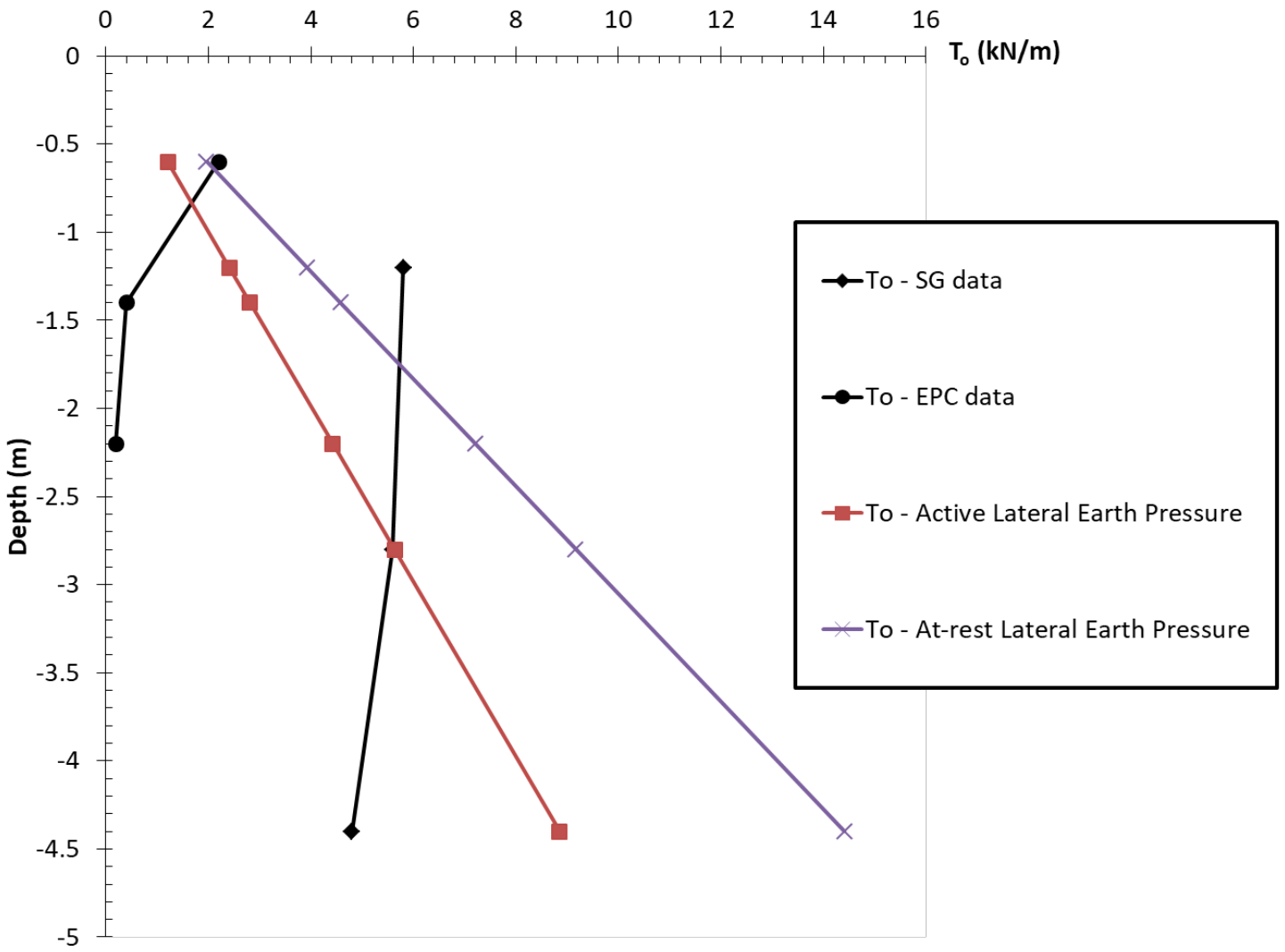

Fig. 4.6.23: T_o versus depth profiles due to self-weight of backfill loading

4.6.6 SUMMARY OF EVALUATION OF FIELD MONITORING DATA FROM OTHER PROJECTS

4.6.6.1 ASSESSMENT OF T_{MAX} VERSUS S_V AND T_{MAX} VERSUS DEPTH

Overall, T_{max} profile estimated from strain gages showed that the reinforcement load distribution versus depth can be interpreted as relatively uniform for different vertical reinforcement spacing (S_v). T_{max} remained nearly constant with depth despite what is predicted using active or at-rest lateral earth pressure theories. However, this speculation is considered with the acceptance of a rescannable variation in data. The design recommendation in chapter 8 related to a uniform distribution of reinforcement unit tension with depth is supported by the observations from the GRS-IBS and load-carrying GMSE abutment projects.

4.6.6.2 ASSESSMENT OF T_O VERSUS S_V

T_o profile obtained from the field follows the lateral stress distribution with a uniform distribution with depth for different vertical reinforcement spacing (S_v). The observed connection loads were reasonably uniform with depth, despite what is predicted using active or at-rest lateral earth pressure theories. T_o values in the observed uniform distribution were found to be within the range to what would be obtained using the triangular distribution assumed for T_{max} distribution. The design recommendation in chapter 8 related to a uniform distribution of reinforcement connection load with depth is supported by the observations from the GRS-IBS and load-carrying GMSE abutment projects. Values of T_o estimated using lateral stresses measured by earth pressure cells appear to be lower than values of T_o estimated using reinforcement strains measured by strain gages installed close to the facing. The discrepancy between T_o estimate with the two approaches may occur due the condition that T_o estimate from lateral stress data may not reflect the actual condition in a frictionally connected system as it is hard measure the load at the connection between the reinforcement and the facing using earth pressure cells. As a result, theoretical force equilibrium between T_o and lateral earth pressure acting in the reinforcement tributary area may not be fully satisfied.

4.6.6.3 ASSESSMENT OF PRESENCE OF BEARING BED

The influence of presence of bearing bed zone in the GRS-IBS and GMSE structures on vertical stress distribution was studied by quantifying the vertical stress distribution due to surcharge load using AASHTO 2:1 and FHWA Boussinesq stress distributions methods and comparing the computed results with the results obtained from the field. It was observed that both theoretical stress distribution methods provided similar stress distribution trends and comparable stress levels as obtained from the field.

4.6.6.4 ASSESSMENT OF SETTLEMENT

The maximum observed foundation settlement on GRS-IBS and GMSE abutments that had an abutment height of 4.3, 4.8, 5.9, and 7 m (14.1, 15.7, 19.4 and 23 ft.) were 6, 5, 20, and 50 mm (0.23, 0.19, 0.78 and 2 in.) respectively. It was observed that settlement in the structures increased with an increase in height of the abutments.

5 EXPERIMENTAL INVESTIGATION

5.1 DEVELOPMENT OF SOIL-GEOSYNTHETIC COMPOSITE INTERACTION EXPERIMENTAL APPROACH

5.1.1 INTRODUCTION

The use of soil reinforcement has been widely recognized as an alternative technology to address many challenges in the geotechnical and transportation projects (e.g. reinforced soil walls, reinforced soil steep slopes, soil reinforced structures as part of load-carrying bridge abutments, reinforced soil load transfer platforms over pile foundations, reinforced soil mats, reinforced subgrade soils in unpaved roadways). The interaction between the soil and reinforcement plays a key role in load transfer forming a composite material that has the appropriate strength to bear the applied loads. The spacing between reinforcement layers governs the degree of interaction not only between the reinforcement layer and surrounding soil, but also between the soil-reinforcement interfaces of neighboring reinforcement layers. This complex interaction has revealed that vertical spacing between reinforcement layers may play a key role in the overall mechanical response of the reinforced soil composite mass. Reinforcement spacing has been reported to have a greater effect on the reinforced soil composite strength than that of the reinforcement tensile strength. This observation was reported as occurring in conditions where reinforcement spacing was small (e.g. Nicks et al. 2013). However, there is need for further understanding of the mechanisms and extent of such effect.

This chapter presents a new experimental approach to assess the behavior of reinforced soil structures. This evaluation includes: (1) a review of the soil-reinforcement interaction experimental modeling of reinforced soil structures based on pullout loading; (2) a description of newly developed testing approach and equipment used in soil-reinforcement interaction behavior assessment; and (3) a description of the experimental testing procedure implemented; and (4) typical testing results to show the capabilities of the proposed testing approach.

5.1.2 TECHNICAL REVIEW

The interaction of reinforcements with the surrounding soil involves complex shear stress transfer mechanisms, the manifestation of which is a shear band that develops in the vicinity of the reinforcement (e.g. Palmeira 2009). Beyond this zone, the soil is no longer affected by the reinforcement. The thickness of this band may be affected by a number of factors, including the reinforcement type and tensile stiffness, particle size, angularity, deformability and shear strength of the reinforced fill material, and the characteristics of the soil-geosynthetic interface. A composite response is expected to result when the shear bands of two contiguous reinforcements interact with each other (Leshchinsky et al. 1994). Accordingly, the thickness of the shear band represents the limit beyond which the composite behavior of reinforcements no longer occurs. That is, the shear bands of closely-spaced reinforcements interfere with each other and change the interaction from a simple tie-back mechanism to a more complex, composite

mechanism that has been reported to include increased confinement, reduced lateral movements and reduced soil dilation (e.g. Adams et al. 2012).

This section includes a detailed literature review on pullout testing equipment, which serves as basis for the development of the new equipment. This review focuses on the reported limitations of soil-geosynthetic interaction equipment (e.g. dimensions, materials, instrumentation) in order to benefit from the experience of other studies. While much of the focus in the evaluation of soil-reinforcement interaction corresponds to pre-failure conditions, the pullout testing technique is a good basis to investigate the interaction behavior. Pullout tests have been proven to be suitable for different types of geosynthetics and soil types (ASTM D6706). The pullout resistance was found to be function of variables such as soil gradation, plasticity, relative compaction, moisture content, and geosynthetic characteristics (ASTM D6706). Pullout tests involve embedding a geosynthetic within soil mass and imposing axial loads to mobilize soil-geosynthetic interaction mechanisms. The soil mass is subjected to a normal pressure to reproduce a representative state of stresses on the soil-reinforcement interface. Much of the previous research has been on different boundary effects, testing procedures, preparation methods, and compaction techniques (e.g., Juran et al. 1988; Farrag et al. 1993). The test is standardized in ASTM D6706 with resent revision made to mimic the as-built conditions as closely as possible. The characteristics and limitations of pullout testing equipment, as reported in the technical literature, are summarized next.

5.1.2.1 BOX DIMENSIONS

According to ASTM D6706, the length of a pullout box should exceed 0.6 m (2 ft.), and should be larger than 5 times the maximum aperture size if a geogrid reinforcement is used. The width of the box should be larger than 0.75 m (2.5 ft.) in devices with rough side walls, and 0.45 m (1.5 ft.) in devices with smooth side walls. Also, the width should exceed 20 times the D85 of the soil, as well as 6 times the maximum soil particle size. The box depth should accommodate soil thickness above and below the geosynthetic and be greater than 0.15 m (0.5 ft.), greater than six times the D85 of the soil, and greater than three times the maximum soil particle size. Ladeira (1995) developed a box measuring 1.53 m (5 ft.) long by 1.00 m (3.3 ft.) wide by 0.80 m (2.6 ft.) high, and demonstrated that these dimensions minimized lateral and horizontal boundary effects.

The height of the newly developed equipment in this study was chosen 1.20 m (4 ft.) to allow varying the vertical reinforcement spacing up to 0.6 m (2 ft.). The width of the equipment was chosen 0.75 m (2.5 ft.) to avoid any potential arching of the fill material with the side walls, especially when adopting the full-height configuration of the box and soils of relatively large-sized granules. The length of the equipment was 1.5 m (5 ft.) to reasonably suit the chosen width. The aspect ratio of the length to width is particularly important in controlling the aspect ratio of the reinforcement specimens. Note that the objective of the pullout device developed in this work was to determine soil-reinforcement interaction not only at failure but also during the stage in which the load carried by the reinforcement increases. That is, the objective was to also observe the shear band development around one and multiple geosynthetic sheets as their strength is being mobilized.

5.1.2.2 REINFORCEMENT LENGTH

According to ASTM D6706, the specimen length in pullout tests should extend 0.6 m (2 ft.) beyond the sleeve and measure at least twice the sample width (i.e. length-to-width ratio should exceed two). Lopes and Ladeira (1996) defined an adherence factor as the ratio of the tangential stress at the soil-reinforcement interface to the product of normal stress at the interface and the tangent of the soil friction angle at the testing stress level. They reported a decrease in the adherence factor as the specimen length increased. However, they noted that the factor should have been greater than the values reported, as the specimens failed because tension exceeded the tensile capacity, rather than because of a deficiency in adherence. Lopes (1992) demonstrated that the influence of specimen length on interface shear resistance was minimal beyond a certain length. However, Moraci and Recalcati (2006) reported that pullout behavior depended on specimen length. They indicated that the pullout interaction mechanism developed progressively along the length of the specimen, with a gradual increase in pullout resistance and displacement.

5.1.2.3 REINFORCEMENT WIDTH/SIDE BOUNDARIES

According to ASTM D6706, there should be a clearance between the edge of the specimen and both side walls. This clearance should exceed 0.075 m (3 in) in devices with smooth side walls, and 0.15 m in devices with rough side walls (ASTM D6706; Farrag et al. 1993). The width of the specimen should exceed 0.3 m (1 ft.) and include at least five tensile elements. The friction of the side walls was found to reduce the amount of normal stresses applied at the soil-reinforcement interface (Farrag et al. 1993). Jewell (1980) recommended lining the side walls with lubricated membranes to minimize friction. Lopes and Ladeira (1996) studied the effect of specimen width on pullout resistance and did not observe a significant influence. However, the results showed a slight increase in pullout resistance and a slight decrease in the adherence factor with a decrease in specimen width.

5.1.2.4 SOIL THICKNESS/UPPER AND LOWER BOUNDARIES

ASTM D6706 requires that the box depth accommodate a soil thickness above and below the geosynthetic greater than 0.15 m (6 in.), greater than 6 times the D85 of the soil, and greater than 3 times the maximum particle size of the soil. Interaction may develop between the upper and lower boundaries and the soil-reinforcement interface. Farrag et al. (1993) developed a box measuring 1.52 m (5 ft.) long by 0.90 m (3 ft.) wide by 0.76 m (2.5 ft.) high. They reported that this interaction increased as soil thickness decreased, and thus influenced test results. They also reported the development of shear forces between the soil and horizontal boundaries, and the bottom boundary in particular. Brand and Duffy (1987) studied the effect of soil thickness on pullout resistance. Based on a limited number of tests, the authors observed that pullout resistance decreased as soil thickness increased, but only up to a certain value, beyond which there was no further change. Lopes and Ladeira (1996) showed that the predicted friction angle of the soil may increase beyond values measured using conventional techniques due to an increased confining pressure as a result of repressing soil dilatancy (Lopes and Ladeira 1996; Farrag et al. 1993). Lopes and Ladeira (1996) reported that specimen length significantly affects the impact of the upper and lower boundaries on test results. Palmeira and Milligan (1989) reported that an increasing specimen length to soil thickness ratio led to greater influence of the

upper and lower boundaries of the pullout box. Farrag et al. (1993) reported that soil thickness should exceed 0.3 m (1 ft.) above and 0.3 m (1 ft.) below the reinforcement to eliminate the effect of the horizontal boundaries. Farrag et al. (1993), Ladeira (1995), and Lopes and Ladeira (1996) used a modular structured box to facilitate changes in soil thickness in various tests.

5.1.2.5 SLEEVE LENGTH

According to ASTM D6706, the box should have a metal sleeve consisting of two thin plates less than 12.5 mm (0.5 in) thick. Inside the box the sleeve should extend to a distance greater than 0.15 m (6 in) and preferably equivalent to the thickness of the soil above the geosynthetic. The interior sleeve end should be tapered to reach a maximum contact thickness of 3 mm (0.12 in). Palmeira and Milligan (1989) reported that interaction developed between the reinforced soil mass and the rigid front wall of the pullout box. They showed that this interaction increased as friction along the front wall increased. During pullout tests, the lateral earth pressure developed on the front wall of the box increased, resulting in an increase in pullout resistance (Farrag et al. 1993). The sleeve allowed the pullout force application line to be transferred away from the soil adjacent to the front wall to the inner soil mass (Christopher 1993; Farrag et al. 1993). Williams and Houlihan (1987) used flexible front walls in an attempt to reduce the effect of rigid walls. Lopes and Ladeira (1996) investigated the effect of the sleeve on pullout resistance. They observed an increase of approximately 10% in the apparent pullout resistance in the absence of the sleeve. They reported that the frictional stresses developed on the front wall of the box resulted in increased vertical stress acting on the reinforcement. Lateral pressure was measured in their study and in the absence of the sleeve, higher pressure on the front wall was observed during testing. This increased lateral pressure resulted in increased shear stresses developed at the soil-reinforcement interface at the front section of the specimen, and in decreased shear stresses developed at the back section of the specimen. They recommended using a 0.2 m (8 in) long sleeve inside the box to reduce the frictional effects of the front wall boundary. Farrag et al. (1993) reported that a sleeve at least 0.3 m (1 ft.) long should be used to eliminate the front wall effect.

5.1.2.6 REINFORCEMENT PULLOUT LOADING SYSTEM

The axial force must be at the same level as the geosynthetic plane so as not to interfere with the soil-reinforcement shear surface (ASTM D6706). According to ASTM D6706, the pullout force should be applied at a constant displacement rate of 1 mm/min (0.04 in/min) +/-10%. However, a constant stress loading approach can also be adopted. This approach may be achieved by three different methods. The first method involves a controlled stress rate, which simulates short-term conditions. In this method a uniform rate of loading is applied to a maximum value of 2 kN/m/min (11.42 lbs/in/min). The second method involves incremental stress, which is also suitable for short-term conditions. In this method, the pullout load is increased incrementally. The third method involves constant stress (creep), which is suitable for long-term conditions. In this method one of the two previous methods is adopted until the desired loading level is reached, and then constant stress is maintained for a period of time.

The pullout force has been reported to be applied using displacement rates ranging from 0.1 to 20 mm/min (4 mil/min to 0.8 in/min). The pullout force is typically applied at a controlled

displacement rate (Farrag et al. 1993). However, some researchers have carried out pullout tests using load controlled systems (e.g. Tzong and Cheng-Kuang 1987). Farrag et al. (1993) also studied the effect of displacement rates on pullout resistance. They conducted tests using displacement rates of 2, 6, 10 and 20 mm/min (0.08, 0.24, 0.4, 0.8 in/min). They reported that high displacement rates affected the pullout force and displacement distribution. Specifically, it was reported that at high displacement rates, reinforcement strains were minimally mobilized, resulting in a higher contribution to the interface resistance than to the passive resistance of the transverse ribs. They recommended displacement rates below 6 mm/min (0.24 in/min) to minimize the displacement rate effects. Fannin and Raju (1993) studied the influence of the pullout displacement rate on pullout resistance at low rate levels. They adopted displacement rates of 0.25, 0.50 and 1.00 mm/min (0.01, 0.02 and 0.04 in/min). They reported that pullout resistance is independent of the pullout displacement rate at low rate values. Yet, their data showed a slight increase in pullout resistance with an increase in the displacement rate.

5.1.2.7 REINFORCEMENT CLAMPING SYSTEM

A clamp is used to attach the geosynthetic to the pulling system. The design should be such that the specimen is held without any slipping, breaking or weakening. The clamp should ensure uniform pullout stress distribution along the width of the specimen so as not to interfere with the shear stress on the soil-reinforcement interface (ASTM D6706). The clamping system typically consists of two steel plates sandwiching the geosynthetic (Farrag et al. 1993; Stadler 2001). Roller grips have also been used to clamp the geosynthetic specimen to the pullout box. Zornberg et al. (2009) used a roller grip consisting of a steel cylinder with a slit to which the specimen could be attached and bolted. Zornberg et al. (2009) reported that the roller grip design helped prevent stress concentration at a single plane throughout the specimen by distributing it uniformly over a wider area.

5.1.2.8 UNCONFINED REINFORCEMENT PORTION

Some studies reported clamping of the reinforcement outside the box, thus leaving a portion of the reinforcement unconfined outside the box (Koerner 1986; Brand and Duffy 1987; Stadler 2001; Zornberg et al. 2009). Other researchers either used clamps or confine the reinforcements between two metal plates with an adhesive inside the sleeve to avoid having unconfined zones (e.g. Farrag et al. 1993; Ladeira 1995; Lopes and Ladeira 1996).

5.1.2.9 CONFINING NORMAL STRESS LOADING

Normal stress is applied to the top of the soil such that the soil-reinforcement interface reaches the desired level of confinement. The applied normal stress should be uniform and remain constant throughout the test. In order to maintain constant normal stress, ASTM D6706 recommends using a flexible pneumatic or hydraulic diaphragm-loading device that covers the entire area of the box. Normal stress has commonly been applied by an air-bag fixed to the interior top side of the box and covers the entire area to ensure a constant uniform stress on top of the soil (Ingold 1983; Palmeira and Milligan 1989; Farrag et al. 1993). Lopes and Ladeira (1996) used a thick neoprene rubber layer and wooden plates to achieve uniform stress distribution on top of the soil. They applied confining stress to the wooden plates using 10 pressure cylinders. Zornberg et al. (2009) and Hanumasagar et al. (2014) used six air pressure cylinders jacking

against a steel lid. Jayawickrama et al. (2014) utilized nine pressure plates hydraulically jacked against three wide flange cross beams.

5.1.2.10 REINFORCEMENT STRAINING MEASUREMENTS

To measure the internal displacements in reinforcement layers and assess their elongation along the specimen, inextensible wires are typically attached to the reinforcement at different locations. Attached to the other end of the inextensible wires are linear potentiometers (Lopes and Ladeira 1996; Zornberg et al. 2009), or LVDTs (ASTM D6706; Farrag et al. 1993), that are fixed outside the pullout box. Tubes protect the wires from the confining pressure applied to the soil mass (ASTM D6706; Farrag et al. 1993). Displacement have also been measured using magnets attached to reinforcements with adhesive with sensors to measure movement of the magnets (Salomone, 1978). Movements that develop at different locations along the extensible reinforcement during pullout testing have been reported to involve two components: (1) displacement due to the shear strain of the soil-reinforcement interface; and (2) reinforcement elongation.

5.1.2.11 SOIL DEFORMATION MEASUREMENTS

Other research studies aimed to generally measure internal displacements within the backfill. Some pullout testing devices have utilized transparent boundary surfaces to monitor soil grain trajectories (Fannin and Raju 1993; Leshchinsky et al. 1994; Zhou et al. 2012). Transparent boundaries were also used in a number of other devices that investigated soil-reinforcement interaction (Jacobs et al. 2002a, 2002b, 2003). These surfaces allow visualization of the kinematic response of soil particles in general, and those adjacent to the geosynthetic reinforcement layers in particular. In addition, Fannin and Raju (1993) used LVDTs on the top of a reinforced soil mass in pullout testing equipment, which allowed for the measurement of dilation.

5.1.2.12 COMPACTION AND SPECIMEN PREPARATION

Soil layers are placed and compacted in the box to its mid-height and then the reinforcement specimen is placed and then the rest of the soil layers are compacted on its top to the full height of the box. The required number of lifts and compaction effort depend upon the type of the soil and the desired compaction moisture content (ASTM D6706). Farrag et al. (1993) and Lopes and Ladeira (1996) placed and compacted soil layers 0.15 m (6 in) thick. Sand has been placed in the box by pouring it from a constant height (Jewell 1980; Palmeira and Milligan 1989; Farrag et al. 1993; Lopes and Ladeira 1996). Compaction has also been performed using electric vibratory hammers (Lopes and Ladeira 1996), electric jack hammers, standard proctor hammers (Saxena and Budiman 1985), mechanical compaction (Chang et al. 1977; Farrag et al. 1993; Alfaro et al. 1995a; Stadler 2001), hand tamping (Elias 1979; Hanumasagar et al. 2014), and pluviation (Palmeira and Milligan 1989; Farrag et al. 1993; Min et al. 1995; Ochiai et al. 1996). Relative density of the compacted layer can be verified by using density gauges (Farrag et al. 1993; Lopes and Ladeira 1996), conducting sand cone tests (Stadler 2001), or weighing the box before and after soil placement (Alfaro et al. 1995a; Cuelho 1998).

Table 5.1.1 shows the characteristics of pullout equipment used in several studies along with the requirements of GRI GT6 (1991) and EN 13738 (2004).

Table 5.1.1. Reinforcement pullout test devices (Modified after Minažek and Mulabdić 2013).

Reference	Dimensions L (m) x W (m) x H (m)	Pullout force generation, with increase D – deformation (mm/min), N – stress (description)	Sleeve: exist (yes/no, description, width (m))/clamping system (description)	Soil thickness bellow/above reinforcement (m)	Force and displacement sensors	Compaction and density
Chang *et al.* (1977)	1.30 x 0.91 x 0.51	D	-	-	-	Mechanical compaction
Salomone (1978) and Salomone et al., 1980	1.90 x 0.70 x 0.7	N (incremental 1,8, 2.7, 4,4 and 6.7 kN)	No	0.30/0.30	Load cell, magnets glued to geotextile	89% relative density
Yuan and Chua (1985)	0.76 x 0.71 x 0.61	D (hydraulic)	-	0.30/0.30	Load cell, displacement transducers	-
Palmeira and Milligan (1989)	0.25 x 0.15 x 0.15 1.10 x 1.10 x 1.10	D (0.5 mm/min, hydraulic)	No (just opening in front box side) // clamps (connected with bolts and aluminum alloy to reinforcement)	-	Photo measurement of wires out of the box, 8 load cells on the front box side, LVDT – on the piston, load cell	Pluviation, vibrocompactor, cylinders in the box
Bonczkiewicz et al., (1990) and Christopher (1993)	1.30 x 0.80 x 0.50	D (1 mm/min, hydraulic)	Yes (width 0.15 m)	0.15 m /0.15 m	Load cell, LVDT	Vibratory Compaction
Farrag *et al.* (1993)	1.52 x 0.90 x 0.76	D, N (max 6 mm/min, hydraulic)	Yes (width 0.3 m) // clamps (plates inside sleeve and soil)	Min. 0.30/0.30	LVDT, velocity transducers and load cells, pressure cell on front box side	Pluviation, mechanical compaction, nuclear densimeter
Alfaro *et al.* (1995b)	1.60 x 0.70 x 0.50	D (1 mm/min)	Yes (width 0.2 m) // clamps (plates inside sleeve)	0.25/0.15	LVDT, load cells	-
Fannin and Raju (1993)	1.30 x 0.64 x 0.60	D	No // clamps (there is upper and lower clamps)	-	Load cell, 2 displacement transducers, piezometers, 5 extensometers	-
Kharchafi and Dysli (1993)	-	-	-	-	x-ray records	-
Bergado *et al.* (1994)	1.30 x 0.80 x 0.50	D (1 mm/min, hydraulic)	-	-	Load cell, LVDT	-
Koerner (2005)	1.90 x 0.91 x 1.10	D, N (1 mm/min, hydraulic)	Yes // clamps (no)	Min. 0.30/0.30	Load and displacement transducers	-
Min *et al.* (1995)	0.60 x 0.60 x 0.20	N (hydraulic, electric, cyclic load, force increments for 24 h)	No // clamps (grid glues on metal plates which extend 0.1 m in the box)	-	Load cells, LVDT at front, 4 extensometers on grid	Pluviation
Alfaro *et al.* (1995a)	1.60 x 0.50 x 0.60	D	Yes // clamps (inside the box)	0.25/0.15	Load cell, LVDT	Mechanical compaction, weighing
Lopes and Ladeira (1996)	1.53 x 0.80 x 1.00	D (hydraulic)	No or yes (width 0.2 m) // clamps (exist)	0.30/0.30	Load cell. LVDT, vertical pressure cell LVDT on grid	Nuclear densimeter
Ochiai *et al.* (1996)	0.60 x 0.40 x 0.40	D (1 mm/min, reducer, cyclic)	Yes // -	-	Load cell, displacement transducers	Pluviation

Table 5.1.1. Reinforcement pullout test devices (Modified after Minažek and Mulabdić 2013) (Continued).

Reference	Dimensions L (m) x W (m) x H (m)	Pullout force generation, with increase D – deformation (mm/min), N – stress (description)	Sleeve: exist (yes/no, description, width (m))/clamping system (description)	Soil thickness bellow/above reinforcement (m)	Force and displacement sensors	Compaction and density
Bernal *et al.* (1997)	1.22 x 0.50 x 1.22	D (1 mm/min, 2 hydraulic cylinders)	Yes (width 0.15 m) // clamps (reinforcement sample in resin, bolted to two plates)	0.205/0.205	Load cell, LVDT, 3 displacement transducers on sample, total cell on box bottom	Hand compaction
Cuelho (1998)	1.25 x 1.10 x 0.90	D, N (0-2 mm/min, electrical-reducer, 2 air cylinders)	Yes (width 0.26 m) // clamps (plates with reinforcement samples glued)	-	Load cell, extensometers (5), glued deflectometers	Vibro-compactor, weighing
Teixeira (2003)	1.50 x 0.48 x 0.70	D (4,6 mm/min, electrical, reducer)	Yes (width 0.2 m) // clamps (bolted to the reinforcement samples, passing through sleeve)	-	Load cell, 3 total cells, 6 extensometers on the sample, deflectometers	-
Alagiyawanna *et al.* (2001)	0.68 x 0.625 x 0.30	D (1 mm/min)	No, sponge to prevent soil loss, // -	-	Displacement transducer, laser sensors for grid displacements, load cell for vertical and horizontal direction	-
Bergado and Teerawattanasuk (2001)	1.27 x 0.76 x 0.51	D (1 mm/min, hydraulic)	-	-	-	Pluviation
Meyer *et al.* (2003)	1.50 x 0.70 x 0.60	D (2 mm/min, hydraulic, cyclic load up to 4 Hz)	Yes (width 0.2 m) // clamps (reinforcement is rolled or pulled with two rods)	-	3 load cells on bottom, LVDT	Weighing, nondestructive methods
Marques (2005)	1.53 x 1.00 x 0.80	(hydraulic)	Yes (width 0.2 m) // -	0.40/0.40	Different measuring instruments	Mechanical compaction, weighing system on the box bottom
Moraci and Gioffrè (2006)	1.70 x 0.60 x 0.68	(electrical)	Yes (width 0.25 m) // clamps (inside soil)	-	RVDT (6 on grid sample), load cell	-
Abdelrahman *et al.* (2007)	1.20 x 1.16 x 0.70	(hydraulic, hand)	No // clamps (two steel plates with thickness of 6 mm)	-	2 sensors: 1 vertical, 1 horizontal, 2 LVDT on sample	Mechanical compaction
Aydogmus and Klapperich (2008)	0.60 x 0.50 x 0.20	D (0.000001-12 mm/min)	No // clamps (outside the box)	0.10/0.10	Load cell, pressure measurement at box bottom and in airbags	Pluviation, mechanical
Abdelouhab *et al.* (2008)	2.00 x 1.10 x 1.10	-	-	-	Load cell and total cell (front and bottom box side)	-
Requirements of EN 13738 (2004)	1.50 x 0.60 x 0.30	D, N (2+/-0.2 mm/min, hydraulic)	Yes (width 0.20 m), clamps (articularly connected)	$6D_{max}/6D_{max}$	LVDT, load cells	-

Table 5.1.1. Reinforcement pullout test devices (Modified after Minažek and Mulabdić 2013) (Continued).

Reference	Dimensions L (m) x W (m) x H (m)	Pullout force generation, with increase D – deformation (mm/min), N – stress (description)	Sleeve: exist (yes/no, description, width (m))/clamping system (description)	Soil thickness bellow/above reinforcement (m)	Force and displacement sensors	Compaction and density
Requirements of GRI GT6 (1991)	1.20 x 0.75 x 0.60 or > $20D_{85}$	D (1 mm/min)	Yes (width 0.15 m) // clamps (2 plates width 0.20 m)	Min. 0.30/0.30	LVDT, measuring ring, load cells	-
Stadler (2001)	0.95-1.50 x 1.20 x 0.60 (adjustable length)	D (1 mm/min, hydraulic)	Yes (width 0.15 m) // clamps (outside the box)	0.18/0.18	3 LVDTs for confined geosynthetic, 2 LVDT for pullout bar, 1 LVDT for unconfined geosynthetic, 2 pressure transducers for pullout actuators	Mechanical and hand compaction, sand cone test
Jayawickrama *et al.* (2014)	3.60 x 3.60 x 1.20	(hydraulic)	-	-	5 vertical pressure cells, pressure transducer for normal stress jacks, load cell for pullout jack, optical and digital measures for geosynthetic displacement	-
Hanumasagar *et al.* (2014)	1.50 x 0.60 x 0.30	D (1 mm/min, hydraulic)	Yes (width 0.075 m) // clamps (roller grips outside the box)	0.15/0.15	-	Hand tamping and jack hammer
Zornberg *et al.* (2009)	1.50 x 0.60 x 0.30	D (1 mm/min, hudraulic)	Yes (width 0.075 m) // clamps (roller grips outside the box)	0.15/0.15	Load cell for pullout force and LVDTs for geosynthetic displacement	Hand tamping and jack hammer

5.1.3 EXPERIMENTAL APPROACH

A new experimental setup was designed and developed at the University of Texas at Austin to evaluate the soil-reinforcement composite behavior and to quantify the thickness of the soil shear band that develops in the vicinity of the soil-reinforcement interface upon shear stress generation (Morsy 2017). The box was designed to accommodate soil specimens up to 1.2 m (3 ft.) deep, 1.50 m (5 ft.) long, and 0.75 m (2.5 ft.) wide. Six pneumatic actuators are placed on wooden pyramids that cover the top surface of the reinforced soil mass. The actuators react against a stiff reaction frame, which conveys the reaction load exerted by the actuators to the bottom of the box. This normal pressure system allows for assessment of soil dilatancy. In addition, this system can maintain a zero-volume-change condition to allow for comparison of the soil-reinforcement interaction under conditions that either fully allow or fully suppress soil dilation. The axial pullout loading system consists of two hydraulic actuators reacting against the front wall of the box. The pullout system is connected to a clamping system that conveys the applied tensile load to the active reinforcement. The embedded geosynthetic is subjected to increasing loads, with particular focus on the responses under loads representative of working stress and ultimate loads. In addition to the active reinforcement layer, two other passive reinforcement layers of the same type are used as upper and lower boundaries to represent the presence of contiguous reinforcements. Soil is placed between the boundary geosynthetics and the top and bottom boundaries of the box. Note that tests conducted using varying soil thicknesses resulted in differences in the unit tension carried by the reinforcement. A combination of collars (to heighten the box) is used to control the soil thickness. The equipment is heavily instrumented to monitor the potential interaction that takes place between the closely-spaced contiguous reinforcement layers. The following sections provide a detailed description of the developed testing equipment and the adopted instrumentation and monitoring techniques.

5.1.3.1 TESTING EQUIPMENT

Figure 5.1.1 shows a schematic layout of the testing equipment, which is based on the framework of a large-scale pullout test. Of particular relevance, this experimental system has the ability to vary the thickness of the soil layer above and below the active reinforcement system, as well as the characteristics of the materials used as top and bottom boundaries of the reinforced soil mass. The equipment includes a geosynthetic-reinforced soil mass that contains three reinforcement layers as shown in the schematic cross-section in Figure 5.1.2. Additionally, the equipment is extensively instrumented to facilitate: (1) evaluation of the effect of the shear stress generated at soil-reinforcement interfaces of one reinforcement layer on the neighboring reinforcement layers; (2) mapping the pressure within the entire reinforced soil mass to assess local changes in confining pressure on the soil-reinforcement interface with increasing shear stresses; (3) mapping the straining of geosynthetic reinforcements; (4) characterizing the evolution of the shear band in the vicinity of the soil-reinforcement interface; (5) quantifying the stiffness of the soil-reinforcement interface; (6) evaluating the unit tension in the reinforcement at working stress and ultimate stress levels; (7) assessing the unconfined tensile properties of the tested reinforcement specimen corresponding to every soil-reinforcement interaction test; (8) assessing the dilation of the reinforced soil mass upon shear stress generation at the soil-

reinforcement interface when volume changes are allowed; (9) assessing the suppressed-dilation pressure within the reinforced soil mass upon shear stress generation at the soil-reinforcement interface when volume changes are restricted; and (10) evaluating the creep effect on soil-reinforcement interface strength. The equipment mainly consists of: (1) box in which the reinforced soil mass is placed; (2) normal loading system; (3) reinforcement clamping system; and (4) pullout loading system. Each of these components is described in detail in the following sub-sections.

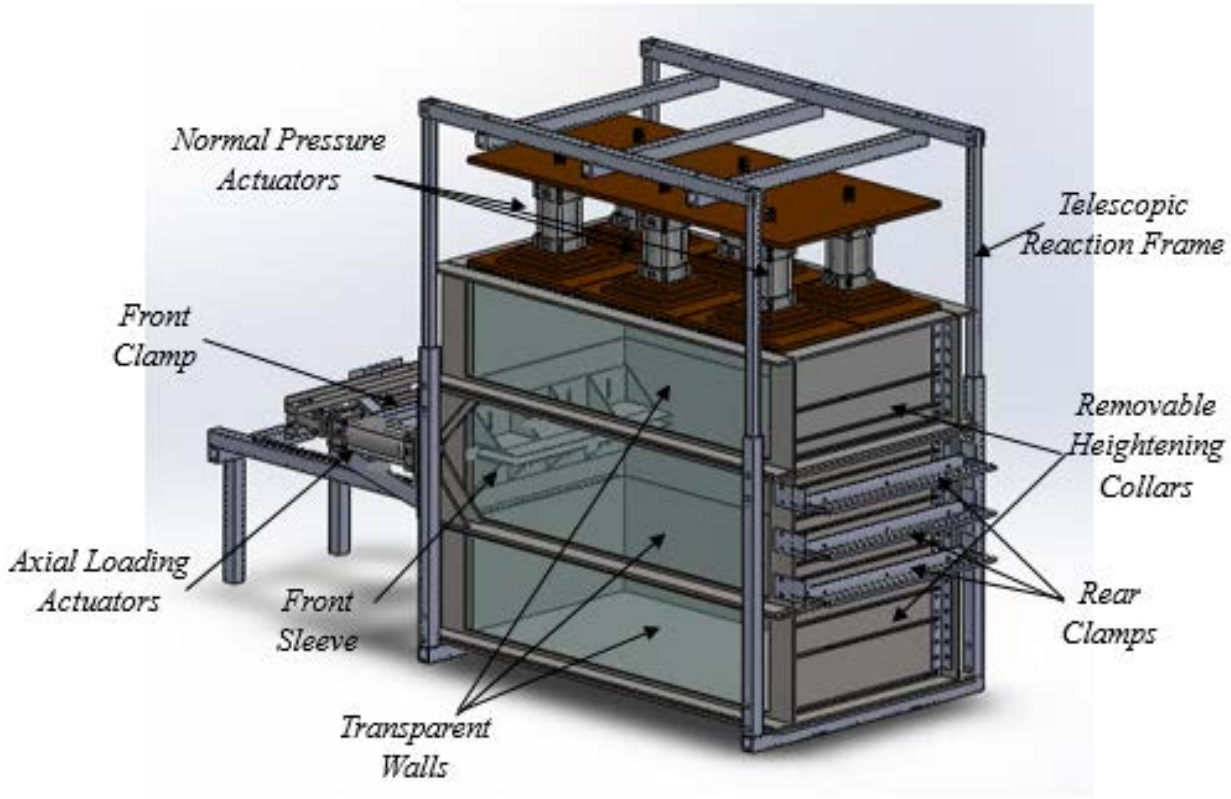

Figure 5.1.1. General layout of the experimental equipment.

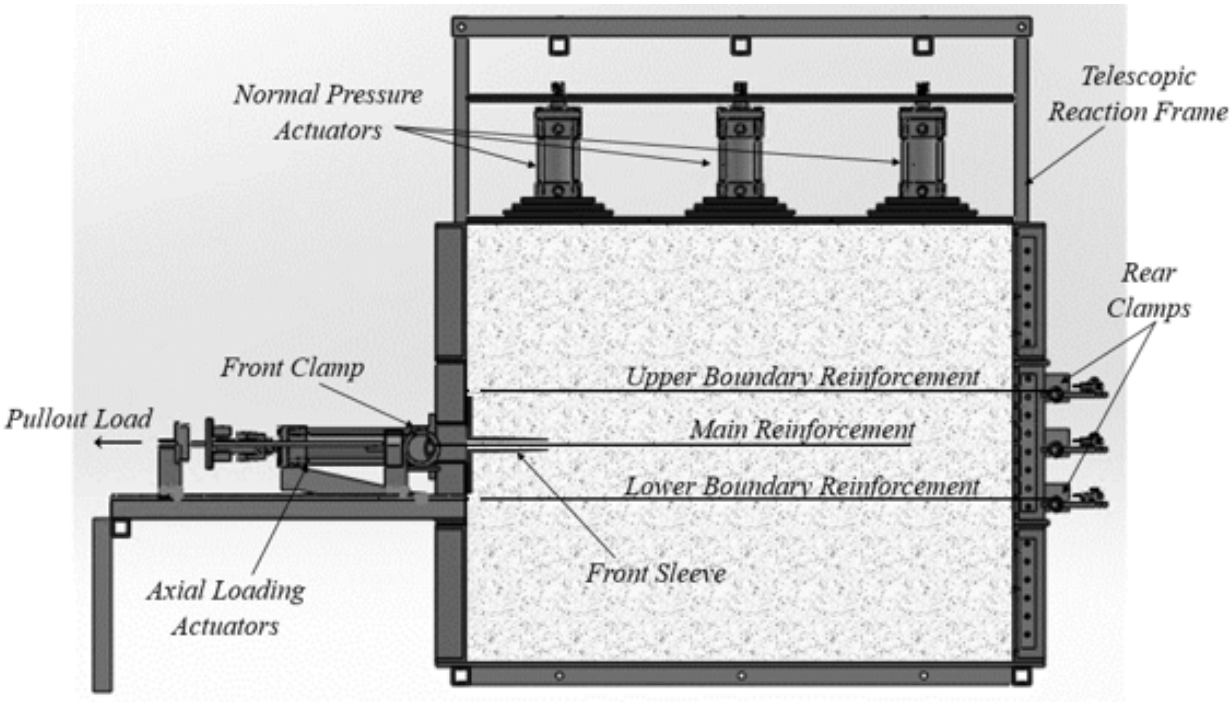

Figure 5.1.2. Schematic sectional side view of the experimental equipment.

5.1.3.2 REINFORCED SOIL BOX

The reinforced soil mass is accommodated in a steel box that is 1.5 m (5 ft.) long, 0.75 m (2.5 ft.) wide, and up to 1.2 m (4 ft.) deep. These dimensions are selected to allow varying the reinforcement vertical spacing from 0.05 to 0.6 m (2 in. to 2 ft.). The box consists of three stacked collars; the middle collar is the main collar and is 0.45 m (18 in) deep, and the top and bottom collars are removable and are 0.375 m (1.2 ft.) deep. That is, the box depth can be either 1.2 m (4 ft.) when the three collars are used or 0.45 m (1.5 ft.) when only the middle collar is used as shown in Figures 5.1.3a and 5.1.3b, respectively. Every collar consists of four steel channel beams forming its walls. One of the side walls of each collar is windowed to accommodate transparent acrylic walls. These transparent walls slide in fabricated grooves lined with rubber behind the windowed steel channels.

(a)

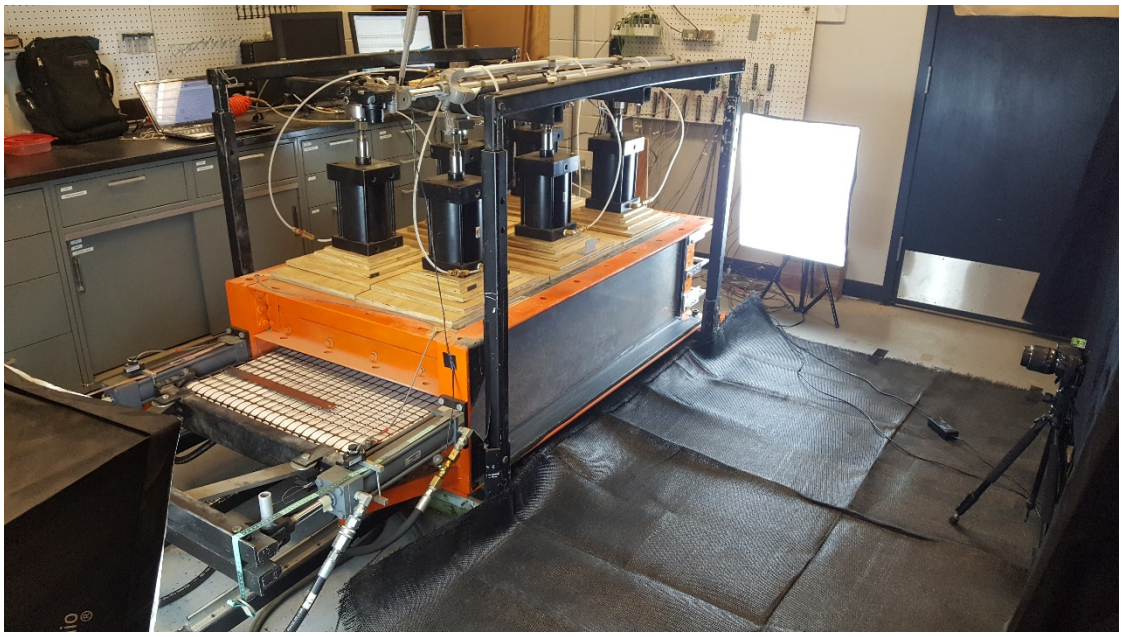

(b)

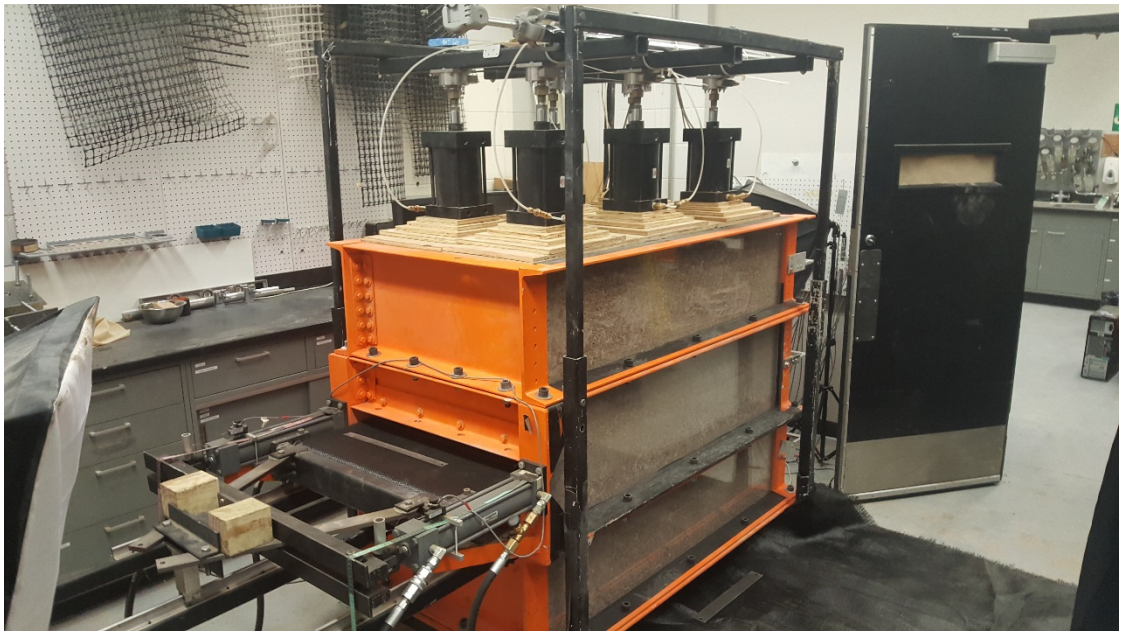

Figure 5.1.3. General view of the equipment: (a) 0.45 m (1.5 ft.) configuration; and (b) 1.2 m (4 ft.) configuration.

The front wall of the middle collar consists of two built-up steel channels 0.175 m (7 in) high forming a gap of 0.1 m (4 in) in the mid height of the front wall. The height of this gap is controlled by an adjustable sleeve such that the smallest gap height is 13 mm (0.5 in) and the largest is 0.1 m (4 in). This gap is adjusted according to the maximum grain size of the backfill material used in testing. The bigger the particle size, the wider the gap has to be to avoid particle jamming against

the sleeve during the test, hence avoiding apparent false increase in the pullout force. The front sleeve attached to the inner side of the middle collar's front wall as shown in Figure 5.1.4. The sleeve consists of two built-up steel angles 0.713 m (2.3 ft.) long. Each angle has 0.225 m (9 in) long cantilevered leg and 0.125 m (5 in) long leg facing the front wall. Five wedges are attached to each angle to stiffen the free legs against bending. The free legs are tapered end such that its thickness is reduced to 0.3 m (0.12 in). The rear wall of each collar has a number of slits, which allow placement of instrumentation (e.g., telltales), seating load, and rear clamping of the passive reinforcement layers at various reinforcement spacing ranging from 0.05 to 0.60 m (2 in. to 2 ft.) as shown in Figure 5.1.1.

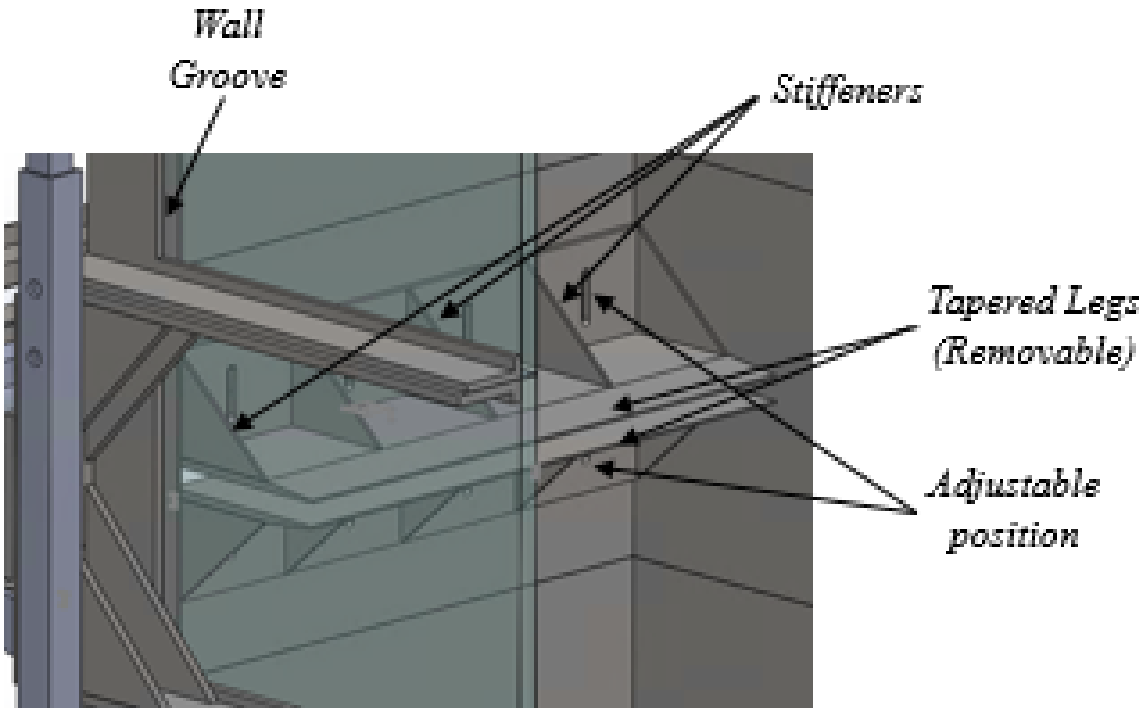

Figure 5.1.4. Front sleeve.

The inside walls of the box were lined with Mylar sheets to alleviate the interface friction that might take place between the backfill material and the interior of the walls at high confining pressures. Mylar sheets were selected for their high ductility and for being transparent, which is important to allow visualization through the transparent side walls. The Mylar sheets placed on the steel walls have adhesive backs. To ascertain the interface friction is low enough, interface shear testing has been conducted to identify the interface friction parameters. Three interface tests have been carried out in a large-scale direct shear machine at various confining pressure levels, specifically 24, 38, and 52 kPa (3.5, 5.5 and 7.5 psi). Using the peak interface shear strength values from Figure 5.1.5a, the strength envelope was constructed as shown in Figure 5.1.5b. The interface friction angle was identified as 5.1 degrees. However, the friction angle was identified as zero for shear displacements less than 5 mm (0.2 in), as shown in Figure 5.1.5a, which is higher than the displacement range expected in testing. This figure shows the interface shear strength

envelope at the instability state identified by the turning points of the stress-displacement curves past yield. For the data obtained in this study, the turning points of the curves were found to be very close to the yielding points and very close to each other.

(a)

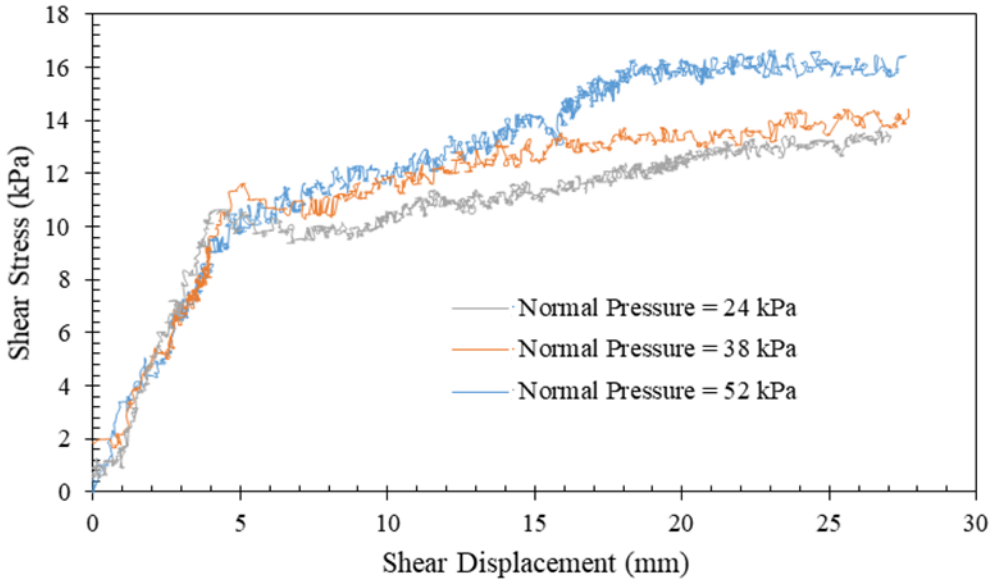

(b)

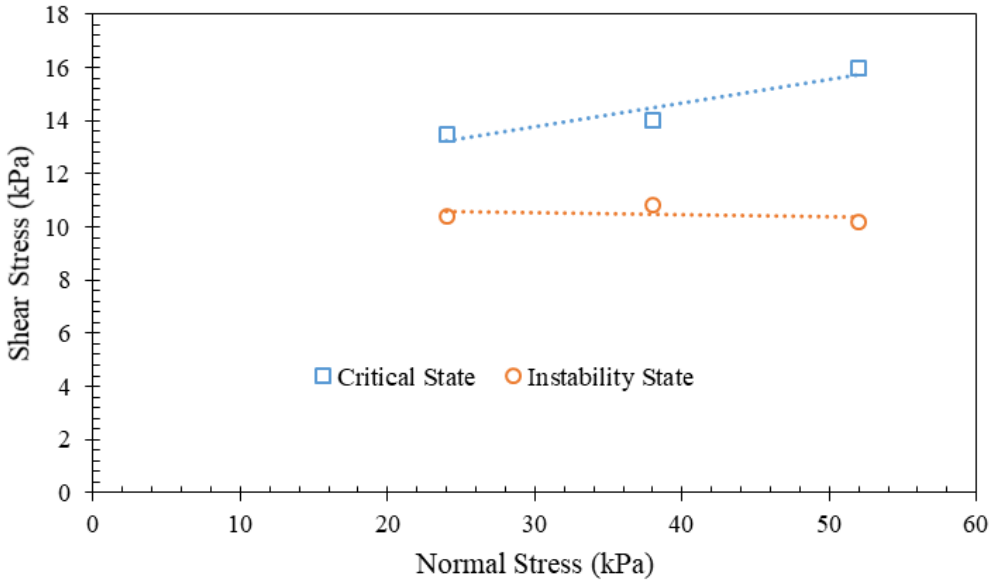

Figure 5.1.5. Soil-Mylar interface shear behavior: (a) Shear stress-displacement behavior; (b) Interface shear resistance envelopes.

5.1.3.3 NORMAL LOADING SYSTEM

The normal loading is applied on the top surface of the reinforced soil mass. The system consists of a set of six pneumatic actuators that exert pressure on the top surface of the reinforced soil mass as shown in Figure 5.1.6. The pressure cylinders react against three transverse beams. The transverse beams convey their load to two longitudinal beams, which in turn convey their loads to four columns located at the four corners of the box. The columns work in tension during operation and convey the load to two transverse beams mounted underneath the box where the load goes eventually to the base plate of the box (i.e., the bottom surface of the reinforced soil mass). The bottom side of the box is stiffened by two other longitudinal beams. Note that the reaction columns are telescopic to fit the two configurations of the box (i.e., 1.2 m (4 ft.) deep and 0.45 m (1.5 ft.) deep configurations).

Stepped wooden pyramids are used underneath each air pressure cylinder to distribute the pressure uniformly on the surface of the reinforced soil mass. The wooden pyramids sit on neoprene rubber mats to properly distribute uniform pressure on the top of the soil. This system provides a flexible normal pressure where the pistons of the air cylinders extend and retract to maintain the desired pressure throughout the test. The pistons are adjusted initially at the mid distance of their stroke length to allow compression and heave. Thus, the system allows the measurement of soil dilatancy and its sensitivity to changing the testing parameters without intervention of the top boundary. In addition, the system can apply pressure at constant reinforced soil volume (i.e., pressure changes during the test such that the volume change is maintained zero). That is, the system can measure the pressure change due to suppressed dilation. In this case the pistons are locked after applying the desired initial normal pressure. Also, the system can provide partial control thus producing information on an intermediate testing condition.

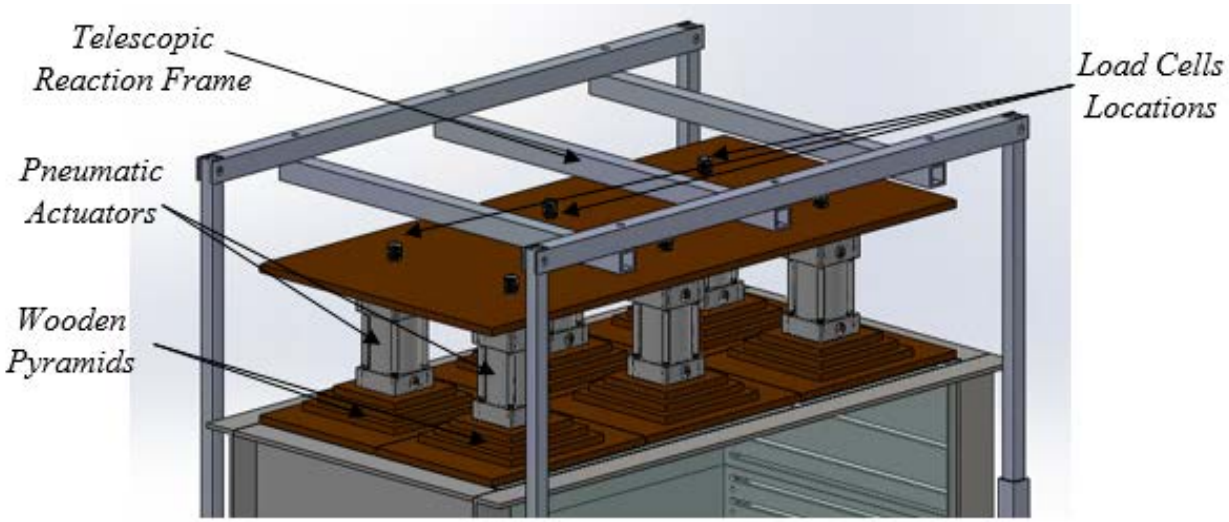

Figure 5.1.6. Normal pressure system.

5.1.3.4 REINFORCEMENT PULLOUT LOADING SYSTEM

Pullout loading of the active reinforcement layer is applied on the grip in which the reinforcement layer is clamped. The pullout loading system consists of two hydraulic actuators connected to a hydraulic pumping system. These actuators are connected by a stiffened beam, which pushes against a clamping system as shown in Figure 5.1.7. The clamping system is mounted on three ball bearing carriages, which run on three linear guide motion rails. This linear guide system significantly reduces the friction against the movement of the clamping system, hence minimizing the contribution of the friction in the measured pullout loading. The total friction force for the linear guide system is approximately 0.01 kN (2.25 lbs). That is, the unit friction force added to the pullout force is 0.01 kN/m (0.7 lbs/ft.), which is within the noise range of the load cell (i.e., exact value could not be identified). In addition, this value is less than 0.03% of the average pullout force measured in the typical tests. The loading system also allows maintaining the load level to investigate the creep effect on the soil-reinforcement interface behavior.

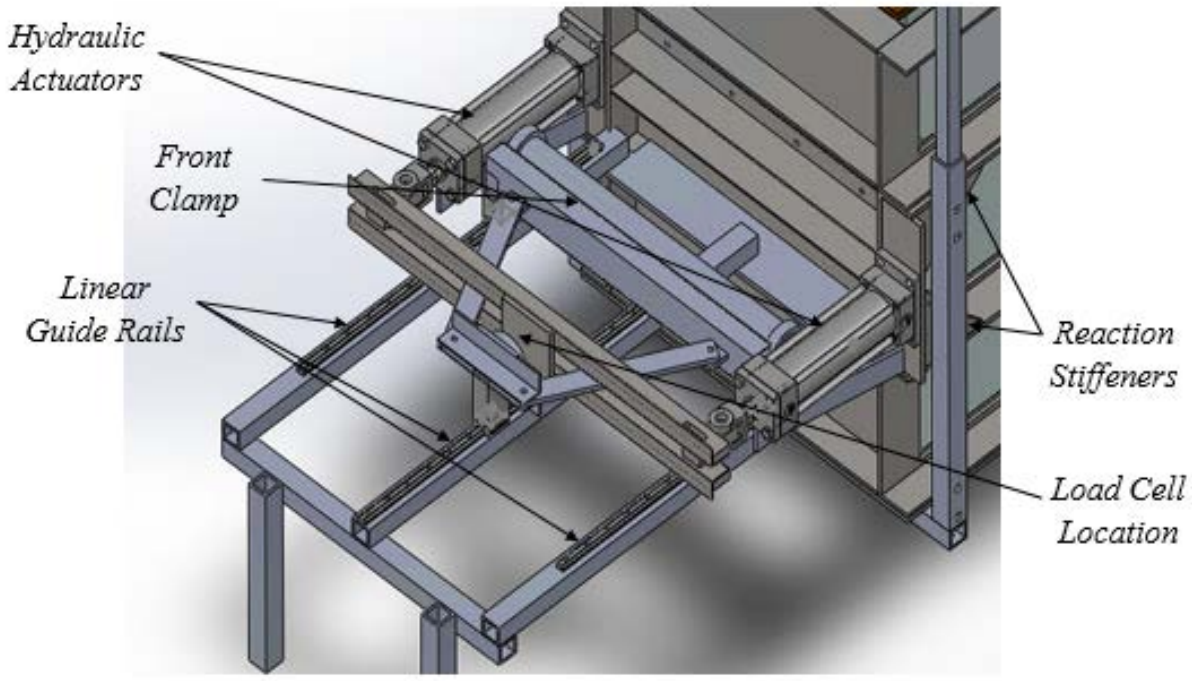

Figure 5.1.7. Reinforcement pullout loading system.

Figures 5.1.8 and 5.1.9 show a schematic diagram and a general view of the hydraulic system, respectively. The system includes the following: (1) hydraulic pump, to provide the required pressure for oil the hydraulic circuit. The pump is accompanied with an oil tank to feed the system with hydraulic oil; (2) pump flow control valve, to control the flow induced by the pump and return the excessive flow to the pump's oil tank; (3) oil filter, mounted on the return inlet of the pump's oil tank to clarify the oil; (4) 4-way directional hydraulic valve, to provide control on the oil pressure direction either to the rear or the front side of the hydraulic actuators (i.e., either to extend or retract the pistons); (5) hydraulic bridging meter valve; (6) two flow control valves mounted on the rear side of the two hydraulic actuators. These valves help controlling the

movement of the pistons in the pushing direction (i.e., while loading the active reinforcement layer).

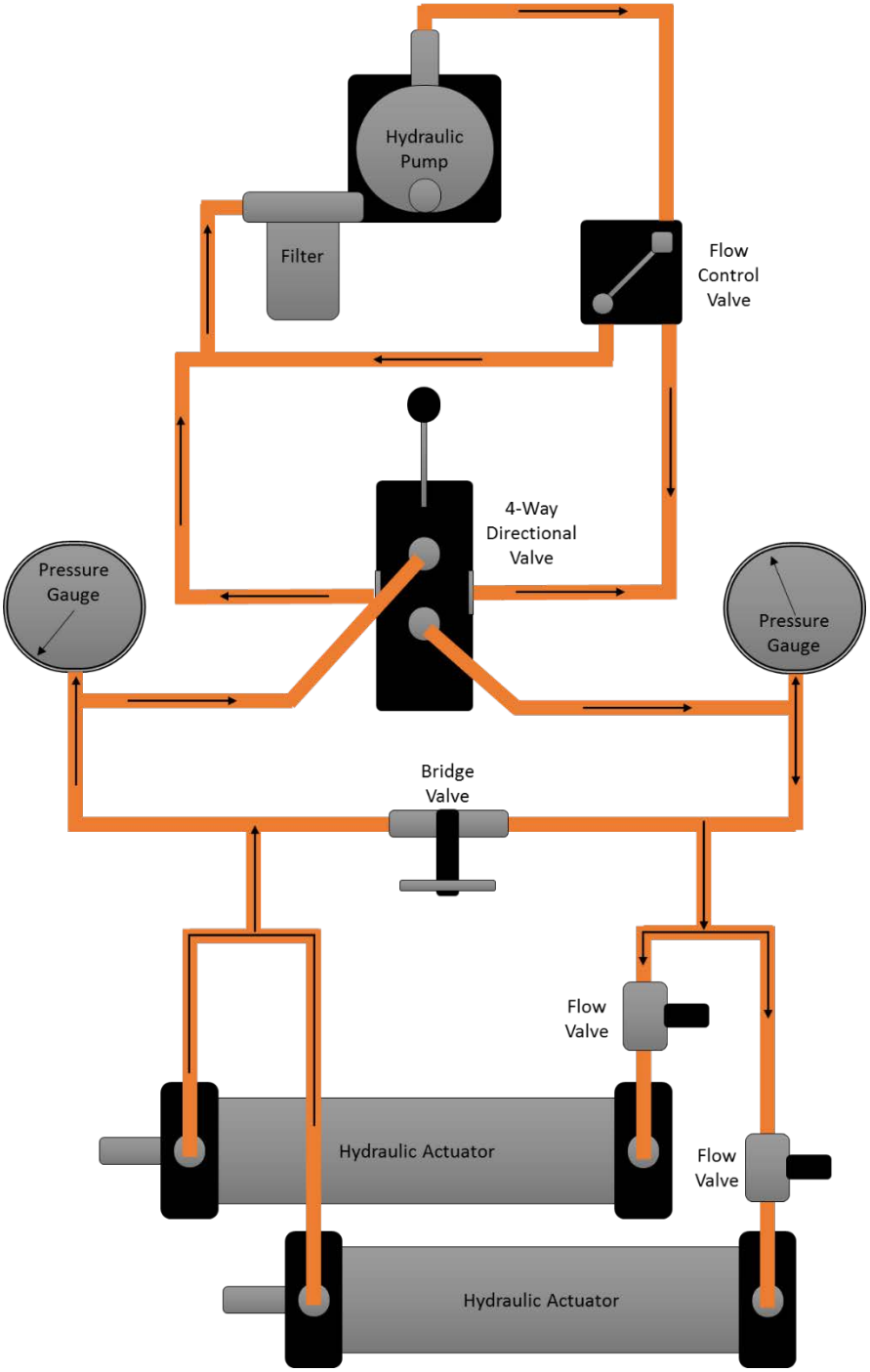

Figure 5.1.8. Schematic diagram for the hydraulic loading system (arrows denotes direction of flow during loading).

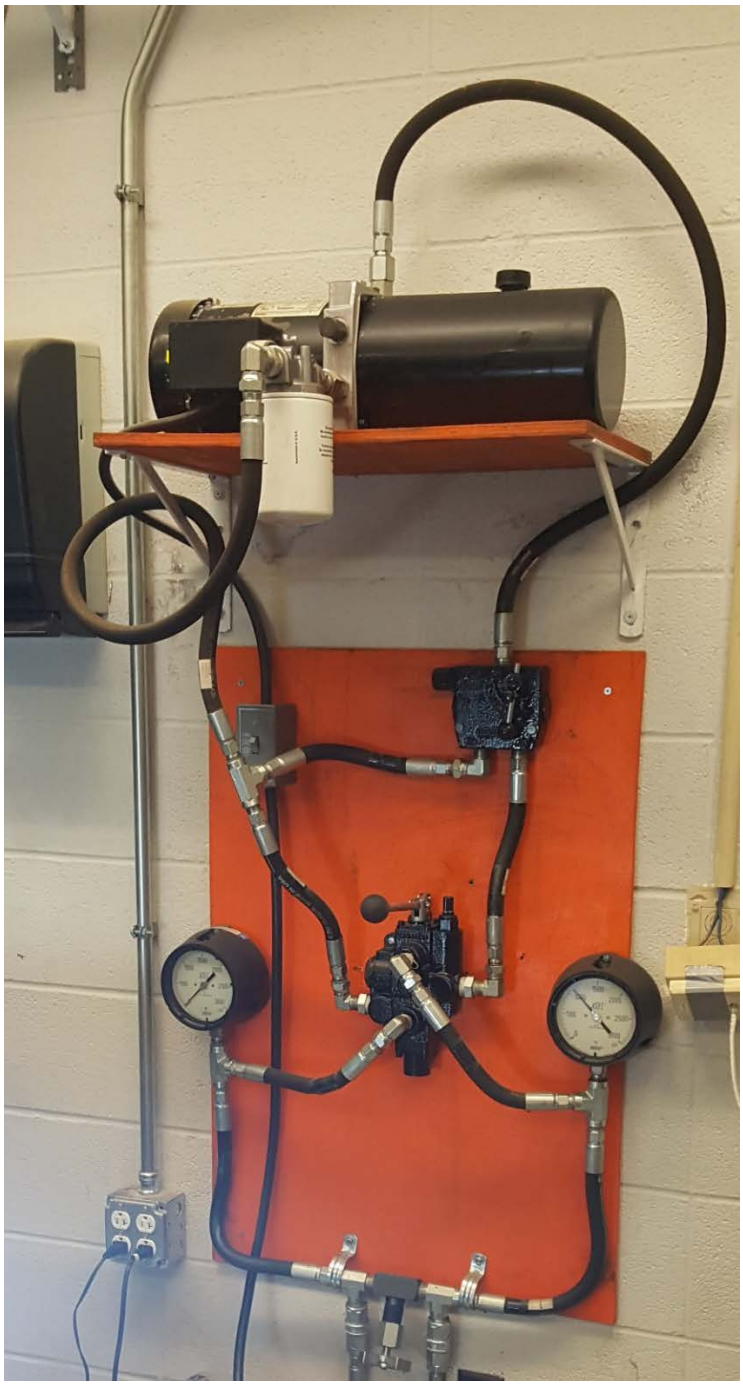

Figure 5.1.9. General view of the hydraulic loading system.

5.1.3.5 REINFORCEMENT CLAMPING SYSTEM

The active reinforcement layer, which is always placed in the middle of the box, is clamped from the front side to a movable clamp placed in front the box. This clamp is attached to a pullout loading system as shown in Figure 5.1.10. The passive reinforcement layers are clamped at the rear side of the box to stationary clamps. The rear ends of the passive reinforcement are not allowed to move.

(a)

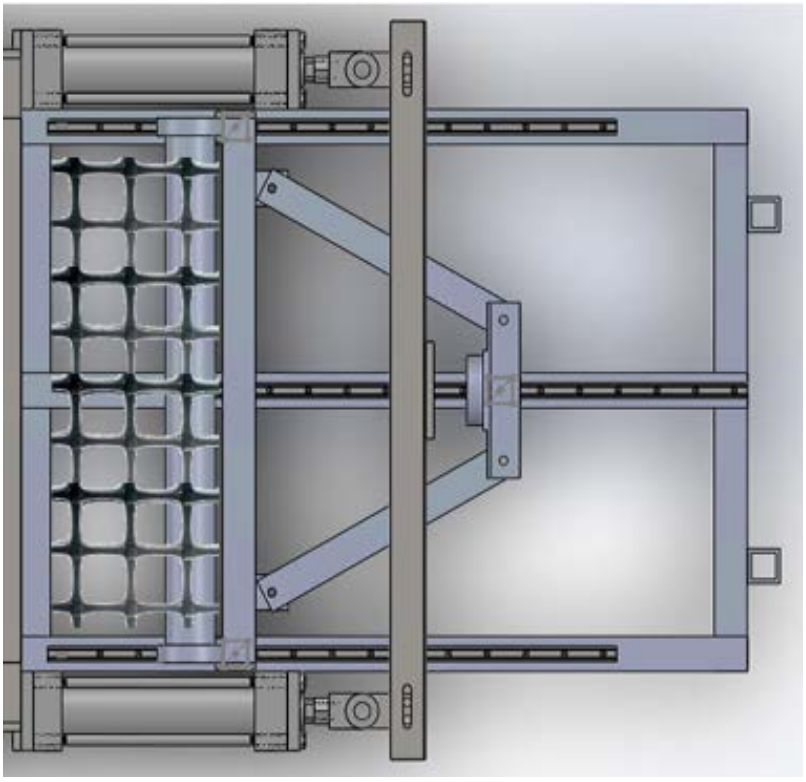

(b)

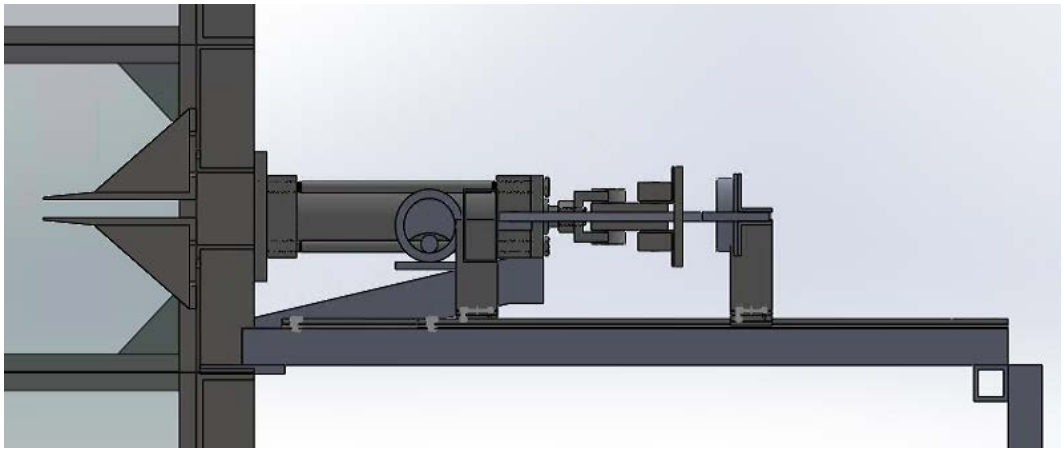

Figure 5.1.10. Front clamp and pullout loading system: (a) top view; (b) sectional side view.

5.1.3.6 ACTIVE REINFORCEMENT CLAMP

The active reinforcement is placed in the middle of the box and clamped to a roller grip as shown in Figure 5.1.11a. The roller grip consists of a steel solid cylinder with a crescent cut. The reinforcement makes a 270-degree round around the cylinder and clamped by a steel rod bolted to the steel cylinder by five screws against the crescent cut, such that the clamping point is facing

the front wall as shown in Figure 5.1.11a. The grip is accommodated in a grip holder that has two steel rings at both ends, which are connected by a steel box tube. Two rods connect the box tube with a steel part, which is in direct contact with the pullout loading system as shown in Figure 5.1.10. These rods are perfectly aligned with the top tangent plane of the grip (i.e., reinforcement plane) which is in turn aligned with the horizontal axial plane at the mid-height of the box.

For geogrid reinforcement, the layer is clamped such that a transverse rib is maintained beyond the clamping rod; whereas, for geotextile reinforcement, a knitted double-layer strip is maintained beyond the clamping rod to avoid potential slippage. In addition, the clamp is lined with sandpaper to enhance avoidance of reinforcement slippage. The edge of the crescent cut in contact with the reinforcement is lined with a neoprene foam strip to mitigate potential stress concentration at this location. Forensic investigation after every test was made to ensure no reinforcement slippage occurred during testing. Figures 5.1.12a and 5.1.12b show a clamped geotextile reinforcement and a clamped geogrid reinforcement, respectively, during testing. The clamping system used allows a reinforcement unconfined portion (i.e., outside the box). This allows evaluation of the tensile behavior of the geosynthetic specimen corresponding to its interaction test.

5.1.3.7 PASSIVE REINFORCEMENT CLAMP

The rear wall of each collar has a number of slits that allow clamping of the passive reinforcement layers at various reinforcement spacing ranging from 0.05 to 0.6 m (1.97 in to 2 ft.). In addition, these slits allow placement of instrumentation and seating load, as needed. The rear ends of the passive reinforcement layers are fixed in place to investigate the effect of the active reinforcement layer where interaction takes place. In addition, having the boundary geosynthetics fixed in place allows the assessment of the effect of the shear stress generation at the soil-reinforcement interface of the active reinforcement layer on each of them. The passive reinforcement layers are clamped to roller grips mounted on the rear side of the box as shown in Figure 5.1.1.

The locations of these clamps can be changed according to the locations of the passive reinforcement layers in the soil mass (i.e., according to the desired reinforcement spacing). The clamps are supplemented with instrumentation holders as shown in Figure 5.1.11b. The clamps are also lined with sandpaper to avoid reinforcement slippage. A similar holder is in place for the active reinforcement layer to hold its instrumentation and to enable placement of the seating load when desired.

(a)

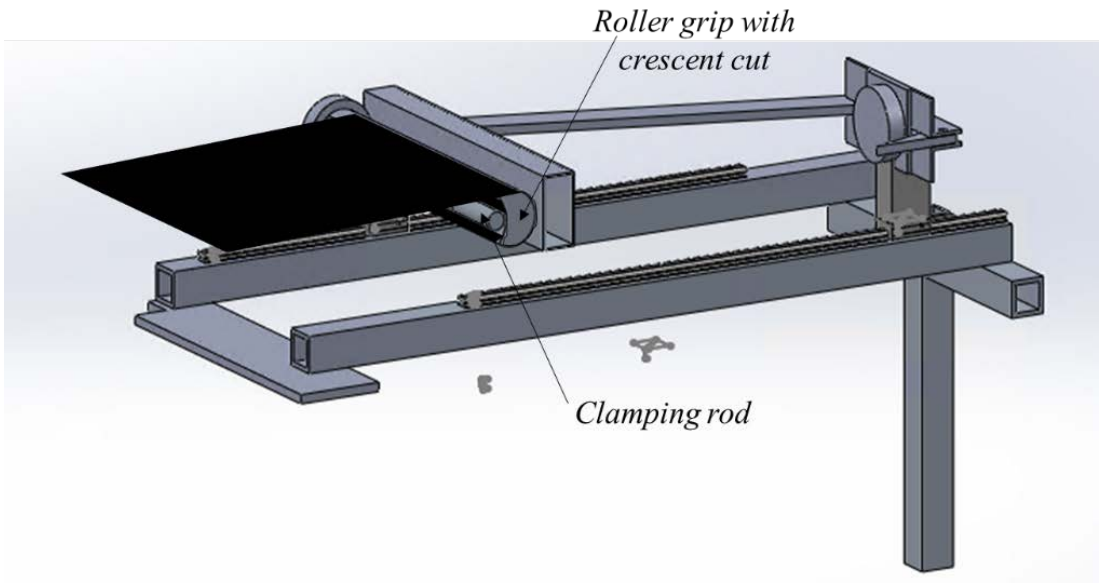

(b)

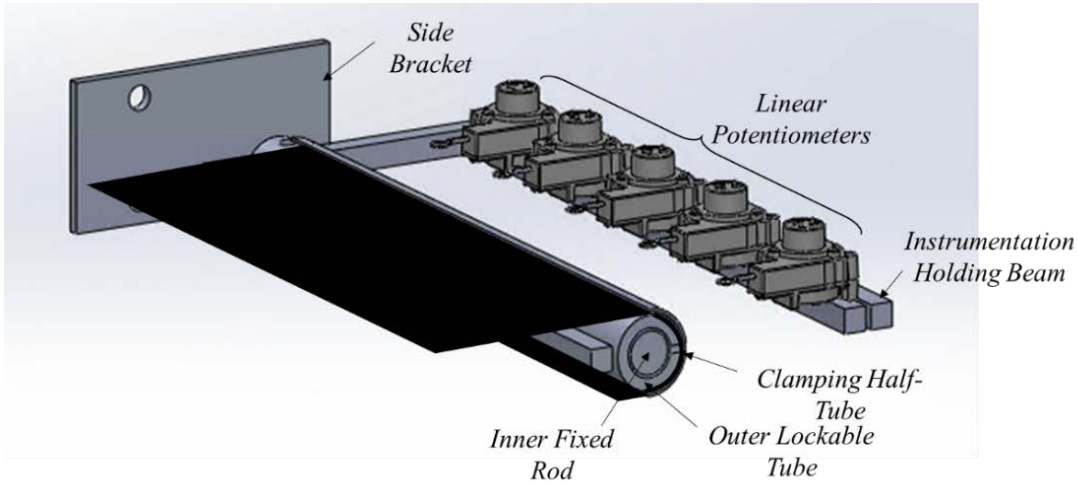

Figure 5.1.11. Reinforcement clamping systems: (a) Sectional view for the active reinforcement clamp; (b) Sectional view for the passive reinforcement clamp

(a)

(b)

Figure 5.1.12. View of clamped reinforcement during testing: (a) Geotextile reinforcement; and (b) Geogrid reinforcement.

5.1.3.8 INSTRUMENTATION AND MONITORING

The instrumentation includes: (1) a load cell to measure the load applied to the active reinforcement; (2) load cells at the normal pressure pneumatic actuators to monitor the actual applied normal pressure on top of the soil throughout the test; (3) a camera that shoots against the transparent side wall that allows for measurement of the shear band as well as direct

observation of the soil-reinforcement interaction. The width of the reinforcements extends to the sides of the box in this case. On the inner surface of the box, Mylar sheets are used to minimize side friction against the fill soil. Markers are placed in the soil at the interface to follow soil movement as the tensile load in the geosynthetic is increased; (4) displacement sensors installed away from the sidewall, to allow for comparison of internal displacements with those obtained through the transparent wall; (5) displacement sensors on the surface that measure vertical displacements to assess the angle of dilation of the reinforced soil mass; (6) an earth pressure mat, placed on the floor of the box, to evaluate the normal pressures conveyed through the reinforced soil mass; (7) lateral earth pressure sensors, fixed to the inside of the front wall, that monitor the change in lateral earth pressure on the front wall during testing to allow for evaluation of the front wall rigidity effect on generated soil-reinforcement shear stresses; (8) displacement sensors to measure displacements at multiple locations within the active reinforcement, as well as within the passive reinforcements; and (9) a camera that measures displacement within the unconfined portion of the active reinforcement to evaluate the tensile behavior of the geosynthetic corresponding to the interaction test.

5.1.3.8.1 Reinforcement axial load

Pullout loading of the active reinforcement layer is applied by hydraulic loading system on a roller grip on which the reinforcement layer is clamped. The clamping system is mounted on three ball bearing carriages which run on three linear guide motion rails. This linear guide system significantly reduce the friction against the movement of the clamping system, hence minimizing the contribution of the friction in the measured pullout loading as discussed earlier. The applied load is measured in real time by a load cell placed at the only contact point between the clamp and the loading system as shown in Figure 5.1.10. The load cell used in the system is a high-accuracy low-profile cell shown in Figure 5.1.13.

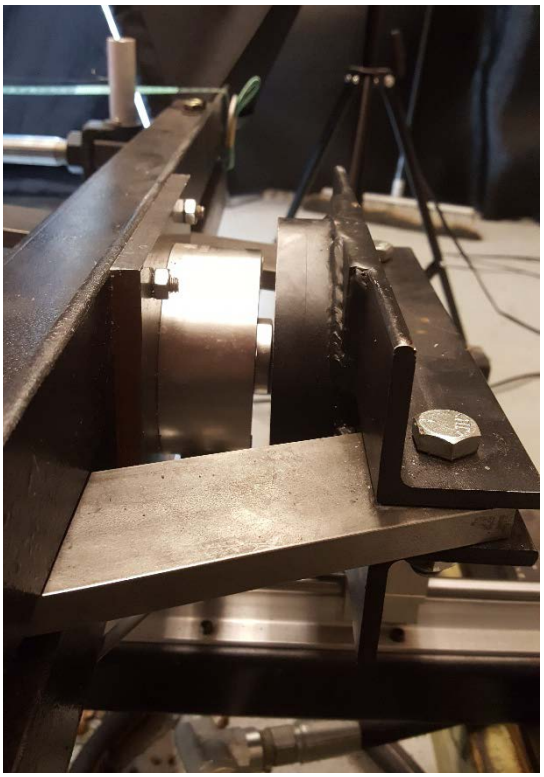

Figure 5.1.13. Low-profile load cell for pullout load measurement.

5.1.3.8.2 Reinforced soil confining pressure

Monitoring the confining pressure within the soil mass is fulfilled by monitoring the normal pressure imposed on the top of the reinforced soil mass and the distributed pressure within the reinforced soil mass.

5.1.3.8.3 Applied normal pressure

Six load cells are mounted on the reaction points of the six pressure cylinders to measure the real-time load exerted by each cylinder during the test. The load cells used in the system are high-accuracy low-profile cells as shown in Figure 5.1.14. This allows measuring the real-time pressure exerted by each cylinder during the test. In turn, this verifies the normal pressure level and its uniformity on the top of the reinforced soil mass during testing. In addition, the load cells allows assessment of the soil dilatant behavior in allowed-volume-change condition (i.e., fully free dilation) and zero-volume-change condition (i.e., fully suppressed dilation). That is, the system allows quantification of the increase in soil normal stress due to dilation suppression. The system also allows for more configurations (i.e., partially allowed volume change).

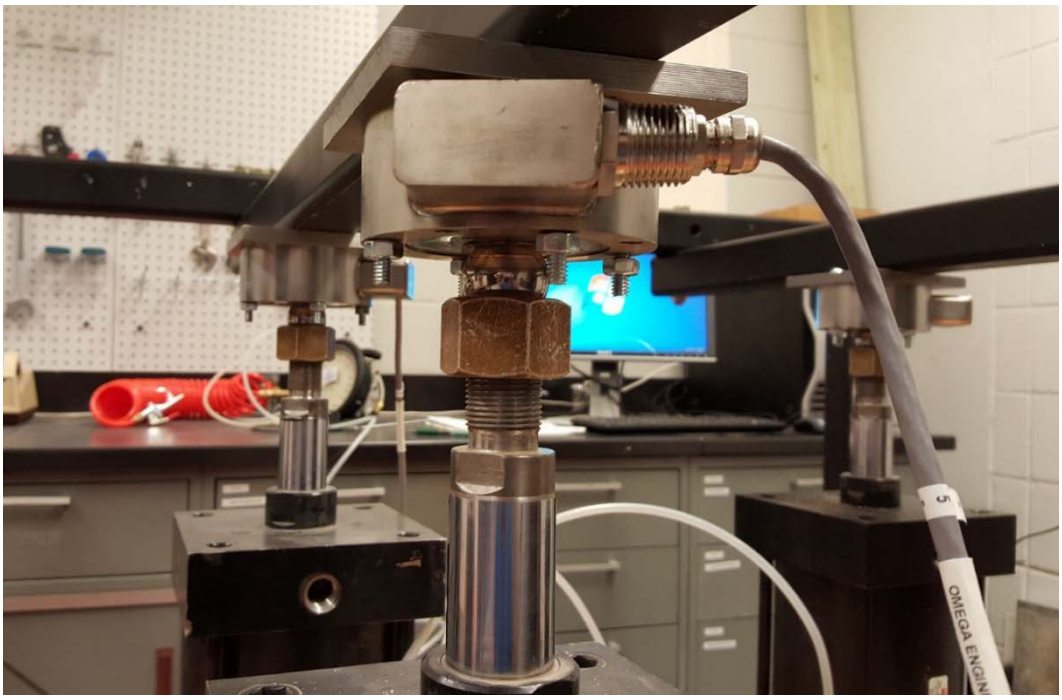

Figure 5.1.14. Load cells for applied normal pressure measurement.

5.1.3.8.4 Distributed normal pressure

A pressure sensing mat was placed on the floor of the reinforce soil box to monitor the pressure changes during the test. The pressure mat was placed on a compacted sand layer (Figure 5.1.15a) and was covered by another compacted sand layer (Figure 5.1.15b). The sand was covered by a latex membrane to prevent contamination of the fill material, which allowed reusing it in the testing program (Figures 5.1.15c and 5.1.15d). In addition, pressure cells are added in the reinforced soil mass and on the box internal surfaces at different locations to monitor the real-time change in stress during the test. This includes vertical and lateral earth pressure sensors. The lateral earth pressure sensors are fixed to the inner surface of the front wall to monitor the change in lateral earth pressure on the front wall during the test. This allows evaluation of the front wall rigidity effect on the generated soil-reinforcement shear stresses.

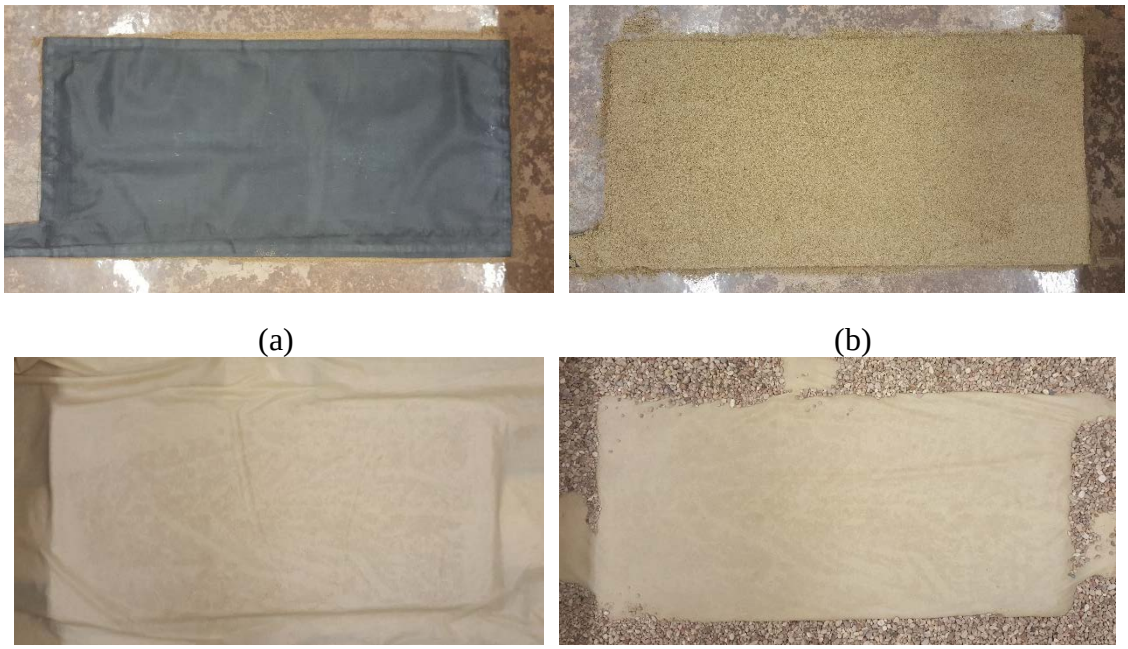

(a) (b)

(c) (d)

Figure 5.1.15. Pressure mat placement: (a) Placing the mat on top of compacted sand layer; (b) Placing another compacted sand layer on top of the mat; (c) Placing a latex membrane on top of the sand; and (d) Placing the fill material on top of the latex membrane.

5.1.3.8.5 Reinforcement straining

While the active reinforcement layer is pulled out from the front side of the box, the rear ends of the passive reinforcement layers will be fixed in place to investigate their effect of the active reinforcement layer where interaction takes place. The straining of the three reinforcement layers is monitored by tell-tales connected to draw-wire linear potentiometers mounted on holders at the rear side of the box. The tell-tales are placed to multiple junctions along the embedment length of the reinforcement layers. The boundary geosynthetic layers are also instrumented to quantify the amount of load transferred from one geosynthetic to the other. Different patterns are adopted to different geosynthetics based on their geometry and testing conditions.

The tell-tales used were made of spring-back music wire (also known as piano wire), which is made of tempered stainless steel. The used music wire was 0.4 mm (0.016 in) in diameter and its mechanical properties meet with ASTM A313 and A555 standards; the tensile strength is 205,000 psi. The wires in turn run through tubes used for bike cables. These tubes have smooth jackets that covers steel coils, which in turn cover lubricated tubes. These tubes are very stiff radially to accommodate the high normal confining pressures without being squeezed. In addition, these wires are very flexible that it tend to straighten out after being released from its spool, which avoids any curving tendency during installation. Ten tell-tales were installed on the middle reinforcement layer (i.e., active reinforcement layer) to serve ten linear potentiometers; whereas, five tell-tales were installed on each of the passive reinforcement layers to serve five linear potentiometers each. Locations of the tell-tales may vary slightly when geogrid

reinforcement is used so that the tell-tales match grid junctions. Figure 5.1.16 shows a geotextile reinforcement layer with the tell-tales connected to it placed in the reinforced soil box.

If geogrid reinforcement is used, the music wire is knotted to the grid junctions. This knot has to be as tight as possible so as not to deform during the test resulting in underestimated displacement values of the grid junctions. On the other hand, if geotextile reinforcement is used, a unique rapid adhesive is employed at the locations of tell-tales attachment. The music wire forms a hook and rests by solidifying an area of approximately 100 mm^2 of the geotextile fabric in which the tell-tale hook is centered. This adhesive comprises a powder component and a liquid component. The surface on which the adhesive is applied has to be cleaned well. The hardening time for the adhesive is 20 to 30 minutes in temperature of 20 Celsius.

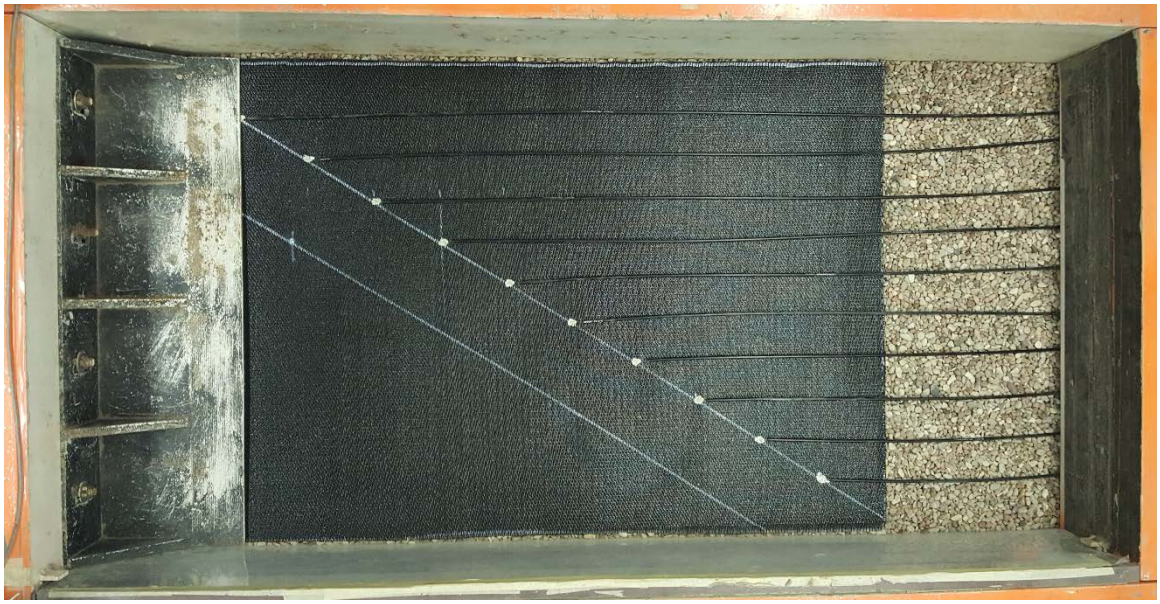

Figure 5.1.16. Telltales attached to an active reinforcement placed on the central horizontal plane of the reinforced soil mass.

5.1.3.8.6 Soil mass deformation

The reinforced soil mass deformation was monitored entirely over the sectional elevation plane adjacent to the transparent side of the box. Real-time imaging of the transparent side during the test, as shown in Figure 5.1.17, allowed post-processing of the tethered images and provided the full soil displacement field. Visualization of the development of the shear band provided particularly valuable insight into the mechanisms leading to an improved soil-reinforcement interaction when the vertical spacing of reinforcements was relatively small. A camera connected to an image tethering software program was placed vertically against the side window. Blackouts are used behind the camera and on the floor under the camera to reduce reflections on the transparent windows. Lighting equipment is placed on the sides of the window to enhance the light intensity and uniformity. A measuring tape is mounted behind the window to allow calibration of the image pixels, which accounts for camera distance and any refraction through the acrylic window.

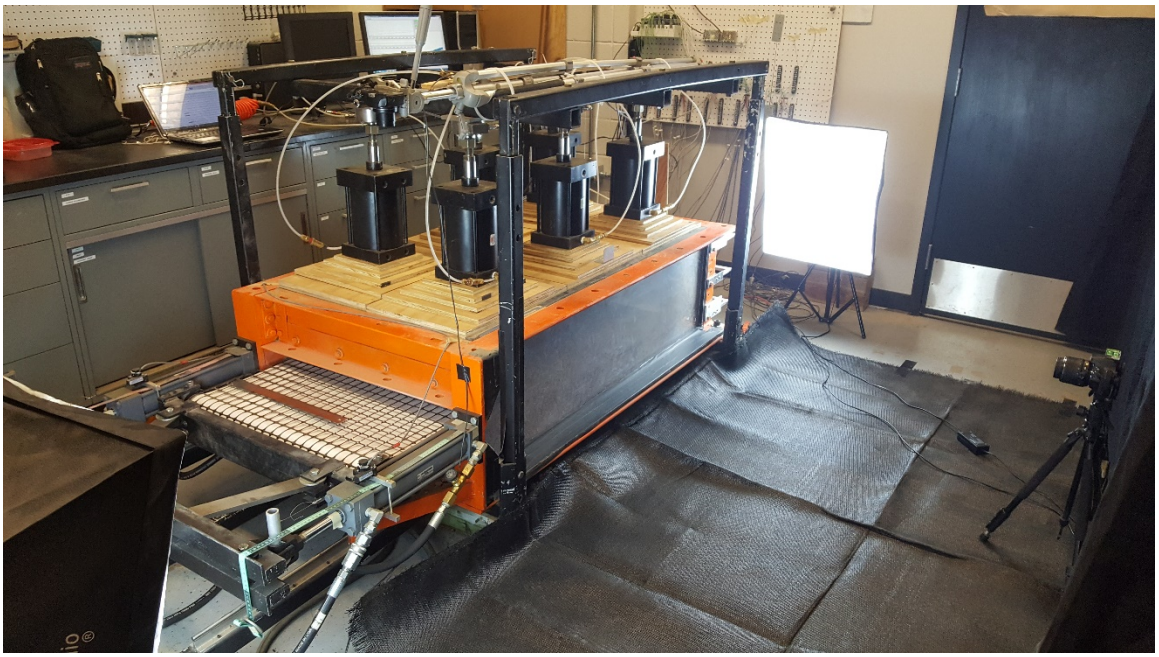

Figure 5.1.17. Camera shooting against a transparent side of the box containing the reinforced soil mass.

In addition, artificial gravel particles made of plastic of similar particle characteristics as the real soil are buried in the soil at the center of the box. These artificial particles are connected to tell-tales, which are in turn connected to draw-wire linear potentiometers. This allows real-time monitoring of the horizontal or vertical displacement representative soil particles at specific locations in the reinforced soil mass as shown in Figures 5.1.18a and 5.1.18b, respectively.

(a)

(b)

Figure 5.1.18. Artificial gravel particle connected to a tell-tale: (a) Horizontal tell-tale; and (b) Vertical tell-tale.

5.1.3.8.7 Reinforcement unconfined tensile behavior

The clamping system used produced a reinforcement unconfined portion (i.e., outside the box). This allowed evaluation of the tensile behavior of the geosynthetic specimen corresponding to its interaction test as mentioned earlier. Also, it allowsed evaluation of the creep effect on the reinforcement tensile behavior in creep tests or in tests operated at different strain rates. A camera was mounted to capture real-time top view frame images during the test. For continous reinforcements (e.g., geotextiles), the exposed portion of the reinforcement was speckled by spray paint and randomly dappled with a white paint marker as shown in Figure 5.1.19a. For gridded reinforcements (e.g., geogrids), a white sheet is placed underneath the geosynthetic to provide an appropriate contrast and facilitate image analysis as shown in Figure 5.1.19b. This serves to create two levels of pattern that enhanced the accuracy of the image analysis. A metal ruler is placed on the unconfined zone to allow calibration of the image pixels.

(a)

(b)

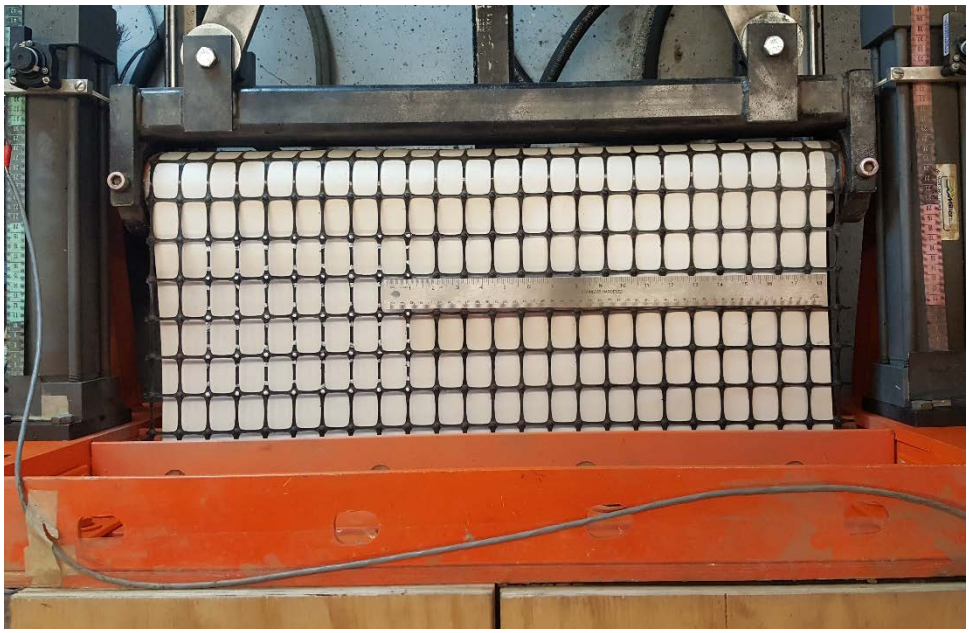

Figure 5.1.19. Unconfined reinforcement zone: (a) Geotextile reinforcement; and (b) Geogrid reinforcement.

5.1.4 ILLUSTRATIVE TESTING

This section describes the testing configuration for an illustrative test that was conducted to exhibit the abilities of the new equipment developed based on the newly proposed experimental approach. The configuration was chosen to magnify the capabilities of the new proposed experimental approach. In this test, the equipment was set in its short configuration; i.e., the

depth of the reinforced soil is 0.225 m (18 in.). Three reinforcement layers were placed at a vertical spacing of 0.051 m (2 in.). The target confining pressure was set to 21 kPa (3 psi) at the level of the active reinforcement layer. This confining pressure was intended to be low enough to allow pullout failure to occur before reinforcement rupture. The backfill material used was gravel to exaggerate on the capabilities of the newly proposed approach. The reinforcement used was woven geotextile, which is very commonly employed in geosynthetic-reinforced soil structures in which reinforcement spacing is small enough for interaction to take place. The embedment length of the active reinforcement layer was 1.016 m (40 in). On the other hand, the passive reinforcement layers were extended to the end of the reinforced soil mass, where they were clamped.

The backfill material used in the pilot test was washed river pea gravel deposited by Colorado River near Austin, Texas. This material is uniformly graded clean gravel classified as GP (poorly graded gravel) according to the Unified Soil Classification System (USCS) and classified as A-1-a according to American Association of State Highway and Transportation Officials (AASHTO) classification (AASHTO M 145). The gravel has gradation that conforms to the standard range of AASHTO No. 8 grain size distribution. The gravel has irregular sub-rounded particles as described Mitchell and Soga (2005). The backfill material was placed in lifts of 3 in. and 2 in. thickness and gently hand tamped until satisfying a target relative density (D_r) of 70%, which is corresponding to dry unit weight of 16.58 kN/m^3 (106 pcf) and void ratio of 0.551.

The reinforcement material used in the illustrative test is HP570 polypropylene woven geotextile. This geotextile has multi-filament yarns oriented in the rollway direction (i.e., machine direction) and mono-filament yarns oriented in the cross-rollway direction (i.e., cross-machine direction). The unconfined tensile properties reported by the manufacturer are summarized in Table 5.1.2. It was reported that the listed tensile strength properties were obtained in accordance with ASTM D4595.

Table 5.1.2. Reinforcement tensile properties (TenCate 2015).

Mechanical Properties	***Minimum Average Roll Value (MARV)***	
	Machine Direction	***Cross-machine Direction***
Ultimate Tensile Strength	70.0 kN/m @_10% Strain	70.0 kN/m
Tensile Strength at 2% Strain	14.0 kN/m	19.3 kN/m
Tensile Strength at 5% Strain	35.0 kN/m	39.4 kN/m
Tensile Strength at 10% Strain	70.0 kN/m	Not applicable

5.1.5 IMAGE ANALYSIS

Digital Image Correlation (DIC) is widely used in surface displacement analysis of solid mechanics and particle image velocimetry (PIV) in fluid mechanics. DIC employs cross-correlation between successive images in an image stack. This cross-correlation provides the best match of targets (sub-image or group of pixels) in successive images compared to their preceding ones. This match allows motion detection (movement, deformation, velocity, and acceleration profiles). A cross-

correlation function C(x) can be applied on any two real functions F and G in 1D and 2D problems. For image correlation, which is a 2D problem, F(m,n) and G(m,n) functions can be a quantifiable property for the images such as grayscale intensity [0,255], which was adopted in this study. The correlation function C(x,y) formula scan the G function that over x,y space around sub-image (m,n) in image (k+1) to search the sub-image that has G(m+Δx,n+Δy) that matches the F(m,n) of sub-image (m,n) in image (k) the best. This is done by computing the integral of F(m,n)*G(m+Δx,n+Δy) using values associated with corresponding pixels in the sub-images. F and G match the best when the integral value is maximum, and the corresponding Δx and Δy are the 2D displacement of the sub-image (m,n) from image (k) to image (k+1). Note that the search zone can be limited to specific extent to optimize the search process. This process is presented schematically in Figure 5.1.20 (Sadek et al. 2003).

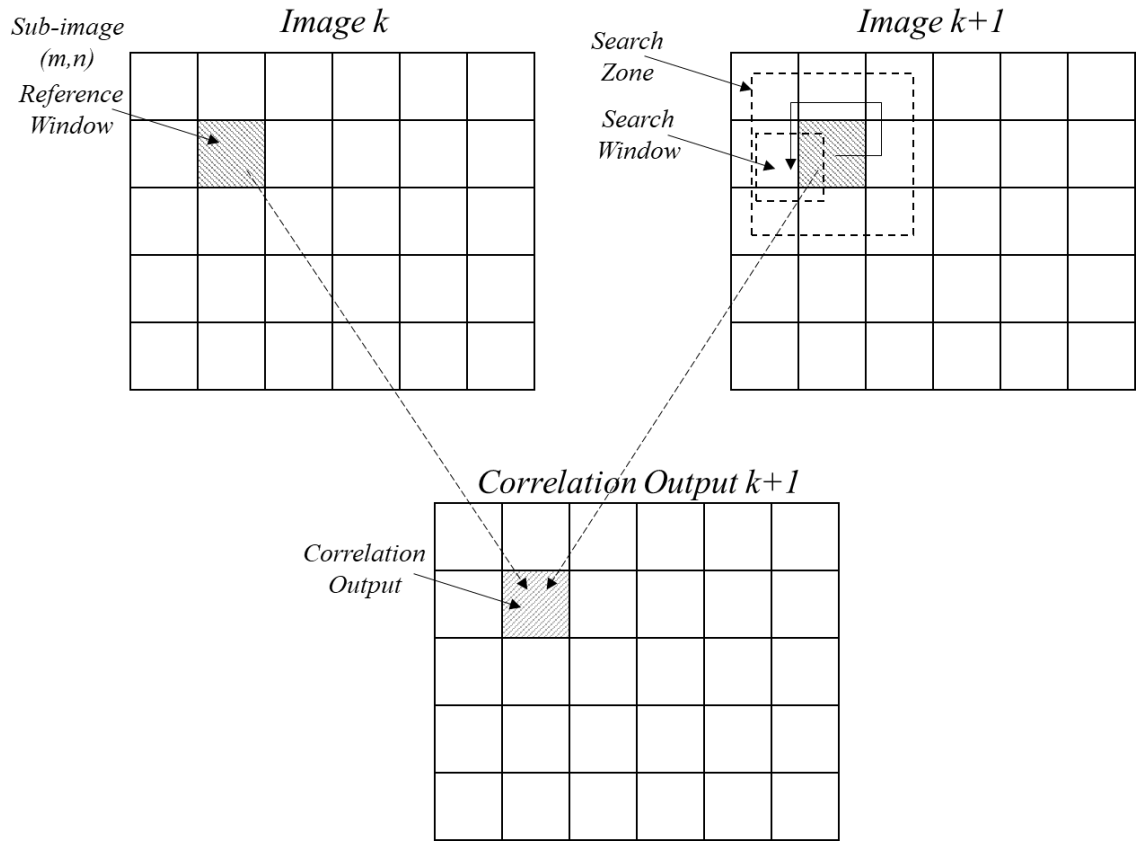

Figure 5.1.20. Schematic for cross-correlation process.

5.1.6 TYPICAL RESULTS AND ANALYSIS

This section presents typical results for one of the tests. The results are presented to illustrate the capabilities of the experimental approach. Note that this experimental approach proposes significant redundancy in various measurements for the purposes of validation. The notations for the data measured from the various instruments are summarized in Table 5.1.3

Table 5.1.3. Instrument and measurement notations.

Measurement	*Instrument Notation*	*Measurement Notation*
Nodal displacements of the active reinforcement layer	LP1	u1
	LP2	u2
	LP3	u3
	LP4	u4
	LP5	u5
	LP6	u6
	LP7	u7
	LP8	u8
	LP9	u9
	LP10	u10
Nodal displacements of the upper passive reinforcement layer	LP11	v1
	LP12	v2
	LP13	v3
	LP14	v4
	LP15	v5
Nodal displacements of the lower passive reinforcement layer	LP16	w1
	LP17	w2
	LP18	w3
	LP19	w4
	LP20	w5
Horizontal displacements of 7 artificial gravel particles	LP21	N/A*
	LP22	N/A*
	LP23	N/A*
	LP24	N/A*
	LP25	N/A*
	LP26	N/A*
	LP27	N/A*
Vertical displacements of 3 artificial gravel particles	LP28	N/A*
	LP29	N/A*
	LP30	N/A*
Clamp displacement	S1	uc1
	S2	uc2
Frontal pullout load	LC1	P
Front normal stress	LC2	σ_{front}
	LC3	σ_{front}
Middle normal stress	LC4	σ_{middle}
	LC5	σ_{middle}
Rear normal stress	LC6	σ_{rear}
	LC7	σ_{rear}

5.1.6.1 PULLOUT RESISTANCE

Figure 5.1.21 shows the frontal load-displacement behavior of the active reinforcement layer. The frontal load is defined as the total pullout force applied per unit width of the active reinforcement layer; the frontal load is measured by the load cell mounted in the loading system. The frontal displacement is defined as the movement of the front end of the confined length of the active reinforcement layer. The frontal displacement is measure by a linear potentiometer attached to a telltale, which is in turn attached to the front end of the confined reinforcement

zone. The difference between the displacement of the clamp and the reinforcement pullout front represents the straining of the entire unconfined reinforcement zone. The failure observed was pullout failure, which enabled a full-range investigation of the soil-reinforcement interface behavior (i.e., at working stress and failure conditions).

(a)

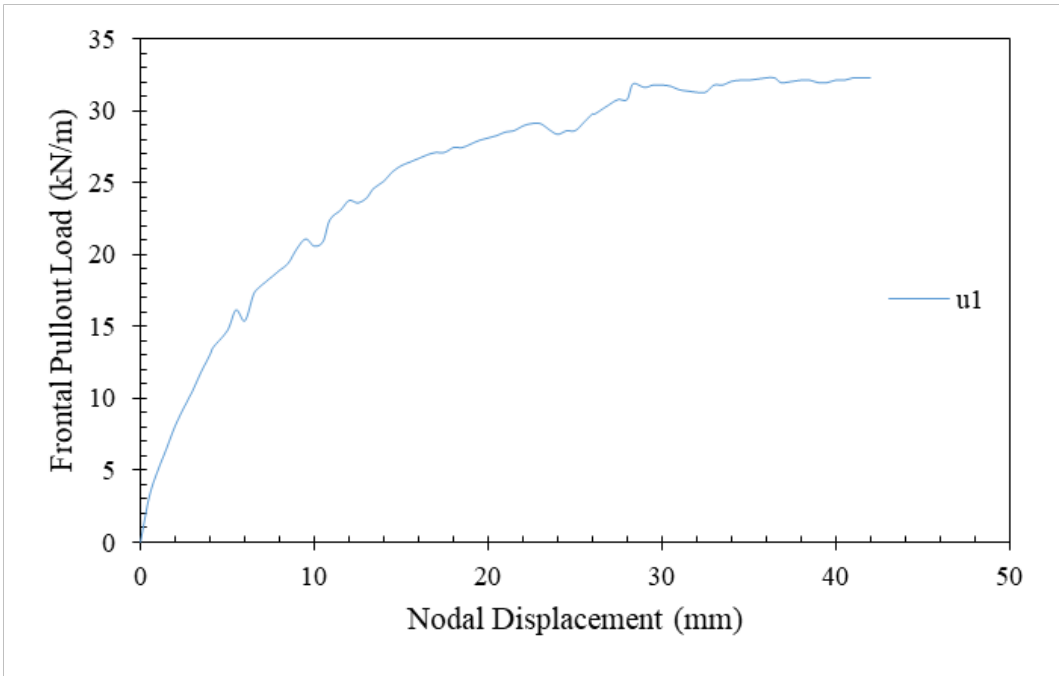

(b)

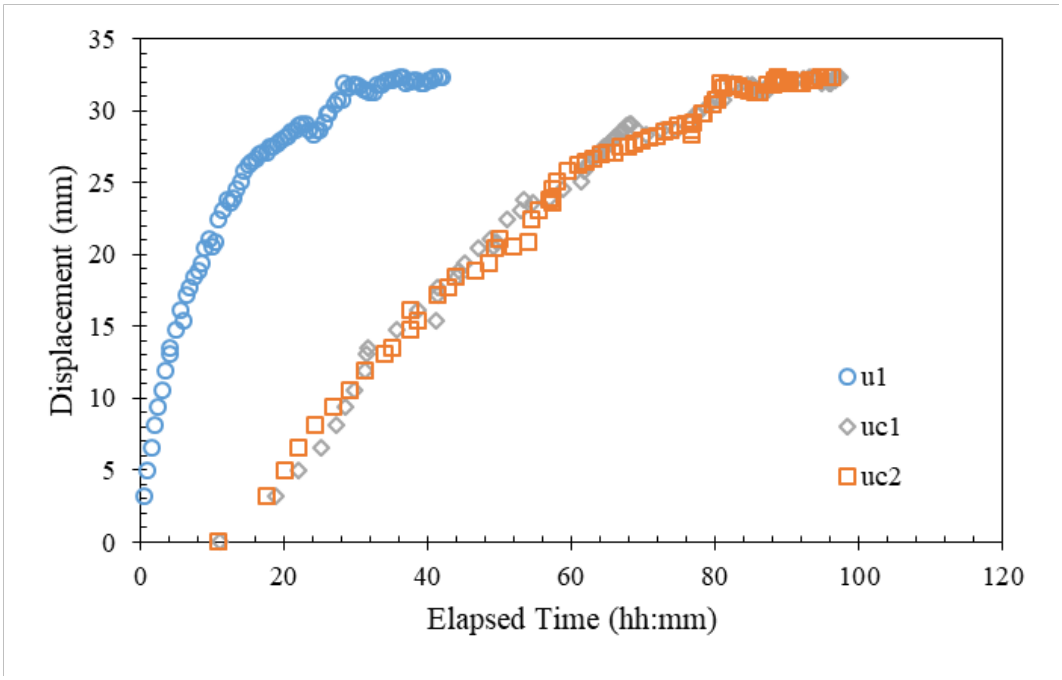

Figure 5.1.21. Frontal pullout load-displacement behavior: (a) Frontal load-displacement curve; and (b) Frontal and clamp load-displacement curves.

5.1.6.2 CONFINED REINFORCEMENT STRAINING

Reinforcement deformation is measured at various nodes along its embedment length. These nodes are connected to tell-tales that are attached to them; these tell-tales are in turn connected to linear potentiometers at the rear side of the box. The locations of these nodes are illustrated in Figures 5.1.22a and 5.1.22b for the main and passive reinforcement layers, respectively. The figures show the location of the nodes on a plan sectional view of the reinforced soil, where the location of the sleeve and the rear bound of the active reinforcement layer are showed. Note that the location of the nodes designated for the passive reinforcement layers coincide some of the nodes on the active reinforcement layer.

Figure 5.1.23 shows the displacement of the various nodes on the reinforcement layers at several load levels. Figure 5.1.23b shows the nodal displacement for the active reinforcement layer; whereas, Figures 5.1.23a and 5.1.23c show the nodal displacement for the upper and the lower passive reinforcement layers, respectively. To transform this to displacement profile, discretized values at specific frontal displacement *u1* were used. Figure 5.1.24a shows the nodal displacement profile for the active reinforcement layer; whereas, Figures 5.1.24b and 5.1.24c show the nodal displacement profile for the upper and the lower passive reinforcement layers, respectively. The displacement profiles were fit to their best parabolic representation to allow calculating reinforcement strains. Figure 5.1.25a shows the strain profile for the active reinforcement layer; whereas, Figures 5.1.25b and 5.1.25c show the strain profile for the upper and the lower passive reinforcement layers, respectively.

(a)

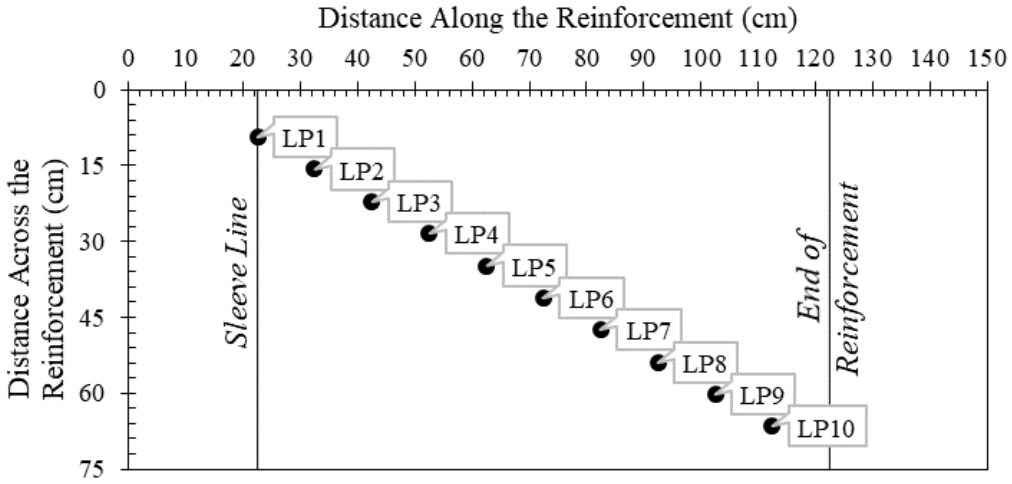

(b)

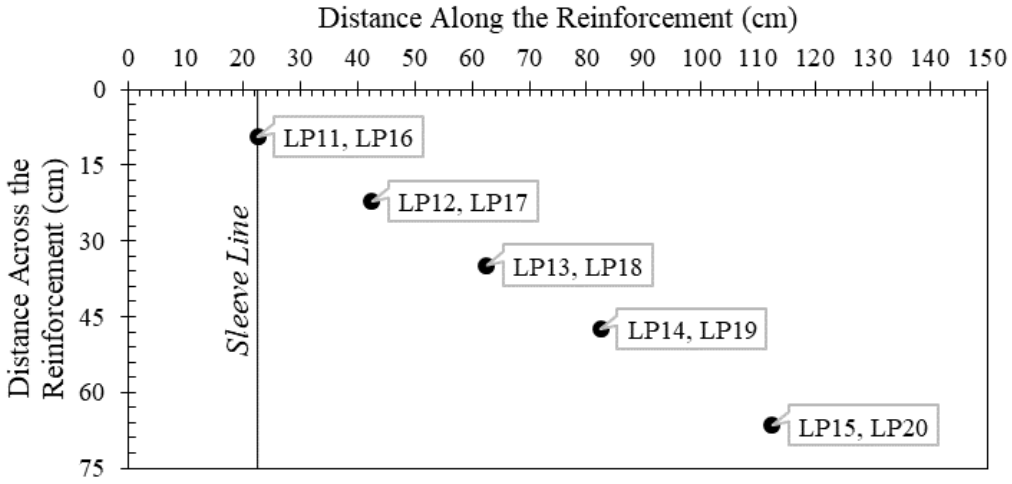

Figure 5.1.22. Locations of tell-tale connections: (a) Active reinforcement layer; and (b) Passive reinforcement layers.

(a)

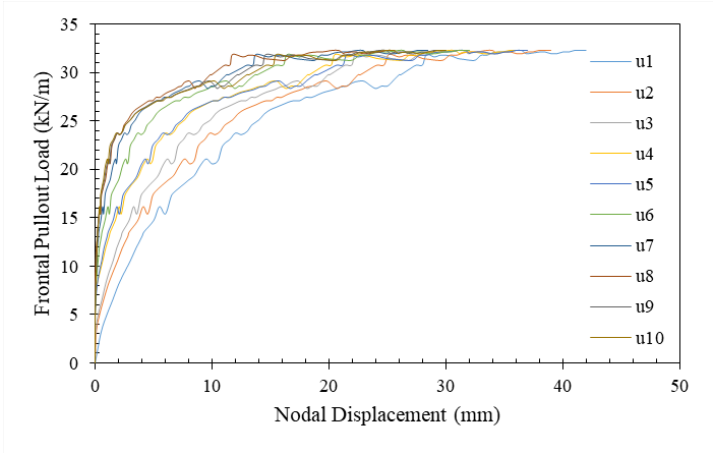

(b)

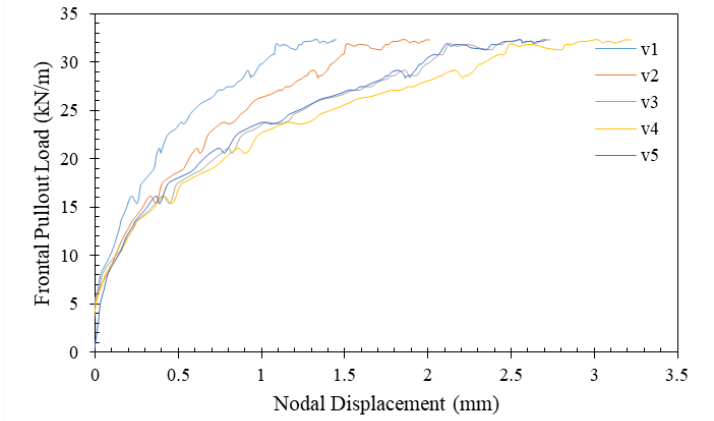

(c)

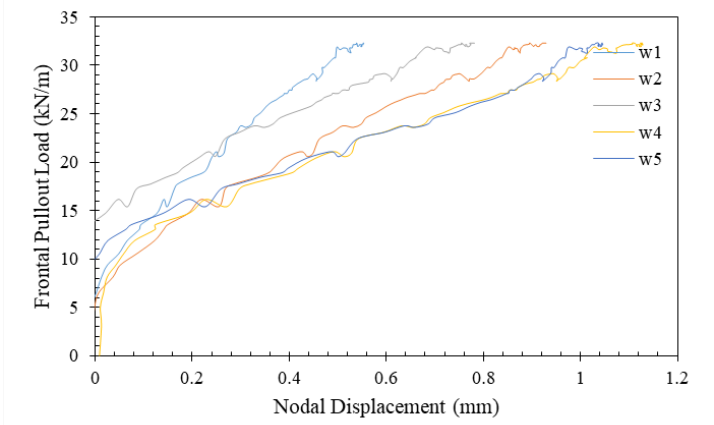

Figure 5.1.23. Reinforcement frontal load versus nodal displacement behavior: (a) Upper passive reinforcement layer; (b) Active reinforcement layer; and (c) Lower passive reinforcement layer.

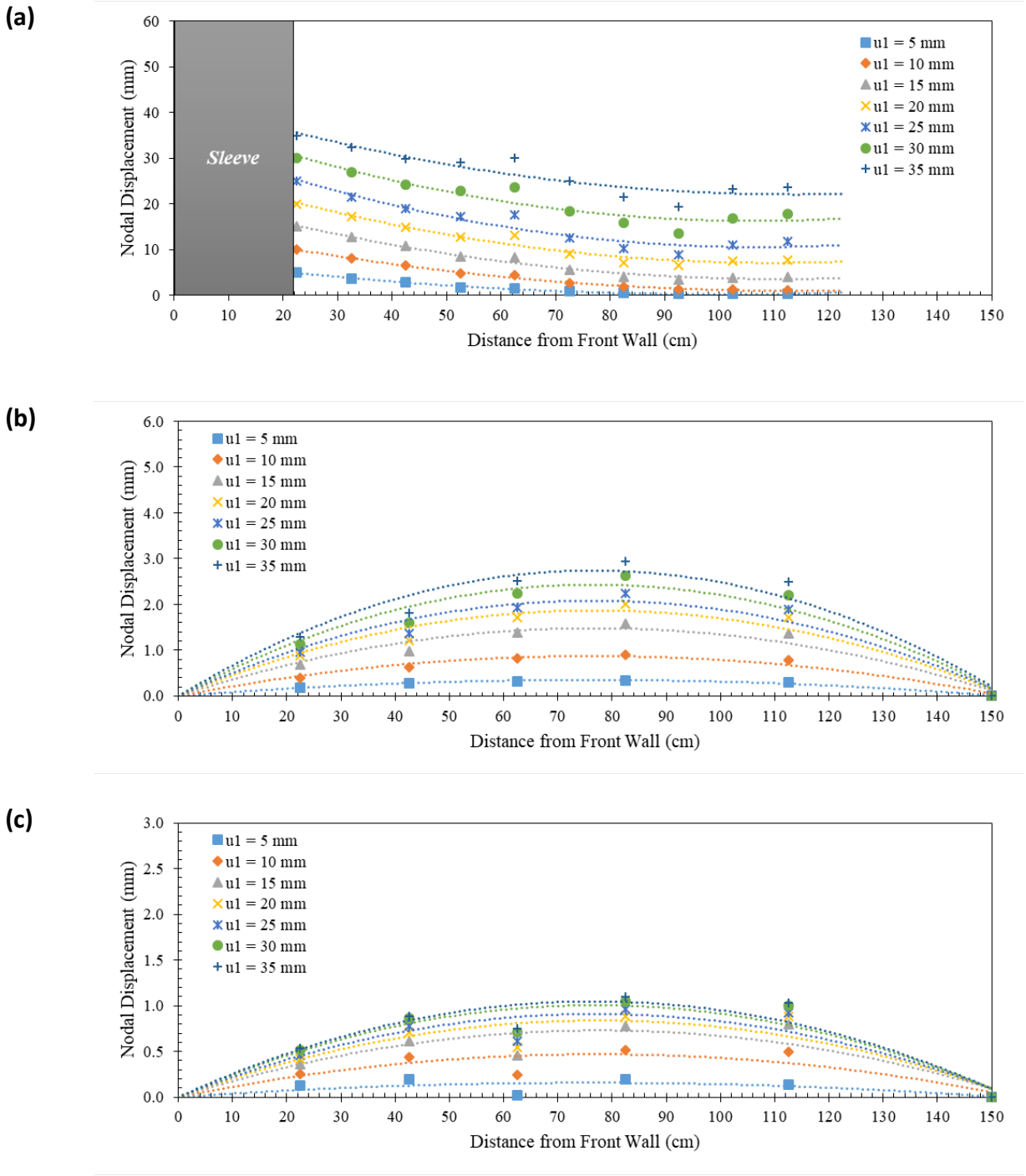

Figure 5.1.24. Reinforcement nodal displacement profiles: (a) Active reinforcement layer; (b) Upper passive reinforcement layer; and (c) Lower passive reinforcement layer.

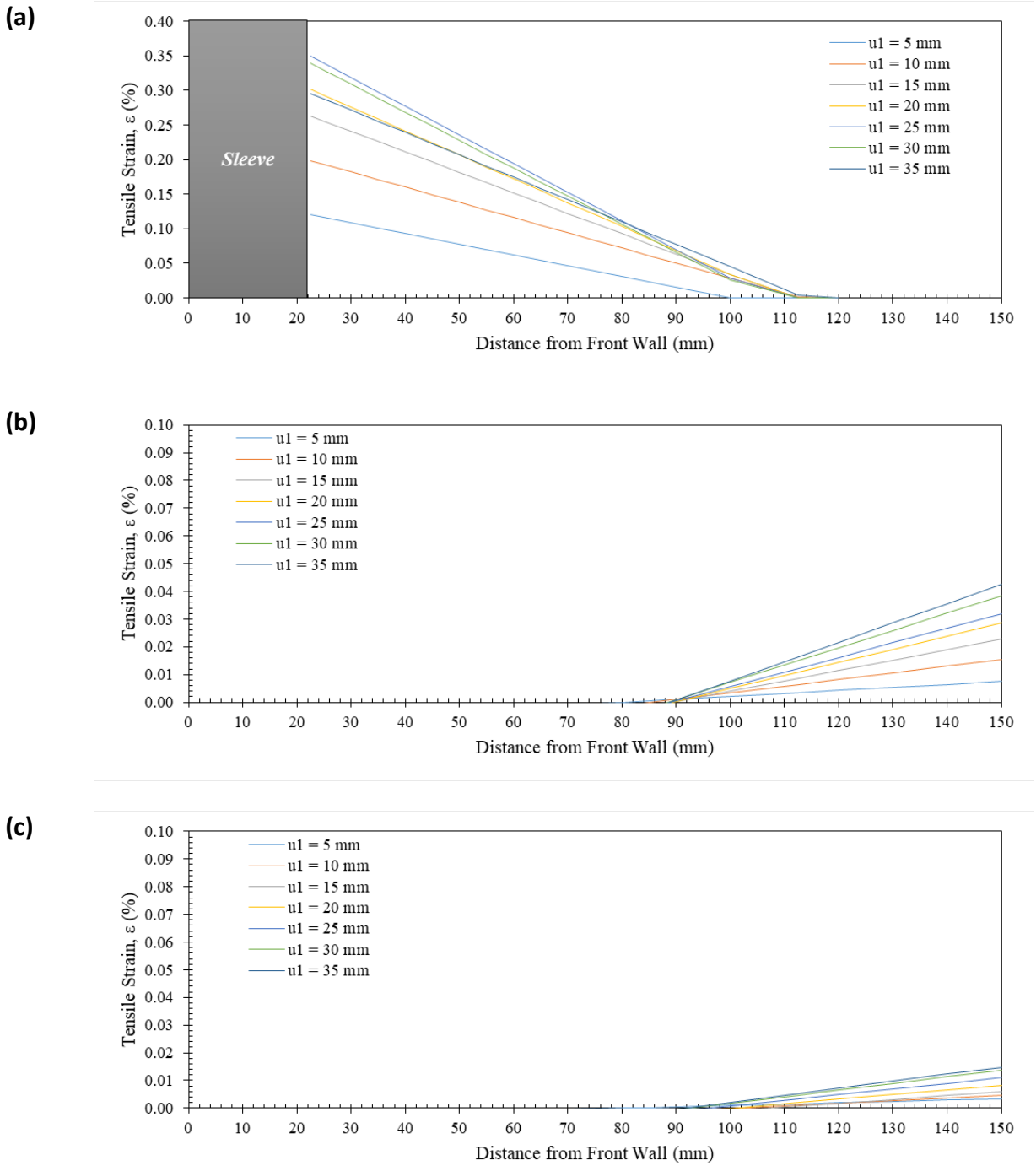

Figure 5.1.25. Reinforcement strain profiles: (a) Active reinforcement layer; (b) Upper passive reinforcement layer; and (c) Lower passive reinforcement layer.

5.1.6.3 REINFORCED SOIL DEFORMATION

Soil deformation was measured through the transparent side of the equipment, which allowed for direct visualization of the kinematic response of soil particles adjacent to the geosynthetic

reinforcement layers as well. Figures 5.1.26 through 5.1.28 show the displacement field of the reinforced soil mass in both horizontal and vertical directions. To validate the measurements taken from the boundary of the reinforced soil mass, artificial gravel particles of a size and shape similar to those of the backfill material were employed. These particles were attached to tell-tales, which were then attached to linear potentiometers to measure the displacement of the artificial particles in real-time during testing. Figure 5.1.29 shows the locations of the artificial particles buried in the reinforced soil mass.

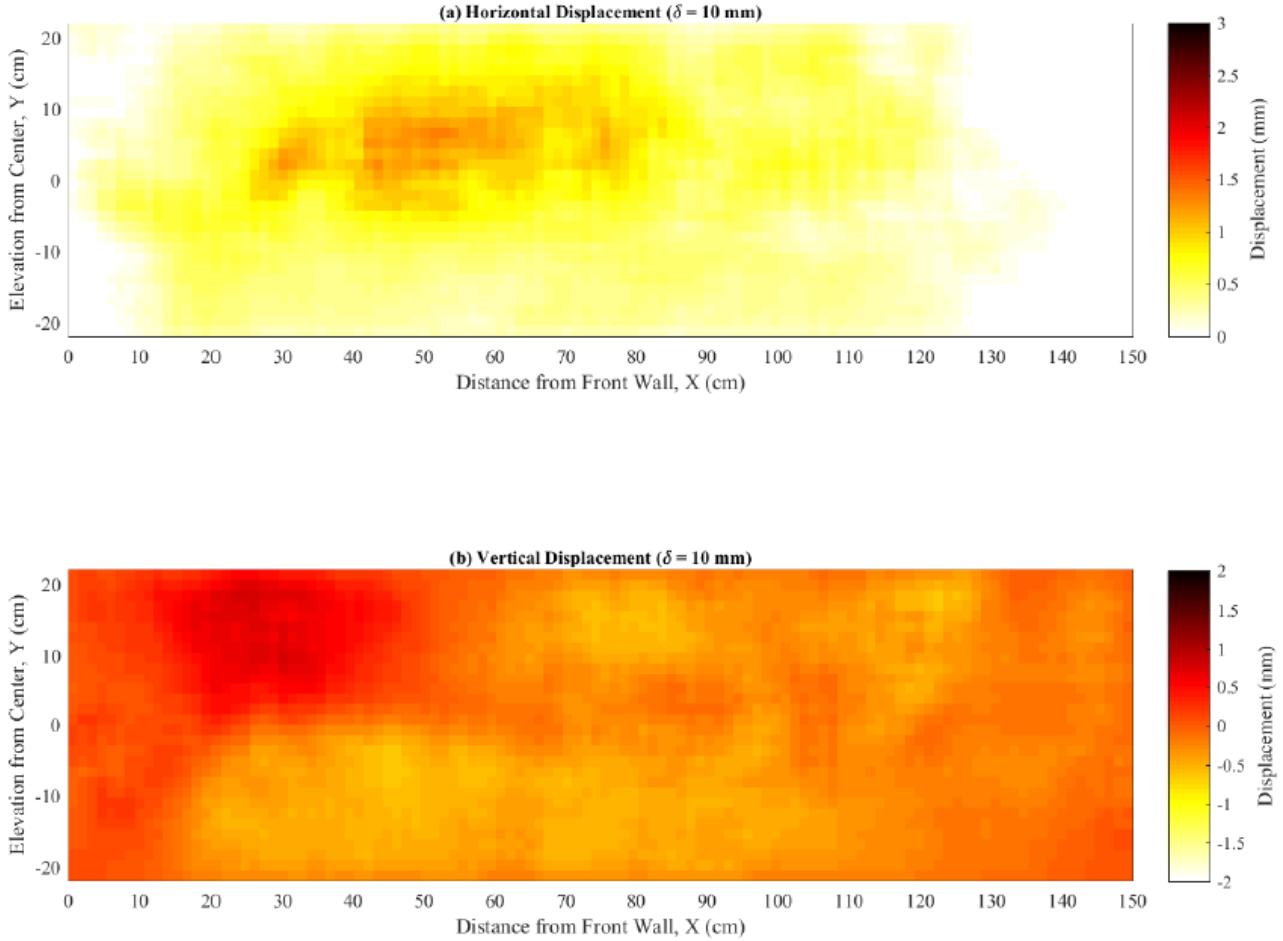

Figure 5.1.26. Displacement maps at 10 mm (0.4 in) frontal displacement: (a) Horizontal displacement; and (b) Vertical displacement.

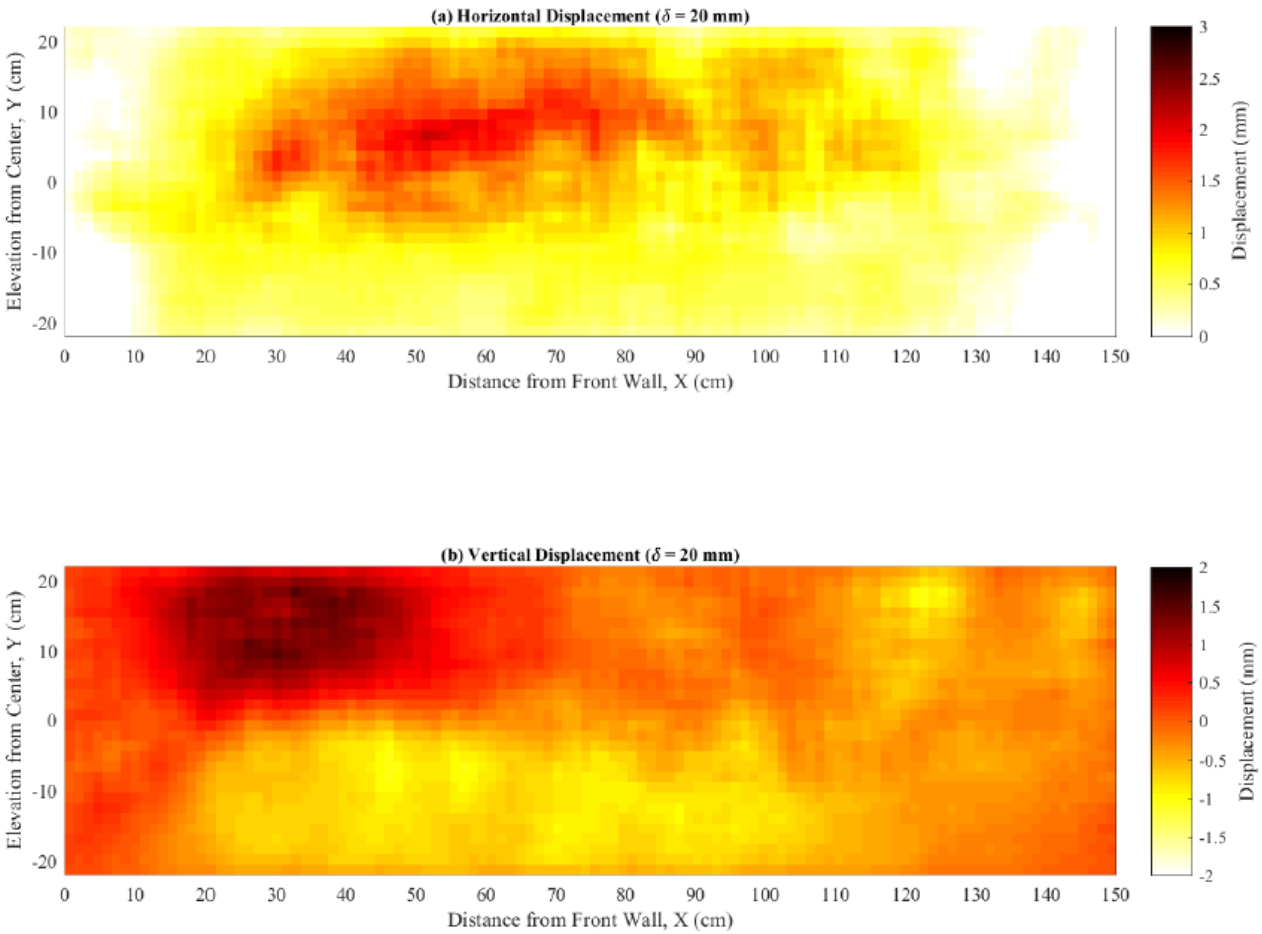

Figure 5.1.27. Displacement maps at 20 mm (0.8 in) frontal displacement: (a) Horizontal displacement; and (b) Vertical displacement.

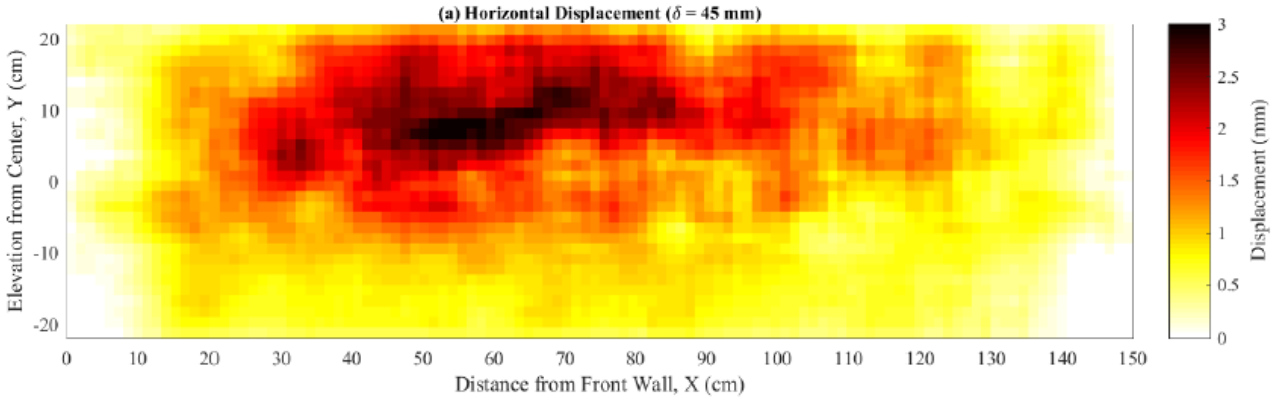

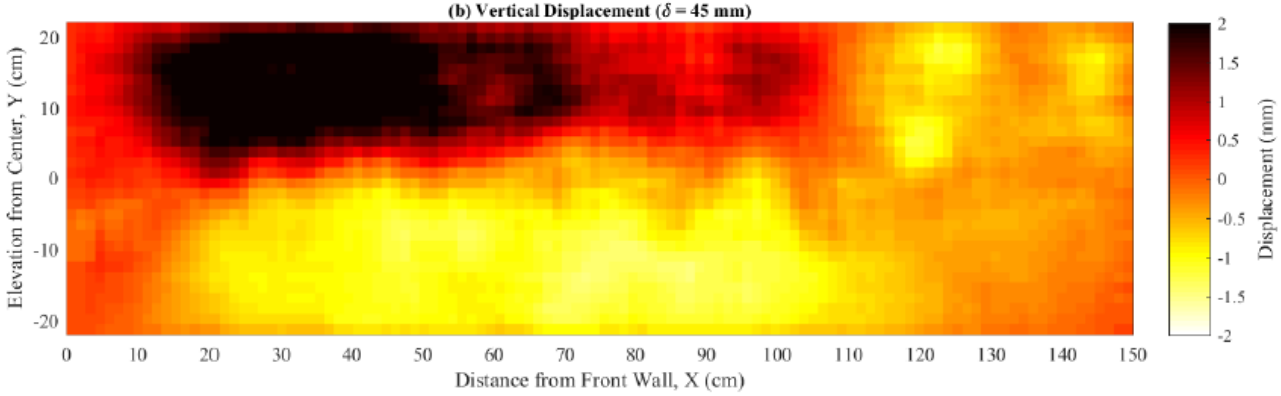

Figure 5.1.28. Displacement maps at 45 mm (1.8 in) frontal displacement: (a) Horizontal displacement; and (b) Vertical displacement.

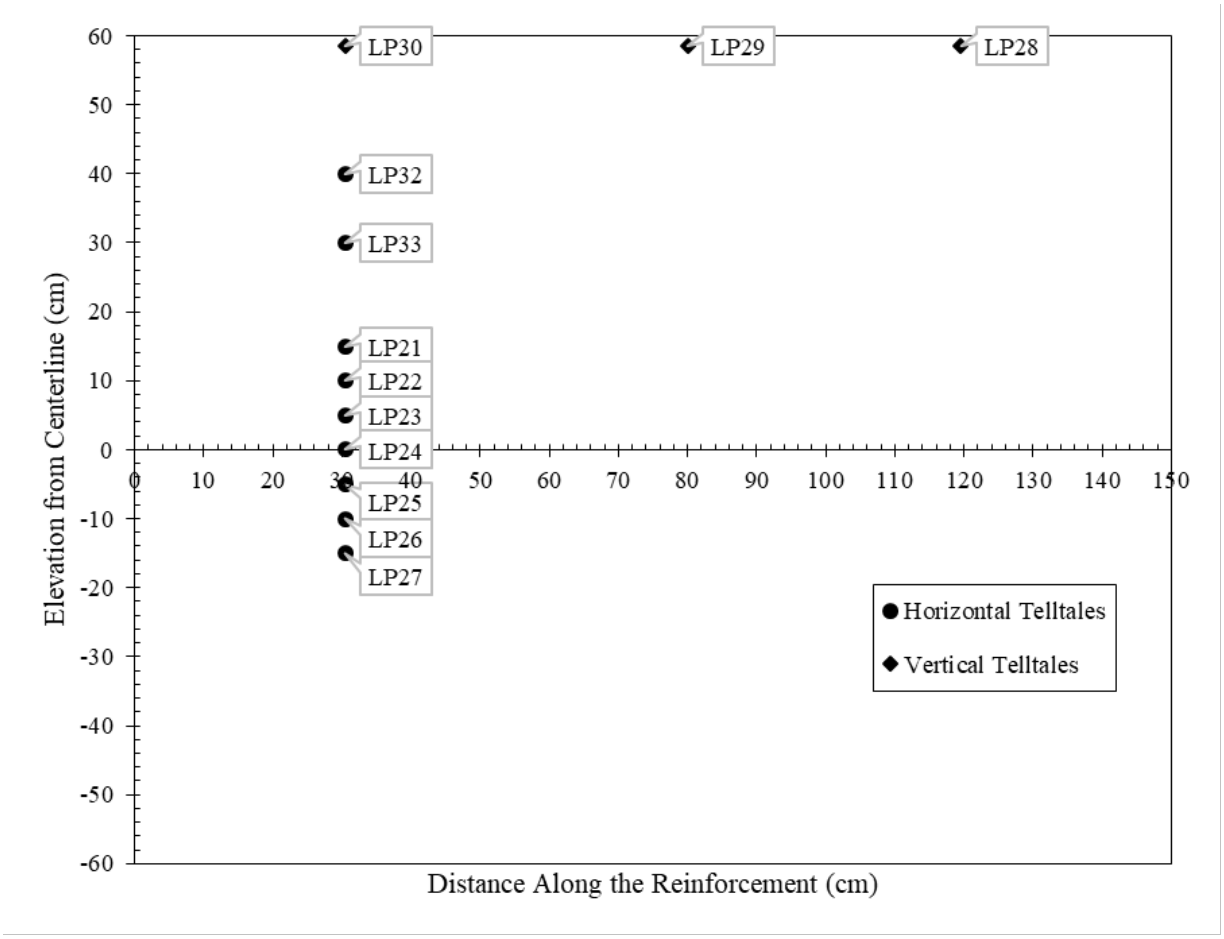

Figure 5.1.29. Locations of the artificial gravel particles

5.1.6.3.1 Soil-reinforcement interface shear band

Six artificial gravel particles were stacked on the top of each other centered in the box and located 0.305 m (1 ft.) (X = +0.305 m (1 ft.)) away from the front wall. This aimed at measuring the horizontal deformation of an imaginary vertical line centered in the box as shown in Figure 5.1.30. Figure 5.1.30 shows the horizontal displacement measured at the middle of the box using linear potentiometers attached to artificial gravel particles by means of tell-tales (see Figure 5.1.29). In addition, Figure 5.1.30 shows the horizontal displacement measured at the side of the box by analyzing the images tethered through the side transparent wall. The two sets of data show a good agreement at the various load levels. That is, the shear band evolution with the increase in the soil-reinforcement interface load can be identified by analyzing images tethered from the side of the reinforced soil mass as long as proper precautions are maintained. In addition, the observed displacement at the front wall of the box (X = 0) was almost zero over the depth of the reinforced soil. This shows that the sleeve almost eliminates the front wall rigidity problem.

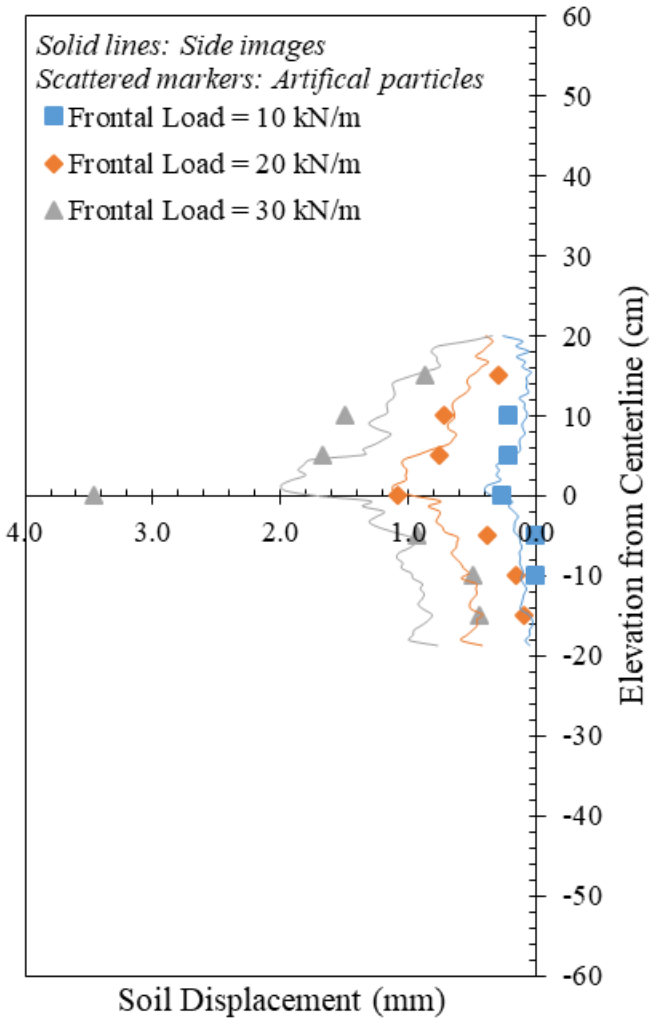

Figure 5.1.30. Horizontal displacement at X = +0.305 m (1 ft.) from the front wall of the box measured at the center of the box by linear potentiometers and at the side of the box by imaging.

5.1.6.3.2 Dilation of the reinforced soil mass

Three particles were placed on the top of the reinforced soil mass and underneath the normal pressure system. This aimed at measuring the vertical deformation of an imaginary horizontal line centered in the box and located near the top of the reinforced soil mass as shown in Figure 5.1.31. Figure 5.1.31 shows the vertical displacement measured at the middle of the box using linear potentiometers attached to artificial gravel particles by means of tell-tales. The artificial particles are placed on the top of the reinforced soil mass at Y = +0.215 m (8.5 in) (see Figure 5.1.29). Additionally, Figure 5.1.31 shows the vertical displacement measured at the side of the box at Y = +0.2 m (8 in) by analyzing the images tethered from through the transparent side wall. The two datasets show a good agreement at the various load levels. That is, the dilative/compressive behavior that can be assessed with the increase in the soil-reinforcement

interface load can be identified by analyzing images tethered from the side of the reinforced soil mass as long as proper precautions are maintained.

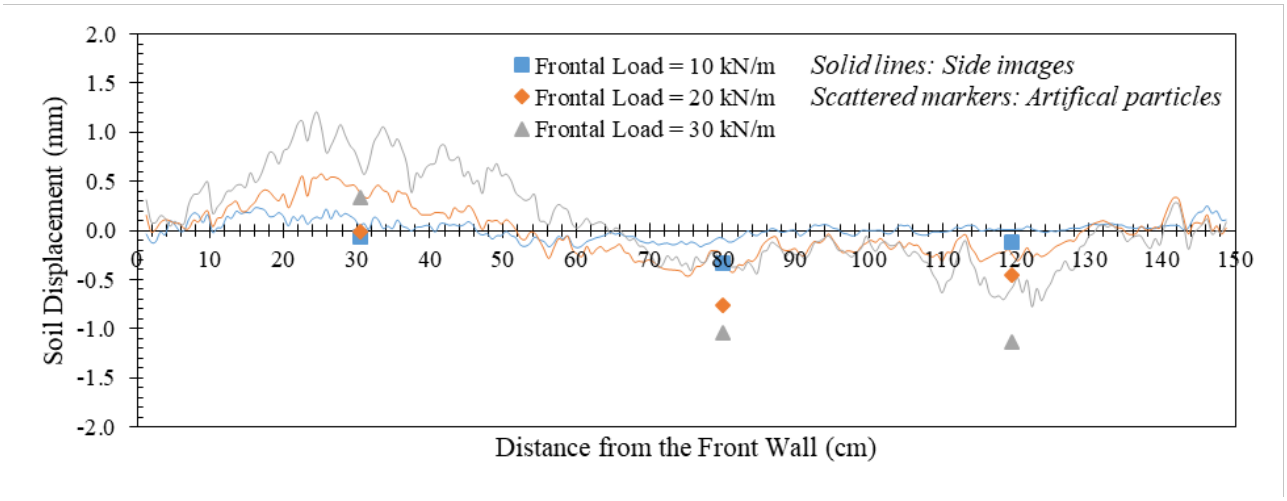

Figure 5.1.31. Vertical displacement at Y = +0.215 m (8.5 in) from the active reinforcement measured at the center of the box on the soil surface by linear potentiometers and at Y = +0.2 m (8 in) from the active reinforcement measured by imaging.

5.1.6.4 CONFINING PRESSURE

Figure 5.1.32 shows the pressure measured on top of the reinforced soil mass. This pressure was estimated from the load measured by the load cells mounted on the reaction frame at the reaction point of each pneumatic actuator. Figure 5.1.32 shows that normal pressure remained constant until 30% of the ultimate pullout load was applied. However, beyond this load level, the normal pressure at the front of the reinforced soil mass increased, up to about 30% of the original normal pressure. Note that limited dilation was allowed during testing to highlight the capabilities of the equipment in assessing the fully-allowed and fully-suppressed volume change conditions. The investigation of intermediate conditions facilitated understanding the full-scale behavior of the volume change, which would most likely happen in real structures.

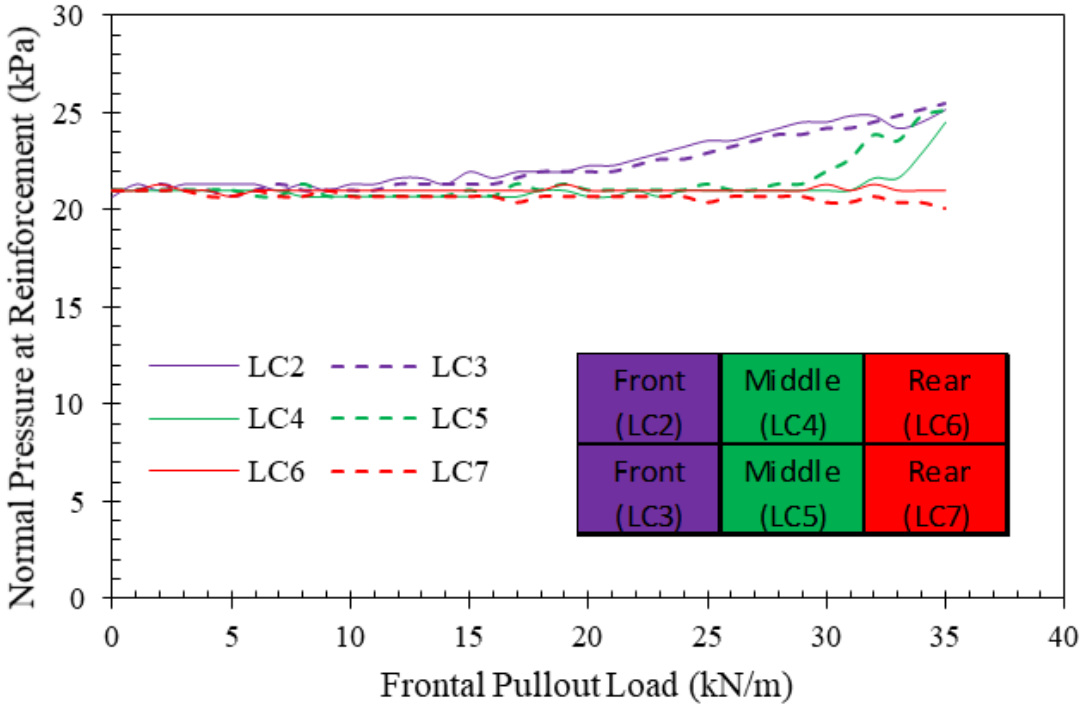

Figure 5.1.32. Normal pressure on the top of the reinforced soil mass.

5.1.6.5 REINFORCEMENT UNCONFINED TENSILE BEHAVIOR

The experimental approach aimed at including an unconfined portion of reinforcement so that the unconfined tensile behavior of the reinforcement specimen used in each test could be evaluated. This was done by analyzing tethered images taken of the unconfined portion of the reinforcement. The exposed portion of the reinforcement was speckled by spray paint and randomly dappled with a white paint marker. This served to create two levels of pattern that enhanced the accuracy of the image analysis. The average strain rate was deliberately maintained at less than 0.1% throughout testing. The average strain rate in the test conducted was approximately 0.02 %/min. Figure 5.1.33 shows the strain data measured from images at various locations in the reinforcement unconfined zone. The average of the measured points is plotted as well. Figure 5.1.33 also shows two data points provided in the technical specifications of the reinforcement manufacturer, which show good agreement with the measured values.

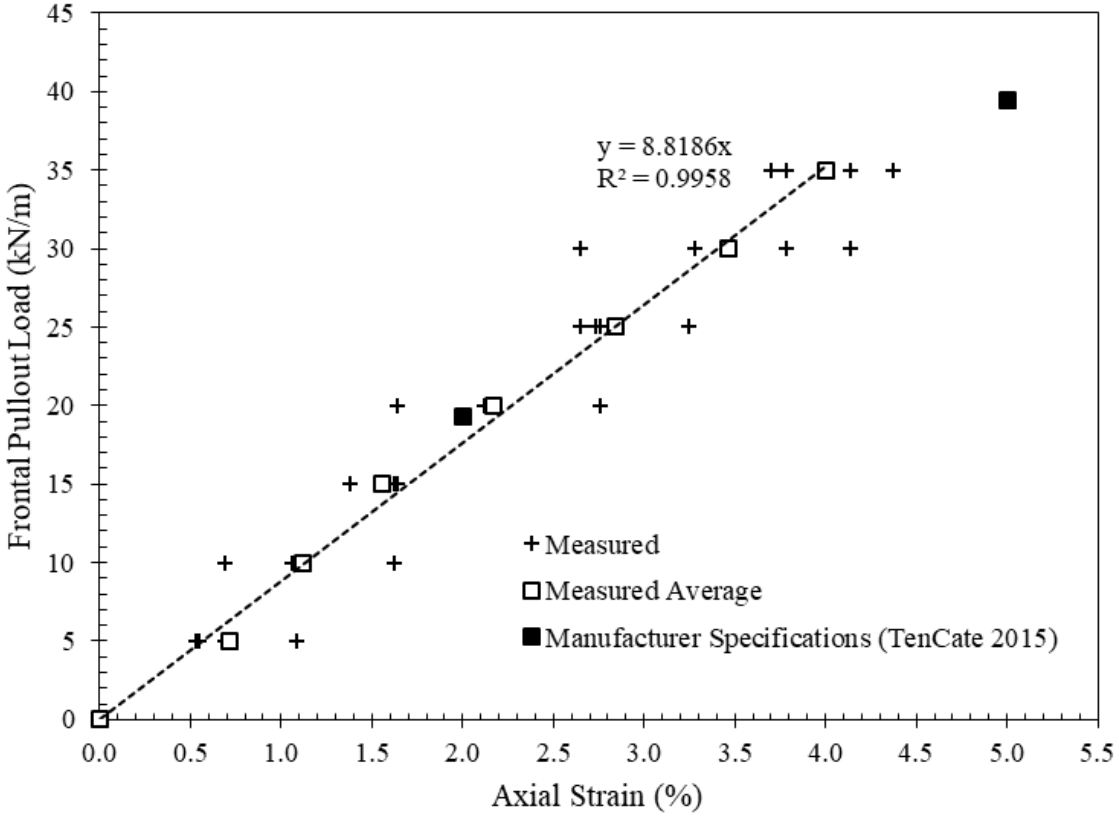

Figure 5.1.33. Reinforcement unconfined tensile behavior.

5.1.7 CONCLUSIONS

A new equipment was developed at the University of Texas at Austin to evaluate soil-reinforcement composite behavior. The equipment includes a geosynthetic-reinforced soil mass that contains three reinforcement layers. This study led to the following findings:

1. The device was found to provide suitable measurements of reinforcement straining in both a loaded geosynthetic reinforcement and in the adjacent reinforcement layers.
2. The device allowed measurement of soil deformation field via digital image analysis, which was found to provide good basis for determination of the shear band.
3. The equipment was found to be able to successfully monitor the dilatant behavior of the reinforced soil mass, which provides significant insight into the effect of reinforcement vertical spacing on the performance of geosynthetic-reinforced soil structures.

5.1.8 REFERENCES

Abdelouhab, A., Dias, D., and Freitag, N. (2010). "Physical and Analytical Modelling of Geosynthetic Strip Pull-out Behaviour." Geotextiles and Geomembranes, Vol. 28, No. 1, pp. 44–53.

Abdel-Rahman, A.H., Ibrahim, M.A., and Ashmawy, A.K. (2007). "Utilization of a Large-Scale Testing Apparatus in Investigating and Formulating the Soil/Geogrid Interface Characteristics in Reinforced Soils." Australian Journal of Basic and Applied Sciences, Vol. 1, No. 4, pp. 415-430.

Adams, M.T., Nicks, J.E., Stabile, T., Wu, J.T.H., Schlatter, W., and Hartmann, J. (2012). Geosynthetic Reinforced Soil Integrated Bridge System Interim Implementation Guide. Report No. FHWA-HRT-11-026, Federal Highway Administration, McLean, VA.

Alagiyawanna, A.M.N., Sugimoto, M., Sato, S., and Toyota, H. (2001). "Influence of Longitudinal and Transverse Members on Geogrid Pullout Behavior during Deformation." Geotextiles and Geomembranes, Vol. 19, No. 8, pp. 483–507.

Alfaro, M.C., Hayashi, S., Miura, N., and Watanabe, K. (1995a). "Pullout Interaction Mechanism of Geogrid Strip Reinforcement." Geosynthetics International, Vol. 2, No. 4, pp. 679-698.

Alfaro, M.C., Miura, N., and Bergado, D.T. (1995b). "Soil-Geogrid Reinforcement Interaction by Pullout and Direct Shear Tests." Geotechnical Testing Journal, GTJODJ, Vol. 18, No. 2, pp. 157-167.

ASTM D4595-11 (2011). "Standard Test Method for Tensile Properties of Geotextiles by the Wide-Width Strip Method." ASTM Standards, American Society for Testing and Materials (ASTM), West Conshohocken, PA.

ASTM D6706-01 (2013). "Standard Test Method for Measuring Geosynthetic Pullout Resistance in Soil." ASTM Standards, American Society for Testing and Materials (ASTM), West Conshohocken, PA.

Aydogmus, T. and Klapperich, H. (2008). "Design and Evaluation of an Enhanced Shear and Pull-Out Testing Device." Proceedings of the 4th European Geosynthetics Conference, paper 170.

Bergado, D.T. and Chai, J.-C. (1994). "Pullout Force/Displacement Relationship of Extensible Grid Reinforcements." Geotextiles and Geomembranes, Vol.13, No.5, pp. 295-316.

Bergado, D.T. and Teerawattanasuk, C. (2001). "Analytical Models for Predicting the Pullout Capacity and Interaction between Hexagonal Wire Mesh and Silty Sand Backfill." Tamakang Journal of Science and Engineering, Vol. 4, No. 4, pp. 227-238.

Bernal, A., Salgado, R., Swan Jr., R.H., and Lovell C.W. (1997). "Interaction between Tire Shreds, Rubber-Sand and Geosynthetics." Geosynthetics International, Vol. 4, No. 6, pp. 623-643.

Bonczkiewicz, C., Christopher, B.R. and Atmatzidis, D.K. (1990). "Evaluation of Soil-Reinforcement Interaction by Large Scale Pullout Test", Transportation Research Record 1188, TRB, Washington, DC, Jan 1990

Brand, S.R. and Duffy, D.M. (1987). "Strength of Pull-Out Testing of Geogrids." Proceedings of Geosynthetics 1987, Vol. 1, New Orleans, LA, pp. 226-236.

Chang, J.C., Hannon, J.B., and Forsyth, R.A. (1977). "Pullout Resistance and Interaction of Earthwork Reinforcement and Soil." Transportation Research Record 640, National Research Council, Washington, DC, pp. 1-7.

Christopher, B.R. (1993). Deformation Response and Wall Stiffness in Relation to Reinforced Soil Wall Design. Ph.D. Dissertation, Department of Civil Engineering, Purdue University, West Lafayette, IN, 354 p.

Cuelho, E.V. (1998). Determination of Geosynthetic Constitutive Parameters and Soil/Geosynthetic Interactions by In-Air and In-Soil Experiments. MS Thesis, Montana State University, MT.

Dyer, M.R. (1985). Observation of the Stress Distribution in Crushed Glass with Applications to Soil Reinforcement. Ph.D. Thesis, The University of Oxford, UK.

Elias, V. (1979). "Friction in Reinforced Earth Utilizing Fine Grained Backfills." International Conference on Soil Reinforcement, Paris, France.

European Standards (2004). Geotextiles and Geotextile-related Products. Determination of Pullout Resistance in Soil. European Standards EN 13738:2004.

Fannin, R.J. and Raju, D.M. (1993). "On the Pullout Resistance of Geosynthetics." Canadian Geotechnical Journal, Vol. 30, No. 3, pp. 409-417.

Farrag, K., Acar, Y.B., and Juran, I. (1993). "Pull-Out Resistance of Geogrid Reinforcements." Geotextiles and Geomembranes, Vol. 12, No. 2, pp. 133-159.

Geosynthetic Institute (1991). Geogrid Pullout. GRI Test Methods GRI GG5. Geosynthetic Institute (GRI).

Hanumasagar, S.S., Roodi, G.H., and Zornberg, J.G. (2014). "Pullout Characterization of Geogrids Embedded in Blends of Dredged Material and Steel Slag Fines." Proceedings of the 10th ICG Conference, Berlin, Germany.

Ingold, T.S. (1983). "A Laboratory Investigation of Grid Reinforcements in Clay." Geotechnical Testing Journal, Vol. 6, No. 3, pp. 112-119.

Jacobs, F., Ruiken, A., and Ziegler, M. (2012a). "Experimental Investigation of Geogrid Reinforced Soil under Plane Strain Conditions." Geosynthetics Asia 2012, 5th Asian Regional Conference on Geosynthetics, 10 to 14 December 2012, Bangkok, Thailand.

Jacobs, F., Ruiken, A., and Ziegler, M. (2012b). "Investigation of Geogrid Reinforced Soil with Large Scale “Element” Testing." GeoAmericas 2012, Lima, Perú, May 2012.

Jacobs, F., Ziegler, M., and Ruiken, A. (2013). "Experimental Investigation of the Stress-Strain Behaviour of Geogrid Reinforced Soil." GeoAfrica 2013, Accra, Ghana, 18–20 November 2013.

Jayawickrama, P.W., Lawson, W.D., Wood, T.A., and Surles, J.G. (2014). "Pullout Behavior of Welded Grid Reinforcements Embedded in Coarse Granular Backfill." ASCE Geo-Congress, Atlanta, GA, February 2014.

Jewell, R.A. (1980). Some Effects of Reinforcement on the Mechanical Behavior of Soils. Ph.D. Dissertation, Cambridge University, Cambridge, UK.

Juran, I., Guermazi, A., Chen, C.L., and Ider, M.H. (1988). "Modelling and Simulation of Load Transfer in Reinforced Soil: Part 1." International Journal for Numerical and Analytical Methods in Geomechanics, Vol. 12, No. 2, pp. 141-155.

Kharchafi, M. and Dysli, M. (1993). "Study of Soil-Geotextile Interaction by an X-Ray Method." Geotextiles and Geomembranes, Vol. 12, No. 4, pp. 307-325.

Koerner, R.M. (2005). Designing with Geosynthetics, Fifth Edition. Pearson Prentice Hall.

Koerner, R.M. (1986). Direct Shear/Pull-Out Tests on Geogrids. Report No. 1, Department of Civil Engineering, Drexel University, Philadelphia, PA.

Ladeira, M.A.S.A. (1995). Estudo dos Fenômenos de Interação Solo-Geossintetico Através de Ensaios de Arranque. (In Portuguese) MS Thesis, University of Porto, Portugal.

Leshchinsky, D., Kaliakin, V., Bose, P., and Collin, J. (1994). "Failure Mechanism in Geogrid-Reinforced Segmental Walls: Experimental Implications." Soils and Foundations, Vol. 34, No. 4, pp. 33-41.

Lopes, M.L. (1992). Walls Reinforced with Geosynthetics. (In Portuguese) Ph.D. Thesis, University of Porto, Portugal, 335 p.

Lopes, M.L. and Ladeira, M. (1996). "Role of Specimen Geometry, Soil Height and Sleeve Length on the Pull-Out Behaviour of Geogrids." Geosynthetic International, Vol. 3, No. 6, pp. 701-719.

Marques, J.M.M.C. (2005). "Finite Element Modelling of the Pull-Out Test of Geosynthetics." VIII International Conference on Computation Plasticity, E. Onate and D.R. Owen (eds.).

McGown, A., Andrawes, K.Z., and Kabir, M.H. (1982). “Load Extension Testing of Geotextiles Confined in Soil.” In Proceedings of the 2nd International Conference on Geotextiles, Vol. 3, pp. 793-798. Roseville, Minnesota, August 1982.

Meyer, N., Nernheim, A., and Emersleben, A. (2003). "Influence of Confining Pressure, Soil Density and Types of Geogrids on Soil-Geogrid Interaction Coefficient." E-Conference "Modern Trends in Foundation Engineering: Geotechnical Challenges and Solutions", IITM, India.

Min, Y., Leshchinsky, D., Ling, H.I., and Kaliakin, V.N. (1995). "Effects of Sustained and Repeated Tensile Loads on Geogrid Embedded in Sand." Geotechnical Testing Journal, Vol. 18, No. 2, pp. 204-225.

Minažek, K. and Mulabdić, M. (2013). "A Review of Soil and Reinforcement Interaction Testing in Reinforced Soil by Pullout Test." Građevinar 2013, Vol. 65, No. 3, pp. 235-250.

Moraci, N. and Gioffre, D. (2006). "A Simple Method to Evaluate the Pullout Resistance of Embedded in a Compacted Granular Soil Extruded Geogrids." Geotextiles and Geomembranes, Vol. 24, No. 2, pp. 116–128.

Moraci, N. and Recalcati, P. (2006). "Factors Affecting the Pullout Behaviour of Extruded Geogrids Embedded in a Compacted Granular Soil." Geotextiles and Geomembranes, Vol. 24, No. 4, pp. 220–242.

Morsy, A. M. (2017). Evaluation of soil-reinforcement composite interaction in geosynthetic-reinforced soil structures. Doctoral dissertation, The University of Texas at Austin, Austin, Texas, USA.

Myles, B. (1982) “Assessment of Soil Fabric Friction by Means of Shear.” Proceedings 2nd International Conference on Geotextiles, Las Vegas, p. 787-791.

Ochiai, H., Otani, J., Hayashic, S., and Hirai, T. (1996). "The Pull-Out Resistance of Geogrids in Reinforced Soil." Geotextiles and Geomembranes, Vol. 14, No. 1, pp. 19-42.

Palmeira, E.M. (2009). "Soil-Geosynthetic Interaction: Modelling and Analysis." Geotextiles and Geomembranes, Vol. 27, No. 5, pp. 368–390.

Palmeira, E.M. and Milligan, G.W.E. (1989). "Scale and Other Factors Affecting the Results of Pull-Out Tests of Grids Buried in Sand." Geotechnique, Vol. 39, No. 3, pp. 511-524.

Salomone, W.G. (1978), Soi-Reinforcement Interaction,” PH.D. Thesis, Purdue University, West Lafayette, Indiana, 70 pp.

Salomone, W. G., Boutrup, E., Holtz, R. D., Kovacs, W. D. and Sutton, C. D. (1980) “Fabric Reinforcement Design Against Pullout Failure”, The Use of Geotextiles for Soil Improvement, ASCE Convention and Exposition, Portland, Oregon, Preprint 80-177, pp.

75-87.cSaxena, S.K. and Budiman, J.S. (1985). "Interface Response of Geotextiles." Proceedings of the 11th International Conference on Soil Mechanics and Foundation Engineering.

Schuettpelz, C., Fratta, D., and Edil, T. (2009). "Evaluation of the zone of influence and stiffness improvement from geogrid reinforcement in granular materials." Transportation Research Record: Journal of the Transportation Research Board, Vol. 2116, pp. 76-84.

Stadler, A.T. (2001). Geogrid Reinforcement of Piedmont Residual Soil. Report No. HWY-2001-02, North Carolina Department of Transportation, Raleigh, NC.

Teixeira, S.H.C. (2003). Estudo da Interação Solo-Geogrelha em Testes de Arrancamento e a sua Aplicação na Análise e Dimensionamento de Maciços Reforçados. (In Poruguese) Ph.D. Thesis, School of Engineering, Univerity of São Paulo, São Carlos.

TenCate Geosynthetics (2015). Mirafi® HP570 Specifications. Nicolon Corporation.

Tzong, W.H. and Cheng-Kuang, S. (1987). "Soil-Geotextile Interaction Mechanism in Pullout Test." Proceedings of Geosynthetics 1987, Vol. 1, New Orleans, LA, pp. 250-259.

Williams, N.D. and Houlihan, M.F. (1987). "Evaluation of Interface Friction Properties between Geosynthetics and Soils." Proceedings of Geosynthetics 1987, Vol. 2, New Orleans, LA, pp. 616-627.

Yuan, Z. and Chua, K.M. (1991). "Numerical Evaluation of the Pullout Box Method for Studying Soil-Reinforcement Interaction." Transportation Research Record 1278, Transportation Research Board, Washington, D.C., pp. 116-124.

Zhou, J., Chen, Chen, J.-F., Xue, J.-F., and Wang, J.-Q. (2012). "Micro-Mechanism of the Interaction between Sand and Geogrid Transverse Ribs." Geosynthetics International, 2012, Vol. 19, No. 6, pp. 1072-6349.

Zornberg, J.G., Ferreira, J.A.Z., Gupta, R.V., Joshi, R.V., and Roodi, G.H. (2009). Geosynthetic-Reinforced Unbound Base Courses: Quantification of the Reinforcement Benefits. Center for Transportation Research (CTR), Report No. FHWA/TX-10/5-4829-1, Austin, Texas, December 2009, Revised February 2012, 170 p.

Zornberg, J.G. and Mitchell, J.K. (1994). "Reinforced Soil Structures with Poorly Draining Backfills. Part I: Reinforcement Interactions and Functions." Geosynthetics International, Vol. 1, No. 2, pp. 103-147.

Zornberg, J.G., Roodi, G.H., Ferreira, J.Z., and Gupta, R. (2013). "Characterization of Soil-geosynthetic Interaction under Small Displacement Conditions." Proceedings of the 18th International Conference on Soil Mechanics and Geotechnical Engineering, 02-06 September, Paris, France, pp. 1385-1388.

5.2 SOIL-GEOSYNTHETIC COMPOSITE INTERACTION PARAMETRIC EVALUATION

5.2.1 INTRODUCTION

A comprehensive testing program has been conducted adopting the developed experimental approach and equipment detailed in Chapter 5.1. The testing program was tailored to evaluate the following aspects: (1) testing repeatability; (2) effect of reinforced soil confinement; (3) effect of reinforcement vertical spacing; (4) effect of reinforcement properties; (5) effect of boundary type; and (6) effect of backfill properties.

5.2.2 TESTING PROGRAM

This section describes the testing scheme adopted to fulfill the objectives of this study. The following subsections include the testing configurations for the various tests and the characteristics of the materials used in the testing program.

The equipment is designed to have two configurations: (1) 0.45 m (1.5-ft.) Configuration, whose dimensions are 1.5 m (5 ft.) (L) x 0.3 m (1 ft.) (W) x 0.45 m (1.5 ft.) (H), as shown in Figure 5.2.1a; and (2) 1.2 m (4-ft.) Configuration, whose dimensions are 1.50 m (5 ft.) (L) x 0.3 m (1 ft.) (W) x 1.2 m (4 ft.) (H), as shown in Figure 5.2.1b. Three reinforcement layers were placed at a vertical spacing ranging from 50 mm (2 in.) to 150 mm (6 in.) in the first configuration and ranging from 20 mm (0.8 in.) to 400 mm (16 in.) for the second configuration. The target confining pressure ranged from 15 kPa (2.25 psi) to 50 kPa (7.3 psi) at the level of the main (middle) reinforcement layer. This confining pressure was intended to be low enough to allow pullout failure to occur before reinforcement rupture. This, particularly, allows excessive deformation to take place in the reinforcement and the surrounding soil (mostly pullout failure). This allows complete understanding of the soil-reinforcement load-transfer mechanisms and assessment of the soil-reinforcement composite interaction behavior. The embedment length of the main reinforcement layer was 1016 mm (40 in). On the other hand, the boundary reinforcement layers were extended to the rear end of the reinforced soil mass, where they were clamped. Table 5.2.1 shows the detailed experimental program adopted in this study.

(a)

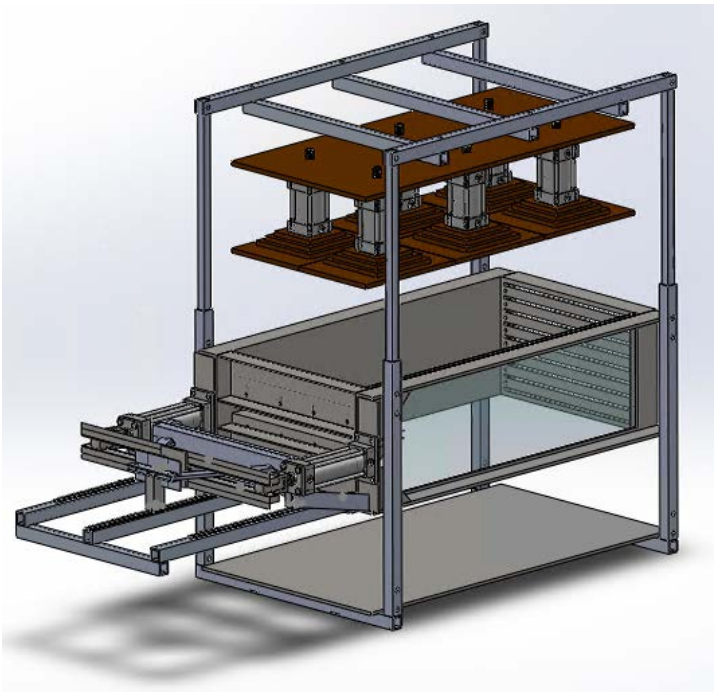

(b)

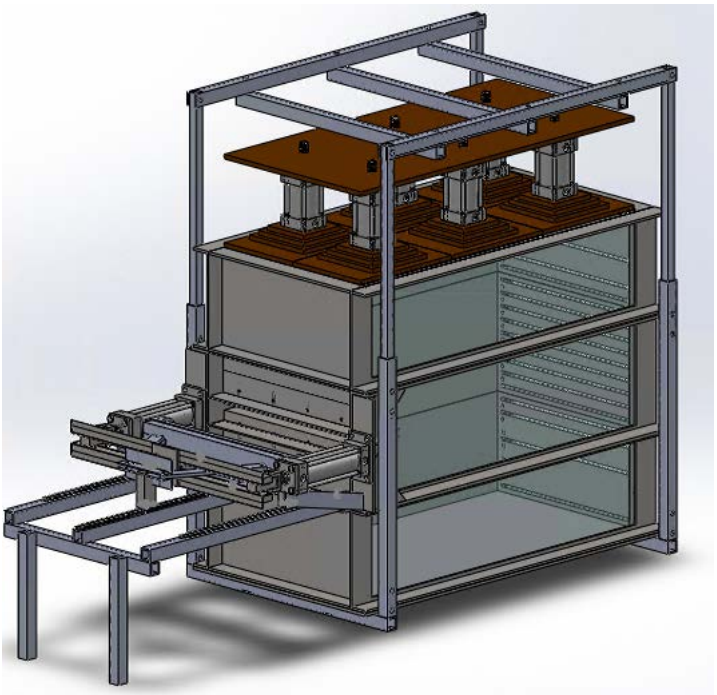

Figure 5.2.1. Equipment testing configurations: (a) 0.45 m configuration (short); and (b) 1.20 m configuration (4 ft.) (tall)

Table 5.2.1. Testing scheme (Morsy 2017).

Test Series	***Theme of the Series***	***Test Number***	***Test ID***	***Testing Variables***					
				Fill Material	***Reinforcement Spacing, S_v***	***Normal Stress, σ_v***	***Geosynthetic Type***	***Boundary Type***	***Dilation Control***
A	***Baseline***	1	GP-06-03-G1-G	AASHTO Gravel No. 8	0.15 m	21 kPa	HP570	Geosynthetic	Allowed
B	***Reinforcement Spacing, S_v***	2	GP-02-03-G1-G	AASHTO Gravel No. 8	0.05 m	21 kPa	HP570	Geosynthetic	Allowed
		3	GP-04-03-G1-G		0.10 m				
		4	GP-02-07-G1-G		0.05 m	50 kPa			
		5	GP-04-07-G1-G		0.10 m				
		6	GP-04-07-G1-G(R)		0.10 m				
		7	GP-06-07-G1-G		0.15 m				
		8	GP-08-07-G1-G		0.20 m				
		9	GP-12-07-G1-G		0.30 m				
		10	GP-16-07-G1-G		0.40 m				
C	***Boundary Type***	11	GP-06-03-G1-S	AASHTO Gravel No. 8	0.15 m	21 kPa	HP570	Mylar	Allowed
D	***Geosynthetic Type***	12	GP-06-03-G2-G	AASHTO Gravel No. 8	0.15 m	21 kPa	RS580i	Geosynthetic	Allowed
		13	GP-06-02-G3-G			15 kPa	BX1100		
		14	GP-06-03-G4-G			21 kPa	BX1200		
		15	GP-06-03-G5-G			21 kPa	80T		
E	***Normal Stress, σ_v***	16	GP-06-02-G1-G	AASHTO Gravel No. 8	0.15 m	15 kPa	HP570	Geosynthetic	Allowed
		17	GP-06-05-G1-G			35 kPa			
F	***Fill Material***	18	SP-06-03-G1-G	Montery Sand No. 30	0.15 m	21 kPa	HP570	Geosynthetic	Allowed
G	***Dilation Control***	19	GP-06-03S-G1-G	AASHTO Gravel No. 8	0.15 m	21 kPa	HP570	Geosynthetic	Reduced

*Conversions: 1 m = 0.0254 in.
1 kPa = 20.89 psf

5.2.3 PARAMETRIC EVALUATION

5.2.3.1 TEST REPEATABILITY

A comparison was conducted to assess the repeatability of the test. Two identical tests were conducted at the same conditions. Specifically, two tests were conducted using HP570 polypropylene woven geotextile reinforcements. The reinforcement has ultimate tensile strength 70 kN/m (399.7 lbs/in) and tensile stiffness of 876 kN/m (5002 lbs/in) at 5% tensile strain in the cross-rollway direction (i.e., cross-machine direction). Three reinforcement layers, one active and two passive, were used in each test and were placed at vertical spacing of 0.10 m (4 in). the passive reinforcement layers are of the same type as the active layers. Both tests used AASHTO No. 8 fill material and conducted at confining normal stress of 50 kPa (7.3 psi) at the active reinforcement level (i.e., central horizontal plane of the reinforced soil mass). Table 5.2.2 summarizes the properties of the tests involved in this comparison.

Table 5.2.2. Summary of repeated tests.

Test ID	***Testing Variables***					
	Fill Material	S_v^*	σ_v^*	***Active GS***	***Passive GS***	***Dilation***
GP-06-03-G1-G GP-06-03-G1-G(R)	AASHTO No. 8	0.10 m	50 kPa	HP570	HP570	Allowed

*Conversions: 1 m = 0.0254 in.

1 kPa = 20.89 psf

Figure 5.2.2 shows the frontal pullout load-displacement experimental curves for both tests. It was observed that both curves well coincide to each other. Figures 5.2.3 through 5.2.6 show the displacement profiles for the active and passive reinforcement layers at active reinforcement frontal displacement (*u1*) of 5, 10, 15, and 20 mm (0.2, 0.4, 0.6 and 0.8 in), respectively. The displacement profiles obtained from both tests matched well at the various loading stages. Similar observation was made for the displacement profiles of the passive reinforcement layers. Figures 5.2.7a through 5.2.7d present the horizontal soil displacement measured for nodal displacements of 5, 10, 15, and 20 mm (0.2, 0.4, 0.6 and 0.8 in), respectively. These displacements were measured at specific locations by tracking artificial gravel particles making a vertical array within the soil at 0.305 m (1 ft.) from the front wall. It was observed that the soil displacement is very similar for both tests at the various loading stages.

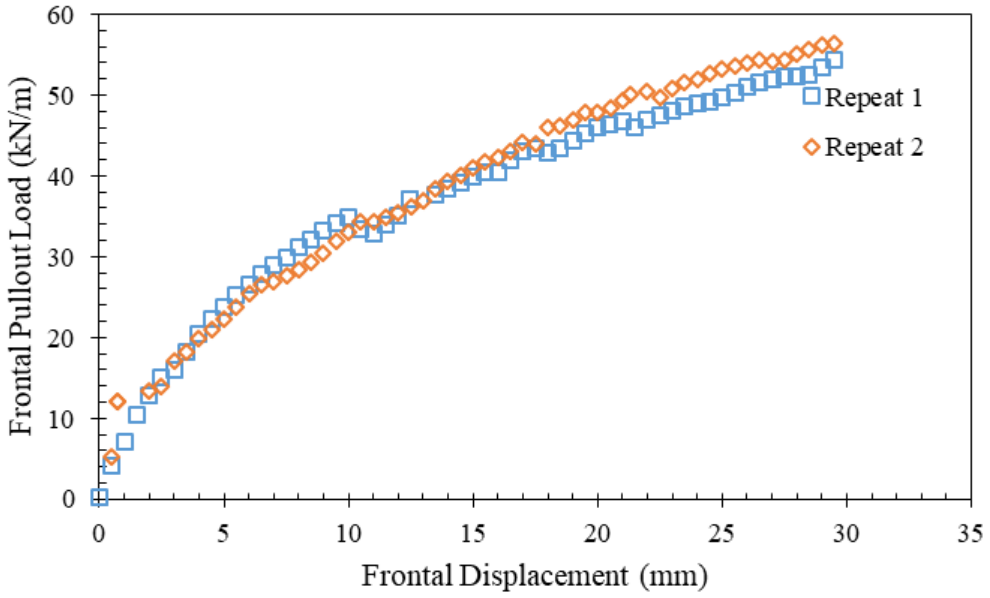

Figure 5.2.2. Frontal pullout load-displacement curves.

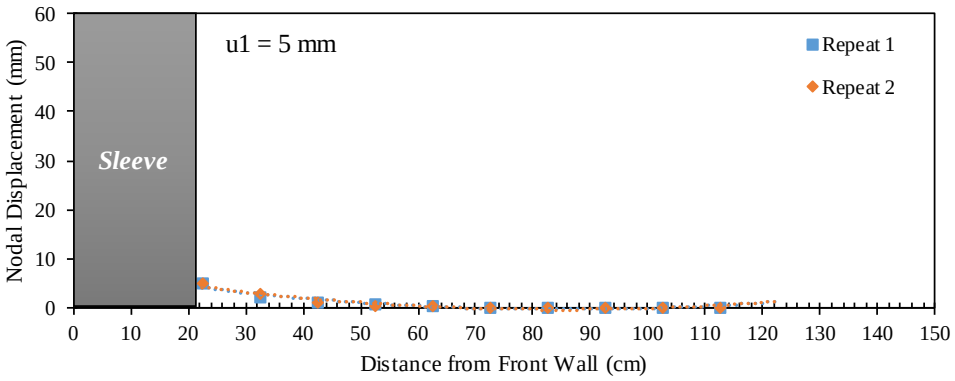

(a)

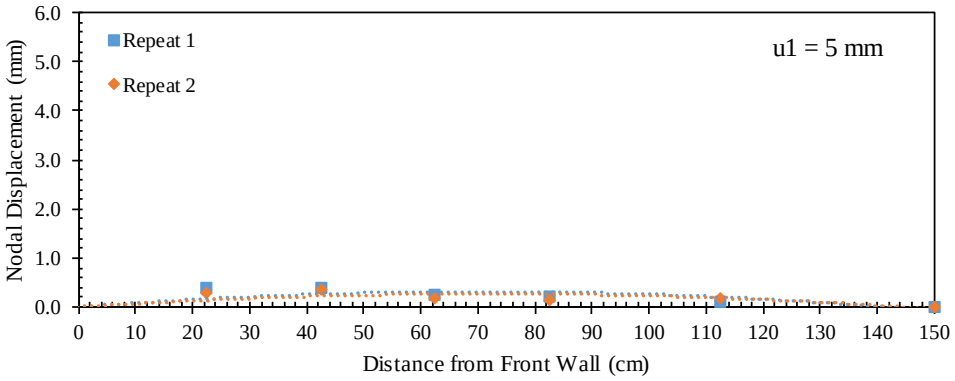

(b)

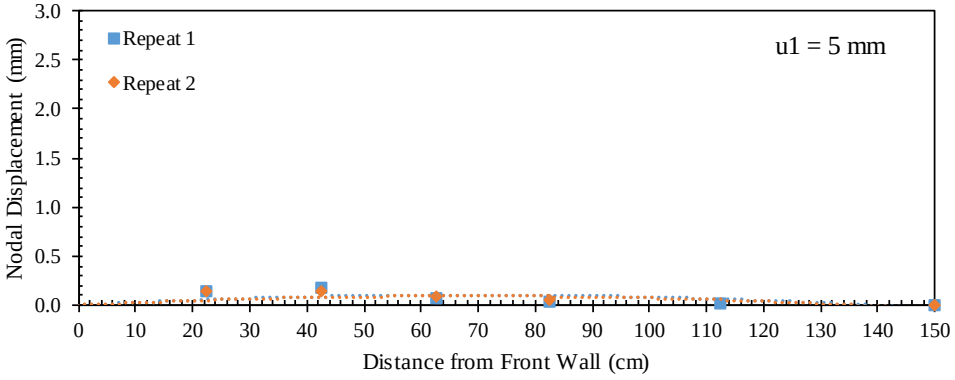

(c)

Figure 5.2.3. Reinforcement displacement profiles at frontal displacement u1 = 5 mm (0.2 in): (a) Active reinforcement; (b) Upper passive reinforcement; and (c) Lower passive reinforcement.

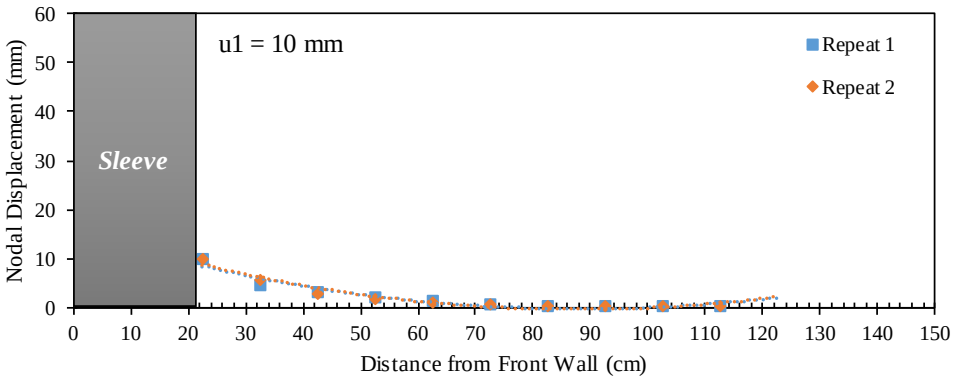

(a)

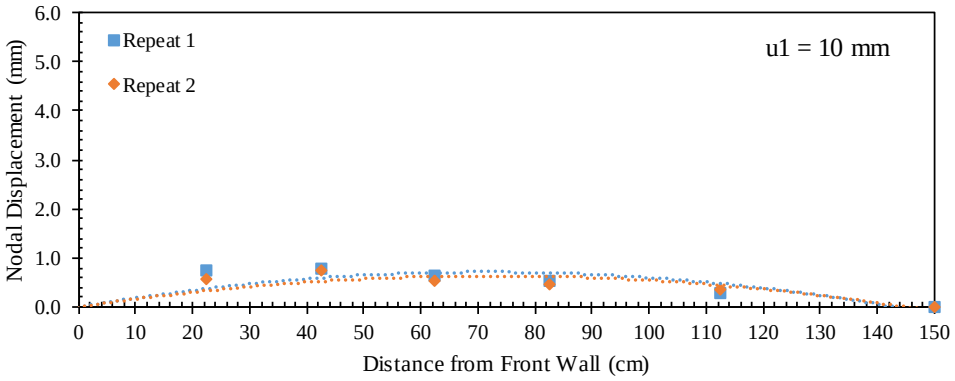

(b)

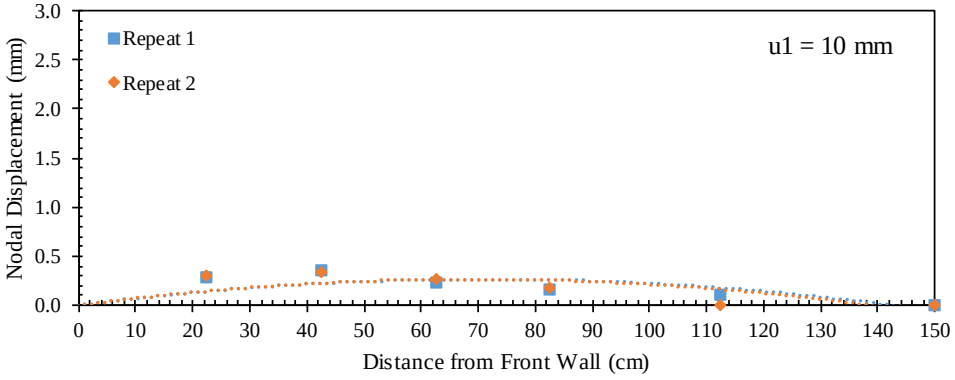

(c)

Figure 5.2.4. Reinforcement displacement profiles at frontal displacement u1 = 10 mm (0.4 in): (a) Active reinforcement; (b) Upper passive reinforcement; and (c) Lower passive reinforcement.

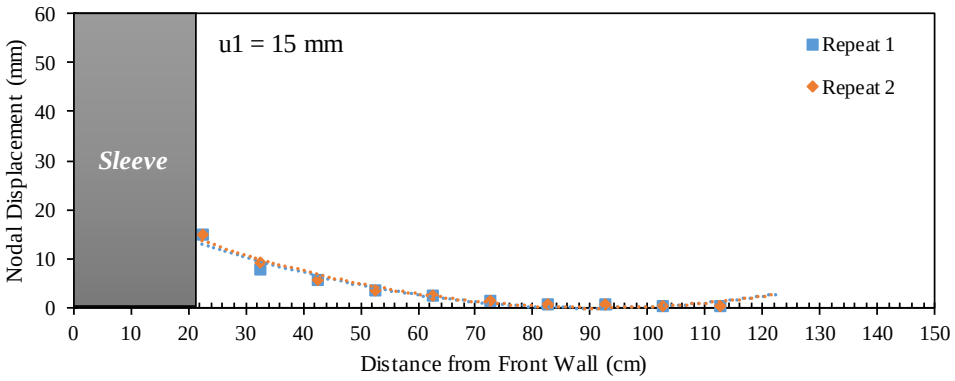

(a)

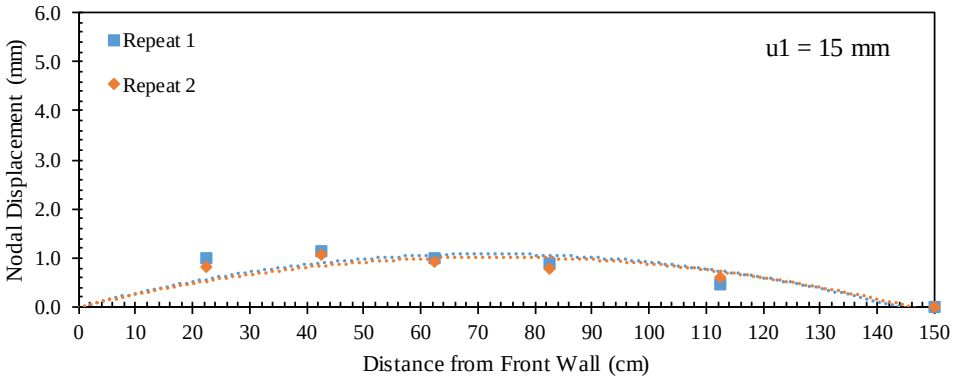

(b)

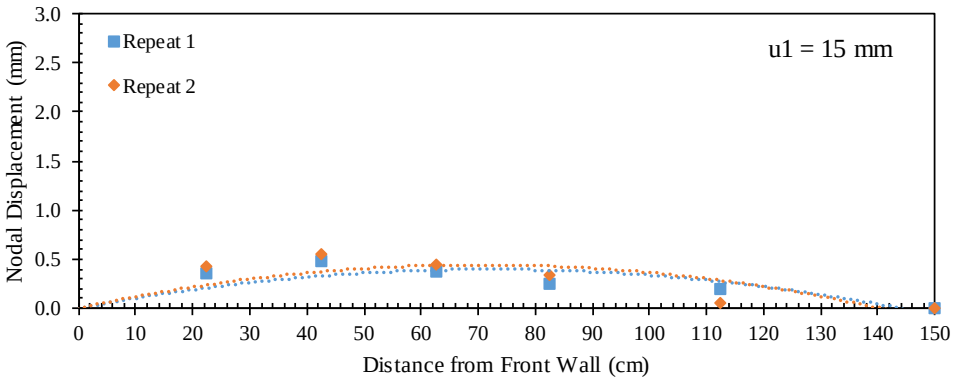

(c)

Figure 5.2.5. Reinforcement displacement profiles at frontal displacement u1 = 15 mm (0.6 in): (a) Active reinforcement; (b) Upper passive reinforcement; and (c) Lower passive reinforcement.

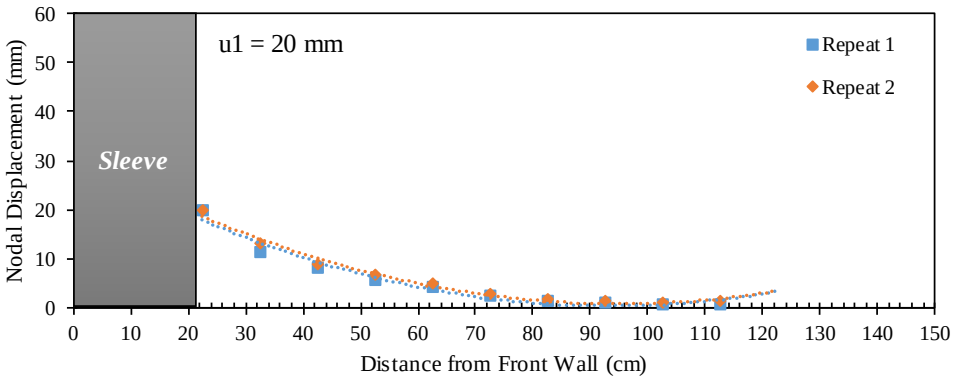

(a)

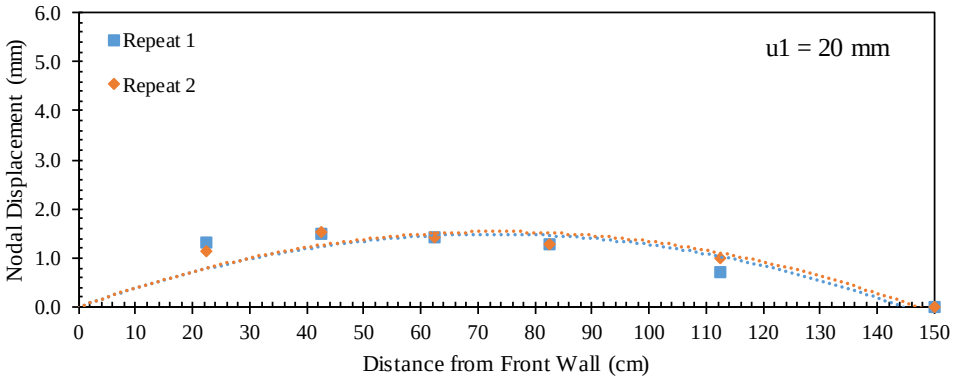

(b)

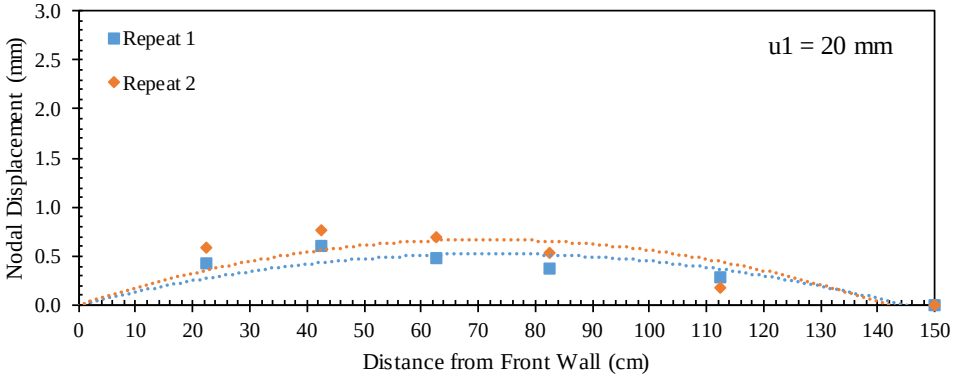

(c)

Figure 5.2.6. Reinforcement displacement profiles at frontal displacement u1 = 20 mm (0.8 in): (a) Active reinforcement; (b) Upper passive reinforcement; and (c) Lower passive reinforcement.

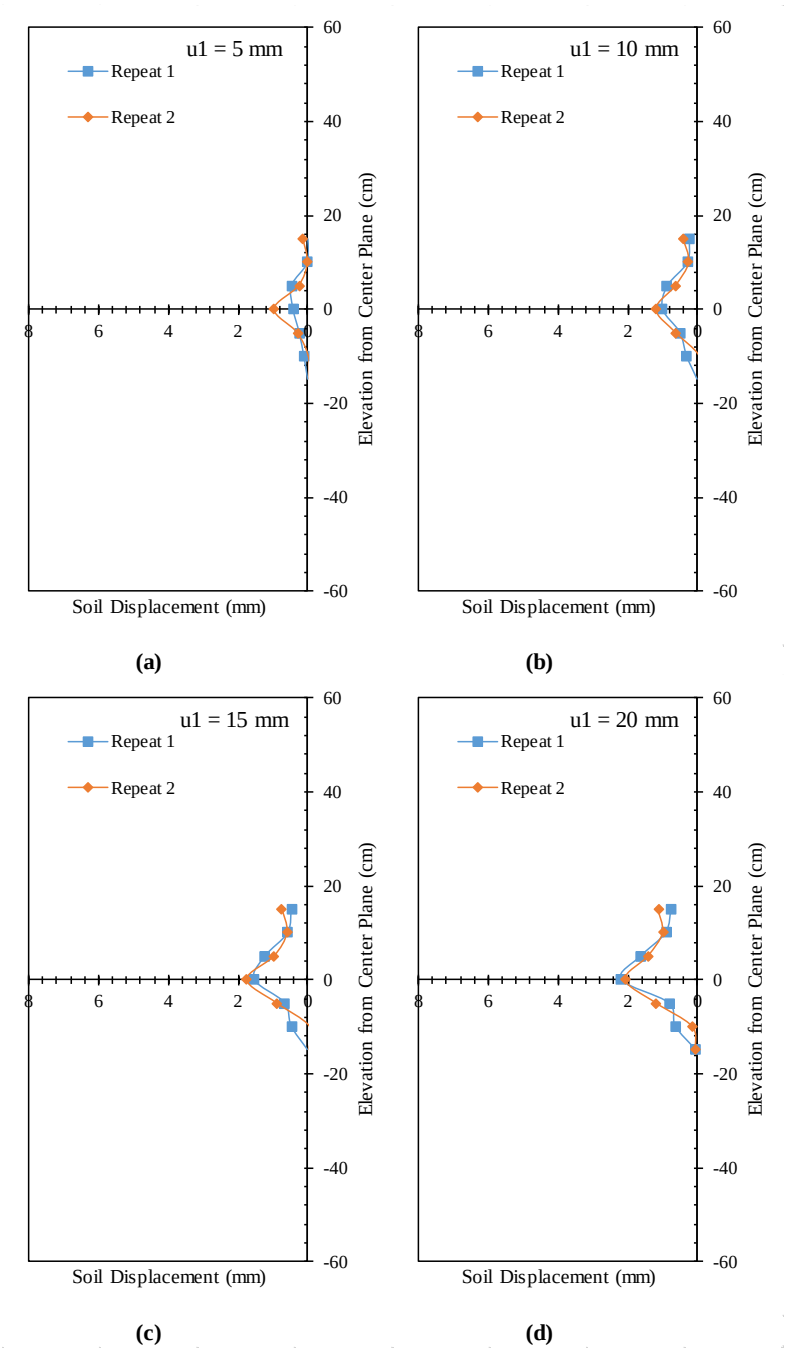

Figure 5.2.7. Horizontal soil displacement profiles (measured by means of artificial gravel particles): (a) At frontal displacement u1 = 5 mm (0.2 in); (b) At frontal displacement u1 = 10 mm (0.4 in); (b) At frontal displacement u1 = 15 mm (0.6 in); and (d) At frontal displacement u1 = 20 mm (0.8 in).

5.2.3.2 EFFECT OF REINFORCED SOIL CONFINEMENT

In order to assess the effect of overburden pressure on the interaction between the contiguous reinforcement layers in GRS structures, the testing program included tests

conducted at the same testing configuration but various confinement levels. Specifically, four tests were conducted for reinforcements spaced at 0.15 m (6 in), two tests were conducted for reinforcements spaced at 0.10 m (4 in), and two tests were conducted for reinforcements spaced at 0.05 m (2 in). The confinement levels in which the tests were conducted at ranged from 15 to 50 kPa (2.25 to 7.3 psi) at the level of main reinforcement layer. This confinement range was adopted to force as many tests as possible to fail in pullout. This allows assessing the full range of soil-reinforcement interaction strength in both working stress and ultimate strength conditions. Table 5.2.3 summarizes the tests in which the confinement level was varied.

Table 5.2.3. Summary of tests in which confinement level was varied.

Test ID	***Testing Variables***					
	Fill Material	***S_v***	***σ_v****	***Active GS***	***Passive GS***	***Dilation***
GP-06-02-G1-G	AASHTO No. 8	0.15 m	15 kPa	HP570	HP570	Allowed
GP-06-03-G1-G			21 kPa			
GP-06-05-G1-G			35 kPa			
GP-06-07-G1-G			50 kPa			
GP-04-03-G1-G	AASHTO No. 8	0.10 m	21 kPa	HP570	HP570	Allowed
GP-04-07-G1-G			50 kPa			
GP-02-03-G1-G	AASHTO No. 8	0.05 m	21 kPa	HP570	HP570	Allowed
GP-02-07-G1-G			50 kPa			

*Conversions: 1 m = 0.0254 in.

1 kPa = 20.89 psf

Three comparisons were made between tests conducted at various confinement levels and with reinforcements placed at different vertical spacing: (1) a comparison between four tests conducted at confining normal stress of 15, 21, 35, and 50 kPa (2.2, 3, 5.1, 7.3 psi) at the active reinforcement level (i.e., central horizontal plane of the reinforced soil mass). These tests were conducted with reinforcements placed at vertical spacing of 0.15 m (6 in.); (2) a comparison between two tests conducted at confining normal stress of 21 and 50 kPa (3 and 7.3 psi) at the active reinforcement level. These tests were conducted with reinforcements placed at vertical spacing of 0.10 m (4 in.); and (3) a comparison between two tests conducted at confining normal stress of 21 and 50 kPa (3 and 7.3 psi) at the active reinforcement level. These tests were conducted with reinforcements placed at vertical spacing of 0.05 m (2 in.). Note that tests of the same comparison group were carried out at the same testing conditions and using the same reinforcement type and fill material. The active and passive reinforcements for all tests were HP570 geotextiles, and the fill material was AASHTO No. 8 aggregate. That is, the only difference in confining normal stress.

Figures 5.2.8a through 5.2.8c show the frontal pullout load-displacement experimental curves for the tests conducted with reinforcements placed at vertical spacing of 0.15, 0.10, and 0.05 m (5.9, 3.9, 2 in), respectively. As anticipated, it was observed that the resistance of the active reinforcement to pullout increases with the increase in the confining normal stress. This observation was made for tests conducted with reinforcements placed different vertical spacings. In addition, the soil-reinforcement interface shear strength increases with the increase in the confining normal stress.

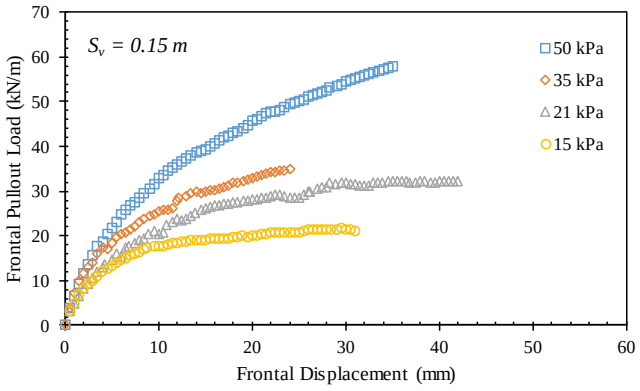

(a)

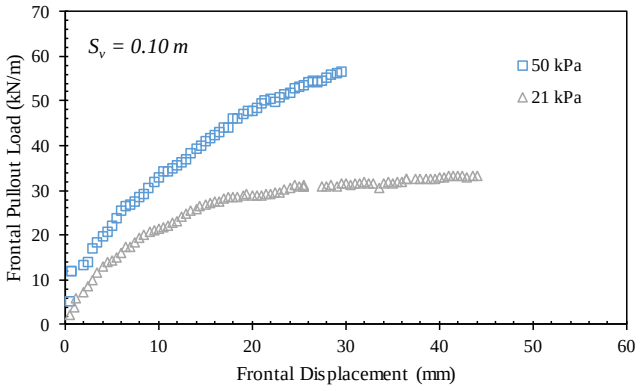

(b)

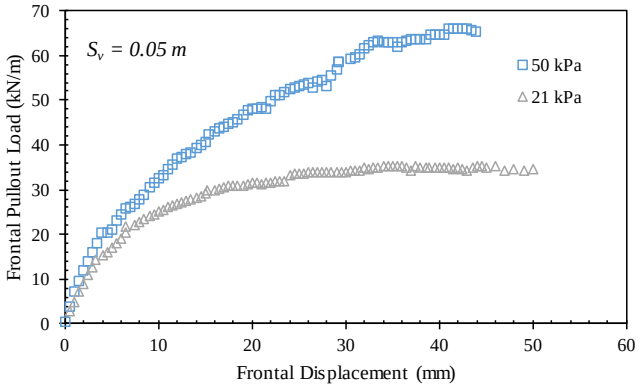

(c)

Figure 5.2.8. Frontal pullout load-displacement curves: (a) Tests conducted with S_v = 0.15 m (6 in); (b) Tests conducted with S_v = 0.10 m (4 in); and (c) Tests conducted with S_v = 0.05 m (2 in).

Figure 5.2.9 shows a comparison between the interface shear strength back-calculated from the pullout test results at ultimate condition and that obtained from large-scale direct shear testing. It was observed that the interface friction angle resulting from the pullout testing is

higher than that resulting from the direct shear testing. This is attributed to additional passive resistance that mobilizes in pullout tests with flexible fabrics. Forensic investigation of the reinforcement layers after the test completion revealed many perforations between filaments in the HP570 fabric that resulted from the adjacent gravel particles. This type of interaction resembles the interaction takes place due to passive resistance of transverse ribs in geogrid reinforcements.

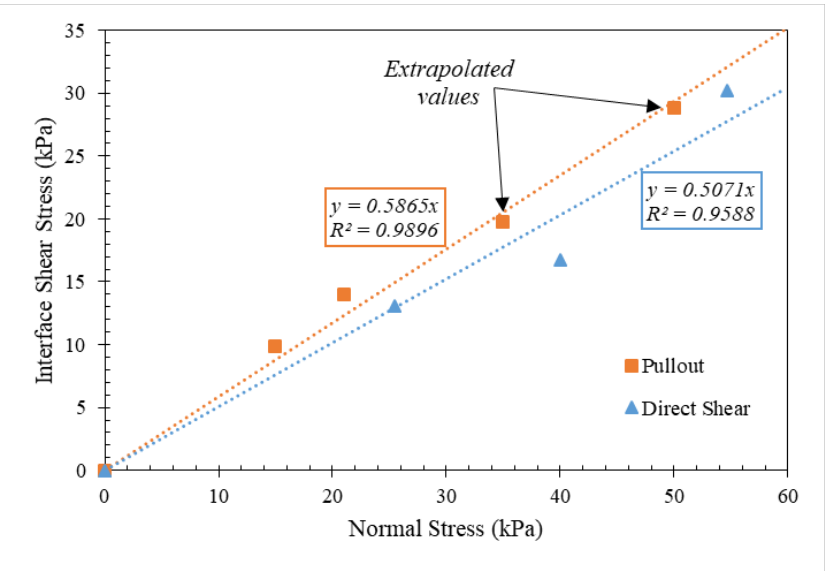

Figure 5.2.9. Soil-reinforcement interfaced shear strength envelopes (AASHTO No. 8 aggregate and HP570 geotextile interface).

Figures 5.2.10 and 5.2.11 present the nodal displacement for the upper and lower passive reinforcement layers, respectively. Specifically, Figures 5.2.10a through 5.2.10d show the nodal displacements in the upper passive reinforcement corresponding to nodal displacements in the active reinforcement *u1*, *u3*, *u5*, and *u7*, respectively. Similarly, Figures 5.2.11a to 5.2.11d show the nodal displacements in the lower passive reinforcement corresponding to nodal displacements in the active reinforcement *u1*, *u3*, *u5*, and *u7*, respectively. Figures 5.2.10 and 5.2.11 reflect the load transfer from the active reinforcement to the passive reinforcements at the same nodal reinforcement of the active reinforcement; i.e., the same soil-reinforcement interface shear displacement. It was observed that the relationship between the nodal displacements for of the passive reinforcements are linear with the nodal displacements of the active reinforcement at early loading stages. This relationship then become non-linear as the load-displacement relationship of the active reinforcement curves. That is, Figures 5.2.10 and 5.2.11 reflect the effect of interface condition of the passive reinforcement on the interaction between the contiguous reinforcement layers. The tests conducted at low confining stresses tend to mobilize displacement in the passive reinforcements more those conducted at higher confining

stresses at early pullout loading stages. This is because the flexibility of soil to deform at low confining stresses resulting in higher load transfer and thus higher interaction between reinforcements. However, as pullout progressed the soil-reinforcement interface stiffness yielded more in the tests conducted at low confining stresses compared to this of the tests conducted at higher confining stresses.

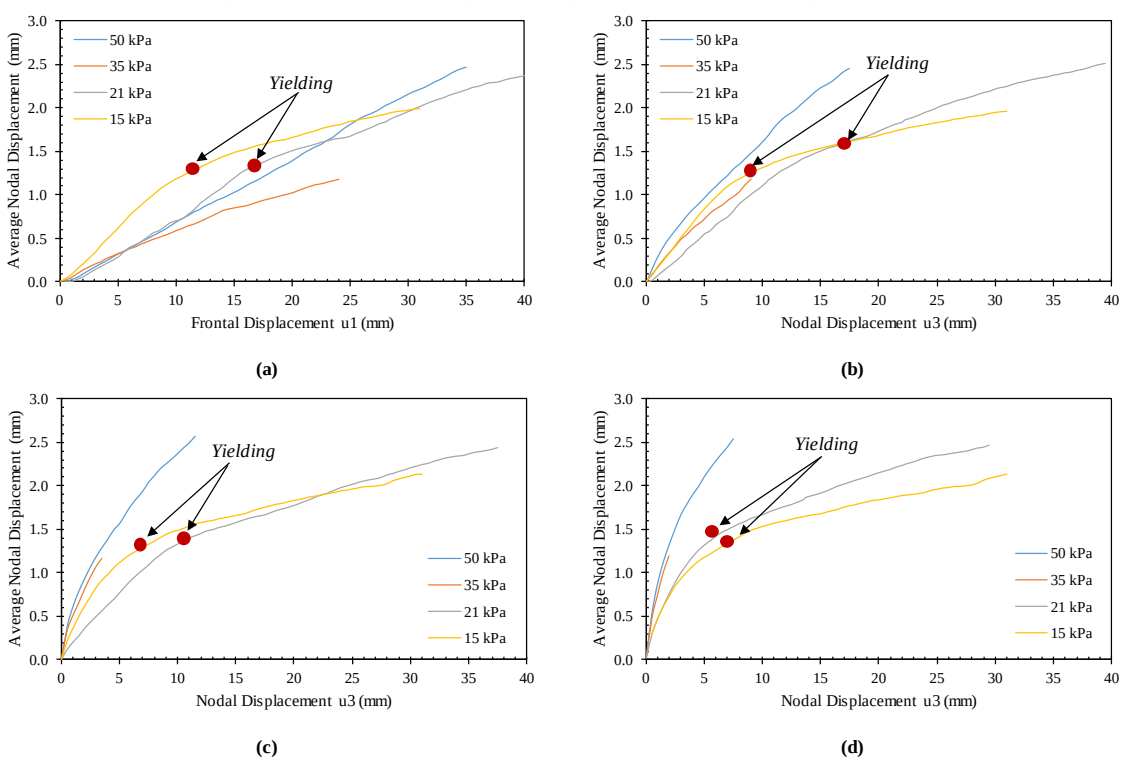

Figure 5.2.10. Average nodal displacements at the upper passive reinforcement with respect to various nodal displacements at the active reinforcement: (a) nodal displacement u1; (b) nodal displacement u3; (c) nodal displacement u5; and (d) nodal displacement u7 (tests conducted at S_v = 0.15 m (6 in)).

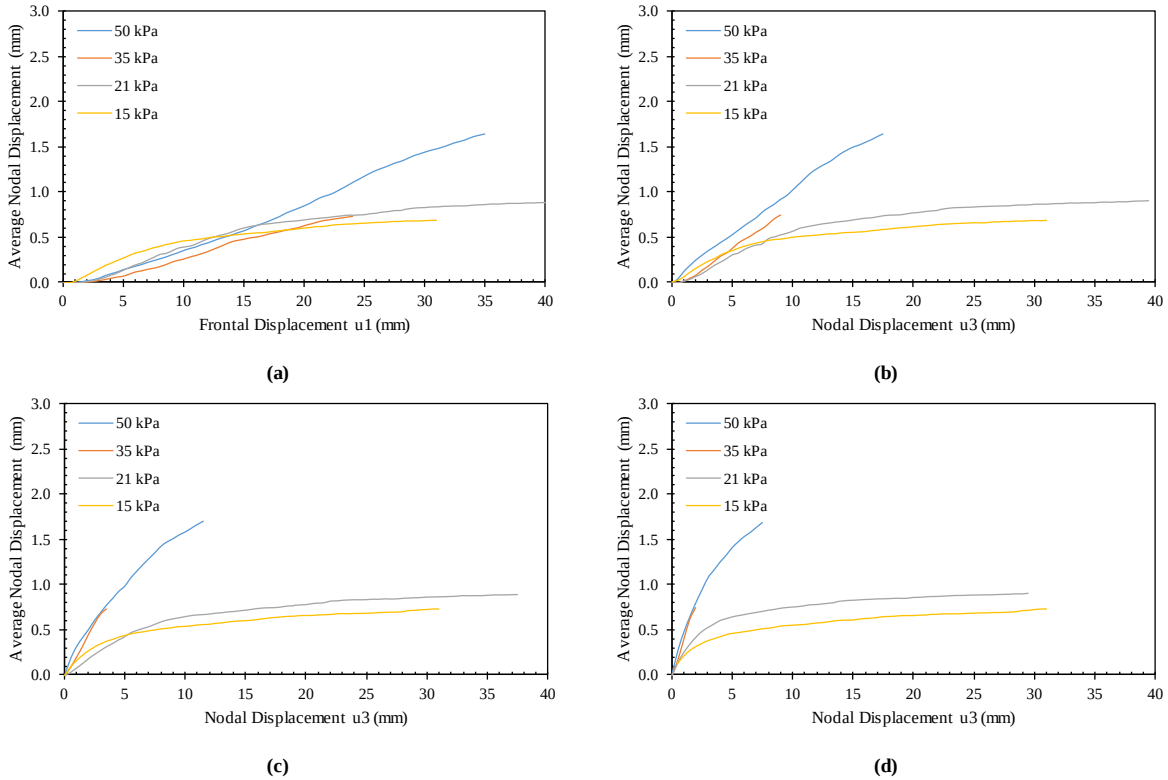

Figure 5.2.11. Average nodal displacements at the lower passive reinforcement with respect to various nodal displacements at the active reinforcement: (a) Nodal displacement u1; (b) Nodal displacement u3; (c) Nodal displacement u5; and (d) Nodal displacement u7 (tests conducted at S_v = 0.15 m (6 in)).

Figures 5.2.12a and 5.2.12b show the average nodal displacement measured for the active reinforcement and the corresponding average nodal displacement for the upper and lower passive reinforcements, respectively. The average nodal displacement represents the area under displacement profile normalized by the reinforcement length. Assuming the constitutive law for the interface shear behavior, Figures 5.2.12a and 5.2.12b provide insight into the effect of confining normal stress on the interaction between neighboring reinforcements. It was concluded that the higher the confining stress the higher the interaction between neighboring reinforcements. At high confining pressures, the soil, which the medium responsible to transfer the load, is stiffer and can more readily transfer load before yielding either internally or at the interface with reinforcements.

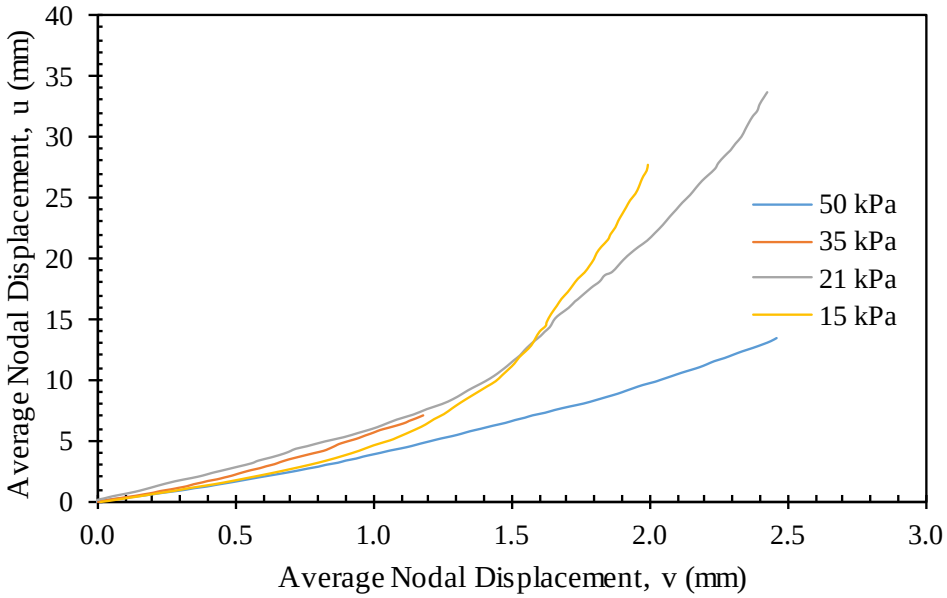

(a)

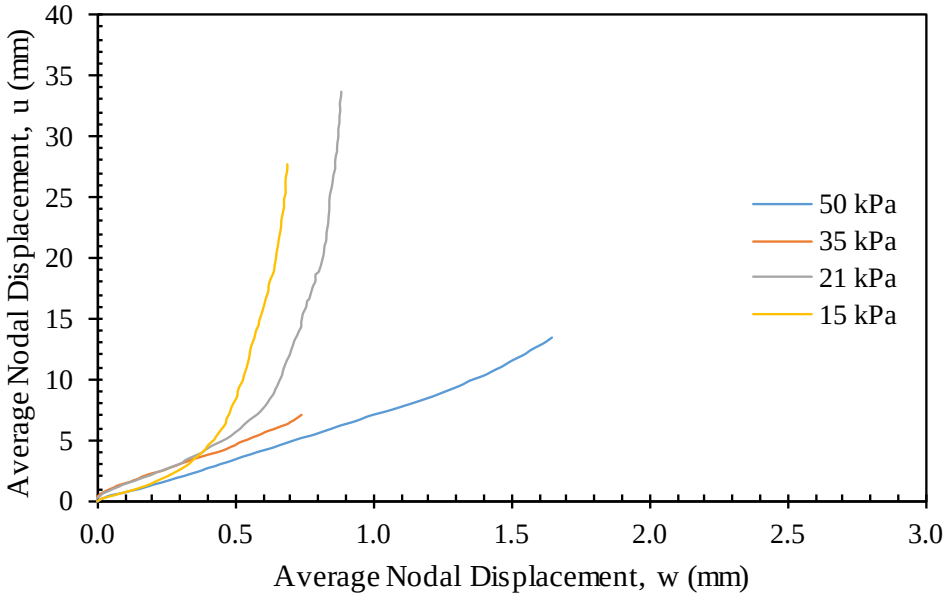

(b)

Figure 5.2.12. Average nodal displacement of passive reinforcements with respect to average nodal displacement of active reinforcement: (a) Upper passive reinforcement; and (b) Lower passive reinforcement.

Figures 5.2.13 through 5.2.17 show the displacement profiles for the active and passive reinforcement layers spaced at 0.15 m (6 in) at active reinforcement frontal displacement (*u1*) of 5, 10, 15, 20, and 30 mm (0.2, 0.4, 0.6, 0.8 and 1.2 in), respectively. Figures 5.2.18 through 5.2.21 show the displacement profiles for reinforcement layers spaced at 0.10 m (4

in) at active reinforcement frontal displacement (*u1*) of 5, 10, 15, and 20 mm (0.2, 0.4, 0.6, 0.8 in), respectively. Figures 5.2.22 through 5.2.26 show the displacement profiles for reinforcement layers spaced at 0.05 m (2 in) at active reinforcement frontal displacement (*u1*) of 5, 10, 15, 20, and 30 mm (0.2, 0.4, 0.6, 0.8 and 1.2 in), respectively. Note that the comparison is based on the same frontal displacement for the different reinforcements rather than the same pullout frontal load. The profiles of tests conducted at low confining stress showed higher displacement along the length of the active reinforcement compared to those conducted at high confining stress. This difference increased as pullout progressed. On the other hand, the profiles of the passive reinforcement layers showed higher displacement values for the tests conducted at low confining stress compared to those conducted at high confining stress. The difference tends to vanish and reverse at high pullout loads. This is explained by the displacement profile of the active reinforcement. The reinforcement tested at low confining pressure could mobilize more soil to transfer load for the same frontal displacement value. That is, the comparison between displacement profiles of passive reinforcements tested at different confining stresses cannot evaluate the effect of confinement magnitude on the interaction between neighboring reinforcements.

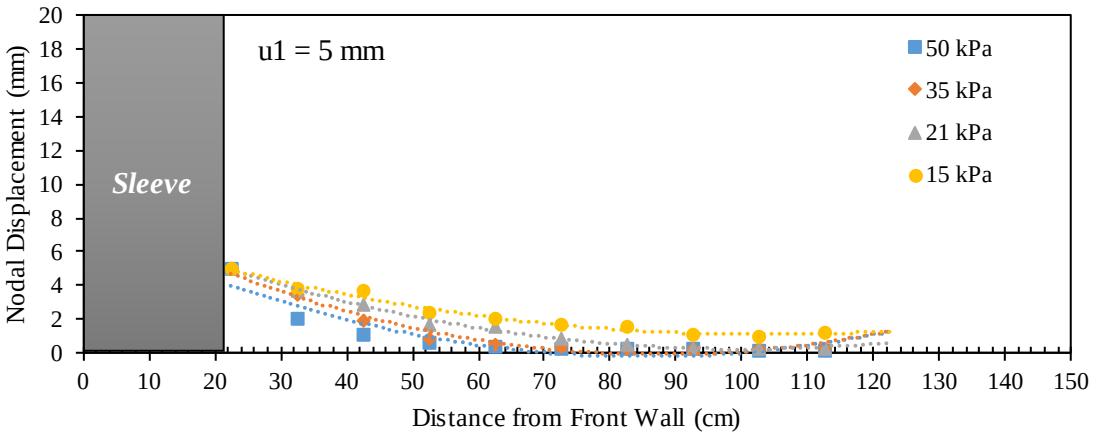

(a)

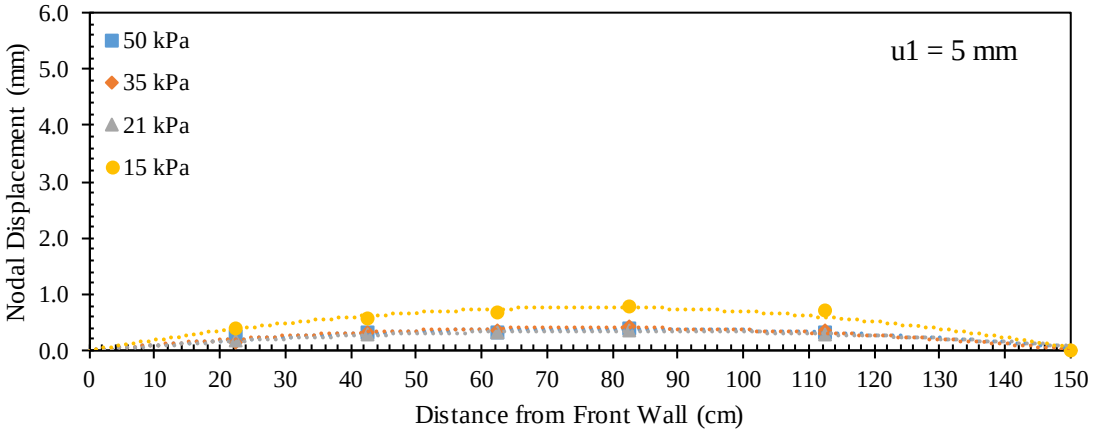

(b)

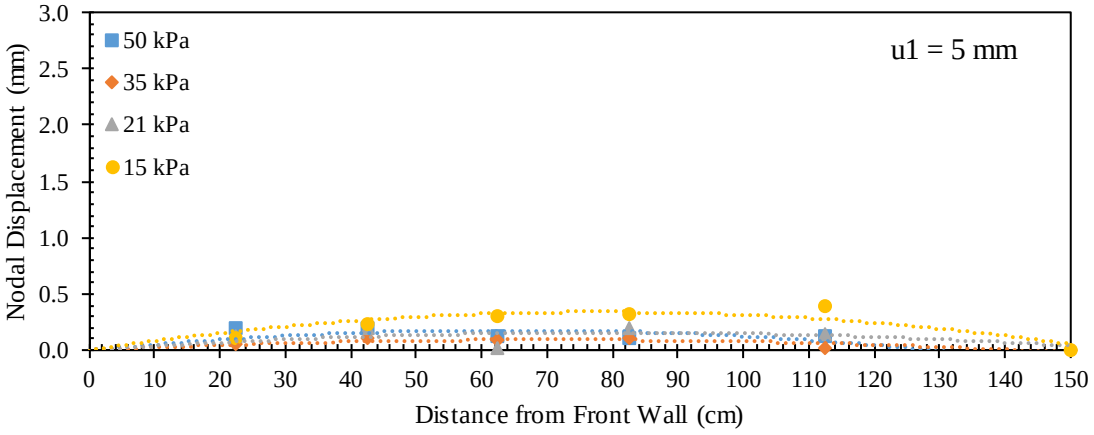

(c)

Figure 5.2.13. Reinforcement displacement profiles for S_v = 150 mm (6 in) at frontal displacement u1 = 5 mm (0.2 in): (a) Active reinforcement; (b) Upper passive reinforcement; and (c) Lower passive reinforcement.

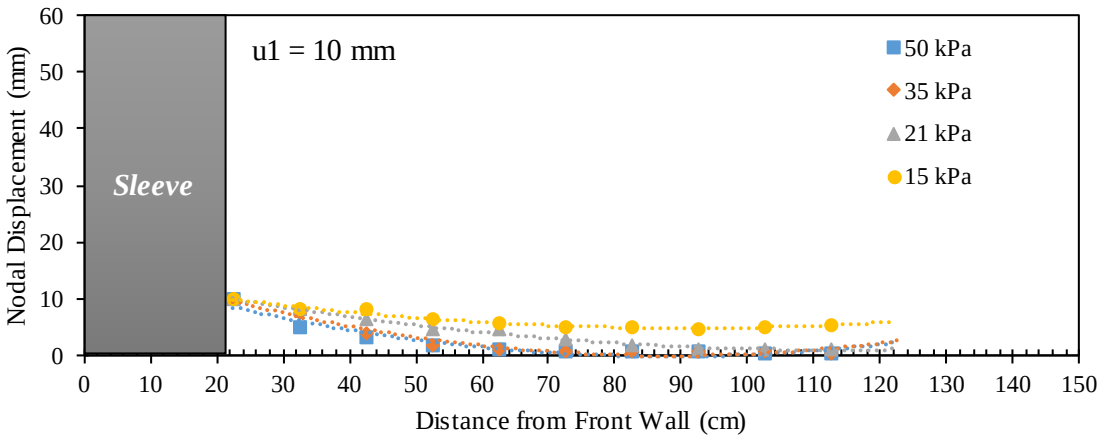

(a)

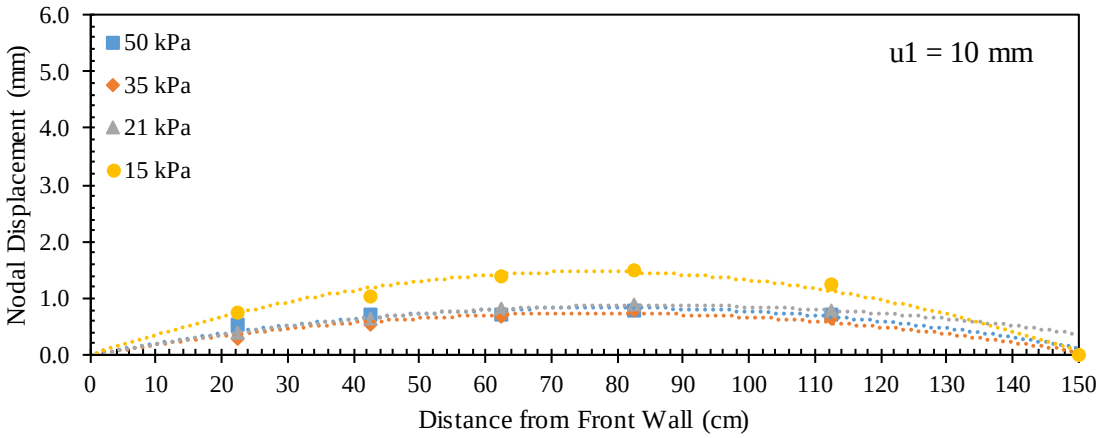

(b)

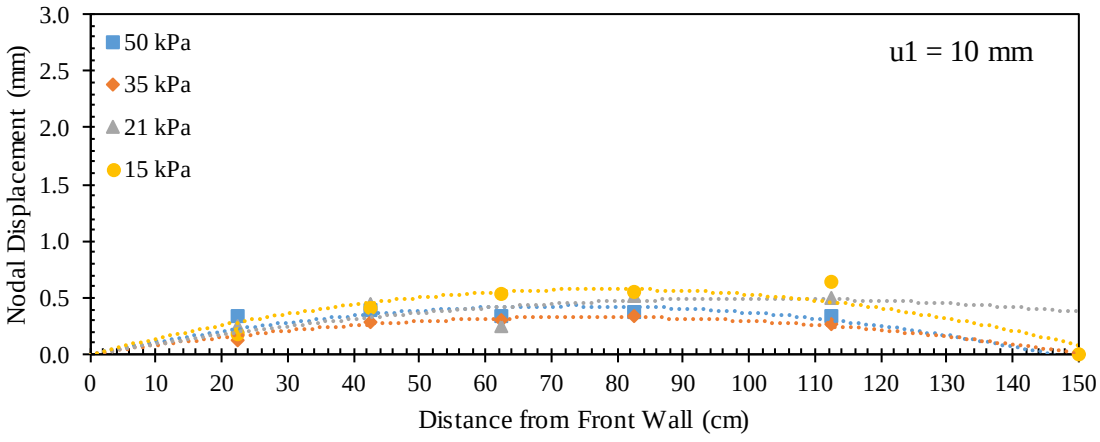

(c)

Figure 5.2.14. Reinforcement displacement profiles for S_v = 150 mm (6 in) at frontal displacement u1 = 10 mm (0.4 in): (a) Active reinforcement; (b) Upper passive reinforcement; and (c) Lower passive reinforcement.

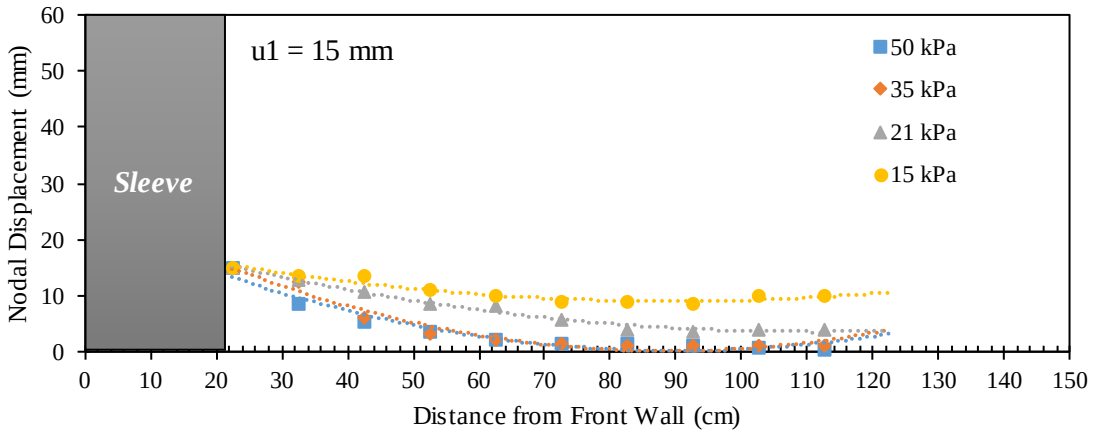

(a)

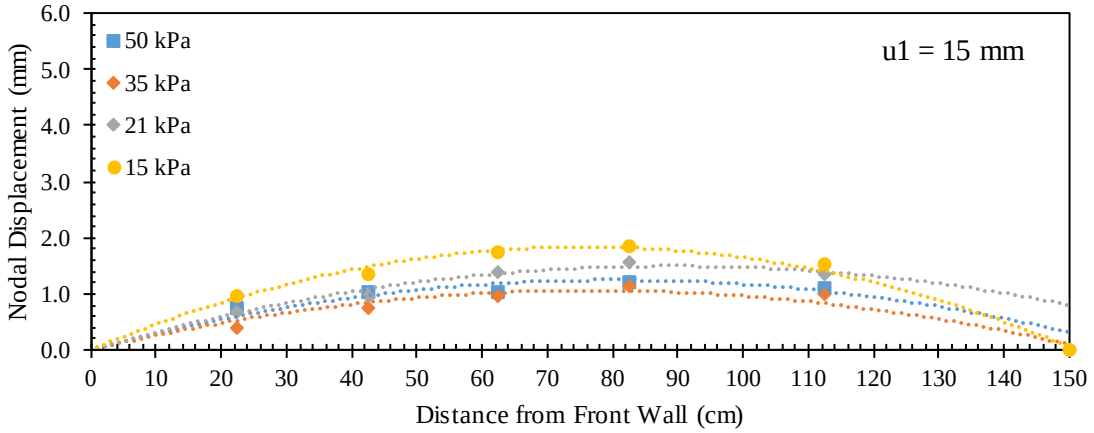

(b)

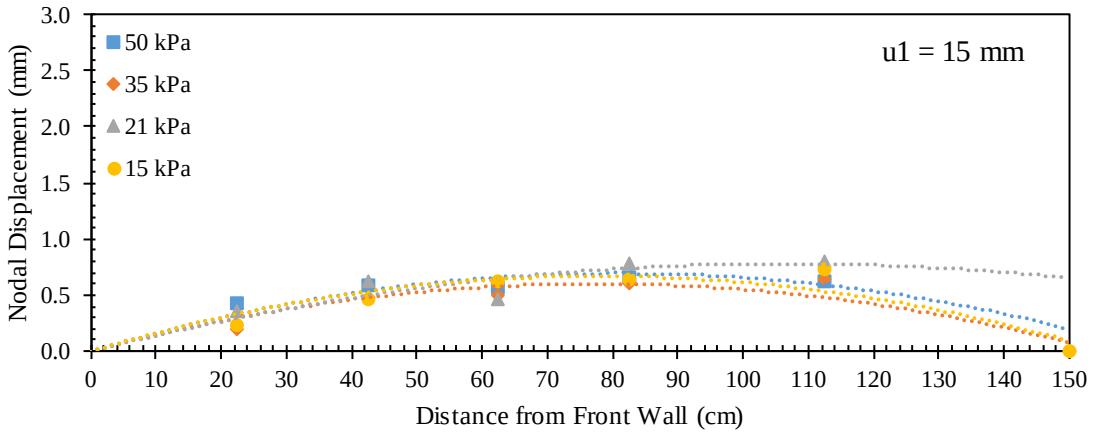

(c)

Figure 5.2.15. Reinforcement displacement profiles for S_v = 150 mm (6 in) at frontal displacement u1 = 15 mm (0.6 in): (a) Active reinforcement; (b) Upper passive reinforcement; and (c) Lower passive reinforcement.

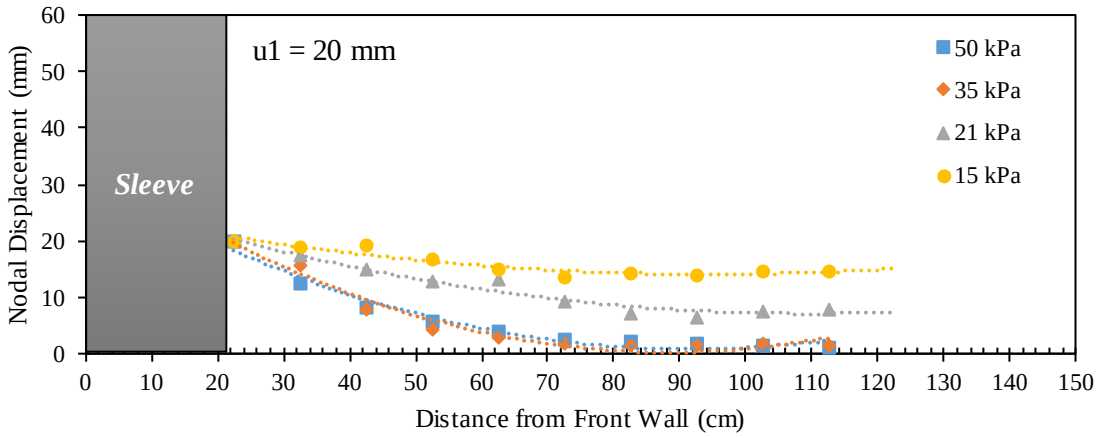

(a)

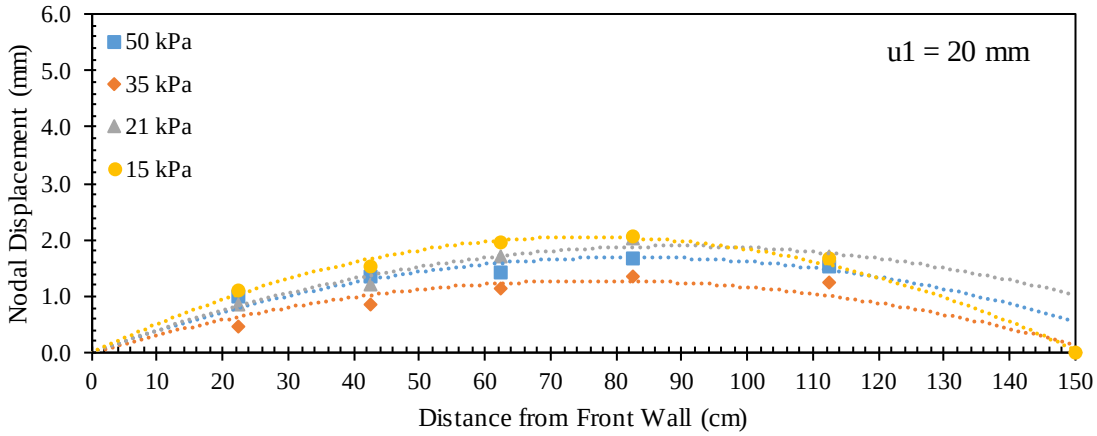

(b)

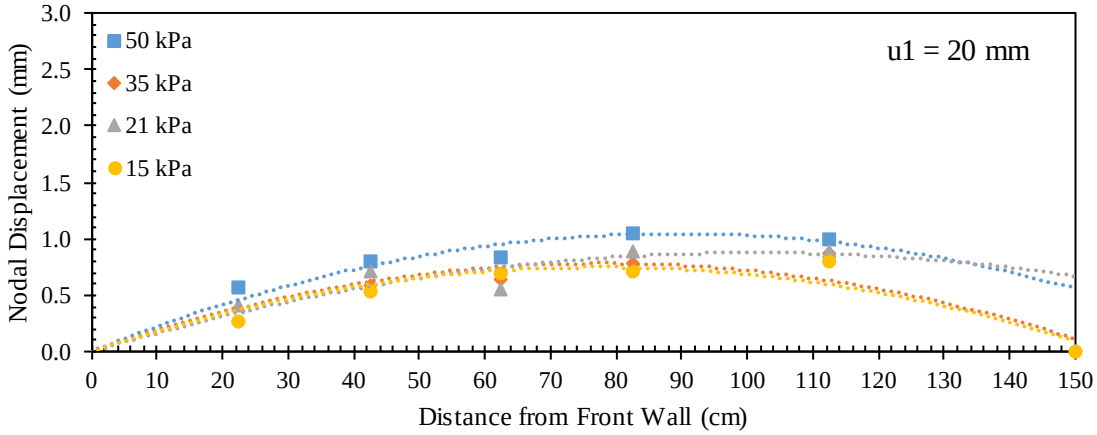

(c)

Figure 5.2.16. Reinforcement displacement profiles for S_v = 150 mm (6 in) at frontal displacement u1 = 20 mm (0.8 in): (a) Active reinforcement; (b) Upper passive reinforcement; and (c) Lower passive reinforcement.

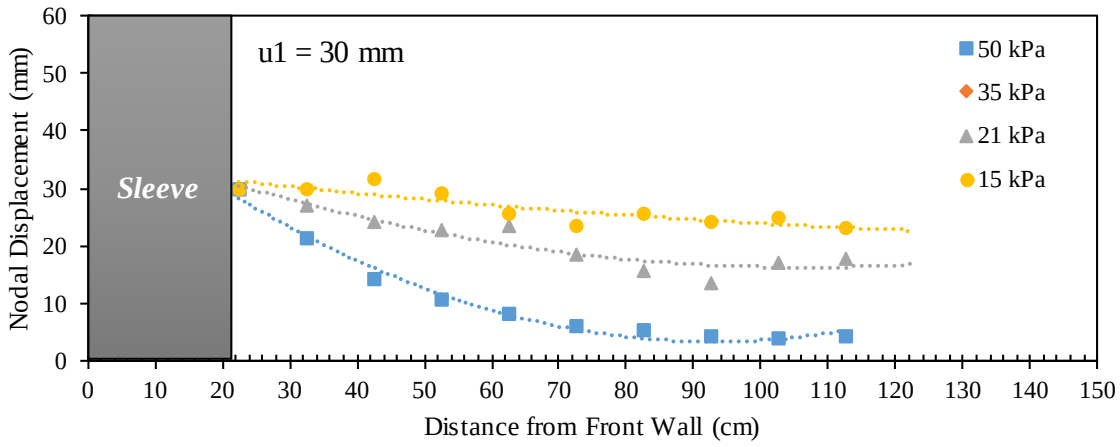

(a)

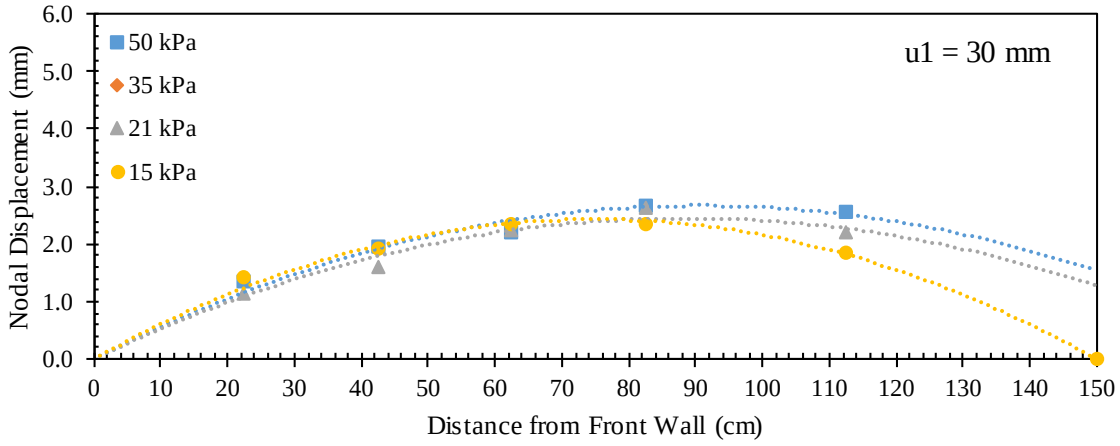

(b)

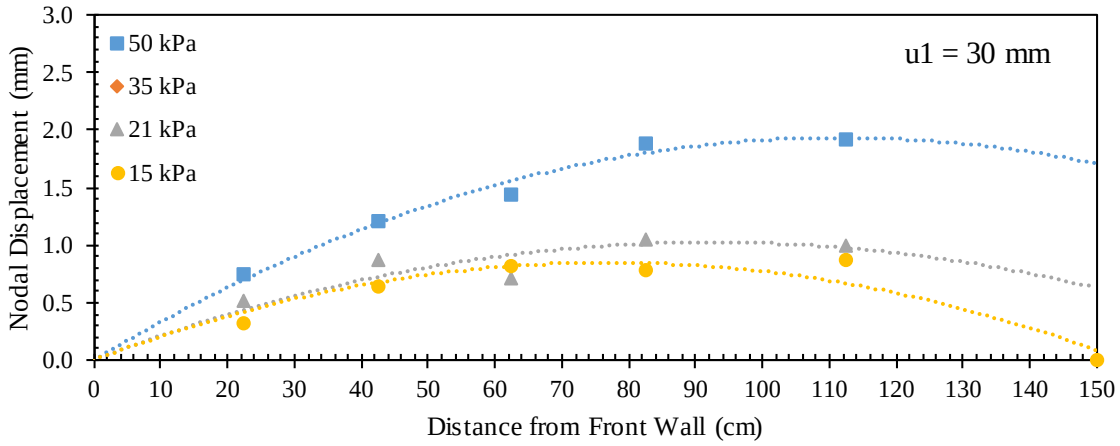

(c)

Figure 5.2.17. Reinforcement displacement profiles for S_v = 150 mm (6 in) at frontal displacement u1 = 30 mm (1.2 in): (a) Active reinforcement; (b) Upper passive reinforcement; and (c) Lower passive reinforcement.

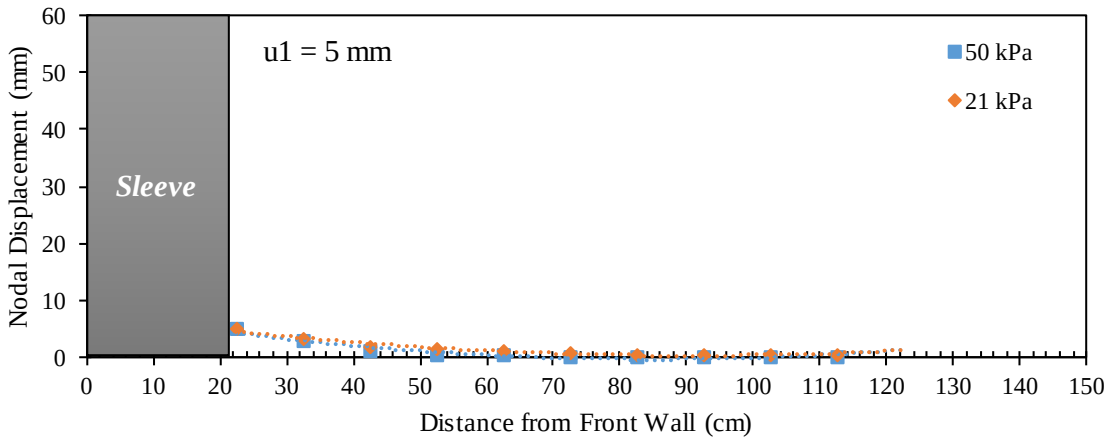

(a)

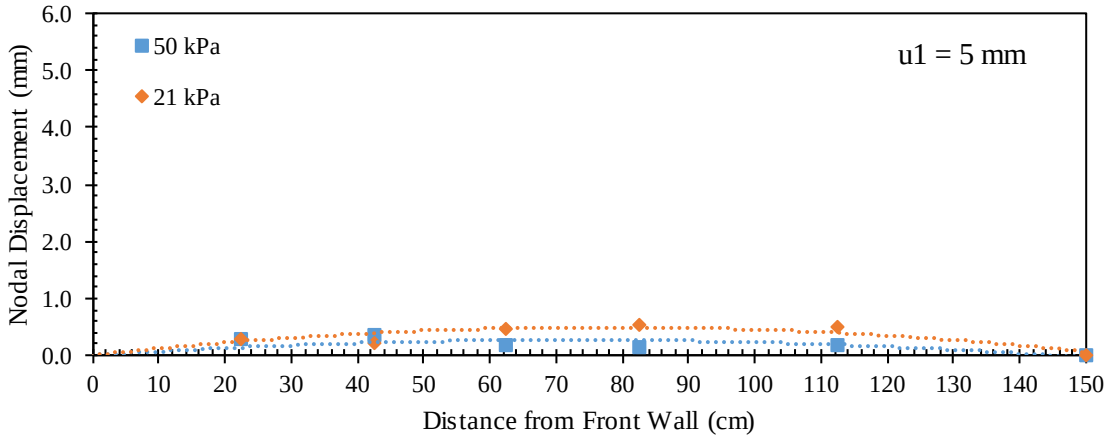

(b)

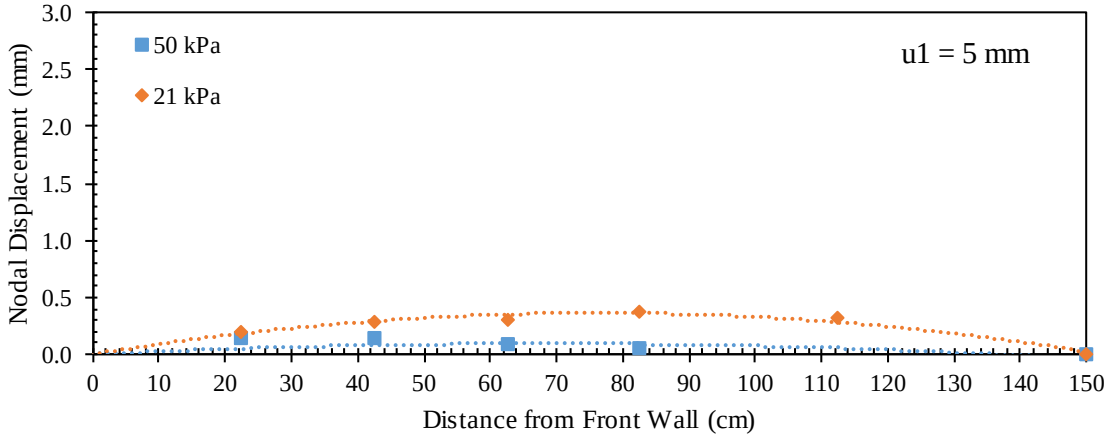

(c)

Figure 5.2.18. Reinforcement displacement profiles for S_v = 100 mm (4 in) at frontal displacement u1 = 5 mm (0.2 in): (a) Active reinforcement; (b) Upper passive reinforcement; and (c) Lower passive reinforcement.

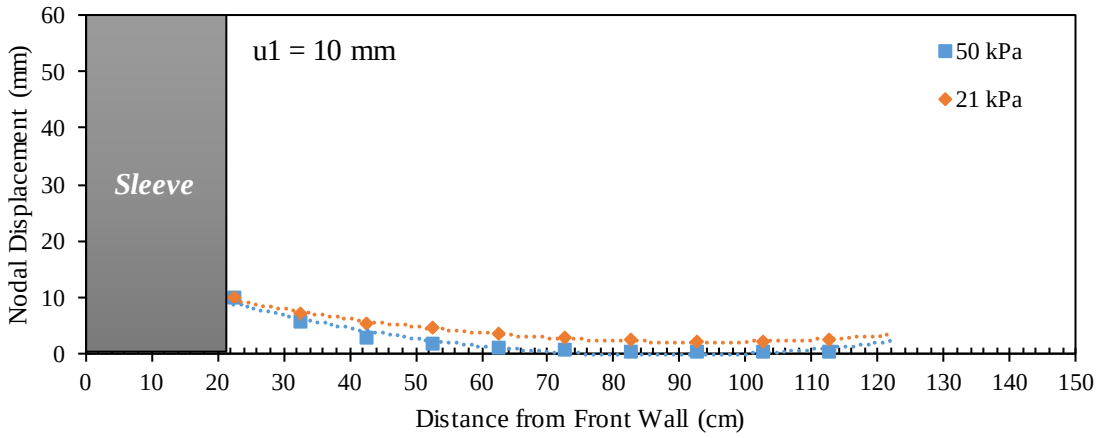

(a)

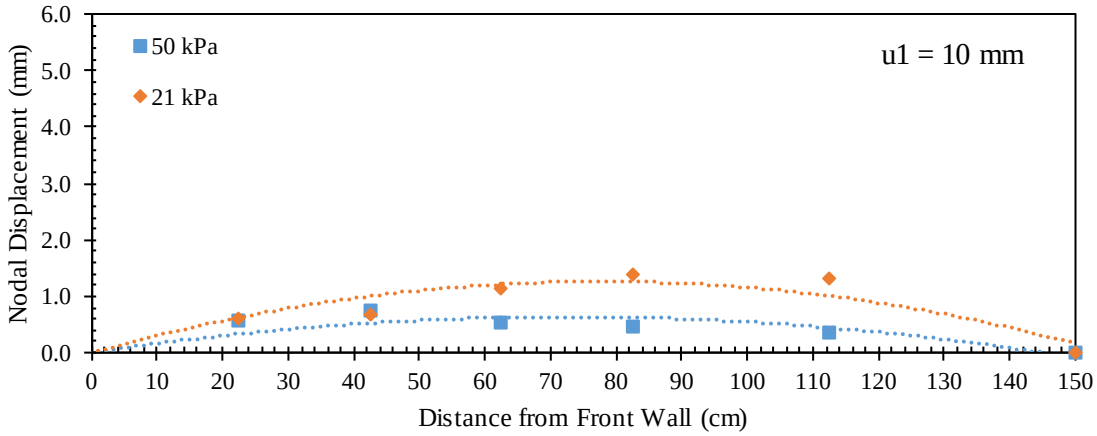

(b)

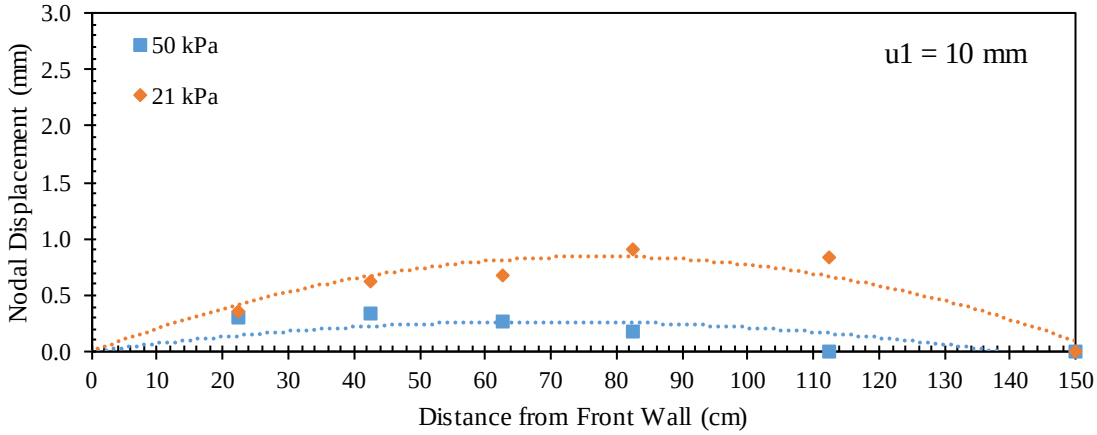

(c)

Figure 5.2.19. Reinforcement displacement profiles for S_v = 100 mm (4 in) at frontal displacement u1 = 10 mm (0.4 in): (a) Active reinforcement; (b) Upper passive reinforcement; and (c) Lower passive reinforcement.

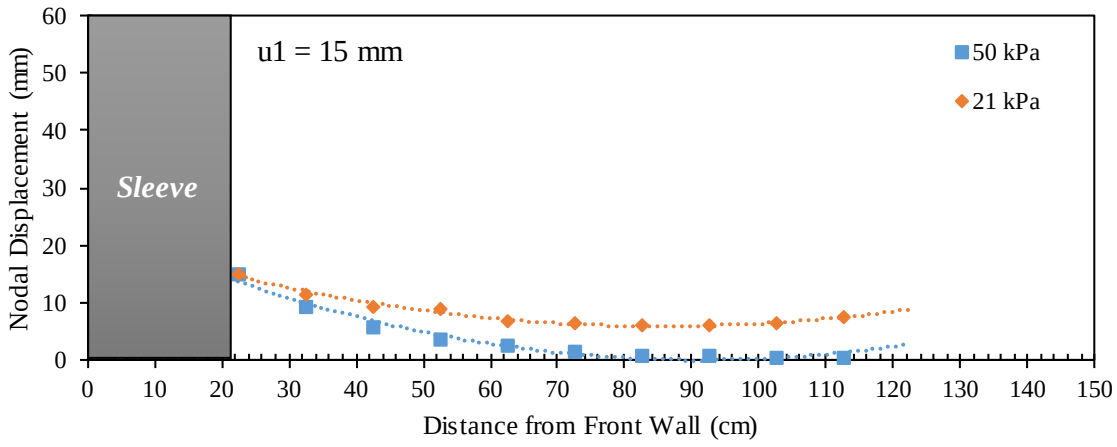

(a)

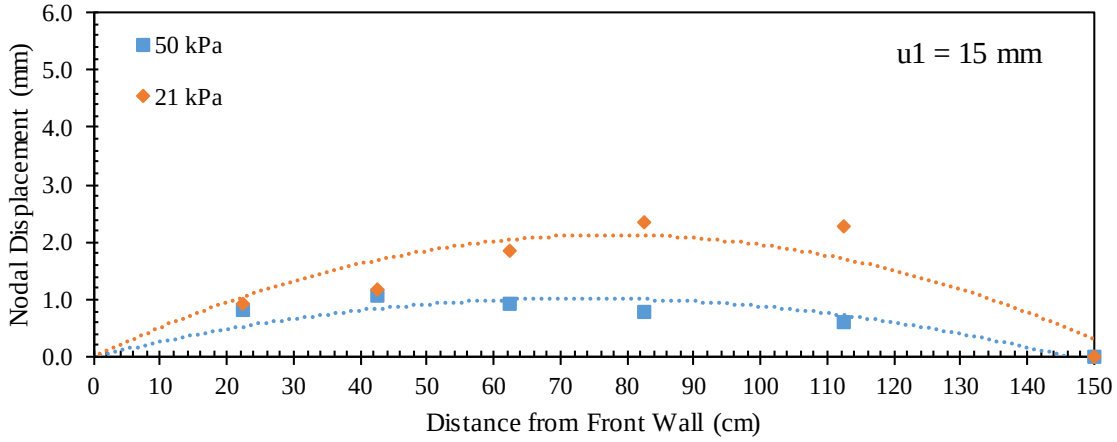

(b)

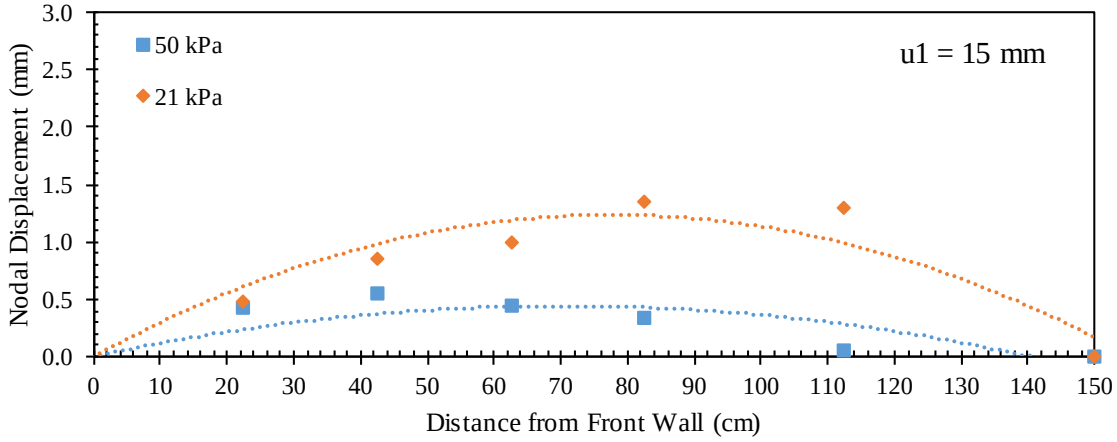

(c)

Figure 5.2.20. Reinforcement displacement profiles for S_v = 100 mm (4 in) at frontal displacement u1 = 15 mm (0.6 in): (a) Active reinforcement; (b) Upper passive reinforcement; and (c) Lower passive reinforcement.

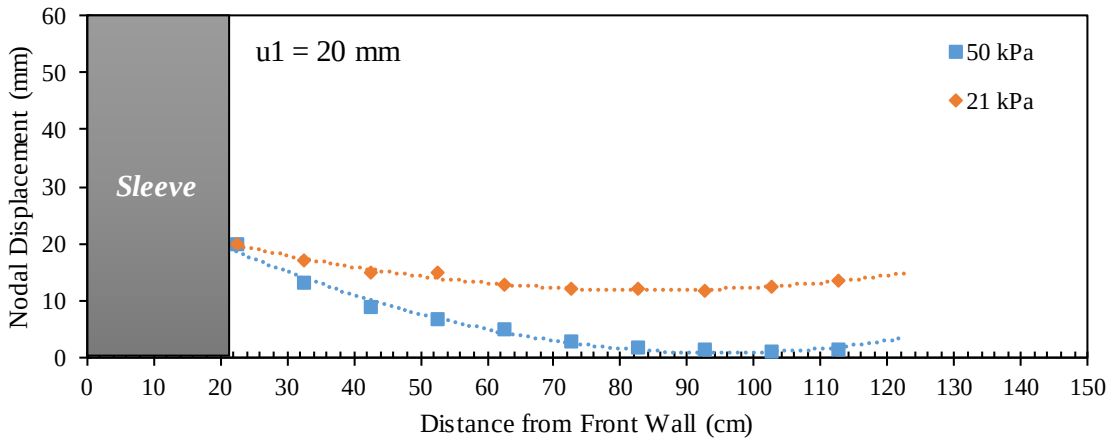

(a)

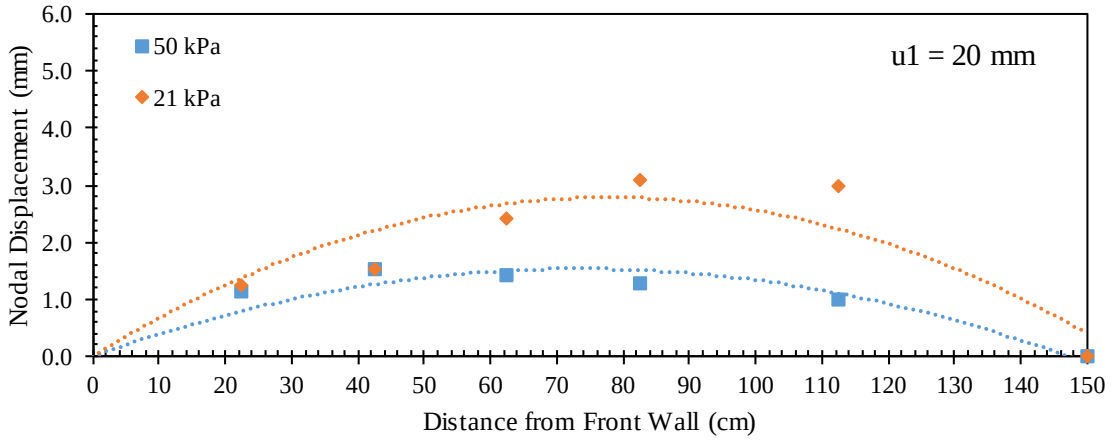

(b)

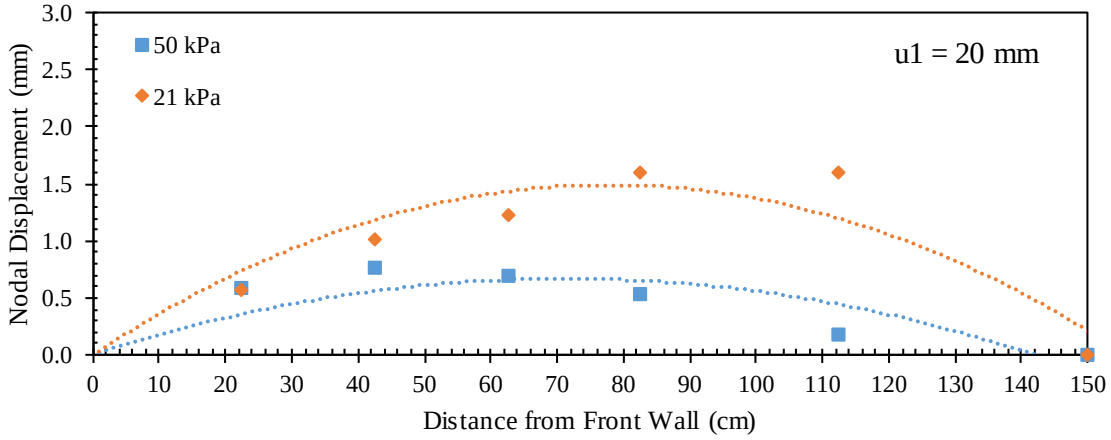

(c)

Figure 5.2.21. Reinforcement displacement profiles for S_v = 100 mm (4 in) at frontal displacement u1 = 20 mm (0.8 in): (a) Active reinforcement; (b) Upper passive reinforcement; and (c) Lower passive reinforcement.

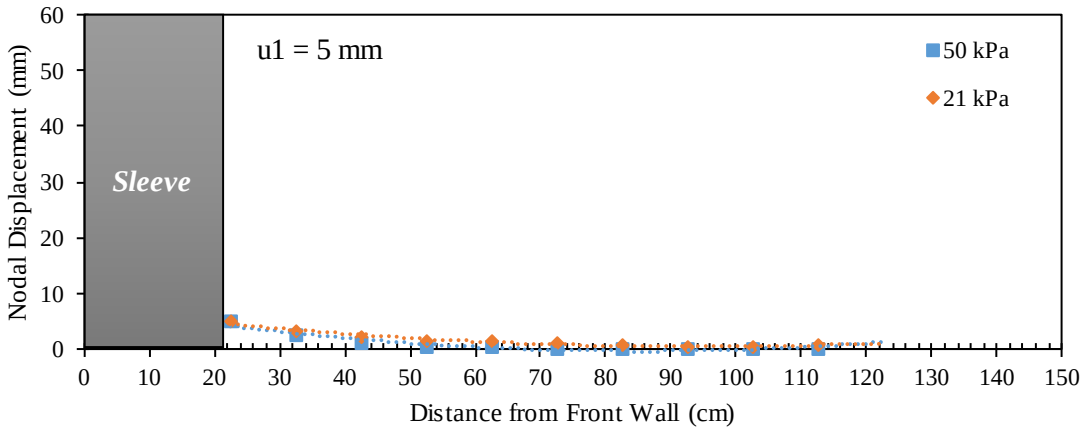

(a)

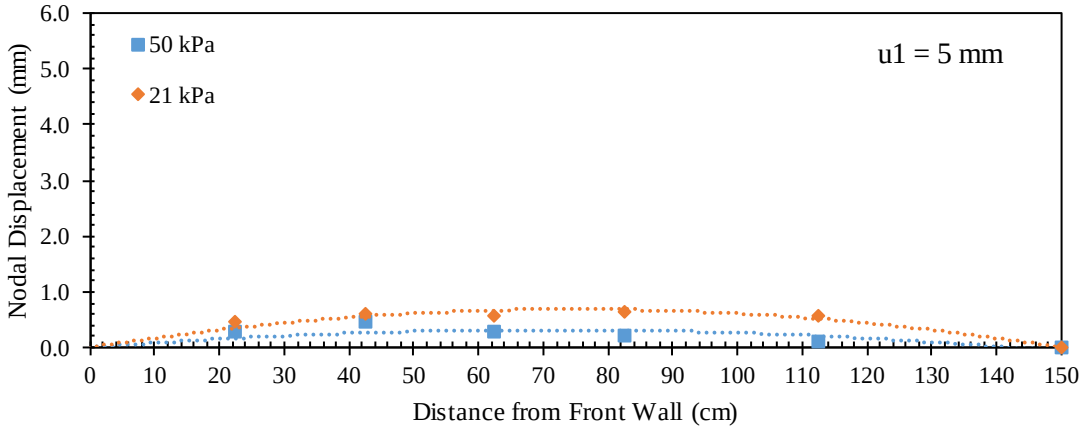

(b)

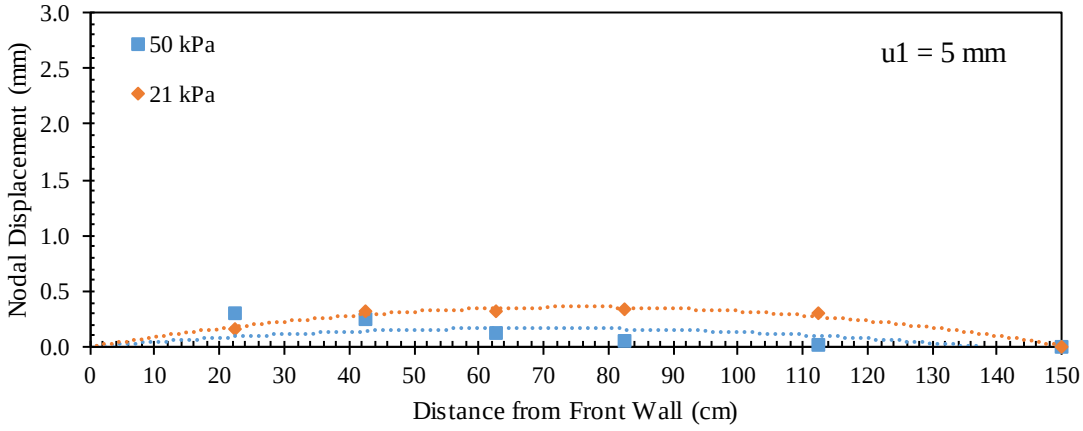

(c)

Figure 5.2.22. Reinforcement displacement profiles for S_v = 50 mm (2 in) at frontal displacement u1 = 5 mm (0.2 in): (a) Active reinforcement; (b) Upper passive reinforcement; and (c) Lower passive reinforcement.

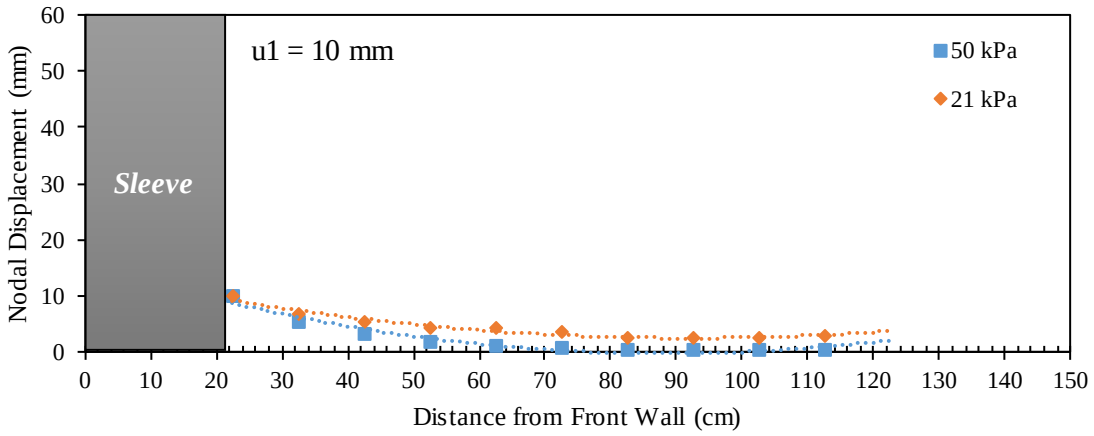

(a)

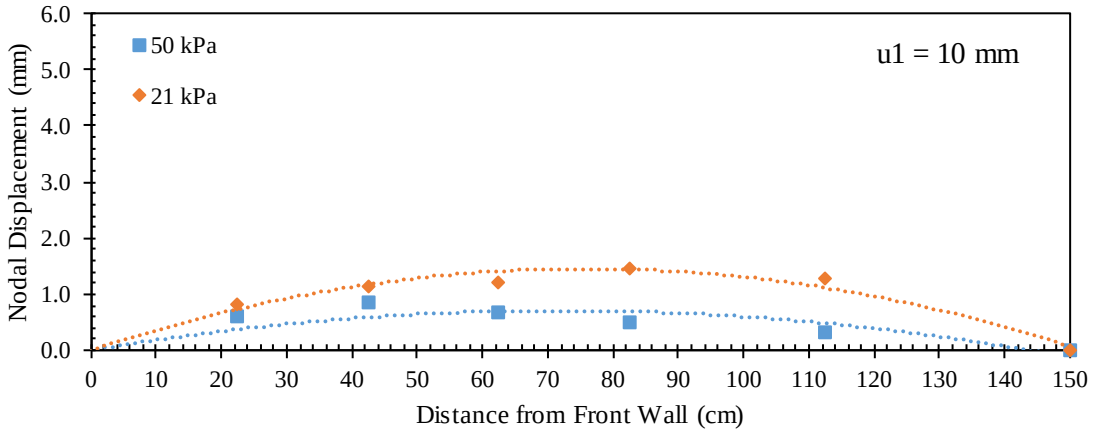

(b)

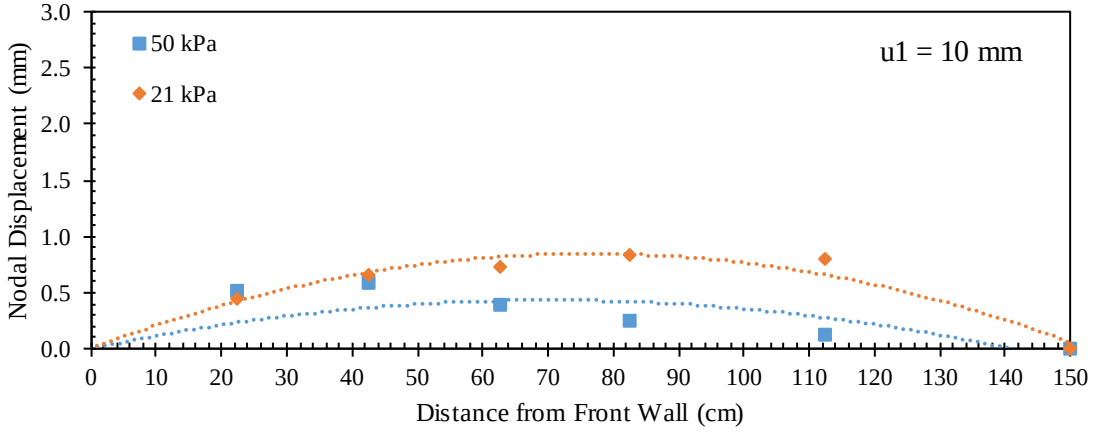

(c)

Figure 5.2.23. Reinforcement displacement profiles for S_v = 50 mm (2 in) at frontal displacement u1 = 10 mm (0.4 in): (a) Active reinforcement; (b) Upper passive reinforcement; and (c) Lower passive reinforcement.

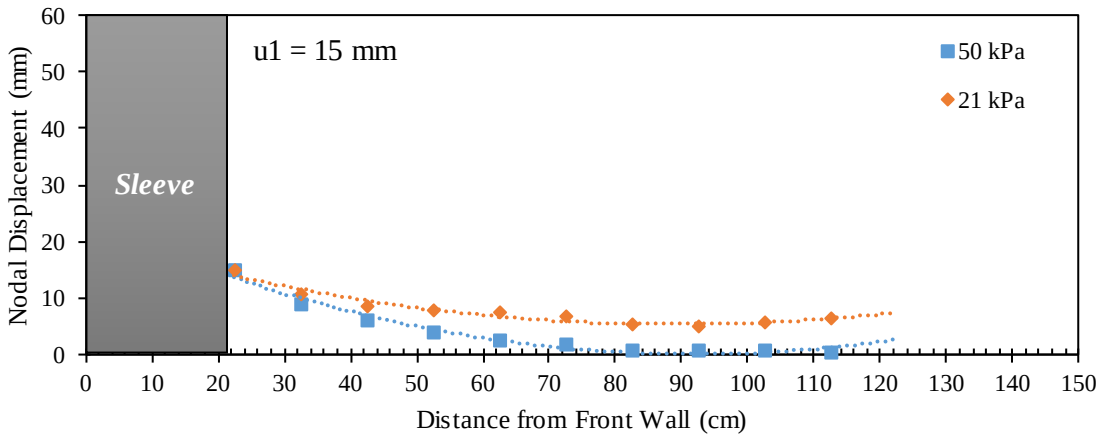

(a)

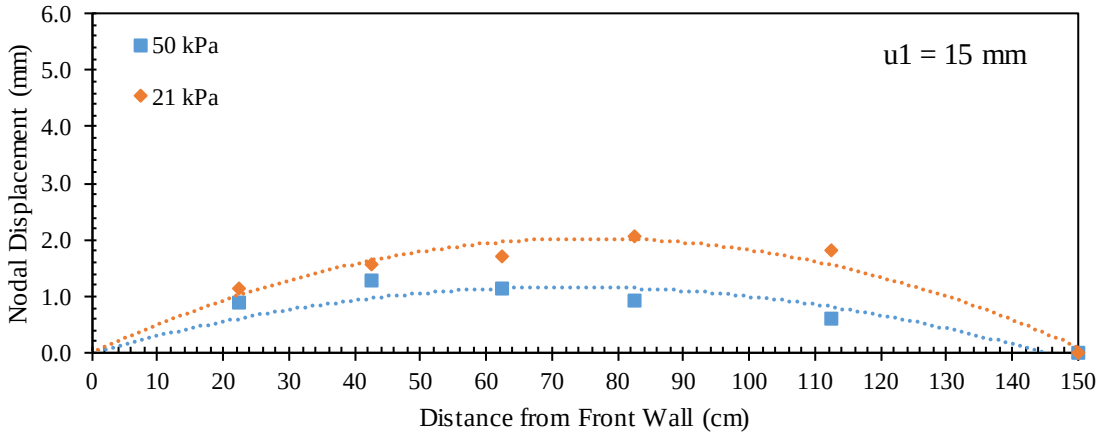

(b)

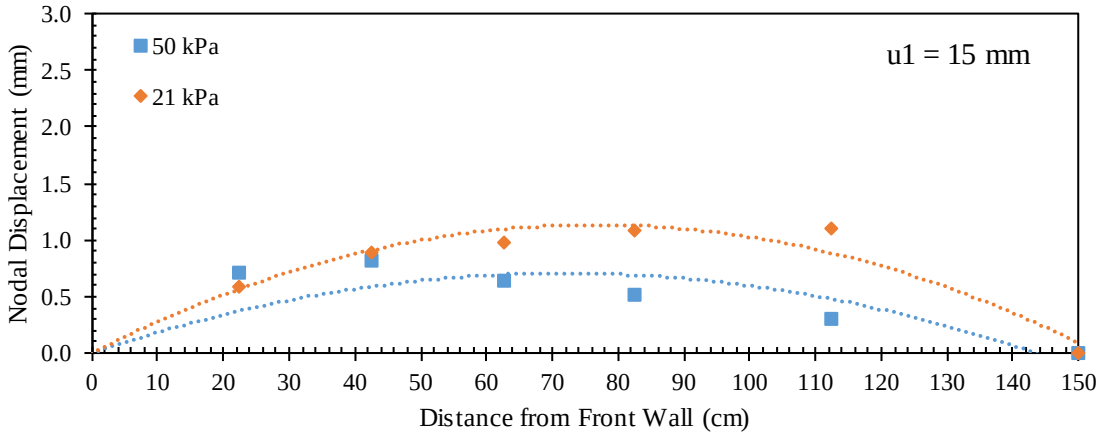

(c)

Figure 5.2.24. Reinforcement displacement profiles for S_v = 50 mm (2 in) at frontal displacement u1 = 15 mm (0.6 in): (a) Active reinforcement; (b) Upper passive reinforcement; and (c) Lower passive reinforcement.

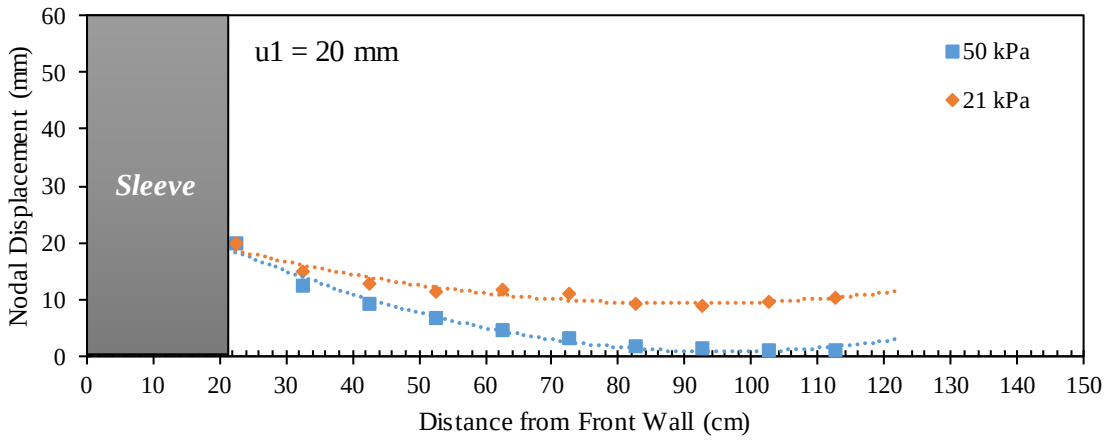

(a)

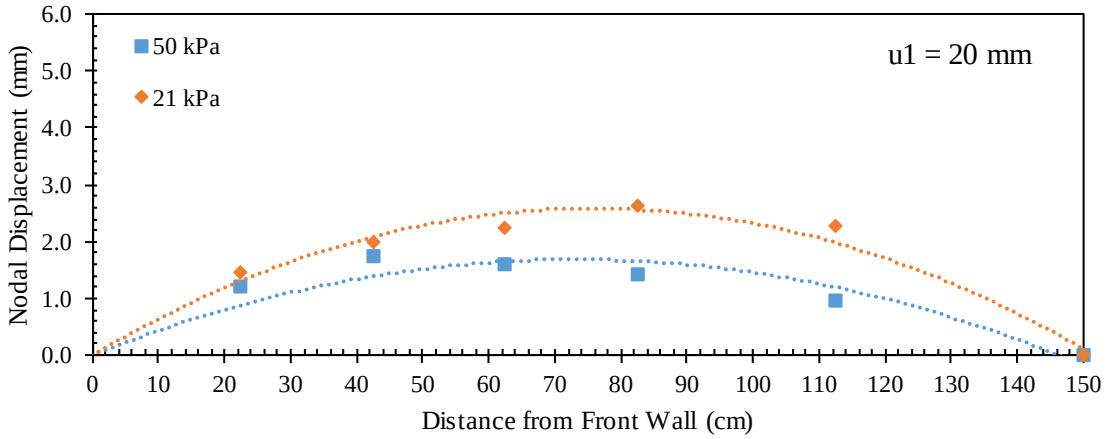

(b)

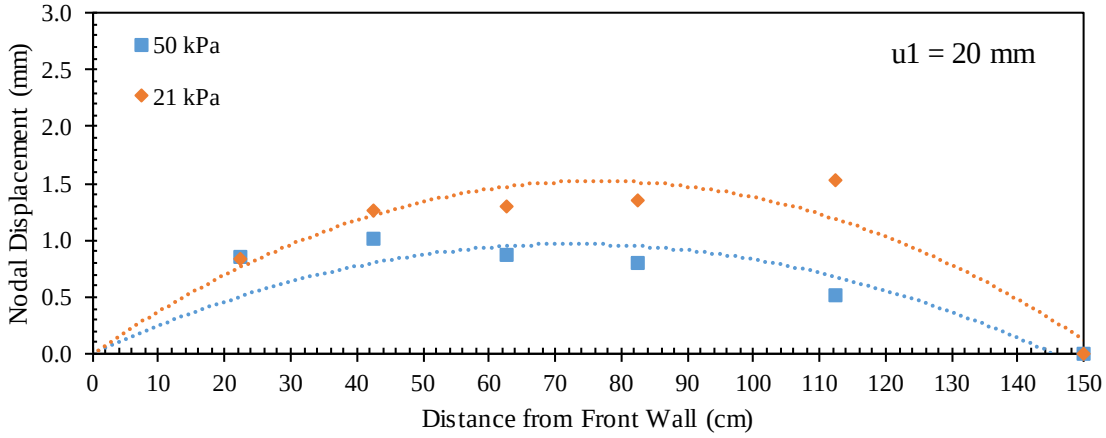

(c)

Figure 5.2.25. Reinforcement displacement profiles for S_v = 50 mm (2 in) at frontal displacement u1 = 20 mm (0.8 in): (a) Active reinforcement; (b) Upper passive reinforcement; and (c) Lower passive reinforcement.

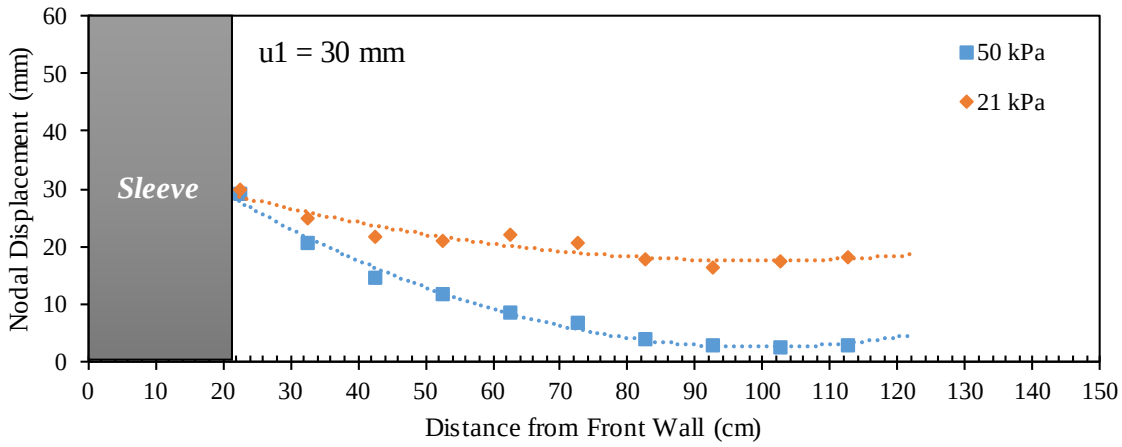

(a)

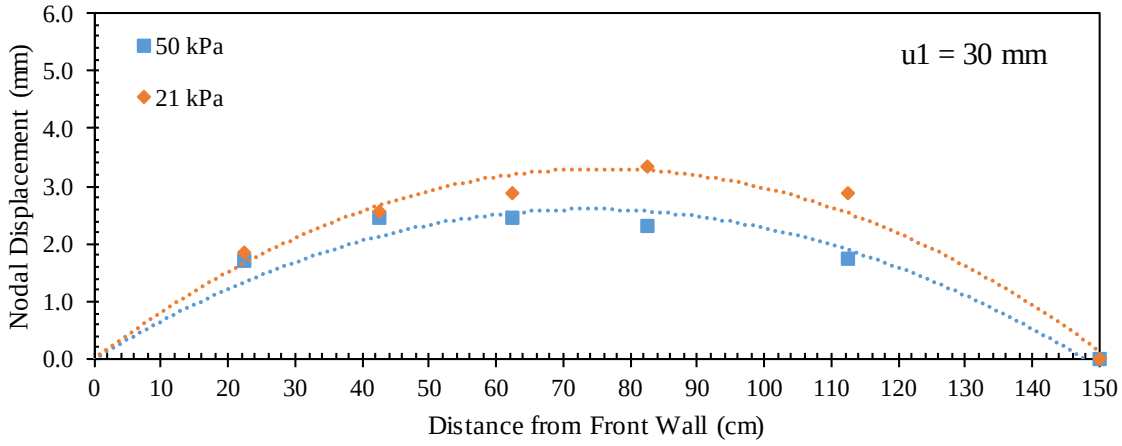

(b)

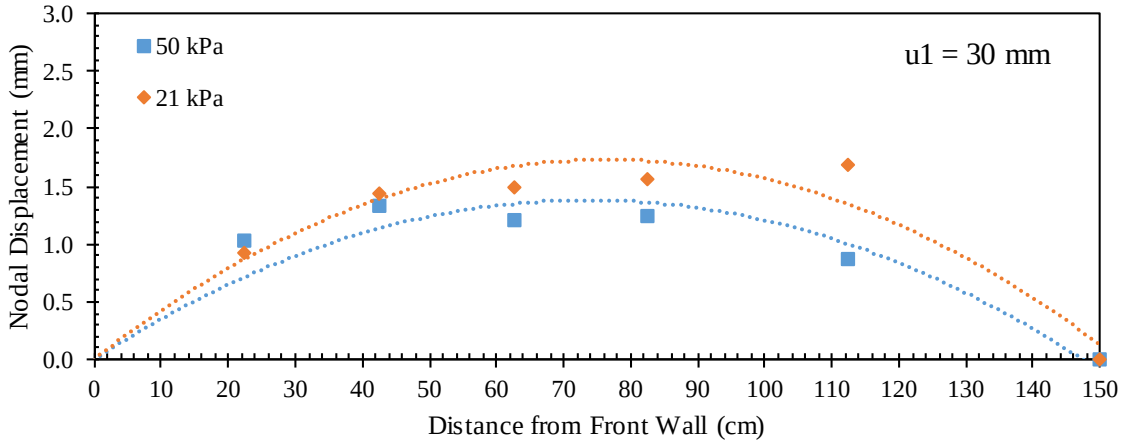

(c)

Figure 5.2.26. Reinforcement displacement profiles for S_v = 50 mm (2 in) at frontal displacement u1 = 30 mm (1.2 in): (a) Active reinforcement; (b) Upper passive reinforcement; and (c) Lower passive reinforcement.

For a better comparison, Figures 5.2.27 through 5.2.29 show the passive reinforcement displacement profiles for tests conducted with reinforcements spaced at 0.15 m (6 in) for various intermediate nodal displacements of the active reinforcement of 5, 10, and 15 mm (0.2, 0.4 and 0.6 in), respectively. Figures 5.2.30 through 5.2.33 show the passive reinforcement displacement profiles for tests conducted with reinforcements spaced at 0.10 m (4 in) for various intermediate nodal displacements of the active reinforcement of 5, 10, 15, and 20 mm (0.2, 0.4, 0.6, 0.8 in), respectively. Figures 5.2.34 through 5.2.37 show the passive reinforcement displacement profiles for tests conducted with reinforcements spaced at 0.05 m (2 in) for various intermediate nodal displacements of the active reinforcement of 5, 10, 15, and 20 mm (0.2, 0.4, 0.6, 0.8 in), respectively. Specifically, each figure consists of a, b, c, and d subfigures that provide comparisons of the upper passive reinforcement profiles for same nodal displacements *u1*, *u3*, *u5*, and *u7*, respectively. Note that some subfigures are missing since the nodal displacements *u3*, *u5*, and *u7* did not reach the values 5, 10, 15, and 20 mm (0.2, 0.4, 0.6, 0.8 in) in all tests. That is, the comparisons were conducted for the similar soil-reinforcement induced interface displacement. This provides more insight into the comparison between the ability of the neighboring reinforcements to interact at different confinement level for a given soil medium and reinforcement type. It was observed from Figures 5.2.27 through 5.2.37 that the interaction between the reinforcement layers is higher at high confinement levels. In addition, reinforcement vertical spacing has no effect on the sensitivity of the reinforcement interaction to the confinement level.

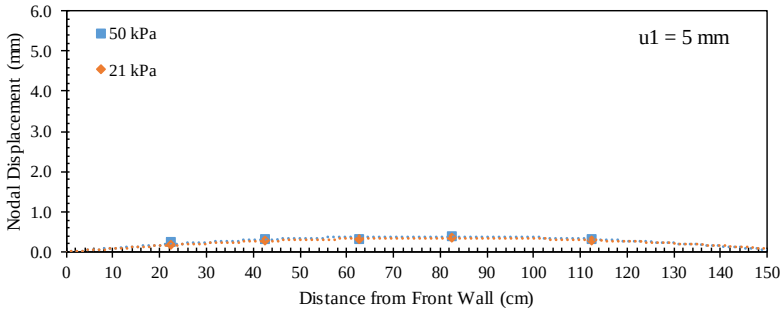

(a)

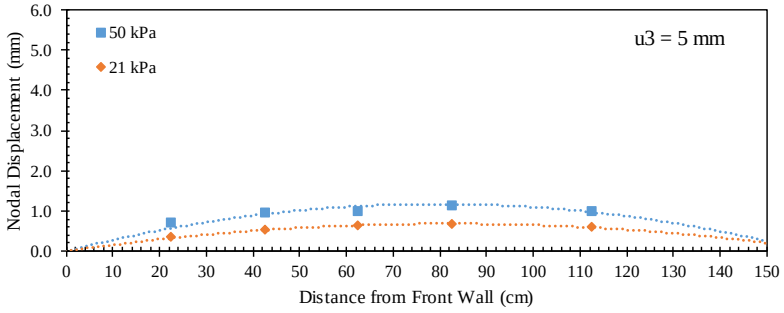

(b)

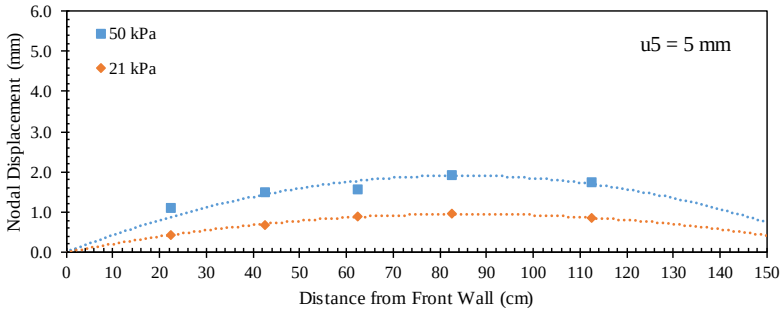

(c)

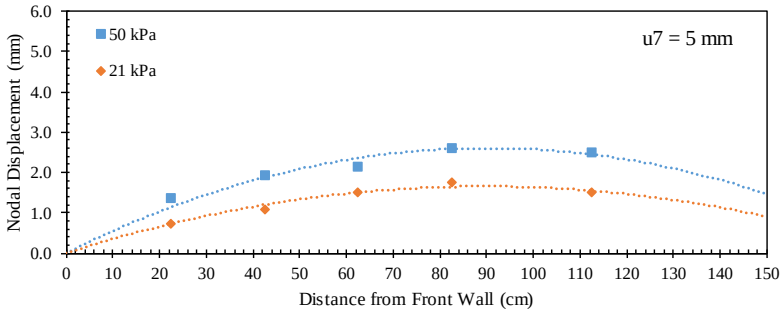

(d)

Figure 5.2.27. Upper passive reinforcement displacement profiles for S_v = 150 mm (6 in): (a) At nodal displacement u1 = 5 mm (0.2 in); (b) At nodal displacement u3 = 5 mm (0.2 in); (c) At nodal displacement u5 = 5 mm (0.2 in); and (d) At nodal displacement u7 = 5 mm (0.2 in).

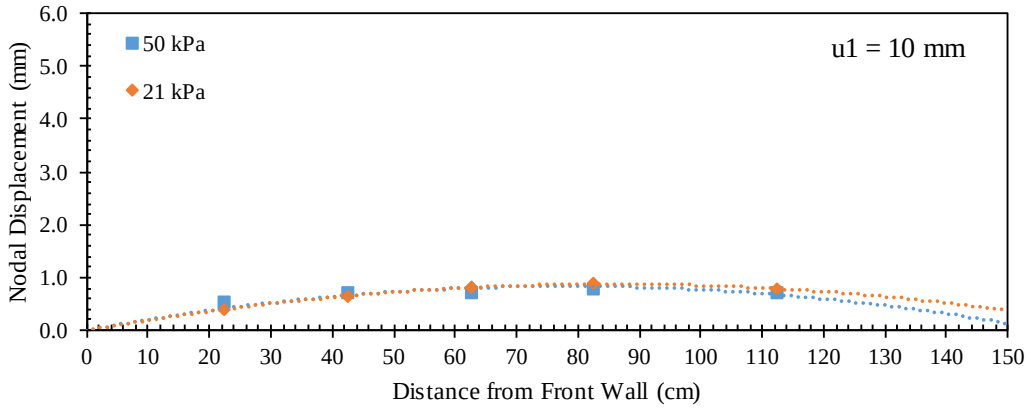

(a)

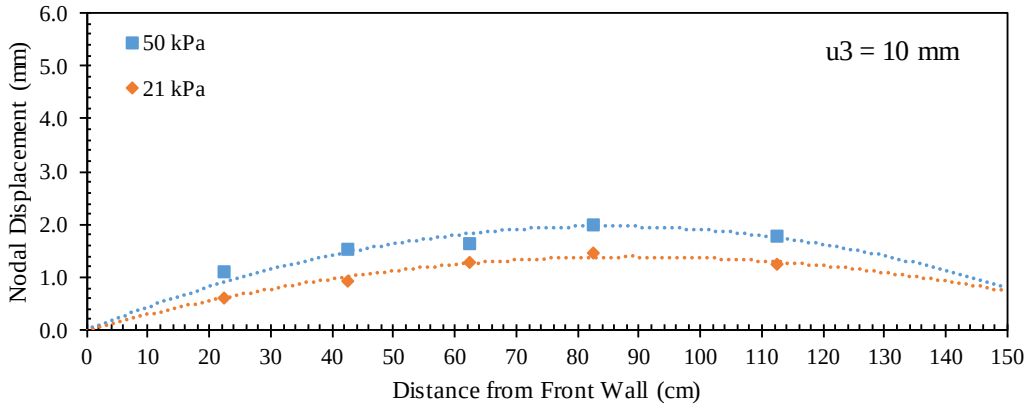

(b)

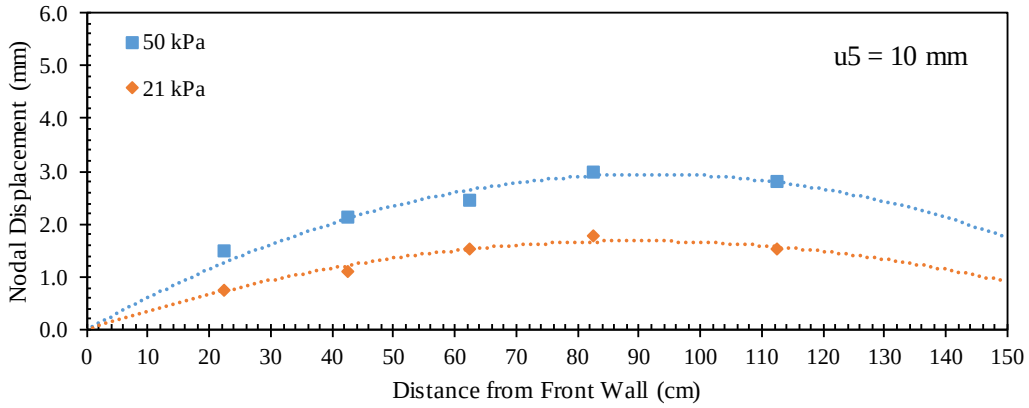

(c)

Figure 5.2.28. Upper passive reinforcement displacement profiles for S_v = 150 mm (6 in): (a) At nodal displacement u1 = 10 mm (0.4 in); (b) At nodal displacement u3 = 10 mm (0.4 in); and (c) At nodal displacement u5 = 10 mm (0.4 in).

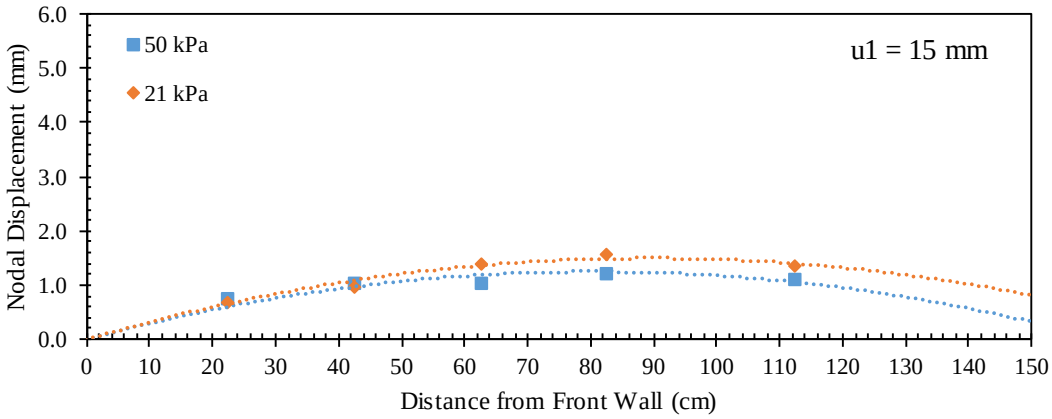

(a)

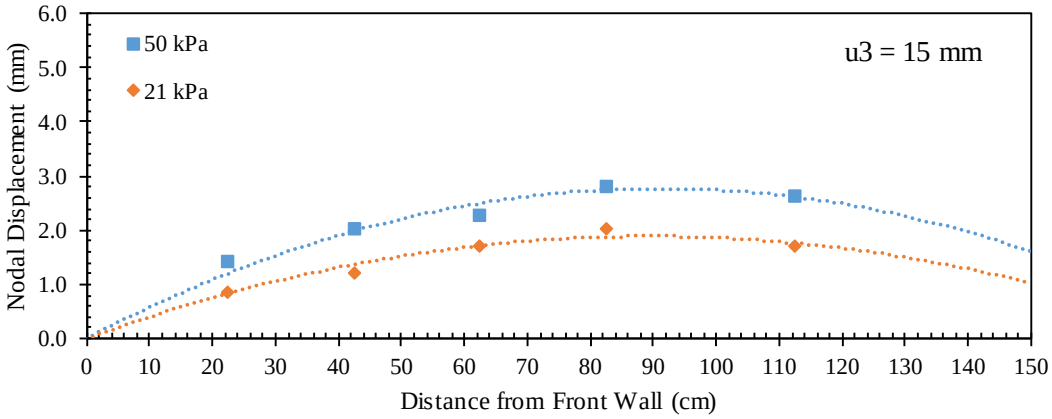

(b)

Figure 5.2.29. Upper passive reinforcement displacement profiles for S_v = 150 mm (6 in): (a) At nodal displacement u1 = 15 mm (0.6 in); and (b) At nodal displacement u3 = 15 mm (0.6 in).

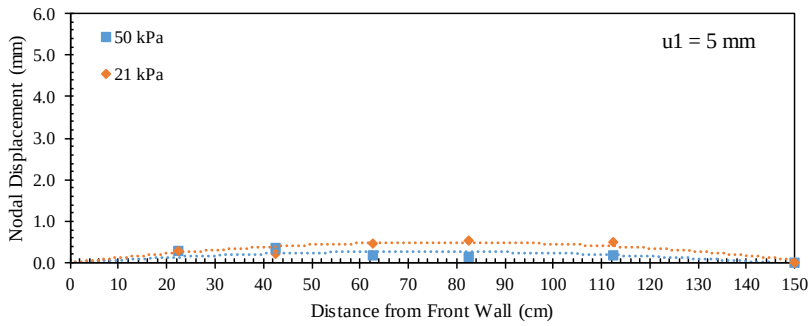

(a)

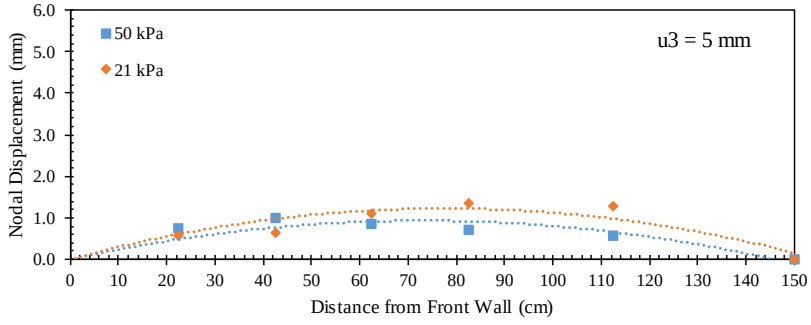

(b)

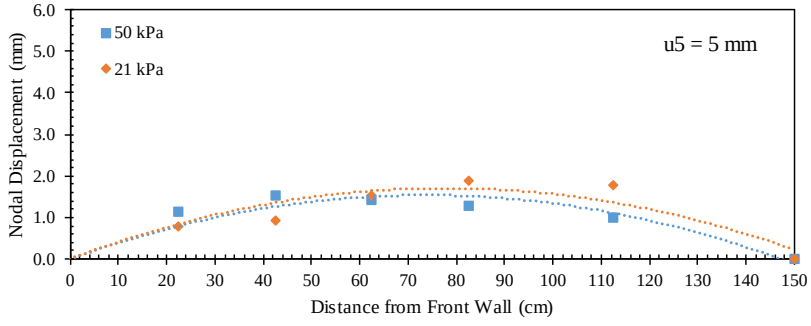

(c)

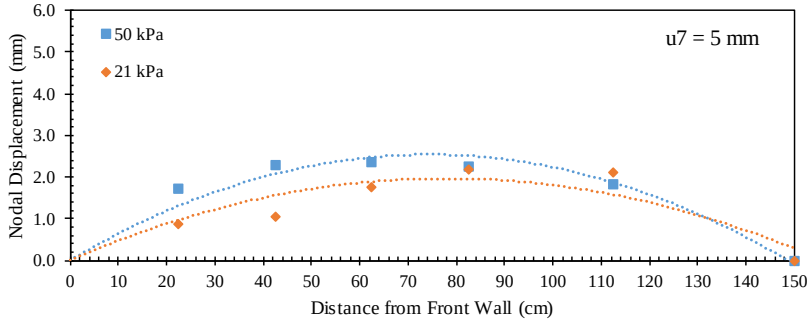

(d)

Figure 5.2.30. Upper passive reinforcement displacement profiles: for S_v = 100 mm (4 in) (a) At nodal displacement u1 = 5 mm (0.2 in); (b) At nodal displacement u3 = 5 mm (0.2 in); (c) At nodal displacement u5 = 5 mm (0.2 in); and (d) At nodal displacement u7 = 5 mm (0.2 in).

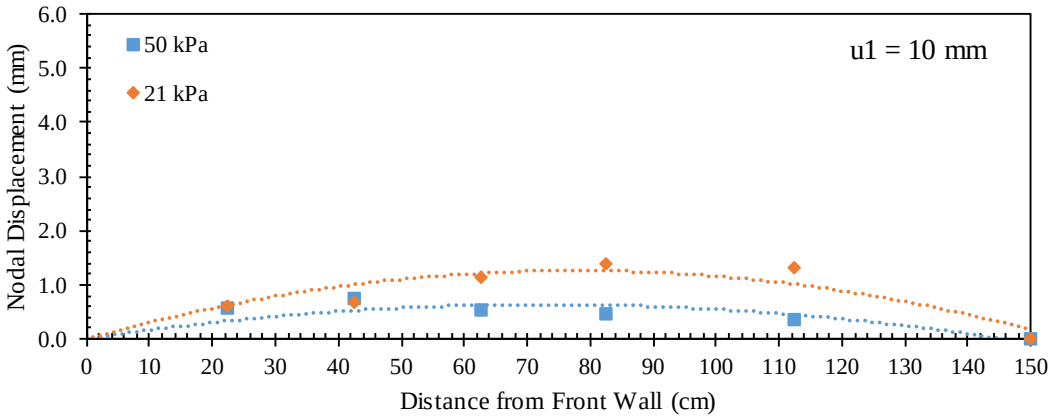

(a)

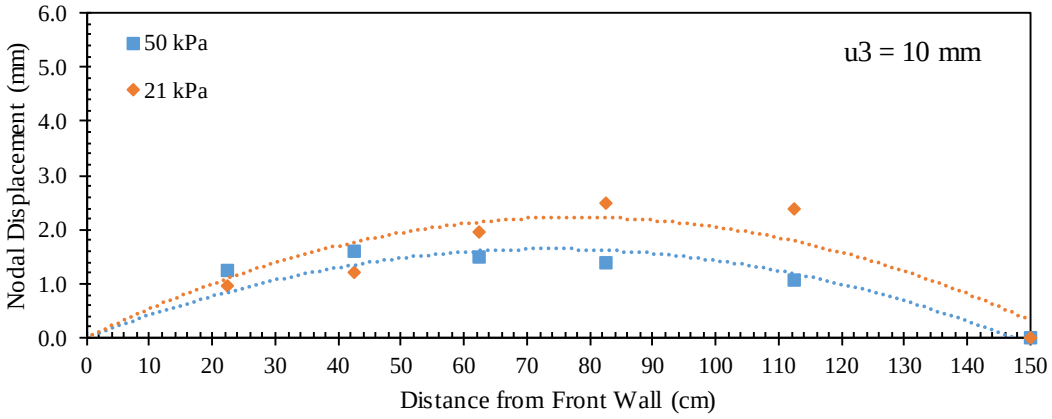

(b)

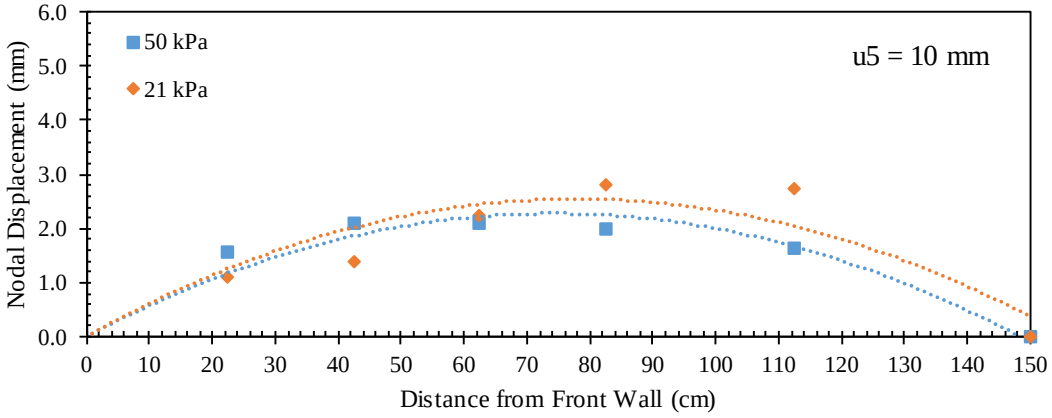

(c)

Figure 5.2.31. Upper passive reinforcement displacement profiles for S_v = 100 mm (4 in): (a) At nodal displacement u1 = 10 mm (0.4 in); (b) At nodal displacement u3 = 10 mm (0.4 in); and (c) At nodal displacement u5 = 10 mm (0.4 in).

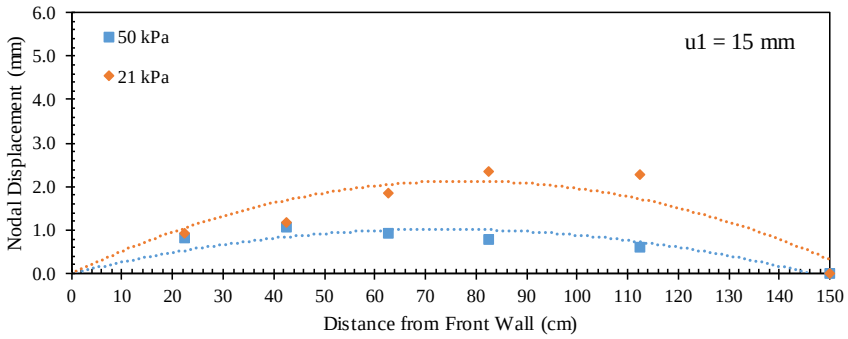

(a)

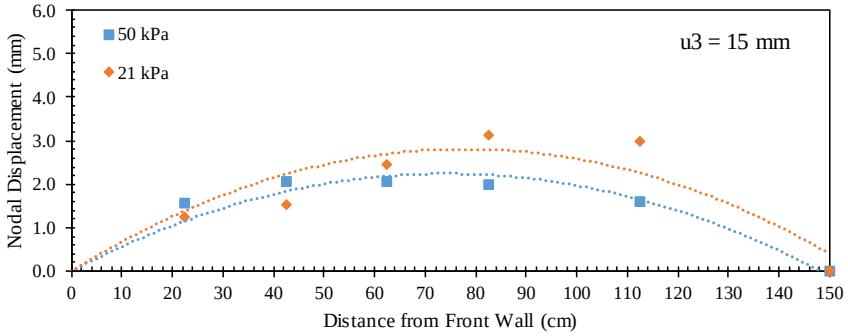

(b)

Figure 5.2.32. Upper passive reinforcement displacement profiles for S_v = 100 mm (3.9 mm): (a) At nodal displacement u1 = 15 mm (0.6 in); and (b) At nodal displacement u3 = 15 mm (0.6 in).

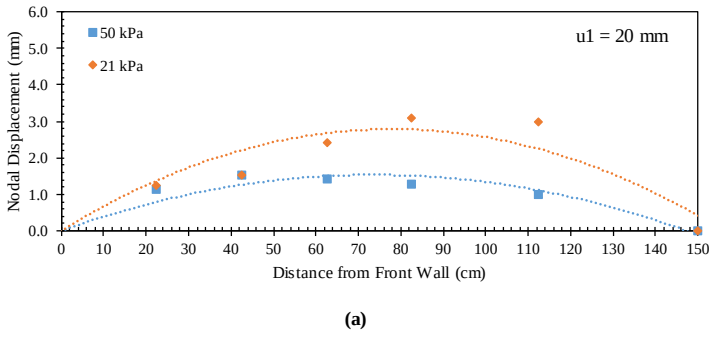

(a)

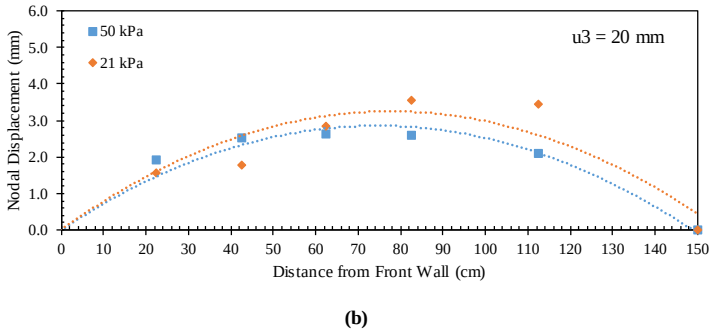

(b)

Figure 5.2.33. Upper passive reinforcement displacement profiles for S_v = 100 mm (4 in): (a) At nodal displacement u1 = 20 mm (0.8 in); and (b) At nodal displacement u3 = 20 mm (0.8 in).

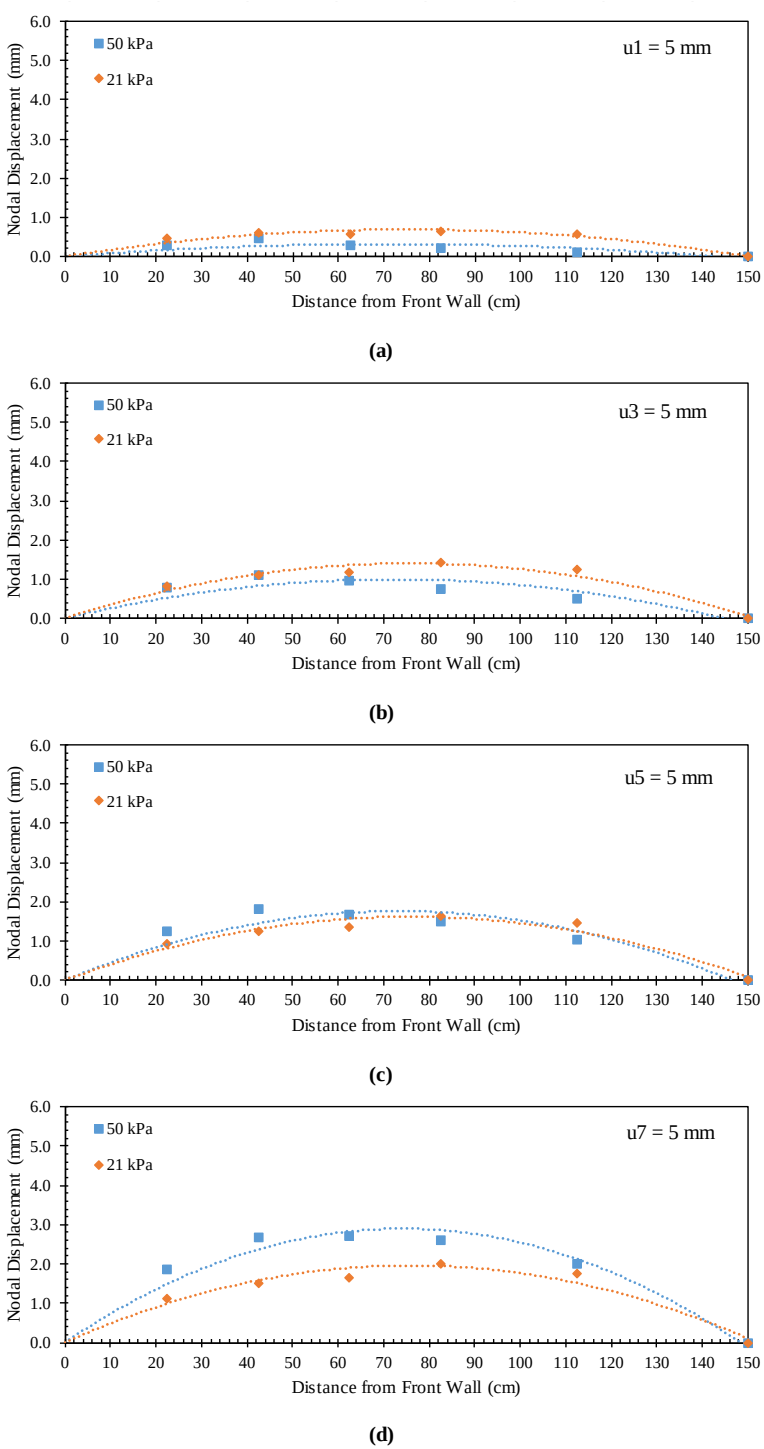

Figure 5.2.34. Upper passive reinforcement displacement profiles for S_v = 50 mm (2 in): (a) At nodal displacement u1 = 5 mm (0.2 in); (b) At nodal displacement u3 = 5 mm (0.2 in); (c)

At nodal displacement u5 = 5 mm (0.2 in); and (d) At nodal displacement u7 = 5 mm (0.2 in).

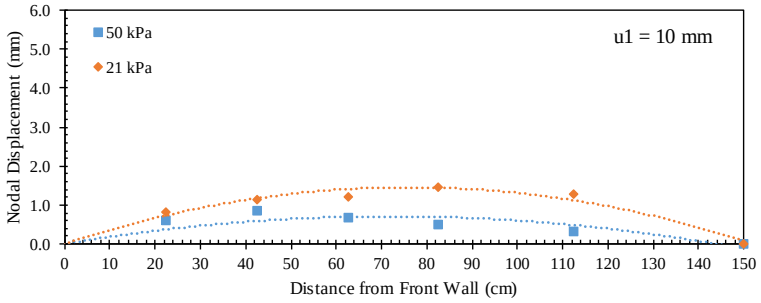

(a)

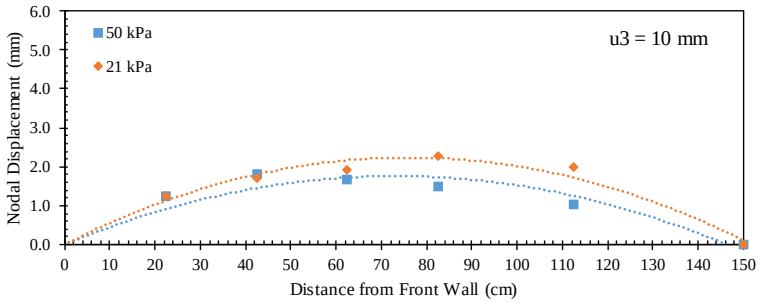

(b)

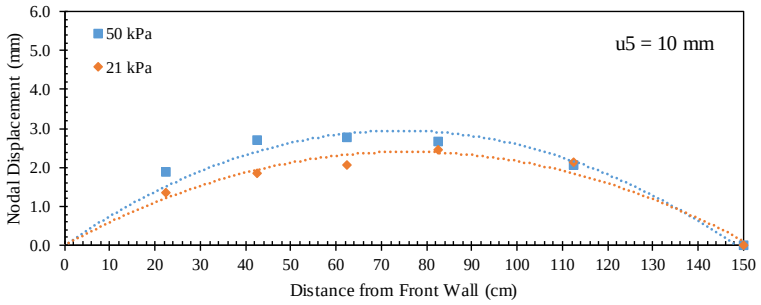

(c)

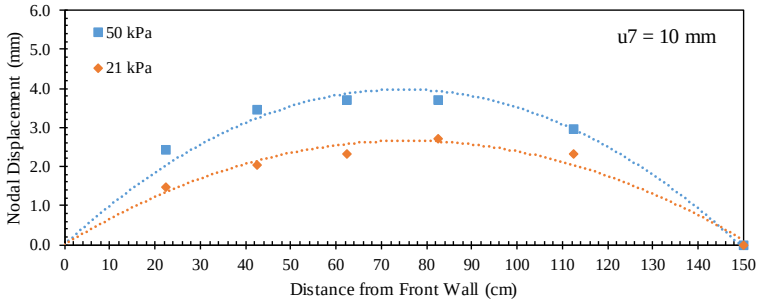

(d)

Figure 5.2.35. Upper passive reinforcement displacement profiles for S_v = 50 mm (2 in): (a) At nodal displacement u1 = 10 mm (0.4 in); (b) At nodal displacement u3 = 10 mm (0.4 in); (c) At nodal displacement u5 = 10 mm (0.4 in); and (d) At nodal displacement u7 = 10 mm (0.4 in).

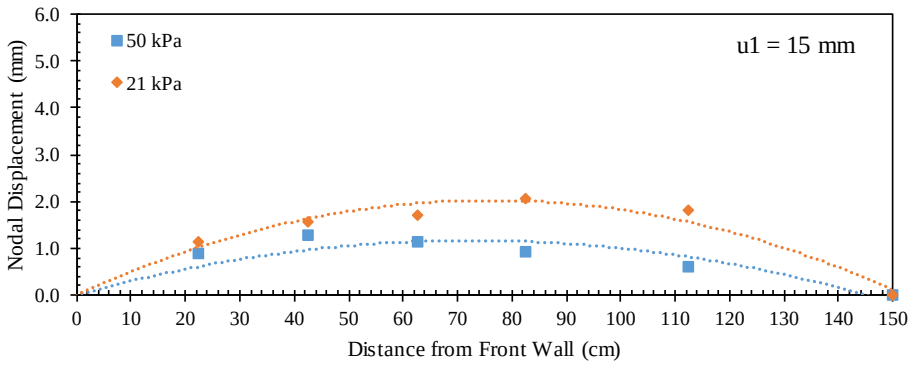

(a)

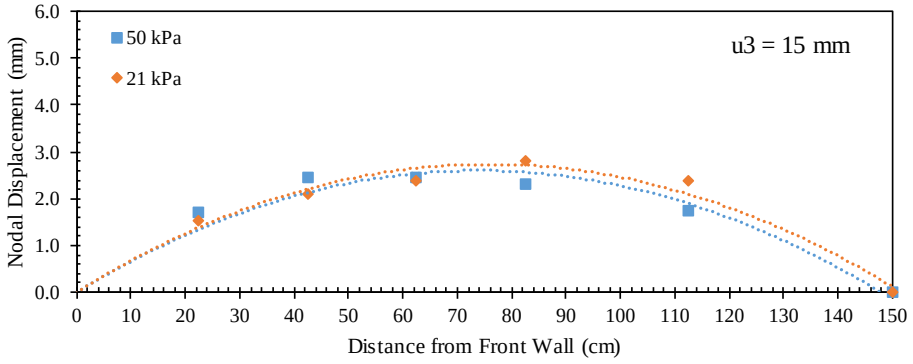

(b)

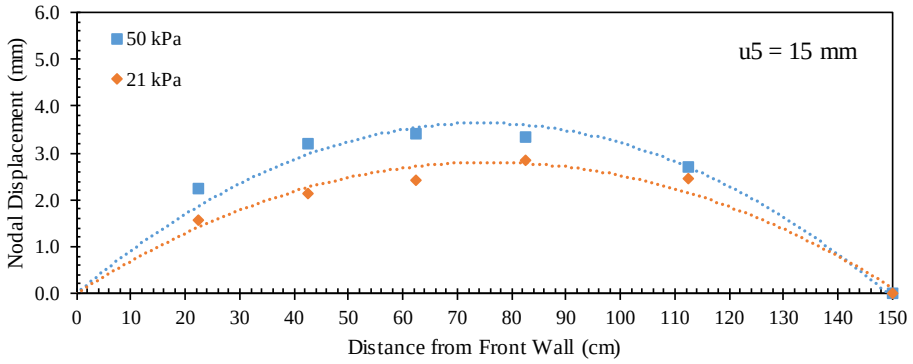

(c)

Figure 5.2.36. Upper passive reinforcement displacement profiles for S_v = 50 mm (2 in): (a) At nodal displacement u1 = 15 mm (0.6 in); (b) At nodal displacement u3 = 15 mm (0.6 in); and (c) At nodal displacement u5 = 15 mm (0.6 in).

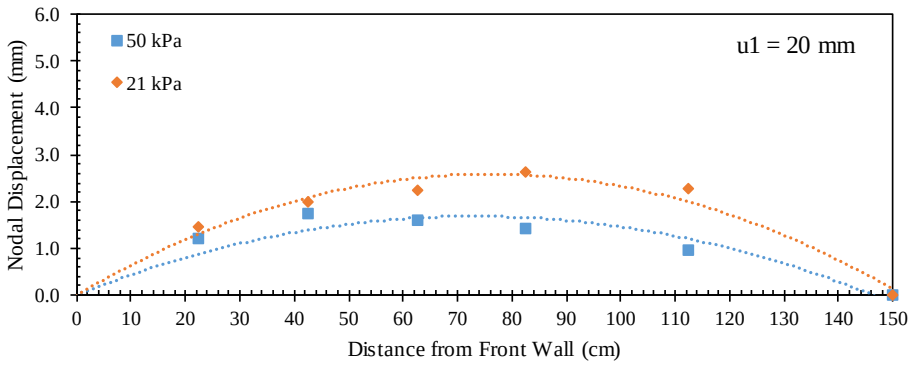

(a)

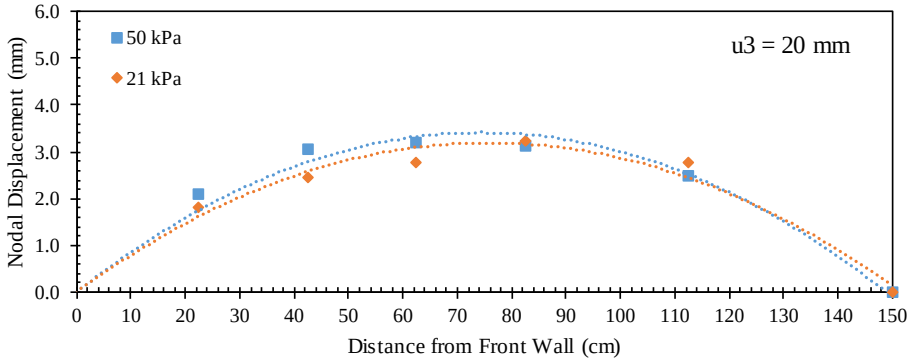

(b)

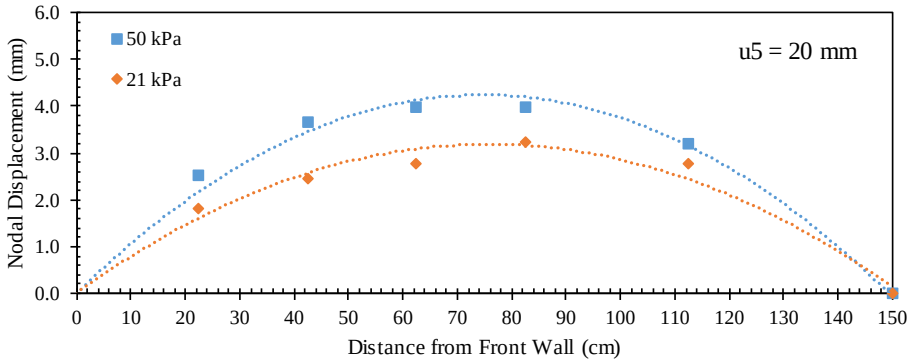

(c)

Figure 5.2.37. Upper passive reinforcement displacement profiles for S_v = 50 mm (2 in): (a) At nodal displacement u1 = 20 mm (0.8 in); (b) At nodal displacement u3 = 20 mm (0.8 in); and (c) At nodal displacement u5 = 20 mm (0.8 in).

Figures 5.2.38a through 5.2.38c show the soil-reinforcement relative displacement magnitude at 0.305 m (1 ft.) from the front wall for tests conducted with reinforcements spaced at 0.15, 0.10, and 0.05 m (6 in, 4 in, 2 in), respectively. This slippage was obtained by subtracting the reinforcement displacement at this location (by interpolation between *u1* and u3) and the soil displacement measured by the artificial gravel particle adjacent to the reinforcement (LP24). It was observed that the slippage (relative displacement) at the interface of the active reinforcement was lower in the tests conducted at low confining normal stresses compared to those conducted at high confining stresses.

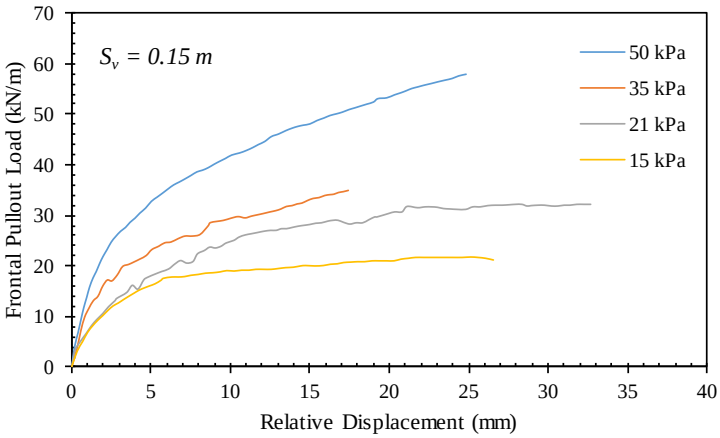

(a)

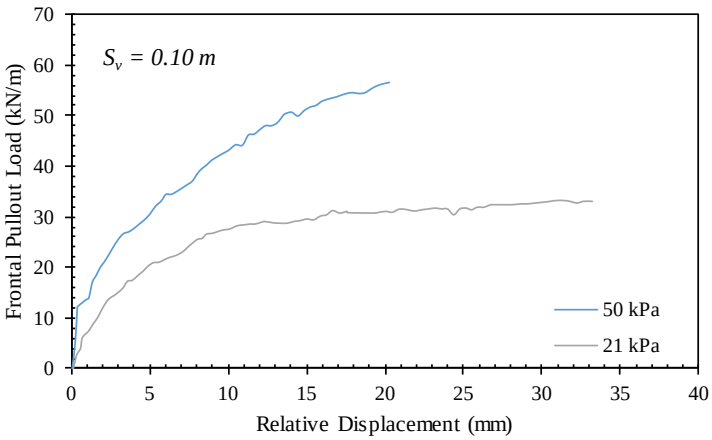

(b)

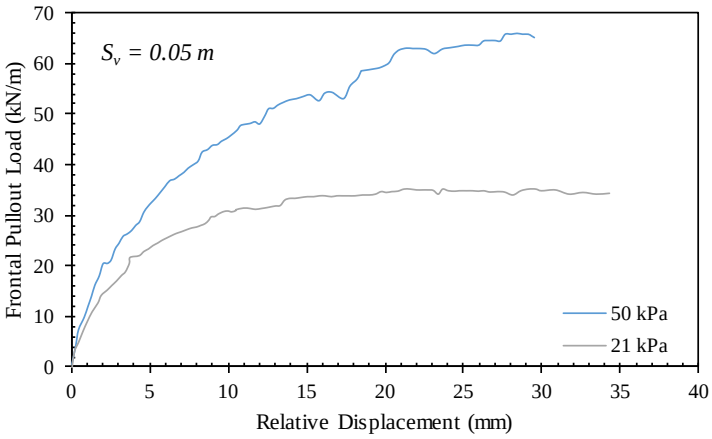

(c)

Figure 5.2.38. Soil-reinforcement relative displacement for tests conducted with reinforcement placed at different spacings: (a) S_v = 0.15 m (6 in); (b) S_v = 0.10 m (4 in); and (c) S_v = 0.05 m (2 in).

Figure 5.2.39 shows the vertical soil displacement measured by means of the artificial gravel particles placed on top of the reinforced soil mass. Figures 5.2.39a through 5.2.39c show the soil displacement with respect to reinforcement frontal displacement of the active reinforcement *u1* for the back, middle, and front of the reinforced soil mass, respectively. The figures include tests conducted at confining stresses of 15, 21, and 35 kPa at the active reinforcement level (i.e., central horizontal plane of the reinforced soil mass). It was observed that the soil tends to dilate near the front and settle near the back as pullout loading progressed. It was observed that the dilation is higher in tests conducted at low confining normal stresses compared to those conducted at high confining stresses. At low confining stresses soils tend to dilate more when subjected to shear compared to soils at high confining stresses. Similar observation were made for tests conducted with reinforcements placed at different reinforcement vertical spacings.

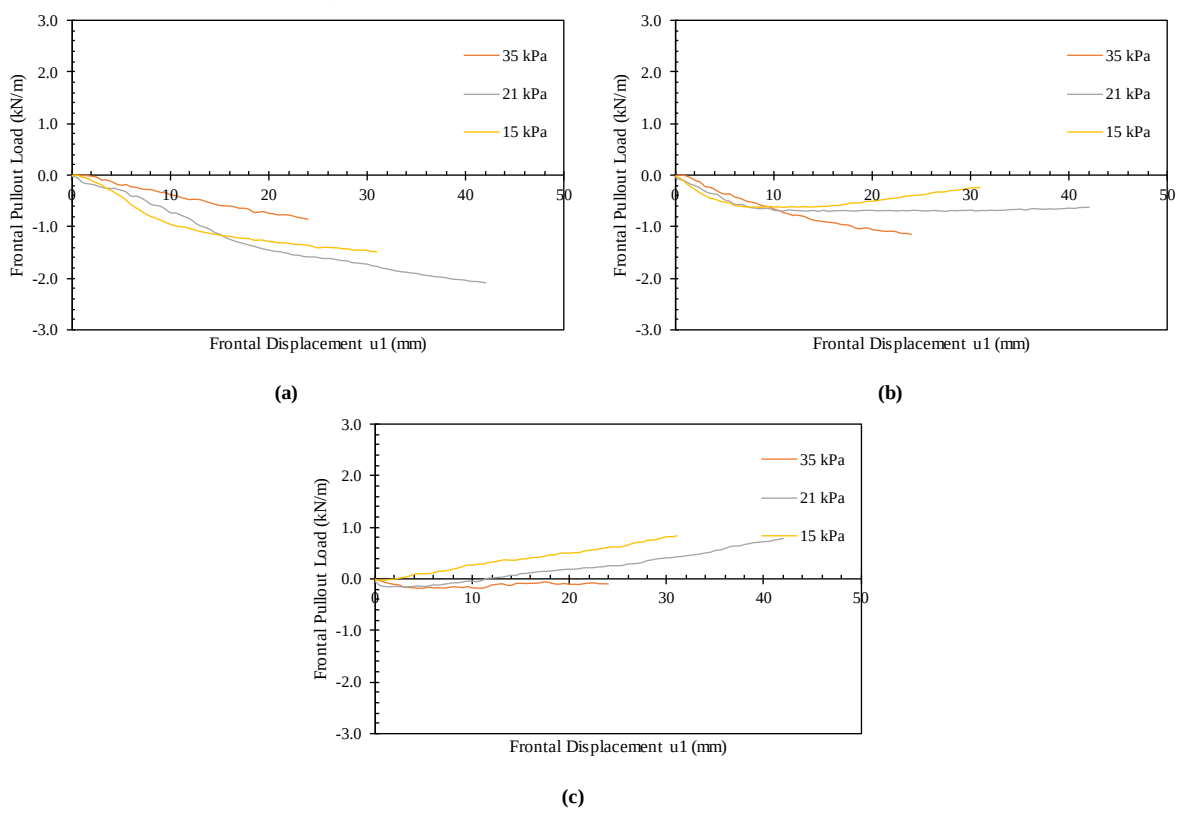

Figure 5.2.39. Vertical soil displacements profiles (measured by means of artificial gravel particles) with respect to frontal displacement at the active reinforcement: (a) At the back of the soil mass; (b) At the middle of the soil mass; and (c) At the front of the soil mass.

5.2.3.3 EFFECT OF REINFORCEMENT VERTICAL SPACING

A comparison was conducted between tests performed with reinforcement layers placed at different vertical spacing. Three layers were used in each test, one active and two passive reinforcement layers, all of which are of the same type. The same reinforcement type used for was the same among the tests, polypropylene woven geotextile reinforcements. This reinforcement has ultimate tensile strength of 70 kN/m (400 lb/in) and tensile stiffness of 876 kN/m (5 kips/in) at tensile strain of 5% in the cross-rollway direction (i.e., cross-machine direction). The fill material used in these tests was AASHTO No. 8 aggregate. Two comparisons were made among tests conducted at the same confining normal stress but with reinforcements placed at different vertical spacings: (1) a comparison between six tests conducted at confining normal stress of 50 kPa (7.3 psi) at the level of active reinforcement layer (i.e., central horizontal plane of the reinforced soil mass); and (2) a comparison between three tests conducted at confining normal stress of 21 kPa (3 psi) at the level of active reinforcement. Table 5.2.4 summarizes the testing conditions of the tests involved in the two comparisons. The findings from both comparisons were used to assess the effect of confining normal stress on the impact of the reinforcement vertical spacing on the behavior of the reinforced soil mass.

Table 5.2.4. Summary of tests in which reinforcement vertical spacing was varied.

Test ID	***Testing Variables***					
	Fill Material	***S_v***	***σ_v***	***Active GS***	***Passive GS***	***Dilation***
GP-02-07-G1-G	AASHTO No. 8	0.05 m	50 kPa	HP570	HP570	Allowed
GP-04-07-G1-G		0.10 m				
GP-06-07-G1-G		0.15 m				
GP-08-07-G1-G		0.20 m				
GP-12-07-G1-G		0.30 m				
GP-16-03-G1-G		0.40 m				
GP-02-03-G1-G	AASHTO No. 8	0.05 m	21 kPa	HP570	HP570	Allowed
GP-04-03-G1-G		0.10 m				
GP-06-03-G1-G		0.15 m				

*Conversions: 1 m = 0.0254 in.
1 kPa = 20.89 psf

Figures 5.2.40a and 5.2.40b show the frontal pullout load-displacement experimental curves tests conducted at confining normal pressure of 50 and 21 kPa (7.3 and 3 psi), respectively. It was observed that the curves coincide well at early pullout loading stages and then fairly agree with slight scatter near pullout failure. This observation shows that the reinforcement vertical spacing has insignificant interference with the soil-reinforcement interaction. A slight difference was observed in Figure 5.2.40b, which shows a comparison at low confining normal stress. For these tests, the reinforced soil tended to dilate more than the tests conducted at high confining pressure. It was observed that for tests conducted at smaller reinforcement vertical spacing, the dilation tendency is smaller. That is, the smaller vertical spacing results in some dilation reduction, which may result in an increase in the soil-reinforcement interface strength.

Figures 5.2.41 and 5.2.42 show the average nodal displacement measured for the active reinforcement and the corresponding average nodal displacement for the passive reinforcements for tests conducted at confining normal stress of 50 and 21 kPa (7.3 and 3 psi), respectively. Every figure consists of a and b showing the average nodal displacement measured for the upper and lower passive reinforcement layers, respectively. Note that, the average nodal displacement represents the area under displacement profile normalized by the reinforcement length. Assuming the constitutive law for the interface shear behavior, Figure a and b provide insight into the effect of confining normal stress on the interaction between neighboring reinforcements. It was concluded that the tests conducted with reinforcements placed at larger vertical spacing resulted in small interaction between neighboring reinforcements. The effect of the reinforcement spacing may have a bigger impact at high confining normal stresses.

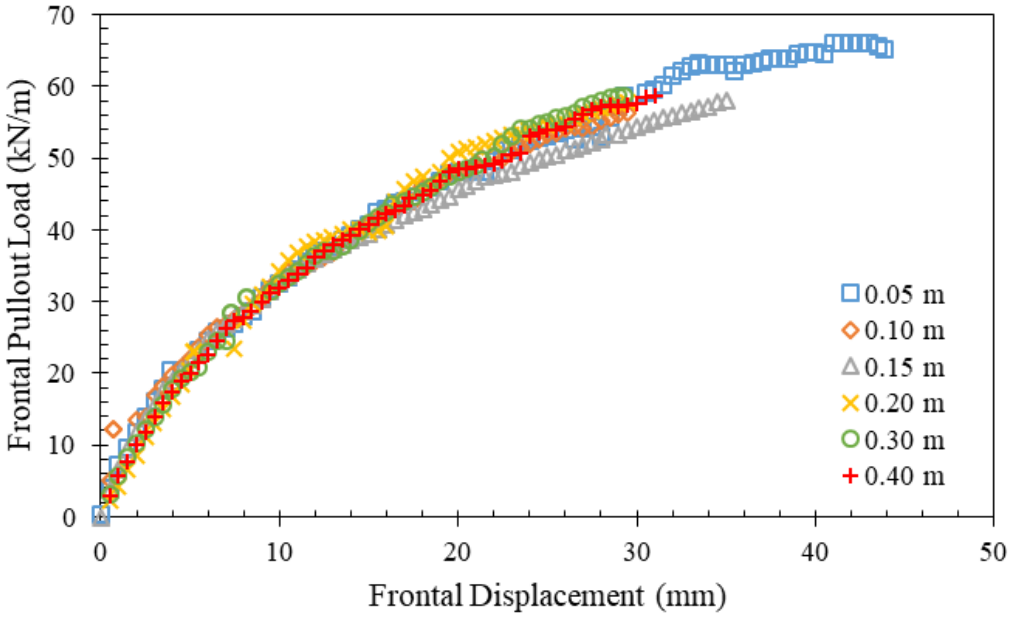

(a)

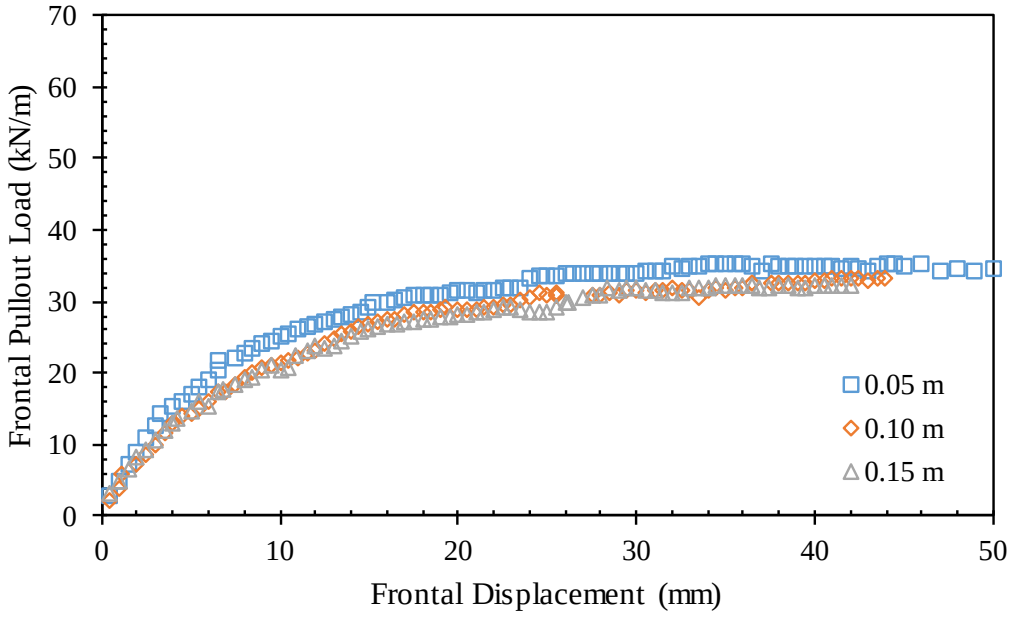

(b)

Figure 5.2.40. Frontal pullout load-displacement curves: (a) At normal confining stress, σ_v = 50 kPa (7.3 psi); and (b) At normal confining stress, σ_v = 21 kPa (3 psi) (legend denotes spacing values).

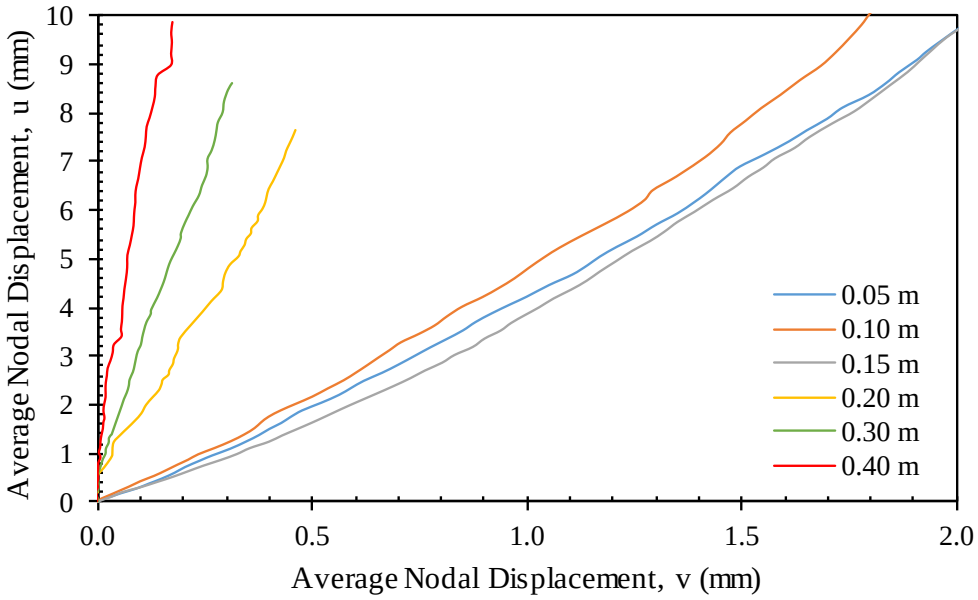

(a)

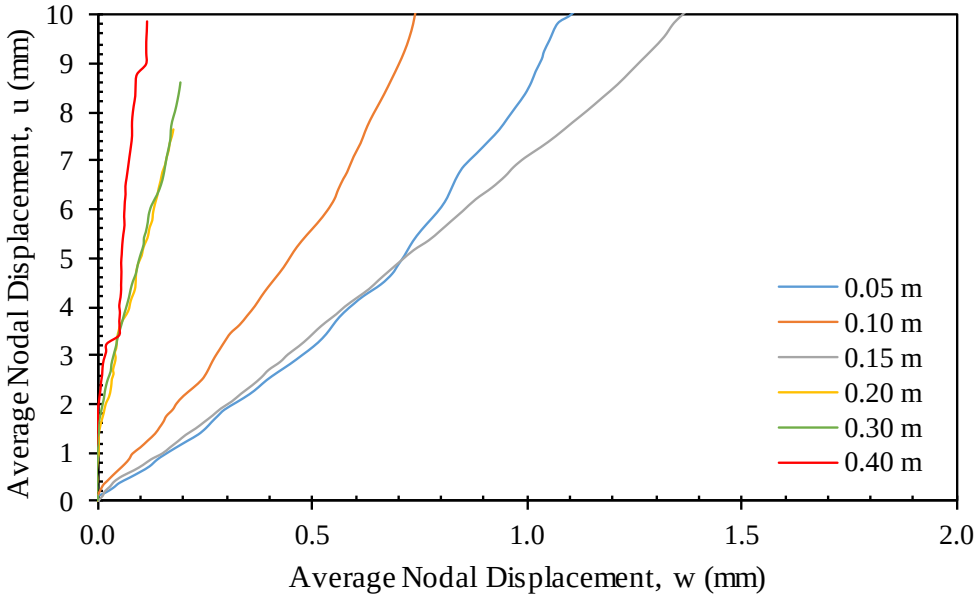

(b)

Figure 5.2.41. Average nodal displacement of passive reinforcements with respect to average nodal displacement of active reinforcement: (a) Upper passive reinforcement; and (b) Lower passive reinforcement (σ_v = 50 kPa (7.3 psi)) (legend denotes spacing values).

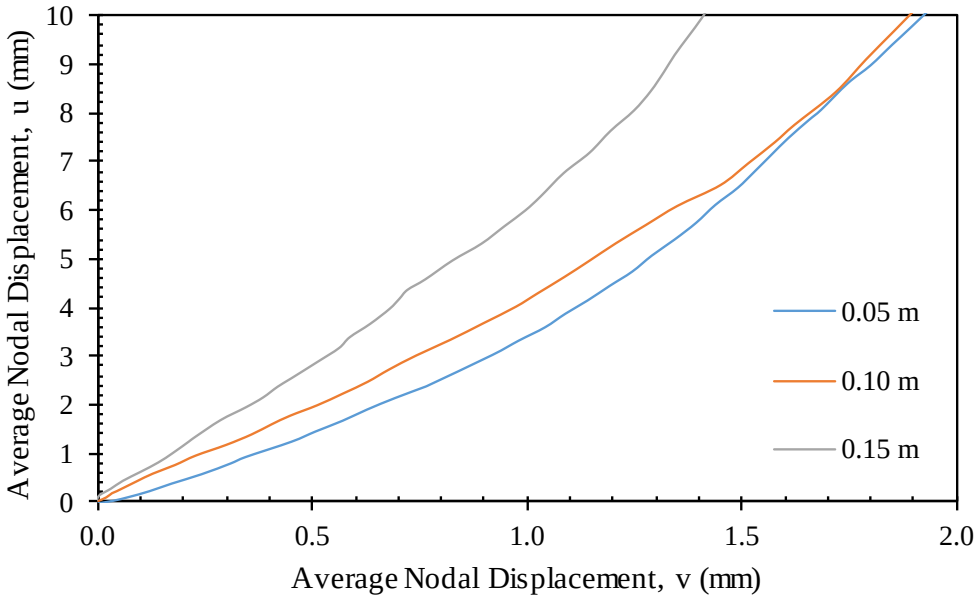

(a)

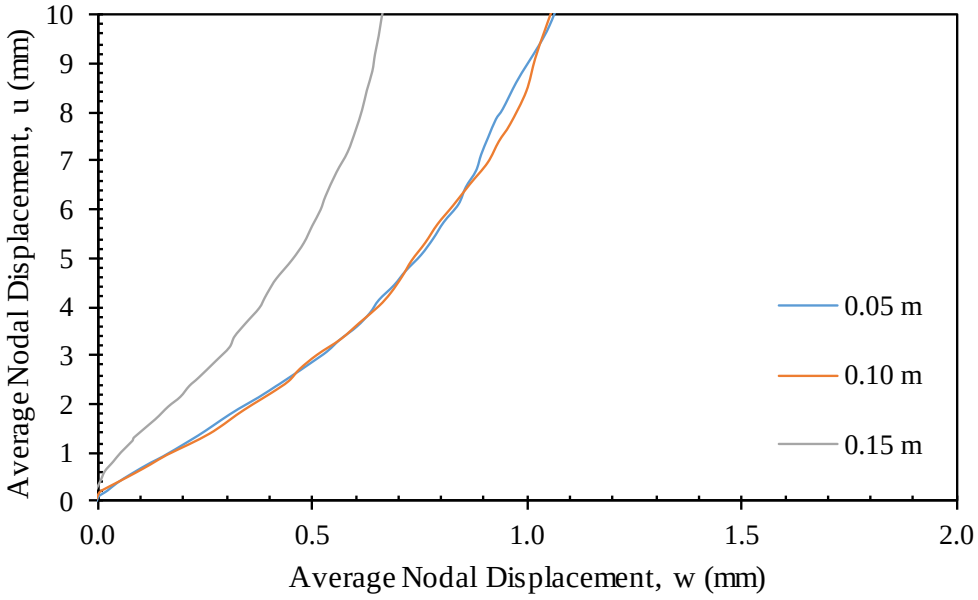

(b)

Figure 5.2.42. Average nodal displacement of passive reinforcements with respect to average nodal displacement of active reinforcement: (a) Upper passive reinforcement; and (b) Lower passive reinforcement (σ_v = 21 kPa (3 psi)) (legend denotes spacing values).

Figures 5.2.43 through 5.2.47 show the displacement profiles for the active and passive reinforcement layers at active reinforcement frontal displacement (*u1*) of 5, 10, 15, 20, and 30 mm (0.2, 0.4, 0.6, 0.8 and 1.2 in) for tests conducted at confining normal stress of 50 kPa (7.3 psi). Similarly, Figures 5.2.48 through 5.2.52 show the displacement profiles for

reinforcement layers at active reinforcement frontal displacement (*u1*) of 5, 10, 15, 20, and 30 mm (0.2, 0.4, 0.6, 0.8 and 1.2 in) for tests conducted at confining normal stress of 21 kPa (3 psi). These figures show comparisons for the reinforcement strains measured at the same displacement of the active (middle) reinforcement. This ensures that the load (strain) propagated along the reinforcement length and generated shear stresses at the soil-reinforcement interface. The profiles for the active reinforcements show the displacement for all tests conducted at the same confining normal stress. That is, the reinforcement vertical spacing has insignificant impact on the soil-reinforcement interaction behavior of the active reinforcement. On the other hand, the profiles of the passive reinforcements showed higher displacements for tests conducted with reinforcements placed at small vertical spacings compared to those conducted with reinforcements placed at larger spacings. The difference in displacement increased as the pullout loading progressed. Note that, however, there was no significant difference between the displacements measured for passive reinforcements in the tests conducted with reinforcements spaced at 0.05, 0.10, and 0.15 m (2, 4 and 6 in) at confining stress of 50 kPa (7.3 psi). Similar observation was made in tests conducted with reinforcements spaced at 0.05 and 0.10 m (2 and 4 in) at confining stress of 21 kPa (3 psi). This observation points towards a threshold vertical spacing below which the effect of the spacing is maximum for specific confining normal stress, soil medium, and reinforcement. This threshold vertical spacing can be identified as 0.15 and 0.10 m (6 and 4 in) for confining stress of 50 and 21 kPa (7.3 and 3 psi), respectively. In addition, the interaction between reinforcement layers almost vanished beyond vertical spacing of 0.3 m (1 ft.) for tests conducted at confining stress of 50 kPa (7.3 psi). This observation points to another boundary beyond which there is no longer an effect for the reinforcement spacing on the interaction between neighboring reinforcements for specific confining normal stress, soil medium, and reinforcement. This value can be can be identified as 0.3 m (1 ft.) for confining stress of 50 kPa (7.3 psi).

It should be noted that the passive reinforcements in tests conducted with reinforcements placed at different spacings are subject to different confining normal stress due to the difference in the overburden pressure (different elevation from the central horizontal plane of the reinforced soil mass). If a comparison is made between passive reinforcements placed at the same elevation in soil masses reinforced at different vertical spacing, the effect of the spacing on the interaction among the neighboring reinforcements will increase. In such comparison, more layers will be placed in the soil mass with closely-spaced reinforcements than that of with largely-spaced reinforcements. In the closely-spaced reinforced system, the intermediate reinforcement layers will reduce the interaction between the active reinforcement and the passive reinforcements layers placed at the same elevation as that in the largely-spaced reinforced system.

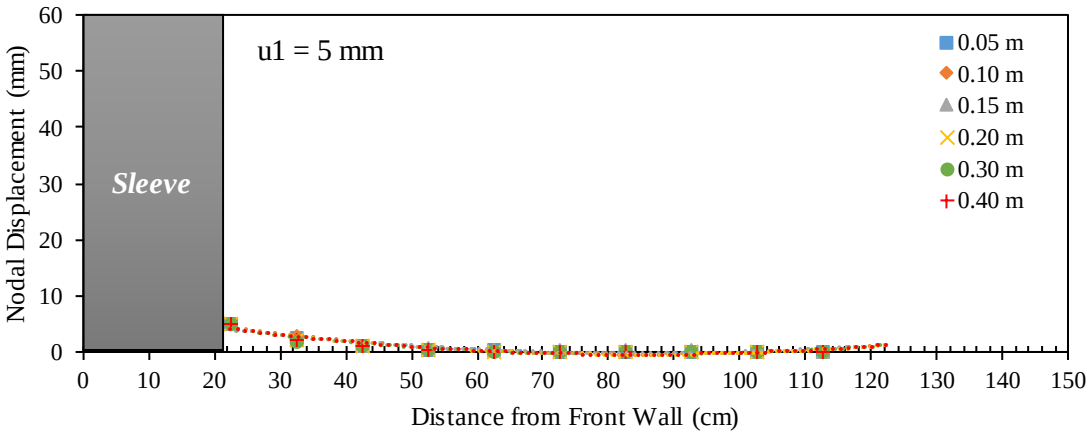

(a)

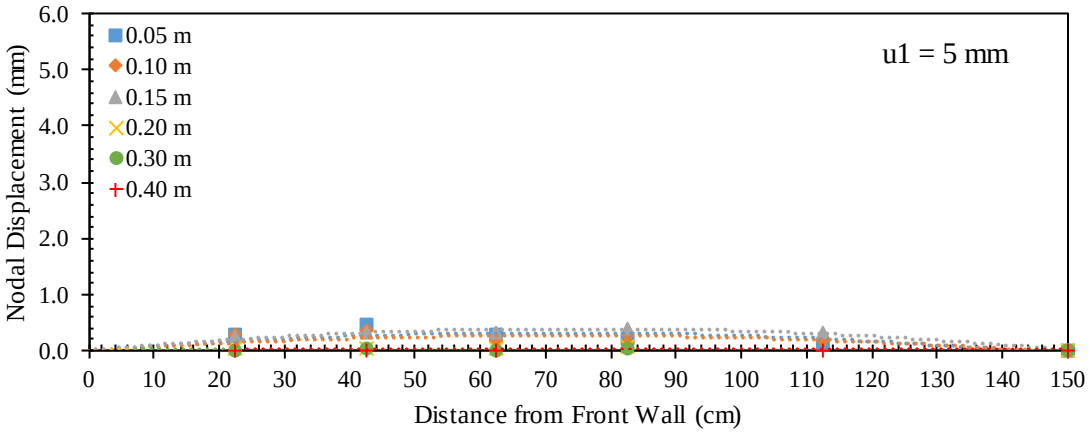

(b)

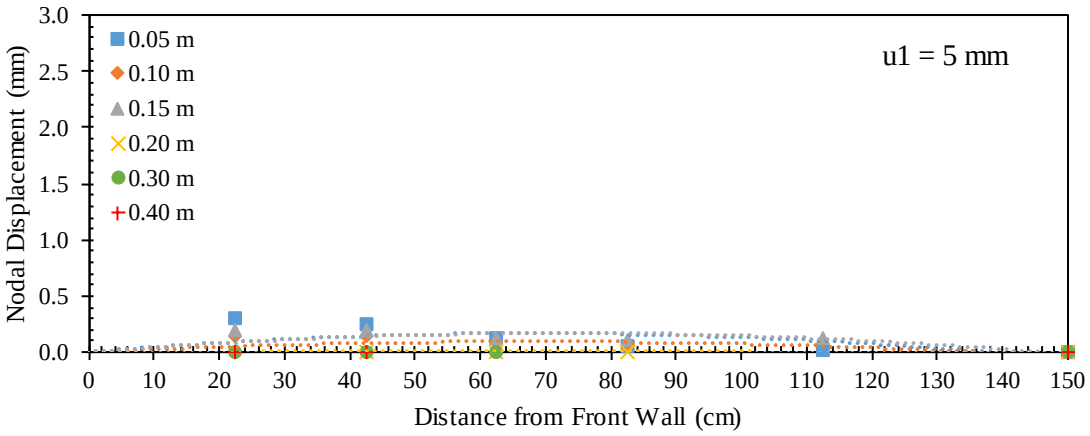

(c)

Figure 5.2.43. Reinforcement displacement profiles at frontal displacement u1 = 5 mm (0.2 in): (a) Active reinforcement; (b) Upper passive reinforcement; and (c) Lower passive reinforcement (σ_v = 50 kPa (7.3 psi)).

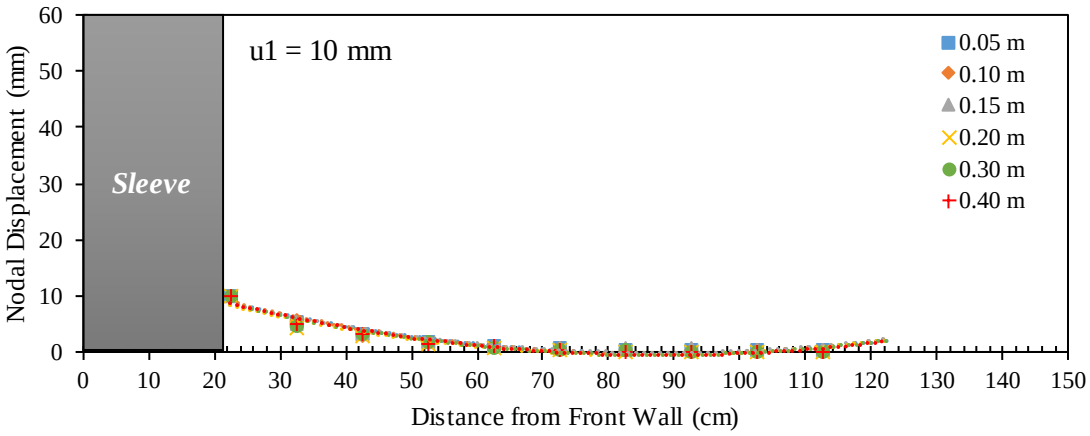

(a)

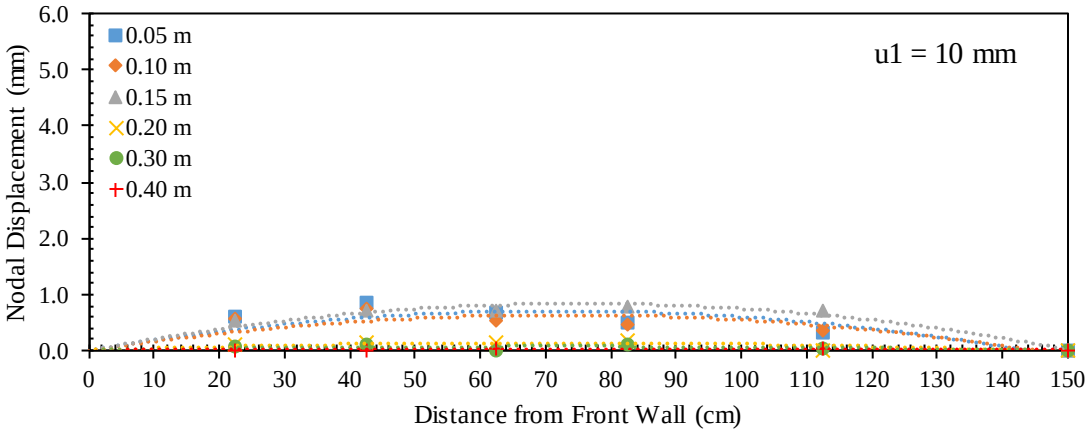

(b)

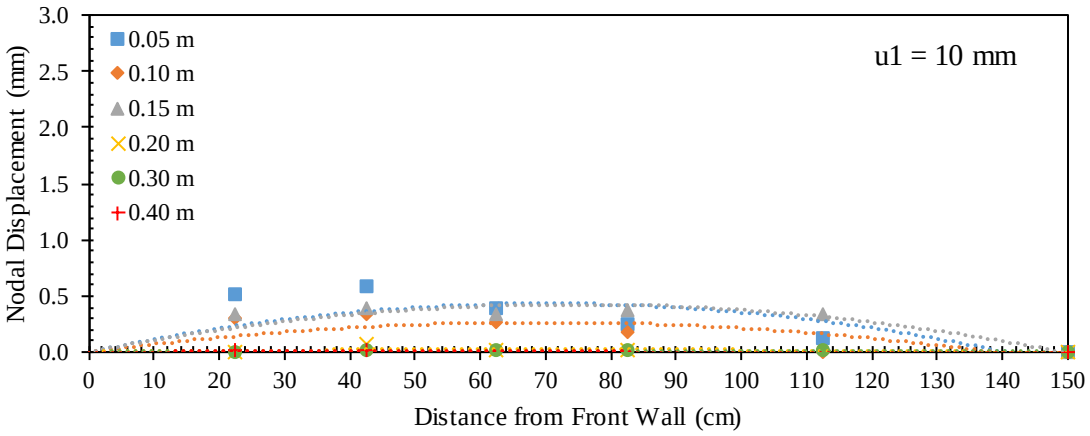

(c)

Figure 5.2.44. Reinforcement displacement profiles at frontal displacement u1 = 10 mm (0.4 in): (a) Active reinforcement; (b) Upper passive reinforcement; and (c) Lower passive reinforcement (σ_v = 50 kPa (7.3 psi)).

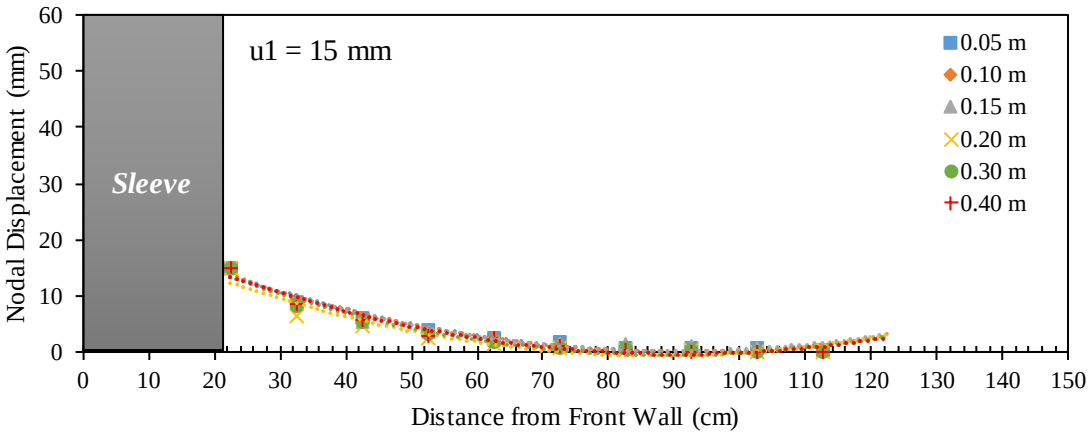

(a)

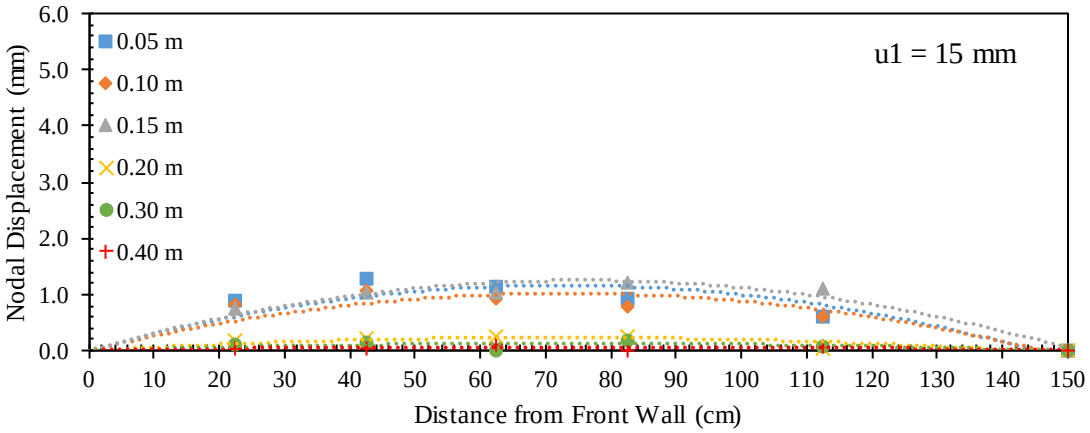

(b)

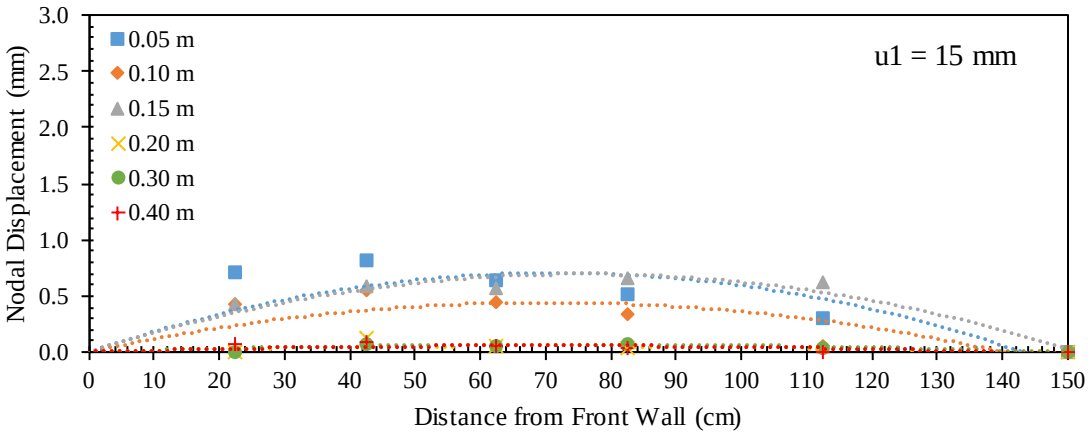

(c)

Figure 5.2.45. Reinforcement displacement profiles at frontal displacement u1 = 15 mm (0.6 in): (a) Active reinforcement; (b) Upper passive reinforcement; and (c) Lower passive reinforcement (σ_v = 50 kPa (7.3 psi)).

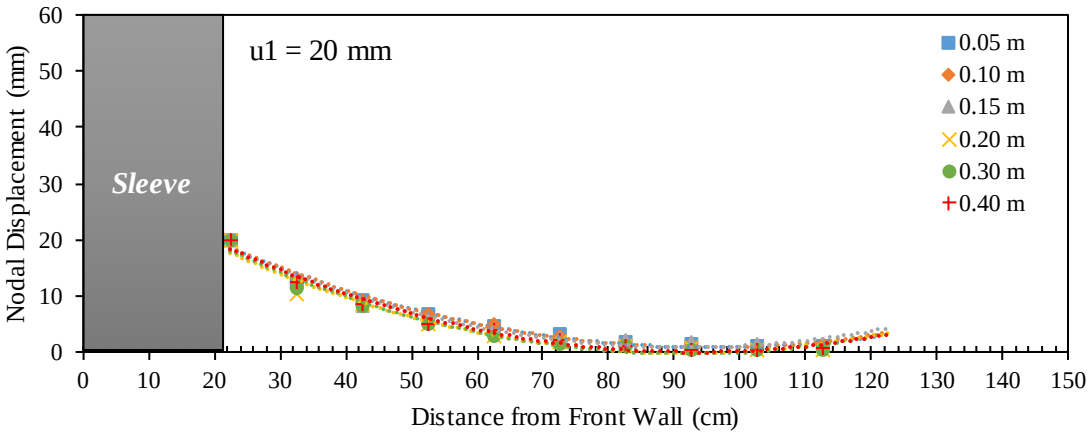

(a)

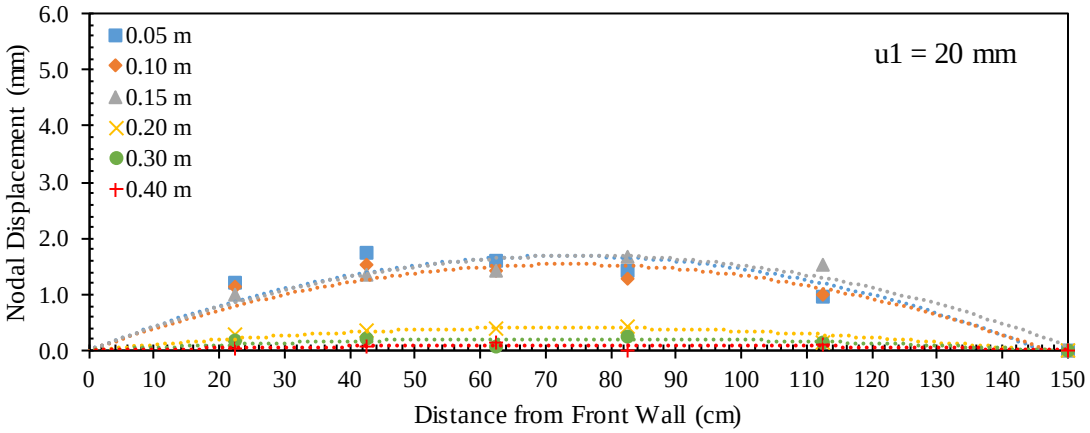

(b)

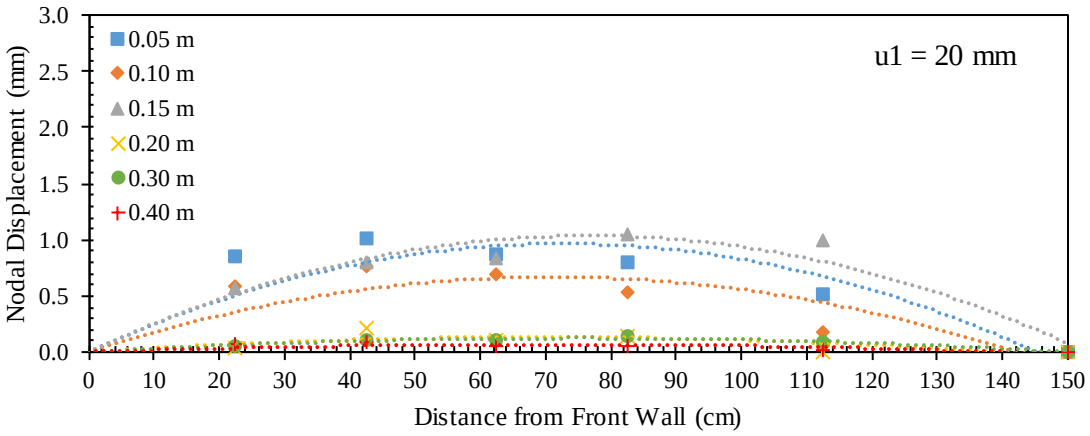

(c)

Figure 5.2.46. Reinforcement displacement profiles at frontal displacement u1 = 20 mm: (a) Active reinforcement; (b) Upper passive reinforcement; and (c) Lower passive reinforcement (σ_v = 50 kPa (7.3 psi)).

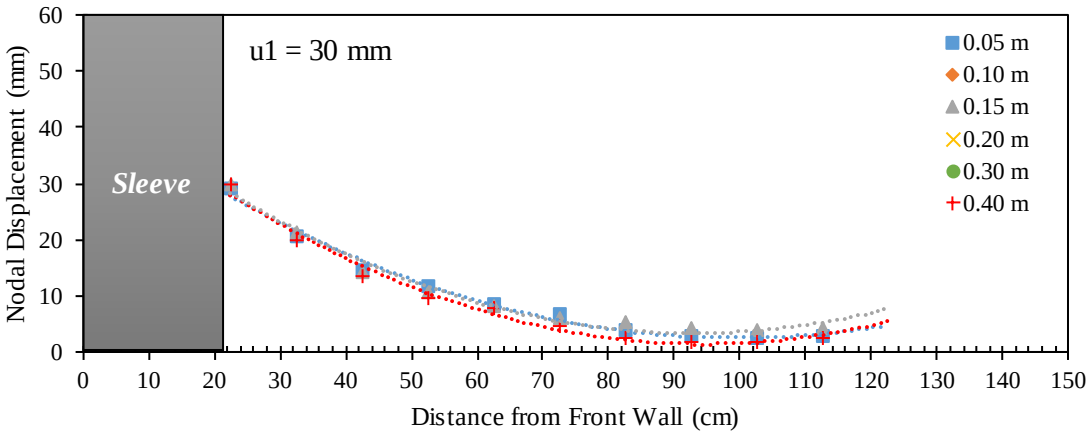

(a)

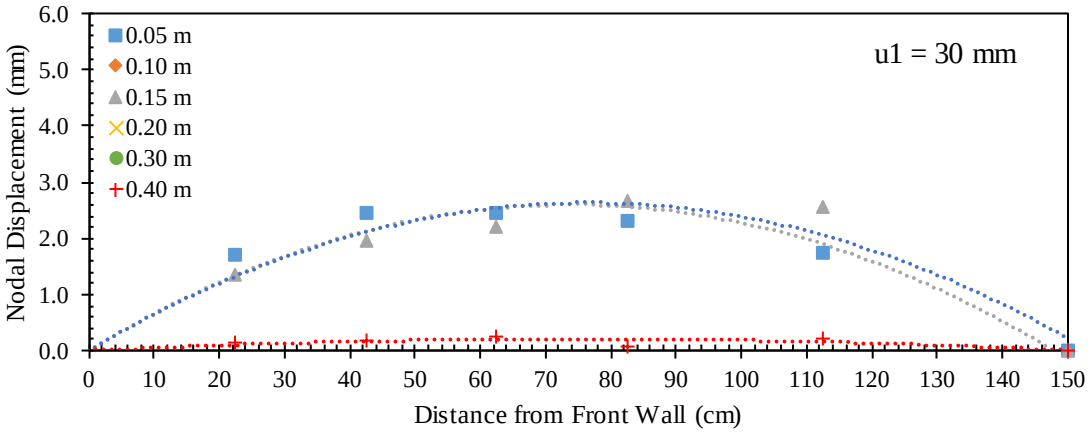

(b)

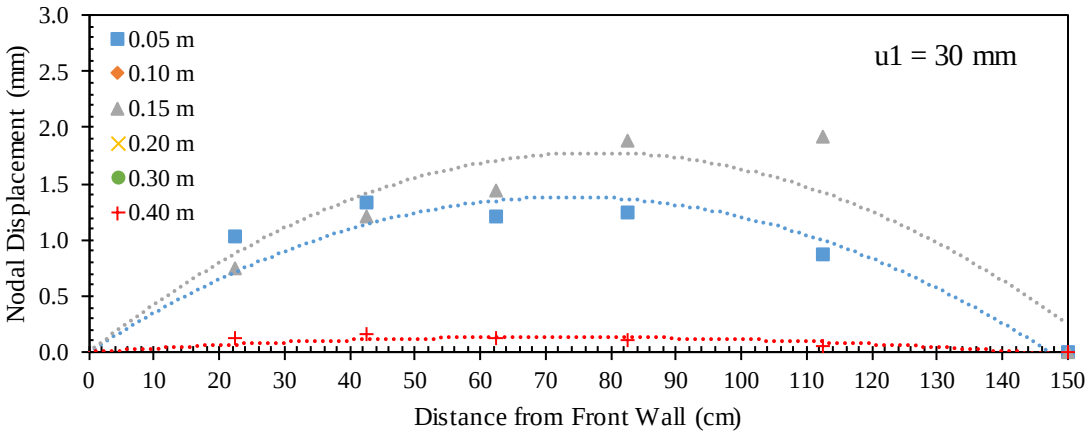

(c)

Figure 5.2.47. Reinforcement displacement profiles at frontal displacement u1 = 30 mm (1.2 in): (a) Active reinforcement; (b) Upper passive reinforcement; and (c) Lower passive reinforcement (σ_v = 50 kPa (7.3 psi)).

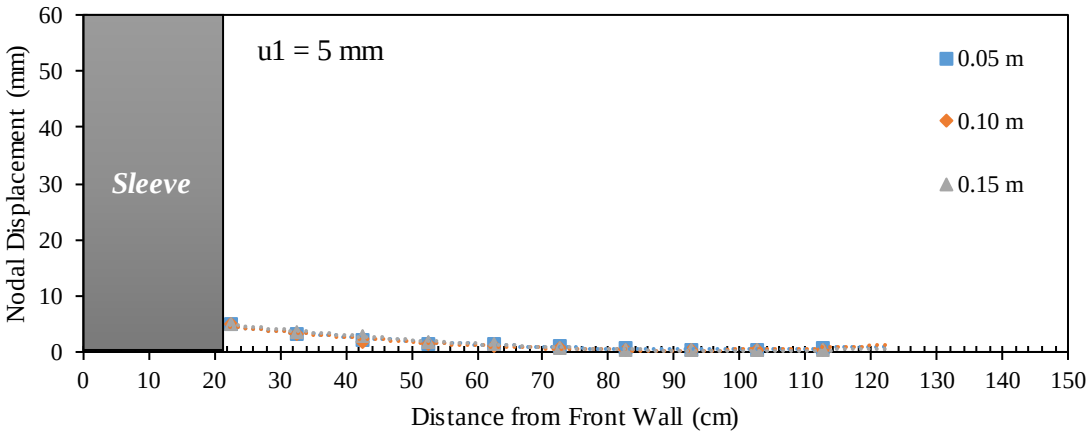

(a)

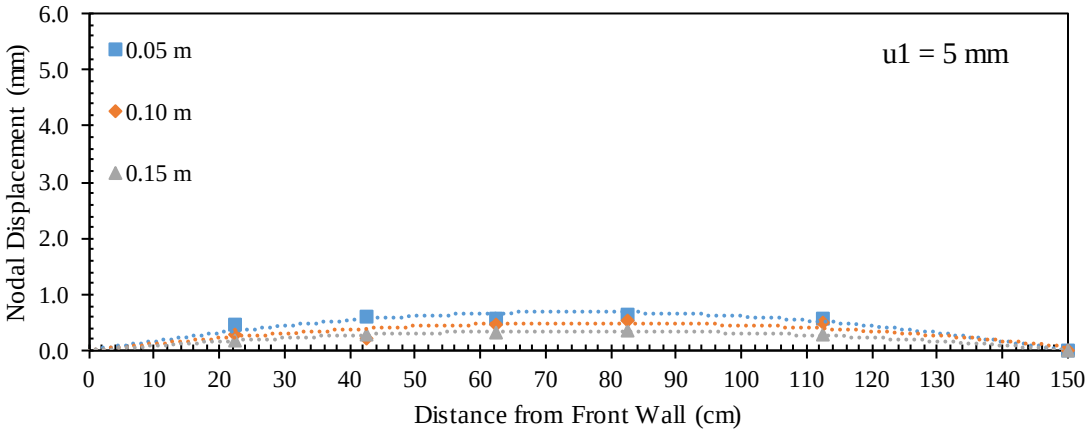

(b)

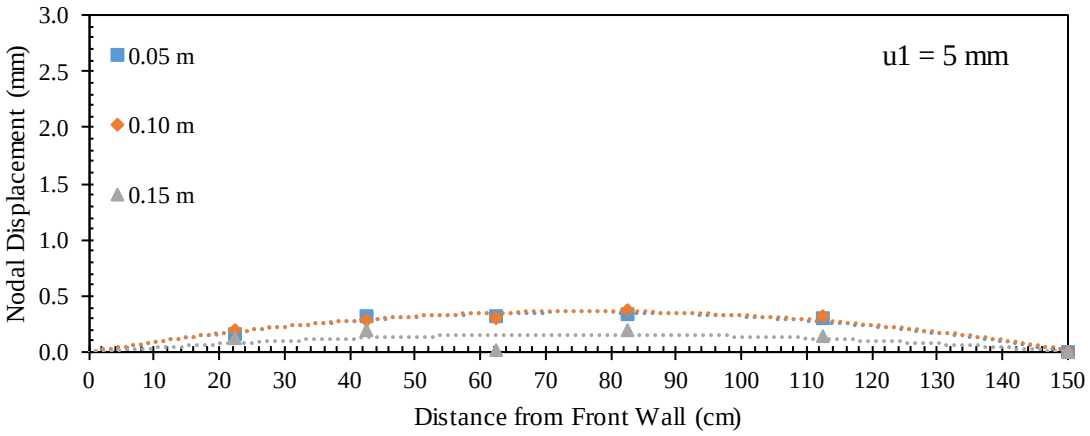

(c)

Figure 5.2.48. Reinforcement displacement profiles at frontal displacement u1 = 5 mm (0.2 in): (a) Active reinforcement; (b) Upper passive reinforcement; and (c) Lower passive reinforcement (σ_v = 21 kPa (3 psi)).

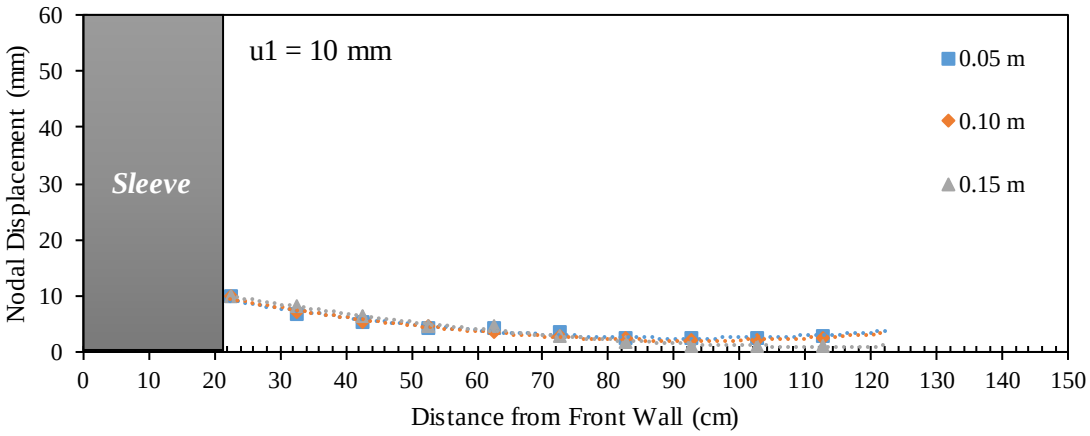

(a)

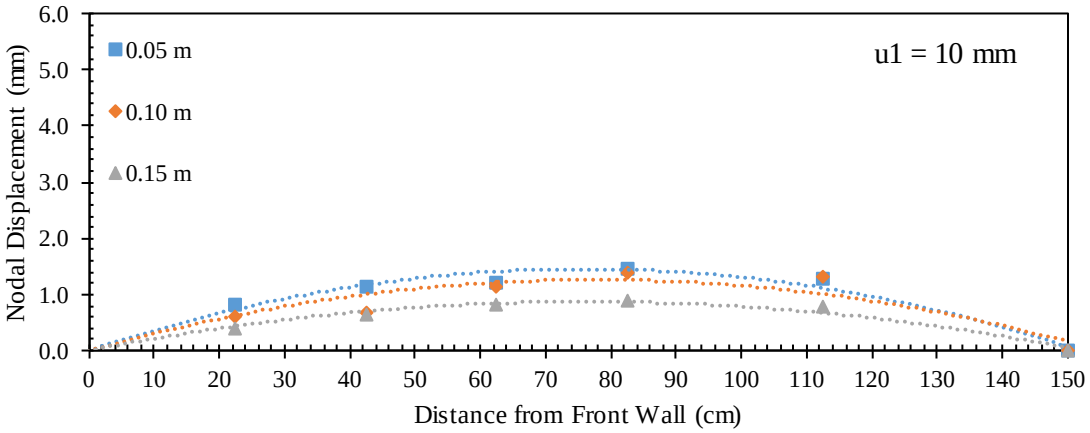

(b)

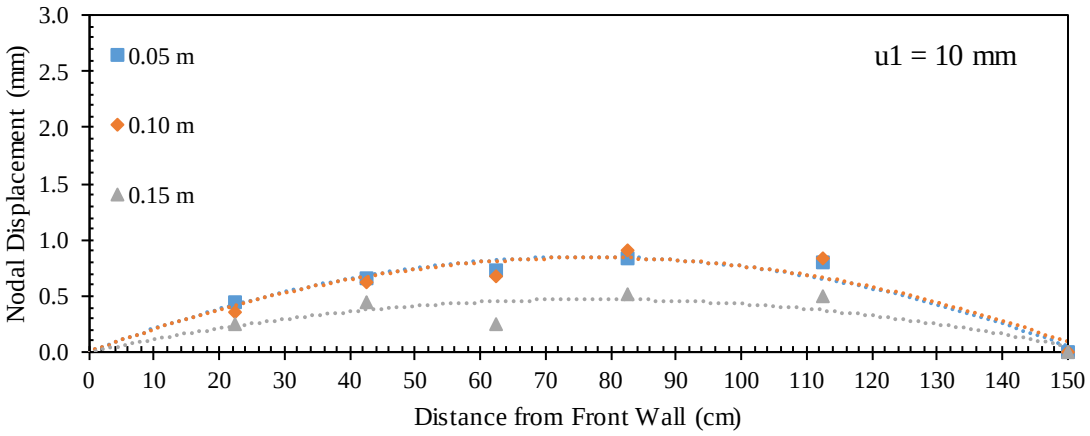

(c)

Figure 5.2.49. Reinforcement displacement profiles at frontal displacement u1 = 10 mm (0.4 in): (a) Active reinforcement; (b) Upper passive reinforcement; and (c) Lower passive reinforcement (σ_v = 21 kPa (3 psi)).

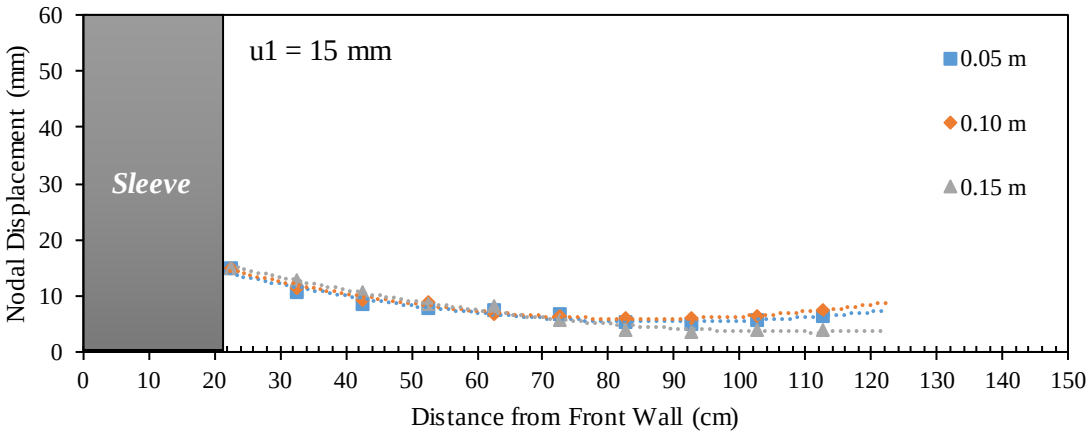

(a)

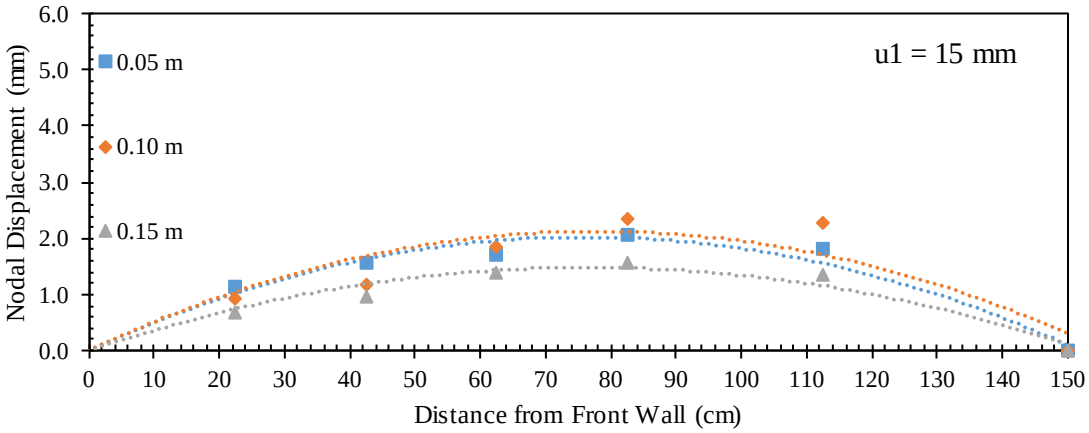

(b)

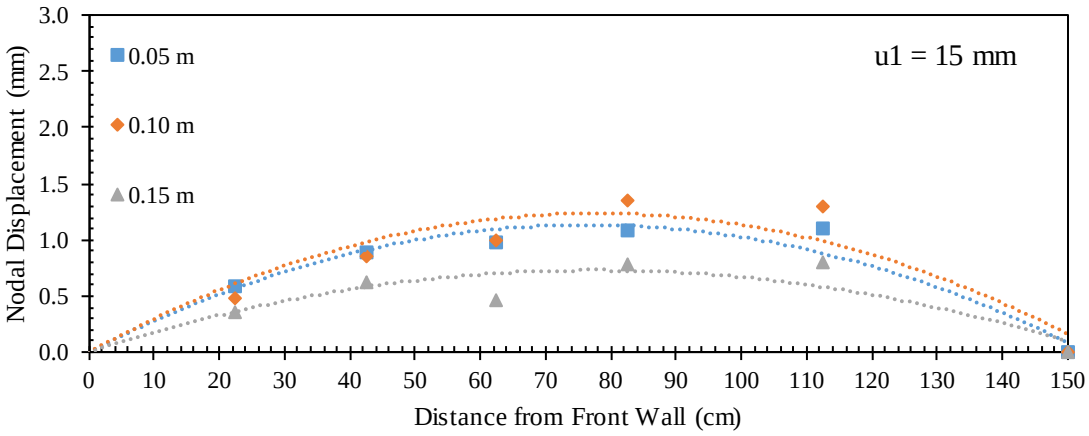

(c)

Figure 5.2.50. Reinforcement displacement profiles at frontal displacement u1 = 15 mm (0.6 in): (a) Active reinforcement; (b) Upper passive reinforcement; and (c) Lower passive reinforcement (σ_v = 21 kPa (3 psi)).

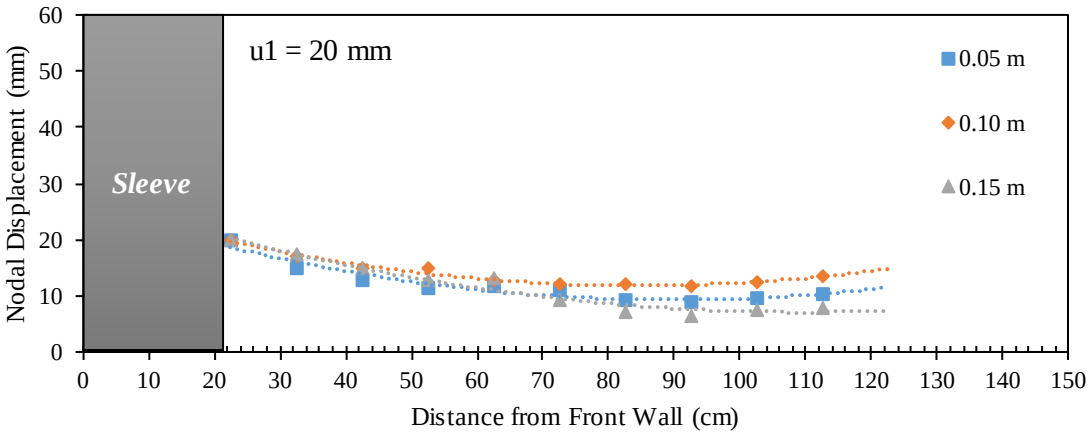

(a)

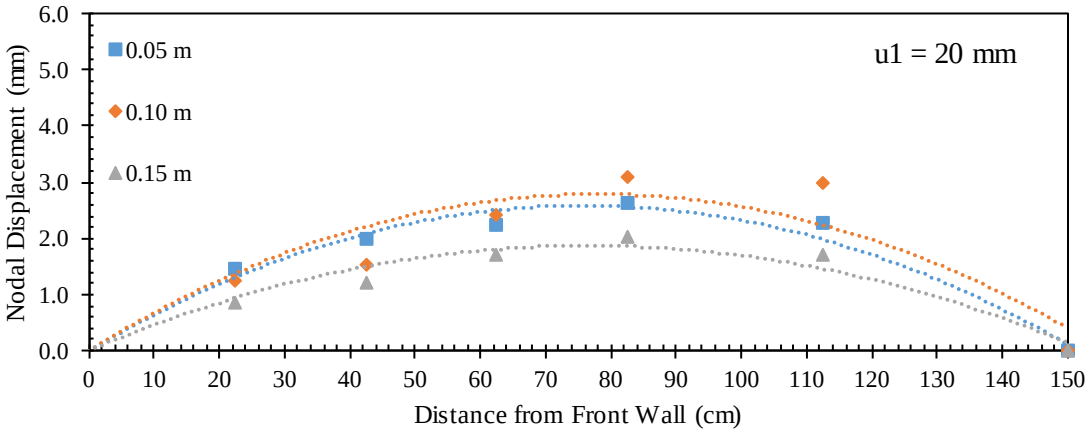

(b)

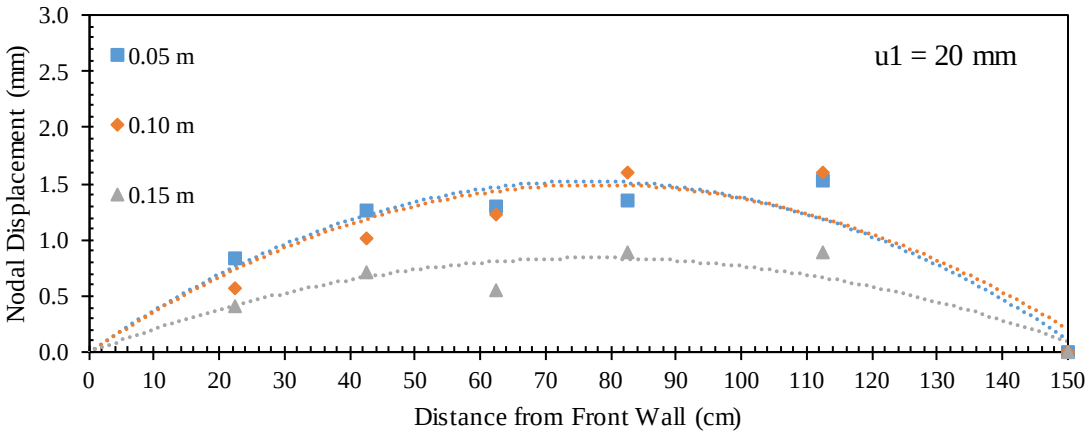

(c)

Figure 5.2.51. Reinforcement displacement profiles at frontal displacement u1 = 20 mm (0.8 in): (a) Active reinforcement; (b) Upper passive reinforcement; and (c) Lower passive reinforcement (σ_v = 21 kPa (3 psi)).

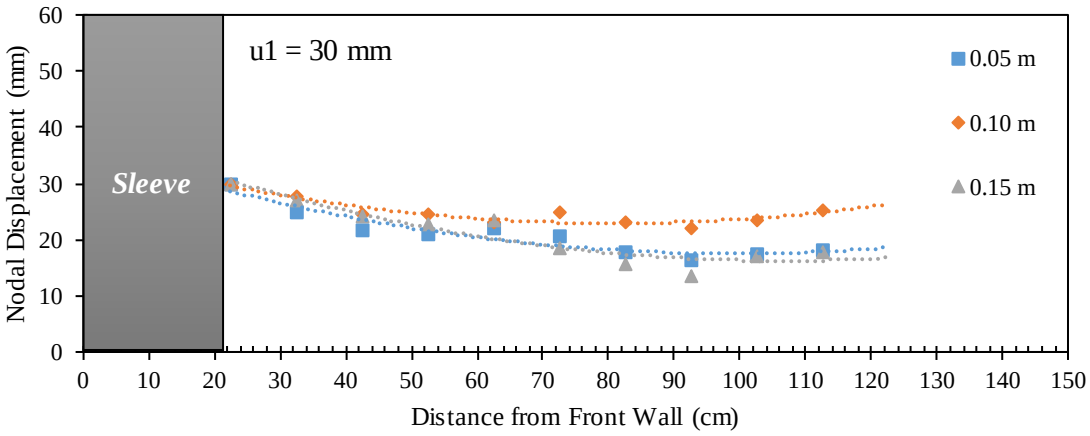

(a)

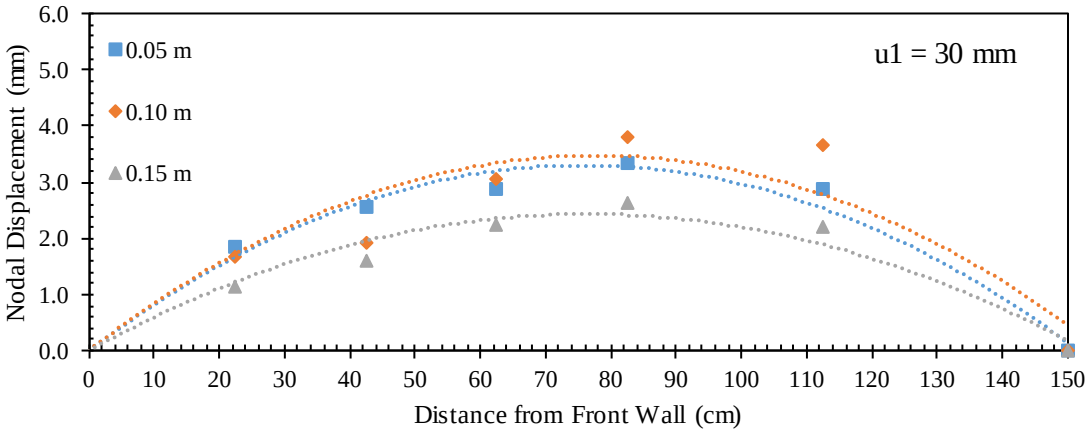

(b)

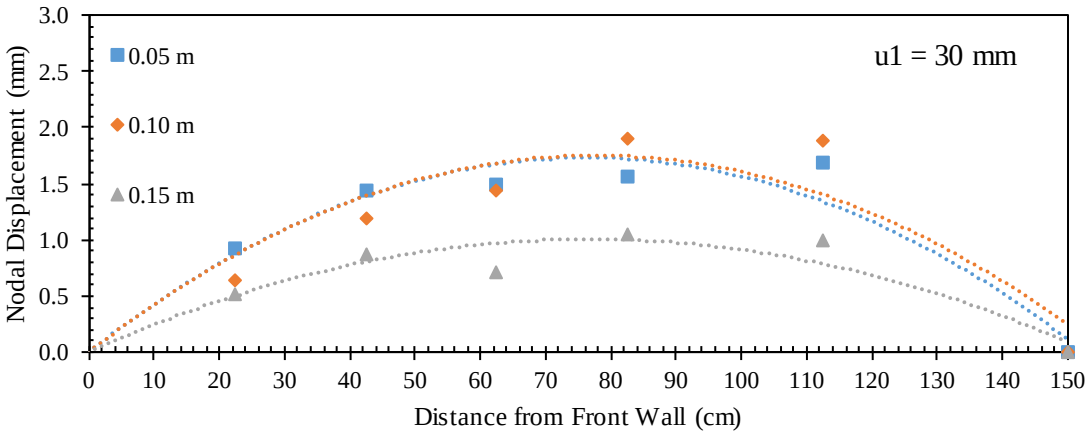

(c)

Figure 5.2.52. Reinforcement displacement profiles at frontal displacement u1 = 30 mm (1.2 in): (a) Active reinforcement; (b) Upper passive reinforcement; and (c) Lower passive reinforcement (σ_v = 21 kPa (3 psi)).

Figures 5.2.53 through 5.2.57 present the horizontal soil displacement measured for nodal displacements of 5, 10, 15, 20, and 30 mm (0.2, 0.4, 0.6, 0.8 and 1.2 in), respectively, for the tests conducted with confining normal stress of 50 kPa (7.3 psi). Similarly, Figures 5.2.58 through 5.2.62 present the horizontal soil displacement measured for nodal displacements of 5, 10, 15, 20, and 30 mm (0.2, 0.4, 0.6, 0.8 and 1.2 in), respectively, for the tests conducted with confining normal stress of 21 kPa (3 psi). Each figure consists of an a and b that show the soil displacement with respect nodal displacements *u1* and *u3*, respectively. These displacements were measured at specific locations by tracking artificial gravel particles making a vertical array within the soil at 0.305 m (1 ft.) from the front wall. Note that the soil adjacent to the reinforcement exhibited higher rate of displacement, which is due to yielding in the internal shear strength of the fill material that limits the load transfer from the reinforcement to larger distance away from the reinforcement.

It was observed that the horizontal soil displacement was higher in the tests conducted with reinforcements spaced at small spacings than that measured in the tests conducted with reinforcements spaced at large spacings. The active reinforcement delivers the load to the surrounding soil medium, which is then transferred to the passive reinforcements. The soil-reinforcement interfaces of the passive reinforcements have weaker shear strength than the internal strength of the soil. These weaker interfaces allow the soil in between the reinforcement layers to displace more than in the case of no passive reinforcements. However, the passive reinforcements reduce the load transfer from the active reinforcement to the soil masses on the other sides of the passive reinforcements.

Note that the active reinforcement in each test delivers the same load to the surrounding soil since the reinforcement spacing was found not to affect the soil-reinforcement interaction behavior of active reinforcements as discussed earlier in this section. That is, the same energy is delivered to the soil and the passive reinforcements in each test. For the tests conducted with reinforcements placed at small vertical spacings, the soil mass in between the active and passive reinforcements displaces more compared to that in the tests conducted with reinforcements placed at large vertical spacings as it receives more energy per unit soil volume from the active reinforcement. Conversely, the soil masses on the other sides of the passive reinforcements displaces less than that in the tests conducted with reinforcements placed at small vertical spacings.

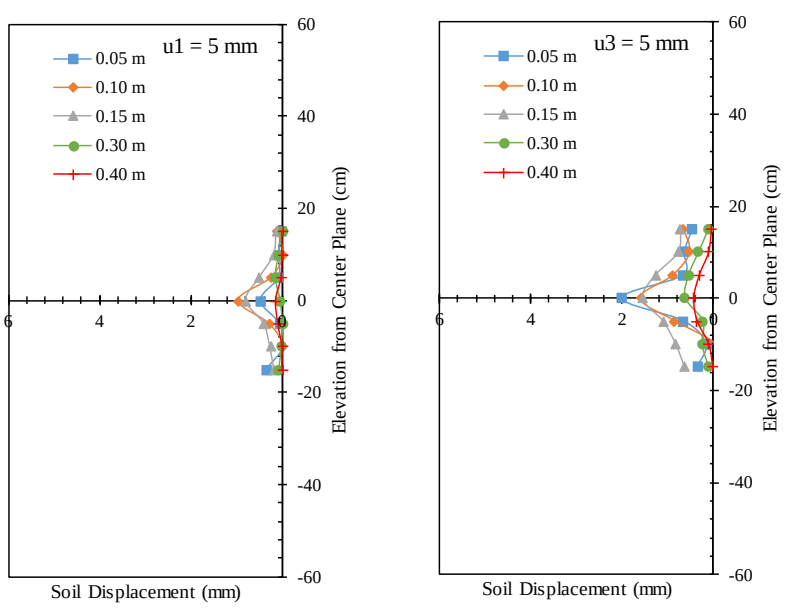

(a) **(b)**

Figure 5.2.53. Horizontal soil displacement profiles (measured by means of artificial gravel particles): (a) At nodal displacement u1 = 5 mm (0.2 in); and (b) At nodal displacement u3 = 5 mm (0.2 in) (σ_v = 50 kPa (7.3 psi)).

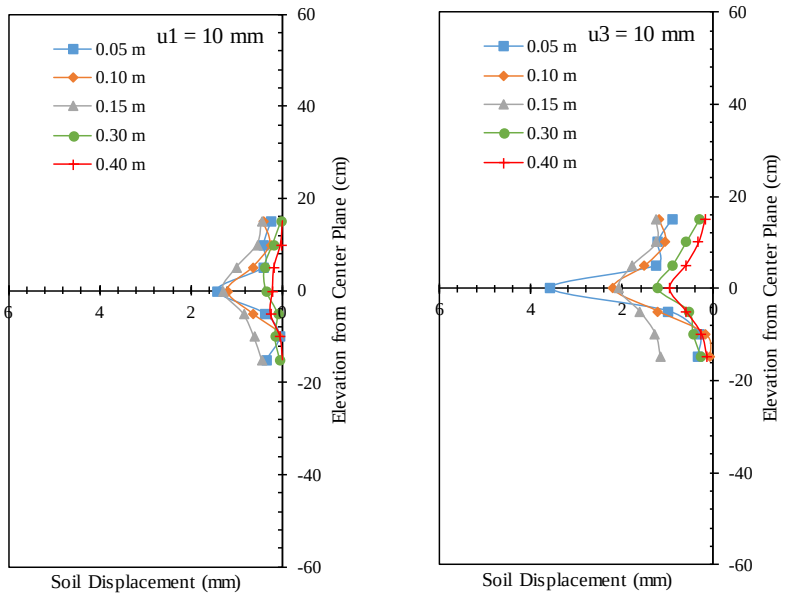

(a) **(b)**

Figure 5.2.54. Horizontal soil displacement profiles (measured by means of artificial gravel particles): (a) At nodal displacement u1 = 10 mm (0.4 in); and (b) At nodal displacement u3 = 10 mm (0.4 in) (σ_v = 50 kPa (7.3 psi)).

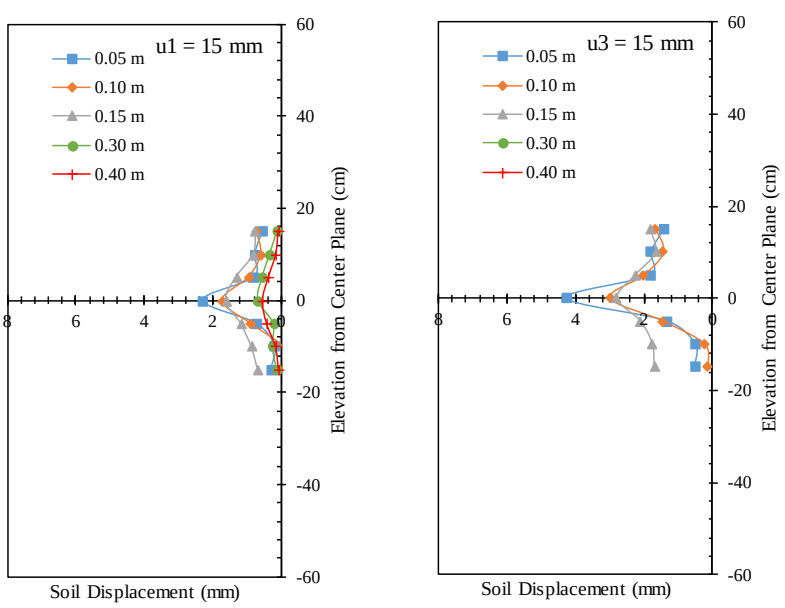

(a) **(b)**

Figure 5.2.55. Horizontal soil displacement profiles (measured by means of artificial gravel particles): (a) At nodal displacement u1 = 15 mm (0.6 in); and (b) At nodal displacement u3 = 15 mm (0.6 in) (σ_v = 50 kPa (7.3 psi)).

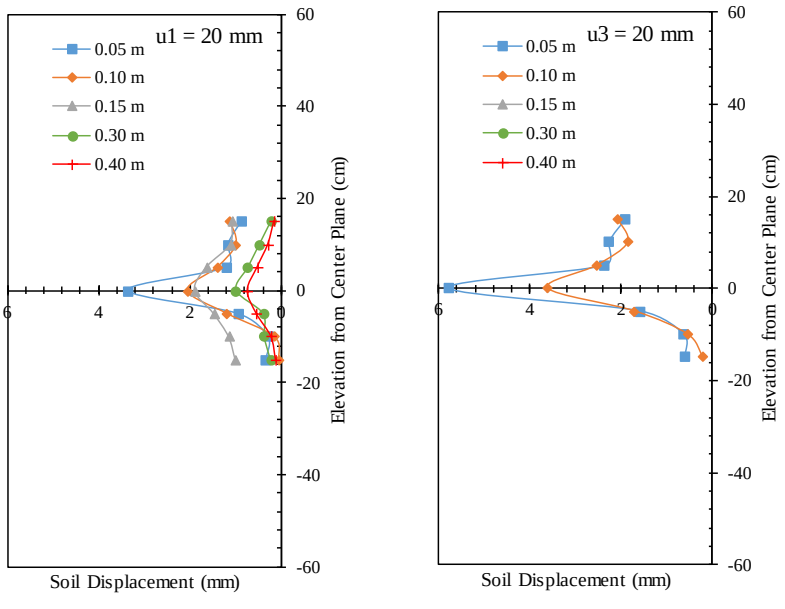

(a) **(b)**

Figure 5.2.56. Horizontal soil displacement profiles (measured by means of artificial gravel particles): (a) At nodal displacement u1 = 20 mm (0.8 in); and (b) At nodal displacement u3 = 20 mm (0.8 in) (σ_v = 50 kPa (7.3 psi)).

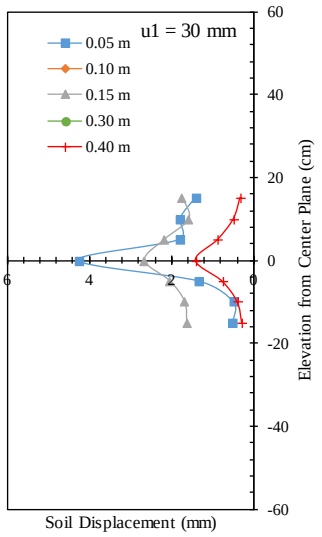

Figure 5.2.57. Horizontal soil displacement profiles (measured by means of artificial gravel particles): (a) At nodal displacement u1 = 30 mm (1.2 in) (σ_v = 50 kPa (7.3 psi)).

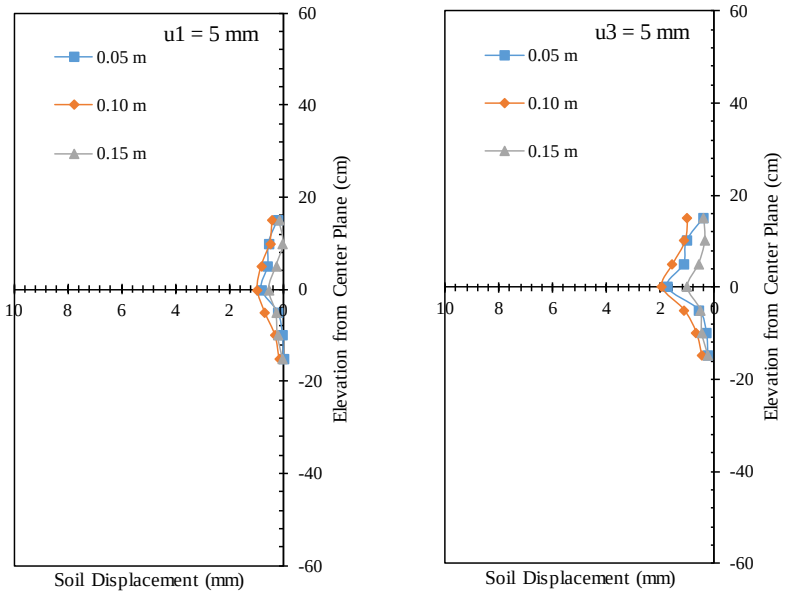

(a) **(b)**

Figure 5.2.58. Horizontal soil displacement profiles (measured by means of artificial gravel particles): (a) At nodal displacement u1 = 5 mm (0.2 in); and (b) At nodal displacement u3 = 5 mm (0.2 in) (σ_v = 21 kPa (3 psi)).

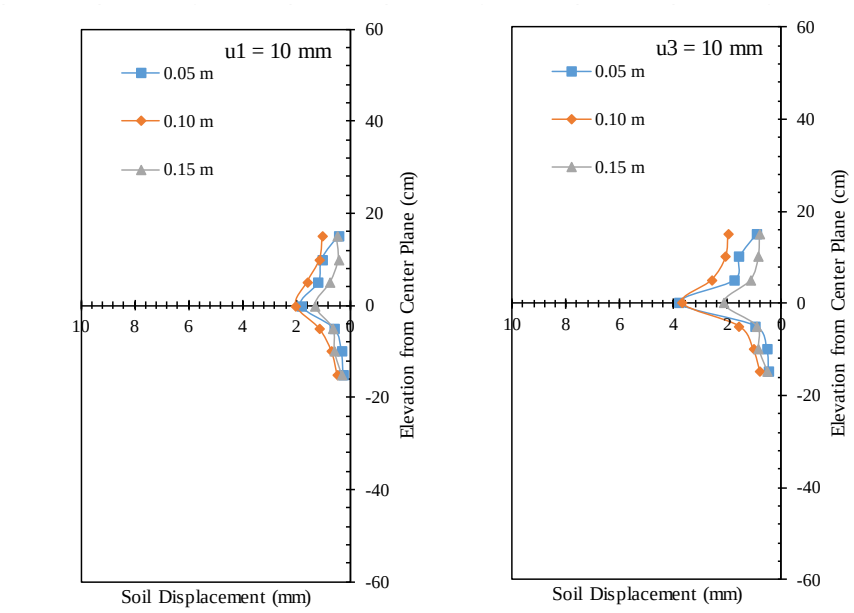

(a) **(b)**

Figure 5.2.59. Horizontal soil displacement profiles (measured by means of artificial gravel particles): (a) At nodal displacement u1 = 10 mm (0.4 in); and (b) At nodal displacement u3 = 10 mm (0.4 in) (σ_v = 21 kPa (3 psi)).

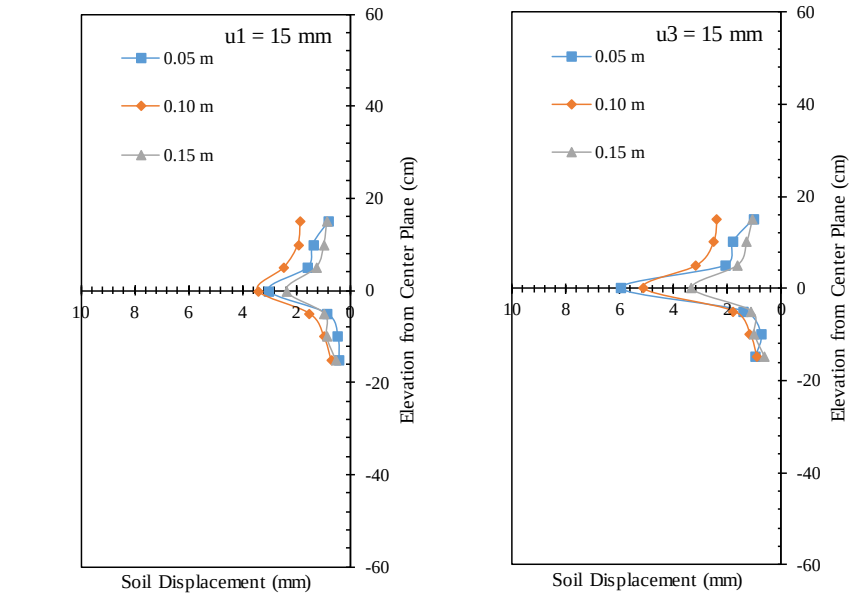

(a) **(b)**

Figure 5.2.60. Horizontal soil displacement profiles (measured by means of artificial gravel particles): (a) At nodal displacement u1 = 15 mm (0.6 in); and (b) At nodal displacement u3 = 15 mm (0.6 in) (σ_v = 21 kPa (3 psi)).

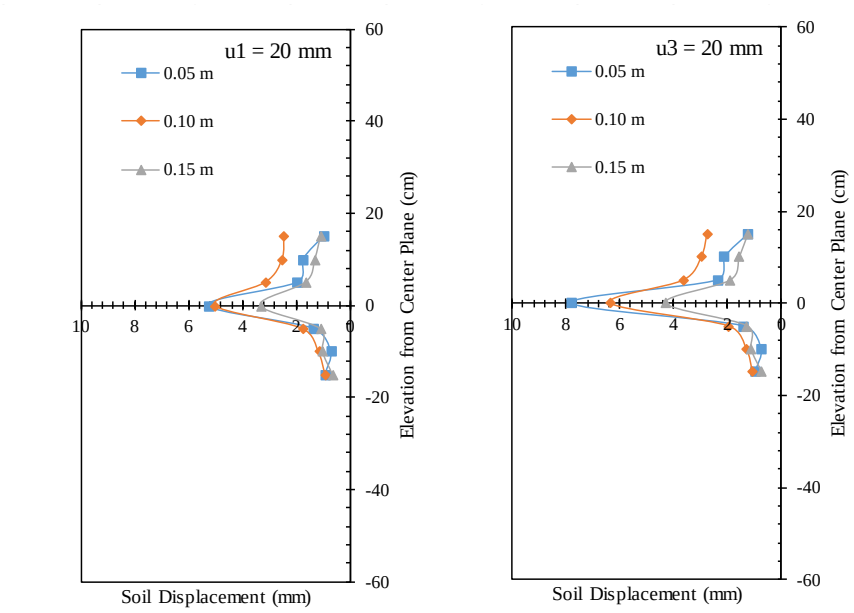

(a) **(b)**

Figure 5.2.61. Horizontal soil displacement profiles (measured by means of artificial gravel particles): (a) At nodal displacement u1 = 20 mm (0.8 in); and (b) At nodal displacement u3 = 20 mm (0.8 in) (σ_v = 21 kPa (3 psi)).

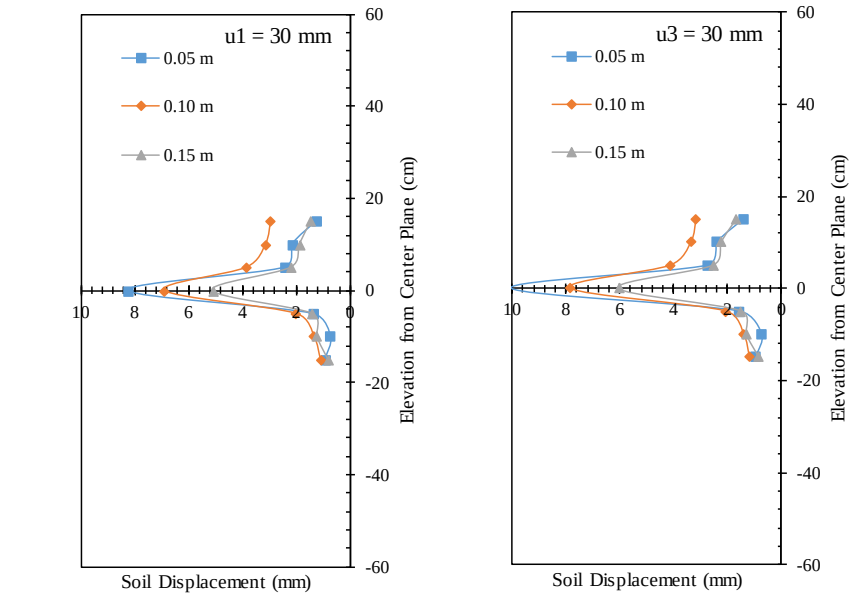

(a) **(b)**

Figure 5.2.62. Horizontal soil displacement profiles (measured by means of artificial gravel particles): (a) At nodal displacement u1 = 30 mm (1.2 in); and (b) At nodal displacement u3 = 30 mm (1.2 in) (σ_v = 21 kPa (3 psi)).

Figures 5.2.63a and 5.2.63b show the soil-reinforcement relative displacement at 0.305 m (1 ft.) from the front wall for tests conducted at confining stress of 50 and 21 kPa (7.3 and 3 psi),

respectively. This slippage was obtained by subtracting the reinforcement displacement at this location (by interpolation between *u1* and *u3*) and the soil displacement measured by the artificial gravel particle adjacent to the reinforcement (LP24). This figure exhibits the reduction in the soil-reinforcement interface shear stiffness during the test. It was observed that the slippage is higher in tests conducted with reinforcements placed at large vertical spacings compared to that in tests conducted with reinforcements placed at small vertical spacings. The displacement of the soil adjacent to the reinforcements in the tests conducted with reinforcements placed at small vertical spacings is higher than that in the tests conducted with reinforcements placed at large vertical spacings. Meanwhile, the reinforcement displacement is the same in all tests regardless the reinforcement vertical spacing. Figure 5.2.64 shows the effect of reinforcement vertical spacing on the sensitivity of soil-reinforcement slippage to confining normal stress. No difference in slippage was observed at early pullout loading stages between tests conducted at confining stress of 50 kPa (7.3 psi).

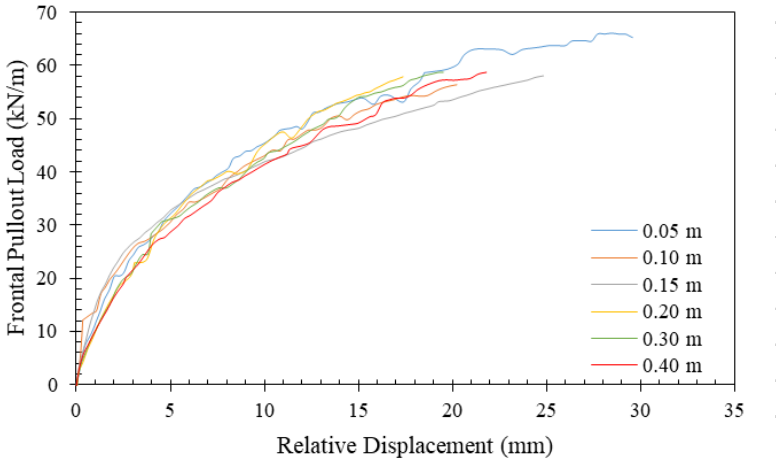

(a)

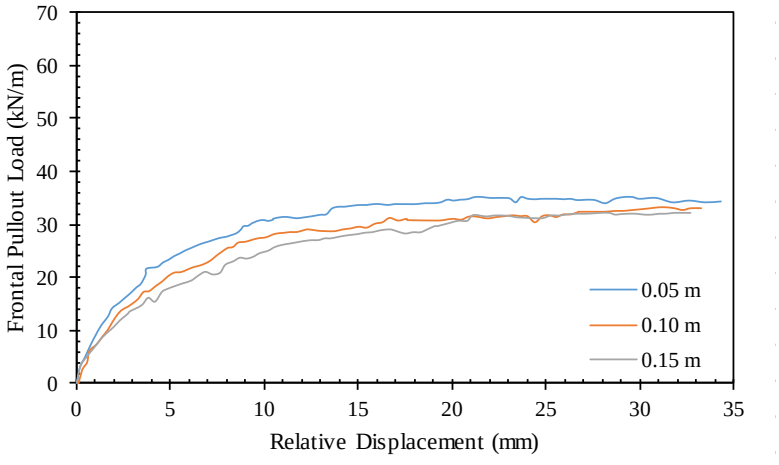

(b)

Figure 5.2.63. Soil-reinforcement relative displacement for tests conducted with reinforcement placed at different spacings: (a) σ_v = 50 kPa (7.3 psi); and (b) σ_v = 21 kPa (3 psi).

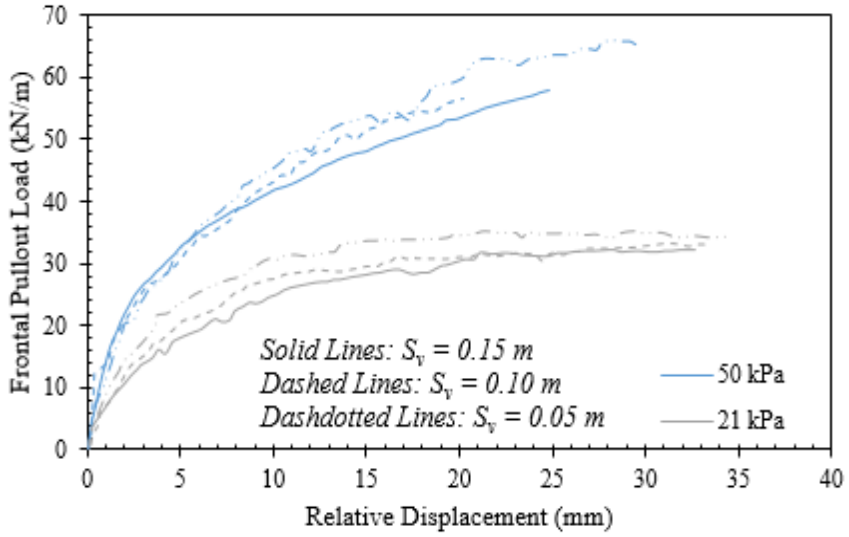

Figure 5.2.64. Soil-reinforcement relative displacement.

Figures 5.2.65 and 5.2.66 show the vertical soil displacement measured by means of the artificial gravel particles placed on top of the reinforced soil mass for tests conducted at confining normal stress of 50 and 21 kPa (7.3 and 3 psi), respectively. Each figure consists of a, b, and c subfigures that show the soil displacement with respect to reinforcement frontal displacement of the active reinforcement *u1* for the back, middle, and front of the reinforced soil mass, respectively. The figures include tests conducted with reinforcements placed at various vertical spacings. It was observed that the soil tends to dilate near the front and settle near the back as pullout loading progressed. The dilation tendency near the front takes place after settlement in early loading stages as shear stresses are generated at the soil-reinforcement interface. It was observed that the dilation tendency is higher in the tests conducted with reinforcements placed at smaller spacings compared to that in the tests conducted with reinforcements placed at large spacings. Note that the dilation tendency is high in tests conducted at low confining stresses compared to those conducted at high confining stresses. That is, the impact of reinforcement vertical spacing on the soil-reinforcement behavior was more pronounced in the tests conducted at 21-kPa (3 psi) confining stress.

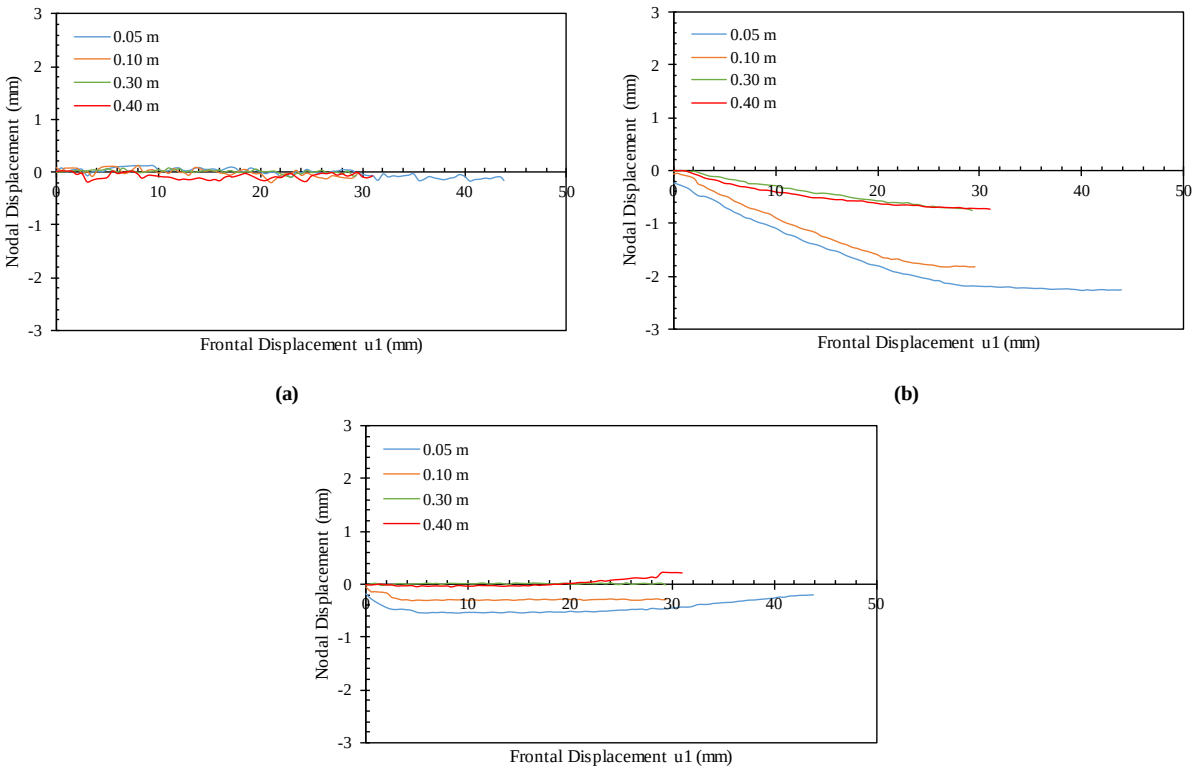

Figure 5.2.65. Vertical soil displacements profiles (measured by means of artificial gravel particles) with respect to frontal displacement at the active reinforcement: (a) At the back of the soil mass; (b) At the middle of the soil mass; and (c) At the front of the soil mass (σ_v = 50 kPa (7.3 psi)).

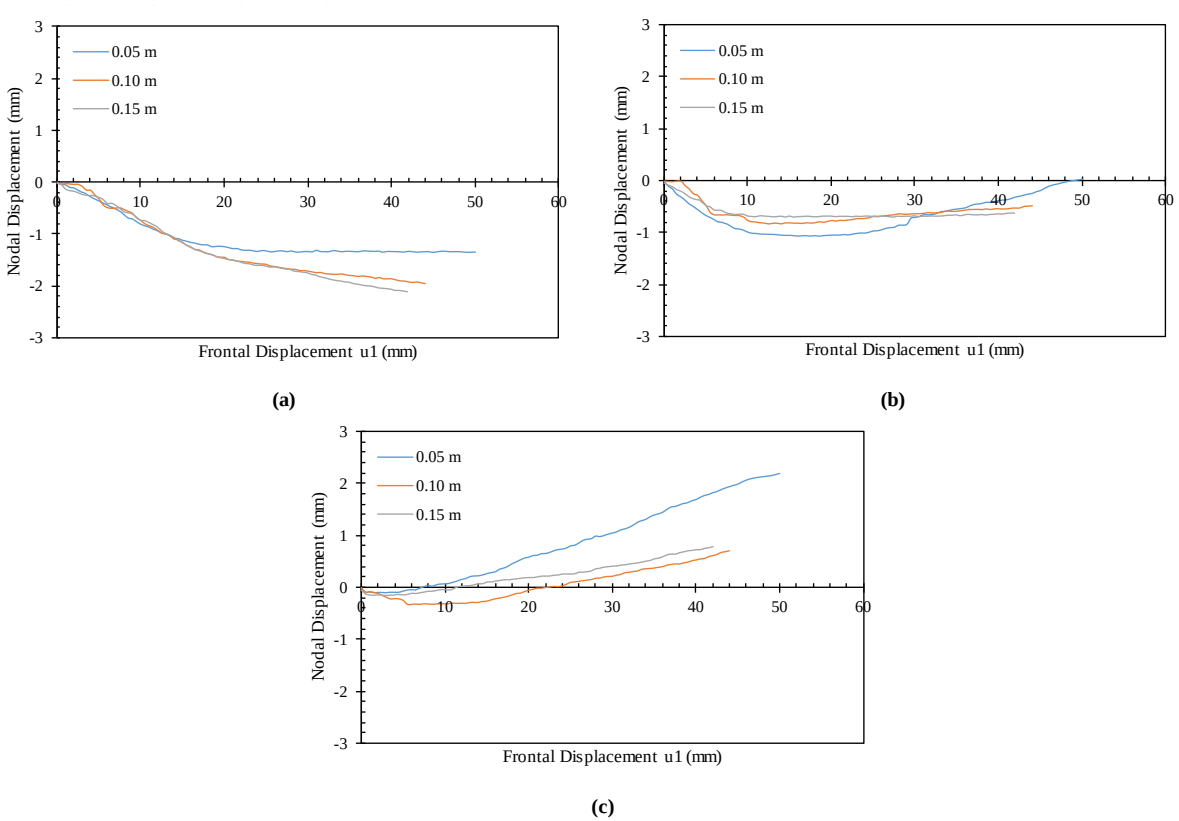

Figure 5.2.66. Vertical soil displacements profiles (measured by means of artificial gravel particles) with respect to frontal displacement at the active reinforcement: (a) At the back of the soil mass; (b) At the middle of the soil mass; and (c) At the front of the soil mass (σ_v = 21 kPa (3 psi)).

5.2.3.4 EFFECT OF REINFORCEMENT PROPERTIES

In order to assess the effect of reinforcement properties (type, tensile stiffness, soil-reinforcement interaction, and ultimate strength) on the interaction between the contiguous reinforcement layers in GRS structures, the testing program included tests conducted at the same testing conditions using various reinforcement types. Specifically, six tests were conducted using AASHTO #8 fill material and three reinforcement layers placed at a vertical spacing of 0.15 m (6 in.). The confinement at the active (middle) reinforcement layer was 15 kPa (2.25 psi) for two tests and 21 kPa (3 psi) for the other four tests. This confinement was selected to allow ultimate pullout failure to occur for most of the reinforcement types. This allowed investigating the soil-reinforcement interaction over a wider range of deformation up to (or close to) pullout failure.

The reinforcements involved in the six tests were (1) HP570 woven polypropylene geotextile with Tu = 70 kN/m (400 lbs/in) at 10% strain strain (approximately J = 1098 kN/m (6270 lbs/in))_ ; (2) RS580i woven polypropylene geotextile with T_u = 70 kN/m (400 lbs/in) at 5% tensile strain (approximately, J = 1400 kN/m (7994 lbs/in)); (3) BX1100 extruded (rigid) polypropylene biaxial geogrid with T_u = 13.4 kN/m (76.5 lbs/in) at 5% tensile strain (approximately, J = 268 kN/m (1530 lbs/in)) and 19.0 kN/m (108.5 lbs/in) at failure; (4) BX1200 extruded (rigid) polypropylene geogrid with T_u = 19.6 kN/m (112 lbs/in) at 5% tensile strain (approximately, J = 392 kN/m (2238 lbs/in)) and 28.8 kN/m (164.5 lbs/in) at failure; and (5) 80T knitted (flexible) polyester uniaxial geogrid with T_u = 45.7 kN/m (261 lbs/in) at 5% tensile strain (approximately, J = 914 kN/m (5219 lbs/in)) and 89.6 kN/m (511.6 lbs/in) at failure. Reinforcements (1) and (3) were tested at 15-kPa (2.25-psi) confinement and reinforcements (1), (2), (4), and (5) were tested at 21-kPa (3-psi) confinement. Table 5.2.5 summarizes the tests in which reinforcement type was varied.

Table 5.2.5. Summary of tests in which reinforcement type was varied.

Test ID	***Testing Variables***					
	Fill Material	***S_v***	***σ_v***	***Active GS***	***Passive GS***	***Dilation***
GP-06-03-G1-G	AASHTO No. 8			HP570	HP570	
GP-06-03-G2-G	AASHTO No. 8			RS580i	RS580i	
GP-06-03-G4-G	AASHTO No. 8	0.15 m	21 kPa	BX1200	BX1200	Allowed
GP-06-03-G5-G	AASHTO No. 8			80T	80T	
SP-06-03-G1-G	Monterey No. 30			HP570	HP570	

*Conversions: 1 m = 0.0254 in.
1 kPa = 20.89 psf

The comparisons were conducted to evaluate one reinforcement property. Three comparisons were made: (1) a comparison between HP570 and RS580i reinforcements to evaluate the effect of reinforcement tensile stiffness; (2) a comparison between HP570 and 80T reinforcements to compare the behavior of geotextiles and geogrids; and (3) a comparison between 80T and BX1200 to evaluate the effect of reinforcement rigidity.

5.2.3.4.1 HP570 geotextile versus RS580i geotextile

This comparison was conducted between two woven geotextile reinforcements made of polypropylene (same material) and produced by the same manufacturer. Both materials have the same ultimate tensile strength 70 kN/m (400 lbs/in). The major difference between both materials is the tensile stiffness and the fabric rigidity. The tensile stiffness for HP570 (XMD) and RS580i (XMD) is 876 and 1400 kN/m (5002 and 7994 lbs/in) at 5% tensile strain, respectively. In addition, RS580i is more rigid due to the high tenacity polly propylene polymer used to manufacturer this geotextile. Its longitudinal and transversal yarns are also more integrated compared to HP570. Figure 5.2.67 shows the frontal pullout load-displacement experimental curves for both tests. It was observed that both curves coincide up to 10-mm (0.4 in) frontal displacement. However, beyond the 10-mm (0.4 in) frontal displacement, RS580i exhibited lower pullout resistance. This observation revealed information about the soil-reinforcement interface shear behavior for both reinforcements with the AASHTO No. 8 aggregate used in the tests. The interface shear stiffness might be very similar for both reinforcements, however, the interface shear strength is larger for the HP570 compared to the RS580i. This is attributed to the fabric rigidity that plays a significant role in the interaction between the fabric and the surrounding soil medium that adds additional resistance to the interface friction. Forensic investigation of the reinforcement layers after the test completion revealed many perforations between filaments in the HP570 fabric that resulted from the adjacent gravel particles. This type of interaction resembles the interaction takes place due to passive resistance of transverse ribs in geogrid reinforcements. On contrary, such perforations were not clear in the RS580i fabric due to the high integration and fabric rigidity it possesses.

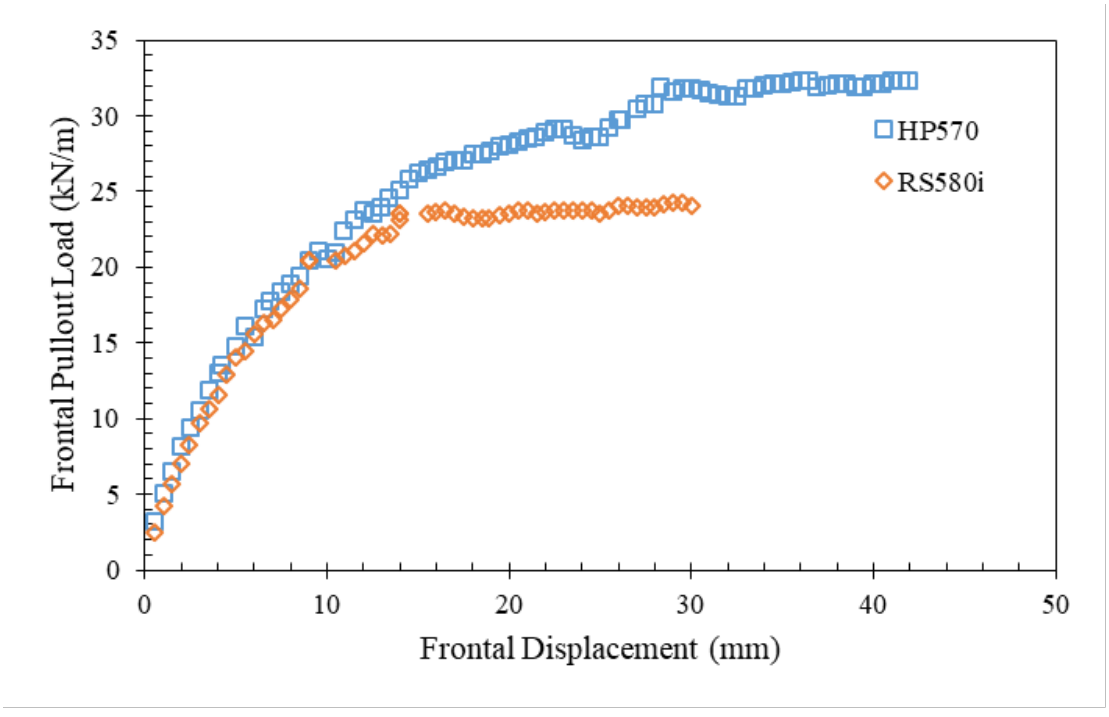

Figure 5.2.67. Frontal pullout load-displacement curves.

Figures 5.2.68 and 5.2.69 present the nodal displacement for the upper and lower passive reinforcement layers, respectively. Specifically, Figures 5.2.68a through 5.2.69d show the nodal displacements in the upper passive reinforcement corresponding to nodal displacements in the active reinforcement *u1*, *u3*, *u5*, and *u7*, respectively. Similarly, Figures 5.2.69a through 5.2.69d show the nodal displacements in the lower passive reinforcement corresponding to nodal displacements in the active reinforcement *u1*, *u3*, *u5*, and *u7*, respectively. Figures 5.2.68 and 5.2.69 reveal the load transfer from the active reinforcement to the passive reinforcements at the same nodal reinforcement of the active reinforcement; i.e., the same soil-reinforcement interface shear displacement.

It was observed that the relationship between the nodal displacements for of the passive reinforcements are linear with the nodal displacements of the active reinforcement at early loading stages. This relationship then become non-linear as the load-displacement relationship of the active reinforcement curves. That is, Figures 5.2.68 and 5.2.69 reflect the reduction in shear stiffness at the soil-reinforcement interface. It was observed that HP570 has a lower rate of interface shear stiffness reduction, which result in reduction of interaction with the neighboring reinforcement layers, compared to that of RS508i.

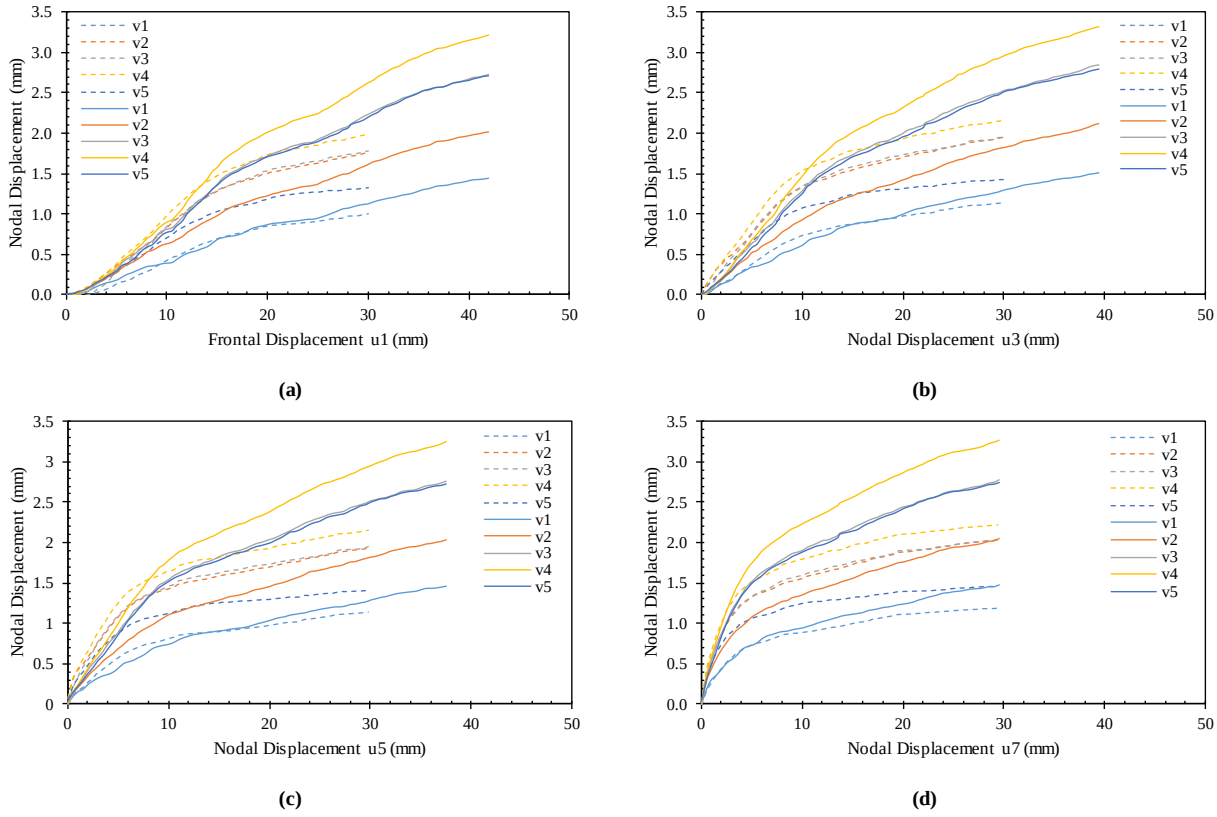

Figure 5.2.68. Nodal displacements at the upper passive reinforcement with respect to various nodal displacements at the active reinforcement: (a) nodal displacement u1; (b) nodal displacement u3; (c) nodal displacement u5; and (d) nodal displacement u7 (solid lines belong to HP570 and dashed lines belong to RS580i).

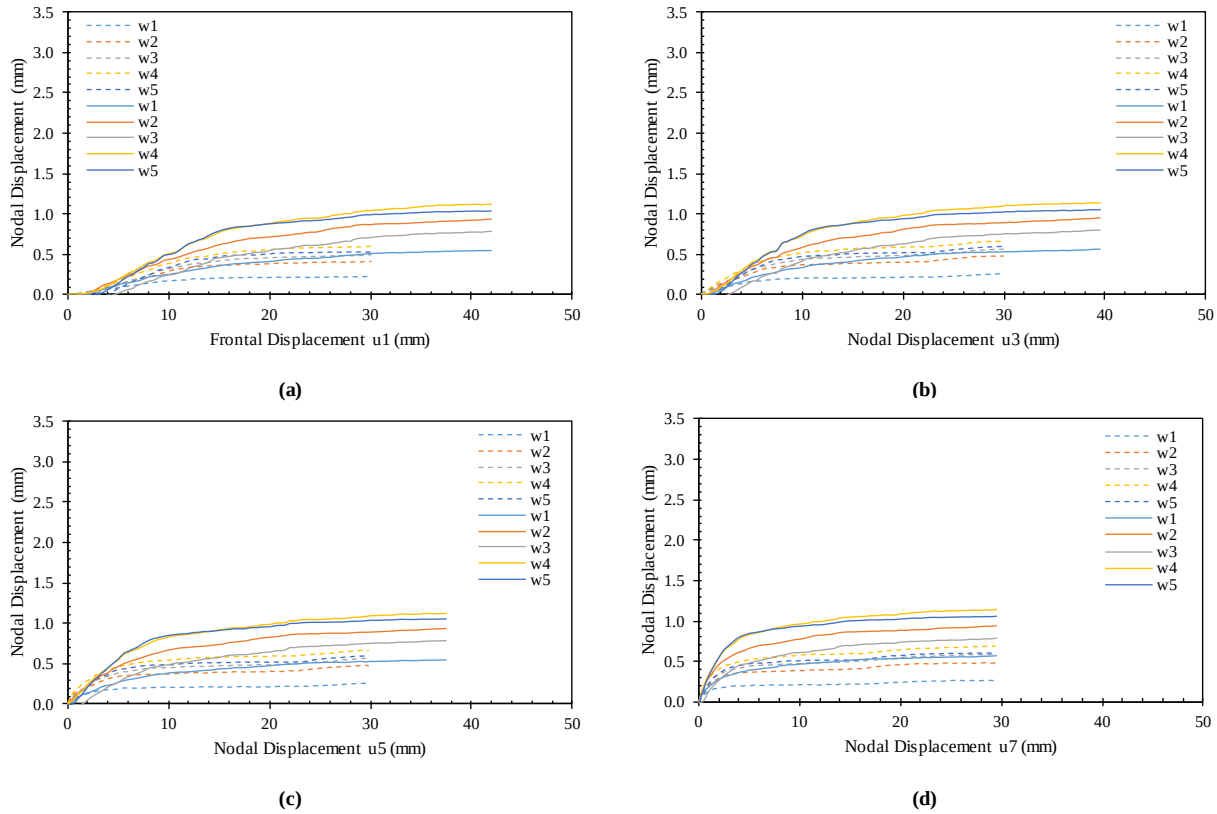

Figure 5.2.69. Nodal displacements at the lower passive reinforcement with respect to various nodal displacements at the active reinforcement: (a) Nodal displacement u1; (b) Nodal displacement u3; (c) Nodal displacement u5; and (d) Nodal displacement u7 (solid lines belong to HP570 and dashed lines belong to RS580i).

Figures 5.2.70 through 5.2.74 show the displacement profiles for the active and passive reinforcement layers at active reinforcement frontal displacement (*u1*) of 5, 10, 15, 20, and 30 mm (1.2 in). The displacement profiles for both reinforcement types, HP570 and RS580i, are very similar up to frontal displacement of 30 mm (1.2 in). Similar observation was made for the displacement profiles of the passive reinforcement layers. However, the measured displacements of the passive reinforcements were higher in case of HP570 reinforcement compared to those measured for the RS580i reinforcement. This is because the reduction in the soil-reinforcement interface shear strength in the case of RS580i reinforcement beyond frontal displacement of 10 mm (0.4 in). That is, the higher the soil-reinforcement interface shear strength, the higher the ability of the reinforcement to transfer load to the soil and the neighboring reinforcement layers for a given soil medium and confinement level.

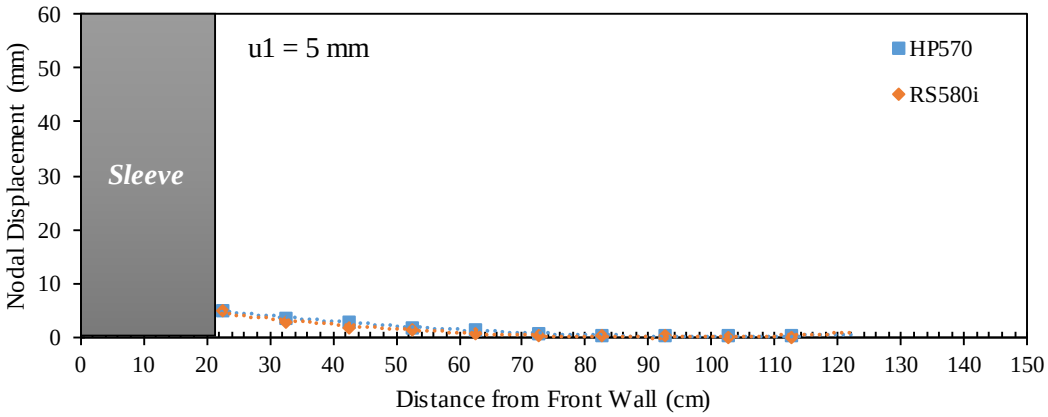

(a)

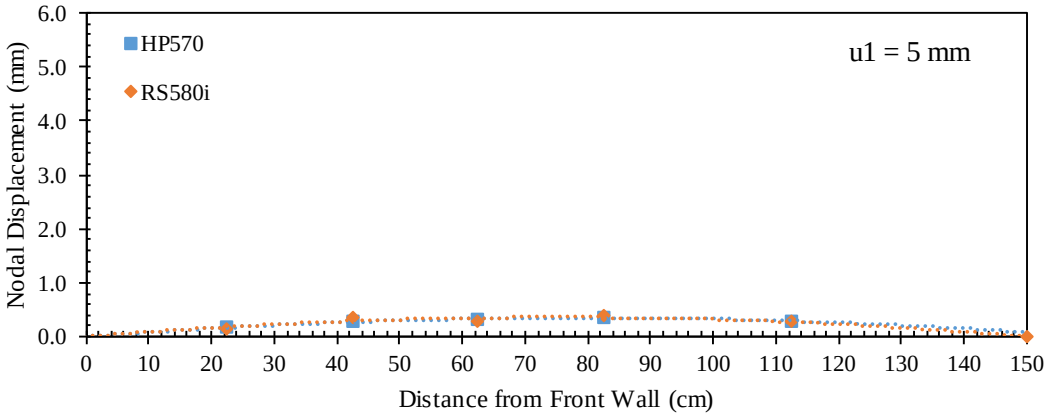

(b)

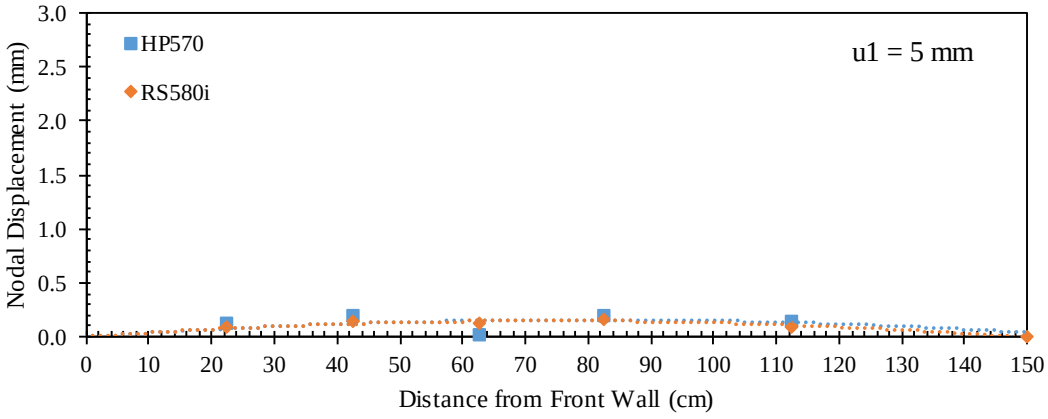

(c)

Figure 5.2.70. Reinforcement displacement profiles at frontal displacement u1 = 5 mm (0.2 in): (a) Active reinforcement; (b) Upper passive reinforcement; and (c) Lower passive reinforcement.

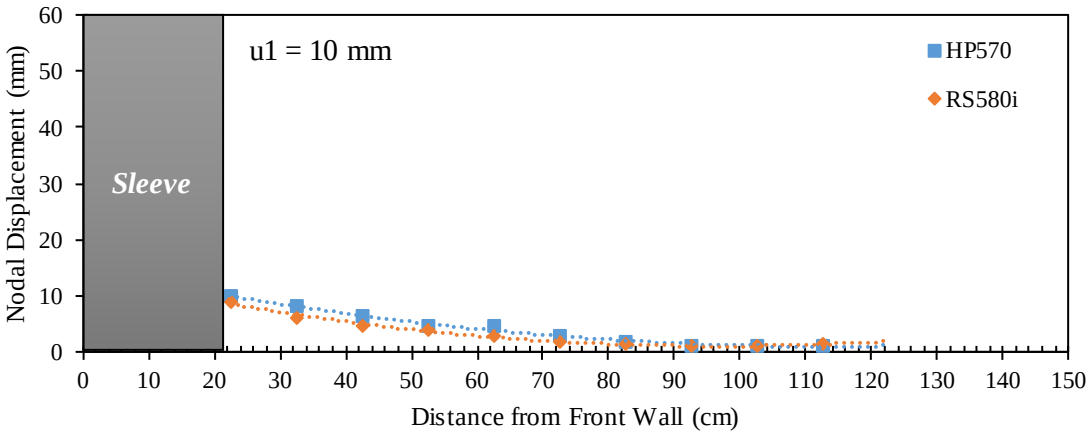

(a)

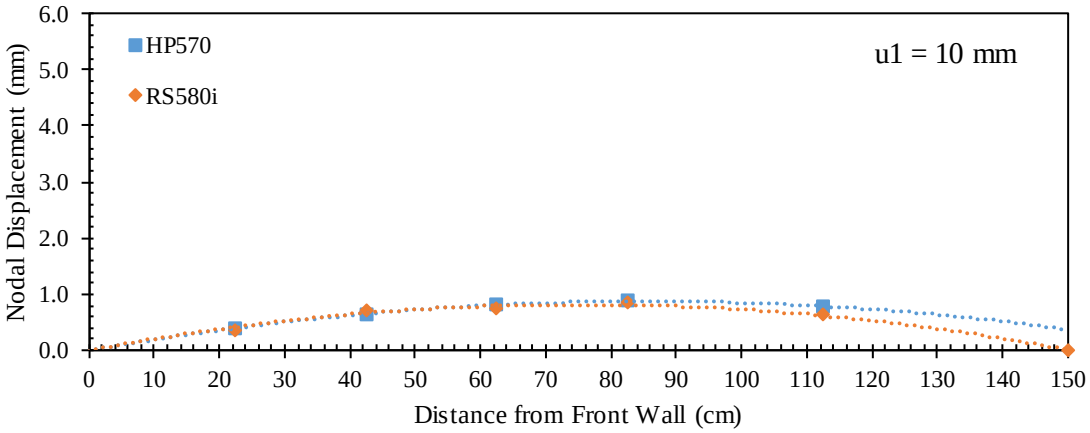

(b)

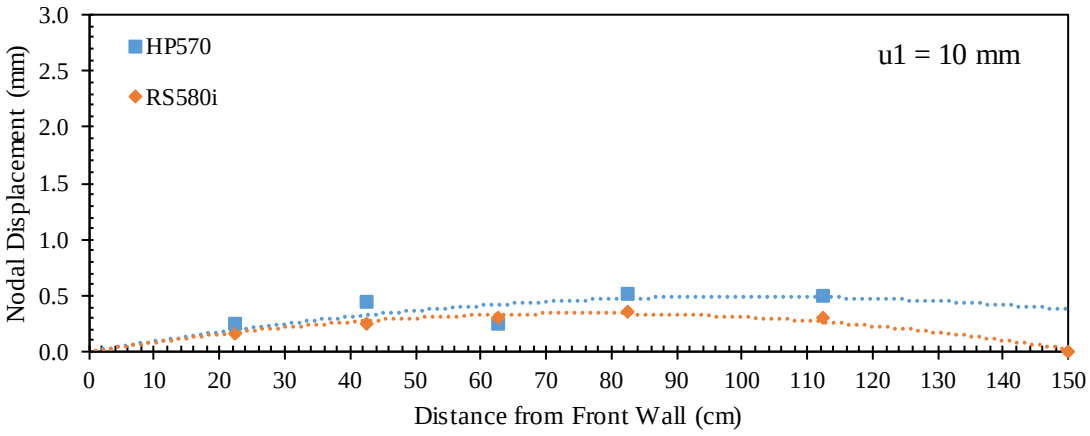

(c)

Figure 5.2.71. Reinforcement displacement profiles at frontal displacement u1 = 10 mm (0.4 in): (a) Active reinforcement; (b) Upper passive reinforcement; and (c) Lower passive reinforcement.

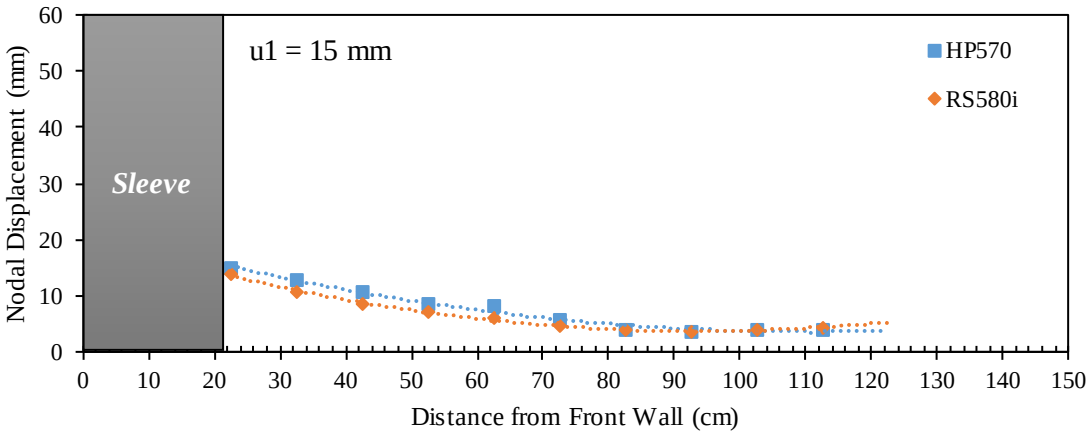

(a)

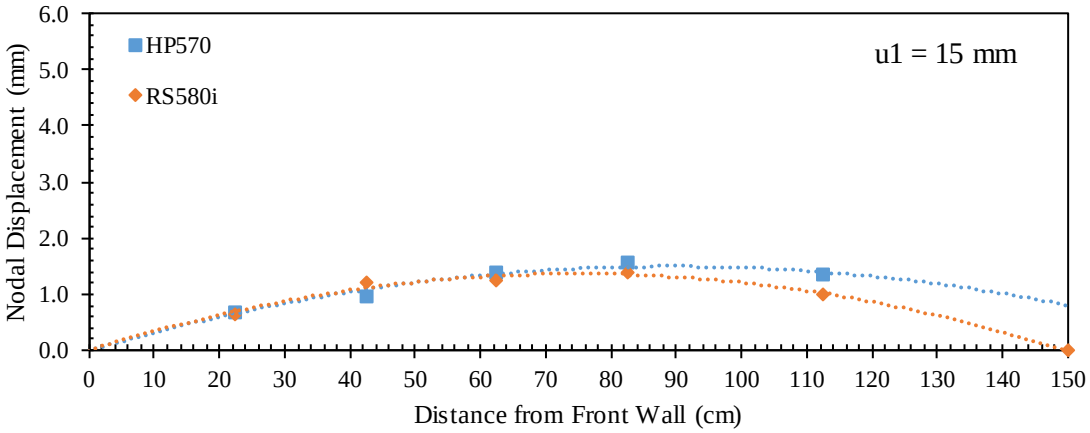

(b)

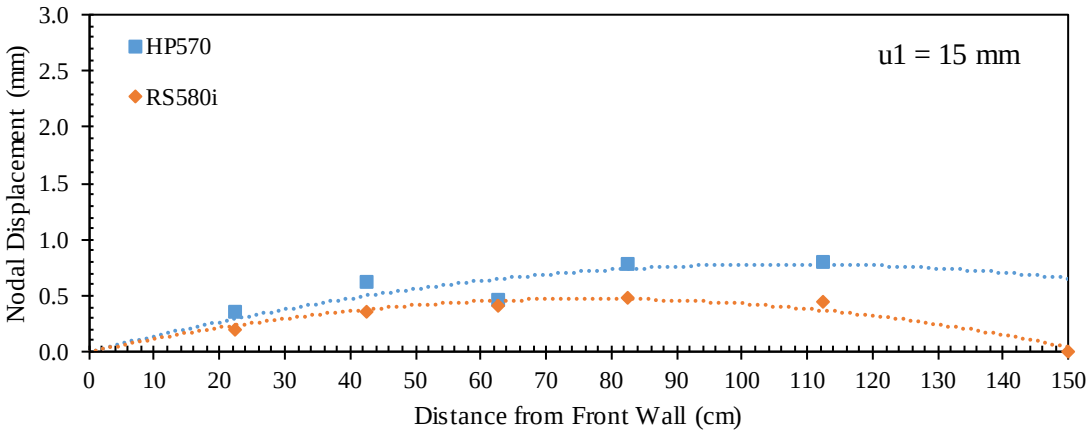

(c)

Figure 5.2.72. Reinforcement displacement profiles at frontal displacement u1 = 15 mm (0.6 in): (a) Active reinforcement; (b) Upper passive reinforcement; and (c) Lower passive reinforcement.

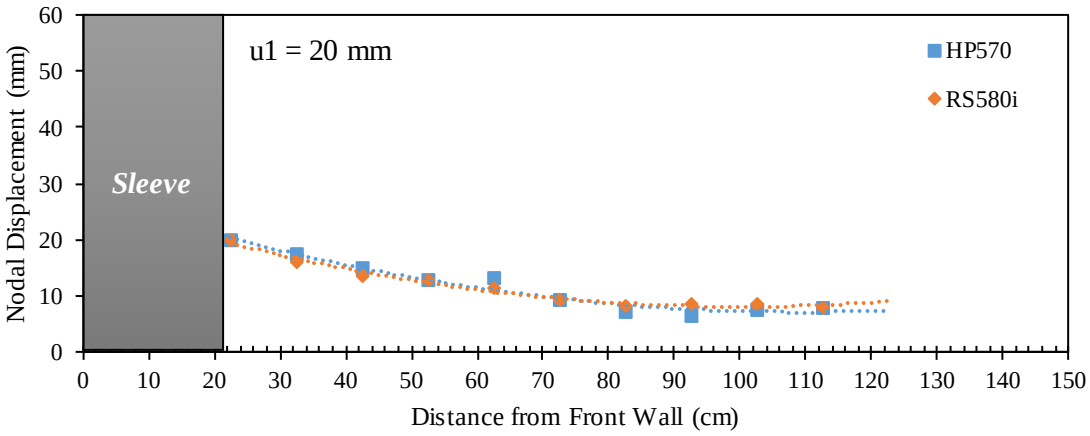

(a)

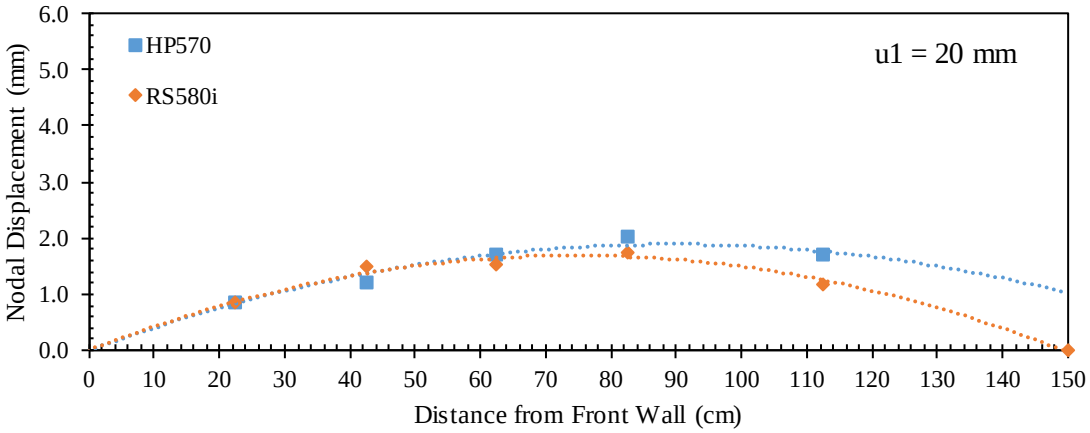

(b)

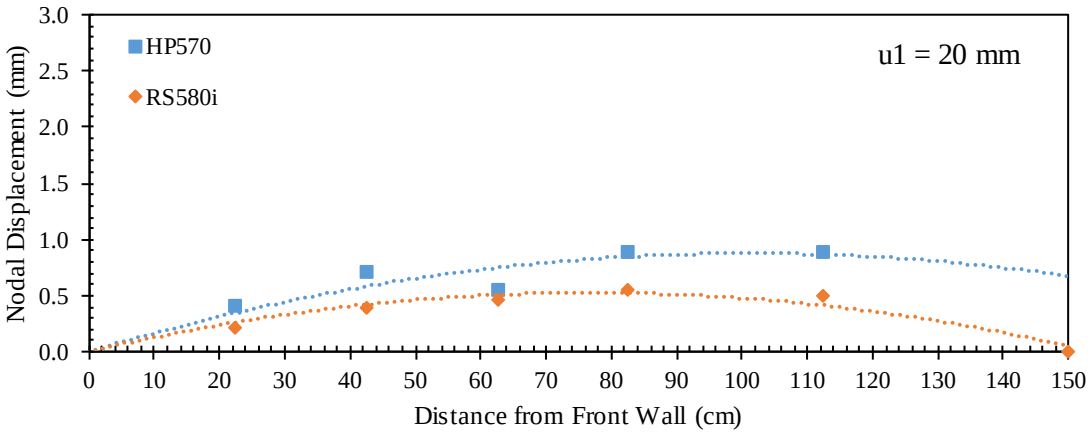

(c)

Figure 5.2.73. Reinforcement displacement profiles at frontal displacement u1 = 20 mm (0.8 in): (a) Active reinforcement; (b) Upper passive reinforcement; and (c) Lower passive reinforcement.

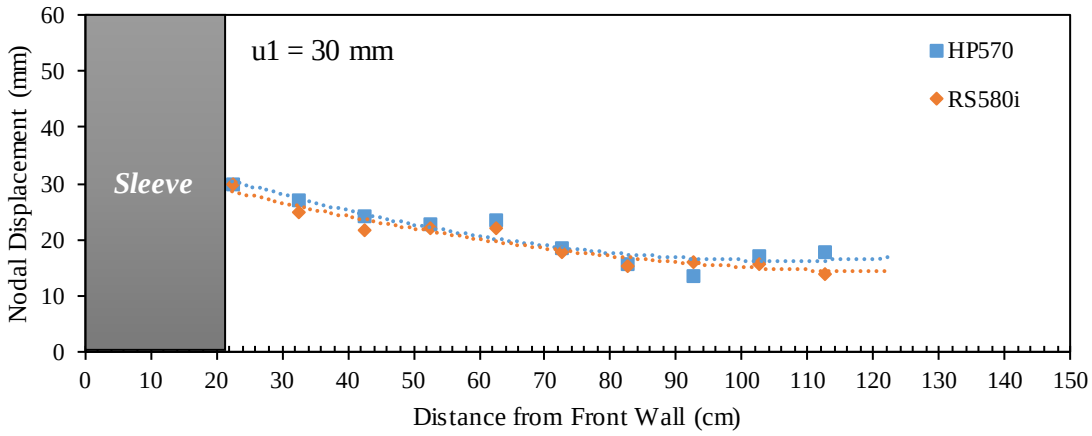

(a)

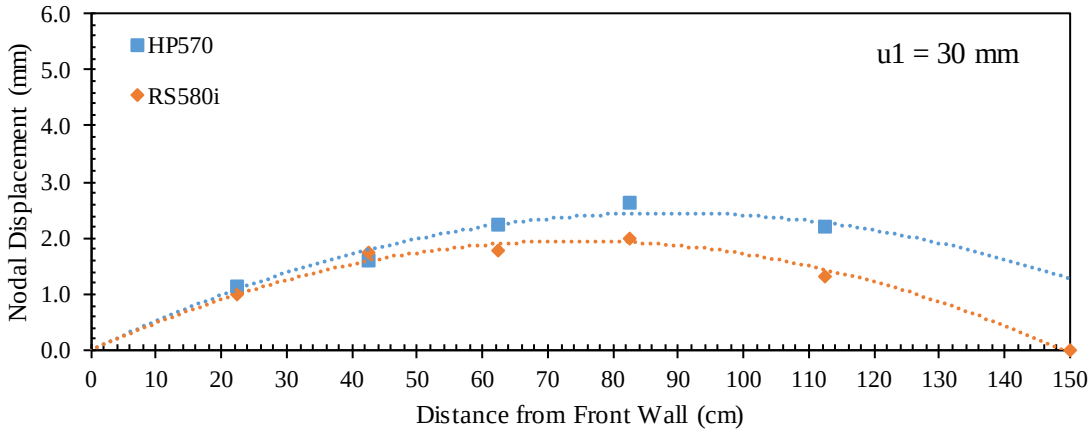

(b)

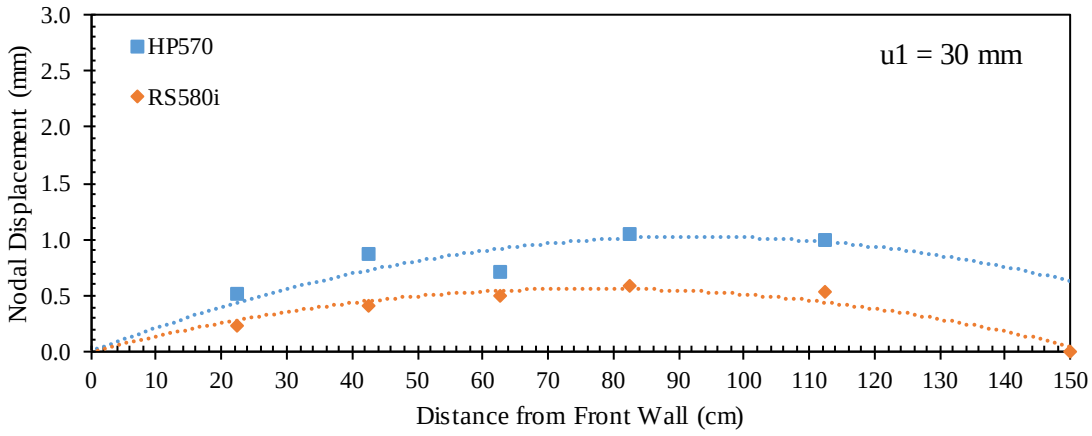

(c)

Figure 5.2.74. Reinforcement displacement profiles at frontal displacement u1 = 30 mm (1.2 in): (a) Active reinforcement; (b) Upper passive reinforcement; and (c) Lower passive reinforcement.

Figures 5.2.75 through 5.2.79 present the horizontal soil displacement measured for nodal displacements of 5, 10, 15, 20, and 30 mm (0.2, 0.4, 0.6, 0.8 and 1.2 in), respectively. Each figure consists of a and b that show the soil displacement with respect nodal displacements *u1* and *u3*, respectively. These displacements were measured at specific locations by tracking artificial gravel particles making a vertical array within the soil at 0.305 m (1 ft.) from the front wall. It was observed that the soil displacement is very similar for the HP570 and RS580i reinforcements at early stages, up to nodal displacements of 10 mm (0.4 in), until a difference appeared in the soil-reinforcement interface shear strength. Thereafter, soil displacements measured in case of the HP570 were higher than those measured in case of the RS580i. Note that the soil adjacent to the reinforcement exhibited higher rate of displacement, which is due to yielding in the internal shear strength of the fill material that limits the load transfer from the reinforcement to larger distance away from the reinforcement.

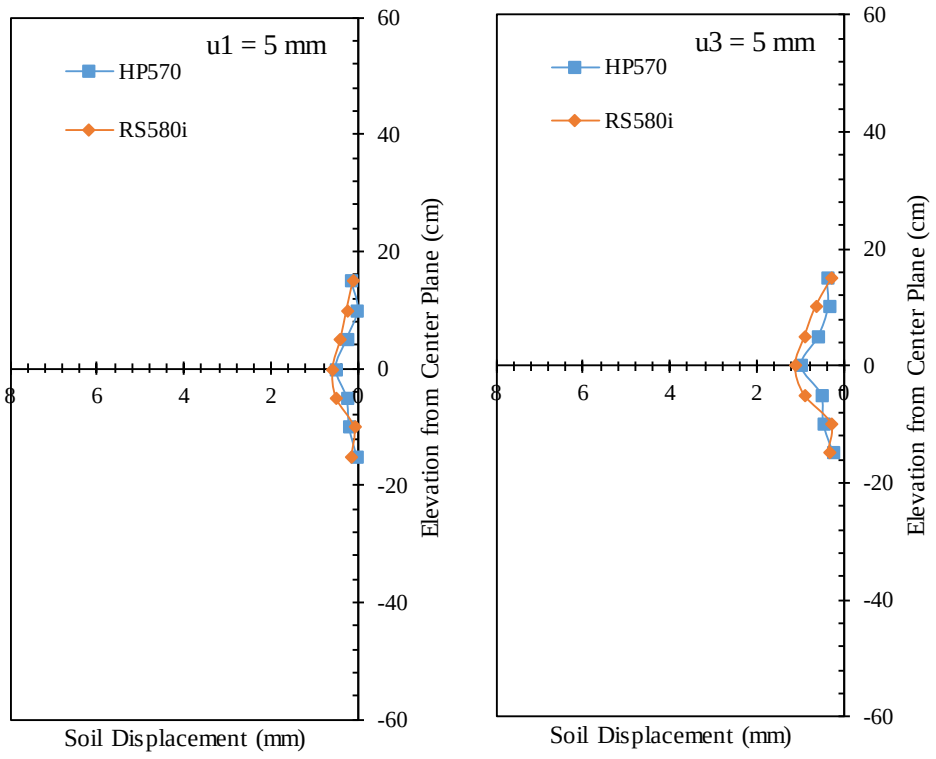

(a) **(b)**

Figure 5.2.75. Horizontal soil displacement profiles (measured by means of artificial gravel particles): (a) At nodal displacement u1 = 5 mm (0.2 in); and (b) At nodal displacement u3 = 5 mm (0.2 in).

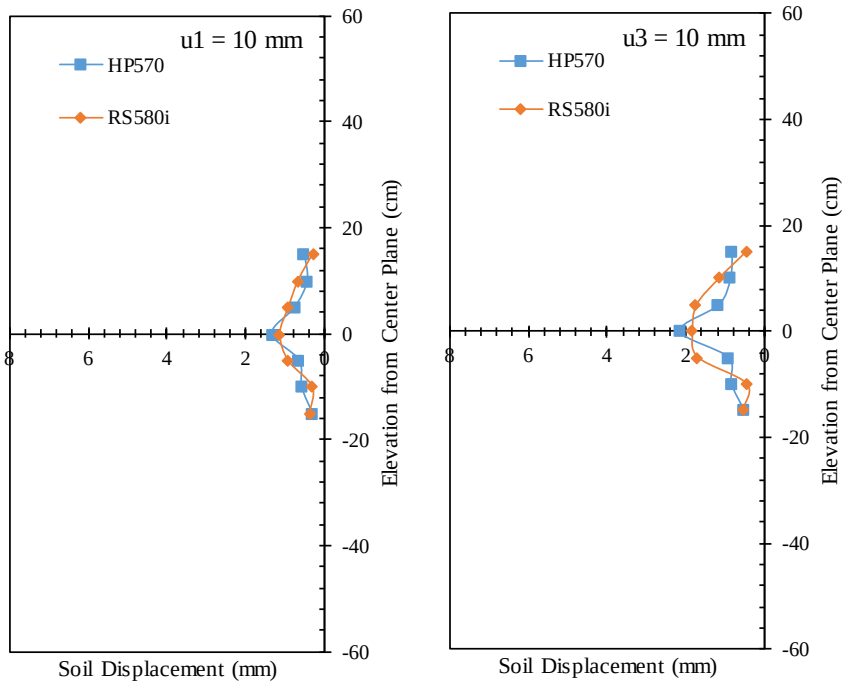

(a) **(b)**

Figure 5.2.76. Horizontal soil displacement profiles (measured by means of artificial gravel particles): (a) At nodal displacement u1 = 10 mm (0.4 in); and (b) At nodal displacement u3 = 10 mm (0.4 in).

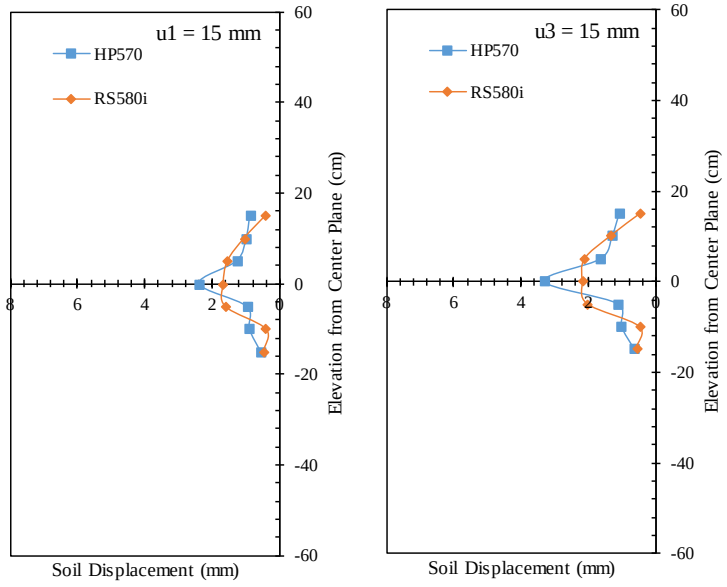

(a) **(b)**

Figure 5.2.77. Horizontal soil displacement profiles (measured by means of artificial gravel particles): (a) At nodal displacement u1 = 15 mm (0.6 in); and (b) At nodal displacement u3 = 15 mm (0.6 in).

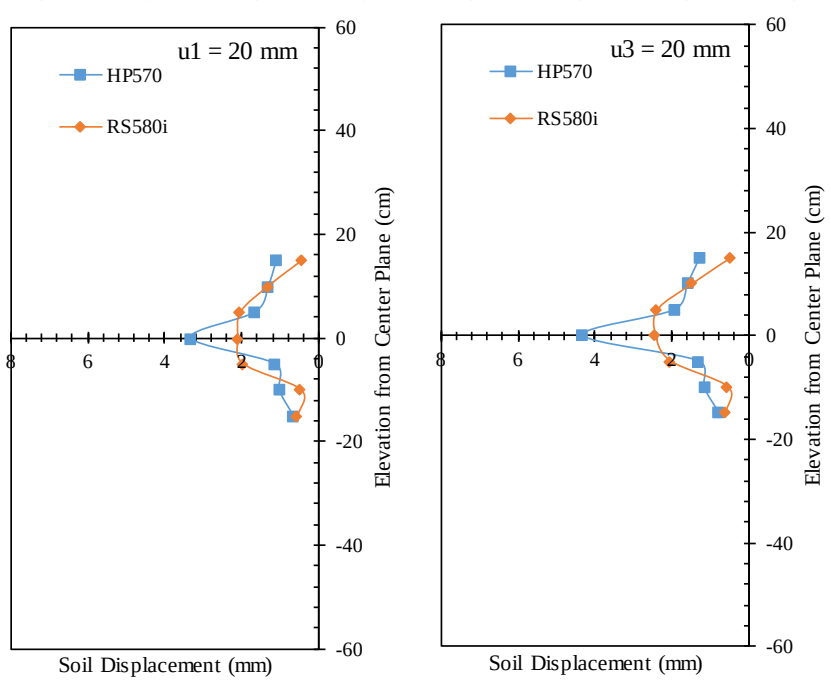

(a) **(b)**

Figure 5.2.78. Horizontal soil displacement profiles (measured by means of artificial gravel particles): (a) At nodal displacement u1 = 20 mm (0.8 in); and (b) At nodal displacement u3 = 20 mm (0.8 in).

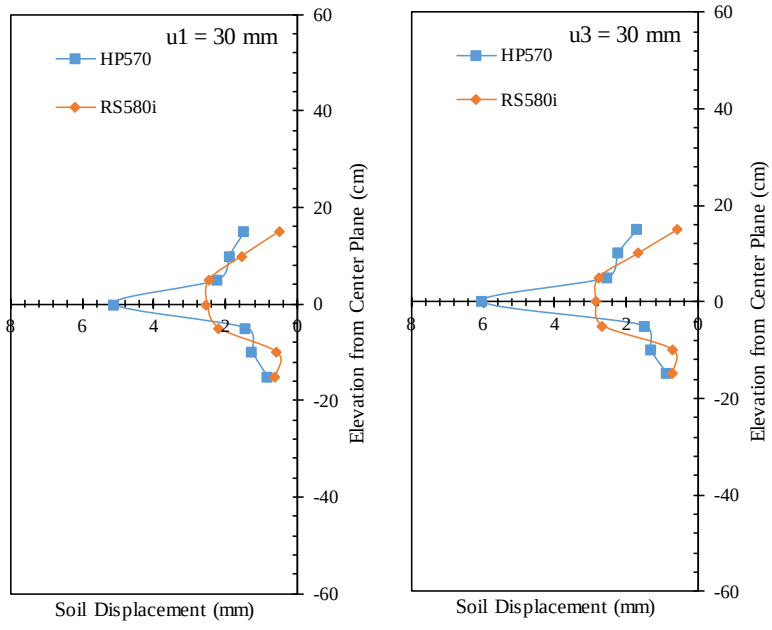

(a) **(b)**

Figure 5.2.79. Horizontal soil displacement profiles (measured by means of artificial gravel particles): (a) At nodal displacement u1 = 30 mm (1.2 in); and (b) At nodal displacement u3 = 30 mm (1.2 in).

Figure 5.2.80 shows the soil-reinforcement relative displacement at 0.305 m (1 ft.) from the front wall. This slippage was obtained by subtracting the reinforcement displacement at this location (by interpolation between *u1* and *u3*) and the soil displacement measured by the artificial gravel particle adjacent to the reinforcement (LP24). This figure exhibits the reduction in the soil-reinforcement interface shear stiffness during the test. It was observed that the slippage at the HP570 interface was similar to that at the RS580i interface up to 10-mm (0.4 in) frontal displacement. However, a significant difference appeared beyond 10-mm (0.4 in) displacement due to the difference in the soil-reinforcement interaction between the two reinforcements, mainly which comes from the passive resistance in the HP570 fabric.

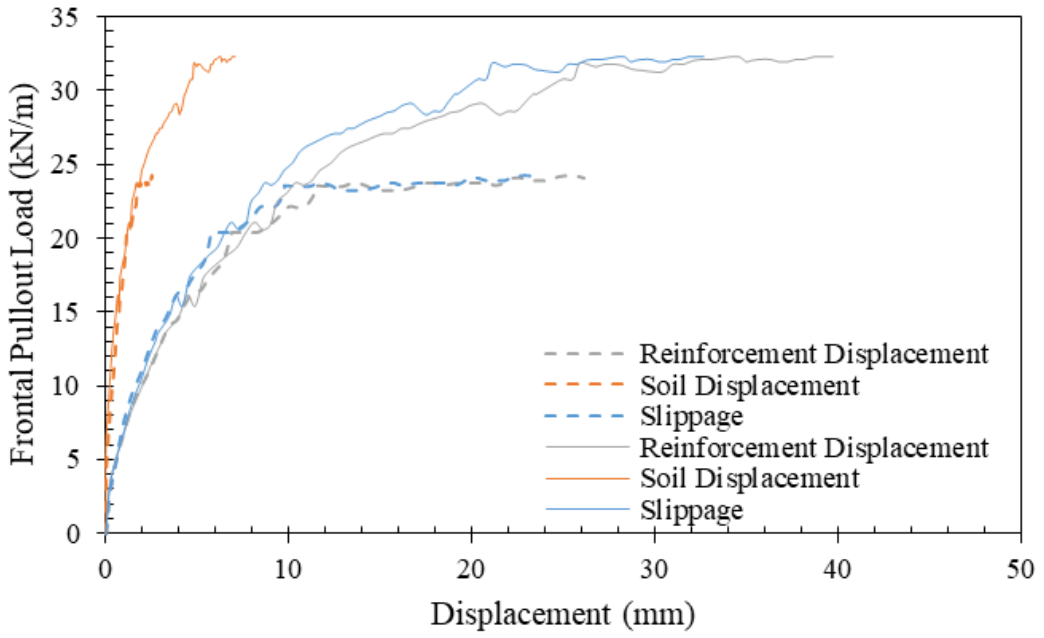

Figure 5.2.80. Soil-reinforcement relative displacement (solid lines belong to HP570 and dashed lines belong to RS580i).

Figure 5.2.81 shows the vertical soil displacement measured by means of the artificial gravel particles placed on top of the reinforced soil mass. Figures 5.2.81a through 5.2.81d show the soil displacement with respect to reinforcement nodal displacement *u1*, *u3*, *u5*, and *u7*. Both tests showed dilation near the front side of the reinforced soil mass and settlement near the rear side. It was observed that the dilation at the front was higher in case of HP570 than that in case of RS580i. At the back, settlement was higher in case of HP570 compared to that in case of RS580i.

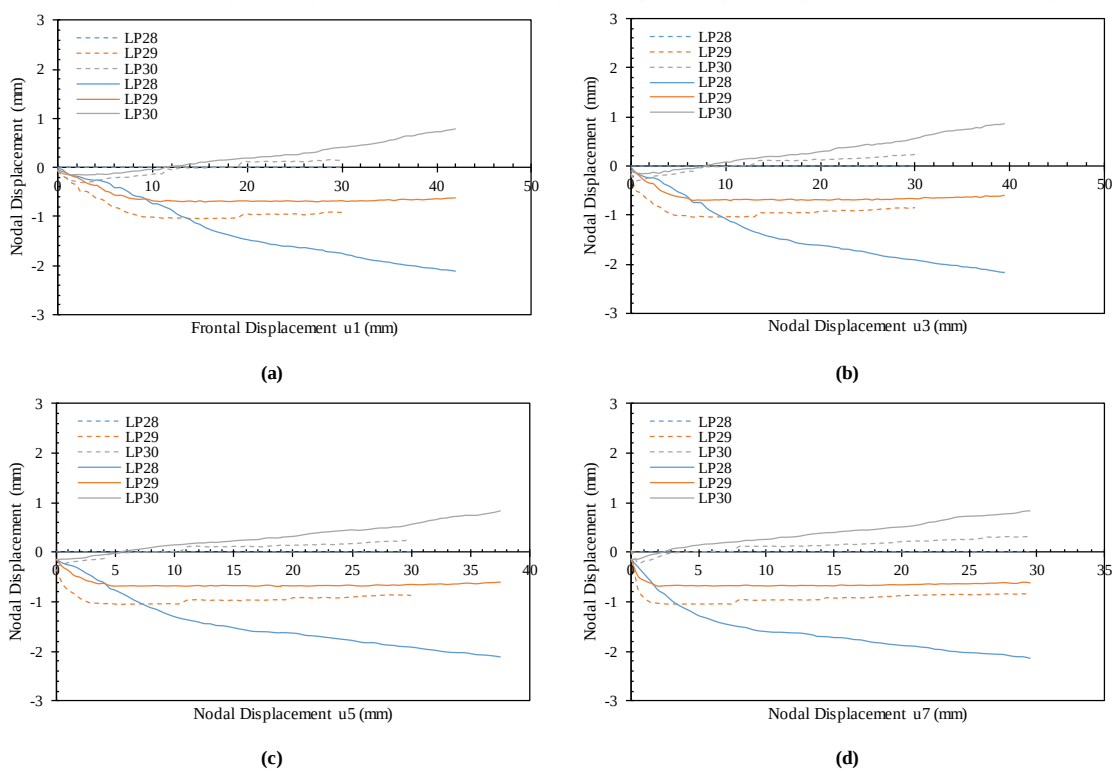

Figure 5.2.81. Vertical soil displacements profiles (measured by means of artificial gravel particles) with respect to various nodal displacements at the active reinforcement: (a) Nodal displacement u1; (b) Nodal displacement u3; (c) Nodal displacement u5; and (d) Nodal displacement u7 (solid lines belong to HP570 and dashed lines belong to RS580i).

5.2.3.4.2 HP570 geotextile versus 80T geogrid

This comparison was conducted between HP570 woven geotextile and 80T knitted uniaxial geogrid reinforcements. Even though the geotextile and geogrid are manufactured from different polymers (i.e., respectively polypropylene and polyester), both reinforcements have very similar tensile stiffness. The tensile stiffness for HP570 (XMD) and 80T (MD) is 876 and 914 kN/m (5002 and 5219 lbs/in) at 5% tensile strain, respectively. Figure 5.2.82 shows the frontal pullout load-displacement experimental curves for both tests. It was observed that the resistance to pullout for the 80T geogrid was higher than that of HP570 geotextile. The difference in resistance increased as the pullout progressed. This observation revealed information about the soil-reinforcement interaction.

Note that the soil-reinforcement interaction here comprises two components: (1) the passive resistance that can be mobilized by the transverse members. The members can be transverse ribs in geogrids or transverse yarns in geotextiles if particles were able to interfere with the geotextile fabric as mentioned earlier; and (2) the soil-reinforcement interface friction (interface shear resistance). The soil-reinforcement interaction was observed to be higher in the 80T geogrid compared to that of the HP570 geotextile.

While the 80T reinforcement is a uniaxial geogrid that has a weak junction (longitudinal and transverse ribs knitted forming square-aperture grid), the contribution of the passive resistance in the soil-reinforcement interaction was considerable. Forensic investigation of the reinforcement after that test revealed good integrity between the longitudinal and transverse ribs. This passive resistance in the 80T geogrid was found to outweigh the interface friction and the associated passive resistance that comes from the interlocking of punching soil particles in the case of HP570 geotextile.

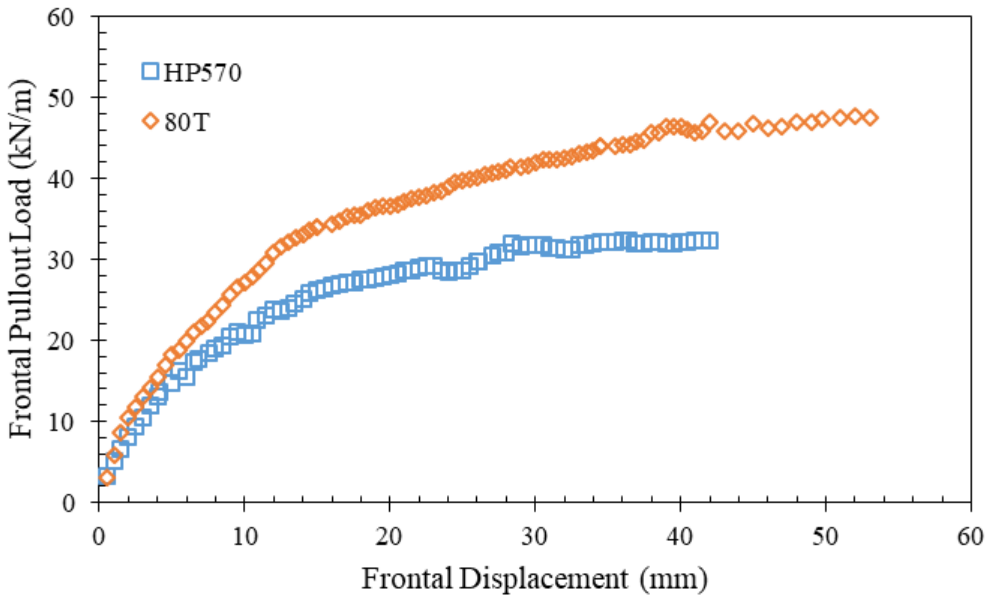

Figure 5.2.82. Frontal pullout load-displacement curves.

Figures 5.2.83 and 5.2.84 present the nodal displacement for the upper and lower passive reinforcement layers, respectively. Specifically, Figures 5.2.83a through 5.2.83d show the nodal displacements in the upper passive reinforcement corresponding to nodal displacements in the active reinforcement *u1*, *u3*, *u5*, and *u7*, respectively. Similarly, Figures 5.2.84a through 5.2.84d show the nodal displacements in the lower passive reinforcement corresponding to nodal displacements in the active reinforcement *u1*, *u3*, *u5*, and *u7*, respectively. Figures 5.2.83 and 5.2.84 reflect the load transfer from the active reinforcement to the passive reinforcements at the same nodal reinforcement of the active reinforcement (the same soil-reinforcement interface shear displacement). It was observed that the relationship between the nodal displacements for of the passive reinforcements are linear with the nodal displacements of the active reinforcement at early loading stages. This relationship then become non-linear as the load-displacement relationship of the active reinforcement curves. That is, Figures 5.2.83 and 5.2.84 reflect the reduction in soil-reinforcement interaction stiffness. It was observed that HP570 geotextile has a higher rate of interaction stiffness reduction, which result in reduction of interaction with the neighboring reinforcement layers, compared to that of 80T geogrid.

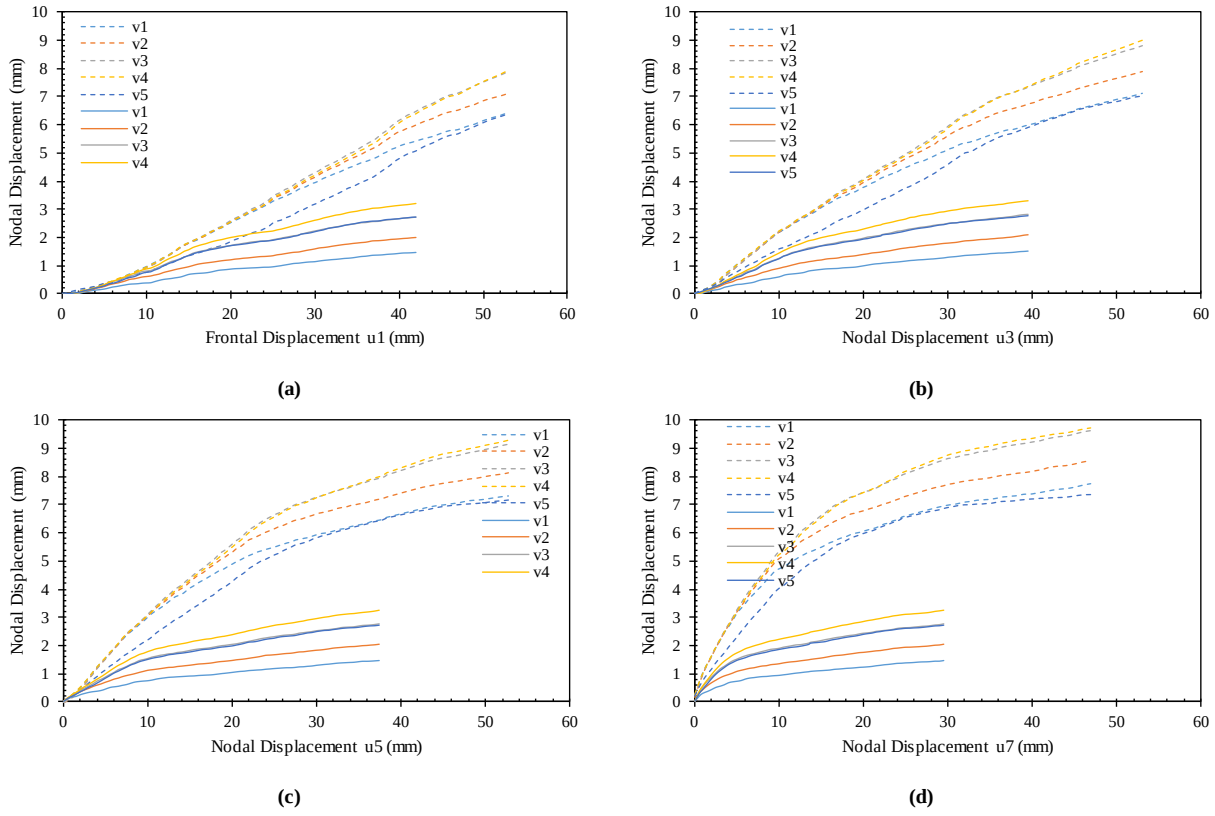

Figure 5.2.83. Nodal displacements at the upper passive reinforcement with respect to various nodal displacements at the active reinforcement: (a) nodal displacement u1; (b) nodal displacement u3; (c) nodal displacement u5; and (d) nodal displacement u7 (solid lines belong to HP570 and dashed lines belong to 80T).

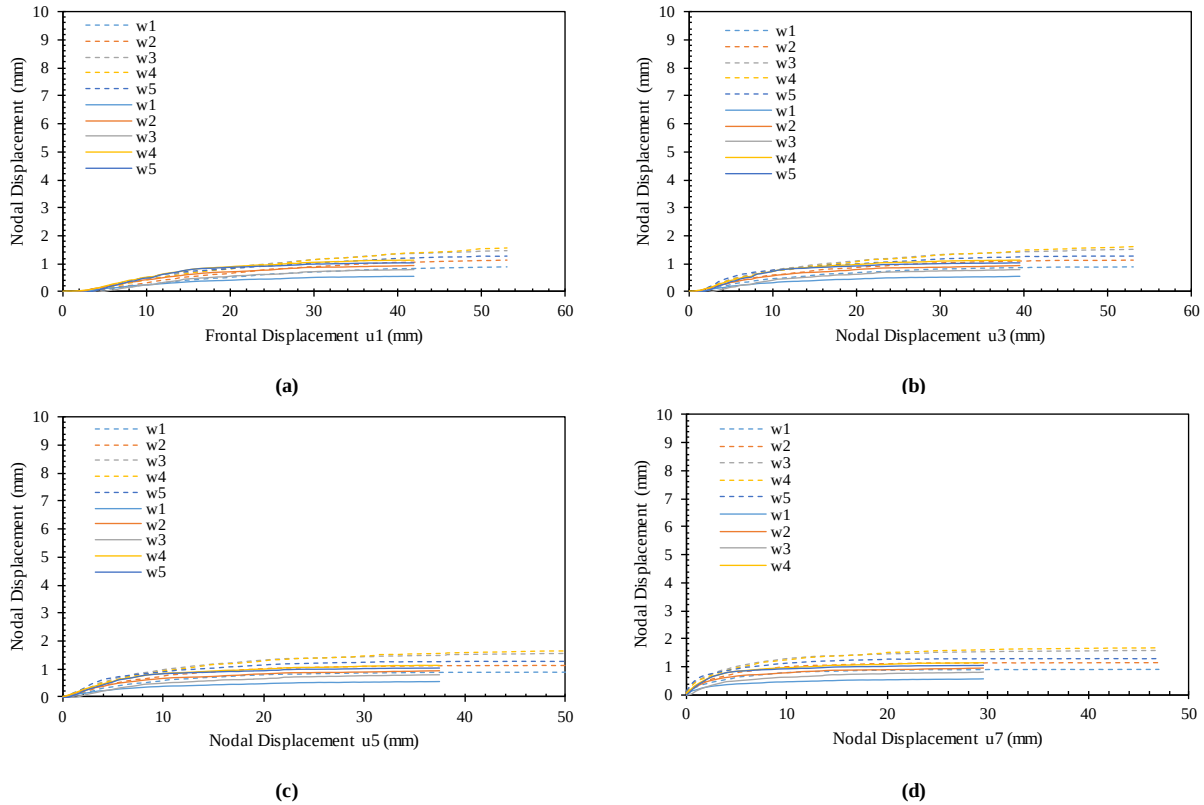

Figure 5.2.84. Nodal displacements at the lower passive reinforcement with respect to various nodal displacements at the active reinforcement: (a) Nodal displacement u1; (b) Nodal displacement u3; (c) Nodal displacement u5; and (d) Nodal displacement u7 (solid lines belong to HP570 and dashed lines belong to 80T).

Figures 5.2.85 through 5.2.89 show the displacement profiles for the active and passive reinforcement layers at active reinforcement frontal displacement (*u1*) of 5, 10, 15, 20, and 30 mm (0.2, 0.4, 0.6, 0.8 and 1.2 in). Note that the comparison is based on the same frontal displacement for the different reinforcements rather than the same pullout frontal load. The profiles of HP570 geotextile show higher displacement along the length of the active reinforcement compared to those of 80T geogrid. This difference increased as pullout progressed. On contrary, the profiles of the passive reinforcement layers showed lower displacement values for the HP570 geotextile compared to those measured for the 80T geogrid. This observation points towards higher reinforcement interaction with the neighboring layers in case of the 80T geogrid compared to the HP570 geotextile. This is a result of the higher soil-reinforcement interaction of the 80T that resulted in a higher load transfer ability and a bigger zone of influence. Note that, although, the reinforcement displacement in the active reinforcement was smaller in the case of 80T geogrid, it showed a bigger interaction than that of HP570 geotextile, which has a bigger reinforcement displacement.

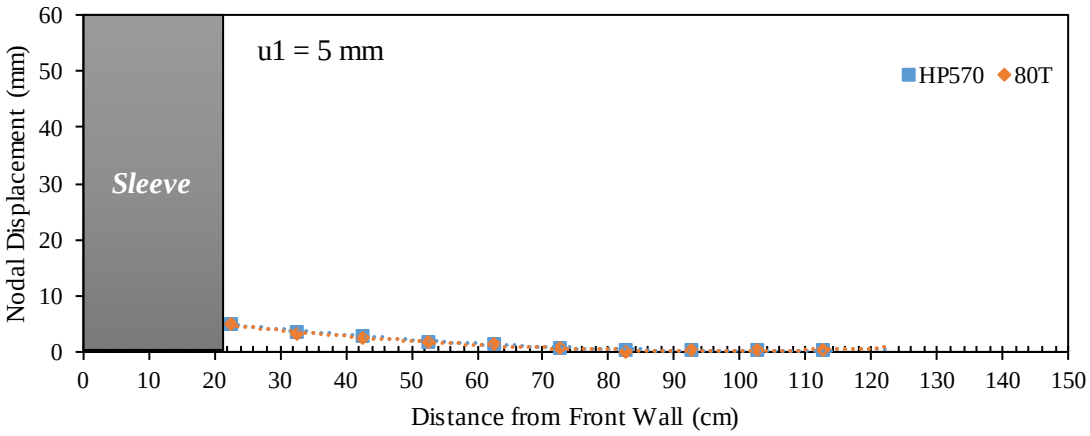

(a)

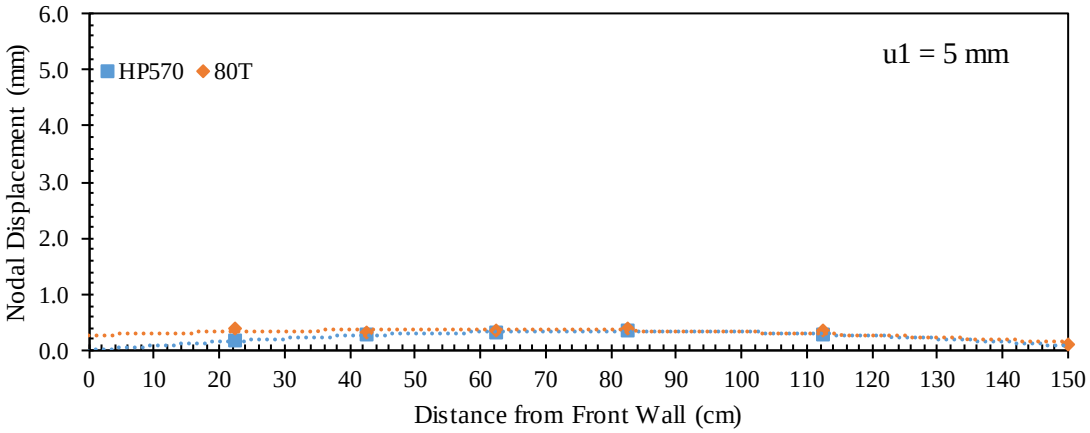

(b)

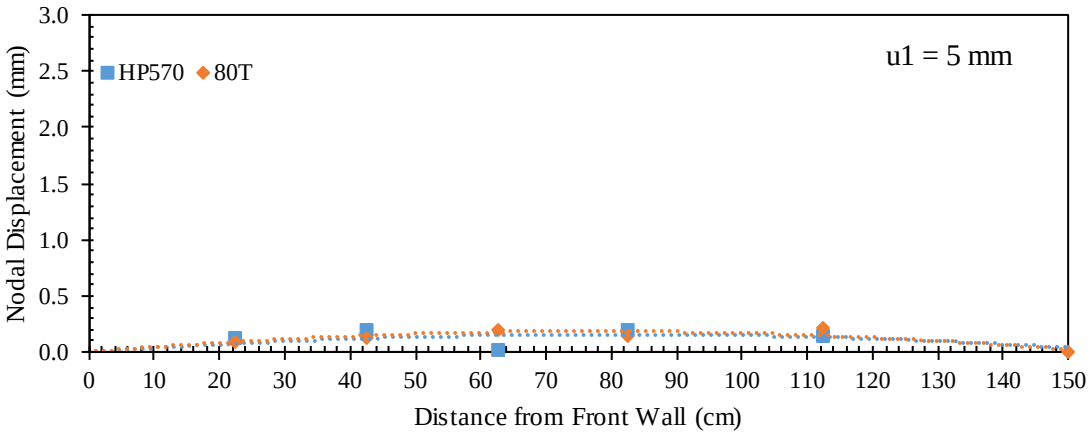

(c)

Figure 5.2.85. Reinforcement displacement profiles at frontal displacement u1 = 5 mm (0.2 in): (a) Active reinforcement; (b) Upper passive reinforcement; and (c) Lower passive reinforcement.

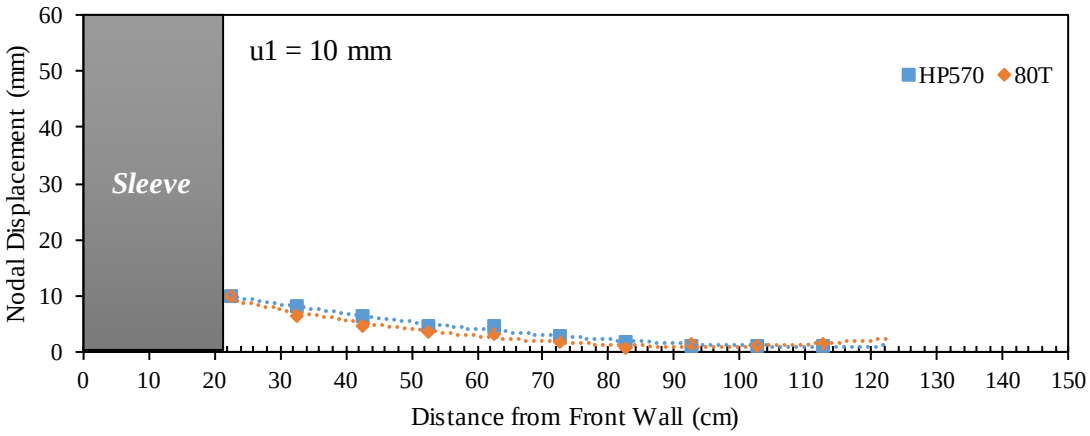

(a)

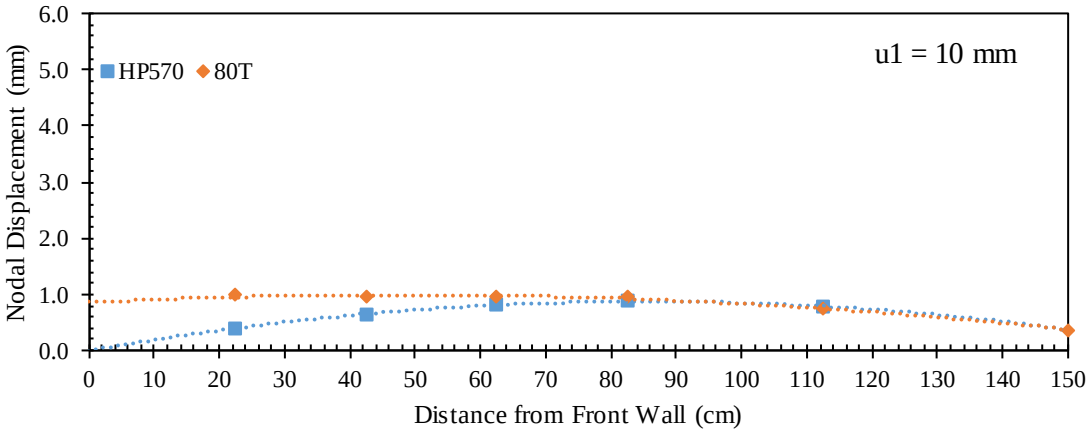

(b)

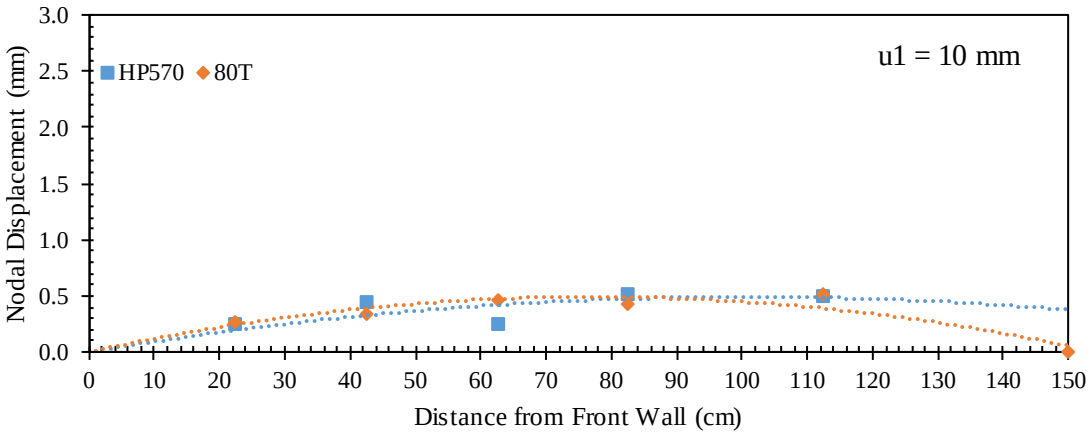

(c)

Figure 5.2.86. Reinforcement displacement profiles at frontal displacement u1 = 10 mm (0.4 in): (a) Active reinforcement; (b) Upper passive reinforcement; and (c) Lower passive reinforcement.

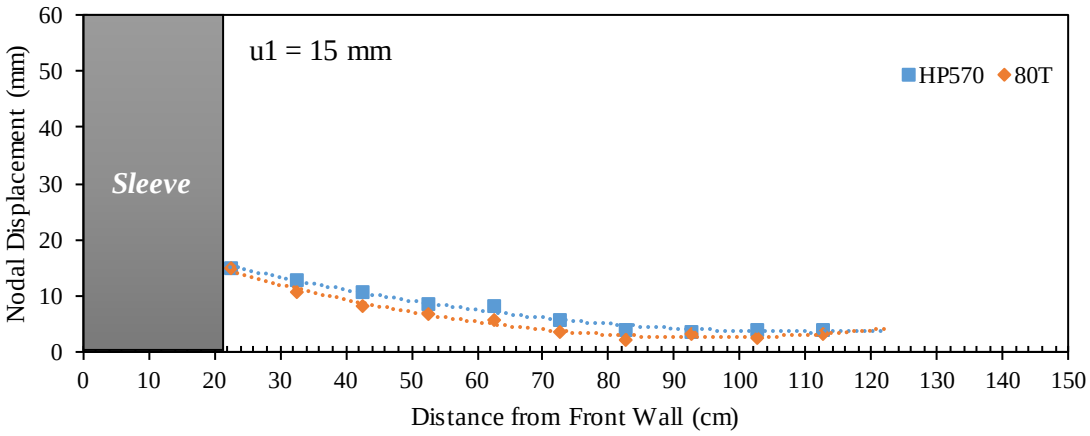

(a)

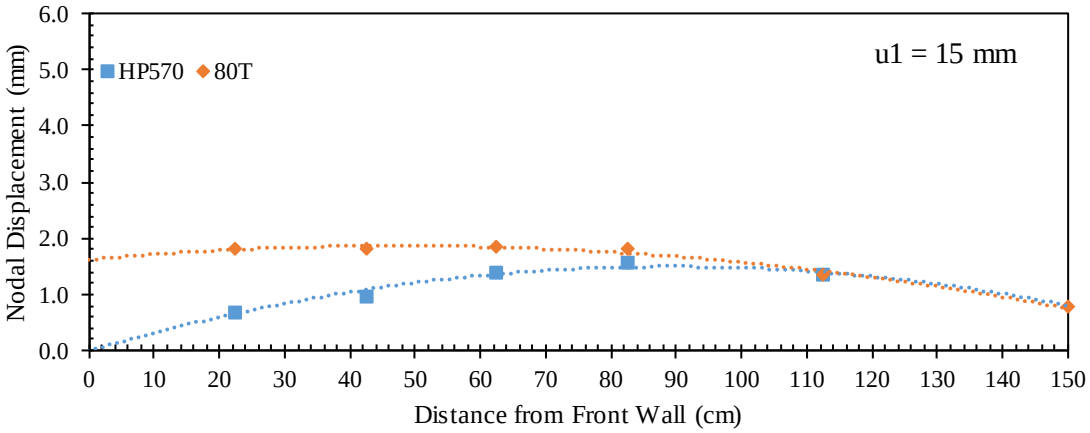

(b)

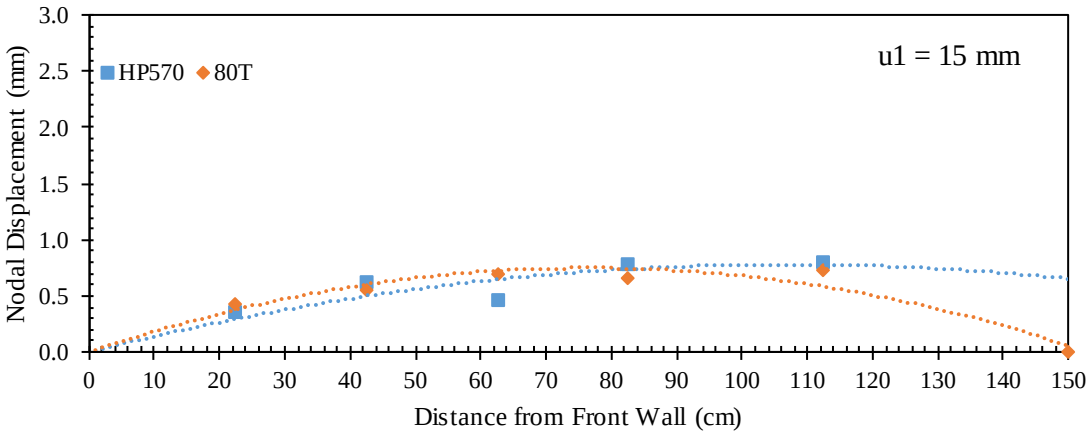

(c)

Figure 5.2.87. Reinforcement displacement profiles at frontal displacement u1 = 15 mm (0.6 in): (a) Active reinforcement; (b) Upper passive reinforcement; and (c) Lower passive reinforcement.

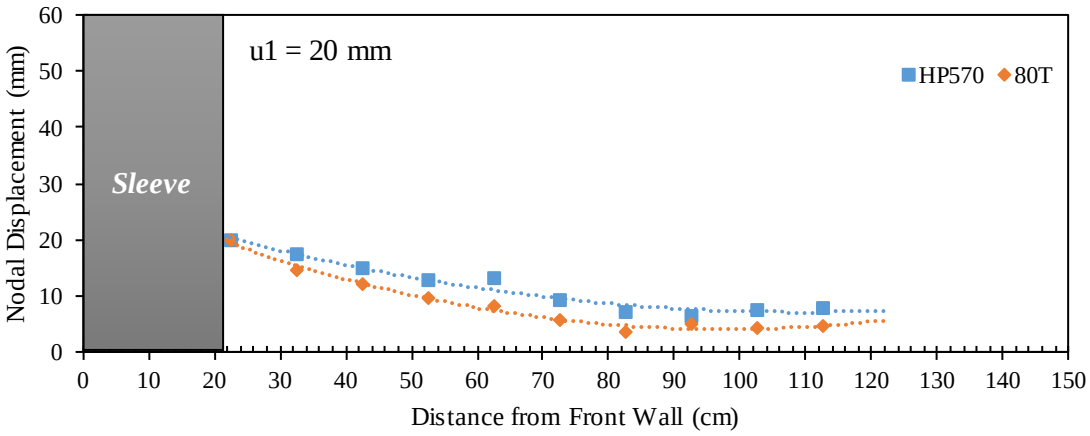

(a)

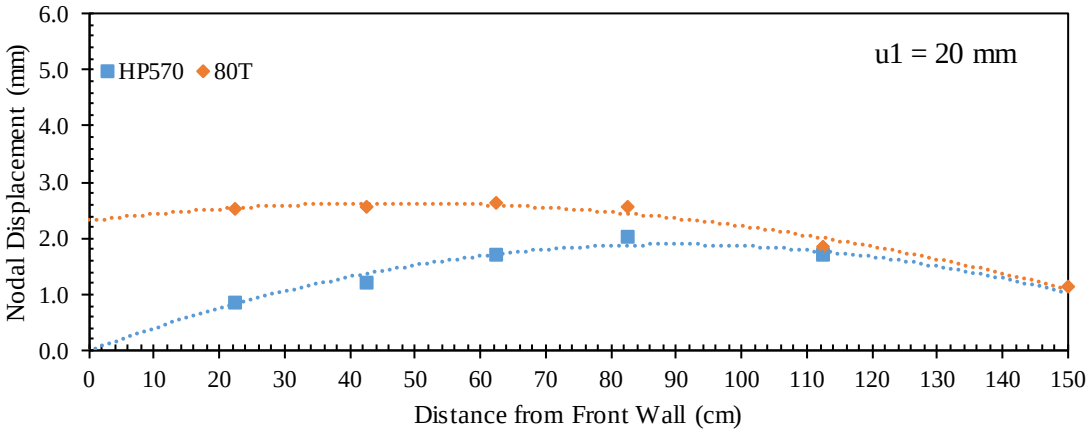

(b)

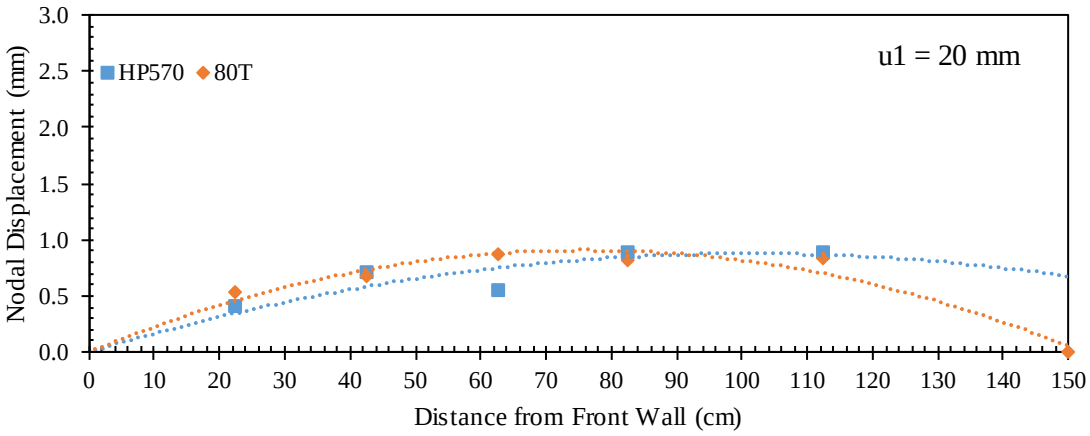

(c)

Figure 5.2.88. Reinforcement displacement profiles at frontal displacement u1 = 20 mm (0.8 in): (a) Active reinforcement; (b) Upper passive reinforcement; and (c) Lower passive reinforcement.

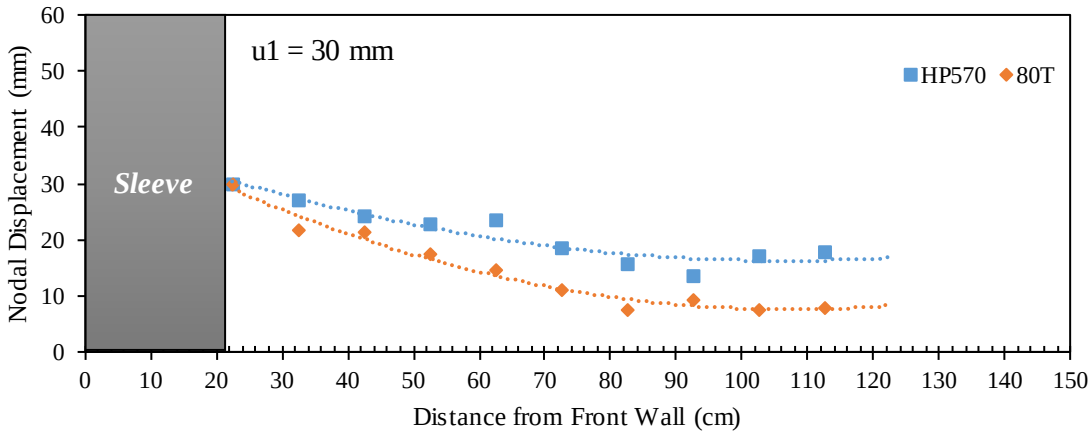

(a)

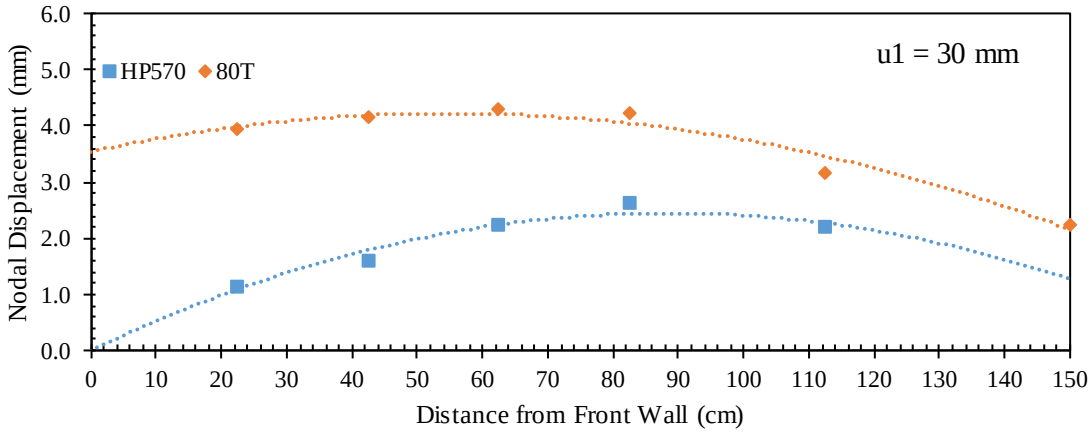

(b)

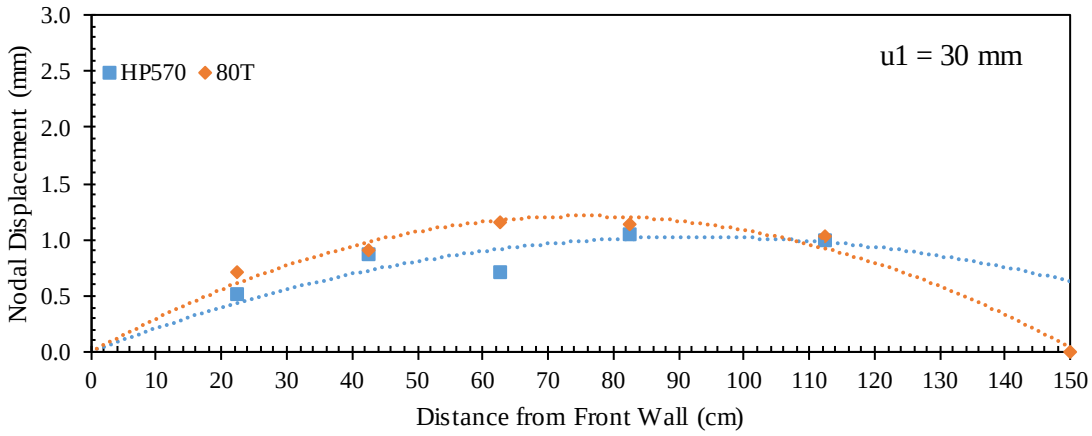

(c)

Figure 5.2.89. Reinforcement displacement profiles at frontal displacement u1 = 30 mm (1.2 in): (a) Active reinforcement; (b) Upper passive reinforcement; and (c) Lower passive reinforcement.

For a better comparison, Figures 5.2.90 through 5.2.94 show the passive reinforcement displacement profiles for various intermediate nodal displacements of the active reinforcement of 5, 10, 15, 20, and 30 mm (0.2, 0.4, 0.6, 0.8 and 1.2 in), respectively. Specifically, each figure consists of a, b, c, and d subfigures that provide comparisons of the upper passive reinforcement profiles for same nodal displacements *u1*, *u3*, *u5*, and *u7*, respectively. That is, the comparisons were conducted for the similar soil-reinforcement induced interface displacement. This provides more insight into the comparison between the different reinforcement types in their ability to interact with their neighboring reinforcement layers for a given soil medium and confinement level. It was observed from Figures 5.2.90 through 5.2.94 that the interaction between the reinforcement layers in case of the 80T geogrid is significantly higher than that in case of the HP570 geotextile.

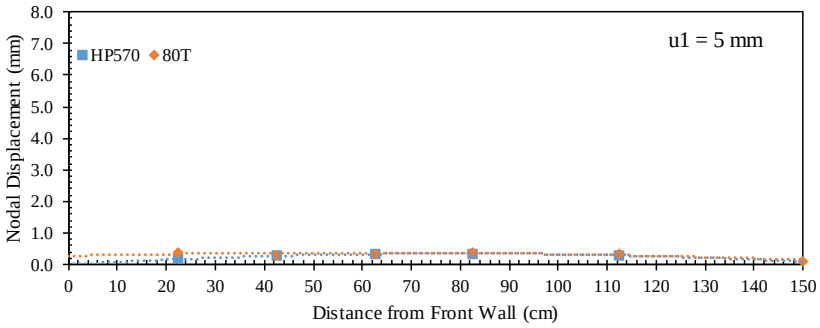

(a)

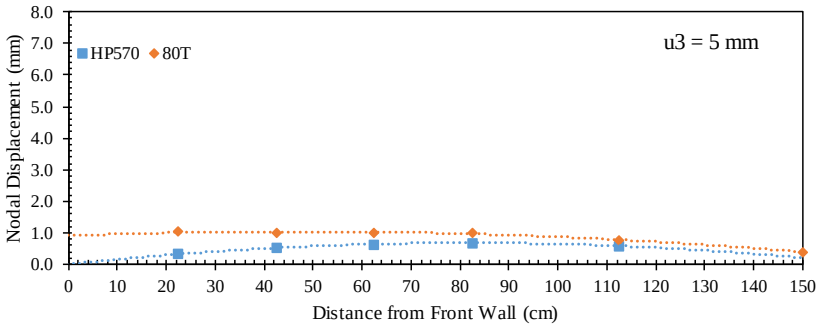

(b)

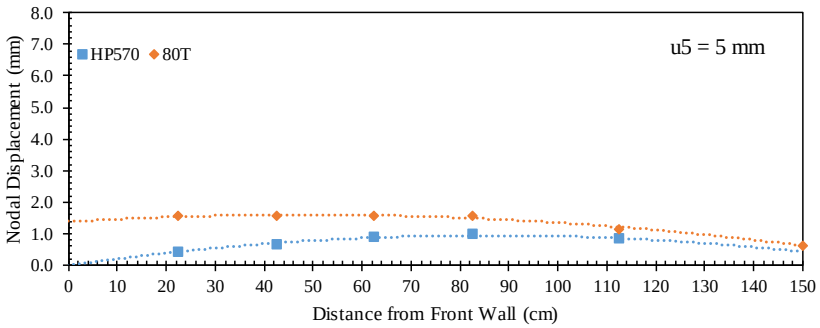

(c)

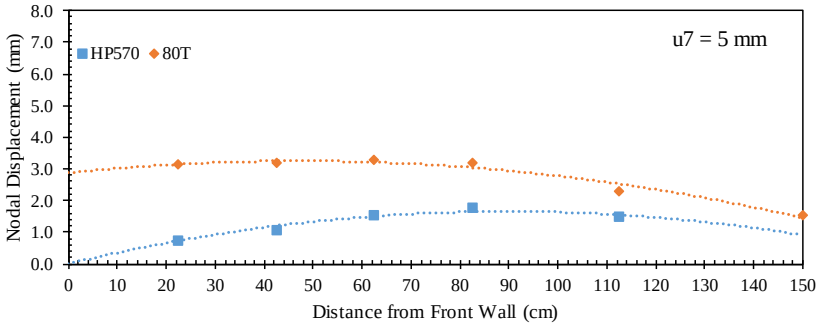

(d)

Figure 5.2.90. Upper passive reinforcement displacement profiles: (a) At nodal displacement u1 = 5 mm (0.2 in); (b) At nodal displacement u3 = 5 mm (0.2 in); (c) At nodal displacement u5 = 5 mm (0.2 in); and (d) At nodal displacement u7 = 5 mm (0.2 in).

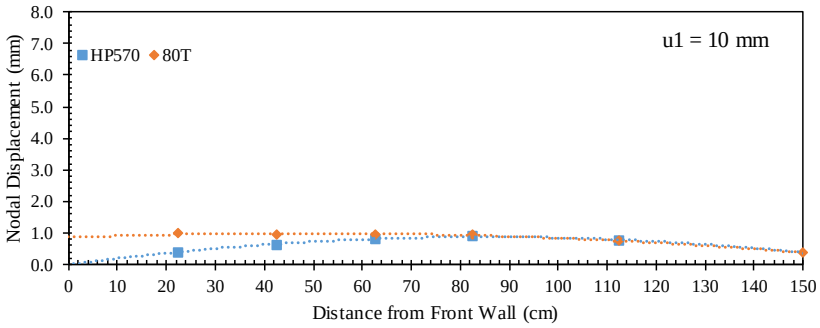

(a)

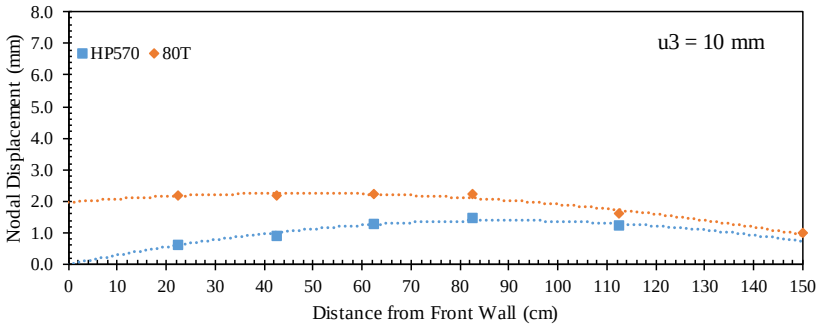

(b)

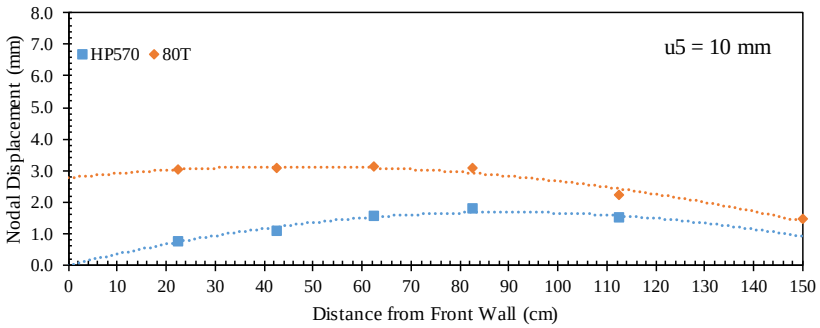

(c)

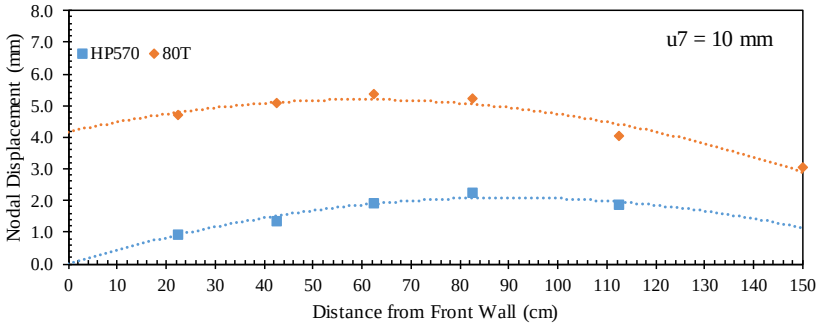

(d)

Figure 5.2.91. Upper passive reinforcement displacement profiles: (a) At nodal displacement u1 = 10 mm (0.4 in); (b) At nodal displacement u3 = 10 mm (0.4 in); (c) At nodal displacement u5 = 10 mm (0.4 in); and (d) At nodal displacement u7 = 10 mm (0.4 in).

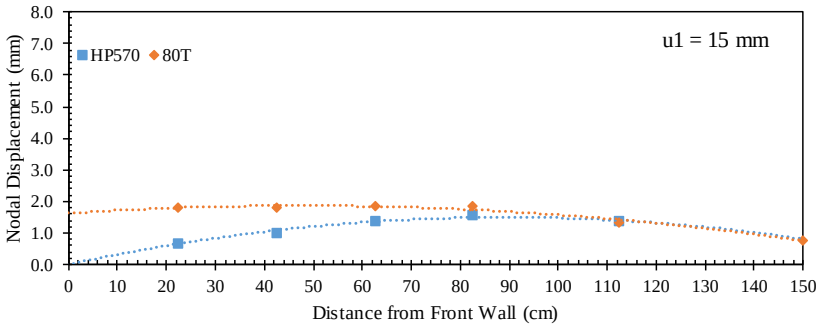

(a)

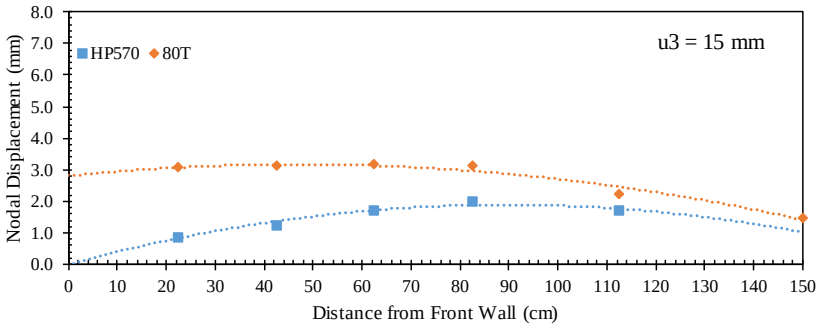

(b)

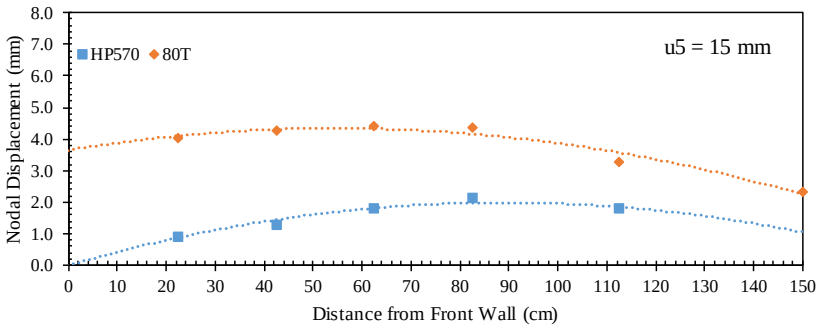

(c)

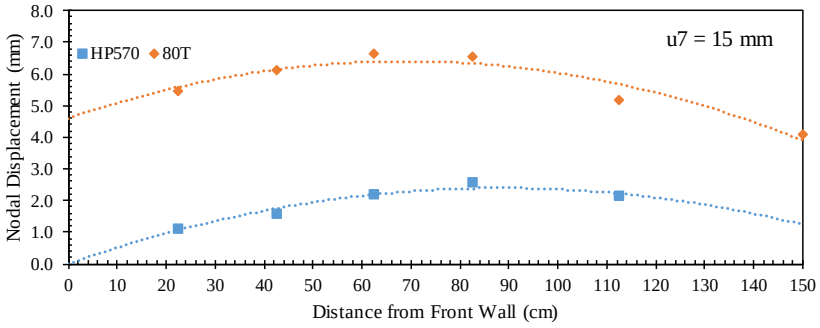

(d)

Figure 5.2.92. Upper passive reinforcement displacement profiles: (a) At nodal displacement u1 = 15 mm (0.6 in); (b) At nodal displacement u3 = 15 mm (0.6 in); (c) At nodal displacement u5 = 15 mm (0.6 in); and (d) At nodal displacement u7 = 15 mm (0.6 in).

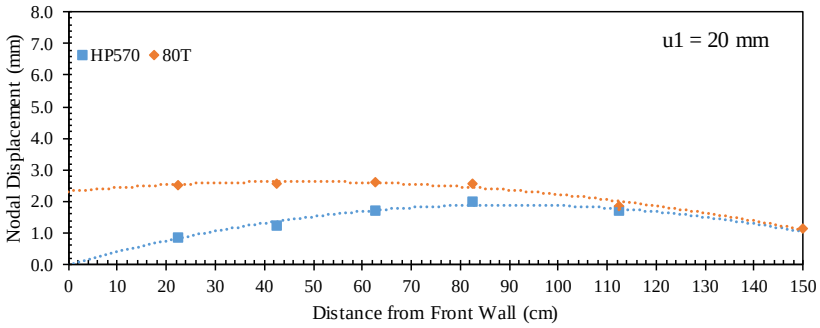

(a)

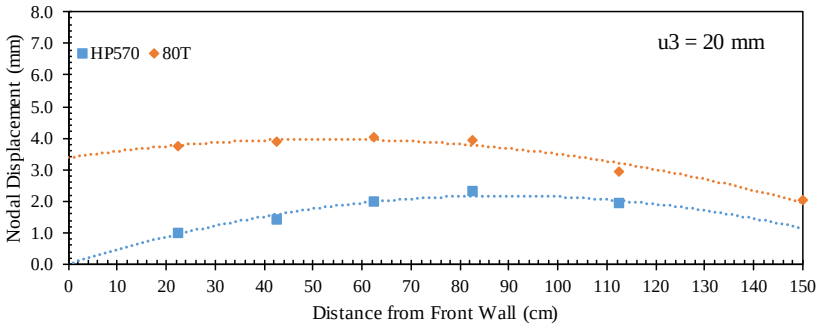

(b)

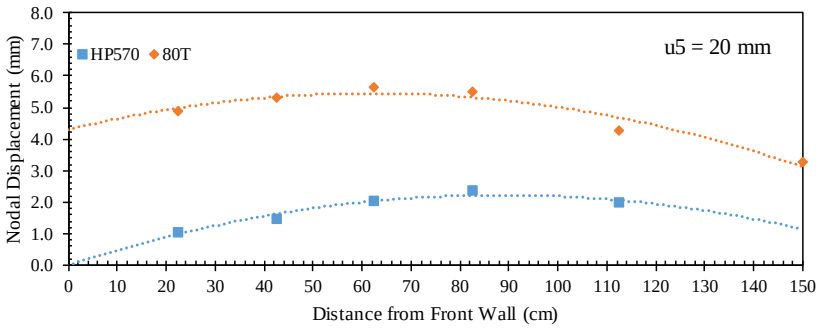

(c)

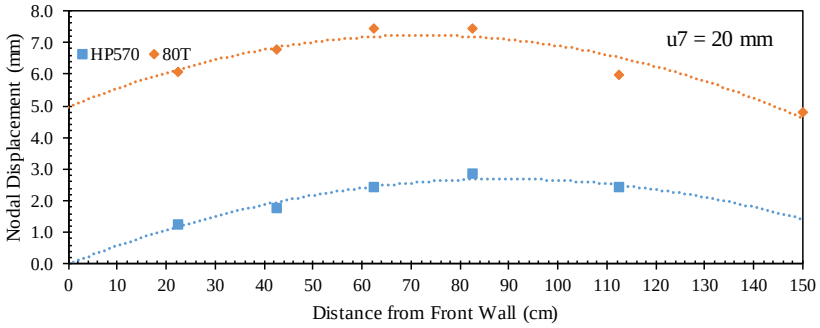

(d)

Figure 5.2.93. Upper passive reinforcement displacement profiles: (a) At nodal displacement u1 = 20 mm (0.8 in); (b) At nodal displacement u3 = 20 mm (0.8 in); (c) At nodal displacement u5 = 20 mm (0.8 in); and (d) At nodal displacement u7 = 20 mm (0.8 in).

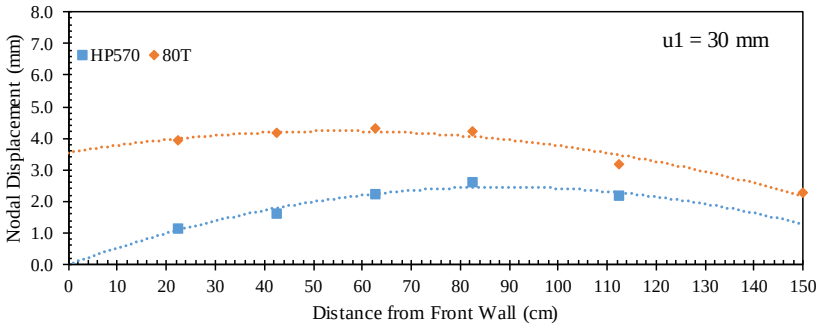

(a)

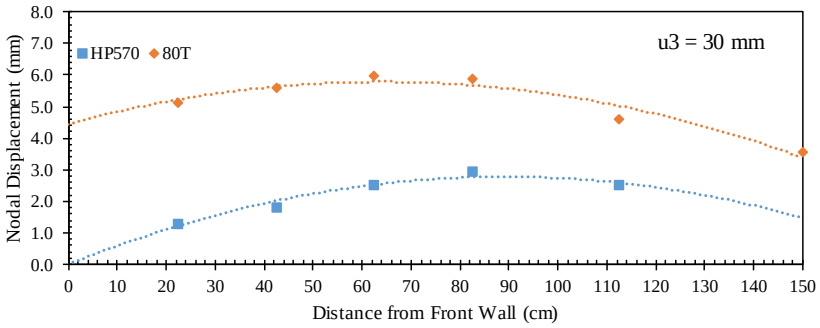

(b)

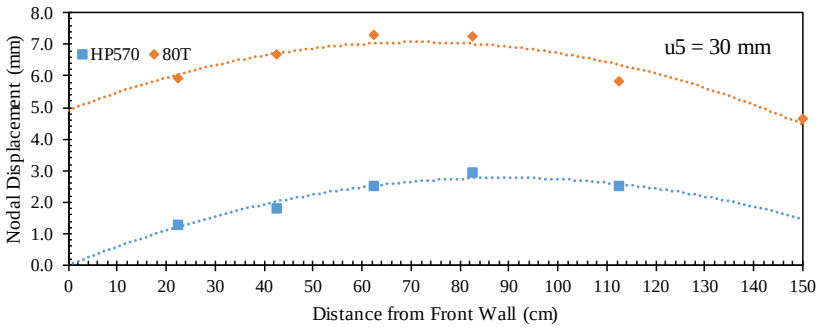

(c)

Figure 5.2.94. Upper passive reinforcement displacement profiles: (a) At nodal displacement u1 = 30 mm (1.2 in); (b) At nodal displacement u3 = 30 mm (1.2 in); and (c) At nodal displacement u5 = 30 mm (1.2 in).

Figures 5.2.95 through 5.2.99 present the horizontal soil displacement measured for nodal displacements of 5, 10, 15, 20, and 30 mm (0.2, 0.4, 0.6, 0.8 and 1.2 in), respectively. Each figure consists of a and b that show the soil displacement with respect nodal displacements *u1* and *u3*, respectively. These displacements were measured at specific locations by tracking artificial gravel particles making a vertical array within the soil at 0.305 m (1 ft.) from the front wall. It was observed that the soil displacement is smaller in case of HP570 geotextile compared to that of 80T geogrid. This difference was observed to increase as pullout progressed due to the difference the soil-reinforcement interaction between the two reinforcements. Note that the soil adjacent to the reinforcement exhibited higher rate of displacement compared to those away from the reinforcement. This is due to yielding in the

internal shear strength of the fill material that limits the load transfer from the reinforcement to larger distance away from the reinforcement.

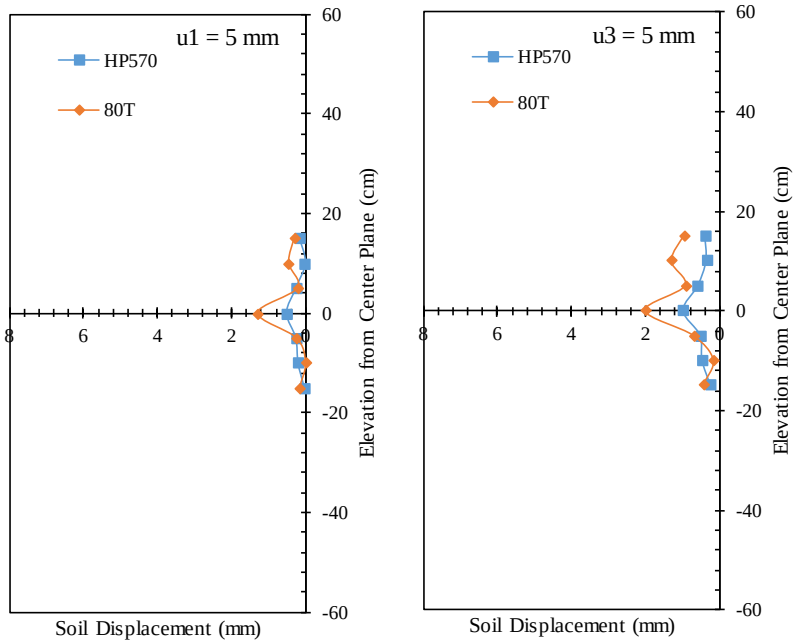

(a) **(b)**

Figure 5.2.95. Horizontal soil displacement profiles (measured by means of artificial gravel particles): (a) At nodal displacement u1 = 5 mm (0.2 in); and (b) At nodal displacement u3 = 5 mm (0.2 in).

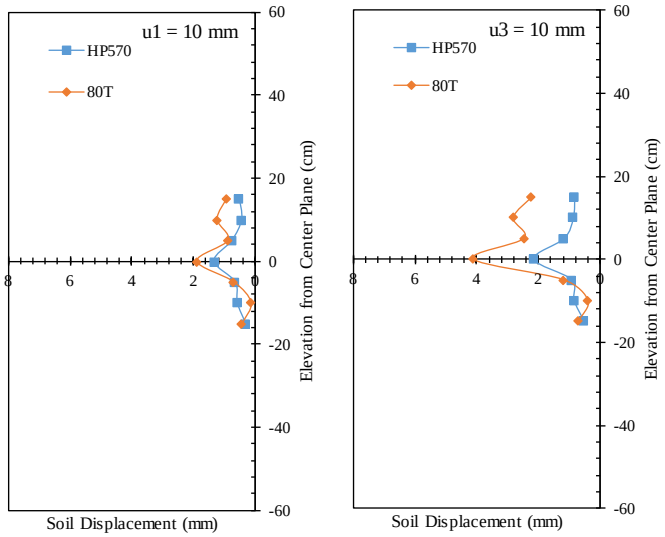

(a) **(b)**

Figure 5.2.96. Horizontal soil displacement profiles (measured by means of artificial gravel particles): (a) At nodal displacement u1 = 10 mm (0.4 in); and (b) At nodal displacement u3 = 10 mm (0.4 in).

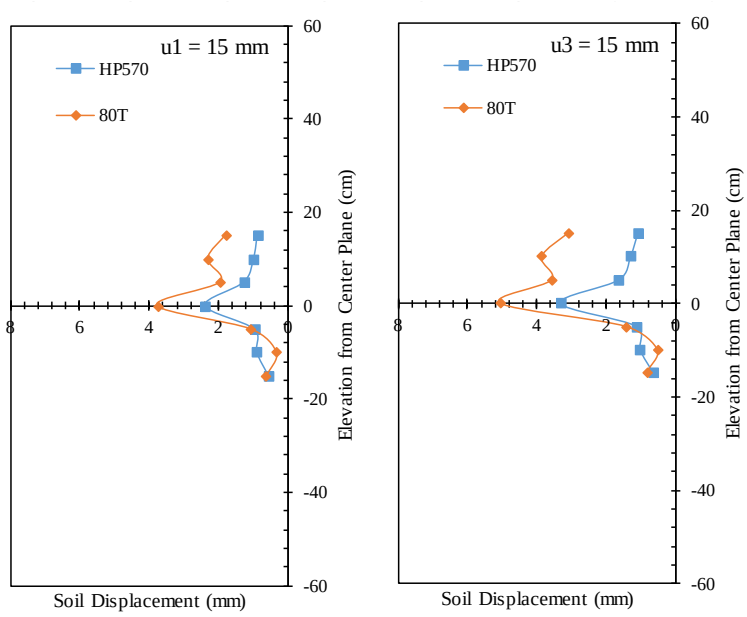

(a) **(b)**

Figure 5.2.97. Horizontal soil displacement profiles (measured by means of artificial gravel particles): (a) At nodal displacement u1 = 15 mm (0.6 in); and (b) At nodal displacement u3 = 15 mm (0.6 in).

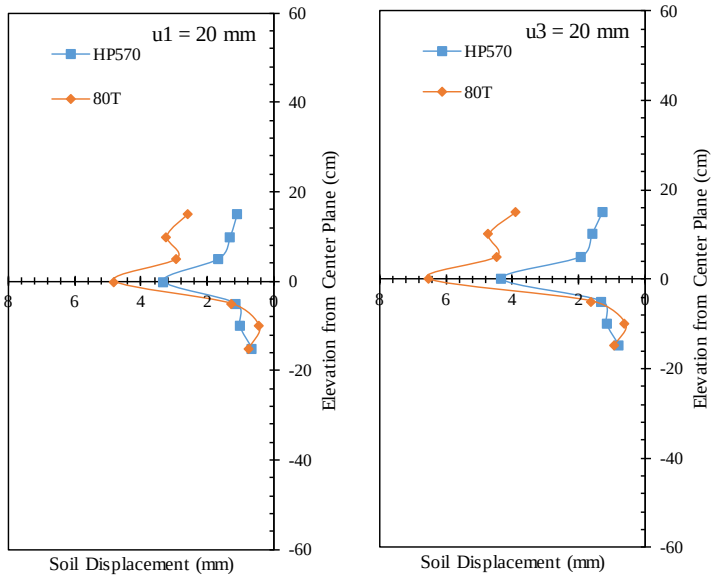

(a) **(b)**

Figure 5.2.98. Horizontal soil displacement profiles (measured by means of artificial gravel particles): (a) At nodal displacement u1 = 20 mm (0.8 in); and (b) At nodal displacement u3 = 20 mm (0.8 in).

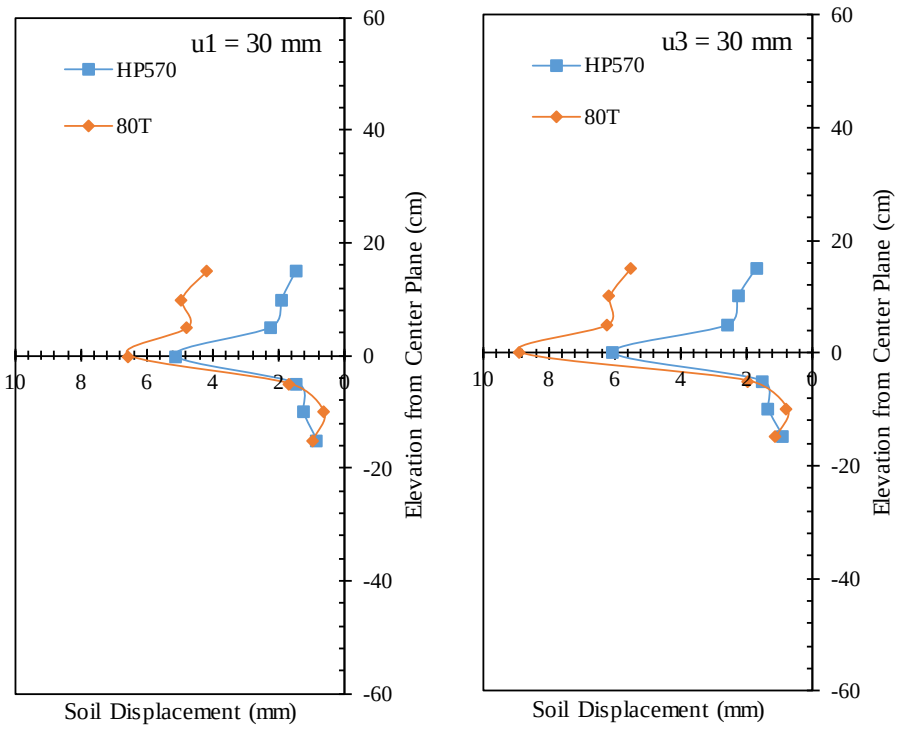

(a) **(b)**

Figure 5.2.99. Horizontal soil displacement profiles (measured by means of artificial gravel particles): (a) At nodal displacement u1 = 30 mm (1.2 in); and (b) At nodal displacement u3 = 30 mm (1.2 in).

Figure 5.2.100 show the soil-reinforcement relative displacement at 0.305 m (1 ft.) from the front wall. This slippage was obtained by subtracting the reinforcement displacement at this location (by interpolation between *u1* and *u3*) and the soil displacement measured by the artificial gravel particle adjacent to the reinforcement (LP24). This figure exhibits the reduction in the soil-reinforcement interface shear stiffness during the test. It was observed that the slippage at the HP570 interface was higher than that at the 80T interface due to the difference in the soil-reinforcement interaction between the two reinforcements.

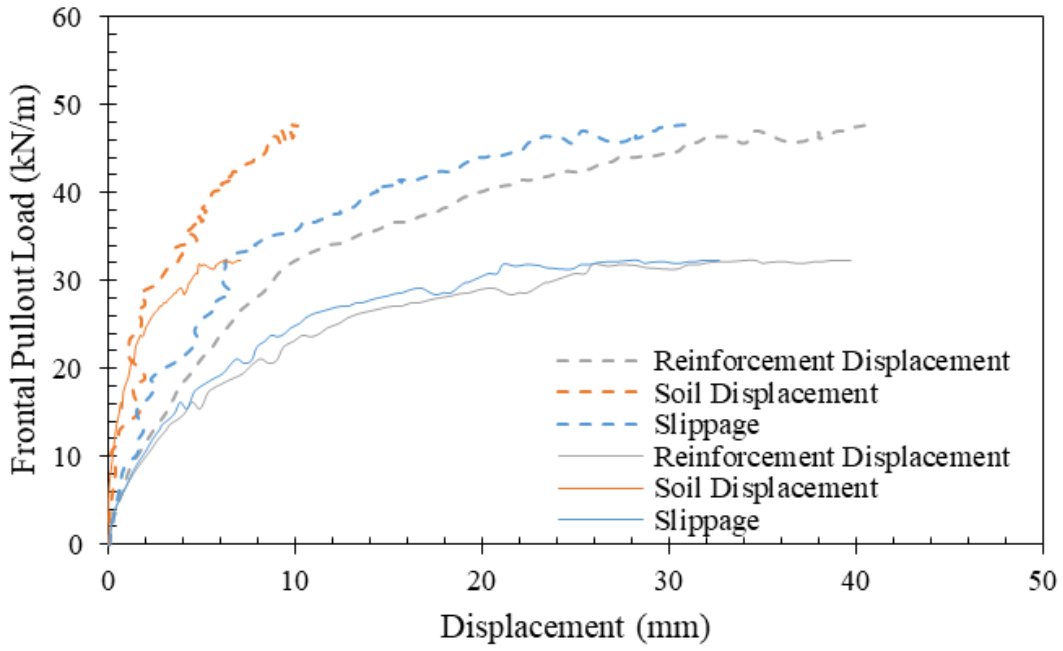

Figure 5.2.100. Soil-reinforcement relative displacement (solid lines belong to HP570 and dashed lines belong to 80T).

Figure 5.2.101 shows the vertical soil displacement measured by means of the artificial gravel particles placed on top of the reinforced soil mass. Figures 5.2.101a through 5.2.101d show the soil displacement with respect to reinforcement nodal displacement *u1*, *u3*, *u5*, and *u7*. Both tests showed dilation near the front side of the reinforced soil mass and settlement near the rear side. It was observed that the dilation at the front was lower in case of HP570 geotextile than that in case of 80T geogrid, which was significantly high. At the back, settlement was higher in case of HP570 geotextile compared to that in case of 80T geogrid. In addition, in case of the 80T geogrid, settlement was observed at the middle of the reinforced soil mass followed by dilation as shear stresses increased at the soil-reinforcement interface.

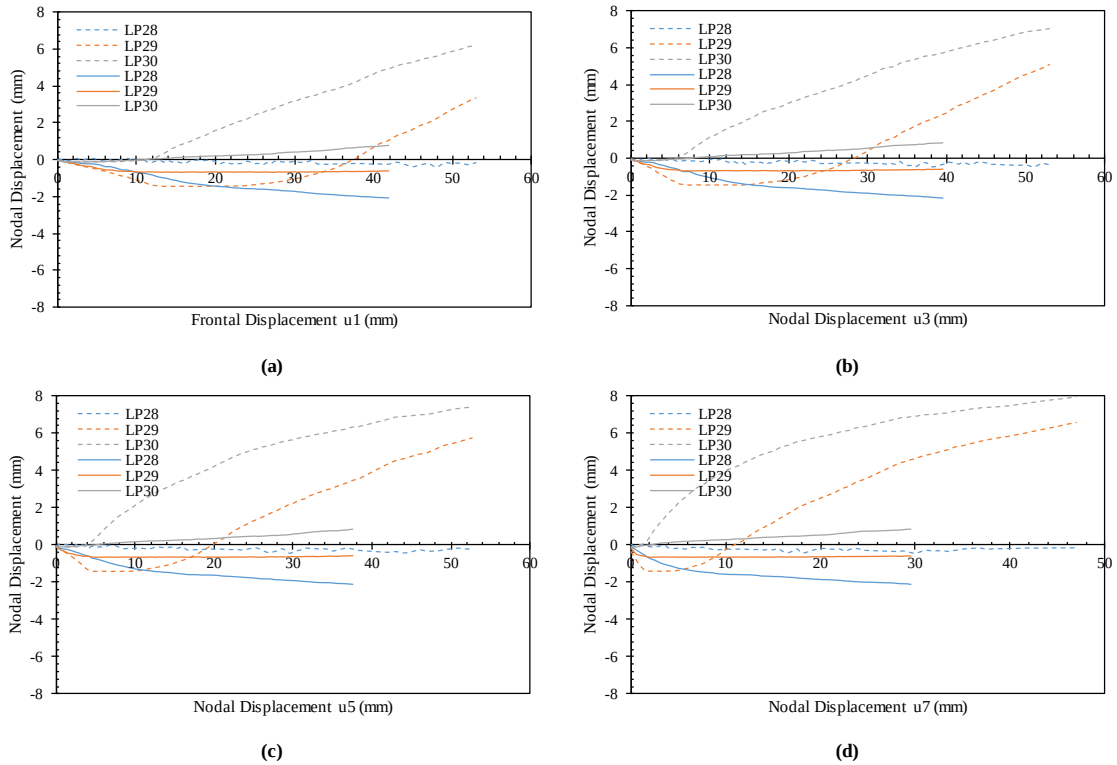

Figure 5.2.101. Vertical soil displacements profiles (measured by means of artificial gravel particles) with respect to various nodal displacements at the active reinforcement: (a) Nodal displacement u1; (b) Nodal displacement u3; (c) Nodal displacement u5; and (d) Nodal displacement u7 (solid lines belong to HP570 and dashed lines belong to 80T).

5.2.3.4.3 80T geogrid versus BX1200 geogrid

This comparison was conducted between BX1200 extruded biaxial geogrid and 80T knitted uniaxial geogrid reinforcements. BX1200 is made of polypropylene and 80T is made of polyester. The tensile stiffness for BX1200 (XMD) and 80T (MD) is 392 and 914 kN/m at 5% tensile strain, respectively. Figure 5.2.102 shows the frontal pullout load-displacement experimental curves for both tests. It was observed that the resistance to pullout for the 80T geogrid was higher than that of BX1200 geogrid. The difference in resistance increased as the pullout progressed. However, due to the low tensile strength and stiffness of the BX1200 geogrid, it failed in rupture before considerable soil-reinforcement interface displacement unlike the 80T geogrid. The comparison between the frontal pullout load-displacement curves in this case cannot provide full understanding of the soil-reinforcement interaction between both reinforcements. This is because the tensile stiffness is quite different between both reinforcements. A deeper look into the behavior of each reinforcement along their embedment length is needed to complement the information retrieved about the front.

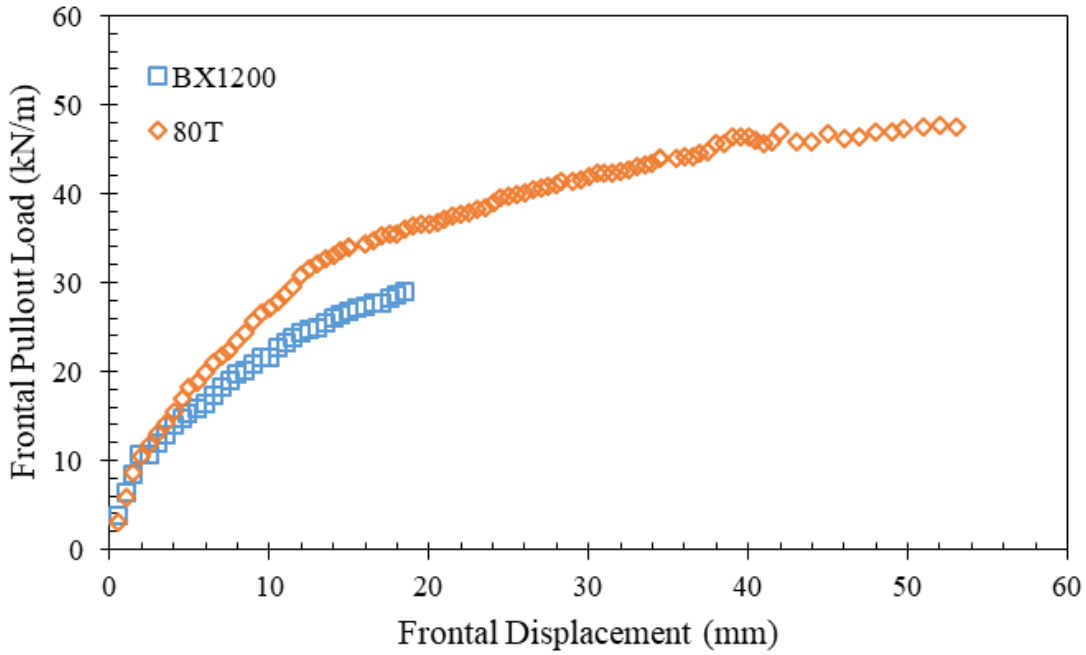

Figure 5.2.102. Frontal pullout load-displacement curves.

A comparison of the behavior at the early loading stage, up to failure of BX1200, was conducted. Figures 5.2.103 and 5.2.104 present the nodal displacement for the upper and lower passive reinforcement layers, respectively. Specifically, Figures 5.2.103a through 5.2.103d show the nodal displacements in the upper passive reinforcement corresponding to nodal displacements in the active reinforcement *u1*, *u3*, *u5*, and *u7*, respectively. Similarly, Figures 5.2.104a through 5.2.104d show the nodal displacements in the lower passive reinforcement corresponding to nodal displacements in the active reinforcement *u1*, *u3*, *u5*, and *u7*, respectively. Figures 5.2.103 and 5.2.104 reflect the load transfer from the active reinforcement to the passive reinforcements at the same nodal reinforcement of the active reinforcement.

Figures 103a, 103b, 104a, and 104b show that the interaction 80T has on its neighboring reinforcements is higher than that of BX1200. However, Figures 103c, 103d, 104c, and 104d show similar effect for both reinforcements. This observation is a result of the higher elongation BX1200 had compared to that of 80T. Overall, the comparison revealed information about the soil-reinforcement interaction stiffness. It was concluded that BX1200 geogrid has a slightly lower soil-reinforcement interaction stiffness, which resulted in a slightly less interaction with the neighboring reinforcement layers, compared to that of 80T geogrid.

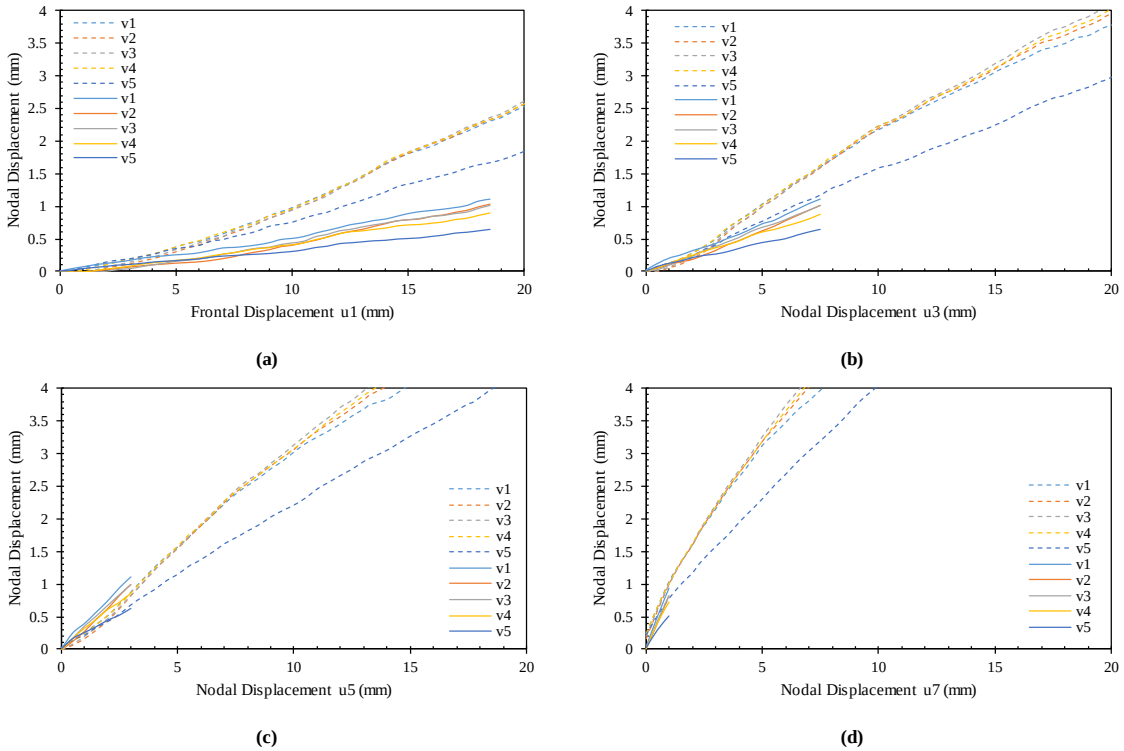

Figure 5.2.103. Nodal displacements at the upper passive reinforcement with respect to various nodal displacements at the active reinforcement: (a) nodal displacement u1; (b) nodal displacement u3; (c) nodal displacement u5; and (d) nodal displacement u7 (solid lines belong to BX1200 and dashed lines belong to 80T).

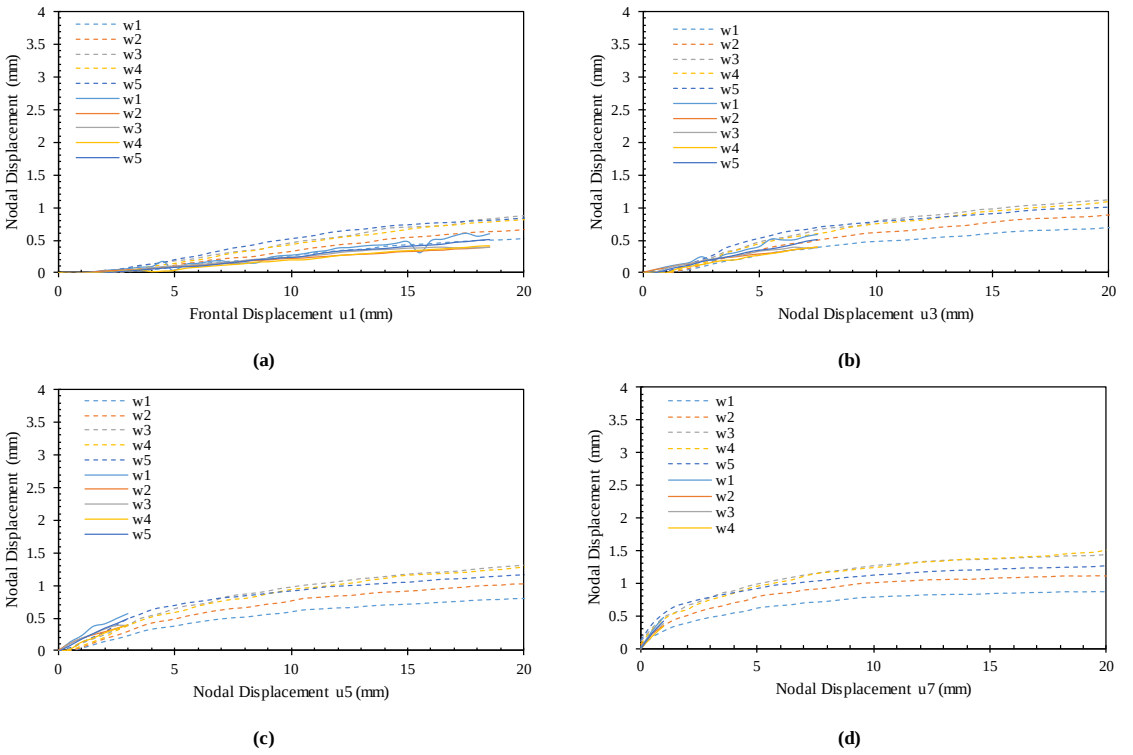

Figure 5.2.104. Nodal displacements at the lower passive reinforcement with respect to various nodal displacements at the active reinforcement: (a) Nodal displacement u1; (b) Nodal displacement u3; (c) Nodal displacement u5; and (d) Nodal displacement u7 (solid lines belong to BX1200 and dashed lines belong to 80T).

Figures 5.2.105 through 5.2.107 show the displacement profiles for the active and passive reinforcement layers at active reinforcement frontal displacement (*u1*) of 5, 10, and 15 mm (0.2, 0.4 and 0.6 in). Note that the comparison is based on the same frontal displacement for the different reinforcements rather than the same pullout frontal load. The profiles of BX1200 geogrid show slightly lower displacement along the reinforcement length compared to those of 80T geogrid. This was observed for both active and passive reinforcement layers.

For a better comparison, Figure 5.2.108 show the passive reinforcement displacement profiles for intermediate nodal displacements of the active reinforcement of 5 mm (0.2 in). Specifically, Figures 5.2.108a and 5.2.108b provide comparisons of the upper passive reinforcement profiles for same nodal displacements *u1* and *u3*, respectively. That is, the comparisons were conducted for the similar soil-reinforcement induced interface displacement. It was observed that the interaction between the reinforcement layers in case of the 80T geogrid is slightly higher than that in case of the BX1200 geogrid.

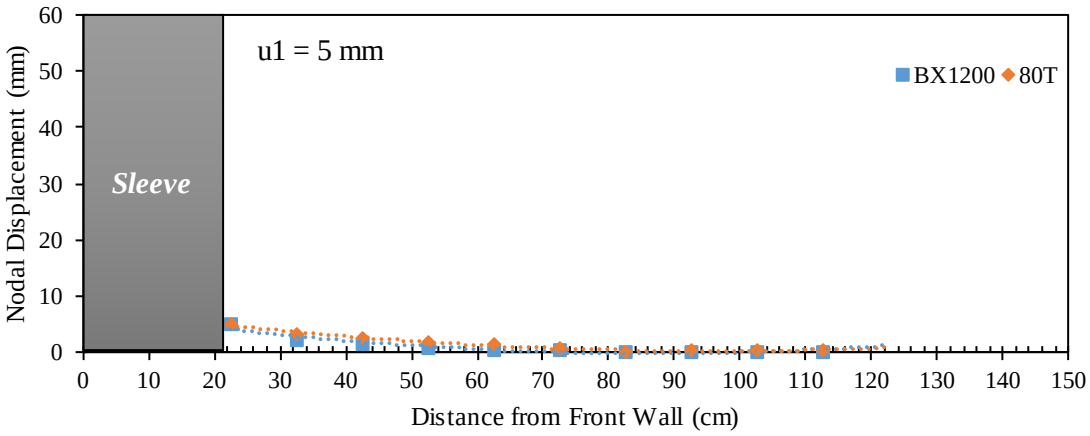

(a)

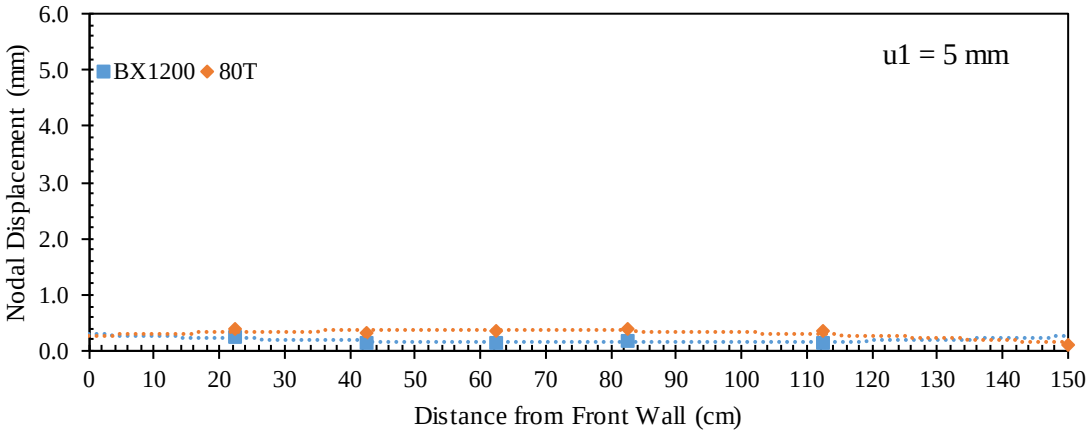

(b)

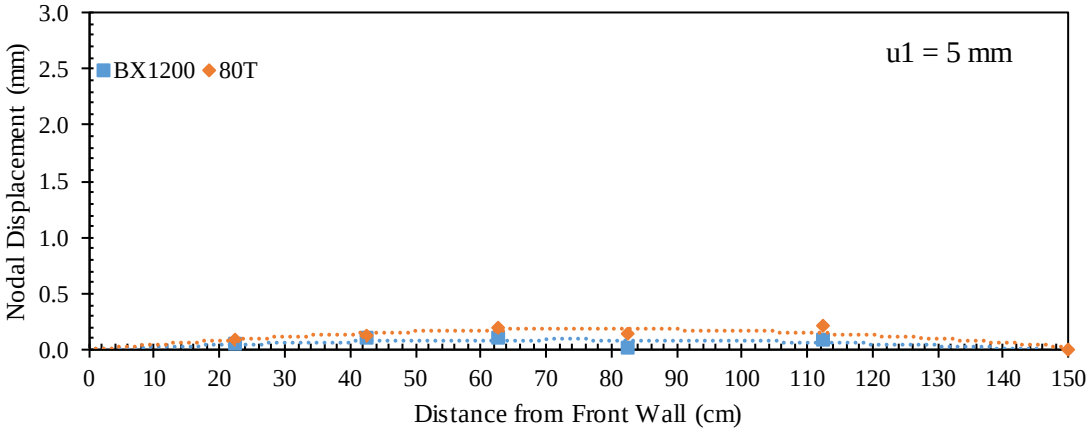

(c)

Figure 5.2.105. Reinforcement displacement profiles at frontal displacement u1 = 5 mm (0.2 in): (a) Active reinforcement; (b) Upper passive reinforcement; and (c) Lower passive reinforcement.

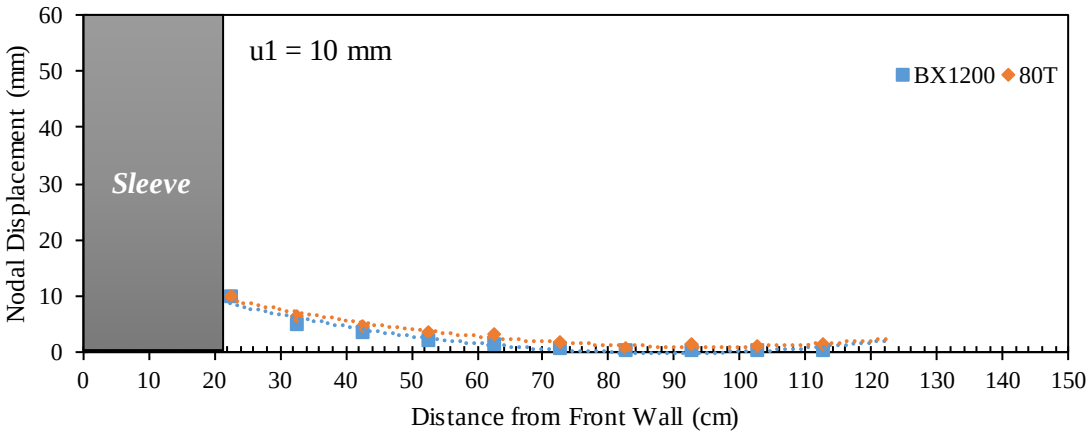

(a)

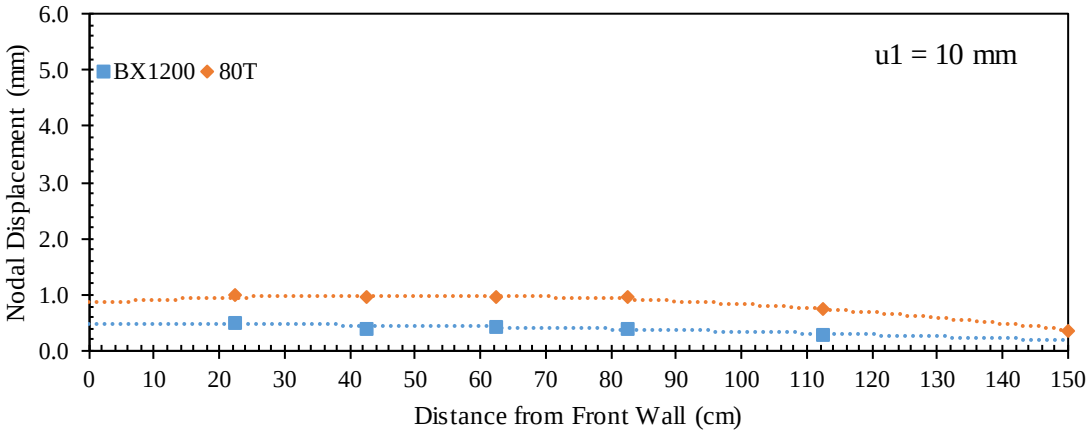

(b)

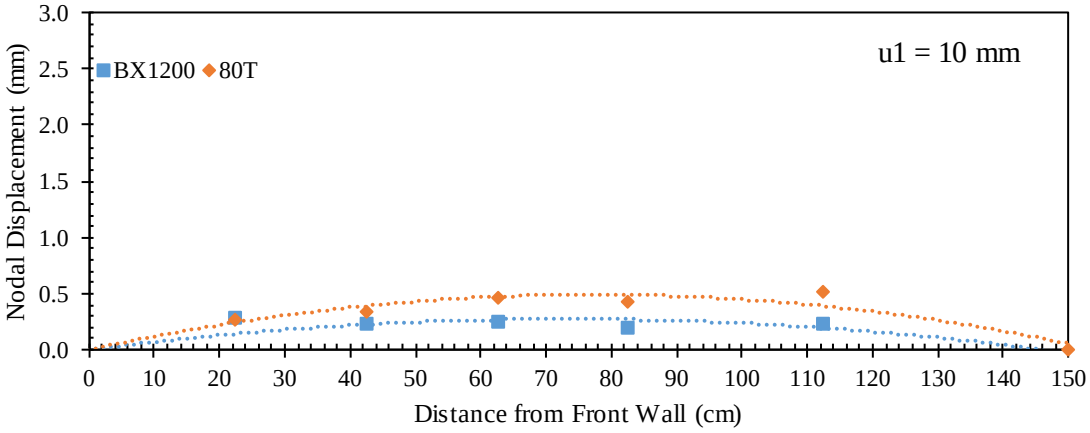

(c)

Figure 5.2.106. Reinforcement displacement profiles at frontal displacement u1 = 10 mm (0.4 in): (a) Active reinforcement; (b) Upper passive reinforcement; and (c) Lower passive reinforcement.

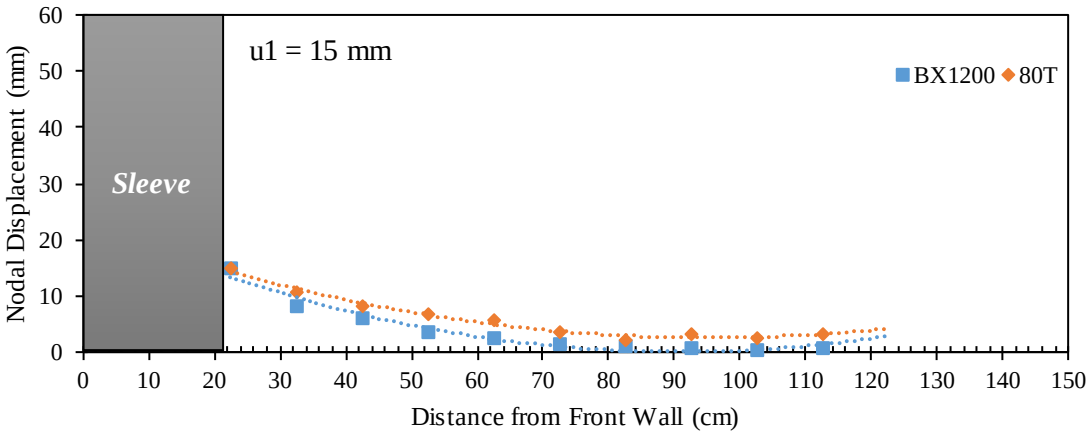

(a)

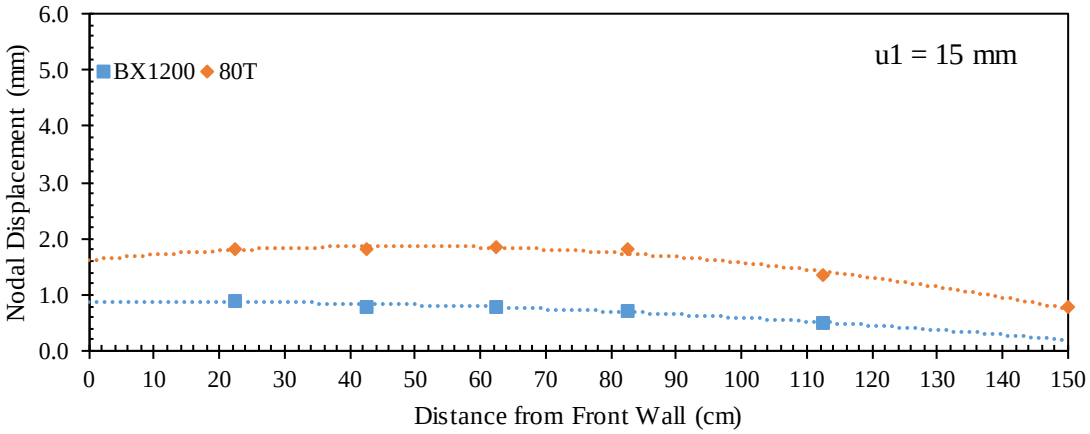

(b)

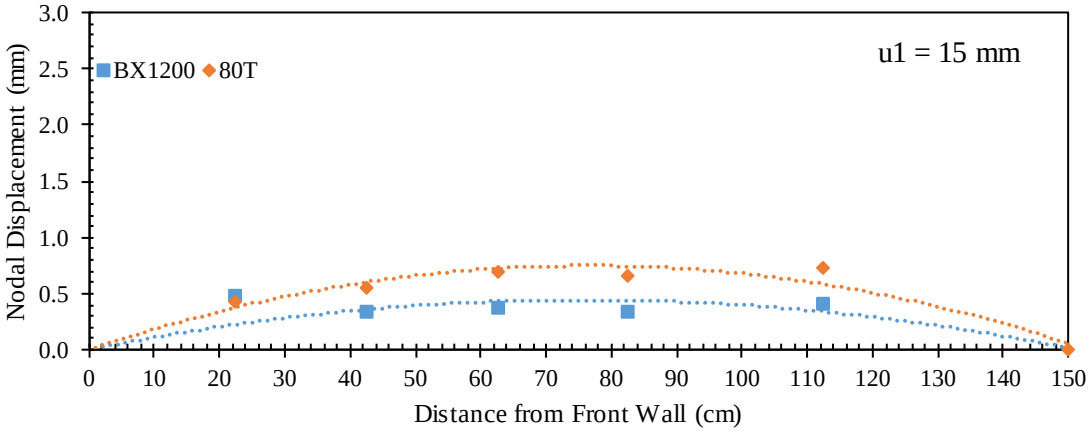

(c)

Figure 5.2.107. Reinforcement displacement profiles at frontal displacement u1 = 15 mm (0.6 in): (a) Active reinforcement; (b) Upper passive reinforcement; and (c) Lower passive reinforcement.

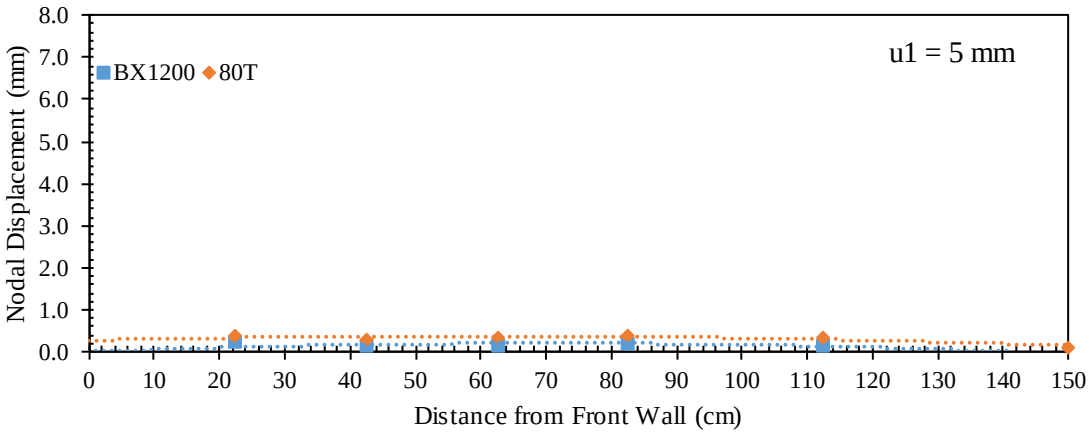

(a)

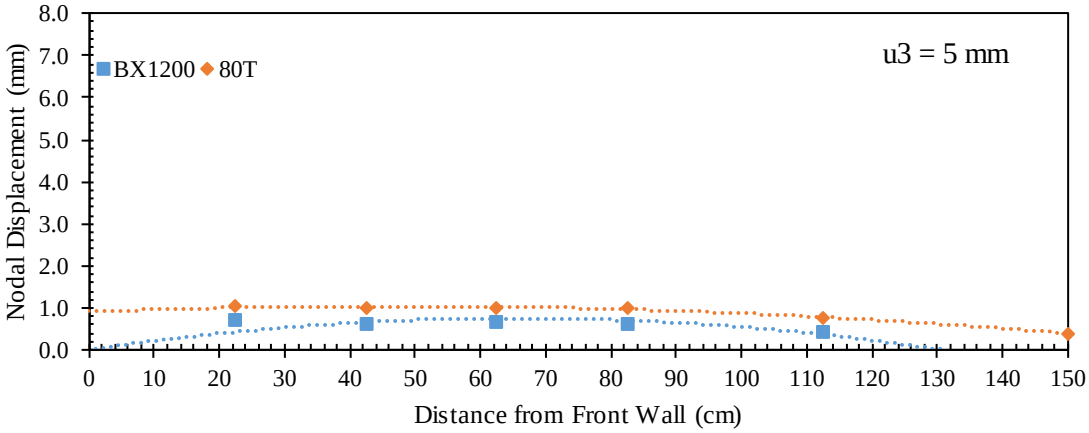

(b)

Figure 5.2.108. Upper passive reinforcement displacement profiles: (a) At nodal displacement u1 = 5 mm (0.2 in); and (b) At nodal displacement u3 = 5 mm (0.2 in).

Figures 5.2.109 through 5.2.111 present the horizontal soil displacement measured for nodal displacements of 5, 10, and 15 mm (0.2, 0.4 and 0.6 in), respectively. Each figure consists of an a and b that show the soil displacement with respect nodal displacements *u1* and *u3*, respectively. These displacements were measured at specific locations by tracking artificial gravel particles making a vertical array within the soil at 0.305 m (1 ft.) from the front wall. It was observed that the soil displacement is smaller in case of BX1200 geogrid compared to that of 80T geogrid. This difference was observed to increase as pullout progressed due to the difference the soil-reinforcement interaction between the two reinforcements.

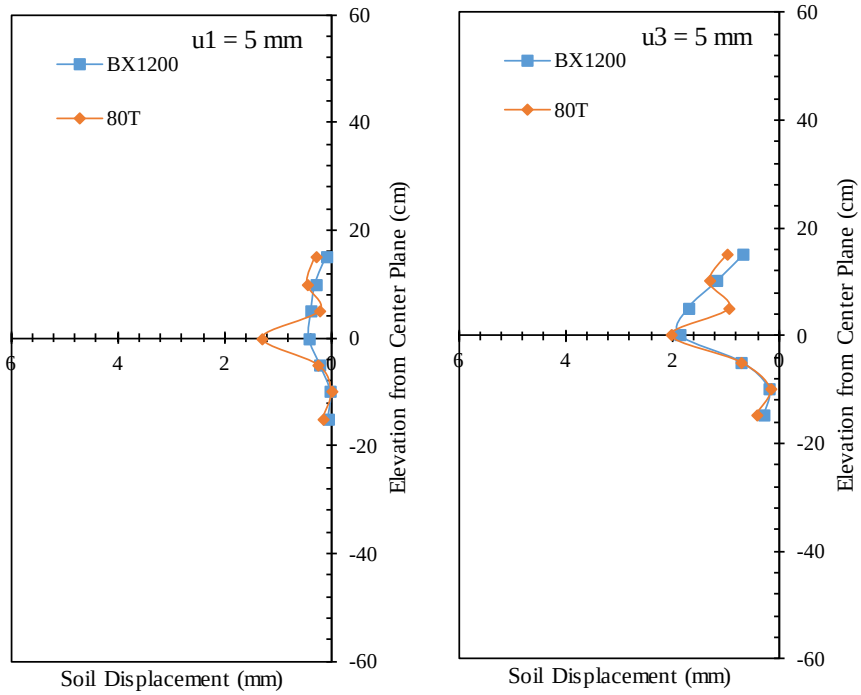

(a) **(b)**

Figure 5.2.109. Horizontal soil displacement profiles (measured by means of artificial gravel particles): (a) At nodal displacement u1 = 5 mm (0.2 in); and (b) At nodal displacement u3 = 5 mm (0.2 in).

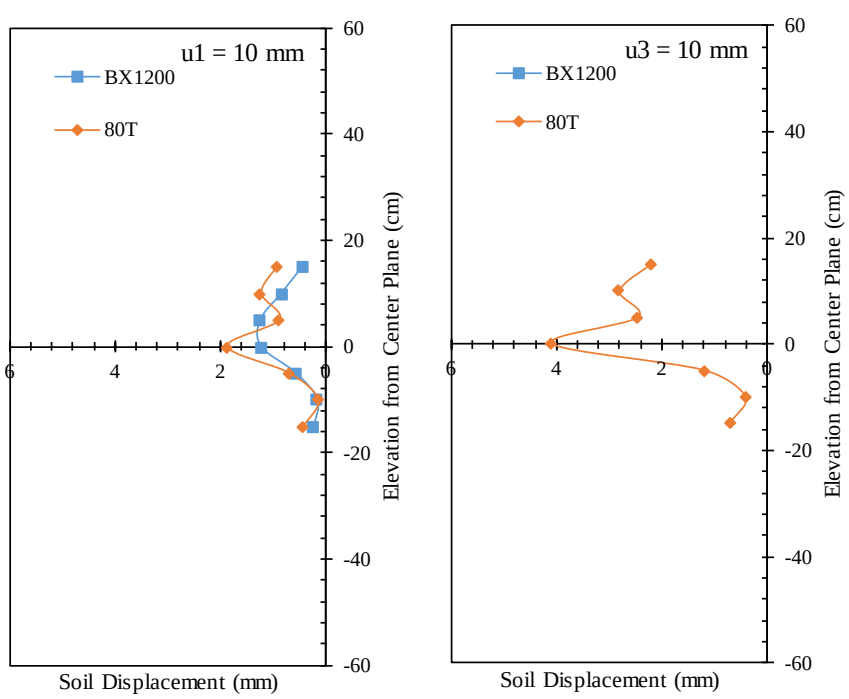

(a) **(b)**

Figure 5.2.110. Horizontal soil displacement profiles (measured by means of artificial gravel particles): (a) At nodal displacement u1 = 10 mm (0.4 in); and (b) At nodal displacement u3 = 10 mm (0.4 in).

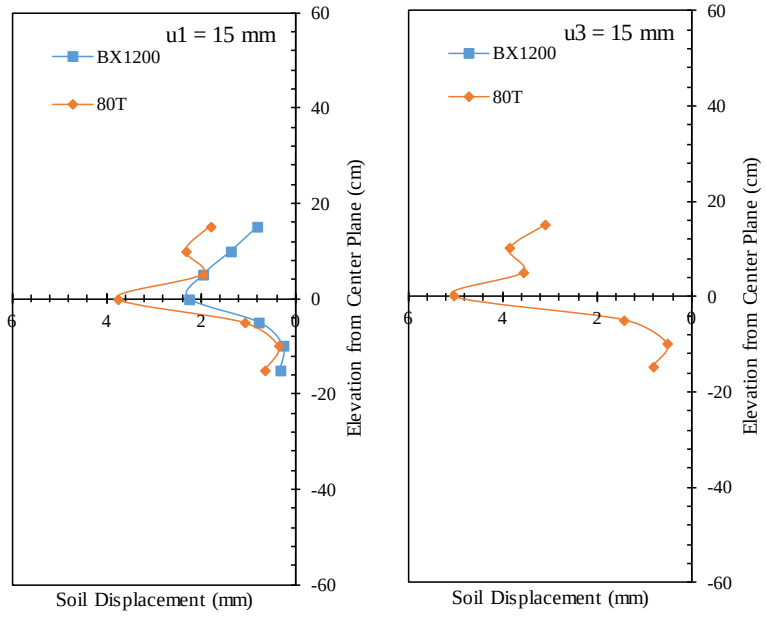

(a) **(b)**

Figure 5.2.111. Horizontal soil displacement profiles (measured by means of artificial gravel particles): (a) At nodal displacement u1 = 15 mm (0.6 in); and (b) At nodal displacement u3 = 15 mm (0.6 in).

Figure 5.2.112 show the soil-reinforcement relative displacement at 0.305 m (1 ft.) from the front wall. This slippage was obtained by subtracting the reinforcement displacement at this location (by interpolation between *u1* and *u3*) and the soil displacement measured by the artificial gravel particle adjacent to the reinforcement (LP24). It was observed that the slippage at the BX1200 interface was higher than that at the 80T interface due to the difference in the soil-reinforcement interaction between the two reinforcements.

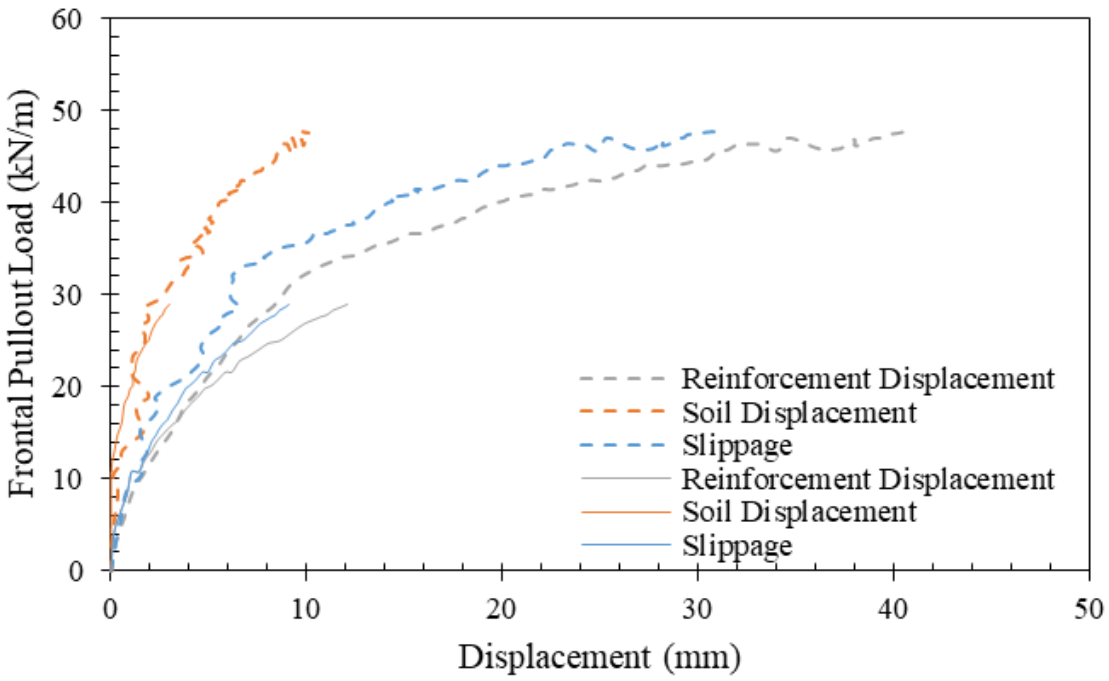

Figure 5.2.112. Soil-reinforcement relative displacement (solid lines belong to BX1200 and dashed lines belong to 80T).

Figure 5.2.113 shows the vertical soil displacement measured by means of the artificial gravel particles placed on top of the reinforced soil mass. Figures 5.2.113a through 5.2.113d show the soil displacement with respect to reinforcement nodal displacement *u1*, *u3*, *u5*, and *u7*. Both tests showed very similar dilation near the front side of the reinforced soil mass and similar settlement near the rear side.

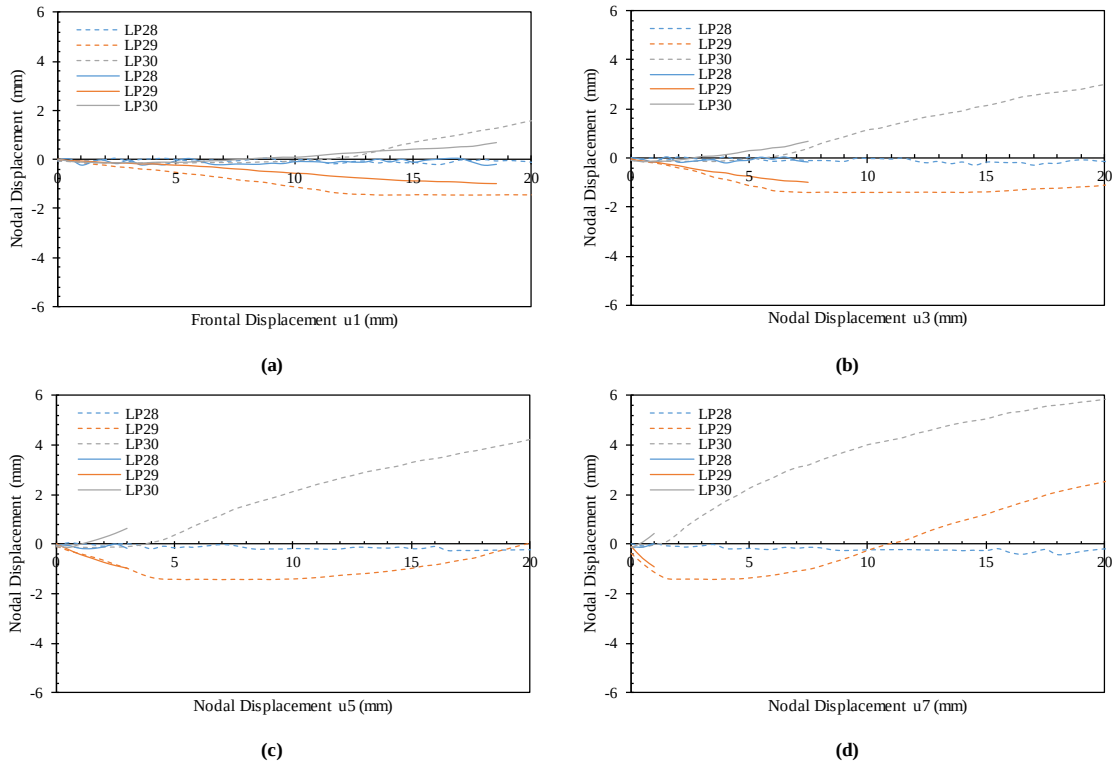

Figure 5.2.113. Vertical soil displacements profiles (measured by means of artificial gravel particles) with respect to various nodal displacements at the active reinforcement: (a) Nodal displacement u1; (b) Nodal displacement u3; (c) Nodal displacement u5; and (d) Nodal displacement u7 (solid lines belong to BX1200 and dashed lines belong to 80T).

5.2.4 CONCLUSIONS

A comprehensive testing program has been conducted adopting the developed experimental approach and equipment detailed in Chapter 5.1. The testing program was tailored to evaluate the following aspects: (1) testing repeatability; (2) effect of reinforced soil confinement; (3) effect of reinforcement vertical spacing; (4) effect of reinforcement properties; (5) effect of boundary type; and (6) effect of backfill properties. The findings from this study are summarized in the following subsections:

5.2.4.1 EVALUATION OF TESTING REPEATABILITY

Two identical tests were conducted to evaluate the testing repeatability of the developed experimental approach and equipment. This evaluation led to the following findings:

1. The frontal pullout load-displacement experimental curves for both tests almost coincided.
2. The displacement profiles for the active and passive reinforcement layers were found to match well at the various loading stages. Similar observation was made for the displacement profiles of the passive reinforcement layers.

3. The horizontal soil displacement was very similar for both tests at the various loading stages.

5.2.4.2 EVALUATION OF THE EFFECT OF REINFORCED SOIL CONFINEMENT

This evaluation was carried out through three comparisons for test groups having different reinforcement vertical spacing: (1) a comparison between four similar tests conducted at different confining stresses with reinforcements spaced at 0.15 m (6 in.); (2) a comparison between two similar tests conducted at different confining stresses with reinforcements spaced at 0.10 m (4 in.); and (3) a comparison between two tests conducted at different confining stresses with reinforcements spaced at 0.05 m (2 in.). This evaluation led to the following findings:

1. The frontal pullout load-displacement experimental curves showed that the resistance of the active reinforcement to pullout increases with the increase in the confining normal stress. Same observation was made for test groups of different reinforcement vertical spacing.
2. The soil-reinforcement interface shear strength increases with the increase in the confining normal stress.
3. The interface shear strength back-calculated from the pullout test results at ultimate condition were found higher than that resulting from direct shear testing conducted as a part of the study detailed in Chapter 7. This was attributed to the additional passive resistance that mobilizes in pullout tests with flexible reinforcements through perforations between filaments by adjacent gravel particles. These perforations were absent in case of the direct shear testing.
4. The tests conducted at low confining stresses tend to mobilize displacement in the passive reinforcements more those conducted at higher confining stresses at early pullout loading stages. This is because the flexibility of soil to deform at low confining stresses resulting in higher load transfer and thus higher interaction between reinforcements. However, as pullout progressed the soil-reinforcement interface stiffness yielded more in the tests conducted at low confining stresses compared to this of the tests conducted at higher confining stresses.
5. By comparing the integrated nodal displacement measured for the passive reinforcements occurring at the same corresponding integrated nodal displacement for the active reinforcement, it was concluded that the higher the confining stress the higher the interaction between neighboring reinforcement layers.
6. The interaction between neighboring reinforcement layers was higher at high confinement levels.
7. At high confining pressures, the soil, which is the medium responsible to transfer the load, is stiffer and can more transfer load before yielding either internally or at the interface with reinforcements.
8. The reinforcement vertical spacing has insignificant effect on the sensitivity of the reinforcement interaction to the confinement level.
9. The slippage at the interface of the active reinforcement was lower in the tests conducted at low confining normal stresses compared to those conducted at high confining stresses.

10. The vertical soil displacement measured at the top of the reinforced soil mass showed that the soil tended to dilate near the front and settle near the back as pullout loading progressed. It was observed that the dilation was higher in tests conducted at low confining normal. At low confining stresses soils tend to dilate more when subjected to shear compared to soils at high confining stresses. Similar observation was made for tests conducted with reinforcements placed at different reinforcement vertical spacing.

5.2.4.3 *EVALUATION OF THE EFFECT OF REINFORCEMENT VERTICAL SPACING*

Two comparisons were carried out between test groups having different confining normal stress: (1) a comparison between six tests conducted at confining normal stress of 50 kPa (7.3 psi) and with reinforcements placed at different vertical spacings; and (2) a comparison between three tests conducted at confining normal stress of 21 kPa (3 psi) and with reinforcements placed at different vertical spacings. This evaluation led to the following findings:

1. At high confining normal stress, the frontal pullout load-displacement experimental curves coincided well at early pullout loading stages and then fairly agree with slight scatter near pullout failure. This observation shows that the reinforcement vertical spacing has insignificant interference with the soil-reinforcement interaction. However, at low confining normal stress, the frontal pullout load-displacement experimental curves, tests conducted at smaller reinforcement vertical spacing.
2. The reinforced soil tended to dilate more than the tests conducted at high confining pressure. The dilation tendency was smaller in tests conducted at smaller reinforcement vertical spacing. That is, the smaller vertical spacing results in some dilation reduction, which may result in an increase in the soil-reinforcement interface strength.
3. The tests conducted with reinforcements placed at larger vertical spacing resulted in small interaction between neighboring reinforcements. The effect of the reinforcement spacing may have a bigger impact at high confining normal stresses.
4. The reinforcement vertical spacing has insignificant impact on the soil-reinforcement interaction behavior of the active reinforcement.
5. A lower threshold bound for reinforcement vertical spacing below which the effect of the spacing is maximum was identified. This spacing is specific for a confining normal stress, soil medium properties, reinforcement properties, soil-reinforcement interaction properties. For the testing program implemented in this study, the lower threshold vertical spacing was identified as 0.15 and 0.10 m (6 and 4 in) for confining stress of 50 and 21 kPa (7.3 and 3 psi), respectively.
6. An upper threshold bound for reinforcement vertical spacing beyond which the interaction between reinforcement layers almost vanished was identified. Similarly, this spacing is specific for a confining normal stress, soil medium properties, reinforcement properties, soil-reinforcement interaction properties. For the testing program implemented in this study, the upper threshold vertical spacing was identified as 0.3 m (1 ft.) for tests conducted at confining stress of 50 kPa (7.3 psi).

7. The horizontal soil displacement was higher in the tests conducted with reinforcements placed at small spacings. That was because the soil-reinforcement interfaces of the passive reinforcements have weaker shear strength than the internal strength of the soil. These weaker interfaces allowed the soil in between the reinforcement layers to displace more than in the case of no passive reinforcements. However, the passive reinforcements reduced the load transfer from the active reinforcement to the soil masses on the other sides of the passive reinforcements.
8. For each testing group, the same energy was delivered from the active reinforcement to the soil and the passive reinforcements. For the tests conducted with reinforcements placed at small vertical spacings, the soil mass in between the active and passive reinforcements displaced more as it received more energy per unit soil volume from the active reinforcement. On contrary, the soil masses on the other sides of the passive reinforcements displaces less than that in the tests conducted with reinforcements placed at small vertical spacings.
9. The slippage at the soil-reinforcement interface was smaller in tests conducted with reinforcements placed at small vertical spacings. That was because the displacement of the soil adjacent to the reinforcements in tests conducted with reinforcements placed at small vertical spacings was higher.
10. The vertical soil displacement measured at the top of the reinforced soil mass showed that the soil tended to dilate near the front and settle near the back as pullout loading progressed. The dilation tendency near the front takes place after settlement in early loading stages as shear stresses were generated at the soil-reinforcement interface. The dilation tendency was higher in the tests conducted with reinforcements placed at smaller spacings.
11. The dilation tendency was high in tests conducted at low confining stresses compared to those conducted at high confining stresses. That is, the impact of reinforcement vertical spacing on the soil-reinforcement behavior was more pronounced in the tests conducted at 21-kPa confining stress.

5.2.4.4 EVALUATION OF THE EFFECT OF REINFORCEMENT PROPERTIES

Three comparisons were carried out to evaluate various reinforcement properties: (1) a comparison between HP570 and RS580i reinforcements to evaluate the effect of reinforcement tensile stiffness; (2) a comparison between HP570 and 80T reinforcements to compare the behavior of geotextiles and geogrids; and (3) a comparison between 80T and BX1200 to evaluate the effect of reinforcement rigidity. This evaluation led to the following findings:

1. The frontal pullout load-displacement curves cannot provide full understanding about the soil-reinforcement interaction. A deeper look into the behavior of each reinforcement along their embedment length is needed to complement the information retrieved about the front.
2. The higher the soil-reinforcement interaction, the higher the ability of the reinforcement to transfer load to the soil and the neighboring reinforcement layers for a given soil medium and confinement level.

3. The soil-reinforcement interaction comprises two components: (1) the passive resistance that can be mobilized by the transverse members. The members can be transverse ribs in geogrids or transverse yarns in geotextiles if particles were able to interfere with the geotextile fabric; and (2) the soil-reinforcement interface friction (interface shear resistance).
4. Geotextile reinforcements with similar soil-reinforcement interface friction may have different soil-reinforcement interaction. The fabric rigidity plays a significant role in the interaction between the fabric and the surrounding soil medium that adds additional resistance to the interface friction. Passive resistance against adjacent soil particles punching in the fabric can contribute to the soil-reinforcement interaction. This interaction resembles the interaction takes place due to passive resistance of transverse ribs in geogrid reinforcements.
5. The contribution of the passive resistance to the soil-reinforcement interaction are likely to outweigh the contribution of the interface friction.
6. The higher the soil-reinforcement interaction, the lower the slippage at the soil-reinforcement interface.
7. The higher the soil-reinforcement interaction, the larger the horizontal soil displacement.
8. The soil adjacent to active reinforcements exhibited higher rate of displacement than the soil away from reinforcements. This is because of the yielding in internal shear strength of the fill material that limits the load transfer from the reinforcement to larger distance away from the reinforcement.
9. The vertical soil displacement measured at the top of the reinforced soil mass showed dilation near the front side of the reinforced soil mass and settlement near the rear side. The higher the soil-reinforcement interaction, the higher the dilation at the front and the settlement at the back.

5.2.5 REFERENCES

Morsy, A. M. (2017). Evaluation of soil-reinforcement composite interaction in geosynthetic-reinforced soil structures. Doctoral dissertation, The University of Texas at Austin, Austin, Texas, USA.

5.3 FUNDAMENTAL ASSESSMENT OF SOIL-GEOSYNTHETIC SHEAR BAND DEVELOPMENT USING TRANSPARENT SOIL

5.3.1 INTRODUCTION

The interaction of reinforcements with the surrounding soil in geosynthetic-reinforced soil structures involves complex shear stress transfer mechanisms. The manifestation of which is a shear band that develops in the vicinity of the reinforcement. The interface shear between reinforcement surface and soil has been generally estimated considering the surface area of the reinforcement and the interface shear strength properties between the soil and reinforcement. This study evaluates the soil-geosynthetic interaction by capitalizing on recent technologies that would allow generating information, in significant volumes and unprecedented detail, on deformations due to soil-geosynthetic interaction. New small-scale transparent soil-geosynthetic equipment has been recently developed at the University of Texas at Austin. This equipment allows monitoring the interaction between the soil and the geosynthetic under tension load.

Load transfer between the geosynthetic and the soil at interior locations is not measured directly and their estimate from stress transfer models is very limited because either no measurements or only point displacement measurements. Instead, the experimental program proposed in this study obtained the entire field of internal reinforcement displacements (reinforcement and soil straining), which will ultimately provide the rich source of information that needed to develop and calibrate stress transfer models. A number of geosynthetics were used to investigate the effect of the reinforcement type, tensile strength, tensile stiffness, and in-plane rigidity on the soil-reinforcement interface load transfer. It was concluded that geogrid reinforcement has larger shear band than geotextile reinforcement. In addition, reinforcements of smaller grid aperture size results in larger shear band than those with larger aperture size. Reinforcements of higher tensile strength and higher stiffness results in smaller shear band. Also, the higher the normal pressure on the soil-geosynthetic interface the larger the shear band.

This research evaluated the soil-geosynthetic interaction by capitalizing on recent technologies that would allow generating information, in significant volumes and unprecedented detail, on deformations due to soil-geosynthetic interaction. A major disadvantage of previous soil-reinforcement interaction research studies has been that the deformation of the embedded reinforcement and its surrounding soil is not measured directly. This study presents an experimental evaluation that allowed mapping of the entire displacement field of reinforcement and its surrounding soil (i.e., the development of soil-reinforcement interface shear band).

5.3.2 BACKGROUND

5.3.2.1 TRANSPARENT SOIL TECHNOLOGY

Transparent soil technology was used in order to provide significant insight into many geotechnical engineering problems (Wakabayashi 1950; Jewel 1984; Gill and Lehane 2001; Sadek et al. 2003; McKelvey et al. 2004; Song et al. 2009; Iskander and Liu 2010). This section includes a detailed background on previous studies that are relevant to this study. The principle of transparent soils is based on submerging a translucent granular material into a liquid with the same refractive index. This approach makes the translucent material becomes transparent when saturated. The characteristics of previous research involving transparent soil techniques are summarized next.

Use of glass beads: Crushed glass or glass beads were used in the past with a fluid having the same refractive index (Wakabayashi 1950; Drescher 1976; Allersma 1982). However, these glass beads were more translucent than transparent, which did not provide adequate transparency through the granular media. In addition, the resulted media were deemed not to satisfactorily represent the properties of natural soils (Manngeimer and Oswald 1993; Sadek et al. 2002). Wakabayashi (1950) applied this principle using crushed glass mixed with a solution of carbon-disulphide and benzene to conduct photo-elastic studies of stress distribution generated by a loaded footing on the soil surface. Dyer (1985) produced a transparent soil with crushed Pyrex glass and a colorless liquid paraffin to conduct photo-elastic experiments with direct shear and pullout tests. However, transparent soils obtained from crushed glass have been reported not to have similar geotechnical properties to sands (Sadek et al. 2002).

Use of silica gel beads: Silica powder or silica gel was used with colorless pore fluids having the same refractive index. Iskander et al. (1994, 2002a, 2002b), Gill and Lehane (2001), Sadek et al. (2002), Liu et al. (2003), Zhao and Ge (2007), and Hird and Stanier (2010) used precipitated and flumed silica powder and silica gel beads as soil simulants. Sadek et al. (2002) used transparent soil obtained from silica gel beads saturated with a blend of white mineral oil and paraffinic solvent. The authors reported geotechnical properties of this transparent soil to be comparable to those of sands. However, the use of the silica gel particles was also found to have important drawbacks. Specifically, they were found to deform plastically even under low confining pressures (Iskander 1998; Iskander et al. 2003; Zhao and Ge 2007). Also, silica gel particles were found to be difficult to de-air (Iskander et al. 2002b, 2003) and to be affected by high humidity and water (hydroscopic). This was reported to affect the particles color and stability. In addition, silica gel particles may undergo chemical reactions with time that cause changes in color and reduce their transparency (Iskander 2010). Sadek et al. (2002) reported using a paraffinic solvent with some mineral oil as a pore-fluid. This solvent is volatile, thus classified as hazardous material.

Use of crushed fused quartz: Ezzein and Bathurst (2011a, 2011b) have recently proposed using crushed quartz submerged in a mixture of mineral oil. The transparent soil was reported to have a geotechnical behavior comparable to that of sands. In addition, the matching

refractive index fluid is composed of non-volatile, non-hazardous liquids. Also, the transparent soil is non-porous and incompressible, with transparency that does not degrade over time. Surveys of reported combinations of transparent granular materials with matching transparent fluids by Iskander (2010) and Ezzein and Bathurst (2011a) indicate that the combination of fused quartz and mineral oil material has the greatest viewing depth. Ferreira and Zornberg (2016) compared the behavior of fused quartz to that of conventional soil. They concluded that the transparent soil makes a good surrogate for sands in reinforcement pullout testing.

5.3.2.2 TRANSPARENT SOIL IN SOIL-REINFORCEMENT INTERACTION

Ezzein and Bathurst (2011a) conducted a study on the pullout resistance of reinforcements embedded in soil using the transparent soil technology. They developed a large transparent pullout device that accommodated transparent soil, which constituted of crushed fused quartz granules submerged in mineral oil with the same refractive index. Ezzein and Bathurst (2011b, 2014) conducted an experimental evaluation of reinforcement pullout resistance using this developed transparent setup, which allowed for direct visualization of the reinforcement layer embedded in the transparent soil.

Ferreira and Zornberg (2014, 2015), and Peng and Zornberg (2016, 2017) to allow for direct visualization to deformations of geogrid reinforcement embedded under pullout load, which helped understanding the soil-reinforcement load transfer mechanisms. Ferreira and Zornberg (2016) mapped the deflection of the transverse ribs for biaxial geogrid reinforcements. Subsequent studies investigated the contribution of transverse ribs in the soil-reinforcement load transfer mechanisms for biaxial and triaxial extruded polypropylene geogrids (Peng and Zornberg 2016, 2017). Ferreira and Zornberg (2016) successfully measured the deformation of soil near the soil-reinforcement interface.

5.3.2.3 DIGITAL IMAGING IN GEOTECHNICAL ENGINEERING

Although digital image analysis techniques have found widespread application in disciplines such as medicine, biology, and geography, applications within civil engineering are more incipient (Mora et al. 1998). However, recent advances in hardware and software for digital image processing and analysis have opened the way for major breakthroughs in areas relevant to geotechnical engineering. In fact, promising advances involving image-processing techniques have recently been made for the purposes of granular soil characterization, including evaluation of porosity, fabric, structure, and uniformity of cohesionless soils (Kemeny et al. 1993, Thomas et al. 1994, Kuo and Frost 1996, Frost and Kuo 1996, Obaidat et al. 1998, Jang and Frost 1998, Jang et al. 1999). Progress has also been made in the use of digital image analysis for assessment of deformation of granular soils and shear band development (Gustafsson et al. 1994, Raschke et al. 1996, Liang et al. 1997) as well as for measurement of geomembrane surface roughness (Dove and Frost 1996, 1999). In addition, the use of digital image analysis techniques has been adopted for evaluation of the pore opening size distribution of geotextiles (Aydilek et al. 2002) and for measurement of strain distribution under tensile testing (Kutay et al. 2006).

Particle Image Velocimetry (PIV) is a technique used to obtain velocity measurements through digital image correlations. It has been traditionally used in studies of fluid mechanics. In these studies, seeding particles are added to the fluid and worked as tracers since these seeding particles are chosen such that they create a significant contrast against the fluid. Images are obtained at a specific rate and are later processed and compared to determine the velocity vectors at each time step. This technique has also been used in geotechnical applications, and has become the technique of choice in studies involving tracking the movement of soil. White et al. (2003), Raffel et al. (2007), and Pan et al. (2009) provided detailed description of this technique.

While the use of transparent soil and digital image analysis is proposed for this study, other techniques (e.g. photo-elastic methods, X-ray tomography) have also been used in previous studies. These techniques are not practical for evaluation of soil-geosynthetic interaction but these studies provide further insight into transfer mechanisms. Wakabayashi (1950) determined the stress distribution in a powdered mass using photo-elastic methods. Specifically, by placing phenolite in locations where determination of stresses was desired, Wakabayashi (1950) was able to define the direction of the principal stresses within the soil mass. Dyer (1985) subsequently used photo-elastic methods to observe stress concentrations in reinforced soil systems. Computerized X-ray tomography (CT) has more recently been used in geology, geosciences, and rock mechanics. It was used to study soil and rock properties such as density, porosity, water content, solute concentration, macroscopic size, and fracture size (Shi et al. 1999). CT is based on the attenuation of X-rays after penetrating objects and on their collection by detectors behind the object. The resulting images have been used to define properties that depend on the material density and atomic number (Colletta et al. 1991). CT has been used in geotechnical research to quantify shear strains and fracture features (e.g. Leung et al. 1995, Walters 1995, Desrues et al. 1996, Wibowo 1996). Shi et al. (1999) utilized CT to monitor the evolution of the internal failure in soil masses and visualize shear bands, while Wong (1999) used CT to visualize shear fractures. Otani et al. (2001) used similar CT techniques to observe the soil displacement field in sand confined geogrids.

A new technique for quantifying spatial deformation throughout transparent synthetic soil models using digital image correlation (DIC) and evaluating its accuracy based on predefined digital movement of soil image (e.g. Sadek et al. 2003). A digital camera is used to capture images of the slices before and after deformation.

5.3.3 TESTING EQUIPMENT

This study employs a small-scale soil-reinforcement interaction equipment initially designed and developed by Ferreira and Zornberg (2016) at the University of Texas at Austin. The setup involves a transparent box that is filled with soil surrogate, which is crushed fused quarts mixed with a mixture of mineral oils of the same refractive index as the fused quarts. When the fused quartz is saturated with the oil mixture it turns transparent (i.e., forming a transparent soil), which allows direct visualization of the reinforcement layer embedded.

5.3.3.1 EQUIPMENT DESCRIPTION

This equipment was designed to study the soil-geogrid interaction under small soil-reinforcement relative displacements. The box has three transparent faces: one face parallel to the reinforcement layer (to visualize the reinforcement deformation) and two side faces along the direction of reinforcement loading (to visualize the deformation of soil in vicinity to the reinforcement layer. The device used in this study has smaller dimensions that the standard pullout device dimensions recommended by ASTM D6707. However, the test targets evaluation of the soil-reinforcement interaction that takes place at very small interface displacements, which are likely to occur in several soil-reinforcement applications. In addition, the box is filled such that no dilation can take place. That is, the test allows for investigation of soil-reinforcement interaction in applications where dilation can be suppressed. Figure 5.3.1 shows a general view of the testing station: Figures 5.3.1a and 5.3.1b show a front view and side view of the device when mounted on the loading frame, respectively. The testing setup involves a loading frame, which similar to that used for geosynthetic wide-width tensile strength tests (ASTM D4595; ASTM D6637), except that the base clamp of the loading frame is replaced by a confined soil box, which the transparent soil device, and the top clamp is a roller grip, on which the reinforcement is clamped. Thus, the device is mounted on the frame such that the reinforcement layer is pulled out vertically. The reinforcement clamp is attached to the loading frame motor through a universal connection that ensures a point tensile load on the reinforcement. More information about the testing setup can be found in Zornberg et al. (2013), Ferreira (2013), and Ferreira and Zornberg (2015).

The box has a slit at the top where the reinforcement exists which is 12.7-mm (0.5 in) thick and 241.3-mm (9.5 in) wide. This slit is boosted with a tapered sleeve that extends by 12.7 mm (0.5 in) into the box. The interior of the transparent pullout box is 300-mm (1 ft.) wide, 250-mm (0.8 ft.) long, and 150-mm (0.6 ft.) deep. The box is closed with a lid that is backed with an air pressure bladder that, which can apply confining pressure on the soil mass in a perpendicular direction to the reinforcement plane. More information about the testing setup can be found in Ferreira (2013), and Ferreira and Zornberg (2015).

5.3.3.2 INSTRUMENTATION/MONITORING PROGRAM

The reinforcement clamp is connected to an S-type load cell that measures the tensile force applied to the reinforcement specimen in real time. The motor power is calibrated to displacement rate, which was set to 1 mm/min (40 mil/min) clamp displacement. Ferreira and Zornberg (2016) used markers (opaque black particles) embedded in the transparent soil mass to track deformation in vicinity of the soil-reinforcement interface upon loading the reinforcement layer. Peng (2017) upgraded the testing setup and used laser to create an illuminated plane in the middle of the transparent soil mass perpendicular to the reinforcement plane. This illuminated plane exhibited the boundaries of the particles (locations of potential refraction due to discrepancies in the values of the refractive indices). The setup upgraded by Peng (2017) was employed in this study.

Three cameras were used in each test: (1) a camera shooting against the front of the box to capture the reinforcement deformation (camera focused on the reinforcement layer confined plane); (2) a camera shooting against the side of the box to capture the soil deformation in a plane perpendicular to the reinforcement plane. This plane was illuminated by a set of two red-light lasers that are synchronized to switch on while the camera shoots and to switch off while the camera shooting against the front shoots (camera focused on the plane illuminated by the laser perpendicular to the reinforcement plane); and (3) a camera that shoots against the unconfined reinforcement portion (camera focused on the reinforcement unconfined plane), which allows evaluating the tensile behavior of the tested specimen. A lighting system was used to enhance the brightness and the contrast of the tethered images. A bandpass filter lens was used on the camera shooting the side view of the box that allow only the reflected laser light to integrated on the camera's sensor. The laser was synchronized to turn on and off so as to allow capturing front images that are contaminated with reflections from the laser beam. Images were tethered from the three cameras simultaneously every 5 seconds, which is synchronized with the same data acquisition reading schedule.

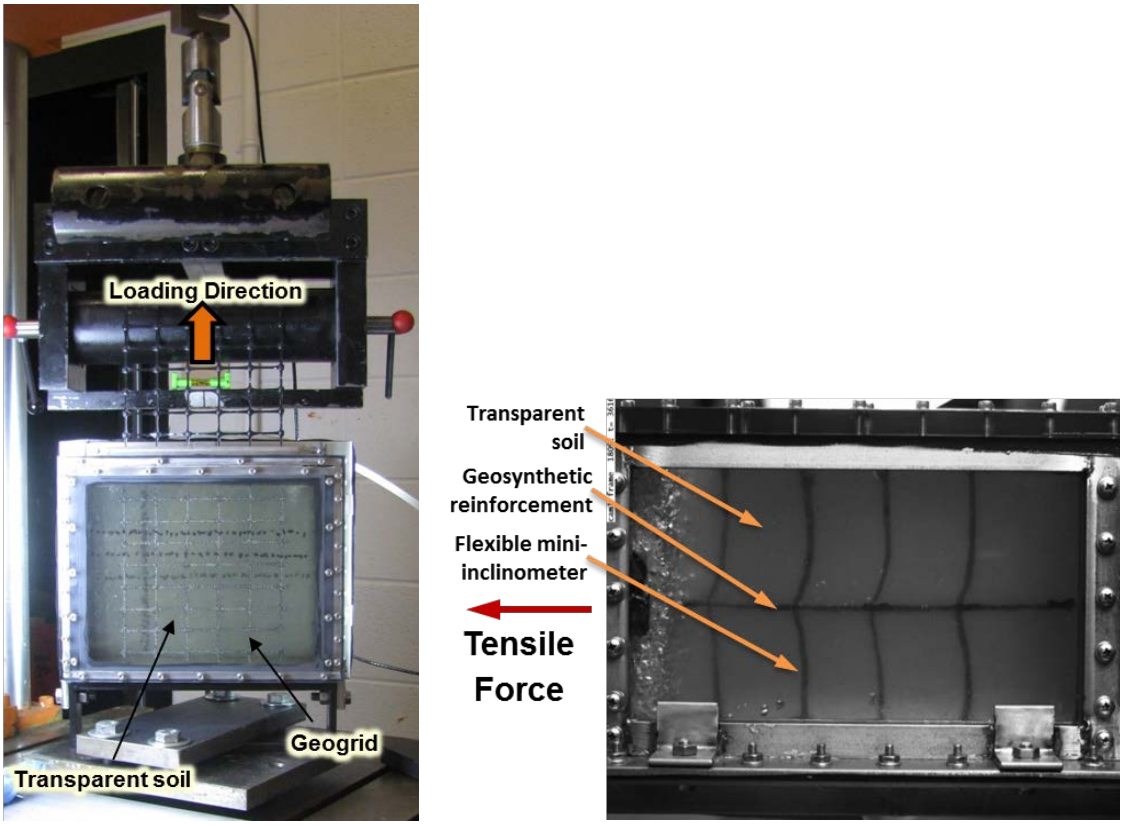

Figure 5.3.1: (a) Testing in progress of a geosynthetic embedded in transparent soil in the transparent box, at UT-Austin (Test conditions: 3psi of normal stress, biaxial geogrid, fused quartz in mineral oil); (b) development of Shear bands during testing using transparent soil techniques (Ferreira 2013).

5.3.4 TESTING MATERIALS

5.3.4.1 FILL MATERIALS

This study involved crushed fused quartz fill materials of different grain sizes. Fused quartz has been reported to be a good surrogate to conventional soil in soil-reinforcement applications (Ezzein and Bathurst 2011a, 2011b; Ferriera 2013; Ferriera and Zornberg 2016). The fused quartz used in this study is the same as that adopted in Ferriera (2013), Ferriera and Zornberg (2014, 2016), Peng and Zornberg (2016, 2017). This study involved two different gradations of the fused quartz, as shown in Figure 5.3.2, which represent coarse sand and fine gravel. The particle size for the fused quartz representing coarse sand ranges from 2.00 to 4.76 mm (0.1 to 0.2 in); whereas, that of for the fused quartz representing fine gravel ranges from 4.76 to 9.51 mm (0.2 to 0.4 in). Table 5.3.1 summarizes the properties of the two soils used in this study.

To quantify the angularity of the crushed fused quartz particles, the roundness index (Rn) proposed by Wilson et al. (1997) was adopted to quantify the particle roundness. This was implemented by analyzing the SEM images. Roundness index (Rn) is defined as $4\pi A/P2$ where A is the particle area and P is the particle perimeter as they appear on a 2D image for the particle. The angularity index (AI) was proposed by Reddy (2007) as the reciprocal of Rn to provide a wider range of particle roundess evaluation (i.e., AI ranges from 1 “rounded” to infinity “angular”, whereas Rn ranges from 0 “angular” to 1 “rounded”). The average Rn was found 0.725, wheras the average AI was found 0.387.

(a) (b)

Figure 5.3.2. Photographs of fused quartz: (a) Coarse Sand; and (b) Fine Gravel.

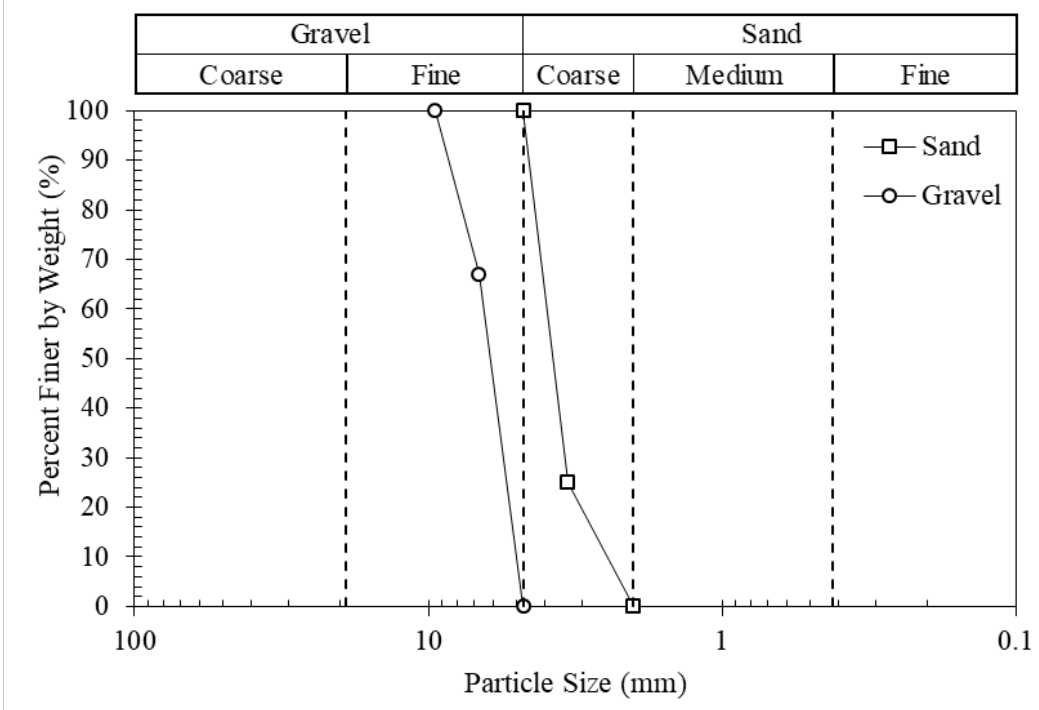

Figure 5.3.3. Grain size distribution of the transparent soils (fused quartz).

Table 5.3.1. Characteristics of the transparent soils (fused quartz).

	D_{10} [1] (mm)	D_{50} [2] (mm)	C_u [3]	C_c [4]	e_{max} [5]	e_{min} [6]	e [7]	γ [8] (Mg/m^3)	USCS [9]	G_s [10]
Coarse Sand	2.3	3.7	1.7	1.2	0.83	0.65	0.69	1.30	SP	2.20
Fine Gravel	5.1	6.1	1.3	1.0	0.87	0.69	0.73	1.27	GP	2.20

[1] D_{10}: Effective grain size.
[2] D_{50}: Mean grain size.
[3] C_u: Coefficient of Uniformity.
[4] C_c: Coefficient of Curvature.
[5] e_{max}: Maximum void ratio.
[6] e_{min}: Minimum void ratio.
[7] e: Constituted soil void ratio.
[8] γ: Constituted soil unit weight.
[9] USCS: Unified Soil Classification System.
[10] G_s: Specific gravity.

5.3.4.2 REINFORCEMENT MATERIALS

Multiple reinforcement types were used in this experimental program. These reinforcements has a wide range of properties. The unconfined tensile properties reported by the manufacturers of the reinforcements are summarized in Table 5.3.2. However, these properties are susceptible to variability during manufacturing, transportation, and storage. In addition, tensile strength and stiffness vary with the strain rate during axial loading. Also, the tensile strength increases with confinement.

Table 5.3.2. Reinforcement tensile properties.

Mechanical Properties	***HP570 (XMD[a])***	***RS580i (XMD[a])***	***BX1100 (XMD[a])***	***BX1200 (XMD[a])***	***80T (MD[b])***
Type	Woven Geotextile	Woven Geotextile	Extruded Geogrid	Extruded Geogrid	Knitted Geogrid
T_{ult}[c] (kN/m)	70.0	70.0	19.0	28.8	89.6
$T_{@5\%}$[d] (kN/m)	39.4	70.0	13.4	19.6	45.7
J[e] (kN/m)	876	1400	268	392	914

[a]XMD: Cross-machine direction (cross-rollway direction)
[b]MD: Machine direction (rollway direction)
[c]T_{ult}: Ultimate tensile strength
[d]$T_{@5\%}$: Tensile strength at 5% axial strain
[e]J: Approximate tensile stiffness, J = $T_{@5\%}$/5%

5.3.5 TESTING PROCEDURE

5.3.5.1 SOIL PREPARATION

The fused quartz was cleaned by washing them with oil on sieve #10 (2 mm (0.1 in)). This reduces the fines and dust particles that may have contaminated the fused quartz from preceding tests. The box was filled with fused quartz on eight lifts, 1.875-mm (0.1 in) thick each (four below the reinforcement level and four above the reinforcement level). Additional 0.2-mm (8 mil) thick layer was placed. The fused quartz required for every lift was weighed and placed to fill the corresponding volume that would render the targeted unit weight. The surface of every lift was leveled-out and gently hand-tamped to compact the fill material. After placing every lift, trapped air bubbles were eliminated by punching them gently with a thin open-ended tube.

5.3.5.2 REINFORCEMENT PREPARATION

Reinforcement layers were marked with a white color to provide a high contrast with the black geosynthetics. This contrast facilitates image processing thereafter. After placing the first four lifts of fused quartz, the reinforcement layer was placed such that the markers were facing downward (towards the transparent face of the box). The front slit of the box from which the reinforcement layer exits was sealed by two foam strips. These foam strips prevented the oil from seeping out from the box while filling the top half of the box. Note that these foam strips were removed after the box was rotated to its vertical orientation and fixed to the loading frame. After the box was filled, a stiffened steel lid was used to seal the box. The lid had a groove and that enclosed rubber ring. The rubber ring was daubed with vacuum grease to enhance the seal of the lid. The desired confining normal pressure was added to the air pressure bladder attached to the lid.

5.3.5.3 BOX SETUP

After the pressure was added to the soil mass, the box was adjusted to its vertical orientation and secured to a mounting base fixed on the loading frame. The reinforcement layer was then clamped to the roller grip fixed to the other side of the loading frame. A very small load was

applied to the reinforcement to allow adjusting the alignment of the box and the reinforcement layer to ensure that the reinforcement was pulled perfectly vertical. This was done be moving the box on its mounting base until the plumpness of the unconfined portion of the reinforcement layer was confirmed, after which the securing bolts of the box to the mounting base were tightened.

5.3.5.4 CAMERA SETUP

The cameras were located in their predefined positions and their plumpness, centration, shooting plane were checked. The lighting system was set such that a uniformly bright view of the box was ensured as seen by the cameras.

After the termination of the test, the transparent box was replaced with a calibration box. This was essential to (1) establish a correlation between the images pixel coordinate space to true spatial coordinate system; and (2) account for refraction through the transparent media: the transparent soil and the transparent polycarbonate wall. This calibration box was composed of the same type of transparent soil and transparent walls with a metallic rigid ruler buried in located at the same location as the geosynthetic/laser plane from the transparent wall. The calibration box was placed at the same distance and orientation from the camera to account for the camera location in a given test.

5.3.6 TESTING SCHEME

Table 5.3.3 shows the testing scheme implemented in this study. The program comprises four series: (1) baseline series, which includes one test that was used a pivot test in subsequent parametric evaluations; (2) geosynthetic type series, which includes tests conducted with the same configuration as the baseline test but with different reinforcement types. Four reinforcement types other than the baseline reinforcement were used; (3) normal stress series, which includes tests conducted with the same configuration as the baseline test but at different confining normal stress levels. Two stress levels other than the baseline stress level were used; and (4) grain size series, which include a test conducted with the same configuration as the baseline test but with fused quartz of different grain size.

Table 5.3.3. Testing scheme (Morsy 2017).

Test Series	*Series Theme*	*Test Number*	*Test ID*	*Testing Variables*			
				Fill Material	*Mean Grain Size*	*Normal Stress*	*Geosynthetic Type*
A	Baseline	1	FQ-21-G1-S	Fused Quartz	3.8 mm	21 kPa	HP570
B	Geosynthetic Type	2	FQ-21-G2-S	Fused Quartz	3.8 mm	21 kPa	RS580i
		3	FQ-21-G3-S				80T
		4	FQ-21-G4-S				BX1200
		5	FQ-21-G5-S				20/20
C	Normal Stress	6	FQ-35-G1-S	Fused Quartz	3.8 mm	35 kPa	HP570
		7	FQ-50-G1-S			50 kPa	
D	Grain Size	8	FQ-21-G1-G	Fused Quartz	6.1 mm	21 kPa	HP570

*Conversions: 1 m = 0.0254 in.
1 kPa = 20.89 psf

5.3.7 RESULTS AND ANALYSIS

5.3.7.1 EFFECT OF NORMAL STRESS

Figure 5.3.4 shows the effect of normal stress on the pullout resistance for normal stresses ranging from 21 to 50 kPa (3 to 7.3 psi) for two different reinforcement types (HP570 geotextile and BX1100 geogrid). The frontal pullout load increased with increasing the normal stress. Note that the effect of reinforcement type is not discussed as they have multiple different characteristics.

(a)

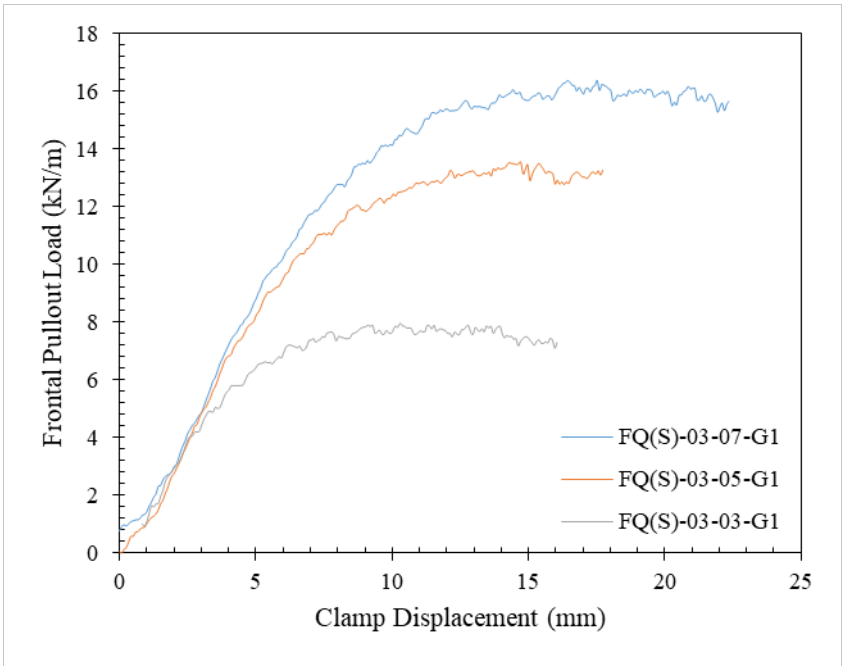

(b)

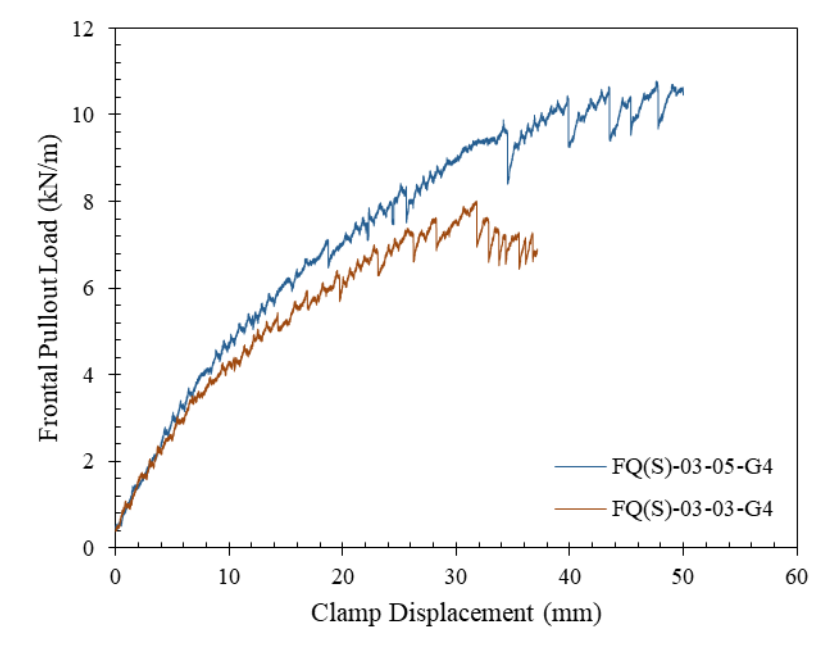

Figure 5.3.4. Frontal pullout load versus clamp displacement: (a) Effect of confinement on geotextiles; and (b) Effect of confinement on geogrids

5.3.7.2 EFFECT OF GRAIN SIZE

Figure 5.3.5 shows the effect of particle size on the pullout resistance for two different particle sizes ranging from fine gravel to coarse sand for HP570 geotextile reinforcement. The

frontal pullout load increased with increasing particle size. The effect of particle size was not purely studied since the increase in particle size is more likely to increase the friction angle of the soil and the soil-reinforcement interaction for the particle size range usually used with geosynthetic reinforcement (Dmax < 0.75 in.). The effect of the particle size on the performance of reinforced soil is significantly affected by the characteristics of the reinforcement, so the soil-reinforcement interaction (or equivalent interface strength) has been the focus of the study as they incorporate many parameters that their effects on the reinforced soil performance are hard to purely investigate

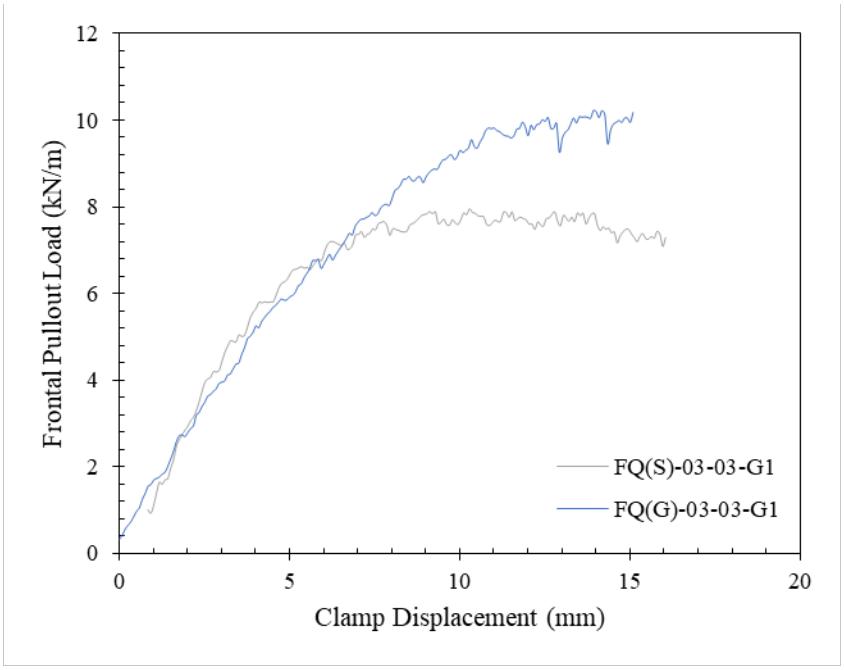

Figure 5.3.5. Frontal pullout load versus clamp displacement: Effect of grain size.

5.3.8 REFERENCES

Alfaro, M.C., Miura, N., and Bergado, D. (1995). "Soil-Geogrid Reinforcement Interaction by Pullout and Direct Shear Tests." ASTM Geotechnical Testing Journal, Vol. 18, No. 2, pp. 157–167.

Allersma, H., (1982). Photoelastic Investigation of the Stress Distribution during Penetration. Proceedings of the 2nd European Symposium on Penetration Testing, Amsterdam, May 24–27, ESOPT-II, Netherlands, pp. 79–83.

Bergado, D.T. and Chai, J.C. (1994). "Pullout Force-Displacement Relationship of Extensible Grid Reinforcement." Geotextiles and Geomembranes, Vol. 13, No. 5, pp. 295–316.

Bergado, D.T., Shivashankar, R., Alfaro, M.C., Chai, J.C., and Balasubramaniam, A.S. (1993). “Interaction Behavior of Steel Grid Reinforcements in Clayey Sand.” Géotechnique, Vol. 43, No. 4, pp. 589–603.

Bergado, D.T., Chai, J.C., Alfaro, M.C., and Balasubramaniam, A.S. (1994). Improvement Techniques of Soft Ground in Subsiding and Lowland Environment. A. A. Balkema, Rotterdam, Netherlands.

Chai, J.C. (1992). Interaction between Grid Reinforcement and Cohesive-frictional Soil and Performance of Reinforced Wall/embankment on Soft Ground. Ph.D. Dissertation, Asian Institute of Technology, Bangkok, Thailand.

Colletta, B., Letouzey, J., Pinedo, R., Ballard, J.F., and Bale, P. (1991). "Computerized X-ray Tomography Analysis of Sandbox Models: Examples of Thin-Skinned Thrust Systems." Geology, Vol. 19, pp. 1063–1067.

Desrues, J., Chambon, R., Mokni, M., and Mazerolle, F. (1996). "Void Ratio Evolution Inside Shear Bands in Triaxial Sand Specimens Studied by Computed Tomography." Géotechnique, Vol. 46, No. 3, pp. 529–546.

Dove, J.E. and Frost, J.D. (1996). "A Method for Measuring Geomembrane Surface Roughness." Geosynthetics International, Vol. 3, No. 3, pp. 369–392.

Dove, J.E., and Frost, J.D. (1999). "Peak Friction Behavior of Smooth Geomembrane-Particle Interfaces." Journal of Geotechnical and Geoenvironmental Engineering, ASCE, Vol. 125, No. 7, pp. 544–555.

Drescher, A. (1976). "An Experimental Investigation of Flow Rules for Granular Materials using Optically Sensitive Glass Particles." Geotechnique, Vol. 26, No. 4, pp. 591–601.

Dyer, M.R. (1985). Observations of the Stress Distribution in Crushed Glass with Applications to Soil Reinforcement. Ph.D. Dissertation, University of Oxford, Oxford, UK.

Ezzein, F.M., and Bathurst, R. (2011a). "A Transparent Sand for Geotechnical Laboratory Modeling." Geotechnical Testing Journal, Vol. 34, No. 6, pp. 1–12.

Ezzein, F.M., and Bathurst, R. (2011b). Development of a Geosynthetic Pullout Test Apparatus with Transparent Granular Soil. Proceedings 2011 Pan-American Canadian Geotechnical Society Geotechnical Conference, Toronto, Canada, 6p.

Farrag, K., Acar, Y.B., and Juran, I. (1993). "Pull-out Resistance of Geogrid Reinforcements." Geotextiles and Geomembranes, Vol. 12, No. 2, pp. 133–160.

Ferreira, J.A.Z. and Zornberg, J.G. (2014). “Behavior of Transverse Ribs in a Tensioned Geogrid Embedded in Transparent Soil.” Proceedings of the 10th ICG—International Conference on Geosynthetics, Berlin, Germany, Sept 21–25, German Geotechnical Society, Essen, Germany.

Ferreira, J.A.Z. and Zornberg, J.G. (2015). “A Transparent Pullout Testing Device for 3D Evaluation of Soil–Geogrid Interaction.” Geotechnical Testing Journal, Vol. 38, No. 5, pp. 686–707.

Franca, F.A.N., Bueno, B.S., and Zornberg, J.G. (2011). "Confined, Accelerated Creep Tests on Geosynthetics." Foundations and Geotechnical Projects. Vol. 2, No. 12, December, pp. 56–63.

Frost, J.D. and Kuo, C.-Y. (1996). "Automated Determination of the Distribution of Local Void Ratio from Digital Images." ASTM Geotechnical Testing Journal, Vol. 19, No. 2, pp. 107–117.

Gill, D.R. and Lehane, B.M. (2001). "An Optical Technique for Investigating Soil Displacement Patterns." Geotechnical Testing Journal, Vol. 24, No. 3, pp. 324–329.

Gustafsson, L. and Knutsson, S. (1994). "An Image Analysis Method for Studying Movement in Granular and Solid Bodies." ASTM Geotechnical Testing Journal, Vol. 17, No. 1, pp. 95–100.

Hird, C.C. and Stanier, S.A. (2010). Modelling Helical Screw Piles in Clay using a Transparent Soil. Proceedings of the 7th International Conference on Physical Modelling in Geotechnics, Zurich, International Society for Soil Mechanics and Geotechnical Engineering, Jun 28–July 1, Switzerland, p. 6.

Ingold, T.S. (1983). "Laboratory Pull-Out Testing of Grid Reinforcements in Sand." Geotechnical Testing Journal. ASTM, Vol. 6, pp. 101–111.

Iskander, M., Lai, J., Oswald, C., and Mannheimer, R. (1994). "Development of a Transparent Material to Model the Geotechnical Properties of Soils." Geotechnical Testing Journal, Vol. 17, No. 4, pp. 425–433.

Iskander, M. (1998). Transparent Soils to Image 3D Flow and Deformation. Proceedings of the 2nd International Conference on Imaging Technologies: Techniques and Applications in Civil Engineering, Davos, Switzerland, May 25–30, 1997, ASCE, New York, pp. 255–264.

Iskander, M., Liu, J., and Sadek, S. (2002a). "Transparent Amorphous Silica to Model Clay." Journal of Geotechnical and Geoenvironmental Engineering, Vol. 128, No. 3, pp. 262–273.

Iskander, M., Sadek, S., and Liu, J. (2002b). "Optical Measurement of Deformation using Transparent Silica Gel to Model Sand." International Journal of Physical Modelling in Geotechnics, Vol. 2, No. 4, pp. 13–26.

Iskander, M., Liu, J., and Sadek, S. (2003). Modeling 3D Flow and Soil Structure Interaction using Optical Tomography. Final Report, NSF Project No. CMS 9733064, p. 280.

Iskander, M. and Liu, J. (2010). "Spatial Deformation Measurement Using Transparent Soil." Geotechnical Testing Journal, Vol. 33, No. 4, pp.1–8.

Iskander, M. (2010). "Modeling with Transparent Soils, Visualizing Soil Structure Interaction and Multiphase Flow, Non-intrusively." Springer, New York, p. 331.

Jang, D.J., and Frost, D.J. (1998). "Sand Structure Differences Resulting from Specimen Preparation Procedures." ASCE Geotechnichal Special Publication no. 75, Geotechnical Earthquake Engineering and Soil Dynamics III, Dakuolas, Yegian, and Holtz (eds.), Seattle, Vol.1, pp. 234–245.

Jang, D.J., Frost, J.D., and Park, J.K. (1999). "Preparation of Epoxy Impregnated Sand Coupons for Image Analysis." ASTM Geotechnical Testing Journal, Vol. 22, No. 2, pp. 147–158.

Jewel et al. (1984) “Interaction Between Soil and Geogrids. Polymer Grid Reinforcement”as published in Polymer Grid Reinforcement: proceedings of a conference sponsored by the Science and Engineering Research Council and Netlon Ltd and held in London on 22 and 23 March 1984, London, Thomas Telford, 1985, c1984

Jewell, R.A. (1990a). "Reinforcement Bond Capacity." Géotechnique, Vol. 40, No. 3, pp. 513–518.

Jewell, R.A. (1990b). "Strength and Deformation in Reinforced Soil Design." Proceedings of the 4th International Conference on Geotextiles, Geomembranes and Related Products, The Hague, Netherlands, Vol. 3, pp. 913–946.

Jewell, R.A. (1996). Soil Reinforcement with Geotextiles. Ciria Special Publication 123, Thomas Telford Ltd., UK, 332 p.

Jewell, R.A., Milligan, G.W.E., Sarsby, R.W., and Dubois, D. (1984). Interaction between Soil and Geogrids. Proceeding of the Symposium on Polymer Grid Reinforcement in Civil

Engineering, Science and Engineering Research Council and Netlon Limited, pp. 18–30.

Kemeny, J.M., Devgan, A., Hagaman, R.M. and Wu, X. (1993). "Analysis of Rock Fragmentation Using Digital Image Processing." Journal of Geotechnical Engineering, Vol. 119, No. 7, pp. 1144–1160.

Koerner, R.M., Wayne, M.H., and Carroll, R.G., Jr. (1989). "Analytic Behavior of Geogrid Anchorage." Proceedings of the Geosynthetics'89 Conference, San Diego, CA, IFAI, pp. 525–536.

Kuo, C.-Y. and Frost, J.D. (1996). "Uniformity Evaluation of Cohesionless Specimens Using Digital Image Analysis." Journal of Geotechnical Engineering, Vol. 122, No. 5, pp. 390–396.

Leung, S.K., Kry, P.R., and Wong, R.C.K. (1995). Visualization of deformation in unconsolidated Athabasca oil sand. Proceedings of the International Heavy Oil Symposium, Calgary, Alta., 18–21 June 1995. Society of Petroleum Engineers, Publication SPE 30315.

Li, C. and Zornberg, J.G. (2013). "Mobilization of Reinforcement Forces in Fiber-Reinforced Soil." Journal of Geotechnical and Geoenvironmental Engineering, ASCE, Vol. 139, No. 1, January, pp. 107–115.

Liang, L., Saada, A., Figueroa, J.L., and Cope, C.T. (1997). "The Use of Digital Image Processing in Monitoring Shear Band Development." ASTM Geotechnical Testing Journal, GTJODJ, Vol. 20, No. 3, September, pp. 324–339.

Liu, C., Zornberg, J.G., Chen, T-C., Ho, Y., and Lin, B. 2009. "Behavior of Geogrid-Sand Interfaces in Direct Shear Mode." Journal of Geotechnical and Geoenvironmental Engineering, ASCE, Vol. 135, No. 12, December, pp. 1863–1871.

Liu, J., Iskander, M. and Sadek, S. (2003). "Consolidation and Permeability of Transparent Amorphous Silica." Geotechnical Testing Journal, Vol. 26, No. 4, pp. 390–401.

Lopes, M.L. and Ladeira, M. (1996). "Influence of the Confinement, Soil Density and Displacement Ratio on Soil-Geogrid Interaction." Geotextiles and Geomembranes, Vol. 14, No. 10, pp. 543–554.

Mannheimer, R. and Oswald, C. (1993). "Development of Transparent Porous Media with Permeabilities and Porosities Comparable to Soils, Aquifers, and Petroleum Reservoirs." Ground Water, Vol. 31, No. 5, pp. 781–788.

McKelvey, D., Sivakumar, V., Bell, A. and Graham, J. (2004). Modeling Vibrated Stone Columns in Soft Clay. Proceedings of the Institution of Civil Engineers: Geotechnical Engineering 157, Issue GE3, pp. 137–149.

Milligan, G.W.E. and Palmeira, E.M. (1987). "Prediction of Bond between Soil and Reinforcement." Symposium on Prediction and Performance in Geotechnical Engineering, Calgary, pp. 147–153.

Mora, C.F., Kwan, A.K.H. and Chan, H.C. (1998). "Particle Size Distribution Analysis of Coarse Aggregate Using Digital Image Processing." Cement and Concrete Research, Vol. 28,

Morsy, A. M. (2017). Evaluation of soil-reinforcement composite interaction in geosynthetic-reinforced soil structures. Doctoral dissertation, The University of Texas at Austin, Austin, Texas, USA.

No. 6, pp. 921–932.

Obaidat, M.T., Al-Masaeid, H.R., Gharaybeh, F., and Khedaywi, T.S. (1998). "An Innovative Digital Image Analysis Approach to Quantify the Percentage of Voids in Mineral Aggregates of Bituminous Mixtures." Canadian Journal of Civil Engineering, Vol. 25, pp. 1041-1049.

Ochiai, H, Otani, J., Hayashic, S., and Hirai, T. (1996). "The Pullout Resistance of Geogrids Reinforced Soil." Geotextiles and Geomembranes, Vol. 14, No. 1, pp. 19–42.

Otani, J., Miyamoto, K., and Mukunoki, T. 2001. "Visualization of Interaction Behavior Between Soil and Reinforcement Using X-ray CT." Proceedings of Landmarks in Earth Reinforcement, Ochiai, H., Otani, J., Yasufuku, N., Omine, K (editors), A.A. Balkema, Tokyo, Japan, Vol. 1, pp. 117–120.

Palmeira, E.M. (1987). The Study of Soil-Reinforcement Interaction by Means of Large Scale Laboratory Tests. Ph.D. Thesis, University of Oxford, UK, 238 p.

Palmeira, E.M. and Milligan, G.W.E., (1989a). "Large Scale Direct Shear Tests on Reinforced Soil." Soil and Foundations, Vol. 29, No. 1, pp. 18–30.

Palmeira, E.M. and Milligan, G.W.E. (1989b). "Scale and Other Factors Affecting the Results of the Pullout Tests of Grids Buried in Sand." Géotechnique, Vol. 39, No. 3, pp. 551–584.

Palmeira, E.M. (2004). "Bearing Force Mobilization in Pull-out Tests on Geogrids." Geotextiles and Geomembranes, Vol. 22, pp. 481–509.

Palmeira, E.M. (2009). "Soil-Geosynthetic Interaction: Modelling and Analysis." Geotextiles and Geomembranes, Vol. 27, No. 5, pp. 368–390.

Pan, B., Qian, K., Xie, H. and Asundi, A. (2009). "Two-Dimensional Digital Image Correlation for In-plane Displacement and Strain Measurement: A Review." Measurement Science and Technology, Vol. 20, No. 6, 17 p.

Peng, X., and Zornberg, J.G. (2016). “Evaluation of Load Transfer in Triaxial Geogrids using Transparent Soil.” Proceedings of the 3rd Pan-American Conference on Geosynthetics, Miami, Florida, 10-13 April, Vol. 2, pp. 1520-1531.

Peterson, L. M. and Anderson, L.R. (1980). Pullout Resistance of Welded Wire Mats Embedded in Soil. Research Report Submitted to Hilfiker Co., Civil and Envir. Eng. Dept., Utah State Univ., Utah, USA.

Raffel M., Willert, C., and Kompenhans, J. 2007. "Particle Image Velocimetry: A Practical Guide." Springer, Berlin.

Raju, D.M. and Fannin R.J. 1998. "Load–Strain–Displacement Response of Geosynthetics in 614 Monotonic and Cyclic Pullout." Canadian Geotechnical Journal, Vol. 35, No. 2, pp. 183–193.

Raschke, S.A., Hryciw, R.D. and Donohoe, G.W. (1996). "Micro-Deformations in Sands by Digital Image Processing and Analysis." Transportation Research Record 1548, pp. 31–37.

Sadek, S., Iskander, M.G. and Liu, J. (2002). "Geotechnical Properties of Transparent Silica." Canadian Geotechnical Journal, Vol. 39, No. 1, pp. 111–124.

Sadek, S., Iskander, M.G. and Liu, J. (2003). "Accuracy of Digital Image Correlation for Measuring Deformations in Transparent Media." Journal of Computing in Civil Engineering, Vol. 17, No. 2, pp. 88–96.

Sarsby, R.W. (1985). "The Influence of Aperture Size/Particule Size on Efficiency of Grid Reinforcement." Proceedings of the 2nd Canadian Symposium on Geotextiles and Geomembranes, Edmonton, Alberta, pp. 7–12

Shi, B., Murakami, Y., Wu, Z., Chen, J. and Inyang, H. (1999). "Monitoring of Internal Failure Evolution in Soils Using Computerization X-ray Tomography." Eng. Geol. (Amsterdam), Vol. 54, No. 3–4, pp. 321–328.

Song, Z., Hu, Y., O'Loughlin, C., and Randolph, M.F. (2009). "Loss in Anchor Embedment During Plate Anchor Keying in Clay." Journal of Geotechnical and Geoenvironmental Engineering, Vol. 135, No. 10, pp. 1475–1485.

Sugimoto, M., Alagiyawanna, A. M. N. and Kadoguchi, K. (2001). "Influence of Rigid and Flexible Face on Geogrid Pullout Tests." Geotextiles and Geomembranes, Vol. 19, No. 5, pp. 257–328.

Teixeira, S.H.C., Bueno, B.S. and Zornberg, J.G. (2007). "Pullout Resistance of Individual Longitudinal and Transverse Geogrid Ribs." Journal of Geotechnical and Geoenvironmental Engineering, ASCE, January, Vol. 133, No. 1, pp. 37–50.

Thomas, T.W., White, T.D., and Kuczek, T. (1994). "Siliceous content determination of sands using automatic image analysis." Transportation Research Record 1437, pp. 51–58.

Wakabayashi, T. (1950). "Photo-Elastic Method for Determination of Stress in Powdered Mass." Journal of the Physical Society of Japan, Vol. 5, No. 5, pp. 383–385.

Walters, D.A. (1995). Fracturing in Oil Sands. M.Sc. thesis, Department of Civil Engineering, The University of Calgary, Calgary, Alta.

White, D.J., Take, W.A. and Bolton, M.D. 2003. "Soil Deformation Measurement Using Particle Image Velocimetry (PIV) and Photogrammetry." Geotechnique, Vol. 53, No. 7, pp. 619–631.

Wong, R. (1999). "Mobilized strength components of athabasca oil sand in triaxial compression." Canadian Geotechnical Journal, Vol. 36, No. 4, pp. 718–735.

Wibowo, R. (1996). Bioremediation and Fracturing in Soil. M.Sc. thesis, Department of Civil Engineering, The University of Calgary, Calgary, Alta.

Zhao, H. and Ge, L. (2010). Camera Calibration Using Neural Networks. Appendix in Moddeling with Transparent Soils by M.G. Iskander, Springer, pp.299–312.

Zornberg, J.G., Sitar, N., and Mitchell, J.K. (1998). "Limit Equilibrium as Basis for Design of Geosynthetic Reinforced Slopes." Journal of Geotechnical and Geoenvironmental Engineering, ASCE, Vol. 124, No. 8, pp. 684–698.

Zornberg, J.G., Prozzi, J.A., Gupta, R., Luo, R., McCartney, J.S., Ferreira, J.Z. and Nogueira, C. (2008). Validating Mechanisms in Geosynthetic Reinforced Pavements. Center for Transportation Research (CTR), Report No. 0-4829-1, Austin, Texas, February 2008.

Zornberg, J.G., Ferreira, J.A.Z. and Roodi, G.H. (2012). Experimental Results on Soil-Geosynthetic Interaction Stiffness. Center for Transportation Research (CTR), Report No. FHWA/TX-12/5-4829-01-3, Austin, Texas, September 2012, 232 p.

Zornberg, J.G., Ferreira, J.A.Z. and Roodi, G.H. (2013). Geosynthetic-reinforced Unbound Base Courses: Quantification of the Reinforcement Benefits. Center for Transportation Research (CTR), Report No. FHWA/TX-12/5-4829-01-2, Austin, Texas, August 2013, 757 p.

6. FIELD MONITORING INVESTIGATION

The main purpose of the field monitoring component of this research was to evaluate the performance of a GRS-IBS structure that is constructed as an actual bridge abutment to a size that is similar to the one used in the FHWA's mini-pier laboratory tests. This was targeted to minimize the differences in results due to different scales. The initial goal was also to compare the actual strains and lateral displacements recorded during the mini-pier tests with the field measurements, however, the relevant data is not available in the literature and has not been shared by the FHWA with the research team. The goal of the monitoring was to develop design parameters based on different loading scenarios and differences in vertical reinforcement spacing in the field. The data obtained from this field monitoring program is used to validate available design methods and to evaluate the performance (as it relates to lateral deformations and stress/strain distributions) of the GRS-IBS structure under field loading and reinforcement spacing. The constructed abutment was subjected to stage loading during construction and the data collected from this phase was used to evaluate the conditions associated with both 0.1 m (4 in.) and 0.2 m (8 in.) spaced reinforcements. The GRS-IBS used in this study was constructed by Virginia Department of Transportation (VDOT) between August and September in 2015 and is located in Harrisonburg, Virginia. This chapter presents the characterization of the construction site, properties of the materials used for construction, details of the field instrumentation program, and evaluation and assessment of field instrumentation data.

6.1 CHARACTERIZATION OF CONSTRUCTION SITE AND MATERIALS USED FOR CONSTRUCTION

The GRS-IBS constructed for this study is approximately 2.4 m (8 ft.) high and 9 m (30 ft) wide with reinforcement spacing of 0.2 m (8 in.) in the primary reinforcement zone and secondary reinforcement spacing of 0.1 m (4 in.) in the bearing bed zone. Primary reinforcements in this GRS-IBS structure are frictionally connected to the facing blocks. However, the secondary reinforcements within bearing bed were terminated right behind the facing blocks and are not connected to them. The structure was constructed on competent foundation using AASHTO No. 8 aggregate. The construction site is located in Virginia's Staunton district (approximately 2.5 hrs. southwest of Washington D.C.) (Figure 6.1.1).

The bridge site was within VDOT right of the way and the entire design and construction was done by VDOT using its in-house capabilities. East and west abutments (abutments A and B) were designed to have different beam seats dimensions. The beam seat in abutments A and B have a width of 0.6 m (2ft) and 1.2 m (4 ft), respectively. This deviation from standard practices of GRS-IBS design was to enable the research team to study the effect of beam seat width on the vertical stress distribution resulted from super-structure loads. Additionally, a loading test by placing Jersey barriers was done for each layer of reinforcement with overlaying aggregate in order to investigate the effect of reinforcement spacing on vertical and lateral stress distribution, reinforcement strains and backfill deformation in the bearing bed zone and primary reinforcement zones.

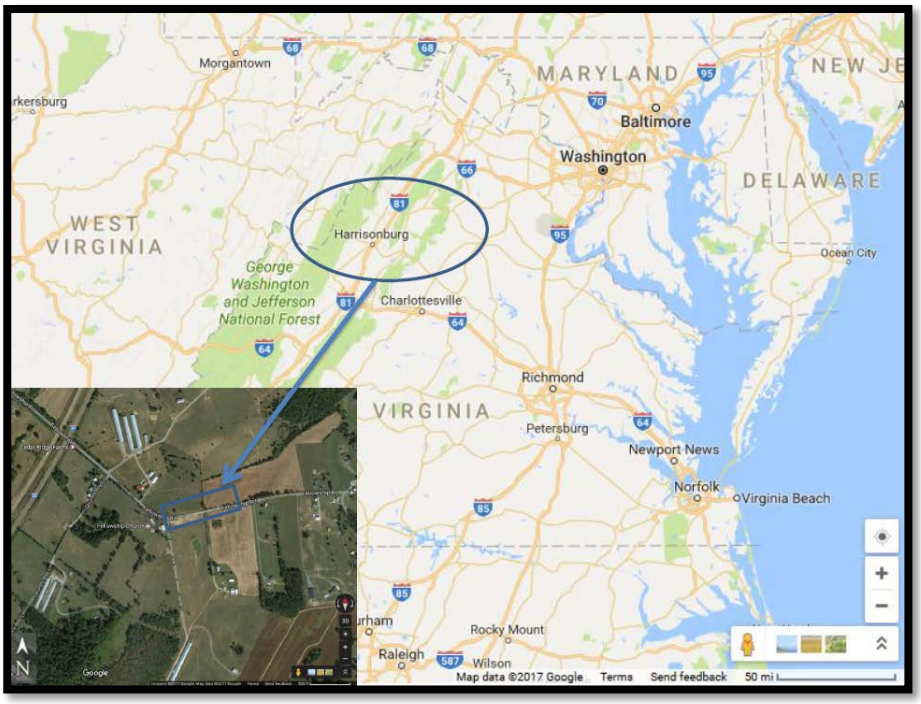

Fig. 6.1.1: Location of field monitored VDOT GRS-IBS site

Geotechnical subsurface exploration and laboratory tests were conducted to identify subsurface stratigraphy and to evaluate geotechnical properties of materials underlying the site. Standard penetration tests (SPT) were conducted at selected depths in drilled borings. Figure 6.1.2a shows locations of boreholes drilled to conduct SPT and collect soil samples for laboratory testing. Figure 6.1.2b shows the soil profile at the site, as interpreted from results of geotechnical subsurface exploration and laboratory tests conducted using soil samples collected from the two boreholes. The foundation soil (where the new GRS-IBS was built on) was characterized as a stiff clayey soil underlain by bedrock within a seasonal dry streambed. However, at the time of excavation to construct the foundation, it was observed that the bed rock level was close to the surface in most locations. The clay is classified as CH with a liquid limit (LL) of 72 and plasticity index (PI) of 45. The fill material (CL) shown in Figure 6.1.2 was excavated together with the existing culvert and replaced with the newly constructed GRS-IBS. No groundwater was encountered during geotechnical site investigation. Consequently, the foundation soil was only compacted before constructing the RSF and no ground improvement was implemented to increase the strength of the foundation soil.

The GRS-IBS abutment involves a 3.6 m (12 ft) long bridge span compensating a two-lane traffic access that is approximately 8.4 m (28 ft) wide. The GRS-IBS abutment was constructed using a high quality aggregate, AASHTO No. 8, which was reinforced with a woven geotextile with an ultimate tensile strength of 70 kN/m (4800 lb/ft). The AASHTO No. 8 aggregate fill was collected from Frazier quarry in Harrisonburg, Virginia. The grain size distribution of AASHTO No. 8 aggregate is shown in Figure 6.1.3. According to USCS classification, the material can be classified as a poorly graded gravel (GP) with no fines. The maximum particle size for this backfill was 12.5

mm (0.5 in.). Standard Proctor tests were carried out to estimate the maximum dry density of the aggregate following procedures outlined in ASTM D698. The compaction curve obtained from Standard Proctor Test (Method B) is shown in Figure 6.1.4a. The maximum dry density was found to be 1600 kg/m^3 (100 pcf). The aggregate used for construction did not have fines and was not sensitive to moisture content changes during compaction.

The relevant materials used for construction of the VDOT GRS-IBS are described as follows:

AASHTO No. 8: Density measurements in the field have shown that the ASSHTO No. 8 aggregate used in this study has a dry density of 1700 kg/m^3 (105 pcf). Triaxial test results obtained from the AASHTO No. 8 aggregate used during this study showed that the friction angle of the aggregate is 47.6 degrees with a 3.5 kPa cohesion intercept as shown in Figure 6.1.4b. Figure 6.1.4b presented in this section was taken from a report provided by an outside source that conducted the triaxial test.

Geosynthetic reinforcements: Mirafi HP570 woven geotextile was used both to construct the reinforced soil foundation (RSF) and the reinforced abutment. This geotextile is consistent with the geotextile used by FHWA TFHRC mini-pier tests as reported in FHWA-HRT-13-066 manual. The properties of the geotextile are summarized in Table 6.1a. The ultimate tensile strength of the geotextile was 70 kN/m (4800 lb/ft). The stiffness of the geotextile at 2 percent and higher strain levels was 700 kN/m (48000 lb/ft). However, the stiffness of the geotextile at 0 to 1 and 0.6 to 0.8 percent strains were approximately 590 kN/m (40457 lb/ft) and 770 kN/m (52800 lb/ft), respectively. In the research component described in this Chapter, the stiffness of the geotextile was estimated to be the average of the stiffness values at 0 to 2 percent strain levels, which has an approximate magnitude of 700 kN/m (48000 lb/ft).

21B Aggregate: Per FHWA design guidelines, the RSF was constructed using VDOT 21 B aggregate. Density measurements in the field have shown that the maximum dry density of this aggregate is 2200 kg/m^3 (140 pcf) and optimum moisture content is approximately 8%. The unit weight and friction angle of the aggregate used for this project is reported by VDOT as 2200 kg/m^3 (140 pcf) and 40 degrees respectively.

Facing blocks: The facing of the abutment was constructed using standard concrete masonry unit (CMU) blocks. The CMU blocks have a width and height of 200 mm (8 in) and a length of 400 mm (16 in). Solid CMU blocks were used for the first four layers and split face CMU blocks were used for the remaining of the layers to construct the facing element.

Bridge superstructure and integrated approach: The bridge superstructure was built using a segmental precast concrete slab and the integrated approach was built with the same materials used to build the RSF.

Table 6.1a. Properties of the geotextile used in this research component (Tencate geosynthetics)

Mechanical properties	Test method	Unit	Average value
Tensile strength (at ultimate)	ASTM D4595	kN/m (lbs/ft)	70 (4800)
Tensile strength (at 2% strain)	ASTM D4595	kN/m (lbs/ft)	14 (960)
Tensile strength (at 5% strain)	ASTM D4595	kN/m (lbs/ft)	35 (2400)
Tensile strength (at 10% strain)	ASTM D4595	kN/m (lbs/ft)	70 (4800)
Factory sewn seam	ASTM D4884	kN/m (lbs/ft)	43.8 (3000)
Flow rate	ASTM D4491	$l/min/m^2$ ($gal/min/ft^2$)	1222 (30)
Permeability	ASTM D4492	cm/sec	0.05
Permittivity	ASTM D4493	Sec^{-1}	0.4
Apparent opening size	ASTM D4751	U.S. sieve (mm)	0.6 (30)
UV resistance (at 500 hours)	ASTM D4355	% strength retained	80

6.2 DESIGN OF FIELD MONITORING PROGRAM

The field instrumentation program was designed to generate data that provides relevant information related to the behavior of GRS-IBS structures under field loading and boundary conditions (with a different loading level and geometry of the structure when compared to FHWA mini-piers that were loaded up to failure and confined in four sides of the structure). Based on information gathered from the previous field monitored review of load-carrying GMSE bridge abutments in general, and of GRS-IBS structures in particular (Sections 2.3.1 and 2.3.2 of Chapter 2 of the report) and goals of this research, the field monitoring program was designed to evaluate the following specific issues that have not been addressed in previous research including:

i. Vertical stress distribution (close to and away from the facing) within the primary reinforcement zone with S_v = 0.2 m (8 in.) and bearing bed zone with S_v = 0.1 m (4 in.).
ii. Horizontal stresses behind the facing of the structure,
iii. Horizontal strains and displacements right behind the facing blocks and 0.9 m (3 ft) away from the facing both within the primary reinforcement and bearing bed zones,
iv. Vertical deformation (settlement) beneath the foundation and lateral movements of the facing.
v. Overall performance of the structure during construction (short-term response) as well as after construction (long-term response).

6.2.1 GENERAL OVERVIEW

For the purpose of this research, both the primary reinforcement zone and bearing bed zone were loaded independently using Jersey barriers during construction and the whole GRS-IBS abutment was loaded using a parked truck on the super-structure after construction. The field instrumentation program was designed with the following types of instruments:

- **Earth pressure cells** – To measure vertical stresses in the GRS-IBS abutment.

- **Rectangular pressure cells** - To evaluate stresses on the back of facing blocks and to assess differential stresses from superstructure loads
- **Load cells** - To evaluate the overall load due to downdrag stresses carried by the facing units
- **Wire line extensometers** – To measure lateral displacements (elongations) in the geotextile reinforcements
- **Soil extensometers** – To measure lateral deformations within the backfill material
- **Settlement gages** – To measure settlement in CH layer beneath the foundation
- **Strain gages** – To evaluate the lateral strains on geotextile reinforcements right behind the facing blocks and 0.9 m (3ft) away from the facing blocks
- **Surveying targets** – To measure facing lateral and vertical movements
- **Water content reflectometers** – To measure the potential changes in volumetric water content of the backfill material
- **Temperature gages** – To evaluate temperature changes in the backfill material through sensors embedded in some of the instruments (e.g. earth pressure cells, water content reflectometers)

The primary purpose of installing rectangular earth pressure cells and strain gages right behind the facing was to evaluate the assumption of uniform distribution of lateral earth pressure behind the wall facing and the conditions of the connection strength between wall facing and reinforcement (T_o) as outlined in FHWA's manual (Adams et al., 2011). The purpose of installing vertical earth pressure cells was to primarily evaluate the structure's response to slab loading both within bearing bed and primary reinforcement zones.

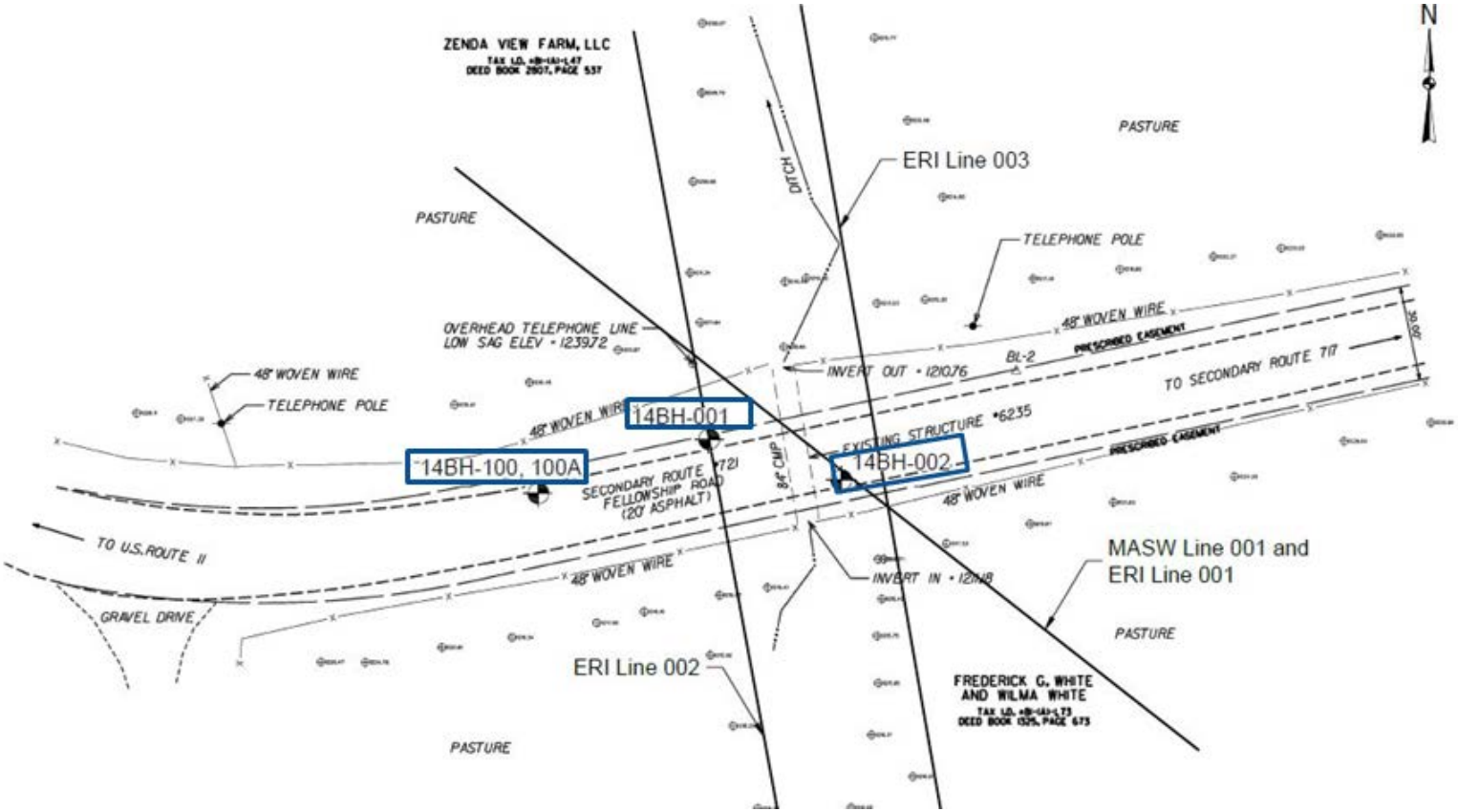

(a)

Fig. 6.1.2: Geotechnical site investigation: (a) Boring Location Diagram; (b) Interpreted soil profile at the site before construction (continued)

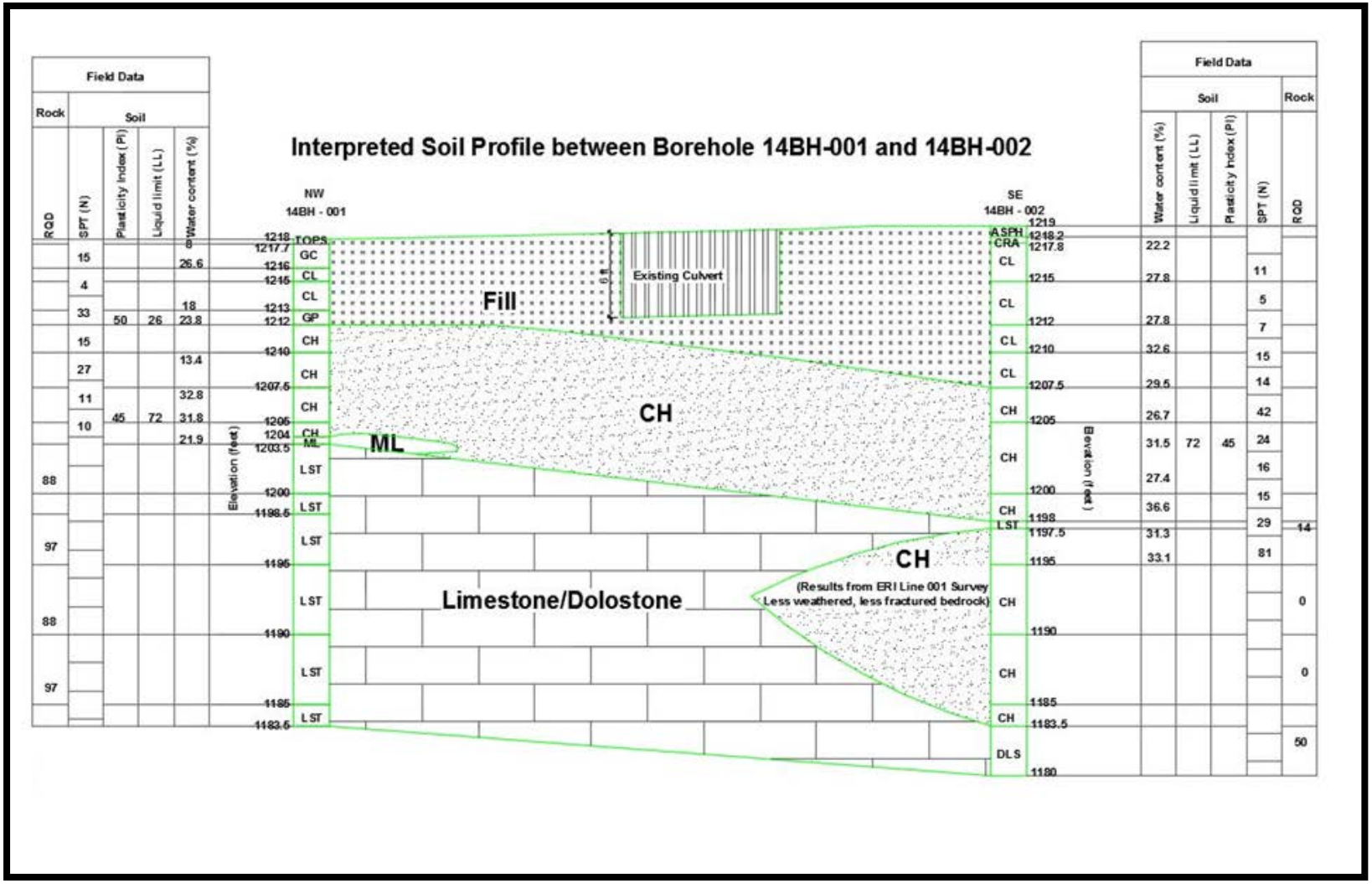

(b)

Note: The CH layer as interpreted in this cross section was not correct. During construction, it was noted that majority of the foundation rested on limestone rather than a continuous CH layer as shown in this figure.

Fig. 6.1.2: Geotechnical site investigation: (a) Boring Location Diagram; (b) Interpreted soil profile at the site before construction (continued)

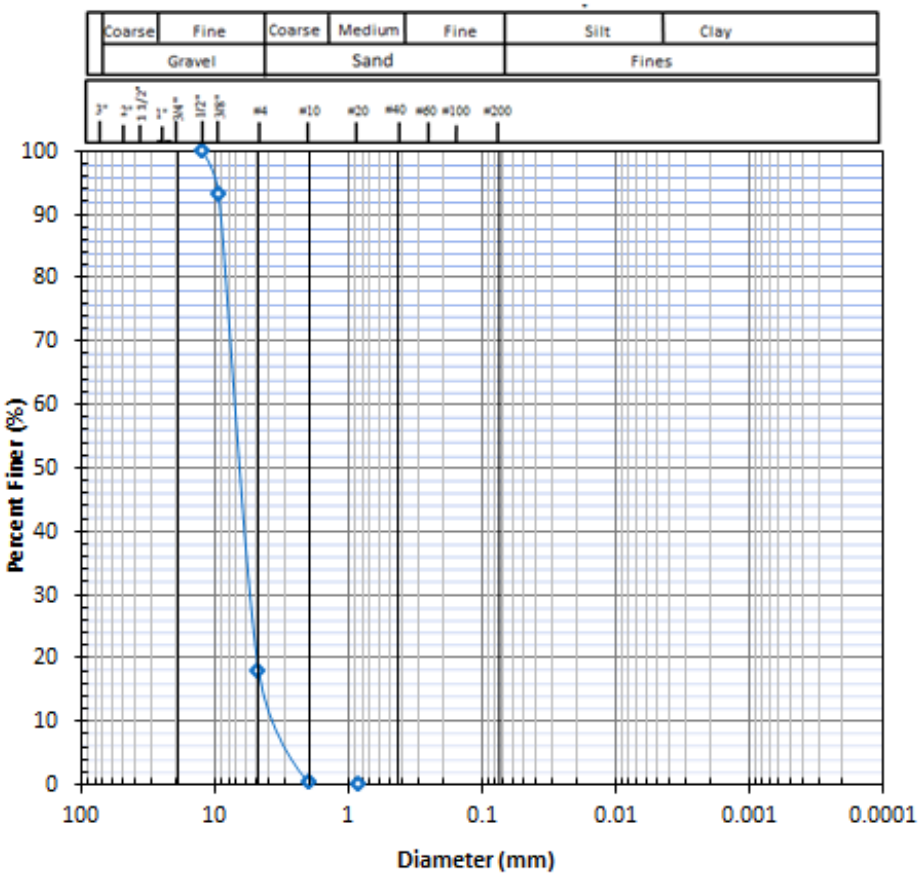

Fig. 6.1.3: Grain size distribution of AASHTO No. 8 aggregate

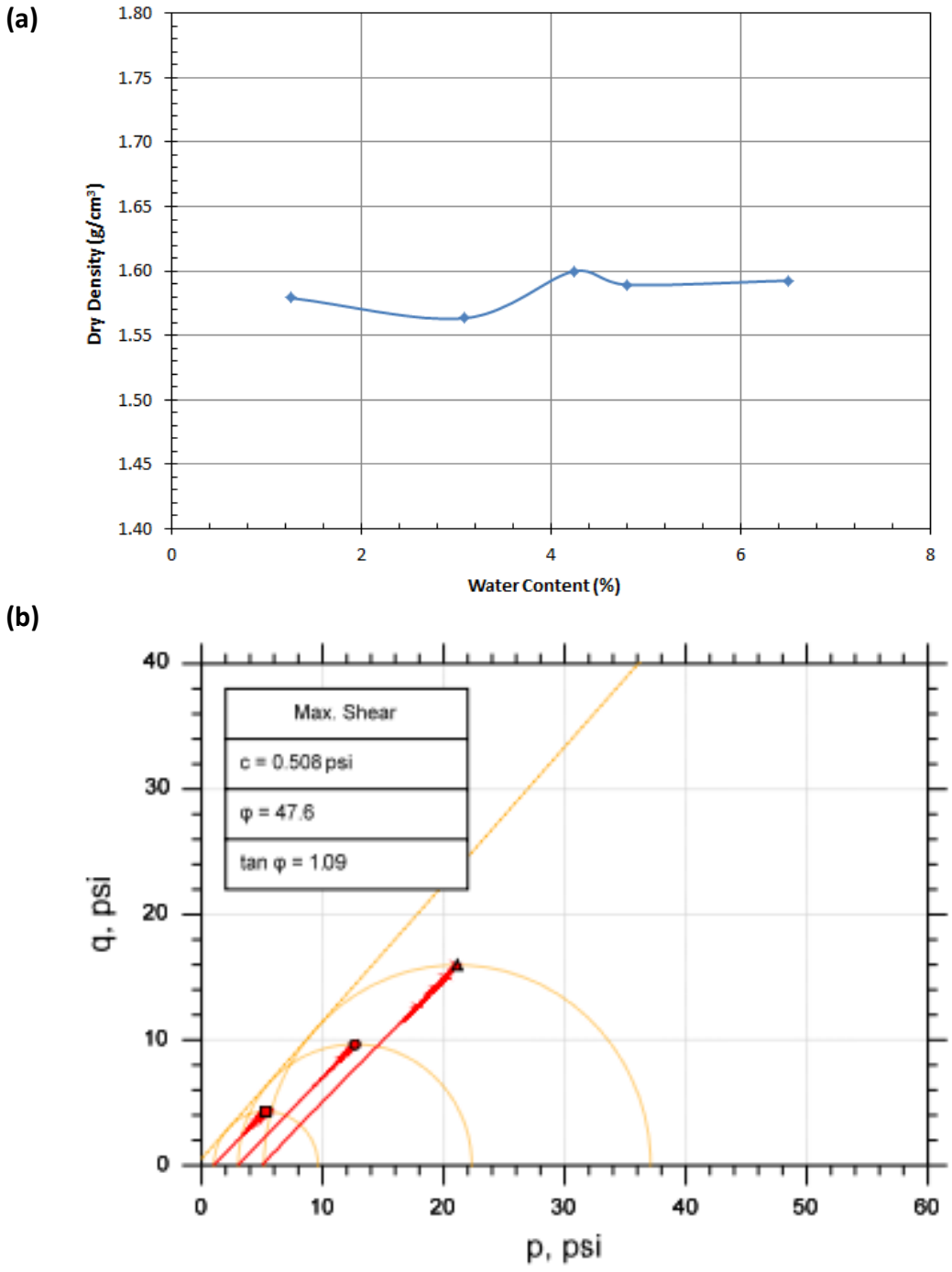

Fig. 6.1.4: Properties of AASHTO No.8 aggregate: (a) Compaction curve; (b) Triaxial test result.

The design of the field instrumentation program was conducted in communication with the VDOT design team in order to avoid practical challenges that may occur while installing instruments and data collection system during the construction of the GRS-IBS. **Figures 6.2.1 and 6.2.2** show the layout of the instrumentation in Abutments A and B of the GRS-IBS. As it can be seen in the figures, the instruments were placed within the bearing bed zone and primary reinforcement

zone along the height of the abutments. The instruments were positioned in the transverse direction (middle, North, and South sections) and longitudinal direction (close to and away from the facing of the structure). The measurement range of the instruments were determined by estimating the magnitude of the applied loads and expected range of performances such as stress and deformation levels in the GRS-IBS structure. For instance, the maximum vertical stress to be applied on the abutment due to self-weight and super-structure load was pre-calculated to be greater than 50 kPa (1045 psf). Therefore, the type of earth pressure cell that was selected to measure vertical stress for this project was the one that has a capacity to measure stress level up 300 kPa (6265 psf). The instruments were calibrated at the GMU laboratory using actual materials used to construct the GRS-IBS with the exceptions of load cells, soil extensometers, settlement cells, and water content reflectometers. For these instruments, the manufacturer's calibration equations were tested to confirm that the provided equations resulted in accurate results. The data acquisition system was designed to have a wirelessly automated datalogger that received power from a solar panel. A Campbell Scientific's CR 1000 datalogger was used as a readout device to collect data generated from all instruments except the surveying work. The design of the data acquisition system involved independent data collection systems for abutments A and B.

Additional details regarding the types of instruments used in the field instrumentation program are discussed in Sections 6.2.1 to 6.2.9.

6.2.2 EARTH PRESSURE CELLS (EPC)

Vibrating Wire model 4800 earth pressure cells (EPC) manufactured by Geokon Inc., were used to measure vertical stresses. Model 4800 consists of two circular stainless steel plates with a diameter of 230 mm (9 in.) welded at the edge and the space in between filled with a hydraulic fluid. Calibration of this sensor was performed by developing a relationship between applied pressure (using AASHTO No.8 aggregate as a load) and response (frequency) of the earth pressure cell in the laboratory. Additional validation of the accuracy of the earth pressure cell was performed by developing a relationship between self-weight of the backfill material load and response of the earth pressure cell in the field.

The earth pressure cells were installed in the field following the pre-determined field instrumentation layout as shown in Figures 6.2.1 and 6.2.2. A total of 28 earth pressure cells (15 on Abutment A and 13 on Abutment B) were installed. One of the earth pressure cells was installed inside a wooden box, outside the abutments. This approach was adopted to assess the sensitivity of this instrument to the changes of weather conditions such as temperature and precipitation. All EPC sensors were installed by placing sand at bottom and top of each cell before placing the backfill. The purpose of placing the sand was to avoid point loading from aggregate particles and to enhance the uniformity of the contact pressures acting on the cell.

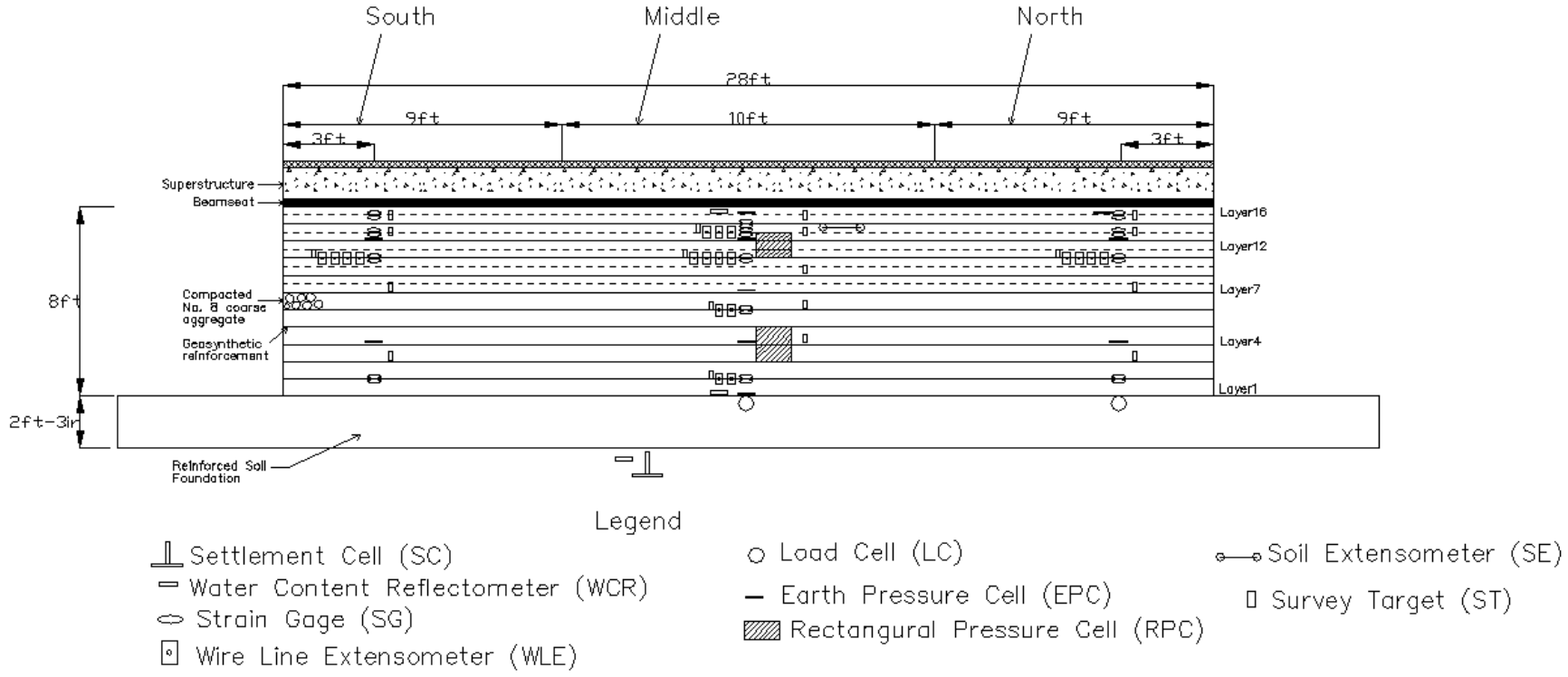

Fig. 6.2.1: Layout of instrumentation in the transverse direction in abutment A

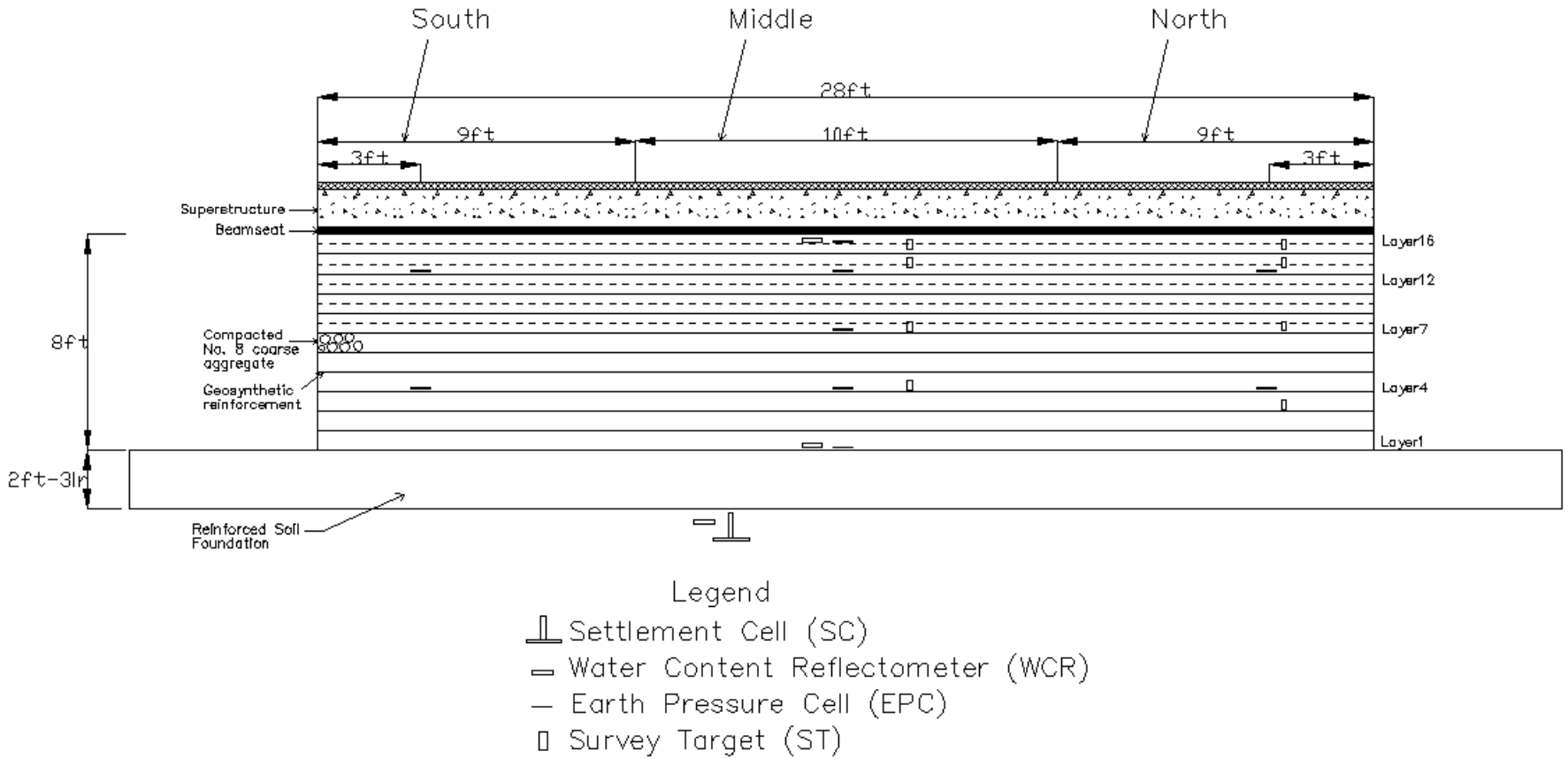

Fig. 6.2.2: Layout of instrumentation in the transverse direction in abutment B

Figure 6.2.3 illustrates an installed earth pressure cells being installed within Abutment A. Figure 6.2.3a shows placement of a single earth pressure cell on a geotextile layer. Figure 6.2.3b shows installation of earth pressure cells in transverse and longitudinal directions of the abutment.

(a)

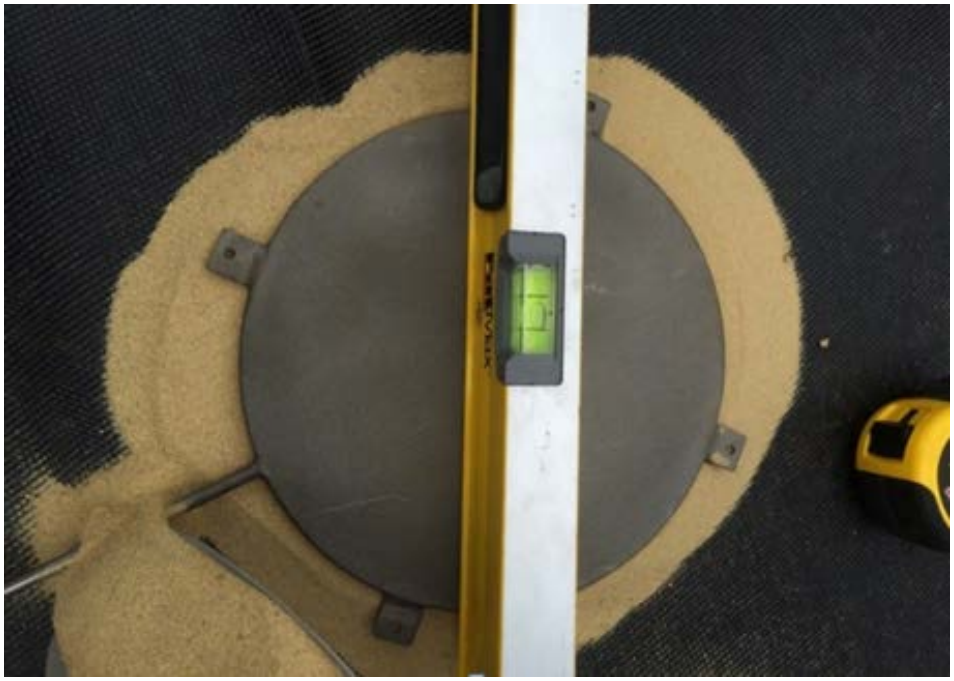

(b)

Fig. 6.2.3: Installation of earth pressure cells in abutment A and B(a) single earth pressure cell ; (b)multiple earth pressure cells in transverse and longitudinal directions of the abutment

All earth pressure cells were installed at the same height in relation to the height from the ground surface on both abutments. The instruments were installed on five different reinforcement layers (1, 4, 7, 13, and 16), where Layer 1 is located at the bottom of the abutment. The distances of

these layers from the super-structure are 2.4, 1.8, 1, 0.4, and 0.1 m (96, 72, 40, 16, and 4 in.), respectively (i.e., layer 1 is 2.4 m (96 in.) from the bottom of the super-structure). The layout of the instrumentation was designed to include instruments within both primary reinforcement zone and bearing bed zone and to obtain data within each abutment along the north, middle, and south sides of the abutments. The instruments were placed approximately 300 mm (1 ft) away from the facing of the GRS-IBS to capture the pressure behind the set-back of the superstructure and underneath the beam seat. Additionally, some of the earth pressure cells were positioned in the longitudinal direction 1.2 m (4 ft) and 2.2 m (7 ft) from the facing to assess the changes in stress distribution within each abutment away from the facing. During construction, Abutment A was loaded with Jersey barriers to simulate stage loading and the specific locations of the earth pressure cells in Abutment A were also determined to capture the effect in vertical reinforcement spacing in primary reinforcement and bearing bed zones.

6.2.3 RECTANGULAR PRESSURE CELLS (RPC)

Rectangular pressure cells (RPC) were used in the field instrumentation program to primarily measure the lateral stresses (lateral earth pressure) behind the facing of the GRS-IBS abutment. This sensor consists of a hydraulic pressure pad and pressure sensor where the pressure pad is connected to an electric transducer, which is filled with a hydraulic fluid in a closed system. Hydraulic pressure is generated when a load is applied on the pressure pad and this hydraulic pressure is transferred to the diaphragm of the electric transducer and converted to a stress measurement. The instrument adopted in this study was manufactured by Gloetzl Company in Germany. The instrument had a capacity to measure pressure in the range of 0 to 100 kPa (14.5 psi). The RPCs were custom designed to fit the dimensions of the facing blocks in the primary reinforcement zone and bearing bed zones. The dimensions of the RPCs were 0.1 m (4 in.) by 0.4 m (16 in) and 0.2 m (8 in.) by 0.4 m (16 in). This sensor was calibrated in GMU laboratory using AASHTO No 8 aggregate as a source of loading. Figure 6.2.4 shows installation of RPCs in the field. Two RPCs were installed in the primary reinforcement zone and three RPCs were installed in the bearing bed zone (Figure 6.2.1).

6.2.4 LOAD CELLS (LC)

The vertical loads carried by the facing blocks were monitored using load cells placed below the first (bottom) layer of CMU blocks. The main purpose of the load cells was to measure the downdrag forces that may develop at the connection between geotextile reinforcement and CMU blocks in the reinforced layers of the GRS-IBS abutment. Load cells with capacity of measuring forces of up to 60 kN (13490 lbs) were used as part of the field instrumentation program. Two circular load cells with a diameter of 140 mm (5.5 in.) were installed below the first CMU blocks (Figure 6.2.1). The first load cell was installed in middle section of the abutment and the second one was placed 3 m from the first load cell in the North side of the abutment. Figure 6.2.5 shows a view of the installation of one of the load cells in the field. The load cells were mounted on a wooden plate that was placed inside the RSF. Proper contact between the CMU blocks and the load cells was maintained without the load cells settling to ensure the load from all layers can be measured by the load cells.

(a)

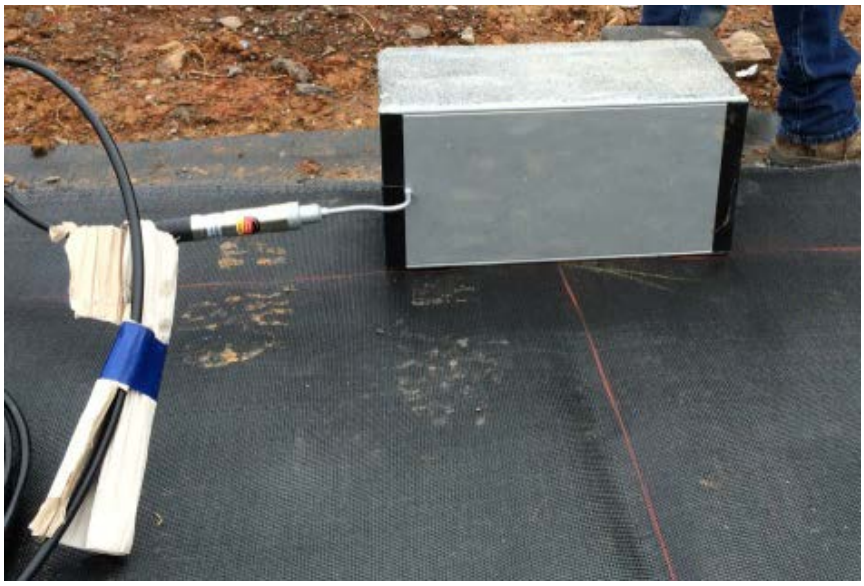

(b)

Fig. 6.2.4: Installation of Rectangular Pressure Cells (RPC) in Abutment A: (a) View of the 0.2 m (8 in.) by 0.4 m (16 in) RPC during installation; (b) View of the 0.1 m (4 in.) by 0.4 m (16 in) RPC during installation.

Fig. 6.2.5: Installation of load cell in Abutment A

6.2.5 STRAIN GAGES (SG)

Foil strain gages were used to evaluate the strains on geotextile reinforcements right behind facing blocks and away from the facing blocks. The selected strain gage (SG), known as HBM LY-41, has a grid length of 50 mm (2 in.) and it has a resistance of 120 ohms. A three-wire circuit configuration was used to generate data from the strain gages.

Calibration of the strain gages was performed according to the procedures outlined in wide-width strip tensile strength test for geotextiles (ASTM D4595) (Figure 6.2.6). The calibration was performed on 0.2 m (8 in.) by 0.2 m (8 in.) geotextile specimen using universal testing machine (UTM). The strain gage was glued on the center of geotextile specimen with an epoxy type adhesive (HBM X-60). During the calibration, strains were recorded both directly from the strain gage and from the internal displacement recordings of the UTM. This allowed the comparison between the local strains on the geotextile (via the glued strain gage) and the global strains in the geotextile specimen defined using displacements measured with sensor in the UTM during tensile loading. The results from three replicate calibration tests are shown in Figure 6.2.7. The results in all three tests show that the strains obtained from the UTM were higher than the strains from the strain gages. To be able to relate this information for use in the field, a correlation between UTM strain (global strain) and strain gage strain (local strain) was developed. Figure 6.2.8 shows the developed correlation. Based on this information, a calibration equation was selected from the trend line with a higher R^2 value to interpret field strain gage data.

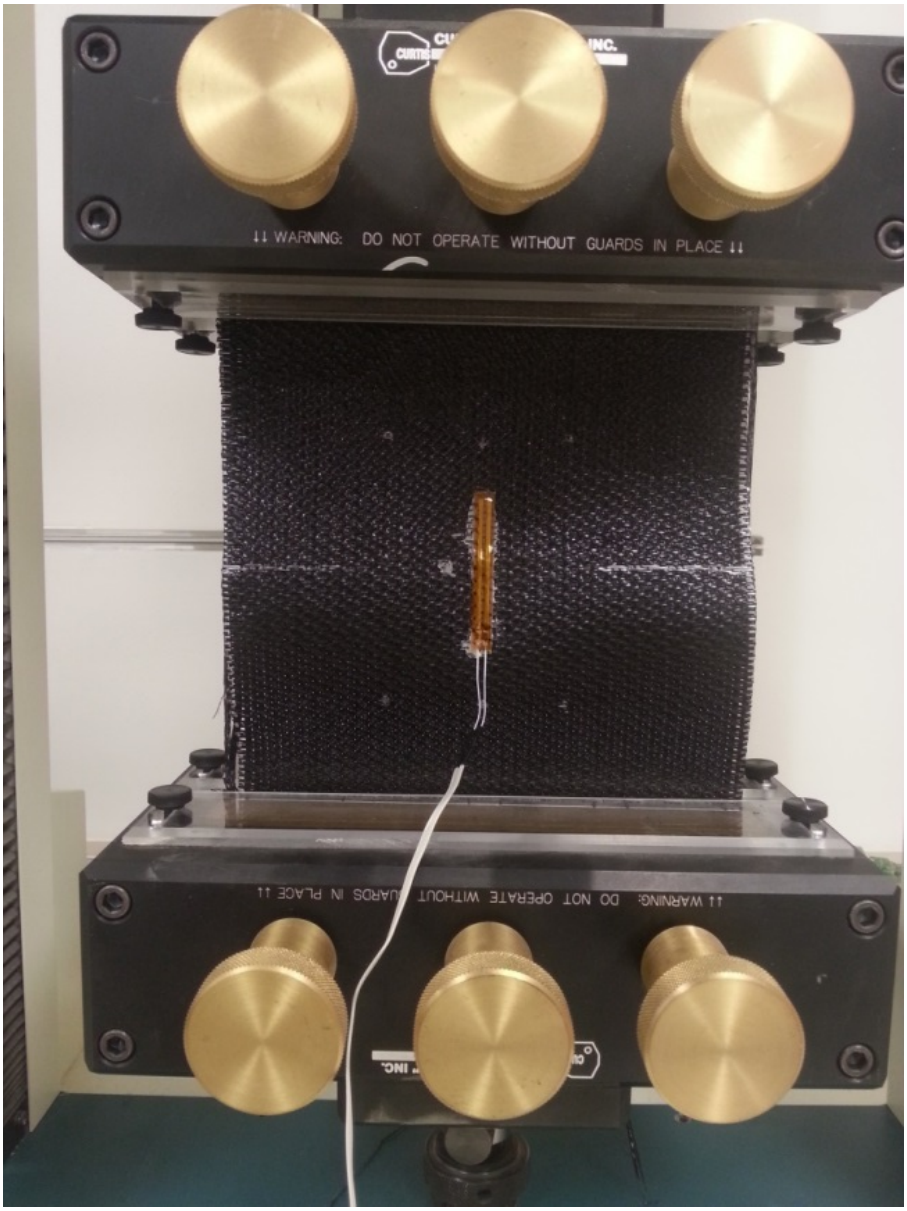

Fig. 6.2.6: Wide-width strip test for calibration of strain gage in GMU laboratory (ASTM D4595)

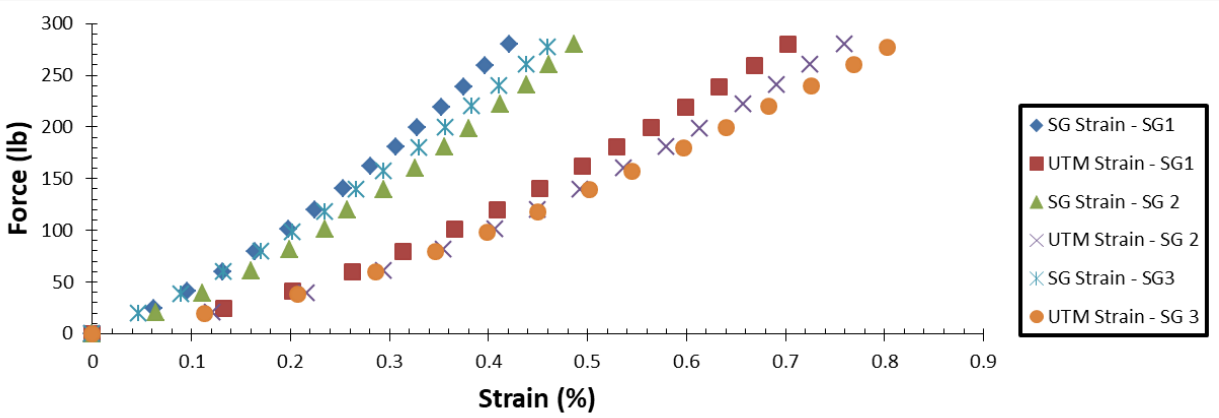

Fig. 6.2.7: Strain data generated from UTM and strain gages during calibration tests

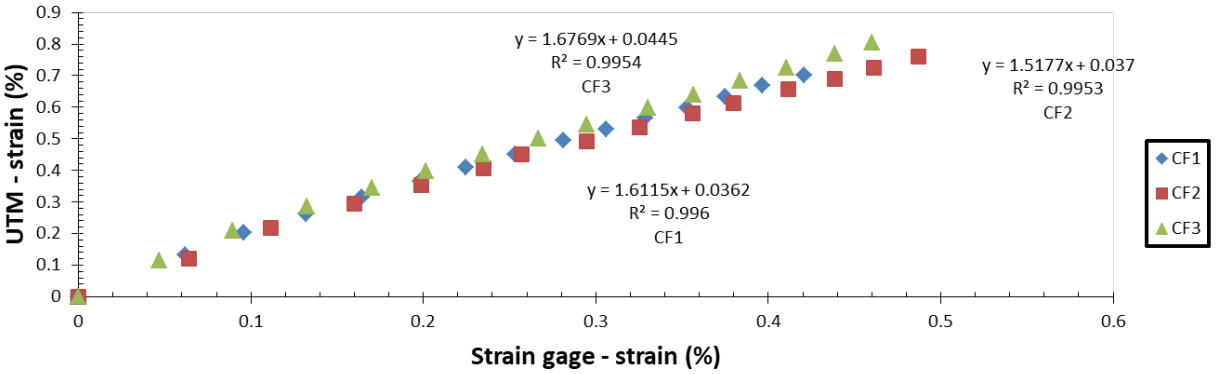

Fig. 6.2.8: Calibration equations developed from UTM (global strain) and strain gage data

Forty-four strain gages were included in the field instrumentation program. For redundancy, the strain gages were designed to be installed on both sides of the geotextile, each paired at the same location. Strain gages were positioned in the field in 2 layers of the primary reinforcement zone and in 4 layers of the bearing bed zone (Figure 6.2.1). Thirty-six strain gages were located right behind the facing blocks and 8 strain gages were located 0.9 m (3 ft) from the back of the facing blocks. They were distributed in the middle, north, and south sides of the abutment. All strain gages were installed prior to the construction on geotextiles that were used to build the GRS-IBS. The installations were conducted at a VDOT facility close to the field site. Silicon (Dow Corning RTV) adhesive was applied on top of the strain gages to protect them from damages by aggregate particles and infiltrations in the abutment. Figure 6.2.9 shows installed strain gages prior to construction and Figure 6.2.10 shows their placement in the field. The cables of the strain gages in the field were placed in PVC conduits for protection.

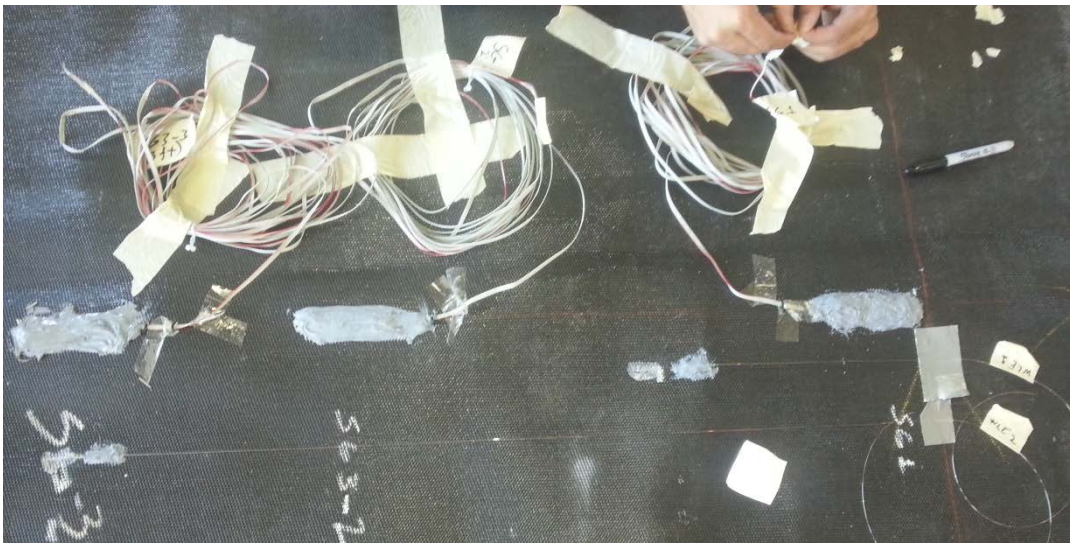

Fig. 6.2.9: Installation of strain gages on to the geotextile

Fig. 6.2.10: Installation of strain gages in reinforcement layer 14 in Abutment A

6.2.6 WIRE LINE EXTENSOMETERS (WLE)

Wire line extensometers (WLE) were used to measure lateral displacement in the geotextile due to imposed vertical loading. The WLE used in this research involves a displacement transducer, stainless steel wire, and tubing. The stainless-steel wire used to construct the WLE has a thickness

of 0.33 mm (0.013 in.), which corresponds to a wire used in pianos. The tubing had an approximate diameter of 5 mm (0.2 in.), which was a tubing used in bicycles to protect brake wires. The displacement transducer adopted in this field program was a Celesco model SP1-4-3 string pot, which involved a chord that extended to a full stroke range of 120 mm (4.75 in.).

The set-up of the WLE included a stainless-steel wire that was attached to the geotextile on one end and was connected to an eyelet of the displacement transducer on the other end. Movements in the geotextile were detected by the wire connected to the eyelet as it started to move by pulling or pushing a chord that moves from the displacement transducer. This displacement was recorded as a change in voltage by the displacement transducer that was supplied with a given voltage. In the field, the stainless-steel wire was installed inside a tubing that protected the wire from damages from the aggregate placed on top of the wire.

Calibration of the WLE was performed in the laboratory by following the procedures outlined by Warren (2010). The calibration was conducted to relate the voltage reading (change in voltage) from the string pots to displacements. During the calibration process, the effect of potential slacks in the wire and friction between the wire and the bicycle tubing were also evaluated. Figure 6.2.11 shows set-up used to calibrate WLEs.

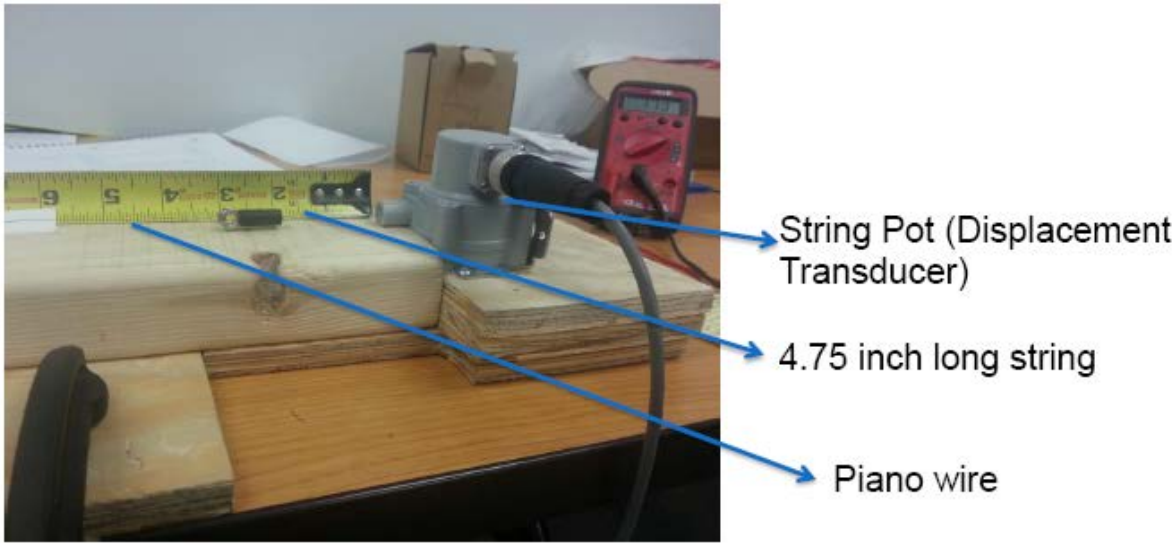

Fig. 6.2.11: Wire line extensometer set-up during calibration of string pot

Nineteen WLEs were included in the field instrumentation program. The WLEs were positioned in 2 layers of the primary reinforcement zone and in 2 layers of the bearing bed zone (Figure 6.2.1). They were positioned in the same locations as the strain gages and were installed adjacent to the strain gages. The WLEs were located 0.3 m (1 ft), 0.9 m (3 ft), 1.5 m (5 ft), and 2.75 m (9 ft) from the facing blocks. The WLEs were located mainly in the middle section of the Abutment A and in north, and south sides of the abutment only in one layer. The WLEs were placed in a plastic housing and mounted to metal bars. The metal bars were then mounted to the facing of the GRS-

IBS (CMU blocks). The piano wire connected to the string pot and bicycle tubing runs through a conduit drilled at the intersection of two CMU blocks. Figure 6.2.12 shows installation of single and multiple WLEs in the field.

(a)

(b)

Fig. 6.2.12: Installation of wire line extensometers in Abutment A: (a) View of one wire line extensometer; (b) View of four wire line extensometers

6.2.7 SOIL EXTENSOMETERS (SE)

Two vibrating wire soil extensometers (SE) were adopted in the field instrumentation program to measure lateral deformations within the backfill material. Geokon's vibrating soil extensometer (model 4435) was selected in the instrumentation. The SE has flanges made from L-shaped steel on both ends and a rod that has a string inside that is bolted to the flanges. The length of the rod is 600 mm (24 in.). The SEs were installed 0.3 m (I ft) and 2.75 m (9 ft) from the facing blocks in the bearing bed zone (Figure 6.2.1). This approach was adopted to evaluate the lateral deformations in the 0.1 m (4 in.) and 0.2 m (8 in.) reinforcement zones, where the instruments installed 0.3 m (I ft) and 2.75 m (9 ft) from the facing capture the 0.1 m (4 in.) and 0.2 m (8 in.) reinforcement zones respectively. The layout of the SEs in the field is shown in Figure 6.2.13. The time required to manufacture these instruments required the instruments to be directly shipped to the site (as opposed to GMU's laboratory). Therefore, data obtained from the field was interpreted using the calibration equations provided by the manufacturer.

Fig. 6.2.13: Installation of soil extensometers in Abutment A

6.2.8 SETTLEMENT CELLS (SC)

To monitor settlement below the foundation of the GRS-IBS abutment, two settlement cells (SC) were installed in the field underneath Abutments A and B (Figures 6.2.1 and 6.2.2). A relevant focus of this research component was to measure the settlement right underneath the reinforced soil foundation (RSF), therefore conventional settlement plates could not be used as they would have required a rod that penetrates through both RSF and GRS-IBS. Therefore, vibrating wire settlement cells manufactured by Slope Indicator Company were used. These systems consist of a reservoir, a pressure transducer, and liquid-filled tubing. In the field, the reservoir was installed on stable ground outside the GRS-IBS abutments on a higher elevation. The pressure transducer was installed in the soil layer below the RSF (in this case the CH layer). Although Figure 6.1.2b

shows a uniform CH layer at the site, during construction majority of the RSF was constructed on bedrock as the CH layer was only observed in pockets of small areas (Figure 6.2.14a). In order to install the instruments, the small clayey area underneath each GRS-IBS was dug out and square steel plates that are 0.3 m (12 in.) by 0.3 m (12 in.) were placed in these holes. The pressure transducers were mounted onto these steel plates (Figure 6.2.14b). The liquid-filled tubing that was connected to the pressure transducers was then extended to the reservoir mounted at a high ground (away from the GRS-IBS) (Figure 6.2.14c). The tubing was filled with a 50/50 mixture of water and ethylene glycol, which is about 7% heavier than water and does not freeze during winter season. The level of the liquid in the tubing was maintained by adding de-aired water to the reservoir in regular time intervals as recommended by the manufacturer.

(a)

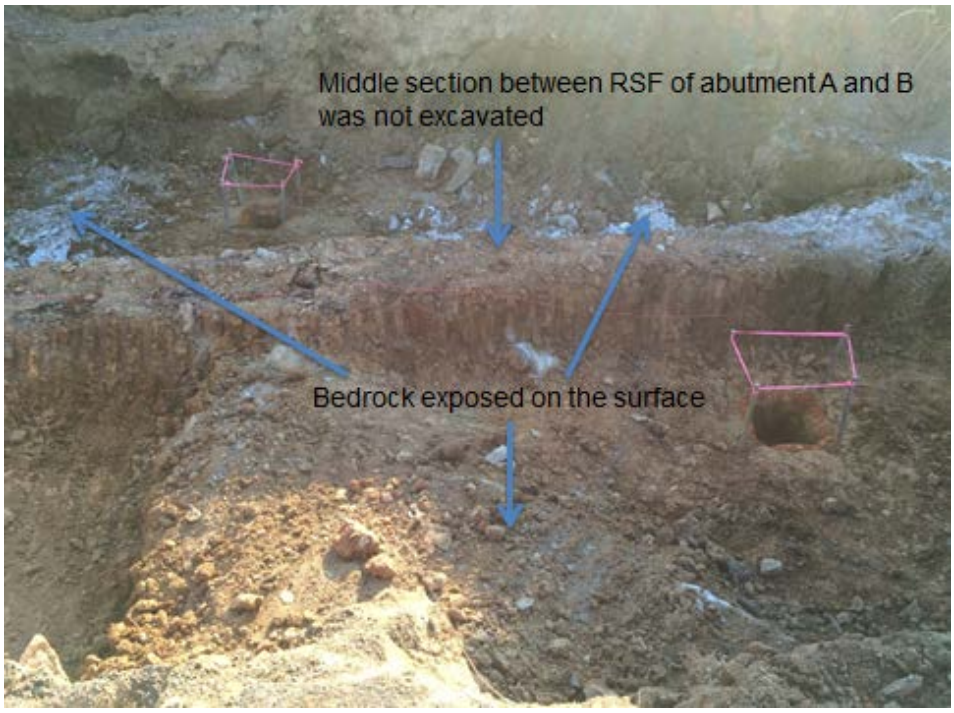

(b)

(c)

Fig. 6.2.14: Installation of settlement cells in Abutments A and B: (a) Exposed area underneath the RSF; (b) Placement of the pressure transducer inside the hole in the clay layer: (c) Installed reservoir away from the abutments

6.2.9 SURVEY TARGETS (ST)

To monitor the long-term displacements of the CMU blocks, survey targets (ST) were installed on 16 blocks in abutment A and 8 blocks in abutment B (Figures 6.2.1 and 6.2.2). A Leica GMP104 monitoring mini-prism that was manufactured by Leica Geosystems was used as a survey target

in this project. This survey target has a circular shape with a diameter of 25.4 mm (1 in.). Figure 6.2.15 shows the installed survey targets in the field. The surveying of these targets was conducted by the VDOT team, which took place right before and after the placing of the bridge slab and during the four-truck loading that took place over a one-year period after construction. Surveying during construction was not available. The total station used by VDOT for surveying had an accuracy of 1 mm (0.04 in) both in lateral and vertical directions. The results obtained from the surveys were plotted to monitor the changes over time.

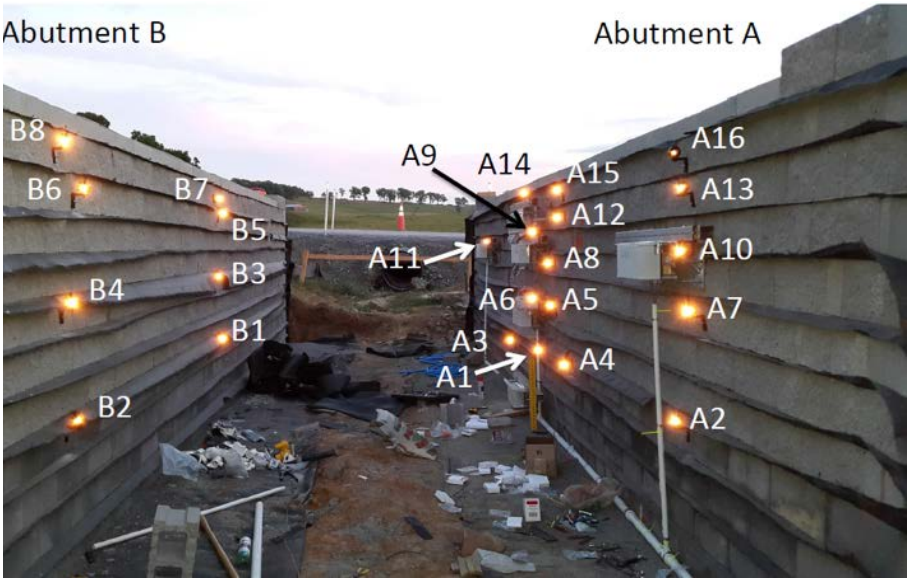

Fig. 6.2.15: Survey targets installed on CMU blocks in Abutments A and B

6.2.10 WATER CONTENT REFLECTOMETERS (WCR)

Water content of the foundation soil (CH) and the backfill material (AASHTO No. 8 aggregate) were monitored using water content reflectometers (WCR) installed in the soils. Campbell Scientific's CS655-LC water content reflectometers were used in this project. This model consists of two 120 mm (4.8 in) stainless steel rods connected to a circuit board. The sensor measures the dielectric constant of the soil, which correlates well with the soil volumetric water content. The volumetric water content was used along with the soil unit weight to define the gravimetric water content. Six WCRs were used, with 3 WCRs being installed on each abutment (Figures 6.2.1 and 6.2.2). One of the WCR was installed in the foundation soil and the two were installed in the first and last layer of the abutment. The WCRs used in this project were also capable of measuring temperature. Figure 6.2.16 shows the installation of a WCR (next to EPC) in the first layer of Abutment A.

Fig. 6.2.16: Installation WCR (next to EPC) in first layer of Abutment A

6.3 EVALUATION OF FIELD INSTRUMENTATION DATA

Overall, a total of 142 instruments were installed as part of the field component of this study, using the instrumentation layouts shown in Figures 6.2.1 and 6.2.2. Table 6.3.1 summarizes the type and number of instruments installed in each abutment. During construction, data from each instrument was collected every five minutes and was monitored through a cell phone application called "logger link," which communicated with the data loggers and displayed the data collected at a given time. After construction, data from all instruments was automatically collected in intervals of every 30 minutes and stored in a server.

The main purposes of the field monitoring program were to:

- evaluate vertical stresses (close to and away from the facing);
- horizontal stresses behind the facing of the structure;
- horizontal deformations in the reinforced zones (right behind the facing blocks and away from the facing); and
- vertical deformation (settlement) beneath the foundation.

The information obtained from the instruments were subsequently used to calibrate numerical models, as documented in Chapter 7 of this report, and to evaluate relevant design aspects, as documented in Chapter 8 of this report. The performance of Abutments A and B were evaluated based on the data generated from:

- self-weight of the backfill material (during construction),
- placement of the bridge slab, and
- loading of the slab with a truck after the construction.

Table 6.3.1. Type and number of instruments used in the field instrumentation program

No	Instrument	Quantity		
		Abutment A	Abutment B	Total
1	Earth Pressure Cell	15	13	28
2	Rectangular Pressure Cell	5		5
3	Load Cell	2		2
4	Strain Gage	44		44
5	Wire Line Extensometer	19		19
6	Soil Extensometer	2		2
7	Settlement Cell	2		2
8	Survey Targets	24		24
9	Water Content Reflectometer	3	3	6

Note: Additional earth pressure cell was installed in a box outside the GRS-IBS abutment to observe the effects of seasonal variation on stress distribution. This makes the total number of earth pressure cells used in the field instrumentation program as 29.

The construction of the GRS-IBS took place between August 3rd and September 15th of 2015. Figure 6.3.1 shows the construction of the structure with the backfill and geotextile. The bridge slab was placed on August 26, 2015 and consisted of seven pre-cast concrete segments that were connected using a steel rod to form one solid slab. The slab was approximately 9 m (30 ft) wide and 5.7 m (18.7 ft.) long and it had a thickness of 0.4 m (1.25 ft). Figure 6.3.2 shows the placement of the slab. Loading of the slab with a truck took place on September 2015, December 2015, March 2016, and November 2016. These four different loading dates were selected to capture the effect of seasonal variations on the performance of the structure. The truck used for this loading was VDOT's GMC C7500 model with single axle and was loaded with 21B aggregate (Figure 6.3.3). The weigh station ticket showed that the total loads from this application equated to 150 kN (15 tons). The truck selected for loading had a length such that it allowed for all tires to sit directly on the slab. During loading, due to traffic control limitations, the truck was parked in 4-hour intervals on each side of the traffic lanes (north and south bounds).

In addition, the performance of Abutment A was evaluated with stage loadings using single and multiple Jersey barriers that were placed at different levels during construction. There were seven stage loadings, four of which involved use of 8 Jersey barriers and three of them involved use of a single Jersey barrier. Four stage loadings were applied on primary reinforcement zone and three stage loadings were applied on bearing bed zone. The loading duration ranged from 30 minutes to 24 hours due to the scheduling constraints during construction. Locations where the loading was applied within abutment A are shown in Figure 6.3.4 (a). The methods used for applying stage loading in the field are shown in Figure 6.3.4 (b) and (c).

Evaluation and assessment of field instrumentation data based on the above described loading conditions during and after construction are presented in detail in the Sections 6.3.1 and 6.3.2.

Fig. 6.3.1: Construction of abutments using AASHTO No.8 backfill (Self-weight)

(a)

(b)

Fig. 6.3.2: Placement of bridge slab: (a)On Abutments A and B; (b)On Abutment B showing the gap between the bottom of the slab and top of the reinforced aggregate

Fig. 6.3.3: Truck parked on the north bound of the super-structure after construction

(a)

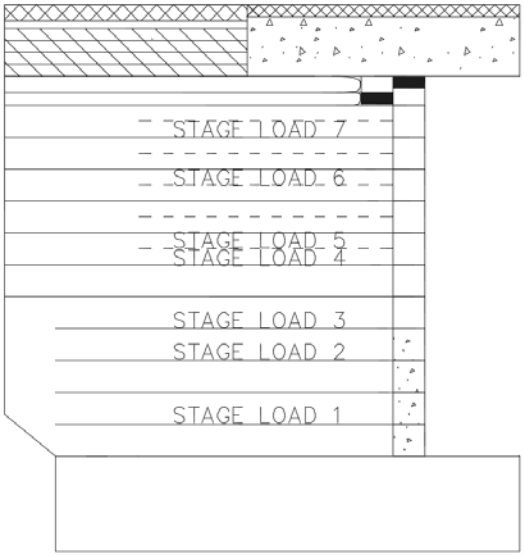

(b)

(c)

Fig. 6.3.4: Characteristics of the stage loading operations: (a) Locations within GRS-IBS where stage loadings were applied during construction; (b) single Jersey barrier loading; (c) multiple Jersey barriers loading

6.3.1 FIELD DATA GENERATED DURING CONSTRUCTION (SHORT-TERM BEHAVIOR)

6.3.1.1 SELF-WEIGHT OF BACKFILL MATERIAL AND BRIDGE SLAB LOADING

Vertical stresses measured using pressure cells at the elevation of five reinforcement layers in Abutments A and B due to self-weight of the backfill and to the subsequent bridge slab loading are shown in Figures 6.3.5 through 6.3.14. It should be noted that the inserts drawn in each of these figures show the locations of the installed pressure cells. These figures also show the results from the stage loadings in Abutment A. However, additional details regarding observations during these loading operations are discussed in Section 6.3.1.2.

When the results from the vertical stresses measured in the field due to the self-weight of backfill material were compared against the calculated theoretical vertical stresses (based on the unit weight of the backfill material (γ_b) multiplied by depth of stress point), it can be stated that the two data are in good agreement. For instance, the stress measured from all EPCs in Layer 1 of Abutments A and B in Figures 6.3.5 and 6.3.6 before the slab was placed is around 36 kPa (5.2 psi). The calculated pressure for unit weight of backfill of 1700 kg/m^3 (107 pcf) and depth of 2.2 m is approximately is 36 kPa (5.2 psi). This comparison was made for all layers where stresses were measured and the data from the field was in good agreement with calculated values. This confirms the validity of the calibration of the instruments and their accuracy to estimate stress purely based on self-weight of the material.

In order to evaluate the data from the placement of bridge slab, it should be recalled that the beam seat widths in the two abutments were purposely constructed differently. In abutment A, the beam seat was 0.6 m (2 ft) whereas in abutment B was 1.2 m (4 ft). Because of this difference, the magnitude of slab load in abutments A and B were estimated as 42 kPa and 21 KPa (6 and 3 kPa) respectively. Figures 6.3.15 and 6.3.16 show vertical stress distribution profiles developed in each abutment due to bridge slab load.

The field monitoring results were compared against the predictions obtained using theoretical stress distributions estimated based on the following three methods:

AASHTO 2:1 method: For strip footing in GMSE structures, this method estimates the stress distribution, as follows:

$$\Delta\sigma = q/D \qquad \text{(Equation 6.3.1)}$$

$$with\ D = (b - 2e) + Z \quad for\ Z \leq Z1, \qquad \text{(Equation 6.3.2)}$$

$$with\ D = d + \frac{(b-2e)+Z}{2} \quad forZ > Z1, \qquad \text{(Equation 6.3.3)}$$

$$Z1 = (2 * d) - b \qquad \text{(Equation 6.3.4)}$$

where: *q* is load per linear feet of strip footing,
D is effective width of the applied load at a given depth,
Z is depth of stress point below footing,
*Z*1 is depth at which the effective width intersects the back of wall facing,
b is width of applied load,

e is eccentricity of footing load, and
d is the distance from the facing to the center of footing width.

The eccentricity of the footing load, in this case the slab load, as obtained from the design of the GRS-IBS was 5 mm (0.2 in).

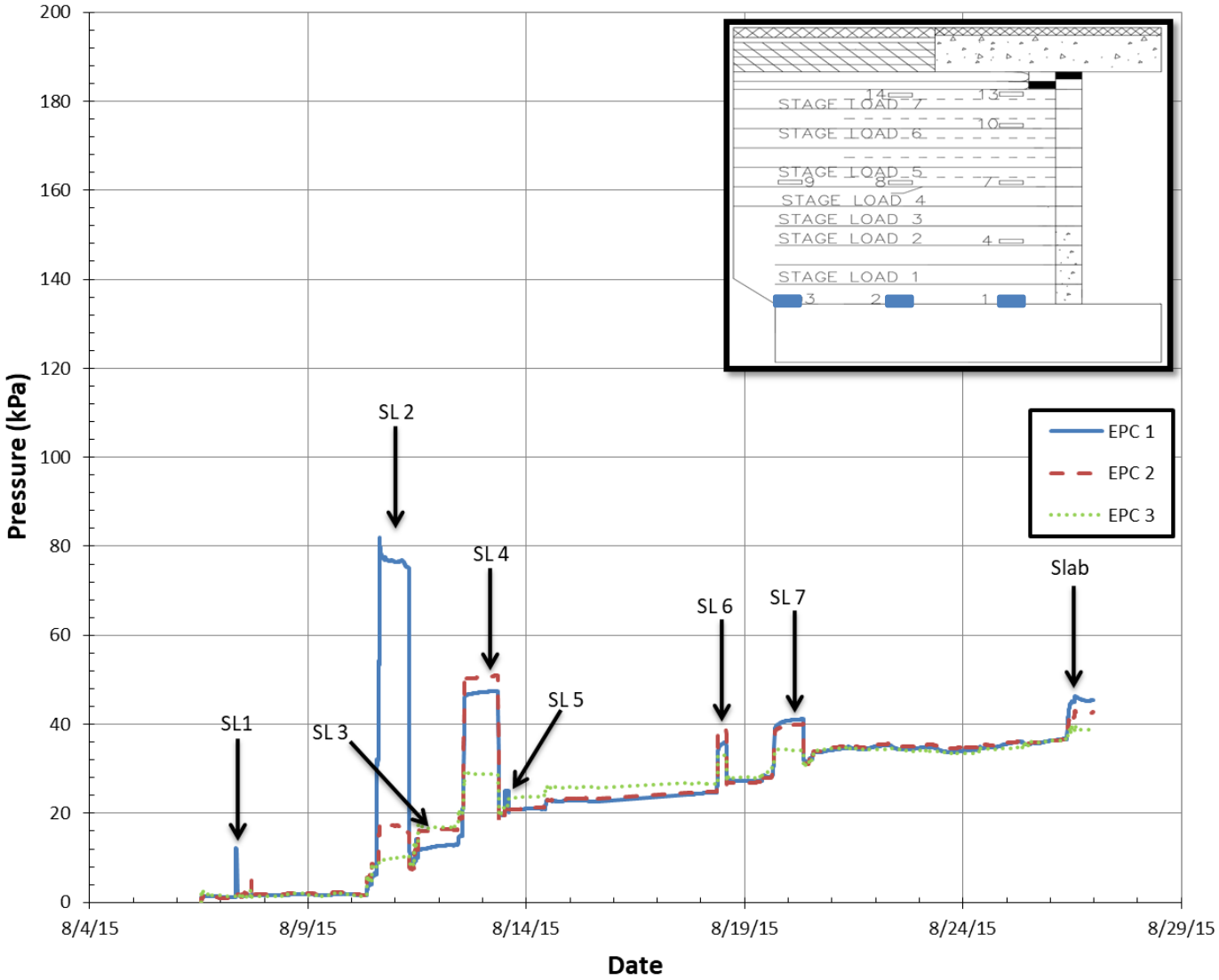

Note: The insert in the figure shows the locations of the pressure cells in Abutment A and the stage loadings (SL) SL1 through SL7.

Fig. 6.3.5: Vertical stresses developed in Layer 1 of Abutment A

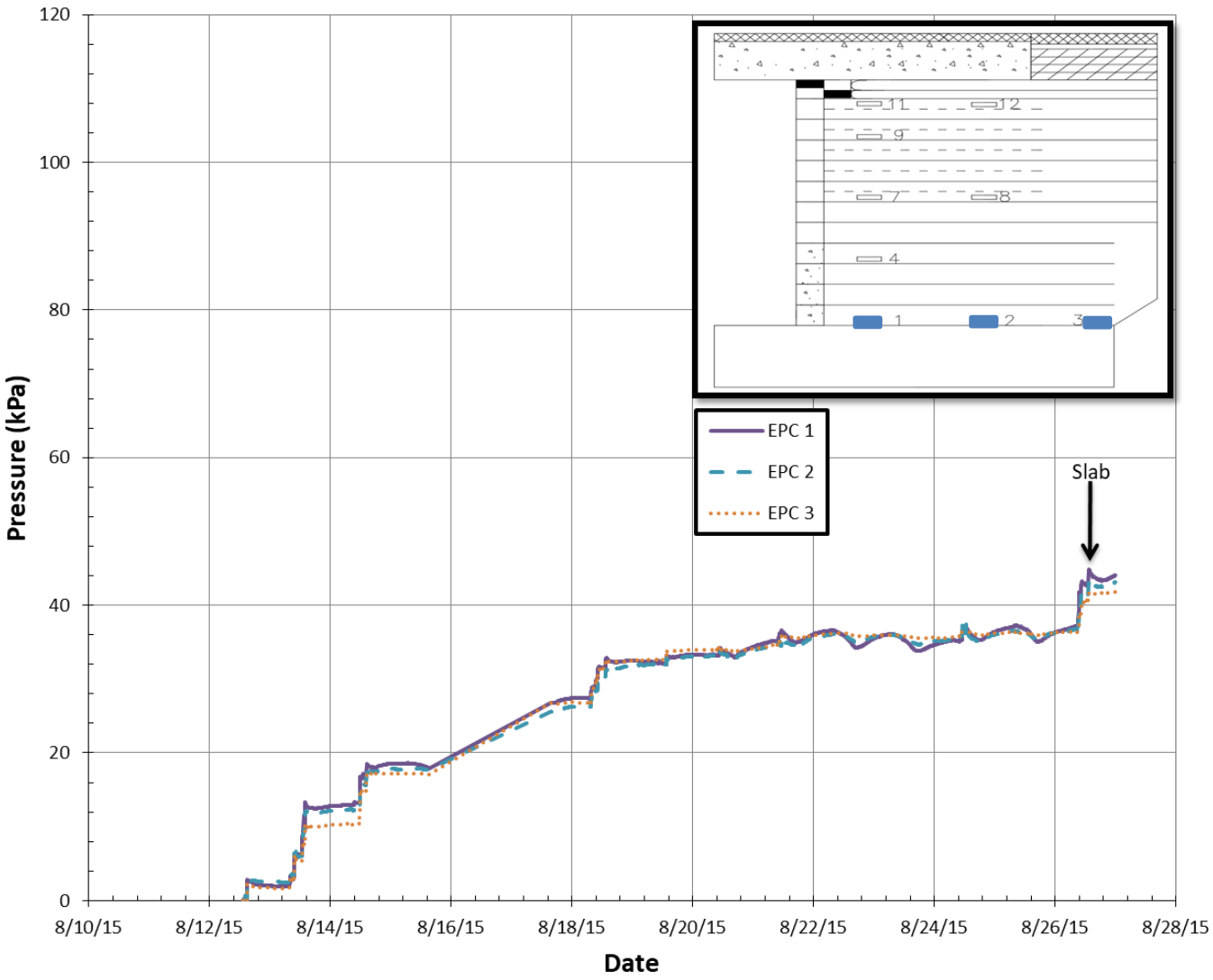

Note: The insert in the figure shows the locations of the pressure cells in Abutment B.

Fig. 6.3.6: Vertical stresses developed in Layer 1 on Abutment B

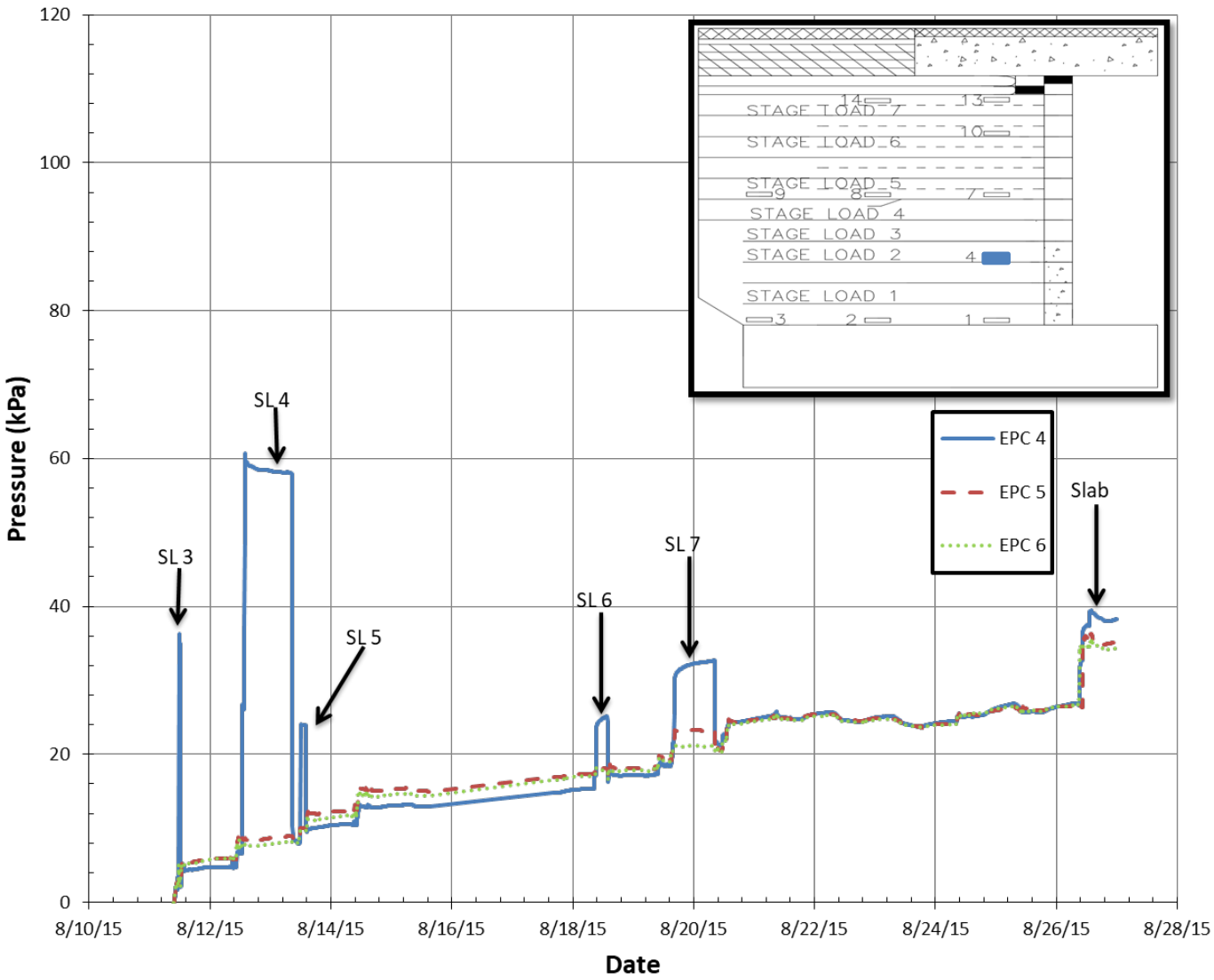

Fig. 6.3.7: Vertical stresses developed in Layer 4 on Abutment A (EPC 5 and 6 are located on the north and south sides – See Fig. 6.2.1)

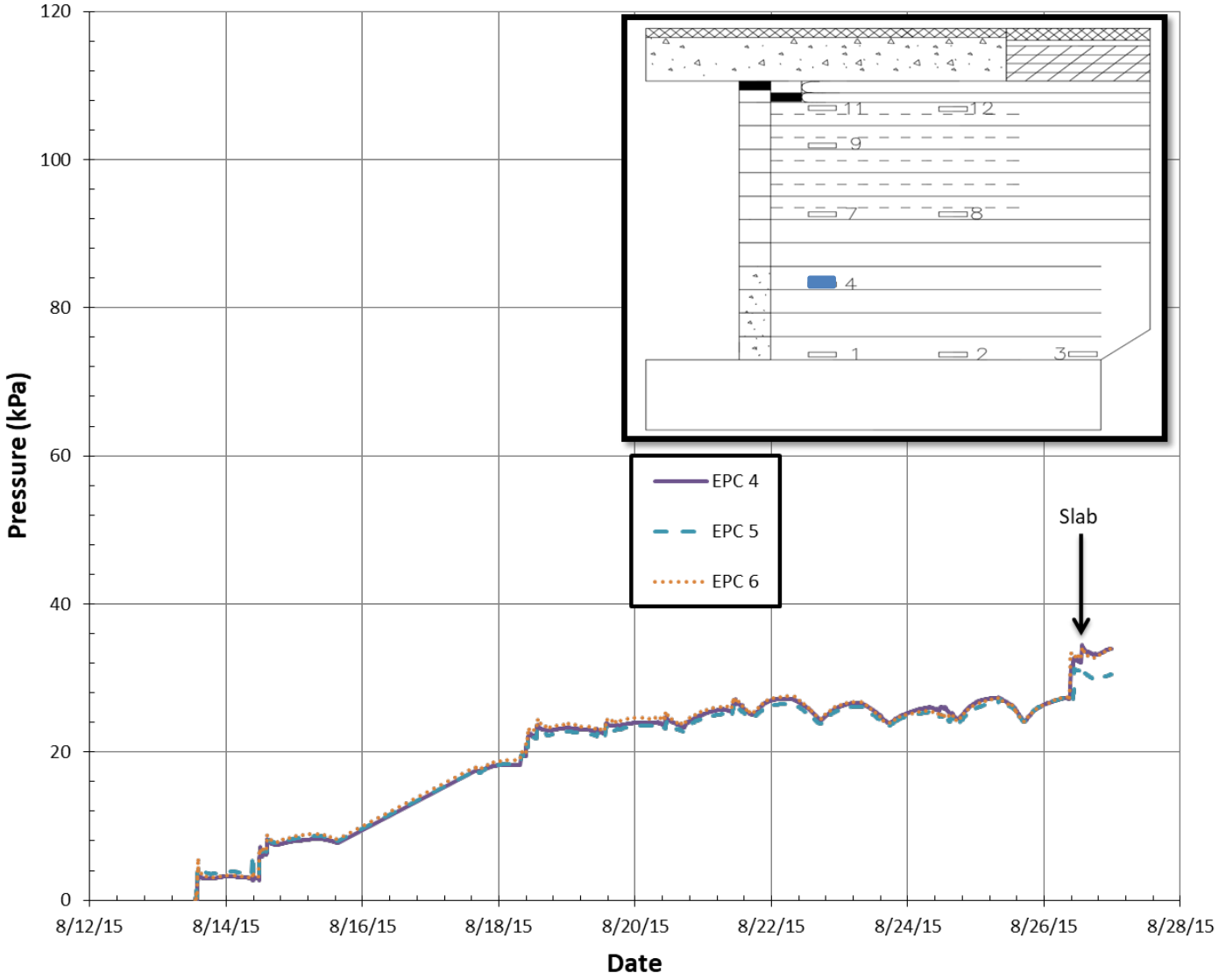

Fig. 6.3.8: Vertical stresses developed in Layer 4 on Abutment B (EPC 5 and 6 are located on the north and south sides – see Fig. 6.2.2)

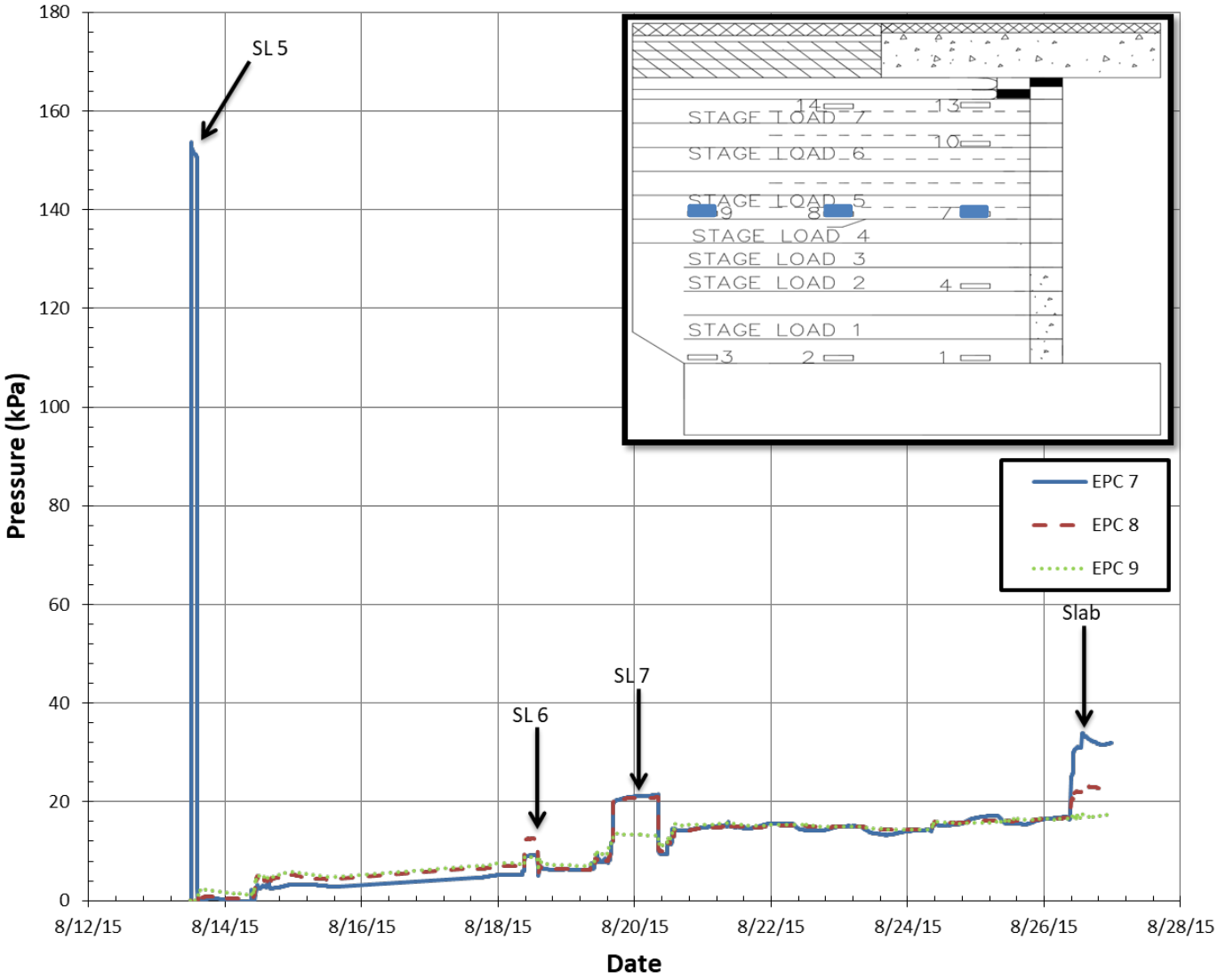

Fig. 6.3.9: Vertical stresses developed in Layer 7 on abutment A

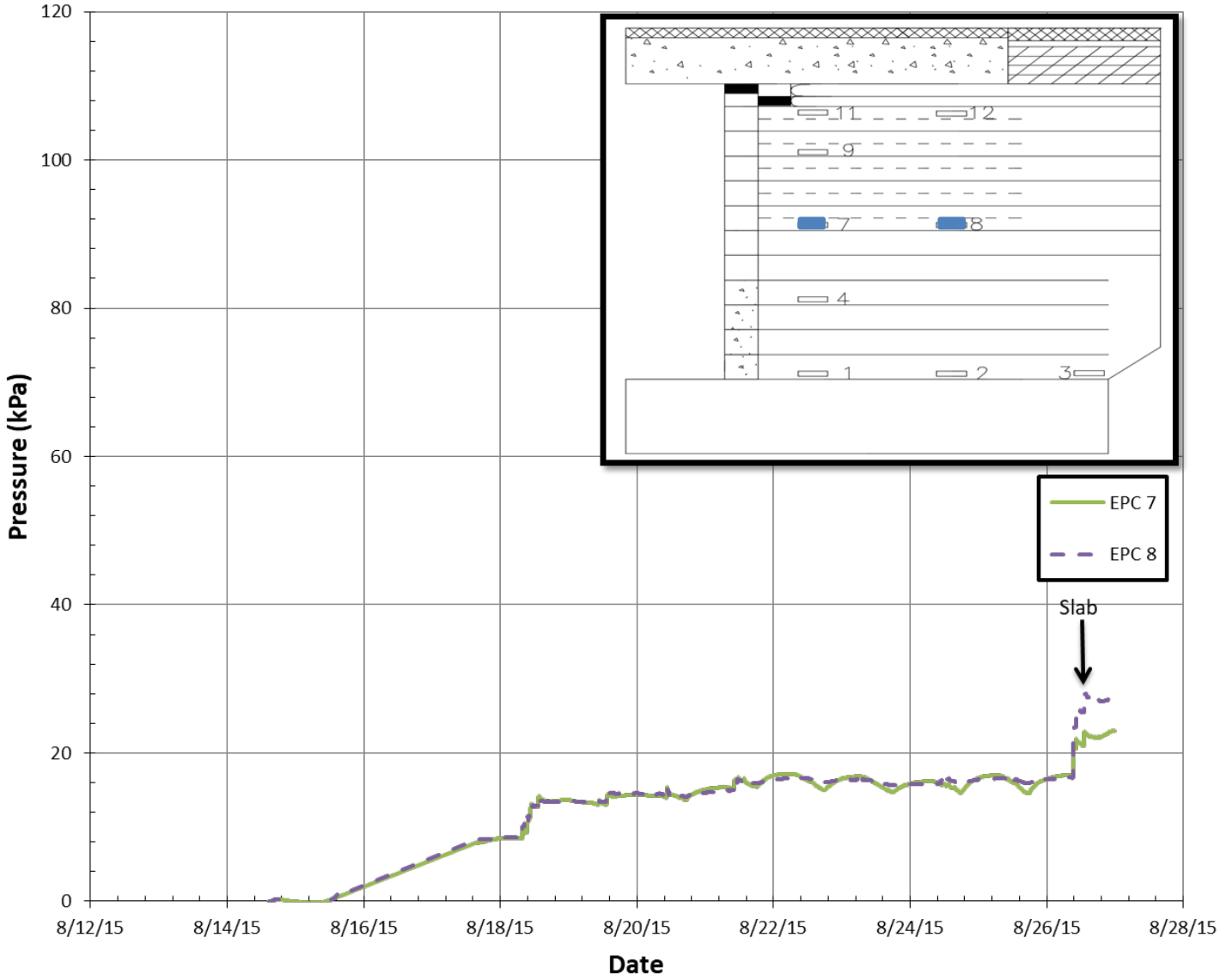

Fig. 6.3.10: Vertical stresses developed in Layer 7 on abutment B

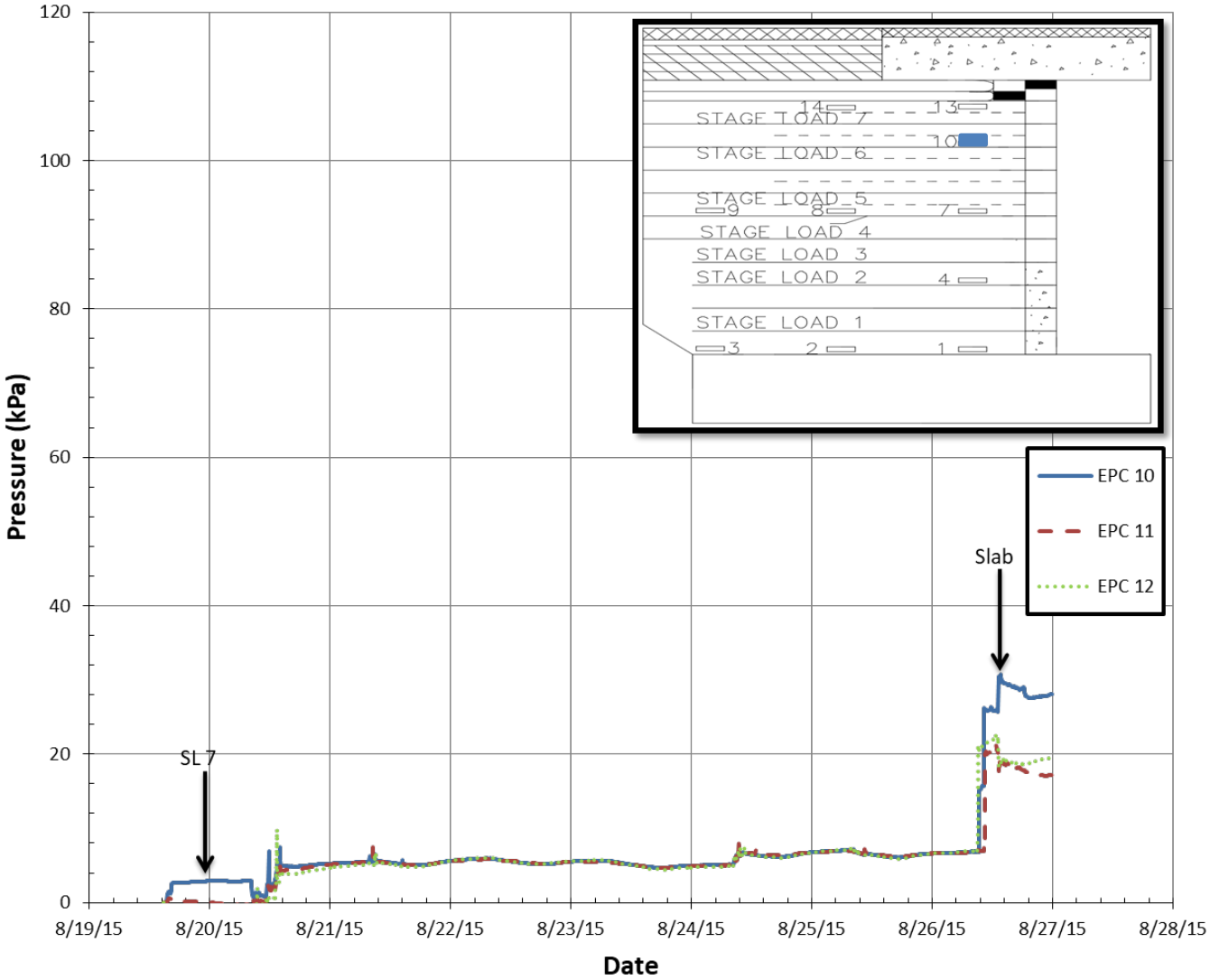

Fig. 6.3.11: Vertical stresses developed in Layer 13 on Abutment A (EPC 11 and 12 are located on the north and south sides – see Fig. 6.2.1)

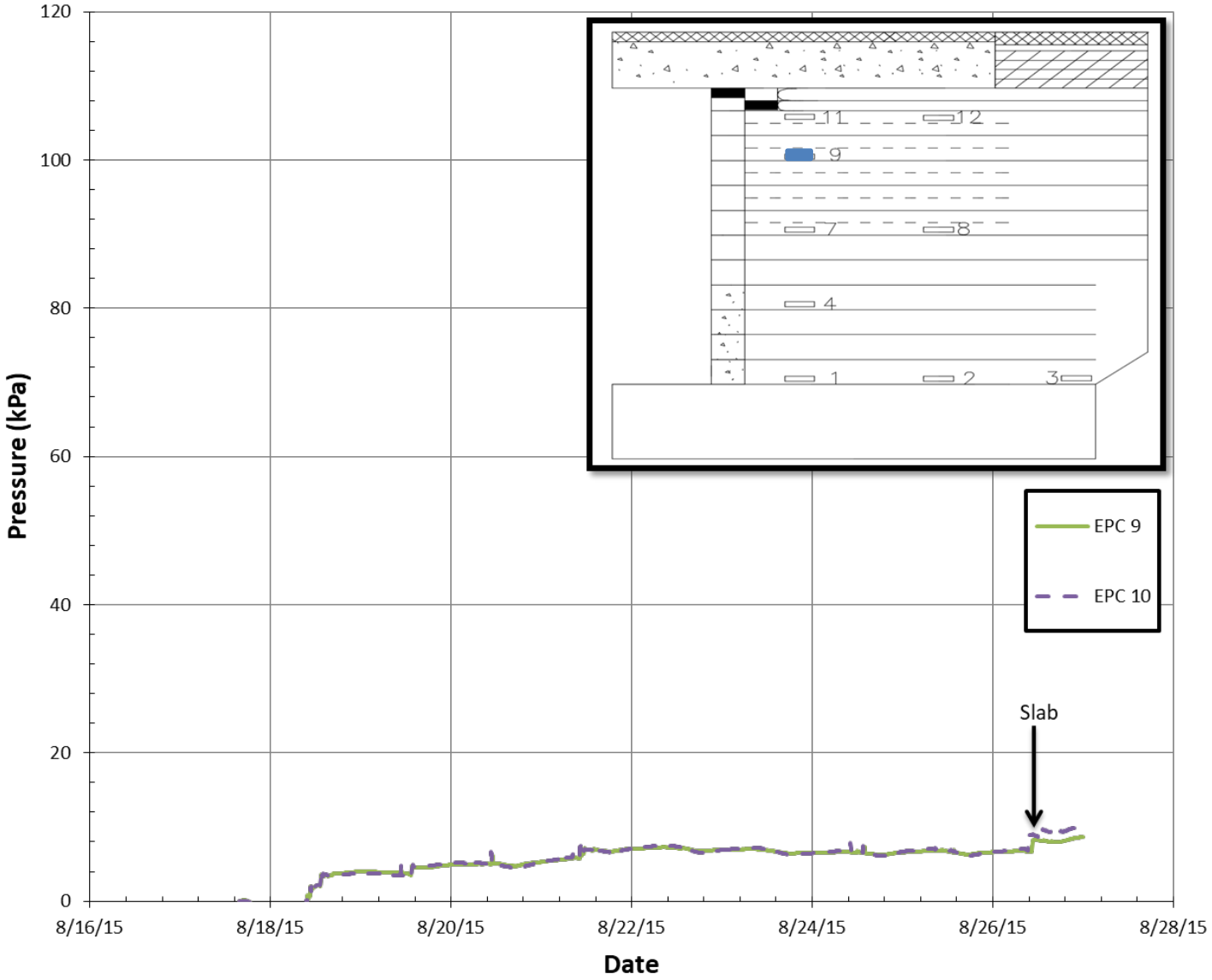

Fig. 6.3.12: Vertical stresses developed in Layer 13 on Abutment B (EPC 10 is located on the north side – see Fig. 6.2.2)

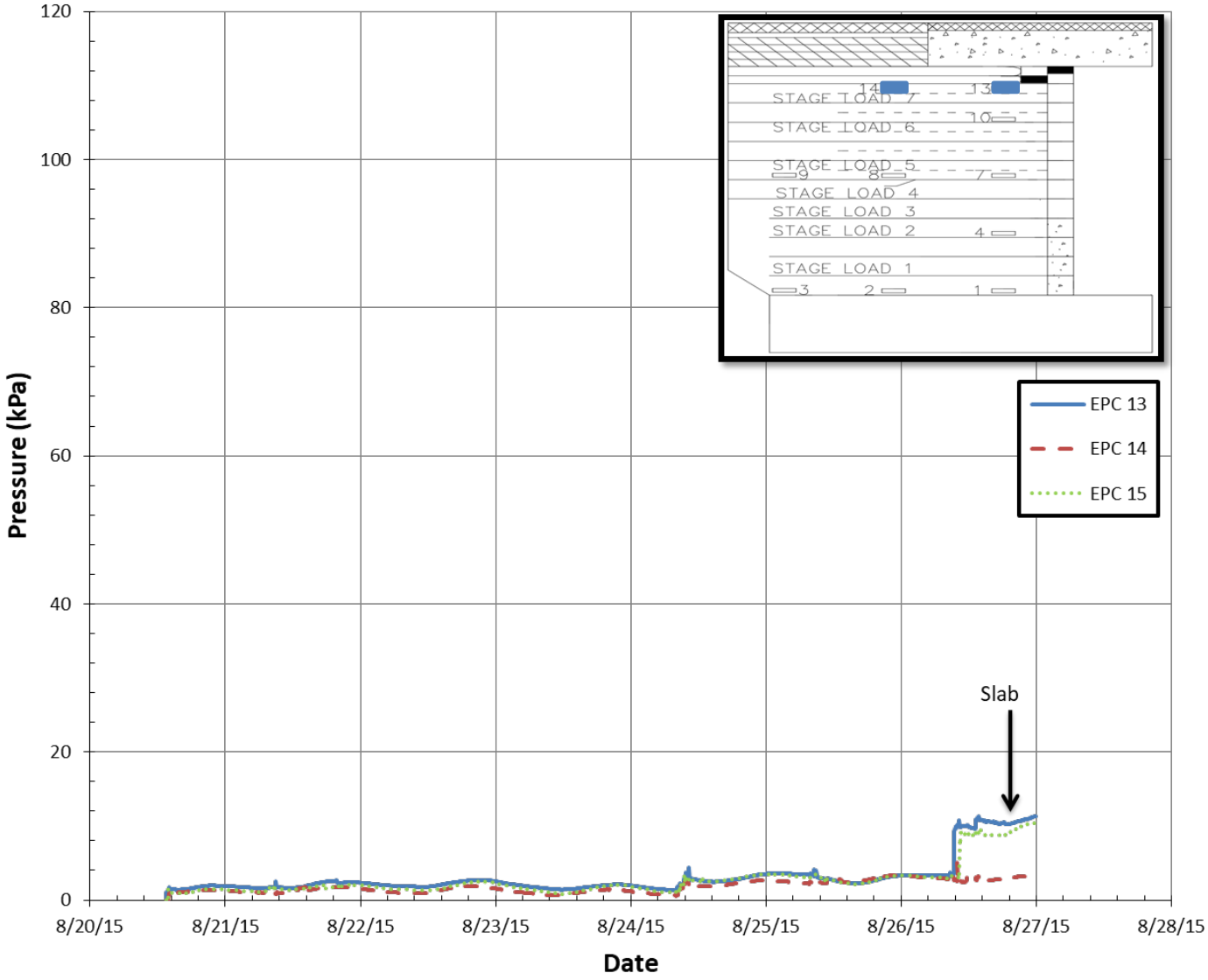

Fig. 6.3.13: Vertical stresses developed in Layer 16 on Abutment A (EPC 15 is located on the north side – see Fig. 6.2.1)

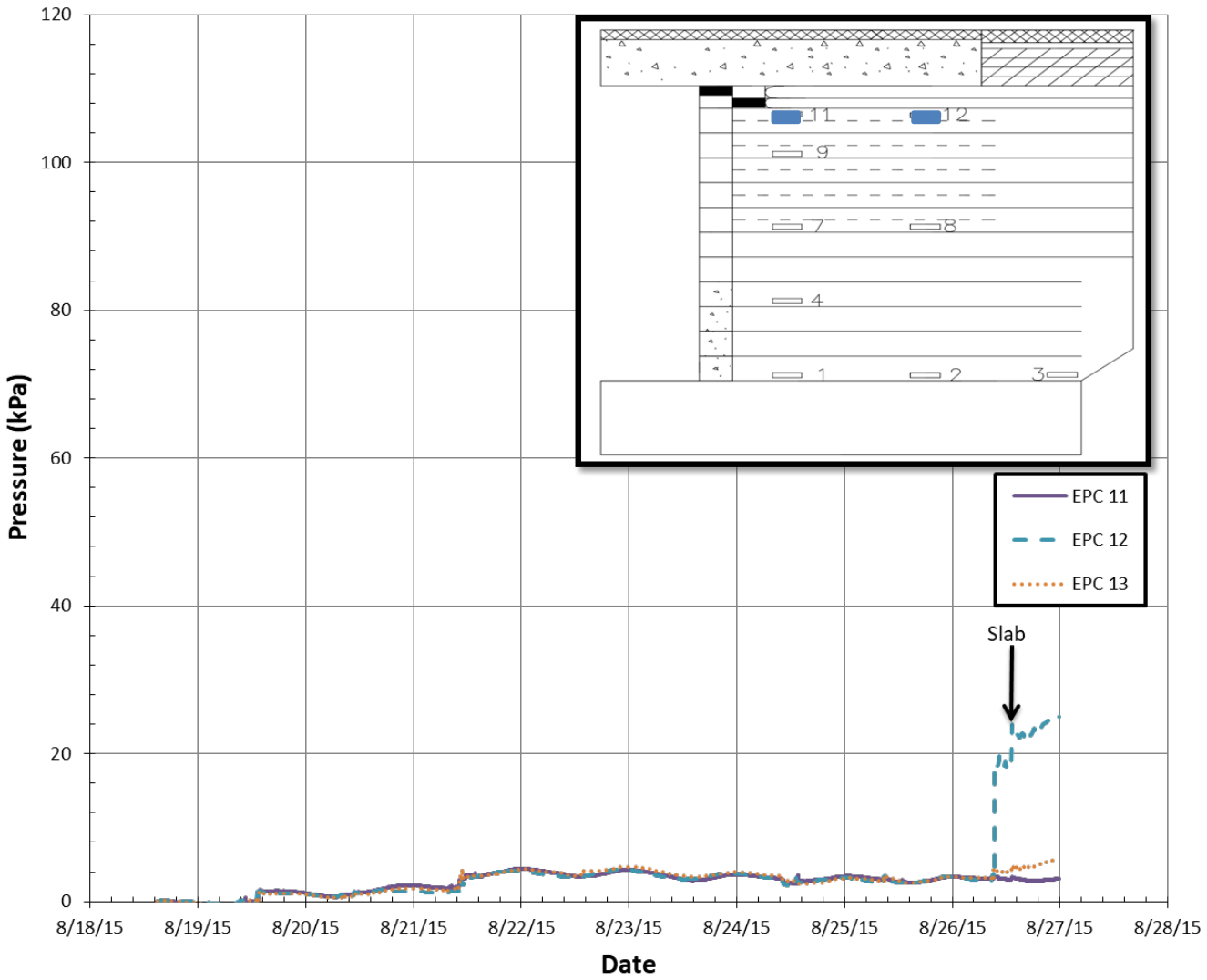

Fig. 6.3.14: Vertical stresses developed in Layer 16 on Abutment B (EPC 13 is located on the South side - see Fig. 6.2.1)

2:1 method: This method differs from the AASHTO 2:1 method by not considering the effect of the wall facing on stress distribution. In this method, the stress from the surcharge load is assumed to be distributed with a 2 to 1 slope and the stress distribution is estimated as:

$$\Delta\sigma = q/D \quad \text{(Equation 6.3.5)}$$

$$D = (b - 2e) + Z \quad \text{(Equation 6.3.6)}$$

where: *q* is load per linear feet of strip footing,
D is effective width of applied load at any depth,
Z is depth of stress point below footing,
b is width of applied load, and
e is eccentricity of footing load.

Boussinesq method: This method is used by FHWA (2018) to calculate stress distribution from the surcharge load with the following expression:

$$\Delta\sigma = (q/\pi) * (\alpha + sin(\alpha)cos(\alpha + 2\beta)) \quad \text{(Equation 6.3.7)}$$

where: *q* is surcharge pressure, and
α and *β* are inclination angles for point interest located at horizontal distance (*x*) from the centerline of the strip footing and depth (*Z*) from width of beam seat where the bridge surcharge is applied.

The data presented in Figures 6.3.15 and 6.3.1.16 was from the pressure cells located in the middle, north, and south sides of Abutments A and B as shown in Figures 6.2.1 and 6.2.2. When the vertical stresses measured in the field after the placement of the slab in the abutments are compared, the data from the middle section of the Abutment A shows a higher stress value on a layer at a close distance from the location of slab load and then decreases with depth. However, data points from EPCs installed in on a layer at a close distance from the location of slab of north and south sides provided lower stresses than what was observed from the top of the middle section. This is believed to be due to a gap that may have developed between some of the slab segments and the top of the reinforced aggregate within the abutment as can be seen from Figure 6.3.2b.

The data from the middle part of the abutment B also shows a similar trend as seen at the top of the abutment A from north and south sides. As in the abutment A, this is also believed to be due to the gap underneath the placed slab and the top of the reinforced aggregate (see **Figure 6.3.2b**). However, with depth, the measured stress distribution matches well with the stress distributions calculated based on theoretical approaches (Figure 6.3.16). Additionally, the foam placed below the super-structure (behind the facing blocks) may have contributed to the reduction of stresses at top sections of the abutment B.

Overall, EPC instruments were found to adequately capture the stress distribution but due to the gaps underneath the slab, some of the data should not be considered for the comparison of stress distribution in Abutments A and B. With this information kept in mind, comparison of field data from Abutments A and B shows that the width of the beam seat has an effect on the stress

distribution within the GRS-IBS. The wider the beam seat the lower the stress measurement within the abutment. In this study, the beam seat width of one abutment was twice the other abutment and the difference in measured stress at the same locations was in the order of 2 (closer to the top) to 1.3 (deeper in the abutment) times.

In addition to the comparison of the vertical stress distributions from Abutments A and B in terms of the effect of beam seat width on stress distribution, vertical stresses distribution observed in the field was compared against the stress distribution estimated based on theoretical calculations. This comparison also shows the effect of the beam seat width. The theoretical calculations show that the difference in stress magnitudes as a result of change of beam seat width is in between the order of 1.5 to 2 close to the top of the abutment. As expected, these differences get smaller with depth as the magnitude of distributed stress is reduced at a higher depth. The theoretical stress distribution methods considered in this study show similar trends. However, when their magnitudes of stress are compared with the field data, the Boussinesq method appears to provide stress magnitudes that were closer to the field data than the AASHTO 2:1 method. As it can be seen in Figures 6.3.15 and 6.3.16, at higher depth the stress distribution from the field was reasonably in agreement with the theoretical distribution methods. However, in the top sections of the abutment, the stresses measured in the field were lower than stresses calculated using the theoretical methods. This is due to the gap underneath the slab segments and the top of the reinforced aggregate (Fig. 6.3.2b). The gap was created during slab installation operation as a result of dimension variations. Although, these variations were within the accepted construction tolerances, it clearly had an effect on the vertical stress distribution transferred over installed EPCs. The earth pressure cells installed on top sections of the abutment were experiencing a reduced load because some of the slab segments were not in full-contact with the abutment close to the facing. In all cases, the AASHTO 2:1 method appears to be over predicting the field measurements by 10 to 20%. The differences between AASHTO 2:1 and Boussinesq method were found to increase with depth. Overall, vertical stress distribution predicted by the theoretical stress distribution methods were in agreement with stress distribution observed from the middle section of the abutment in the field.

Horizontal (lateral) stresses developed from self-weight of backfill and bridge slab during construction, as recorded from the five RPCs installed in abutment A, are shown in Figures 6.3.17 to 6.3.21. The figures also show the response of the instruments to stage loading, the analyses of that data is discussed in Section 6.3.1.2.

The stress distribution profile obtained from the field at the end of the construction (right before the placement of the slab – August 26, 2015) is compared with the theoretical active and at-rest earth pressure distributions that are calculated using the properties of the backfill based on the following formula as provided by AASHTO:

$$\sigma_H = K\,((\gamma\, x\, Z) + \Delta\sigma_V \qquad \text{(Equation 6.3.8)}$$

where, σ_H is the lateral earth pressure, γ is the unit weight of the backfill material, Z is the depth at a given stress point, and σ_V is the vertical stress distributed from slab load.

The earth pressure coefficient, *K*, which is a function of friction angle (ϕ) is calculated as follows:

$$K_a = tan^2(45 - \frac{\phi}{2}) \quad \text{(Equation 6.3.9)}$$

$$K_o = 1 - sin\phi \quad \text{(Equation 6.3.10)}$$

where K_a is active lateral earth pressure coefficient (Rankine's theory for a wall with no sloping backfill) and K_o is the at-rest lateral earth pressure coefficient (Jaky, 1944).

Additionally, lateral earth pressure distribution was calculated based on a theoretical concept referred to as bin pressure, where the pressure is assumed to increase within a given layer and becomes zero at the next reinforcement layer (Wu et al., 2001 and Adams et al., 2011). The lateral earth pressure predicted using this method is assumed to be a function of reinforcement spacing (S_v), not a function of height of the abutment (*H*). The pressure is calculated using Equation 6.3.7, however instead of *H*, the computations are made with S_v. The friction angle (φ) used in the calculations was obtained from the triaxial test of actual AASHTO No. 8 aggregate used to construct the abutments as 47.6 degrees.

Comparison of the lateral stress distribution profile from the field at the end of construction (before the slab is placed) with the lateral stress distributions computed from the above discussed theoretical methods is shown in Figure 6.3.22. The field data used to generate the information provided in Figure 6.3.22 was obtained from the Figures 6.3.17 to 6.3.21. The lateral earth pressure values from the field instruments were selected based on the one-day average of recorded data prior to placement of the slab (August 26, 2015). A close look at the general trend shown in Figure 6.3.22 show that the data from RPC 3 is higher than the data from the other RPCs. This is believed to be due to the end result of a stage loading (SL 6) that this instrument has experienced. A close look at Figure 6.3.19 shows the response of this instrument to the stage loading that was placed 4 inches above the location of this instrument and the applied load was considered as "high load" (please see section 6.3.1.2 for further discussion on stage load testing). This resulted in a higher lateral stress condition in this instrument compared to the other RPCs located within the GRS-IBS (Figures 6.3.17 thru 6.3.21). Despite this fact, a fitted linear regression line (black line shown in Figure 6.3.22) shows a relatively uniform distribution of stresses within the GRS-IBS with depth. This trend appears to be similar to the stress distribution estimated based on Wu's method but with much higher magnitudes. When the magnitudes of each lateral stress points shown in Figure 6.3.22 are compared with the stress distributions computed based on earth pressure theories. The results show that the lateral stress distribution obtained in the field under self-weight conditions is follows a reasonably uniform trend, although the total magnitude is similar to those that defined using the at-rest lateral earth pressure coefficient in the bearing bed zone of the abutment.

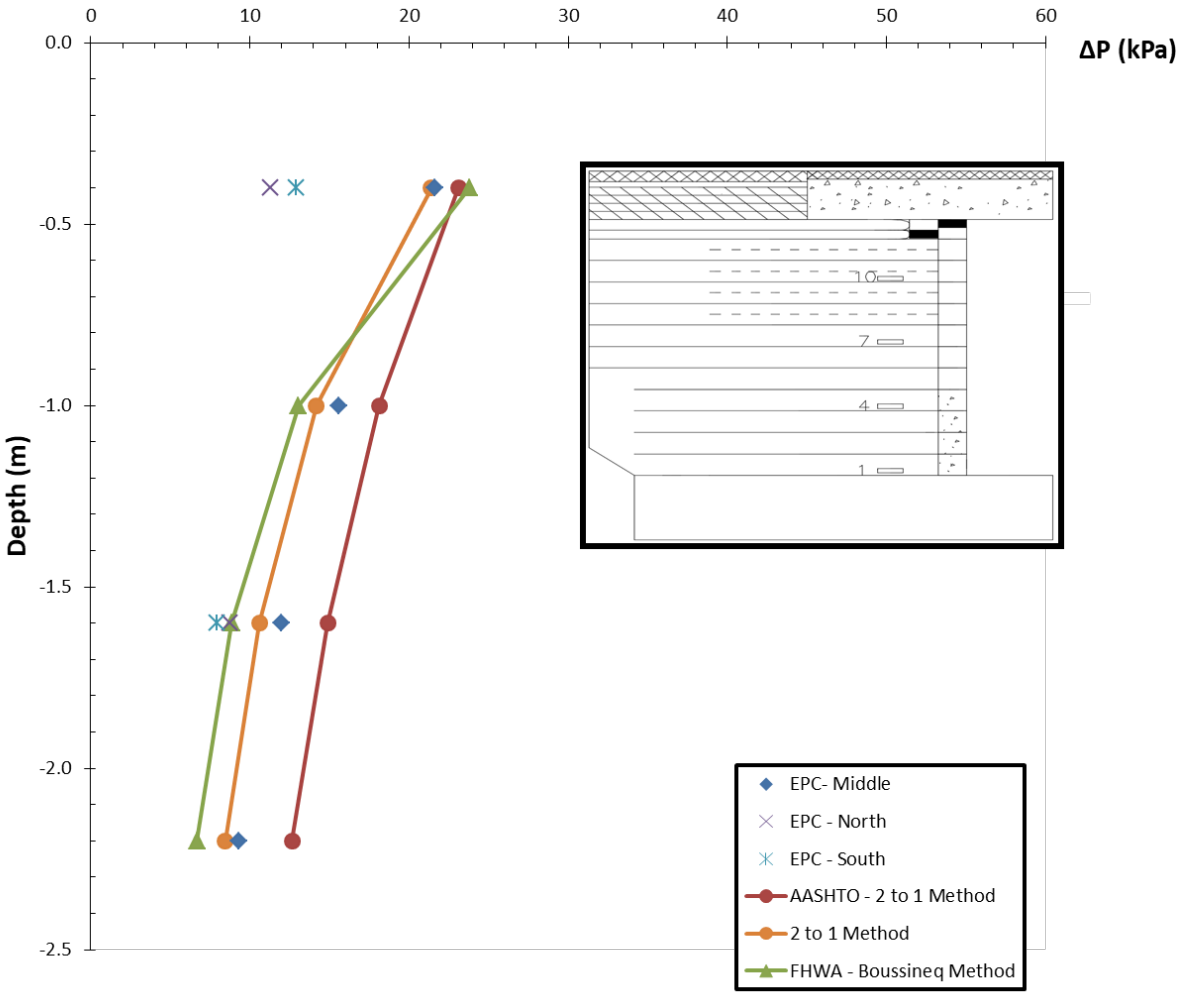

Fig. 6.3.15: Vertical stress distribution due to bridge slab load in Abutment A (both from field measurements and theoretical estimations)

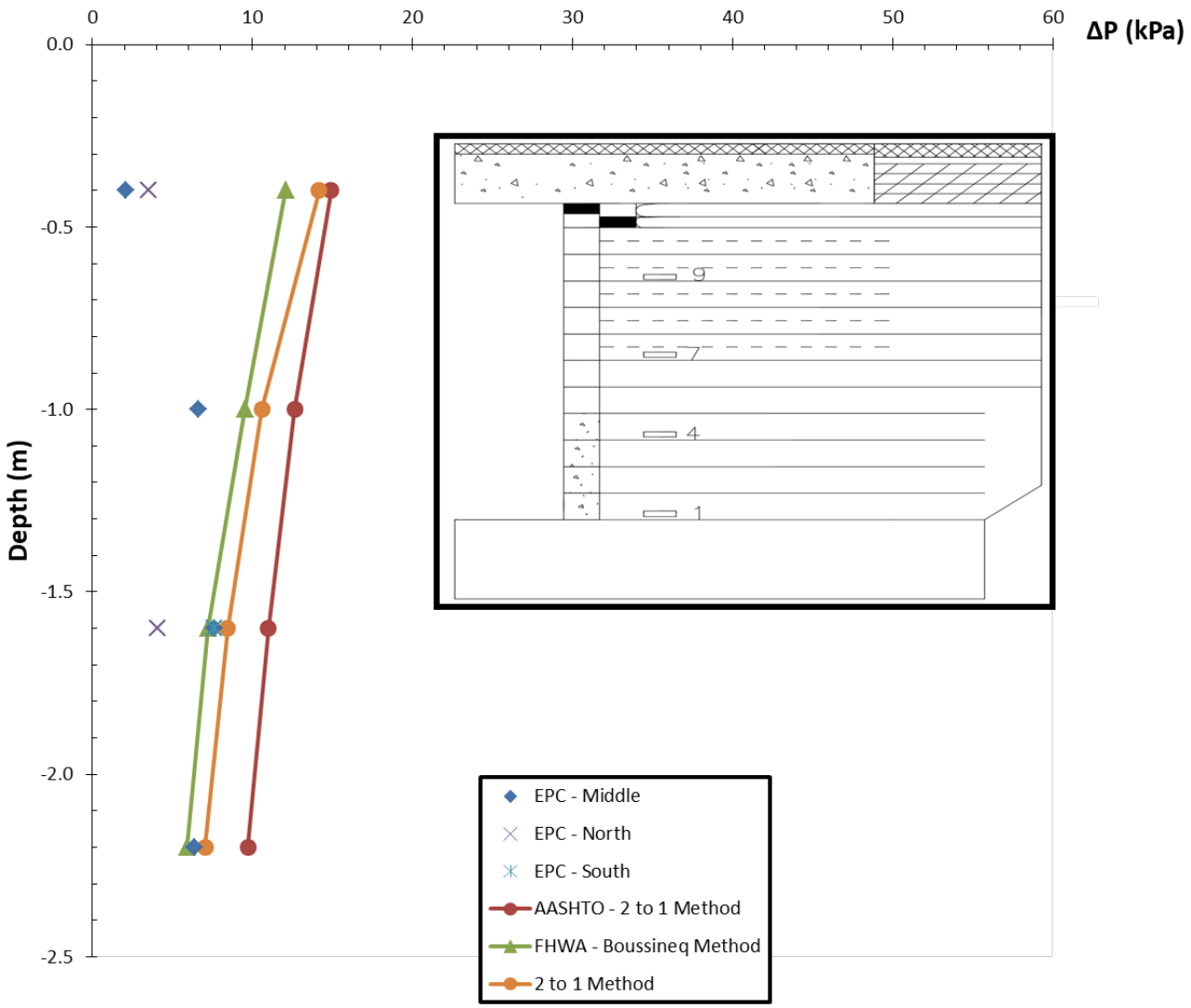

Fig. 6.3.16: Vertical stress distribution due to bridge slab load in Abutment B (both from field measurements and theoretical estimations)

Comparison of the lateral stress distribution profile for combined self-weight and bridge slab loading with the lateral stress distributions computed from the theoretical methods is shown in Figure 6.3.23. Figure 6.3.23 was created based on the data shown in Figures 6.3.17 to 6.3.21 at locations noted as "slab". The lateral earth pressures for this loading condition were predicted by using the formula in Equation 6.3.8. The vertical stress distributed from the slab load ($\Delta\sigma_V$) was calculated using the AASHTO 2:1 method (Equation 6.3.1) and it was calculated in all layers where the lateral stresses were measured in the field. The magnitude of the slab load was 42 kPa (6.1 psi) and the vertical stresses distributed from the slab at depths where RPC 5, 4, 3, 2, and 1 were located were 31.8, 28.9, 26.6, 13.3, and 12.3 kPa (4.6, 4.2, 3.9, 1.9 and 1.8 psi), respectively. The data from Figure 6.3.23 shows that with the placement of slab, the lateral stress distribution in the field became closer to the active condition (just as was the case without the bridge slab, the actual magnitude from the field in general, is less than the estimated active earth pressures).

Unfortunately, Load cells installed at the site only operated for a very short time. The first load cell functioned for one and half months and the second one only functioned for one week after installation. The result obtained from the first load cell is shown in Figure 6.3.24. The data shows the response of the load cell during construction and right after the placement of slab. The magnitude of the vertical force obtained from the load cell is less than the total weight CMU blocks in all layers. Therefore, although there was a trend, the magnitude of the data makes the vertical force measurement in the field using these load cells not successful.

Geotextile strains were measured from SGs installed within the geotextiles placed at five reinforcement layers in Abutment A. Although forty-four strain gages were installed as part of the field instrumentation program, only 24 of them ended up working. The data from all operational strain gages are presented in this report. The strain gages were installed only right behind the facing and 0.9 m (3 ft) from the facing blocks. Specifically, data obtained from the SGs located right behind the facing blocks of the abutment are shown on Figures 6.3.25 to 6.3.29. Data obtained from SGs located 0.9 m (3 ft) from the facing are shown on Figure 6.3.30. As with the stress distribution data, these figures also show the response of the gages during stage loading. Discussion and interpretation of this field data is provided in Section 6.3.1.2.

Data from Figures 6.3.25 shows that in Layer 2 the highest strains (~0.15%) recorded from SGs installed right behind the facing were obtained from the middle section of the abutment. The strains measured from the north and south sides showed less strains than the middle section (~ 0.1%). The difference between the strains is attributed to the fact that the middle part of the section was exposed to stage loading. In Figure 6.3.25 the initial strain value for SG7 was zero until sometime on 8/13/15, in which the gage started to show readings. The strain data presented in the figure is based on the readings generated by the gages after they started to respond to load or experienced the load. Data from Figures 6.326 shows that the maximum strain (~0.3 %) was recorded from SG9 and SG10 that were located in the middle section of the abutment when compared to SG15 and SG16 located in south side of the abutment. The effect of stage loading in generation of locked-in strains was also pronounced in this layer. Figures 6.3.27 to 6.3.29 show that the maximum strain level recorded from SGs installed in the bearing bed zone was less than 0.2%. The strain levels in bearing bed zone were comparatively smaller than the strain levels in

the primary reinforcement zone. This may occur due to closely spaced reinforcement in this zone reducing the lateral deformations and/or SGs in this zone were not subjected to stage loading as much as SGs in the primary reinforcement zone. When all of the strains from all strain gages located right behind the facing blocks in the middle, north and south sections of the abutment are compared, it appears that the strains from both bearing bed and primary reinforcement zones are generally comparable with few exceptions where the strain gages recorded slightly higher strains from the primary reinforcement zone. In all cases, the maximum strains obtained from the field (~0.3%) was significantly below the maximum allowed geosynthetic strains in design of abutments reinforced with geosynthetics (2%) (Adams et al., 2011).

Unfortunately, among the strain gages that were placed 0.9 m (3 ft) from the facing, only SG33 and SG34 survived after construction. These strain gages are located in layer 14 and unfortunately all other strain gages installed at that layer did not work. Therefore, it is not possible to compare this data with the strain gages located closer to the facing, although it would be expected that the strains would decrease farther away from the facing. The strains recorded from these strain gages (~0.13%) were also significantly below the maximum allowed threshold by the design.

The purpose of the instrumentation program was to specifically focus on the strain measurements right behind the facing and compare these values with strains obtained 0.9 m (3 ft) from the facing. Therefore, the instrumentation program did not include the installation of strain gages along the entire length of the reinforcement layers. As a result, the locus of maximum strain cannot be estimated at this particular site.

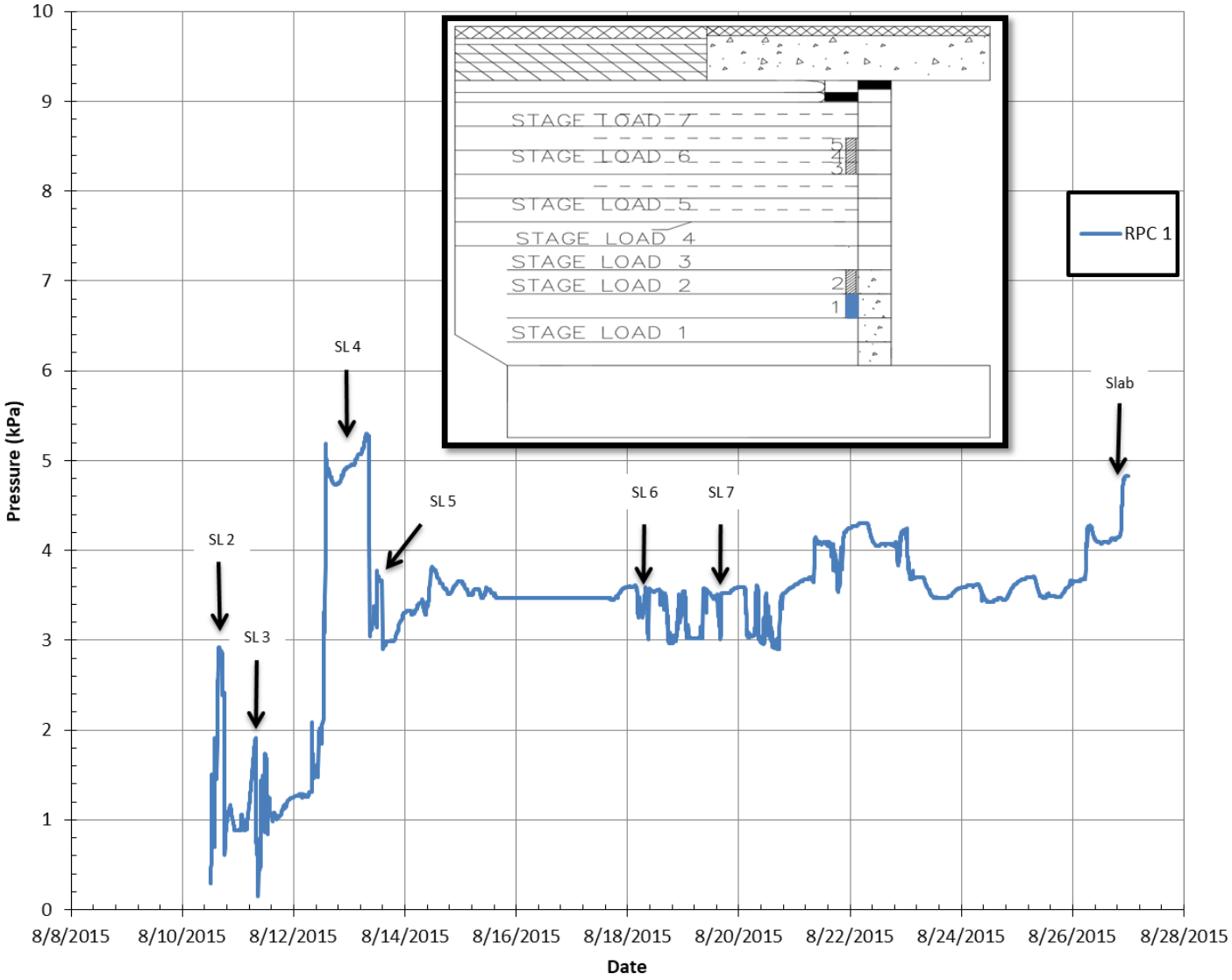

Fig. 6.3.17: Lateral stresses developed behind the facing blocks in Layer 3 as recorded by RPC 1

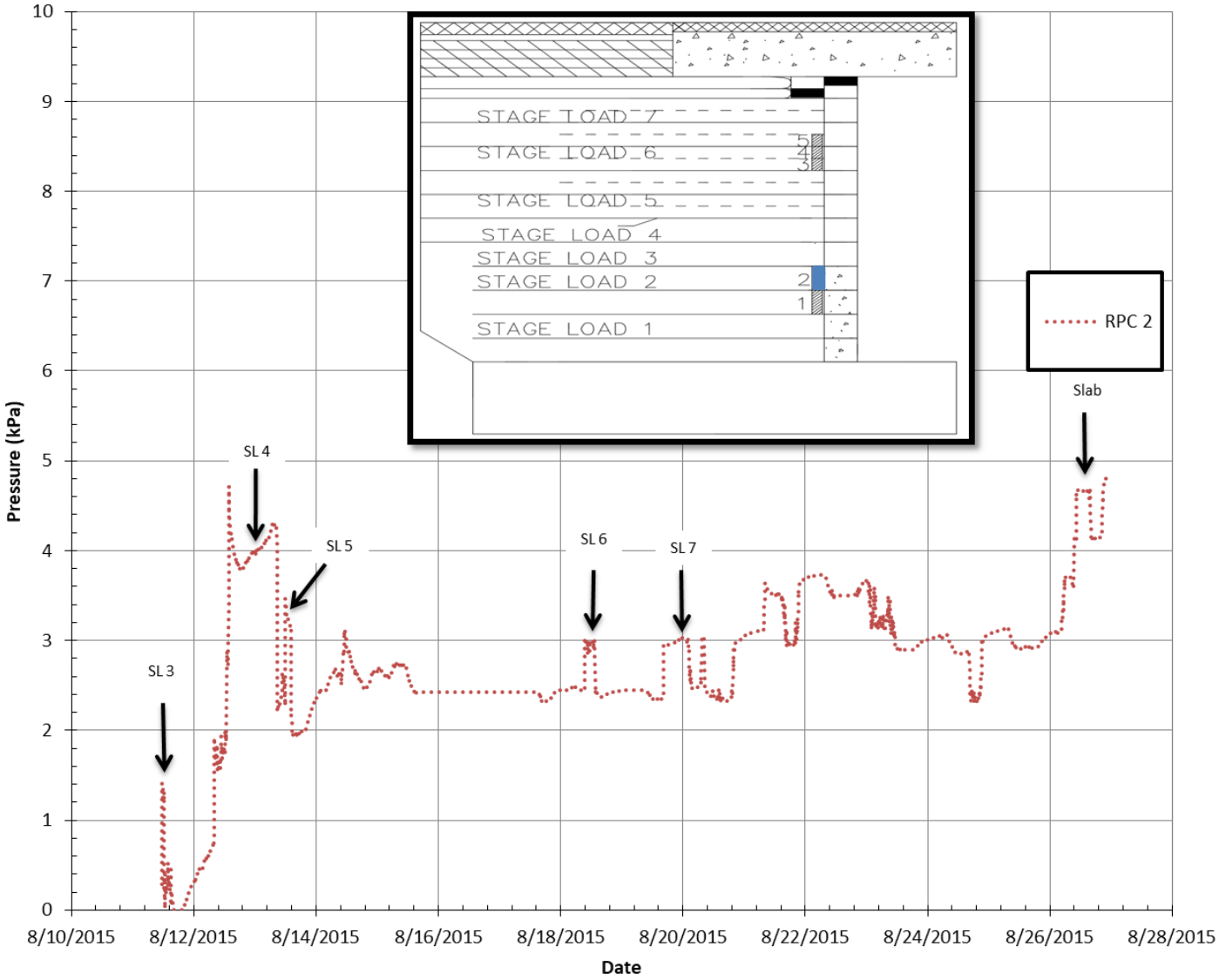

Fig. 6.3.18: Lateral stresses developed behind the facing blocks in Layer 4 as recorded by RPC 2

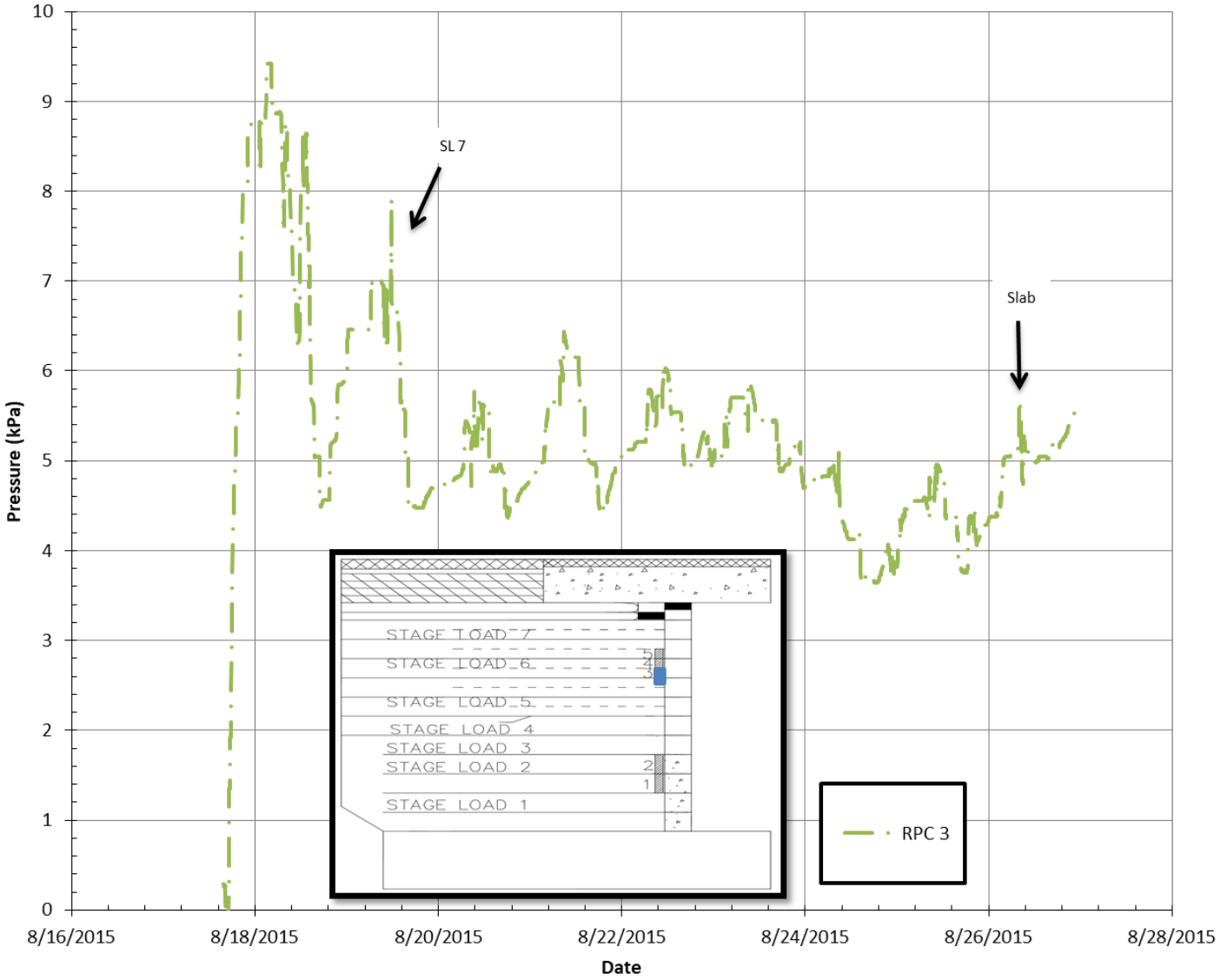

Fig. 6.3.19: Lateral stresses developed behind the facing blocks in Layer 11 as recorded by RPC 3

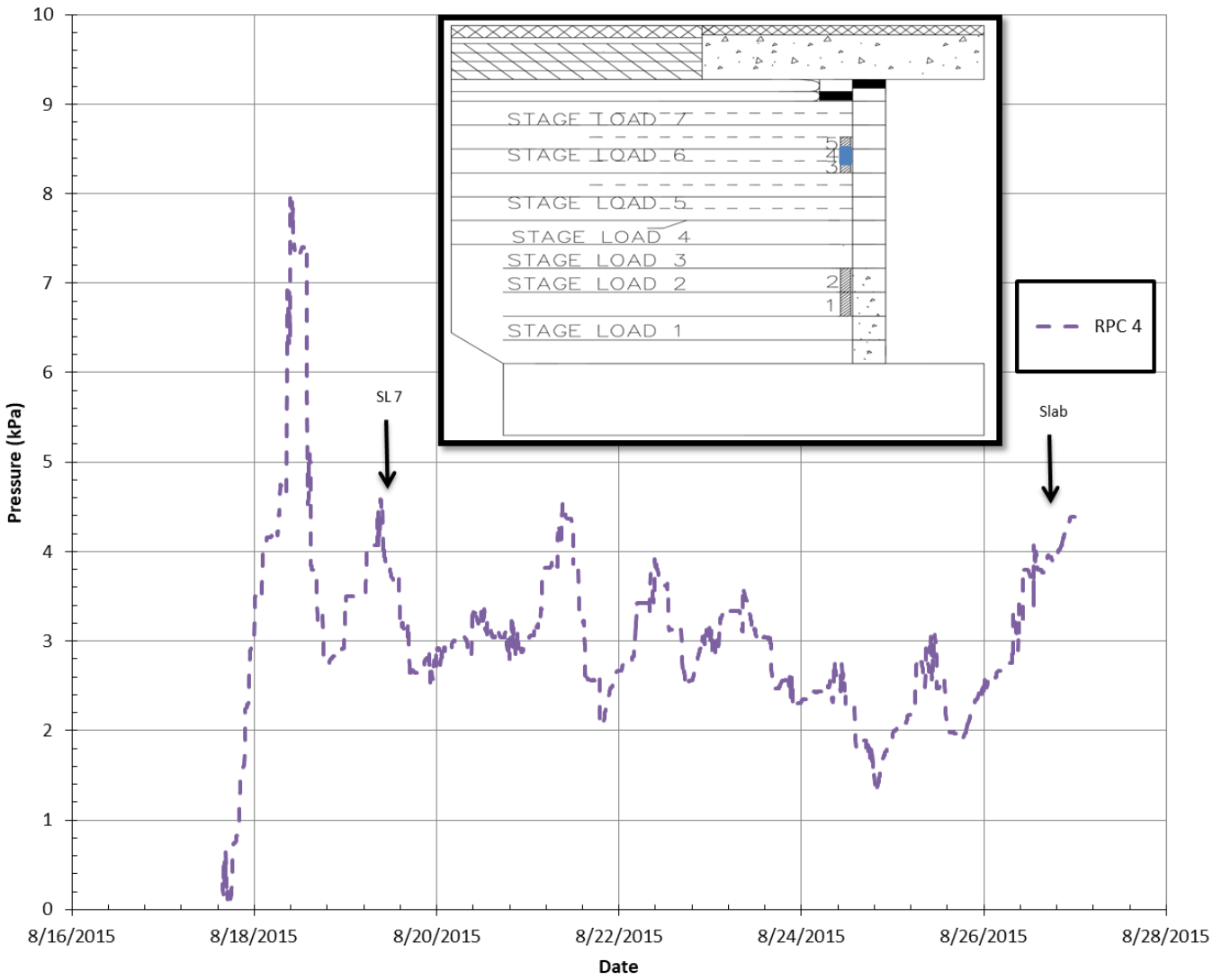

Fig. 6.3.20: Lateral stresses developed behind the facing blocks in Layer 12 as recorded by RPC 4

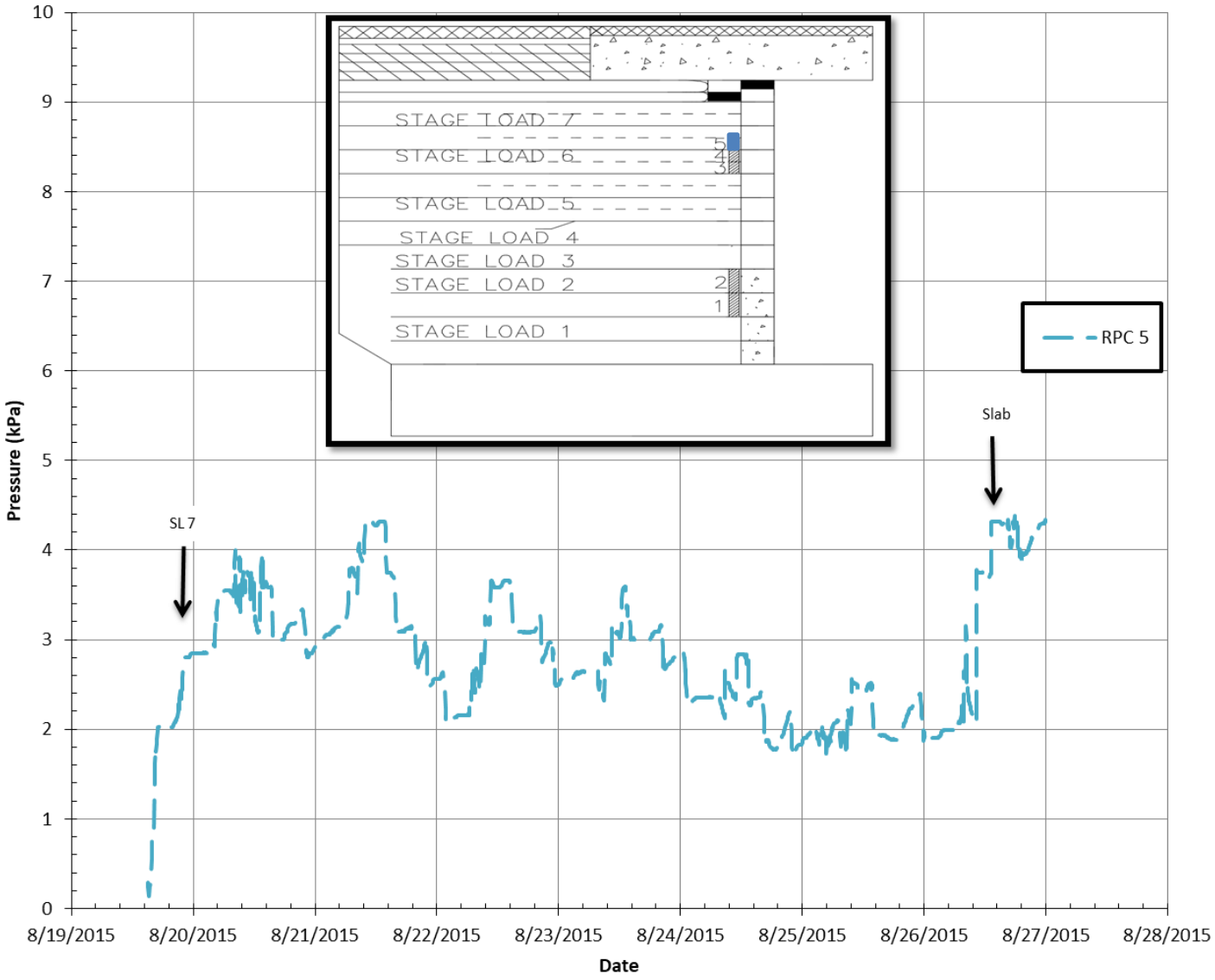

Fig. 6.3.21: Lateral stresses developed behind the facing blocks in Layer 13 as recorded by RPC 5

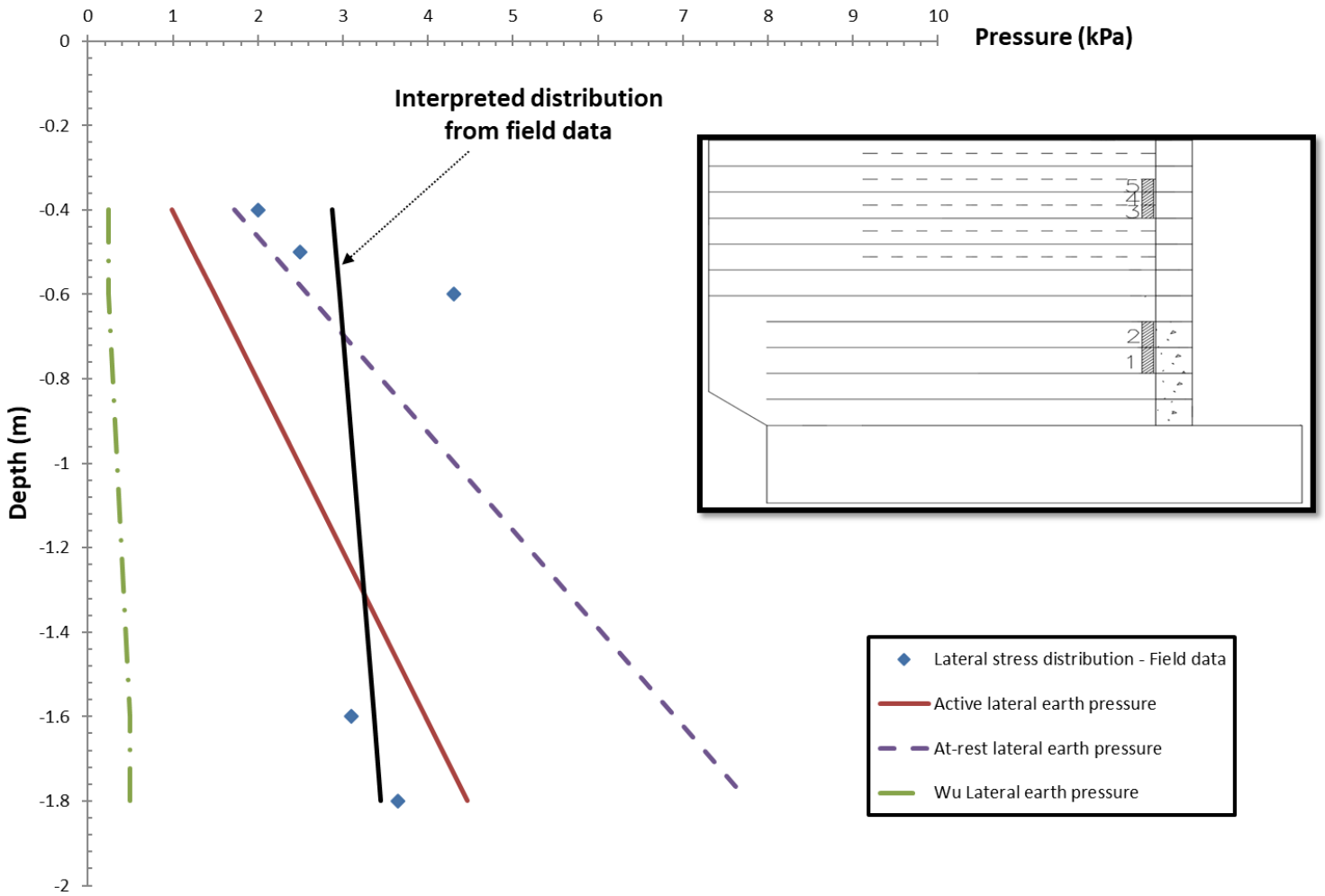

Fig. 6.3.22: Lateral stress distribution due to self-weight of backfill load at the end of construction (before the slab is placed)

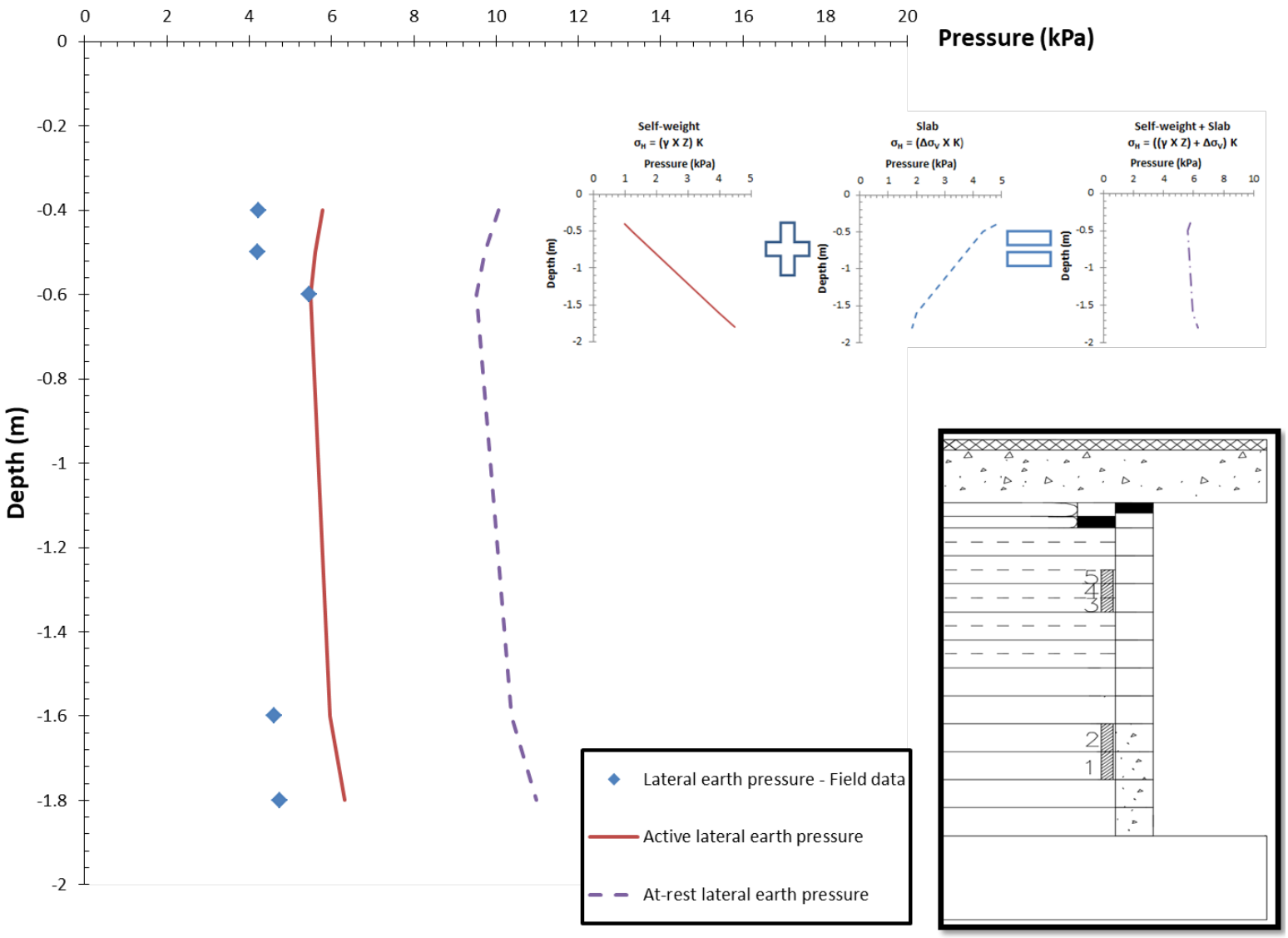

Fig. 6.3.23: Cumulative lateral stress distribution due to self-weight of backfill and slab load

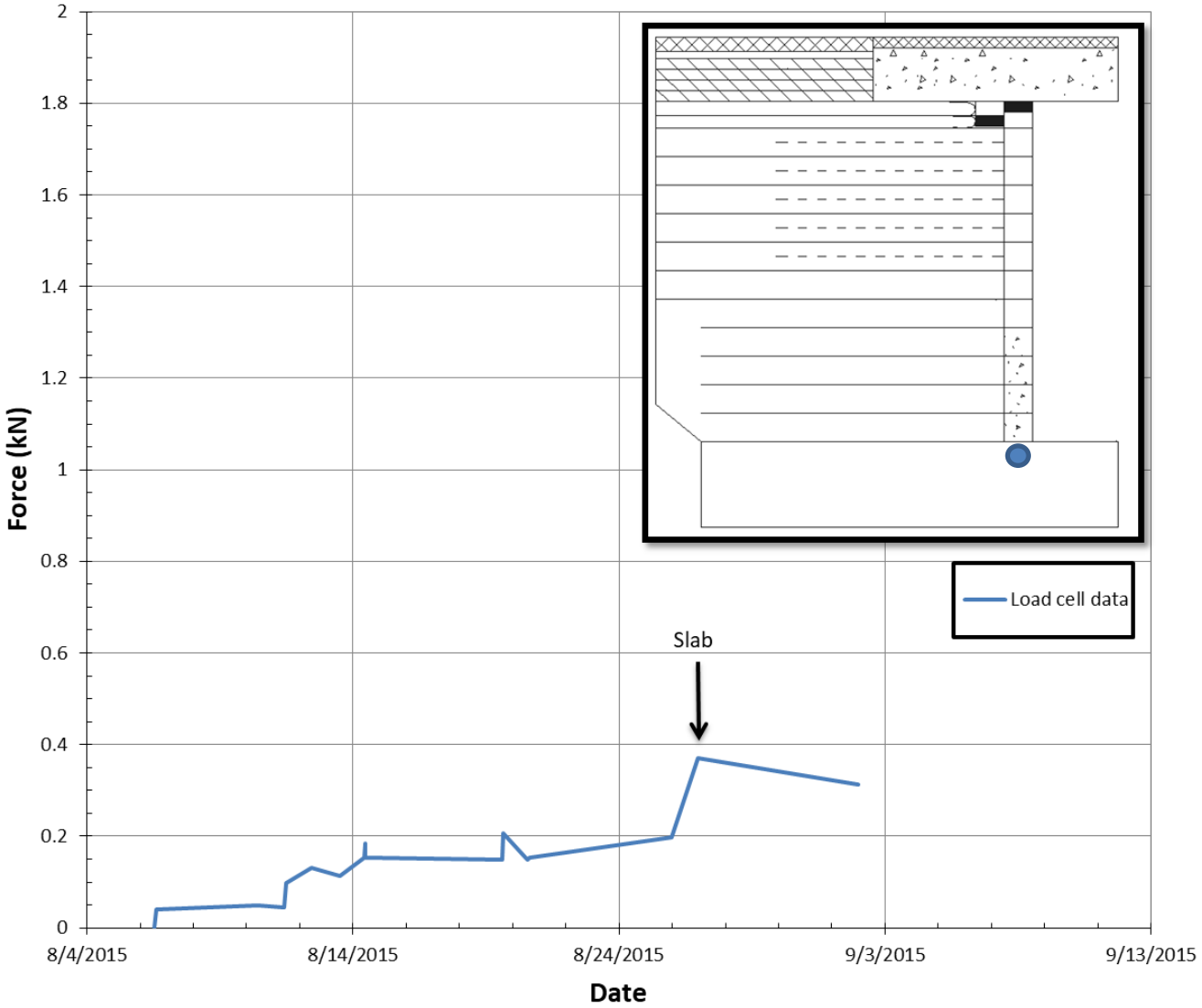

Fig. 6.3.24: Vertical force measurements below facing blocks

Wire line extensometers were used to interpret the lateral geotextile displacements. The data obtained from four different reinforcement layers in Abutment A are shown in Figures 6.3.31 to Figure 6.3.34. While data shown in these figures included the response of the WLEs during stage loading, details of those results are provided in Section 6.3.1.2. The maximum observed lateral displacement was 3 mm (0.12 in). And attempt was made to convert the displacements measured from the field into global strains by evaluating the differences in measured lateral displacements (*Δs*) and the horizontal distance between WLEs (*L*) between the zone of 0.3 m (1 ft) and 0.9 m (3 ft). Table 6.32 shows calculation of strains from geotextile and backfill lateral displacements occurred due to self-weight and combined self-weight and slab loading. Based on this conversion, the maximum lateral strains obtained in the field from WLE data was less than 0.07%, which was significantly below FHWA's design geosynthetic strain level of 2%.

Table 6.3.2. Calculation of global strains from geotextile displacements due to self-weight loading from wire line extensometer data

WLE	SW	SW + SL	SW	SW + SL	L (mm)	SW	SW + SL
	s (mm)	s (mm)	Δs (mm)	Δs (mm)		ε (Δs/L)(%)	ε (Δs/L)(%)
1	0.30	0.28	0.15	0.154	600	0.03	0.03
2	0.45	0.43					
3	1.76	1.67	0.28	0.3	600	0.05	0.05
4	2.04	1.97					
5	0.27	0.46	0.23	0.38	600	0.04	0.06
6	0.04	0.08					
17	0.14	0.14	0.03	0.03	600	0.01	0.01
18	0.11	0.11					

Note: WLE is designation of the wire line extensometers. *s* is displacement. *Δs* is change in displacement between WLEs located on the same geotextile. *L* is horizontal distance between the two wire line extensometers in a given layer. *SW* is self-weight. *SW*+*SL* is self-weight and slab load.

As shown in Table 6.3.2, the displacements in the geotextile layers mainly occurred as result of the self-weight load during construction period. Additionally, as it can be seen in Figures 6.3.31 to 6.3.34 the stage loadings appear to generate displacements in the geotextile layers. The displacements generated due to the stage loadings did not decrease after the Jersey barriers were unloaded and the displacements increased with progress of construction of the abutment. However, on a layer close to the foundation, the additional displacements generated as result of stage loadings showed a decrease when the Jersey barriers were unloaded and the displacements were mainly due to the self-weight load (Figure 6.3.31). The displacements in the geotextile layers did not show a significant change after applying the bridge slab load.

By combining all of the data from SGs, profiles showing the strain distribution with depth due to self-weight and combined self-weight slab load were created. Figure 6.3.35 shows this profile based on only self-weight of the backfill and Figure 6.3.36 shows this profile based on combined

self-weight of backfill and bridge slab load. These profiles were developed using all of the working strain gages, which included the ones installed in the middle, north, and south of the abutment. The strain data from the strain gages is shown as an average of strain obtained from SGs installed on top and bottom of a given point on the geotextile layer. For instance, strain data obtained from SG1 and SG2 was converted to an average strain value in layer 2 (located at 2 m depth) in middle section of the abutment. When evaluating this data, it should be kept in mind that due to the stage loading during construction, the strain gages in the middle might have been exposed to loading depending on their location compared to the applied load. The strain gages used in these figures are all located right behind the facing blocks and therefore only reflect the conditions at those locations. Whereas the WLE data shows the global strains between the zone of 0.3 m (1 ft) and 0.9 m (3 ft) from the back of the facing blocks. Therefore, WLE data reflect the strains farther away from the facing. When the data is evaluated based on this information, the following conclusions can be made:

- In general, strain gages reflect the effects of stage loading. At the locations where the stage loading was applied (data from the middle part of the abutment) the strains were 60 to 80% larger than the strains measured from the north and south sides of the abutment (where no stage loading was applied).
- The recorded strain values on all three sections of abutment A (north, middle and south sections) show a fairly uniform distribution of experienced strains with wall height on all reinforcement layers (Figures 6.3.35 and 6.3.36). The magnitude of the strains in the middle section are, generally, higher than the strain magnitudes in north and south sections. Since the stage loading was applied in the middle section of the abutment, it is expected that this test affected the reinforcement strains. With the application of the slab load, minute changes were observed in recorded strain values on all gages. However, these changes do not affect overall observed behavior of the reinforcement strain distribution (the uniform distribution with depth). Strains observed from WLE are lower than the strains measured from the strain gages. This information is consistent with the expected strain distribution along the length of the reinforcements.
- Overall the magnitude of the strains measured in the field was very small (in the range of 0.05 to 0.3%), which may affect the ability to establish adequate comparison among different data sources.

In design of GRS, it is assumed to be internally supported by closely spaced reinforcement, hence, the facing element is not considered as a structural component except providing frictional connection. Because of this, evaluation of connection strength criterion is not required (Adams et al. 2011). The purpose of installing the strain gages right behind the facing blocks (Figure 6.2.10) was to evaluate the load at the connection between the reinforcement and the facing blocks and investigate the existence of connection strength (T_o) that results primarily due to the lateral stresses on the facing blocks. The reinforcement strain measured by the strain gages was used to estimate the load at the connection using the modulus of geotextile reinforcement. The relationship between T_o and ε is provided by Allen and Bathurst (2001) as:

$$T_o = J \, x \, \varepsilon \qquad \text{(Equation 6.3.11)}$$

where, J is modulus of the geotextile and ε is geotextile strain.

In this study, the modulus of the geotextile at 2% strain is reported as 700 kN/m (4 kips/in) (as discussed in Section 6.1). However, it is important to note that this modulus value was determined based on ASTM D4595 where the geotextile sample is tested without being confined in between the reinforced soil. This condition may not reflect the conditions in the field.

Figure 6.3.37 shows T_o profile with depth developed using average of strains measured by strain gages located right behind the facing blocks in the middle, north, and south sections of the Abutment A. In Figure 6.3.37 the T_o profile was calculated under self-weight load only and combined self-weight and slab loads.

The T_o profile showed a small increase with depth under self-weight load, however, it shows a decrease in layers close to the foundation level. The maximum T_o, was observed in the lower half of the structure. T_o values in the top section of the abutment showed an increase with application of the slab load. However, T_o values in lower section of the abutment did not show a significant increase with application slab load. Although the magnitude of T_o showed a small increase with depth, the overall distribution trend was reasonably uniform.

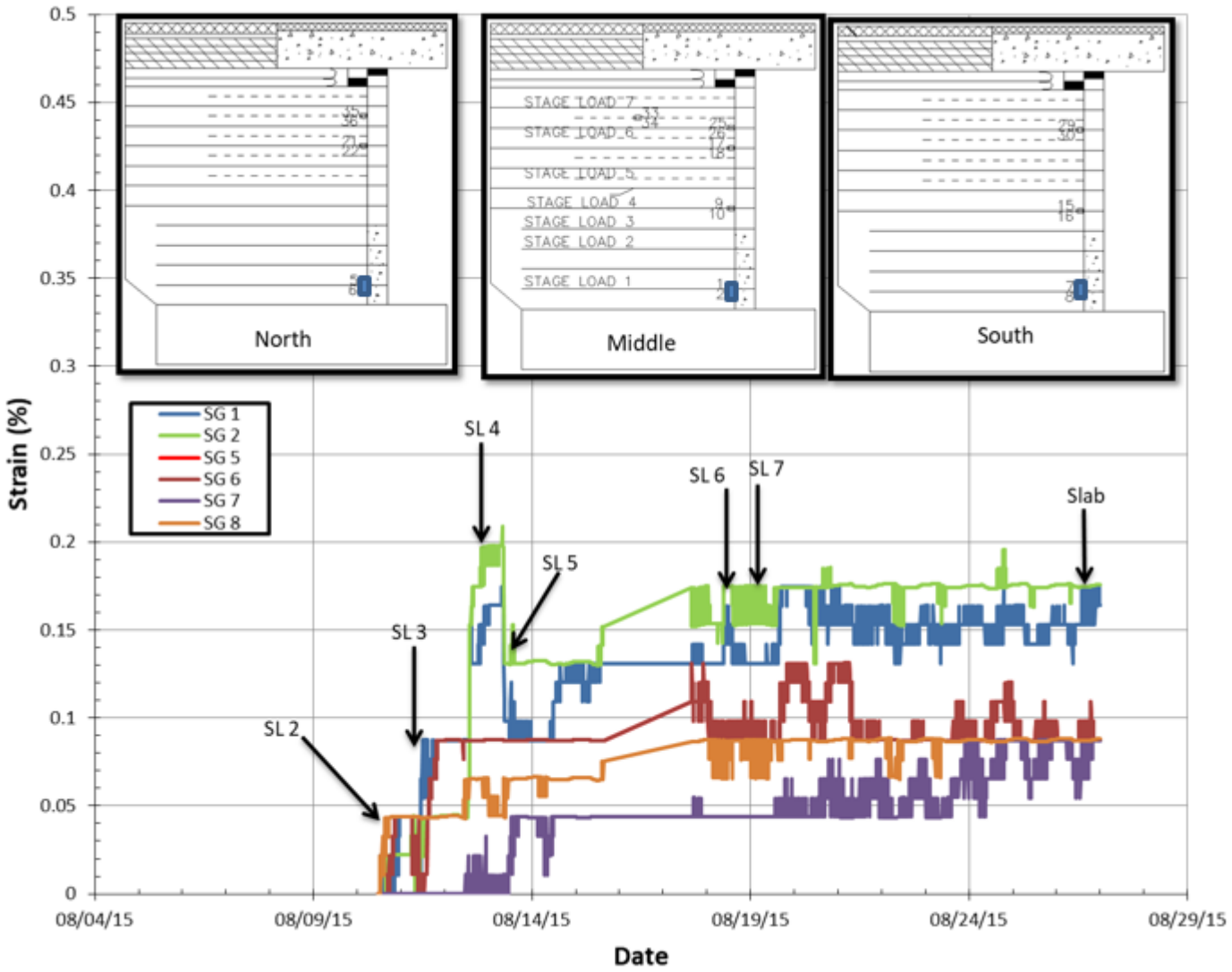

Note: SGs 5, 6, 7, and 8 are located at the same level as SGs 1 and 2 except they are on the north and south sides of the abutment respectively (see Fig. 6.2.1).

Fig. 6.3.25: Geotextile strains recorded from strain gages in Layer 2 of Abutment A

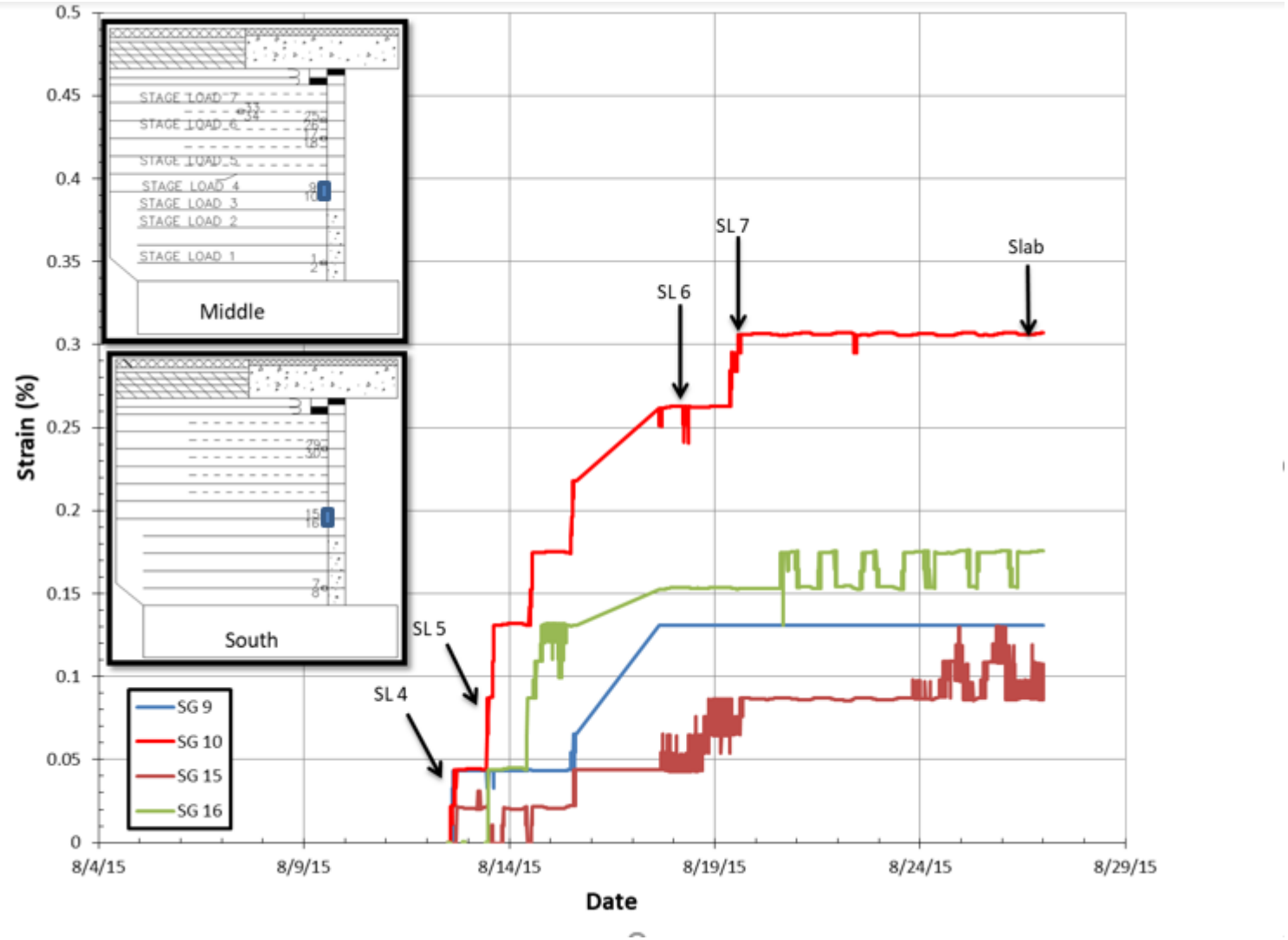

Fig. 6.3.26: Lateral geotextile strains recorded from strain gages in Layer 6 on Abutment A (SG 15 and 16 are located on south side – See Fig.6.2.1)

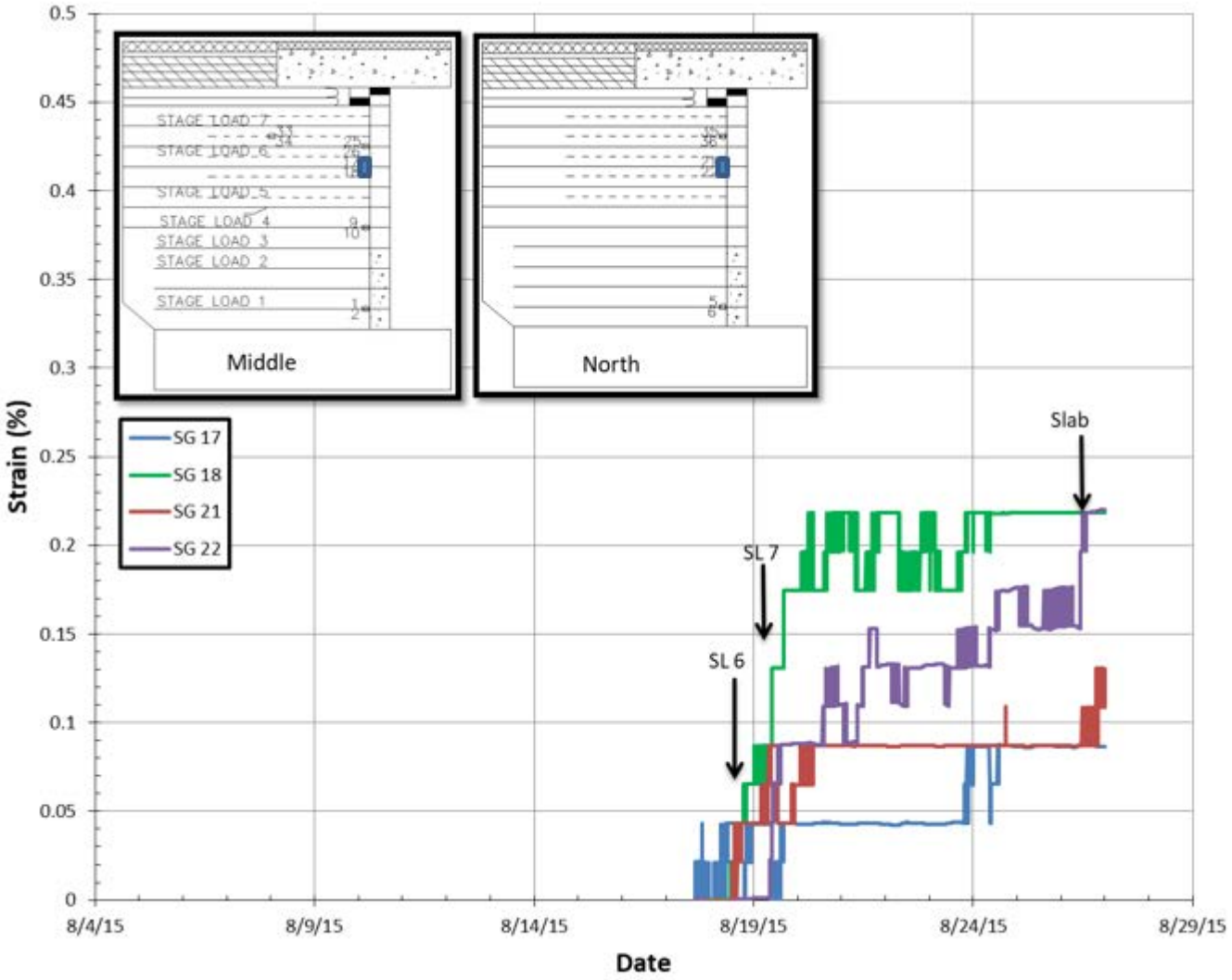

Fig. 6.3.27: Lateral geotextile strains recorded from strain gages in Layer 11 on Abutment A (SG 21 and 22 are located on north side – See Fig. 6.2.1)

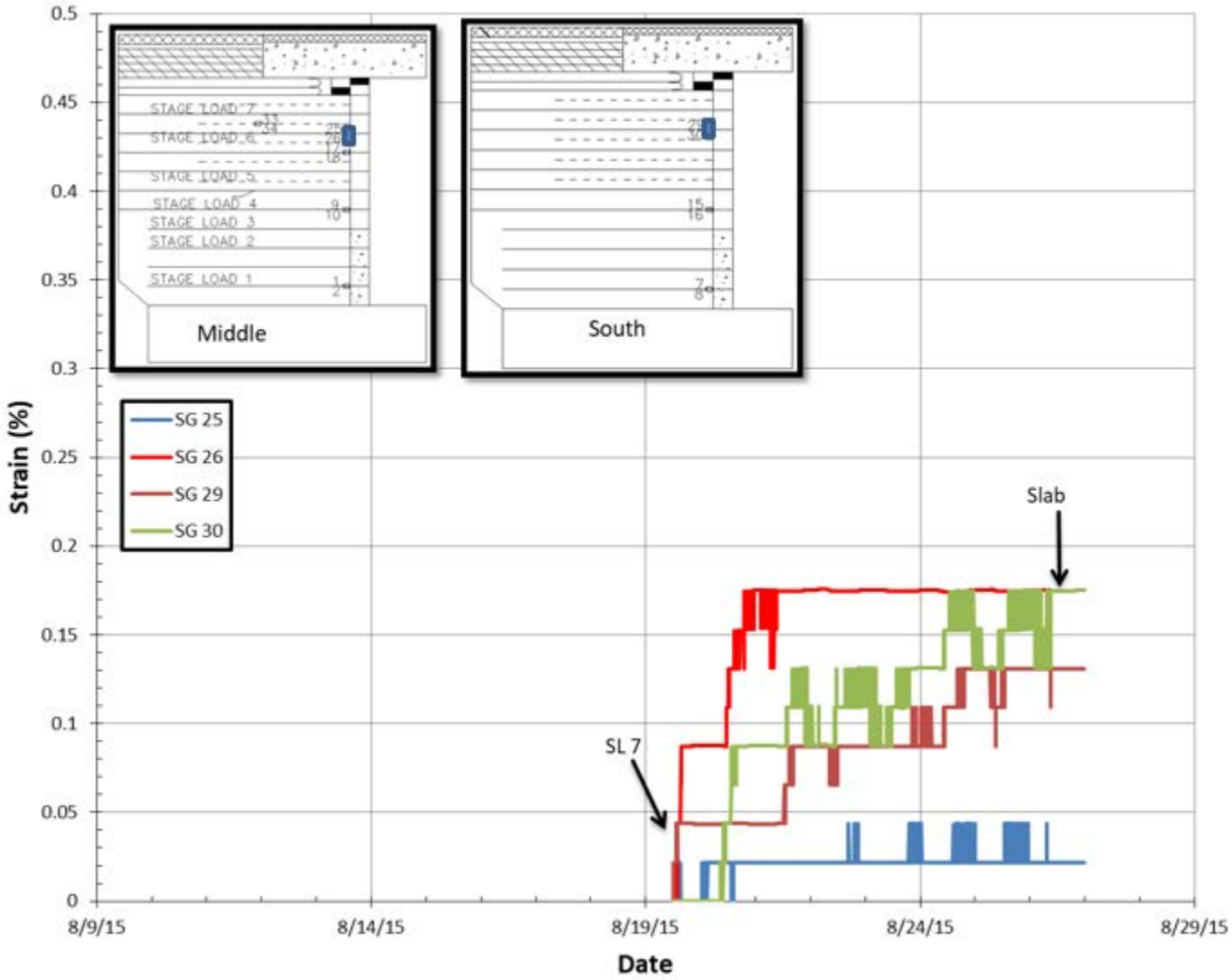

Fig. 6.3.28: Lateral geotextile strains recorded from strain gages in Layer 13 on Abutment A. (SG 29 and30 are located on south side – See Fig. 6.2.1)

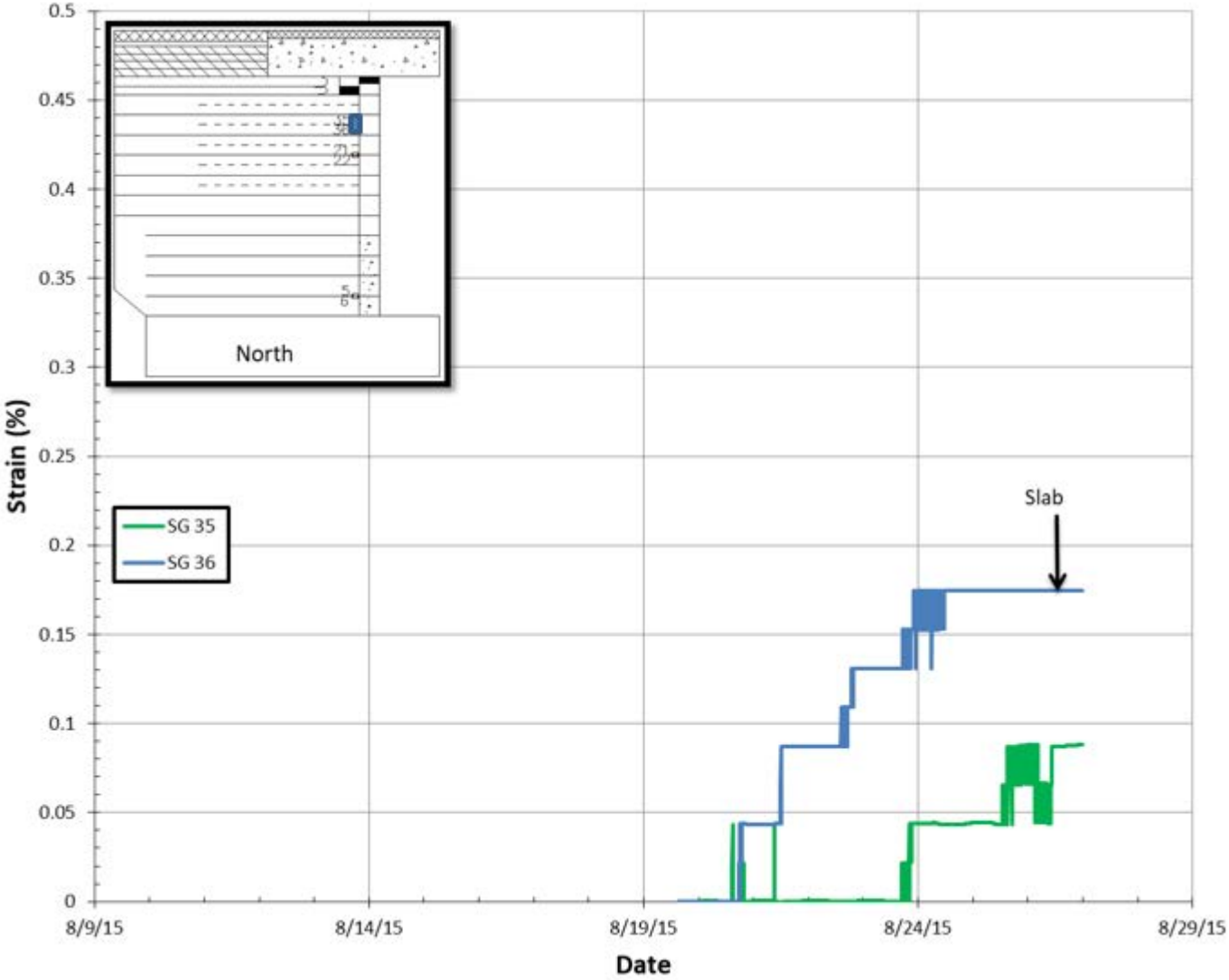

Fig. 6.3.29: Lateral geotextile strains recorded from strain gages in Layer 14 on Abutment A (SG 35 and 36 are located on north side – See Fig. 6.2.1)

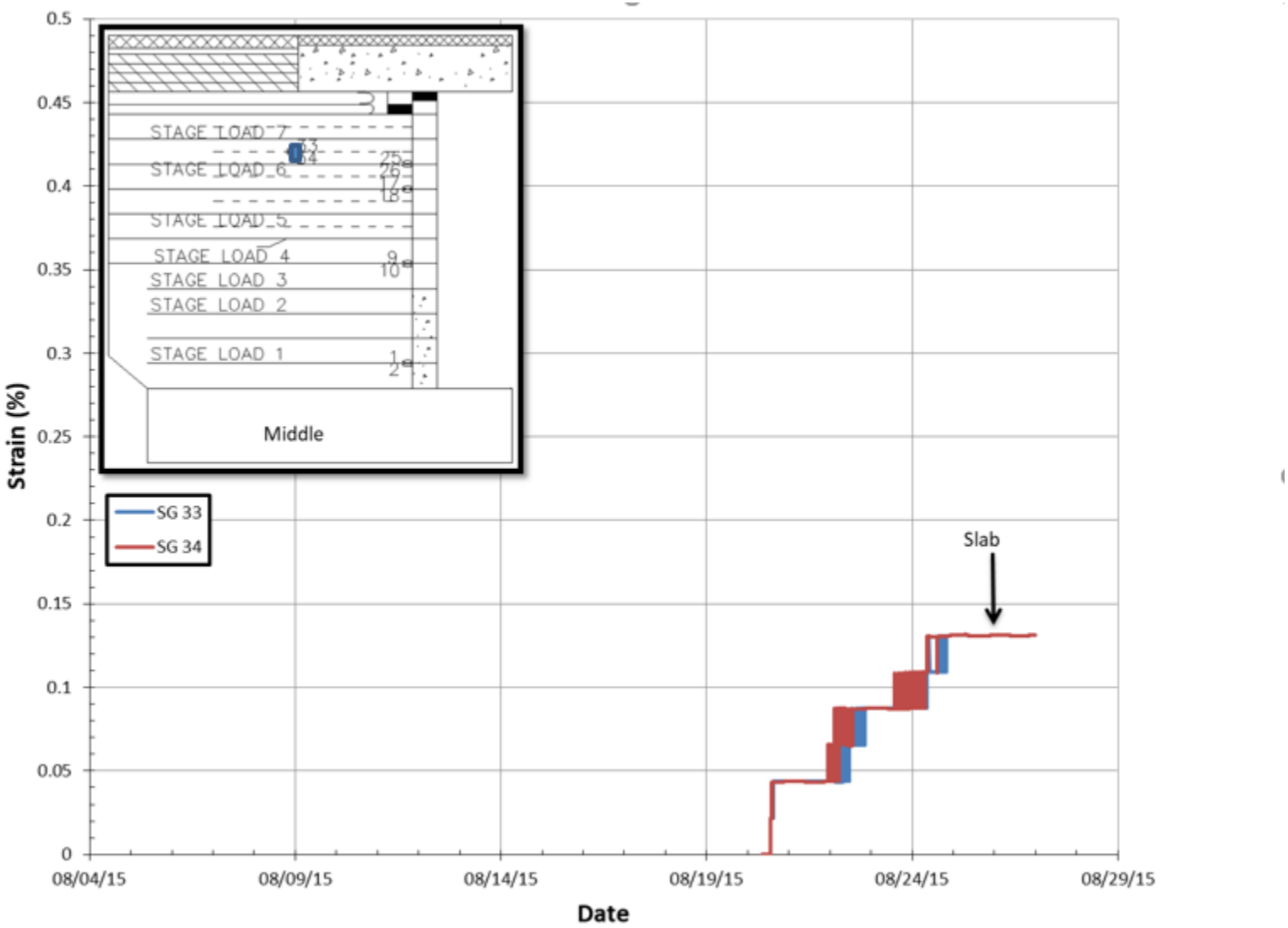

Fig. 6.3.30: Lateral geotextile strains recorded from strain gages in Layer 14 on Abutment A

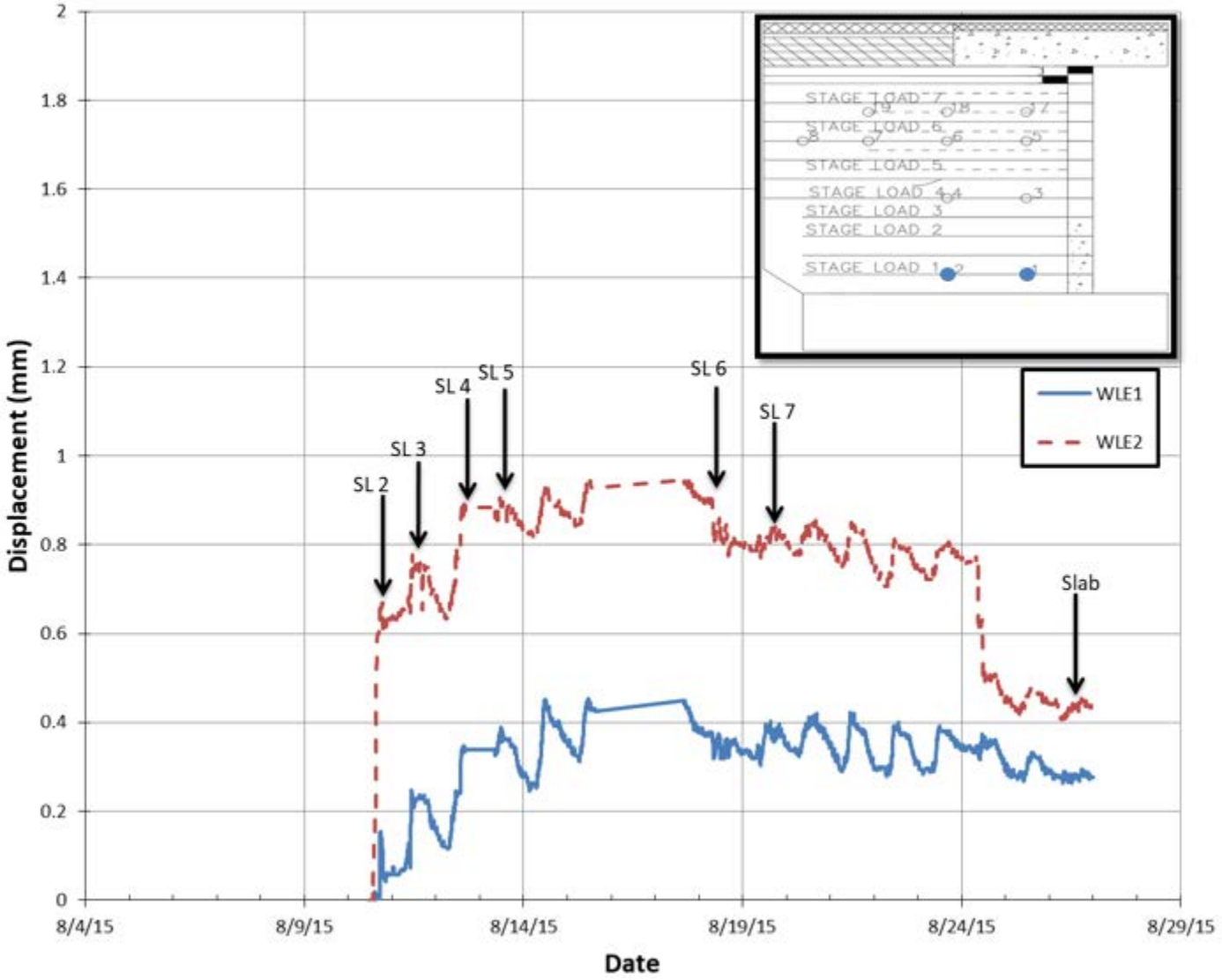

Fig. 6.3.31: Lateral geotextile displacements recorded from WLEs in Layer 2 on Abutment A

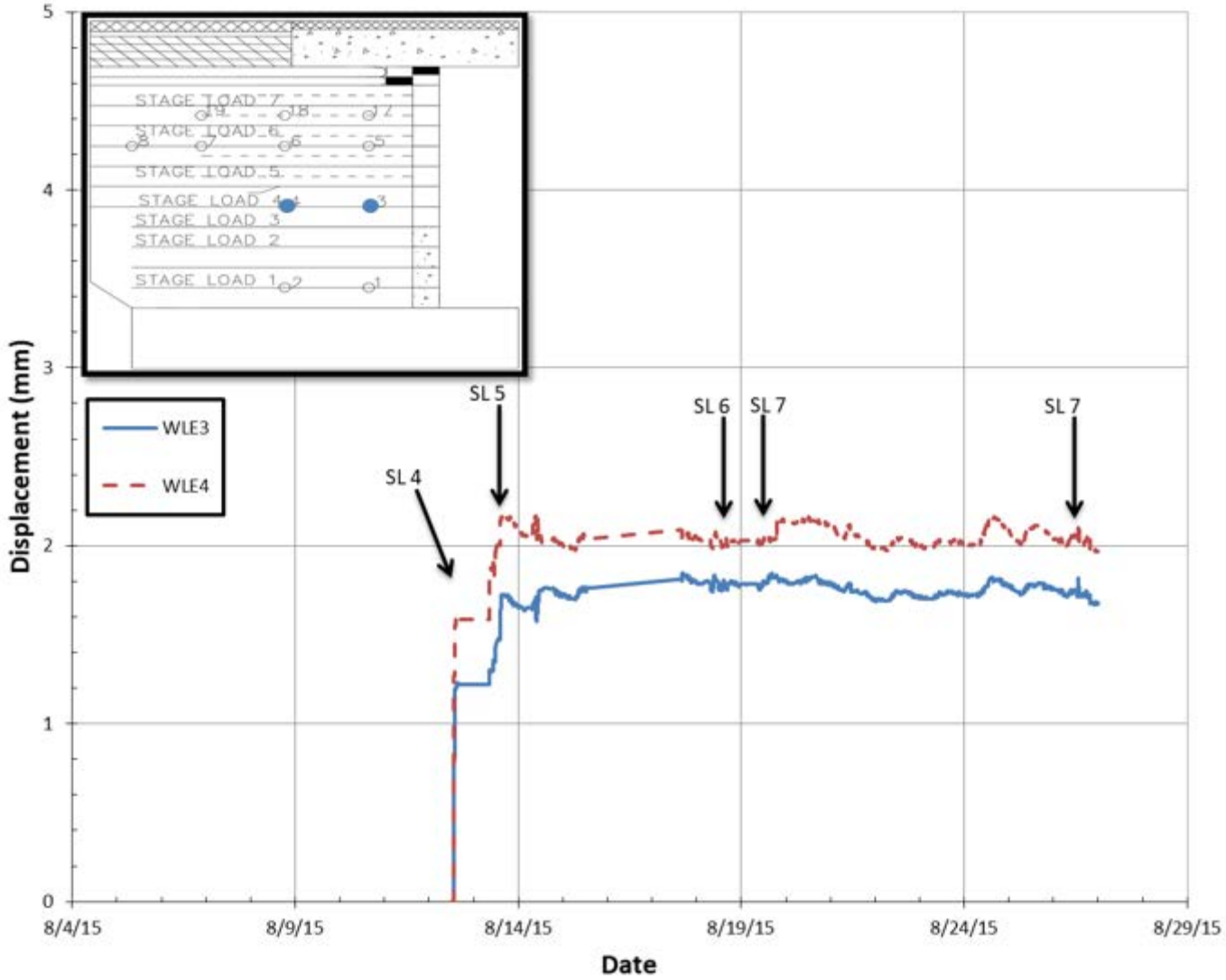

Fig. 6.3.32: Lateral geotextile displacements recorded from WLEs in Layer 6 on Abutment A

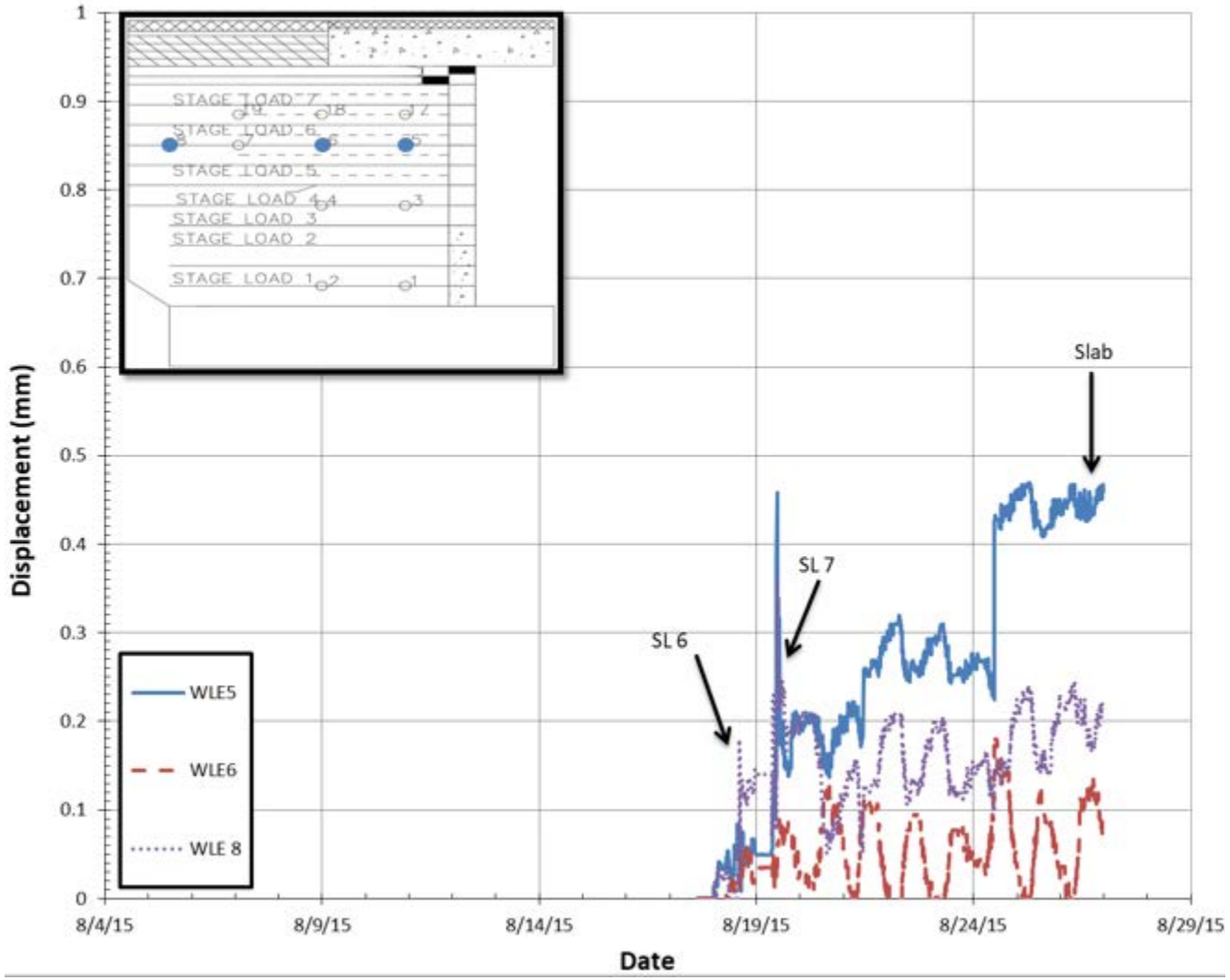

Fig. 6.3.33: Lateral geotextile displacements recorded from WLEs in Layer 11 on Abutment A (WLE 7 was not working and the data from this sensor is not included in this figure)

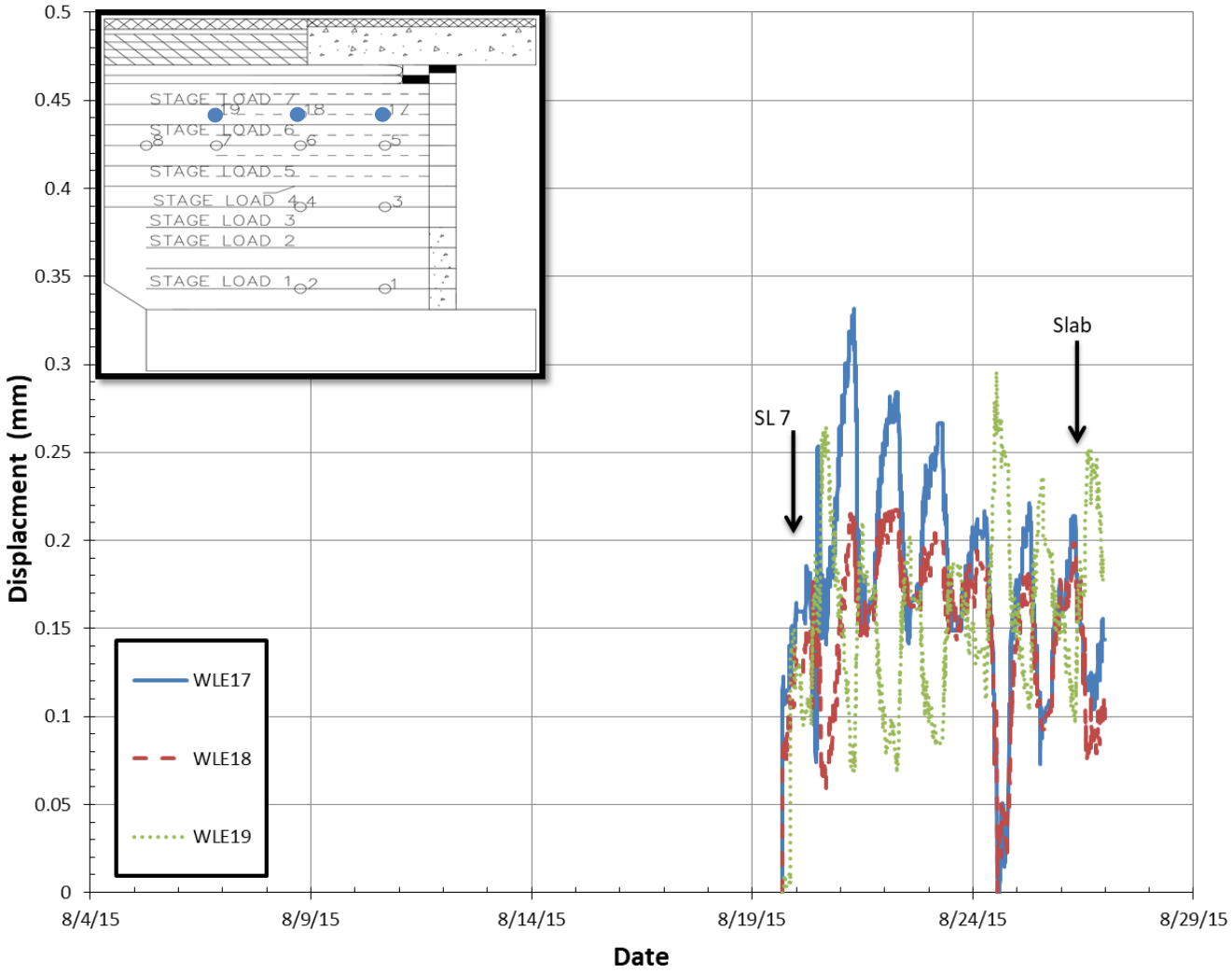

Fig. 6.3.34: Lateral geotextile displacements recorded from WLEs in Layer 14 on Abutment A

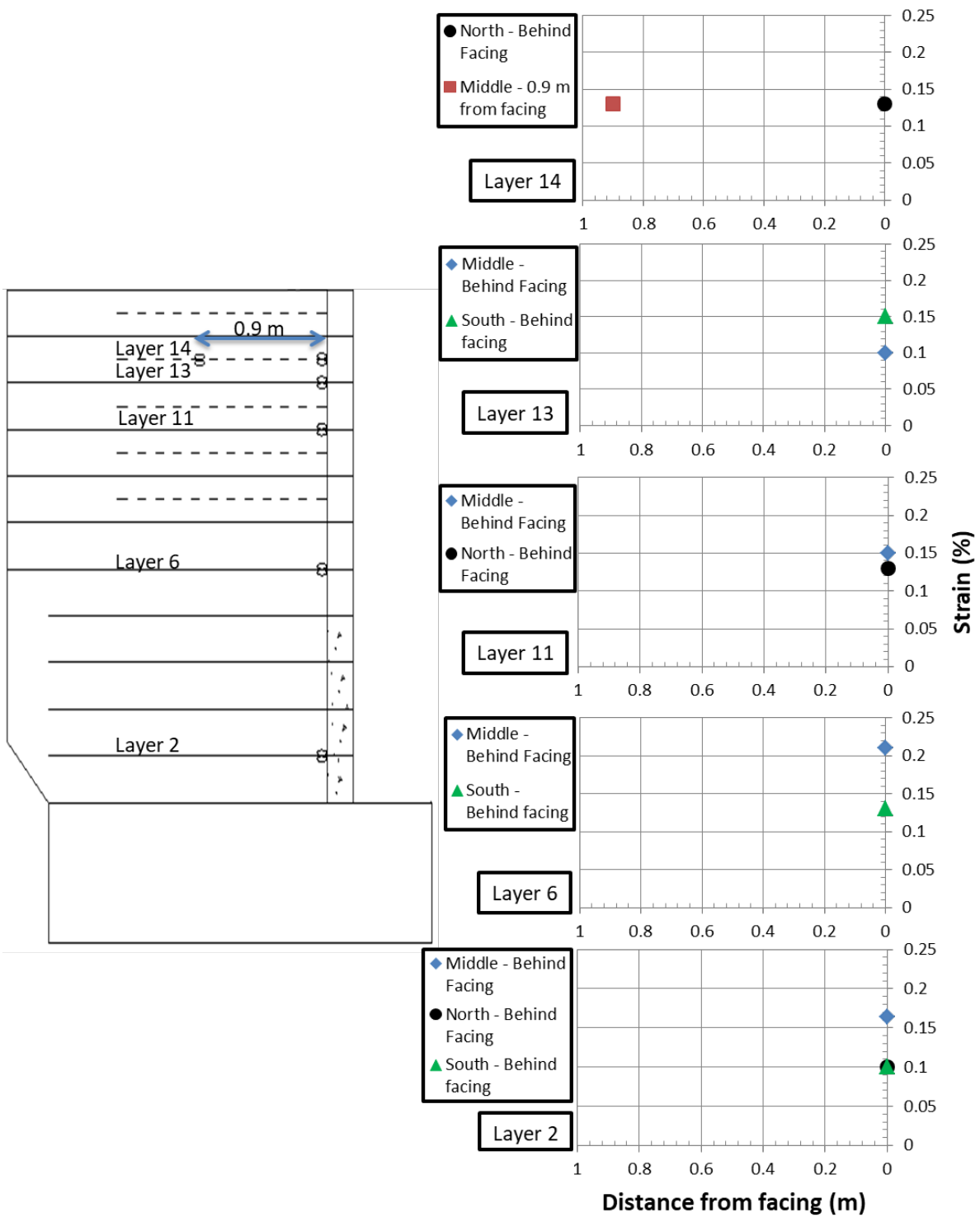

Fig. 6.3.35: Strain versus depth plot within abutment A due to self-weight of backfill load. The SGs are located right behind the facing block and away from the facing block (0.9 m or 3 ft from the back of the facing block).

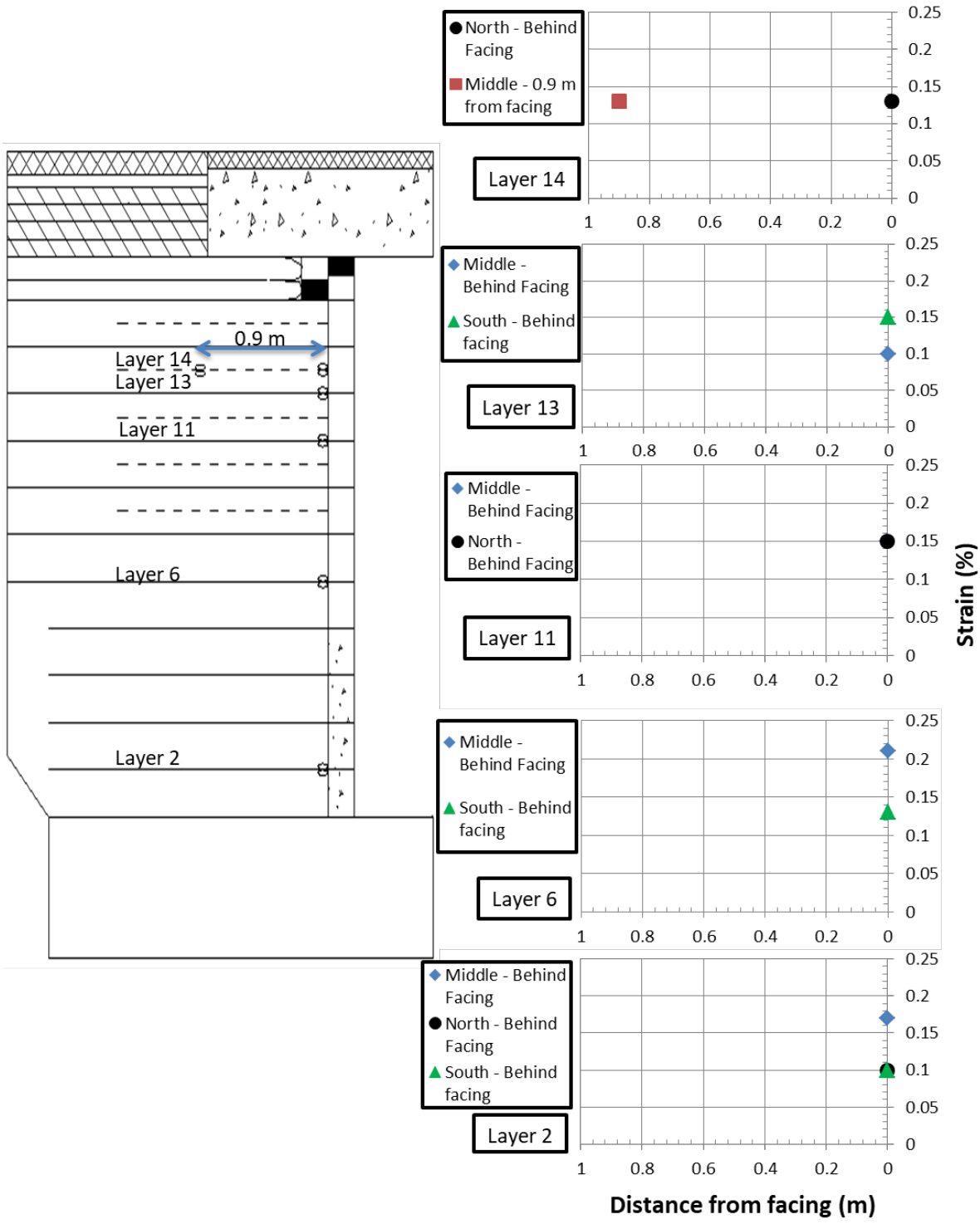

Fig. 6.3.36: Strain versus depth plot within abutment A for combined self-weight of backfill and bridge slab loads. The SGs are located right behind the facing block and away from the facing block (0.9 m or 3 ft from the back of the facing block).

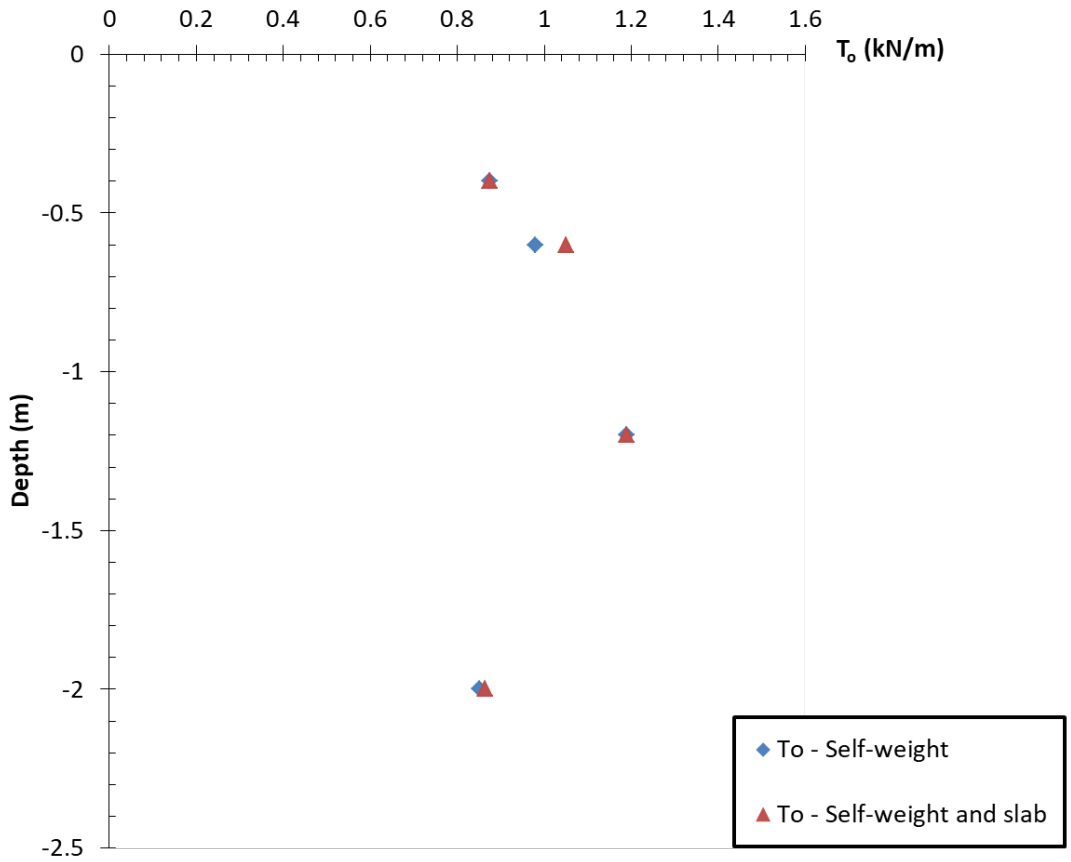

Fig. 6.3.37: T_o versus depth plot within abutment A for self-weight and combined self-weight of backfill and bridge slab loads (The SGs are located right behind the facing blocks)

Soil extensometers were used to estimate the strains within the backfill. Figure 6.3.38 shows the data obtained from the two soil extensometers installed at the same height of the abutment, although one of the extensometers was located within the bearing bed (and the other one within the primary reinforcement zone. The data shown on Figure 6.3.38 is the result of the combined load applied from the self-weight of backfill and bridge slab load. The data also shows the response of the gages to the stage loading, which is discussed in Section 6.3.1.2. The data shows that the soil extensometer located within the primary reinforcement zone shows deformations approximately within 1.65 mm (0.065 in.) and within the bearing bed approximately 1.05 mm (0.042 in.). The backfill deformation in the bearing bed zone (measured by SE 1) was lower than the deformation beyond the bearing bed zone (measured by SE 2), in a location where no secondary reinforcement was placed. This shows that the confinement in closely spaced reinforcement has an effect in reducing lateral backfill deformation. Overall, the maximum observed lateral backfill deformation from both extensometers was less than 2.5 mm (0.1 in.). The observed lateral deformations were comparatively very small, but not negligible as the measured deformations were comparable with the geosynthetic displacements measured by the wire line extensometers. In the same way lateral geotextile displacements were converted to strain, the lateral backfill displacements measured by the soil extensometers were converted to soil strains using the measured displacements (Δs) and length of the rod (L). The calculated backfill strains due to self-weight in bearing bed zone and primary reinforcement zone were 0.16 % and 0.26, % respectively. The calculated backfill strains due to combined self-weight and slab load in bearing bed zone and primary reinforcement zone were 0.17 % and 0.27 %, respectively. The soil strain in bearing bed zone was comparable with the geosynthetic strain measured by strain gages installed in the same layer as the soil extensometers. However, the soil strain in primary reinforcement zone was higher than the geosynthetic strain measured by strain gages. The soil strains were found to be much higher than the global geosynthetic strain estimated using wire line extensometer installed in the same layer as the soil extensometers.

Settlement measurements from the abutment are shown in Figure 6.3.39. The data shown is within the accuracy of the instrument. Consequently, the overall conclusion from this data is that settlements were negligible within the soil below the abutments. This information was expected as the soil below the reinforced soil mass was found to have large areas of exposed bedrock as discussed in Section 6.2.7.

Movements of the facing of the abutment after construction are shown in Figures 6.3.40 and 6.3.41 from Abutments A and B, respectively. The data shown in these figures were obtained from the survey targets installed in middle and north sides of the abutments right after the placement of the slab. The accuracy of the surveying conducted in this research is reported to be 1 mm (0.04 in). In general, considering the accuracy of the surveying, the data shows that the maximum movement of the facing blocks was observed in the top half section of the abutment and the movement close to the foundation was within the accuracy of surveying. Overall, the data from survey results show that vertical and lateral deformations in the structure during construction period were very small.

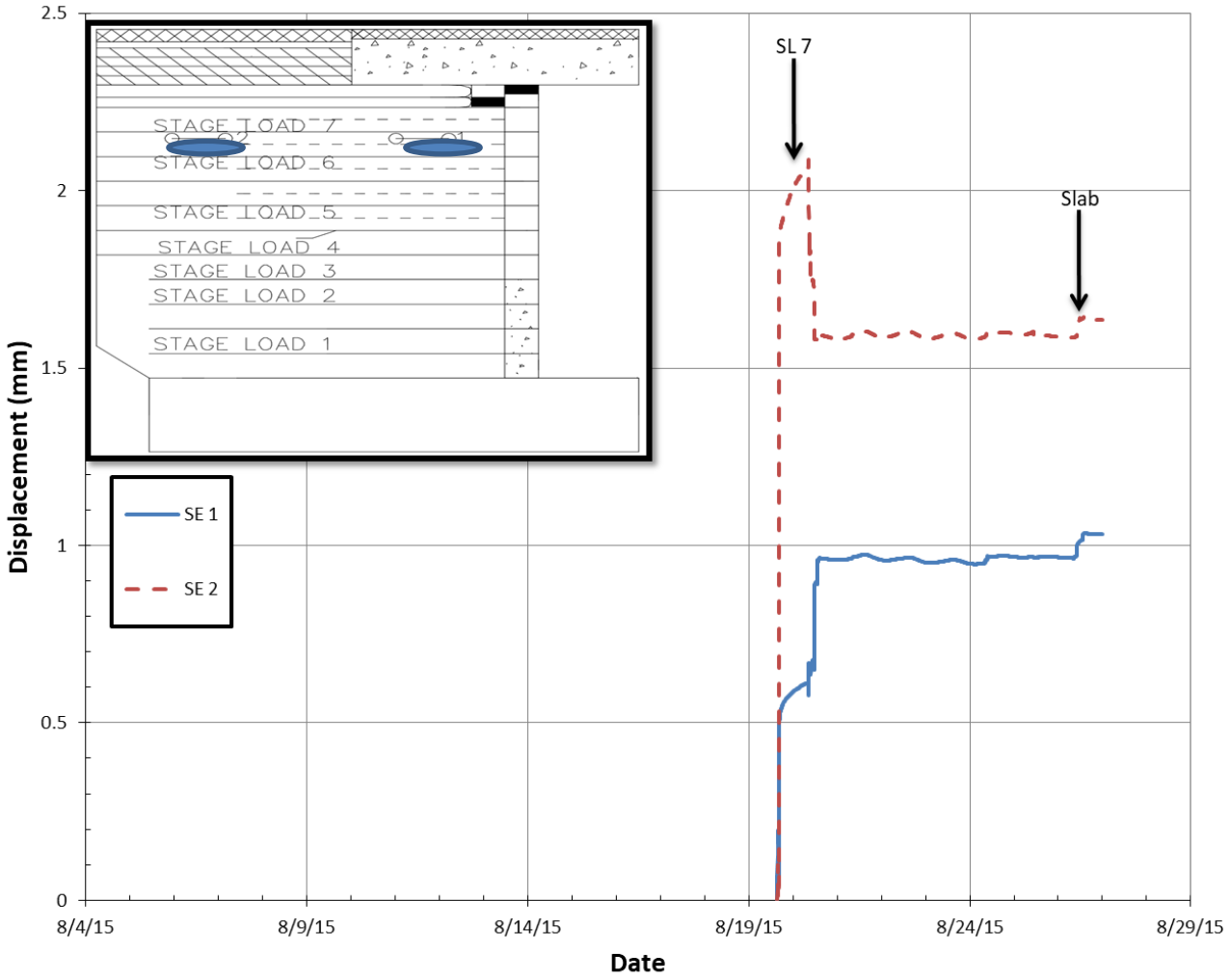

Fig. 6.3.38: Lateral deformations measured in Layer 14 on Abutment A due to combined self-weight of backfill and slab loading (The SEs were located 0.3 m (I ft) and 2.75 m (9ft) from the facing)

Fig. 6.3.39: Settlement measurements recorded below the reinforced soil foundation in Abutments A and B

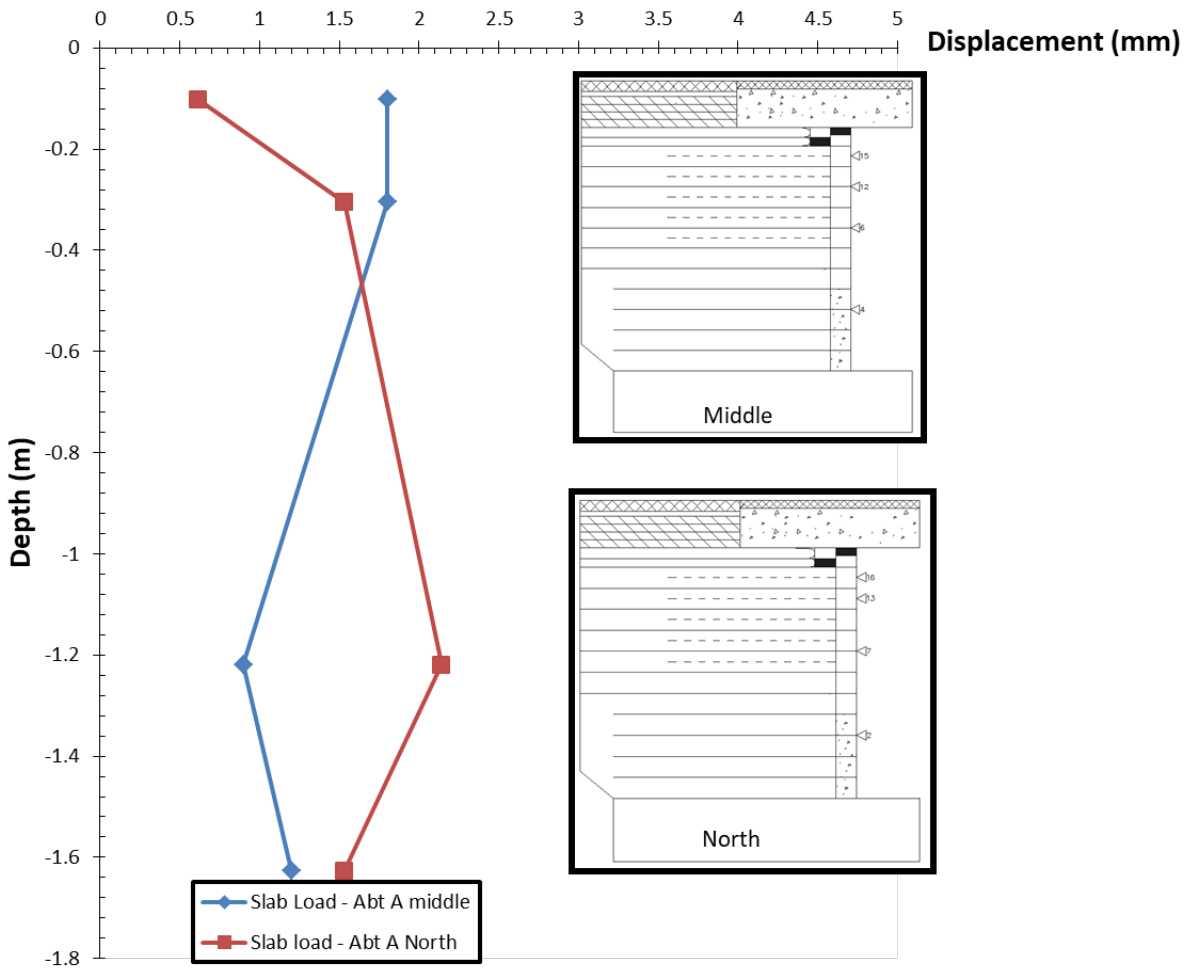

Fig. 6.3.40: Lateral movements of facing blocks due to slab load (without self-weight) as observed from survey targets in Abutment A

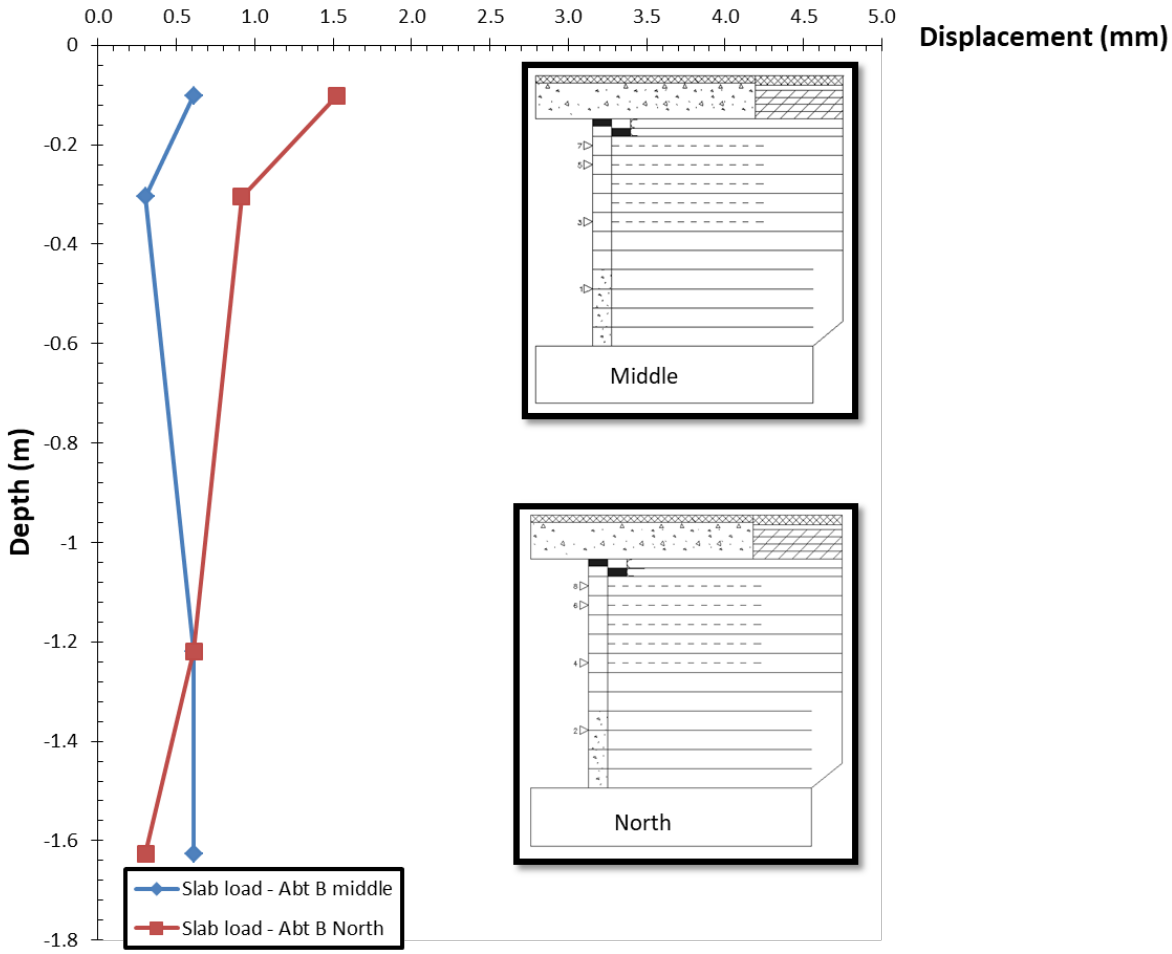

Fig. 6.3.41: Lateral movements of facing blocks due to slab load (without self-weight) , as observed from survey targets in Abutment B

6.3.1.2 STAGE LOADING

The purpose of the stage loading conducting during construction of Abutment A was to document the response of the primary reinforcement zone and bearing bed zone of the GRS-IBS structure to the applied load. The bearing bed sections were constructed with half of the reinforcement spacing compared to the primary reinforcement section. Therefore, the comparison of the stress distribution and measured strains in each of these zones could be used to evaluate the effects of reinforcement spacing.

The stage loading was achieved in the field by placing Jersey barriers at different stages on the fill surface during GRS-IBS abutment construction. As discussed in Section 6.3, there were seven stage loadings, four of which were applied using 8 Jersey barriers (stage load 2, 4, 6, and 7) and three of which were applied using a single Jersey barrier (stage load 1, 3, and 5). Single Jersey barriers had to be used due to the construction schedule restrictions as applying multiple Jersey barriers took longer time, which was not always available.

Figure 6.3.4a shows the locations of all stage loads. Stage loads 1, 2, 3, and 4 were applied on in the primary reinforcement zone and stage loads 5, 6, and 7 were applied on bearing bed zone. The load from a single Jersey barrier had a magnitude of 11 kPa (1.6 psi). In the case of 8 Jersey barrier applications, 3 Jersey barriers were placed directly on the geotextile layer and the remaining 5 Jersey barriers were stacked up on top of the 3 Jersey barriers (Figure 6.3.4c). However, the second barrier of the 3 lower barriers was not in contact with the top 5 barriers due to the construction of the Jersey barriers used in this study (Figure 6.3.4c). Therefore, the calculation of the load was conducted based on the first and third barriers of the 3 lower barriers to carry the load from the top 5 barriers. This resulted in the total load of 89 kPa (13 psi) (i.e., first and third barrier was each approximately applying 39 kPa (5.7 psi) and the middle barrier was applying 11 kPa (1.6 psi)).

During stage loading, both the measured vertical and lateral stresses within the aggregate and the strains on the geotextile were recorded as discussed below:

Vertical pressures recorded from each EPC were compared against the theoretical stress distributions estimated using the AASHTO 2 to 1 and Boussinesq theoretical methods. In single stage loading, the AASHTO 2 to 1 method was applied in a way that the load from a given stage was distributed to the layer of interest and EPCs that fall within the trapezoid of stress distribution were only evaluated. In 8 Jersey barrier loading, the load over the width of each one of the bottom three barriers was distributed to the geosynthetic reinforcement layer of interest and the load distributed from each zone was summed up on EPCs that fall within the trapezoid of stress distribution. However, in case of Boussinesq method, the load from each zone was distributed to the layer of interest using super-position and the stress on locations of EPCs was the sum of stresses distributed from each zone of loading. Figures 6.3.42 to 6.3.47 show the responses of EPCs to 6 single stage loadings. Figures 6.3.48 to 6.3.50 show the responses of EPCs to the 8 Jersey barriers loadings. During the multiple Jersey barrier application, the first set of data was always collected from the application of a single Jersey barrier for 30 minutes. This meant, when it comes to data comparison, all stage loads had a single Jersey barrier application

(stage load 1 to 7) and additionally some layers also had multiple Jersey barriers application (Stage load 2, 4, 6, and 7).

The data collected from EPCs showed that these instruments do not give accurate measurements when the applied load is very close to the instrument. In those cases, the EPCs generated higher stresses than the applied pressure. This condition was observed in different stage loadings such as response of EPC 4 to stage load 4 and 5 as shown in Figure 6.3.44 and 6.3.45. Additionally, the responses of EPC 1, 2, and 3 to stage load 2, EPC 4 to stage load 3, and EPC 7 to stage load 5 showed stresses that were much higher than the expected range and results from these stage loadings are not presented in this section. In general, the theoretical distributions (AASHTO 2:1 and Boussinesq) did not agree well with each other. The differences between the theoretical estimations are believed to be due to the complexity of the geometry under the stage loading where the load is applied very close to the facing of the abutment. Hence, the distributions are affected by the presence of the facing blocks even though the AASHTO 2:1 method equation used in this study (Equation 6.3.1 to 6.3.4) is already supposed to capture this effect. When the theoretical calculations were compared against the field measurements there were also discrepancies except in some cases both the field measurements and the theoretical calculations matched well with each other (please see Figures 6.3.46, 6.3.47, and EPCs 1 and 4 in 6.3.48). These matching results primarily observed in the zone of primary reinforcement where the spacing between the reinforcements were 8 -inches apart. Potentially the discrepancy between the theoretical and field measurements occurred not only because of the limitations of the theoretical calculations to accurately capture the field conditions but also due to the point loading effect on some instruments. The aggregate used in this study could have the potential to result in point loading on the instrument, where the potential evidence of this exist in the EPC 4 data shown in Figure 6.3.45. It should be kept in mind that the field measurements are affected by the magnitude of the applied load, the duration of the applied load, and potentially the presence of the reinforcements and the spacing between them. However, when the field measurements are carefully evaluated by comparing both the theoretical estimations (AASHTO 2:1 and Boussinesq) and numerical calculations (Cap-yield and Mohr-Coulomb methods) (as shown in Chapter 7), we believe that overall the field measurements are telling an accurate story with the exception of pressure cells that show the signs of point loading.

From Figures 6.3.42 to 6.3.47 it can be observed that the responses of EPCs in the primary reinforcement zone to stage loadings were higher than EPCs in the bearing bed zone This trend provides evidence that closely spaced reinforcement contributes to reduce vertical stresses in the bearing bed zone.

Lateral earth pressures recorded from RPCs during stage loading are shown in Figures 6.3.17 to 6.3.21. The results showed that the stresses generated due to the stage loadings were higher in primary reinforcement zones. This indicates that the presence of secondary reinforcement or close reinforcement spacing has an effect in reducing both the vertical and lateral stresses in GRS-IBS structures.

Strains recorded by the strain gages attached to the geotextile reinforcements are shown in Figures 6.3.25 to Figure 6.3.29. From these figures, it can be observed that the geotextile strains induced due to the stage loading in the primary reinforcement zone were higher than geotextile strains in the bearing bed zone. This indicates the presence of secondary reinforcement in the bearing bed zone plays a role in restraining lateral geotextile strains.

Lateral strains recorded from the wire line extensometers that were attached to the geotextile are shown in Figures 6.3.31 to Figure 6.3.34. The results showed that the lateral deformations due to stage loading in the bearing bed zone were lower than the ones recorded in the primary reinforcement zone.

Strains recorded within the aggregate used to construct the GRS-IBS are shown in Figure 6.3.38. The results reveal that the backfill deformation in the bearing bed zone was lower than in the zone that had the same vertical spacing between the reinforcements as in the primary reinforcement zone.

One of the objectives of the stage loading evaluations was to determine if there was a boundary below which having smaller spacing would not affect the stress and strain measurements within the geosynthetic reinforced soil mass. However, this boundary condition could not be determined from the field study as the responses of stress sensors and deformation gages to stage loadings indicate that reduction of vertical spacing (i.e., from 0.2 m (8 in) to 0.1 m (4 in)) had an impact on the stress and strain measurements. The decrease in vertical reinforcement spacing or an increase in number of reinforcements resulted in an increase in the confinement and stiffness of the geosynthetic reinforced soil mass and reduced the stress distribution and lateral deformations within the reinforced zone.

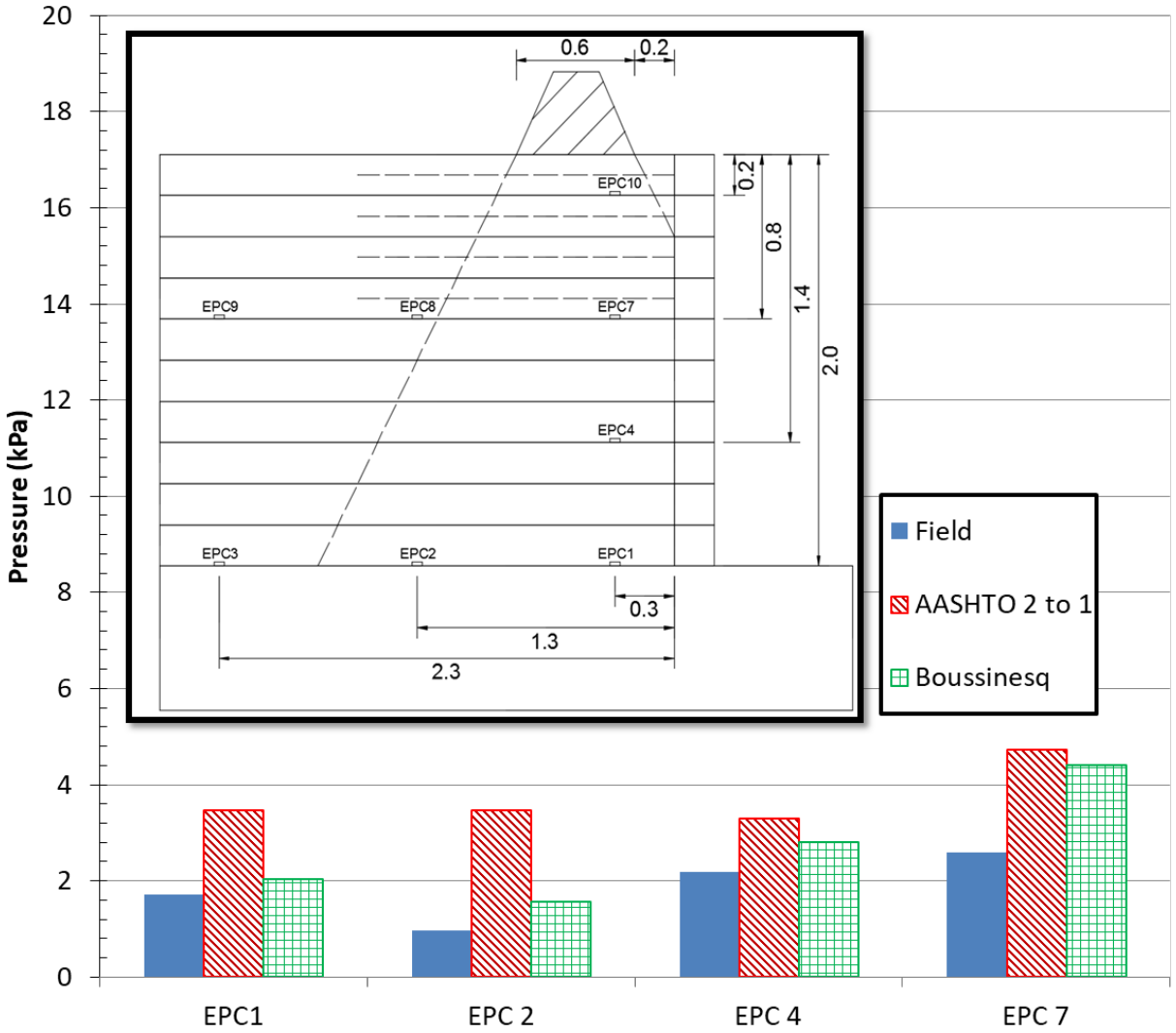

Fig. 6.3.42: Stage load 7 – single Jersey barrier application: Comparison of EPC data and theoretical stress distributions

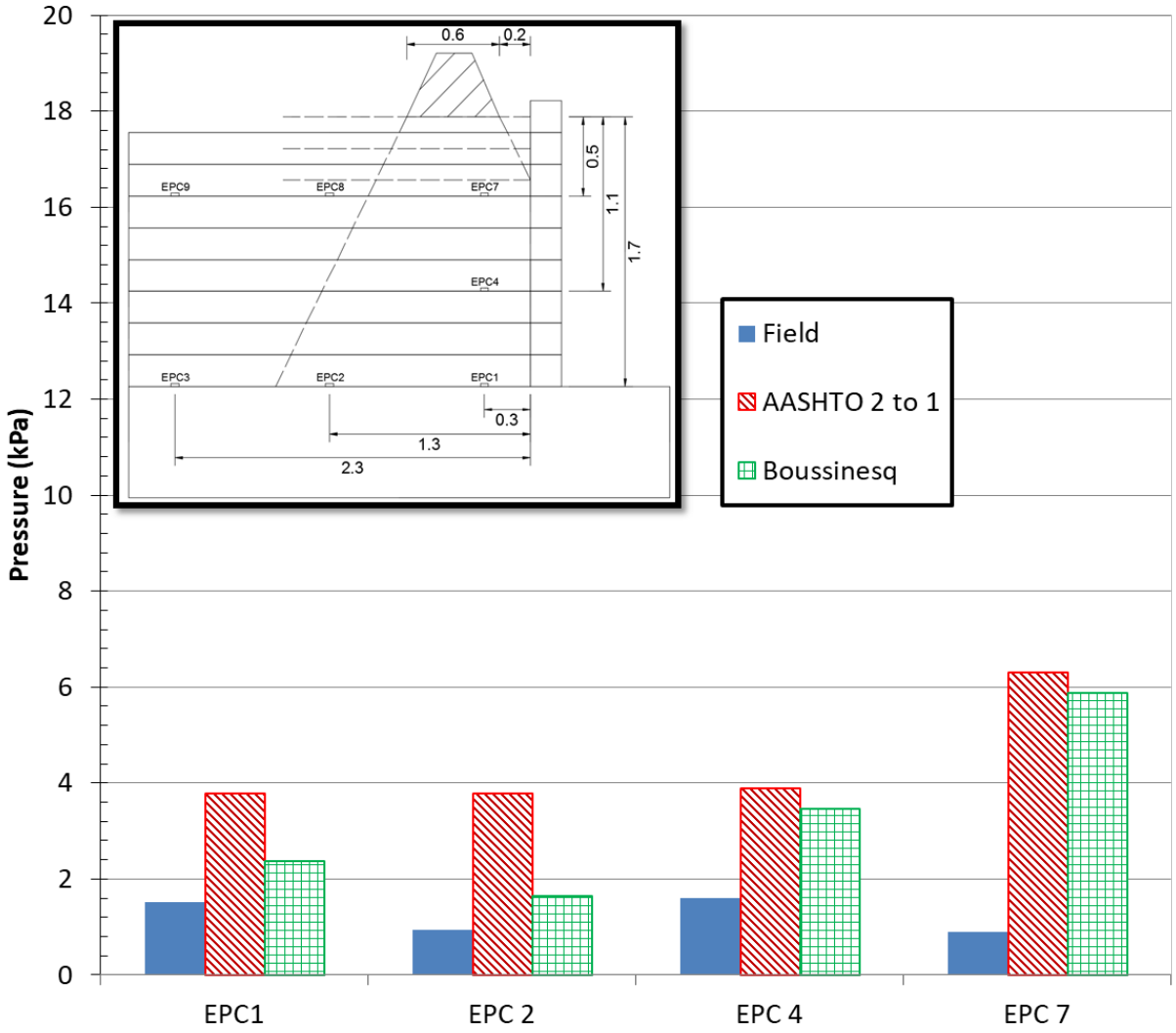

Fig. 6.3.43: Stage load 6 – single Jersey barrier application: Comparison of EPC data and theoretical stress distributions

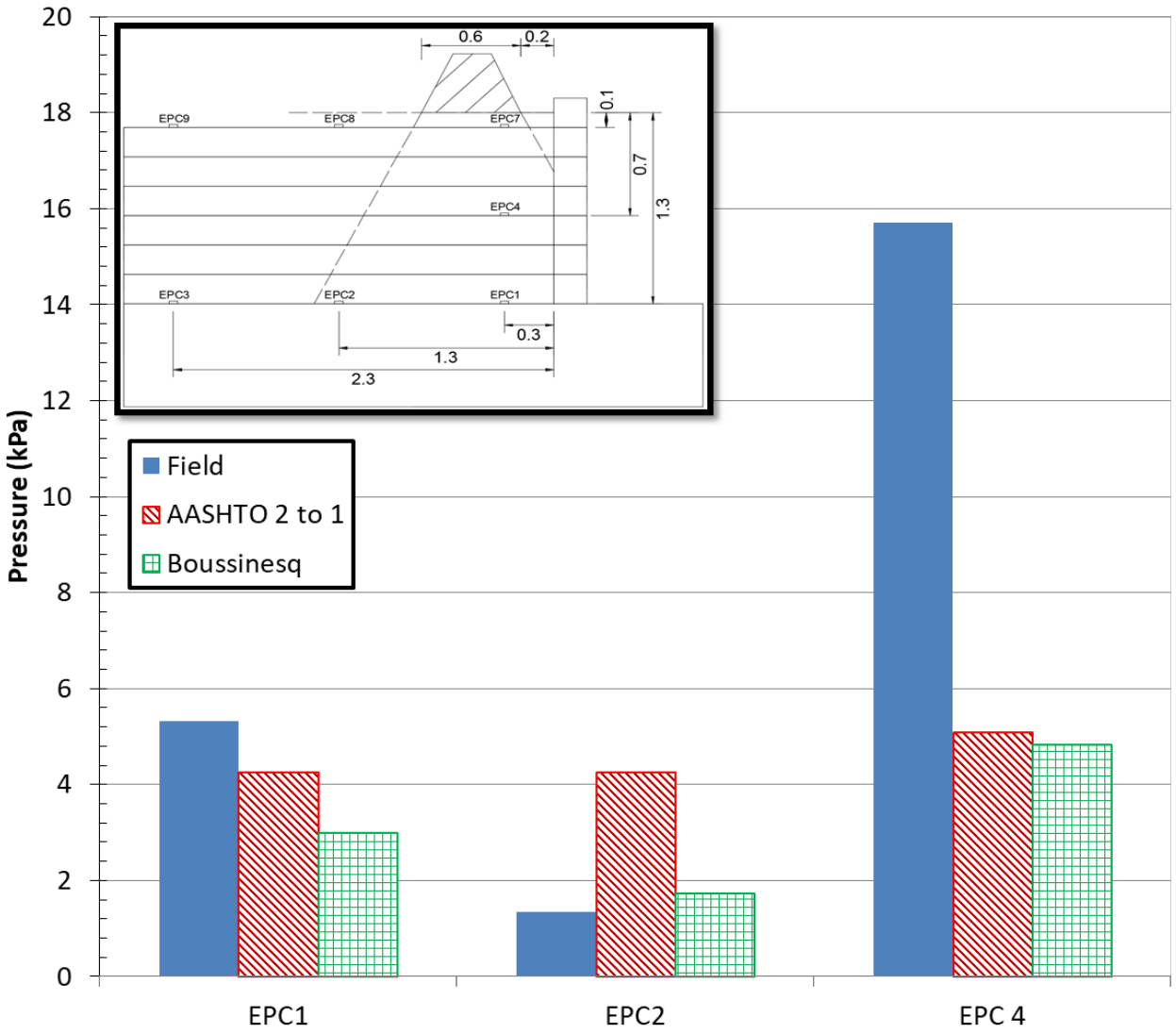

Fig. 6.3.44: Stage load 5 – single Jersey barrier application: Comparison of EPC data and theoretical stress distributions

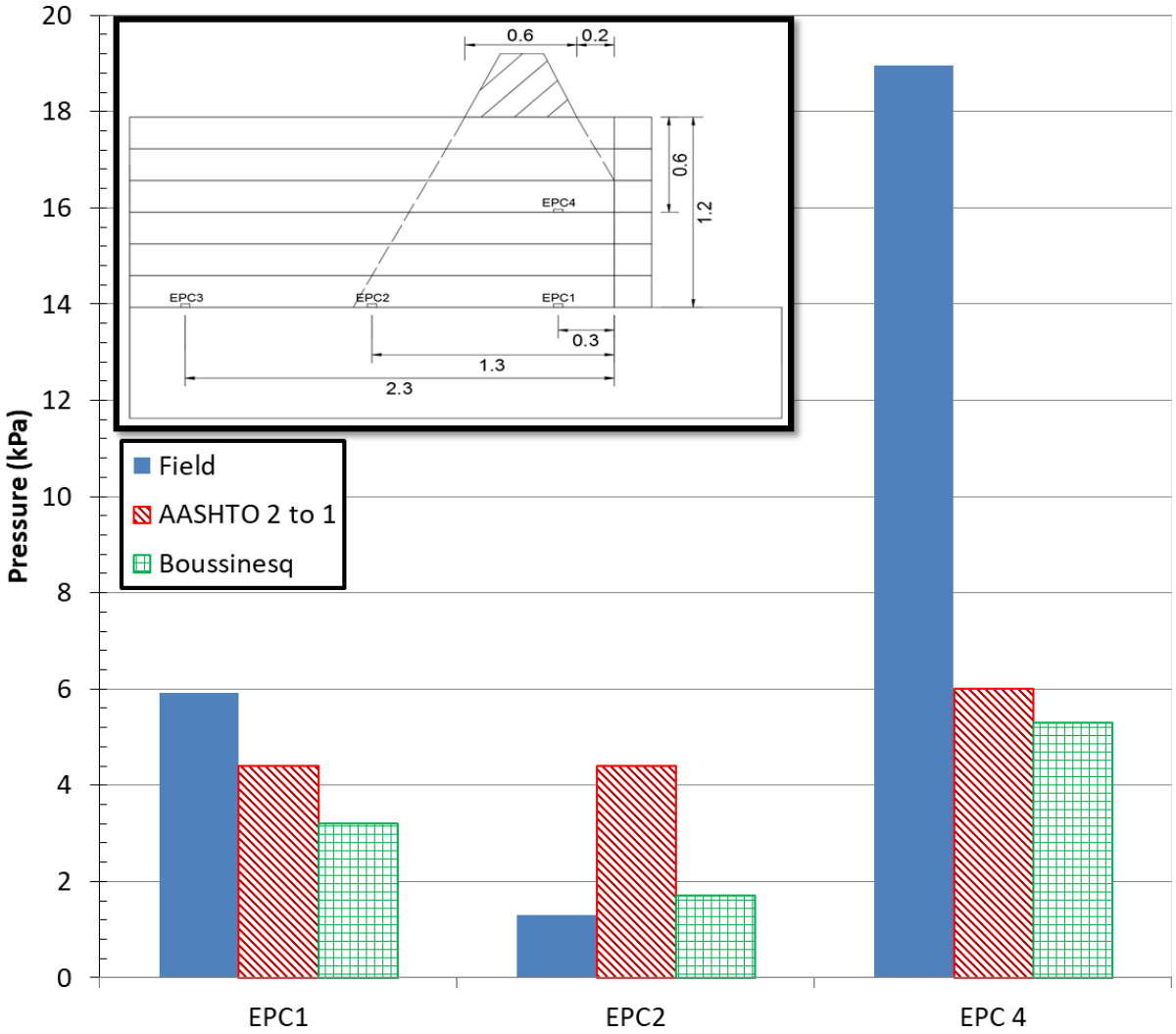

Fig. 6.3.45: Stage load 4 – single Jersey barrier application: Comparison of EPC data and theoretical stress distributions

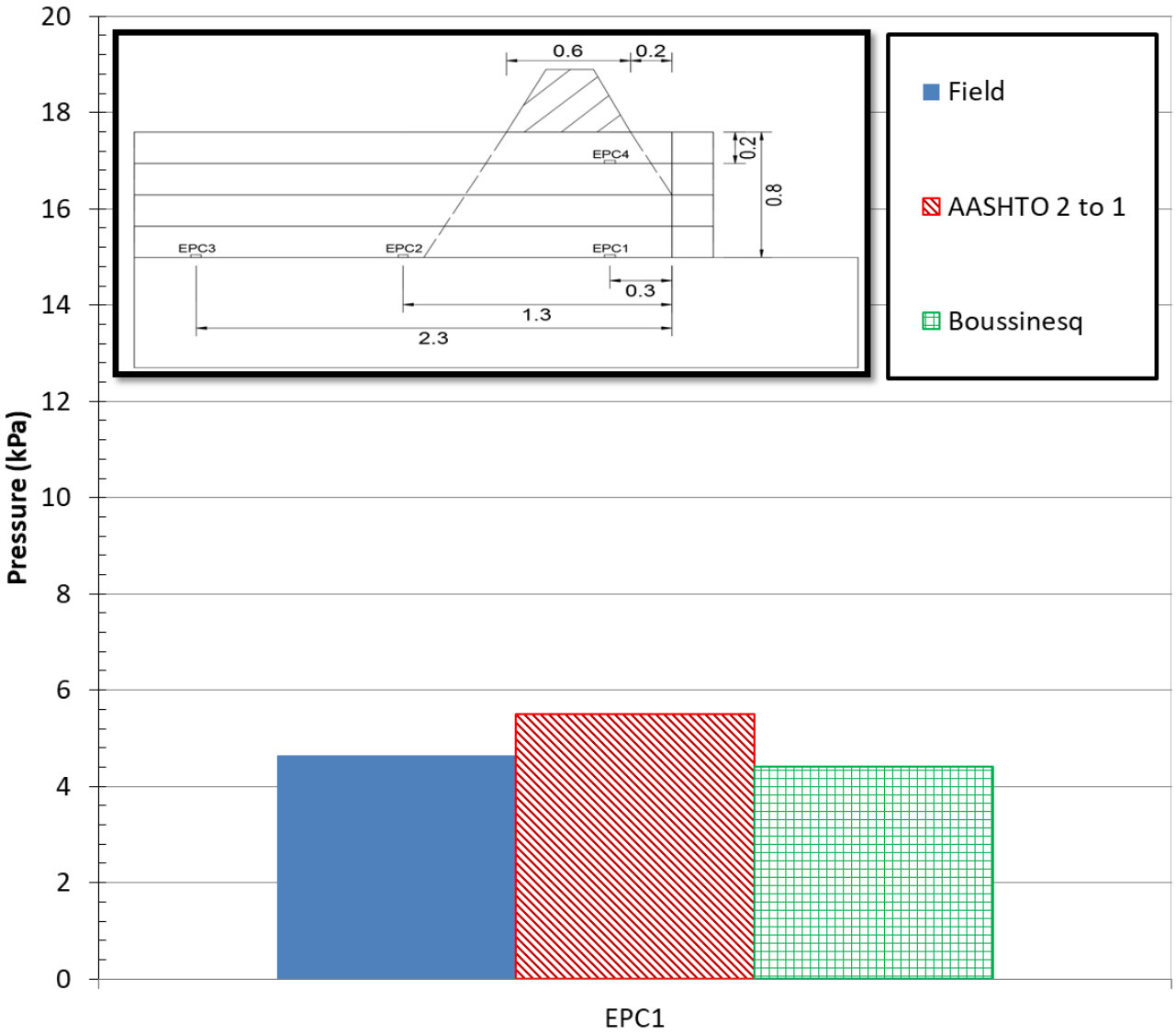

Fig. 6.3.46: Stage load 3 – single Jersey barrier application: Comparison of EPC data and theoretical stress distributions

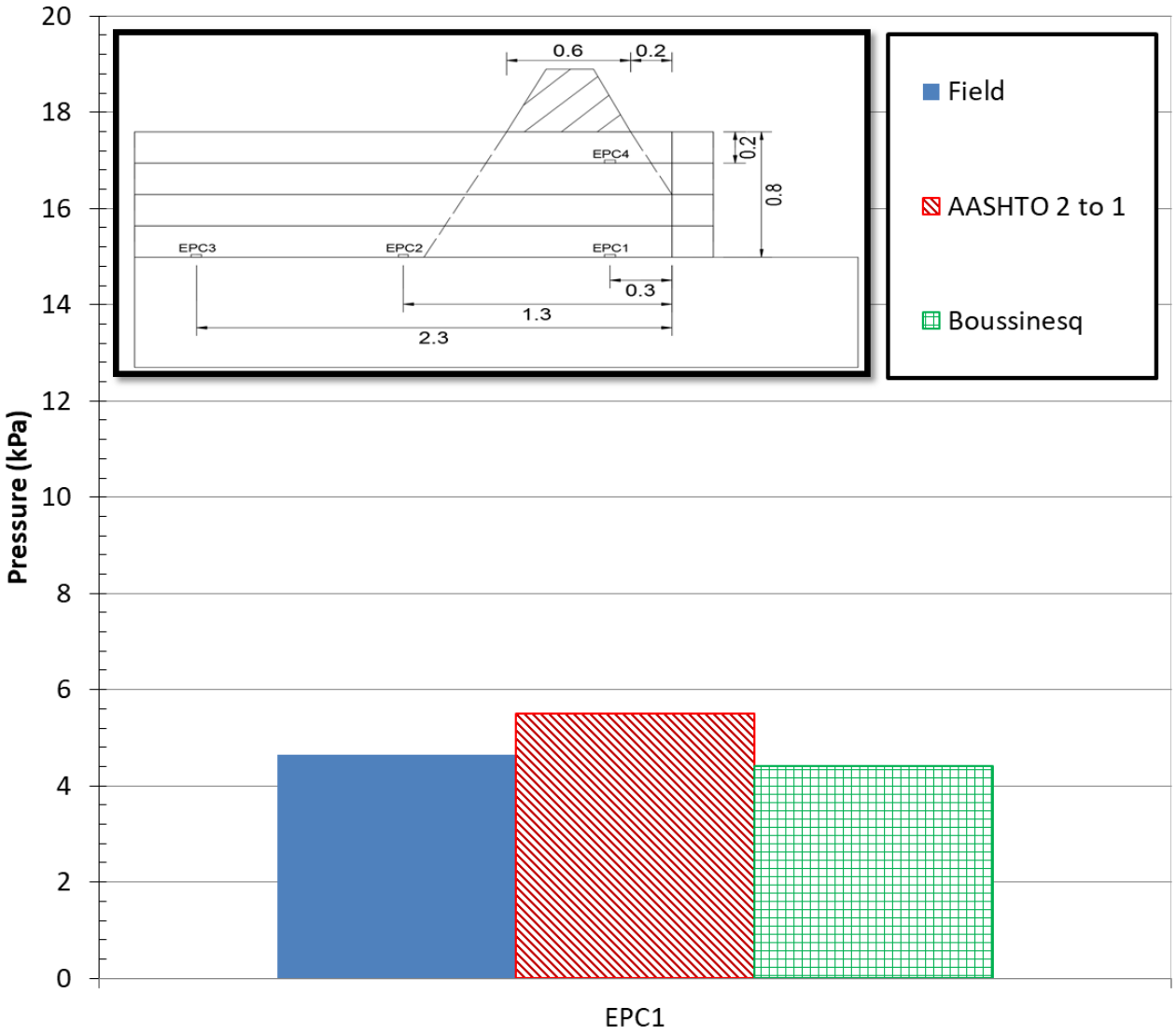

Fig. 6.3.47: Stage load 1 – single Jersey barrier application: Comparison of EPC data and theoretical stress distributions

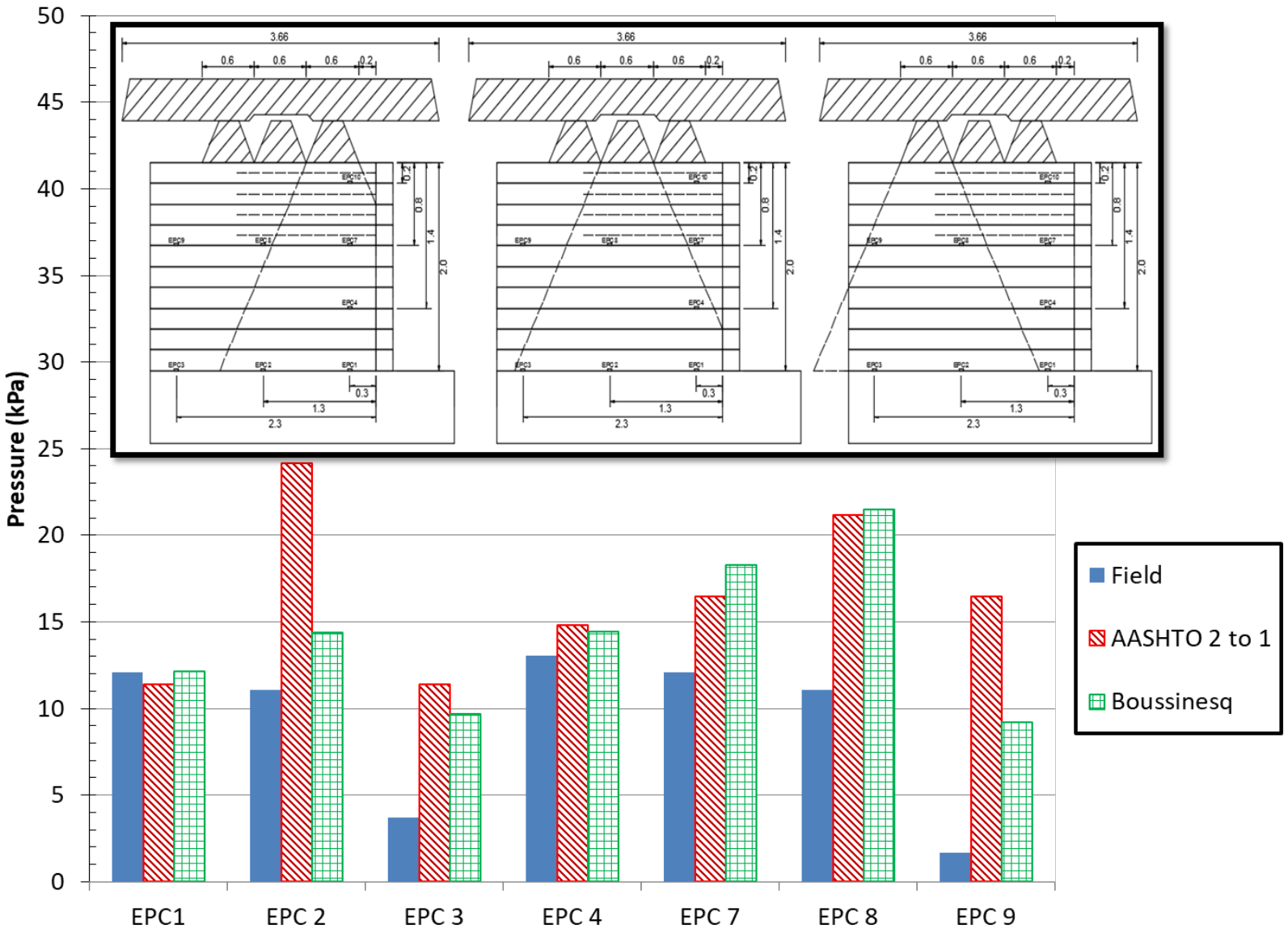

Fig. 6.3.48: Stage load 7 – multiple Jersey barrier application: Comparison of EPC data and theoretical stress distributions

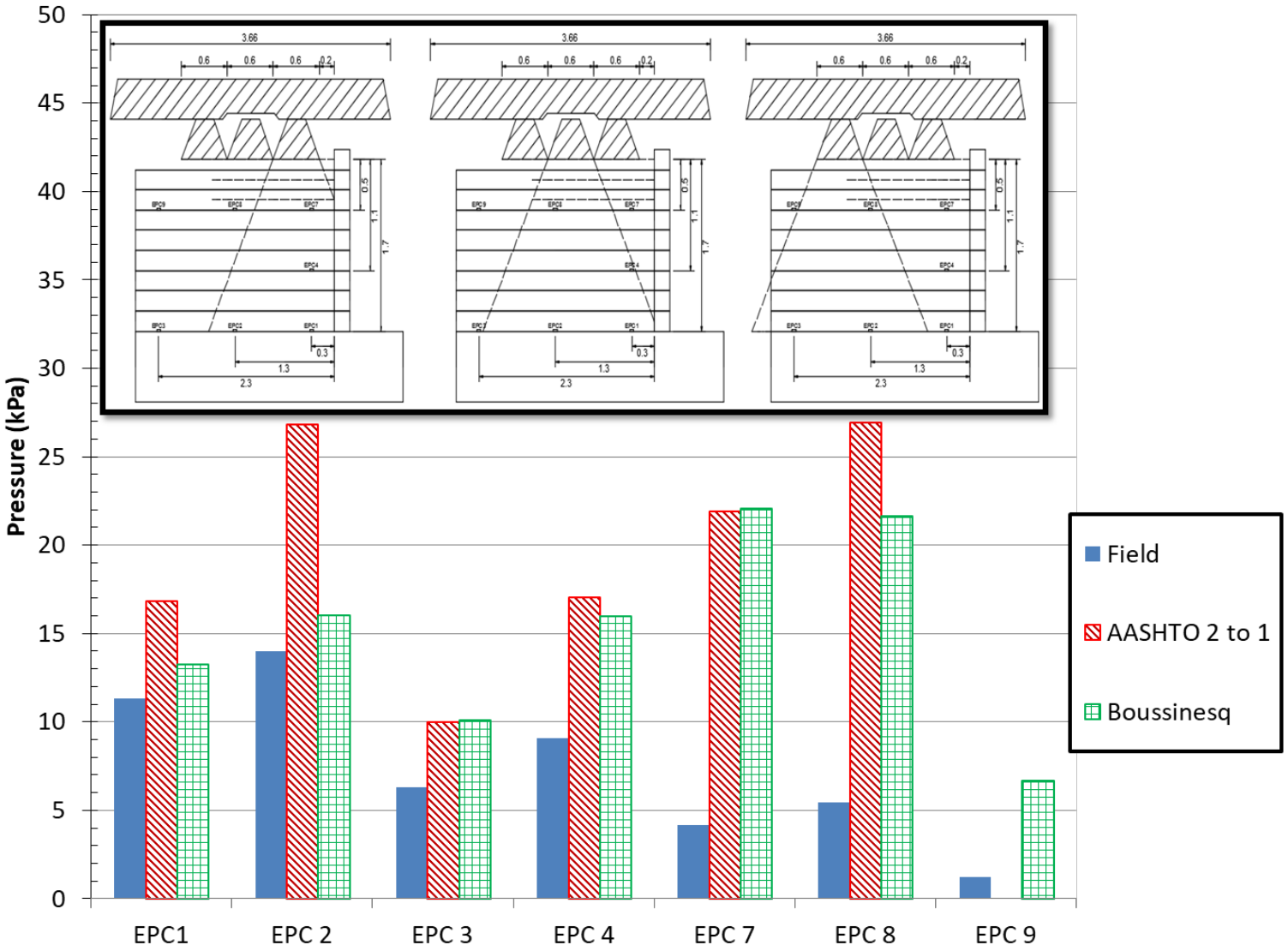

Fig. 6.3.49: Stage load 6 – multiple Jersey barrier application: Comparison of EPC data and theoretical stress distributions

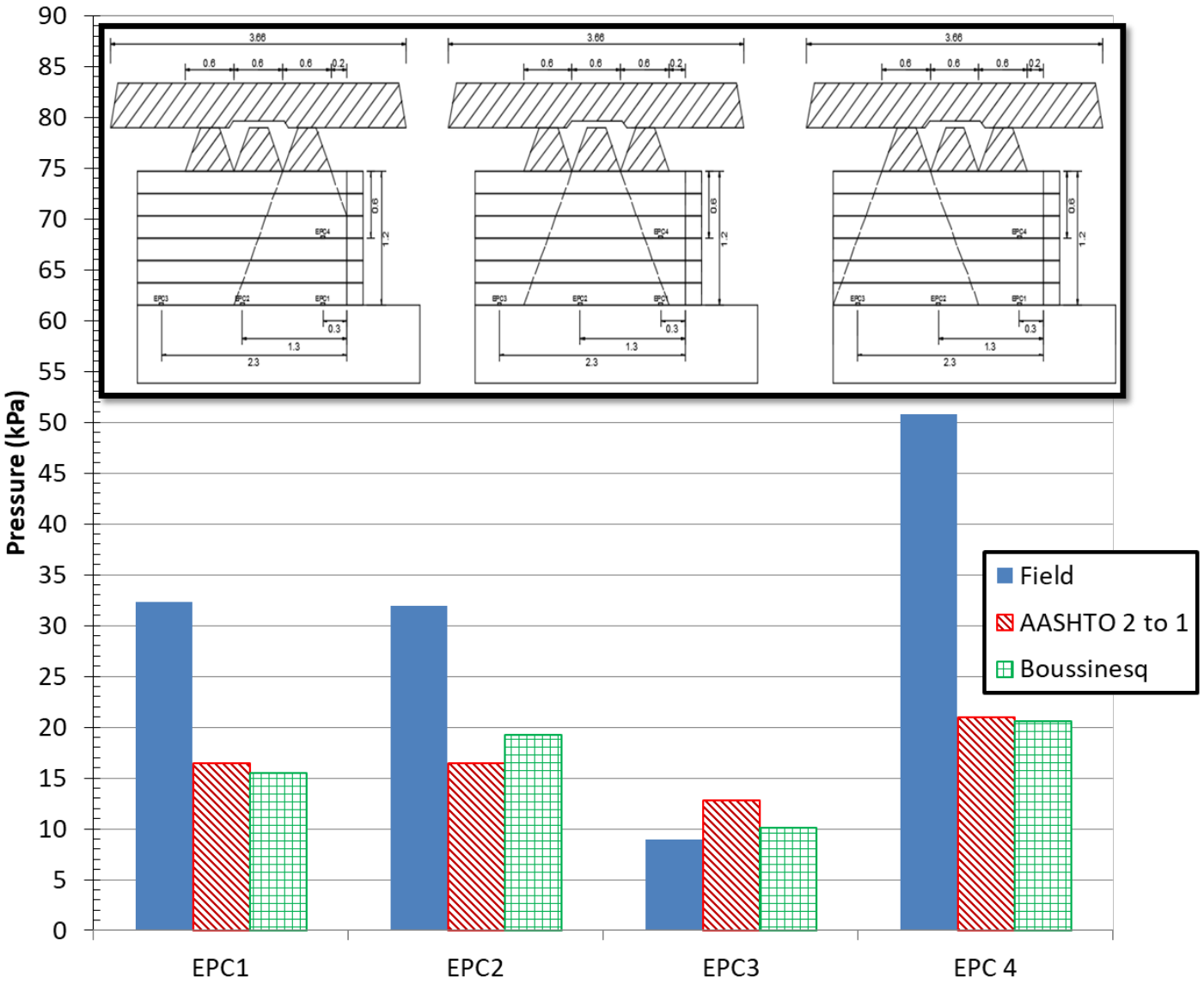

Fig. 6.3.50: Stage load 4 – multiple Jersey barrier application: Comparison of EPC data and theoretical stress distributions

6.3.2 FIELD DATA GENERATED AFTER CONSTRUCTION (LONG-TERM BEHAVIOR)

After construction, a loaded truck was parked over the bridge super-structure at four different times to evaluate the effect of seasonal variations on the performance of the structure. The dates of these load applications were September 2, 2015 (response right after construction), December 21, 2015 (response during winter season), March 29, 2016 (response during spring season), and November 17, 2016 (response during fall season, also corresponding to one year of service). The truck used for this load application was filled with AASHTO No. 8 aggregate and had a gross weight of 150 kN (15 tons). The surcharge from the truck load was approximately 14 kPa (2 psi) in abutment A and 7 kPa (1 psi) in abutment B. The surcharge in abutment A was twice of the surcharge in abutment B because of the beam seat width in abutment A being half of the beam seat width in abutment B. The truck was parked for 4 hours on North and South lanes of the super-structure.

Abutment B was only instrumented using EPCs, therefore the comparison of the response to truck loading on both abutments could only be conducted by comparing the vertical stress distributions. Figures 6.351 and 6.352 show the stress distribution profiles due to the truck load in abutments A and B, respectively. The recorded earth pressure distributions were also compared against the theoretical stress distributions based on AASHTO 2 to 1 and FHWA Boussinesq methods. As shown in the figures, the stress distribution profiles obtained from field measurements was in agreement with the distributions predicted by theoretical methods. The results also show that stress distribution in the GRS-IBS abutment that is composed of AASHTO No.8 aggregate is not significantly influenced by seasonal variations. However, the stresses in September 2015 and March 2016 truck loadings were found to be slightly higher than those measured during the December 2015 and November 2016 truck loadings. Such difference in response could be attributed to stress increase as a result of infiltrations in to the abutment from the surroundings in spring and summer seasons as shown in Figures B1 to B10 (Appendix B).

Potential changes in stress measurements with seasonal variations were also monitored using an earth pressure cell that was installed outside of the GRS-IBS abutment inside a wooden box filled with AASHTO No. 8 aggregate. The box has square dimensions of 0.6 m (23.6 in.) width and height of 0.5 m (19.7 in.). the earth pressure cell was placed at the bottom of the box and a 0.18 m (7.1 in.) thick aggregate layer was placed on top of it. Figure 6.353 shows the set-up of the box in the field. The result obtained from the EPC in the control box is shown in Figure 6.354 along with average monthly temperature and cumulative monthly precipitation data obtained from nearby weather station. Temperature correction was applied to the stress data obtained from the EPC using a factor provided by the manufacturer. The result shows that there is an increase of stress magnitude at times where high precipitation and snow accumulation was recorded in the area. However, the amount of load applied by the aggregate was very small and the observed stress fluctuation in the figure was well within the accuracy of the sensor. Pore-water pressure that could develop due to precipitation did not appear to generate additional stress to the expected level. This is because of the fact that AASHTO No. 8 aggregate is a free draining granular material with no fines content and water could easily pass through the pores of the aggregate. In addition, any water that may be stored in the box would drain out through a hole created on one side of

the box for drainage purpose. No water rise was observed in the box as a result of precipitation during regular site visits after construction.

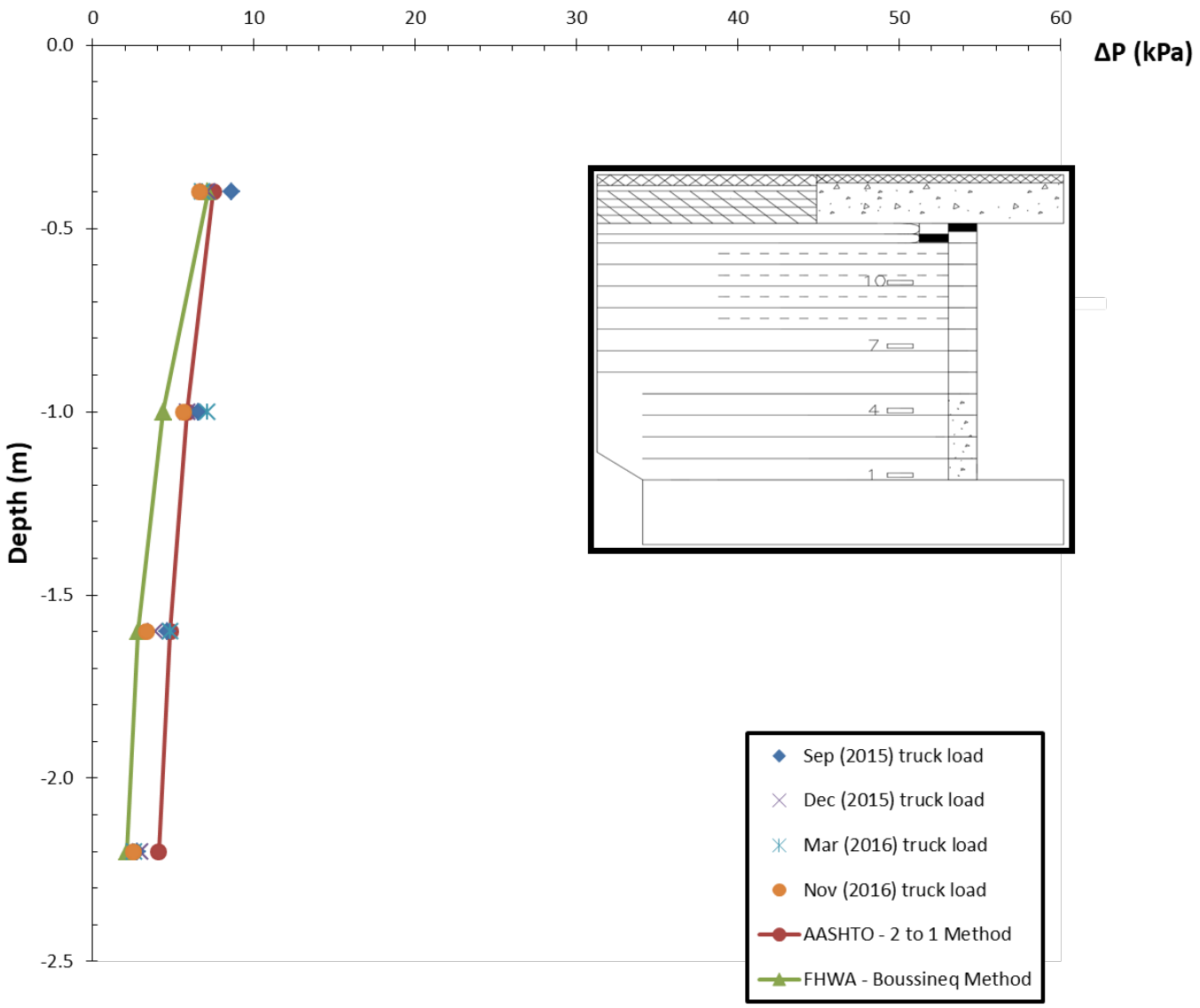

Fig. 6.3.51: Vertical stress distribution in Abutment A due to truck load

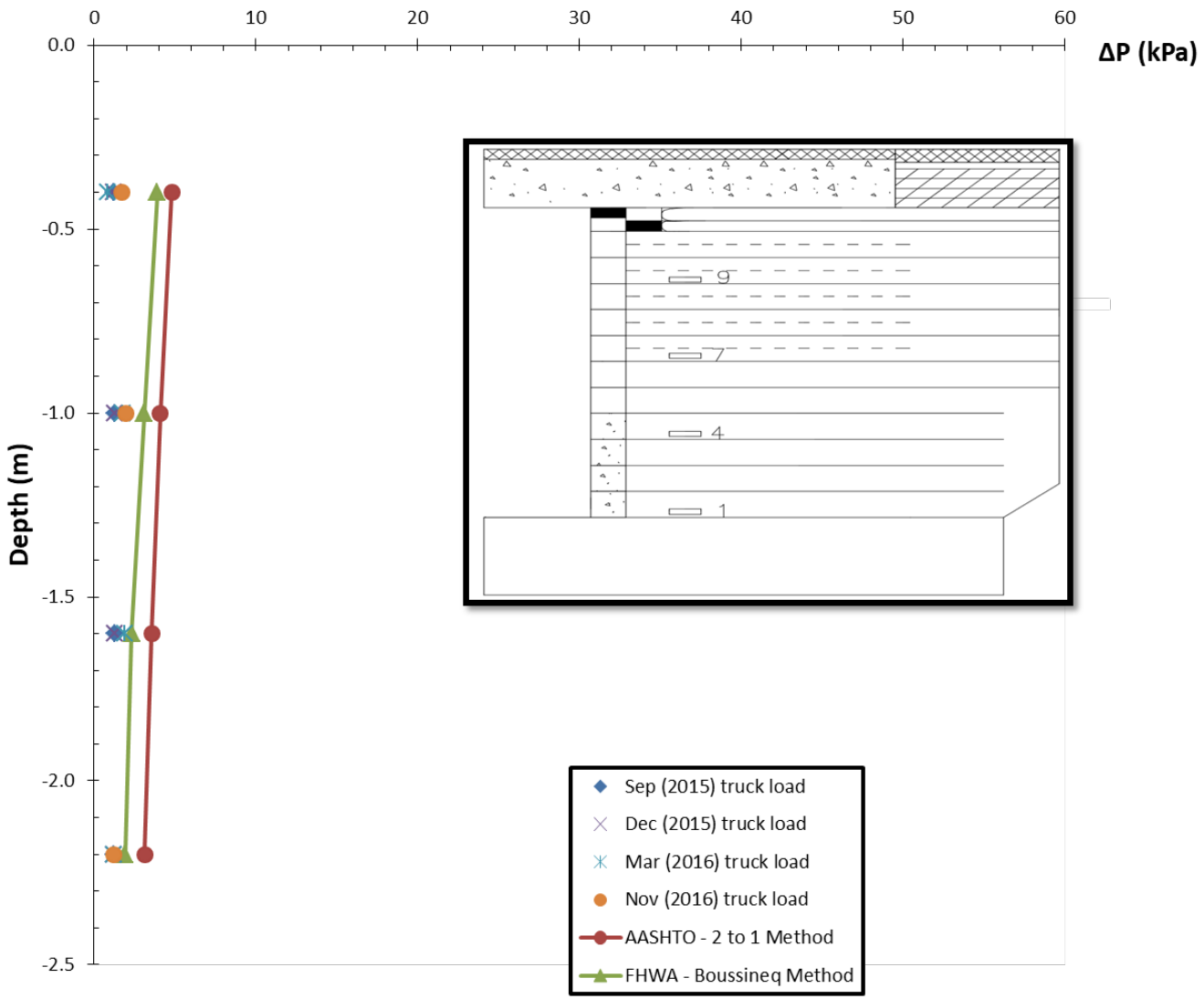

Fig. 6.3.52: Vertical stress distribution in Abutment B due to truck load

(a)

(b)

Fig. 6.3.53: Installation of one earth pressure cell outside of the GRS: a) Earth pressure cell placed inside a control box; b) AASHTO No.8 aggregate placed on top of the earth pressure cell

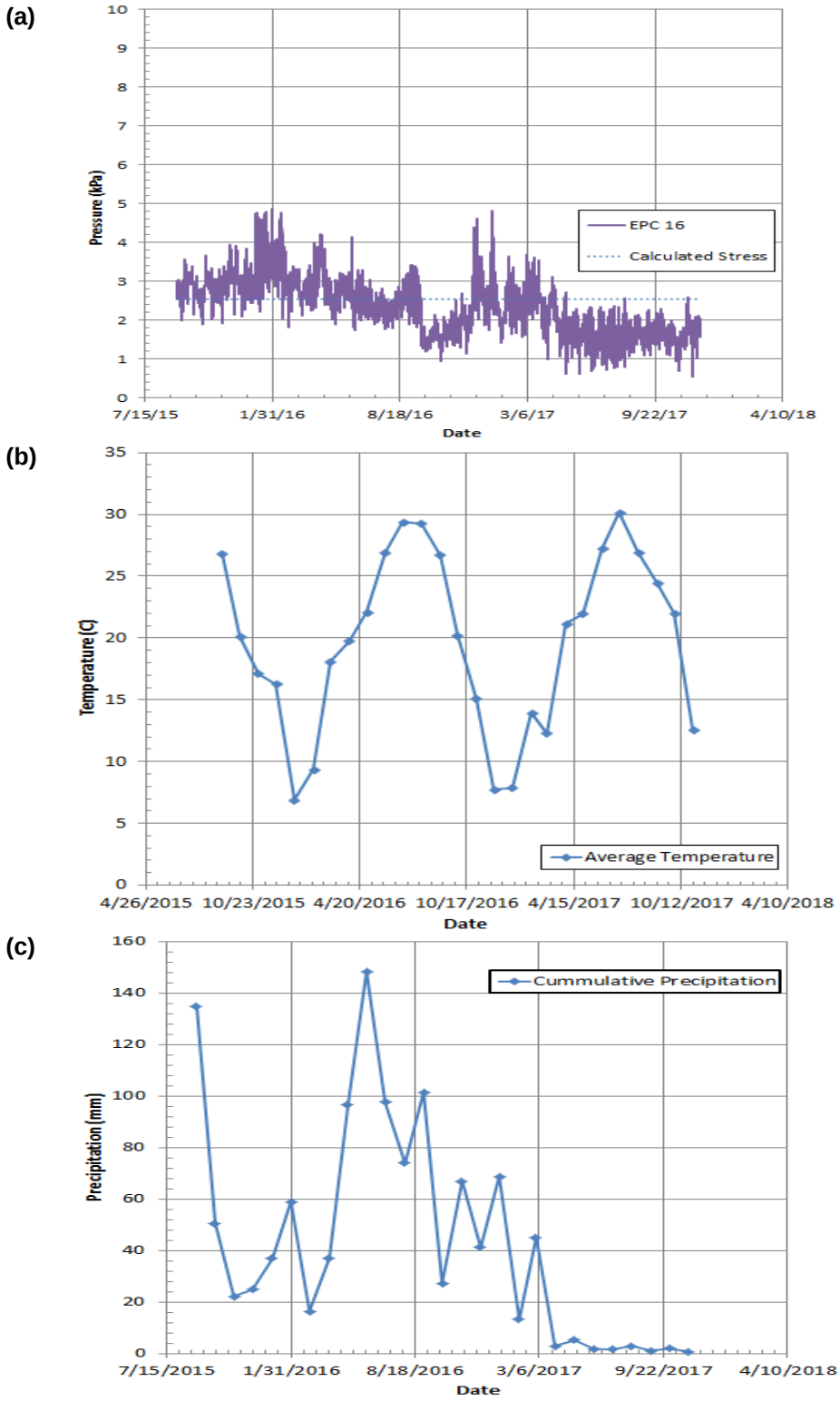

Fig. 6.3.54: Fluctuations of stresses, temperature, and precipitation with seasonal changes: (a) vertical stresses recorded from EPC inside the box; (b) average monthly temperature; (c) cumulative monthly precipitation

In addition to the vertical stress distributions, lateral stresses, geosynthetic displacements and strains, and vertical and lateral deformations were evaluated in Abutment A as part of the long-term field instrumentation data assessment. The results related to lateral stresses are presented in Appendix B (Figures B11 to B15). Lateral stress measurements from the RPCs showed higher lateral stresses during spring and summer seasons and lower lateral stresses during fall and winter seasons. It was observed that the instruments were sensitive to seasonal variations. Temperature correction factor was not provided by the manufacturer and temperature correction was not applied to the stresses measured by the RPCs. This may contribute to the observed fluctuation of stresses with seasonal variations.

The lateral geotextile displacements and strains and backfill deformations (Appendix B, Figures B16 to B26) were not significantly influenced by seasonal variations although some of the deformation gages stopped working properly three to six months after construction. The maximum geosynthetic strains measured in the field were less than 0.5 %, which were less than FHWA's required design geosynthetic strain level of 2%. The deformations in the backfill did not show a significant change after construction.

Figures 6.3.55 and 6.3.56 (Abutment A) and Figures 6.3.57 and 6.3.58 (Abutment B) show results obtained from monitoring of the lateral movements of facing blocks as the structure got loaded with the placement of the slab and trucks parked on top of the slab. The results show that although there was a continuous outward deflection of the facing blocks in both abutments, in abutment A the magnitude of the maximum recorded value was 4.5 mm (0.18 in.) and in abutment B, it was 2.3 mm (0.1 in.). The increase in facing deflections at the time of the truck load tests are cumulative of deformation of the facing due to the truck loads and live loads after the GRS-IBS was open to traffic.

The results obtained from the settlement cells after construction period are shown in Figure 6.3.59. The maximum observed foundation settlement was less than 3 mm (0.12 in.).

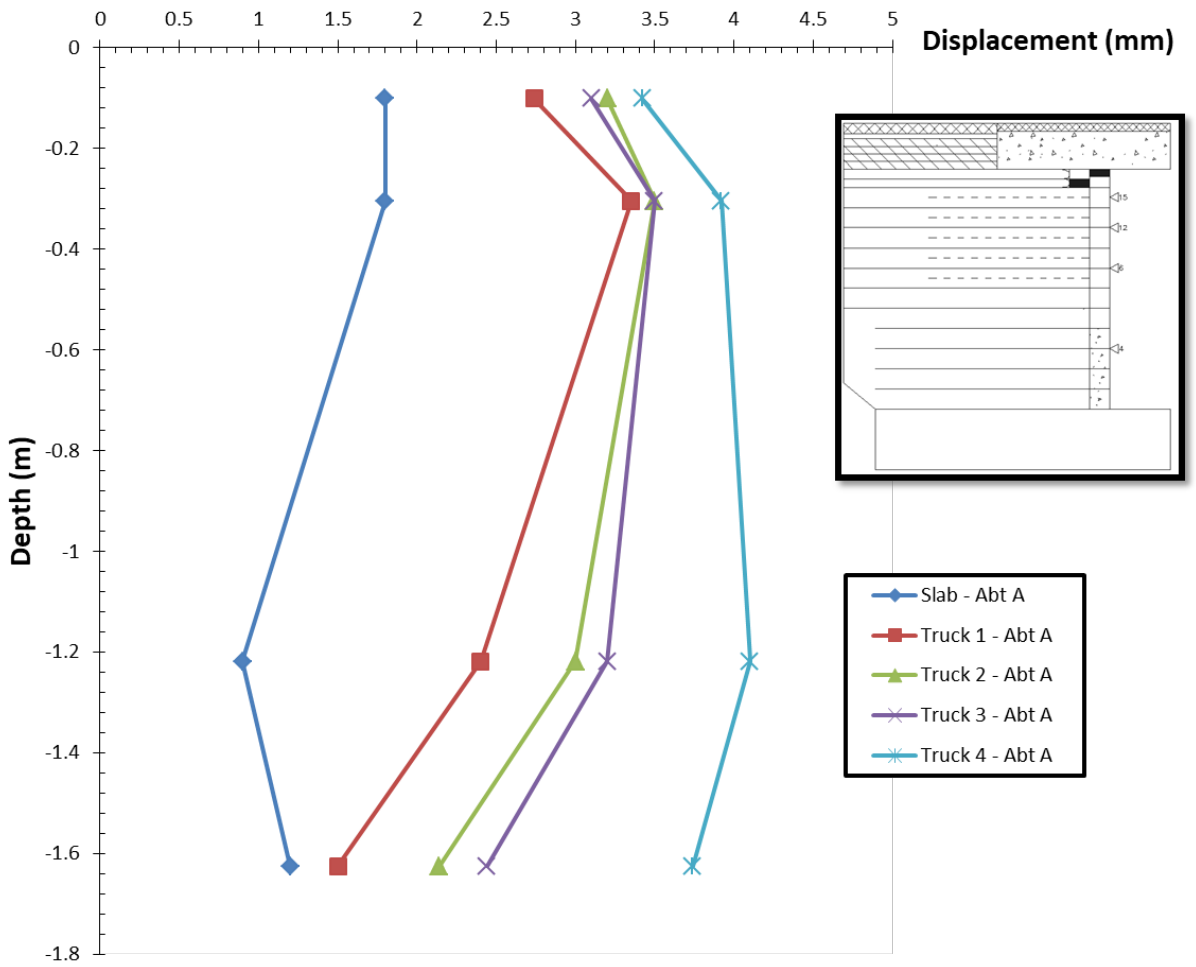

Fig. 6.3.55: Lateral movements of facing blocks in middle section of Abutment A

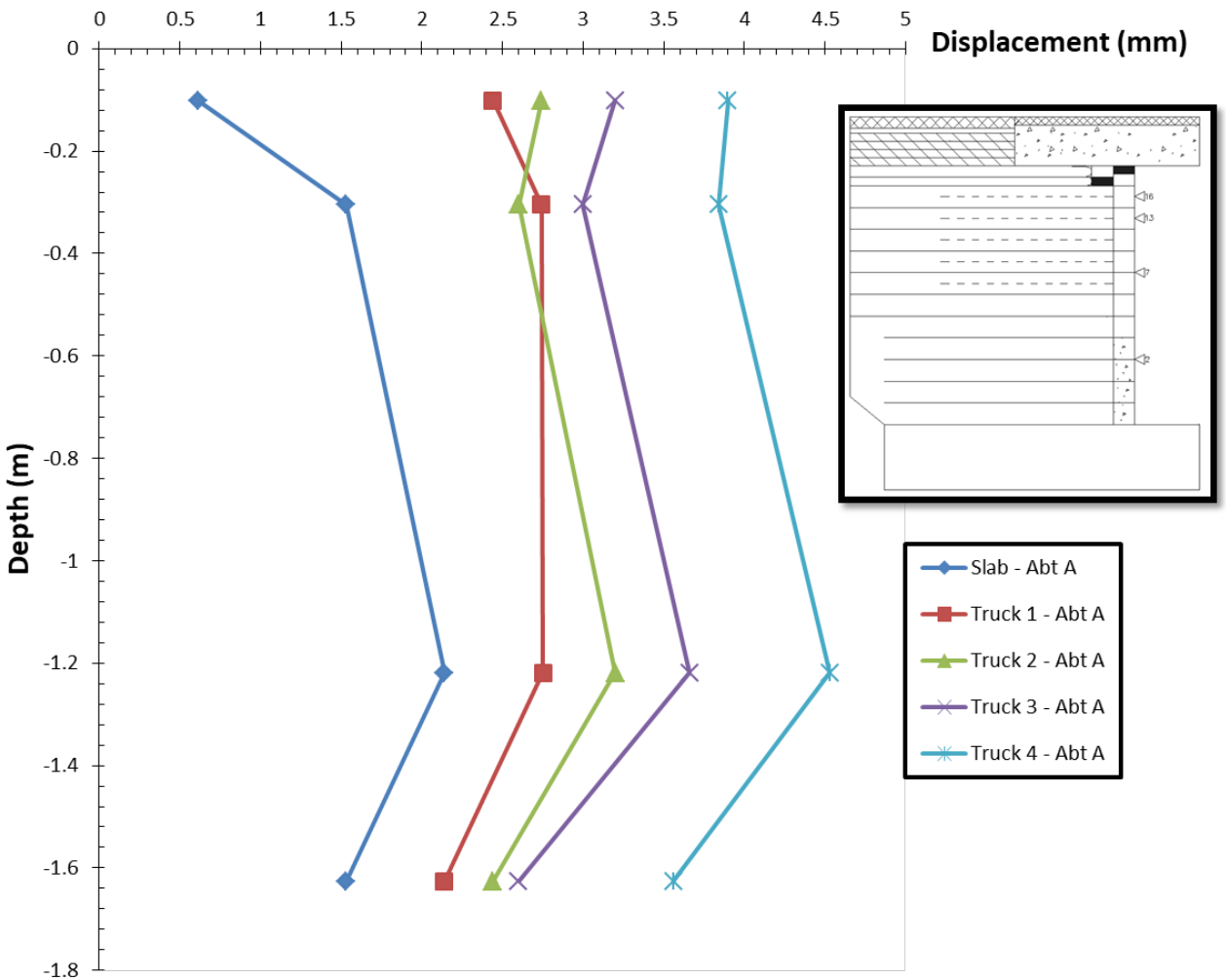

Fig. 6.3.56: Lateral movements of facing blocks in north side of Abutment A

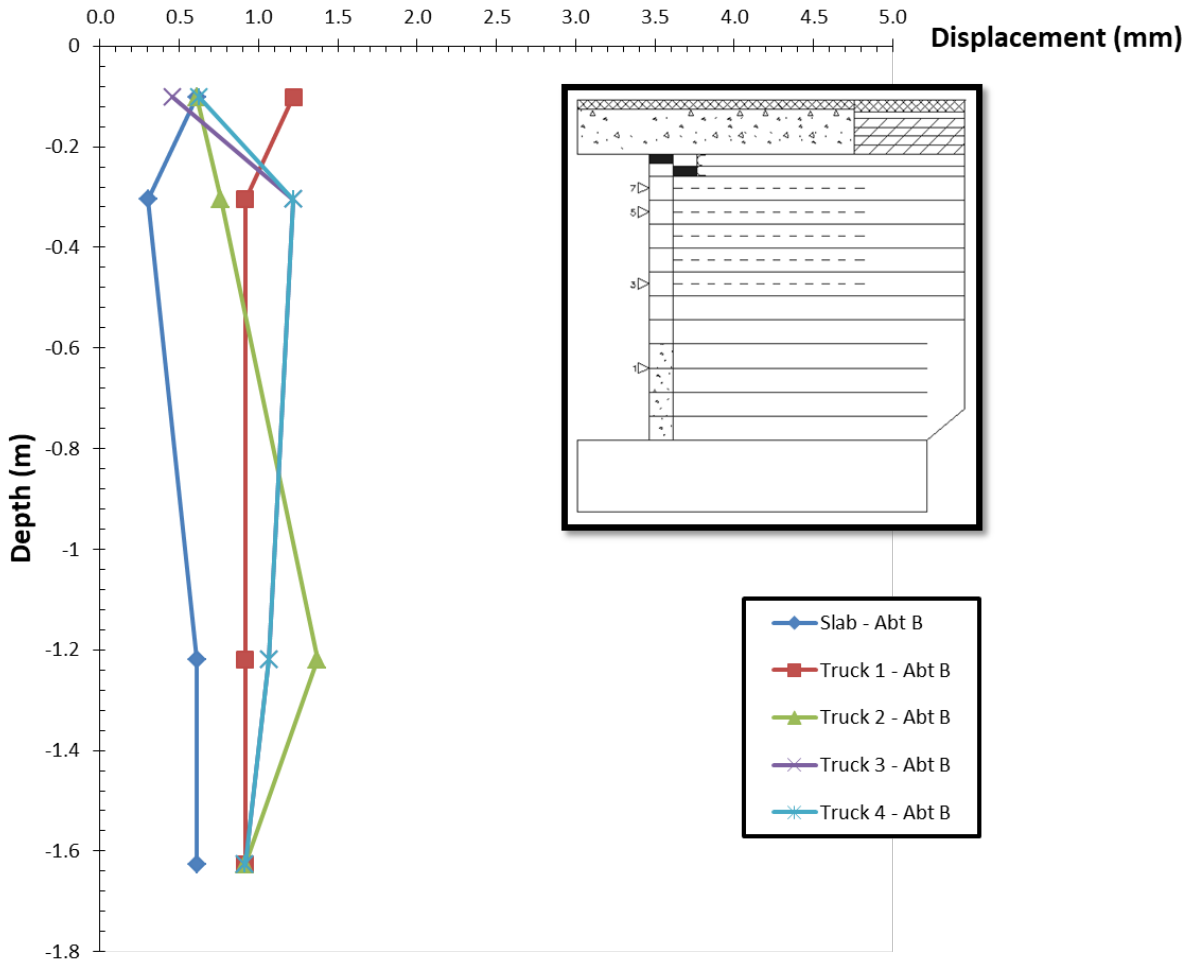

Fig. 6.3.57: Lateral movements of facing blocks in middle section of Abutment B

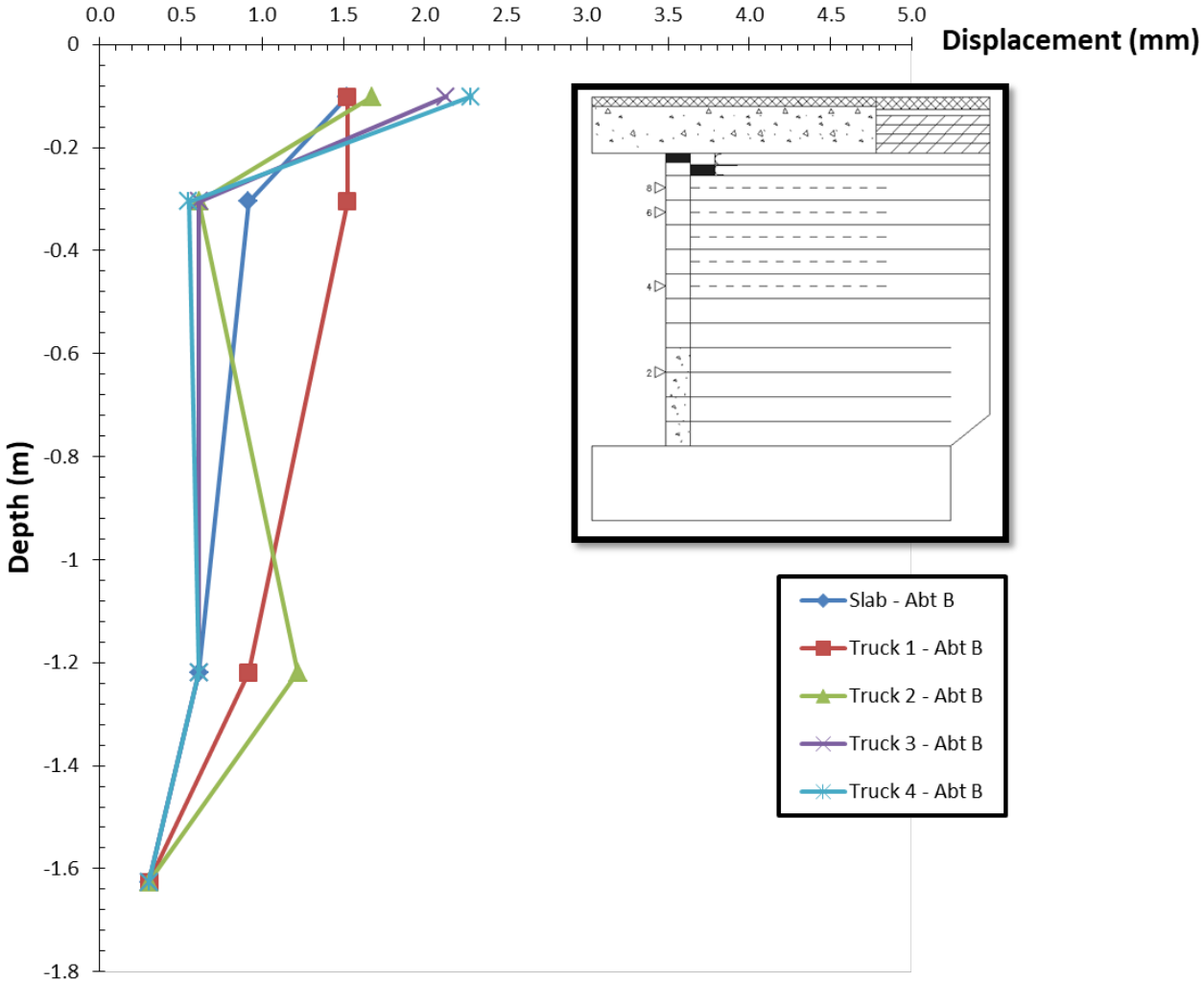

Fig. 6.3.58: Lateral movements of facing blocks in north side of Abutment B

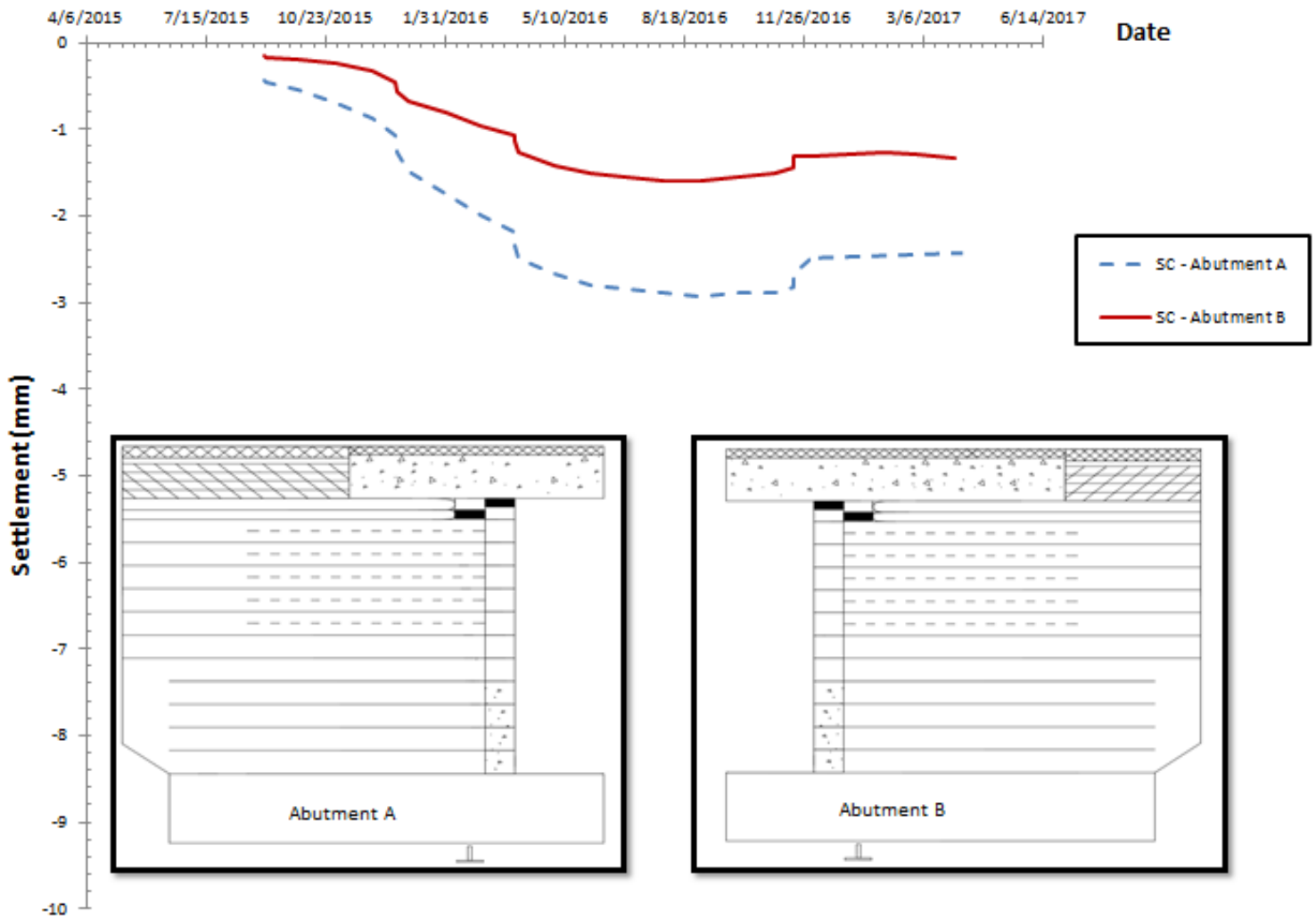

Fig. 6.3.59: Settlement below the reinforced soil foundation after construction in Abutments A and B

Water content reflectometers allow measurement of volumetric water content of the soil. The gravimetric water content of the soil can be obtained using the soil density and the measured volumetric water content or specific gravity of the soil and the volumetric water content. In this project, the volumetric water content of the soil measured by the water content reflectometers was converted to gravimetric water content using specific gravity (Gs) of the foundation soil and backfill, which have Gs values of 2.7 and 2.65 respectively. The results obtained from WCRs installed in Abutments A and B are shown in Figures 6.3.60 and 6.3.61 respectively. As discussed in section 6.2.8, the WCRs were installed in the foundation soil and in the first and last backfill layers of both abutments A and B. WCR installed in the foundation soil of abutment A was not functioning properly and the result from this WCR is not included in Figure 6.3.60. The results show that the water content of the backfill in first and last layers were 1 to 1.5% in both abutments A and B. The water content obtained from the WCRs are in good agreement with water content measured using field density gauge tests that showed the water content of the backfill to be 1 to 1.4%. The water content of the foundation soil in abutment B was around 1.9%. The water content of the backfill slightly increased after construction. This could occur due to infiltrations into the abutment from the surroundings. The water content of the backfill material showed an increase at times where higher precipitation was recorded. However, the water content of the foundation soil in abutment B did not show alteration during and after construction.

The WCRs were also used to measure temperature through sensors embedded inside them. Temperature readings obtained from the WCRs in Abutments A and B are shown in Figure 6.3.62. The results show that the temperature in the backfill and foundation soil shows changes with seasonal variations. The temperature was maximum during summer season and minimum during winter season. In addition, peak temperature readings were observed from WCRs installed in the last layers of Abutments A and B. This could occur because the WCRs are located close to the super-structure and they are exposed to the environment outside the abutment more than the WCRs installed in the first layer and the foundation soil. Temperature readings obtained from the WCRs were compared with temperature readings measured by thermistors embedded in the EPCs. The WCRs were installed right next to EPCs in the first and last backfill layers of both Abutments A and B. Figure 6.3.63 shows comparison of temperature measured in the first and last backfill layers of both Abutments A and B using WCRs and EPCs. The results show that temperature measured by WCRs and EPCs have similar trends and very close magnitude of measured temperature over 2.5 years of monitoring period. However, the temperature measured by using the two instruments showed variation with temperature obtained from nearby weather station (Figure 6.3.54 b), which may occur due to insulation effect of the backfill material and the geotextile reinforcement.

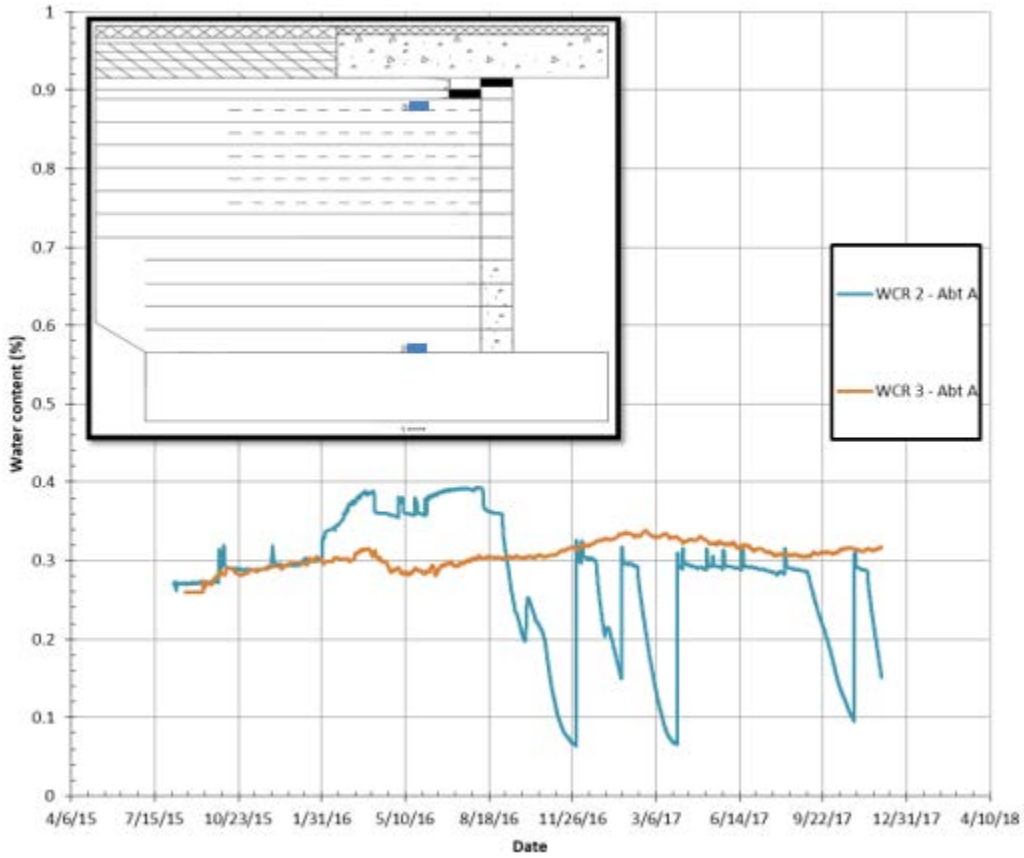

Fig. 6.3.60: Gravimetric water content in backfill in Abutment A

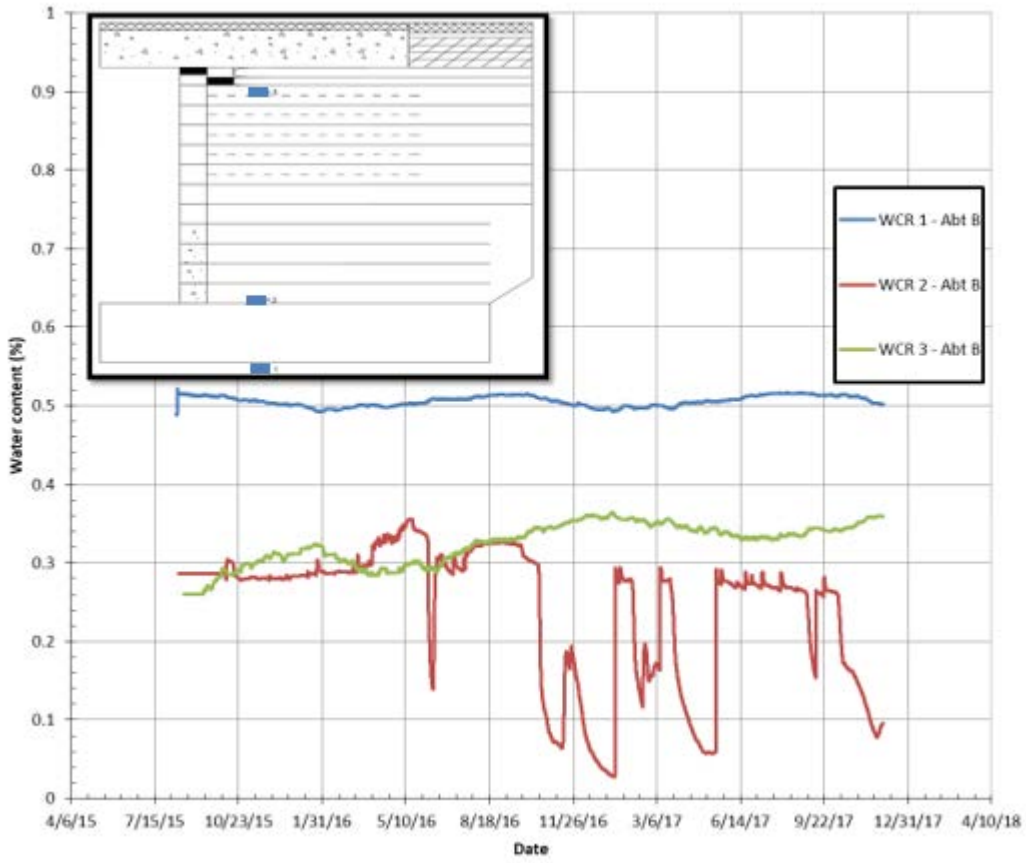

Fig. 6.3.61: Gravimetric water content in backfill and foundation soil in Abutment B

(a)

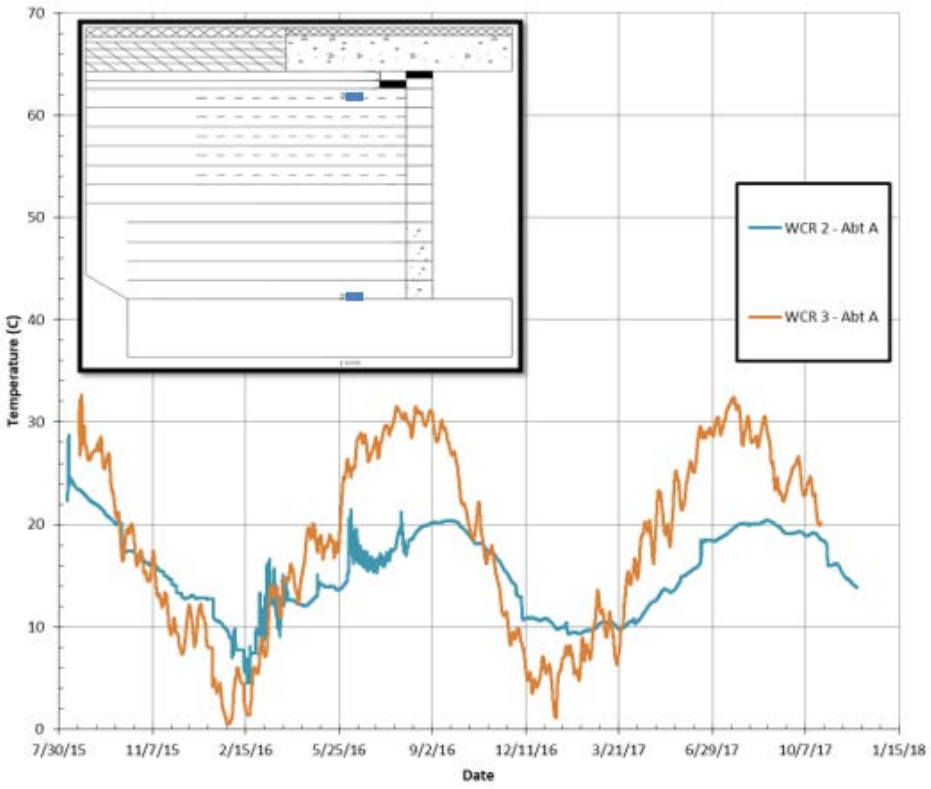

(b)

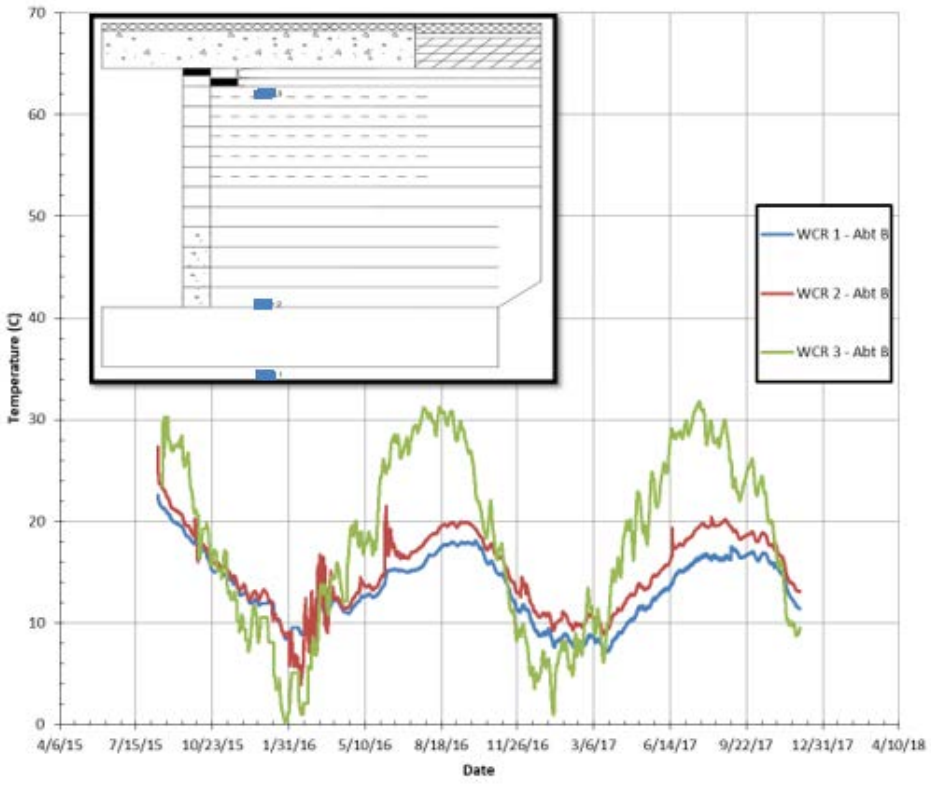

Fig. 6.3.62: Temperature measurement in backfill and foundation soil: a) Abutment A; b) Abutment B

(a)

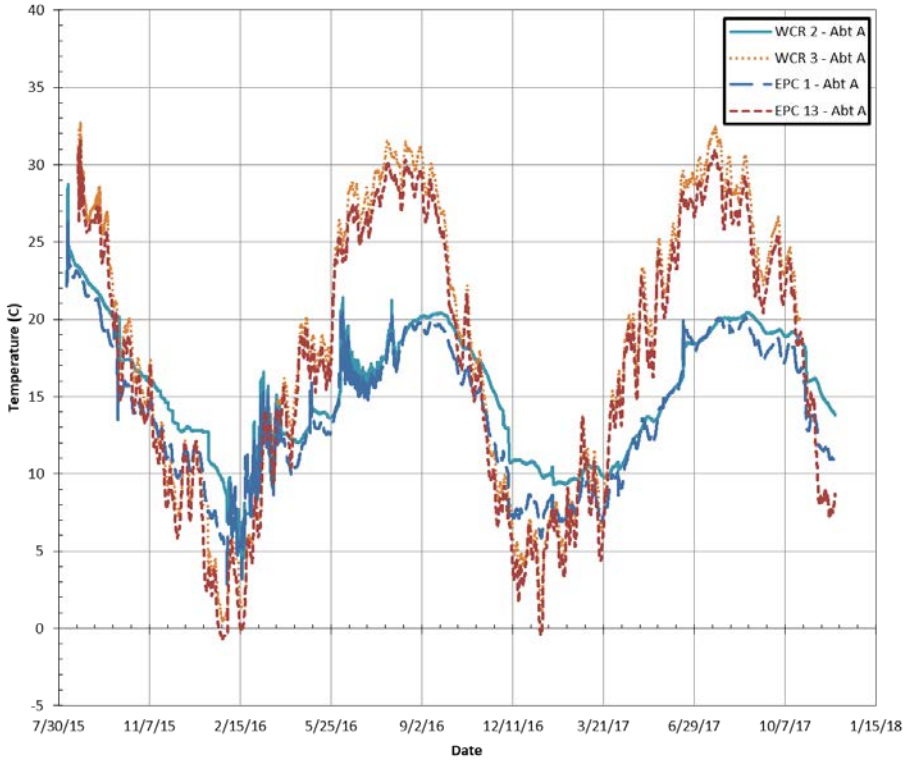

(b)

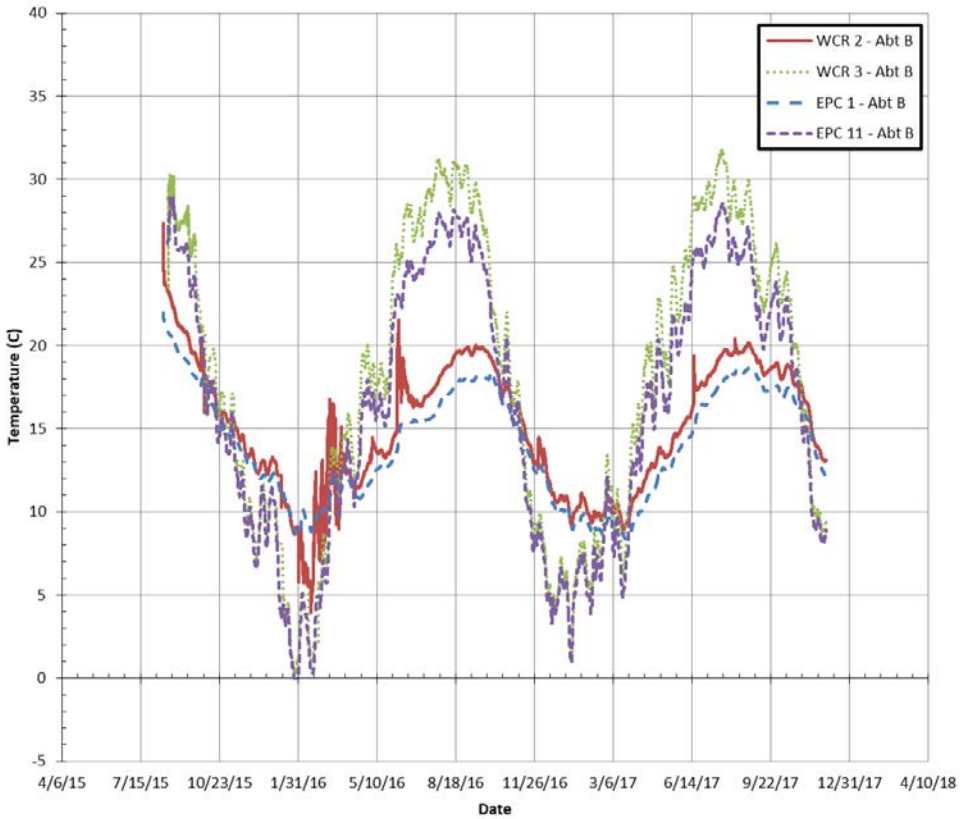

Fig. 6.3.63: Comparison of backfill temperature measurements using WCRs and EPCs: a) Abutment A; b) abutment B

6.4 SUMMARY OF MAIN FINDINGS FROM FIELD MONITORING

The main purpose of the field monitoring was to study the behavior of a GRS-IBS structure under field loading and boundary conditions. The field monitoring program was implemented to monitor the performance the GRS-IBS in relation to stresses, strains, deformations, and water content and temperature aspects. The key findings from this study are presented as follows:

- Based on the observations of the vertical stress distribution profiles after the placement of the slab, the measurements obtained from the field from the middle of the abutment were in agreement with the theoretical AASHTO 2:1 and FHWA Boussinesq stress distribution methods.
- Wider beam seat will result in a larger contact area between the superstructure and the abutment which also means a smaller applied pressure from superstructure. The abutment with wider beam seat showed a better overall performance in terms of vertical stress distribution, maximum lateral displacement of facing, and total foundation settlement.
- The lateral earth pressure distribution based on recorded stresses may be interpreted as relatively uniform distribution along the abutment height. This distribution is closer to the stress distribution estimated based on Wu's method but with much higher magnitudes.
- The presence of secondary reinforcement or close reinforcement spacing has an effect in reducing both the vertical and lateral stresses in the GRS-IBS abutment.
- Tensile strain distribution increases with depth in the top section of the abutment, but then decreases in layers close to the foundation. The overall trend of distribution with depth was reasonably uniform.
- The staged loading on reinforcement layers with different configurations (i.e. bearing bed zone and primary reinforcement) showed that the closely spaced reinforcement (bearing bed zone) appears to have an effect in reducing strains in the geotextile and backfill.
- Calculated T_0 values from strain gages installed right behind the facing blocks, ranges from 0.8 to 1.2 kN/m (4.6 to 6.9 lb/in) with a maximum value observed at approximately half depth of the abutment. The distribution of the T_0 values with depth follows a reasonably uniform trend. The design recommendation in chapter 8 related to a uniform distribution of reinforcement connection load with depth is supported by the observation from this site.
- The maximum measured strains in the geotextile were less than 0.5%, which were below the maximum allowable geosynthetic strains in design of GRS.
- The maximum observed lateral backfill deformation was less than 2.5 mm (0.1 in.). The strains in the backfill were found to be higher than the global geosynthetic strains.
- Vertical deformation (settlement) of the foundation and lateral facing deformations were very small and below the maximum vertical and lateral deformation allowed by the design of GRS.

- The water content of the backfill measured using water content reflectometers were in good agreement with water content measured using field density gauge tests. Temperature measured in backfill layer close to the super-structure was in agreement with temperature measured outside the abutment. However, temperatures measured in backfill layer close to the foundation was lower than temperature measured outside the abutment, which may occur due to insulation effect of the backfill material and the geotextile reinforcement.

6.5 REFERENCES

Abernathy, C. (2013). "Experimental Projects Construction Report - Geosynthetic Reinforced Soil - Integrated Bridge System (GRS-IBS)." Report No. MT-12-04, Montana Department of Transportation, Montana, November 2013, 26 p.

Abu-Hejleh, N., Zornberg, J. G., Elias V., and Watcharamonthein, J (2003). " Design Assessment Of The Founders/Meadows GRS Abutment Structure." Proceedings of Annual Meeting, Transportation Research Board, Washington, D.C. (CD-ROM).

Adams, M.T., and Saunders, S.A. (2007). "Upper Ouachita National Wildlife Refuge GRS Abutments for Replacement Bridges." Presentation by Adams, M., and Saunders, S.A., FHWA.

Adams, M.T., Nicks, J.E., Stabile, T., Wu, J.T.H., Schlatter, W., and Hartmann, J. (2012). "Geosynthetic Reinforced Soil Integrated Bridge System Interim Implementation Guide." Report No. FHWA-HRT-11-026, Federal Highway Administration, McLean, VA.

Adams, M.T., Nicks, J.E., Stabile, T., Wu, J.T.H., Schlatter, W., and Hartmann, J. (2011). "Geosynthetic Reinforced Soil Integrated Bridge System, Synthesis Report." Report No. FHWA-HRT-11-027, Federal Highway Administration, McLean, VA.

Adams, M.T., Schlatter, W., and Stabile, T. (2011). "Geosynthetic Reinforced Soil Integrated Bridge System." EuroGeo4 Paper number 271.

Adams, M.T., Schlatter, W., and Stabile, T. (2007). "Geosynthetic Reinforced Soil Integrated Abutments at the Bowman Road Bridge in Defiance County, Ohio." Proceedings of Geo-Denver, 2007, pp. 01-11.

Allen, T.M., and Bathurst, R.J. (2001). "Prediction of Soil Reinforcement Loads in Mechanically Stabilized Earth (MSE) Walls." Report No. WA-RD 522.1, Washington Department of Transportation, Washington, 2001.

Allen, T.M., Christopher, B.R., and Holtz, R.D. (1992). "Performance of a 41-Foot High Geotextile Wall." Report No. WA-RD 257.1, Washington Department of Transportation, Washington, 1992.

Bathurst, R.J., Walters, D., Vlachopoulos, N., Burgess, P., and Allen, T.M. (2000). "Full Scale Testing of Geosynthetic Reinforced Walls." ASCE Special Publication, Proceedings of GeoDenver 2000.

Benjamim, C.V.S., Bueno, B.S., and Zornberg, J.G. (2007). "Field Monitoring Evaluation of Geotextile-Reinforced Soil-Retaining Walls." Geosynthetics International, April, Vol. 14, No. 2, pp. 100-118.

Berg, R.R., Christopher, B.R. and Samtani, N.C. (2009). "Design and Construction of Mechanically Stabilized Earth Walls and Reinforced Soil Slopes." FHWA NHI-10-024 Vol I and NHI-10-025 Vol II, U.S. DOTFHWA-NHI-09-083 and FHWA GEC-011, Federal Highway Administration, Washington, D.C., 2009, pp 306 (Vol I) and pp. 378 (Vol II).

Bloser, S., Shearer, D., Corradini, K., and Scheetz, B. (2012). "Geosynthetically Reinforced Soil-Integrated Bridge Systems (GRS-IBS) Specification Development for PennDOT Publication 447." Publication No. 447 (10-14), Pennsylvania Department of Transportation.

Budge, A., Dasenbrock, D., Mattison, D., Bryant, G., Grosser, A., Adams, M., and Nicks, J. (2014). "Instrumentation and Early Performance of a Large Grade GRS-IBS Wall." Geo-Congress 2014 Technical Papers@ sGeo-characterization and Modeling for Sustainability, ASCE.

Bueno, B.S., Benjamim, C.V.S., and Zornberg, J.G (2005). "Field Performance of a Full-Scale Retaining Wall Reinforced with Nonwoven Geotextiles." Slopes and Retaining Structures Under Seismic and Static Conditions, 2005, pp. 1-9.

Christopher, B.R. (1993). "Deformation Response and Wall Stiffness in Relation to Reinforced Soil Wall Design." Ph.D. Dissertation, Department of Civil Engineering, Purdue University, West Lafayette, IN, 354 p.

Christopher, B.R. (2013). "Review of June 18, 2013 GRS-IBS Showcase at Clarkson University, Potsdam, New York and St. Lawrence County Wall Visits." Memorandum by Christopher, B.R.

Coduto, P.D., Yeung, M.R., and Kitch, W.A. (2011), "Geotechnical Engineering: Principles and Practices", Pearson Higher Education, Inc., New Jersey, U.S.A

Desai, C.S., and Hoseiny, K.E.E. (2005). "Prediction of Field Behavior of Reinforced Soil Wall Using Advanced Constitutive Model." Journal of Geotechnical and Geoenvironmental Engineering, ASCE, Vol. 131, No. 6, pp. 729-739.

FHWA (2014). "Yauco Bridges PR-2 Km 20.5 Instrumentation." FHWA Presentation, Sent by Alzamora, D., Federal Highway Administration.

Jiang Y., Han, J., Parsons R. L., and Cai H. (2015). "Field Monitoring of MSE Walls to Investigate Secondary Reinforcement Effects." Report, The Kansas Department of Transportation, Kansas.

Helwany, S.M.B., Wu, J.T.H., and Froessl, B. (2003). "GRS Bridge Abutments-an Effective Means to Alleviate Bridge Approach Settlement." Geotextiles and Geomembranes, Vol. 21, pp. 177-196.

Helwany, S.M.B., Wu, J.T.H. et al (2012). "Seismic Design of Geosynthetic Reinforced Soil Abutments". Web document Report 187, National Cooperative Highway Research Program, Washington D.C. (January 2012).

Ho, S.K. and Rowe, R.K. (1996). "Effect of Wall Geometry on the Behaviour of Reinforced Soil Walls." Geotextiles and Geomembranes, Vol. 14, pp. 521-541.

Holtz, R.D. and Lee, W.F. (2002). "Internal Stability Analyses of Geosynthetic Reinforced Retaining Walls." Report No. WA-RD 532.1, Washington State Department of Transportation, January, 379 p.

Ketchart, K. and Wu, J.T.H. (1996). "Long-Term Performance Tests of Soil-Geosynthetic Composites." Report No. CDOT-CTI-96-1, Colorado Department of Transportation, Denver, CO.

Ling, P. and Leshchinsky, D. (1996). "Mesa Walls: Field Data Reduction, Finite Element Analysis, and Preliminary Design Recommendations." Report to Tensar Earth Technologies, Inc., Atlanta, GA.

Morrison, K. F., Harrison, F. E., Collin J. G., Dodds A., and Arndt B. (2006). "Shored Mechanically Stabilized Earth (SMSE) Wall Systems Design Guidelines." Report No. FHWA-CFL/TD-06-001, Federal Highway Administration.

Saghebfar, M., Abu-Farsakh, M., Ardah A., Chen, Q., and Fernandez, B.A. (2016). " Performance monitoring of Geosynthetic Reinforced Soil Integrated Bridge System (GRS-IBS) in Louisiana." Geotextiles and Geomembranes 45 (2017) 34-47.

Stulgis, R.P. (2006). "Full-Scale MSE Test Walls." Proceedings of the 19th Geosynthetic Research Institute Conference, 2005.

TFHRC (2013). "Instrumentation and Monitoring Program on GRS-IBS." FHWA Presentation, Sent by Alzamora, D., Federal Highway Administration.

Vennapusa, P., White, D. J., Klaiber, F.W., Wang, S., and Gieselman, H. (2012). "Geosynthetic Reinforced Soil for Low-Volume Bridge Abutments." Report No. IHRB Project TR-621, Iowa Department of Transportation, Ames, IA, January 2012.

Wu, J.T.H., Ketchart, K., and Adams, M.T. (2001). "GRS Bridge Piers and Abutments." Report No. FHWA-RD-00-038, Federal Highway Administration, McLean, VA.

Wu, J.T.H., Ketchart, K., and Adams, M.T. (2001). "GRS Piers and Abutments." Report No. FHWA-RD-00-038, Federal Highway Administration, McLean, VA.

Wu, J.T.H., Lee, K.Z.Z., Helwany, S.B., and Ketchart, K. (2006a). "Design and Construction Guidelines for Geosynthetic-Reinforced Soil Bridge Abutments with a Flexible Facing." Report No. 556, National Cooperative Highway Research Program, Washington, DC.

Wu, J.T.H., Pham, T.Q., and Adams, M.T. (2013). "Composite Behavior of Geosynthetic Reinforced Soil Mass." Report No. FHWA-HRT-10-077, Federal Highway Administration, McLean, VA.

Zornberg, J.G., Abu-Hejleh, N., and Wang, T. (2001). "Geosynthetic-Reinforced Soil Bridge Abutments." Geotechnical Fabrics Report, Vol. 19, No. 2, March, pp. 52-55.

7 NUMERICAL INVESTIGATION

A series of numerical simulations were carried out by KU in this study to extend the investigation of GRS from the laboratory tests as discussed in Section 5 and GRS-IBS from the field tests as discussed in Section 6. Numerical simulations of Geosynthetic-Reinforced Soil (GRS) structures allow investigating the performance of GRS structures under both serviceability and limit strength states. Numerical models were firstly calibrated and validated against laboratory or field test data to the reliability and accuracy of the models that simulate the behavior of GRS structures. Once the models were properly calibrated, the numerical study was then performed involving a parametric study related to: (a) the experimental data generated as ended part of the soil-geosynthetic interaction tests as discussed in Section 5, (b) the performance of FHWA GRS piers as discussed in Section 4.1.3.8, and (c) the monitored performance of the VDOT GRS-IBS as discussed in Section 6. In addition, this section includes a numerical analysis to investigate the effect of boundary conditions on the performance of GRS structures. Finally, this section includes a stability analysis of GRS structures to investigate the behavior of GRS structures under a limit state.

FLAC, ABAQUS, and PLAXIS are three commonly used numerical software for geotechnical applications in the United States. FLAC and PLAXIS have been mainly developed for geotechnical applications while ABAQUS has been mainly developed for structural applications. ABAQUS has limited geotechnical models and is not friendly for some geotechnical applications; therefore, it was not selected for the numerical analysis in this study. The soil-geosynthetic interaction tests as discussed in Section 5 were simulated using PLAXIS 2D due to its availability at UT-Austin. FLAC 2D and 3D have a long track record and they have been used for many projects and well verified by researchers and engineers. The unique feature of FLAC 2D and 3D is to have greater flexibility for users to incorporate user-defined constitutive models than ABAQUS and PLAXIS. In this study, the performance of FHWA GRS piers as discussed in Section 6 was simulated using FLAC 3D due to its ability to represent a true 3D condition. The performance of the VDOT GRS structure, on the other hand, was simulated using FLAC 2D. Abu-Farsakh et al. (2018) confirmed that 2D and 3D models of GRS-IBS structures yielded similar numerical results.

After model calibration or verification, three series of numerical parametric studies were conducted to investigate the effects of influence factors (e.g. wall height, reinforcement spacing, backfill and reinforcement properties, facing rigidity, foundation conditions, and loading conditions) on the performance of GRS structures. These parametric studies include: (1) numerical investigation of soil-geosynthetic interaction tests, (2) numerical investigation of GRS piers, and (3) numerical investigation of GRS-IBS structures. The influence factors investigated in each parametric study are presented in Table 7.1. The key influencing factor, geosynthetic reinforcement vertical spacing, was investigated at 0.2 m (8 in), 0.4 m (16 in), and 0.6 m (24 in). Structure heights ranged from 2 m (6.6 ft), 3 m (10 ft) to 6 m (20 ft). All the parameters used in the numerical study were unfactored. The effects of key influence factors on the performance of GRS structures (e.g. maximum tension and connection force in geosynthetic reinforcement,

facing deformation, additional vertical stress induced by loading, and settlement) were evaluated as part of the parametric study.

Table 7.1: Influence factors investigated in the parametric study

Case	Wall	Fill	Geosynthetic	Fill/geosynthetic	Foundation	Load
Soil-geosynthetic interaction	N/A	Frictional angle, dilation angle, cohesion	Stiffness, strength	Coefficient of interaction	N/A	Normal stress
GRS piers	Height, facing rigidity	Frictional angle, dilation angle	Stiffness, strength, spacing	coefficient of interaction	Incompressible	Confining stress, uniform vertical stress
GRS-IBS	Height, facing rigidity	Frictional angle, dilation angle	Stiffness, strength, length, spacing	coefficient of interaction	Compressibility	Footing load, surcharge

7.1 CONSTITUTIVE MODEL SELECTION

7.1.1 SOILS AND FACING BLOCKS

Constitutive models were selected to properly represent the behavior of reinforced backfill, retained soil, foundation, wall facing blocks, and geosynthetic reinforcement. The wall facing blocks are often masonry blocks, which were modeled as discrete elastic bricks with interfaces. The foundation soil was modeled using a linearly-elastic model due to its incompressibility for most cases. The retained soil was represented by a linearly-elastic perfectly-plastic material with the Mohr-Coulomb failure criterion. The selection of the constitutive model for the reinforced backfill was carefully evaluated as it is particularly important for the behavior of GRS structures. Accordingly, an elastoplastic model (so-called Cap-Yield model, as available in FLAC), which has been successfully used to characterize the compression and shear hardening/softening behavior of reinforced backfill (Huang et al. 2013), was used in this study. The Cap-Yield model simulates soil behavior using three types of hardening laws: (1) a cap hardening law, to capture the volumetric power law behavior observed in isotropic compression tests, (2) a friction-hardening law, to reproduce the hyperbolic stress-strain law behavior observed in drained triaxial tests, and (3) a contraction/dilation law to model irrecoverable volumetric strain taking place as a result of

soil shearing. It combines the features of the Mohr-Coulomb failure criterion, the Cam-Clay model volumetric cap yield criterion, and the Duncan-Chang stress-dependent hyperbolic behavior. This advanced model is capable of accounting for both shear and compression yielding. Of particular importance is that this model accounts for confining stress and soil dilation, which are critical for the behavior of the GRS structure since recent research has shown that closely-spaced geosynthetic reinforcement can minimize soil dilation (Pham, 2009). Therefore, the Cap-Yield model was used to simulate the behavior of the backfill soil used in VDOT GRS-IBS since laboratory tests results (i.e., triaxial tests) were available. Unfortunately, triaxial test results of the backfill soil used in FHWA GRS piers were not available at the time when the numerical simulation was conducted. Therefore, the backfill soil used in FHWA GRS piers was simulated using a linearly elastic-perfectly plastic model with the Mohr-Coulomb failure criterion. The linearly elastic-perfectly plastic model has been found to simulate similar behavior of geosynthetic-reinforced walls as the stress-dependent model (e.g. the Cap-Yield model by Jiang et al. (2018); the hyperbolic model by Hatami and Bathurst (2005)).

7.1.2 GEOSYNTHETIC REINFORCEMENT

Geosynthetic reinforcement was modeled as linearly-elastic cable elements in the FLAC 2D software or linearly-elastic geogrid elements in the FLAC 3D software. Interfaces were assigned or attached to both sides of the structural elements. The interfaces between facing blocks, block and soil, and geosynthetic and soil were modeled using the linearly elastic-perfectly plastic Mohr-Coulomb interface elements (i.e. 0-thickness). Interface properties between block and soil and block and geosynthetic were be determined either experimentally or empirically.

7.1.3 COMPACTION-INDUCED STRESS

Compaction-induced residual stresses, which are identified as the additional lateral stresses in the fill of GRS structures, were considered in the numerical simulations. Literature review shows different techniques used to simulate compaction-induced residual stresses. These techniques include, but not limited to, the compaction model proposed by Duncan and Seed (1986) developed for unreinforced fill, the modified models by Pham (2009) considering the presence of geotextiles or geogrids, and the model by Yang et al. (2013) considering the presence of geocell. In the numerical modeling of GMSE structures, Hatami and Bathurst (2005) modeled the compaction-induced stresses by applying 8 kPa (1.2 psi) distributed pressure on the top of every lift. Huang et al. (2013) simulated the effect of compaction-induced stress by applying additional lateral stress of 10 kPa (1.5 psi) to each lift if a heavy compactor is used or 8 kPa (1.2 psi) if a light compactor is used. In this study, the approach proposed by Hatami and Bathurst (2005) was adopted due to its convenience for application and the numerical results were further verified in the numerical analysis against field data.

7.1.4 REFERENCES

Abu-Farsakh, M., Ardah, A., and Voyiadjis, G. (2018). 3D Finite element analysis of the geosynthetic reinforced soil-integrated bridge system (GRS-IBS) under different loading conditions. Transportation Geotechnics, 15, 70-83.

Duncan, J. M. & Seed, R. B. (1986). Compaction-Induced Earth Pressures Under K0-Conditions. Journal of Geotechnical Engineering, 112(1), 1-22.

Hatami, K. & Bathurst, R. J. (2005). Development and verification of a numerical model for the analysis of geosynthetic-reinforced soil segmental walls under working stress conditions. Canadian Geotechnical Journal, 42(4), 1066-1085.

Huang, J., Han, J., Parsons, R. L. & Pierson, M. C. (2013). Refined numerical modeling of a laterally-loaded drilled shaft in an MSE wall. Geotextiles and Geomembranes, 37, 61-73.

Jiang, Y., Han, J., Zornberg, J., Parsons, R.L., Leshchinsky, D., and Tanyu, B. (2018). Numerical analysis of field geosynthetic-reinforced retaining walls with secondary reinforcement. *Geotechnique*, https://doi.org/10.1680/jgeot.17.P.118.

Pham, T.Q. (2009). Investigating Composite Behavior of Geosynthetic-reinforced Soil (GRS) Mass. Ph.D. dissertation, the University of Colorado at Denver, 358 p.

Yang, X., Han, J., Leshchinsky, D. & Parsons, R. L. (2013). A three-dimensional mechanistic-empirical model for geocell-reinforced unpaved roads. Acta Geotechnica, 8(2), 201-213.

7.2 NUMERICAL INVESTIGATION OF SOIL-GEOSYNTHETIC INTERACTION TESTS

7.2.1 INTRODUCTION

This chapter includes a numerical simulation of the soil-geosynthetic interaction tests previously reported in Chapter 5 of this report. Specifically, this chapter includes a detailed description of the numerical model developed to represent the conditions during testing using the soil-geosynthetic interaction equipment, which was designed to comprehensively assess soil-reinforcement interaction under both working stress and failure conditions. As discussed in Chapter 5, the experimental device was found capable of assessing the mechanical behavior of a geosynthetic-reinforced soil mass considering variable reinforcement vertical spacing. In addition, it was found to facilitate investigation of the interface shear stress transfer mechanisms as well as visualization of the kinematic response of soil particles adjacent to the geosynthetic reinforcements. In addition to the findings that resulted from direct evaluation of the experimental data, additional insight was sought out through numerical simulations. Specifically, the numerical investigation conducted as part of this research component aimed at quantifying, for range of properties beyond those used in the experimental research component, the effect of influence factors (e.g., soil and reinforcement properties) on the soil-reinforcement interaction and the thickness of the shear band.

The numerical simulations included in this section of the report involve parametric evaluations conducted using a numerical model that was calibrated using the experimental results discussed in Chapter 5. As previously discussed, the new experimental device successfully captured key aspects of the soil-reinforcement interaction. The numerical evaluation allowed extrapolating the findings of the experimental efforts to include configurations that are difficult to simulate experimentally in the laboratory. This includes the effect of several key parameters that are expected to control the behavior of reinforced soil structures: (1) reinforcement vertical spacing; (2) normal pressure; (3) soil friction angle; (4) soil cohesion; (5) soil-reinforcement interface friction angle; and (6) reinforcement tensile stiffness.

7.2.2 DEVELOPMENT AND VALIDATION OF THE NUMERICAL MODELS

The objective of the numerical simulations conducted as part of this research component is to extend the results from the laboratory soil-reinforcement interaction tests by examining variables and states (serviceability and strength limits) beyond those investigated experimentally. Specifically, numerical simulations were conducted to investigate the effects of factors influencing the soil-reinforcement interaction and reinforcement interlayer interaction. A description of the details needed for proper modeling of the soil-reinforcement interaction equipment and the materials. In addition, the scope of the numerical simulations is also presented below.

7.2.2.1 SIMULATION OF THE TESTING BOUNDARY CONDITIONS

The boundary conditions for the numerical model used in this research component were selected to represent those of the laboratory experiment. The experimental device had rigid walls on four sides, rigid floor, and flexible top surface. Consequently, the numerical model involved two-dimensional plane strain conditions with horizontal fixities on the vertical boundaries and vertical fixities on the bottom horizontal boundaries (the bottom of the box), as shown in Figure 7.2.1. The front wall had a gap at the central on which a sleeve was installed at the reinforcement exist. This sleeve extended into the box and was modeled at the front wall by extending two boundaries with vertical fixities.

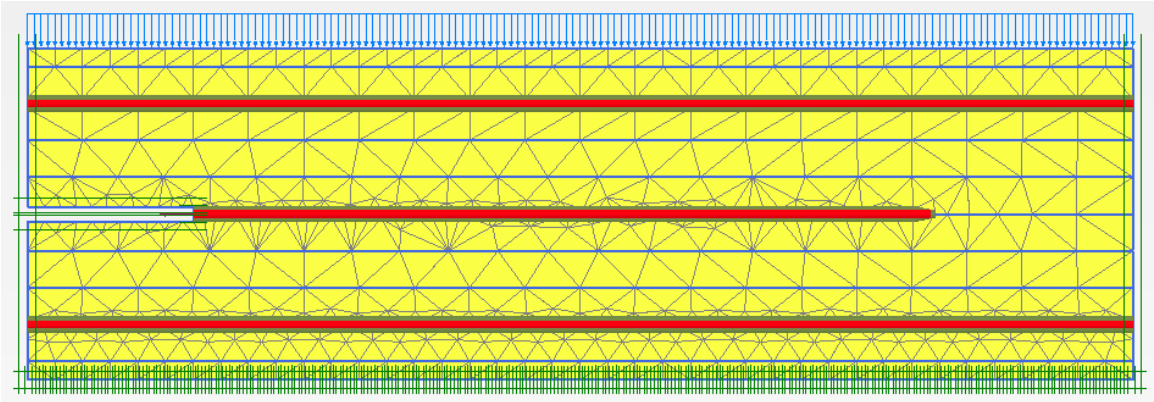

Fig. 7.2.1: View of the numerical model used for simulation of the soil-geosynthetic interaction tests.

7.2.2.2 MATERIALS CONSTITUTIVE MODELS

Constitutive models were selected to properly represent the behavior of the fill material, geosynthetic reinforcement, soil-reinforcement interface, and equipment boundaries. Note that material constitutive models were established for the materials used as baseline in the experimental program (Chapter 5). The reminder of this section discusses the selection of the various constitutive models as well as validation of their parameters against laboratory test results used to experimentally determine the model parameters.

7.2.2.2.1 Fill material (AASHTO No. 8 river-washed pea gravel)

The constitutive model selected for the fill material was carefully evaluated as it is particularly important to properly simulate the behavior of Geosynthetic-Reinforced Soil structures. The fill material was modeled using the Mohr-Coulomb linear elastic, perfectly plastic model. Triaxial compression laboratory tests were conducted to determine the parameters adopted in this study to model the fill material used in the soil-reinforcement interaction tests. Figure 7.2.2 provides a comparison of the AASHTO No. 8 experimental data from triaxial tests to the stress-strain response predicted using the finite elements simulation. The soil stiffness was selected 18,000 kPa (2.6 ksi), the friction angle was selected 37 degrees, and the cohesion intercept was selected 15 kPa (2.2 psi).

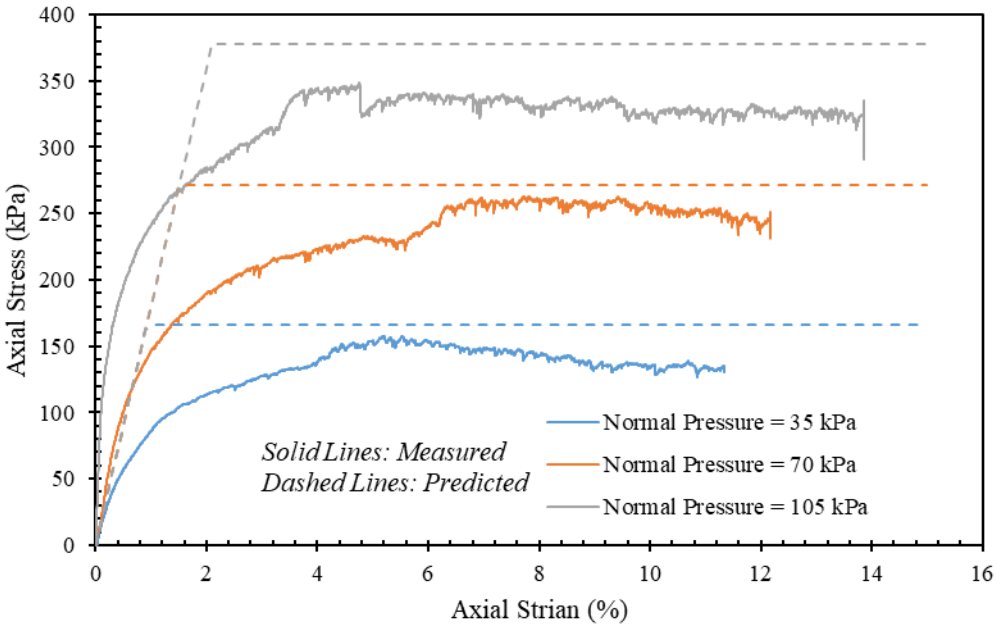

Figure 7.2.2. Comparison between measured triaxial test data and numerically predicted results.

7.2.2.2.2 Geosynthetic reinforcement (HP570 woven geotextile)

A linear elastic constitutive model was selected for the geosynthetic reinforcement. While the tensile behavior of geosynthetic reinforcement may exhibit some nonlinearity at comparatively high tensile strain levels, these levels were not typically reached in the soil-reinforcement interaction tests. The reinforcement stiffness was determined from the tensile stress-strain data measured during the soil-geosynthetic interaction tests on the unconfined portion of the reinforcement. The stiffness values obtained experimentally as part of this investigation were found to be consistent with the reinforcement stiffness reported in the manufacturer specifications for a tensile strain of 2%. The reinforcement stiffness (*EA*) measured using this information was 1,095 kN/m (6.25 kips/in). Figure 7.2.3 shows a comparison between the tensile stress-strain data measured from the unconfined portion of the reinforcement zone and the prediction using the linear elastic model adopted in this study. In addition, the Figure 7.2.shows the nominal values reported in the manufacturer specifications for a 2% strain and for breakage.

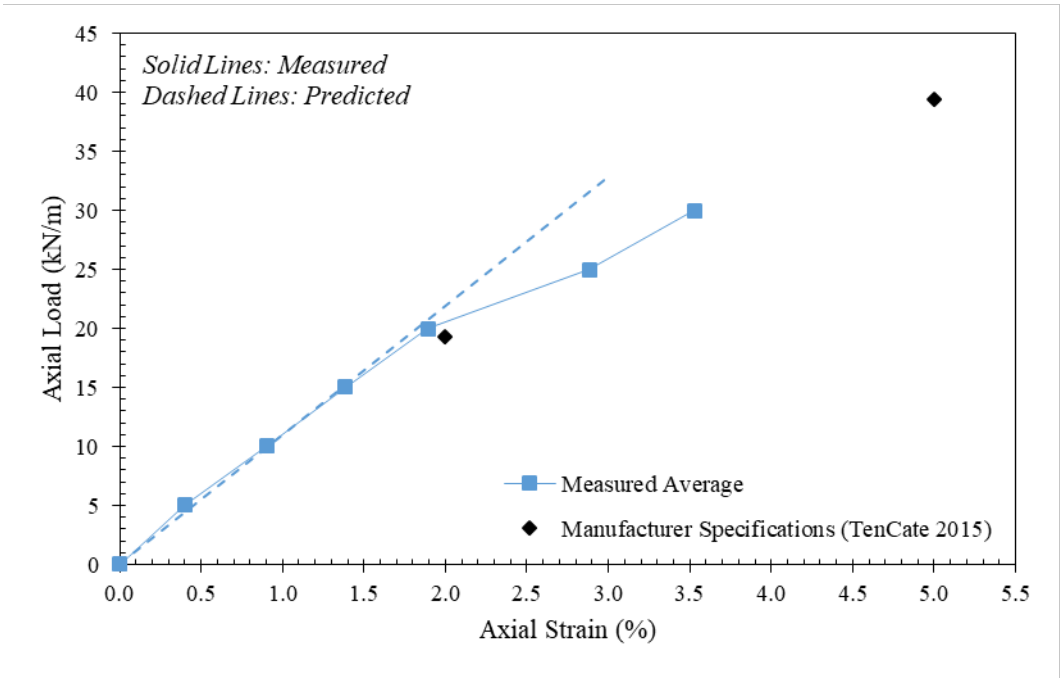

Figure 7.2.3. Comparison between measured reinforcement tensile stress-strain data and values predicted by the linear-elastic model.

7.2.2.2.3 Soil-reinforcement interface (AASHTO No. 8 against HP570 geotextile)

A large-scale direct shear device was used to test the soil-reinforcement interface between the soil and reinforcement materials used as baseline materials in the soil-geosynthetic interaction tests. The constitutive model selected to simulate the interface shear behavior was the linearly-elastic perfectly-plastic Mohr-Coulomb interface model. The parameters used in this model were determined by conducting interface direct shear tests using the materials adopted in this investigation. The shear stiffness was selected as 5,000 kPa (725 psi) and the effective angle of interface friction was selected as 31 deg (the ratio between the angle of interface friction to the angle of internal friction was 0.84).

7.2.2.3 NUMERICAL SIMULATION OF THE EXPERIMENTAL PROCEDURE

Placement of soil layers in the box were simulated using consecutive construction stages. The first and the last layers were 0.025-m (1-in.) thick and the intermediate layers were 0.05-m (2-in.) thick. Additional intermediate stages were introduced at elevations where reinforcement layers were placed. During these stages, reinforcement layers were placed, and soil-reinforcement interface elements were assigned to both sides of the reinforcement layers. The penultimate stage involved the application of the normal pressure on top of the reinforced soil mass. The normal stress applied on top of the reinforced soil mass is less than the target normal stress by stress magnitude equivalent to the overburden pressure exerted by the backfill material at the elevation of the active reinforcement layer (center of the box). The ultimate stage involves the application of prescribed displacement at the free end of the middle (active) reinforcement layer.

7.2.2.4 MODEL VALIDATION

The developed numerical model was validated by comparing laboratory results obtained experimentally from several soil-reinforcement interaction tests with numerically predicted results obtained from the corresponding numerical simulations of the tests. Specifically, the load-displacement curves predicted numerically considering the frontal load were compared against the experimental results. In addition, the reinforcement displacement profiles were compared for both active and passive reinforcement layers obtained numerically and experimentally were compared. Also, the soil displacement profiles across the reinforcement planes obtained numerically and experimentally were compared. The soil-reinforcement interaction tests used in the validation of the numerical model were conducted using various normal stress levels, frontal pullout load (and displacement) levels, and vertical reinforcement spacings.

7.2.2.4.1 Reinforcement frontal pullout load-displacement

Figure 7.2.4 shows a comparison between the force-displacement curves defined using the frontal load, obtained experimentally from soil-reinforcement interaction tests conducted at various normal pressures and the predicted curves obtained from corresponding numerical simulations. Figure 7.2.4a shows the full range of the frontal load-displacement curves, whereas Figure 7.2.4b shows a close-up on the curves at the first 15 mm (0.6 in) frontal displacement range. The curves obtained experimentally and numerically were found to match very well, especially at the early loading stages, which usually corresponds to comparatively low soil-reinforcement relative displacements in reinforced soil systems.

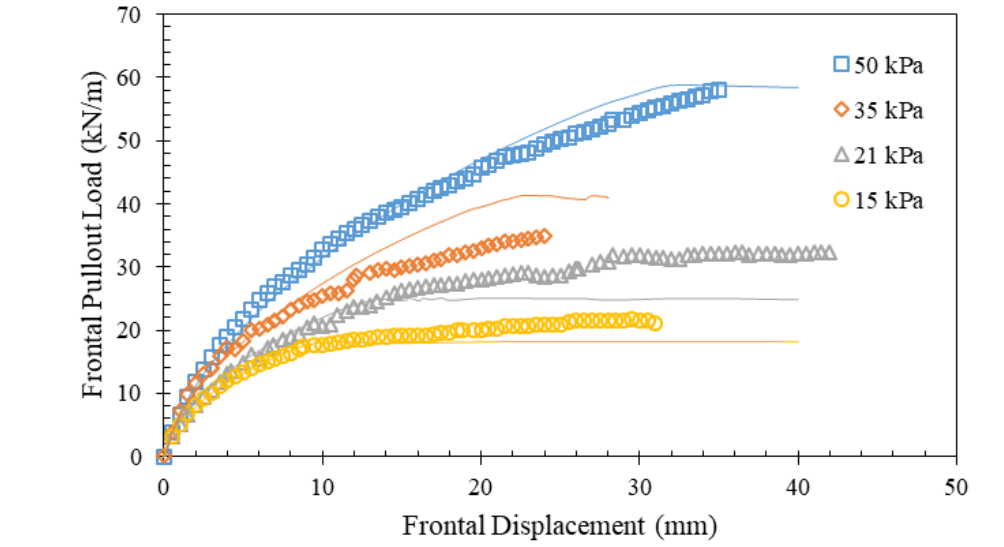

(a)

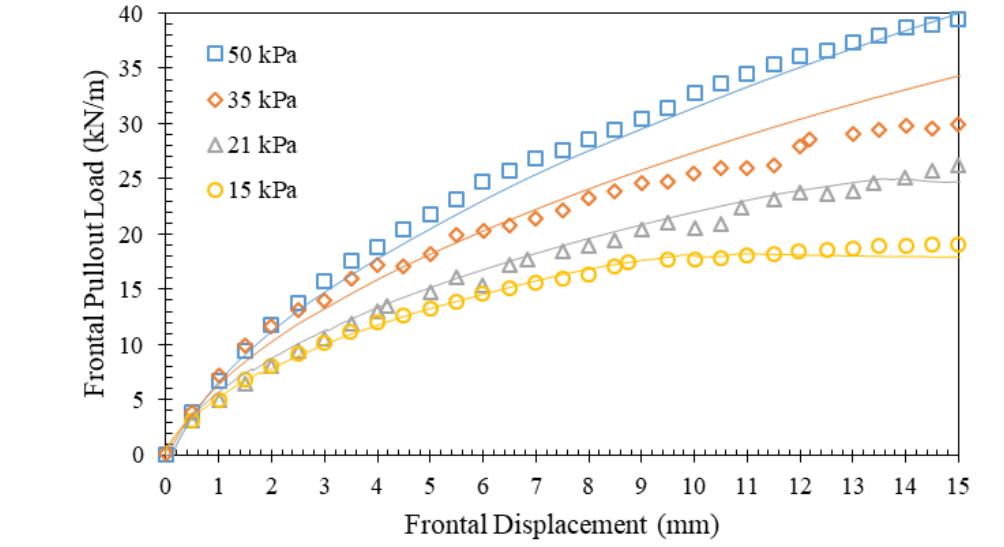

(b)

Figure 7.2.4. Reinforcement frontal pullout load-displacement behavior: (a) full frontal displacement range; (b) first 15 mm (0.6 in) front displacement range.

7.2.2.4.2 Reinforcement displacement profiles

Figure 7.2.5 shows a comparison between the active reinforcement displacement profiles obtained from soil-reinforcement interaction tests, conducted at various loading stages (frontal displacements of 10, 20, and 30 mm (0.4, 0.8 and 1.2 in)), and the numerically predicted curves . Figures 7.2.5a through 7.2.5c show the reinforcement displacement profiles obtained from the experimental tests and the numerical simulations conducted at normal stresses of 50, 21, and 15 kPa (7.3, 3 and 2.2 psi). The displacement profiles obtained experimentally and numerically were found to match very well. Similarly, the displacement

profiles obtained experimentally for the upper passive reinforcement layer were compared against the numerical predictions, as shown in Figure 7.2.6. Also in this case, the displacement profiles obtained experimentally and numerically were found to match very well.

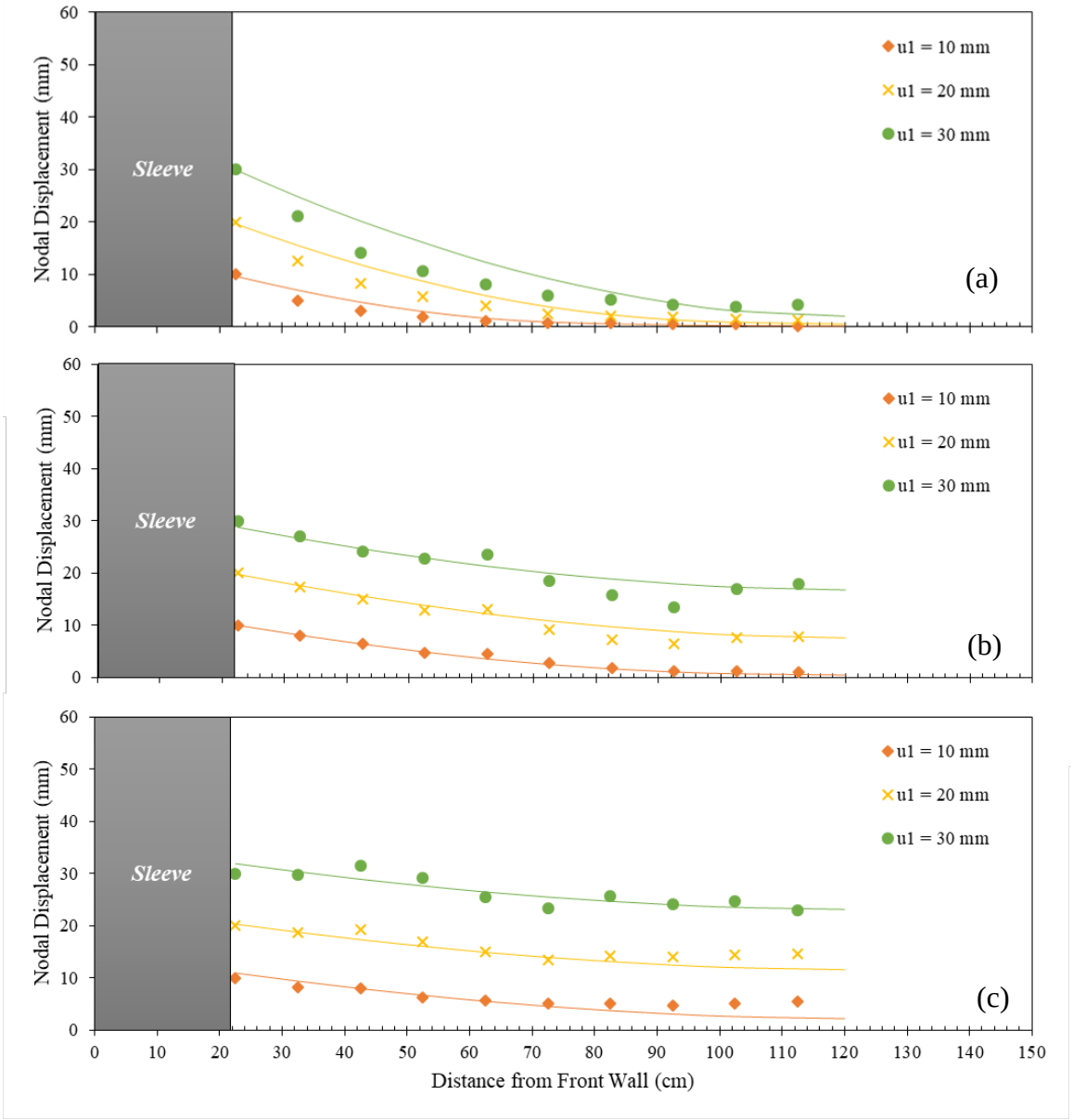

Figure 7.2.5. Active reinforcement displacement profiles: (a) 50 kPa (7.3 psi) normal stress; (b) 21 kPa (3 psi) normal stress; (c) 15 kPa (2.2 psi) normal stress.

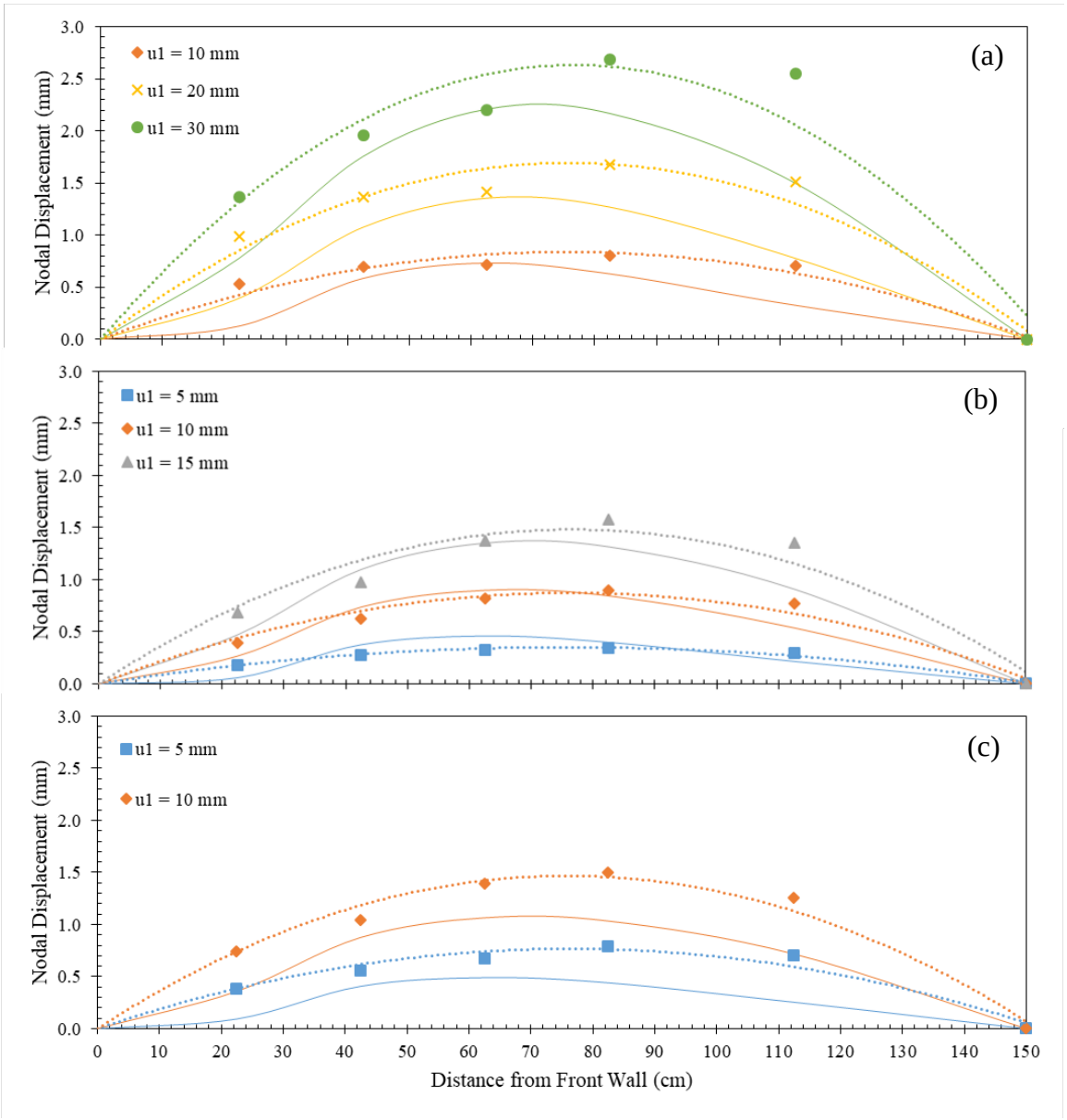

Figure 7.2.6. Upper passive reinforcement displacement profiles: (a) 50 kPa (7.3 psi) normal stress; (b) 21 kPa (3 psi) normal stress; (c) 15 kPa (2.2 psi) normal stress.

7.2.2.4.3 Soil displacement profiles

Figure 7.2.7 shows a comparison between the horizontal soil displacement profiles obtained from soil-reinforcement interaction tests conducted at various loading stages and predicted curves obtained from corresponding numerical simulations. The soil displacement was determined at a vertical cross-section located at 0.3 m (1 ft) from the front wall (7.6 m (25 ft) from the line of loading application). Figures 7.2.7a and 7.2.7b show the reinforcement displacement profiles obtained from experimental tests and numerical simulations conducted at normal stresses of 50 and 21 kPa (7.3 and 3 psi), respectively. The displacement profiles obtained experimentally and numerically were found to match reasonably well.

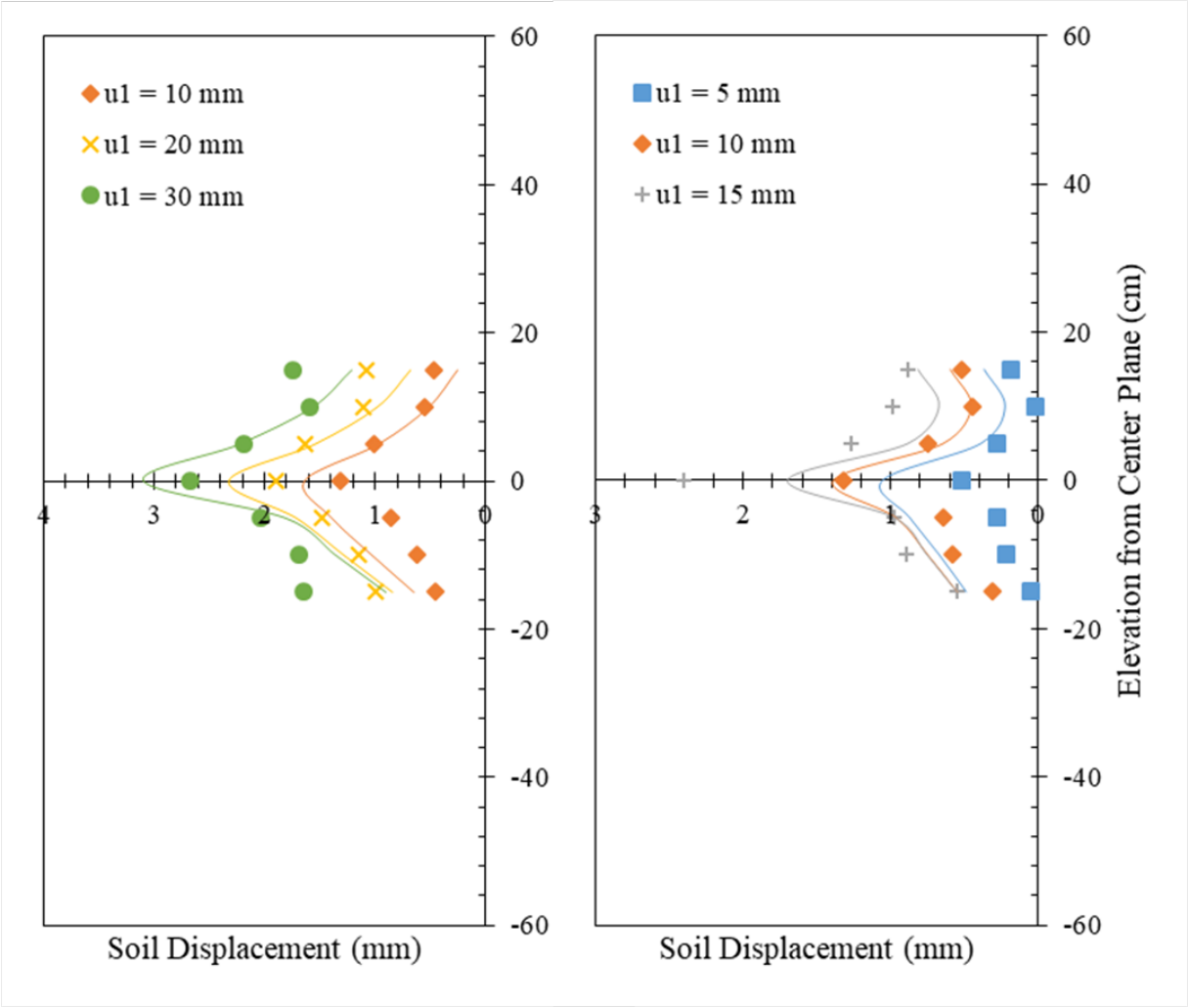

Figure 7.2.7. Horizontal soil displacement profiles: (a) 50 kPa (7.3 psi) normal stress; (b) 21 kPa (3 psi) normal stress.

7.2.2.5 SCOPE OF THE NUMERICAL SIMULATIONS

The numerical investigation conducted as part of this research component involved a series of simulations conducted to evaluate the soil-reinforcement interaction and reinforcement interlayer interaction for both serviceability (small strain) and ultimate strength (large strain) conditions. In addition, a parametric study was also conducted, which aimed at identifying the key factors which have an impact on the thickness of the shear band. In particular, the effect on the soil-reinforcement interaction and reinforcement interlayer interaction of the following parameters was evaluated: (1) reinforcement vertical spacing; (2) normal pressure; (3) soil friction angle; (4) soil cohesion; (5) soil-reinforcement interface friction angle; and (6) reinforcement tensile stiffness. Table 7.2.2 shows the simulation configurations, a total number of 16 numerical simulations were performed in this study.

Table 7.2.2. Numerical simulation configurations

#	Theme	S_v (m)	σ (kPa)	φ (deg)	ψ (deg)	c (kPa)	E_s (kPa)	φ' (deg)	EA (kN/m)
1	Baseline	0.15	50	37	7	15	18000	31	1095
2			15						
3			21						
4	Confining Normal Stress	0.15	35	37	7	15	18000	31	1095
(1)			50						
5			100						
6			200						
7	Soil Friction Angle	0.15	50	37	7	15	18000	31	1095
(1)				50	20				
8						1			
(1)	Soil Cohesion	0.15	50	37	7	15	18000	31	1095
9						30			
10								20	
(1)	Interface Friction Angle	0.15	50	37	7	15	18000	31	1095
11								40	
12									500
(1)	Reinforcement Tensile Stiffness	0.15	50	37	7	15	18000	31	1095
13									2000
14		0.05							
15	Reinforcement Vertical Spacing	0.10	50	37	7	15	18000	31	1095
(1)		0.15							
16		0.20							

7.2.3 PARAMETRIC EVALUATION

7.2.3.1 EFFECT OF REINFORCEMENT SPACING

Figure 7.2.8 shows the frontal load-displacement curves predicted by the numerical simulations conducted with reinforcement vertical reinforcement spacing values ranging from 0.05 to 0.20 m (2 to 8 in.). The results presented in this figure show the effect of the reinforcement spacing on the frontal load-displacement response. As shown by the numerical predictions, It was observed that changing the reinforcement spacing has no effect on the load displacement response, including the maximum load (i.e. pullout resistance). This is consistent with the fact that the soil-reinforcement interface, and its corresponding strength, was the same in the different simulations.

Figure 7.2.9a shows the horizontal soil displacement profiles predicted at the vertical plane located 0.3 m (1 ft) behind the frontal wall (i.e. 7.6 mm (0.3 in) from the point within the geosynthetic where load is applied). The numerical simulations were conducted using

different reinforcement spacings. The displacement profiles shown in Figure 7.2.9a correspond to a 5 mm (0.2 in) frontal displacement of the Central Geosynthetic. It was observed that the location of the passive reinforcement layers reduces the load transfer in the soil mass beyond their locations.

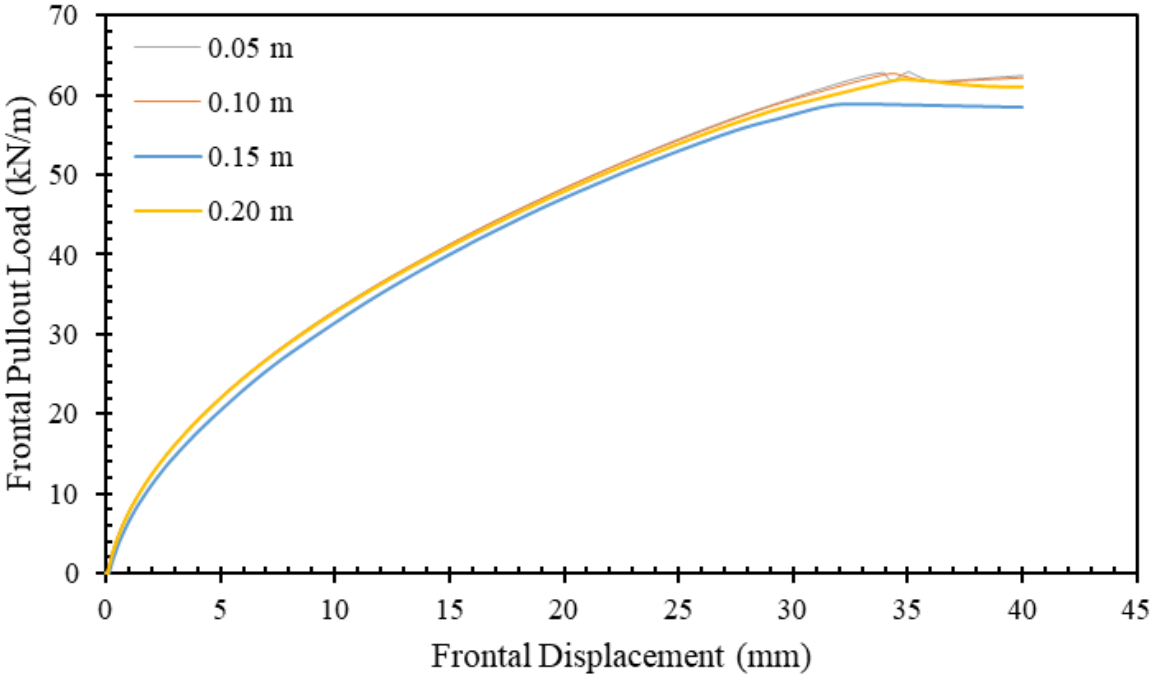

Figure 7.2.8. Reinforcement frontal pullout load-displacement behavior for various reinforcement spacing.

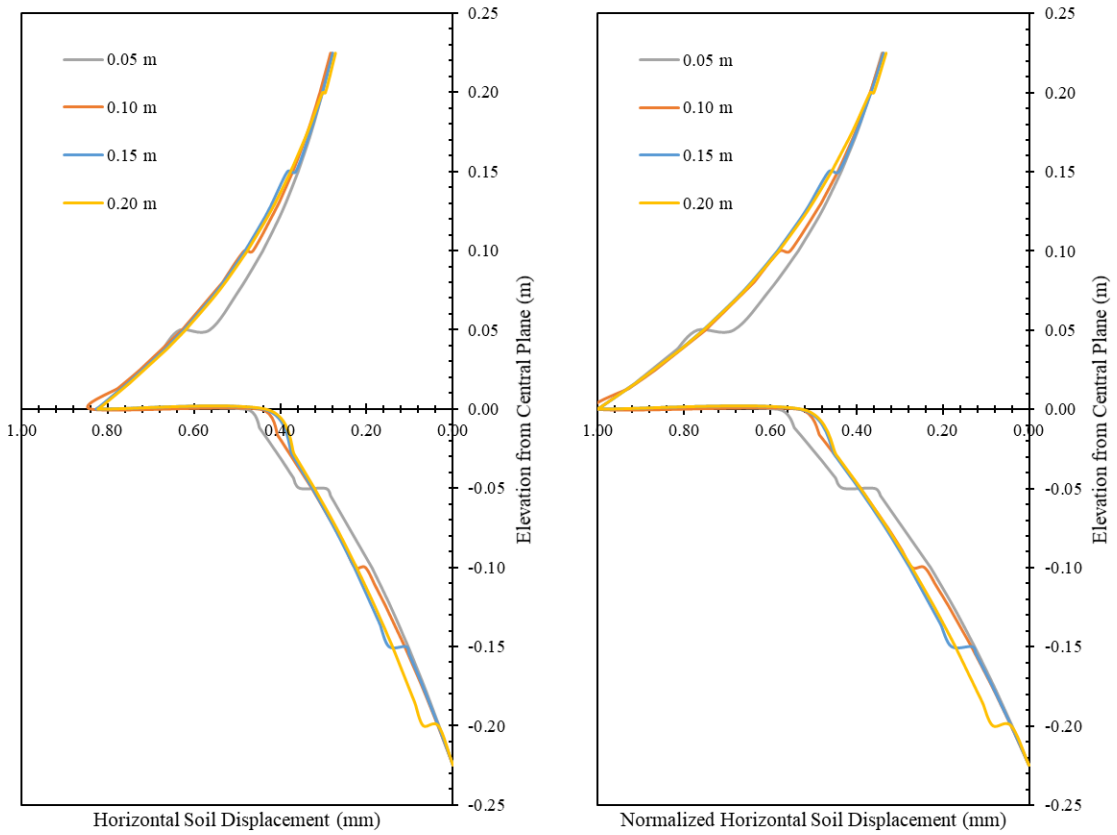

(a) (b)

Figure 7.2.9. Horizontal soil displacement profiles: (a) Absolute displacement; (b) Displacement normalized to the maximum displacement.

7.2.3.2 EFFECT OF NORMAL PRESSURE

Figure 7.2.10 shows the frontal load-displacement curves obtained for numerical simulations conducted at various normal stresses ranging from 15 to 200 kPa (2.25 to 30 psi). This figure shows the effect of the normal stress applied at the active reinforcement elevation on the reinforcement pullout resistance. It was observed that the pullout resistance increases with increasing the normal stress. This is because the soil-reinforcement interface strength increases with increasing the normal stress.

Figure 7.2.11a shows the horizontal soil displacement profiles predicted at the vertical plane located at 0.3 m (1 ft) from the frontal wall (7.6 mm (0.3 in) from the line of load application) for the numerical simulations conducted at the various normal stresses. The displacements shown in Figure 7.2.11a correspond to a 5 mm (0.2 in) frontal displacement of the active reinforcement. It was observed that the soil displacement increases with increasing the normal stress for the same frontal displacement. This is because the soil-reinforcement interface strength increases with increasing the normal stress, which allows for a larger load transfer from the reinforcement (actively loaded) to the soil in vicinity.

Figure 7.2.11b shows the profiles of the horizontal soil displacements normalized to the maximum displacement (i.e., the soil displacement at the soil-reinforcement interface). It was observed that the normalized soil displacement decreases with increasing the normal stress. This is because the shear stiffness of the soil increases with increasing the normal stress providing high resistance to deformation compared to soils with lower normal stresses.

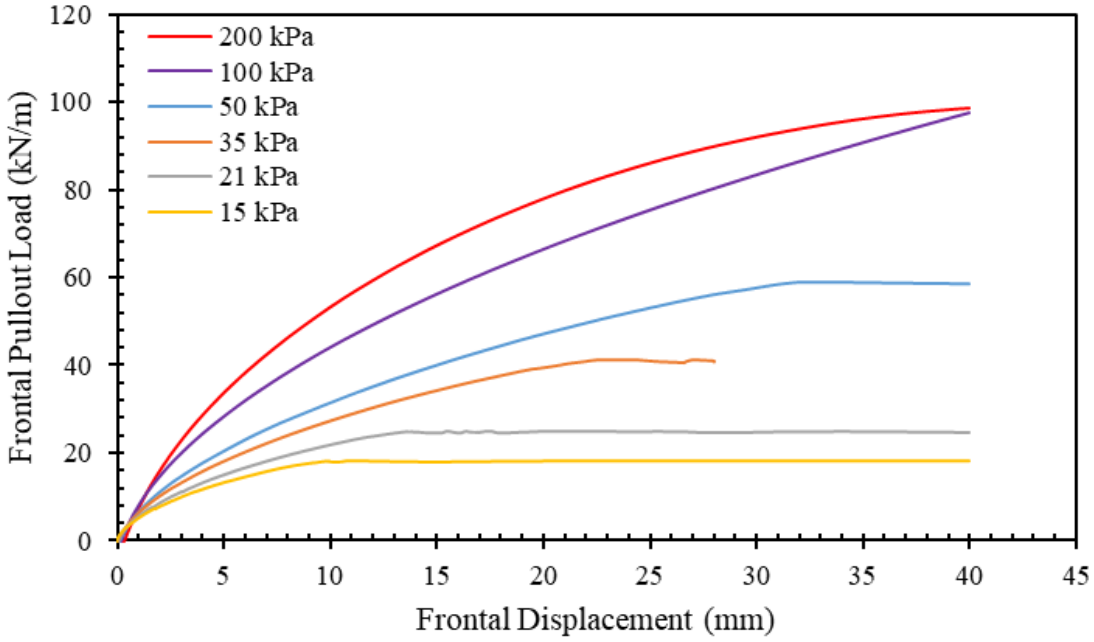

Figure 7.2.10. Reinforcement frontal pullout load-displacement behavior.

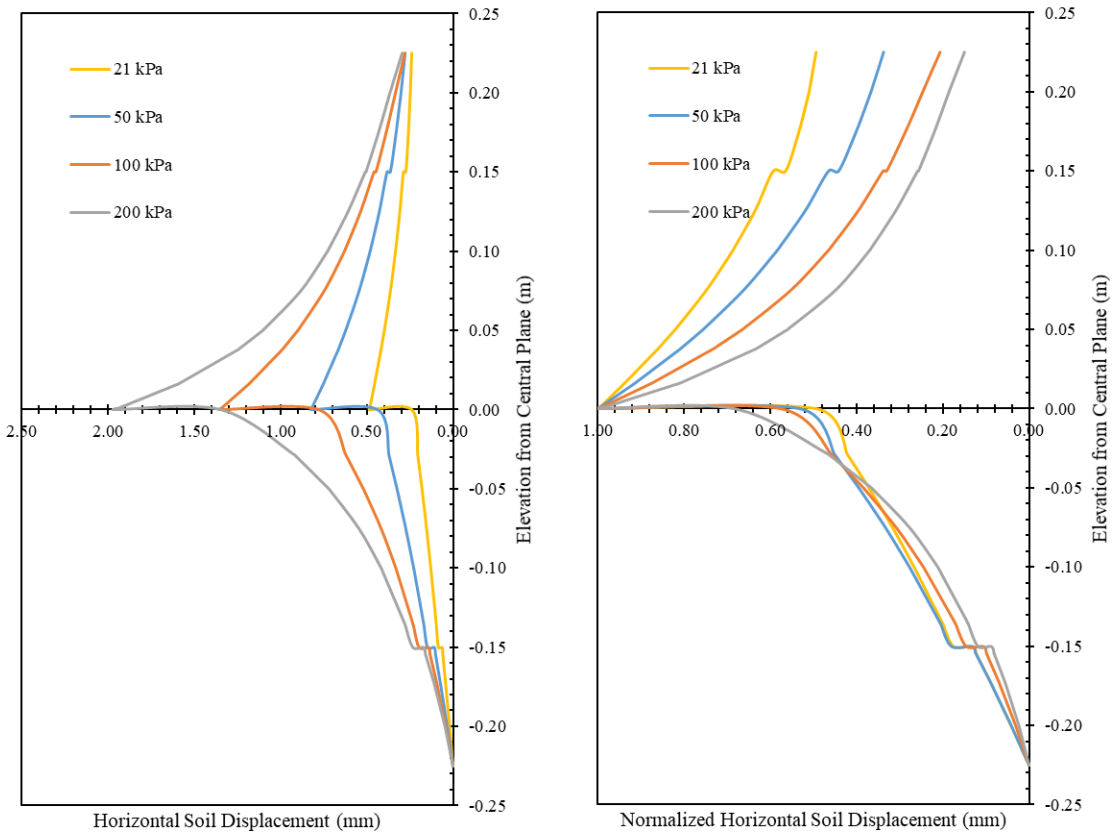

(a) (b)

Figure 7.2.11. Horizontal soil displacement profiles: (a) Absolute displacement; (b) Displacement normalized to the maximum displacement.

7.2.3.3 EFFECT OF SOIL FRICTION ANGLE

Figure 7.2.12 shows the frontal pullout load-displacement curves obtained for numerical simulations conducted using various backfill material friction angles 37 and 50 degrees. This figure shows the effect of the soil friction angle on the reinforcement pullout resistance. It was observed that the ultimate pullout resistance increases with increasing the soil friction angle with negligible effect on the resistance at working stress levels. This is because the soil-reinforcement interface friction angle was kept the same for both simulations. Note that in this comparison the friction angle was changed while the soil-reinforcement interface friction angle was maintained the same. Another comparison was made to assess the effect of the interface friction angle. This way, the impact of the soil strength could be separated from the impact of the interface strength, which is the key parameter in the soil-reinforcement load transfer.

Figure 7.2.13a shows the horizontal soil displacement profiles predicted at the vertical plane located at 0.3 m (1 ft) from the frontal wall (7.6 mm (0.3 in) from the line of load application) from the numerical simulations conducted using two different soil friction angles. The displacements shown in Figure 7.2.13a correspond to a 5 mm (0.2 in) frontal displacement of

the active reinforcement. No effect was observed for the soil friction angle on the horizontal soil displacement for the same frontal displacement. This is because the soil-reinforcement interface strength and soil stiffness remained the same for both simulations. A larger displacement was observed at loading stages beyond the pullout failure of the simulation conducted with the 37-degree soil friction angle.

Figure 7.2.13b shows the profiles of the horizontal soil displacements normalized to the maximum displacement (i.e., the soil displacement at the soil-reinforcement interface). Likewise, no effect was observed on the normalized soil displacement with changing the soil friction angle.

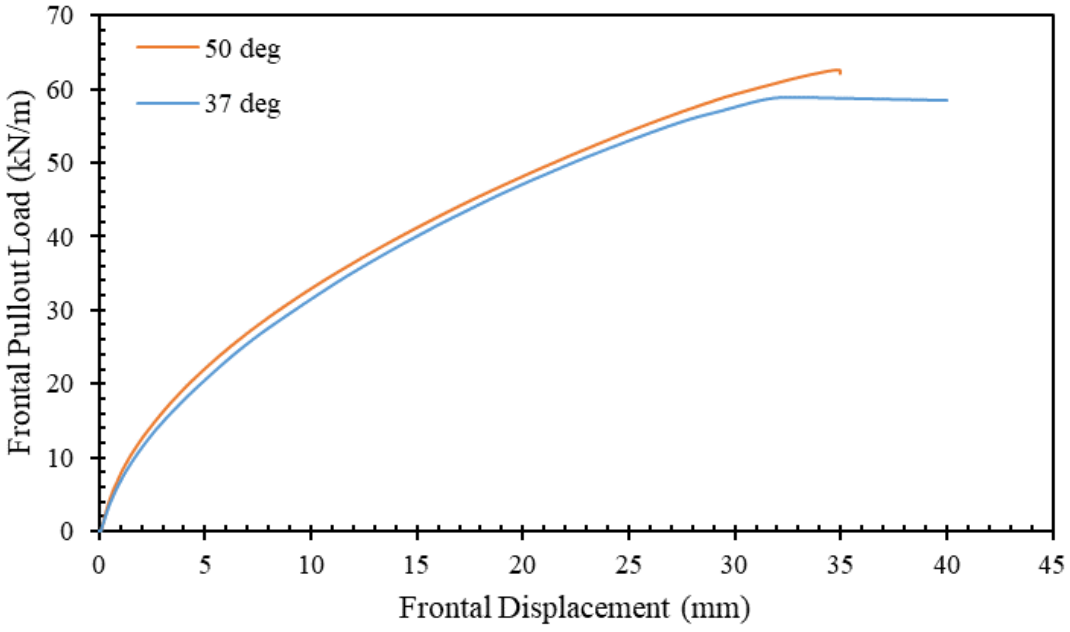

Figure 7.2.12. Reinforcement frontal pullout load-displacement behavior.

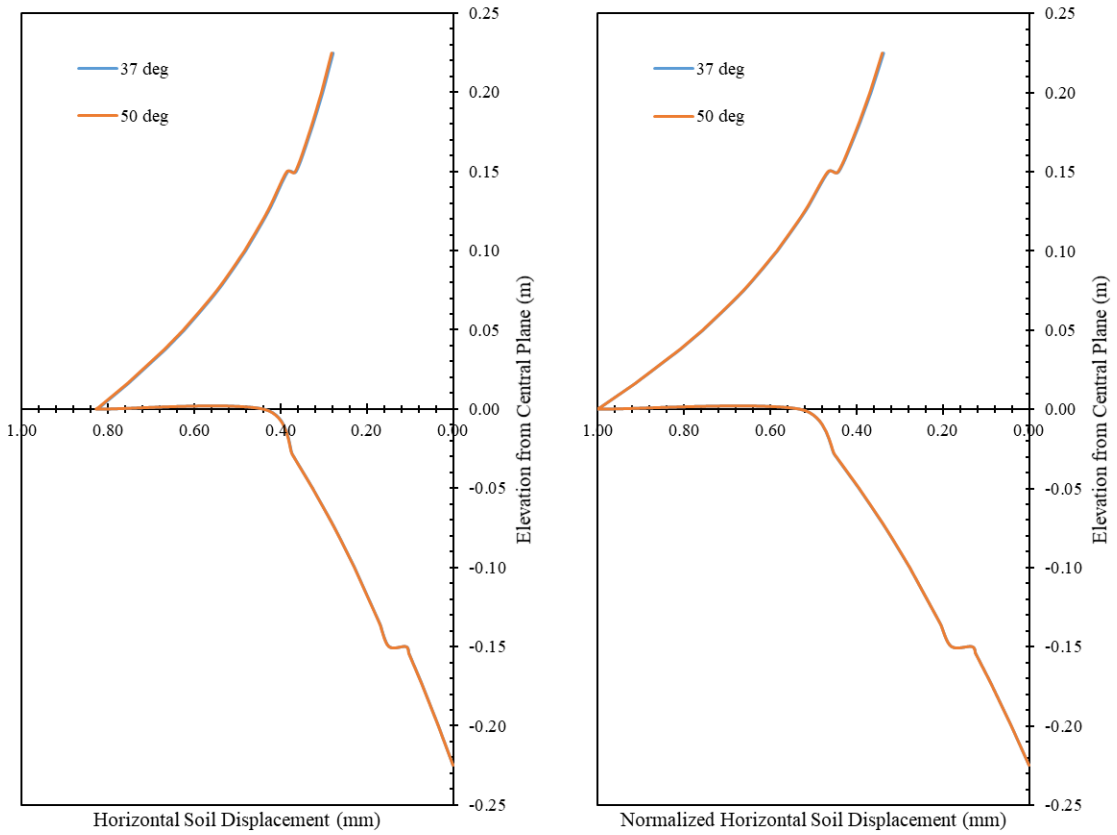

(a) (b)

Figure 7.2.13. Horizontal soil displacement profiles: (a) Absolute displacement; (b) Displacement normalized to the maximum displacement.

7.2.3.4 EFFECT OF SOIL COHESION

Figure 7.2.14 shows the frontal pullout load-displacement curves obtained for numerical simulations conducted using various backfill material cohesion 15 and 30 kPa (2.2 and 4.4 psi). This figure shows the effect of the soil cohesion on the reinforcement pullout resistance. It was observed that the ultimate pullout resistance slightly increases with increasing the soil cohesion with insignificant effect on the resistance at working stress levels. This is because the soil-reinforcement interface friction angle and adhesion were kept the same for both simulations.

Figure 7.2.15a shows the horizontal soil displacement profiles predicted at the vertical plane located at 0.3 m (1 ft) from the frontal wall (7.6 mm (0.3 in) from the line of load application) from the numerical simulations conducted using two different soil cohesions. The displacements shown in Figure 7.2.15a correspond to a 5 mm (0.2 in) frontal displacement of the active reinforcement. No effect was observed for the soil cohesion on the horizontal soil displacement for the same frontal displacement. This is because the soil-reinforcement interface strength and soil stiffness remained the same for both simulations. A larger

displacement was observed at loading stages beyond the pullout failure of the simulation conducted with the 15 kPa (2.2 psi) soil cohesion.

Figure 7.2.15b shows the profiles of the horizontal soil displacements normalized to the maximum displacement (i.e., the soil displacement at the soil-reinforcement interface). Likewise, no effect was observed on the normalized soil displacement with changing the soil cohesion.

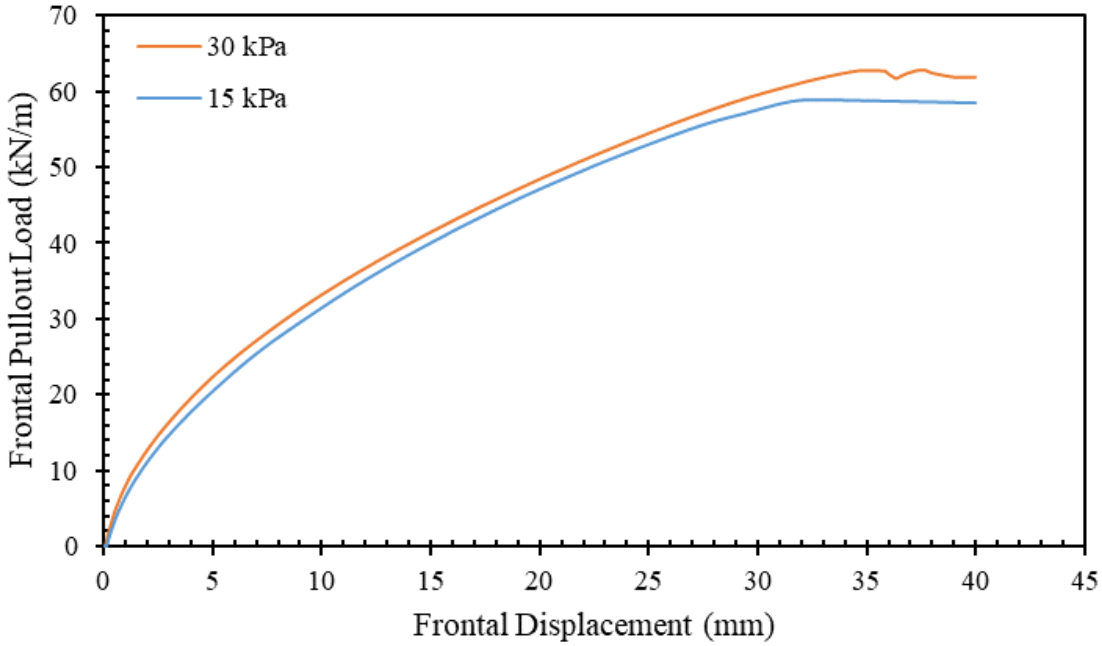

Figure 7.2.14. Reinforcement frontal pullout load-displacement behavior.

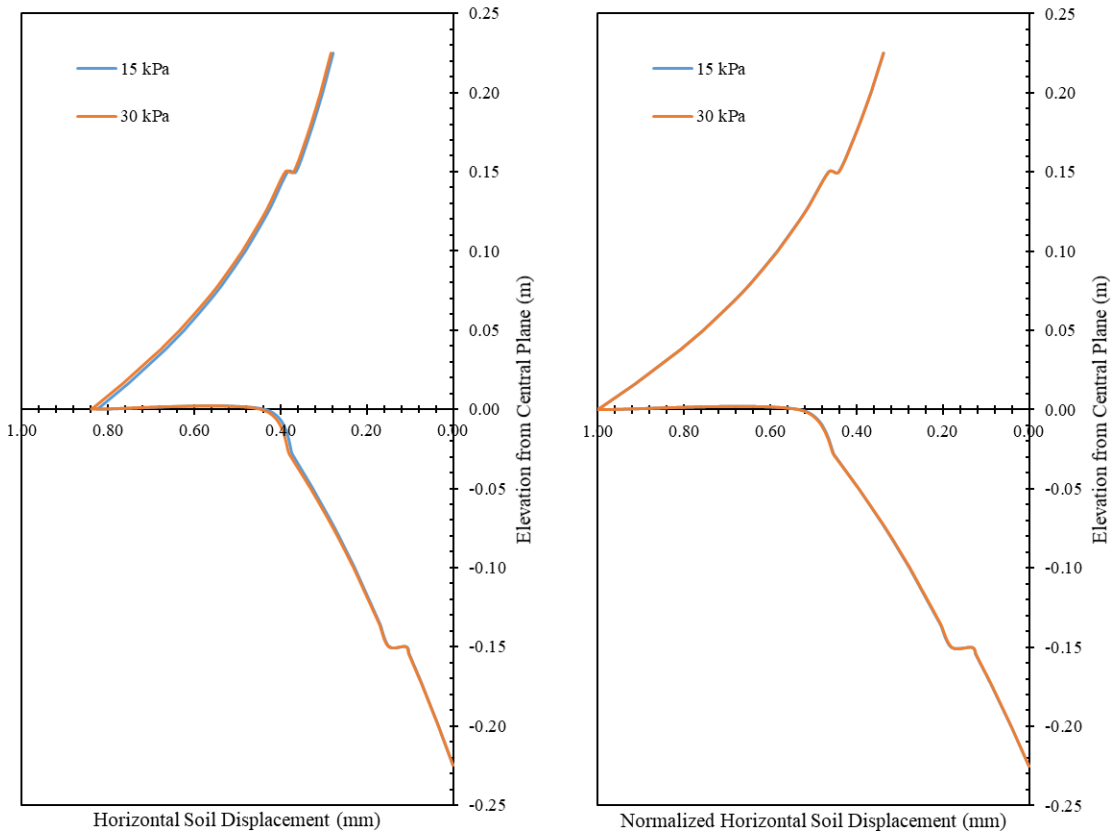

(a) (b)

Figure 7.2.15. Horizontal soil displacement profiles: (a) Absolute displacement; (b) Displacement normalized to the maximum displacement.

7.2.3.5 EFFECT OF SOIL-REINFORCEMENT INTERFACE FRICTION ANGLE

Figure 7.2.16 shows the frontal pullout load-displacement curves obtained for numerical simulations conducted with various soil-reinforcement interface friction angles ranging from 20 to 40 degrees. This figure shows the effect of the soil-reinforcement friction angle on the reinforcement pullout resistance. It was observed that the pullout resistance increases with increasing the soil-reinforcement friction angle.

Figure 7.2.17a shows the horizontal soil displacement profiles predicted at the vertical plane located at 0.3 m (1 ft) from the frontal wall (7.6 mm (0.3 in) from the line of load application) from the numerical simulations conducted with various soil-reinforcement friction angles. The displacements shown in Figure 7.2.17a correspond to a 5 mm (0.2 in) frontal displacement of the active reinforcement. It was observed that the soil displacement increases with increasing the soil-reinforcement friction angle for the same frontal displacement. This is because the increase in the soil-reinforcement interface strength allows for a larger load transfer from the reinforcement (actively loaded) to the soil in vicinity.

Figure 7.2.17b shows the profiles of the horizontal soil displacements normalized to the maximum displacement (i.e., the soil displacement at the soil-reinforcement interface). It was observed that the normalized soil displacement decreases with increasing the soil-reinforcement friction angle. This is because the load shedding reduces with increasing the soil-reinforcement friction angle. The soil shear strength interface yields at smaller reinforcement displacement when the interface strength is high compared to that when the interface strength is low. This is because the load transfer increases with increasing the soil-reinforcement strength.

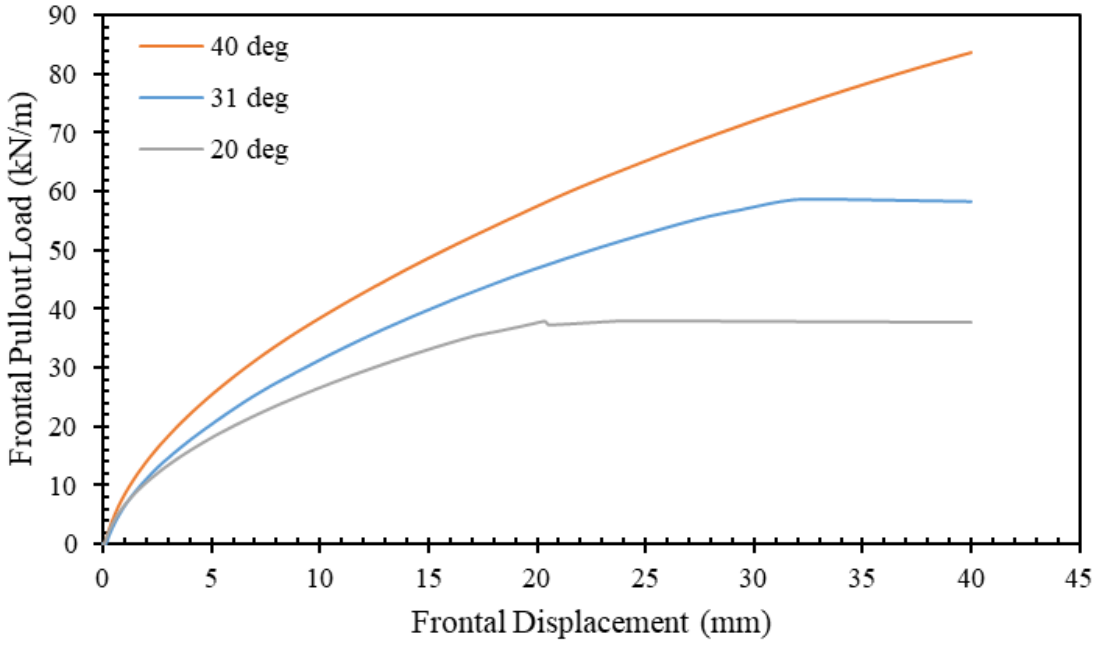

Figure 7.2.16. Reinforcement frontal pullout load-displacement behavior.

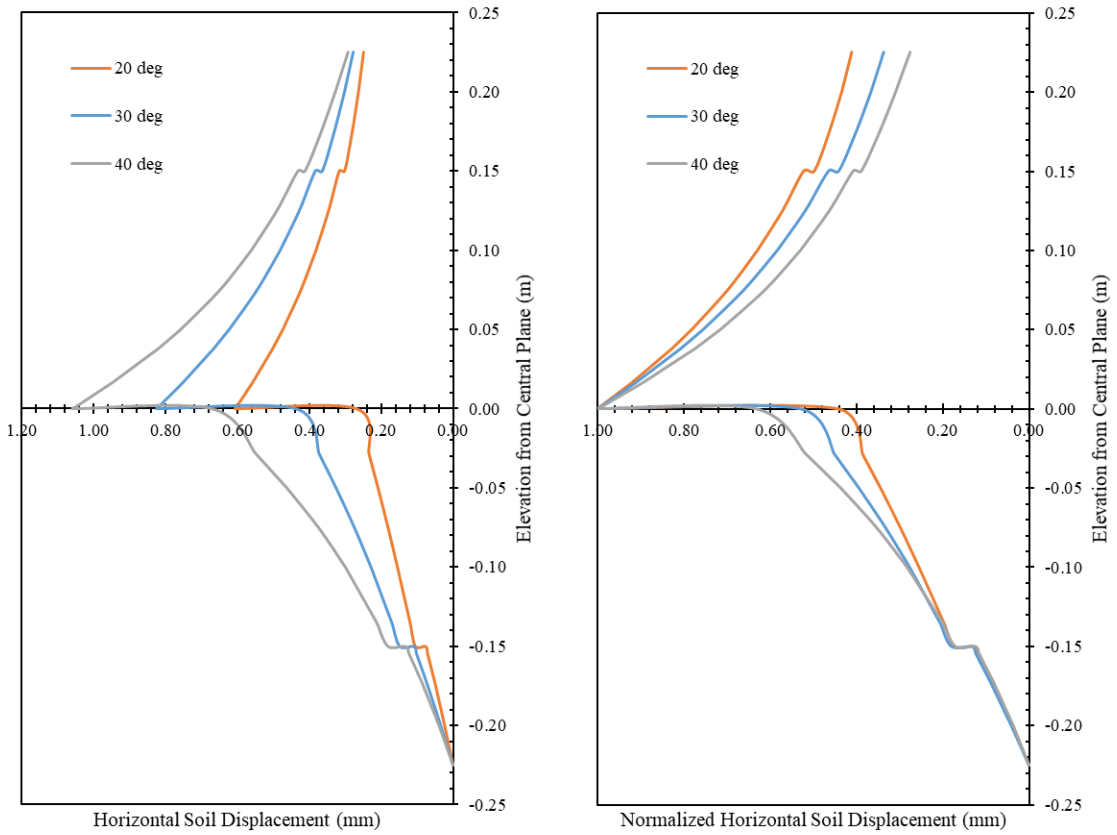

(a) (b)

Figure 7.2.17. Horizontal soil displacement profiles: (a) Absolute displacement; (b) Displacement normalized to the maximum displacement.

7.2.3.6 EFFECT OF REINFORCEMENT TENSILE STIFFNESS

Figure 7.2.18 shows the frontal pullout load-displacement curves obtained for numerical simulations conducted with various reinforcement tensile stiffnesses ranging from 500 to 2000 kN/m (2.9 to 11.4 kips/in). This figure shows the effect of the reinforcement tensile stiffness on the reinforcement pullout resistance. It was observed that the pullout resistance increases with increasing the reinforcement tensile stiffness. This is because reinforcements with high tensile stiffnesses tend to mobilize the soil-reinforcement interface friction along a comparatively large length at early loading stages. Figure 7.2.18 also shows that ultimate pullout resistance is reached earlier for simulations conducted with higher reinforcement tensile stiffness compared to those conducted with lower reinforcement tensile stiffness.

Figure 7.2.19a shows the horizontal soil displacement profiles predicted at the vertical plane located at 0.3 m (1 ft) from the frontal wall (7.6 mm (0.3 in) from the line of load application) from the numerical simulations conducted with various reinforcement tensile stiffnesses. The displacements shown in Figure 7.2.19a correspond to a 5 mm (0.2 in) frontal displacement of the active reinforcement. It was observed that the soil displacement increases with increasing the reinforcement tensile stiffness for the same frontal displacement. This is because the

total load transfer along the reinforcement length increases with increasing the reinforcement tensile stiffness.

Figure 7.2.19b shows the profiles of the horizontal soil displacements normalized to the maximum displacement (i.e., the soil displacement at the soil-reinforcement interface). It was observed that the normalized soil displacement increases with increasing the reinforcement tensile stiffness. Likewise, the total load transfer along the reinforcement length increases with increasing the reinforcement tensile stiffness, which in turn increases the load shedding to the soil in vicinity.

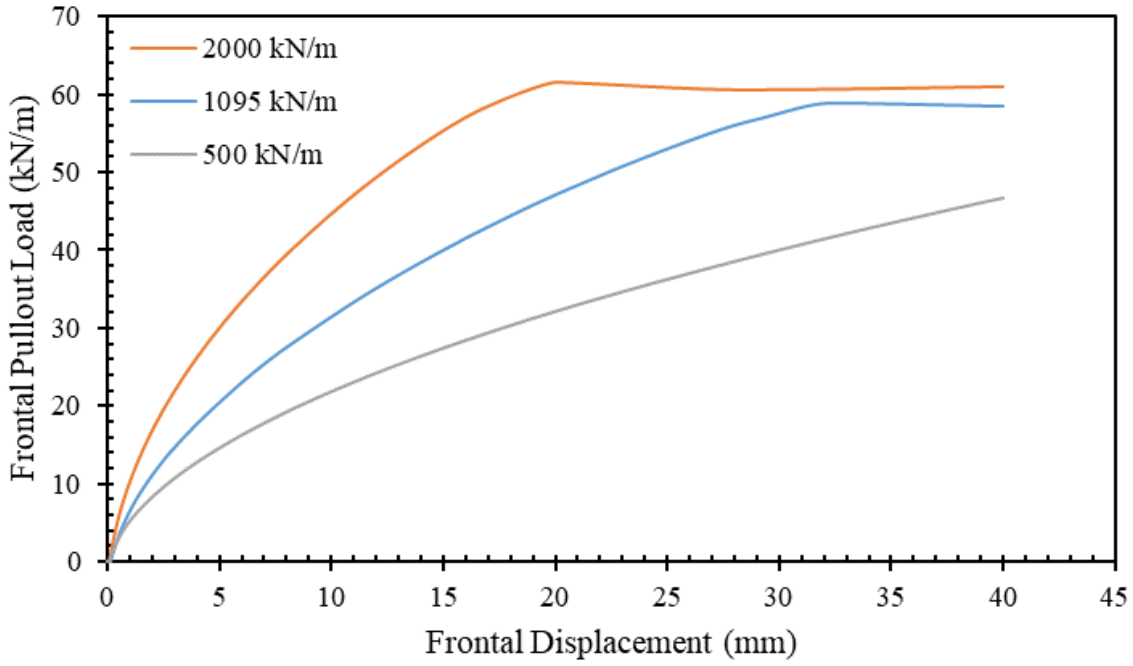

Figure 7.2.18. Reinforcement frontal pullout load-displacement behavior.

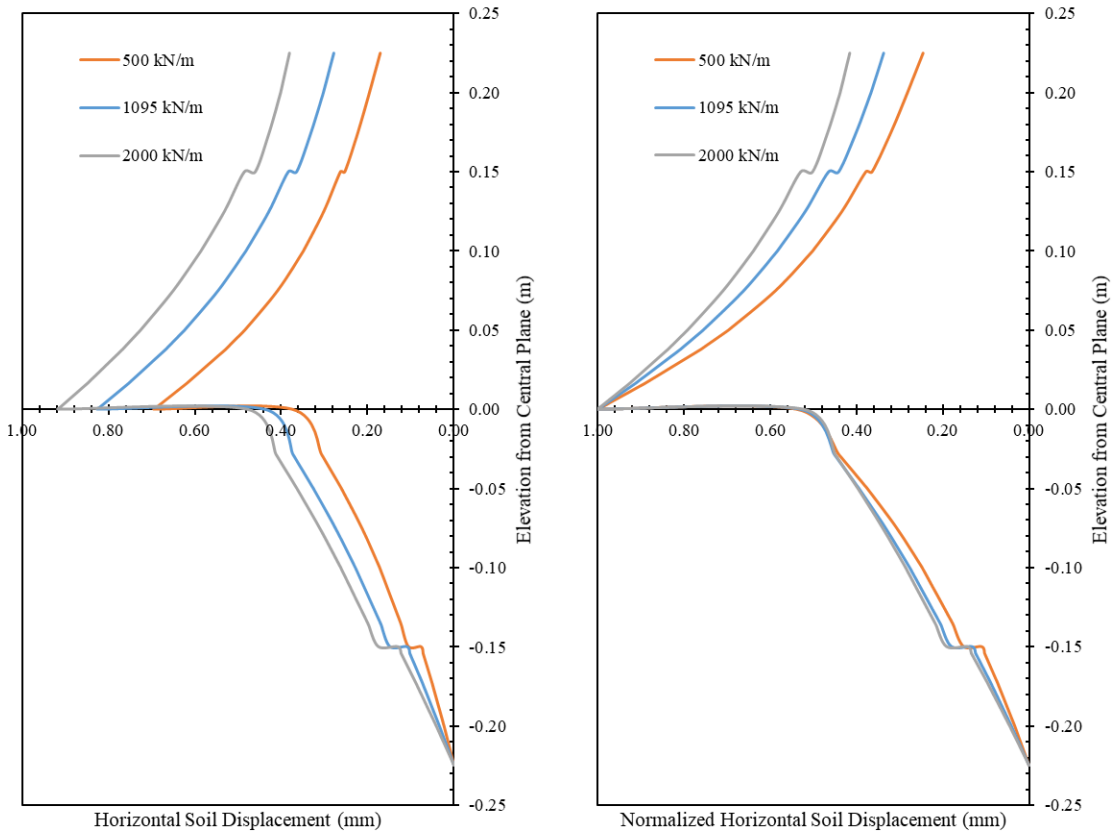

(a) (b)

Figure 7.2.19. Horizontal soil displacement profiles: (a) Absolute displacement; (b) Displacement normalized to the maximum displacement.

7.2.4 CONCLUSIONS

This numerical investigation focused on the factors that influence the soil-reinforcement interaction (e.g., soil and reinforcement properties). This study evaluated the effect of several key parameters that are believed to control the soil-reinforcement interaction, which is key to the behavior of reinforced soil structures. The parameters evaluated include: (1) reinforcement vertical spacing; (2) normal pressure; (3) soil friction angle; (4) soil cohesion; (5) soil-reinforcement interface friction angle; and (6) reinforcement tensile stiffness. The main conclusions from this research component can be summarized as follows:

- The horizontal soil displacement profiles predicted from numerical simulations conducted at the various normal stresses showed that soil displacement increases with increasing the normal stress. This can be attributed to the increase in soil-reinforcement interface shear strength with increasing normal stress, which allows for a larger load transfer from the reinforcement (actively loaded) to the soil in vicinity. It was found that the soil displacement normalized to the soil displacement at the interface decreases with increasing the normal stress. This is because the shear stiffness of the soil increases with

increasing the normal stress providing high resistance to deformation compared to soils with lower normal stresses.

- The horizontal soil displacement profiles predicted from numerical simulations conducted using various backfill material friction angles showed no effect for the soil friction angle on the soil displacement. This is because the soil-reinforcement interface strength and soil stiffness remained the same for the conducted simulations. Likewise, no effect was observed on the soil displacement normalized to the soil displacement at the interface with changing the soil friction angle.

- The horizontal soil displacement profiles predicted from numerical simulations conducted using various backfill material cohesions showed no effect for the soil cohesion on the soil displacement. This is because the soil-reinforcement interface strength and soil stiffness and adhesion remained the same for the conducted simulations. Likewise, no effect was observed on the soil displacement normalized to the soil displacement at the interface with changing the soil cohesion.

- The horizontal soil displacement profiles predicted from numerical simulations conducted with various soil-reinforcement interface friction angles showed that soil displacement increases with increasing the interface friction angle. This is because the increase in the soil-reinforcement interface strength allows for a larger load transfer from the reinforcement (actively loaded) to the soil in vicinity. It was found that the soil displacement normalized to the soil displacement at the interface decreases with increasing the soil-reinforcement friction angle. This is because the load shedding reduces with increasing the soil-reinforcement friction angle. The soil shear strength interface yields at smaller reinforcement displacement when the interface strength is high compared to that when the interface strength is low. This is because the load transfer increases with increasing the soil-reinforcement strength.

- The horizontal soil displacement profiles predicted from numerical simulations conducted with various reinforcement tensile stiffnesses showed that soil displacement increases with increasing the reinforcement tensile stiffness. This is because the total load transfer along the reinforcement length increases with increasing the reinforcement tensile stiffness. It was found that the soil displacement normalized to the soil displacement at the interface increases with increasing the reinforcement tensile stiffness. Likewise, the total load transfer along the reinforcement length increases with increasing the reinforcement tensile stiffness, which in turn increases the load shedding to the soil in vicinity.

7.3 NUMERICAL ANALYSIS OF GEOSYNTHETIC REINFORCED SOIL (GRS) PIERS TESTS

7.3.1 OVERVIEW OF GRS PIER TESTS

Nicks et al. (2013) conducted 19 geosynthetic-reinforced soil (GRS) performance tests, also called mini-pier tests, to investigate the axial load-deformation relationships of the GRS composites with different reinforcement spacings as discussed in Section 4.1.3.8. Concrete Masonry Units (CMU) were used as facing blocks in these tests. For each test, the ratio of the height of the pier to the width of the GRS composite itself was kept constant at approximately 2.0, which is consistent with triaxial test relative dimensions. In all the tests, layers of woven polypropylene geotextile were used as the reinforcement material. After the vertical load was applied onto the pier, the CMU blocks were removed in eight of the 19 tests, leaving the remaining 11 tests conducted with the presence of the CMU blocks. Two of the tests, TF6 and TF9, were chosen to calibrate and validate the numerical model investigated as part of this component of the NCHRP project.

Both TF6 and TF9 were loaded while keeping the CMU blocks. The CMU blocks had dimensions of 0.398 m (15 in) (long) × 0.194 m (7 in) (wide) × 0.194 m (7 in) (high) and weighed approximately 19 kg (42 lb). Two hollow void spaces existed in each CMU block. The GRS pier had a height of 1.94 m (76 $^{1}/_{4}$ in) and a cross section of 1.384 m × 1.384 m (54 ½ in × 54 ½ in) with CMU blocks. The width of the GRS composite itself was 0.995 m (39 ¼ in). A 0.914 m-wide (36 in) concrete slab was applied on top of the GRS composite to serve as a footing for the loading test. Virginia Department of Transportation (VDOT) 21A aggregate was used as the backfill soil, which was placed at a density of 2500 kg/m^3 (156.07 pcf). Large-scale direct shear test results of VDOT 21A showed a friction angle of 53° and cohesion of 5.5 kPa (115 psf) (Nicks et al., 2013). The backfill soil was compacted to reach a 100% relative density using a light-weight electric vibratory plate compactor. The geotextile with wide-width tensile strength of 70 kN/m (4800 lb/ft) at 10% elongation in the machine direction and wide-width tensile strength of 70 kN/m at 8% elongation in the cross-machine direction was used in both TF6 and TF9 as reinforcement material. The CMU blocks were frictionally connected to the geotextile reinforcement. The vertical spacing of the reinforcement layers, S_v, was 0.194 m (7 in) and 0.388 m (15 ¼ in) for TF6 and TF9, respectively.

7.3.2 NUMERICAL MODELING

The finite difference method-based program FLAC3D (Fast Lagrangian Analysis of Continua) was used to simulate the behavior of the GRS piers in a three dimensional (3D) condition. The numerical model included backfill soil, CMU blocks, concrete slab, and geosynthetic layers. Figure 7.3.1 shows the numerical model mesh.

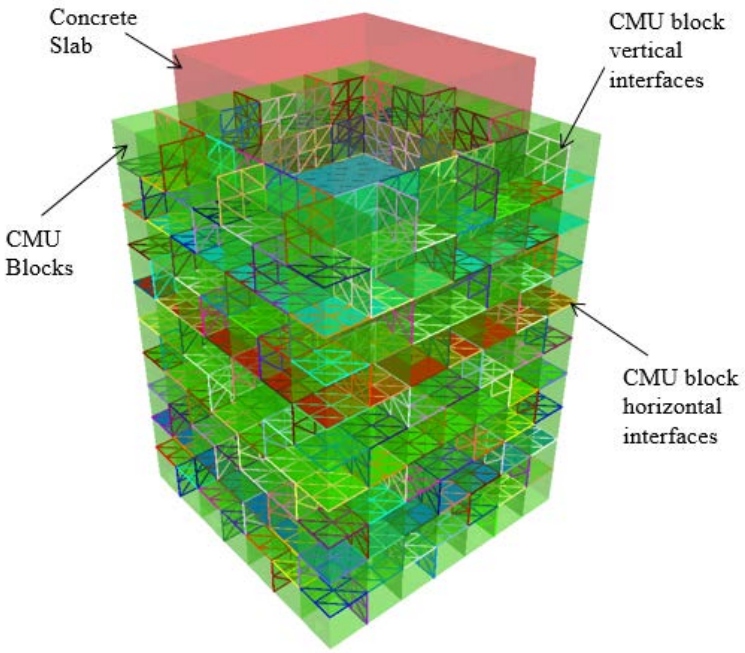

Fig. 7.3.1: Numerical model mesh for the GRS pier

7.3.2.1 CONSTITUTIVE MODELS

The backfill soil VDOT 21A was modeled as a linearly-elastic perfectly-plastic material with the Mohr-Coulomb failure criterion. The backfill soil was compacted to the density of 2500 kg/m^3 (156.07 pcf). An elastic modulus of 25 MPa (3.6 ksi) and Poisson's ratio of 0.25 were used. A friction angle of 53° and cohesion of 5.5 kPa (115 psf) were adopted in the numerical analysis based on large-scale direct shear test results (Nicks et la., 2013). A dilation angle of 23° was used based on the empirical relationship from Bolton (1986) as follows:

$$\psi = \phi - 30^\circ \tag{7.3.1}$$

where ψ and ϕ are the dilation angle and friction angle for the backfill soil respectively.

The geotextile reinforcement was modeled as an isotropic elastic material using "geogrid" structural elements available in the FLAC3D software (Itasca Consulting Group, 2009a). The geogrid structural element is designed to resist only a membrane load. The properties of geogrid structural elements were assumed to be the same as those of the woven polypropylene geotextile used in the tests. The tensile stiffness of the geotextile was estimated as 700 kN/m (48 kip/ft) based on the wide-width tensile stress of the geotextile at 2% elongation used in the GRS pier tests. The thickness of the geotextile was assumed to be 1 mm (0.04 in) and its Poisson's ratio was assumed to be 0.33. Both CMU facing blocks and the concrete slab on top of the GRS pier were modeled as elastic materials with an elastic modulus *E* of 2 GPa (290.08 ksi) and a Poisson's ratio υ of 0.15. A density of 2500 kg/m^3 (156.07 pcf) was used for the concrete slab and an equivalent density of 1230 kg/m^3 (76.79 pcf) was used for the facing blocks CMU to account for the two hollow voids in the actual blocks.

7.3.2.2 INTERFACES

Different types of interfaces were used in the numerical analysis. They were represented by interface elements embedded in the software, which are linearly-elastic perfectly-plastic springs with the Mohr-Coulomb failure criterion. An interaction coefficient C_i, defined as follwos, has been used to characterize frictional interface properties.

$$C_i = \frac{\tan\delta}{\tan\phi} \tag{7.3.2}$$

where δ is the interface friction angle and ϕ is the friction angle for the backfill soil.

For the properties of interfaces between granular backfill and geotextile, an interaction coefficient C_i typically ranges from 0.5 to 0.9 and cohesion of the interface is assumed to be zero. In this study, an interaction coefficient C_i of 0.6 and zero cohesion were assigned to the geotextile–soil interface considering the smooth surface of the geotextile. An interaction coefficient C_i of 0.4 and zero cohesion were used for the vertical interface between soil and CMU facing blocks. For the interface between geotextile and CMU blocks, Awad & Tanyu (2014) conducted direct shear tests and pullout tests to investigate the connection strength between the geotextile and facing blocks. Based on their results, a friction angle δ of 16.2° and a cohesion of 9.5 kPa (1.4 psi) were assigned to the interface between CMU blocks and geotextile. A cohesion of 9.5 kPa (1.4 psi) was justified because some irregularities existing on the rough surfaces of concrete could behave like cohesion by preventing the geotextile from moving. For the interface between CMU facing blocks, a coefficient of friction of 0.6 was adopted in the numerical analysis. In other words, the interface friction angle δ between CMU blocks was equal to $\delta = \arctan(0.6) = 31.0°$. Zero cohesion was assigned to the interface between CMU blocks since no mechanical connection was used in the tests. The horizontal surfaces of the CMU blocks were assumed to have the same roughness as the vertical surfaces of the CMU blocks. The interface between backfill soil and the concrete slab was also considered in this study by assuming that the interface friction angle was equal to the friction angle of the backfill soil.

In addition to the interface friction angle and the cohesion, the relative interface movement was also controlled by the interface normal stiffness k_n and the shear stiffness k_s. Itasca Consulting Group (2009b) recommended estimating the maximum interface stiffness value as follows:

$$k_n = k_s \approx 10 \times \max\left(\frac{K + \frac{4}{3}G}{\Delta z_{\min}} \right) \tag{7.3.3}$$

where the parameters $\Delta z_{\min}$, K, and G are the smallest dimension in a normal direction, the bulk modulus, and the shear modulus of the continuum zone adjacent to the interface, respectively. Equation (7.3.3) was used to estimate the initial input values for the interface stiffness, and these values were subsequently adjusted by comparing the numerical results to the test data and minimizing excessive computation time. Table summarizes the interface properties used in the

numerical model. In all cases, the shear stiffness was refined as 1/100 of the normal stiffness to prevent the interface from penetrating into neighboring zones. The final stiffness values reported in Table are smaller than the values obtained with Eq. (7.3.3).

Table 7.3.1: Interface properties

Interface Properties	Normal Stiffness (MPa/m)	Shear Stiffness (MPa/m)	Interaction Coefficient C_i	Friction Angle δ (°)	Cohesion (kPa)
Soil and geotextile	/	3	0.6	38.5	0
CMU blocks and geotextile	/	210	/	16.2	9.5
Soil and CMU blocks	300	3	0.4	28.0	0
CMU block interfaces (vertical and horizontal)	21000	210	/	31.0	0
Soil and concrete slab	21000	210	1.0	53.0	0

7.3.2.3 MODELING PROCEDURE

Numerical model was activated layer by layer to simulate the construction process. During construction, CMU facing blocks separated by interface were used to provide lateral confinement to the GRS mass. Layers of geotextile reinforcements were placed over the backfill soil based on the reinforcement plan. In the numerical model, the reinforcement overlapped 100% of the block depth instead of 85% used in model tests to simplify the interface connection between "geogrid" structural element and CMU blocks. After simulation of the GRS pier construction was completed, a concrete slab was put on top of the pier and vertical load was applied in increments on the concrete slab according to the loading plan. During the construction and the loading stage, the bottom of the numerical model was fixed in all directions and no fixity was applied to the left, right, front and back sides of the pier.

7.3.2.4 CALIBRATION AND VALIDATION

Figure 7.3.2 shows the applied pressure vs. vertical strain curves from the numerical model and test results for both TF6 and TF9 cases (i.e., S_v = 0.194 m (7 in) and 0.388 m (15 ¼ in) respectively). Figure 7.3.2 shows that for the case with S_v = 0.194 m (7 in), the numerical results agreed well with the test results until the applied pressure reached approximately 1500 kPa (218 psi). For the case with S_v = 0.388 m (15 ¼ in), the numerical results deviated from the test results when the applied pressure exceeded 700 kPa (102 psi). The vertical strain shown in Figure 7.3.2 was defined as the total vertical deformation of the concrete slab divided by the height of the pier. The vertical strains calculated from the numerical model in both cases were smaller than those monitored in the tests when the applied pressure reached comparatively high values. One possible explanation for this difference is that the "geogrid" structural elements in the numerical model was simulated as having a linearly elastic behavior without a failure limit. In other words, the numerical model assumed that failure only occurred at the geotextile-soil interface while

tensile failure of geotextile happened in tests (Nicks et al., 2013) and caused larger deformations of the GRS mini piers.

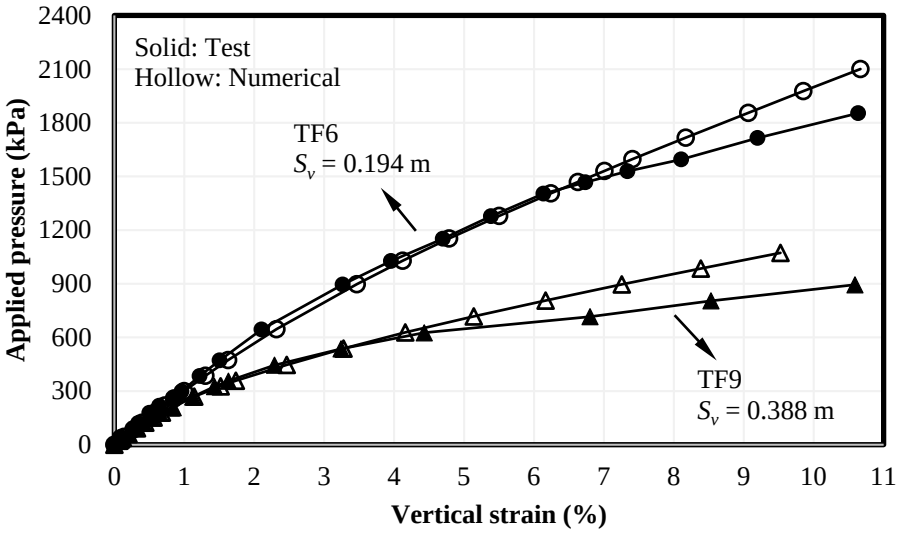

Fig. 7.3.2: Applied pressure vs. vertical strain curves for the GRS piers

Figure 7.3.3 shows the lateral displacement profile of the CMU blocks along the height of the GRS pier at two different applied pressures for Case TF6 (i.e., S_v = 0.194 m (7 in)). Figure 7.3.3 shows that the numerical results matched reasonably well with the test data. As expected, an increase in applied pressure increased lateral displacements. Both the numerical and test results showed that the maximum lateral deformation happened within the upper part to mid-height of the GRS pier. The lateral displacement at the top of the GRS pier was smaller than that towards the base because the surface of the concrete slab on top of the GRS pier was relatively rough as compared to the backfill soil-geotextile interface. The bottom of the GRS pier had the smallest lateral displacement due to the restraint at the bottom of the pier from moving laterally.

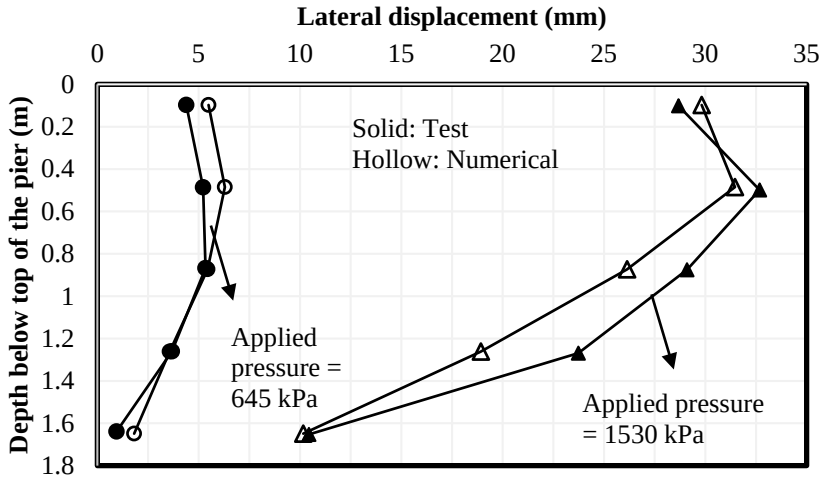

Fig. 7.3.3: Lateral displacement profile of the GRS pier under two applied pressures for Case TF6 (S_v = 0.194 m (7 in))

Figure 7.3.4 shows a comparison of the deformed GRS pier after the loading between the numerical model and the model test results for Case TF6 (S_v = 0.194 m (7 in)). Compared to the photo taken during the model test after loading, the numerical model captured the gaps and slippage developing between CMU blocks. Different interfaces used in the numerical model as mentioned previously were necessary to simulate differential movement between different components (e.g., the slippage between the upper and lower layers of CMU facing blocks or gaps between two CMU facing blocks at the same layer).

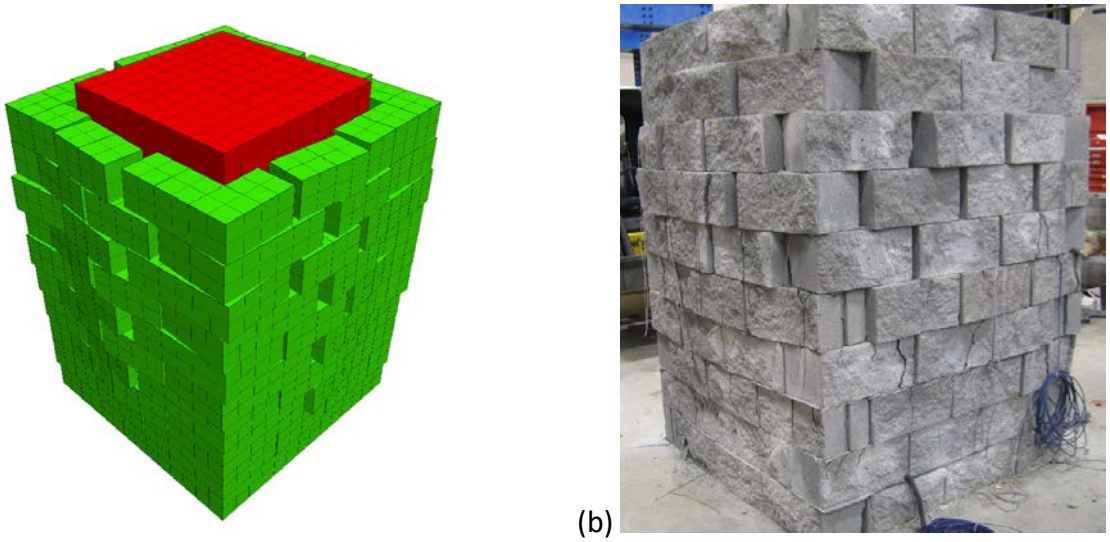

Fig. 7.3.4: Deformed GRS mini pier after loading for Case TF6 (S_v = 0.194 m (7 in)): (a) Deformed numerical mesh (magnified 2 times); (b) Photo of the GRS Pier after test (Nicks et al., 2013).

Figure 7.3.5 shows the calculated additional vertical stress distribution along the width of the GRS pier beneath the concrete slab and at the mid-height of the GRS pier under the applied pressure of 180 kPa (3759 psf) for Case TF6 (S_v = 0.194 m (7 in)). The applied pressure of 180 kPa (3759 psf) is close to the service pressure for GRS abutments recommended by the US Federal Highway Administration (FHWA) (i.e., 4000 psf) (Adams et al., 2011). Figure 7.3.5 shows that the CMU facing blocks did not carry much of the vertical load as compared with the backfill soil in between. The numerical results confirmed that the CMU facing blocks, which were frictionally connected to the GRS pier by geotextile layers, did not directly carry much vertical load (Adams et al., 2012; Saghebfar et al., 2017). However, Nicks et al. (2013) found that the GRS pier tests loaded without CMU facing blocks had much lower ultimate bearing capacities than those loaded with CMU facing blocks when the same backfill soil and reinforcement were used. It was speculated that the effect of CMU facing blocks is to providing lateral confinement rather than to carry vertical load. At the mid-height of the GRS pier, higher pressure was found at the center area of the GRS pier while lower pressure was at the edges because of the side friction provided by the CMU blocks. The stress beneath the concrete slab was not uniformly distributed. Similar to the contact stress beneath a rigid footing resting on cohesive soil, higher stresses developed near the edges of the concrete slab with lower stresses at the center. Salgado (2008) reported that in cohesive soil the stiffness is uniform across the entire base of rigid footing. A uniform contact stress would generate larger displacements near the center because the stress due to the footing load is higher along the axis of the foundation. For a uniform settlement to take place, the contact stresses should not be uniform, with higher stresses developing near edges.

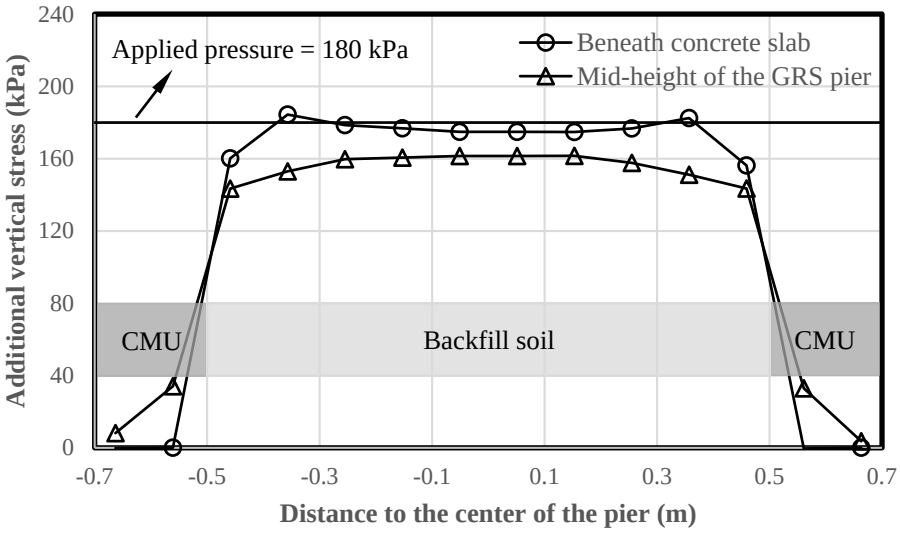

Fig. 7.3.5: Calculated additional vertical stress distribution along the width of the GRS pier under the applied pressure of 180 kPa (3759 psf) for Case TF6 (S_v = 0.194 m (7 in))

Figure 7.3.6 shows the calculated lateral earth pressure profile behind the CMU facing blocks along the height of the GRS pier under the applied pressure of 180 kPa (3759 psf) for Case TF6

(S_v = 0.194 m (7 in)). Figure 7.3.6 also shows, as references, the theoretical lateral earth pressure profiles calculated using the Rankine active earth pressure coefficient K_a and the coefficient at-rest K_0 (i.e., $K_0 = 1 - \sin\phi$). At the top of the GRS pier, the lateral earth pressure behind the CMU facing blocks was slightly higher than K_a because of the interaction between the concrete slab and the backfill soil. In the mid-portion of the GRS pier, the lateral earth pressure behind the CMU facing blocks was lower than K_a. Since the GRS pier was three-dimensional, the lateral earth pressures were lower than the two-dimensional earth pressure calculated by the Rankine method due to the development of arching behind the facing (tom Wörden & Achmus, 2013). Another possible reason for the lower lateral earth pressure behind facing is that the backfill soil behind the CMU facing blocks was limited. The theoretical methods commonly used for estimating active lateral earth pressure are expected to be inaccurate since the thrust wedge (i.e., failure plane) cannot fully develop in the shape and size predicted by these methods (Leshchinsky et al., 2004; Greco, 2013). In other words, the GRS pier in this study was similar to a limited-space retaining wall and the failure plane was not able to fully develop due to lack of space. As a result, lower lateral earth pressures developed behind the CMU blocks. At the bottom of the GRS pier, the lateral earth pressure was close to and even higher than K_0 since the bottom of the GRS pier was fully fixed since no interface between the GRS pier and the concrete floor was assigned in the numerical model.

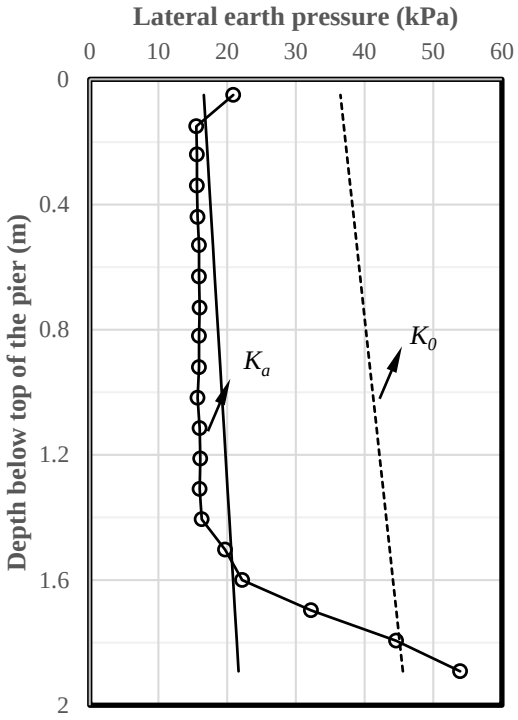

Fig. 7.3.6: Calculated lateral earth pressure behind CMU facing blocks along the height of the GRS pier under the applied pressure of 180 kPa (3759 psf) for Case TF6 (S_v = 0.194 m (7 in))

From the above discussion, it can be concluded that the numerical model was able to predict the behavior of the GRS mini pier reasonably well, although some discrepancies were identified between the numerical predictions and the measured test results. Accordingly, the numerical model was deemed reasonable for adoption in the remainder stages of the numerical study.

7.3.3 PARAMETRIC STUDY OF GRS MINI PIERS

7.3.3.1 BASELINE MODEL

A baseline model was developed considering on the numerical simulation of the GRS pier discussed in last section. Specifically, the baseline model had the same geometry as the numerical model discussed in last section. However, the backfill soil used in the baseline model was different: A cohesionless soil of a friction angle of 38° was selected in the baseline model since Adams et al. (2012) recommend that the friction angle of the backfill soil used for design of GRS walls should not be lower than 38°. Table 7.3.2 to Table 7.3.4 present the information regarding the baseline model. The Baseline model had nine layers of reinforcement with a vertical spacing S_v of 0.194 m (7 in). The behavior of the backfill soil was described using the Mohr-Coulomb model and the behavior of the reinforcement was described using geogrid structural elements. Other than the friction angle and the density of the backfill material, the remaining characteristics and material properties were the same as those adopted in the numerical model discussed in the previous section. Some of the interface friction angles were changed based on the change of the friction angle of the backfill soil. The normal and shear stiffness of different interfaces remained the same as those used in the previsou section, as well as the boundary conditions and the modelling procedure.

A parametric study was carried out by changing one parameter at a time in the baseline model to study its influence on the performance of the GRS mini piers, such as applied pressure – vertical strain curve, lateral deformation, volume change, vertical and lateral earth pressures, and tension in the reinforcement. The influence factors included the friction angle of the backfill soil, the stiffness of the reinforcement material, the reinforcement spacing, the combination of reinforcement stiffness and spacing, the soil – reinforcement interaction coefficient, the facing connection, the pier height, and the confining stress.

Table 7.3.2: Baseline Model Variables (Geometry)

	Model Variable	Value
Geometry	Height H (m)	1.94
	Width with CMU blocks (m)	1.384
	Width without CMU blocks B (m)	0.995
	Reinforcement Vertical Spacing S_v (m)	0.194
	Reinforcement Coverage Ratio (%)	100
	Number of Layers of Reinforcement	9

Table 7.3.3: Baseline Model Variables (Constitutive Models)

Model Variable		Value
Backfill Soil	Constitutive Model	Mohr-Coulomb
	Elastic Modulus E (MPa)	25
	Poisson's Ratio υ	0.25
	Friction Angle ϕ (°)	38
	Dilation Angle ψ (°)	8
	Cohesion (kPa)	1
	Density (kg/m^3)	2000
CMU blocks and Concrete Slab	Constitutive Model	Elastic
	Elastic Modulus E (GPa)	2
	Poisson's Ratio υ	0.15
	Density (kg/m^3)	2500 (for Concrete Slab) 1230 (for CMU blocks)
Geogrid Structural Element	Constitutive Model	Isotropic Elastic
	Stiffness (kN/m)	700
	Thickness (mm)	1

Table 7.3.4: Baseline Model Variables (Interfaces)

Interface Properties	Normal Stiffness (MPa/m)	Shear Stiffness (MPa/m)	Interaction Coefficient C_i	Friction Angle δ (°)	Cohesion (kPa)
Soil and geotextile	/	3	0.6	25.1	0
CMU blocks and geotextile	/	210	/	16.2	9.5
Soil and CMU blocks	300	3	0.4	17.4	0
CMU block interfaces (vertical and horizontal)	21000	210	/	31.0	0
Soil and concrete slab	21000	210	1.0	38.0	0

7.3.3.2 EFFECT OF FRICTION ANGLE OF BACKFILL SOIL

This section discusses the effect of the friction angle of the backfill soil. Two additional values were adopted for the friction angle of the backfill soil in the parametric study: 34° and 42°. The friction angle of 34° corresponds to the value suggested by AASHTO (2014) in the design of MSE walls when no triaxial tests data are available.

In the numerical model the dilation angle of the backfill soil followed the empirical relationship proposed by Bolton (1986) as shown in Equation (7.3.1). The dilation angle changed with the change of the friction angle. Both the soil – geotextile interface friction angle and the soil – CMU block interface friction angle would be affected by the change of the friction angle of the backfill soil. Table 7.3.5 summarizes all the variables because of the change of the friction angle of the

backfill soil. Properties not presented in Table 7.3.5 are the same as those in Table 7.3.2 to Table 7.3.4.

Table 7.3.5: Variables in the parametric study on the effect of thefriction angle of the backfill soil

Model Variable			Baseline	Case 1	Case 2
Backfill	Constitutive Model			Mohr-Coulomb	
	Elastic Modulus E (MPa)			25	
	Poisson's Ratio υ			0.33	
	Friction Angle ϕ (°)		38	34	42
	Dilation Angle ψ (°)		8	4	12
	Cohesion (kPa)			1	
	Density (kg/m^3)			2000	
Interfaces	Backfill soil and geotextile	Shear Stiffness k_s (MPa/m)		3.4	
		Interaction Coefficient C_i		0.6	
		Friction Angle δ (°)	22.0	25.1	28.4
		Cohesion (kPa)		0	
	Backfill soil and CMU blocks	Normal Stiffness k_n (MPa/m)		340	
		Shear Stiffness k_s (MPa/m)		3.4	
		Interaction Coefficient C_i		0.4	
		Friction Angle δ (°)		15.1	
		Cohesion (kPa)		0	

7.3.3.2.1 Applied pressure – vertical strain curve

Figure 7.3.7 shows the calculated applied pressure – vertical strain curves using backfill soils of different friction angles. Different from numerical results of pullout tests as discussed in Section 7.2.3.3, the friction angle of the backfill soil had a significant effect on the performance of the GRS pier. The GRS pier had higher modulus with the increase of the friction angle of the backfill soil. The reason for different results was that the interface friction angle, as shown in Table 7.2.2 in Section 7.2.2.5, did not change with the change of the friction angle of the backfill soil used in the numerical analysis of pullout tests. FHWA (Adams et al., 2011) recommended a 200 kPa (4177 psf) service pressure and a 0.5% vertical deformation service limit for GRS abutments. Under the applied pressure of 200 kPa (4177 psf), the GRS pier had secant moduli of 5.9 MPa (855.7 psi), 12.0 MPa (1740.5 psi), and 19.8 MPa (2871.8 psi) for the cases corresponding to friction angles of 34°, 38°, and 42°, respectively. The increase of the friction angle had a significant effect on the increase of the secant modulus of the GRS pier. The stage loading was terminated when the vertical strain of the GRS pier reached 10%. Adams et al. (2012) defined the ultimate vertical capacity of the GRS pier as the applied pressure at which the GRS pier test reaches a vertical strain of 5%. The ultimate vertical capacities of the GRS piers were 239 kPa (4991 psf), 343 kPa (7164 psf), and 493 kPa (10297 psf) for the cases corresponding to fill friction angles of 34°, 38°, and 42°, respectively.

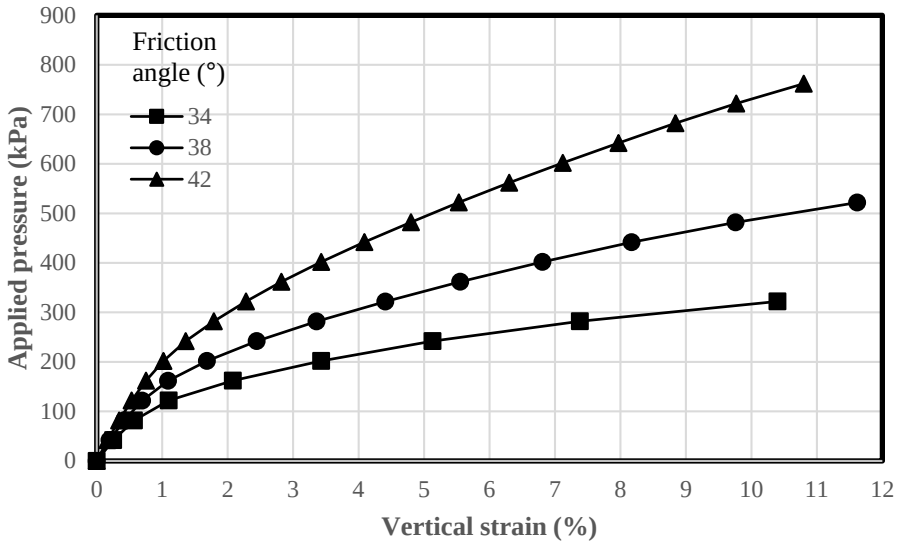

Fig. 7.3.7: Effect of the friction angle of the backfill soil on the applied pressure – vertical strain curves

7.3.3.2.2 Lateral deformation and volume change

Figure 7.3.8 shows the lateral displacement profile of the CMU blocks along the height of the GRS pier under the applied pressure of 200 kPa (4177 psf), as obtained considering backfill soils with different friction angles. As expected, an increasing friction angle of the backfill soil led to decreased lateral deformations of the CMU blocks. For all the cases, the maximum lateral displacements of the CMU blocks happened within the upper to mid portion of the GRS pier with almost no movement at the bottom due to the boundary effect.

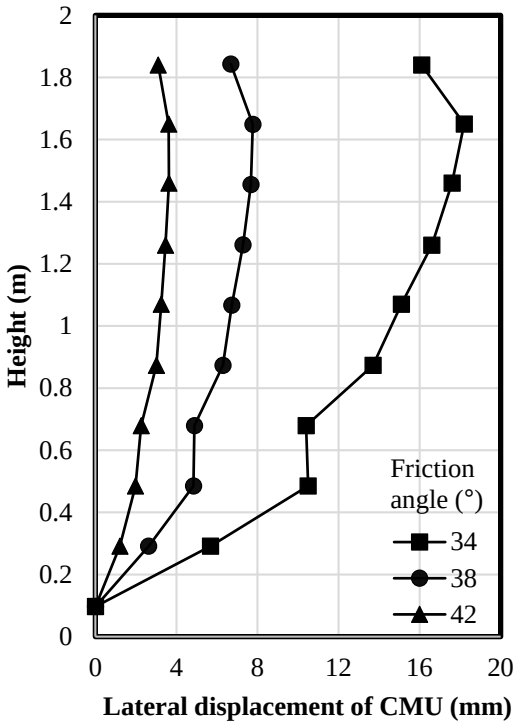

Fig. 7.3.8: Effect of the friction angle of the backfill soil on the lateral displacement of CMU blocks under the applied pressure of 200 kPa (4177 psf)

Adams et al. (2002) reported the results of large-scale GRS pier tests and investigated the relationship between the vertical and lateral deformations. Test results suggested a zero net volume change during vertical loading. Adams et al. (2002) suggested that zero volume change can be assumed to predict the maximum lateral deflection of a GRS structure. In this study, the volume changes of the GRS pier during vertical loading were also investigated.

Figure 7.3.9 shows the schematic of the deformed GRS pier predicted by the numerical simulations. Under the vertical load, the concrete slab settled and the GRS pier expanded laterally. The vertical volume change due to the vertical compression of the GRS pier can be calculated as $\Delta V_v = \delta_v \cdot A_s$ where δ_v is the vertical settlement of the concrete slab (as shown in Figure 7.3.9 (b)) and A_s is the cross-section area of the backfill soil ($A_s = 0.995 \times 0.995 = 0.990\ \mathrm{m}^2$ (10.7 sq. in.) in this study). The normalized vertical volume change is defined as $\Delta V_v/V_0$ where V_0 is the original volume of the GRS pier ($V_0 = 1.384 \times 1.384 \times 1.94 = 3.716\ \mathrm{m}^3$ (131.2 cu. ft.) in this study). The lateral volume change due to the lateral expansion of the GRS pier can be calculated by integrating the lateral displacement of the CMU blocks δ_{li} at the *i*th layer over the whole height. Based on the numerical calculation, the movement of the CMU blocks at the corner of the GRS pier could be ignored. In other words, the lateral displacement of the CMU blocks was assumed to have a triangular distribution at each face of the GRS pier, as shown in Figure 7.3.9 (a). Therefore, the lateral volume change of the GRS pier can be calculated as:

$$\Delta V_l = \int_0^H \left(\frac{1}{2} \delta_{li} \cdot B_{total} \cdot 4 \right) \cdot \mathrm{dz} \tag{7.3.4}$$

where H is the GRS pier height (H = 1.94 m (76 $^1/_4$ in) in this study) and B_{total} is the GRS pier width with CMU blocks (B_{total} = 1.384 m (54 $^1/_2$ in) in this study).

The whole GRS pier was composed of 10 layers of CMU blocks. Assuming that the lateral displacement of the CMU blocks was equally distributed along the height of each CMU block layer, the lateral volume change of the GRS pier can be simplified as:

$$\Delta V_l = \sum_1^{10} \left(\frac{1}{2} \delta_{li} \cdot B_{total} \cdot 4 \cdot h \right) = 2 B_{total} \cdot h \sum_1^{10} \delta_{li} \tag{7.3.5}$$

where h is the height of each CMU block layer (h = 0.194 m (7 in) in this study).

The normalized lateral volume change is defined as $\Delta V_l / V_0$. If there is no volume change of the pier, $\Delta V_v = \Delta V_l$.

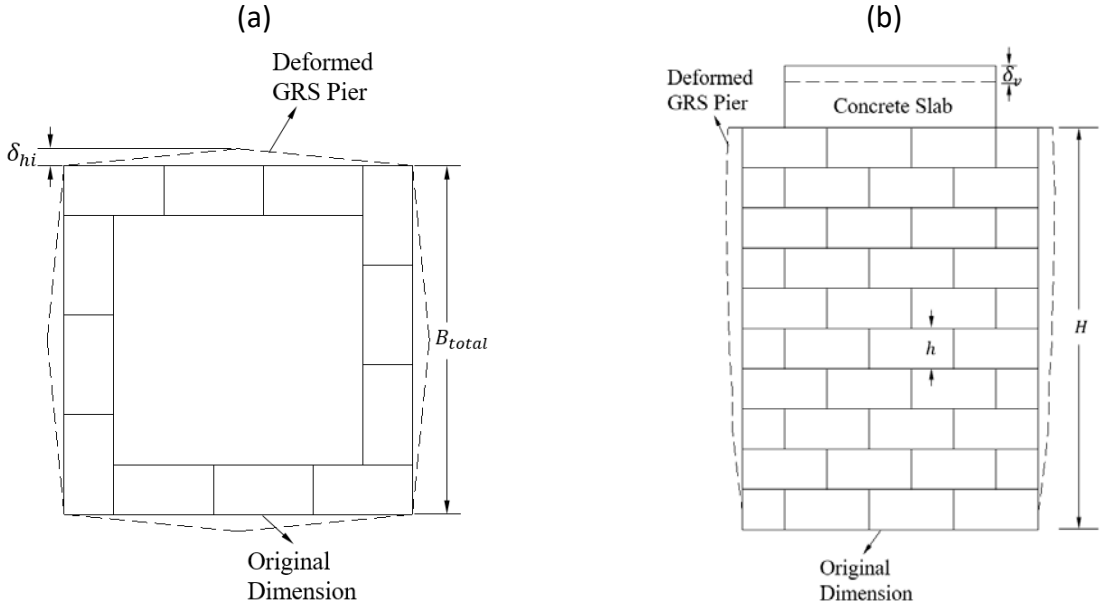

Fig. 7.3.9: Schematic of the deformed GRS pier: (a) Plan view; (b) Side view.

Figure 7.3.10 shows the normalized lateral volume change – normalized vertical volume change curves with the backfill soil of different friction angles. The zero volume change line is also plotted in Fig. 7.3.10 for comparison. The numerical results shown in Fig. 7.3.10 indicate that the volume changes in the GRS pier did not exactly follow the zero volume change assumption. When the applied vertical load was small, all the curves in Fig. 7.3.10 are below the zero volume change line, indicating that the GRS pier had more vertical compression than lateral expansion. On the

other hand, for comparatively higher applied vertical loads, the increase of the lateral volume change was faster than that of the vertical volume change, suggesting that the GRS pier showed more lateral expansion than vertical compression. The GRS pier tended to laterally expand more when the backfill soil had a comparatively higher friction angle since the dilation angle of the backfill soil also increased with increasing friction angle.

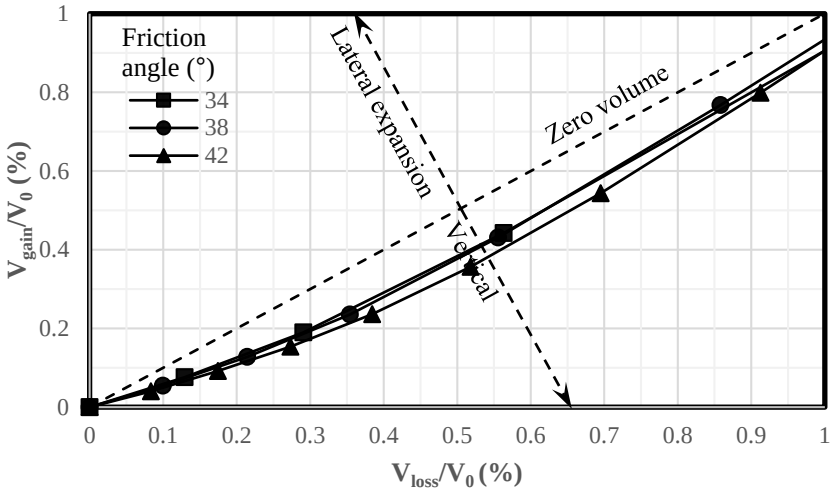

(a)

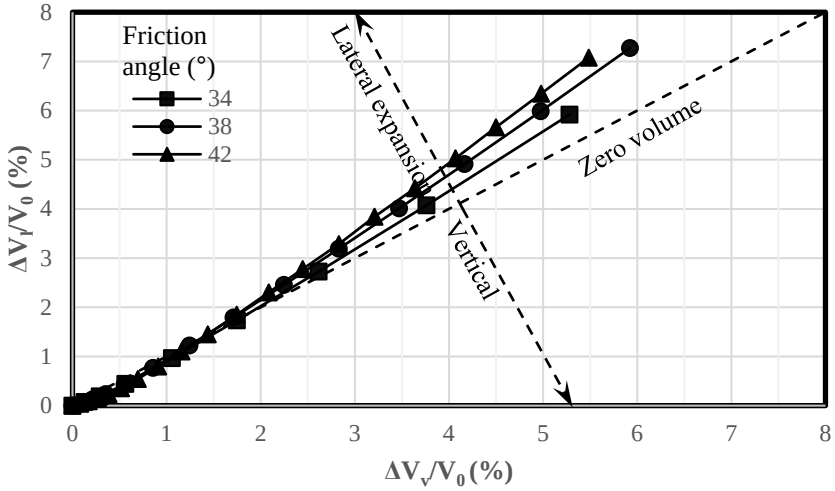

(b)

Fig. 7.3.10: Effect of the friction angle of the backfill soil on the volume change of the pier: (a) scale of volume change up to 1%; (b) scale of volume change up to 8%.

7.3.3.2.3 Additional vertical stress

Figure 7.3.11 shows the additional vertical stress distribution beneath the concrete slab along the width of the GRS pier under the applied pressure of 200 kPa (4177 psf) with the backfill soil of different friction angles. Unlike in cohesive soil, the additional vertical stresses beneath the

concrete slab in the cohesionless soil show a non-uniform distribution with higher stresses near the center and lower stresses around the edge. The stiffness of the cohesionless soil near the center of the rigid concrete slab was higher than that around the edge due to higher confinement. The stress was higher near the center because higher stiffness required higher stress for the settlement to be the same as near the edge (Salgado, 2008). Figure 7.3.11 also shows that the CMU blocks did not carry vertical load as compared with the backfill soil inside. The CMU facing blocks had more effect in constraining the lateral movement of the soil. The additional vertical stresses beneath the concrete slab had a more uniform distribution when the backfill soil had a higher friction angle. The additional vertical stress near the center of the concrete slab for the case with the backfill soil having a friction angle of 34° was approximately 1.5 times that for the case with the backfill soil having a friction angle of 42°.

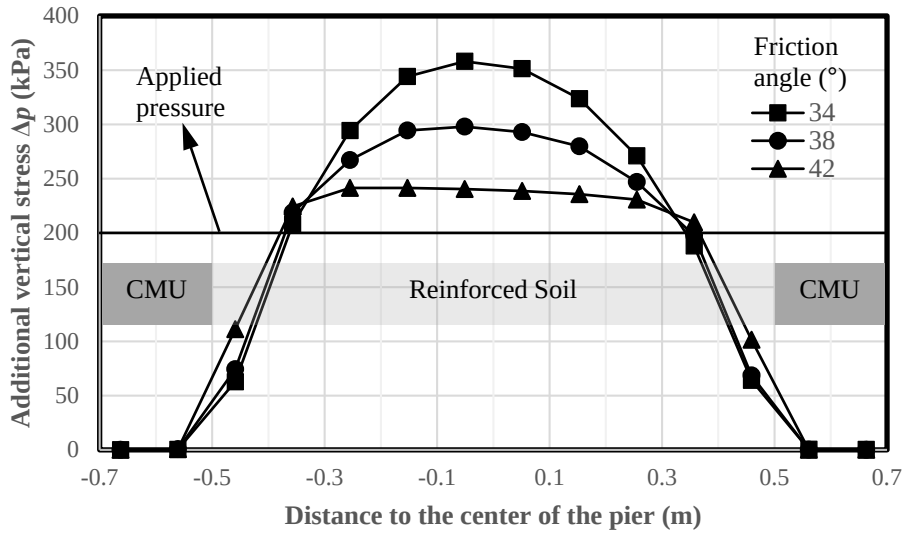

Fig. 7.3.11: Effect of the friction angle of the backfill soil on the additional vertical stress distribution beneath the concrete slab along the width of the pier under the applied pressure of 200 kPa (4177 psf)

7.3.3.2.4 Lateral earth pressures

Figure 7.3.12 presents the lateral earth pressures along the height of the GRS pier both behind the CMU blocks and near the center of the GRS pier for an applied pressure of 200 kPa (4177 psf) and considering backfill soils of different friction angles. As expected, a higher friction angle resulted in lower lateral earth pressures. The lateral earth pressure behind the CMU blocks was lower than that near the center of the GRS pier since the higher vertical stress developed near the center and the lower vertical stress occurred behind the CMU blocks as shown in Fig. 7.3.11. The non-uniform distribution of the vertical stresses within the GRS pier resulted in the non-uniform distribution of the lateral earth pressures. Therefore, treating the applied pressure as a uniform surcharge q to calculate the lateral pressure (i.e., $\sigma_h = K_a(\gamma h + q)$) is not appropriate when load is applied using a rigid footing on top of the GRS pier.

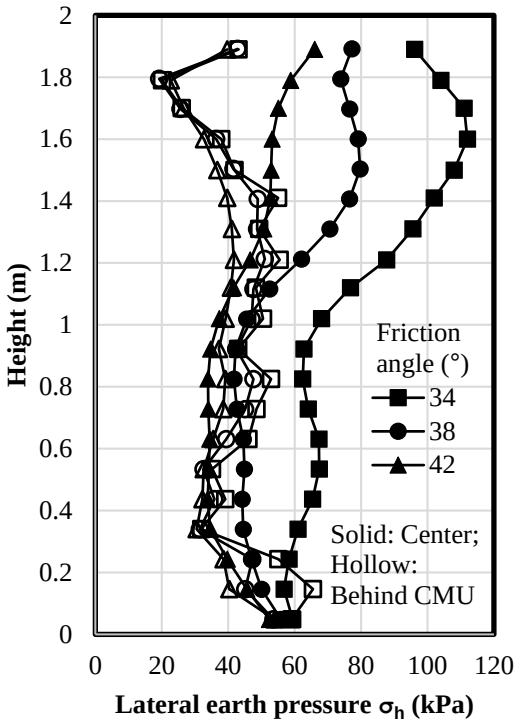

Fig. 7.3.12: Effect of the friction angle of the backfill soil on the lateral earth pressure along height under the applied pressure of 200 kPa (4177 psf)

Figure 7.3.13 shows the calculated lateral earth pressure coefficient *K* under the applied pressure of 200 kPa (4177 psf) considering backfill soils of different friction angles. The calculated lateral earth pressure coefficient *K* is defined as the ratio of the lateral earth pressure to the vertical stress at the same location. The results shown in Fig. 7.3.13 indicate that the calculated lateral earth pressure coefficients near the center of the GRS pier were almost the same as the Rankine active lateral earth pressure coefficients K_a except for locations near the top and bottom of the pier because of boundary effects. The calculated lateral earth pressure coefficients behind the CMU blocks fluctuated between the active lateral earth pressure coefficient K_a and the lateral earth pressure coefficient at-rest K_0. The higher friction angle of backfill soil resulted in the calculated lateral earth pressure coefficients behind the CMU blocks were closer to K_a.

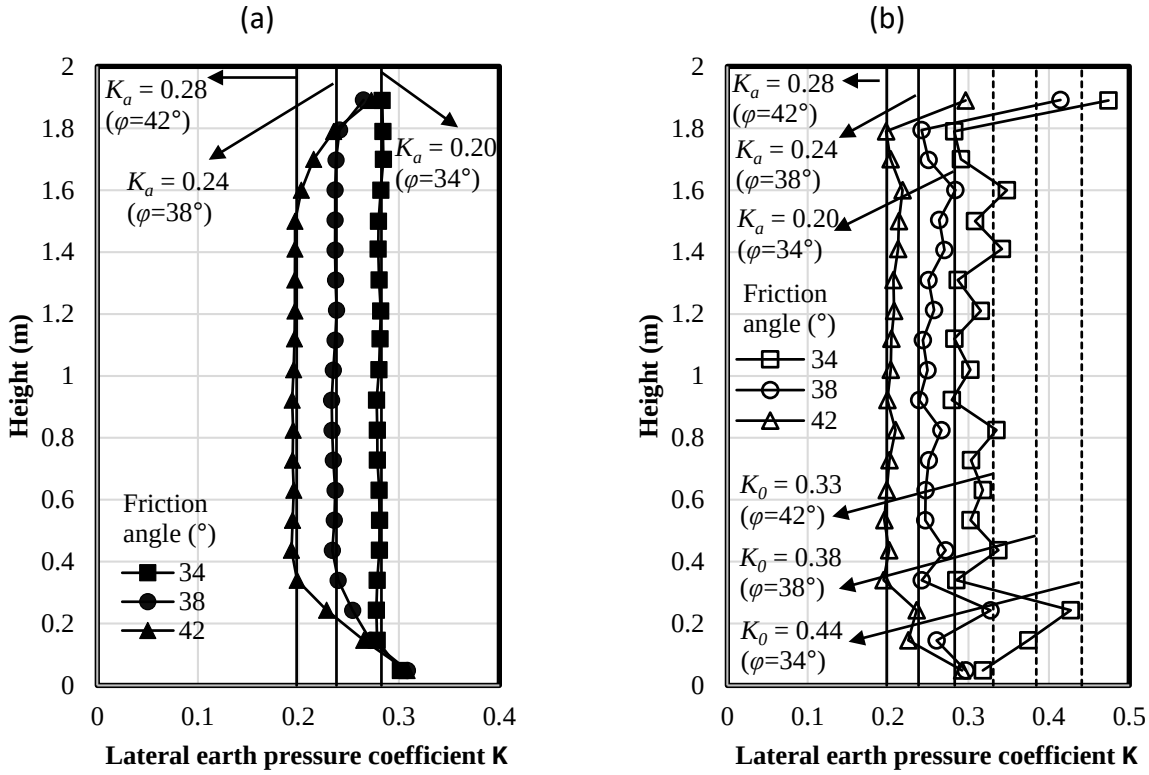

Fig. 7.3.13: Effect of the friction angle of the backfill soil on the calculated lateral earth pressure coefficient K under the applied pressure of 200 kPa (4177 psf): (a) Near the center of the pier; (b) Behind the CMU blocks.

7.3.3.2.5 Tension in the reinforcement

Figure 7.3.14 presents the tensile force in the reinforcement under the applied pressure of 200 kPa (4177 psf) with the backfill soil of different friction angles. Figure 7.3.14(a) shows the contour of the tensile force in the reinforcement for the case of friction angle of 38^{o} . It indicates that the maximum tensile force in the reinforcement happened around the centerline of the GRS pier. Figure 7.3.14(b) shows that the maximum tensile force increased from the top of the pier to the mid-height and then decreased until the bottom layer. The friction angle of the backfill soil had a significant influence on the maximum tensile force in the reinforcement. The maximum tensile force in the reinforcement decreased with the increase of the friction angle of the backfill soil since the higher friction angle resulted in a lower lateral earth pressure in the GRS pier as shown in Figure 7.3.12.

(a)

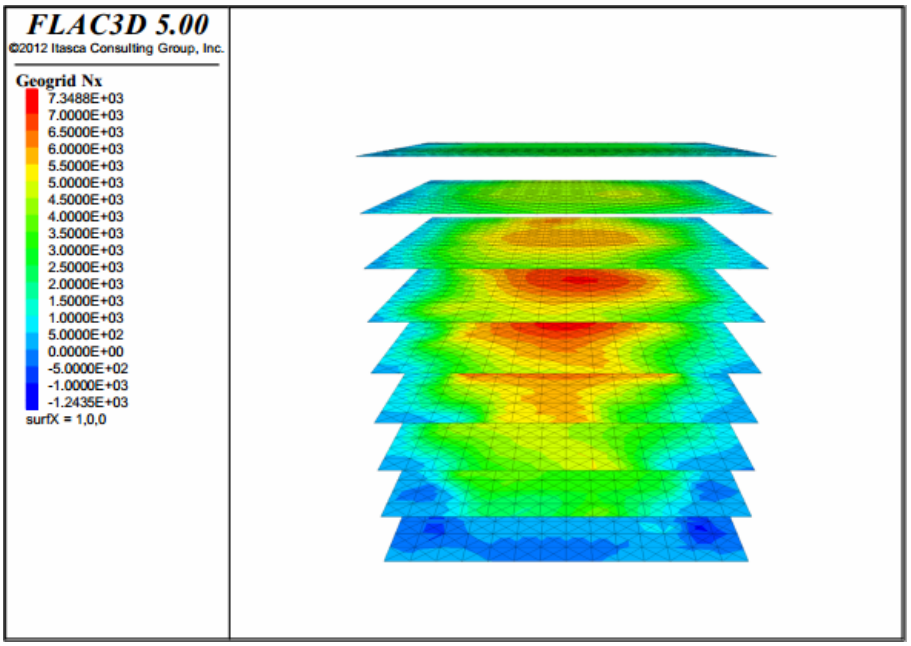

(b)

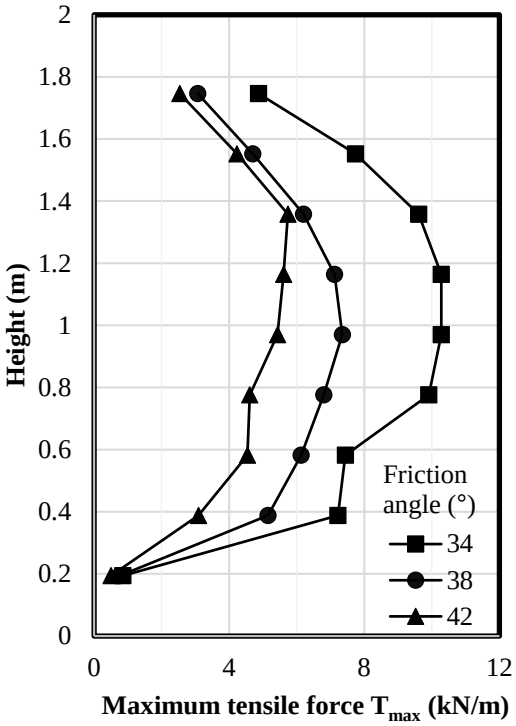

Fig. 7.3.14: Tensile force of the reinforcement under the applied pressure of 200 kPa (4177 psf): (a) Contour of tensile force of the reinforcement for the case of friction angle of 38 ^{o} ; (b) Effect of the friction anlge of backfill soil on the maximum tensile force of the reinforcement.

Figure 7.3.15 presents the connection force in the reinforcement along the height of the GRS pier under the applied pressure of 200 kPa with the backfill soil of different friction angles. Since the geotextile layers were frictionally connected to the CMU blocks, the connection stress in the geotextile was lower than the maximum tensile force. Larger connection force of the reinforcement occurred at approximately mid-height of the GRS pier since the relative movement between the CMU blocks and geotextile was the largest. At the bottom of the GRS pier, the CMU blocks had almost no movement as shown in Fig. 7.3.8, resulting in almost no connection force in the bottom layer of the geotextile reinforcement. Figure 7.3.14 shows that the maximum tensile force of the reinforcement decreased with the increase of the friction angle of the backfill soil. However, the connection force of the reinforcement did not change much with the increase of the friction angle of the backfill soil.

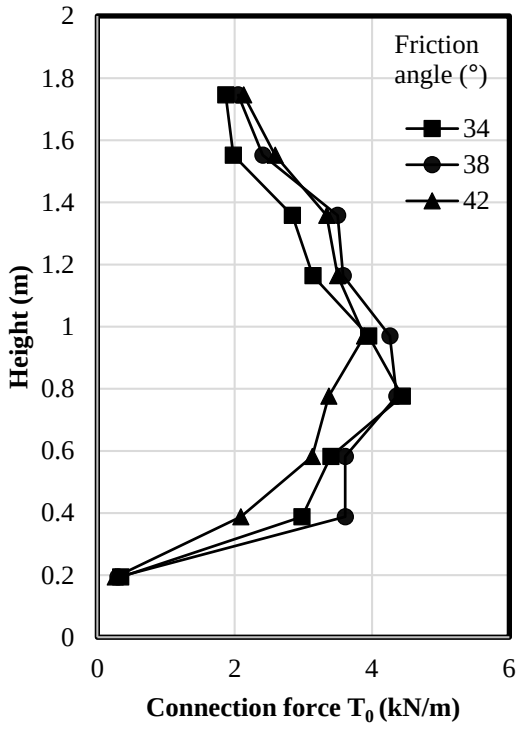

Fig. 7.3.15: Effect of the friction angle of the backfill soil on the connection force of the reinforcement under the applied pressure of 200 kPa (4177 psf)

7.3.3.3 EFFECT OF REINFORCEMENT STIFFNESS

This section discusses the effect of the reinforcement stiffness. In the baseline model, the stiffness of the reinforcement was 700 kN/m (48 kip/ft). Two additional cases, with the stiffness values of the reinforcement being 350 kN/m (24 kip/ft) and 1400 kN/m (96 kip/ft), were evaluated in this study.

7.3.3.3.1 Applied pressure – vertical strain curve

Figure 7.3.16 presents the applied pressure – vertical strain curves with geotextile reinforcement of different tensile stiffness. Figure 7.3.16 shows that the effect of the geotextile reinforcement stiffness on the applied pressure – vertical strain curves was not as significant as the effect of the friction angle of the backfill soil. As expected, geotextile reinforcement with higher tensile stiffness led to comparatively larger ultimate vertical capacity at 5% vertical strain. The ultimate vertical capacity values of GRS piers with geotextile reinforcement tensile stiffness of 350 kN/m (24 kip/ft), 700 kN/m (48 kip/ft), and 1400 kN/m (96 kip/ft) were 312 kPa (6516 psf), 343 kPa (7164 psf), and 362 kPa (7561 psf), respectively. The moduli of the GRS pier at the applied pressure of 200 kPa (4177 psf) were 9.4 MPa (1363.4 psi), 12.0 MPa (1740.5 psi), and 14.1 MPa (2045.0 psi) for the case with the geotextile reinforcement tensile stiffness of 350 kN/m (24 kip/ft), 700 kN/mn (48 kip/ft), and 1400 kN/m (96 kip/ft), respectively. The use of geotextile reinforcement provided lateral restraint to the backfill soil, thus resulting in an apparent cohesion and an increased modulus of the GRS pier (Han, 2015).

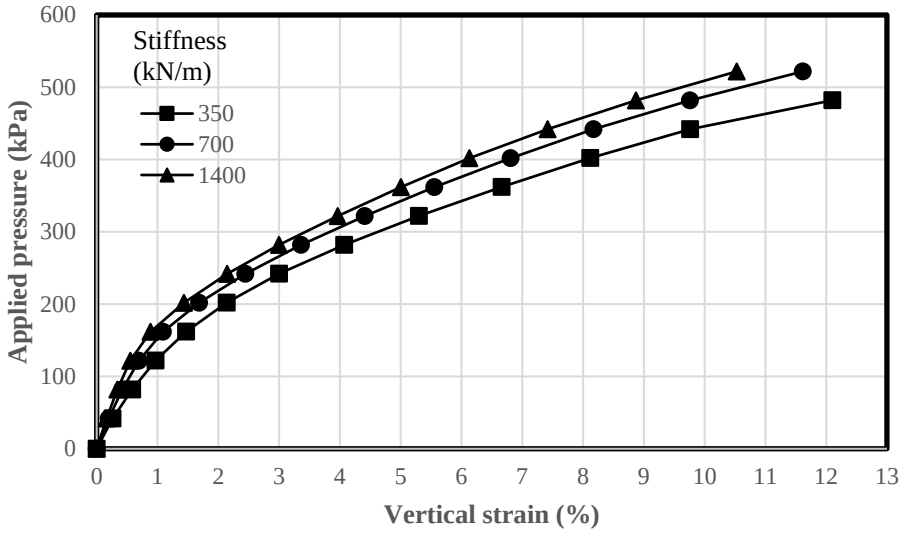

Fig. 7.3.16: Effect of geotextile reinforcement stiffness on the applied pressure – vertical strain curves

7.3.3.3.2 Lateral deformation and volume change

Figure 7.3.17 presents the lateral displacement profile of the CMU blocks along the height of the GRS pier under the applied pressure of 200 kPa (4177 psf) with geotextile reinforcement of different tensile stiffness. The tensile stiffness of the geotextile reinforcement had more influence on the lateral movements of the GRS pier than on the applied pressure – vertical strain curves. The increase of the tensile stiffness reduced the lateral displacement of the CMU blocks since geotextile with high tensile stiffness provided more lateral confinement to the surrounding soil by friction between the geotextile and the backfill soil.

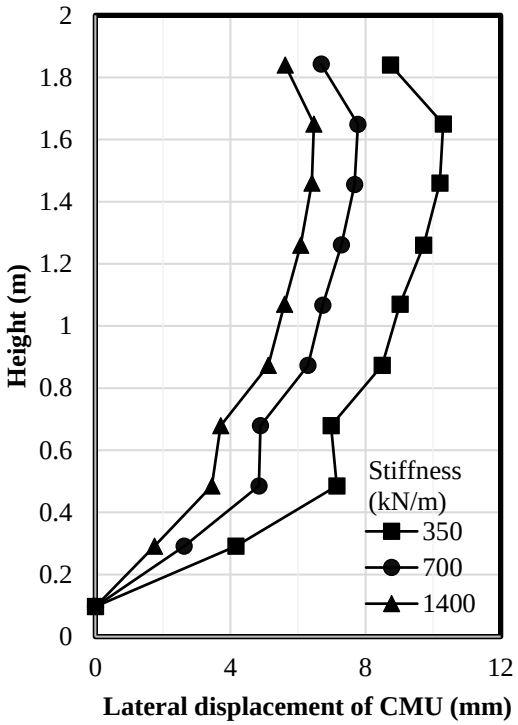

Fig. 7.3.17: Effect of the geotextile reinforcement stiffness on the lateral displacement of CMU blocks under the applied pressure of 200 kPa (4177 psf)

Figure 7.3.18 presents the normalized lateral volume change – normalized vertical volume change curves with geotextile reinforcement of different tensile stiffness. The zero-volume change curve was also plotted on the figure as reference. Figure 7.3.18 shows that the tensile stiffness of the geotextile reinforcement had a little effect on the volume change of the GRS pier. Although the use of geotextile reinforcement with high tensile stiffness reduced the lateral expansion of the CMU blocks as shown in Fig. 7.3.17, it also reduced the vertical compression of the GRS pier under the same applied pressure as shown in Fig. 7.3.16. The GRS pier had more vertical compression than lateral expansion when the applied pressure was small and tended to laterally expand more when the applied pressure was large.

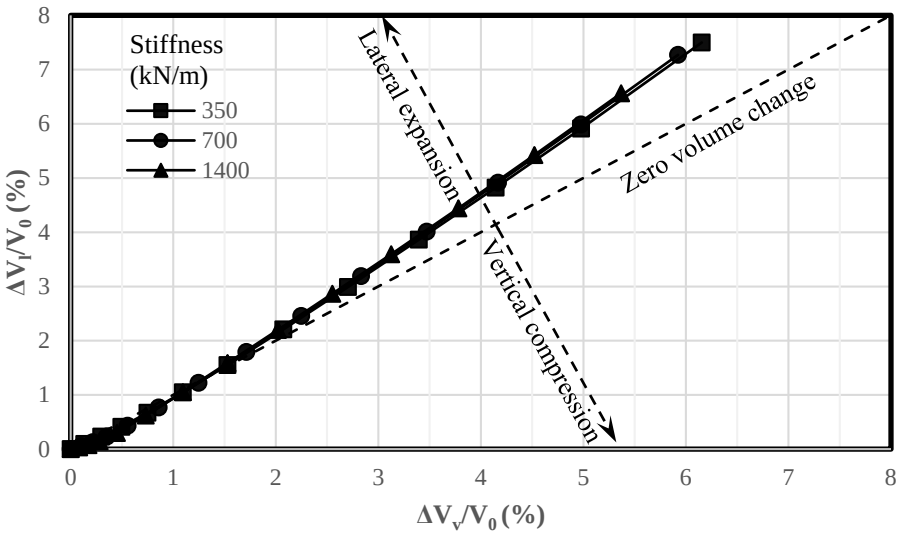

Fig. 7.3.18: Effect of the geotextile reinforcement stiffness on the volume change of the pier

7.3.3.3.3 Additional vertical stress

Figure 7.3.19 presents the additional vertical stress distribution beneath the concrete slab along the width of the GRS pier under the applied pressure of 200 kPa (4177 psf) with geotextile reinforcement of different tensile stiffness. Figure 7.3.19 shows that the additional vertical stress beneath the concrete slab showed a non-uniform distribution with higher stresses near the center and lower stresses at edges due to low confinement. The effect of the tensile stiffness of the geotextile reinforcement on the additional vertical stress distribution beneath the concrete slab was not as significant as that on the lateral displacement of the CMU blocks. The use of the geotextile reinforcement with higher stiffness reduced the additional vertical stress near the center caused by the applied pressure beneath the concrete slab.

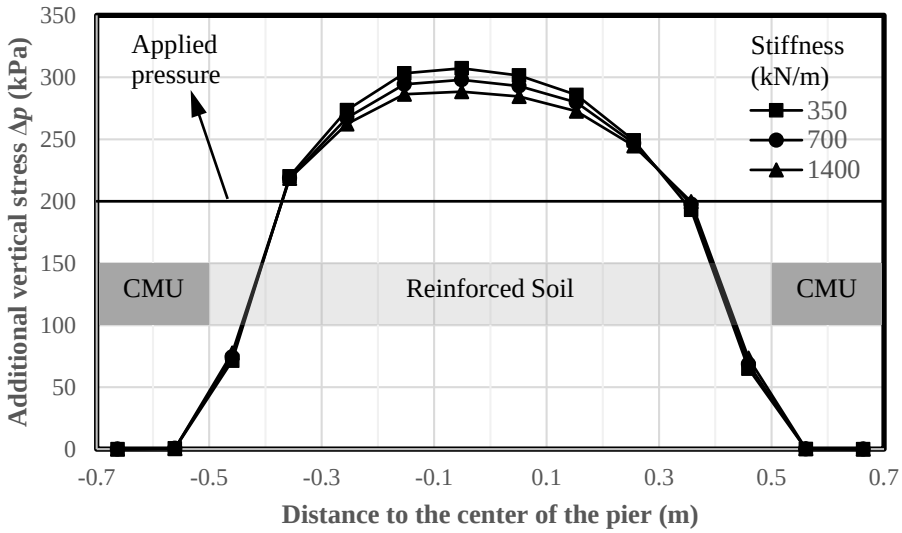

Fig. 7.3.19: Effect of the geotextile reinforcement stiffness on the additional vertical stress distribution beneath the concrete slab along the width of the pier under the applied pressure of 200 kPa (4177 psf)

7.3.3.3.4 Lateral earth pressures

Figure 7.3.20 presents the lateral earth pressure along the height of the GRS pier both behind the CMU blocks and near the center of the GRS pier under the applied pressure of 200 kPa (4177 psf) with geotextile reinforcement of different tensile stiffness. Similar to the additional vertical stress distribution, the effect of the tensile stiffness of the geotextile reinforcement on the lateral earth pressure distribution along the height of the GRS pier was small. The lateral earth pressures behind the CMU blocks were essentially the same for all three cases with different geotextile stiffness. The lateral earth pressure near the center of the GRS pier showed slightly different results within the upper part of the pier with higher lateral earth pressures when geotextile with low stiffness was used. Figure 7.3.19 shows that the use of geotextile with low stiffness increased the additional vertical stress beneath the concrete slab, resulting in higher lateral earth pressure occurring at the same location. Figure 7.3.21 presents the calculated lateral earth pressure coefficients *K* under the applied pressure of 200 kPa (4177 psf) with geotextile reinforcement of different tensile stiffness. Figure 7.3.21 also illustrates that the tensile stiffness of the geotextile reinforcement had little effect on both vertical and lateral earth pressure distributions within the GRS pier. The calculated lateral earth pressure coefficients near the center of the GRS pier were almost the same as the theoretical active lateral earth pressure coefficients K_a except for the locations at the top and bottom of the GRS pier.

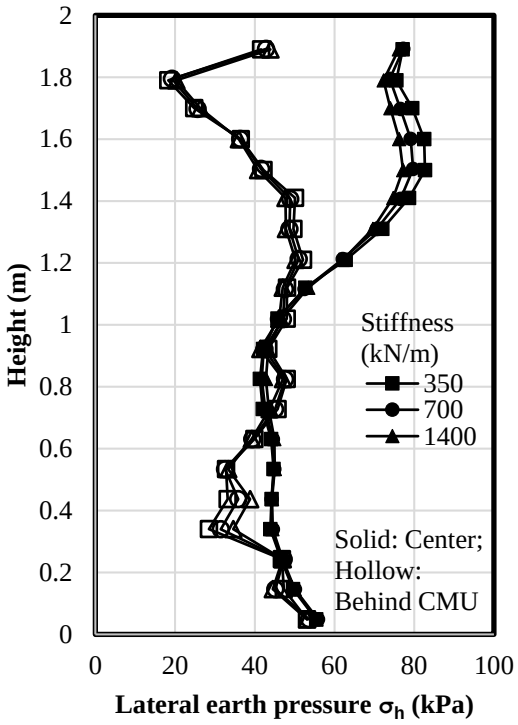

Fig. 7.3.20: Effect of the geotextile reinforcement stiffness on the lateral earth pressure along height under the applied pressure of 200 kPa (4177 psf)

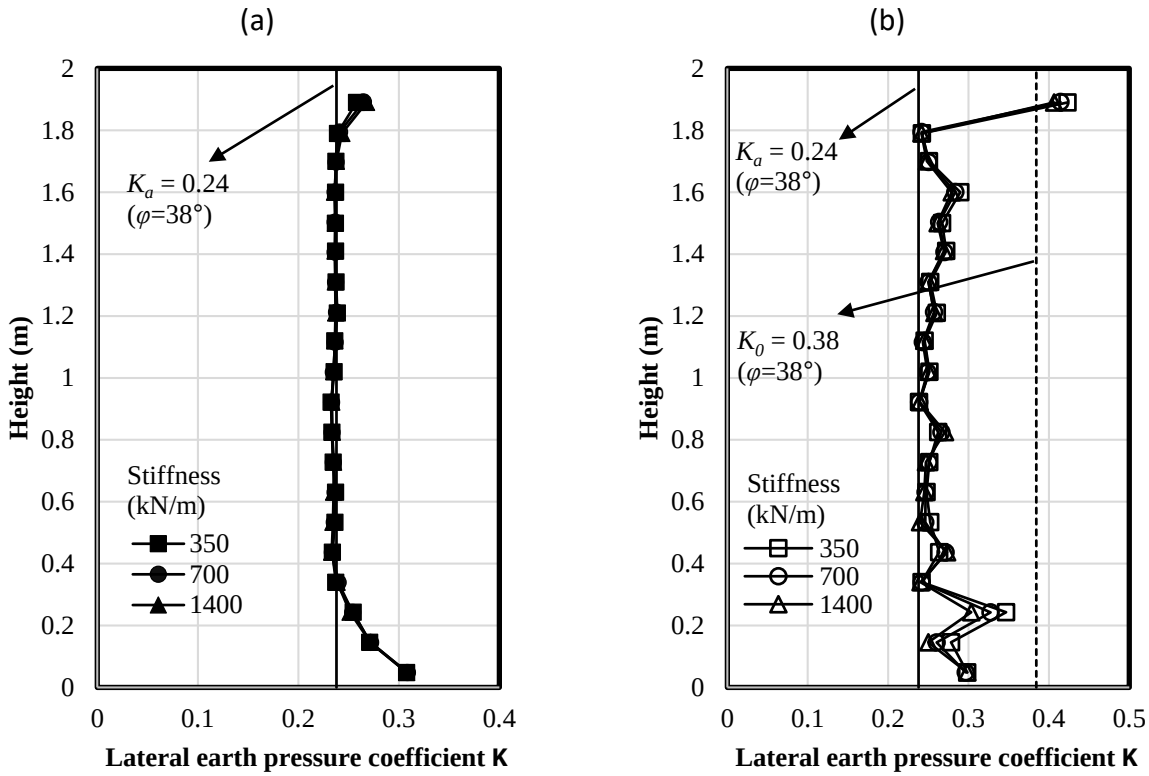

Fig. 7.3.21: Effect of the geotextile reinforcement stiffness on the calculated lateral earth pressure coefficient K under the applied pressure of 200 kPa (4177 psf): (a) Near the center of the pier; (b) Behind the CMU blocks.

7.3.3.3.5 Tension in the reinforcement

Figure 7.3.22 presents the maximum tensile force in the reinforcement under the applied pressure of 200 kPa (4177 psf) with geotextile reinforcement of different tensile stiffness. Figure 7.3.22 shows that the maximum tensile force in the geotextile reinforcement of tensile stiffness of 700 kN/m (48 kip/ft) was slightly larger than the case with the geotextile reinforcement having tensile stiffness of 350 kN/m (24 kip/ft). Meanwhile, for the case with the geotextile reinforcement having tensile stiffness of 1400 kN/m (96 kip/ft), the maximum tensile force was obviously larger, especially at the bottom part of the GRS pier. The maximum tensile force in the reinforcement followed the relationship of $T = J\varepsilon$. Under the same geotextile strain, the increase of the tensile stiffness would result in larger tensile force in the reinforcement.

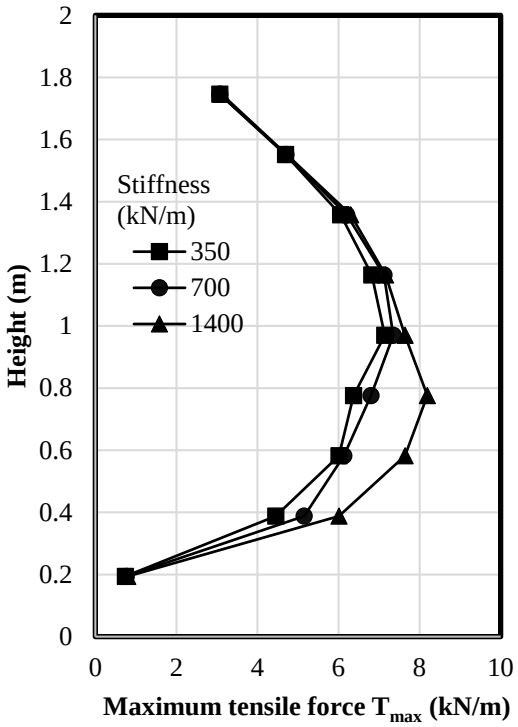

Fig. 7.3.22: Effect of the geotextile reinforcement stiffness on the maximum tensile force of the reinforcement under the applied pressure of 200 kPa (4177 psf)

Figure 7.3.23 presents the connection force in the reinforcement along the height of the GRS pier under the applied pressure of 200 kPa (4177 psf) with geotextile reinforcement of different tensile stiffness. The calculated connection force in the reinforcement was much smaller than the maximum tensile force. The effect of the tensile stiffness of the geotextile reinforcement on the connection force in the reinforcement was minimum, especially at the top of the pier. Similar to the maximum tension in the reinforcement, the difference of connection force between different reinforcement stiffness cases became larger at the mid-height to bottom portion of the pier.

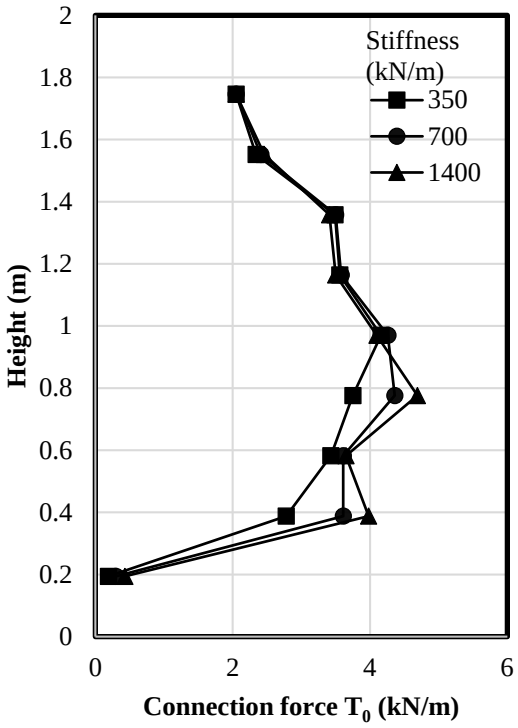

Fig. 7.3.23: Effect of the geotextile reinforcement stiffness on the connection force in the reinforcement under the applied pressure of 200 kPa (4177 psf)

7.3.3.4 EFFECT OF REINFORCEMENT VERTICAL SPACING

This section discusses the effect of the reinforcement vertical spacing. In the baseline model, the reinforcement spacing S_v was 0.194 m (7 in), corresponding to nine layers of geotextile reinforcement. Two additional reinforcement vertical spacings were considered in the study: 0.388 m (15 ¼ in) and 0.097 m (3 $^{13}/_{16}$ in). When the spacing of 0.388 m (15 ¼ in) was used, the GRS pier only incorporated four layers of geotextile reinforcement. When the spacing of 0.097 m (3 $^{13}/_{16}$ in) was used, the GRS pier contained 19 layers of geotextile reinforcement. Since the GRS pier was composed of ten layers of CMU blocks, only nine out of 19 layers of geotextile reinforcement were frictionally connected to the CMU blocks, leaving the remaining ten layers of geotextile reinforcement only placed over the backfill soil without connection to the facing. The geotextile layers frictionally connected to the CMU blocks are considered as primary reinforcement while the geotextile layers only placed above the backfill soil are considered as bearing bed reinforcement layers.

7.3.3.4.1 Applied pressure – vertical strain curve

Figure 7.3.24 presents the applied pressure – vertical strain curves with different reinforcement spacing. Figure 7.3.24 shows that the reinforcement spacing had a significant effect on the applied pressure – vertical strain curves. At 5% vertical strain, the ultimate vertical capacity of the GRS pier was 137 kPa (2861 psf), 343 kPa (7164 psf), and 458 kPa (9566 psf) for the cases

with reinforcement spacing of 0.388 m (15 ¼ in), 0.194 m (7 in), 0.097 m (3 $^{13}/_{16}$ in), respectively. The ultimate vertical capacity of the GRS pier with the reinforcement spacing of 0.388 m (15 ¼ in) was lower than 200 kPa (4177 psf), which was FHWA's recommended service pressure (Adams et al., 2011). The moduli of the GRS piers at the applied pressure of 200 kPa (4177 psf) was 12.0 MPa (1740.5 psi) and 15.4 MPa (2233.6 psi) for the cases with the reinforcement spacing of 0.194 m (7 in) and 0.097 m (3 $^{13}/_{16}$ in), respectively. The ultimate bearing capacity increased significantly from the reinforcement spacing of 0.388 m (15 ¼ in) to 0.194 m (7 in). The increase of the modulus of the GRS pier from the reinforcement spacing of 0.194 m (7 in) to 0.097 m (3 $^{13}/_{16}$ in) was limited. Because of the close spacing between geotextile reinforcement layers (less than 0.3 m (12 in)), the GRS pier had more reinforcement layers, meaning that the geotextile reinforcement had more interaction with the backfill soil. For largely-spaced reinforced GRS piers (larger than 0.3 m (12 in)), the pier had fewer reinforcement layers that provided less lateral restraint to the backfill soil. Since the vertical capacity of the GRS pier with the reinforcement spacing of 0.388 m (15 ¼ in) did not reach 200 kPa (4177 psf), the analyses presented subsequently in this section were conducted at the applied pressure of 160 kPa (3342 psf).

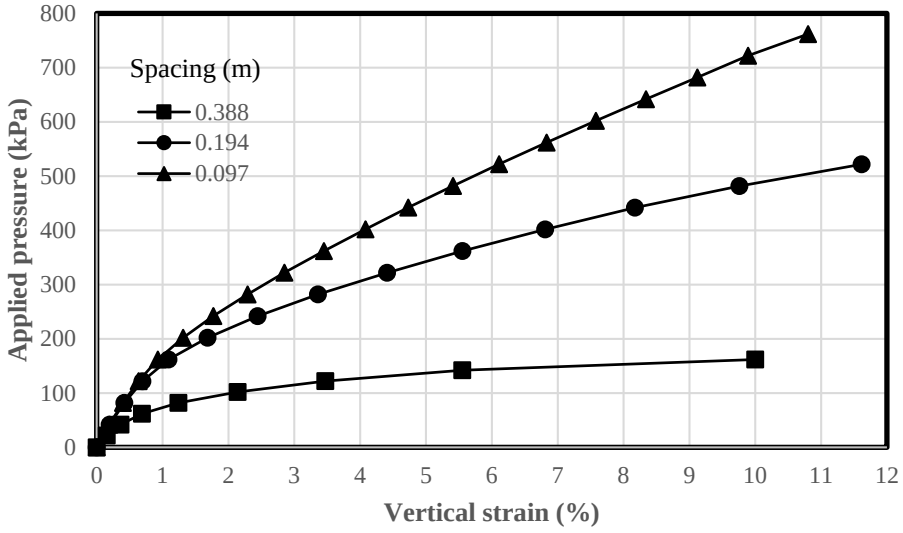

Fig. 7.3.24: Effect of the reinforcement vertical spacing on the applied pressure – vertical strain curves

7.3.3.4.2 Lateral deformation and volume change

Figure 7.3.25 presents the lateral displacement profile of the CMU blocks along the height of the GRS pier under the applied pressure of 160 kPa (3342 psf) with different reinforcement spacing. Figure 7.3.25 shows that at the applied pressure of 160 kPa (3342 psf), the lateral displacement of the CMU blocks was almost the same when the reinforcement spacing was smaller than 0.3 m (12 in). However, when the reinforcement spacing was 0.388 m (15 ¼ in), the lateral displacement of the CMU blocks was much larger with the maximum lateral displacement occurring at the top

of the pier. The GRS pier with the reinforcement spacing of 0.388 m (15 ¼ in) behaved differently from the closely-spaced GRS pier. The reinforcement layers with close spacing imparted an elevated confining stress on the backfill soil and influenced the particle-to-particle interaction of the soil (Saghebfar et al., 2017).

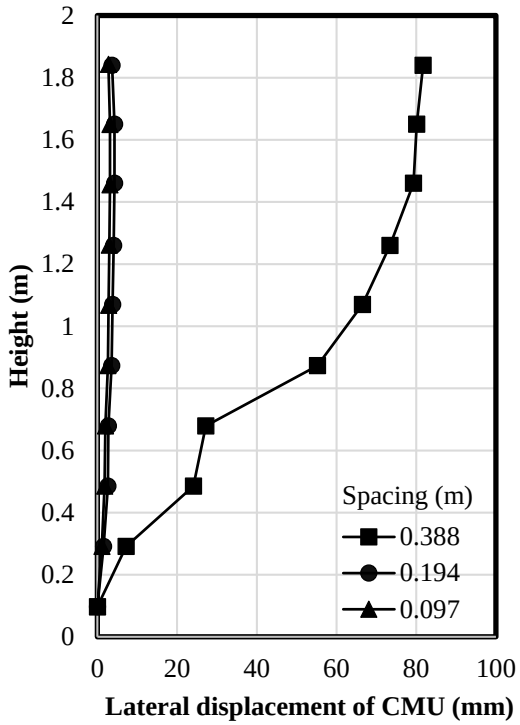

Fig. 7.3.25: Effect of the reinforcement vertical spacing on the lateral displacement of CMU blocks under the applied pressure of 160 kPa (3342 psf)

Figure 7.3.26 presents the normalized lateral volume change – normalized vertical volume change curves with different reinforcement spacing. The zero-volume change curve was also plotted on the figure for the purpose of comparison. Figure 7.3.26 shows that smaller reinforcement spacing resulted in the curve closer to the zero-volume change line. Wu et al. (2014) pointed out that the closely-spaced GRS mass usually shows a higher strength due to suppression of dilation. As a result, the suppression of dilation reduced both the lateral expansion and the volume change of the pier.

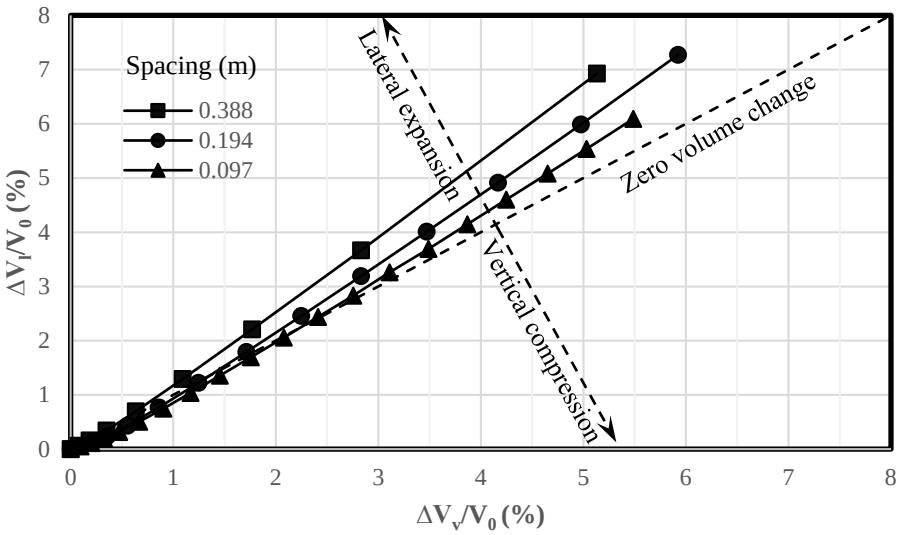

Fig. 7.3.26: Effect of the reinforcement vertical spacing on the volume change of the pier

7.3.3.4.3 Additional vertical stress

Figure 7.3.27 presents the additional vertical stress distribution beneath the concrete slab along the width of the pier under the applied pressure of 160 kPa (3342 psf) with different reinforcement spacing. Figure 7.3.27 shows that the additional vertical stress distribution beneath the concrete slab was almost the same when the reinforcement spacing was smaller than 0.3 m (12 in). However, when the reinforcement spacing was 0.388 m (15 ¼ in), the additional vertical stress near the center of the pier was almost three times the applied pressure and the additional vertical stress decreased sharply towards the edge of the concrete slab. The use of closely-spaced geotextile reinforcement layers made the distribution of additional vertical stress beneath the concrete slab more uniform. The increase of the reinforcement spacing resulted in a more non-uniform vertical stress distribution beneath the concrete slab. Maximum lateral displacement of the CMU blocks happened at the top of the pier as shown in Fig. 7.3.25. The backfill soil under the edges of the concrete slab moved laterally with the CMU blocks and they did not have enough lateral confinement to carry the vertical load. As a result, more stress was concentrated under the center of the concrete slab.

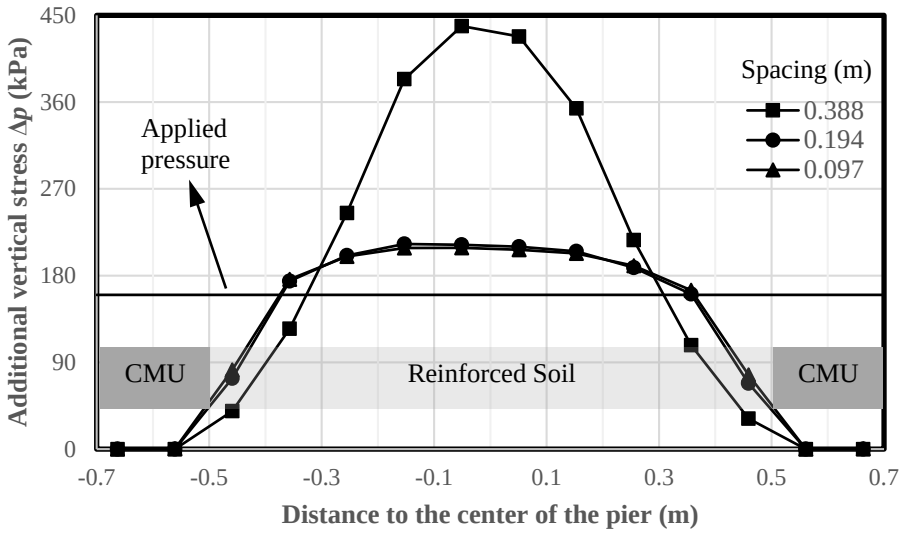

Fig. 7.3.27: Effect of the reinforcement vertical spacing on the additional vertical stress distribution beneath the concrete slab along the width of the pier under the applied pressure of 160 kPa (3342 psf)

7.3.3.4.4 Lateral earth pressures

Figure 7.3.28 presents the lateral earth pressure along the height of the GRS pier both behind the CMU blocks and near the center of the GRS pier under the applied pressure of 160 kPa (3342 psf) with different reinforcement spacing. Similar to the additional vertical stress beneath the concrete slab, the lateral earth pressure did not show obvious difference when the reinforcement spacing was smaller than 0.3 m (12 in). However, when the reinforcement spacing was 0.388 m (15 ¼ in), the lateral earth pressure near the center of the pier was much higher than those in the other two cases due to the vertical stress concentration near the center of the pier as shown in Fig. 7.3.27. Because of the large lateral movement of the CMU blocks as shown in Fig. 7.3.25, the lateral earth pressure behind the CMU blocks was slightly lower as compared with those in the other two cases.

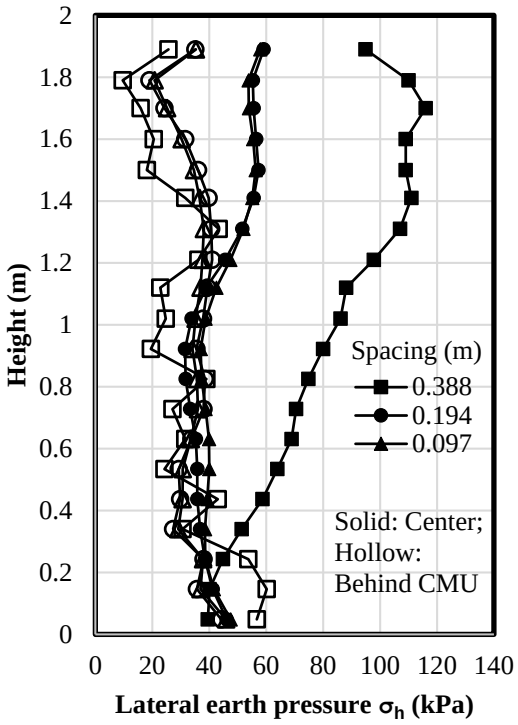

Fig. 7.3.28: Effect of the reinforcement vertical spacing on the lateral earth pressure along height under the applied pressure of 160 kPa (3342 psf)

Figure 7.3.29 presents the calculated lateral earth pressure coefficients *K* under the applied pressure of 160 kPa (3342 psf) with different reinforcement spacing. For the lateral earth pressures at the center of the pier, the calculated lateral earth pressure coefficients in all the cases with three reinforcement spacing were close to the theoretical active lateral earth pressure coefficients K_a. For the lateral earth pressure behind the CMU blocks, the increase of the reinforcement spacing caused the variations of the calculated lateral earth pressure coefficients along the height. At the locations above or below the geotextile reinforcement layers when the reinforcement spacing was 0.388 m (15 ¼ in), the calculated *K* coefficients fluctuated between the theoretical K_a and K_0 coefficients and were sometimes larger than K_0. The existence of the geotextile layers provided lateral confinement to the surrounding soil. However, when the geotextile reinforcement layers were not closely-spaced, the lateral confinement of the geotextile layers were not effective to the locations farther away, thus resulting in the variations in the calculated *K* along the height.

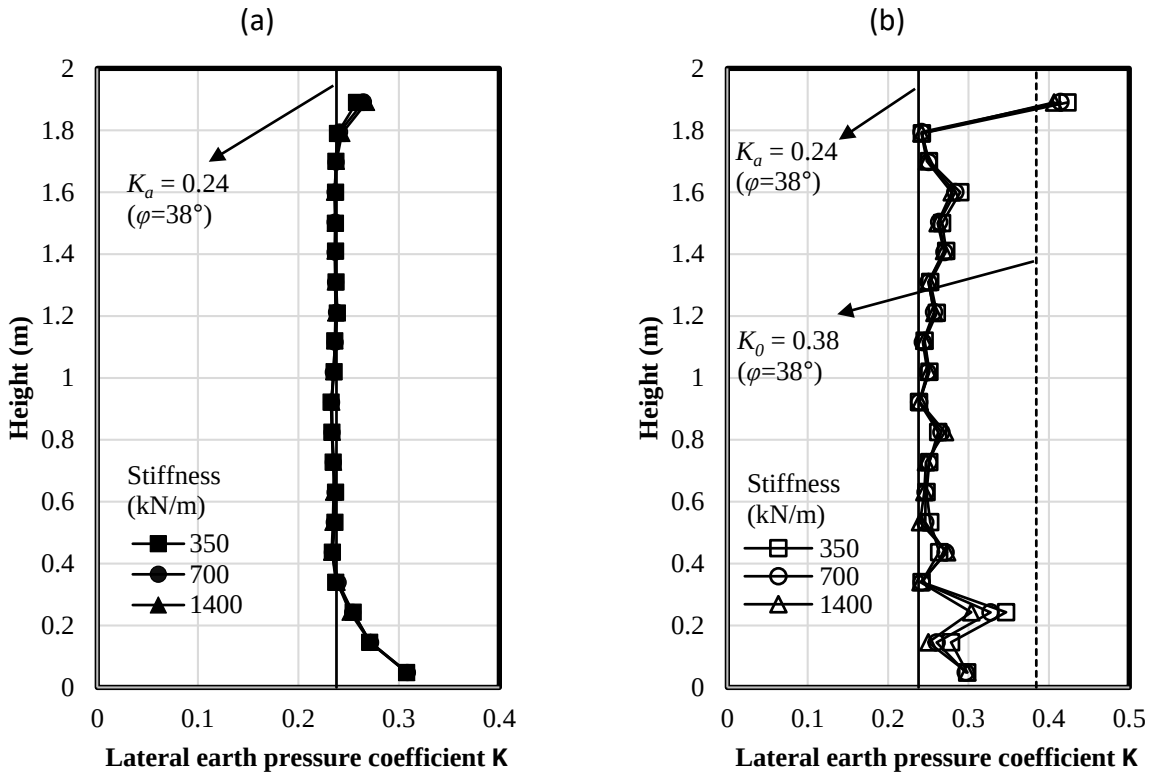

Fig. 7.3.29: Effect of the reinforcement vertical spacing on the calculated lateral earth pressure coefficient K under the applied pressure of 160 kPa (3342 psf): (a) Near the center of the pier; (b) Behind the CMU blocks.

7.3.3.4.5 Tension in the reinforcement

Figure 7.3.30 presents the maximum tensile force in the reinforcement under the applied pressure of 160 kPa (3342 psf) with different reinforcement spacing. When the reinforcement spacing was 0.097 m (3 $^{13}/_{16}$ in), the maximum tensile force in the primary reinforcement was close to that the maximum tensile force in the reinforcement when the spacing was 0.194 m (7 in). The maximum tensile force in the bearing bed reinforcements was much smaller than that in the primary reinforcement when the reinforcement spacing was 0.097 m (3 $^{13}/_{16}$ in). For the case with reinforcement spacing of 0.388 m (15 ¼ in), the maximum tensile force in the reinforcement was much larger than those in the other two cases.

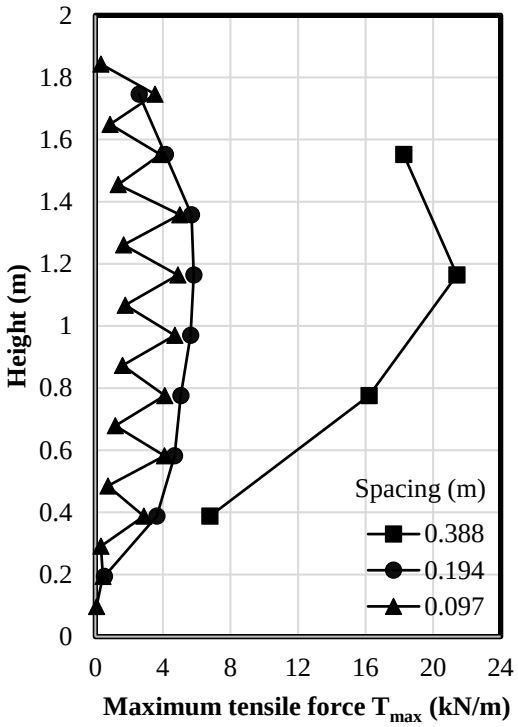

Fig. 7.3.30: Effect of the reinforcement vertical spacing on the maximum tensile force of the reinforcement under the applied pressure of of 160 kPa (3342 psf)

Figure 7.3.31 presents the connection force in the reinforcement along the height of the GRS pier under the applied pressure of 160 kPa (3342 psf) with different reinforcement spacing. Figure 7.3.31 shows that for the cases with reinforcement spacing of 0.194 m (7 in) and 0.097 m (3 $^{13}/_{16}$ in), the connection forces in the primary reinforcement were close to each other. When the reinforcement spacing was 0.388 m (15 ¼ in), however, the connection force in the primary reinforcement increased with the increase of depth.

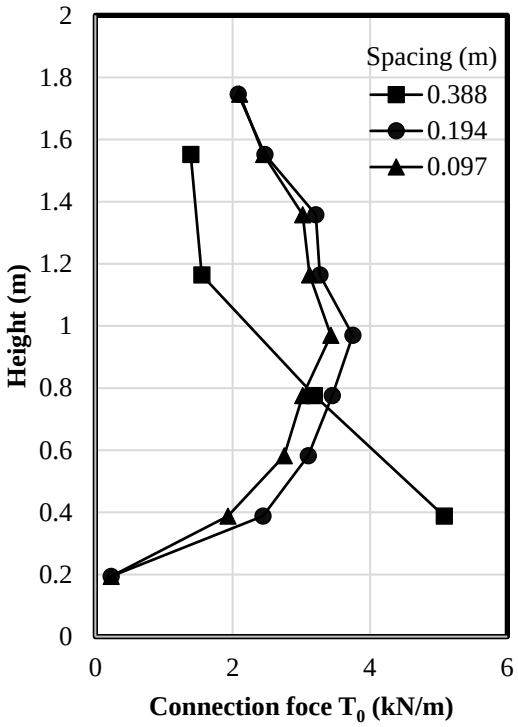

Fig. 7.3.31: Effect of the reinforcement vertical spacing on the connection force of the reinforcement under the applied pressure of of 160 kPa (3342 psf)

7.3.3.5 EFFECT OF COMBINATION OF REINFORCEMENT STIFFNESS AND SPACING

Schlosser & Long (1974) concluded that the presence of geosynthetic reinforcement resulted in an apparent cohesion in the soil. Wu & Pham (2013) used Equation (7.3.6) to evaluate the apparent cohesion c_R due to the existence of geosynthetic reinforcement:

$$c_R = \frac{T_f \sqrt{K_p}}{2S_v} + c \tag{7.3.6}$$

where T_f is the reinforcement strength; K_p is the Rankine passive earth pressure coefficient; S_v is the reinforcement spacing; c is the cohesion of the soil. Equation (7.3.6) implies that the increase in reinforcement strength T_f has the same effect as a proportional decrease in reinforcement S_v (Wu & Pham, 2013). Since the geogrid structural element used to simulate geotextile reinforcement in FLAC3D had constant stiffness J, the reinforcement strength T_f is also proportional to the reinforcement stiffness J ($T_f = \varepsilon J$). Therefore, it is appropriate to use the ratio of reinforcement stiffness J to spacing S_v to evaluate the contribution of the reinforcement layers.

This section discusses the effect of the reinforcement stiffness to spacing ratio. Two cases were studied in this section: Case 1 (J = 700 kN/m (48 kip/ft), S_v = 0.388 m (15 ¼ in))) and Case 2 (J = 350 kN/m (24 kip/ft), S_v = 0.194 m (7 in)). In both cases, the ratio of reinforcement stiffness to spacing was maintained the same as J/S_v = 1804 kN/m/m (37677 lb/ft/ft). However, the first case used larger reinforcement spacing with higher strength reinforcement while the second case used smaller reinforcement spacing with lower strength reinforcement. This section aimed to investigate the effect of different combinations of J and S_v but the same J/S_v on the performance of the pier.

7.3.3.5.1 Applied pressure – vertical strain curve

Figure 7.3.32 presents the applied pressure – vertical strain curves with different combinations of J and S_v while the ratio of J/S_v was maintained the same. Figure 7.3.32 shows significantly different results from these two cases. At 5% vertical strain, the ultimate vertical capacity of the GRS pier was 137 kPa (2861 psf) and 312 kPa (6516 psf) for Case 1 (J = 700 kN/m (48 kip/ft), S_v = 0.388 m (15 ¼ in)) and Case 2 (J = 350 kN/m (24 kip/ft), S_v = 0.194 m (7 in)), respectively. The ultimate vertical capacity of the GRS pier in Case 1 was lower than the FHWA recommended service pressure of 200 kPa (4177 psf) (Adams et al., 2011). Figure 7.3.32 shows that the contribution of close reinforcement spacing was much more significant than that of high stiffness reinforcement. The closely-spaced reinforcement case had more reinforcement layers and the interaction between reinforcement layers and the backfill soil provide higher confinement to the surrounding soil, resulting in the increase of the bearing capacity. However, when the reinforcement spacing was larger than 0.3 m (12 in), there were fewer reinforcement layers and the required connection force of each reinforcement to maintain the stability of the pier became higher. The confinement of the soil provided by the reinforcement was limited by its connection resistance in the largely-spaced reinforcement case.

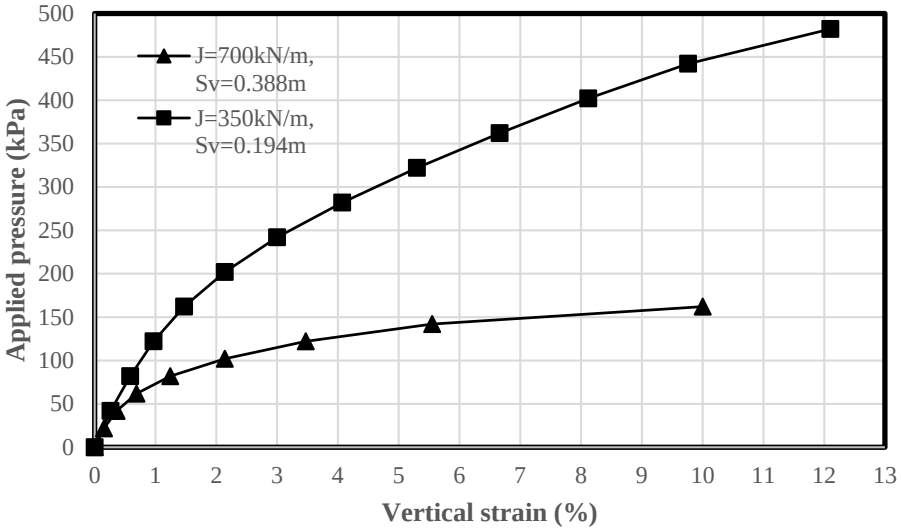

Fig. 7.3.32: Effect of the combination of reinforcement stiffness and spacing on the applied pressure – vertical strain curves

7.3.3.5.2 Lateral deformation and volume change

Figure 7.3.33 presents the lateral displacement profile of the CMU blocks along the height of the GRS pier under the applied pressure of 160 kPa (3342 psf) with different combinations of reinforcement stiffness and spacing. Similar to the applied pressure – vertical strain curves, these two cases had very different lateral displacements of the CMU blocks. Lateral displacement in Case 1 (J = 700 kN/m (48 kip/ft), S_v = 0.388 m (15 ¼ in)) was much larger than that in Case 2 (J = 350 kN/m (24 kip/ft), S_v = 0.194 m (7 in)). When the reinforcement spacing was larger than 0.3 m (12 in) (i.e., case 1), the maximum lateral displacement of the CMU blocks happened at the top of the pier. However, when the close reinforcement spacing was used (i.e., Case 2), the top of the pier was restrained by the top layer of the geotextile reinforcement, resulting the maximum lateral displacement happened below the top of the pier.

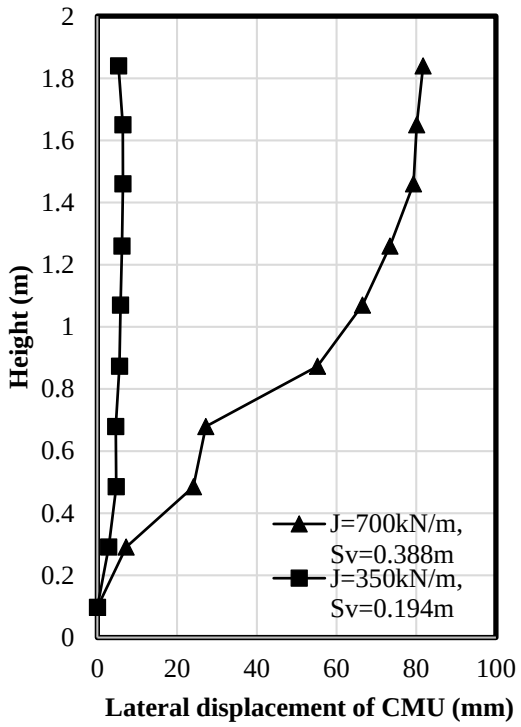

Fig. 7.3.33: Effect of the combination of reinforcement stiffness and spacing on the lateral displacement of CMU blocks under the applied pressure of 160 kPa (3342 psf)

Figure 7.3.34 presents the normalized lateral volume change – normalized vertical volume change curves with different combinations of reinforcement stiffness and spacing. Figure 7.3.34 shows the curve for Case 2 (J = 350 kN/m (24 kip/ft), S_v = 0.194 m (7 in)) was much closer to the zero volume change line as compared with Case 1 (J = 700 kN/m (48 kip/ft), S_v = 0.388 m (15 ¼ in)). The use of closely-spaced geotextile reinforcement significantly reduced the lateral expansion of the GRS pier.

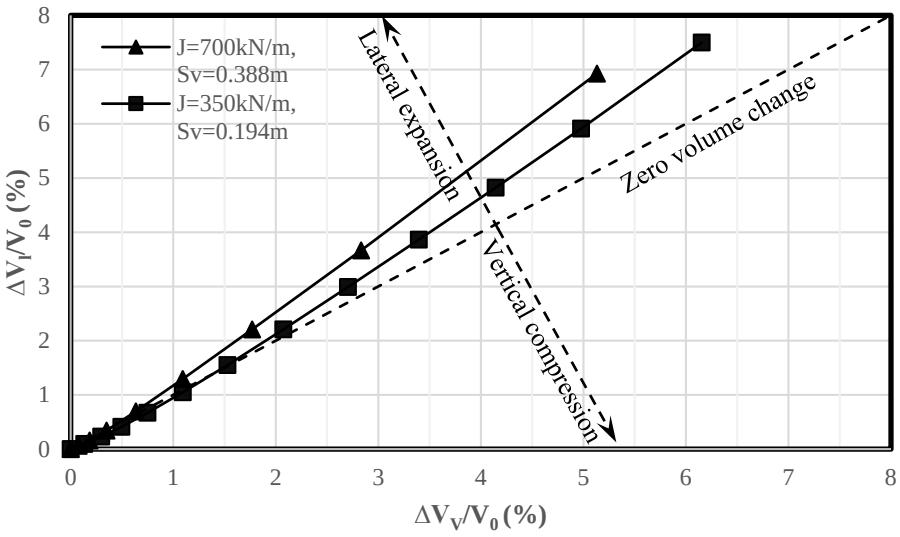

Fig. 7.3.34: Effect of the combination of reinforcement stiffness and spacing on the volume change of the pier

7.3.3.5.3 Additional vertical stress

Figure 7.3.35 presents the additional vertical stress distribution beneath the concrete slab along the width of the pier under the applied pressure of 160 kPa (3342 psf) with different combinations of reinforcement stiffness and spacing. Due to the difference in lateral restraint by different numbers of reinforcement layers, the additional vertical stress distribution beneath the concrete slab along the width of the pier showed very different results for Cases 1 and 2. Cases 1 (J = 700 kN/m (48 kip/ft), S_v = 0.388 m (15 ¼ in)) showed much stress concentration at the center of the pier as compared with Case 2 (J = 350 kN/m (24 kip/ft), S_v = 0.194 m (7 in)). This difference is because fewer reinforcement layers in the larger spacing case (Case 1) provided less lateral restraint behind the facing blocks than more reinforcement layers in the closer spacing case (Case 2).)

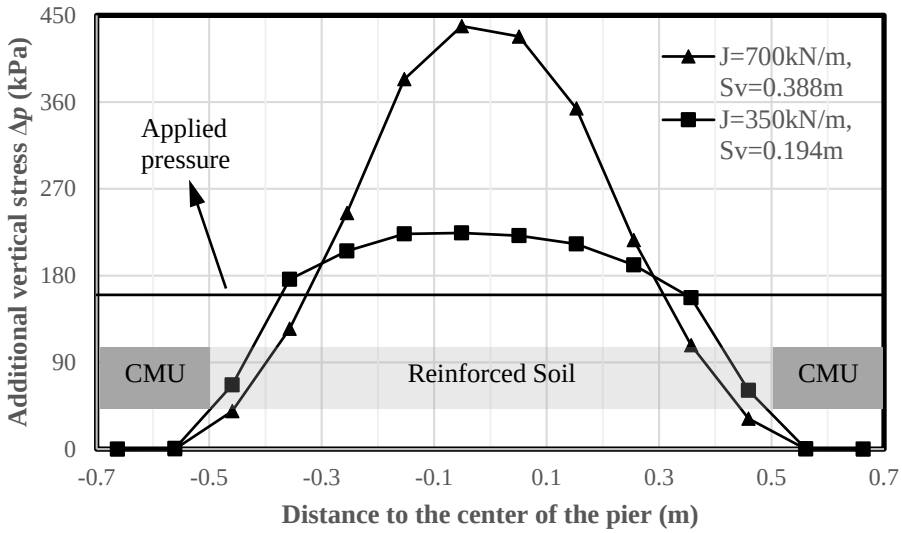

Fig. 7.3.35: Effect of the combination of reinforcement stiffness and spacing on the additional vertical stress distribution beneath the concrete slab along the width of the pier under the applied pressure of 160 kPa (3342 psf)

7.3.3.5.4 Lateral earth pressures

Figure 7.3.36 presents the lateral earth pressures along the height of the GRS pier both behind the CMU blocks and near the center of the GRS pier under the applied pressure of 160 kPa (3342 psf) with different combinations of reinforcement stiffness and spacing. Figure 7.3.37 presents the calculated lateral earth pressure coefficients *K* under the applied pressure of 160 kPa (3342 psf) with different combinations of reinforcement stiffness and spacing. The lateral earth pressure near the center of pier using large spacing but high stiffness reinforcement (i.e., Case 1 J = 700 kN/m (48 kip/ft), S_v = 0.388 m (15 ¼ in)) was much higher than Case 2 (J = 350 kN/m (24 kip/ft), S_v = 0.194 m (7 in)) due to the vertical stress concentration near the center. However, the calculated lateral earth pressure coefficients for the locations near the center of the pier were close to the theoretical K_a despite the change of the combinations of reinforcement spacing and stiffness. Both the calculated lateral earth pressure and coefficient behind the CMU blocks for Case 1 had more variations than those for Case 2.

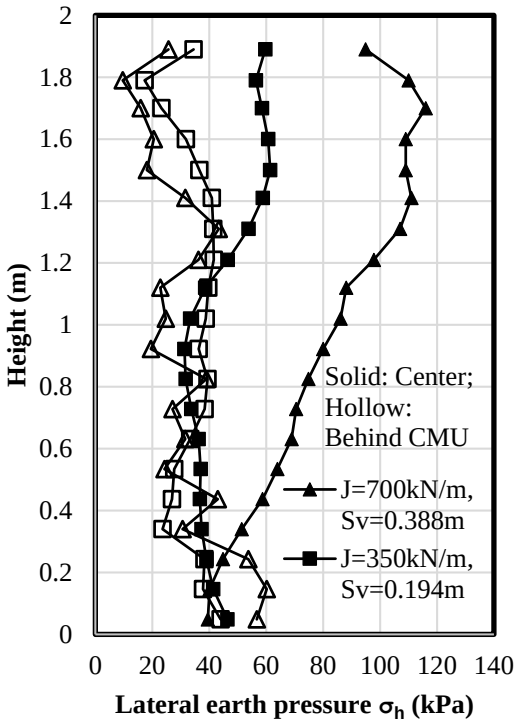

Fig. 7.3.36: Effect of the combination of reinforcement stiffness and spacing on the lateral earth pressure along the height under the applied pressure of 160 kPa (3342 psf)

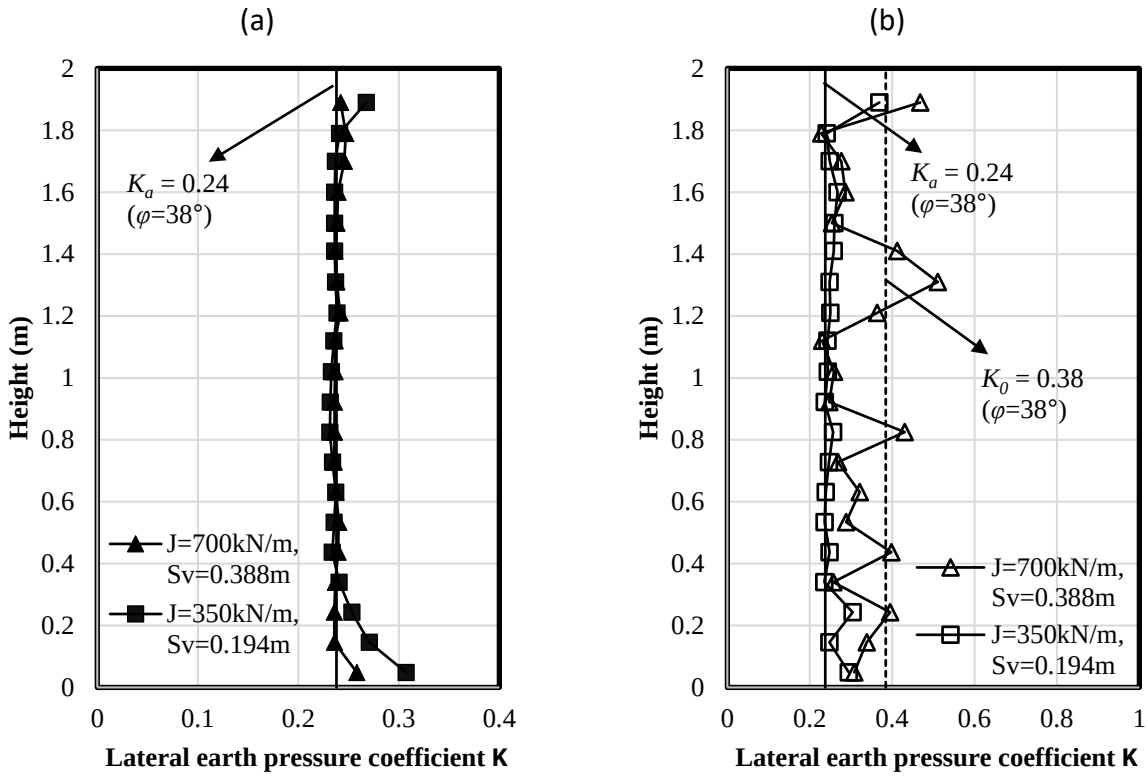

Fig. 7.3.37: Effect of the combination of reinforcement stiffness and spacing on the calculated lateral earth pressure coefficient K under the applied pressure of 160 kPa (3342 psf): (a) Near the center of the pier; (b) Behind the CMU blocks.

7.3.3.5.5 Tension in the reinforcement

Figure 7.3.38 presents the maximum tensile forces of the reinforcement under the applied pressure of 160 kPa (3342 psf) with different combinations of reinforcement stiffness and spacing. Because of different numbers of reinforcement layers, the maximum tensile force of the reinforcement in Case 1 (J = 700 kN/m (48 kip/ft), S_v = 0.388 m (15 ¼ in)) was much higher than that in Case 2 (J = 350 kN/m (24 kip/ft), S_v = 0.194 m (7 in)). When the reinforcement spacing was 0.388 m (15 ¼ in) and the pier had fewer reinforcement layers, each reinforcement layer carried more load. However, when the reinforcement spacing was 0.194 m (7 in) and the pier had more reinforcement layers, each reinforcement layer carried less and more uniform load.

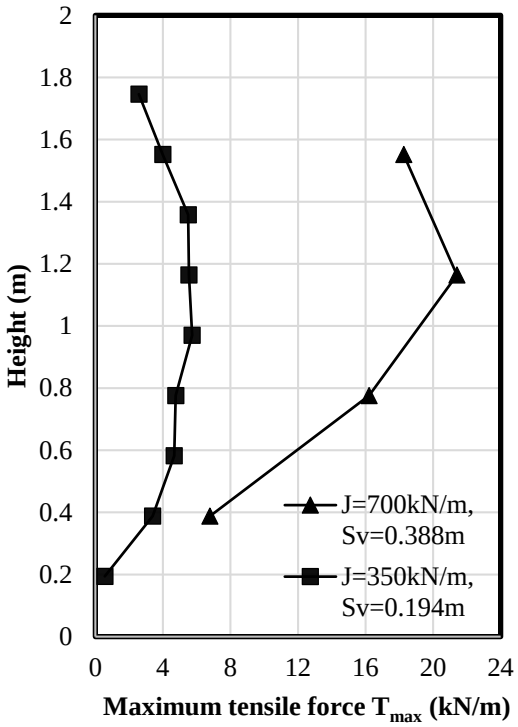

Fig. 7.3.38: Effect of the combination of reinforcement stiffness and spacing on the maximum tensile force of the reinforcement under the applied pressure of 160 kPa (3342 psf)

Figure 7.3.39 (a) presents the connection force in the reinforcement along the height of the GRS pier under the applied pressure of 160 kPa (3342 psf) with different combinations of reinforcement stiffness and spacing. The connection force in the reinforcement was smaller as compared with the maximum tensile force due to frictional connection between the geotextile reinforcement and the CMU blocks. When close spacing reinforcement was used, the connection force in each reinforcement did not change significantly along the depth except for the top and bottom layers. For the case with large spacing reinforcement, on the other hand, the connection force in the reinforcement showed an increase with the depth. Figure 7.3.39 (b) presents the ratio of the connection force to the maximum tensile force in the reinforcement along the depth. For the case with small spacing reinforcement, the connection force was much closer to the maximum tensile force in the reinforcement, resulting in their ratio of approximately 0.6. For the case with large spacing reinforcement, however, their ratio was approximately 0.1 for the top two layers and rapidly increased to 0.76 for the bottom reinforcement layer. The tension in the reinforcement with close spacing was more uniformly distributed than that with large spacing.

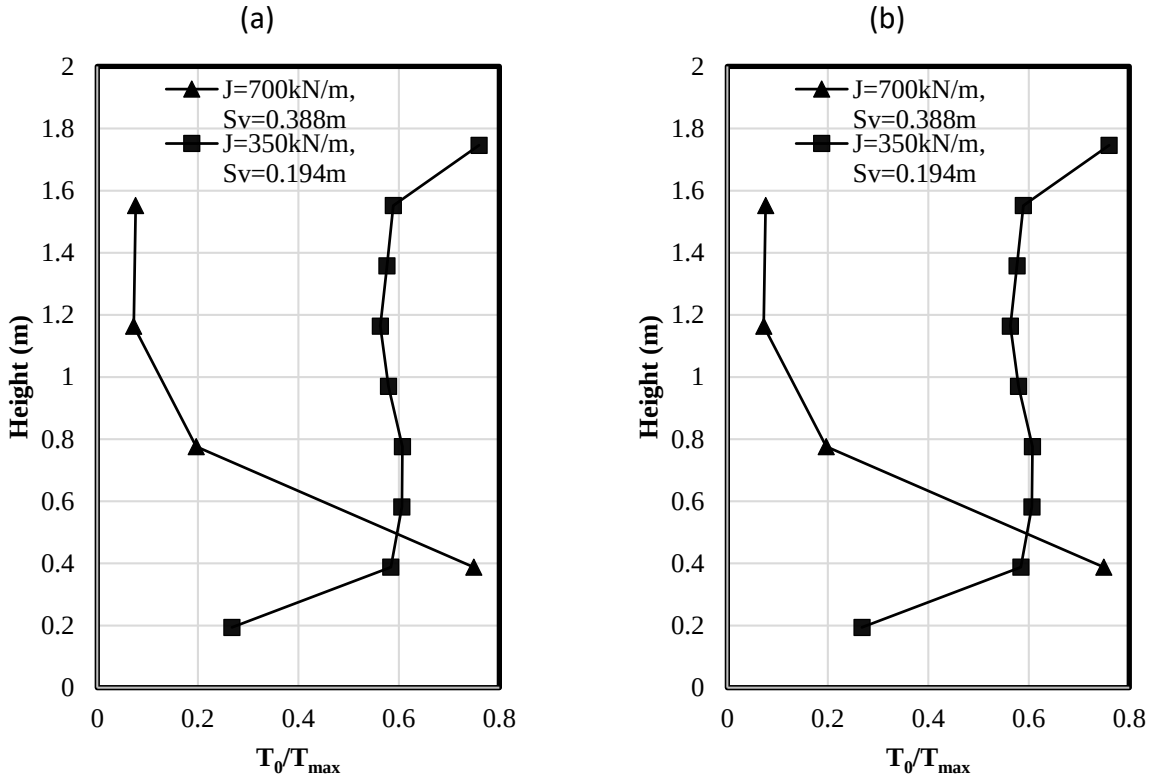

Fig. 7.3.39: Effect of the combination of reinforcement stiffness and spacing on the connection force in the reinforcement under the applied pressure of 160 kPa (3342 psf): (a) Connection force profile along depth; (b) Ratio of connection force to the maximum tensile force profile along depth.

It should be noted that only two cases of same J/S_v were discussed in this section. More cases with same J/S_v would be better to serve the purpose of this section to investigate the effect of different combinations of J and S_v but the same J/S_v on the performance of the pier. However, the geometry of the pier as well as the CMU facing blocks led to difficulties in running additional numerical cases with larger reinforcement spacing. The height of the pier and each CMU facing block were 1.94 m and 0.194 m respectively. In other words, the pier consisted of ten layers of CMU facing blocks. Cases of reinforcement spacing larger than 0.388 m would result in an uneven distribution of reinforcement material along the height of the pier. In addition, numerical results of the pier with reinforcement spacing of 0.388 m showed that the pier had excessively large vertical settlement and lateral displacement under the applied pressure of 160 kPa. If larger spacing were used, the pier would fail under even smaller load. On the other hand, since the height of each CMU block was 0.194 m, smaller reinforcement spacing (e.g., 0.1 m) would cause ten out of 19 layers of reinforcement not connected with CMU facing blocks. Under this condition, the behavior of the pier would be affected not only by the reinforcement spacing and stiffness but also by the facing connection. Therefore, only two cases with same J/S_v were presented in this section regarding the behavior of the pier. However, additional cases will be

presented in the subsequent numerical analyses of GRS-IBS conducted in this study (i.e., Section 7.4) where the height of the GRS abutment was larger and, accordingly, larger reinforcement spacing could be used.

7.3.3.6 EFFECT OF SOIL – REINFORCEMENT INTERACTION COEFFICIENT

This section discusses the effect of interaction coefficient between the backfill soil and the reinforcement. In the baseline model, the soil – reinforcement interaction coefficient C_i was 0.6. Additional two cases with C_i being 0.8 and 1.0 were studied. The soil – reinforcement interface friction angles were 32° and 38° when C_i was equal to 0.8 and 1.0, respectively.

7.3.3.6.1 Applied pressure – vertical strain curve

Figure 7.3.40 presents the applied pressure – vertical strain curves with different soil – reinforcement interaction coefficients. Figure 7.3.40 shows that the effect of the soil – geotextile interaction coefficient was limited. Larger soil – reinforcement interaction coefficient represented better interlocking between geosynthetic reinforcement and backfill. Considering the smooth surface of geotextile, the baseline model used a C_i of 0.6. A coefficient C_i of 0.8 or 1.0 may be used for the interface between geogrid and backfill soil. At 5% vertical strain, the ultimate vertical capacities of the GRS pier with the soil - reinforcement interaction coefficient of 0.6, 0.8, and 1.0 were 343 kPa (7164 psf), 351 kPa (7331 psf), and 359 kPa (7498 psf), respectively. The moduli of the GRS pier at the applied pressure of 200 kPa (4177 psf) were 12.0 MPa (1740.5 psi), 12.5 MPa (1813.0 psi), and 12.9 MPa (1871.0 psi) for the cases with the soil - reinforcement interaction coefficients of 0.6, 0.8, and 1.0, respectively.

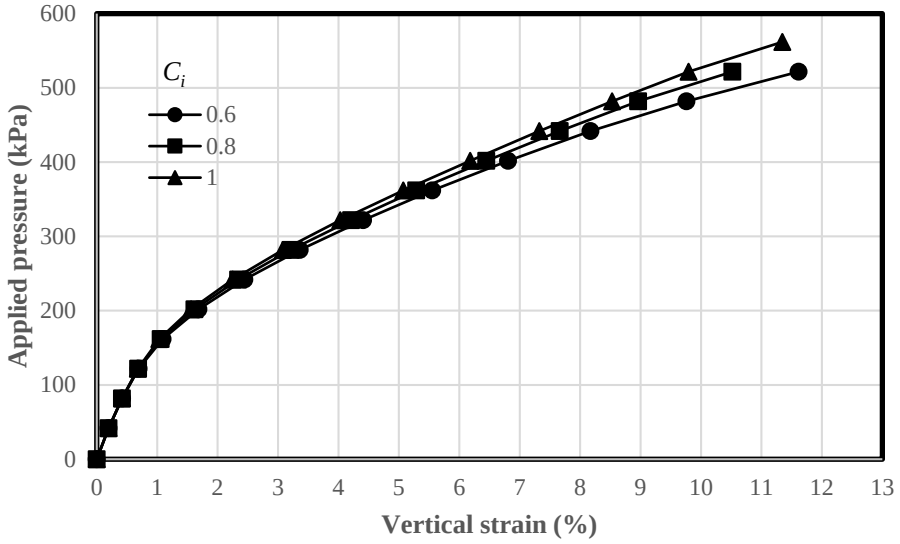

Fig. 7.3.40: Effect of the soil – reinforcement interaction coefficient on the applied pressure – vertical strain curves

7.3.3.6.2 Lateral deformation and volume change

Figure 7.3.41 presents the lateral displacement profiles of the CMU blocks along the height of the GRS pier under the applied pressure of 200 kPa (4177 psf) with different soil – reinforcement interaction coefficients. Figure 7.3.41 shows that the effect of the soil – reinforcement interaction coefficient on the lateral displacement of the CMU blocks was more significant as compared with that on the applied pressure – vertical strain curve. The larger soil – reinforcement interaction coefficient resulted in the smaller lateral displacement since rough interface could provide more lateral restraint to the surrounding soil.

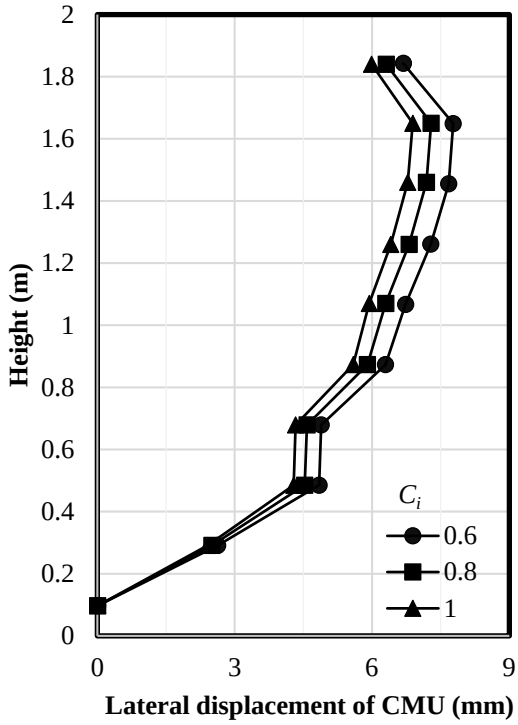

Fig. 7.3.41: Effect of the soil – reinforcement interaction coefficient on the lateral displacement of CMU blocks under the applied pressure of 200 kPa (4177 psf)

Figure 7.3.42 presents the normalized lateral volume change – normalized vertical volume change curves with different soil – reinforcement interaction coefficients. The zero-volume change curve was also plotted on the figure for the purpose of comparison. Figure 7.3.42 shows that the soil – reinforcement interaction coefficient had little effect on the volume change of the pier. Although the increase of the soil – reinforcement interaction coefficient reduced the lateral displacement of the CMU blocks, it also had slightly reduced the vertical compression of the pier (-as shown in Fig. 7.3.40), resulting in all three curves overlapped with each other.

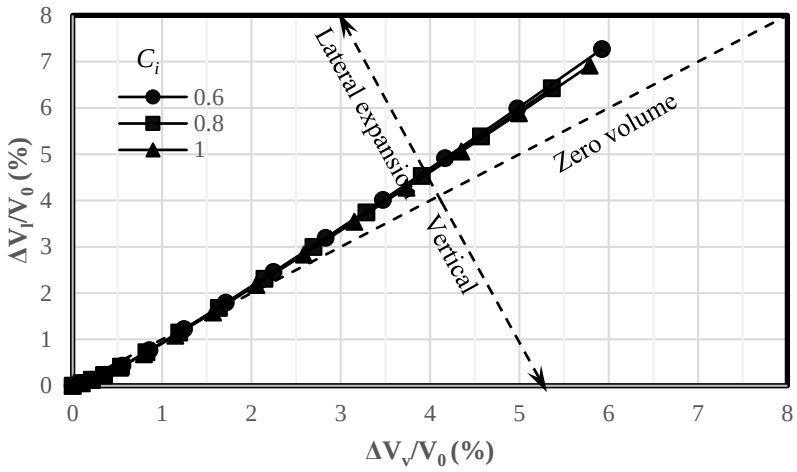

Fig. 7.3.42: Effect of the soil – reinforcement interaction coefficient on the volume change of the pier

7.3.3.6.3 Additional vertical stress

Figure 7.3.43 presents the additional vertical stress distributions beneath the concrete slab along the width of the GRS pier under the applied pressure of 200 kPa (4177 psf) with different soil – reinforcement interaction coefficients. Figure 7.3.43 shows that the increase of the soil – reinforcement interaction coefficient slightly reduced the additional vertical stress beneath the concrete slab, thus resulting in the reduction of the vertical compression of the pier as discussed before.

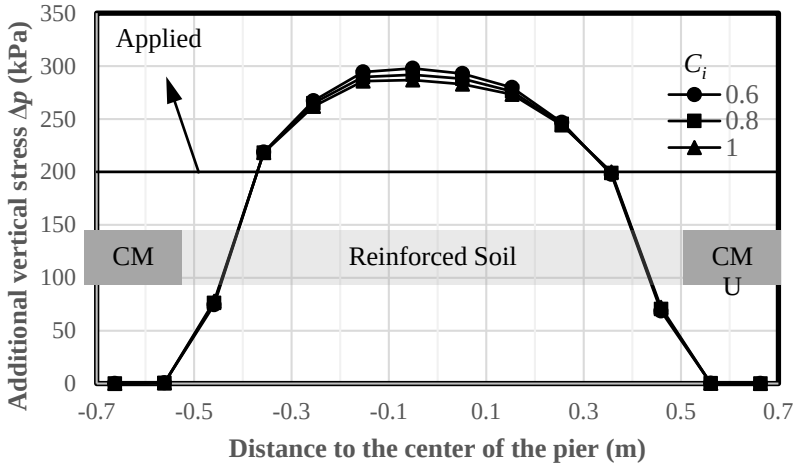

Fig. 7.3.43: Effect of the soil – reinforcement interaction coefficient on the additional vertical stress distribution beneath the concrete slab along the width of the pier under the applied pressure of 200 kPa (4177 psf)

7.3.3.6.4 Lateral earth pressures

Figure 7.3.44 shows the lateral earth pressures along the height of the GRS pier both behind the CMU blocks and near the center of the GRS pier under the applied pressure of 200 kPa (4177 psf) with different soil – reinforcement interaction coefficients. Figure 7.3.45 presents the calculated lateral earth pressure coefficients *K* under the applied pressure of 200 kPa (4177 psf) with different soil – reinforcement interaction coefficients. Both Fig. 7.3.44 and Fig. 7.3.45 show that the effect of the soil – reinforcement interaction coefficient on the lateral earth pressure was limited. The increase of the soil – reinforcement interaction coefficient slightly reduced the lateral earth pressure near the center of the pier. The calculated lateral earth pressure coefficients were essentially the same for all three cases.

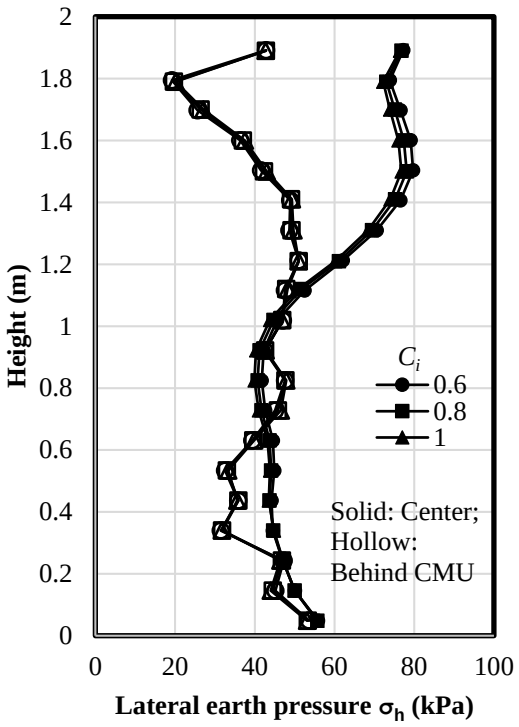

Fig. 7.3.44: Effect of the soil – reinforcement interaction coefficient on the lateral earth pressure along height under the applied pressure of 200 kPa (4177 psf)

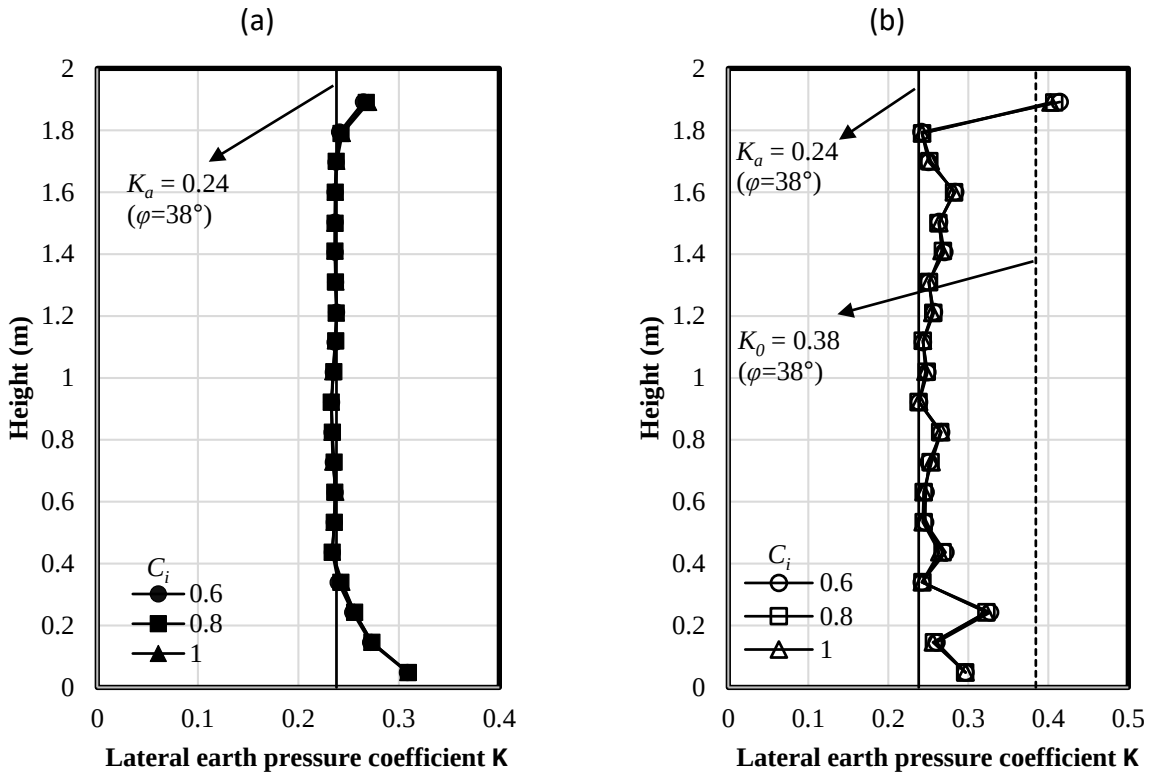

Fig. 7.3.45: Effect of the soil – reinforcement interaction coefficient on the calculated lateral earth pressure coefficient K under the applied pressure of 200 kPa (4177 psf): (a) Near the center of the pier; (b) Behind the CMU blocks.

7.3.3.6.5 Tension in the reinforcement

Figure 7.3.46 presents the maximum tensile forces in the reinforcement under the applied pressure of 200 kPa (4177 psf) with different soil – reinforcement interaction coefficients. Figure 7.3.46 shows that the maximum tensile forces in the reinforcement were almost the same for all three cases. Figure 7.3.47 presents the connection forces in the reinforcement along the height of the GRS pier under the applied pressure of 200 kPa (4177 psf) with different soil – reinforcement interaction coefficients. The connection forces of the reinforcement did not change much with the change of soil – reinforcement interaction coefficients. Overall, the effect of the soil – reinforcement interaction coefficient was limited on both the stress and deformation characteristics of the pier.

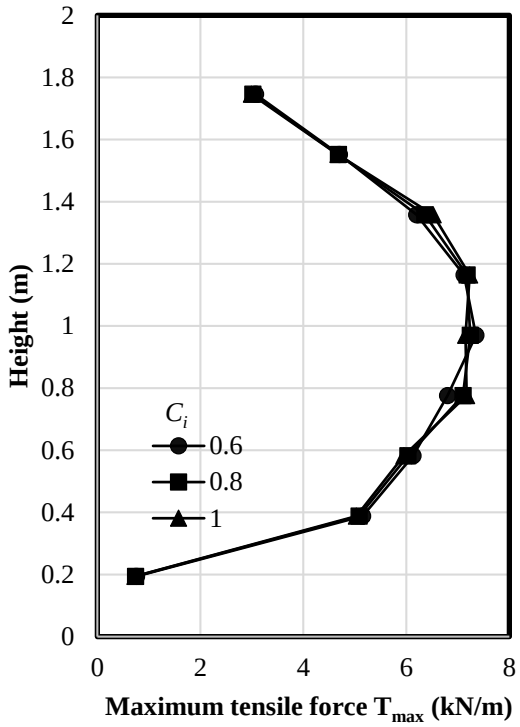

Fig. 7.3.46: Effect of the soil – reinforcement interaction coefficient on the maximum tensile force of the reinforcement under the applied pressure of 200 kPa (4177 psf)

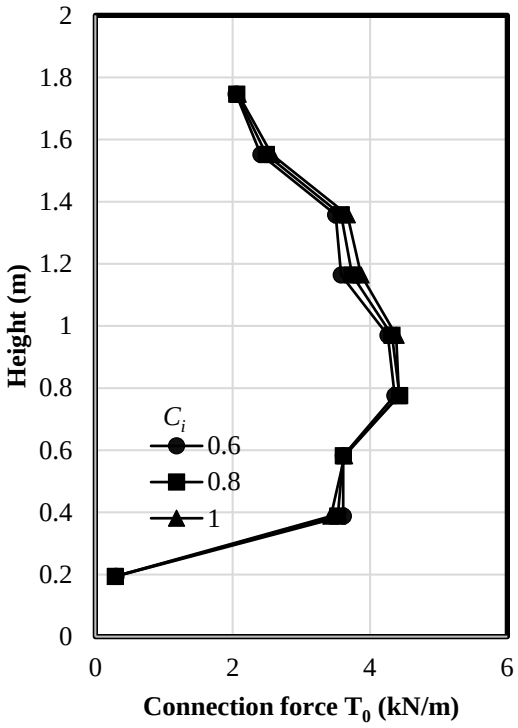

Fig. 7.3.47: Effect of the soil – reinforcement interaction coefficient on the connection force of the reinforcement under the applied pressure of 200 kPa (4177 psf)

7.3.3.7 EFFECT OF FACING CONNECTION STRENGTH

This section discusses the effect of facing connection strength. In the baseline model, the geotextile reinforcement was frictionally connected to the CMU facing blocks. A case in which a mechanical connection was used was investigated in this study. For the case involving a mechanical connection used, an interface friction angle of 57° and a cohesion of 46 kPa were assigned to the geotextile – CMU block interface (Huang et al., 2009).

7.3.3.7.1 Applied pressure – vertical strain curve

Figure 7.3.48 presents the applied pressure – vertical strain curves with different facing connections. The ultimate vertical capacities of the pier at 5% vertical strain were 343 kPa (7164 psf) and 884 kPa (18463 psf) for the cases with frictional and mechanical connection respectively. The moduli of the pier at the applied pressure of 200 kPa (4177 psf) were 12.0 MPa (1740.5 psi) and 20.0 MPa (2900.8 psi) for the cases with frictional and mechanical connection respectively. The use of mechanical connection improved the bearing capacity of the GRS pier significantly because the case with large spacing reinforcement was controlled by the connection strength.

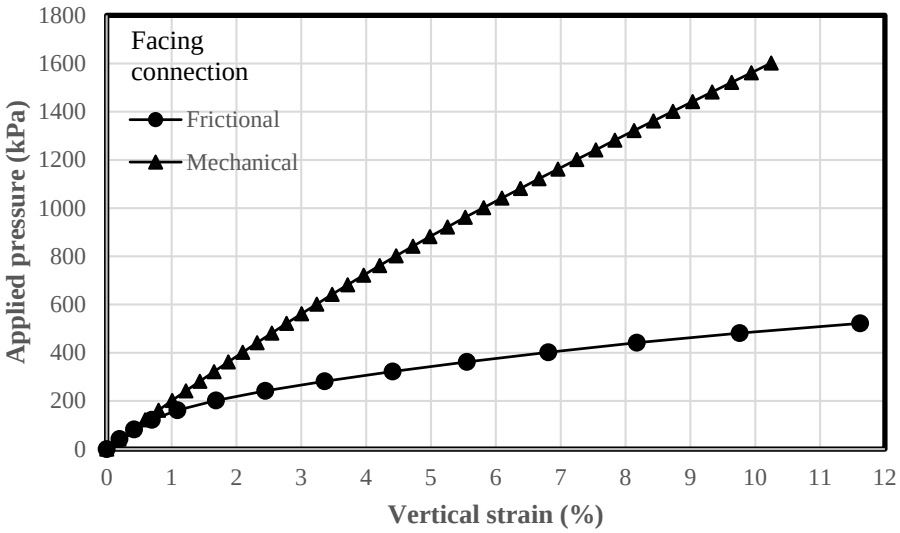

Fig. 7.3.48: Effect of the facing connection strength on the applied pressure – vertical strain curves

7.3.3.7.2 Lateral deformation and volume change

Figure 7.3.49 presents the lateral displacement profiles of the CMU blocks along the height of the GRS pier under the applied pressure of 200 kPa (4177 psf) with different facing connections. Figure 7.3.49 shows that the use of mechanical connection significantly reduced the lateral movement of the CMU blocks as compared with the use of frictional connection. In addition, the use of mechanical connection forced the maximum lateral displacement of the CMU blocks to occur at the height of approximately 1.5 m, which was lower than that in the case with frictional connection. The use of mechanical connection resulted in a more uniform distribution of lateral deformation of the CMU facing blocks.

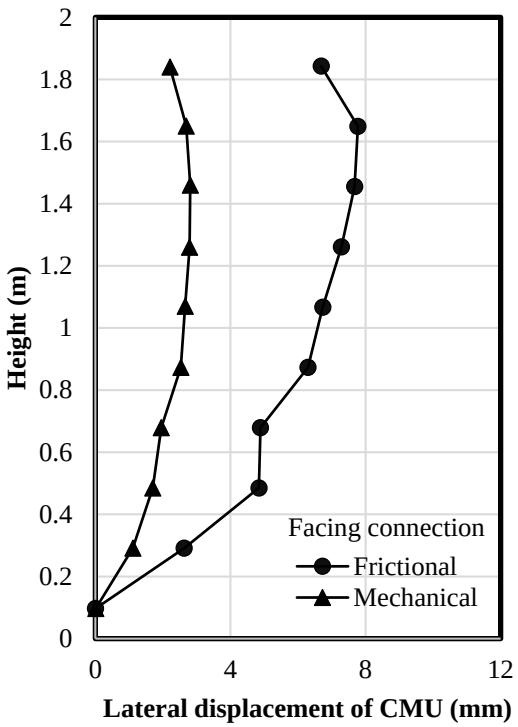

Fig. 7.3.49: Effect of the facing connection strength on the lateral displacement of CMU blocks under the applied pressure of 200 kPa (4177 psf)

Figure 7.3.50 presents the normalized lateral volume change – normalized vertical volume change curves with different facing connections. Figure 7.3.50 shows that the pier with frictional connection had more lateral expansion while the pier with mechanical connection had more vertical compression. For the case with mechanical connection, the curve was farther away from the zero-volume change line as compared with the case with frictional connection. The mechanical connection worked as an anchorage and prevented the CMU blocks from moving laterally, thus resulting in less lateral movement and more vertical compression of the pier.

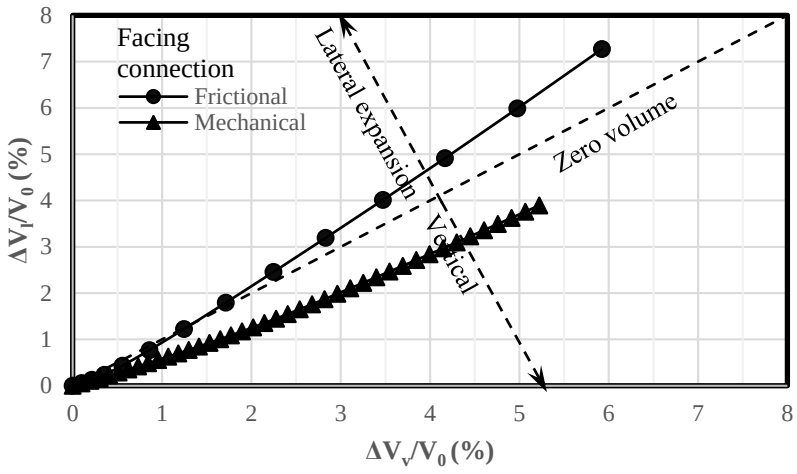

Fig. 7.3.50: Effect of the facing connection strength on the volume change of the pier

7.3.3.7.3 Additional vertical stress

Figure 7.3.51 presents the additional vertical stress distributions beneath the concrete slab along the width of the GRS pier under the applied pressure of 200 kPa (4177 psf) with different facing connections. Figure 7.3.51 shows that the use of mechanical connection resulted in a more uniform distribution of additional vertical stress beneath the concrete slab. Because of the higher lateral confinement provided by the mechanical connection, the backfill soil near the edges of the concrete slab could carry more vertical load.

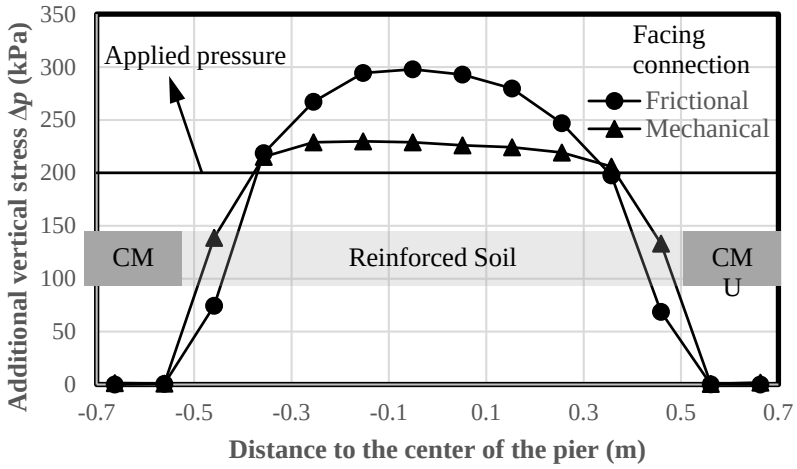

Fig. 7.3.51: Effect of the facing connection strength on the additional vertical stress distribution beneath the concrete slab along the width of the pier under the applied pressure of 200 kPa (4177 psf)

7.3.3.7.4 Lateral earth pressures

Figure 7.3.52 presents the lateral earth pressures along the height of the GRS pier both behind the CMU blocks and near the center of the GRS pier under the applied pressure of 200 kPa (4177 psf) with different facing connections. Figure 7.3.53 presents the calculated lateral earth pressure coefficients K under the applied pressure of 200 kPa (4177 psf) with different facing connections. Figure 7.3.52 shows that within the upper portion of the pier, the mechanical connection reduced the lateral earth pressure both near the center of the pier and increased the lateral earth pressure behind the CMU blocks as compared with the case with frictional connection. Because of the more uniform distribution of the vertical stress as shown in Fig. 7.3.51, the difference between the lateral earth pressures behind the CMU blocks and near the center of the pier was reduced when mechanical connection was used. Figure 7.3.53 (a) shows that except for the top and bottom of the pier, the calculated lateral earth pressure coefficients near the center of the pier were close to the theoretical K_a no matter what kind of connection was used. Figure 7.3.53 (b) shows that as compared with the frictional connection, the mechanical connection resulted in the calculated lateral earth pressure coefficient closer to the theoretical K_a. The slippage and relative movement of the CMU blocks were restrained by the mechanical connection, reducing the variations of the lateral earth pressures behind the CMU blocks.

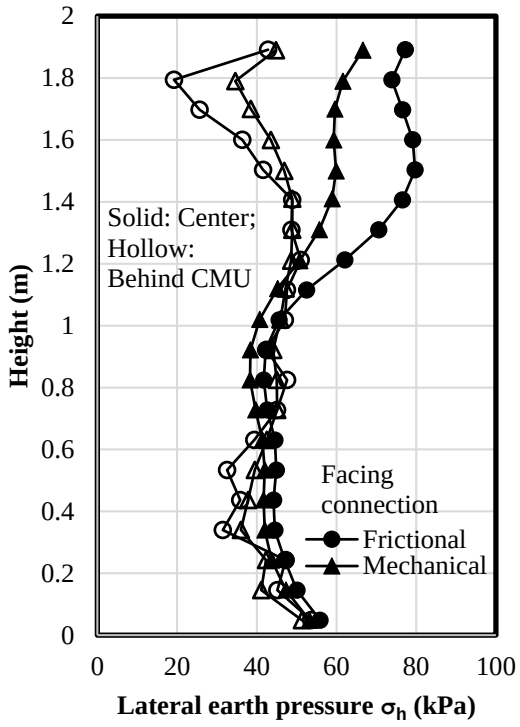

Fig. 7.3.52: Effect of the facing connection strength on the lateral earth pressure along height under the applied pressure of 200 kPa (4177 psf)

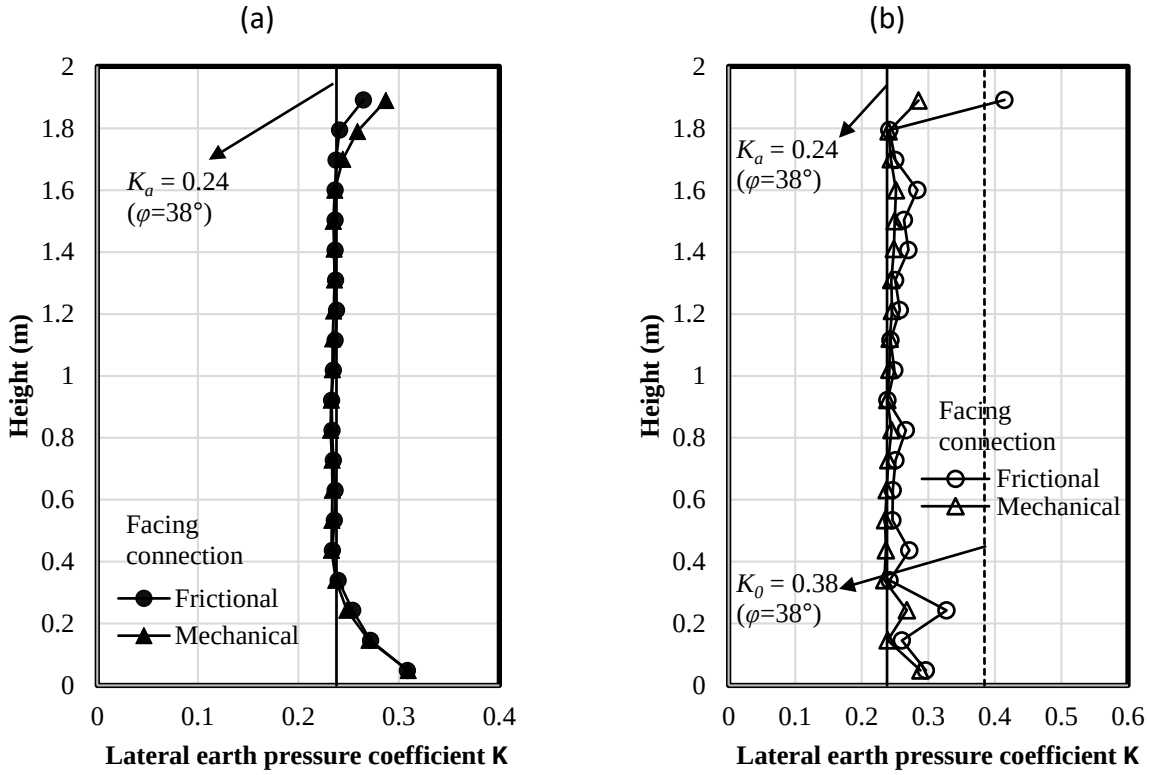

Fig. 7.3.53: Effect of the facing connection strength on the calculated lateral earth pressure coefficient K under the applied pressure of 200 kPa (4177 psf): (a) Near the center of the pier; (b) Behind the CMU blocks.

7.3.3.7.5 Tension in the reinforcement

Figure 7.3.54 presents the maximum tensile forces in the reinforcement under the applied pressure of 200 kPa (4177 psf) with different facing connections. Figure 7.3.54 shows that at the upper portion of the pier, the maximum tensile force in the reinforcement for the case with mechanical connection was larger than the case with frictional connection. When the frictional connection was used, the maximum lateral displacement of the CMU blocks happened within the upper portion of the pier as shown in Figure 7.3.49. The mechanical connection restrained this lateral movement by providing more tensile resistance to the CMU blocks, thus resulting in larger tensile force of the reinforcement.

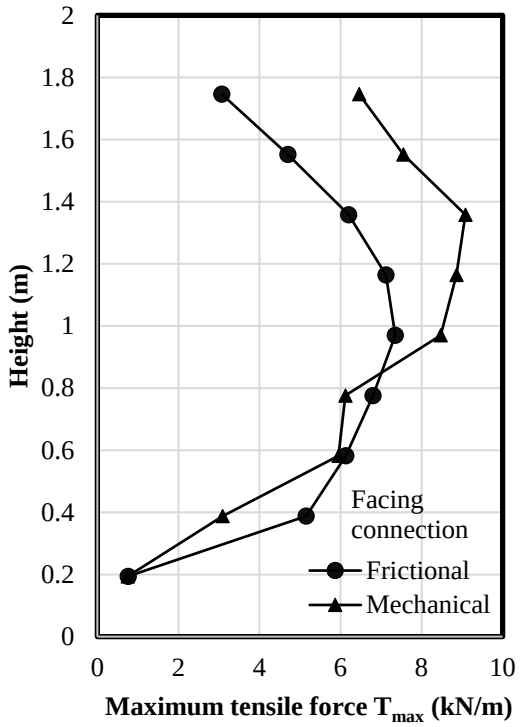

Fig. 7.3.54: Effect of the facing connection strength on the maximum tensile force in the reinforcement under the applied pressure of 200 kPa (4177 psf)

Figure 7.3.55 presents the connection forces in the reinforcement along the height of the GRS pier under the applied pressure of 200 kPa (4177 psf) with different facing connections. Figure 7.3.55 shows that the connection forces in the top five reinforcement layers were larger for the case with mechanical connection than those for the case with frictional connection. As discussed previously, the lateral movement of the CMU facing blocks was larger in the upper portion of the pier. For the lower portion of the pier, since the normal stress became higher due to higher overburden stress from self-weight of the CMU blocks, frictional connection could develop sufficient connection strength. As a result, the effect of mechanical connection was not significant. Numerical results showed that when mechanical connection was used, the maximum tensile force of the reinforcement happened at the connection.

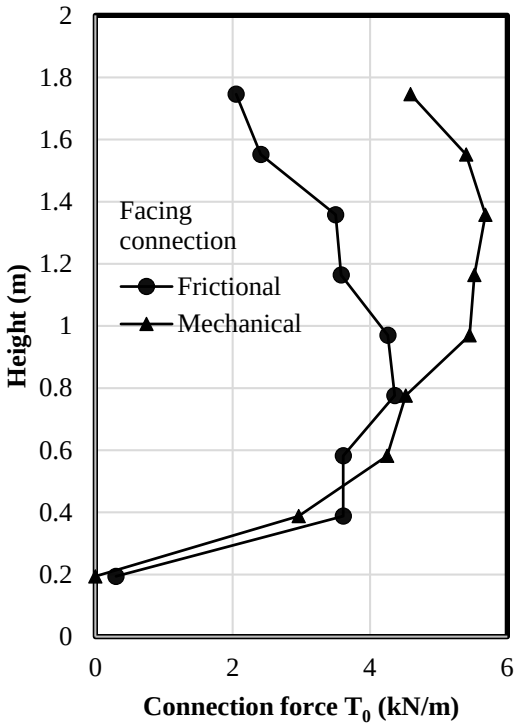

Fig. 7.3.55: Effect of the facing connection strength on the connection force in the reinforcement under the applied pressure of 200 kPa (4177 psf)

7.3.3.8 EFFECT OF PIER HEIGHT

This section discusses the effect of pier height. In the baseline model, the height of the pier was 1.94 m (76 ¼ in). The ratio of the height of the pier to the width of the GRS composite itself was approximately 2.0 to simulate triaxial test relative dimensions. Additional two heights were investigated, which were 0.97 m (38 in) and 2.91 m (114 in), as shown in Fig. 7.3.56. When the pier height was 0.97 m (38 in), five layers of CMU blocks were used and the ratio of the height of the pier to the width of the GRS composite itself was 1.0. Four layers of geotextile reinforcement were used at the spacing of 0.194 m (7 in). When the pier height was 2.91 m (114 in), 15 layers of CMU blocks were used and the ratio of the height of the pier to the width of the GRS composite itself was 3.0. Fourteen layers of reinforcement were used at the spacing of 0.194 m (7 in). For better comparisons, the numerical results of all three GRS piers are presented using both depth from the top of the pier and normalized depth.

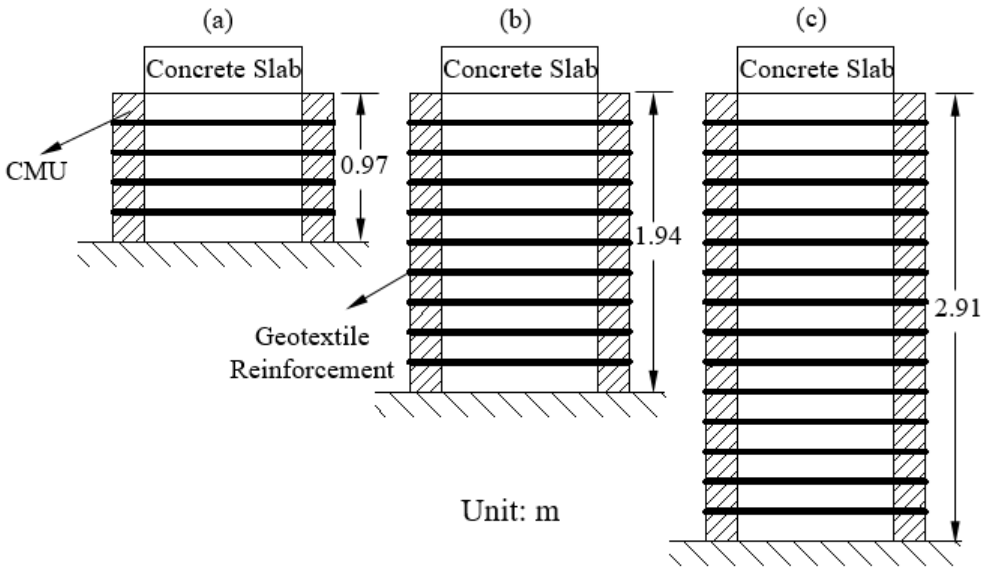

Fig. 7.3.56: Schematic of GRS piers with three different heights: (a) Pier height = 0.97 m (38 in); (b) Pier height = 1.94 m (76 ¼ in); (c) Pier height = 2.91 m (114 in).

7.3.3.8.1 Applied pressure – vertical strain curve

Figure 7.3.57 presents the applied pressure – vertical strain curves with different pier heights. Figure 7.3.57 shows that at 5% vertical strain, the ultimate vertical capacities were 429 kPa (8960 psf), 343 kPa (7164 psf), and 390 kPa (8145 psf) for the pier heights of 0.97 m (38 in), 1.94 m (76 ¼ in), and 2.91 m (114 in), respectively. At the applied pressure of 200 kPa, the moduli of the pier were 14.5 MPa (2103.1 psi), 12.0 MPa (1740.5 psi), and 15.3 MPa (2219.1 psi) for the pier heights of 0.97 m (38 in), 1.94 m (76 ¼ in), and 2.91 m (114 in), respectively. The pier with height of 0.97 m (38 in) had a higher ultimate vertical capacity and modulus than the pier with height of 1.94 m (76 ¼ in) due to a relatively small height to width ratio. The boundary effect was significant in this case. The pier with the height of 2.91 m (114 in) had a higher ultimate vertical capacity and modulus than the pier with the height of 1.94 m (76 ¼ in). Later discussion shows that the pier with the height of 1.94 m (76 ¼ in) had more uniform lateral deformation than that with the height of 2.91 m (114 ⅜ in). This difference caused the differences in their capacities and moduli.

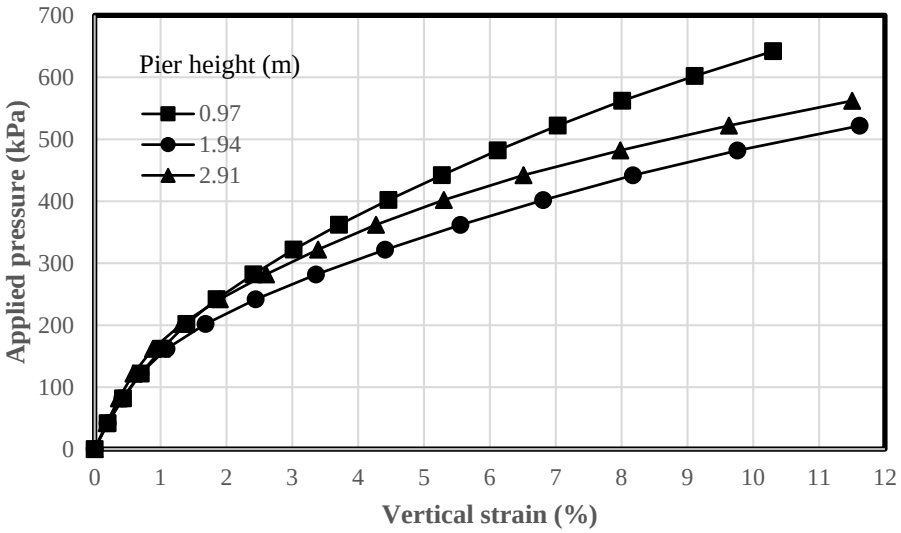

Fig. 7.3.57: Effect of pier height on the applied pressure – vertical strain curves

7.3.3.8.2 Lateral deformation and volume change

Figure 7.3.58 presents the lateral displacement profiles of the CMU blocks along the depth of the GRS pier under the applied pressure of 200 kPa (4177 psf) with different pier heights. The case with the pier height of 0.97 m (38 ⅛ in) had the smallest lateral displacement of CMU blocks due to the boundary effect at the bottom of the pier. From the top of the pier to the normalized depth of approximately 0.1, the lateral displacement of the CMU blocks for the case with the pier height of 1.94 m (76 ¼ in) and 2.91 m (114 ⅜ in) were close. At deeper depths (i.e., from the normailized depth of 0.2 to 1.0), more lateral displacement of the CMU blocks happened when the pier height was 1.94 m (76 ¼ in). The case with the pier height of 2.91 m (114 ⅜ in) had least lateral deformation at deeper depth (i.e., from normalized depth of 0.4 to 0.8), indicating that the influence of the loading on top of the pier was limited at deeper depth.

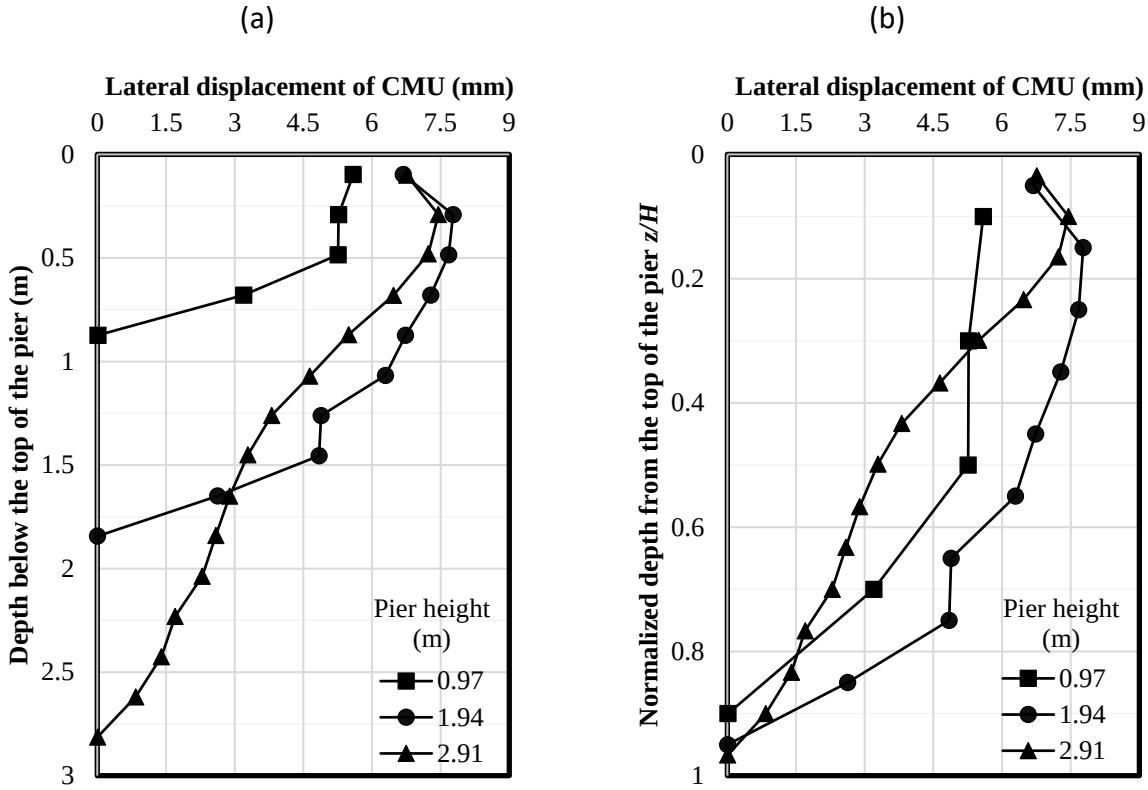

Fig. 7.3.58: Effect of the pier height on the lateral displacement of CMU blocks under the applied pressure of 200 kPa (4177 psf): (a) Depth from the top of the pier; (b) Normalized depth from the top of the pier.

Figure 7.3.59 presents the normalized lateral volume change – normalized vertical volume change curves with different pier heights. The zero-volume change line is also plotted in Fig. 7.3.59 for the purpose of comparison. Figure 7.3.59 shows that all three curves almost overlapped with each other with the least lateral expansion of the pier happening for the case with the pier height of 2.91 m (114 ⅜ in).

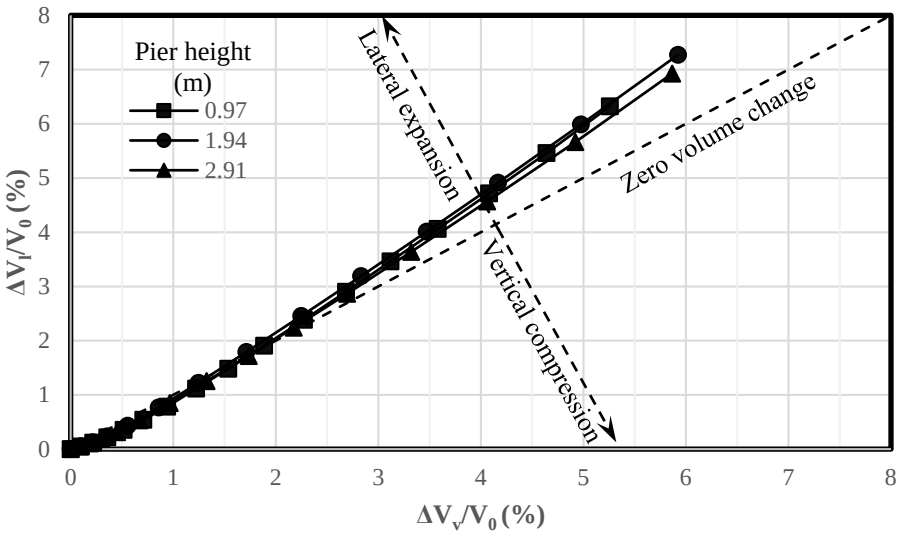

Fig. 7.3.59: Effect of the pier height on the volume change of the pier

7.3.3.8.3 Additional vertical stress

Figure 7.3.60 presents the additional vertical stress distributions under the center of the concrete slab along the height of the pier under the applied pressure of 200 kPa (4177 psf) with different pier heights. Figure 7.3.60 shows that the influence depth of the applied pressure was approximately 1.0 m (39.4 in) below the concrete slab despite the change of the pier height. When the pier height was 0.97 m (38 ⅛ in), Fig. 7.3.60 (b) showed that higher additional stresses occurred at the whole depth of the pier as compared with those with other two pier heights. Within the lower portion of the pier (i.e., the normalized depth of 0.2 to 1.0), the case with the pier height of 2.91 m (114 ⅜ in) resulted in lower additional vertical stresses under the center of the concrete slab as compared with those in the case with the pier height of 1.94 m (76 ¼ in), thus resulting in smaller lateral deformation of the pier as shown in Fig. 7.3.58.

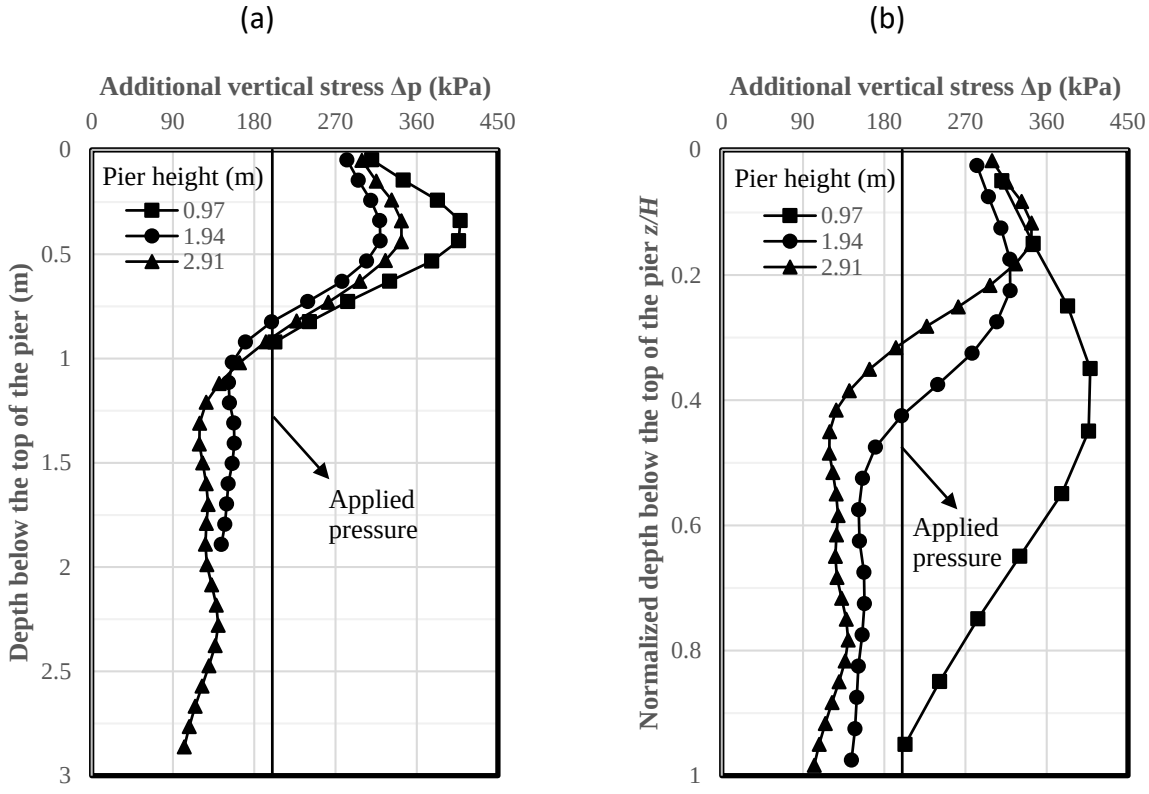

Fig. 7.3.60: Effect of the pier height on the additional vertical stress distribution under the center of the concrete slab along the height of the pier under the applied pressure of 200 kPa (4177 psf): (a) Depth from the top of the pier; (b) Normalized depth from the top of the pier.

7.3.3.8.4 Lateral earth pressures

Figure 7.3.61 presents the lateral earth pressures along the height of the GRS pier both behind the CMU blocks and near the center of the GRS pier under the applied pressure of 200 kPa (4177 psf) with different pier heights. Figure 7.3.61 (b) shows that at the normalized depths from 0 to 0.3 below the top of the pier, the lateral earth pressures behind the CMU blocks were lower than those near the center of the pier for all three cases. However, at the deeper depths (at the normalized depth from 0.1 to 1.0 below the top of the pier), the lateral earth pressures behind the CMU blocks were close to those near the center of the pier except for the case of pier height of 0.97 m (38 ⅛ in) due to the boundary effect of the bottom.

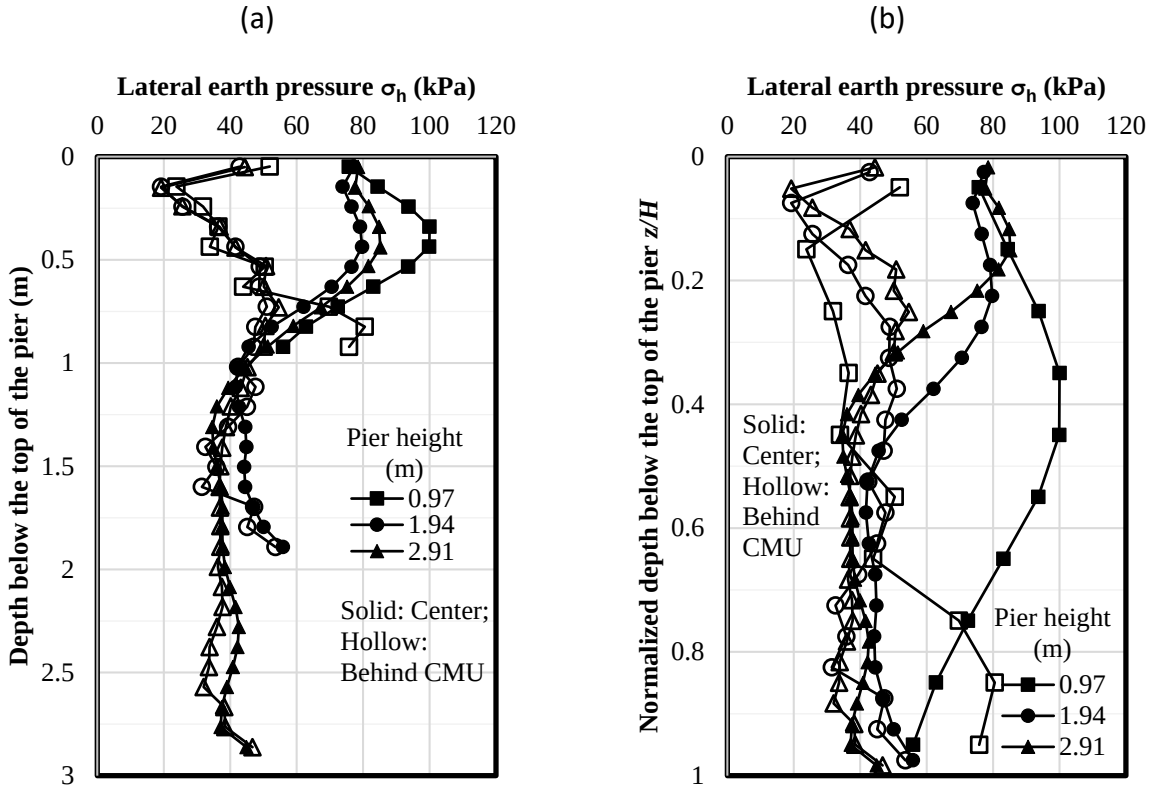

Fig. 7.3.61: Effect of the pier height on the lateral earth pressure along height under the applied pressure of 200 kPa (4177 psf): (a) Depth from the top of the pier; (b) Normalized depth from the top of the pier.

Figure 7.3.62 presents the calculated lateral earth pressure coefficients *K* under the applied pressure of 200 kPa (4177 psf) with different pier heights. Figure 7.3.62 (a) and (b) show that the calculated lateral earth pressure coefficients near the center of the pier were all close to the theoretical K_a except for the locations at the top and bottom of the pier despite the change of pier heights. Figure 7.3.62 (c) and (d) show that when the pier height was 0.97 m (38 ⅛ in), the calculated lateral earth pressure coefficients behind the CMU blocks fluctuated between the theoretical K_a and K_0. For the cases with the pier heights of 1.94 m (76 ¼ in) and 2.91 m (114 ⅜ in), the calculated lateral earth pressure coefficients behind the CMU blocks were closer to the theoretical K_a.

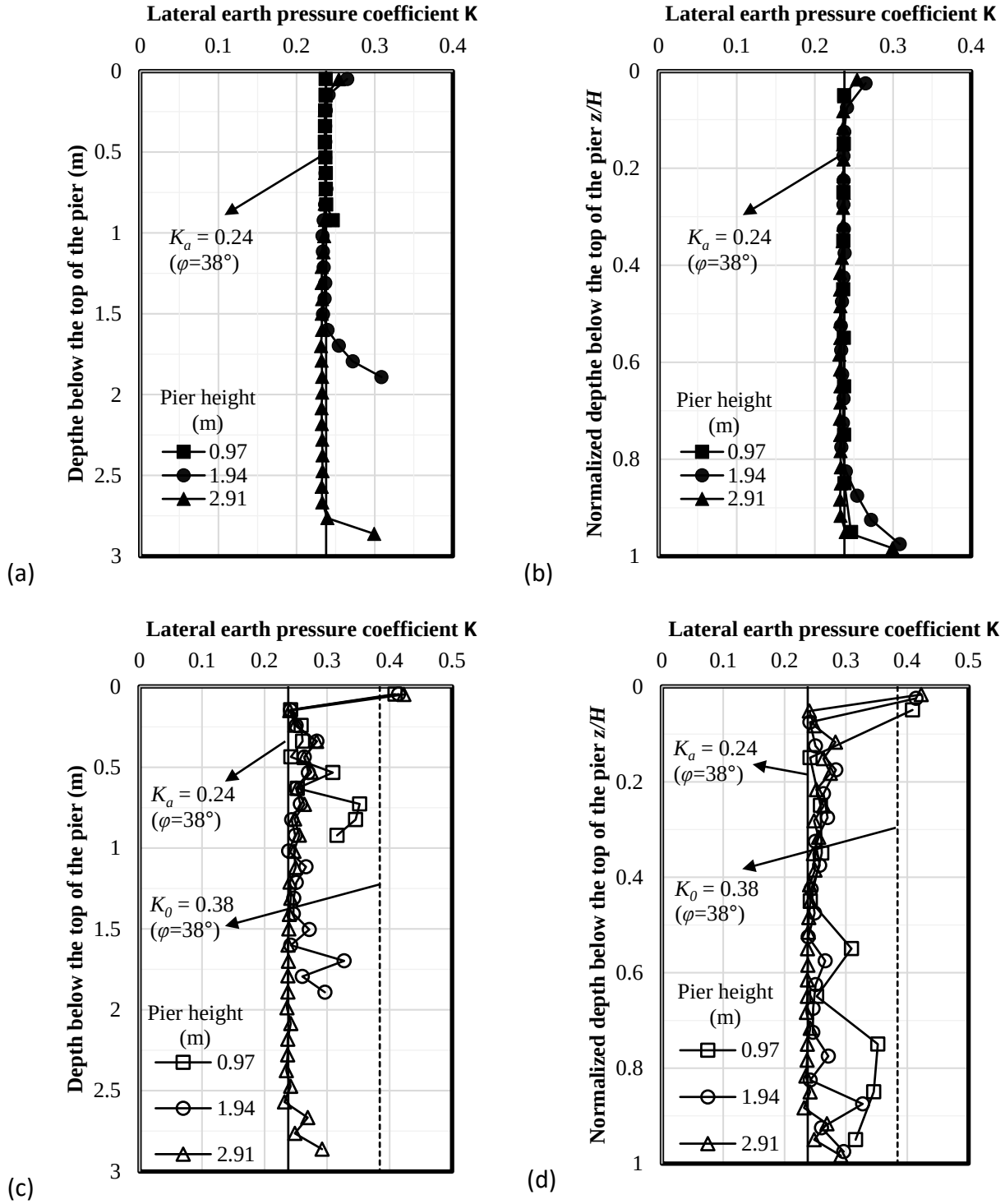

Fig. 7.3.62: Effect of the pier height on the calculated lateral earth pressure coefficient K under the applied pressure of 200 kPa (4177 psf): (a) Near the center of the pier and depth from the top of the pier; (b) Near the center of the pier and normalized depth from the top of the pier; (c) Behind the CMU blocks and depth from the top of the pier; (d) Behind the CMU blocks and normalized depth from the top of the pier.

7.3.3.8.5 Tension in the reinforcement

Figure 7.3.63 presents the maximum tensile forces of the reinforcement under the applied pressure of 200 kPa (4177 psf) with different pier heights. Figure 7.3.63 shows that the maximum tensile force of the reinforcement increased from the top of the pier to the maximum value approximately at the mid-height and then decreased to the minimum value at the bottom of the pier. The maximum tensile force of the reinforcement happened within the upper to mid height of the pier despite the change of pier heights. The maximum tensile force of the reinforcement for the case with the pier height of 0.97 m (38 ⅛ in) was smaller than those in other two cases due to the boundary effect. For the cases with the pier heights of 1.94 m (76 ¼ in) and 2.91 m (114 ⅜ in), the maximum tensile forces of the reinforcement were close to each other.

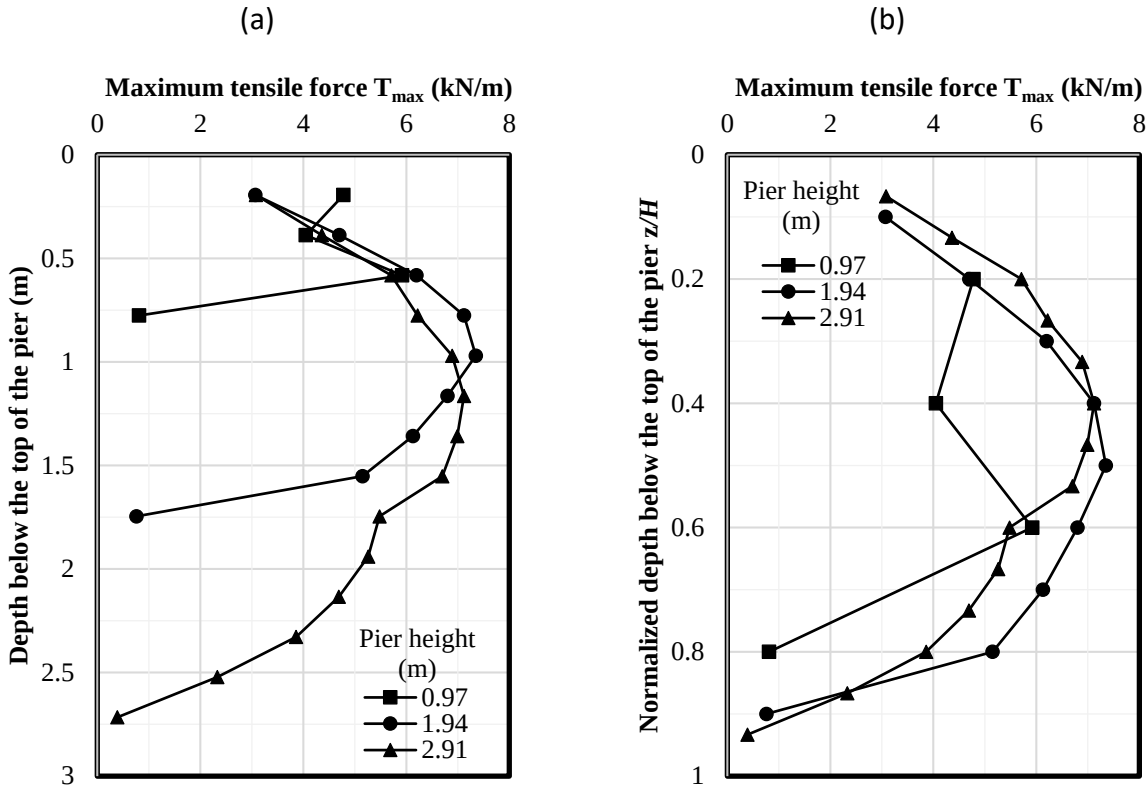

Fig. 7.3.63: Effect of the pier height on the maximum tensile force of the reinforcement under the applied pressure of 200 kPa (4177 psf): (a) Depth from the top of the pier; (b) Normalized depth from the top of the pier.

Figure 7.3.64 presents the connection forces in the reinforcement along the height of the GRS pier under the applied pressure of 200 kPa (4177 psf) with different pier heights. Figure 6.3.64 shows that the connection force was smaller than the maximum tensile force of the reinforcement despite the change of the pier height. For all three cases, the connection forces in the reinforcement were close to zero at the bottom of the pier due to the boundary effect. The connection force had a small increase when the pier height increased from 1.94 m (76 ¼ in) to 2.91 m (114 ⅜ in).

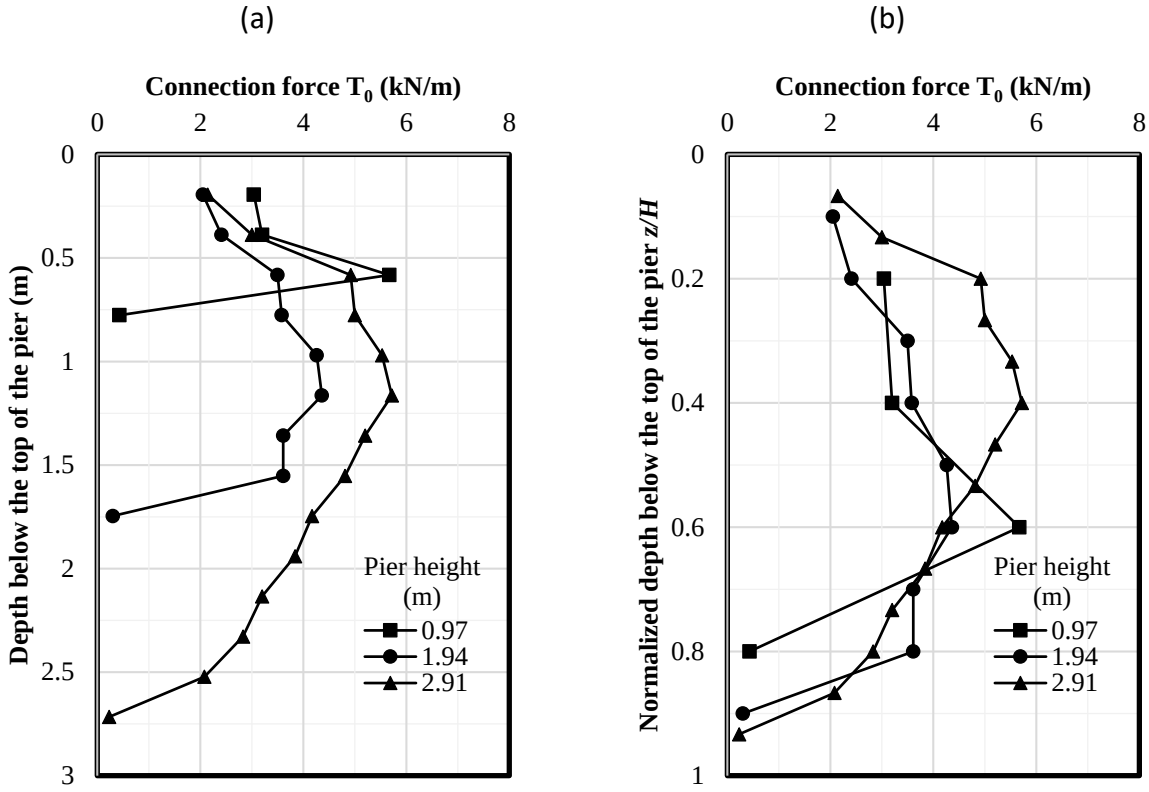

Fig. 7.3.64: Effect of the pier height on the connection force of the reinforcement under the applied pressure of 200 kPa (4177 psf): (a) Depth from the top of the pier; (b) Normalized depth from the top of the pier.

7.3.3.9 EFFECT OF CONFINING STRESS

This section discusses the effect of confining stress. In this section, the pier was loaded without CMU blocks but with different confining stresses. The numerical model in this section simulated the condition of triaxial tests. The height of the pier was 1.94 m (76 ¼ in) and the width of the pier was 0.995 m (39 ¼ in), resulting in the ratio of height to width of approximately 2.0. Nine geotextile reinforcement layers were placed in the GRS pier with a vertical spacing of 0.194 m (7 in). The area of each geotextile reinforcement was the same as the area of the pier itself. An all-around confining stress was first applied on the pier, followed by a vertical deviator stress. Vertical loading stopped until 5% vertical strain was reached. Figure 7.3.65 shows the deformed numerical mesh. This section investigated four confining stress levels, which were 10 kPa (209 psf), 25 kPa (552 psf), 50 kPa (1044 psf), and 100 kPa (2088 psf).

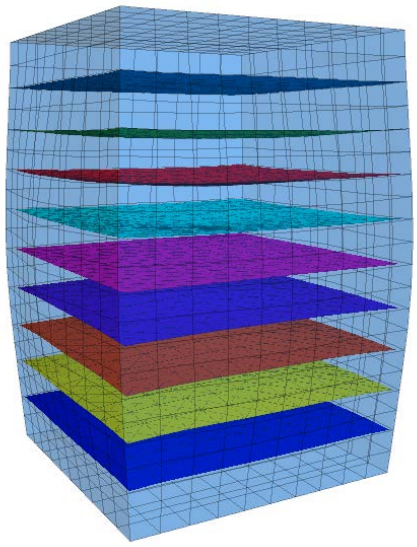

Fig. 7.3.65: Deformed numerical mesh (magnified by 5 times)

Figure 7.3.66 presents the Mohr circles under different confining stresses when the vertical strain reached 5%. The Mohr – Coulomb failure envelope is also plotted in Fig. 7.3.66, which shows a friction angle of 38° (i.e., the same as the friction angle of the backfill soil). In addition, the failure envelope had an intercept of 30.5 kPa (637 psf), indicating that the GRS pier had an apparent cohesion of 30.5 kPa (637 psf). These results proved that the presence of geosynthetic reinforcement resulted in an apparent cohesion in the soil (Schlosser & Long, 1974).

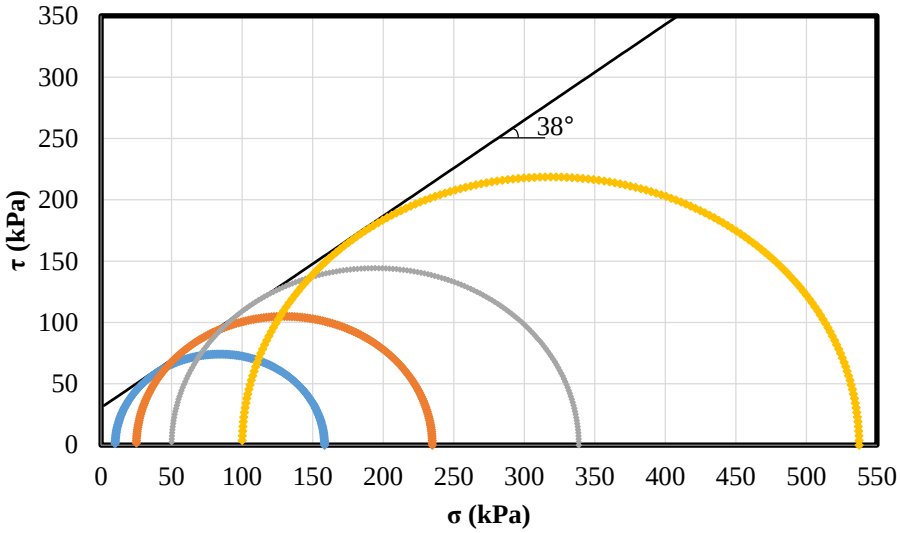

Fig. 7.3.66: Mohr circles and failure envelope (S_v = 0.194 m (7 in))

Two additional reinforcement vertical spacings were investigated in this study: 0.388 m (15 ¼ in) and 0.097 m (3 $^{13}/_{16}$ in). Figure 7.3.67 and Fig. 7.3.68 show the numerical results. Despite the change of the reinforcement spacing, the friction angle remained unchanged as 38°. However, the case with the reinforcement spacing of 0.388 m (15 ¼ in) had an apparent cohesion of 13.5 kPa (282 psf) while the case with the reinforcement spacing of 0.097 m (3 $^{13}/_{16}$ in) had an apparent cohesion of 62.5 kPa (1305 psf).

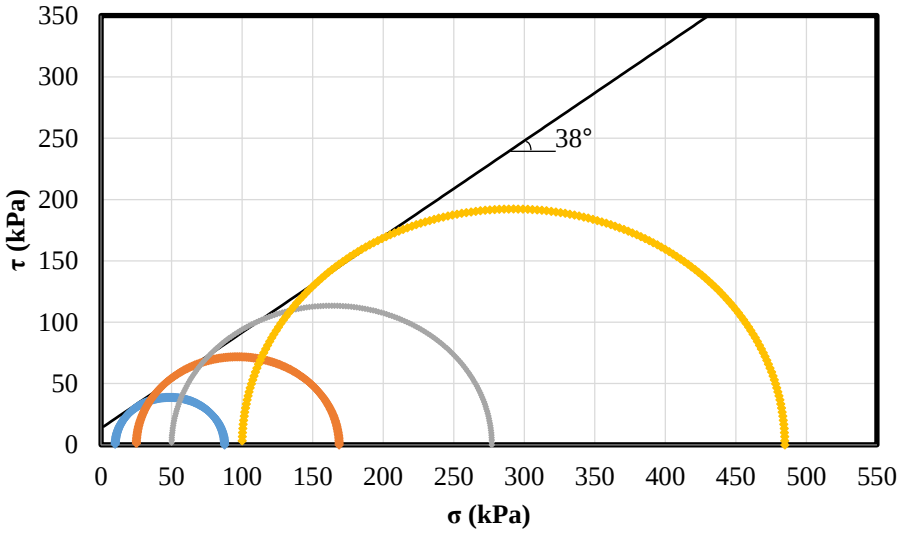

Fig. 7.3.67: Mohr circles and failure envelope (S_v = 0.388 m (15 ¼ in))

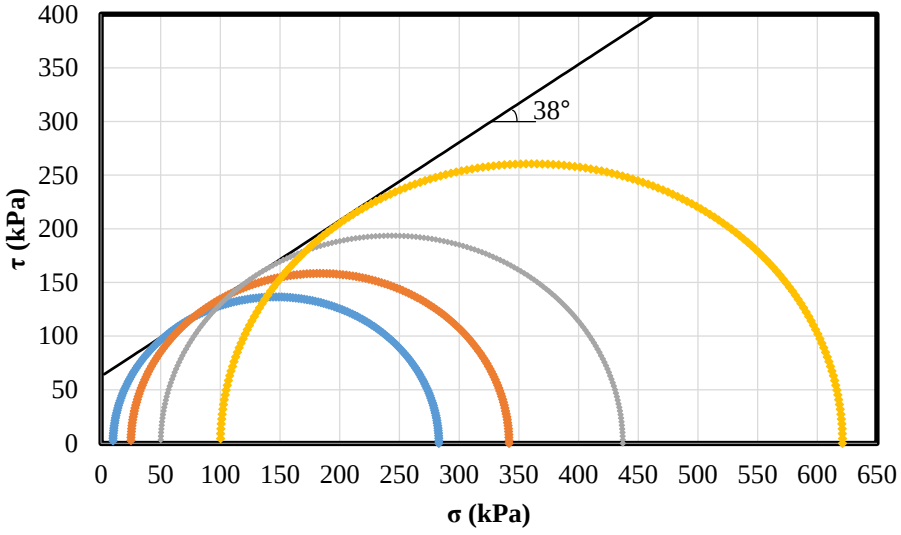

Fig. 7.3.68: Mohr circles and failure envelope (S_v = 0.097 m (3 $^{13}/_{16}$ in))

Table 7.3.6 to Table 7.3.8 summarize the numerical results of the maximum tensile force T_{max} in the reinforcement along the height of the pier under different confining stresses. Since the vertical loading in the numerical model stopped when the vertical strain reached 5%, the maximum tensile force T_{max} in the reinforcement was not the tensile force at failure T_f. In the tables, Avg. T_{max}, Min. T_{max}, and Max. T_{max} represent the average, the minimum, and the maximum values of the maximum tensile force T_{max} in the reinforcement along the height of the pier respectively. Table 7.3.6 to Table 7.3.8 shows that the T_{max} was not uniformly distributed along the pier height. Under different confining stresses, there were small differences between T_{max}.

Table 7.3.6: Distribution of maximum tensile forces Tmax in the reinforcement along the height of the pier for the case S_v = 0.388 m (15 ¼ in) under different confining stresses

Height (m)	**σ_3 (kPa)**			
	10	25	50	100
1.552	5.07	4.55	3.89	3.22
1.164	11.12	13.81	13.59	11.82
0.776	12.70	15.27	15.01	13.00
0.388	7.38	6.55	5.52	4.40
Avg. T_{max} (kN/m)	9.07	10.05	9.50	8.11
Min. T_{max} (kN/m)	5.07	4.55	3.89	3.22
Max. T_{max} (kN/m)	12.70	15.27	15.01	13.00

Table 7.3.7: Distribution of the maximum tensile forces Tmax in the reinforcement along the height of the pier for the case S_v = 0.194 m (7 in) under different confining stresses

Height (m)	**σ_3 (kPa)**			
	10	25	50	100
1.746	2.81	1.94	1.48	1.09
1.552	6.72	5.73	4.69	3.62
1.358	10.02	9.77	8.78	7.19
1.164	11.79	12.84	12.43	10.76
0.97	12.27	14.17	14.13	12.54
0.776	12.49	13.56	13.20	11.52
0.582	11.00	10.90	9.94	8.25
0.388	7.75	6.81	5.73	4.48
0.194	3.61	2.72	2.10	1.55

Table 7.3.7: Distribution of the maximum tensile forces Tmax in the reinforcement along the height of the pier for the case S_v = 0.194 m (7 in) under different confining stresses (continued)

Height (m)	σ_3 (kPa)			
	10	25	50	100
Avg. T_{max} (kN/m)	8.72	8.71	8.05	6.78
Min. T_{max} (kN/m)	2.81	1.94	1.48	1.09
Max. T_{max} (kN/m)	12.49	14.17	14.13	12.54

Table 7.3.8: Distribution of the maximum tensile forces Tmax in the reinforcement along the height of the pier for the case S_v = 0.097 m (3 $^{13}/_{16}$ in) under different confining stresses

Height (m)	σ_3 (kPa)			
	10	25	50	100
1.843	1.52	0.93	0.70	0.49
1.746	3.35	2.56	2.00	1.43
1.649	5.17	4.37	3.52	2.59
1.552	6.85	6.05	5.04	3.85
1.455	8.34	7.62	6.60	5.19
1.358	9.52	8.99	8.10	6.59
1.261	10.36	10.07	9.39	7.91
1.164	10.90	10.84	10.40	9.01
1.067	11.22	11.32	11.05	9.76
0.97	11.38	11.53	11.33	10.09
0.873	11.38	11.47	11.22	9.96
0.776	11.21	11.13	10.72	9.38
0.679	10.78	10.47	9.84	8.42
0.582	10.01	9.46	8.64	7.17
0.485	8.85	8.13	7.18	5.78
0.388	7.37	6.57	5.63	4.40
0.291	5.66	4.89	4.06	3.07
0.194	3.76	3.09	2.47	1.81
0.097	1.73	1.35	1.05	0.77
Avg. T_{max} (kN/m)	7.86	7.41	6.79	5.67
Min. T_{max} (kN/m)	1.52	0.93	0.70	0.49
Max. T_{max} (kN/m)	11.38	11.53	11.33	10.09

Table 7.3.9 presents the apparent cohesion c_R due to the existence of geosynthetic reinforcement from both numerical results and Equation (7.3.6). When T_f in Equation (7.3.6) was substituted by the average of Max. T_{max} in the reinforcement under different confining stresses, the calculated apparent cohesion was labelled as $c_{R\text{-max}}$. When T_f in Equation (7.3.6) was substituted by the average of Avg. T_{max} in the reinforcement under different confining stresses, the calculated apparent cohesion was labelled as $c_{R\text{-avg}}$. Table 7.3.9 shows that Equation (7.3.6) overestimated the contribution of the geotextile reinforcement to the apparent cohesion based on the numerical calculation. Compared to the use of Max. T_{max}, the use of Avg. T_{max} gave closer apparent cohesion values compared to the numerical results. One possible reason for the overestimation of Equation (7.3.6) was that the Rankine passive earth pressure coefficient was adopted. However, the discussion in the previous sections showed that the numerical model calculated the lateral earth pressures both behind the CMU blocks and near the center of the pier were active.

Table 7.3.9: Apparent cohesion c_R due to the contribution of geosynthetic reinforcement

S_v (m)	c_R from numerical analysis (kPa)	Average of Max. T_{max} (kN/m)	$c_{R\text{-max.}}$ (kPa) (Equation (7.3.6)	Average of Avg. T_{max} (kN/m)	$c_{R\text{-avg.}}$ (kPa) (Equation (7.3.6)
0.388	13.5	14.0	37.0	9.2	24.3
0.194	30.5	13.3	70.2	8.1	42.8
0.097	62.5	11.1	117.3	6.9	72.9

7.3.4 CONCLUSIONS

This study involved the use of a three-dimensional finite difference method-based program, FLAC3D, to simulate the performance of geosynthetic-reinforced soil piers under vertical loading. The numerical model was calibrated and verified against the test results using the applied pressure-vertical strain curve and the lateral displacement profile along the height of the GRS pier. A parametric study was then carried out using the numerical model to investigate the influence of the following factors on the performance of the GRS pier: friction angle of backfill soil, reinforcement stiffness, reinforcement spacing, combination of reinforcement stiffness and spacing, soil – reinforcement interaction coefficient, facing connection, pier height, and confining stress. The following conclusions can be made from the parametric study:

1 The numerical results showed that the maximum lateral displacement of the CMU blocks happened within the upper to mid portion of the GRS pier. The numerical results indicate that GRS piers do not necessarily deform following zero volume changes, which has been an assumption recommended for prediction of lateral displacements. When the applied vertical load was comparatively small, the GRS pier was predicted to have comparatively larger vertical compression than lateral expansion. With the increase of the applied vertical load, the lateral expansion increased at at a faster rate than the vertical compression.

2 The numerical results indicated that the CMU facing blocks, which were frictionally connected to the GRS pier by geotextile layers, did not directly carry much vertical load compared to the backfill soil in between.

3 The additional vertical stresses beneath the concrete slab induced by the applied pressure were not uniformly distributed.

4 The non-uniform distribution of the vertical stress within the GRS pier resulted in the non-uniform distribution of the lateral earth pressure. In cohesionless soil, the lateral earth pressure behind the CMU blocks was lower than that near the center of the GRS pier within the upper to mid height of the pier.

5 The calculated lateral earth pressure coefficient K is defined as the ratio of the lateral earth pressure to the vertical stress at the same location. The calculated lateral earth pressure coefficients K near the center of the GRS pier were close to that calculated using Rankine active lateral earth pressure coefficient K_a except for the locations near the top and bottom of the pier. The calculated lateral earth pressure coefficients behind the CMU blocks fluctuated between the Rankine active lateral earth pressure coefficient K_a and the lateral earth pressure coefficient at-rest K_0.

6 The maximum tensile force in the reinforcement increased from the top of the pier to mid-height and then decreased until the bottom layer. Since the reinforcement layers were frictionally connected to the CMU blocks, the connection stress in the reinforceemnt was significantly lower than the maximum tensile force in the reinforcement.

7 The friction angle of the backfill soil had a significant influence on the performance of the GRS pier. The increase of the friction angle resulted in a higher ultimate vertical capacity and reduced the vertical compression of the pier. The use of backfill soil with a higher friction angle made the distribution of additional vertical stress beneath the concrete slab more uniform. In addition, the increase of the friction angle reduced the lateral displacement of the CMU blocks, the lateral earth pressure near the center of the pier, and the maximum tensile force in the reinforcement.

8 The reinforcement stiffness was found to have negligible effect on both the lateral earth pressure and the vertical stress distribution within the GRS pier. However, the use of reinforcement with high stiffness could reduce the lateral displacement of the CMU blocks.

9 Compared to the reinforcement stiffness, the reinforcement spacing had more significant influence on the performance of the GRS pier. The contribution of the reinforcement spacing was more significant than that of the reinforcement stiffness when the ratio of reinforcement stiffness J to spacing S_v was maintained the same. The closely–spaced reinforcement layers provided more lateral confinement to the backfill soil than largely-spaced reinforcement layers. The GRS pier with closely-spaced reinforcement resulted in a higher ultimate vertical capacity, a smaller lateral displacement of CMU blocks, and a lower maximum tensile force in the reinforcement.

10 The soil – geotextile interaction coefficient had little effect on the performance of the GRS pier. A higher interaction coefficient between the soil and the geotextile resulted in a smaller lateral displacement of the CMU blocks.

11 The use of mechanical facing connection improved the performance of the GRS pier by providing more lateral confinement through the connection between the CMU blocks and the geotextile reinforcement. The use of mechanical connection resulted in a comparatively

higher ultimate vertical capacity, smaller lateral expansion, and higher connection force in the reinforcement.

12 Numerical analysis of GRS pier loaded vertically under different confining stresses showed that the use of geosynthetic reinforcement resulted in an apparent cohesion in the GRS composite. The friction anlge of the GRS composite remained the same as the friction angle of the backfill soil. A decrease in the reinforcement vertical spacing resulted in higher apparent cohesion of the GRS composite.

7.3.5 REFERENCES

AASHTO (2014). LRFD bridge design specifications. 7th ed. Washington, DC.:

Adams, M., Lillis, C., Wu, J. & Ketchart, K. (2002). Vegas mini pier experiment and postulate of zero volume change. In (Eds.), Paper presented at Proceedings, Seventh International Conference on Geosynthetics, (pp. 389-394).

Adams, M., Nicks, J., Stabile, T., Wu, J., Schlatter, W. & Hartmann, J. (2011). Geosynthetic Reinforced Soil Integrated Bridge System, Synthesis Report. FHWA-HRT-11-027.

Adams, M., Nicks, J., Stabile, T., Wu, J., Schlatter, W. & Hartmann, J. (2012). Geosynthetic Reinforced Soil Integrated Bridge System, Interim Implementation Guide. FHWA-HRT-11-026.

Awad, M. I. & Tanyu, B. F. (2014). Laboratory evaluation of governing mechanism of frictionally connected MSEW face and implications on design. Geotextiles and Geomembranes, 42(5), 468-478.

Bolton, M. (1986). The strength and dilatancy of sands. Geotechnique, 36(1), 65-78.

Greco, V. (2013). Active thrust on retaining walls of narrow backfill width. Computers and Geotechnics, 50, 66-78.

Han, J. (2015). Principles and practice of ground improvement. John Wiley & Sons, 418p.

Huang, B., Bathurst, R. J. & Hatami, K. (2009). Numerical study of reinforced soil segmental walls using three different constitutive soil models. Journal of Geotechnical and Geoenvironmental engineering, 135(10), 1486-1498.

Itasca Consulting Group (2009a). FLAC3D Structural Elements. Itasca Consulting Group Inc., 254 p.

Itasca Consulting Group (2009b). FLAC3D Theory and Background. Itasca Consulting Group Inc., 226p.

Leshchinsky, D., Hu, Y. & Han, J. (2004). Limited reinforced space in segmental retaining walls. Geotextiles and Geomembranes, 22(6), 543-553.

Nicks, J. E., Adams, M., Ooi, P. & Stabile, T. (2013). Geosynthetic reinforced soil performance testing—Axial load deformation relationships. FHWA-HRT-13-066.

Pham, T. Q. (2009). Investigating Composite Behavior of Geosynthetic-Reinforced Soil (GRS) Mass. Ph.D. dissertation, University of Colorado Denver, Colorado, USA, 3797p.

Saghebfar, M., Abu-Farsakh, M., Ardah, A., Chen, Q. & Fernandez, B. A. (2017). Performance monitoring of Geosynthetic Reinforced Soil Integrated Bridge System (GRS-IBS) in Louisiana. Geotextiles and Geomembranes, 45(2), 34-47.

Salgado, R. (2008). The engineering of foundations. McGraw-Hill New York, 882p.

Schlosser, F. & Long, N. T. (1974). Recent results in French research on reinforced earth. Journal of the construction Division, 100(3), 223-237.

tom Wörden, F. & Achmus, M. (2013). Numerical modeling of three-dimensional active earth pressure acting on rigid walls. Computers and Geotechnics, 51, 83-90.

Wu, J. T., Yang, K.-H., Mohamed, S., Pham, T. & Chen, R.-H. (2014). Suppression of soil dilation—A reinforcing mechanism of soil-geosynthetic composites. Transportation Infrastructure Geotechnology, 1(1), 68-82.

Wu, J. T. H. & Pham, T. Q. (2013). Load-Carrying Capacity and Required Reinforcement Strength of Closely Spaced Soil-Geosynthetic Composites. Journal of Geotechnical and Geoenvironmental Engineering, 139(9), 1468-1476.

7.4 NUMERICAL SIMULATION OF GEOSYNTHETIC REINFORCED SOIL – INTEGRATED BRIDGE SYSTEMS

7.4.1 OVERVIEW OF VDOT GRS-IBS

Section 6 of this report provided a discussion of the field monitored geosynthetic reinforced soil – integrated bridge system (GRS-IBS) build by VDOT (hereinafter referred to as VDOT wall). The VDOT wall was approximately 2.45 m high (H = 2.45 m (8 ft)) and constructed based on the layout recommended by Adams et al. (2012). The cross section of the VDOT wall was reflected in the numerical model used in this investigation, as shown in Fig. 7.4.1. The VDOT wall is composed of reinforced soil foundation, reinforced zone, 11 layers of Concrete Masonry Unit (CMU) facing blocks, geofoam, bridge slab, and integrated approach.

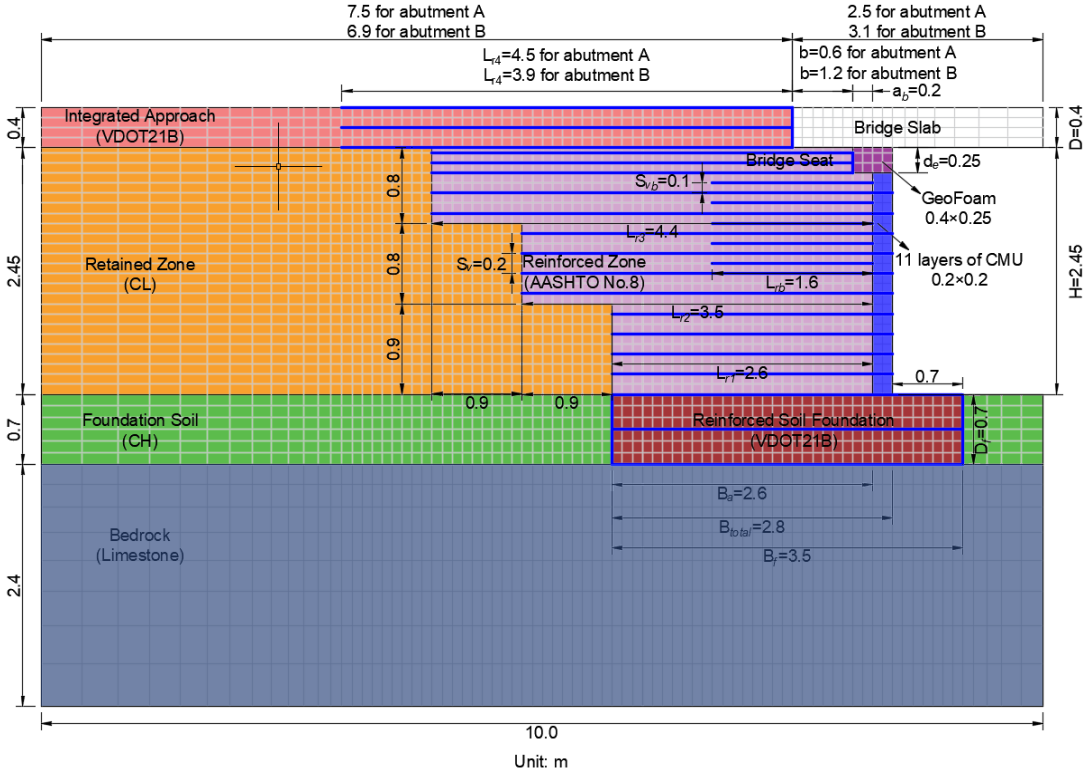

Fig. 7.4.1: Cross section of the VDOT wall

The geometry of the numerical model of the VDOT wall was based on the true dimension of the actural VDOT wall constructed in the field with some minor modifications to simplify the numerical mesh. The numerical model included a reinforced soil foundation (i.e., RSF), constructed using the VDOT21B aggregate, had a depth D_f of 0.7 m (2 ft 3 in) and a length B_f of 3.5 m (11.3 ft). A woven geotextile was used as reinforcement to form the wrapped-around RSF with an additional reinforcement layer in the middle. The RSF was seated on limestone bedrock and was surrounded by the foundation soil. The wall itself had a height H of 2.45 m (8 ft)

(including the bridge seat behind the geofoam) with three vertical cut slopes at back. The base length for the VDOT wall B_a was 2.6 m (8.5 ft) and the total base length including the facing block B_{total} was 2.8 m (9 ft). AASHTO No. 8 aggregate was used as the backfill material for the reinforced zone. The same type of woven geotextile was used as the reinforcement in the reinforced zone with vertical spacing S_v of 0.2 m (8 in) between primary reinforcement layers. The primary reinforcement layers in the reinforced zone extended to the cut slope with three different lengths as shown in Fig. 7.4.1. Five layers of bearing reinforcement (or secondary reinforcement) were used in the reinforced zone. The length of the bearing reinforcement was L_{rb} = 1.6 m (5 ft). The vertical spacing of the bearing reinforcement layers was half of the spacing between the primary reinforcement layers (i.e., S_{vb} = 0.1 m (4 in)). Solid CMU blocks were used for the first four layers and hollow CMU blocks were used for the remaining seven layers to simulate the construction of the facing element. All the CMU facing blocks had a dimension of 0.2 m (8 in) (wide) × 0.2 m (8 in) (high). On top of the CMU facing blocks was the geofoam with a dimension of 0.4 m (1 ft 4 in) (wide) × 0.25 m (10 in) (high). The beam seat width *b* was 0.6 m (2 ft) for Abutment A and 1.2 m (4 ft) for Abutment B and the setback distance a_b for the bridge seat was 0.2 m (8 in). The bridge slab had a length L_b of 5.6 m (18 ft 8 in) and a thickness *D* of 0.4 m (1 ft 4 in). The integrated approach constructed using the VDOT 21B aggregate had two lifts of wrapped-around fill material behind the bridge slab. The same type of woven geotextile was used as the reinforcement.

During the construction of the VDOT wall, the research team performed seven stage loadings on Abutment A using single or multiple Jersey concrete barriers. The seven stage loadings were also simulated in the numerical evaluation of this structure, as will be discussed in Section 7.4.2.4 of this report.

7.4.2 NUMERICAL MODELING

The finite difference method-based program FLAC2D (Fast Lagrangian Analysis of Continua) was used to simulate the VDOT wall. The numerical model mesh is shown in Fig. 7.4.1. To minimize the influence of the boundary condition, the foundation soil was 2.4 m (8 ft) deep (approximately 1.0*H*) and the left lateral boundary was located at 8.5 m (28 ft) (3.5*H*) behind the wall facing. The right lateral boundary was located at 1.5 m (5 ft) in front of the wall facing based on the symmetry of the bridge slab. Lateral boundaries were fixed in the horizontal direction and were free to move in the vertical direction while the bottom boundary was fixed in both horizontal and vertical directions. The numerical evaluations conducted as part of this study included simulation of both Abutment A and Abutment B by changing the beam seat width *b* and the length of the integrated approach.

7.4.2.1 CONSTITUTIVE MODELS

The backfill material AASHTO No. 8 aggregate used in the reinforced zone was poorly graded (GP) with no fines. Both the Mohr-Coulomb (MC) model and the stress-dependent Cap-Yield (CY) model were used as consitutive models for this soil. The parameters used in the MC model are summarized in Table 7.4.1:. Density gauge tests in the field showed that the aggregate had a dry density of 1650 kg/m^3 (100 pcf). The Young's modulus of the aggregate was determined based

on the secant elastic modulus corresponding to 50% of the yield strength E_{50} at the confining pressure of 34.47 kPa (5 psi). The cohesion was assumed to be zero since the AASHTO No. 8 aggregate was a granular material with no fines. The friction angle of the aggregate was determined by triaxial tests conducted using confining stresses of 6.89, 20.68, and 34.47 kPa (1, 3, and 5 psi). The dilation angle of the aggregate was selected based on the relationship of $\psi = \phi - 30^{o}$ recommended by Bolton (1986) for granular materials. Triaxial shear tests were simulated in the numerical analysis, with the results of the numerical simulations being shown in Fig. 7.4.2. The numerical results of the MC model match reasonably well with the experimental test results except that the MC model cannot capture the stress-dependent behavior of soil modulus since the MC model uses a constant elastic modulus. The simulated response for soil dilation was also in reasonable agreement with the measured data using the relationship of $\psi = \phi - 30^{o}$ from Bolton (1986).

Table 7.4.1: Parameters of the Mohr-Coulomb model for the AASHTO No. 8 aggregate

Constitutive Model	Mohr-Coulomb Model
Density ρ (kg/m^3)	1650
Young's Modulus E (MPa)	17.37
Poisson's Ratio υ	0.2
Cohesion c (kPa)	0
Friction Angle ϕ (°)	50
Dilation Angle ψ (°)	20

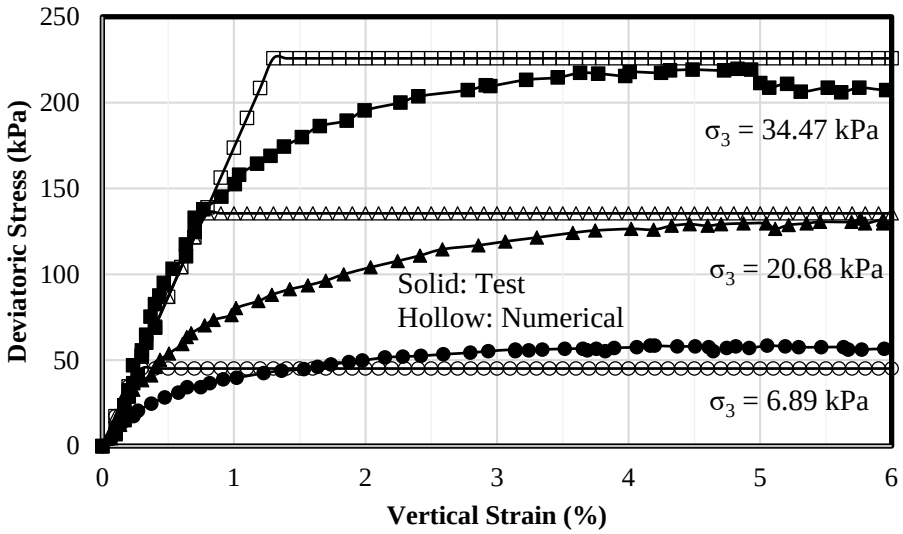

(a)

Fig. 7.4.2: Comparison between the measured and simulated triaxial test results using the MC model: (a) Stress - strain relationship;

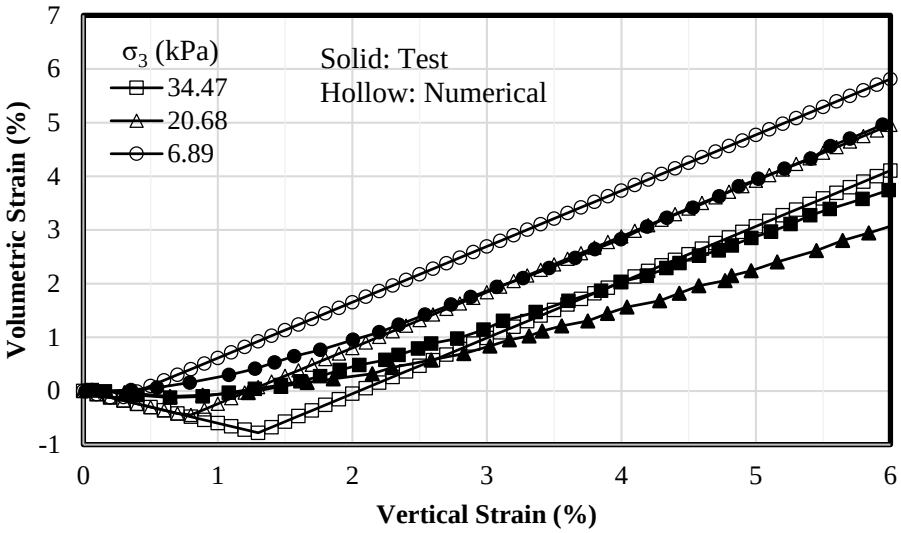

(b)

Fig. 7.4.2: Comparison between the measured and simulated triaxial test results using the MC model: (b) Volumetric strain - vertical strain relationship (continued).

In addition to the MC model, the stress-dependent Cap-Yield (CY) model (Itasca Consulting Group, 2008b) was also used to simulate the backfill soil (AASHTO No. 8 aggregate). The CY model is a double yield model, which considers both isotropic compression yielding and shear yielding. Some of the parameters in the CY model are the same as those in the MC model, such as the density ρ, Poisson's ratio υ_{ur}, cohesion *c*, friction angle ϕ_f, and dilation angle ψ_f. Other parameters, such as the cap-yield surface parameter α, the multiplier *R*, the calibration factor β, the power *m*, the reference elastic shear modulus G^e_{ref}, the reference bulk modulus K^{iso}_{ref}, the reference pressure p_{ref}, and the failure ratio R_f, required additional evaluation for their determination or calibration. In the CY model, the reference pressure p_{ref} was set as 34.47 kPa (5 psi), which was same as one of the confining stresses in the triaxial shear tests conducted as part of this study. The typical failure ratio R_f of 0.9 was used. The Cap-Yield surface was assumed to be spherical and therefore the cap-yield surface parameter $\alpha$was set to be 1. Itasca Consulting Group (2008a) provided three equations to determine the elastic tangent shear modulus at the reference pressure G^e_{ref}, the bulk modulus at the reference pressure K^{iso}_{ref}, and the multiplier *R*, as shown in Equations (7.4.1) to (7.4.3):

$$G^e_{ref} = \frac{E^{ref}_{ur}}{2(1+\upsilon_{ur})} \tag{7.4.1}$$

$$K^{iso}_{ref} = E^{ref}_{oed} \tag{7.4.2}$$

$$R = \frac{E_{ur}^{ref}}{3(1-2\upsilon_{ur})E_{oed}^{ref}} - 1 \qquad (7.4.3)$$

where E_{ur}^{ref} is the unloading and loading modulus at the reference pressure and E_{oed}^{ref} is the tangent modulus for a primary oedometer loading test.

The unloading and loading modulus E_{ur}^{ref} is typically 2 to 5 times the secant elastic modulus at 50% of the yield strength E_{50}^{ref} (Tjie-Liong, 2014). In this study, E_{ur}^{ref} was set to be 5 times E_{50}^{ref} and G_{ref}^{e} was calculated using Equation (7.4.1). Due to lack of reliable oedometer loading test data or isotropic compression test data, the bulk modulus at the reference pressure K_{ref}^{iso} and the power *m* were derived as a result of calibration using the triaxial shear test results. The multiplier *R* was calculated using Equation (7.4.3) once K_{ref}^{iso} was determined. Table 7.4.2 summarizes the parameters used in the CY model. Triaxial shear tests were also simulated in the numerical analysis using the CY model and the results are shown in Fig. 7.4.3. Figure 7.4.3 shows that the stress-dependent CY model can capture the nonlinear stress - strain behavior of the modulus of the soil prior to failure. The simulated soil volumetric strain – vertical strain relationship was also in reasonable agreement with the measured data, indicating that the calibrated bulk modulus at the reference pressure K_{ref}^{iso} and the power *m* were reasonable.

Table 7.4.2: Parameters of the Cap-Yield model for the AASHTO No. 8 aggregate

Constitutive Model	Cap Yield Model
Density ρ (kg/m^3)	1650
Ultimate friction angle ϕ_f (°)	50
Ultimate dilation angle ψ_f (°)	20
Cap-Yield surface parameter α	1
Multiplier R	5.89
Calibration factor β	0.15
Power m	0.55
Unloading and loading modulus E_{ur}^{ref} (MPa)	86.85
Reference elastic shear modulus G_{ref}^{e} (MPa)	36.19
Reference bulk modulus K_{ref}^{iso} (MPa)	7.00
Reference Pressure p_{ref} (kPa)	34.47
Poisson's ratio υ_{ur}	0.2
Cohesion c (kPa)	0
Failure ratio R_f	0.9

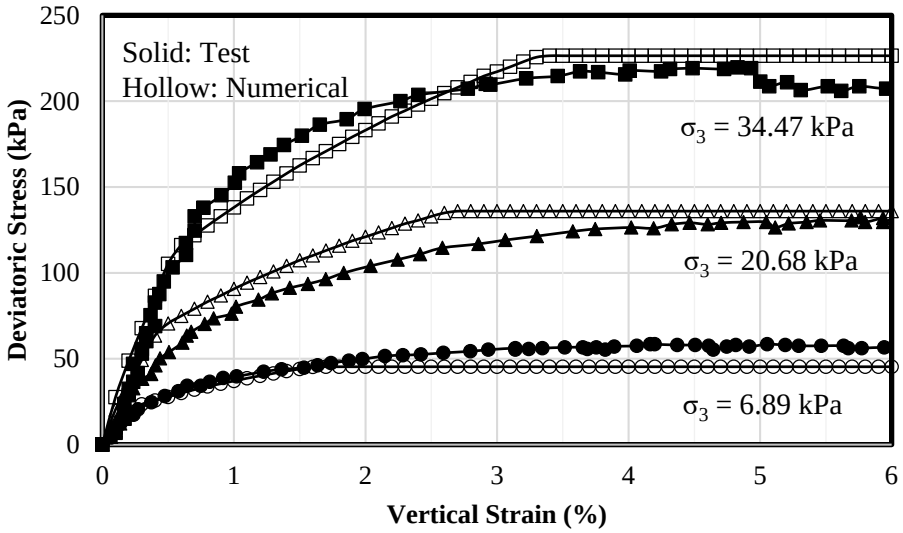

(a)

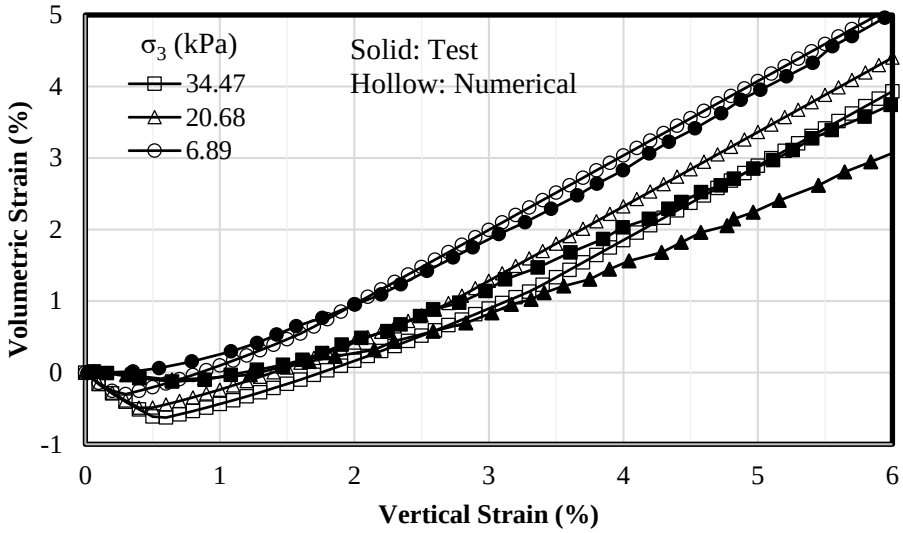

(b)

Fig. 7.4.3: Comparison between the measured and simulated triaxial test results using the CY model: (a) Stress - strain relationship; (b) Volumetric strain - vertical strain relationship.

Results presented in Fig. 7.4.2 and Fig. 7.4.3 show that the MC model cannot capture the nonlinear elastoplastic behavior of the fill material and the CY model is much better. The purpose of using two different models here (i.e., MC and CY models) is to study the influence of different constitutive models on the behavior of the GRS-IBS

The VDOT21B aggregate (i.e., the backfill soil for the RSF and the integrated approach) was modeled using the MC model. An elastic modulus of 25 MPa (3626 psi) and Poisson's ratio of 0.2 were used. A friction angle of 48.3° and cohesion of 5.6 kPa (117 psf) were adopted in the

numerical analysis based on direct shear tests. The correlation from Bolton (1986) as shown in Equation (7.3.1) was also used to determine a dilation angle of 18.3°. The backfill soil was compacted to a density of 2200 kg/m^3 (137 pcf). Table 7.4.3 summarizes the parameters used to model the VDOT21B aggregates.

Table 7.4.3: Parameters of the Mohr-Coulomb model for the VDOT21B aggregate

Constitutive Model	Mohr-Coulomb Model
Density ρ (kg/m^3)	2200
Young's Modulus E (MPa)	25
Poisson's Ratio υ	0.2
Cohesion c (kPa)	5.6
Friction Angle ϕ (°)	48.3
Dilation Angle ψ (°)	18.3

The retained soil classified as CL according to the USCS soil classification. The measured liquid limit (LL) and plasticity limit (PL) for the retained soil were 42 and 19 respectively, resulting in a plasticity index (PI) of 23. The foundation soil classified as CH according to the USCS soil classification. The measured liquid limit (LL) and plasticity limit (PL) for the foundation soil were 50 and 23 respectively, resulting in a plasticity index (PI) of 27. An elastic modulus of 20 MPa (2900 psi) and Poisson's ratio of 0.3 were used for both the retained soil and the foundation soil. A typical density of 1750 kg/m^3 (109 pcf) (Coduto, 2015) and a cohesion of 20 kPa (418 psf) (Subramanian, 2008) were adopted for the clay. The friction angles of 30° and 26° were assigned to the retained soil and the foundation soil respectively based on the correlation between the friction angle and the PI (Mitchell and Soga, 2005) as shown in Equation (7.3.4):

$$\sin\phi \approx 0.8 - 0.094 \ln PI \tag{7.3.4}$$

where ϕ is the effective friction angle and *PI* is the plasticity index.

Table 7.4.4: Parameters of the Mohr-Coulomb model for the retained soil (CL) and the foundation soil (CH)

Constitutive Model	Mohr-Coulomb Model
Density ρ (kg/m^3)	1750
Young's Modulus E (MPa)	20
Poisson's Ratio υ	0.3
Cohesion c (kPa)	20
Friction Angle ϕ (°)	30 for retained soil (CL) 26 for foundation soil (CH)
Dilation Angle ψ (°)	0

The limestone bedrock and the bridge slab were simulated using a linearly elastic model. Densities of 2000 kg/m^3 (125 pcf) and 2500 kg/m^3 (156 pcf) were assigned to the limestone bedrock and the bridge slab respectively. The Young's modulus and Poisson's ratio were selected based on typical values. Table 7.4.5 and Table 7.4.6 summarize the parameters used to model the limestone bedrock and the bridge slab.

Table 7.4.5: Parameters of the linearly elastic model for the limestone bedrock

Constitutive Model	Linearly Elastic
Density ρ (kg/m^3)	2000
Young's Modulus E (GPa)	2
Poisson's Ratio υ	0.2

Table 7.4.6: Parameters of the linearly elastic model for the bridge slab

Constitutive Model	Linearly Elastic
Density ρ (kg/m^3)	2500
Young's Modulus E (GPa)	20
Poisson's Ratio υ	0.15

The CMU facing blocks were also simulated using a linearly elastic model. Solid CMU blocks with a density of 1800 kg/m^3 (112 pcf) were used for the first four layers and hollow CMU blocks with a density of 1250 kg/m^3 (78 pcf) were used for the remaining seven layers to construct the facing elements. The same Young's modulus and Poisson's ratio were assigned to CMU facing blocks as those assigned to the bridge slab. Table 7.4.7 summarizes the parameters used in the numerical analysis to simulate the CMU facing blocks.

Table 7.4.7: Parameters of the linearly elastic model for CMU facing blocks

Constitutive Model	Linearly Elastic
Density ρ (kg/m^3)	1800 for solid CMU blocks 1230 for hollow CMU blocks
Young's Modulus E (GPa)	20
Poisson's Ratio υ	0.15

The linearly elastic model was also used to simulate the geofoam in this study since the main function of the geofoam was not to sustain the vertical load from the bridge slab. The properties of the geofoam, as provided by the manufacturer, were represented by parameters used in the linearly elastic model summarized in Table 7.4.8.

Table 7.4.8: Parameters of the linearly elastic model for the geofoam

Constitutive Model	Linearly Elastic
Density ρ (kg/m^3)	11.2
Young's Modulus E (MPa)	1.5
Poisson's Ratio υ	0.15

7.4.2.2 REINFORCEMENT AND INTERFACES

The woven geotextile with a wide-width tensile strength T_f of 70 kN/m (4800 lb/ft) at 10% strain in the machine direction (MD) was used in the VDOT wall as the reinforcement. At 2% strain, the tensile strength of the geotextile was 14 kN/m (960 lb/ft) according to the manufacturer, resulting in a tensile stiffness *J* of 700 kN/m (48 kip/ft). Both cable structural elements and beam structural elements were evaluated for use in the numerical model to simulate the geotextile reinforcement. Horizontal geotextile between CMU facing blocks, horizontal geotextile between CMU facing blocks and RSF, vertical geotextile between the bridge seat and the geofoam, and vertical geotextile between the integrated approach and the bridge slab were modeled using beam structural elements with zero moment of inertia (i.e., no bending stiffness) and frictional interfaces on both sides. The remaining geotextile reinforcements within the backfill soil were simulated using cable structural elements with frictional interfaces on both sides. Figure 7.4.4 shows different structural elements and their interface details used in the numerical model.

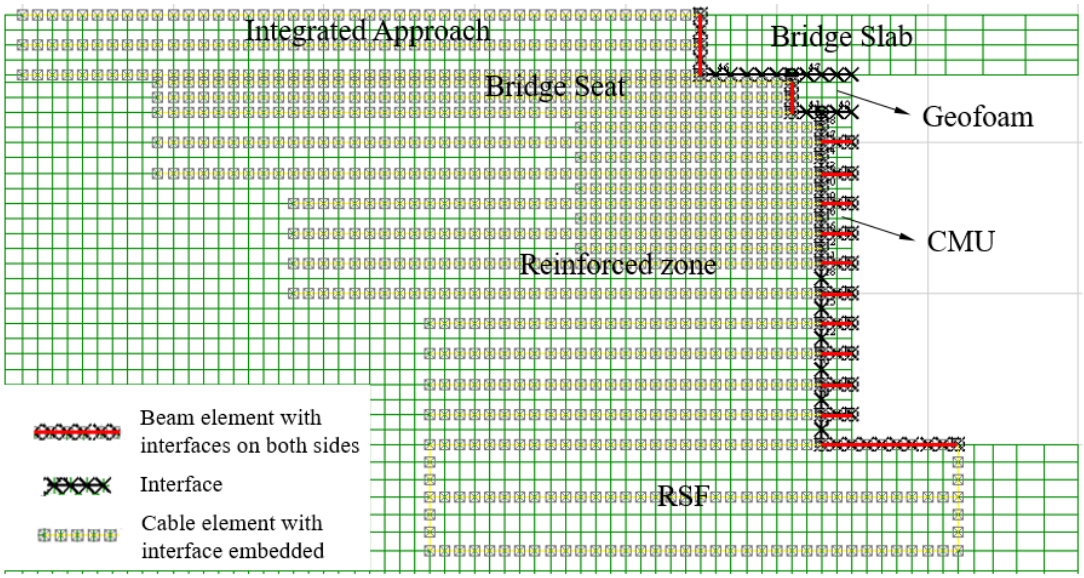

Fig. 7.4.4: Reinforcement and interface details

The properties of both the beam and cable structural elements were determined based on the actual properties of the woven geotextile used for construction of the VDOT wall. Assuming the thickness *t* of the geotextile to be 1 mm (0.04 in), the elastic modulus of the structural elements

was calculated by dividing the tensile stiffness by the thickness. The properties of both beam and cable structural elements are summarized in Table 7.4.9.

Table 7.4.9: Reinforcement properties for beam and cable structural elements

Element properties	Cable	Beam
Stiffness (kN/m)	700	700
Thickness (mm)	1	1
Elastic modulus (MPa)	700	700
Cross-sectional Area (m^2)	0.001	0.001
Perimeter (m)	2.002	2.002
Yield strength T_f (kN/m)	70	/
Moment of inertia (m^4)	/	0

Different types of interfaces were used in the numerical analysis. These interfaces were represented by interface elements included in the software, which are linearly-elastic perfectly-plastic springs with the Mohr - Coulomb failure criterion. For the properties of the interfaces between backfill soil and geotextile, Goodhue et al. (2001) recommended that interaction coefficients C_i ranging from 0.5 to 0.9 could be used for foundry sands in contact with geosynthetics and the cohesion of the soil should be ignored. In the numerical simulations conducted as part of this study, an interaction coefficient C_i of 0.9 and zero cohesion were assigned to the geotextile – soil interface. For the vertical interface between backfill soil and CMU facing blocks, an interaction coefficient C_i of 0.65 and zero cohesion were used. For the interface between geotextile and CMU blocks, Awad & Tanyu (2014) conducted direct shear tests and pullout tests to investigate the connection strength between the geotextile and facing blocks. Based on their results, a friction angle δ of 16.2° and a cohesion of 9.5 kPa (1.4 psi) were assigned to the interface between CMU blocks and geotextile. A cohesion of 9.5 kPa (1.4 psi) was justified because some irregularities existing on the rough surfaces of concrete could behave like cohesion by preventing the geotextile from moving. The top three layers of CMU facing blocks were connected using dowel bars in the field. In the numerical model, the dowel bars were simulated as mechanical connection. A friction angle of 57° and a cohesion of 46 kPa (961 psf) were assigned to the interface to simulate the mechanical connection (Huang et al., 2009). The bearing reinforcement layers were not connected to the CMU facing blocks. For the interface related to the geofoam (e.g., the bridge slab – geofoam interface, the CMU facing blocks – geofoam interface, and the geotextile – geofoam interface), a friction coefficient of 0.5 and zero cohesion were used (Negussey, 2007). In other words, the interface friction angle was equal to $\delta = \arctan(0.5) = 26.6°$.

In addition to the interface friction angle and the cohesion, the relative interface movement was also controlled by the interface normal stiffness k_n and the shear stiffness k_s. Hatami and Bathurst (2005) gave some recommendations on the determination of interface stiffness. Based

on their research, a normal stiffness k_n of 1×10^8 N/m/m was selected for the soil – block interface. The shear stiffness k_s was refined as 1/100 of the normal stiffness k_n to prevent the interface from penetrating into neighboring zones. For the soil – block interface, Hatami and Bathurst (2005) suggested to use a normal stiffness k_n of 1×10^9 N/m/m and a shear stiffness k_s of 4×10^7 N/m/m to avoid numerical effects, such as intrusion of adjacent zones and excessive computation time. Table 7.4.10 summarizes all the interface properties used in the numerical model.

7.4.2.3 CONSTRUCTION SEQUENCE

Field construction of the VDOT wall took place in stages, which were simulated in the numerical modeling conducted in this numerical investigation. The construction stages adopted in the simulations are as follows:

(1) Before the wall construction, the limestone bedrock and the foundation soil CH reached an equilibrium under gravity.
(2) The construction of the RSF was simulated and the geotextile was placed in the RSF.
(3) A layer of the CMU facing block, the backfill soil (AASHTO No. 8 aggregate), the retained soil CL, and the geotextile were installed. Corresponding interfaces and connection were assigned. A uniform vertical stress of 8 kPa (167 psf) was applied on top of each lift of the backfill soil layer and was removed before the placement of next lift to simulate the compaction effect in the field. Hatami and Bathurst (2005) and Zheng and Fox (2017) successfully used an 8 kPa (167 psf) vertical compaction stress in their numerical models to study the effect of compaction. The wall was under self-weight condition after this construction stage was finished.
(4) The geofoam and the bridge seat were installed. Corresponding interfaces and connection were assigned. A uniform vertical stress of 8 kPa (167 psf) was also applied on top of the backfill soil layer to simulate the compaction effect.
(5) After the construction of the wall itself was finished, the bridge slab was placed on top of the bridge seat. The beam seat width b was 0.6 m (2 ft) for Abutment A and 1.2 m (4 ft) for Abutment B and the setback distance a_b for the bridge seat was 0.2 m. Corresponding interfaces and connection were assigned.
(6) The integrated approach was constructed behind the bridge slab. Geotextile was installed in the integrated approach.

Table 7.4.10: Interface properties

Interface	Method	k_n (N/m/m)	k_s (N/m/m)	Interaction coefficient C_i	Friction angle (°)	Cohesion (kPa)
Geotextile – VDOT21B (Geotextile – RSF & Geotextile – Integrated approach)	Embedded in cable element	/	1×10^{6}	0.9	45.3	0
Geotextile – AASHTO No.8 (Geotextile – Reinforced Zone)	Embedded in cable element		1×10^{6}	0.9	47.0	0
AASHTO No.8 – CMU (Vertical interface between soil and CMU)	Interface	1×10^{8}	1×10^{6}	0.65	37.8	0
Geotextile – CMU (Frictional Connection)	Beam elements with interfaces	1×10^{9}	4×10^{7}	/	16.2	9.5
Geotextile – CMU (Mechanical Connection)	Beam elements with interfaces	1×10^{9}	4×10^{7}	/	57.0	46
Geofoam – Geotextile & Geofoam – CMU & Geofoam – Bridge slab	Interface	1×10^{7}	1×10^{5}	/	26.6	0
Bridge slab – AASHTO No.8 (Bridge slab – bridge seat)	Interface	1×10^{8}	1×10^{6}	0.9	47.0	0
Bridge slab – Geotextile	Beam elements with interfaces	1×10^{9}	4×10^{7}	/	16.2	9.5

7.4.2.4 STAGE LOADING

For Abutment A, seven stage loadings (SL) were applied during Construction Stage (3) using single or multiple Jersey barriers. For Abutment B, however, no SL was applied. Figure 7.4.5 shows the schematic of the seven stage loadings simulated as part of the numerical evaluation of Abutment A. Among the seven stage loadings, SL1, SL3, and SL5 were applied using a single Jersey barrier as a load while the remaining four SL used eight Jersey barriers. Four stage loadings were applied on the reinforcement zone with reinforcement spacing S_v of 0.2 m (8 in) (i.e., SL1 to SL4) and three stage loadings were applied on the reinforcement zone with reinforcement spacing S_{vb} of 0.1 m (4 in) (i.e., SL5 to SL7). The load from a single Jersey barrier was approximately 24 kN (5395 lb). The bottom of a single Jersey barrier was 3.66 m (12 ft) long and 0.6 m (2 ft) wide. As a result, the average equivalent vertical stress from a single Jersey barrier was approximately 11 kPa (230 psf). When eight Jersey barriers were used, a single Jersey barrier was placed first and the readings of the earth pressure cells were recorded during a 30 minutes waiting period. The remaining seven Jersey barriers were then placed with no waiting period. The small notch at the bottom of the Jersey barrier resulted in a non-uniform stress distribution when eight Jersey barriers were applied as shown in Fig. 7.4.5. The load from seven Jersey barriers were applied on the left and right Jersey barriers with an average equivalent vertical stress of approximately 38.5 kPa (804 psf) on each end, resulting in an average equivalent vertical stress of 11 kPa (230 psf) from the middle Jersey barrier.

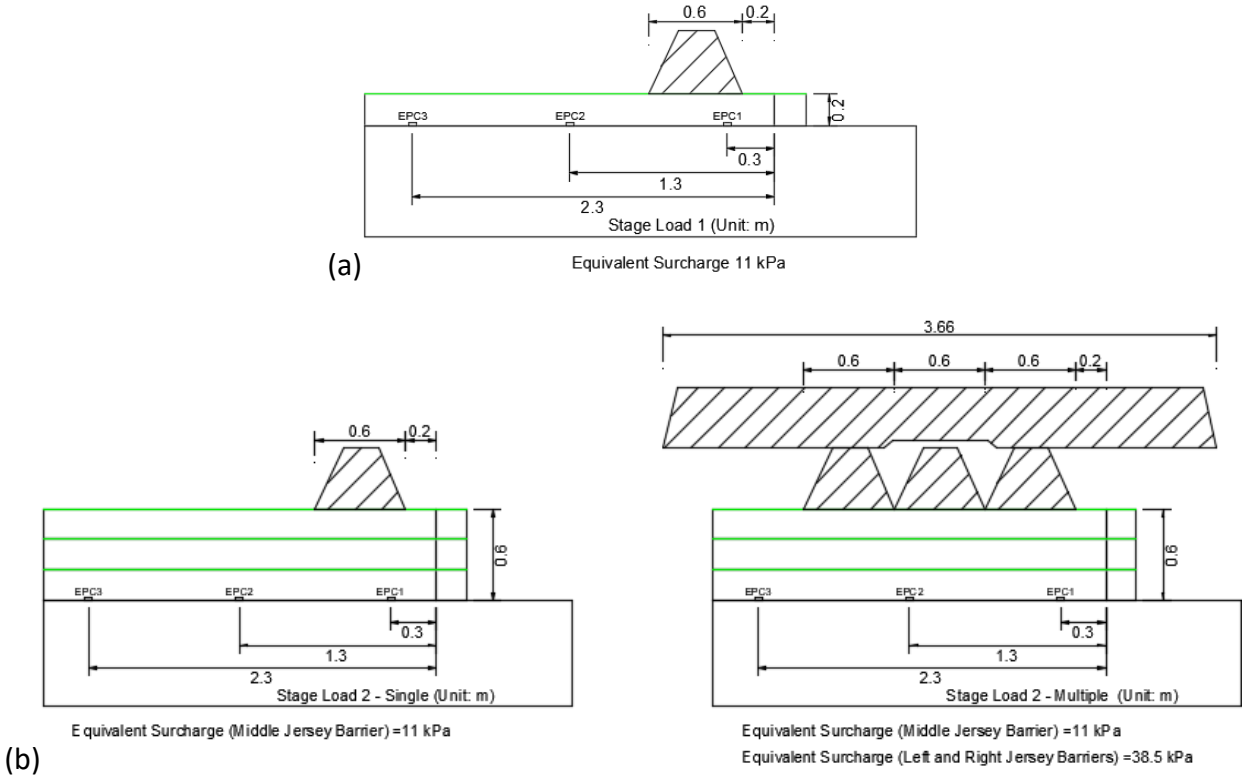

Fig. 7.4.5: Schematic of stage loading adopted in the numerical simulations: (a) SL1; (b) SL2;

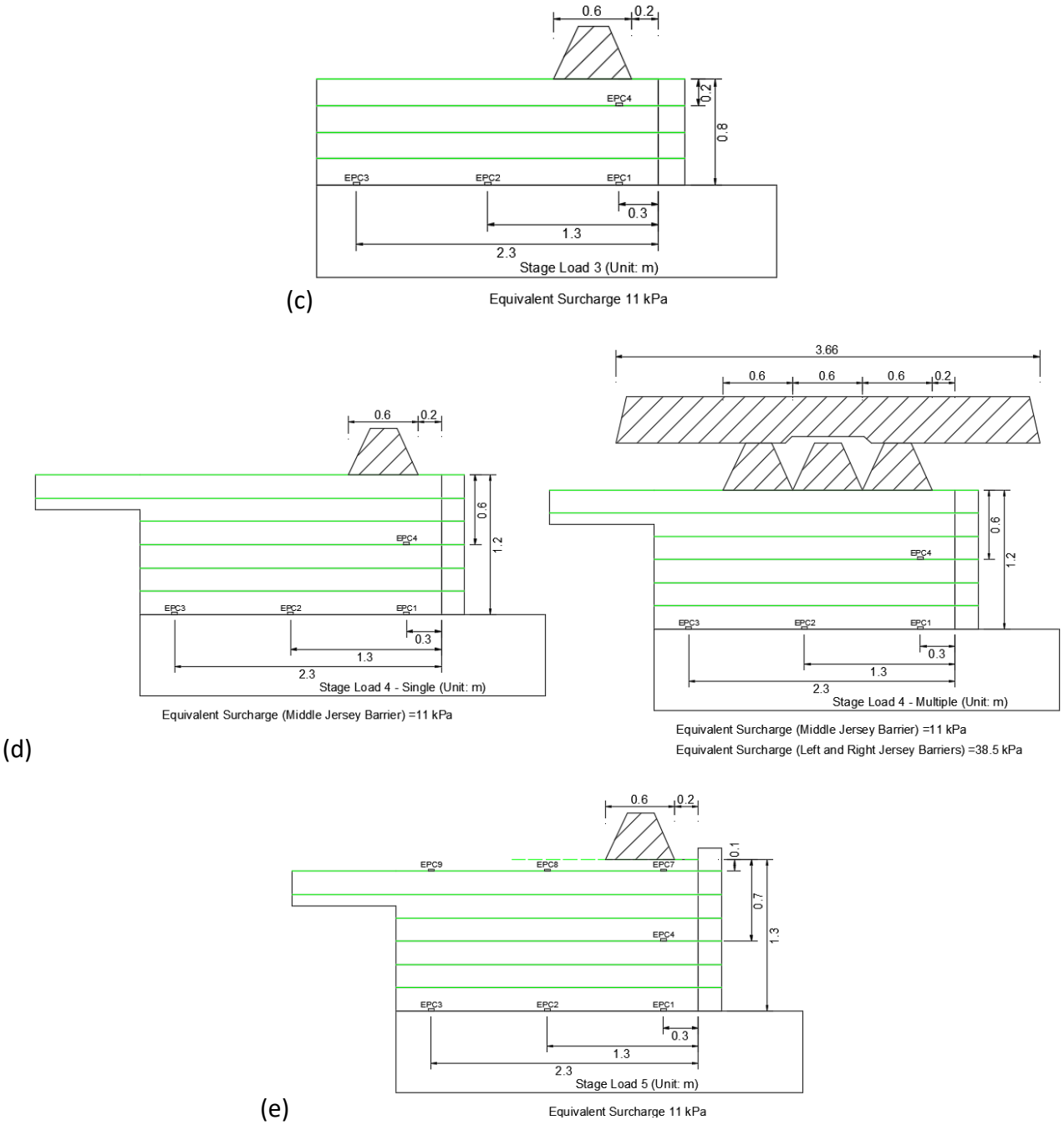

Fig. 7.4.5: Schematic of stage loading adopted in the numerical simulations: (c) SL3; (d) SL4; (e) SL5 (continued);

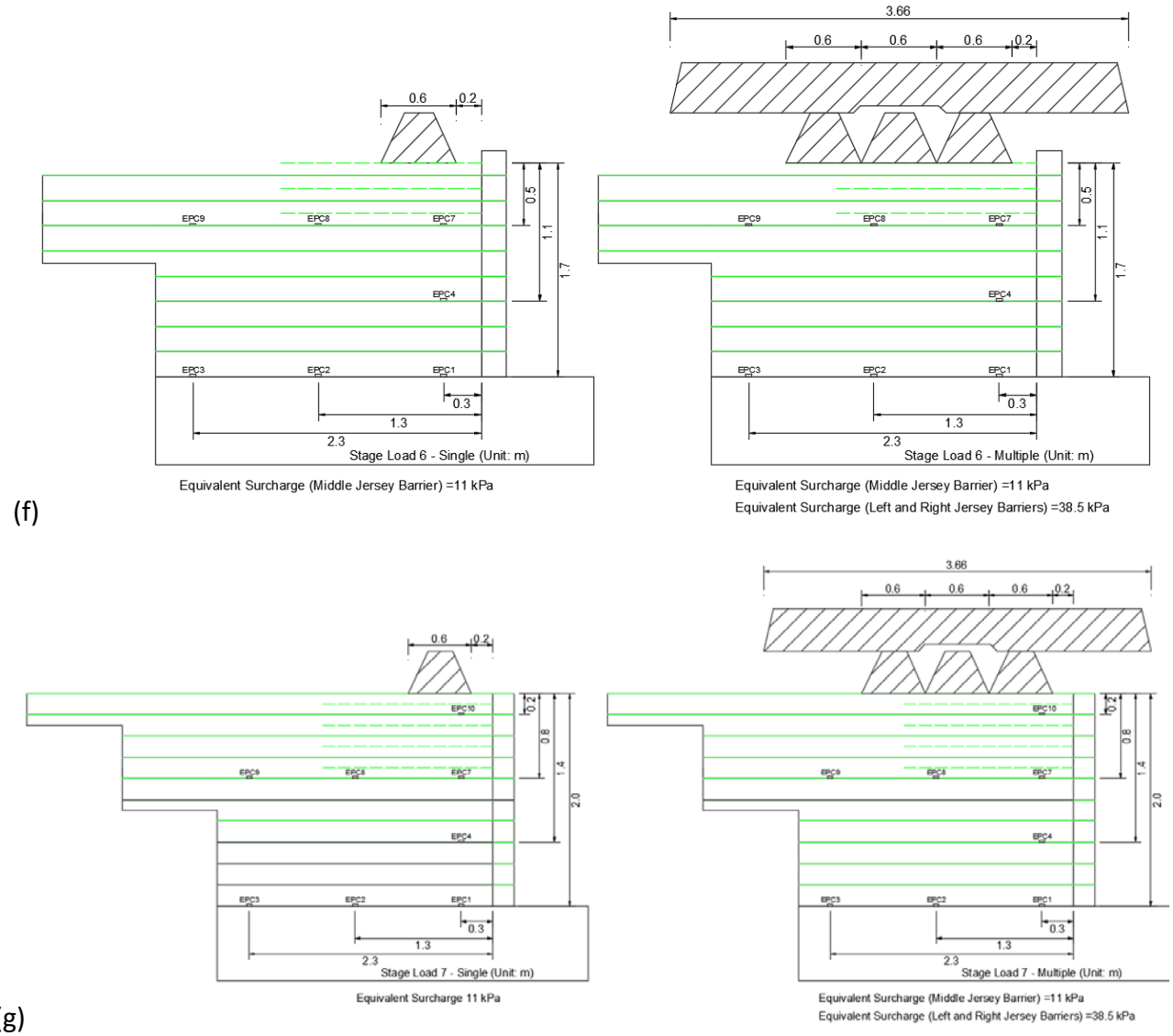

Fig. 7.4.5: Schematic of stage loading adopted in the numerical simulations (f) SL6; (g) SL7 (continued).

The seven stage loadings in Abutment A were also simulated in the numerical modelling. The Jersey barriers used in the field were similar to rigid footings. Using a uniform vertical stress to simulate stage loading was not deemed appropriate since the contact pressure at the bottom of the Jersey barrier was not uniformly distributed. Instead of a uniform vertical stress, the numerical model used rectangular blocks of 0.6 m (2 ft) wide and 0.1 m (4 in) high to simulate the load. Since the Jersey barriers were made of concrete, a typical elastic modulus of 20 GPa (2900 ksi) and Poisson's ratio of 0.15 were assigned to these rectangular blocks. Different densities were assigned to the rectangular blocks as shown in Fig. 7.4.6 in order to simulate the non-uniform stress distribution when eight Jersey barriers were used. For single Jersey barrier

stage loading (i.e., SL1, SL3, and SL5), the rectangular block had a density of 11224.5 kg/m^3 (700 pcf), resulting in an average vertical stress of 11 kPa (230 psf) at the bottom of the block (as shown in Fig. 7.4.6 (a)). For multiple Jersey barriers stage loading (i.e., SL2, SL4, SL6, and SL7), the bottom three rectangular blocks had the same density of 11224.5 kg/m^3 (700 pcf) while the top two blocks had a density of 28061.2 kg/m^3 (1752 pcf) (as shown in Fig. 7.4.6 (b)), resulting in an average vertical stress of 38.5 kPa (804 psf) at the bottom of the left and right blocks.

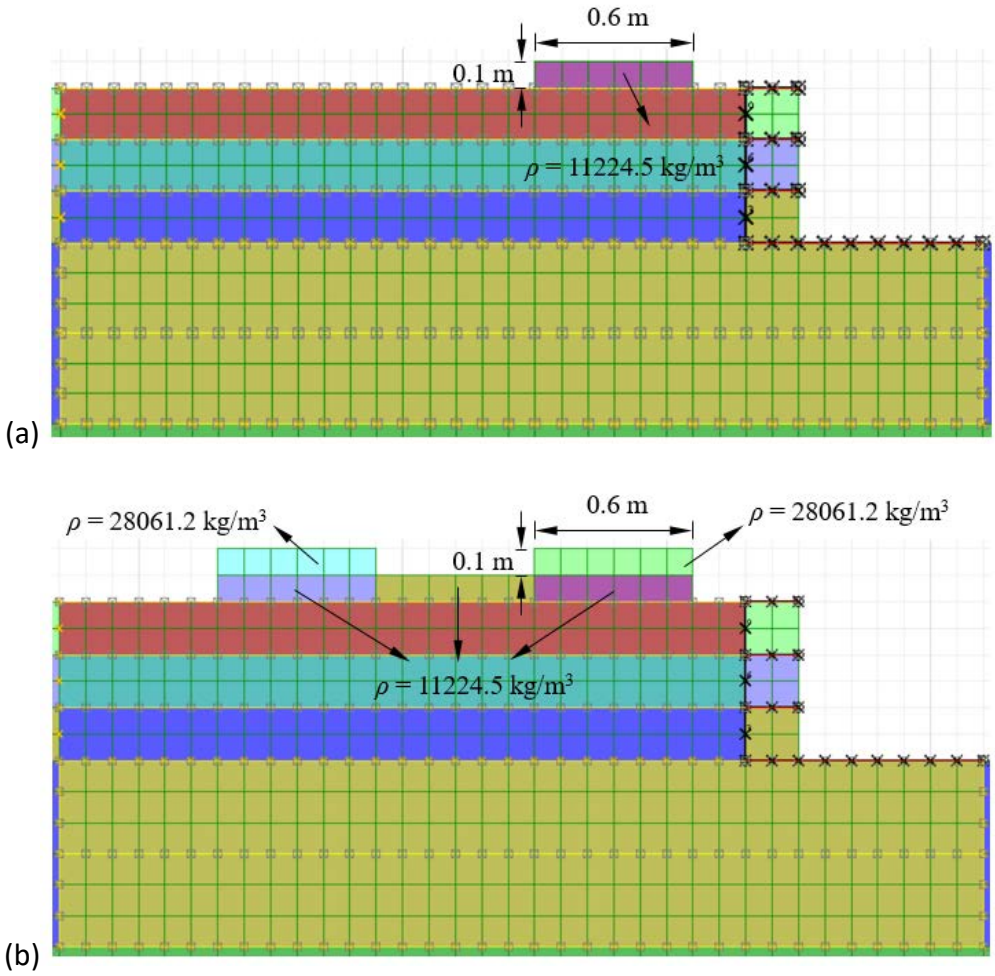

Fig. 7.4.6: Numerical simulation of stage loading: (a) Single Jersey barrier; (b) Multiple Jersey barriers.

7.4.2.5 CALIBRATION AND VALIDATION

The effect of mesh density on the results of the numerical results was considered in this study, as will be discussed in detail in Section 7.4.4. It was concluded that the mesh density adopted in the numerical model was appropriate for the numerical simulations, resulting in adequate accuracy.

Figure 7.4.7 shows the lateral earth pressure behind the wall facing as part of the numerical simulation of Abutment B. Specifically, the calculated stresses are shown for two of the construction stages: The end of construction of the wall itself at the end of Construction Stage (3) (i.e., the wall is under its self-weight condition) and the end of Construction Stage (5) (i.e., after the placement of the bridge slab). Figure 7.4.7 also shows as reference the lateral earth pressure profiles calculated using the Rankine active earth pressure coefficient K_a and the lateral earth pressure coefficient at-rest K_0 under the self-weight condition. The Rankine active lateral earth pressure coefficient was calculated as $K_a = \tan^2(45^o - \phi/2)$ and the at-rest lateral earth pressure coefficient K_0 was calculated as $K_0 = 1 - \sin\phi$ where $\phi = 50^o$ was the friction angle of the backfill material AASHTO No. 8 aggregate. Under the self-weight condition, the lateral earth pressure behind the wall facing were higher than the Rankine active earth pressure due to the compaction effect. The field and laboratory study reported by Filz and Duncan (1996) indicated that permanent lateral earth pressures increase due to compaction. The lateral earth pressure behind the wall facing increased with the placement of the bridge slab. It should be noted that the CY model gave results that were very similar to those calculated using the MC model. *The slab load may be within the elastic range, thus similar predictions are obtained in simulations conducted using the CY and MC models.*

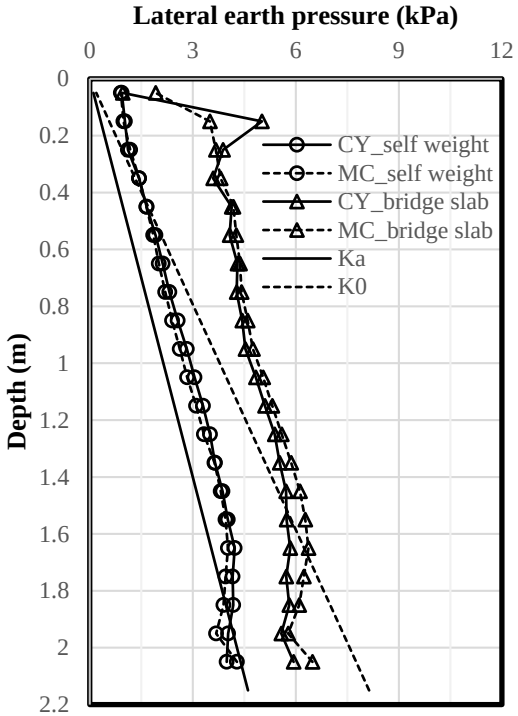

Fig. 7.4.7: Lateral earth pressure in Abutment B

Figure 7.4.8 shows a comparison between the numerically calculated and the measured lateral earth pressures behind the wall facing in Abutment A. The results obtained after two of the

construction stages are shown in Fig. 7.4.8: under its self-weight (i.e., end of Construction Stage (3)) and under the bridge slab load (i.e., end of Construction Stage (5)). Figure 7.4.8 (a) also shows the lateral earth pressure profiles calculated using the Rankine active earth pressure coefficient K_a and the coefficient at-rest K_0 when the construction of the wall itself was completed at the end of Construction Stage (3) (i.e., under self-weight condition). Because of the stage loading applied in Abutment A, the lateral earth pressure behind the wall facing did not show a proportional increase with increasing depth. The calculated lateral earth pressures were similar to the lateral earth pressure at-rest K_0 condition for the upper portion of the wall where the bearing reinforcement layers existed and the reinforcement spacing S_{vb} was 0.1 m (4 in). For the lower portion of the wall where the reinforcement spacing S_v was 0.2 m (8 in), the MC model gave a relatively uniform lateral earth pressure distribution while the results using the CY model reflected the effect of stage loading. When the CY model was used, the lateral earth pressure increased at the elevation where the stage loading using multiple Jersey barriers was applied. Since the CY model is stress-dependent, the stage loading and unloading resulted in the increase of the soil modulus. As a result, the lateral displacement of the CMU facing blocks decreased and the lateral earth pressure behind the facing increased. The field measurements were also shown in Fig. 7.4.8. The measured lateral earth pressures were close to the numerical results, especially under the bridge slab loading as shown in Fig. 7.4.8 (b).

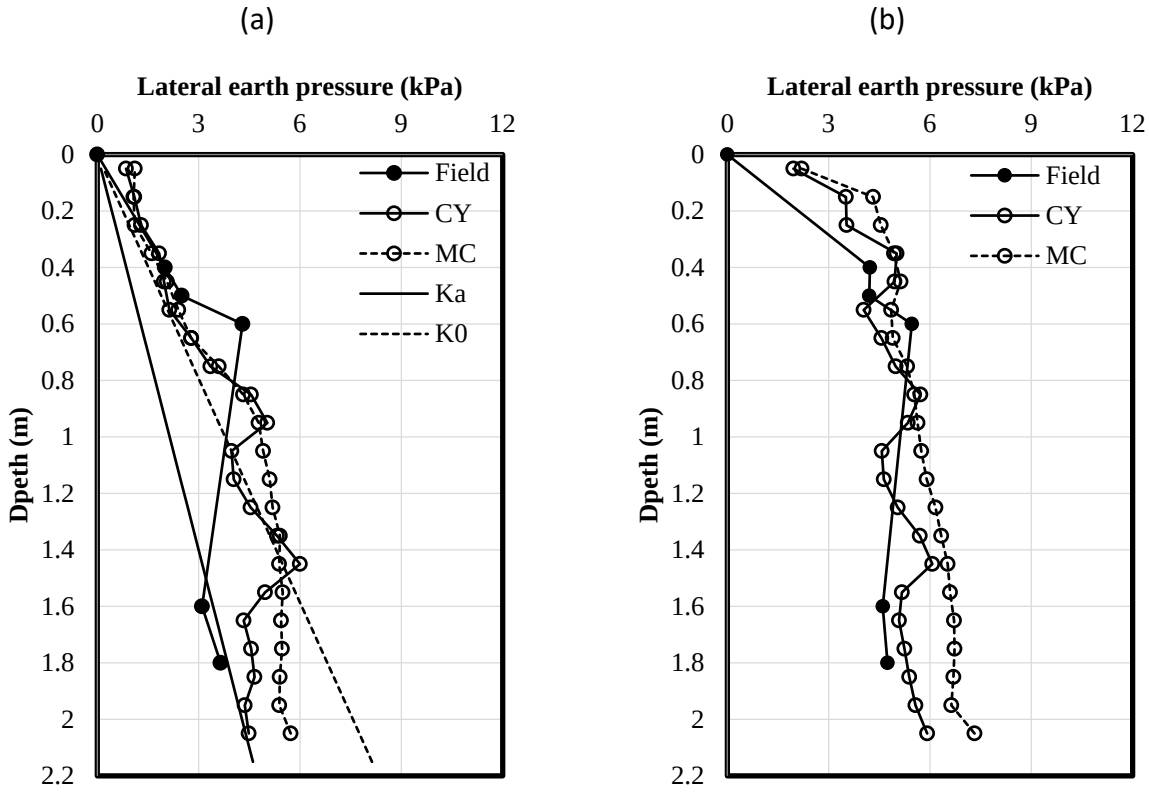

Fig. 7.4.8: Lateral earth pressure in Abutment A: (a) Self-weight; (b) Bridge slab load.

Figure 7.4.9 shows the distribution of additional vertical stress 0.3 m (1 ft) away from back of CMU facing blocks due to the placement of the bridge slab for both Abutments A and B. This addition vertical stress was caused by the bridge slab load only. In other words, the reference "zero" vertical stress was set at the end of Construction Stage (4) (i.e., the end of construction of geofoam and bridge seat). Field measurements are also shown in Fig. 7.4.9. It should be noted that the two abutments were constructed with different beam seat widths *b* (see Section 7.4.1) and that a stage loading process was conducted only on Abutment A (see Section 7.4.2.4). These two aspects led to different results, both in field measurements and numerical predictions, between Abutments A and B.For Abutment A, the numerical results were close to the field data. The additional vertical stress induced by the placement of the bridge slab was higher at top and decreased with depth. For Abutment B, however, the calculated additional vertical stress was higher than the measured ones, especially the earth pressure cell data at the top of the wall. The earth pressure cell at the top of the wall in Abutment B was placed under the geofoam, possibly resulting in an extremely low reading as discussed in Section 6.3.1.1.

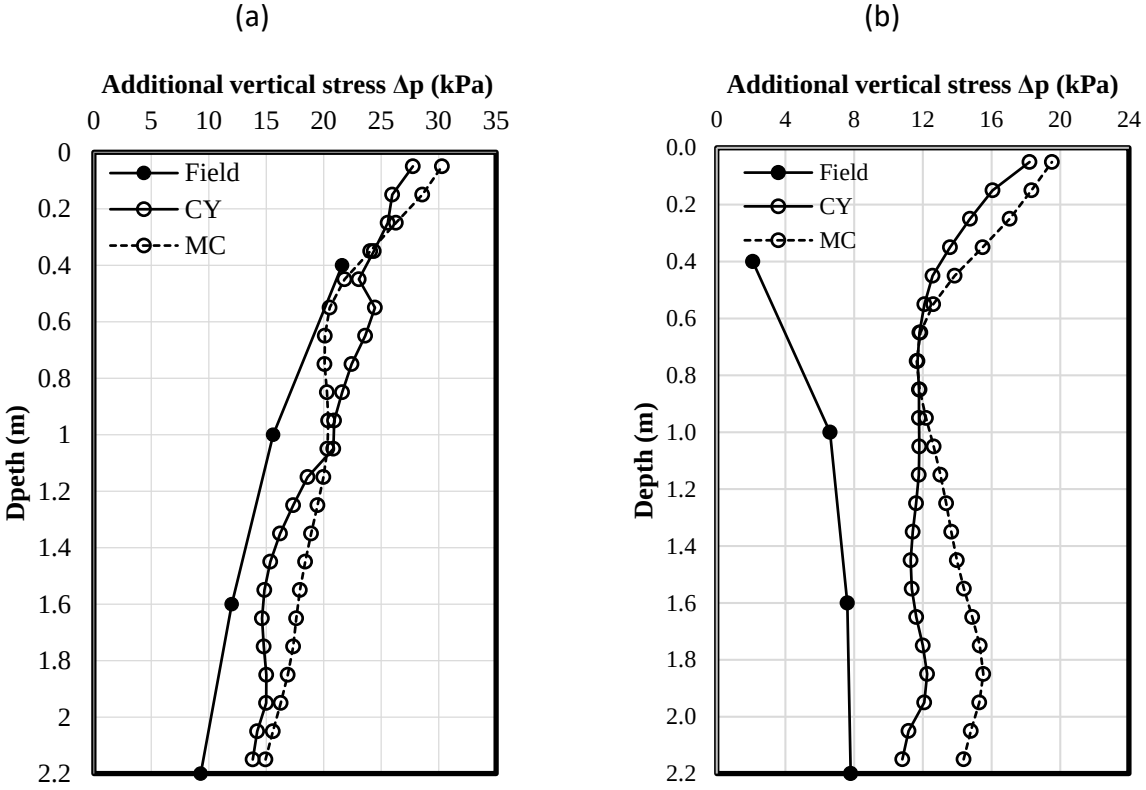

Fig. 7.4.9: Additional vertical stress 0.3 m away from the back of CMU facing blocks due to the bridge slab: (a) Abutment A; (b) Abutment B.

Figure 7.4.10 shows the additional lateral displacement of CMU facing blocks induced by the placement of the bridge slab for both Abutments A and B. This addition lateral displacement was caused by the bridge slab load only. In other words, the reference "zero" lateral displacement was set at the end of Construction Stage (4) (i.e., the end of construction of geofoam and bridge

seat). Figure 7.4.10 shows that the numerical results were close to the measured data even though the magnitude of the lateral displacement was very small. The CY model calculated smaller lateral displacements than the MC model since the modulus of the backfill soil increased with depth in the CY model.

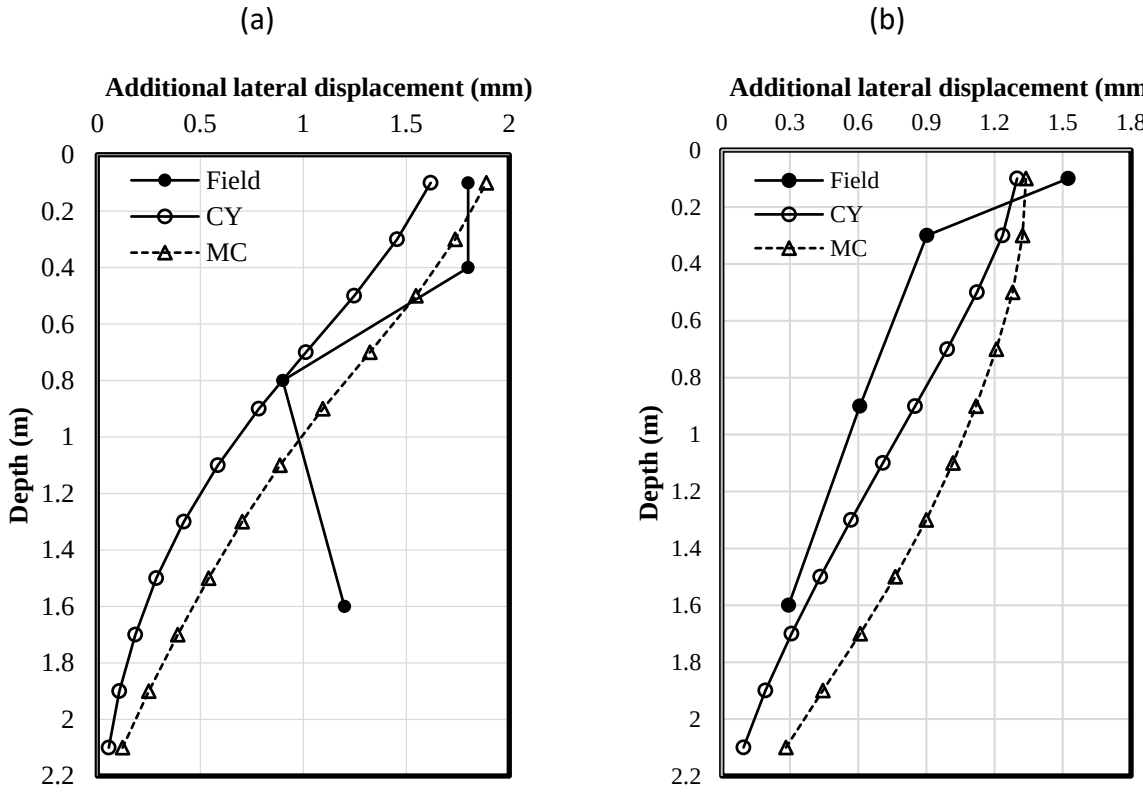

Fig. 7.4.10: Additional lateral displacements of the CMU facing blocks induced by self-weight and bridge slab: (a) Self-weight; (b) Bridge slab load.

Figure 7.4.11 shows the measured and calculated geotextile strains with depth in Abutment A. The strain gauges were located 0.3 m (1 ft) away from the back of CMU facing blocks. Two construction stages are shown in Fig. 7.4.11, which are under self-weight and bridge slab load. Figure 7.4.11 shows that the numerical results were close to the measured data although the measured strain was slightly larger than the calculated under the self-weight of the wall. Numerical results showed that larger strains developed in the primary reinforcement and smaller strains developed in the bearing reinforcement layers. Use of the MC model gave larger strains than the CY model, especially at the bottom of the wall. The increased modulus of the backfill soil restrained the relative movement between the soil and the geotextile when the CY model was used, resulting in smaller strains in the geotextile. Limited number of strain gauges used in the fileds resulted in difficluties in generating the strain distribution along geotextile layers at different depths. Additional results regarding the potential slip surface determined from the strain distribution of geotextile layers at different depths will be presented in Section 7.6 where stability analyses of GRS structures are discussed.

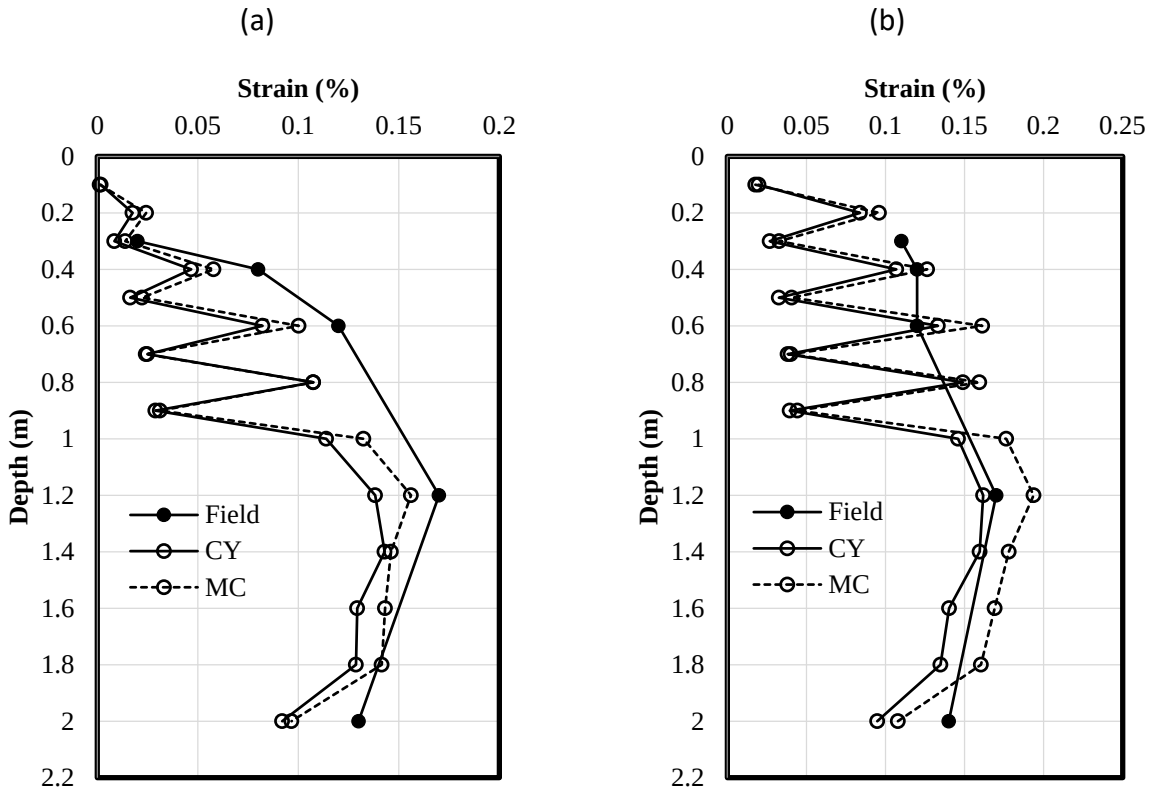

Fig. 7.4.11: Geotextile strain distribution with depth in Abutment A: (a) Self-weight; (b) Bridge slab load.

A numerical evaluation was also conducted to simulate the seven stage loadings applied in Abutment A. The numerical results of additional vertical stress induced by stage loading Δp are compared with the field monitoring data as well as two analytical solutions: (1) Boussinesq's solution for under uniform strip load recommended by Adams et al. (2012) and (2) the AASHTO 2 to 1 truncated distribution (AASHTO, 2012). For the cases of stage loading using eight Jersey barriers, the pressures applied by the left (38.5 kPa (804 psf)), middle (11kPa (230 psf)), and right (38.5 kPa (804 psf)) Jersey barriers were considered separately as shown in Fig. 7.4.12.

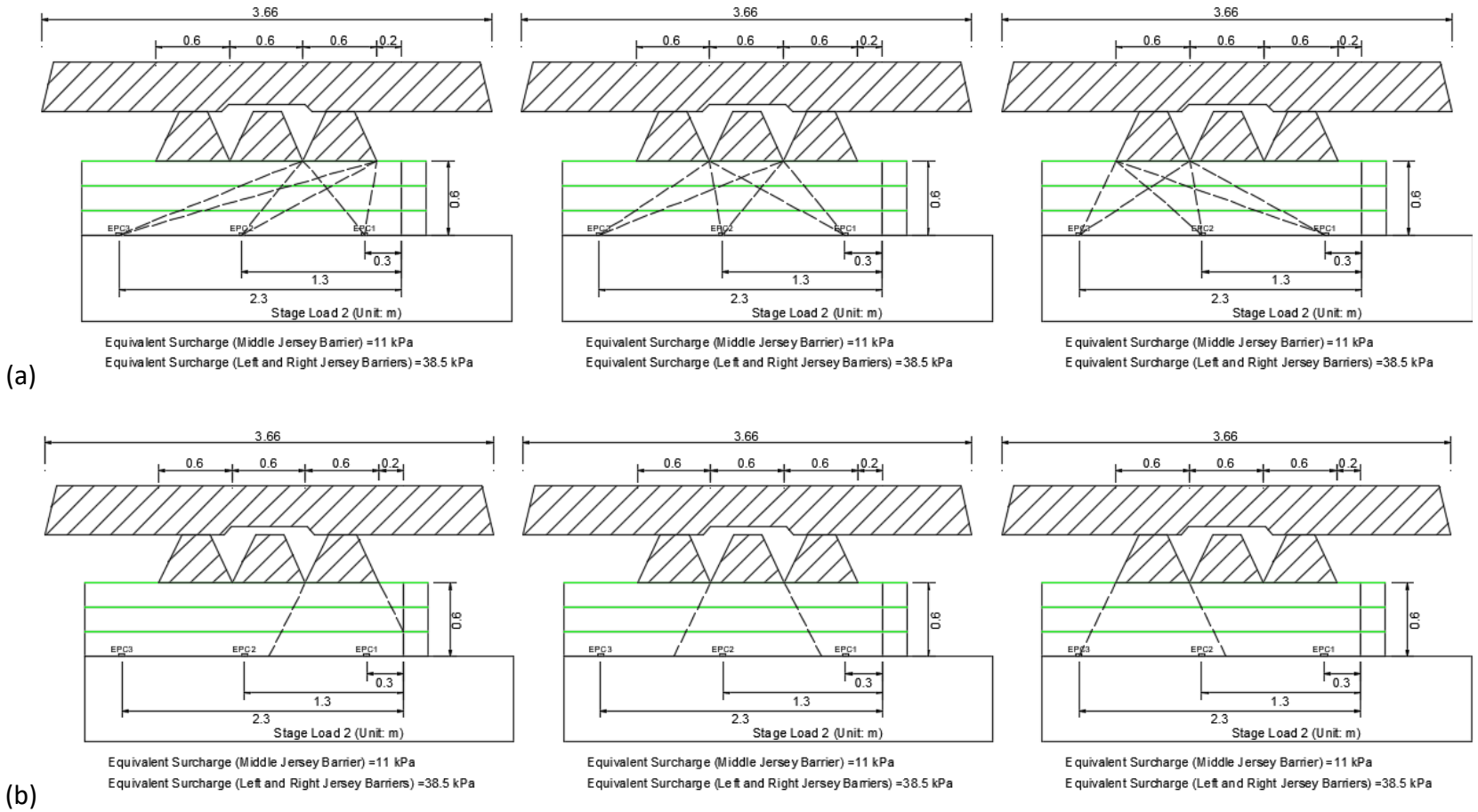

Fig. 7.4.12: Schematic of superposition of stage loadings using multiple Jersey barriers: (a) Boussinesq's solution for uniform strip load (recommended by Adams et al. (2012)); (b) AASHTO 2 to 1 truncated distribution (AASHTO, 2012).

When Boussinesq's solution was used, the distributed additional vertical stress induced by stage loading at each earth pressure cell location was calculated no matter how far the earth pressure cell was from the loading Jersey barrier. When the AASHTO 2 to 1 truncated distribution was used, however, only the earth pressure cell location within the distribution range of the load was considered. For example, epc1, epc2, and epc3 were all considered when the additional vertical stresses Δp were calculated due to the right Jersey barrier using Boussinesq's solution. However, only epc1 was considered when the AASHTO 2 to 1 truncated distribution was used since both epc2 and epc3 were outside the distribution range of the load from the right Jersey barrier as shown in Fig. 7.4.12. The location of each earth pressure cell is shown in Fig. 7.4.5.

The comparisons between the numerical results and the field measurements obtained after each of the seven stage loadings are shown in Fig. 7.4.13 to Fig. 7.4.19. The comparison showed that when stage loading with the single Jersey barrier was applied (i.e., SL1, SL2 single, SL3, SL4 single, SL5, SL6 single, and SL7 single), the numerical results compare well with the theoretical solutions and some of the field measurements. Some earth pressure cell readings in the field were deemed not stable (e.g., epc1 in SL2 single, epc4 in SL3, epc4 in SL4 single, and epc7 in SL5), resulting in large differences between the measured data and the calculated results as discussed in Section 6.3.1.2. When stage loadings with eight Jersey barriers were applied, the difference between the numerical results, the field measurements, and the theoretical solutions became larger. When the reinforcement spacing S_v was 0.2 m (8 in), the calculated additional vertical earth stresses from the numerical model were lower than the measured data from the field. When bearing reinforcement layers were used and the reinforcement spacing S_{vb} was 0.1 m (4 in), however, the numerical model gave a higher additional vertical stress than the field measurements. Overall, the results from the numerical model were found to reasonably match results from the theoretical solutions, especially for those earth pressure cells located not far away from the loading Jersey barriers. It should be noted that the AASHTO 2 to 1 truncated distribution sometimes resulted in higher vertical stresses than Boussinesq's solution. The AASHTO 2 to 1 truncated distribution assumed a uniformly distributed pressure within the distribution range, which was accurate for the locations at the center of the distribution range. For the locations at the edge of the distribution range, however, the AASHTO 2 to 1 truncated distribution was found to overestimate the vertical stress.

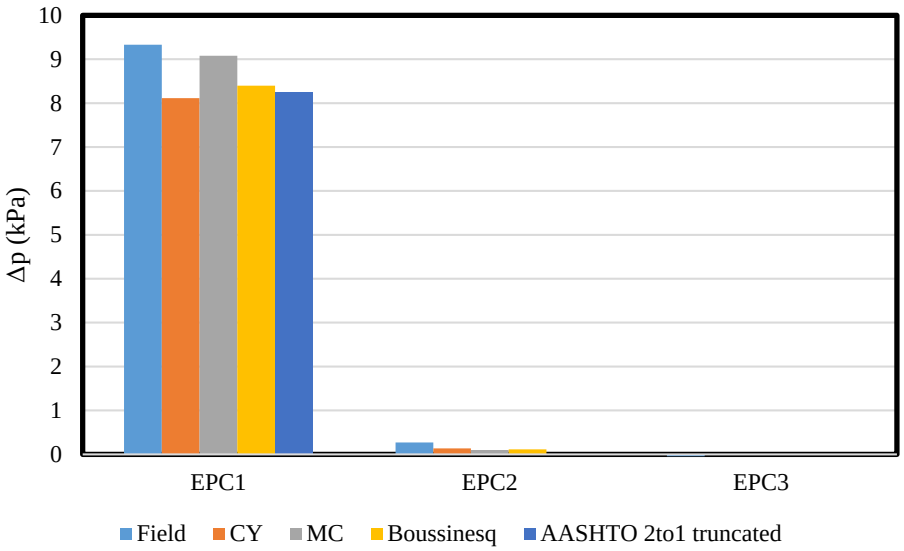

Fig. 7.4.13: Stage loading 1

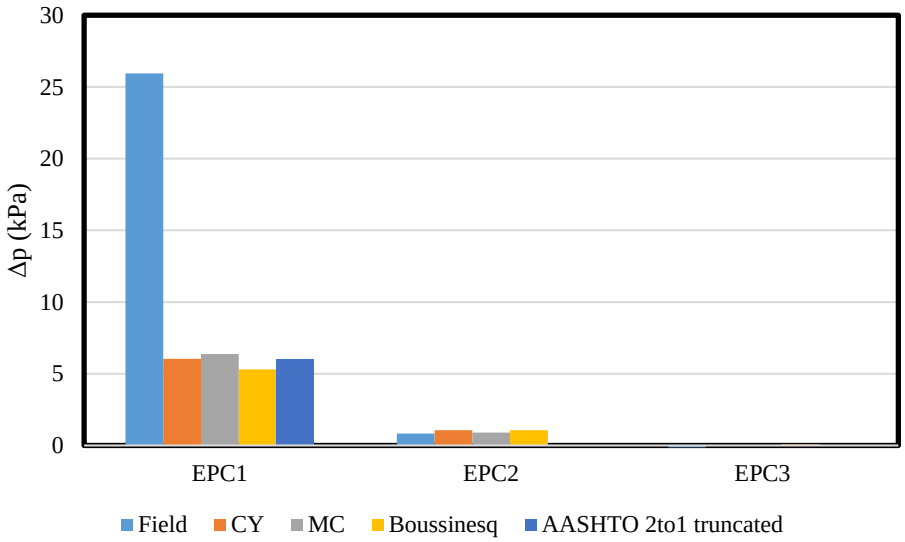

(a)

Fig. 7.4.14: Stage loading 2: (a) Single Jersey barrier;

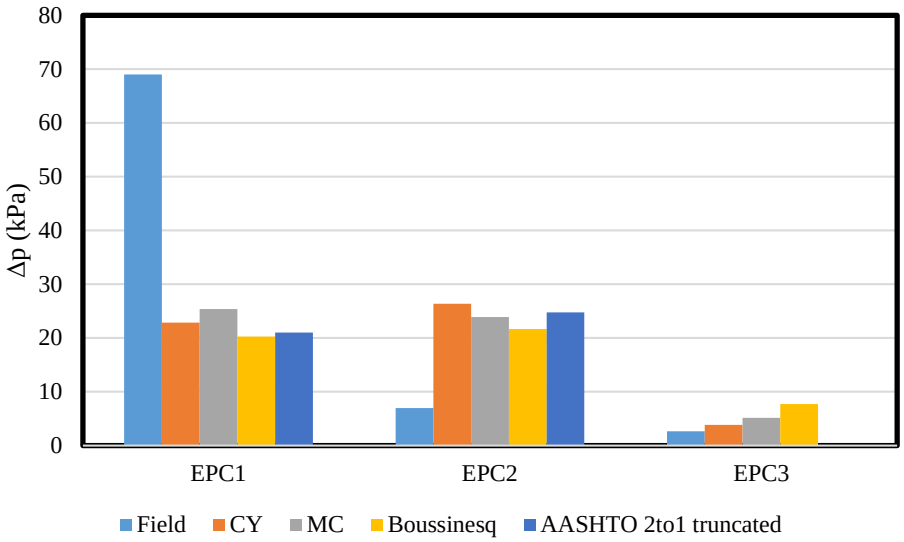

(b)

Fig. 7.4.14: Stage loading 2: (b) Eight Jersey barriers (continued).

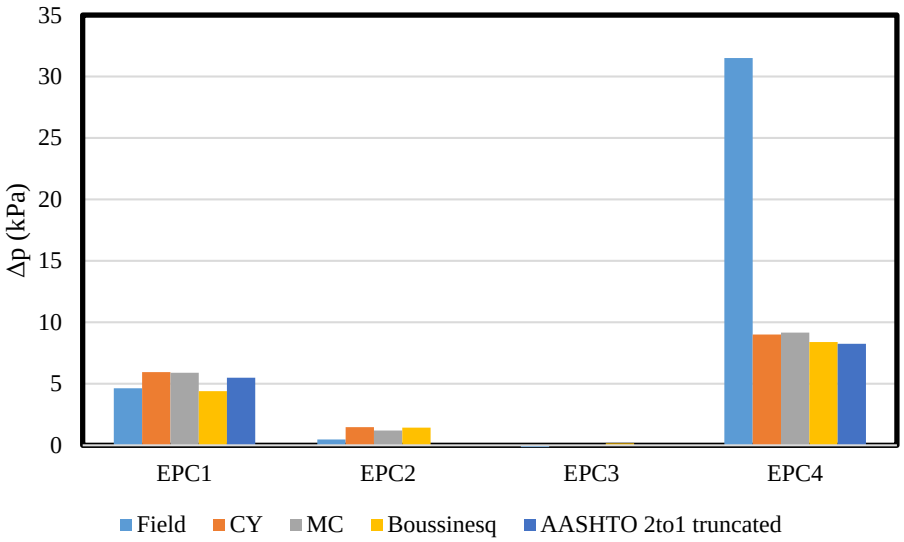

Fig. 7.4.15: Stage loading 3

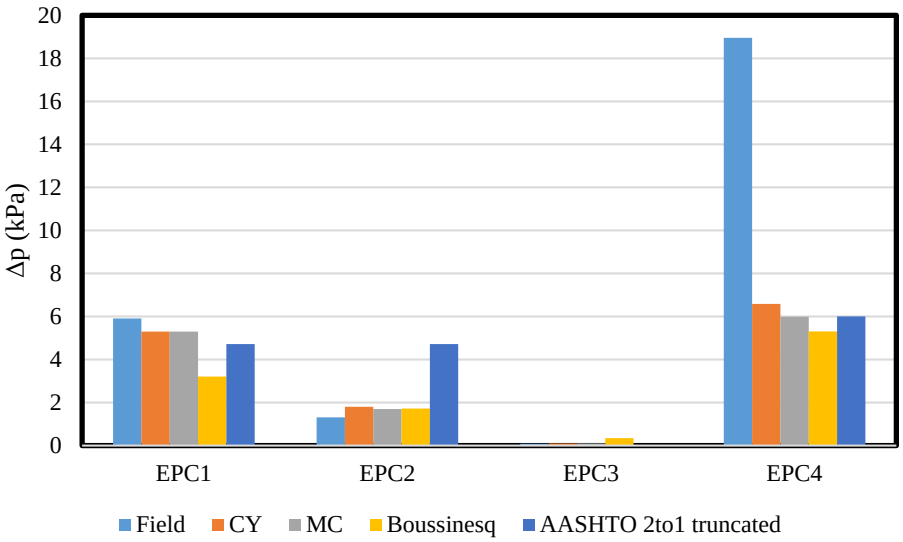

(a)

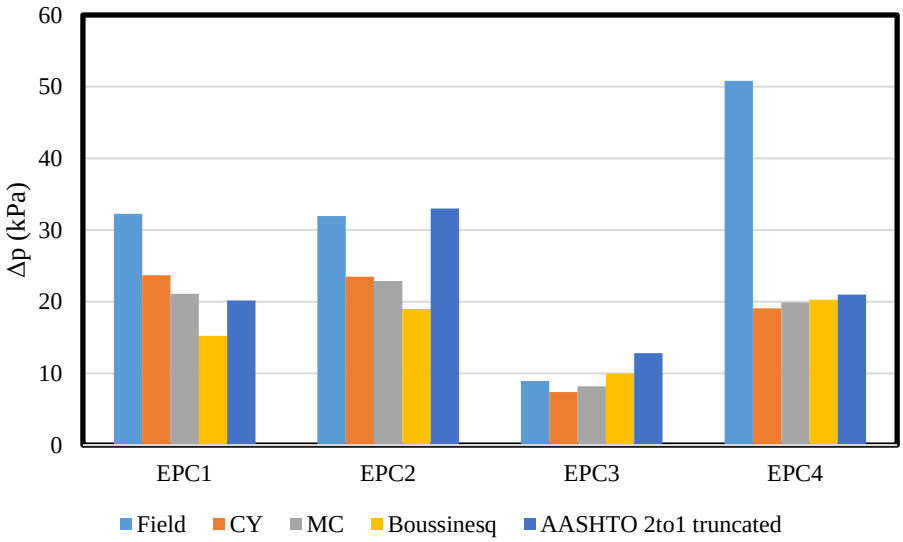

(b)

Fig. 7.4.16: Stage loading 4: (a) Single Jersey barrier; (b) Eight Jersey barriers.

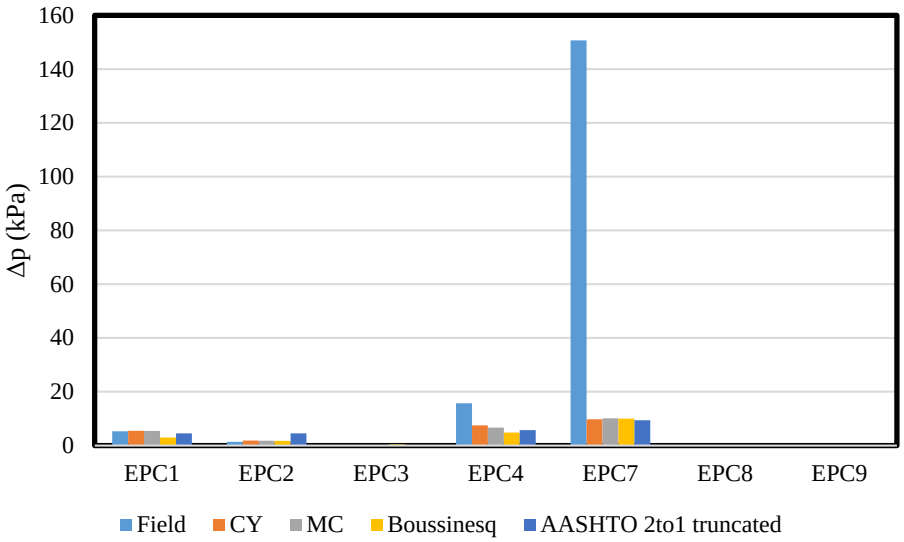

Fig. 7.4.17: Stage loading 5

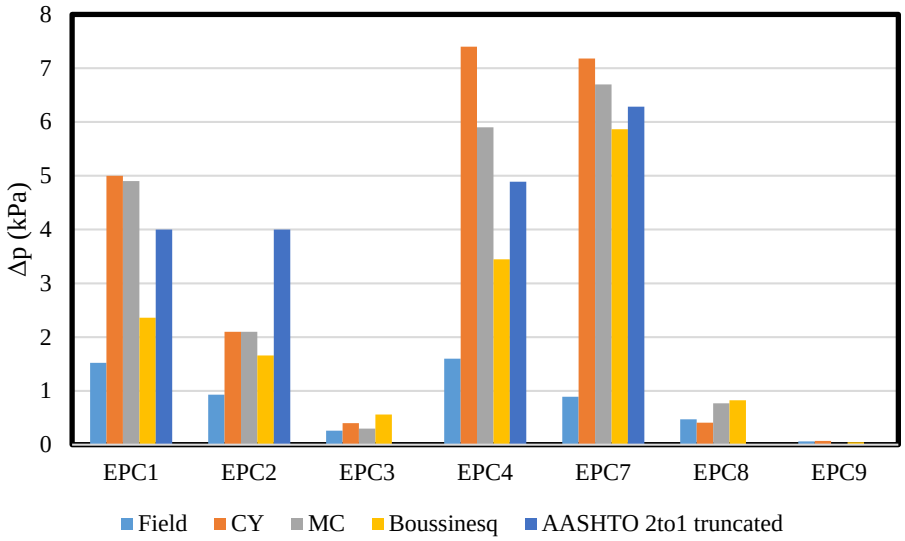

(a)

Fig. 7.4.18: Stage loading 6: (a) Single Jersey barrier;

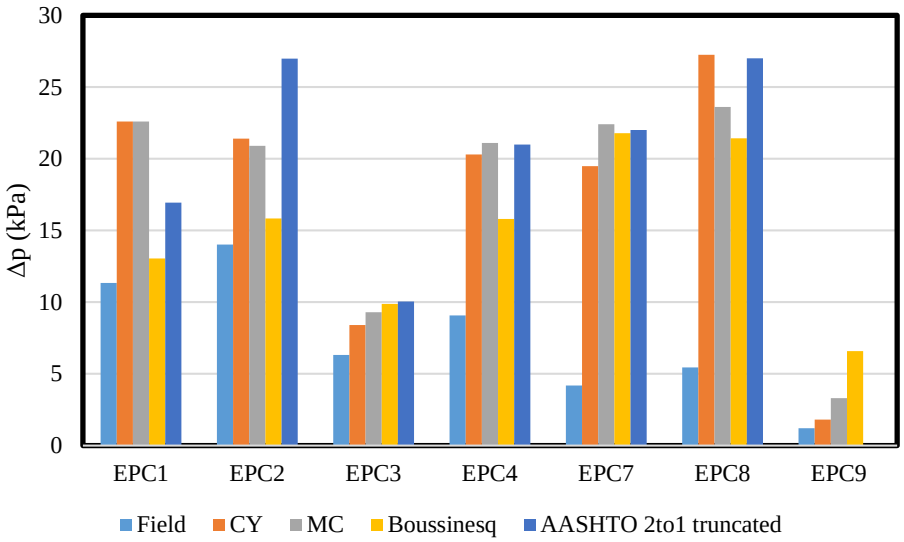

(b)

Fig. 7.4.18: Stage loading 6: (b) Eight Jersey barriers (continued).

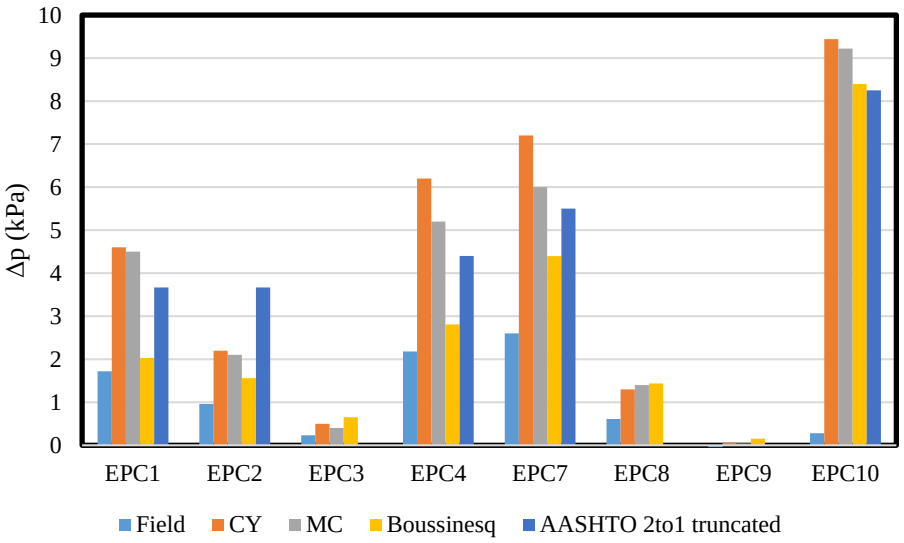

(a)

Fig. 7.4.19: Stage loading 7: (a) Single Jersey barrier;

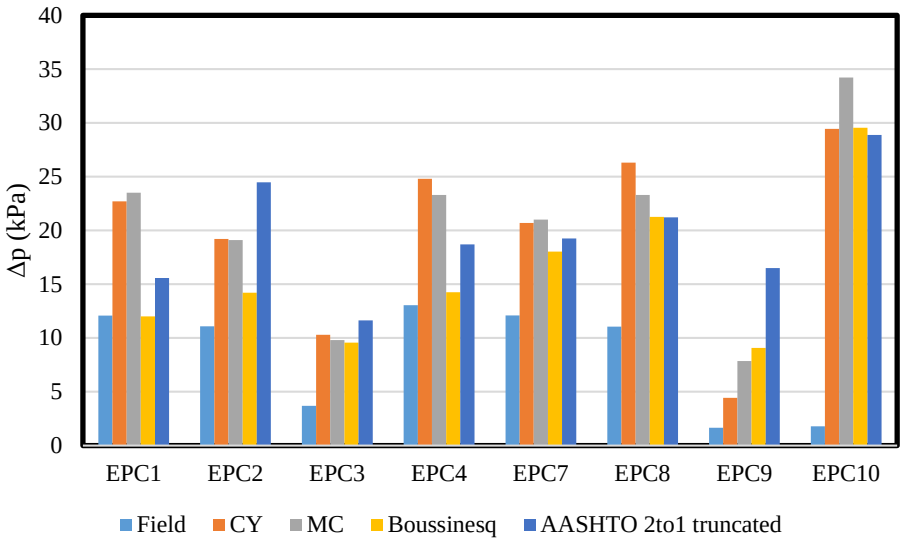

(b)

Fig. 7.4.19: Stage loading 7: (b) Eight Jersey barriers (continued).

From the discussion in Sections 7.4.2, it can be concluded that the numerical model was able to reasonably predict the behavior of the VDOT wall. Therefore, this numerical model was adopted for the numerical study.

7.4.3 EVALUATION OF EFFECT OF THE REINFORCEMENT LAYOUT

7.4.3.1 GEOMETRIES OF THE REINFORCEMENT LAYOUT

The VDOT wall had a layout recommended by Adams et al. (2012) with shorter reinforcement at the bottom (i.e., L_{rb}) and longer reinforcement at the top (hereinafter referred to as a trapezoidal layout). A traditional MSE wall, however, usually uses uniform reinforcement length L_r throughout the whole wall (hereinafter referred to as a uniform layout). In this section, a comparison was made between the trapezoidal layout and the uniform layout. Figure 7.4.20 shows the schematic of these two layouts.

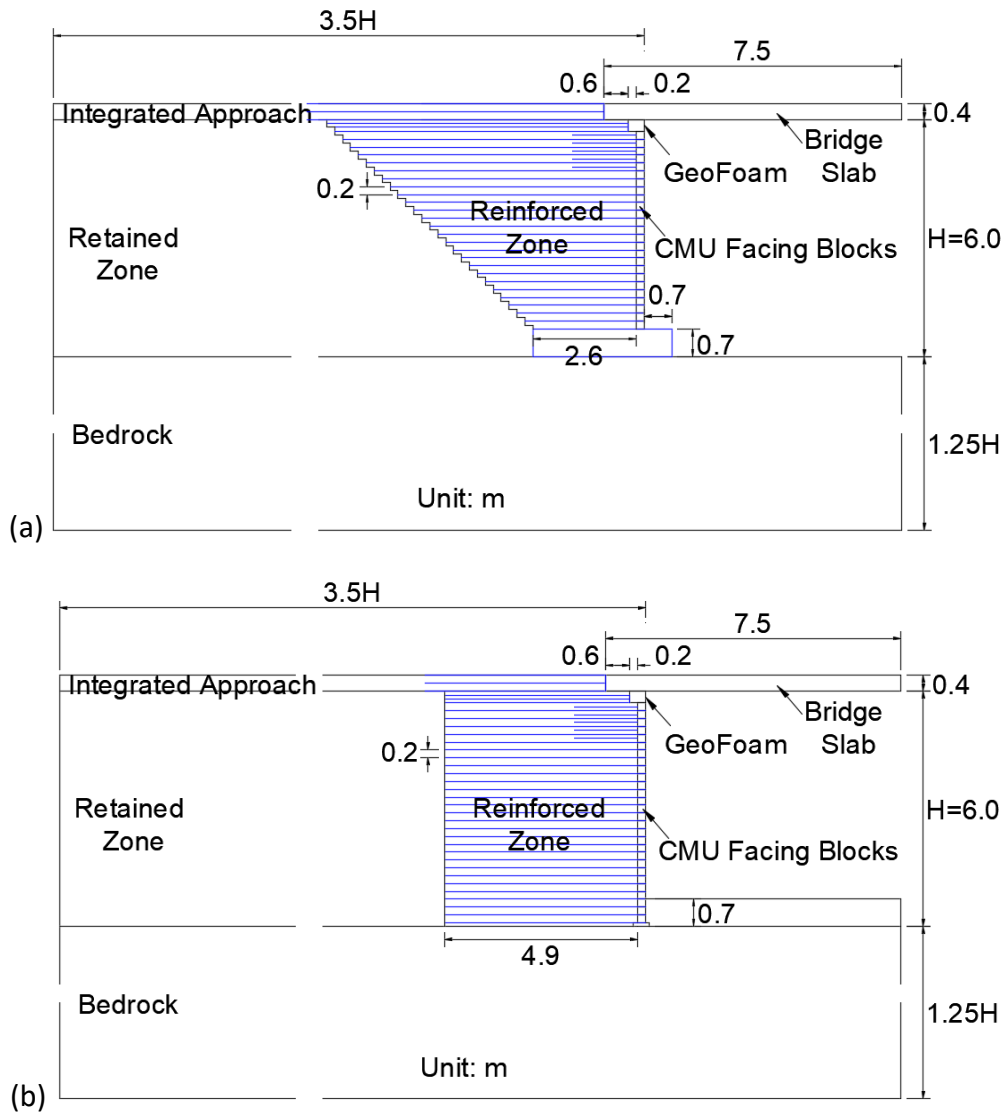

Fig. 7.4.20: Schematic of two layouts: (a) Trapezoidal layout; (b) Uniform layout.

The trapezoidal layout involved a 1:1 cut slope of the retained soil while the uniform layout corresponded to a vertical cut slope of the retained soil. A H= 6 m high wall, which is a typical wall height of MSE walls used in the practice, was selected. To minimize the effect of boundary conditions, the depth of the foundation soil was 7.5 m (25 ft) (approximately 1.25H) and the left lateral boundary was located at 21 m (69 ft) (3.5 H) behind the wall facing. The bridge slab had a length L_b of 15 m (49 ft) and a thickness D of 0.4 m (1.3 ft). The right lateral boundary was located at 6.5 m (21 ft) in front of the wall facing based on the symmetry of the bridge slab. Lateral boundaries were fixed in horizontal direction and were free to move in the vertical direction while the bottom boundary was fixed in both horizontal and vertical directions. The beam seat width b was 0.6 m (2 ft) and the setback distance a_b for the bridge seat was 0.2 m (8 in). The trapezoidal layout had a RSF of thickness D_f of 0.7 m (2.3 ft), resulting in a free wall height of 5.3

m (17 ft). In order to keep the same free wall height for both layouts, a 0.7 m (2.3 ft) thick embedment was assigned to the uniform layout in front of wall facing. The length of all reinforcements was such that they reached the cut slope. The reinforcement length for the trapezoidal layout increased proportionally from the bottom of the wall to the top along the 1:1 cut slope. The reinforcement length at the bottom of the wall for the trapezoidal layout L_{rb} was 2.6 m (8.5 ft) as shown in Fig. 7.4.20 (a). Assuming the reinforcement was extended to the bottom of the RSF along the same 1:1 cut slope, the reinforcement length at the bottom of the RSF was 1.9 m (6 ft). The reinforcement length at the top of the wall for the trapezoidal layout was 7.9 m (26 ft). Therefore, the average length of the reinforcement for the trapezoidal layout was 4.9 m (16 ft). For a consistent comparison, the uniform reinforcement length L_r in the uniform layout was also set as 4.9 m (16 ft) as shown in Fig. 7.4.20 (b). Five bearing reinforcement layers were used at the top of the wall. The spacing between primary reinforcement S_v was set as 0.2 m (8 in) and the bearing reinforcement spacing S_{vb} was half of the spacing between primary reinforcement layers (S_{vb} = 0.1 m (4 in)).

7.4.3.2 CONSTITUTIVE MODELS

The constitutive models and the properties of the retained soil (as shown in Table 7.4.4), the bedrock foundation (as shown in Table 7.4.5), the bridge slab (as shown in Table 7.4.6), the CMU facing blocks (as shown in Table 7.4.7), and the geofoam (as shown in Table 7.4.8) were maintained as the same as those used in the VDOT wall. The CY model was used to simulate the backfill soil for the reinforced zone and the integrated approach. A cohesionless soil with a friction angle of 38° was selected for the backfill soil since Adams et al. (2012) pointed out that the friction angle of the backfill soil used for design of GRS walls should not be lower than 38°. The dilation angle followed the relationship of $\psi = \phi - 30^{o}$ recommended by Bolton (1986) as shown in Equation (7.3.1). Other properties of the backfill soil were kept as the same as those used in the VDOT wall. Table 7.4.11 summarizes the parameters used for the CY model for the backfill soil.

Table 7.4.11: Parameters of the Cap-Yield model for backfill soil

Constitutive Model	Cap Yield Model
Density ρ (kg/m^3)	1650
Ultimate friction angle ϕ_f (°)	38
Ultimate dilation angle ψ_f (°)	8
Cap-Yield surface parameter α	1
Multiplier R	5.89
Calibration factor β	0.15
Power m	0.55
Reference elastic shear modulus G^e_{ref} (MPa)	36.19
Reference bulk modulus K^{iso}_{ref} (MPa)	7.00
Reference Pressure p_{ref} (kPa)	34.47
Poisson's ratio υ_{ur}	0.2
Cohesion c (kPa)	0
Failure ratio R_f	0.9

7.4.3.3 REINFORCEMENT AND INTERFACES

The structural elements used to simulate the geotextile reinforcement were also kept the same as those used in the VDOT wall, as shown in Table 7.4.9. Interface properties were also kept the same as those used in the VDOT wall except that some of the interface friction angles were changed based on the change of the friction angle of the backfill soil. Table 7.4.12 summarizes the interface properties used in the numerical models for the comparison of these two layouts.

Table 7.4.12: Interface properties for comparison between two layouts

Interface	Method	k_n (N/m/m)	k_s (N/m/m)	Interaction coefficient C_i	Friction angle (°)	Cohesion (kPa)
Geotextile – Backfill soil (Geotextile – Reinforced Zone & Geotextile – Integrated approach)	Embedded in cable element		1×10^{6}	0.9	35.1	0
Backfill soil – CMU (Vertical interface between backfill soil and CMU)	Interface	1×10^{8}	1×10^{6}	0.65	26.9	0
Embedment soil – CMU (Vertical interface between embedment soil and CMU)	Interface	1×10^{8}	1×10^{6}	0.65	20.57	0
Geotextile – CMU (Frictional Connection)	Beam elements with interfaces	1×10^{9}	4×10^{7}	/	16.2	9.5
Geotextile – CMU (Mechanical Connection)	Beam elements with interfaces	1×10^{9}	4×10^{7}	/	57.0	46
Geofoam – Geotextile & Geofoam – CMU & Geofoam – Bridge slab	Interface	1×10^{7}	1×10^{5}	/	26.6	0
Bridge slab – Backfill soil (Bridge slab – bridge seat)	Interface	1×10^{8}	1×10^{6}	0.9	35.1	0
Bridge slab – Geotextile	Beam elements with interfaces	1×10^{9}	4×10^{7}	/	16.2	9.5

7.4.3.4 CONSTRUCTION SEQUENCE AND TRAFFIC LOAD

The numerical models for both the trapezoidal layout and the uniform layout were constructed by stages. The construction stages are described as follows:

(1) Before the wall construction, the limestone bedrock reached an equilibrium under gravity.
(2) For the trapezoidal layout, the construction of the RSF was simulated and the geotextile was placed in the RSF. For the uniform layout, however, a layer of the CMU facing blocks, the backfill soil, the retained soil, the embedment soil in front of wall facing, and the geotextile were installed until the wall height reached 0.7 m (2.3 ft). The corresponding interfaces and connection were assigned. No compaction stress was applied on top of the backfill soil.
(3) A layer of the CMU facing block, the backfill soil (the AASHTO No. 8 aggregate), the retained soil CL, and the geotextile were installed for both the trapezoidal layout and the uniform layout until the wall height reached 5.7 m (18.7 ft). The corresponding interfaces and connection were assigned. No compaction stress was applied on top of the backfill soil. The wall was under self-weight condition after this construction stage was finished.
(4) The geofoam and the bridge seat were installed. The corresponding interfaces and connection were assigned. No compaction stress was applied on top of the backfill soil.
(5) After the construction of the wall itself was finished, the bridge slab was placed on top of the bridge seat. The beam seat width b was 0.6 m and the setback distance a_b for the bridge seat was 0.2 m (8 in). The corresponding interfaces and connection were assigned.
(6) The integrated approach was constructed behind the bridge slab. Geotextile was installed in the integrated approach.
(7) Traffic loads on the bridge and approach roadways were simulated as a uniform vertical surcharge stress according to the design guidelines (AASHTO, 2012; Adams et al., 2012; Berg et al., 2009; Zheng and Fox, 2017). A uniform surcharge $\sigma_{traffic\text{-}approach}$ of 12.7 kPa (265 psf) was applied to the integrated approach roadway, which is equivalent to 0.72 m (2.4 ft) thick backfill soil. The traffic load on the bridge slab was determined using the HL-93 LL model and a uniform surcharge $\sigma_{traffic\text{-}slab}$ of 5.4 kPa (113 psf) was applied to the bridge span. Since the beam seat width b was 0.6 m (2 ft), the bridge self-weight and the traffic load resulted in vertical stresses of 122.5 kPa (2558 psf) and 67.5 kPa (1410 psf) respectively on the bridge seat. The total average vertical stress on the bridge seat was 190 kPa (3968 psf), which was lower than the allowable bearing pressure for GRS abutments suggested by Adams et al. (2012).

7.4.3.5 NUMERICAL RESULTS CONSIDERING THE TWO ADOPTED LAYOUTS

Figure 7.4.21 shows the lateral earth pressure behind the CMU facing blocks under the self-weight and the traffic load. Figure 7.4.21 shows that the results from both layouts were essentially the same under the self-weight. Under the traffic load, the results from both layouts were also reasonably close to each other, with slightly higher lateral earth pressures from the case of the trapezoidal layout. For the uniform layout, the lateral earth pressures at the bottom of the wall showed a comparatively significant increase followed by a decrease. The change of the lateral earth pressure at the bottom of the wall was due to the embedment in front of the

CMU facing blocks. Overall, it can be concluded that the two layouts consider in this study did not result in significantly different lateral earth pressures behind the wall facing.

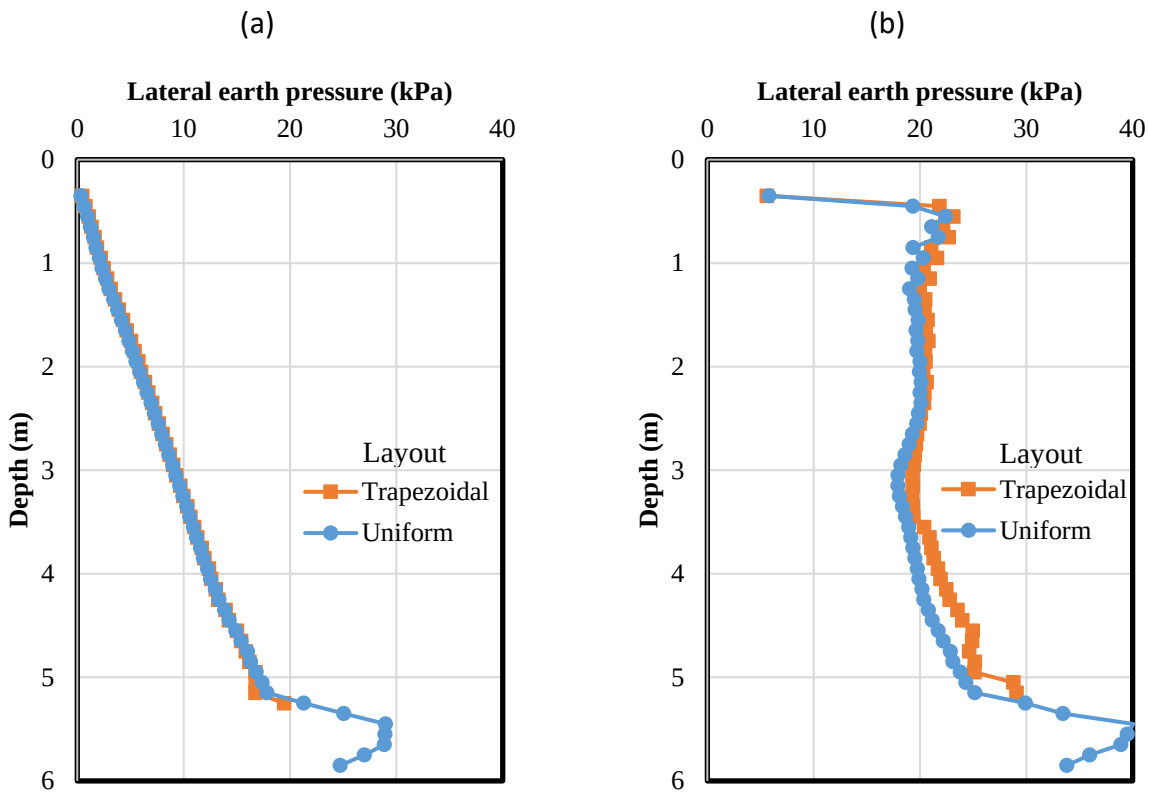

Fig. 7.4.21: Lateral earth pressures in two layouts: (a) Self-weight; (b) Traffic load.

Figure 7.4.22 shows the additional vertical stresses 0.3 m (1 ft) away from the back of CMU facing blocks induced by different loading. Figure 7.4.22 shows that the results from both layouts were close to each other, with slightly higher additional vertical stresses generated by the trapezoidal layout. The additional vertical stress induced by loading was highest at the top of the wall and decreased with depth sharply until a certain depth. At the greater depth, the uniform layout resulted in almost constant additional vertical stresses with a small reduction with depth. The trapezoidal layout, however, resulted in higher additional vertical stresses at the bottom of the wall. This difference may be due to the presence of the RSF in the trapezoidal layout, which was different from the embedment in front of CMU facing blocks in the uniform layout.

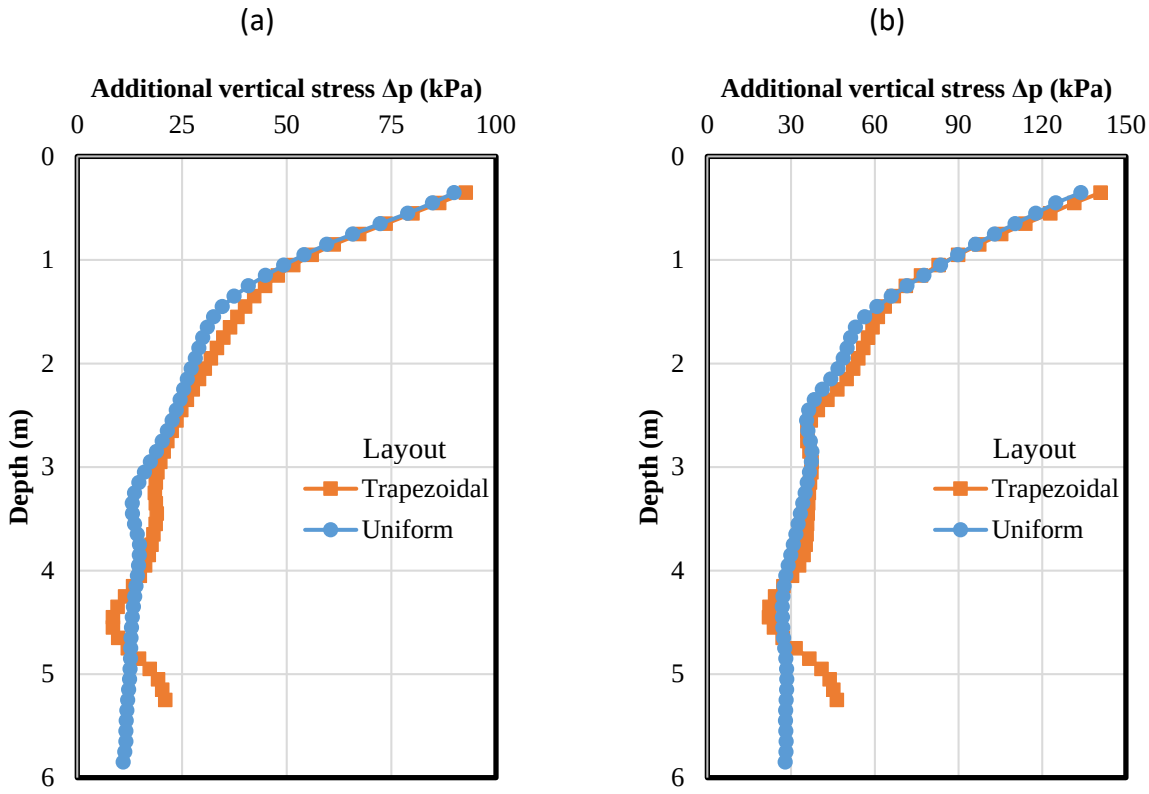

Fig. 7.4.22: Additional vertical stresses due to loading in two layouts: (a) Due to bridge slab; (b) Due to bridge slab, integrated approach, and traffic load.

Figure 7.4.23 shows the total lateral displacements of CMU facing blocks and additional lateral displacements of CMU facing blocks induced by different loading. Figure 7.4.23 shows that the trapezoidal layout calculated larger lateral displacements of CMU facing blocks than the uniform layout, which was expected since the uniform layout had longer reinforcement at the bottom of the wall. However, the difference of additional lateral displacement of CMU facing blocks between the uniform layout and the trapezoidal layout was within a couple of millimeters as shown in Fig. 7.23. (b). Therefore, it can be concluded that the two layouts did not have a significant effect on the lateral displacement of CMU facing blocks.

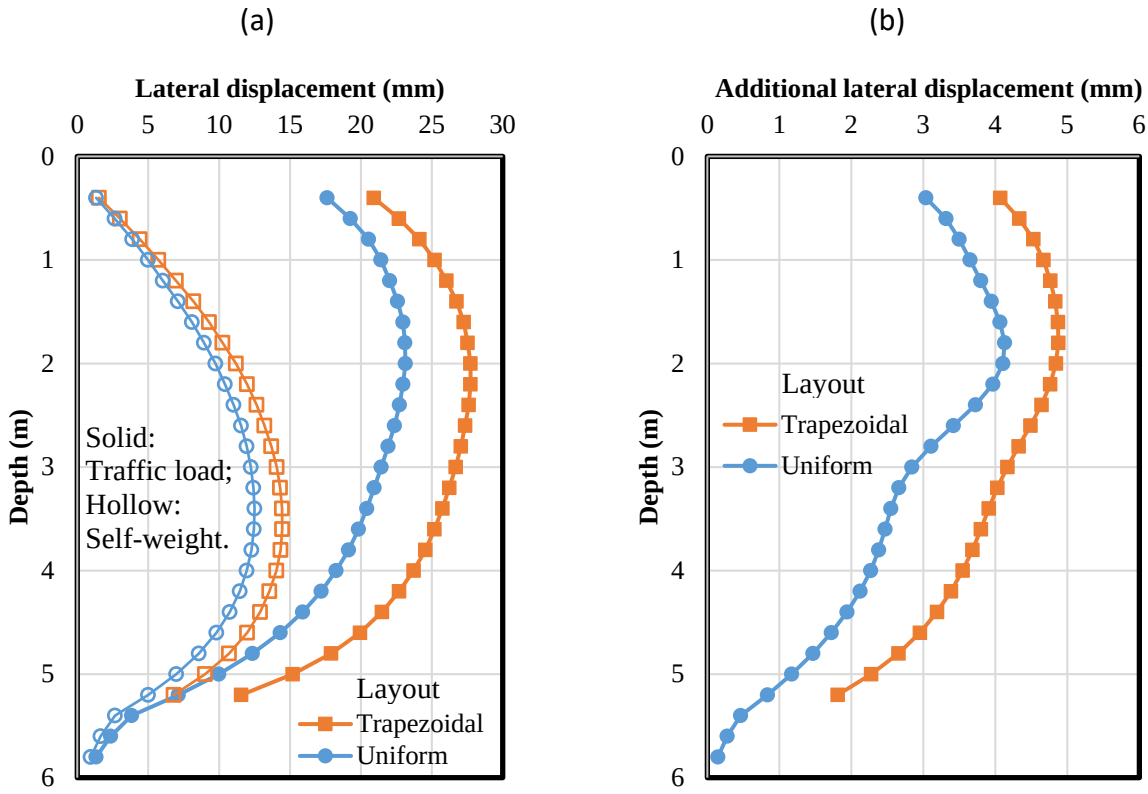

Fig. 7.4.23: Lateral displacement of CMU facing blocks: (a) Total lateral displacement; (b) Additional lateral displacement due to traffic load.

Figure 7.4.24 shows the additional settlement on top of the bridge abutment induced by traffic load. Differential settlement happened at the interface between the bridge slab and the integrated approach way. The bridge slab settled more than the integrated approach way due to a large load on the bridge slab. The trapezoidal layout resulted in larger settlement than the uniform layout. However, the difference between two layouts was within a couple of millimeters as shown in Fig. 7.4.24. Therefore, it can be concluded that the different layouts did not have a significant effect on the settlement of the bridge abutment. It should also be noted that the differential settlement between the bridge slab and the approach way (i.e., bump at the end of the bridge) was approximately 3 mm (0.1 in) for both two layouts. A couple of reasons may contribute to the relatively large bump in the numerical analysis. First, the numerical model used a friction angle of 38º as the baseline, which is much lower than the actual friction angle of approximately 50º used in the field. Parametric study results which will be discussed in Section 7.4.5.2 later showed that the increase of the friction angle of backfill soil from 38º to 42º could reduce the bump at end of bridge from 2.4 mm (0.09 in) to 1.6 mm (0.06 in). Second, the numerical model did not simulate the pavement on top of the approach way, which might result in larger bump at the end of the bridge.

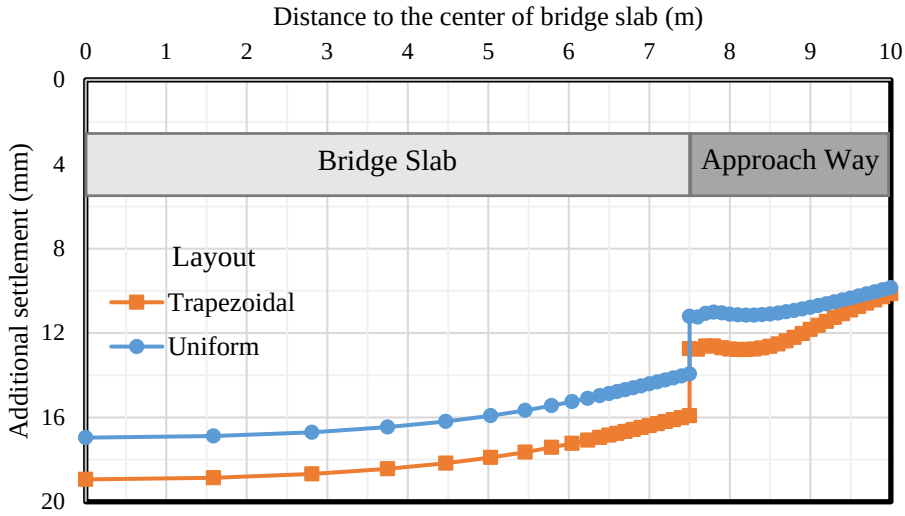

Fig. 7.4.24: Additional settlement of the abutment due to the traffic load

Figure 7.4.25 shows the maximum tension in the reinforcement under the self-weight and the traffic load. Figure 7.4.25 shows that both layouts resulted in almost the same results under the self-weight. Under the traffic load, two layouts gave close results on the top of the wall. At a greater depth (larger than 3 m (10 ft)), the trapezoidal layout resulted in a higher maximum tensile force than the uniform layout. The maximum tension in the bearing reinforcement layers was much smaller than that in the primary reinforcement. The embedment soil in front of the CMU facing blocks in the uniform layout restrained the lateral movement of CMU facing blocks and the lateral deformation of backfill soil. The relative displacement between the geotextile and the backfill soil also decreased, resulting in a lower maximum tensile force in the reinforcement. Figure 7.4.25 also shows a zig-zag distribution of the maximum tensile force in the reinforcement within the upper portion of the wall The locations of the smaller tensile forces in the reinforcement corresponded to the location where bearing reinforcement layers were used. The bearing reinforcement layers were not connected to the CMU facing blocks, thus resulting in a much smaller tensile force in the bearing reinforcement layers than those in the primary reinforcement layers.

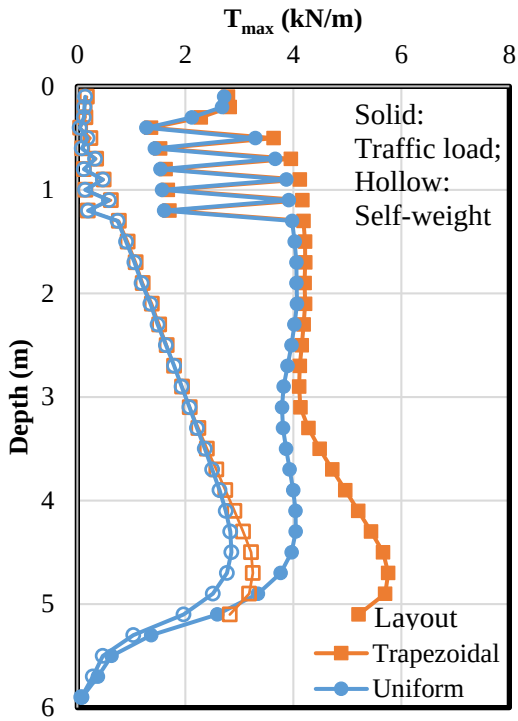

Fig. 7.4.25: Maximum tension in the reinforcement T_{max} along depth in two layouts

From the above discussion, it can be concluded that the two reinforcement layouts evaluated in this study resulted in similar responses of the abutment under both self-weight and traffic loading. The lateral earth pressure behind the wall facing and the additional vertical stress inside the abutment due to loading were almost the same with both layouts. The trapezoidal layout generated larger lateral displacements of CMU facing blocks and larger settlement on top of the abutment than the uniform layout. However, the differences between two layouts were within millimeters. The uniform layout resulted in lower maximum tensile force in the reinforcement at the greater depth of the abutment due to the embedment in front the wall facing. The trapezoidal layout was easy for construction since it only required limited range of excavation at the bottom of the abutment. However, the uniform layout was adopted in this study for the parametric study since AASHTO (2012) adopted the same layout. The effect of close spacing reinforcement should be evaluated without the influence of the different layouts. It would be much easier to incorporate the GRS-IBS design into the current AASHTO design methods if the same uniform reinforcement length layout was used.

7.4.4 Evaluation of Effect of Mesh Density

Prior to the parametric study, the possible mesh density effect was evaluated in this study, as discussed in this section.

7.4.4.1 GEOMETRY

To investigate whether the adopted mesh density is adequate to assess the interaction between geosynthetics and backfill soil, two mesh densities were selected, which are referred to as coarse mesh and fine mesh. The coarse mesh had two zones between two adjacent primary reinforcement layers in the reinforced zone while the fine mesh had 10 zones between two adjacent primary reinforcement layers in the reinforced zone. The spacing between primary reinforcement layers S_v was 0.2 m (8 in). A H = 3 m (10 ft) high wall was selected since the calculation time for a H = 6 m (20 ft) high wall was too long when the fine mesh was used. The wall height H is not expected to be a significant factor affecting the interaction between geosynthetics and backfill soil. No embedment soil in front of the wall facing was used. Figure 7.4.26 shows the numerical model grids adopted to assess the effect of mesh density.

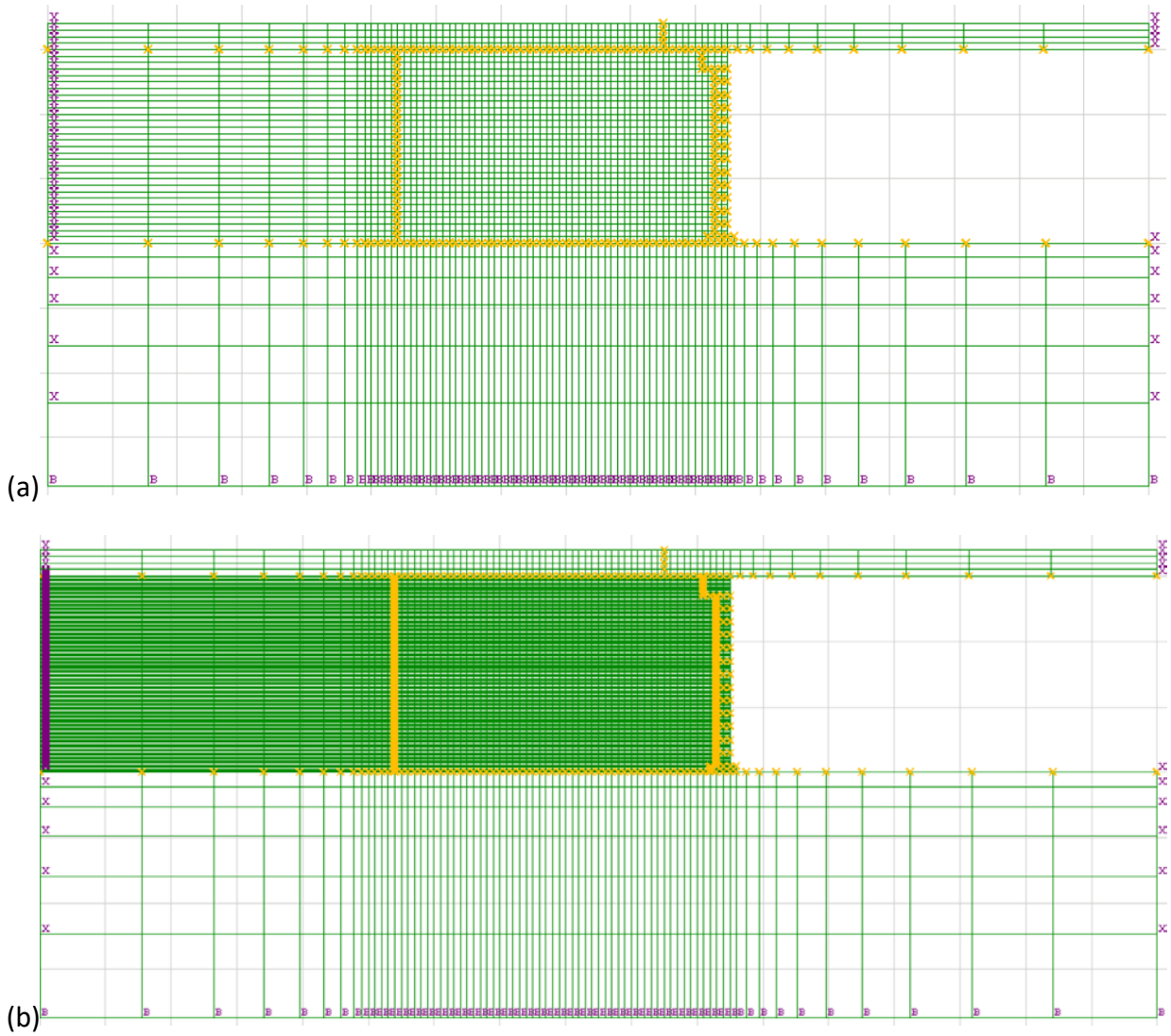

Fig. 7.4.26: Numerical model grids with two mesh densities: (a) Coarse mesh; (b) Fine mesh.

7.4.4.2 CONSTITUTIVE MODELS, REINFORCEMENTS, INTERFACES, AND CONSTRUCTION

The same constitutive models and the properties of the retained soil (as shown in Table 7.4.4), the bedrock foundation (as shown in Table 7.4.5), the bridge slab (as shown in Table 7.4.6), the CMU facing blocks (as shown in Table 7.4.7), the geofoam (as shown in Table 7.4.8), and the backfill soil for the reinforced zone (as shown in Table 7.4.11) presented previously were used in this evaluation. The structural elements used to simulate the geotextile reinforcement (as shown in Table 7.4.9) and the interfaced used in the numerical model (as shown in Table 7.4.12) presented in Section 7.4.3 were used in this evaluation. Same construction sequence and traffic load as in Section 7.4.3 were adopted without the placement of the embedment soil in front of the wall facing. No compaction stress was considered.

7.4.4.3 NUMERICAL RESULTS FROM THE CASES WITH DIFFERENT MESH DENSITIES

Figure 7.4.27 shows that both cases with coarse and fine meshes have similar results. When the fine mesh was used, the calculated lateral earth pressures were found to show fluctuations at the location of the geotextile reinforcement. The presence of geotextile reinforcement changed the distribution of the lateral earth pressure in the neighboring zone. However, these fluctuations could be regarded as a localized effect. The mesh density was found not to change the global behavior of the wall. The calculated lateral earth pressure in the case with the coarse mesh was close to the average lateral earth pressure in the case with the fine mesh.

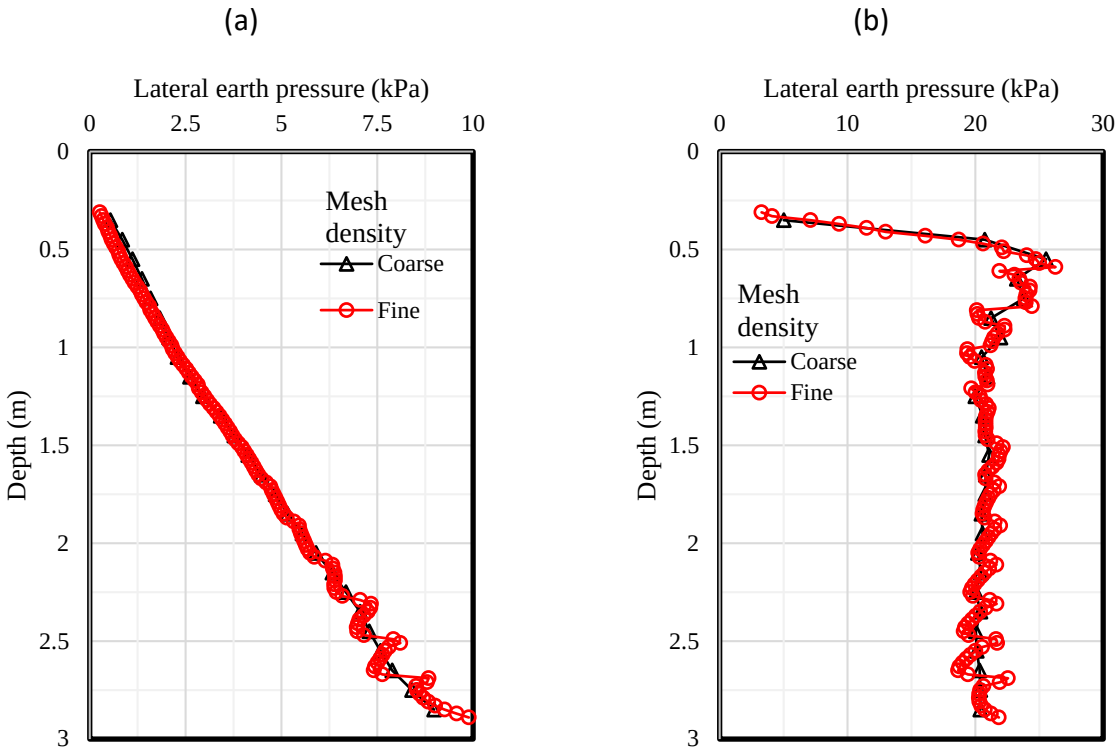

Fig. 7.4.27: Lateral earth pressure behind CMU facing blocks: (a) Self-weight; (b) Traffic load.

Figure 7.4.28 shows the additional vertical stress 0.3 m (1 ft) away from the back of CMU facing blocks. It can be seen that the fine mesh resulted in slightly higher additional vertical stress than the coarse mesh induced by the self-weight of the bridge slab. The difference between the fine and coarse meshes became negligible when the self-weight of the integrated approach way and the traffic load were applied. The mesh density did not affect the additional vertical stress inside the backfill material induced by loading.

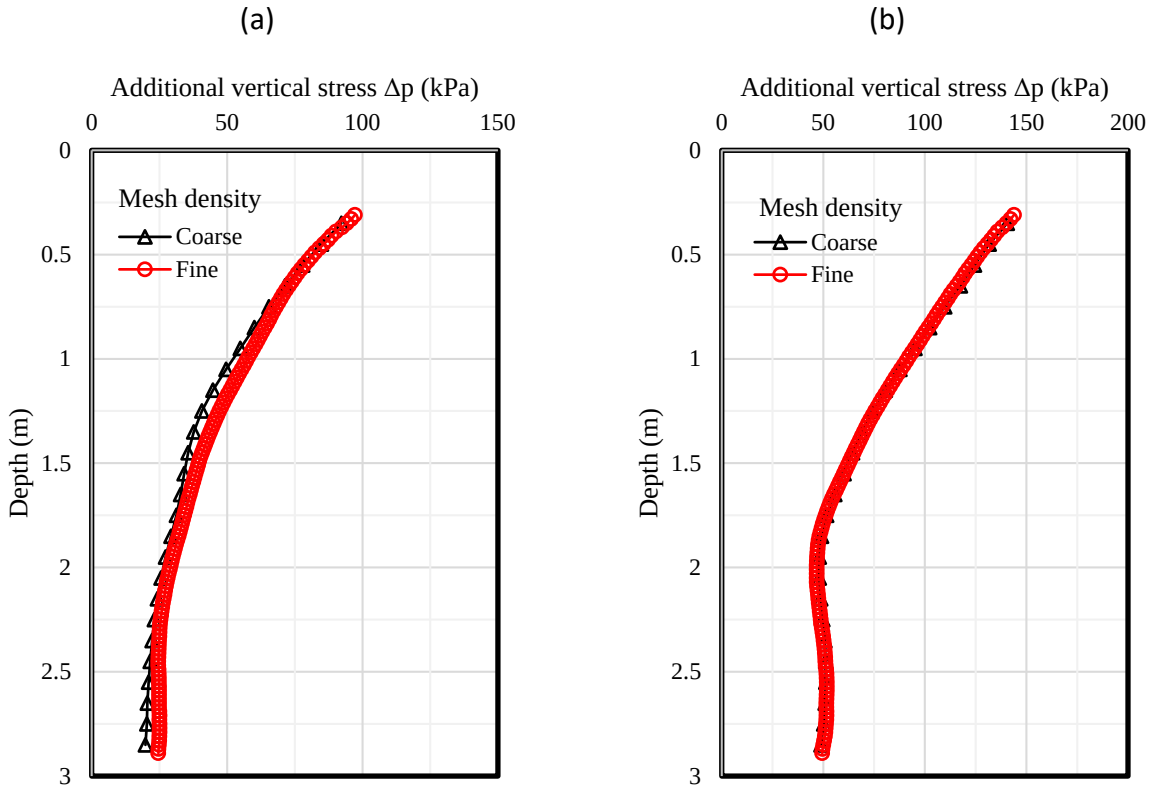

Fig. 7.4.28: Additional vertical stresses due to loading: (a) Induced by bridge slab; (b) Induced by bridge slab, integrated approach, and traffic load.

Figure 7.4.29 shows the total and additional lateral displacements of CMU facing blocks. Figure 7.4.29 shows that both the fine and coarse meshes resulted in almost the same total lateral displacement of CMU facing blocks. For the additional lateral displacement induced by the traffic load, the fine mesh calculated larger values than the coarse mesh at the top of the wall and slightly smaller values at the bottom. However, the difference between the cases with these two mesh densities was within millimeters, which is deemed relevant yet not signficant.

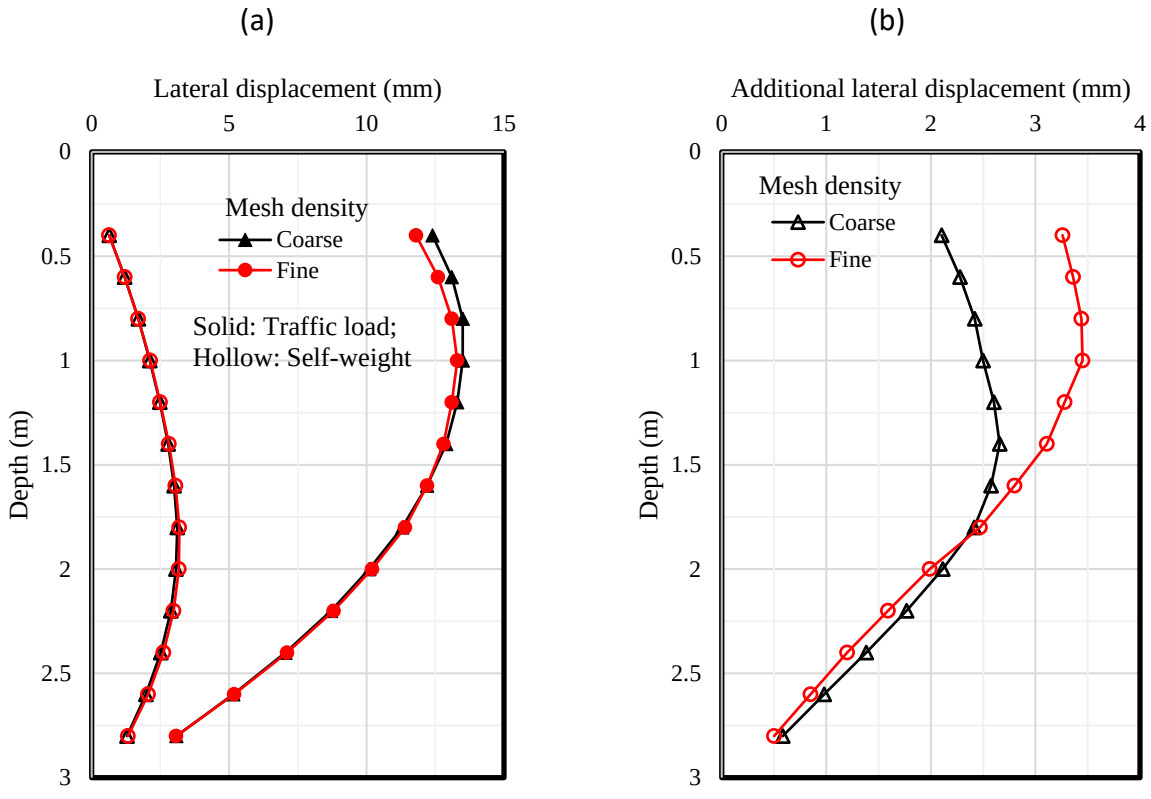

Fig. 7.4.29: Lateral displacement of CMU facing blocks: (a) Total lateral displacement; (b) Additional lateral displacement due to traffic load.

Figure 7.4.30 shows the additional settlement on top of the bridge abutmentinduced by traffic load. Figure 7.4.30 shows that the case with the fine mesh had larger settlement of the bridge slab than that with the coarse mesh. Itasca Consulting Group (2008b) recommended an equation for estimating the maximum interface stiffness value as follows:

$$k_n = k_s \approx 10 \times \max\left(\frac{K + \frac{4}{3}G}{\Delta z_{\min}}\right) \tag{7.4.5}$$

where the parameters $\Delta z_{\min}$, K, and G are the smallest dimension in the normal direction, the bulk modulus, and the shear modulus of the continuum zone adjacent to the interface, respectively.

Equation (7.4.5) indicates that the interface stiffness should be increased if the zone dimension decreases. In other words, higher interface stiffness should be used when the mesh density increases. However, the interface stiffness for both mesh densities was kept the same, resulting in larger settlementwhen the fine mesh was used.

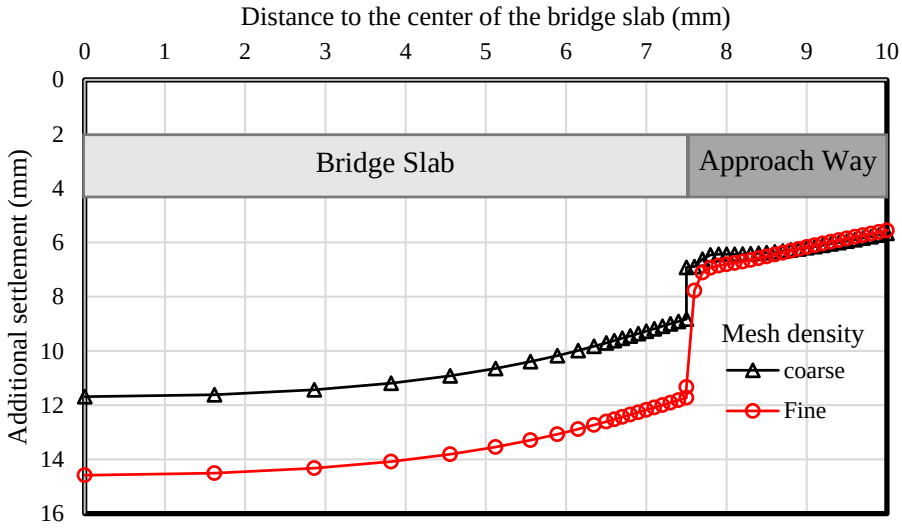

Fig. 7.4.30: Additional settlement of the abutment due to traffic load

Figure 7.3.31 shows the maximum tension in the reinforcement under the self-weight and the traffic load. Figure 7.3.31 shows that the results for both cases with different mesh densities are almost the same except that fine mesh resulted in slightly lower T_{max} at the top of the wall under the traffic load.

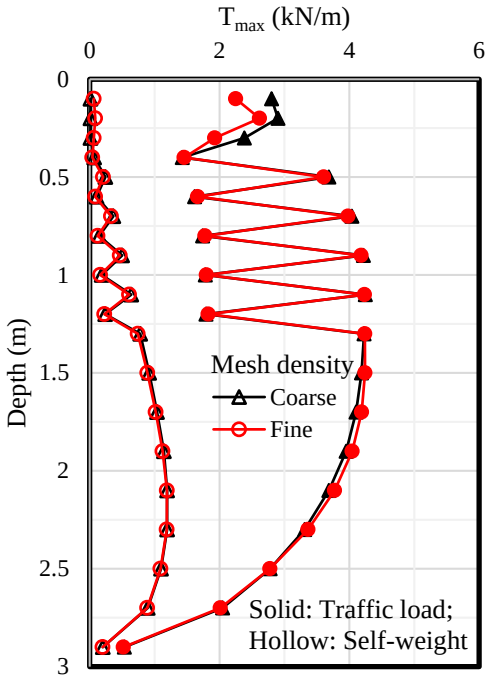

Fig. 7.4.31: Maximum tension in the reinforcement T_{max} with depth

From the above discussion, it was concluded that the coarse mesh density was appropriate for the numerical analysis with sufficient accuracy. Therefore, the coarse mesh was adopted in this study for the parametric study.

7.4.5 PARAMETRIC STUDY

7.4.5.1 BASELINE MODEL

A baseline model was developed based on the uniform layout discussed in Section 7.4.3. Figure 7.4.32 shows the geometry of the baseline model. A H = 6 m high wall was selected as the baseline case without the embedment soil in front of the wall facing.

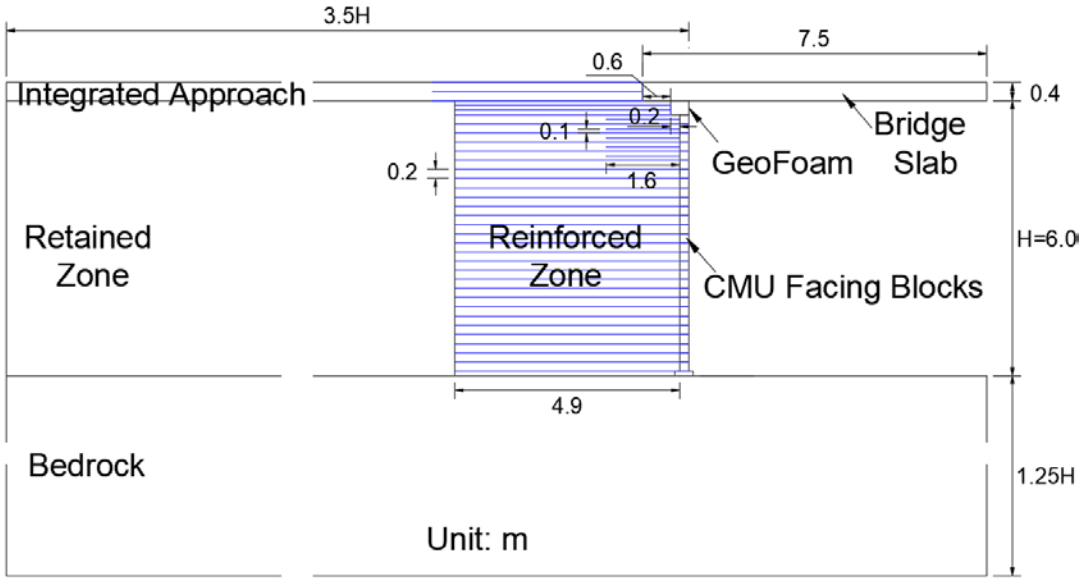

Fig. 7.4.32: Geometry of the baseline model

The parametric study conducted as part of this evaluation adopted the same constitutive models and properties of the retained soil (as shown in Table 7.4.4), the bedrock foundation (as shown in Table 7.4.5), the bridge slab (as shown in Table 7.4.6), the CMU facing blocks (as shown in Table 7.4.7), the geofoam (as shown in Table 7.4.8), and the backfill soil for the reinforced zone (as shown in Table 7.4.11) as presented previously. The same structural elements used to simulate the geotextile reinforcement (as shown in Table 7.4.9) and the same interfaces presented in Section 7.4.3 were used in the baseline model (as shown in Table 7.4.12). Similar construction sequence as presented in Section 7.4.3 was adopted in the parametric study without the placement of the embedment soil in front of the wall facing. This construction sequence is also described as follows:

Stage 1: Before the wall construction, the limestone bedrock reached an equilibrium under gravity.

Stage 2: A layer of the CMU facing block, the backfill soil (the AASHTO No. 8 aggregate), the retained soil CL, and the geotextile were installed until the wall height reached 5.7 m (18.7 ft). The corresponding interfaces and connection were assigned. No compaction stress was applied on top of the backfill soil. The wall was under the self-weight condition after this construction stage was finished.

Stage 3: The geofoam and the bridge seat were installed. The corresponding interfaces and connection were assigned. No compaction stress was applied on top of the backfill soil.

Stage 4: After the construction of the wall itself was finished, the bridge slab was placed on top of the bridge seat. The beam seat width b was 0.6 m (2 ft) and the setback distance a_b for the bridge seat was 0.2 m (8 in). The corresponding interfaces and connection were assigned.

Stage 5: The integrated approach was constructed behind the bridge slab. Geotextile was installed in the integrated approach.

Stage 6: Traffic load on the bridge and the approach roadway was simulated as a uniform vertical stress according to the design guidelines (AASHTO, 2012; Adams et al., 2012; Berg et al., 2009; Zheng and Fox, 2017). A uniform surcharge $\sigma_{traffic\text{-}approach}$ of 12.7 kPa (265 psf) was applied to the integrated approach roadway, which is equivalent to 0.72 m (2.4 ft) thick backfill soil. The traffic load on the bridge slab was determined using the HL-93 LL model and a uniform surcharge $\sigma_{traffic\text{-}slab}$ of 5.4 kPa (113 psf) was applied to the bridge span.

A parametric study was carried out by changing one parameter at a time in the baseline model to study its influence on the performance of the GRS-IBS, such as the lateral earth pressure behind the CMU facing blocks, the additional vertical stress inside the backfill soil due to loading, the lateral displacement of CMU blocks, the settlement on top of the abutment, and the tension in the reinforcement. The influencing factors included the friction angle of the backfill soil, the stiffness of the reinforcement material J, the reinforcement spacing S_v, the combination of reinforcement stiffness and spacing J/S_v, the bearing reinforcement layers, the soil – reinforcement interaction coefficient C_i, the primary reinforcement length L_r, the foundation compressibility E, the beam seat width b, the compaction stress, the facing connection, and the facing connection stiffness.

7.4.5.2 EFFECT OF FRICTION ANGLE OF BACKFILL SOIL

This section discusses the effect of the friction angle of the backfill soil. Additional two friction angles of the backfill soil were used in the parametric study, which were 34° and 42°. The friction angle of 34° was the value suggested by AASHTO (2012) in the design of MSE walls when no tests data were available.

In the numerical model the dilation angle of the backfill soil followed the empirical relationship of $\psi = \phi - 30^{o}$ proposed by Bolton (1986). The dilation angle changed with the change of the friction angle. The geotextile – backfill soil interface friction angle, the backfill soil – CMU interface friction angle, and the bridge slab – backfill soil interface angle would be affected by the change of the friction angle of the backfill soil. Table 7.4.13 summarizes all the changed variables because of the change of the friction angle of the backfill soil.

Table 7.4.13: Parametric study variables (friction angle of the backfill soil)

Model Variable			Baseline	Case 1	Case 2
Backfill	Friction Angle ϕ (°)		38	34	42
	Dilation Angle ψ (°)		8	4	12
Interfaces	Geotextile – Backfill soil	Shear Stiffness k_s (N/m/m)		1×10^6	
		Interaction Coefficient C_i		0.9	
		Friction Angle δ (°)	35.1	31.3	39.0
		Cohesion (kPa)		0	
	Backfill soil – CMU	Normal Stiffness k_n (N/m/m)		1×10^8	
		Shear Stiffness k_s (N/m/m)		1×10^6	
		Interaction Coefficient C_i		0.65	
		Friction Angle δ (°)	26.9	23.7	30.3
		Cohesion (kPa)		0	
	Bridge slab – Backfill soil	Normal Stiffness k_n (N/m/m)		1×10^8	
		Shear Stiffness k_s (N/m/m)		1×10^6	
		Interaction Coefficient C_i		0.9	
		Friction Angle δ (°)	35.1	31.3	39.0
		Cohesion (kPa)		0	

7.4.5.2.1 Lateral earth pressures

Figure 7.4.33 shows the lateral earth pressure behind the CMU facing blocks under both self-weight (i.e., Stage 2) and traffic load conditions (i.e., Stage 6). Three solid lines in Fig. 7.4.33 (a) represent the Coulomb's active earth pressure distribution using the different friction angles of the backfill soil and interface friction angles between backfill soil and CMU (provided in Table 7.4.13). Previous comparisons in Section 7.4.2.5 were made between field measurements, theoretical solutions, and numerical results. Since it was difficult to evaluate the interface friction angle between backfill soil and wall facing in the field, Rankine theory was used to calculate the theoretical active lateral earth pressure. However, the interface friction angle between the backfill soil and the CMU facing blocks was considered in the parametric study discussed in this section. Therefore, the Coulomb's theory instead of Rankine theory was used to calculate the lateral earth pressure behind the CMU facing blocks. The calculated Coulomb's active lateral earth pressure coefficients were 0.25, 0.22, and 0.19 for the cases of backfill soil friction angle of 34^o, 38^o (i.e., the baseline case), and 42^o respectively. Figure 7.4.33 (a) shows that the lateral earth pressures behind wall facing from the numerical model are in good agreement with the

Coulomb's active earth pressures under self-weight except for some deviations at the bottom of the wall due to boundary conditions. Under the traffic loads, as shown in Fig. 7.4.33 (b), the lateral earth pressure was found to increase significantly especially at the top of the wall. This is due to the combined loads from self-weight of the bridge slab, self-weight of the integrated approach, and traffic load. The influence of these loads were found to decrease with increasing depth from the top of the wall, thus resulting in a significant increase of lateral earth pressure towards the top of the wall and a comparatively smaller increase towards the bottom of the wall. As a result, the lateral earth pressure was found to show an essentially uniform distribution with depth. As expected, a larger friction angle of the backfill soil resulted in a lower lateral earth pressure behind the wall facing.

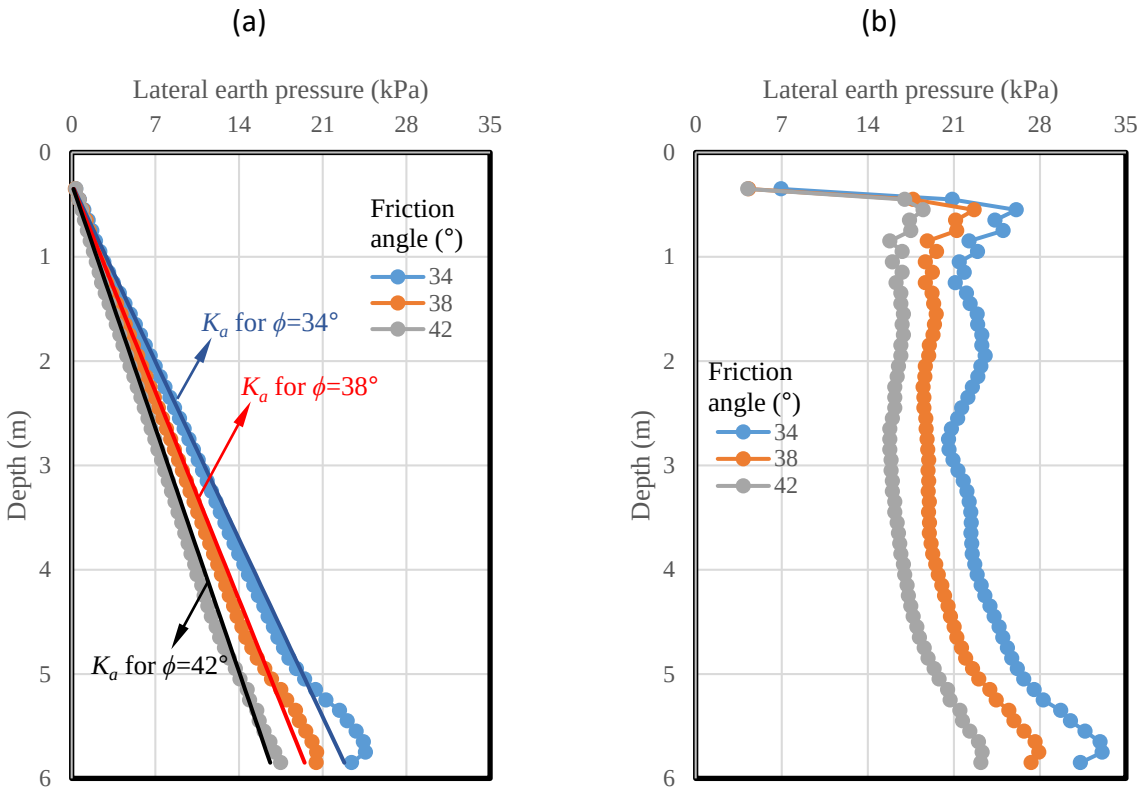

Fig. 7.4.33: Effect of the friction angle of the backfill soil on the lateral earth pressure behind CMU facing blocks: (a) Self-weight; (b) Traffic load.

7.4.5.2.2 Additional vertical stress induced by loading

Figure 7.4.34 shows the effect of the friction angle of backfill soil on the distribution of additional vertical stress Δp at 0.5 m (20 in) from the back of CMU facing blocks with depth induced by loading. The location of 0.5 m (20 in) from the back of CMU facing blocks was selected because it was under the center of the contact area between the bridge slab and the bridge seat (i.e., under the center of the beam seat width *b*). The additional vertical stress induced by the self-weight of the bridge slab as shown in Fig. 7.4.34 (a) was calculated as the difference of the vertical stress between Stage 4 and Stage 3. The additional vertical stress Δp induced by the self-weight

of the bridge slab and the traffic load as shown Fig. 7.4.34 (b) was calculated as the difference of the vertical stress between Stage 6 and Stage 3. In other words, the additional vertical stress Δp as shown in Fig. 7.4.34 (b) was induced not only by the self-weight of the bridge slab and the traffic load applied on the bridge span $\sigma_{traffic\text{-}slab}$ but also by the self-weight of the integrated approach way and the traffic load applied on the approach way $\sigma_{traffic\text{-}approach}$. Figure 7.4.34 shows that the change of the friction angle of backfill soil did not have any significant effect on Δp. The additional vertical stress Δp was highest at the top of the wall just below the bridge slab and then decreased with depth. The rate of stress decrease became slower at a greater depth.

Figure 7.4.34 also shows the calculated additional vertical stress Δp using the AASHTO 2 to 1 truncation method (AASHTO, 2012) as shown in Equation (7.4.6):

$$\Delta p = \frac{P_v}{D_1} \tag{7.4.6}$$

where P_v is the load per linear meter of the strip footing and D_1 is the effective width of the applied load at any depth. When the additional vertical stress induced by the self-weight of the bridge slab was calculated, P_v was equal to 73.5 kN/m (5036 lb/ft). That is:

$$P_v = \rho_{bridge} g D \frac{L_b}{2} = \frac{2500 \times 9.8}{1000} \times 0.4 \times 7.5 = 73.5 \text{ kN/m} \tag{7.4.7}$$

When the additional vertical stress induced by the self-weight of the bridge slab and the traffic load was calculated, P_v was equal to 114 kN/m (7811 lb/ft). That is:

$$P_v = \rho_{bridge} g D \frac{L_b}{2} + \sigma_{traffic-slab} \frac{L_b}{2} = \frac{2500 \times 9.8}{1000} \times 0.4 \times 7.5 + 5.4 \times 7.5 = 114 \text{ kN/m} \tag{7.4.8}$$

The calculation of the effective width of the applied load at any depth is shown in Equations (7.4.9) and (7.4.10):

$$D_1 = b + z, z \le z_2 \tag{7.4.9}$$

$$D_1 = \frac{b+z}{2} + d, z > z_2 \tag{7.4.10}$$

where b is the width of the applied load or the beam seat width (i.e., b = 0.6 m in this study); z is the depth; d is the distance between the centroid of the concentrated vertical load and the back of the wall facing (i.e., $d = b/2 + a_b$ = 0.5 m in this study); z_2 is the depth where the effective width intersects the back of the wall face (i.e., $z_2 = 2d - b$ = 0.4 m in this study).

When Δp induced by the self-weight of the bridge slab and the traffic load was calculated, the influence of the self-weight of the integrated approach and the traffic load applied on the integrated approach $\sigma_{traffic\text{-}approach}$ was unclear. Both the self-weight of the integrated approach

and the traffic load $\sigma_{traffic\text{-}approach}$ had large loading areas. Therefore, they could be treated as a uniform surcharge q along the depth. That is:

$$q = \rho_{backfill} gD + \sigma_{traffic-approach} = \frac{1650 \times 9.8}{1000} \times 0.4 + 12.7 = 19.2\,\text{kPa} \qquad (7.4.11)$$

Fig. 7.4.34 (b) presents the calculated Δp with or without the consideration of the uniform surcharge q. The "AASHTO 2 to 1 truncated plus surcharge q" in Fig. 7.4.34 (b) means $\Delta p = P_v/D_1 + q$.

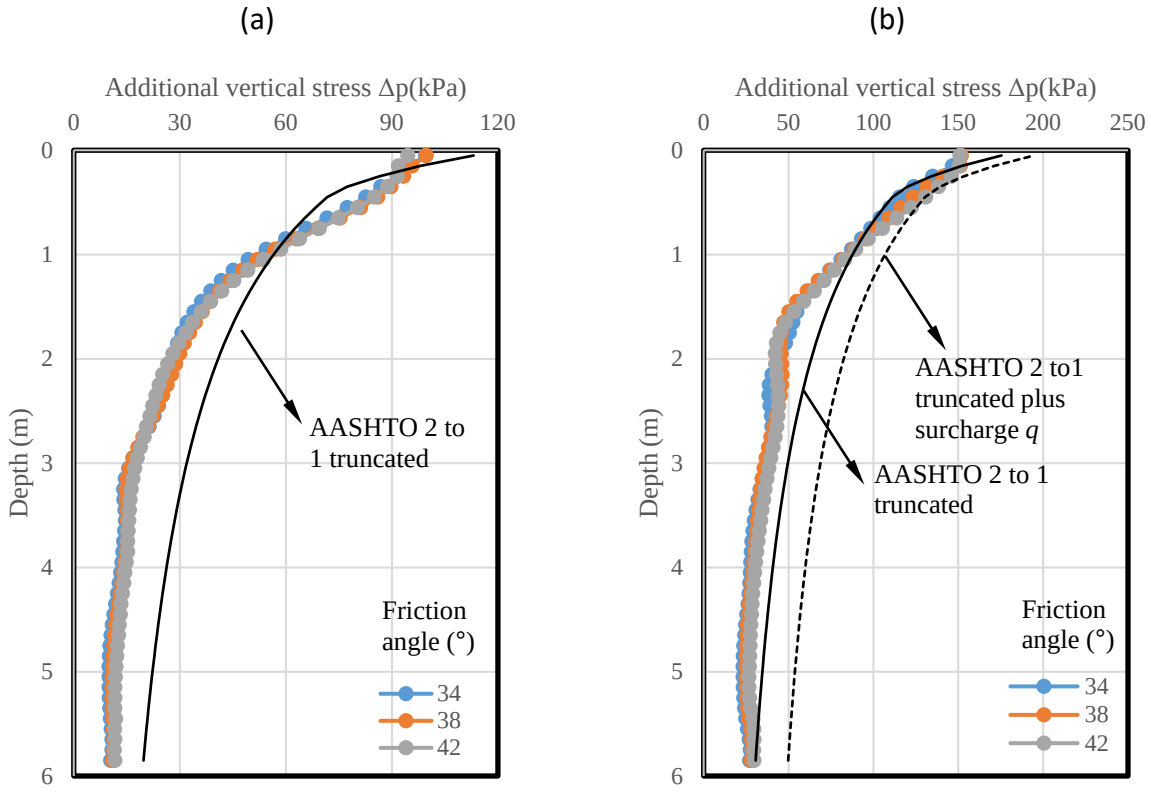

Fig. 7.4.34: Effect of the friction angle of the backfill soil on the additional vertical stress induced by loading: (a) Induced by the self-weight of the bridge slab; (b) Induced by the self-weight of the bridge slab and the traffic load.

Figure 7.4.34 (a) shows that the additional vertical stresses calculated by the AASHTO 2 to 1 truncation method are in reasonable agreement with the numerical results. Figure 7.4.34 (b) shows that Δp calculated using the AASHTO 2 to 1 truncation method without the consideration of a uniform surcharge $q$was closer to the numerical results as compared with those considering a uniform surcharge q. The influence of the self-weight of the integrated approach and the traffic load applied on the integrated approach $\sigma_{traffic\text{-}approach}$ was conservatively considered by adding a uniform surcharge q with the depth to the additional vertical stress.

7.4.5.2.3 Lateral displacement of CMU facing blocks

Figure 7.4.35 shows the lateral displacements of CMU facing blocks under the self-weight (i.e., Stage 2), after the placement of the bridge slab (i.e., Stage 4), and the application of the traffic load (i.e., Stage 6). As expected, the higher friction angle of the backfill soil caused smaller lateral displacements of the CMU facing blocks since the higher friction angle resulted in lower lateral earth pressures behind the wall facing as shown in Fig. 7.4.33 (a). Under the self-weight condition, the maximum lateral displacement occurred around the mid to lower portion of the wall. Under both the bridge slab load and the traffic load, the location of the maximum lateral displacement moved up because of the load applied on the top of the wall. The use of the geofoam in front of the bridge seat led to a reduced lateral displacement of the CMU facing blocks at the top of the wall. The additional lateral displacements of CMU facing blocks induced by the self-weight of the bridge slab were 11.23, 10.63, and 10.35 mm (0.44, 0.42 and 0.41 in) for the cases of backfill soil with friction angles of 34°, 38°, and 42°, respectively. FHWA (Adams et al., 2011) recommended a tolerable lateral strain for GRS-IBS of up to 1% of the beam seat width plus the setback distance. In the predictions obtained in this study, the maximum lateral strains were 1.4%, 1.3%, and 1.3% for the cases of backfill soil with friction angles of 34°, 38°, and 42°, respectively. Consequently, the maximum lateral strains exceeded the tolerable lateral strain recommended by FHWA (Adams et al., 2011).

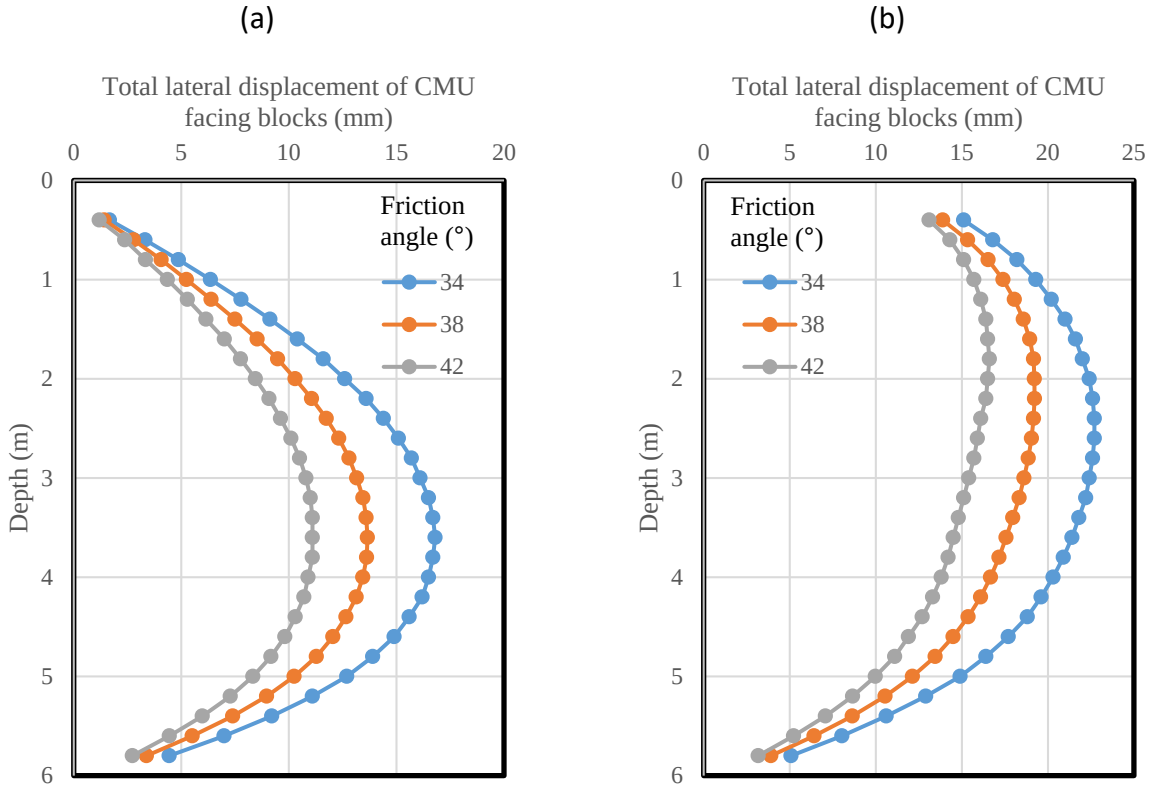

Fig. 7.4.35: Effect of the friction angle of the backfill soil on the lateral displacements of CMU facing blocks: (a) Self-weight; (b) Bridge slab;

(c)

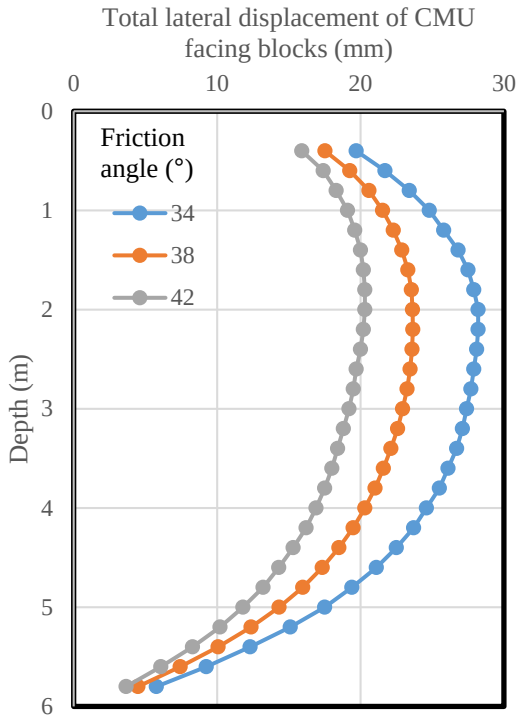

Fig. 7.4.35: Effect of the friction angle of the backfill soil on the lateral displacements of CMU facing blocks: (c) Traffic load (continued).

Figure 7.4.36 shows the additional lateral displacements of CMU facing blocks induced by the traffic load only (i.e., the difference of the lateral displacements between Stage 6 and Stage 5). Figure 7.4.36 shows that the additional lateral displacement of CMU facing blocks was larger near the top of the wall and decreased with depth. As expected, the higher friction angle of the backfill soil resulted in smaller additional lateral displacement. The maximum additional lateral displacements of CMU facing blocks induced by the traffic load only were 44.8, 33.4, and 22.9 mm for the cases of backfill soil with friction angles of 34°, 38°, and 42° respectively. Therefore, the maximum lateral strain induced by the traffic load only were 0.60%, 0.43%, and 0.36% for the cases of backfill soil with friction angles of 34°, 38°, and 42° respectively. In other words, the lateral displacements of CMU facing blocks after open to traffic were minimal.

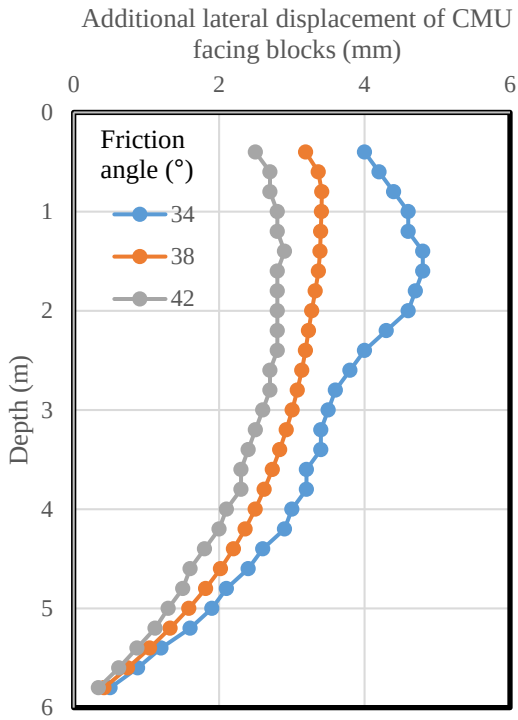

Fig. 7.4.36: Effect of the friction angle of the backfill soil on the additional lateral displacement of CMU facing blocks induced by the traffic load

7.4.5.2.4 Settlement profile for the bridge slab and integrated approach

Figure 7.4.37 shows the effect of the friction angle of backfill soil on the additional settlement on the top of the bridge slab and integrated approach induced by the traffic load (i.e., the difference of the settlement between Stage 6 and Stage 5). Figure 7.4.37 shows that higher friction angle of the backfill soil resulted in smaller settlement of both the bridge slab and the integrated approach. Differential settlement happened at the end of the bridge slab. The bridge slab settled more than the integrated approach due to the high pressure applied on the beam seat. The self-weight of the bridge slab and the traffic load were applied on top of the abutment considering a much smaller contact area (i.e. beam seat width b = 0.6 m) compared to the bridge span, thus resulting in a high applied pressure on the beam seat. As a result, the bridge slab experienced comparatively more settlements than the approaching road. The use of the high soil friction angle also reduced the differential settlement at the end of the bridge slab. As discussed previously in Section 7.4.3.5, the numerical model did not simulate the pavement on top of the approach way, which might result in relatively larger bump (i.e., approximately from 1.6 mm to 3.6 mm) at the end of the bridge

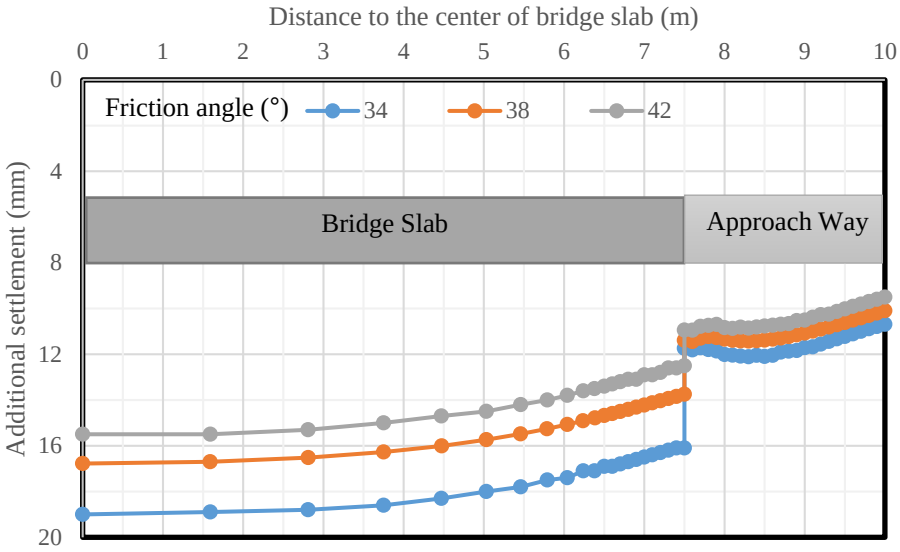

Fig. 7.4.37: Effect of the friction angle of the backfill soil on the additional settlement of the bridge slab and the integrated approach induced by traffic load

7.4.5.2.5 Volume change of the abutment

Adams et al. (2002) conducted large-scale geosynthetic reinforced soil pier tests and investigated the relationship between the vertical and lateral deformations. Test results suggested a zero net volume change during vertical loading. Adams et al. (2002) suggested that the theory of zero volume change should be used to predict the maximum lateral deflection of a GRS structure. In this study, the volume change of the GRS-IBS abutment during vertical loading was also investigated.

Figure 7.4.38 shows the schematic of the deformed GRS-IBS abutment. Only the volume changes of the reinforced zone due to loading was considered in this study. The vertical volume change due to the vertical compression of the GRS-IBS abutment can be calculated by integrating the vertical displacement δ_{vi} of each grid point in the numerical model at the top of the abutment over the entire top width of the abutment, which is shown as follows:

$$\Delta V_v = \int_0^{L_r - a_b} \delta_{vi} \cdot dx \qquad (7.4.12)$$

where L_r is the width of the abutment or the length of the reinforcement and a_b is the setback distance for the bridge seat behind the geofoam (L_r = 4.9 m (16 ft) in the baseline case and a_b = 0.2 m (8 in) in all the cases in this study).

The normalized vertical volume change is defined as $\Delta V_v/V_0$ where V_0 is the original volume of the GRS-IBS abutment. $V_0 = L_r \cdot H$ where H is the wall height (H = 6.0 m (20 ft) in all the cases in this study and V_0 = 29.4 m^3/m (316 cu. ft./ft.) in the baseline case).

The lateral volume change of the GRS-IBS abutment due to the lateral displacement of the CMU facing blocks and geofoam can be calculated by integrating the lateral displacement of the CMU blocks δ_{li} at the *i*th layer over the whole height plus the lateral displacement of the geofoam δ_{foam} over its thickness h_{foam} (h_{foam} = 0.3 m (12 in) in all the cases in this study). The whole GRS-IBS abutment was composed of 28 layers of CMU blocks and one geofoam. Assuming that the lateral displacements of the CMU blocks and the geofoam were equally distributed along their own thicknesses, the lateral volume change of the GRS-IBS abutment can be simplified as follows:

$$\Delta V_l = \delta_{foam} \cdot h_{foam} + \sum_{1}^{28} \left(\delta_{li} \cdot h \right) \tag{7.4.13}$$

where h is the thickness of each CMU facing block (h = 0.2 m (8 in) in all the cases in this study). The normalized lateral volume change of the GRS-IBS abutment is defined as $\Delta V_l / V_0$. If there is no volume change as assumed by Adams et al. (2002), $\Delta V_l = \Delta V_v$.

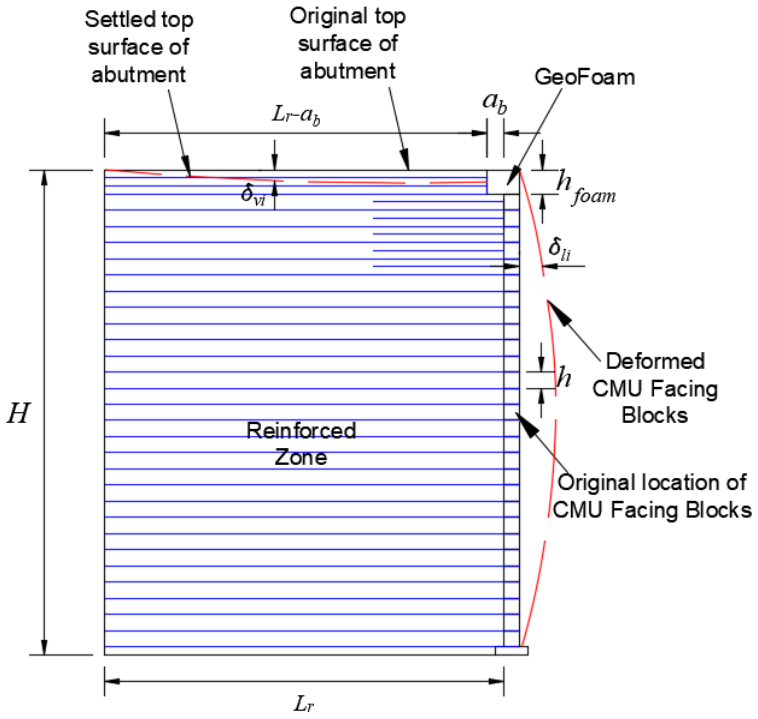

Fig. 7.4.38: Schematic of deformed GRS-IBS abutment

Figure 7.4.39 shows the normalized lateral volume change – normalized vertical volume change curves with the backfill soil of different friction angles. Each line in Fig. 7.4.39 has four points. The first point, located at the origin, represents the condition of Stage 3 when the construction of the abutment itself (including the bridge seat) was finished and both the lateral and vertical displacements were initialized. The second point corresponds to Stage 4 (i.e., the placement of the bridge slab). The third point corresponds to Stage 5 when the integrated approach was

constructed behind the bridge slab. The final point corresponds to Stage 6 when the traffic load was applied on both the bridge slab and the integrated approach. Figure 7.4.39 shows that the volume change of the GRS-IBS abutment did not satisfy the zero-volume change assumption proposed by Adams et al. (2002). The abutment had more vertical compression than the lateral expansion, which is different from the volume change of GRS piers as discussed in Section 7.3. Further calculations regarding the volume change of the GRS-IBS are discussed in the "Contributions to the "SIX DESIGN ASPECTS"". Results showed that when the entire reinforced zone was considered in calculating the vertical volume change of the GRS-IBS, the structure had more vertical compression than lateral expansion. When only the settlement of the reinforced zone within the width of beam seat was considered in calculating the vertical volume change of the GRS-IBS, however, the structure had more lateral expansion than vertical compression. Differnent zone considered in the volume change calculation resulted in different volumetric behavior of the GRS-IBS. Figure 7.4.39 also shows that lower friction angle of the soil caused more lateral displacement of the CMU facing blocks and larger settlement at the top of the abutment, thus resulting in the volume-change line slightly closer to the zero-volume change line.

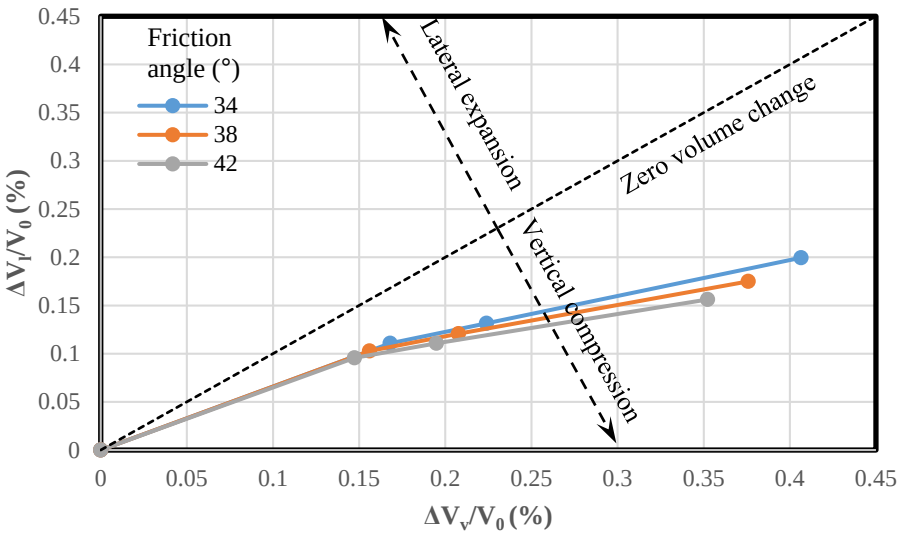

Fig. 7.4.39: Effect of the friction angle of the backfill soil on the volume change of the GRS-IBS abutment

Table 7.4.14 summarizes the effect of the friction angle of the backfill soil on the maximum vertical and lateral displacements of the abutment. Similar to the data presented in Fig. 7.4.39, all the displacements presented in Table 7.4.14 excluded the displacement of the abutment in Stage 3. In other words, the displacement of the abutment was initialized after the construction of the abutment and the beam seat was finished.

Table 7.4.14: Effect of friction angle of the backfill soil on the maximum vertical and lateral displacements of the abutment

Friction angle (°)	Displacement (mm)	Construction stage		
		Stage 4 (bridge slab)	Stage 5 (Integrated approach)	Stage 6 (traffic load)
34	$\delta_{v\text{-max}}$	39.97	42.07	58.07
	$\delta_{l\text{-max}}$	11.23	11.92	16.22
38	$\delta_{v\text{-max}}$	35.36	37.19	51.06
	$\delta_{l\text{-max}}$	10.63	11.18	14.54
42	$\delta_{v\text{-max}}$	31.89	33.49	46.09
	$\delta_{l\text{-max}}$	10.35	10.72	13.42

7.4.5.2.6 Tension in the reinforcement

Figure 7.4.40 shows the maximum tensile forces of the reinforcement T_{max} with the backfill soil of different friction angles under both self-weight (i.e., Stage 2) and traffic load conditions (i.e., Stage 6). Higher friction angle of the backfill soil resulted in lower maximum tensile force in the reinforcement. Under the self-weight, the maximum tensile force in the reinforcement T_{max} increased with depth, reached to the largest value near the lower part of the wall, and then decreased to almost zero at the bottom of the wall. Under the traffic load, the maximum tensile force in the reinforcement T_{max} had a significant increase in the upper protion of the wall due to loading. T_{max} kept almost the same with the depth of the wall and decreased at the bottom. Figure 7.4.40 also shows a zig-zag distribution of the maximum tensile force within the upper portion of the wall. The locations of the smaller tensile forces in the reinforcement corresponded to the location where bearing reinforcement layers were used. The bearing reinforcement layers were not connected to the CMU facing blocks, thus resulting in a much smaller tensile force in the bearing reinforcement layers than those in the primary reinforcement layers.

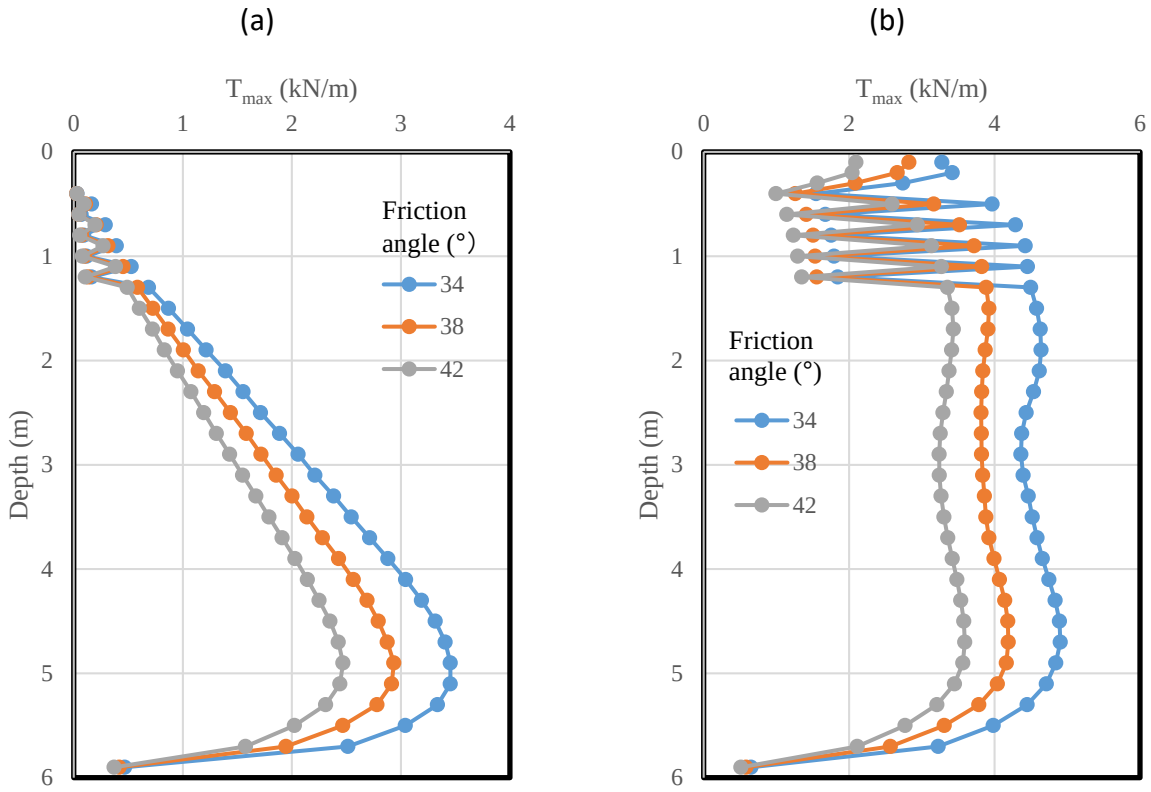

Fig. 7.4.40: Effect of the friction angle of the backfill soil on the maximum tensile force T_{max} in the reinforcement: (a) Self-weight; (b) Traffic load.

Figure 7.4.41 shows the ratio of the connection forces T_0 to the maximum tensile force T_{max} in the reinforcement with the backfill soil of different friction angles under both self-weight (i.e., Stage 2) and traffic load conditions (i.e., Stage 6). Figure 7.4.41 shows that the change of the friction angle of backfill soil did not affect the ratio of the connection force T_0 to the maximum tensile force T_{max} in the reinforcement. The connection force T_0 was essentially the same as the maximum tensile force T_{max} in the reinforcement under both the self-weight and the traffic load. Under the self-weight, the maximum tensile force in the reinforcement happening near the connection was due to the down-drag force. Under the traffic load, the connection force was still close to the maximum tensile force because of the way of load application. The bridge slab was placed on the top of the abutment. The beam seat width *b*, which was the contact width between the bridge slab and the bridge seat, was 0.6 m (2 ft). In other words, the load caused by the self-weight of the bridge slab and the traffic load applied on the bridge span were very close to the CMU facing blocks, thus resulting in larger tensile force near facing. In addition, the self-weight of the bridge slab and the traffic load applied on the bridge span could generate a moment on the abutment, which also contributed to the high connection force in the reinforcement. Another possible reason for T_{max} happening near the facing connection is that the GRS-IBS was under working condition. The location of T_{max} in the reinforcement of the GRS-IBS under limit condition will be discussed later in Section 7.6.

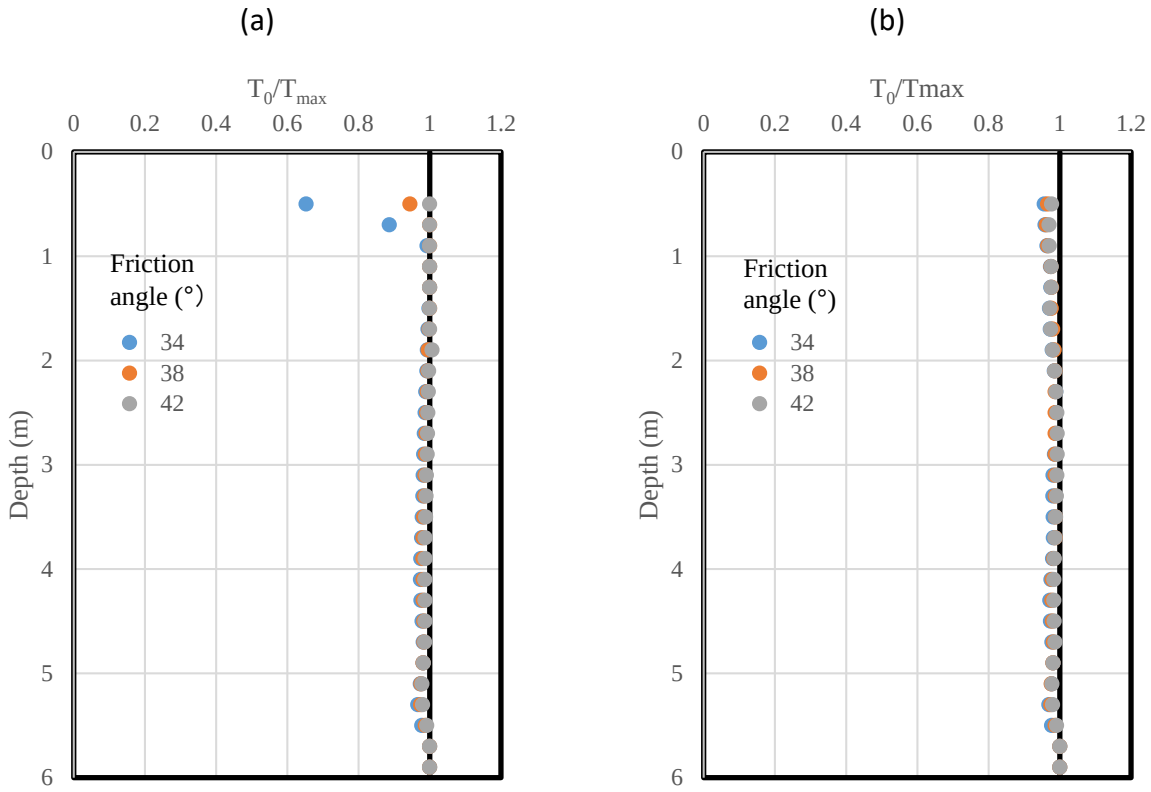

Fig. 7.4.41: Effect of the friction angle of the backfill soil on the ratio of connection force T_0 to the maximum tensile force T_{max} in the reinforcement: (a) Self-weight; (b) Traffic load.

The coefficient of lateral earth pressure behind the wall K_r was estimated using the maximum tensile stress T_{max} from the numerical simulation. Equation (7.4.14) shows the calculation of K_r as follows:

$$K_r = \frac{T_{\max}}{S_v \cdot \sigma_v} \tag{7.4.14}$$

where S_v is the primary reinforcement spacing and σ_v is the vertical stress on the reinforcement. A normalized coefficient of lateral earth pressure is defined as K_r/K_a where K_a is the Rankine active earth pressure coefficient. The method for calculating the coefficient of lateral earth pressure based on the maximum tensile stress in the primary reinforcement was adopted by (AASHTO) (2012) to develop the profile of K_r/K_a with depth. The calculated Rankine active lateral earth pressure coefficients were 0.28, 0.24, and 0.20 for the cases of backfill soil friction angle of 34^o, 38^o (i.e., the baseline case), and 42^o respectively.

Figure 7.4.42 shows the normalized coefficients of lateral earth pressure K_r/K_a with the backfill soil of different friction angles under both self-weight (i.e., Stage 2) and traffic load conditions (i.e., Stage 6). The calculation of σ_v induced by different loading conditions should be considered.

Under the self-weight, σ_v was calculated as the overburden stress. Under the traffic load, however, σ_v was calculated as the sum of both the overburden stress and the additional vertical stress Δp induced by loading using the AASHTO 2 to 1 truncation method without surcharge q. Figure 7.4.42 shows that the change of the friction angle of backfill soil did not have any significant effect on the normalized coefficient of lateral earth pressure. The K_r/K_a ratios from the numerical simulation were less than 1.0 and approximately uniform with the depth at the center of the wall with the smaller values near the top and the bottom of the wall. Comparatively smaller K_r/K_a values obtained towards the bottom of the wall can be attributed to the toe restraint. Leshchinsky and Vahedifard (2012) conducted global stability analyses and concluded that toe restraint can reduce the reinforcement load by as much as 50%. The numerical model did not have an embedded leveling pad. However, the numerical model used a relatively high toe shear stiffness of 4×10^7 N/m/m (Huang et al. 2010, Zheng and Fox, 2017), which may have resulted in a comparatively smaller K_r/K_a values towards the bottom of the wall. Similarly, smaller K_r/K_a values towards the top of the wall can be attributed to the horizontal restraint from the bridge slab to the backfill soil at the top of the wall. Zheng and Fox (2016) concluded that it is relevant to consider the horizontal restraining effect of the bridge slab when modelling load-carrying GMSE bridge abutments. The connection between geotextile reinforcement and CMU facing blocks along the height of the wall may also reduce the load carried by the reinforcement, thus resulting in K_r/K_a smaller than 1.0 and essentially uniform with depth.

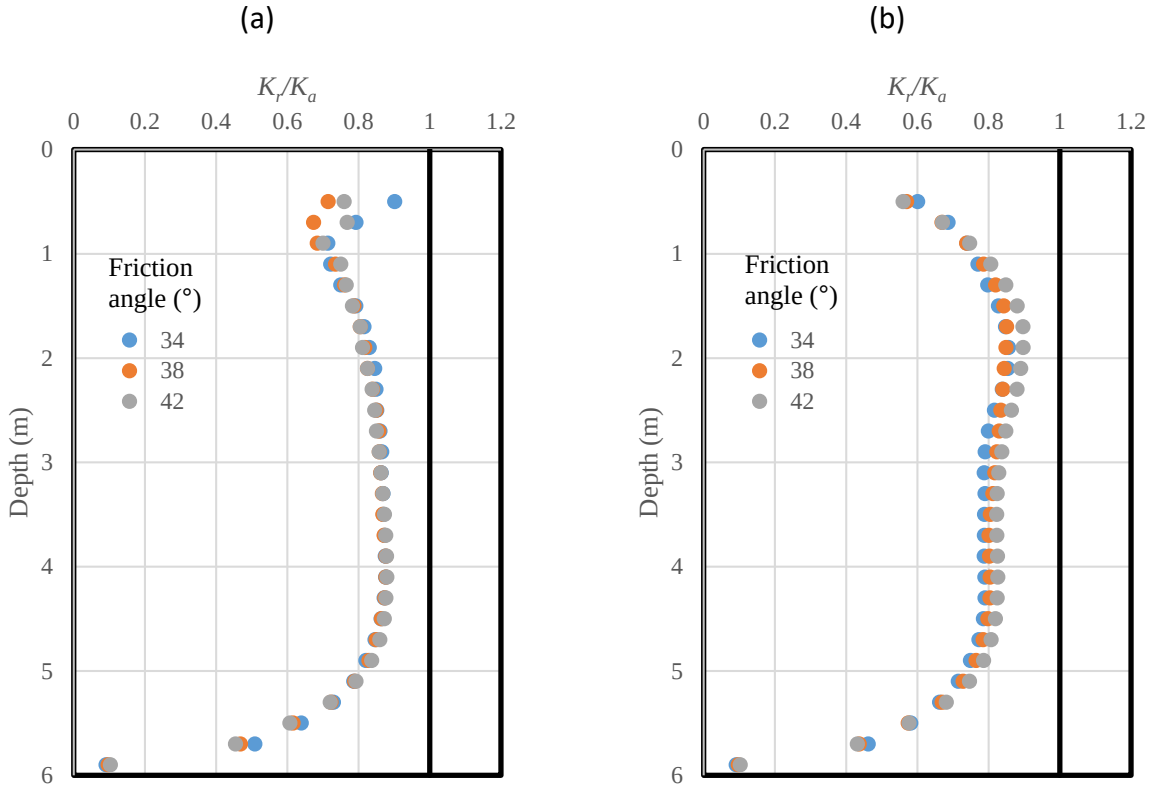

Fig. 7.4.42: Effect of the friction angle of the backfill soil on the normalized coefficient of lateral earth pressure K_r/K_a: (a) Self-weight; (b) Traffic load.

7.4.5.3 EFFECT OF REINFORCEMENT STIFFNESS

This section discusses the effect of the reinforcement stiffness on the performance of the GRS-IBS. In the baseline model, the stiffness of the reinforcement was 700 kN/m (48 kip/ft). Two additional cases were evaluated in this parametric study, which involved reinforcement stiffness values of 350 kN/m (24 kip/ft) and 1400 kN/m (96 kip/ft). It should be noted that the ultimate tensile strength of the reinforcement also changed with the change of the stiffness. Table 7.4.15 summarizes the variables that changed regarding the reinforcement properties.

Table 7.4.15: Variables in the parametric study for the tensile stiffness effect of reinforcement

Properties of cable elements	Baseline	Case 1	Case 2
Stiffness (kN/m)	700	350	1400
Thickness (mm)	1	1	1
Elastic modulus (MPa)	700	350	1400
Cross-sectional Area (m^2)	0.001	0.001	0.001
Perimeter (m)	2.002	2.002	2.002
Yield strength T_f (kN/m)	70	35	140

7.4.5.3.1 Lateral earth pressures

Figure 7.4.43 presents the lateral earth pressure behind the CMU facing blocks under both self-weight (i.e., Stage 2) and traffic load conditions (i.e., Stage 6) with different reinforcement stiffness. Figure 7.4.43 (a) also shows the lateral earth pressure profiles calculated using Coulomb's active earth pressure coefficient. Figure 7.4.43 (a) shows that the lateral earth pressure behind wall facing from the numerical calculation was in good agreement to the Coulomb's active earth pressure under the self-weight. The stiffness of the reinforcement did not affect the lateral earth pressure distribution behind the wall facing under the self-weight. Under the traffic load, the lateral earth pressures profile showed a comparatively large increase towards the top of the wall due to the additional loading. Higher reinforcement stiffness resulted in slightly higher lateral earth pressures. The use of high reinforcement stiffness would restrain the lateral deformation of the wall, as will be discussed later in Section 7.4.5.3.3. The restraint of the lateral deformation of the wall resulted in turn in comparatively higher lateral earth pressures.

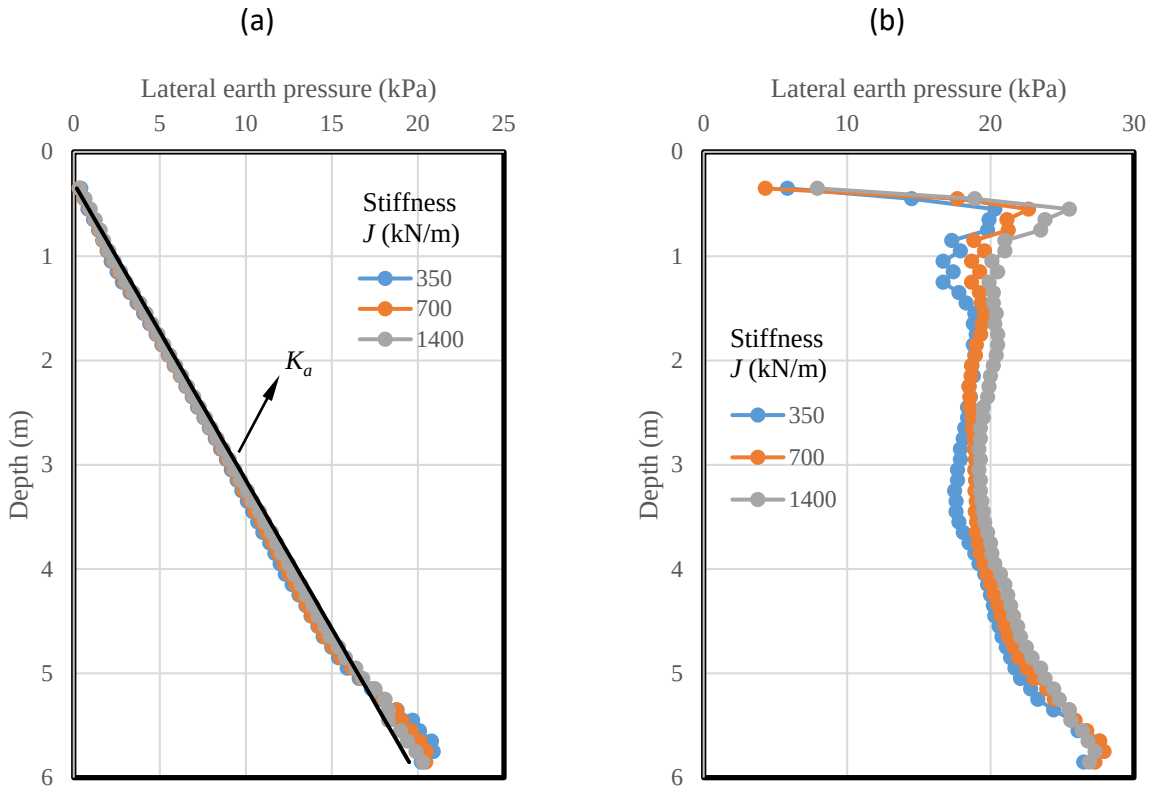

Fig. 7.4.43: Effect of the reinforcement stiffness on the lateral earth pressure behind CMU facing blocks: (a) Self-weight; (b) Traffic load.

7.4.5.3.2 Additional vertical stress induced by loading

Figure 7.4.44 shows the effect of the reinforcement stiffness on the distribution of the additional vertical stress Δp at 0.5 m (20 in) from the back of CMU facing blocks with depth induced by to loading. Figure 7.4.44 shows that the change of the reinforcement stiffness did not have a significant effect on Δp. The use of stiffer reinforcements resulted in slightly higher additional vertical stress underneath the bridge slab. Figure 7.4.44 also shows the calculated additional vertical stress using the AASHTO 2 to 1 truncation method. The AASHTO 2 to 1 truncation method calculated the additional vertical stresses in reasonable agreement with the numerical results.

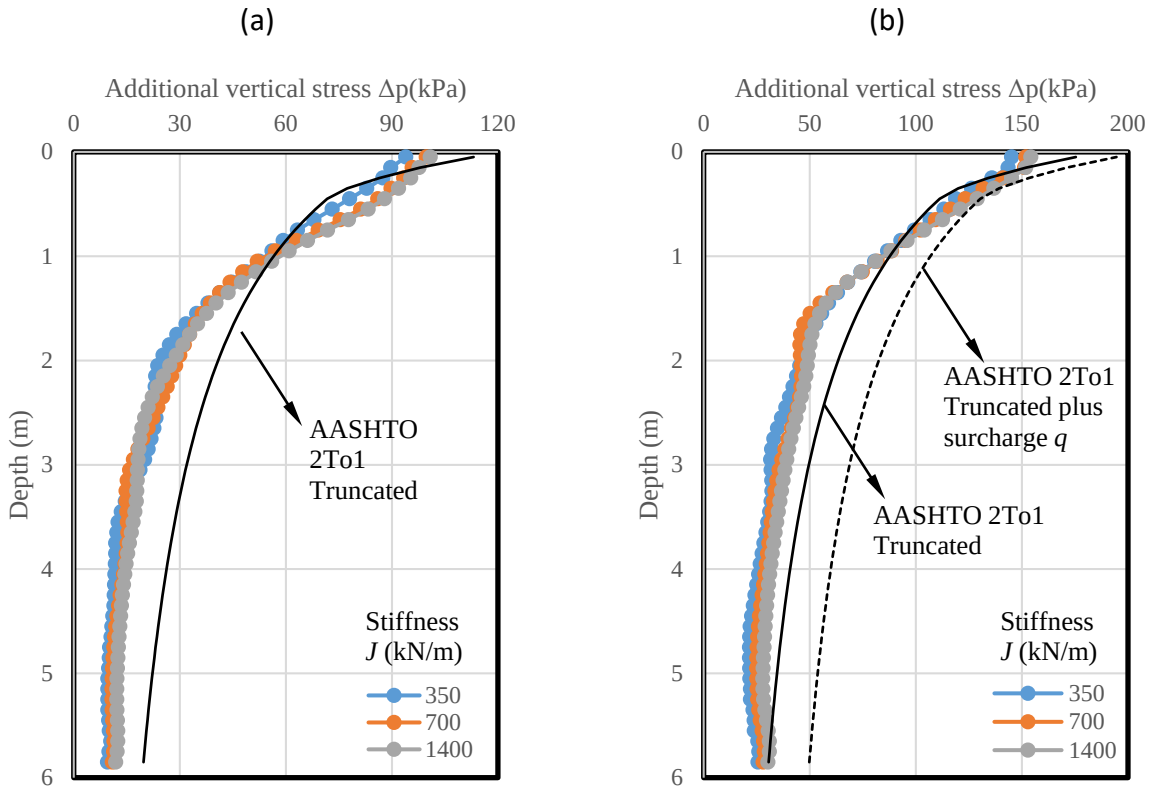

Fig. 7.4.44: Effect of the reinforcement stiffness on the additional vertical stress induced by loading: (a) Induced by the self-weight of the bridge slab; (b) Induced by the self-weight of the bridge slab and the traffic load.

7.4.5.3.3 Lateral displacement of CMU facing blocks

Figure 7.4.45 shows the lateral displacement of CMU facing blocks under self-weight (i.e., Stage 2), bridge slab (i.e., Stage 4), and traffic load conditions (i.e., Stage 6) with different reinforcement stiffness. As expected, the use of stiffer reinforcement resulted in smaller lateral displacement of CMU facing blocks. Under the self-weight, the lateral displacements profile of the CMU facing blocks showed an increasing trend with increasing elevation, reaching a maximum lateral displacement value approximately in the middle of the wall. Lateral displacements then decreased with increasing elevation towards the top of the wall. Under both the bridge slab load and the traffic load, the lateral displacement of CMU facing blocks showed a significant increase in total lateral displacement near the top of the wall since the load was applied on the top of the wall.

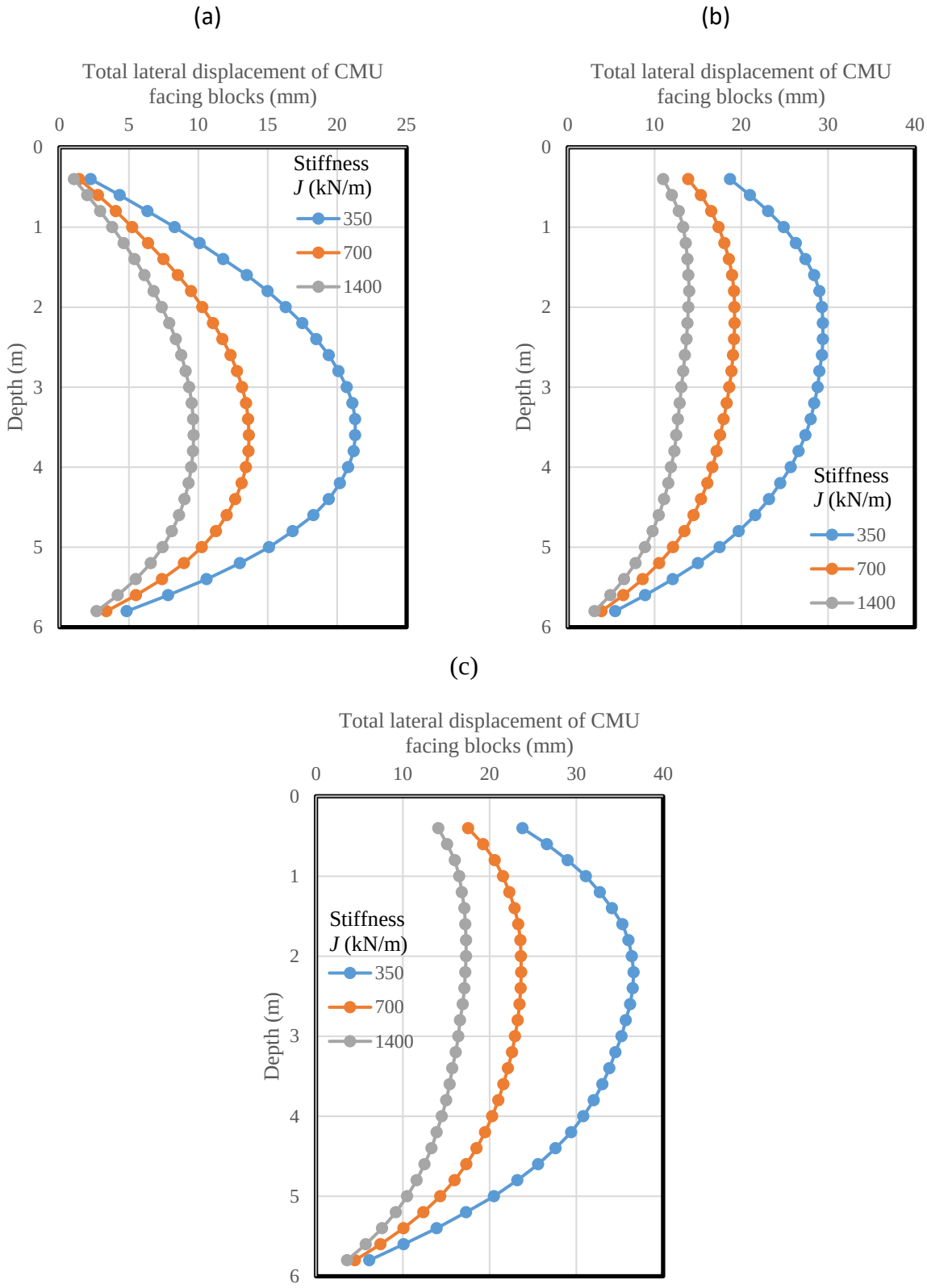

Fig. 7.4.45: Effect of the reinforcement stiffness on the lateral displacement of CMU facing blocks: (a) Self-weight; (b) Bridge slab; (c) Traffic load.

Figure 7.4.46 shows the effect of the reinforcement stiffness on the additional lateral displacement of CMU facing blocks induced bytraffic load only (i.e., the difference of the lateral displacements between Stage 6 and Stage 5). The results in Fig. 7.4.46 show that the use of stiffer reinforcements also led to a reduction in the additional lateral displacements induced by traffic load. The maximum traffic-induced lateral displacements occurred in the upper half of the wall.

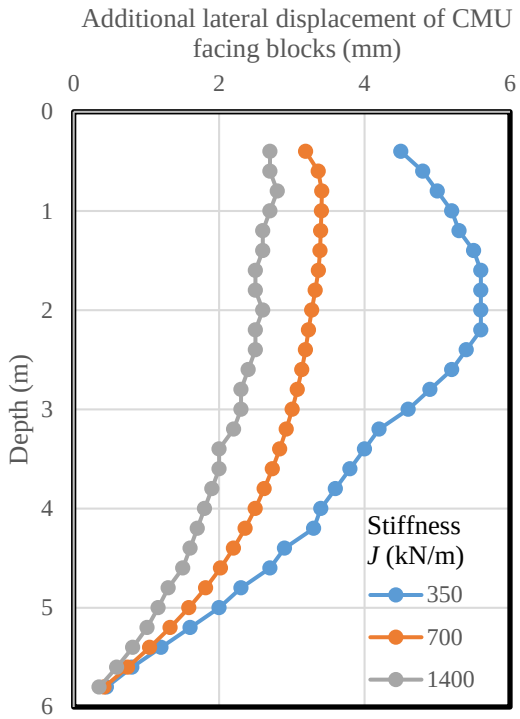

Fig. 7.4.46: Effect of the reinforcement stiffness on the additional lateral displacement of CMU facing blocks induced by traffic load

7.4.5.3.4 Settlement profile for the bridge slab and integrated approach

Figure 7.4.47 shows the effect of the reinforcement stiffness on the additional settlement on top of the bridge slab and integrated approach induced by traffic load (i.e., the difference of the settlement between Stage 6 and Stage 5). Figure 7.4.47 shows that the use of stiffer reinforcement also led to a reduced traffic-induced settlement of both the bridge slab and the integrated approach. Differential settlement happened at the end of the bridge slab. The use of stiffer reinforcement also led to reduced differential settlements.

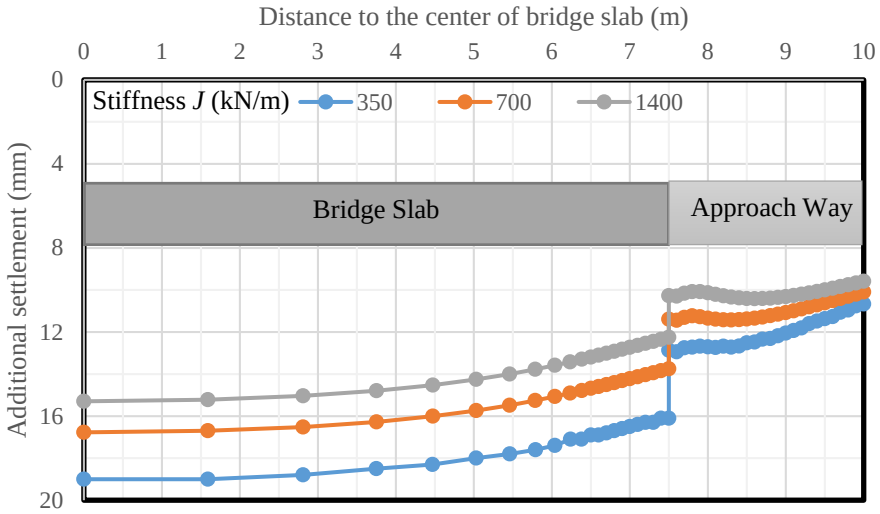

Fig. 7.4.47: Effect of the reinforcement stiffness on the additional settlement of the bridge slab and integrated approach induced by traffic load

7.4.5.3.5 Volume change of the abutment

Figure 7.4.48 shows the normalized lateral volume change – normalized vertical volume change curves with different reinforcement stiffness. Figure 7.4.48 indicate that the abutment underwent more vertical compression than lateral deflection, which is not consistent with the zero volume change assumption reported by Adams et al. (2002). The use of stiffer reinforcement resulted in comparatively smaller vertical compression and lateral deflections. The slope of all three lines are smaller than 1, indicating that reinforcement was more effective in reducing the lateral deflection of the abutment than reducing the vertical compression.

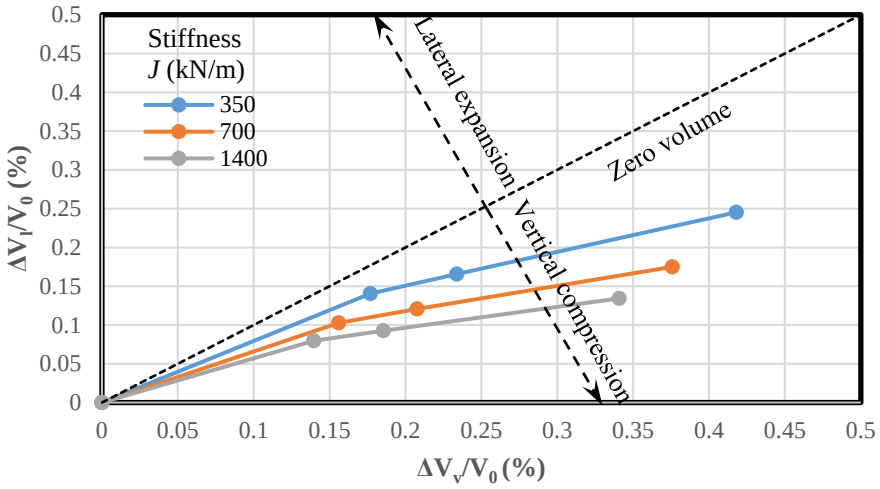

Fig. 7.4.48: Effect of the reinforcement stiffness on the volume change of the GRS-IBS abutment

Table 7.4.16 summarizes the effect of the reinforcement stiffness on the maximum vertical and lateral displacements of the abutment. Consistent with the data presented in Fig. 7.4.48, all the displacements presented in Table 7.4.16 excluded the displacement of the abutment in Stage 3. In other words, the displacement of the abutment was initialized after the construction of the abutment and the beam seat were finished.

Table 7.4.16: Effect of the reinforcement stiffness on the maximum vertical and lateral displacements of the abutment

Stiffness (kN/m)	Displacement (mm)	Construction stage		
		Stage 4 (bridge slab)	Stage 5 (Integrated approach)	Stage 6 (traffic load)
350	$\delta_{v\text{-max}}$	41.28	43.38	59.48
	$\delta_{l\text{-max}}$	13.77	14.67	19.80
700	$\delta_{v\text{-max}}$	35.36	37.19	51.06
	$\delta_{l\text{-max}}$	10.63	11.18	14.54
1400	$\delta_{v\text{-max}}$	31.91	33.61	45.91
	$\delta_{l\text{-max}}$	8.60	9.00	11.70

7.4.5.3.6 Tension in the reinforcement

Figure 7.4.49 shows the maximum tensile force in the reinforcement T_{max} with different reinforcement stiffness under both self-weight (i.e., Stage 2) and traffic load conditions (i.e., Stage 6). Under self-weight, the effect of reinforcement stiffness was not significant. Specifically, T_{max} in the reinforcements was found to be essentially the same except that the increase of reinforcement stiffness resulted in slightly higher T_{max} in the reinforcement towards the bottom of the wall. Under traffic loads, T_{max} showed a comparatively large increase towards the top of the wall. The use of stiffer reinforcement resulted in larger T_{max} in the primary reinforcement throughout the entire wall height. T_{max} in the bearing reinforcement layers, however, decreased with increasing reinforcement stiffness, indicating that the use of stiffer reinforcement reduced the contribution of the bearing reinforcement layers.

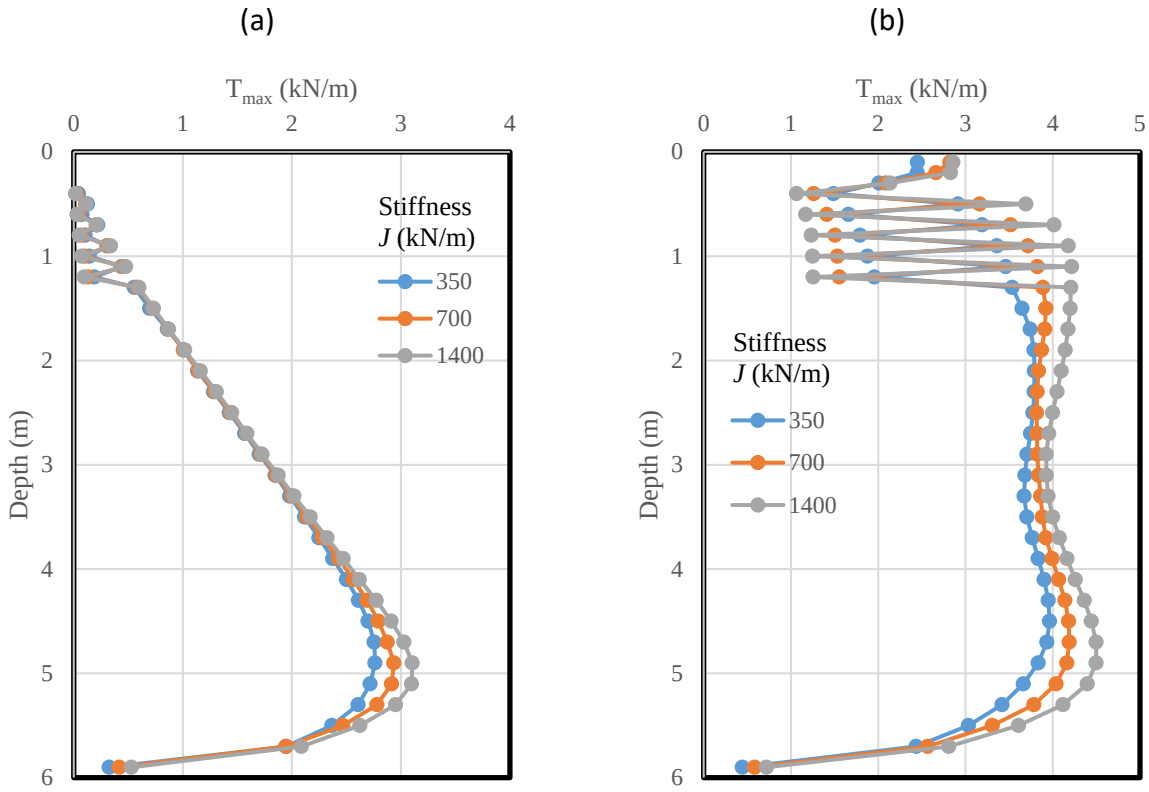

Fig. 7.4.49: Effect of the reinforcement stiffness on the maximum tensile force T_{max} in the reinforcement: (a) Self-weight; (b) Traffic load.

Figure 7.4.50 shows the ratio of the connection force T_0 to the maximum tensile force T_{max} in the reinforcement for different reinforcement stiffness under both self-weight (i.e., Stage 2) and traffic load conditions (i.e., Stage 6). Figure 7.4.50 shows that the magnitude of the connection force T_0 was similar to the maximum tensile force T_{max} in the reinforcement, indicating that T_{max} developed in the vicinity of the wall facing. The magnitude of reinforcement stiffness did not affect significantly the ratio of T_0 to T_{max}.

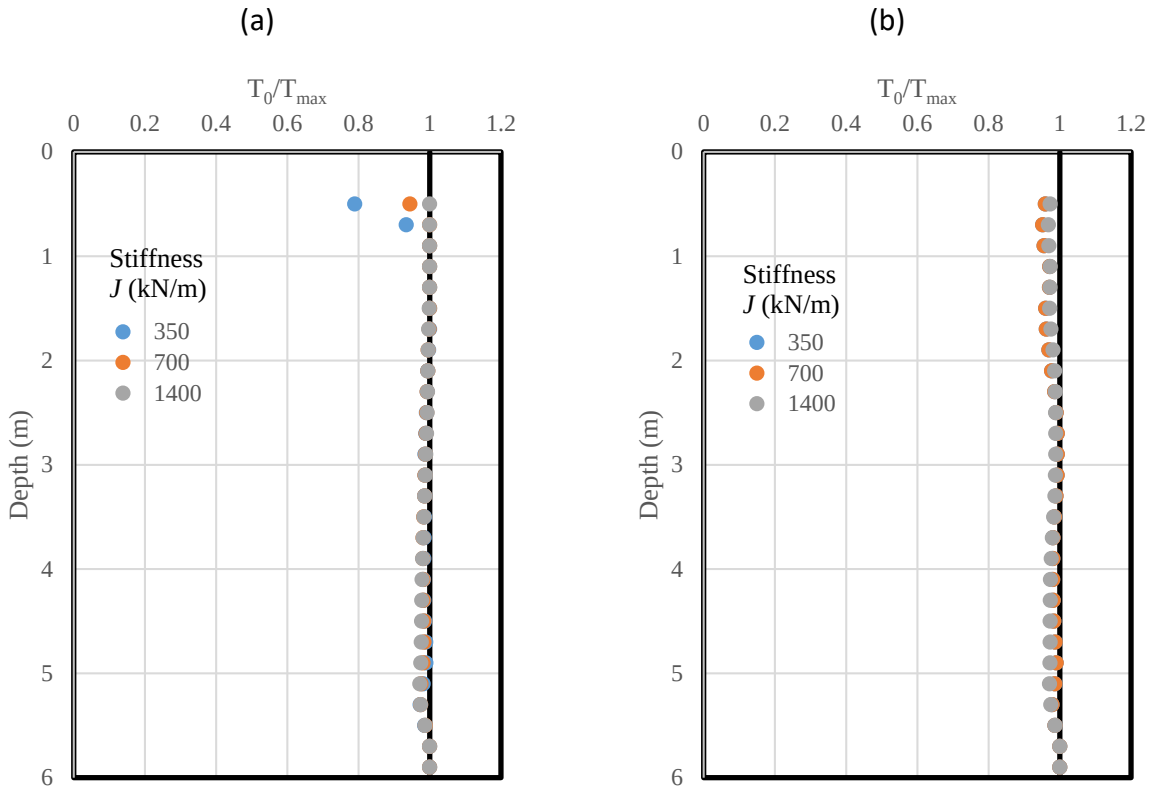

Fig. 7.4.50: Effect of the reinforcement stiffness on the ratio of connection force T_0 to the maximum tensile force T_{max} in the reinforcement: (a) Self-weight; (b) Traffic load.

Figure 7.4.51 shows the normalized coefficient of lateral earth pressure K_r/K_a with different reinforcement stiffness under both self-weight (i.e., Stage 2) and traffic load conditions (i.e., Stage 6). The determination of σ_v under different loading conditions was discussed in Section 7.4.5.2.6 (i.e., using the overburden stress and the AASHTO 2 to1 truncation method without surcharge q). Figure 7.4.51 shows that the distribution of K_r/K_a was similar to that of T_{max}. Under the self-weight, the effect of the reinforcement stiffness on K_r/K_a was minimum. Under the traffic load, however, the increase of the reinforcement stiffness resulted in larger T_{max} and thus larger K_r/K_a since the additional vertical stress σ_v did not change significantly as previously shown in Fig. 7.4.44. The phenomenon of K_r/K_a being approximately 0.8 along depth has already been explained in Section 7.4.5.2.6.

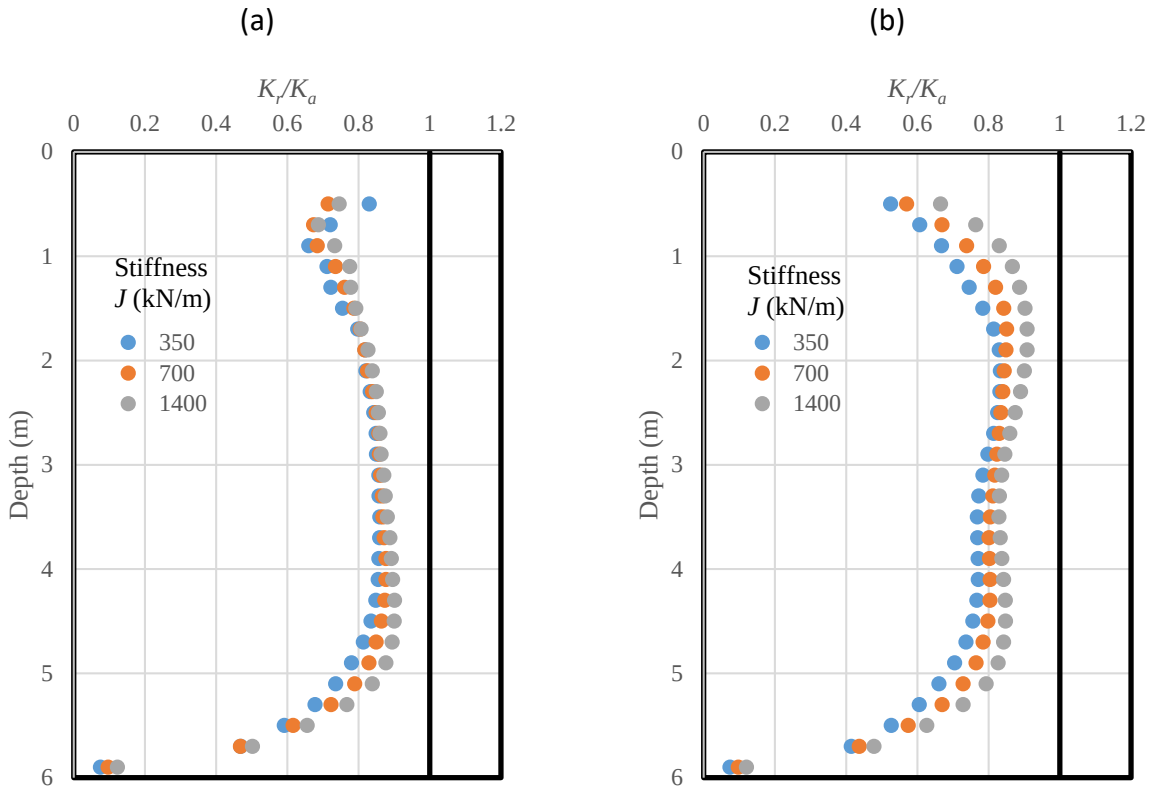

Fig. 7.4.51: Effect of the reinforcement stiffness on the normalized coefficient of lateral earth pressure K_l/K_a: (a) Self-weight; (b) Traffic load.

7.4.5.4 EFFECT OF REINFORCEMENT SPACING

This section discusses the effect of the reinforcement spacing on the performance of GRS-IBS. In the baseline model, the reinforcement spacing S_v was 0.2 m (8 in). Two additional reinforcement vertical spacing values, S_v, were considered in this parametric study: 0.4 m (16 in) and 0.6 m (24 in or 2 ft). When the reinforcement spacing S_v was larger than 0.2 m (8 in), two CMU facing blocks were connected with each other without having a geotextile reinforcement in between. In other words, the interfaces between CMU facing blocks was considered. Based on the recommendation by Eurocode 2 (British Standards Institution, 2004), a friction coefficient of 0.6 was assigned to the interface between CMU facing blocks in the numerical analysis. Consequently, the interface friction angle between CMU blocks was equal to $\arctan(0.6) = 31.0°$. The normal and shear stiffness values of the interface between CMU facing blocks were the same as those adopted for the interface between CMU facing blocks and geotextile reinforcement. Table 7.4.17 summarizes the properties of the interface between CMU facing blocks used in the numerical analysis.

Table 7.4.17: Properties of the interface between CMU facing blocks

Interface	Method	k_n (N/m/m)	k_s (N/m/m)	Frictional coefficient μ	Friction angle (°)	Cohesion (kPa)
CMU – CMU (Frictional Connection)	Interface	1×10^9	4×10^7	0.6	31.0	0

7.4.5.4.1 Lateral earth pressures

Figure 7.4.52 shows the effect of the reinforcement spacing on the lateral earth pressure behind the CMU facing blocks under both self-weight (i.e., Stage 2) and traffic load conditions (i.e., Stage 6). Under self-weight, the lateral earth pressures behind the wall facing were close to the theoretical Coulomb's active lateral pressure distribution and were essentially not affected by the change of reinforcement spacing S_v. Under traffic load, however, increasing reinforcement spacing S_v led to a reduction in the the lateral earth pressures behind wall facing, especially when S_v increased from 0.2 m (8 in) to 0.4 m (16 in). When close reinforcement spacing was used, the lateral displacement of CMU facing blocks decreased, which will be further discussed in Section 7.4.5.4.3. A reduction in the wall facing displacement resulted in higher lateral earth pressures behind the wall.

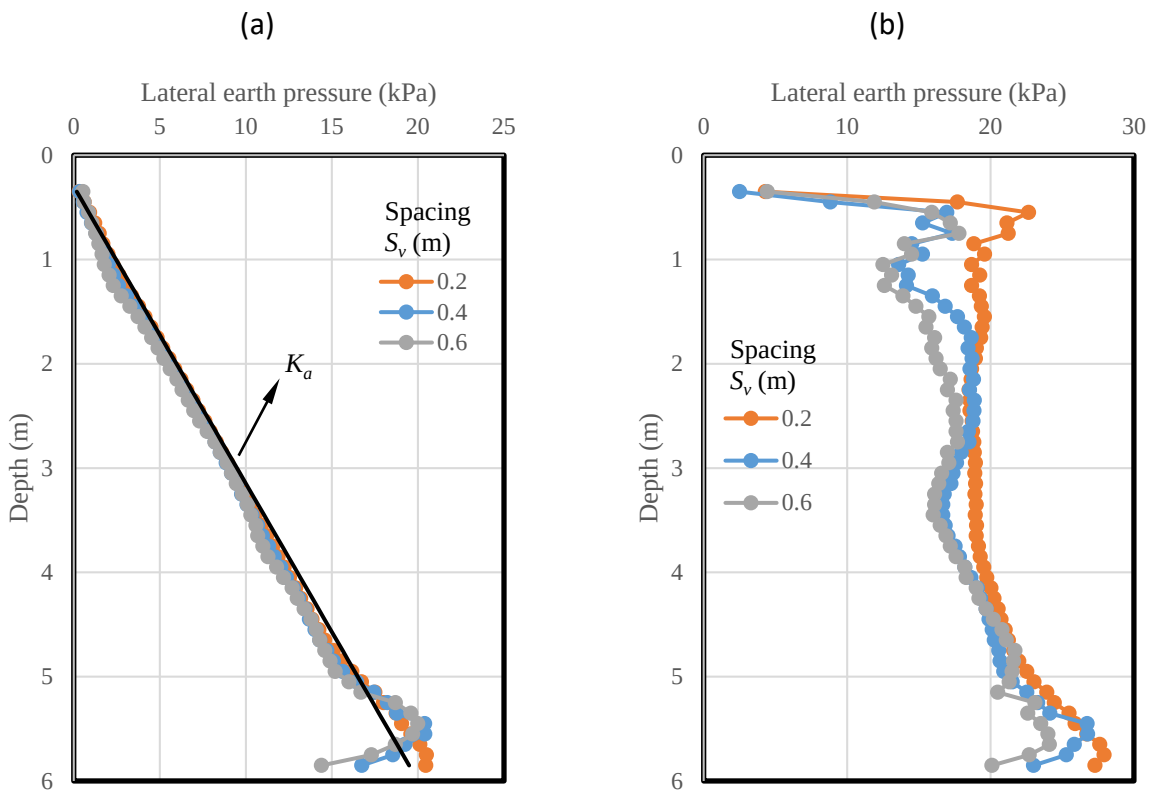

Fig. 7.4.52: Effect of the reinforcement spacing on the lateral earth pressure behind CMU facing blocks: (a) Self-weight; (b) Traffic load.

7.4.5.4.2 Additional vertical stress induced by loading

Figure 7.4.53 shows the effect of the reinforcement spacing on the distribution of additional vertical stress Δp at 0.5 m (20 in) from the back of CMU facing blocks with the depth induced by loading. Figure 7.4.53 also shows the calculated additional vertical stress using the AASHTO 2 to 1 truncation method. Figure 7.4.53 shows that the additional vertical stress Δp did not change much despite the change of the reinforcement spacing. The increase of the reinforcement spacing resulted in slightly lower additional vertical stress induced by loading. The minor change in Δp may be due to the small loading area of the bridge slab (i.e., the beam seat width b = 0.6 m (2 ft) was small). The AASHTO 2 to 1 truncation method resulted in an estimate of the additional stresses that was in reasonable agreement with the numerical results.

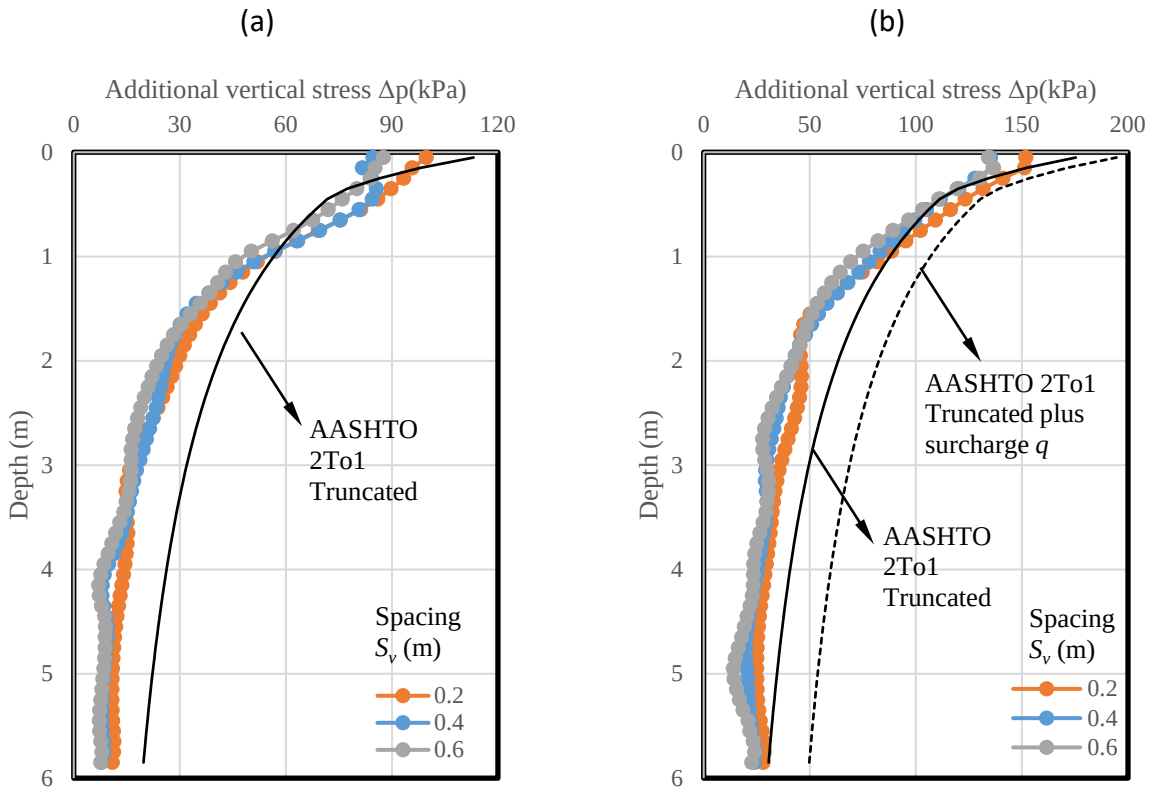

Fig. 7.4.53: Effect of the reinforcement spacing on the additional vertical stress induced by loading: (a) Induced by the self-weight of the bridge slab; (b) Induced by the self-weight of the bridge slab and the traffic load.

7.4.5.4.3 Lateral displacement of CMU facing blocks

Figure 7.4.54 shows the effect of the reinforcement spacing on the lateral displacement of CMU facing blocks under self-weight (i.e., Stage 2), bridge slab (i.e., Stage 4), and traffic load conditions (i.e., Stage 6). As expected, a decrease in reinforcement spacing led to a large reduction in lateral displacements of CMU facing blocks. Specifically, a decrease in reinforcement spacing caused a smaller maximum lateral displacement occurred approximately at mid-height of the wall. In

addition, a decreasing reinforcement spacing led to a more uniform wall deflection profile along depth.

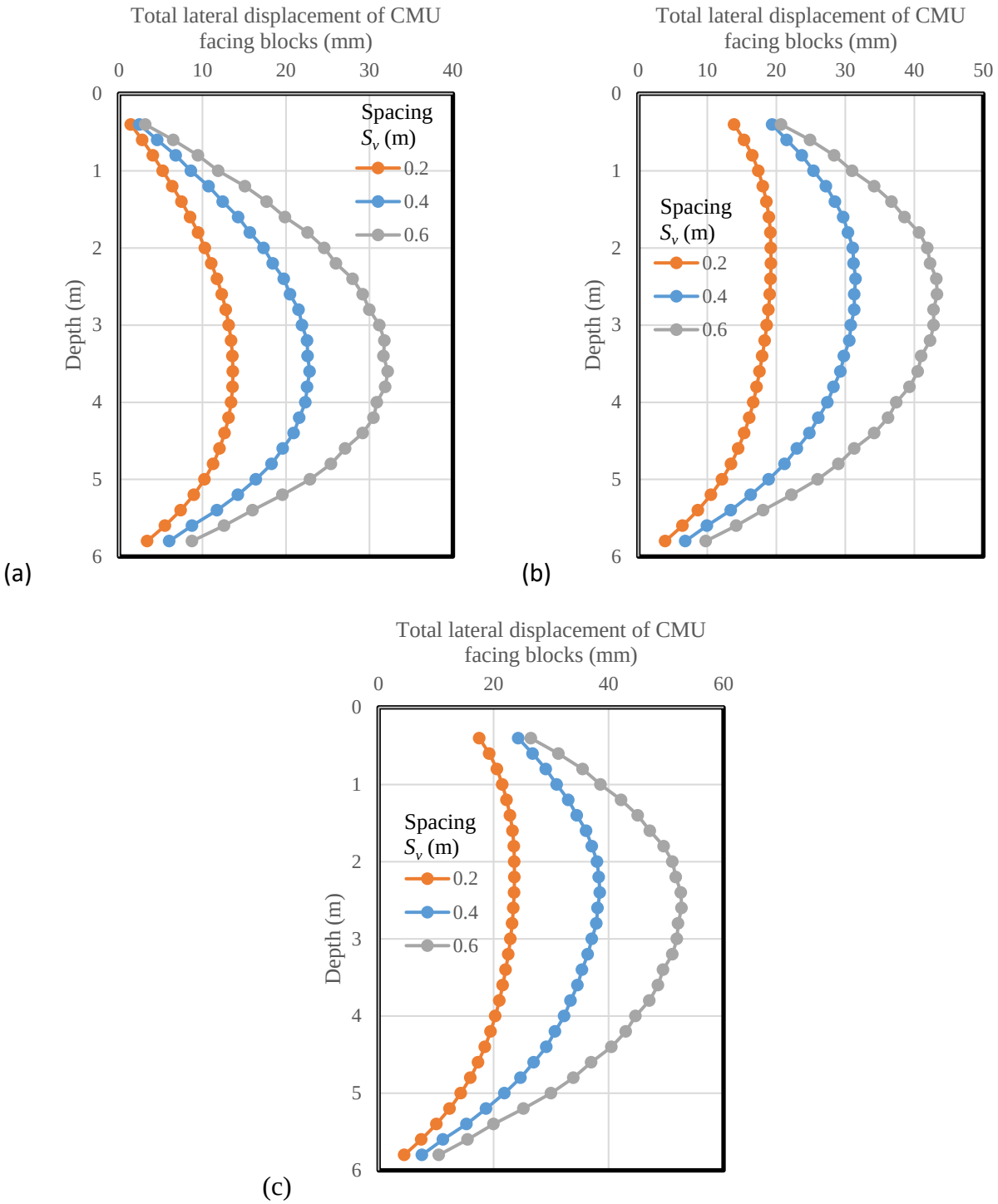

Fig. 7.4.54: Effect of the reinforcement spacing on the lateral displacement of CMU facing blocks: (a) Self-weight; (b) Bridge slab; (c) Traffic load.

Figure 7.4.55 shows the effect of the reinforcement spacing on the additional lateral displacement of CMU facing blocks induced by the traffic load only (i.e., the difference of the lateral displacements between Stage 6 and Stage 5). Figure 7.4.55 indicates that the decreaseof the reinforcement spacing also decreased the additional lateral displacement of wall facing due to the traffic load. When the reinforcement spacing was 0.2 m (8 in), the maximum additional lateral displacement of wall facing happened within the upper portion of the wall. When the reinforcement spacing was larger than 0.2 m (8 in), however, the location of the maximum additional lateral displacement of wall facing moved down to the middle height of the wall. The change of the reinforcement spacing changed the distribution of additional lateral displacement of CMU facing blocks along the height of the wall.

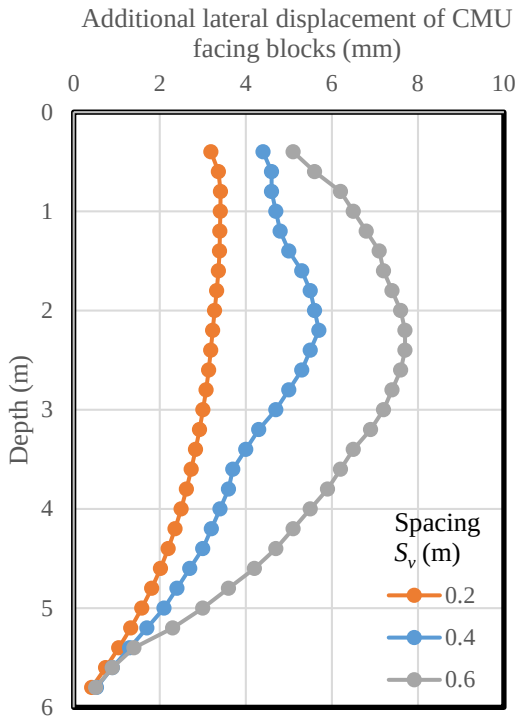

Fig. 7.4.55: Effect of the reinforcement spacing on the additional lateral displacement of CMU facing blocks induced by traffic load

7.4.5.4.4 Settlement profile for the bridge slab and integrated approach

Figure 7.4.56 shows the effect of the reinforcement spacing on the additional settlement on top of the bridge slab and integrated approach induced by traffic load (i.e., the difference of the settlement between Stage 6 and Stage 5). Figure 7.4.56 shows that a reduction in the reinforcement spacing led to reduced settlement of both the bridge slab and the integrated approach. The differential settlement that developed at the end of bridge slab was also reduced. This is because the reduction of the reinforcement spacing reduced the lateral deformation of the wall as shown in Fig. 7.4.55, thus reducing the settlement.

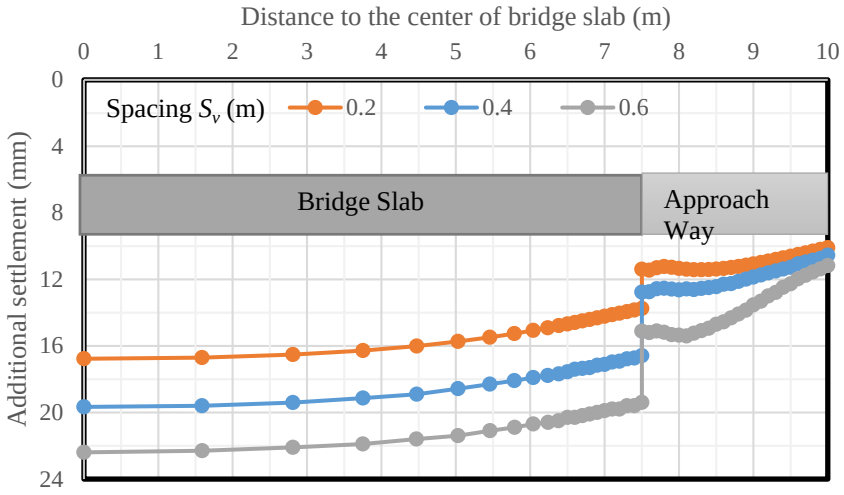

Fig. 7.4.56: Effect of the reinforcement spacing on the additional settlement of the bridge slab and integrated approach induced by traffic load

7.4.5.4.5 Volume change of the abutment

Figure 7.4.57 shows the effect of the reinforcement spacing on the normalized lateral volume change – normalized vertical volume change curves. Figure 7.4.57 shows that the abutment had more vertical compression than lateral deflection. The decrease of the reinforcement spacing reduced both the lateral deflection and the vertical compression, resulting in the relationship in Fig. 7.4.57 further away from the zero volume change line. The line for close reinforcement spacing was below the linefor large reinforcement spacing, indicating that the contribution of close reinforcement spacing to the reduction of the lateral deflection of the abutment was more significant than that to the reduction of the vertical compression.

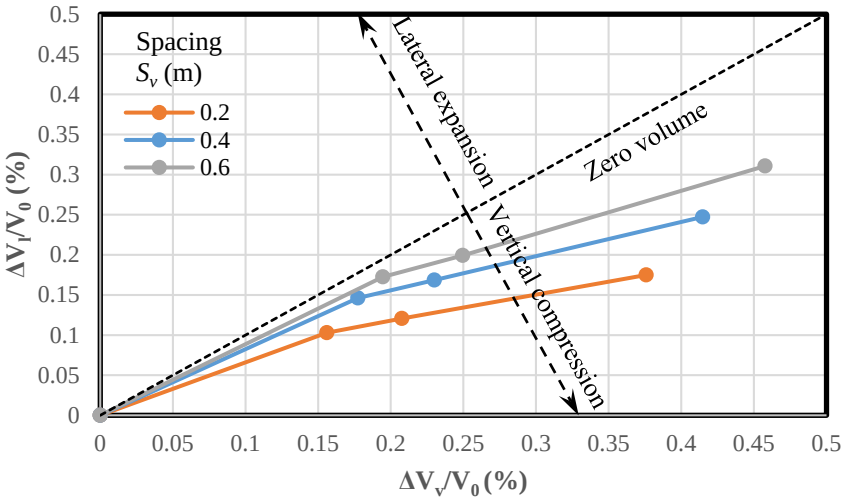

Fig. 7.4.57: Effect of the reinforcement spacing on the volume change of the GRS-IBS abutment

Table 7.4.18 summarizes the effect of the reinforcement stiffness on the maximum vertical and lateral displacements of the abutment. It should be noted that the displacements presented in Table 7.4.18 exclude the displacements of the abutment in Stage 3. In other words, the displacements of the abutment were initialized after the construction of the abutment and the beam seat were finished.

Table 7.4.18: Effect of the reinforcement spacing on the maximum vertical and lateral displacements of the abutment

Spacing (m)	Displacement (mm)	Construction stage		
		Stage 4 (bridge slab)	Stage 5 (integrated approach)	Stage 6 (traffic load)
0.2	$\delta_{v\text{-max}}$	35.36	37.19	51.06
	$\delta_{l\text{-max}}$	10.63	11.18	14.54
0.4	$\delta_{v\text{-max}}$	40.39	42.29	59.09
	$\delta_{l\text{-max}}$	14.02	14.71	19.4
0.6	$\delta_{v\text{-max}}$	44.43	46.63	66.13
	$\delta_{l\text{-max}}$	15.30	16.50	23.60

7.4.5.4.6 Tension in the reinforcement

Figure 7.4.58 shows the effect of the reinforcement spacing on the maximum tensile force of the reinforcement T_{max} under both self-weight (i.e., Stage 2) and traffic load conditions (i.e., Stage 6). As expected, a decrease in the reinforcement vertical spacing resulted in thedecrease of the maximum tensile force T_{max} in the reinforcement. Under the self-weight, the maximum tensile forces T_{max} in the reinforcement with the depth were 2.94 kN/m (201 lb/ft), 5.36 kN/m (367 lb/ft), and 7.69 kN/m (527 lb/ft) for the cases with the reinforcement spacing of 0.2 m (8 in), 0.4 m (16 in), and 0.6 m (24 in or two ft) respectively. Under the traffic load, the maximum tensile forces T_{max} in the reinforcement with depth were 4.19 kN/m (287 lb/ft), 7.52 kN/m (515 lb/ft), and 10.97 kN/m (752 lb/ft) for the cases with the reinforcement spacing of 0.2 m (8 in), 0.4 m (16 in), and 0.6 m (24 in or 2 ft) respectively. Therefore, the numerical results showed that T_{max} decreased with an approximately proportional trend with decreasing reinforcement spacing under both self-weight and traffic load.

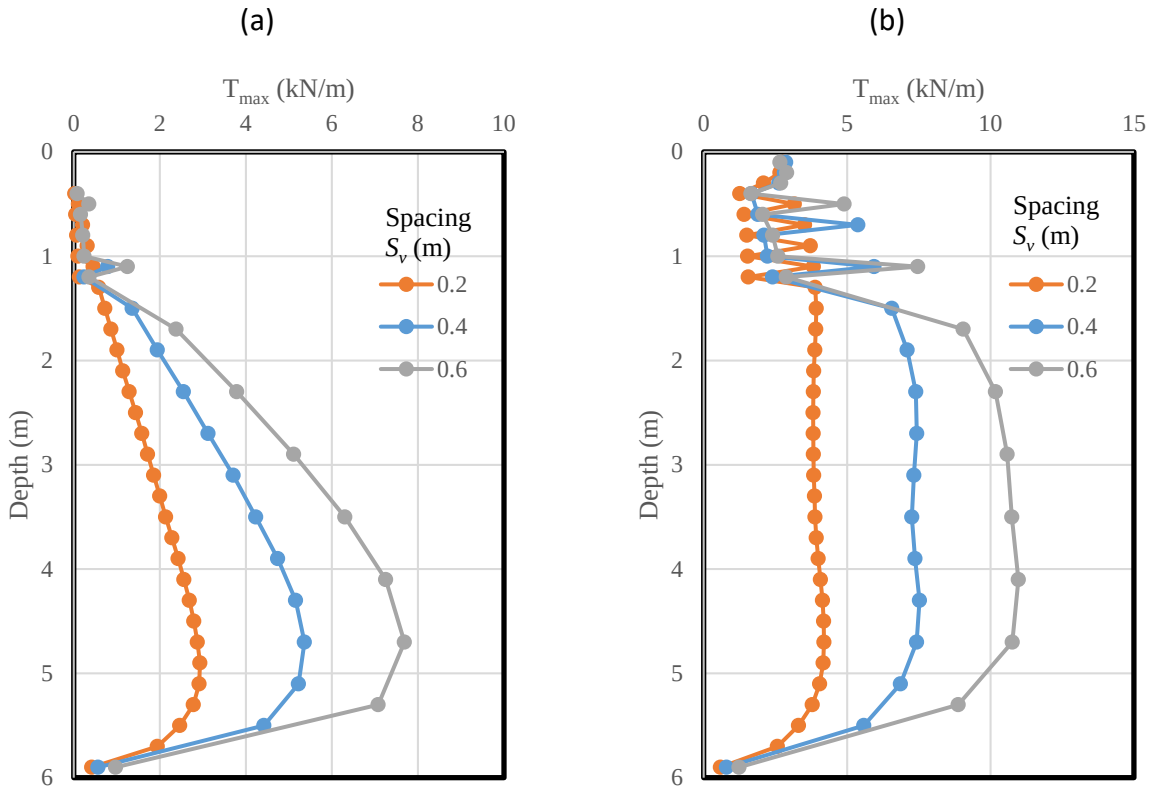

Fig. 7.4.58: Effect of the reinforcement spacing on the maximum tensile force T_{max} in the reinforcement: (a) Self-weight; (b) Traffic load.

Figure 7.4.59 shows the effect of the reinforcement spacing on the ratio of the connection force T_0 to the maximum tensile force T_{max} in the reinforcement under both self-weight (i.e., Stage 2) and traffic load conditions (i.e., Stage 6). Figure 7.4.59 shows that the ratio of T_0 to T_{max} was close to 1.0 under both the self-weight and the traffic load, indicating that the maximum tensile force in the reinforcement happened close to the wall facing connection. The change of reinforcement spacing did not have a significant effect on the ratio of T_0 to T_{max}.

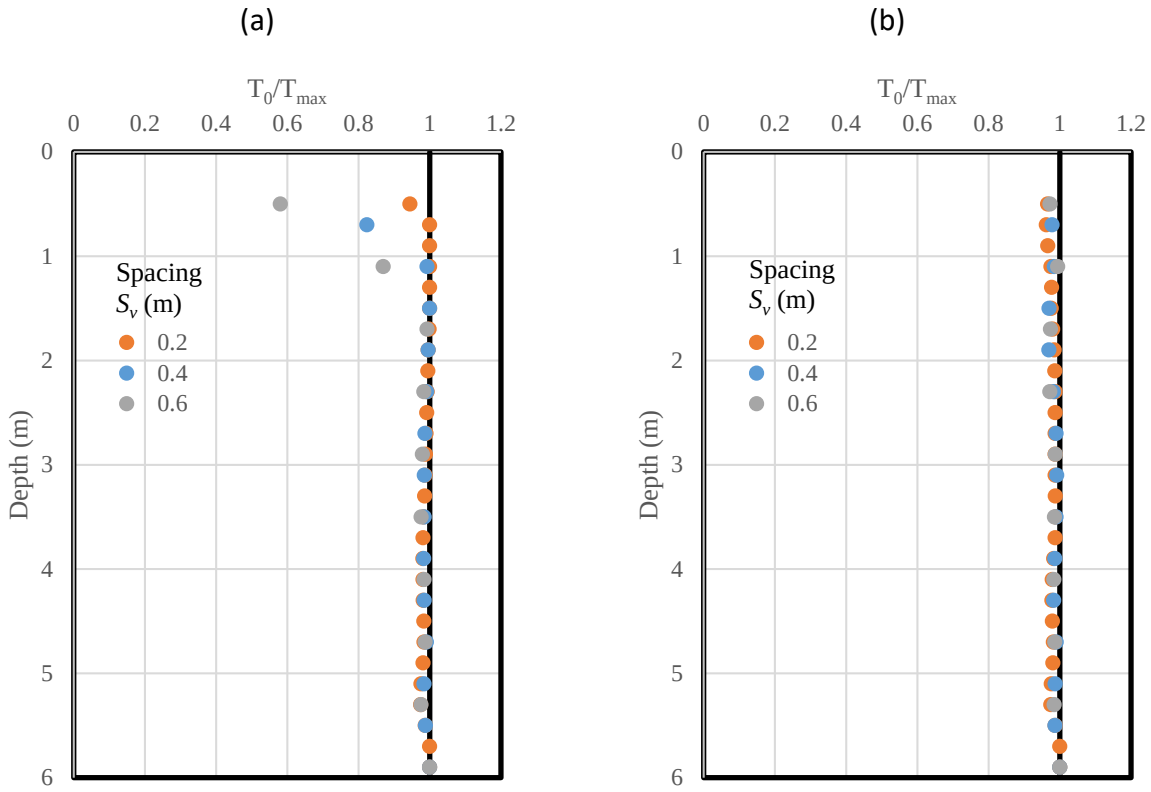

Fig. 7.4.59: Effect of the reinforcement spacing on the ratio of connection force T_0 to the maximum tensile force T_{max} in the reinforcement: (a) Self-weight; (b) Traffic load.

Figure 7.4.60 shows the effect of the reinforcement spacing on the normalized coefficient of lateral earth pressure K_r/K_a under both self-weight (i.e., Stage 2) and traffic load conditions (i.e., Stage 6). The determination of σ_v under different loading conditions was discussed in Section 7.4.5.2.6 (i.e., using the overburden stress and the AASHTO 2 to1 truncation method without surcharge q). Figure 7.4.60 shows that the decrease of the reinforcement spacing resulted in the decrease of the normalized coefficient of lateral earth pressure K_r/K_a, especially near the top and bottom of the wall. At the middle height of the wall, the influence of the reinforcement spacing on the normalized coefficient of lateral earth pressure K_r/K_a was limited. The phenomenon of K_r/K_a being approximately 0.8 along depth has already been explained in Section 7.4.5.2.6.

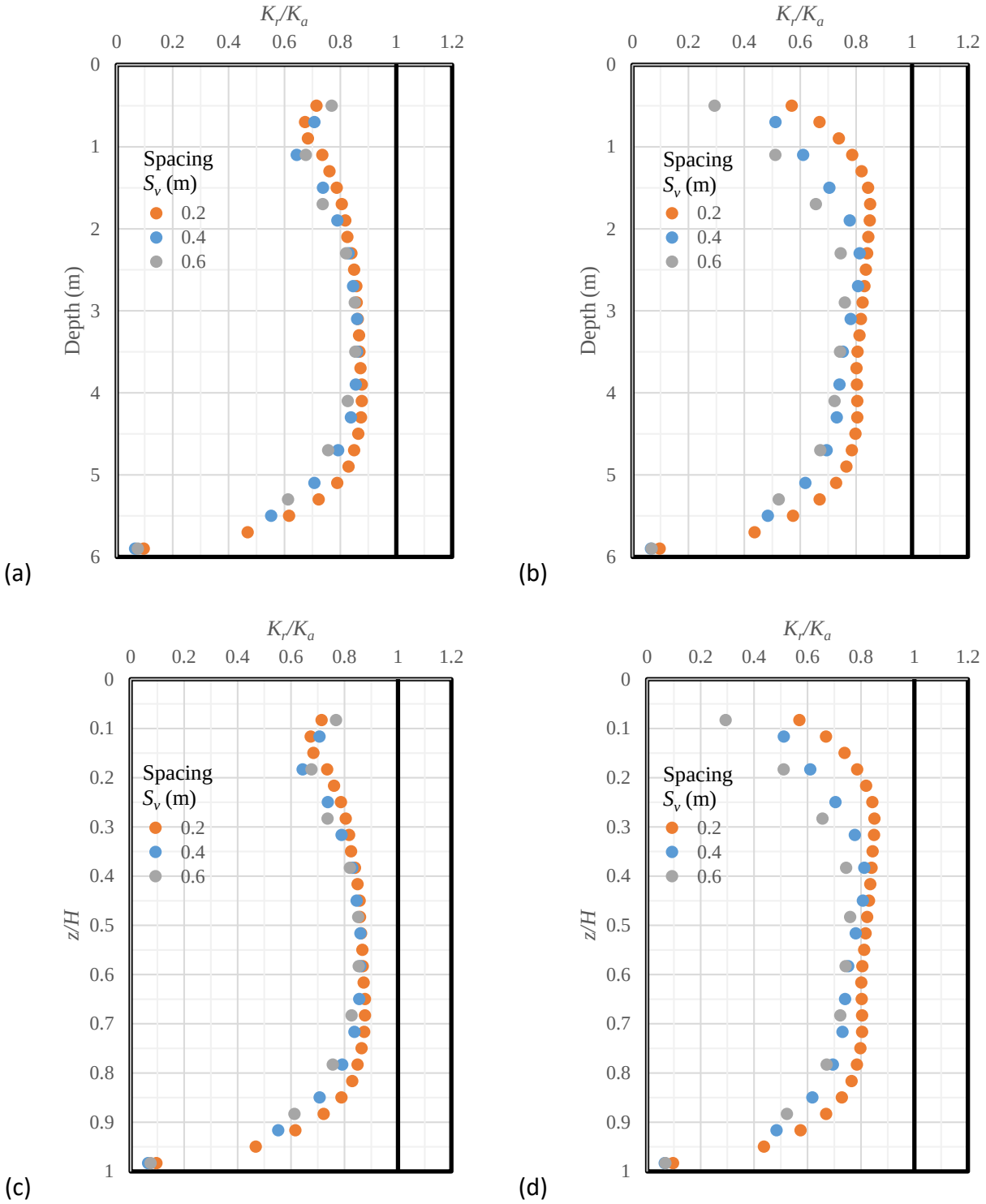

Fig. 7.4.60: Effect of the reinforcement spacing on the normalized coefficient of lateral earth pressure K_r/K_a: (a) Distribution under self-weight with depth; (b) Distribution under traffic load with depth; (c) Distribution under self-weight with normalized depth; (d) Distribution under traffic load with normalized depth.

7.4.5.5 EFFECT OF COMBINATION OF REINFORCEMENT STIFFNESS AND SPACING

This section discusses the combined effect of the reinforcement stiffness (also of the ultimate tensile strength) and the vertical spacing. Three cases were evaluated in this section: Case 1 (J = 1050 kN/m (72 kip/ft), T_f = 105 kN/m (7200 lb/ft), S_v = 0.6 m (24 in or 2 ft)), Case 2 (J = 700 kN/m (48 kip/ft), T_f = 70 kN/m (4800 lb/ft), S_v = 0.4 m (16 in)), and Case 3 (J = 350 kN/m (24 kip/ft), T_f = 35 kN/m (2400 lb/ft), S_v = 0.2 m (8 in)). Case 1, 2, and 3 utilized 10, 14, and 28 primary reinforcement layers respectively. In all three cases, the ratio of reinforcement stiffness to spacing was maintained the same as J/S_v = 1750 kN/m/m (36550 lb/ft/ft). However, the first case involved use of a larger reinforcement vertical spacing with stiffer reinforcement than the other two cases. This study aimed to investigate the effect of different combinations of J and S_v on the performance of the abutment while maintaining the same J/S_v ratio.

7.4.5.5.1 Lateral earth pressures

Figure 7.4.61 shows the effect of reinforcement stiffness and vertical spacing on the lateral earth pressure behind the CMU facing blocks under both self-weight (i.e., Stage 2) and traffic load conditions (i.e., Stage 6). Figure 7.4.61 shows that the lateral earth pressure behind the wall was essentially the same for all three cases under the self-weight and was close to the theoretical Coulomb active lateral earth pressure. Under the traffic load, results from all three cases were also close, except for slight difference near the top of the wall.

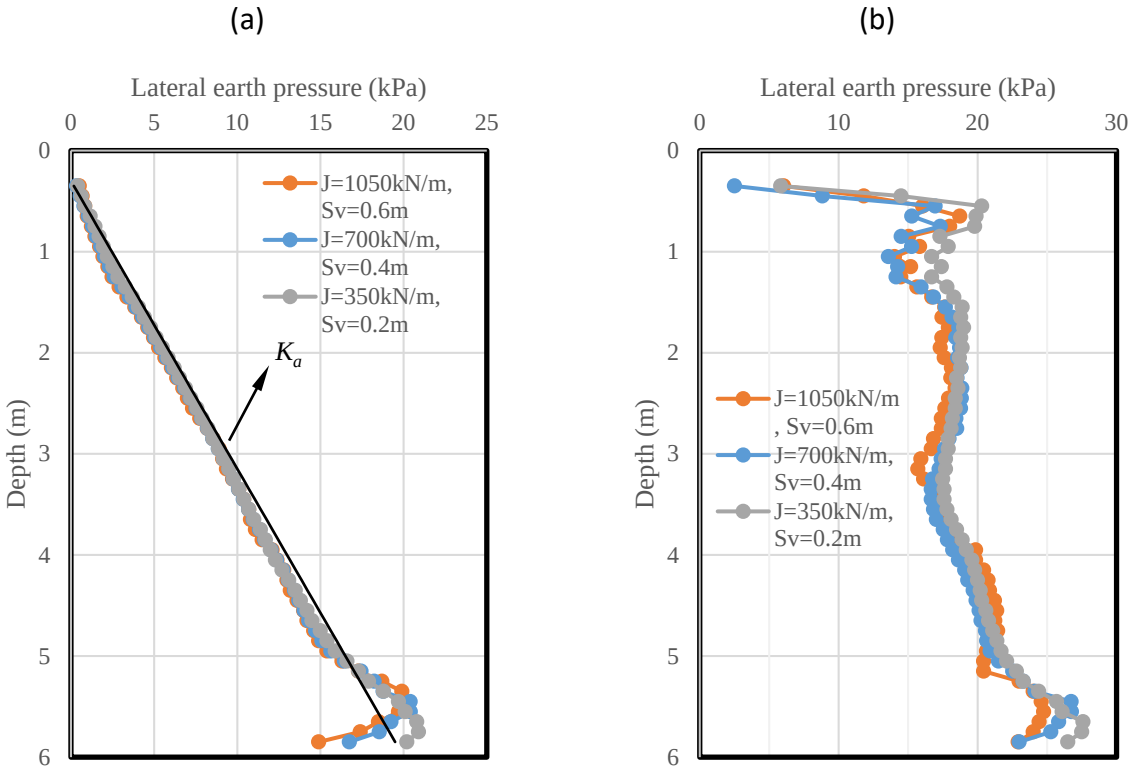

Fig. 7.4.61: Effect of combination of reinforcement stiffness and spacing on the lateral earth pressure behind CMU facing blocks: (a) Self-weight; (b) Traffic load.

7.4.5.5.2 Additional vertical stress induced by loading

Figure 7.4.62 shows the combined effect of reinforcement stiffness and vertical spacing on the distribution of additional vertical stress Δp at 0.5 m (20 in) from the back of CMU facing blocks with the depth induced by loading. Figure 7.4.62 shows that the additional vertical stress induced by loading was almost the same for all three cases except for the small difference near the top of the wall. The AASHTO 2 to 1 truncation method calculated the additional vertical stresses in reasonable agreement with the numerical results.

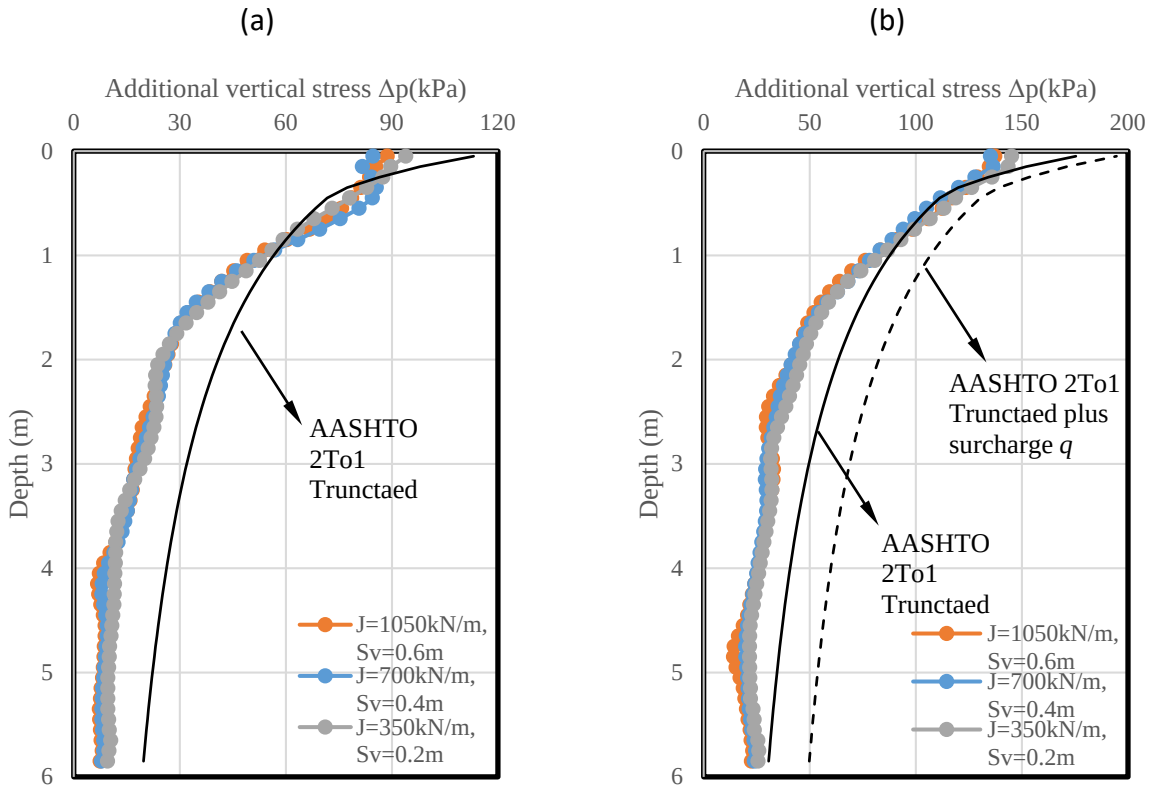

Fig. 7.4.62: Effect of combination of reinforcement stiffness and spacing on the additional vertical stress induced by loading: (a) Induced by the self-weight of the bridge slab; (b) Induced by the self-weight of the bridge slab and the traffic load.

7.4.5.5.3 Lateral displacement of CMU facing blocks

Figure 7.4.63 shows the combined effect of reinforcement stiffness and vertical spacing on the lateral displacements of CMU facing blocks under self-weight (i.e., Stage 2), bridge slab (i.e., Stage 4), and traffic load conditions (i.e., Stage 6). Figure 7.4.63 indicate that the case with the least stiff reinforcement and smallest vertical spacing (i.e., Case 3) resulted in slightly smaller lateral displacements of CMU facing blocks near the mid-height of the wall. At the top or bottom of the wall, the lateral displacements of the wall facing were essentially the same for all three cases.

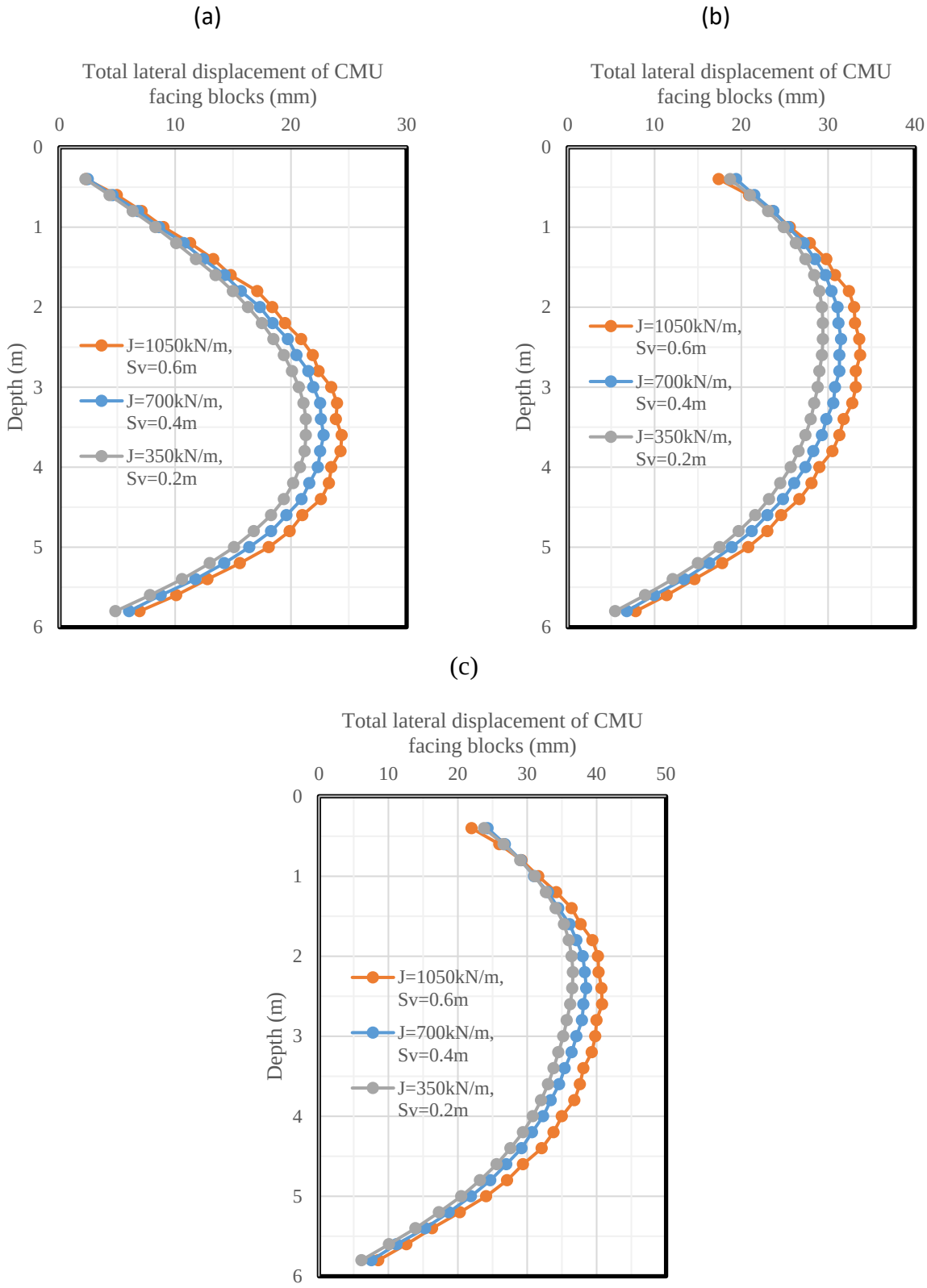

Fig. 7.4.63: Effect of combination of reinforcement stiffness and spacing on the lateral displacement of CMU facing blocks: (a) Self-weight; (b) Bridge slab; (c) Traffic load.

Figure 7.4.64 shows the combined effect of reinforcement stiffness and vertical spacing on the additional lateral displacement of CMU facing blocks induced by traffic load only (i.e., the difference of lateral displacements between Stage 6 and Stage 5). Figure 7.4.64 shows that the case with the stiffest reinforcement and largest spacing (i.e., Case 1) resulted in the largest additional lateral displacements of CMU facing blocks due to the fact that the largest reinforcement spacing provided the least lateral restraint. Figure 7.4.64 also shows that the additional lateral displacements of CMU facing blocks were almost the same for Case 2 and Case 3 from the bottom to the mid-height of the wall. Near the top of the wall (i.e., at the depth smaller than 2 m (6.5 ft)), the case with stiffer reinforcement and larger vertical spacing (i.e., Case 2) resulted in smaller additional lateral displacement. However, their difference was smaller than 1 mm (0.04 in). It could be concluded from the numerical results that the wall deflections were essentially the same for Case 2 and Case 3.

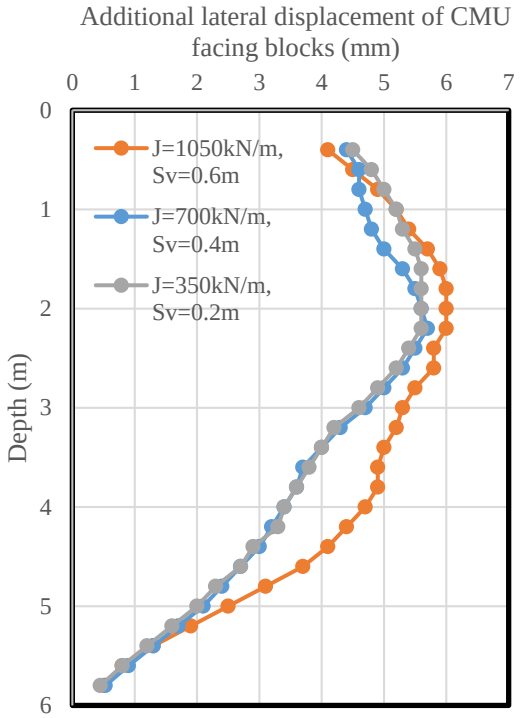

Fig. 7.4.64: Effect of combination of reinforcement stiffness and spacing on the additional lateral displacement of CMU facing blocks induced by traffic load

7.4.5.5.4 Settlement profile for the bridge slab and integrated approach

Figure 7.4.65 shows the combined effect of reinforcement stiffness and vertical spacing on the additional settlement on top of the bridge slab and integrated approach induced by the traffic load (i.e., the difference of settlement between Stage 6 and Stage 5). Figure 7.4.65 shows that the settlement on top of the integrated approach way was essentially the same for all three cases. For the settlement of the bridge slab, Case 2 resulted in slightly small settlement. However, the difference between two cases was smaller than 1.0 mm (0.04 in).

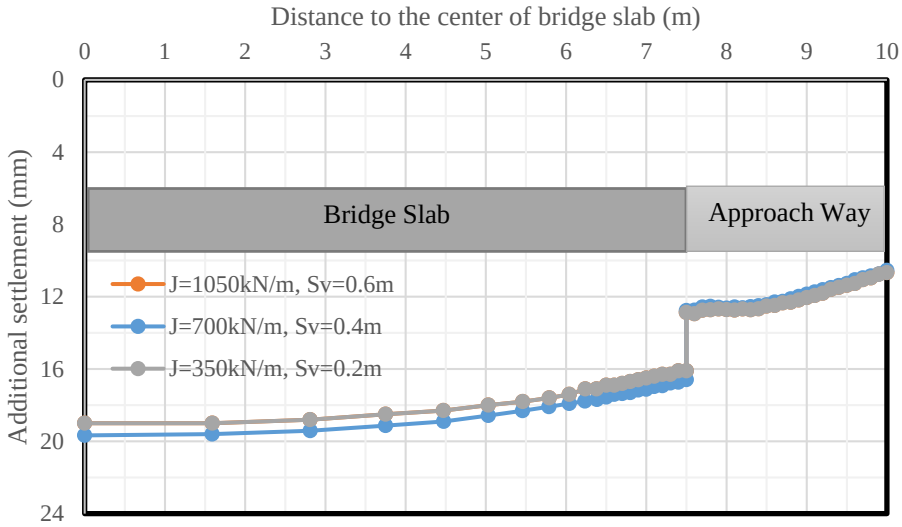

Fig. 7.4.65: Effect of combination of reinforcement stiffness and spacing on the additional settlement of the bridge slab and integrated approach induced by traffic load

7.4.5.5.5 Volume change of the abutment

Figure 7.4.66 shows the combined effect of reinforcement stiffness and vertical spacing on the normalized lateral volume change – normalized vertical volume change curves. Figure 7.4.66 shows that their relationships of all three cases overlapped, indicating that the volume change of the abutment was almost the same under the same ratio of J/S_v despite the change of reinforcement stiffness and vertical spacing.

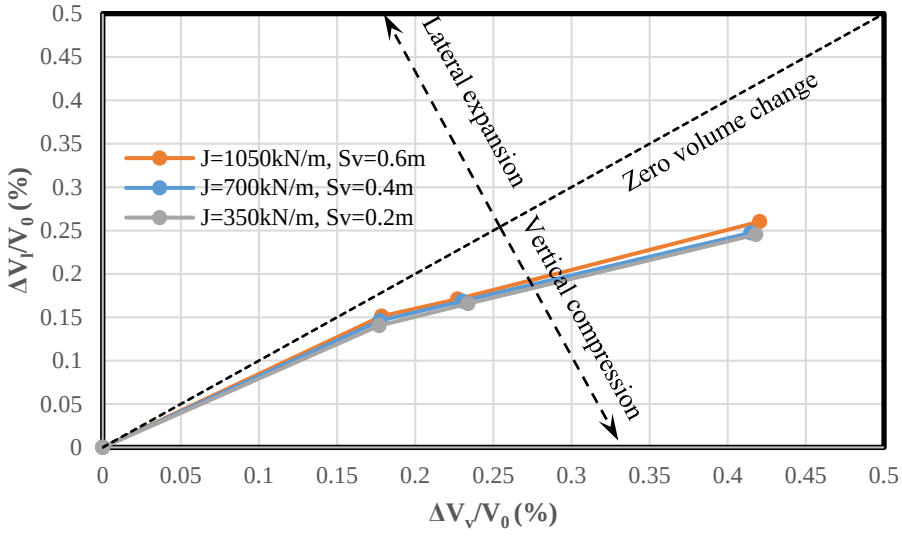

Fig. 7.4.66: Effect of combination of reinforcement stiffness and spacing on the volume change of the GRS-IBS abutment

Table 7.4.19 summarizes the combined effect of reinforcement stiffness and vertical spacing on the maximum vertical and lateral displacements of the abutment. It should be noted that all the displacements presented in Table 7.4.19 excluded the displacements of the abutment in Stage 3. In other words, the displacements of the abutment were initialized after the construction of the abutment and the beam seat were finished.

Table 7.4.19: Effect of combination of reinforcement stiffness and vertical spacing on the maximum vertical and lateral displacements of the abutment

Cases	Displacement (mm)	Construction stage		
		Stage 4 (bridge slab)	Stage 5 (Integrated approach)	Stage 6 (traffic load)
J = 350 kN/m, S_v = 0.2 m	$\delta_{v\text{-max}}$	41.28	43.38	59.48
	$\delta_{l\text{-max}}$	13.77	14.67	19.80
J = 700 kN/m, S_v = 0.4 m	$\delta_{v\text{-max}}$	40.39	42.29	59.09
	$\delta_{l\text{-max}}$	14.02	14.71	19.40
J = 1050 kN/m, S_v = 0.6 m	$\delta_{v\text{-max}}$	40.51	42.41	59.31
	$\delta_{l\text{-max}}$	13.70	14.50	20.10

7.4.5.5.6 Tension in the reinforcement

Figure 7.4.67 shows the combined effect of reinforcement stiffness and vertical spacing on the maximum tensile force of the reinforcement T_{max} under both self-weight (i.e., Stage 2) and traffic load conditions (i.e., Stage 6). Under self-weight conditions, the maximum tensile forces T_{max} in the reinforcement with the depth were 2.77 kN/m (190 lb/ft), 5.36 kN/m (367 lb/ft), and 7.92 kN/m (542 lb/ft) for the cases with vertical reinforcement spacing of 0.2 m (8 in), 0.4 m (16 in), and 0.6 m (24 in or 2 ft) respectively. Under the traffic load, the maximum tensile forces T_{max} in the reinforcement with the depth were 3.96 kN/m (271 lb/ft), 7.52 kN/m (515 lb/ft), and 11.32 kN/m (775 lb/ft) for the cases with vertical reinforcement spacing of 0.2 m (8 in), 0.4 m (16 in), and 0.6 m (24 in or 2 ft) respectively. Therefore, the maximum tensile force in the reinforcement decreased almost proportionally with the decrease in reinforcement spacing under the same load. Under the self-weight, the walls with S_v = 0.6m (24 in or 2 ft), 0.4 m (16 in), and 0.2 m (8 in) required the total maximum tension ΣT_{max} = 43.68 kN/m (2993 lb/ft), 44.37 kN/m (3040 lb/ft), and 45.76 kN/m (3136 lb/ft) respectively. Under the traffic load, the walls with S_v = 0.6m (24 in or 2 ft), 0.4 m (16 in), and 0.2 m (8 in) required the total maximum tension ΣT_{max} = 108.90 kN/m (7462 lb/ft), 108.48 kN/m (7433 lb/ft), and 113.35 kN/m (7767 lb/ft) respectively. Therefore, these three walls required almost the same total maximum tension under the self-weight and the traffic load.

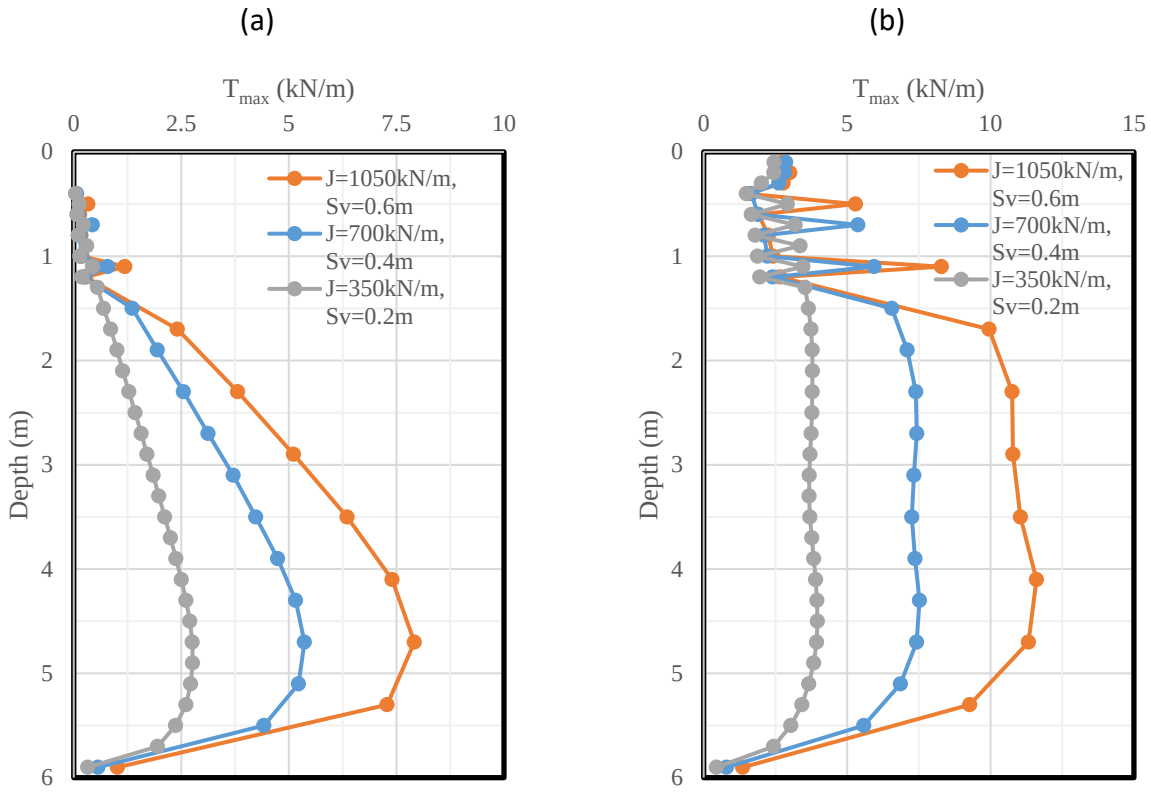

Fig. 7.4.67: Effect of combination of reinforcement stiffness and spacing on the maximum tensile force T_{max} in the reinforcement: (a) Self-weight; (b) Traffic load.

Figure 7.4.68 shows the combined effect of reinforcement stiffness and vertical spacing on the ratio of the connection force T_0 to the maximum tensile force T_{max} in the reinforcement under both self-weight (i.e., Stage 2) and traffic load conditions (i.e., Stage 6). Figure 7.4.68 shows that the ratio of T_0 to T_{max} was close to 1.0 under both the self-weight and the traffic load, indicating that the maximum tensile force in the reinforcement happened near the connection between geotextile reinforcement and wall facing for both cases.

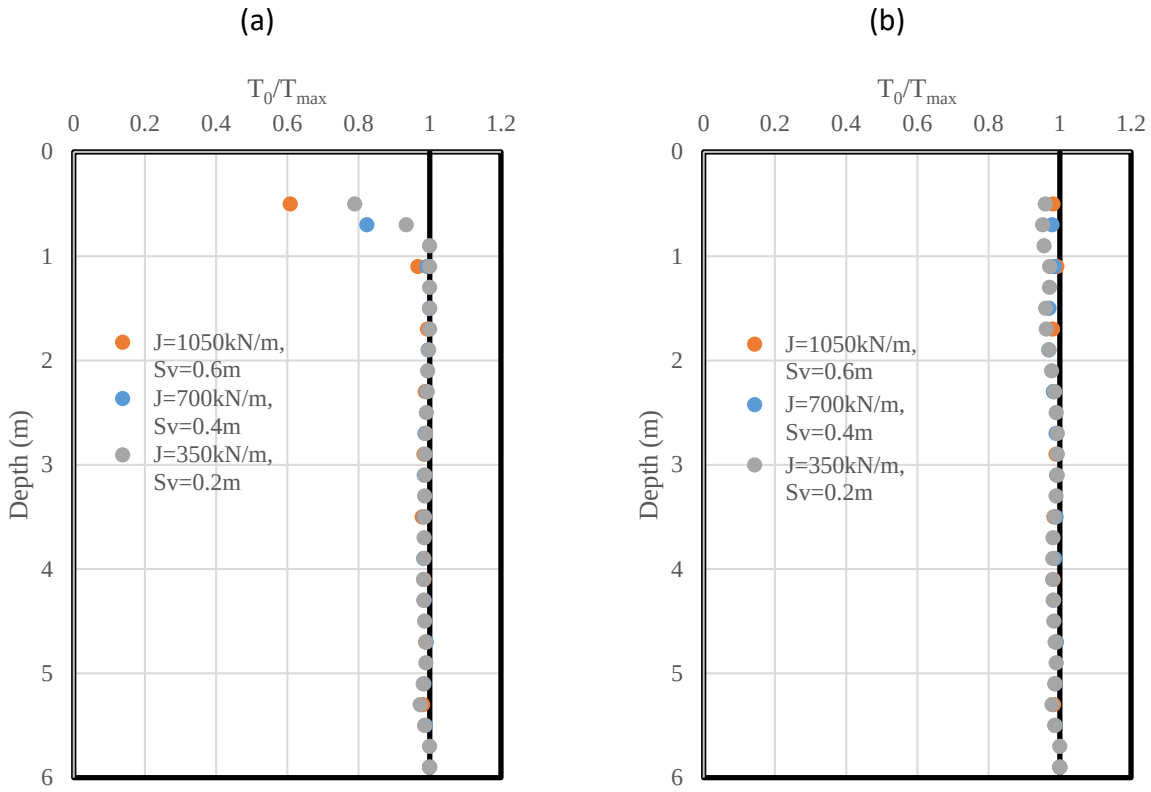

Fig. 7.4.68: Effect of combination of reinforcement stiffness and spacing on the ratio of connection force T_0 to the maximum tensile force T_{max} in the reinforcement: (a) Self-weight; (b) Traffic load.

Figure 7.4.69 shows the combined effect of reinforcement stiffness and vertical spacing on the normalized coefficient of lateral earth pressure K_r/K_a under both self-weight (i.e., Stage 2) and traffic load conditions (i.e., Stage 6). The determination of σ_v under different loading conditions was discussed in Section 7.4.5.2.6 (i.e., using the overburden stress and the AASHTO 2 to1 truncation method without surcharge q). Figure 7.4.69 shows that under the self-weight, the normalized coefficients of lateral earth pressure K_r/K_a were almost the same for all three cases. Under the traffic load, there is small difference in K_r/K_a between these three cases. The cases with stiffer reinforcement and larger vertical spacing resulted in slightly smaller K_r/K_a. The phenomenon of K_r/K_a being approximately 0.8 along depth has already been explained in Section 7.4.5.2.6.

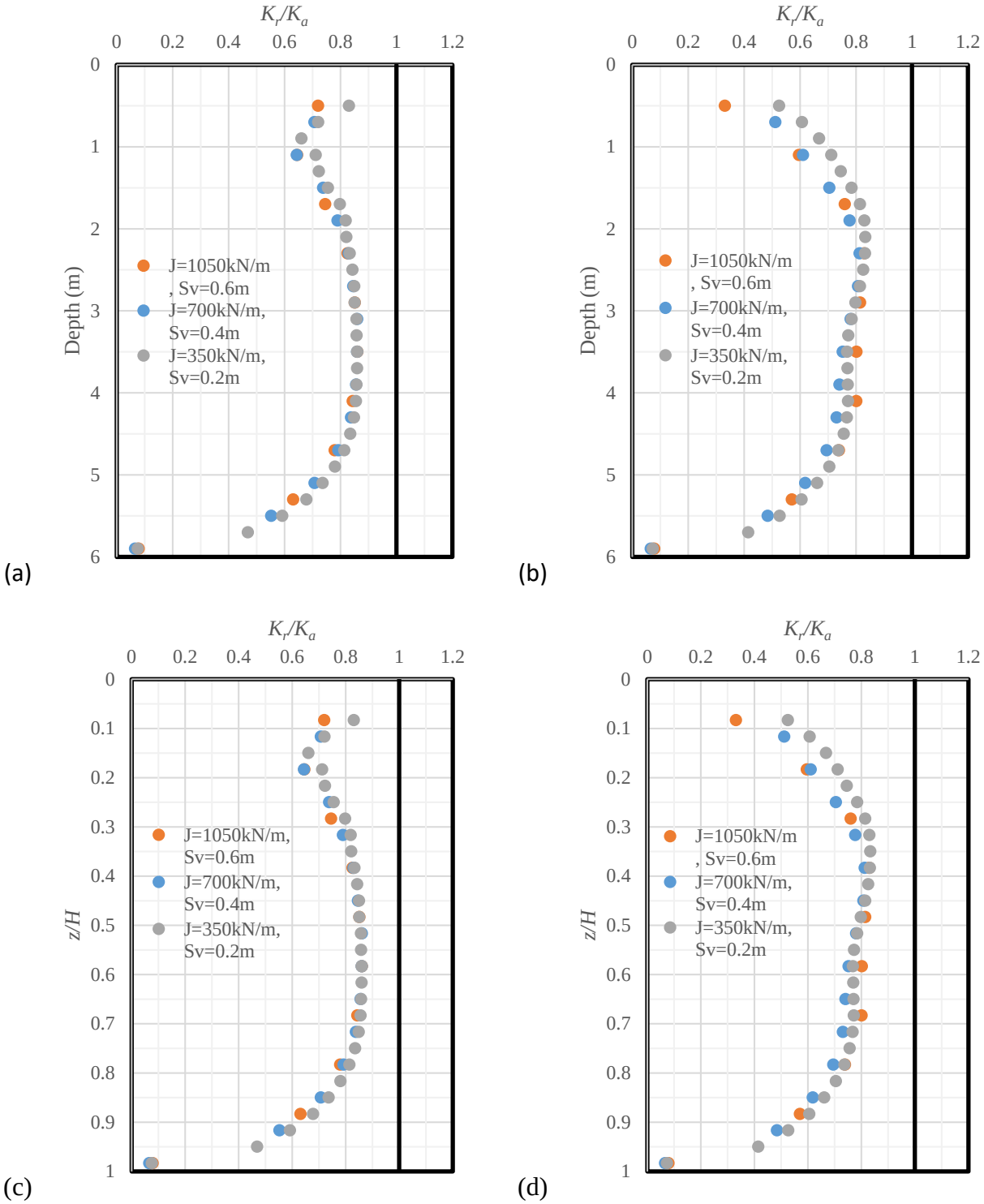

Fig. 7.4.69: Effect of combination of reinforcement stiffness and spacing on the normalized coefficient of lateral earth pressure K_r/K_a: (a) Distribution under self-weight with depth; (b) Distribution under traffic load with depth; (c) Distribution under self-weight with normalized depth; (d) Distribution under traffic load with normalized depth.

7.4.5.6 EFFECT OF BEARING REINFORCEMENT LAYERS

This section discusses the effect of bearing reinforcement layers. In the baseline model, five bearing reinforcement layers were used under the bridge seat from the depth of 0.4 m (16 in) to 1.2 m (4 ft). An additional case with no bearing reinforcement layer was studied.

7.4.5.6.1 Lateral earth pressures

Figure 7.4.70 shows the effect of bearing reinforcement layers on the lateral earth pressure behind the CMU facing blocks under both self-weight (i.e., Stage 2) and traffic load conditions (i.e., Stage 6). Under the self-weight, the number of bearing reinforcement layers did not affect the lateral earth pressure distribution behind the wall facing. Numerical results showed a close agreement with the theoretical Coulomb's active lateral earth pressure. Under the traffic load, the difference between these two cases was larger. When no bearing reinforcement layer was used, higher lateral earth pressure behind wall facing happened from the top of the wall to the depth of approximately 1.6 m (5 ft). In the baseline model, five bearing reinforcement layers were placed at the depth of 0.4 m (16 in) to 1.2 m (4 ft), which was within the range where the lateral earth pressure increased. The closely-spaced bearing reinforcement layers changed the lateral earth pressure distribution in the neighboring area.

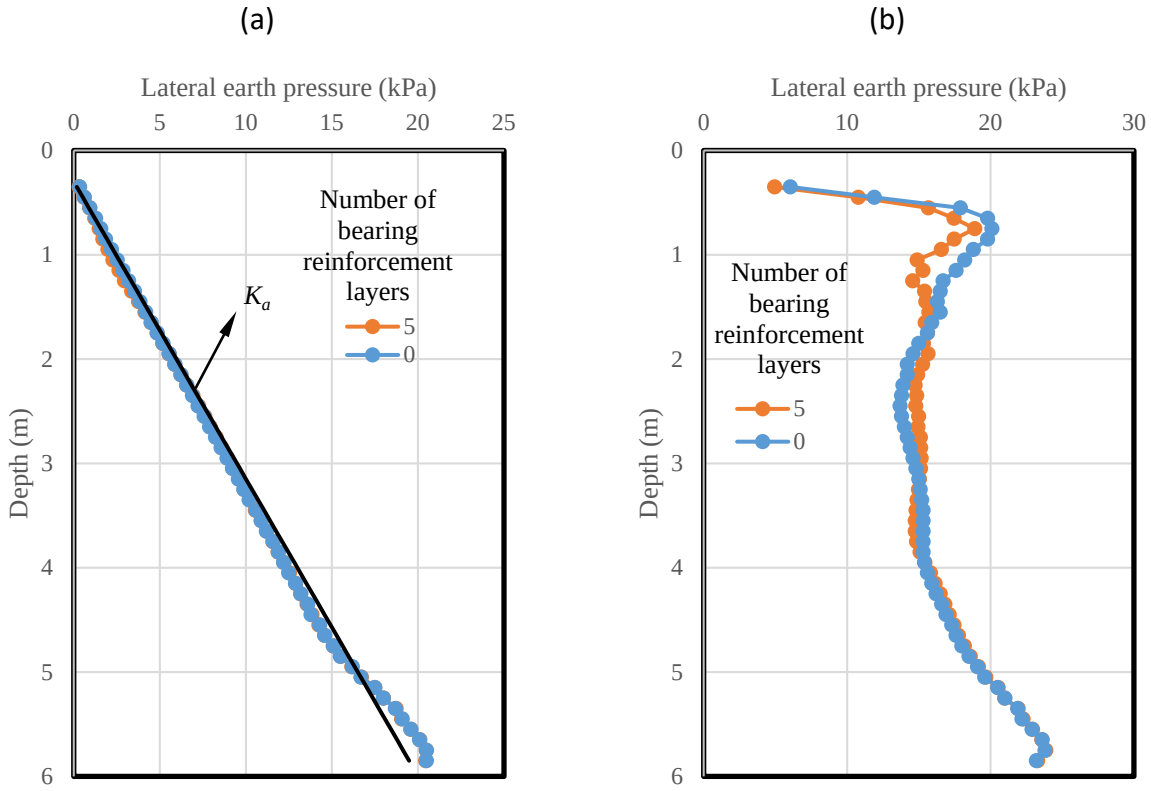

Fig. 7.4.70: Effect of bearing reinforcement layers on the lateral earth pressure behind CMU facing blocks: (a) Self-weight; (b) Traffic load.

7.4.5.6.2 Additional vertical stress induced by loading

Figure 7.4.71 shows the effect of bearing reinforcement layers on the distribution of additional vertical stress Δp at 0.5 m (20 in) from the back of CMU facing blocks with the depth induced by loading. Figure 7.4.71 shows that the bearing reinforcement layers did not have any significant effect on the additional vertical stress distribution induced by loading. The difference between these two cases was minimum. The AASHTO 2 to 1 truncation method calculated the additional vertical stresses in reasonable agreements with the numerical results.

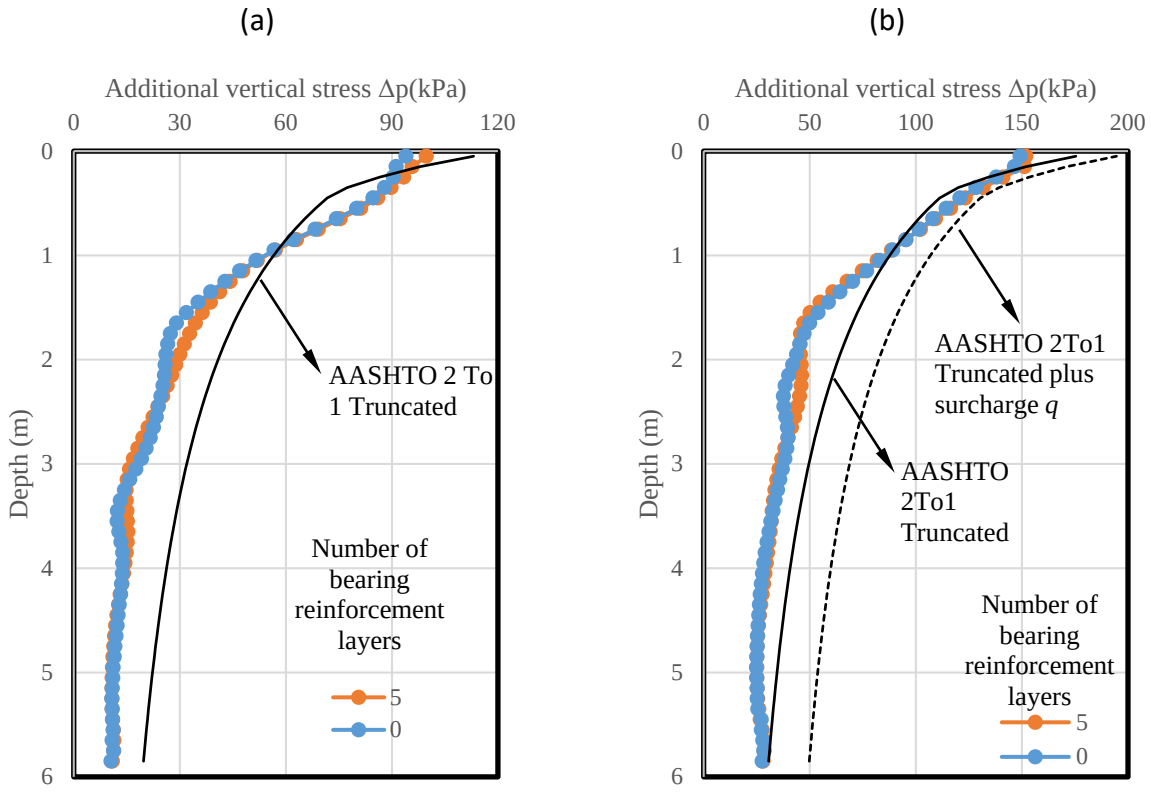

Fig. 7.4.71: Effect of bearing reinforcement layers on the additional vertical stress induced by loading: (a) Induced by the self-weight of the bridge slab; (b) Induced by the self-weight of the bridge slab and the traffic load.

7.4.5.6.3 Lateral displacement of CMU facing blocks

Figure 7.4.72 shows the effect of bearing reinforcement layers on the lateral displacement of CMU facing blocks under self-weight (i.e., Stage 2), bridge slab (i.e., Stage 4), and traffic load conditions (i.e., Stage 6). Under the self-weight, there was almost no difference between these two cases. Under both the bridge slab and the traffic load, the use of five bearing reinforcement layers resulted in slightly smaller lateral displacement of CMU facing blocks where these bearing reinforcement layers were placed.

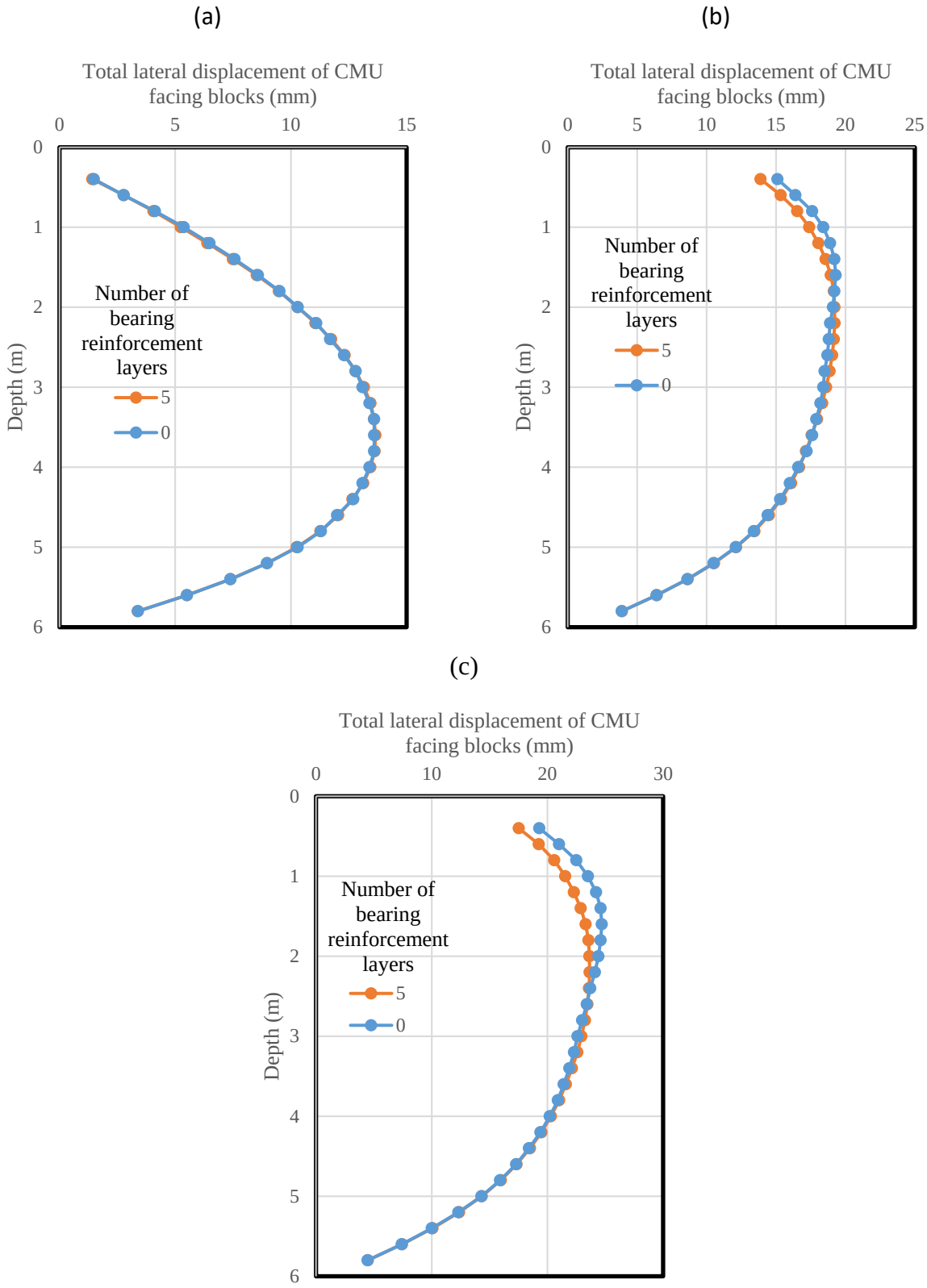

Fig. 7.4.72: Effect of bearing reinforcement layers on the lateral displacement of CMU facing blocks: (a) Self-weight; (b) Bridge slab; (c) Traffic load.

Figure 7.4.73 shows the effect of bearing reinforcement layers on the additional settlement on the top of the bridge slab and integrated approach induced by the traffic load only (i.e., the difference in the lateral displacements between Stage 6 and Stage 5). As expected, the use of bearing reinforcement layers reduced the additional lateral displacement of CMU facing blocks due to the traffic load near the top of the wall where these bearing reinforcement layers were placed. The closely-spaced bearing reinforcement layers provided more lateral restraint to the backfill soil due to more interfaces, hence resulting in the smaller total and additional lateral displacements of wall facing.

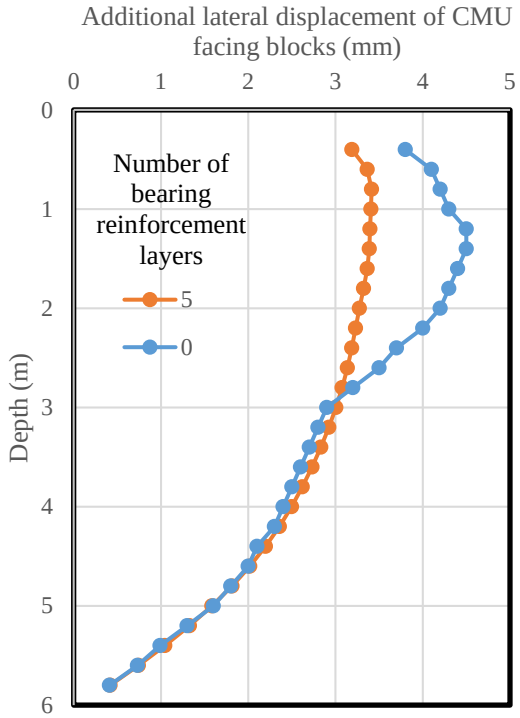

Fig. 7.4.73: Effect of bearing reinforcement layers on the additional lateral displacement of CMU facing blocks induced by traffic load

7.4.5.6.4 Settlement profile for the bridge slab and integrated approach

Figure 7.4.74 shows the effect of bearing reinforcement layers on the additional settlement on the top of the bridge slab and integrated approach induced by the traffic load (i.e., the difference in the settlement between Stage 6 and Stage 5). Figure 7.4.74 shows that the use of bearing reinforcement layers reduced the additional settlement of the bridge slab induced by loading but not the additional settlement in the integrated approach way. The use of bearing reinforcement layers also reduced the differential settlement that developed at the end of the bridge slab. The main function of bearing reinforcement layers was to provide lateral restraint to the backfill soil when subjected to the bridge slab load and the traffic load applied on the top of bridge slab. Therefore, the bearing reinforcement layers were placed below the bridge seat and the length of bearing reinforcement layers was shorter than the length of primary reinforcement. Due to the

limited length and depth of bearing reinforcement layers, they had little influence on the additional settlement of the integrated approach way.

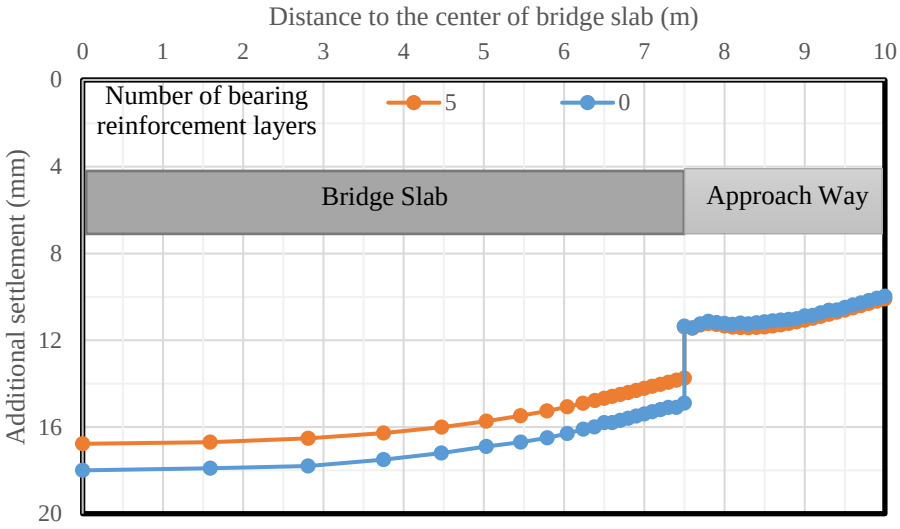

Fig. 7.4.74: Effect of bearing reniforcemeng layers on the additional settlement of the bridge slab and integrated approach induced by traffic load

7.4.5.6.5 Volume change of the abutment

Figure 7.4.75 shows the effect of bearing reinforcement layers on the normalized lateral volume change – normalized vertical volume change curves. Two lines in Fig. 7.4.75 almost overlapped with each other, indicating that bearing reinforcement layers had essentially no effect on the volume change of the abutment. Two reasons may contribute to this trend. First, the length of bearing reinforcement layers was much shorter than the width of the reinforced zone, thus resulting in limited contribution to volume changes. Also, only five layers were placed under the bridge slab. The bearing reinforcement layers did not cover the entire wall height. Therefore, the effect of bearing reinforcement layers on the volume change was minimum.

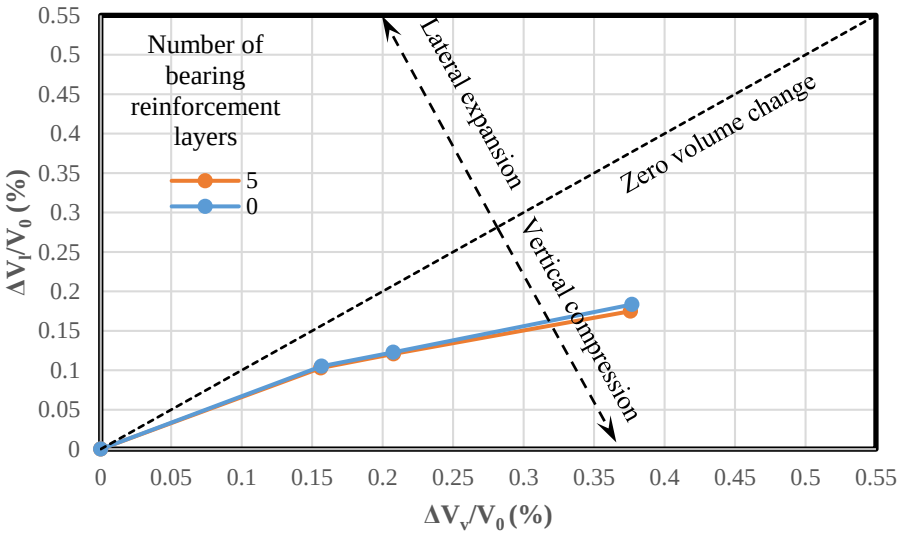

Fig. 7.4.75: Effect of bearing reinforcement layers on the volume change of the GRS-IBS abutment

Table 7.4.20 summarizes the effect of bearing reinforcement layers on the maximum vertical and lateral displacements of the abutment. It should be noted that the displacements presented in Table 7.4.20 excluded the displacements of the abutment in Stage 3. In other words, the displacements of the abutment were initialized after the construction of the abutmentand the beam seat were finished.

Table 7.4.20: Effect of bearing reinforcement layers on the maximum vertical and lateral displacements of the abutment

Number of bearing reinforcement layers	Displacement (mm)	Construction stage		
		Stage 4 (bridge slab)	Stage 5 (Integrated approach)	Stage 6 (traffic load)
5	$\delta_{v\text{-max}}$	35.36	37.19	51.06
	$\delta_{l\text{-max}}$	10.63	11.18	14.54
0	$\delta_{v\text{-max}}$	36.26	37.96	53.06
	$\delta_{l\text{-max}}$	11.71	12.17	16.36

7.4.5.6.6 Tension in the reinforcement

Figure 7.4.76 shows the effect of bearing reinforcement layers on the maximum tensile forces of the reinforcement T_{max} under both self-weight (i.e., Stage 2) and traffic load conditions (i.e., Stage

6). Under the self-weight, their difference between these two cases was small. Under the traffic load, however, the difference between these two cases became more significant towards the top of the wall. When five bearing reinforcement layers were used, smaller T_{max} developed in primary reinforcement as compared to the case without bearing reinforcement layers. When five bearing reinforcement layers were used, the sum of T_{max} in the top six primary reinforcement layers and five bearing reinforcement layers was 27.46 kN/m (1882 lb/ft). When no bearing reinforcement layers was used, the sum of T_{max} in the top six primary reinforcement layers was 25.24 kN/m (1729 lb/ft). These two numbers were close, indicating that bearing reinforcement layers carried part of the load that was supposed to be carried by the primary reinforcement if no bearing layer was used.

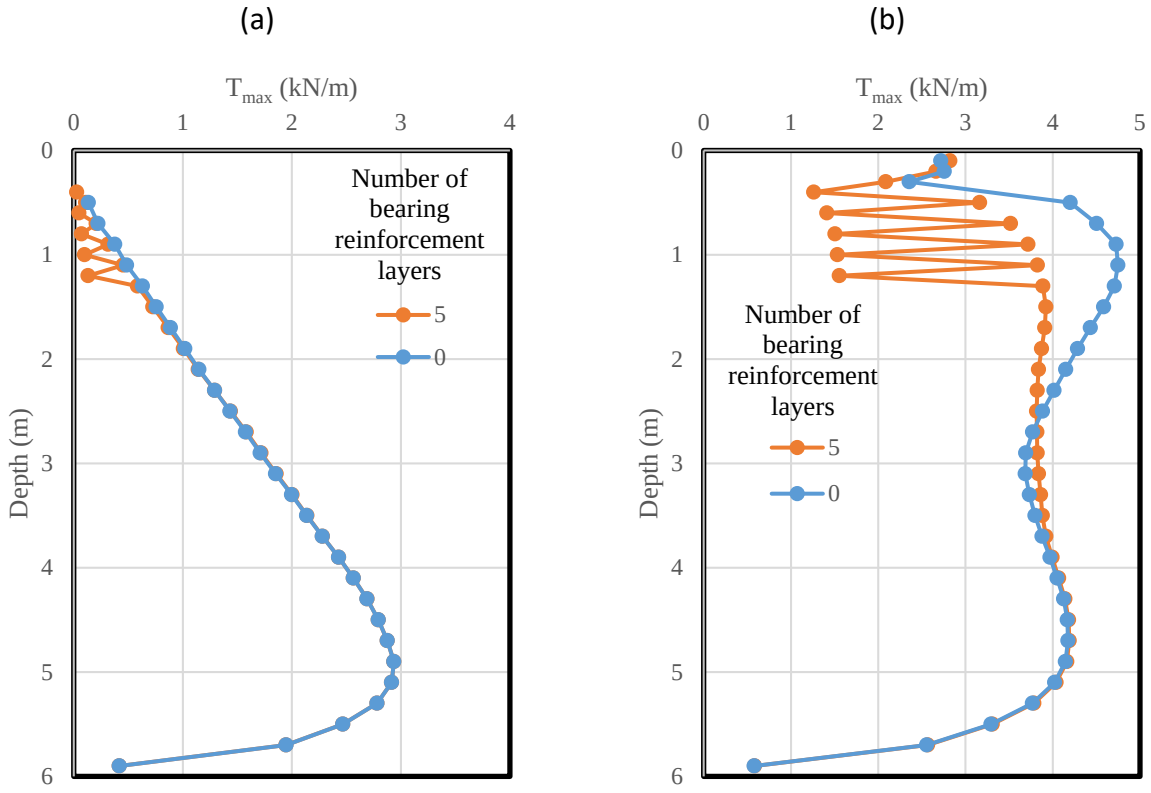

Fig. 7.4.76: Effect of bearing reinforcement layers on the maximum tensile force T_{max} in the reinforcement: (a) Self-weight; (b) Traffic load.

Figure 7.4.77 shows the effect of bearing reinforcement layers on the ratios of the connection force T_0 to the maximum tensile force T_{max} in the reinforcement under both self-weight (i.e., Stage 2) and traffic load conditions (i.e., Stage 6). Under self-weight, the bearing reinforcement layers had no influence on T_0/T_{max}. Under the traffic load, the use of bearing reinforcement layers resulted in slightly larger T_0/T_{max} near the top of the wall where the bearing reinforcement layers were placed since the bearing reinforcement layers reduced T_{max} in the primary reinforcement as shown in Fig. 7.4.76.

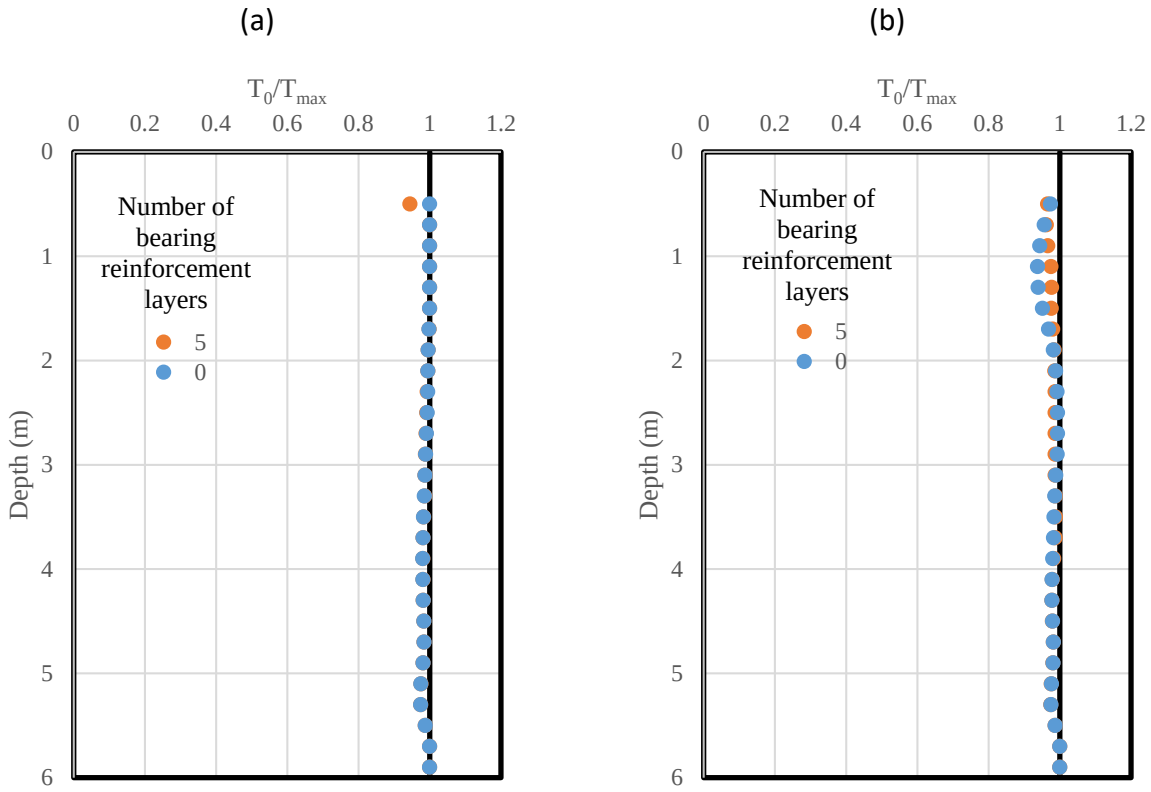

Fig. 7.4.77: Effect of bearing reinforcement layers on the ratio of connection force T_0 to the maximum tensile force T_{max} in the reinforcement: (a) Self-weight; (b) Traffic load.

Figure 7.4.78 shows the effect of bearing reinforcement layers on the normalized coefficients of lateral earth pressure K_r/K_a under both self-weight (i.e., Stage 2) and traffic load conditions (i.e., Stage 6). The determination of σ_v under different loading conditions was discussed in Section 7.4.5.2.6 (i.e., using the overburden stress and the AASHTO 2 to1 truncation method without surcharge q). Their difference between these two cases happened near the top of the wall where the bearing reinforcement layers were placed. The use of bearing reinforcement layers resulted in smaller K_r/K_a due to the decrease of T_{max} in the primary reinforcement as shown in Fig. 7.4.76.

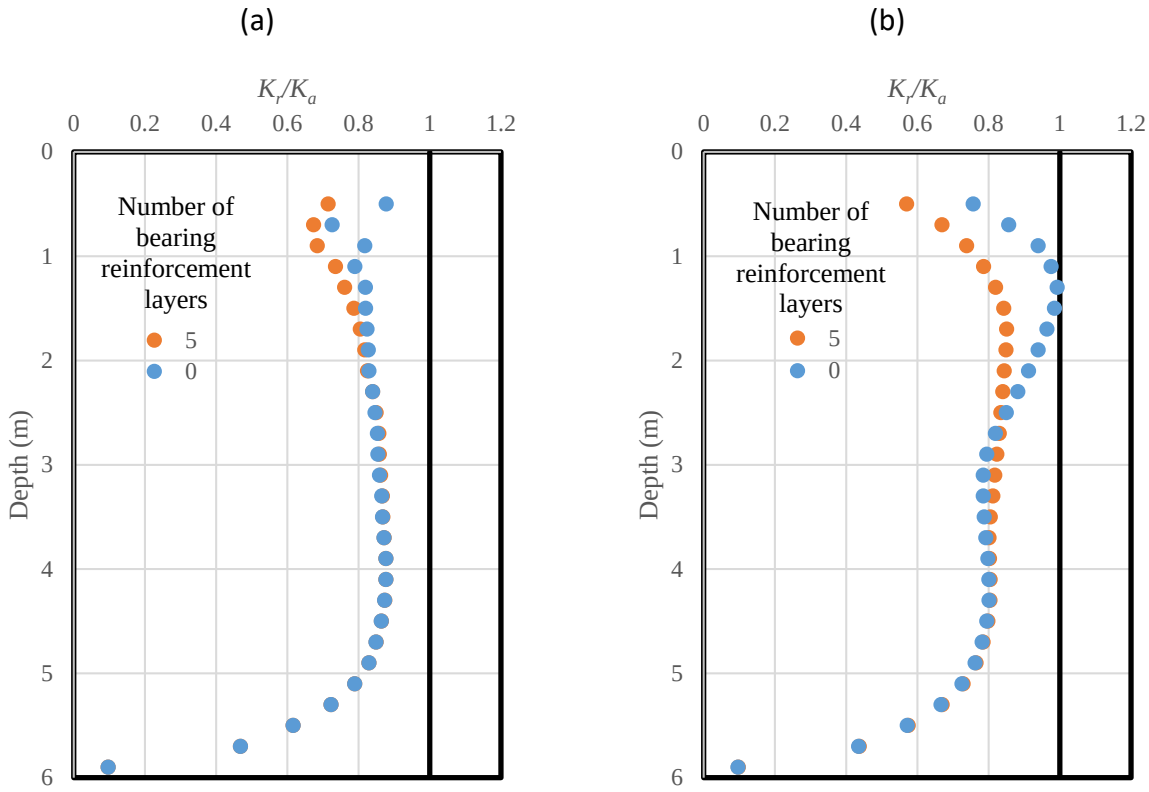

Fig. 7.4.78: Effect of bearing reinforcement layers on the normalized coefficient of lateral earth pressure K_l/K_a: (a) Self-weight; (b) Traffic load.

7.4.5.7 EFFECT OF SOIL – REINFORCEMENT INTERACTION COEFFICIENT

This section discusses the effect of the interaction coefficient between the backfill soil and the reinforcement. In the baseline model, the soil – reinforcement interaction coefficient C_i was 0.9. Additional two cases with C_i being 0.7 and 0.5 were evaluated. The soil – reinforcement interface friction angles were 28.67° and 21.34° when C_i was equal to 0.7 and 0.5 respectively.

7.4.5.7.1 Lateral earth pressure

Figure 7.4.79 shows the effect of the soil-reinforcement interaction coefficient on the lateral earth pressure behind the CMU facing blocks under both self-weight (i.e., Stage 2) and traffic load conditions (i.e., Stage 6). Figure 7.4.79 shows that the change of the soil-reinforcement interaction coefficient did not influence the lateral earth pressure behind the wall facing. Under self-weight, the lateral earth pressure was close to the theoretical Coulomb's active earth pressure. Under the traffic load, the lateral earth pressure near the top of the wall had a large increase due to loading.

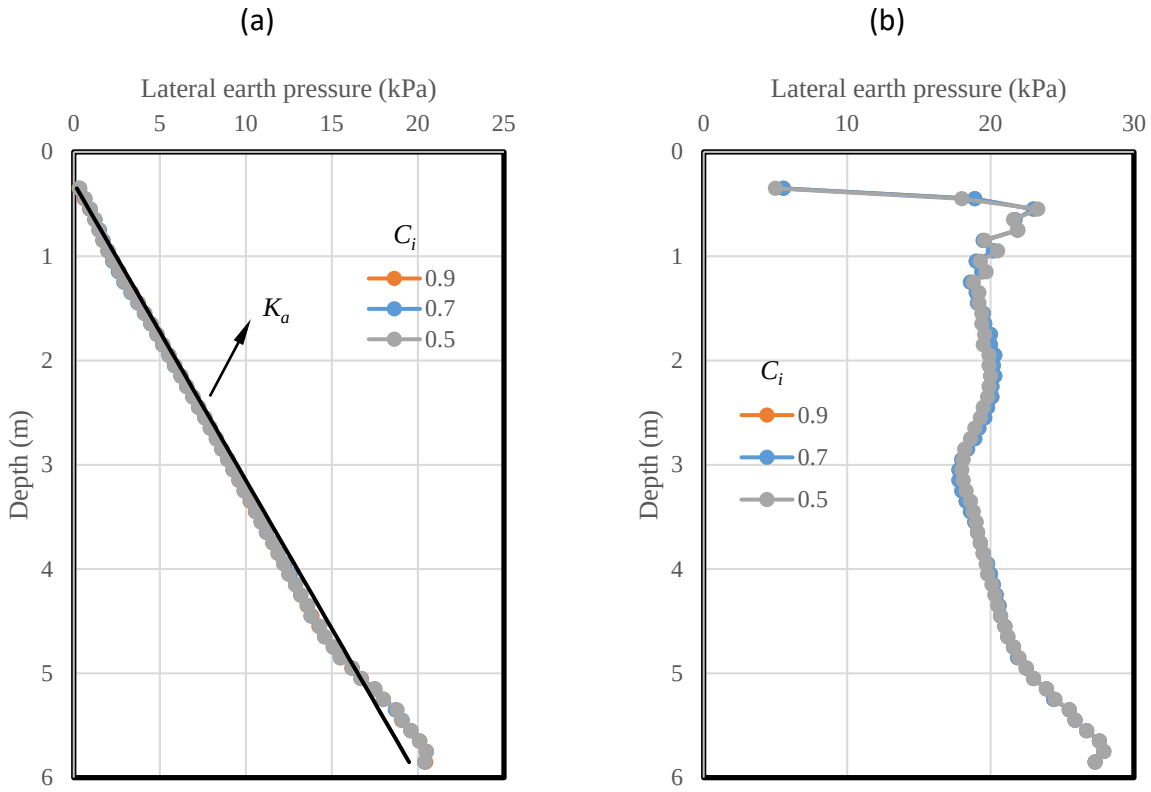

Fig. 7.4.79: Effect of the soil-reinforcement interaction coefficient on the lateral earth pressure behind CMU facing blocks: (a) Self-weight; (b) Traffic load.

7.4.5.7.2 Additional vertical stress induced by loading

Figure 7.4.80 shows the effect of the soil-reinforcement interaction coefficient on the distribution of additional vertical stress Δp at 0.5 m (20 in) from the back of CMU facing blocks with the depth due to loading. Figure 7.4.80 shows that the change of the soil-reinforcement interaction coefficient did not have any significant influence on the additional vertical stress distribution due to loading. The distributions of the additional vertical stress of all three cases overlapped with each other. The AASHTO 2 to 1 truncation method calculated the additional vertical stresses in a reasonable agreement with the numerical results.

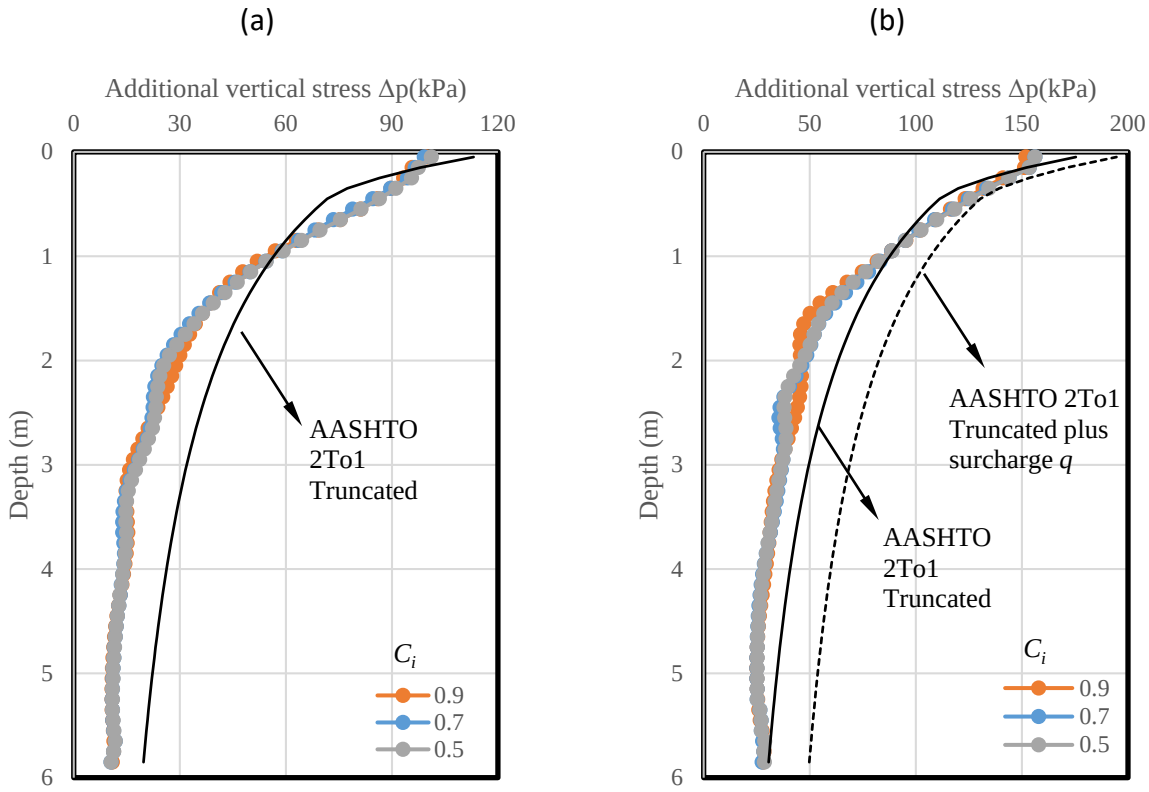

Fig. 7.4.80: Effect of the soil-reinforcement interaction coefficient on the additional vertical stress induced by loading: (a) Induced by the self-weight of the bridge slab; (b) Induced by the self-weight of the bridge slab and the traffic load.

7.4.5.7.3 Lateral displacement of CMU facing blocks

Figure 7.4.81 shows the effect of the soil-reinforcement interaction coefficient on the lateral displacement of CMU facing blocks under self-weight (i.e., Stage 2), bridge slab (i.e., Stage 4), and traffic load conditions (i.e., Stage 6). Figure 7.4.81 shows that the change of the soil-reinforcement interaction coefficient did not affect the total lateral displacement of CMU facing blocks.

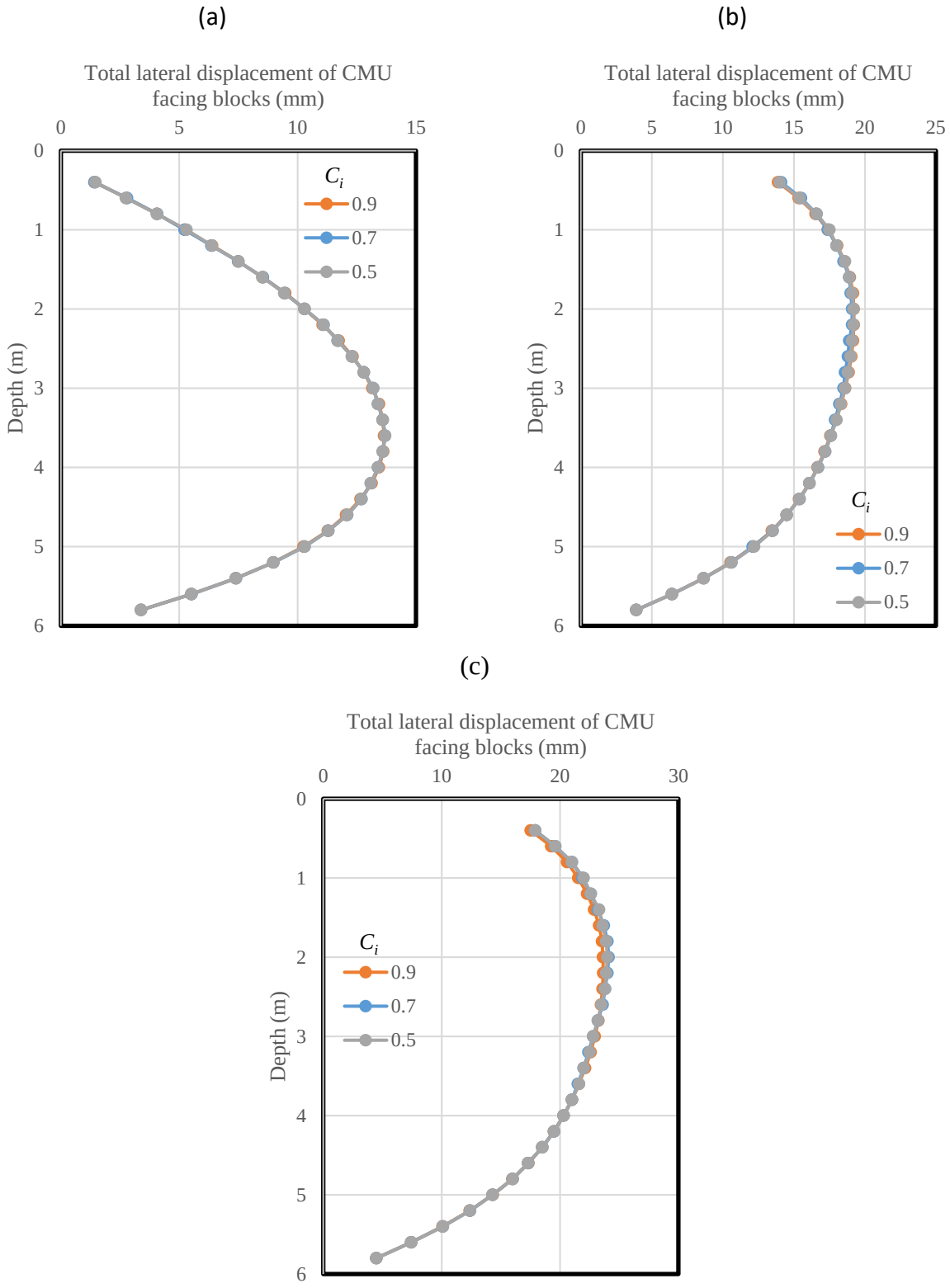

Fig. 7.4.81: Effect of the soil-reinforcement interaction coefficient on the lateral displacement of CMU facing blocks: (a) Self-weight; (b) Bridge slab; (c) Traffic load.

Figure 7.4.82 shows the effect of the soil-reinforcement interaction coefficient on the additional lateral displacement of CMU facing blocks induced by the traffic load only (i.e., the difference in the lateral displacements between Stage 6 and Stage 5). Figure 7.4.82 shows that the influence of the interaction coefficient on the additional lateral displacement of CMU facing blocks induced by traffic load was limited to the upper reinforcement layers (with secondary reinforcements). The use of the soil-reinforcement interaction coefficient of 0.9 resulted in the smallest additional lateral displacement of wall facing due to the traffic load. The reduction of the soil-reinforcement interaction coefficient increased the additional wall deflection. However, this increase was less than 1 mm (0.04 in). The confining stress towards the bottom of the wall was relatively high due to the self-weight of the wall and different types of loading on top of the wall. Therefore, the beneficial reduction in lateral displacements resulting from an increased soil-reinforcement interaction coefficient became negligible towards the bottom of the wall.

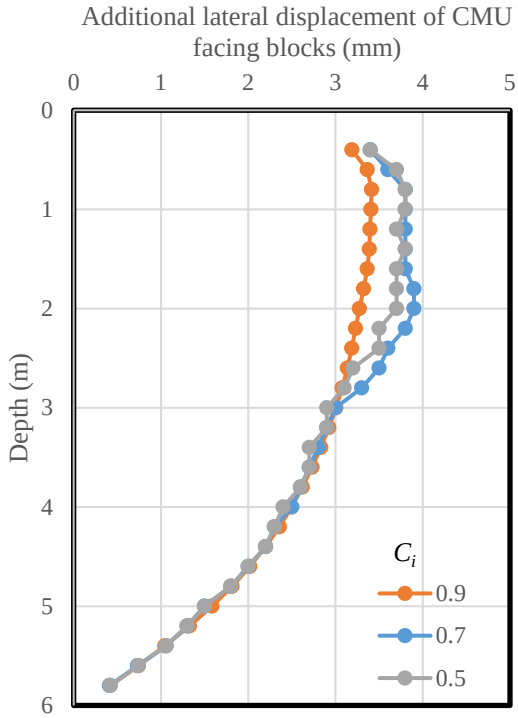

Fig. 7.4.82: Effect of the soil-reinforcement interaction coefficient on the additional lateral displacement of CMU facing blocks induced by traffic load

7.4.5.7.4 Settlement profile for the bridge slab and integrated approach

Figure 7.4.83 shows the effect of the soil-reinforcement interaction coefficient on the additional settlement on the top of the bridge slab and integrated approach induced by the traffic load (i.e., the difference in the settlement between Stage 6 and Stage 5). Figure 7.4.83 shows that the change of the soil-reinforcement interaction coefficient did not have much effect on the additional settlement on the top of the integrated approach way. The decrease of the soil-reinforcement interaction coefficient resulted in larger additional settlement of the bridge slab,

especially when C_i decreased from 0.7 to 0.5. However, the increase of the additional settlement was limited and smaller than 1.0 mm (0.04 in).

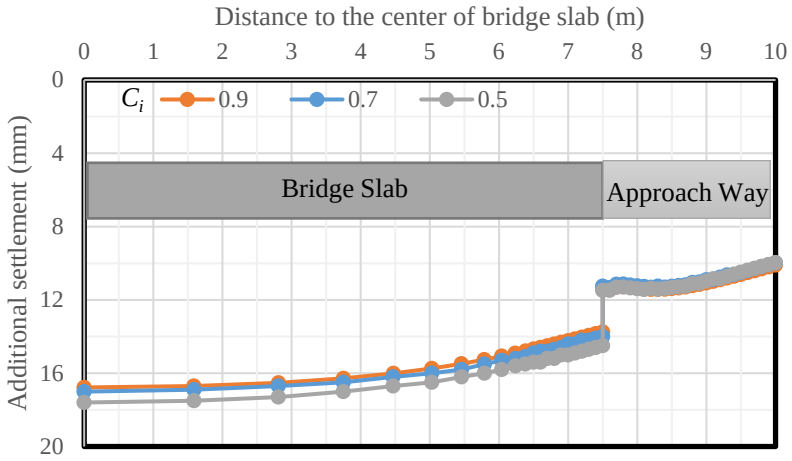

Fig. 7.4.83: Effect of the soil-reinforcement interaction coefficient on the additional settlement of the bridge slab and integrated approach induced by traffic load

7.4.5.7.5 Volume change of the abutment

Figure 7.4.84 shows the effect of the soil-reinforcement interaction coefficient on the normalized lateral volume change – normalized vertical volume change curves. Figure 7.4.84 shows that all three relationships at different soil-reinforcement interaction coefficients overlapped with each other, indicating that the change of C_i did not affect the volume change behavior of the abutment. The abutment had more vertical compression than the lateral deflection, which is different from the zero-volume change assumption.

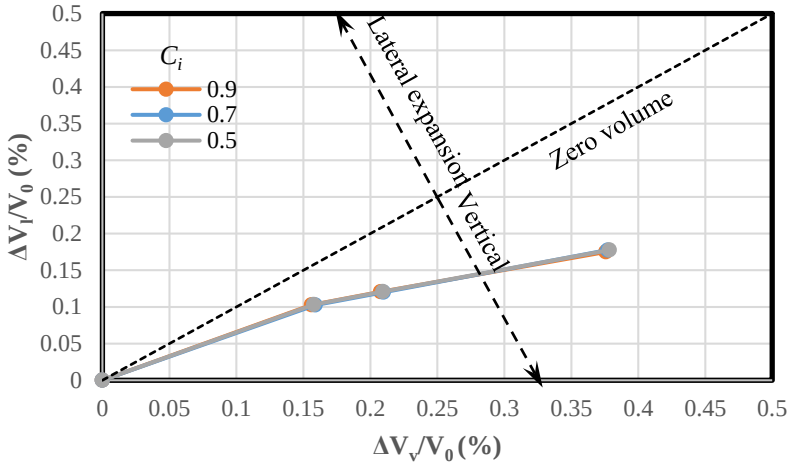

Fig. 7.4.84: Effect of the soil-reinforcement interaction coefficient on the volume change of the GRS-IBS abutment

Table 7.4.21 summarizes the effect of the soil-reinforcement interaction coefficient on the maximum vertical and lateral displacements of the abutment. It should be noted that all the displacements presented in Table 7.4.21 excluded the displacements of the abutment in Stage 3. In other words, the displacements of the abutment were initialized after the construction of the abutmentand the beam seat were finished.

Table 7.4.21: Effect of the soil-reinforcement interaction coefficient on the maximum vertical and lateral displacement of the abutment

Soil-reinforcement interaction coefficient	Displacement (mm)	Construction stage		
		Stage 4 (bridge slab)	Stage 5 (integrated approach)	Stage 6 (traffic load)
0.9	$\delta_{v\text{-max}}$	35.36	37.19	51.06
	$\delta_{l\text{-max}}$	10.63	11.18	14.54
0.7	$\delta_{v\text{-max}}$	35.99	37.79	51.89
	$\delta_{l\text{-max}}$	10.80	11.27	14.95
0.5	$\delta_{v\text{-max}}$	35.09	36.99	51.59
	$\delta_{l\text{-max}}$	10.72	11.22	14.96

7.4.5.7.6 Tension in the reinforcement

Figure 7.4.85 shows the effect of the soil-reinforcement interaction coefficient on the maximum tensile forces of the reinforcement T_{max} under both self-weight (i.e., Stage 2) and traffic load conditions (i.e., Stage 6). Figure 7.4.85 shows that all three lines with different soil-reinforcement interaction coefficients overlapped with each other, indicating that the change of the soil-reinforcement interaction coefficient did not change the maximum tensile force distribution in the reinforcement under both the self-weight and the traffic load.

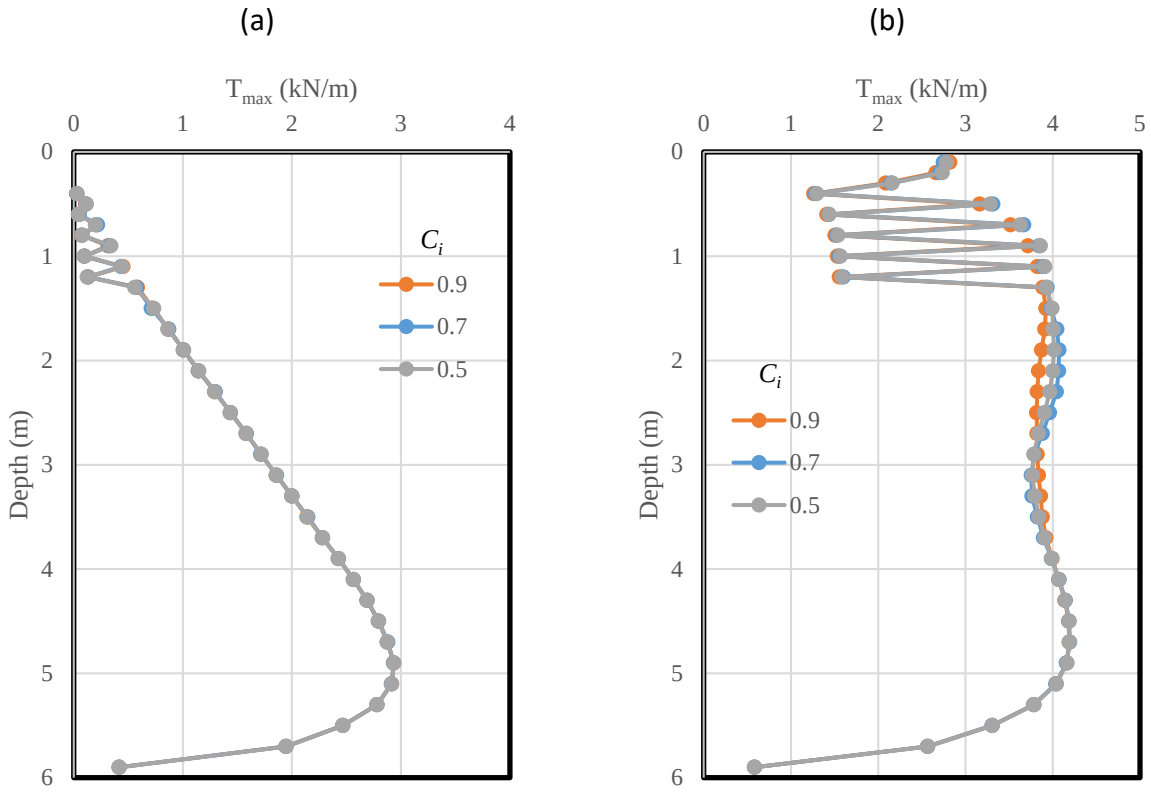

Fig. 7.4.85: Effect of the soil-reinforcement interaction coefficient on the maximum tensile force T_{max} in the reinforcement: (a) Self-weight; (b) Traffic load.

Figure 7.4.86 shows the effect of the soil-reinforcement interaction coefficient on the ratios of the connection force T_0 to the maximum tensile force T_{max} in the reinforcement under both self-weight (i.e., Stage 2) and traffic load conditions (i.e., Stage 6). Figure 7.4.86 shows that the ratios of T_0 to T_{max} were close to 1.0 under both the self-weight and the traffic load, indicating that the maximum tensile force in the reinforcement happened near the connection between geotextile reinforcement and wall facing despite the change of the soil-reinforcement interaction coefficient.

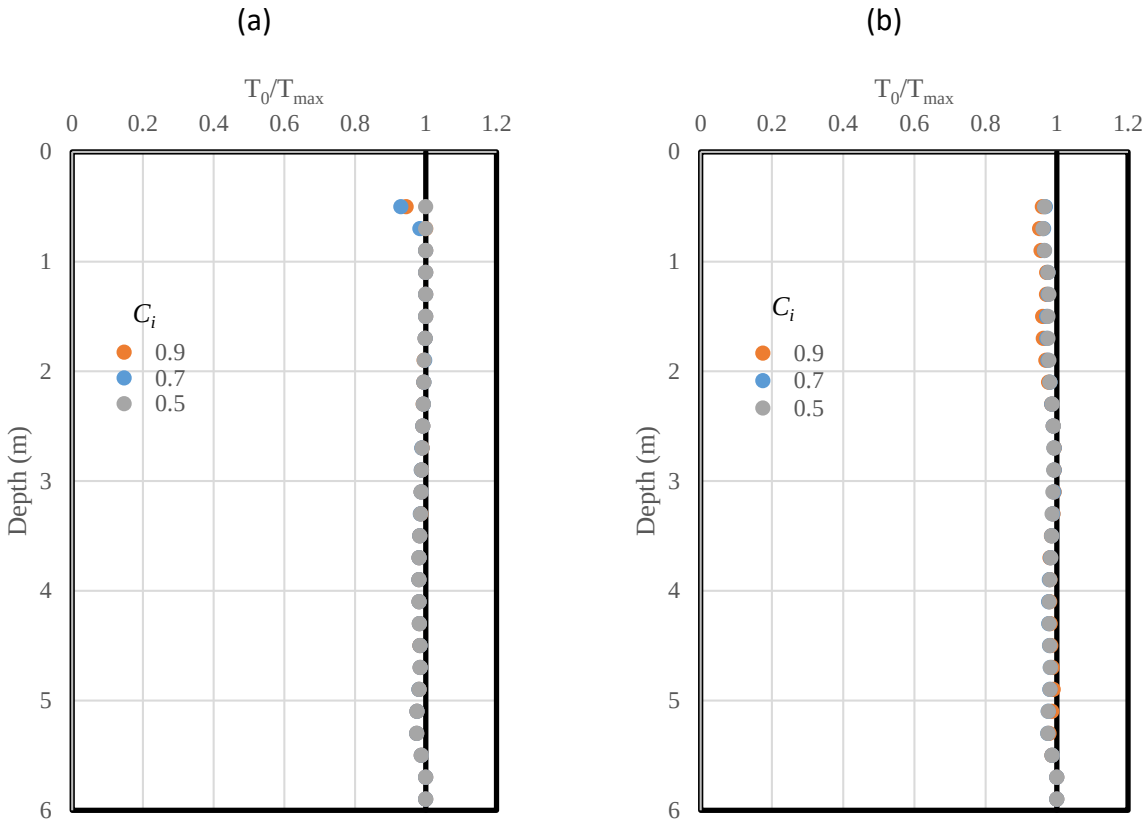

Fig. 7.4.86: Effect of the soil-reinforcement interaction coefficient on the ratio of connection force T_0 to the maximum tensile force T_{max} in the reinforcement: (a) Self-weight; (b) Traffic load.

Figure 7.4.87 shows the effect of the soil-reinforcement interaction coefficient on the normalized coefficients of lateral earth pressure K_r/K_a under both self-weight (i.e., Stage 2) and traffic load conditions (i.e., Stage 6). The determination of σ_v under different loading conditions was discussed in Section 7.4.5.2.6 (i.e., using the overburden stress and the AASHTO 2 to1 truncation method without surcharge q). Figure 7.4.87 shows that the change of the soil-reinforcement interaction coefficient did not affect the normalized coefficient of lateral earth pressure K_r/K_a distribution with the depth. K_r/K_a was close to 1.0 at the mid-height of the wall and less than 1.0 near the top or bottom of the wall for all three cases.

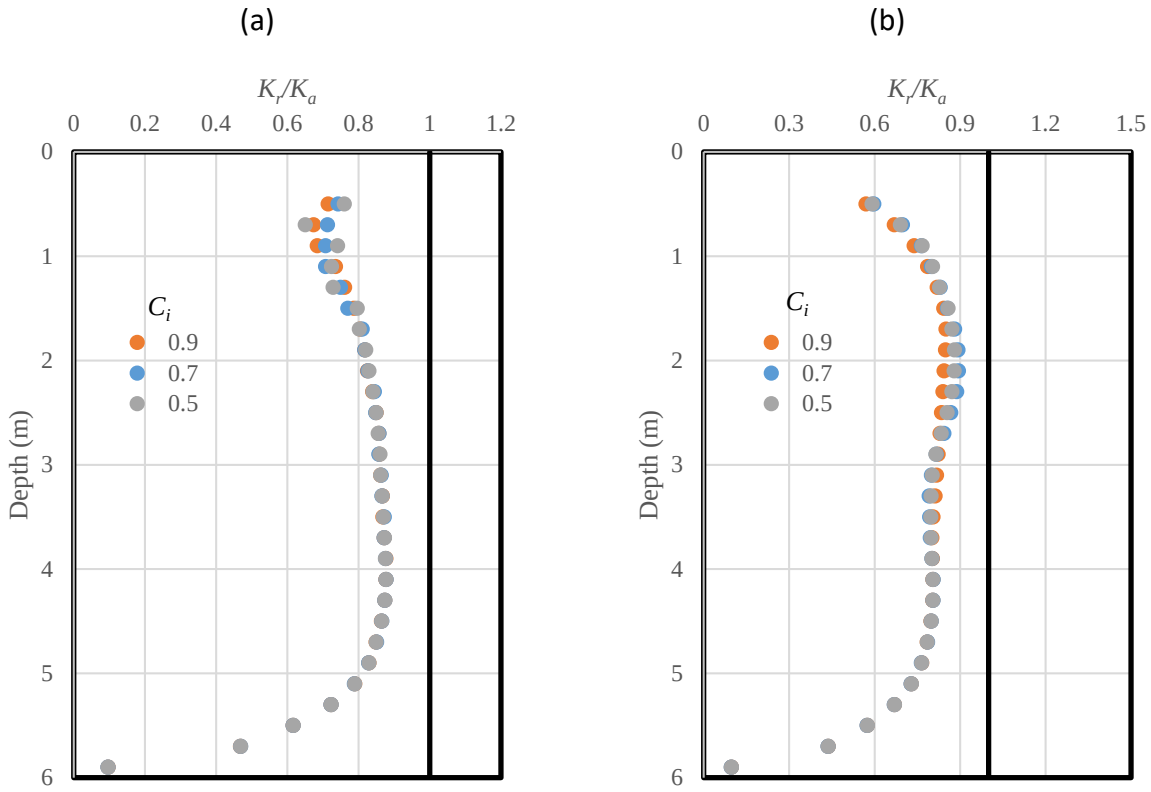

Fig. 7.4.87: Effect of the soil-reinforcement interaction coefficient on the normalized coefficient of lateral earth pressure K_r/K_a: (a) Self-weight; (b) Traffic load.

7.4.5.8 EFFECT OF PRIMARY REINFORCEMENT LENGTH

This section discusses the effect of the primary reinforcement length. The length of the primary reinforcement L_r was normalized by the wall height Has L_r/H. In the baseline model, L_r/H was equal to 0.8. Additional two cases with L_r/H of 0.5 and 0.3 were studied. The primary reinforcement lengths L_r were 3.0 m (10 ft) and 1.8 m (6 ft) when the L_r/H ratios were equal to 0.5 and 0.3 respectively.

7.4.5.8.1 Lateral earth pressure

Figure 7.4.88 shows the effect of the primary reinforcement length on the lateral earth pressure behind the CMU facing blocks under both self-weight (i.e., Stage 2) and traffic load conditions (i.e., Stage 6). Under the self-weight, the reduction of the primary reinforcement length resulted in the lateral earth pressure behind wall facing deviating from the Coulomb active lateral pressure near the bottom of the wall. When the primary reinforcement length was 0.5H or 0.8H, the lateral earth pressure behind wall facing was close to the Coulomb K_a condition from the top of the wall to the depth of approximately 4.5 m (15 ft). Below this depth, the lateral earth pressure was slightly higher than Coulomb's K_a condition. When the primary reinforcement length was 0.3H, however, the lateral earth pressure behind the wall facing was close to Coulomb's K_a condition from the top of the wall to the depth of approximately 3 m (10 ft). Below this depth, the lateral earth pressure was between Coulomb's active lateral earth pressure and the lateral earth

pressure at-rest. This phenomenon may be explained as follows: As the reinforcement length decreases, the lower portion of the wall facing deforms and rotates, resulting in an increase of the lateral earth pressure. This increase can also be explained using the Coulomb theory with a reversely inclined wall back. Under the traffic load, the lateral earth pressure behind the wall facing increased significantly near the top of the wall due to loading. All three primary reinforcement lengths resulted in close lateral earth pressure from the top of the wall to the depth of approximately 3 m (10 ft). Below this depth, the reduction of the primary reinforcement length resulted in the increase of the lateral earth pressure, which was similar to the lateral earth pressure distribution under the self-weight.

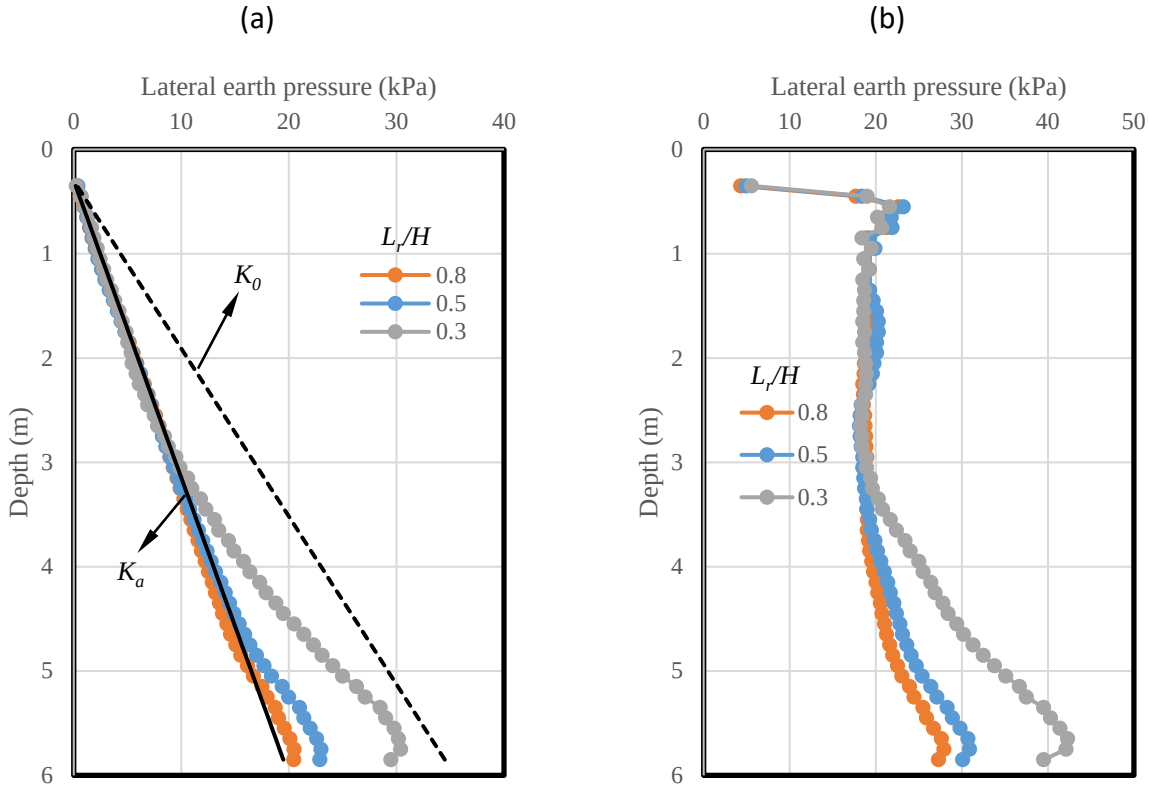

Fig. 7.4.88: Effect of the primary reinforcement length on the lateral earth pressure behind CMU facing blocks: (a) Self-weight; (b) Traffic load.

7.4.5.8.2 Additional vertical stress induced by loading

Figure 7.4.89 shows the effect of the primary reinforcement length on the distribution of additional vertical stress Δp at 0.5 m (20 in) from the back of CMU facing blocks with the depth induced by loading. Figure 7.4.89 shows that the change of the primary reinforcement length did not have any significant effect on the additional vertical stress at 0.5 m (20 in) from the back of wall facing. The limited contact area between the bridge slab and the bridge seat (i.e., b = 0.6 m (20 ft)) might have resulted in little change of Δp. The AASHTO 2 to 1 truncation method calculated the additional stresses in reasonable agreements with the numerical results.

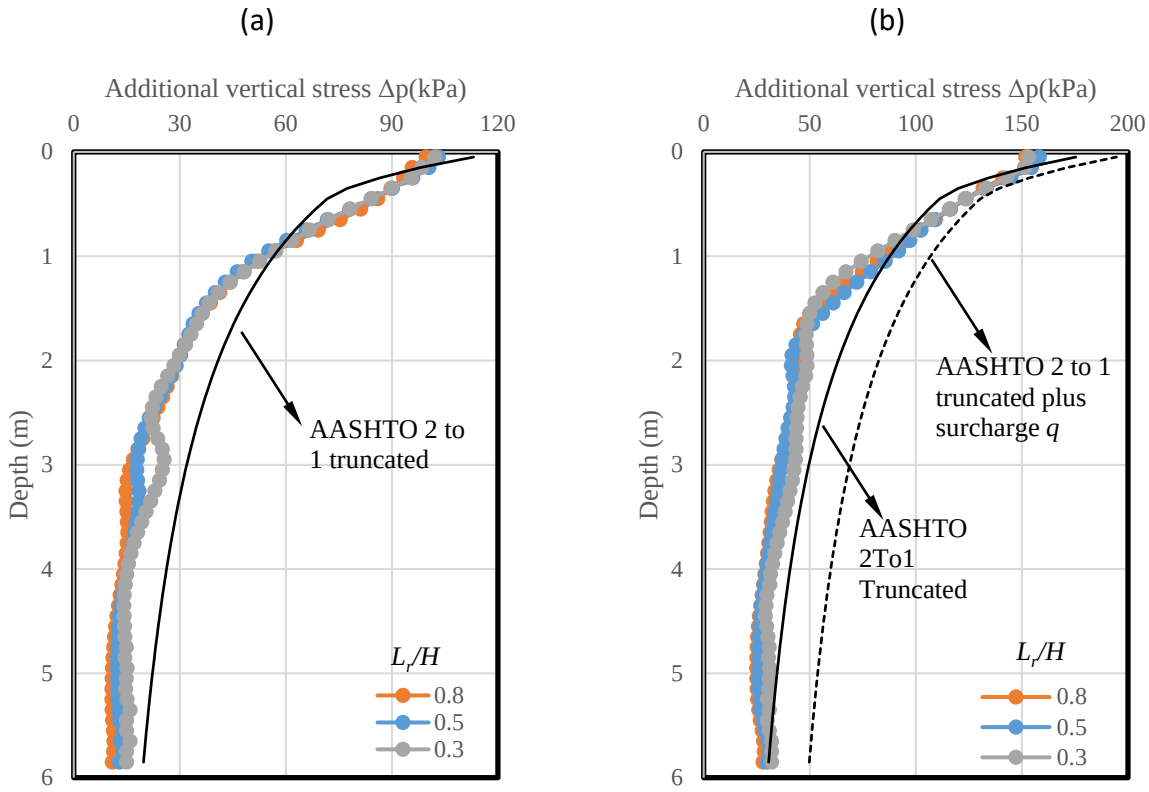

Fig. 7.4.89: Effect of the primary reinforcement length on the additional vertical stress induced by loading: (a) Induced by the self-weight of the bridge slab; (b) Induced by the self-weight of the bridge slab and the traffic load.

7.4.5.8.3 Lateral displacement of CMU facing blocks

Figure 7.4.90 shows the effect of the primary reinforcement length on the lateral displacements of CMU facing blocks under both self-weight (i.e., Stage 2), bridge slab (i.e., Stage 4), and traffic load conditions (i.e., Stage 6). As expected, the reduction of the primary reinforcement length increased the total lateral displacement of CMU facing blocks. The increase of the wall facing deflection was significant when the primary reinforcement length decreased from 0.5*H* to 0.3*H*, indicating that the primary reinforcement length should be at least larger than 0.5*H* to prevent the excessive wall facing deflection.

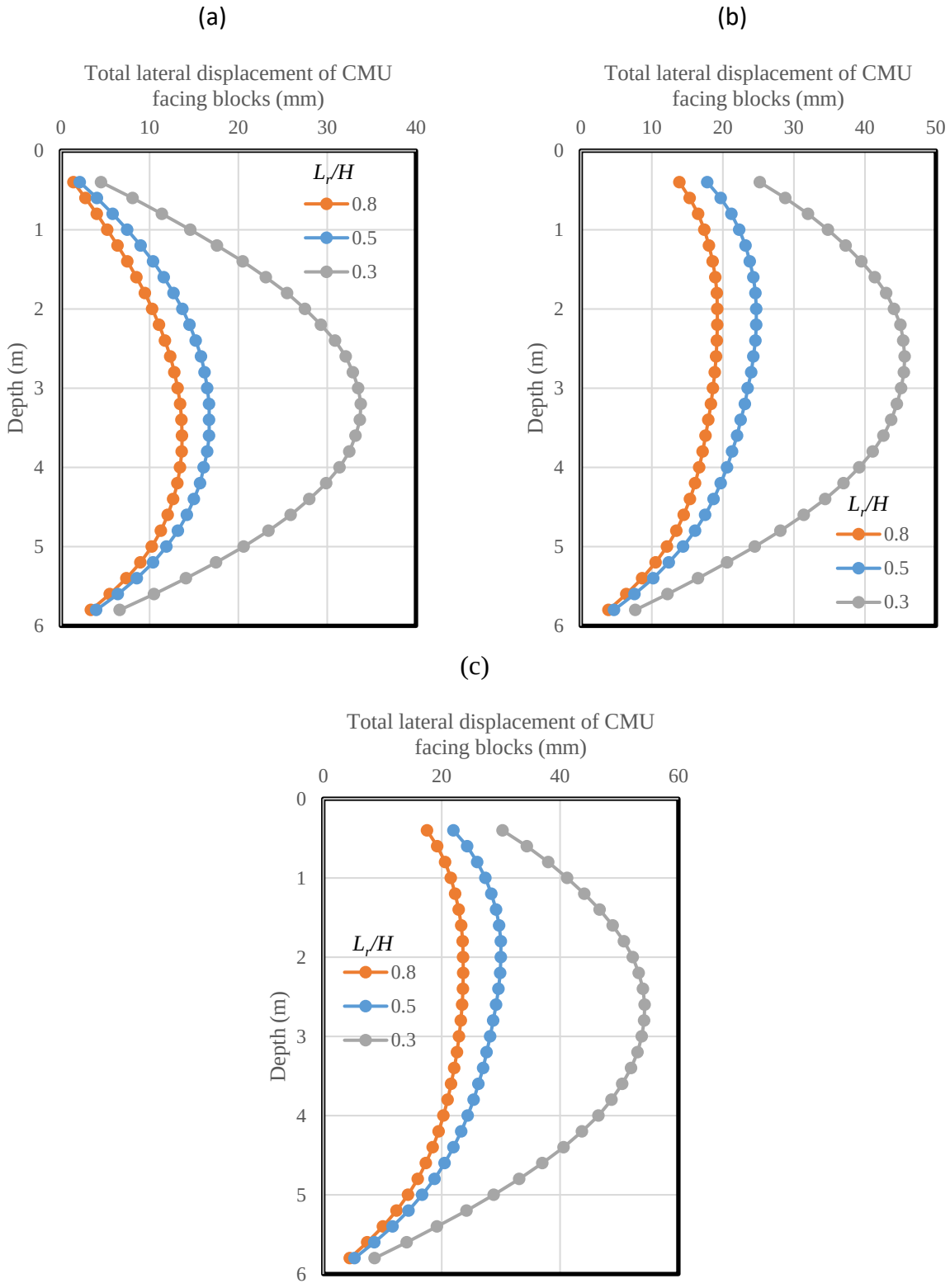

Fig. 7.4.90: Effect of the primary reinforcement length on the lateral displacement of CMU facing blocks: (a) Self-weight; (b) Bridge slab; (c) Traffic load.

Figure 7.4.91 shows the effect of the primary reinforcement length on the additional lateral displacement of CMU facing blocks induced by the traffic load only (i.e., the difference in the lateral displacement between Stage 6 and Stage 5). When the primary reinforcement length decreased from 0.8*H* to 0.5*H*, the additional lateral displacement of CMU facing blocks was almost the same from the bottom of the wall to the depth of approximately 3 m (10 ft). From the top of the wall to the depth of approximately 3 m (10 ft), the case with L_r/H = 0.5 resulted in larger additional wall deflection than the case with L_r/H = 0.8. When the primary reinforcement length decreased from 0.5*H* to 0.3*H*, the additional lateral displacement of the CMU facing blocks increased significantly throughout the entire wall height.

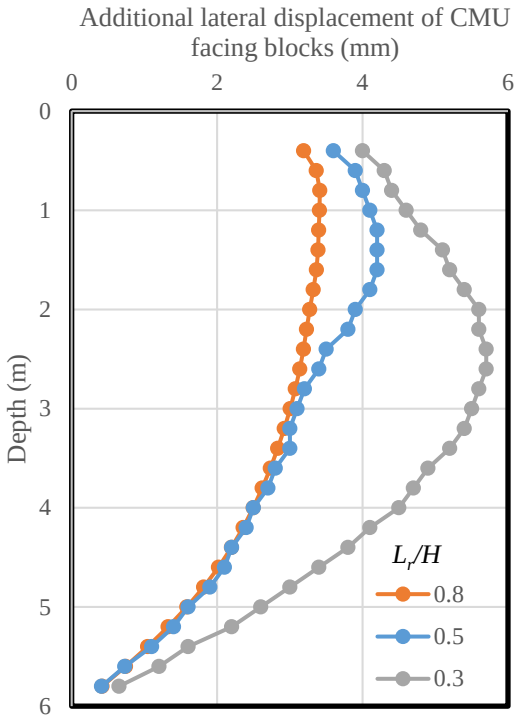

Fig. 7.4.91: Effect of the primary reinforcement length on the additional lateral displacement of CMU facing blocks induced by traffic load

7.4.5.8.4 Settlement profile for the bridge slab and integrated approach

Figure 7.4.92 shows the effect of the primary reinforcement length on the additional settlement on the top of the bridge slab and integrated approach induced by the traffic load (i.e., the difference in the settlement between Stage 6 and Stage 5). Figure 7.4.92 shows that the reduction of the primary reinforcement length did not have any significant effect on the additional settlement of the bridge slab. However, the additional settlement of the integrated approach way had a significant increase when the primary reinforcement length decreased from 0.5*H* to 0.3*H*. When L_r/H = 0.3, the maximum additional settlement of the approach way happened at approximately 8.7 m (28.5 ft) from the center of the bridge slab (i.e., 2 m (6.5 ft) from the back of CMU facing blocks). This location was near the end of the primary reinforcement

since the primary reinforcement ended at 1.8 m (6 ft) from the back of CMU facing blocks. Similar to the findings of the wall facing deflection, the numerical results of the additional settlement of the integrated approach way showed that the primary reinforcement length should be at least equal or larger than 0.5*H* to prevent excessive settlement.

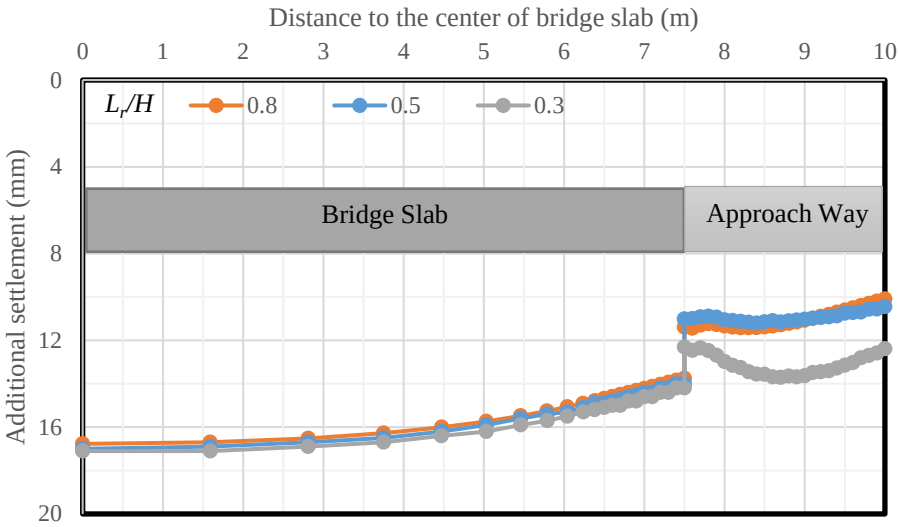

Fig. 7.4.92: Effect of the primary reinforcement length on the additional settlement of the bridge slab and integrated approach induced by traffic load

7.4.5.8.5 Volume change of the abutment

Figure 7.4.93 shows the effect of the primary reinforcement length on the normalized lateral volume change – normalized vertical volume change curves. The original volume of the reinforced zone of GRS-IBS abutment V_0 is calculated as $V_0 = L_r \cdot H$. Due to different L_r considered in this Section, V_0 were different for different L_r/H. The original volume V_0 were 29.4 m^3/m (316 cu. ft./ft.), 17.9 m^3/m (193 cu. ft./ft.), and 10.7 m^3/m (115 cu. ft./ft.) for the cases of L_r/H = 0.8, 0.5, and 0.3 respectively. As expected, Fig. 7.4.93 shows that the reduction of the primary reinforcement length resulted in larger lateral deflection and vertical compression of the abutment. All three relationships in Fig. 7.4.93 are below the zero volume change line, indicating that the increase of the lateral deflection was smaller than the increase of the vertical compression. In other words, the abutment had more vertical compression than lateral deflection.

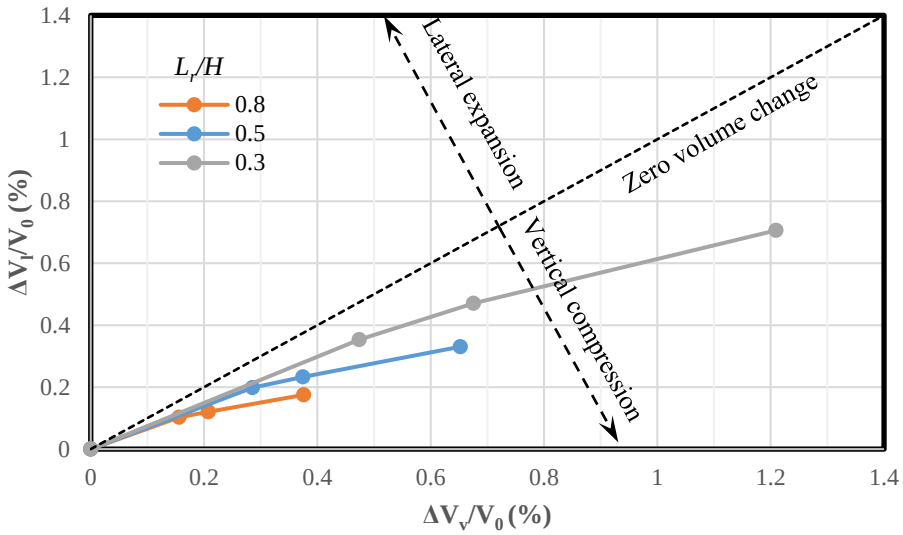

Fig. 7.4.93: Effect of the primary reinforcement length on the volume change of the GRS-IBS abutment

Table 7.4.22 summarizes the effect of the primary reinforcement length on the maximum vertical and lateral displacements of the abutment. It should be noted that all the displacements presented in Table 7.4.22 excluded the displacement of the abutment in Stage 3. In other words, the displacements of the abutment were initialized after the construction of the abutment and the beam seat were finished.

Table 7.4.22: Effect of the primary reinforcement length on the maximum vertical and lateral displacements of the abutment

L_r / H	Displacement (mm)	Construction stage		
		Stage 4 (bridge slab)	Stage 5 (integrated approach)	Stage 6 (traffic load)
0.8	$\delta_{v\text{-max}}$	35.36	37.19	51.06
	$\delta_{l\text{-max}}$	10.63	11.18	14.54
0.5	$\delta_{v\text{-max}}$	36.40	38.10	52.10
	$\delta_{l\text{-max}}$	12.78	13.39	17.29
0.3	$\delta_{v\text{-max}}$	36.07	38.27	52.27
	$\delta_{l\text{-max}}$	13.50	14.70	19.00

7.4.5.8.6 Tension in the reinforcement

Figure 7.4.94 shows the effect of the primary reinforcement length on the maximum tensile forces of the reinforcement Tmax under both self-weight (i.e., Stage 2) and traffic load conditions (i.e., Stage 6). Under both the self-weight and the traffic load, the maximum tensile forces in the reinforcement were close from the top of the wall to the depth of approximately 3 m (10 ft) for all three reinforcement lengths. Below this depth, however, the reduction of the primary reinforcement length resulted in the increase of the maximum tensile force in the reinforcement. Similar to the findings of the lateral earth pressure behind wall facing and the lateral displacement of wall facing, the increase of Tmax in the reinforcement was significant when *Lr*/*H* decreased from 0.5 to 0.3.

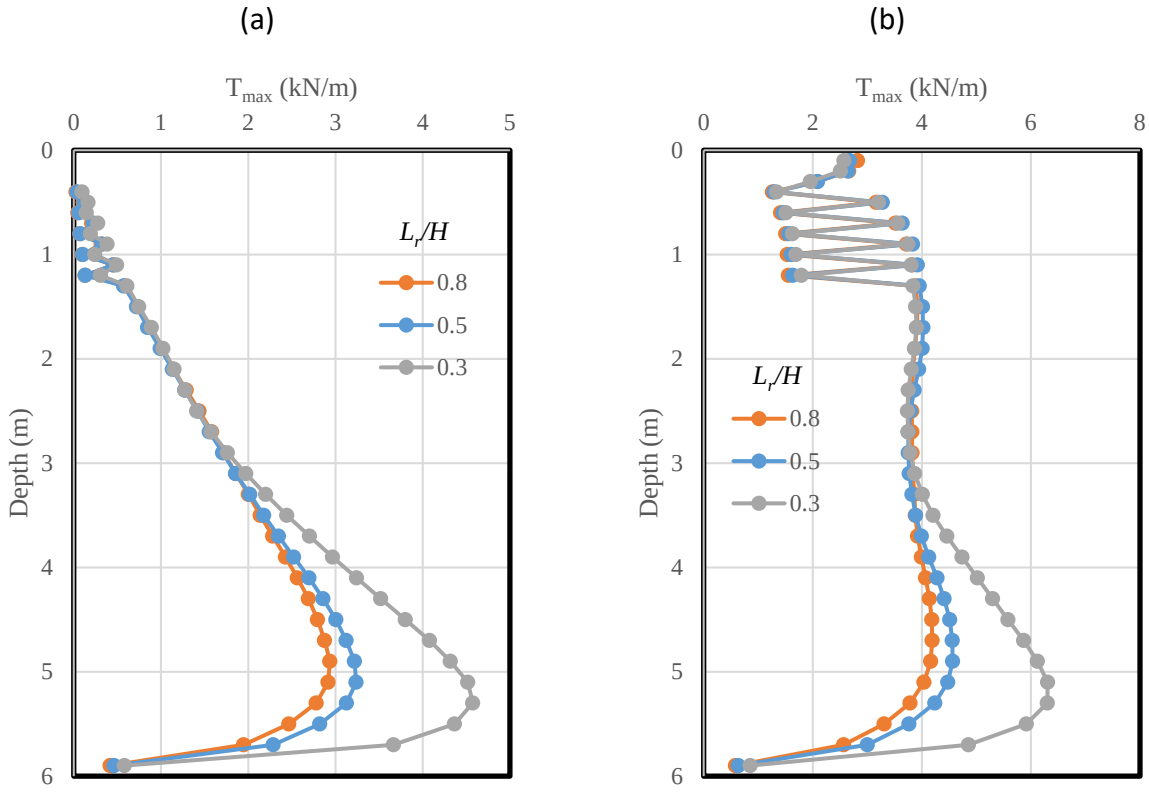

Fig. 7.4.94: Effect of the primary reinforcement length on the maximum tensile force T_{max} in the reinforcement: (a) Self-weight; (b) Traffic load.

Figure 7.4.95 shows the effect of the primary reinforcement length on the ratios of the connection force T_0 to the maximum tensile force T_{max} in the reinforcement under both self-weight (i.e., Stage 2) and traffic load conditions (i.e., Stage 6). The change of the primary reinforcement length had an insignificant influence on the ratio of the connection force T_0 to the maximum tensile force T_{max} in the reinforcement. At the depth of approximately 2 m (6.5 ft), the case with L_r/H = 0.3 resulted in slightly smaller T_0/T_{max}. However, the reduction of T_0/T_{max} was limited. It could be concluded that the maximum tensile force in the reinforcement happened near the facing connection for all three reinforcement lengths.

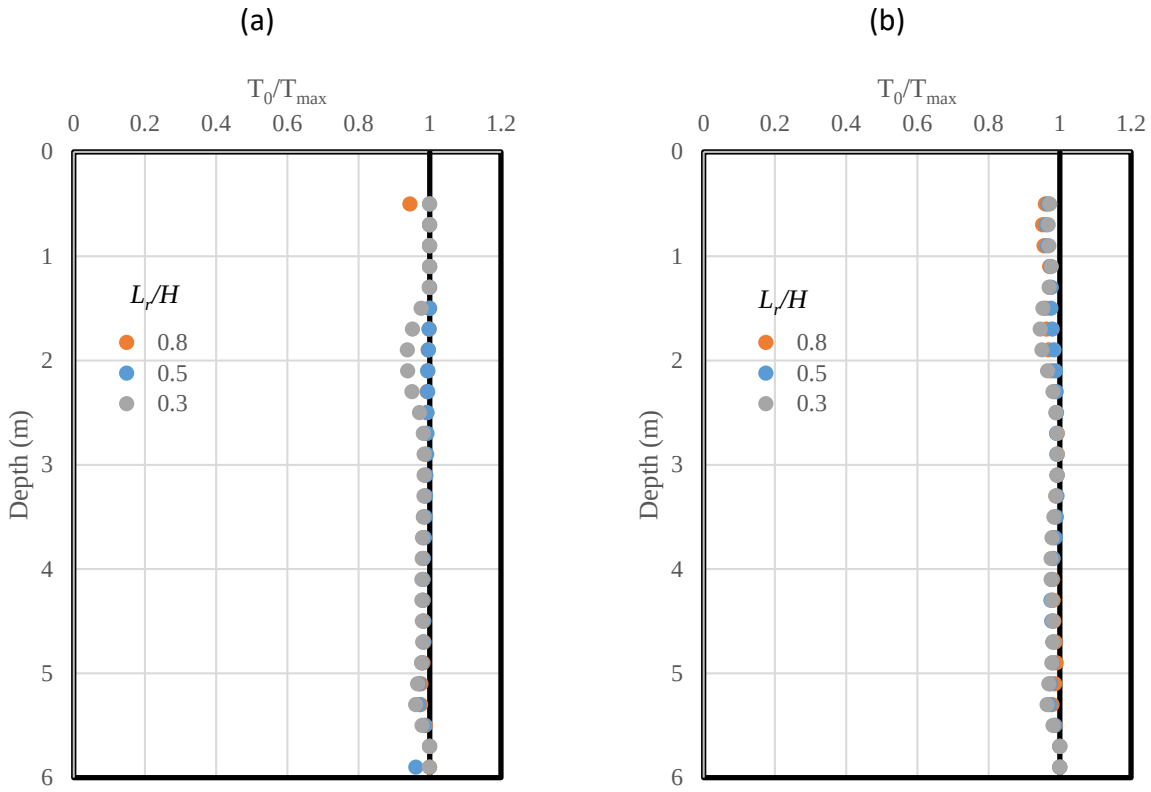

Fig. 7.4.95: Effect of the primary reinforcement length on the ratio of connection force T_0 to the maximum tensile force T_{max} in the reinforcement: (a) Self-weight; (b) Traffic load.

Figure 7.4.96 shows the effect of the primary reinforcement length on the normalized coefficients of lateral earth pressure K_r/K_a under both self-weight (i.e., Stage 2) and traffic load conditions (i.e., Stage 6). The determination of σ_v under different loading conditions was discussed in Section 7.4.5.2.6 (i.e., using the overburden stress and the AASHTO 2 to1 truncation method without surcharge q). Under the self-weight, the reduction of the primary reinforcement length resulted in larger K_r/K_a especially near the top and bottom of the wall. Under the traffic load, the K_r/K_a ratios were close for all three reinforcement lengths from the top of the wall to the depth of approximately 3 m (10 ft). Below this depth, shorter reinforcement length caused larger K_r/K_a. Similar to the findings of T_{max} in the reinforcement, the increase of K_r/K_a was significantly large when L_r/H decreased from 0.5 to 0.3.

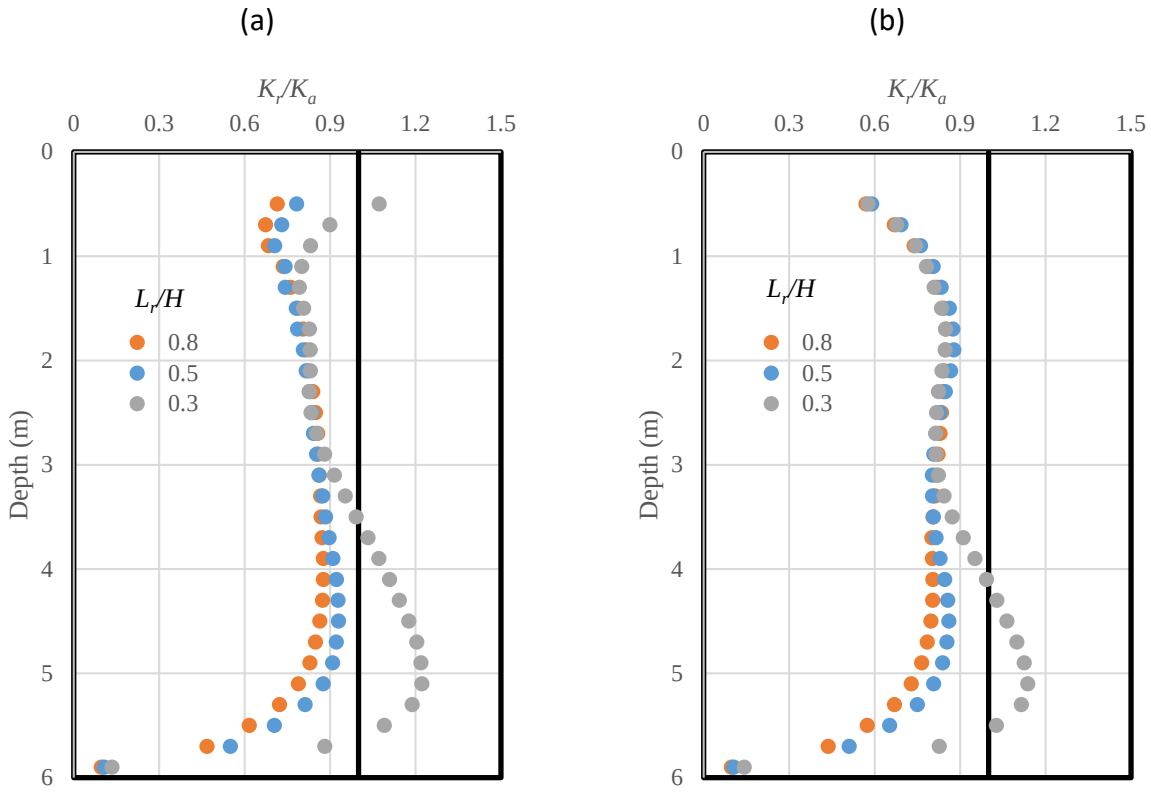

Fig. 7.4.96: Effect of the primary reinforcement length on the normalized coefficient of lateral earth pressure K_r/K_a: (a) Self-weight; (b) Traffic load.

7.4.5.9 EFFECT OF FOUNDATION COMPRESSIBILITY

This section discusses the effect of the foundation compressibility. In the baseline model, the elastic modulus of the foundation soil was 2000 MPa (290 ksi), which represents a bedrock or firm foundation without any settlement. Two additional cases considering the foundation soil with the elastic moduli of 20 MPa (2.9 ksi) and 200 MPa (29 ksi) were studied.

7.4.5.9.1 Lateral earth pressure

Figure 7.4.97 shows the effect of the foundation compressibility on the lateral earth pressures behind the CMU facing blocks under both self-weight (i.e., Stage 2) and traffic load conditions (i.e., Stage 6). Figure 7.4.97 shows that the change of the foundation compressibility had an insignificant influence on the lateral earth pressure behind wall facing. Under the self-weight, the lateral earth pressure behind wall facing was close to Coulomb's active lateral earth pressure. Under the traffic load, the lateral earth pressure increased significantly near the top of the wall due to loading.

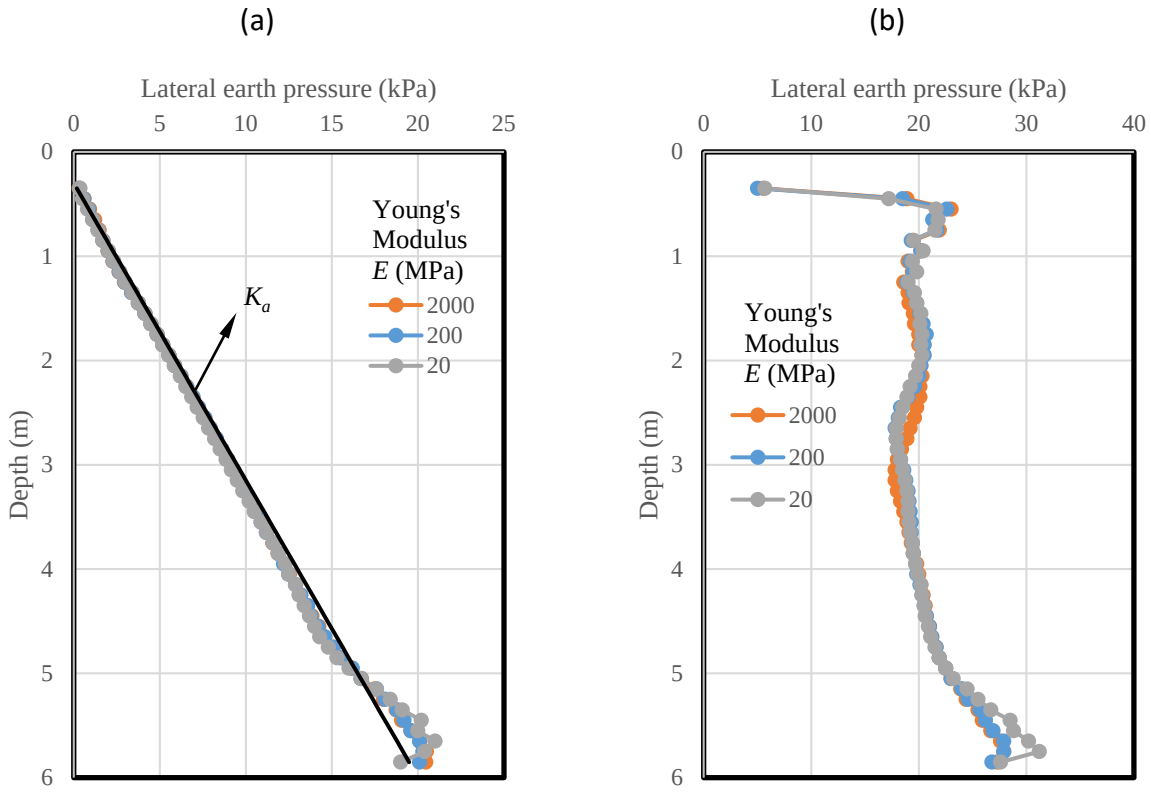

Fig. 7.4.97: Effect of the foundation compressibility on the lateral earth pressure behind CMU facing blocks: (a) Self-weight; (b) Traffic load.

7.4.5.9.2 Additional vertical stress induced by loading

Figure 7.4.98 shows the effect of the foundation compressibility on the distribution of additional vertical stress Δp at 0.5 m (20 in) from the back of CMU facing blocks with the depth due to loading. Figure 7.4.98 shows that the change of the foundation compressibility did not have any significant influence on the additional vertical stress distribution due to loading. The distribution of the additional vertical stresses of all three cases almost overlapped with each other. The AASHTO 2 to 1 truncation method calculated the additional vertical stresses in reasonable agreement with the numerical results.

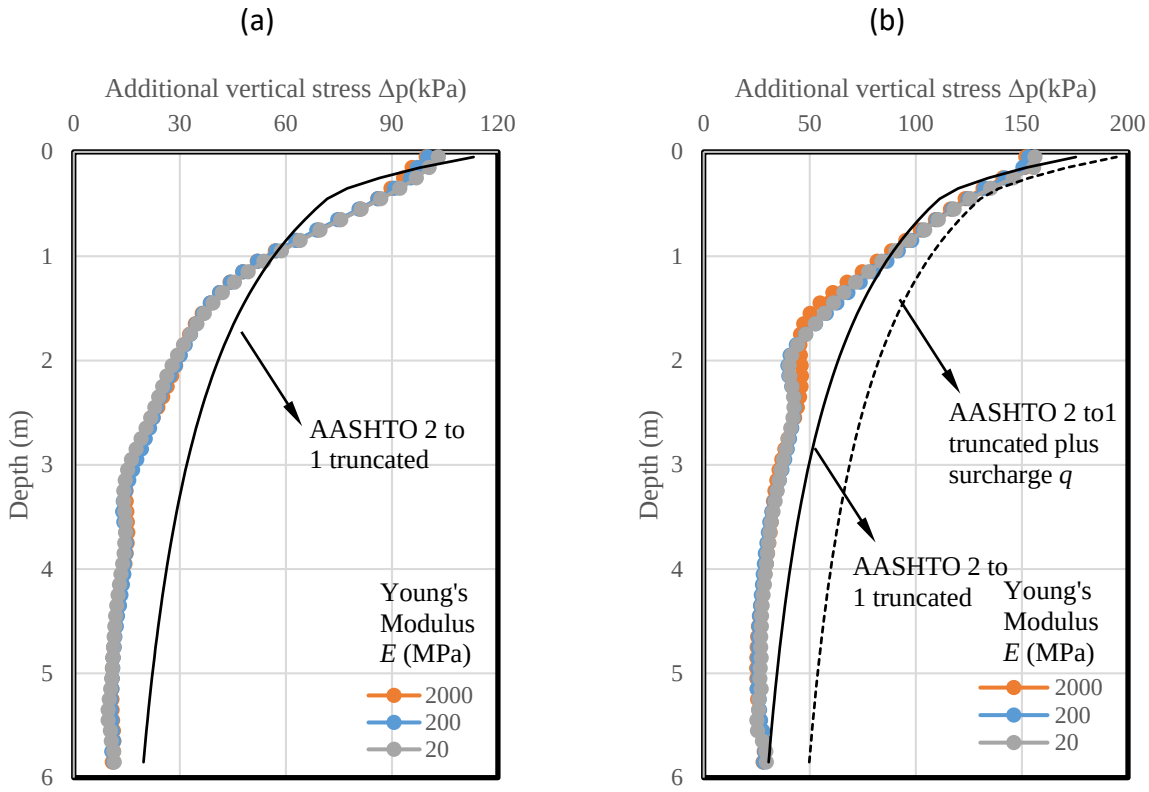

Fig. 7.4.98: Effect of the foundation compressibility on the additional vertical stress induced by loading: (a) Induced by the self-weight of the bridge slab; (b) Induced by the self-weight of the bridge slab and the traffic load.

7.4.5.9.3 Lateral displacement of CMU facing blocks

Figure 7.4.99 shows the effect of the foundation compressibility on the lateral displacement of CMU facing blocks under self-weight (i.e., Stage 2), bridge slab (i.e., Stage 4), and traffic load conditions (i.e., Stage 6). As excepted, the reduction of the Young's modulus of the foundation increased the total lateral displacement of CMU facing blocks. When the Young's modulus of the foundation decreased from 2000 MPa (290 ksi) to 200 MPa (29 ksi), the increase of the lateral displacement of wall facing was minimum. When the Young's modulus of the foundation decreased from 200 MPa (29 ksi) to 20 MPa (2.9 ksi), however, the increase was more obvious as shown in Fig. 7.4.99.

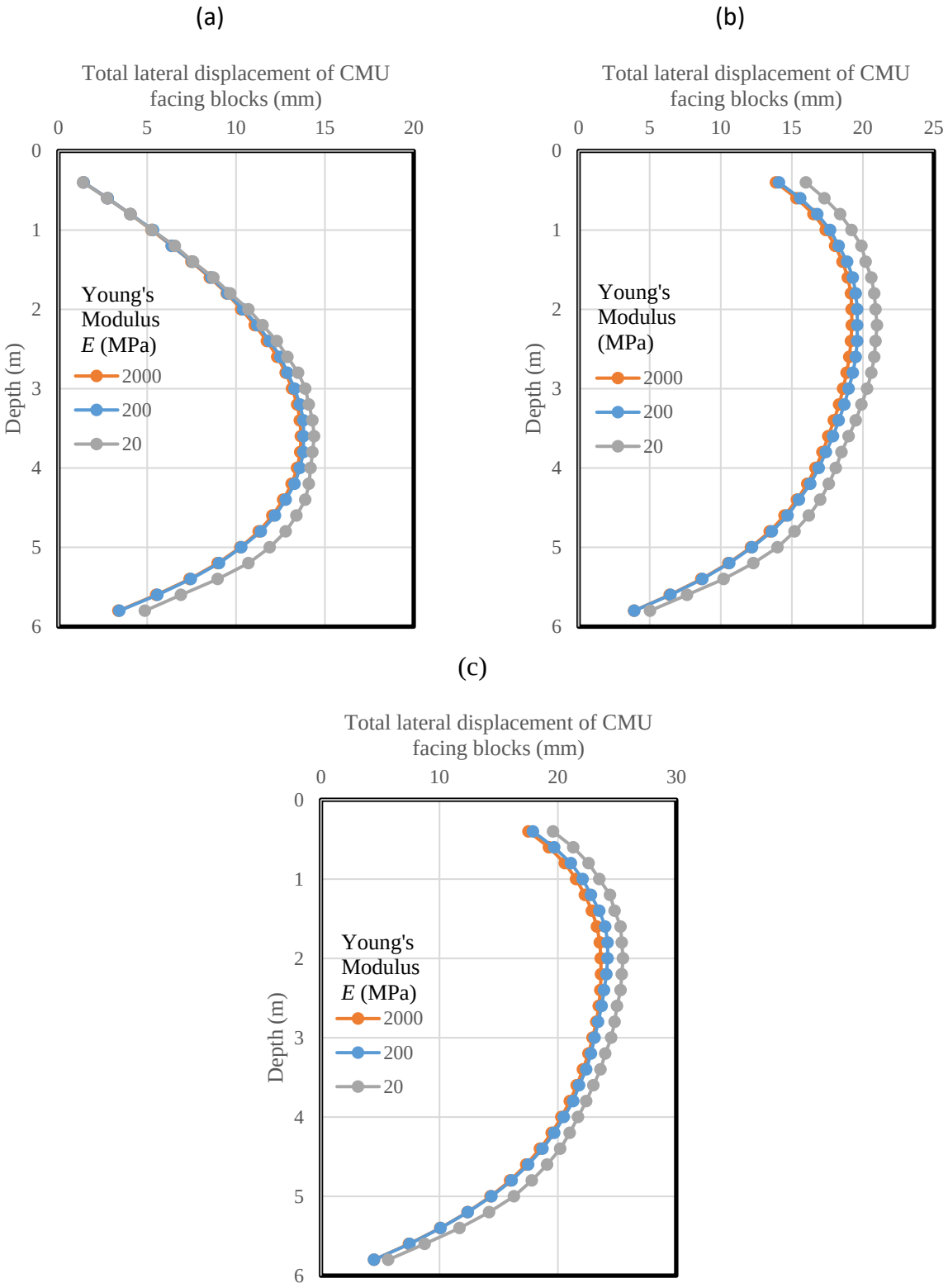

Fig. 7.4.99: Effect of the foundation compressibility on the lateral displacement of CMU facing blocks: (a) Self-weight; (b) Bridge slab; (c) Traffic load.

Figure 7.4.100 shows the effect of the foundation compressibility on the additional lateral displacement of CMU facing blocks induced by the traffic load only (i.e., the difference in the lateral displacements between Stage 6 and Stage 5). Figure 7.4.100 shows that all three cases had almost the same additional lateral displacements of CMU facing blocks from the bottom of the wall to the depth of approximately 3 m (10 ft). From the top of the wall to the depth of approximately 3 m (10 ft), the case with the rigid foundation (i.e., *E* = 2000 MPa (290 ksi)) had the smallest additional wall facing deflection.

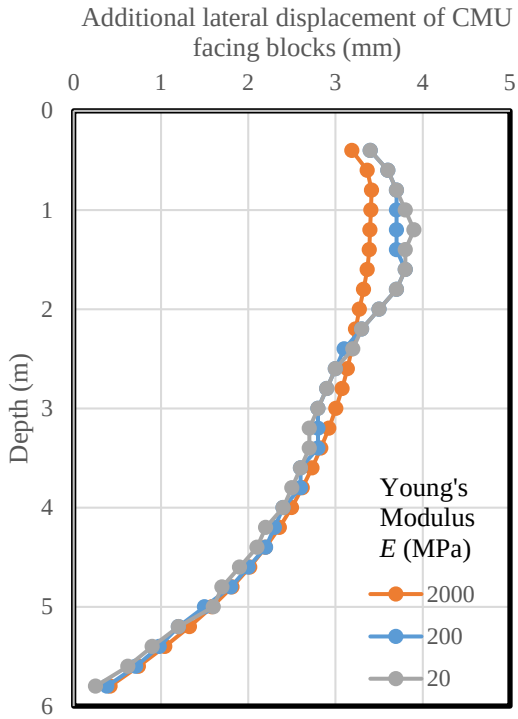

Fig. 7.4.100: Effect of the foundation compressibility on the additional lateral displacement of CMU facing blocks induced by traffic load

7.4.5.9.4 Settlement profile for the bridge slab and integrated approach

Figure 7.4.101 shows the effect of the foundation compressibility on the additional settlement on the top of the bridge slab and integrated approach induced by traffic load (i.e., the difference in the settlement between Stage 6 and Stage 5). As expected, the decrease of the foundation modulus resulted in larger settlement of both the bridge slab and the integrated approach way. When the Young's modulus of foundation decreased from 2000 MPa (290 ksi) to 200 MPa (29 ksi), the increase of settlement was minimum. When the Young's modulus of the foundation decreased from 200 MPa (29 ksi) to 20 MPa (2.9 ksi), however, the increase was much more significant. It should be noted that the increase of the additional settlement of the bridge slab was almost the same as that of the integrated approach way, indicating that the increase of the settlement was due to the compression of the foundation only.

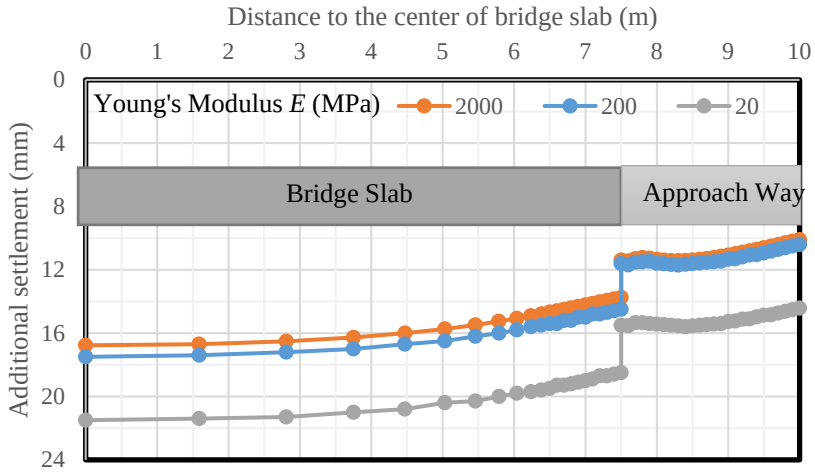

Fig. 7.4.101: Effect of the foundation compressibility on the additional settlement of the bridge slab and integrated approach induced by traffic load

7.4.5.9.5 Volume change of the abutment

Figure 7.4.102 shows the effect of the foundation compressibility on the normalized lateral volume change – normalized vertical volume change curves. As expected, the increase of the foundation compressibility resulted in larger vertical compression and lateral deflection. When the Young's modulus of the foundation decreased from 2000 MPa (290 ksi) to 200 MPa (29 ksi), the volume change of the abutment was almost the same. When the Young's modulus of the foundation decreased from 200 MPa (29 ksi) to 20 MPa (2.9 ksi), however, the foundation settlement became significant, thus resulting in the relationship for the case with E = 20 MPa (2.9 ksi) shifted to the right.

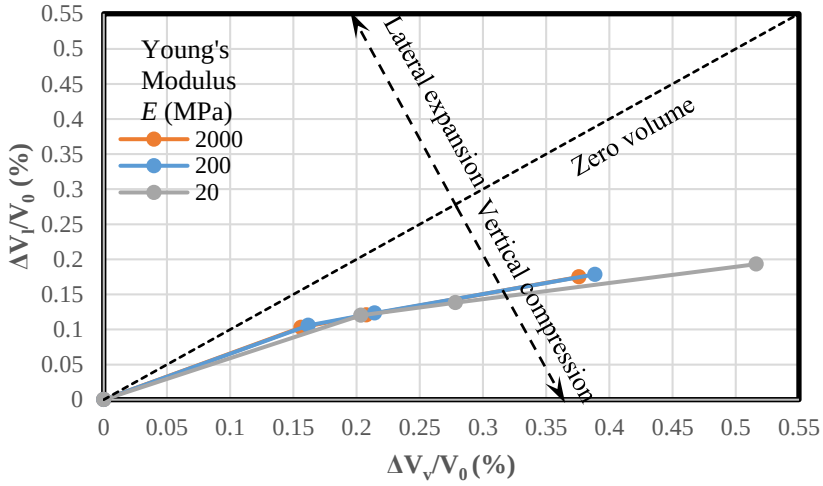

Fig. 7.4.102: Effect of the foundation compressibility on the volume change of the GRS-IBS abutment

Table 7.4.23 summarizes the effect of the foundation compressibility on the maximum vertical and lateral displacement of the abutment. It should be noted that all the displacements presented in Table 7.4.23 excluded the displacements of the abutment in Stage 3. In other words, the displacements of the abutment were initialized after the construction of the abutment and the beam seat were finished.

Table 7.4.23: Effect of the foundation compressibility on the maximum vertical and lateral displacements of the abutment

Young's Modulus (MPa)	Displacement (mm)	Construction stage		
		Stage 4 (bridge slab)	Stage 5 (integrated approach)	Stage 6 (traffic load)
2000	$\delta_{v\text{-max}}$	35.36	37.19	51.06
	$\delta_{l\text{-max}}$	10.63	11.18	14.54
200	$\delta_{v\text{-max}}$	36.03	37.88	52.47
	$\delta_{l\text{-max}}$	10.88	11.38	15.05
20	$\delta_{v\text{-max}}$	38.76	41.86	60.46
	$\delta_{l\text{-max}}$	12.66	12.95	16.55

7.4.5.9.6 Tension in the reinforcement

Figure 7.4.103 shows the effect of the foundation compressibility on the maximum tensile forces of the reinforcement T_{max} under both self-weight (i.e., Stage 2) and traffic load conditions (i.e., Stage 6). Figure 7.4.103 shows that all three curves for the cases with different foundation moduli almost overlapped with each other, indicating that the change of the foundation compressibility did not change the maximum tensile force distribution in the reinforcement under both the self-weight and the traffic load.

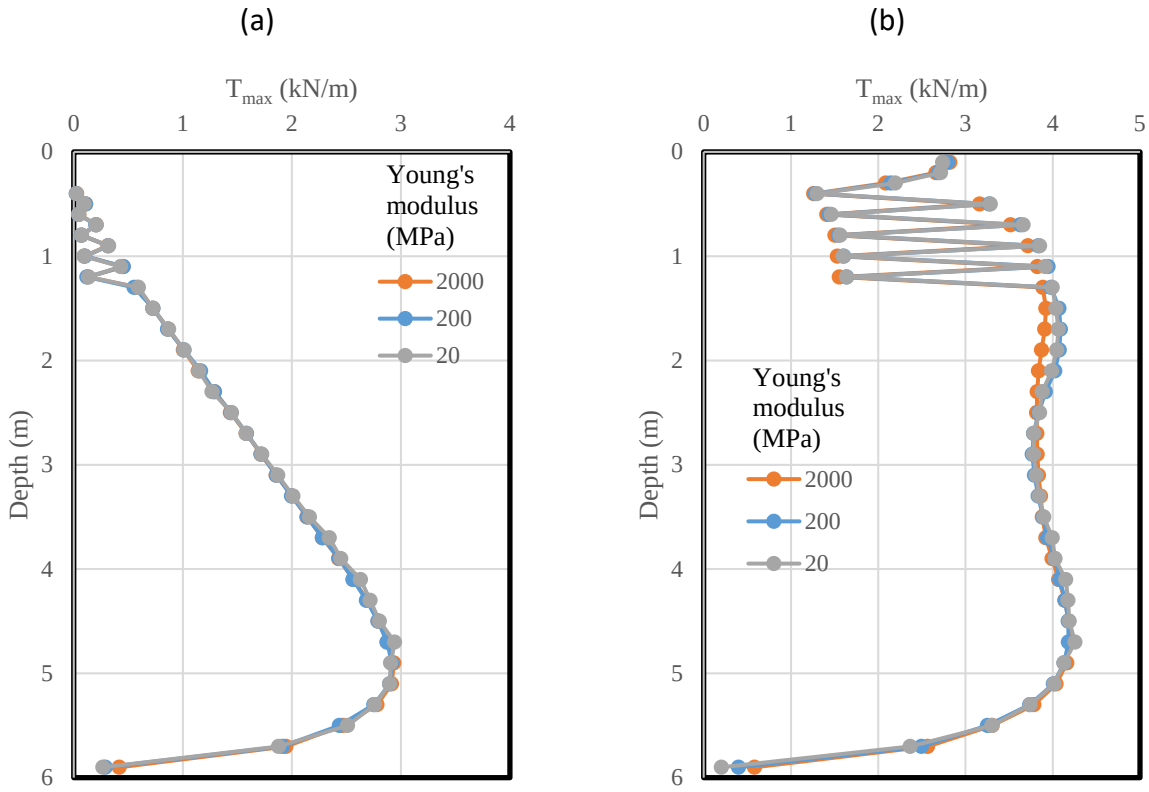

Fig. 7.4.103: Effect of the foundation compressibility on the maximum tensile force T_{max} in the reinforcement: (a) Self-weight; (b) Traffic load.

Figure 7.4.104 shows the effect of the foundation compressibility on the ratios of the connection force T_0 to the maximum tensile force T_{max} in the reinforcement under both self-weight (i.e., Stage 2) and traffic load conditions (i.e., Stage 6). Figure 7.4.104 shows that the ratios of T_0/T_{max} were almost the same for all three cases except that the increase of the foundation compressibility resulted in a slight decrease of the ratio of T_0/T_{max} at the depth of approximately 5 m (16.4 ft). Therefore, it can be concluded that the maximum tensile force in the reinforcement happened near the wall facing connection despite the change of the foundation compressibility.

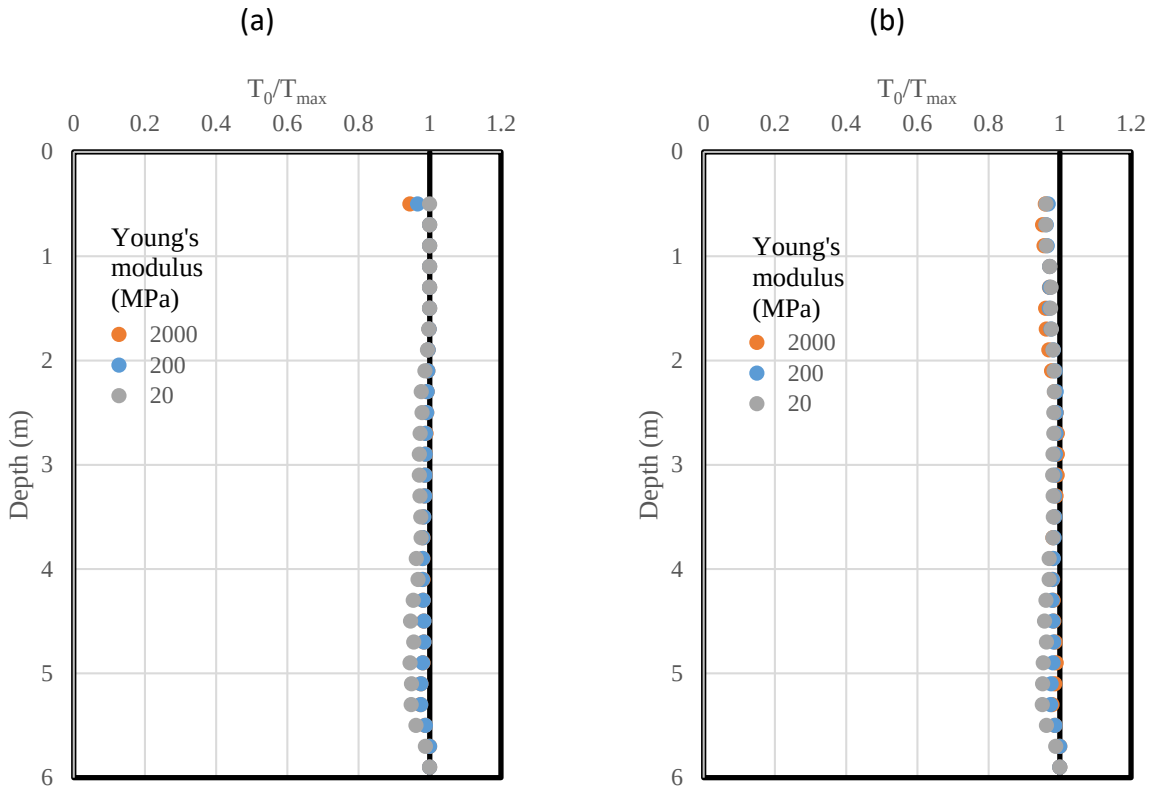

Fig. 7.4.104: Effect of the foundation compressibility on the ratio of connection force T_0 to the maximum tensile force T_{max} in the reinforcement: (a) Self-weight; (b) Traffic load.

Figure 7.4.105 shows the effect of the foundation compressibility on the normalized coefficients of lateral earth pressure K_r/K_a under both self-weight (i.e., Stage 2) and traffic load conditions (i.e., Stage 6). The determination of σ_v under different loading conditions was discussed in Section 7.4.5.2.6 (i.e., using the overburden stress and the AASHTO 2 to1 truncation method without surcharge q). Figure 7.4.105 shows that the change of the foundation compressibility did not affect the normalized coefficient of lateral earth pressure K_r/K_a distribution with the depth. K_r/K_a was close to 1.0 near the mid-height of the wall and smaller than 1.0 near the top or bottom of the wall for all three cases.

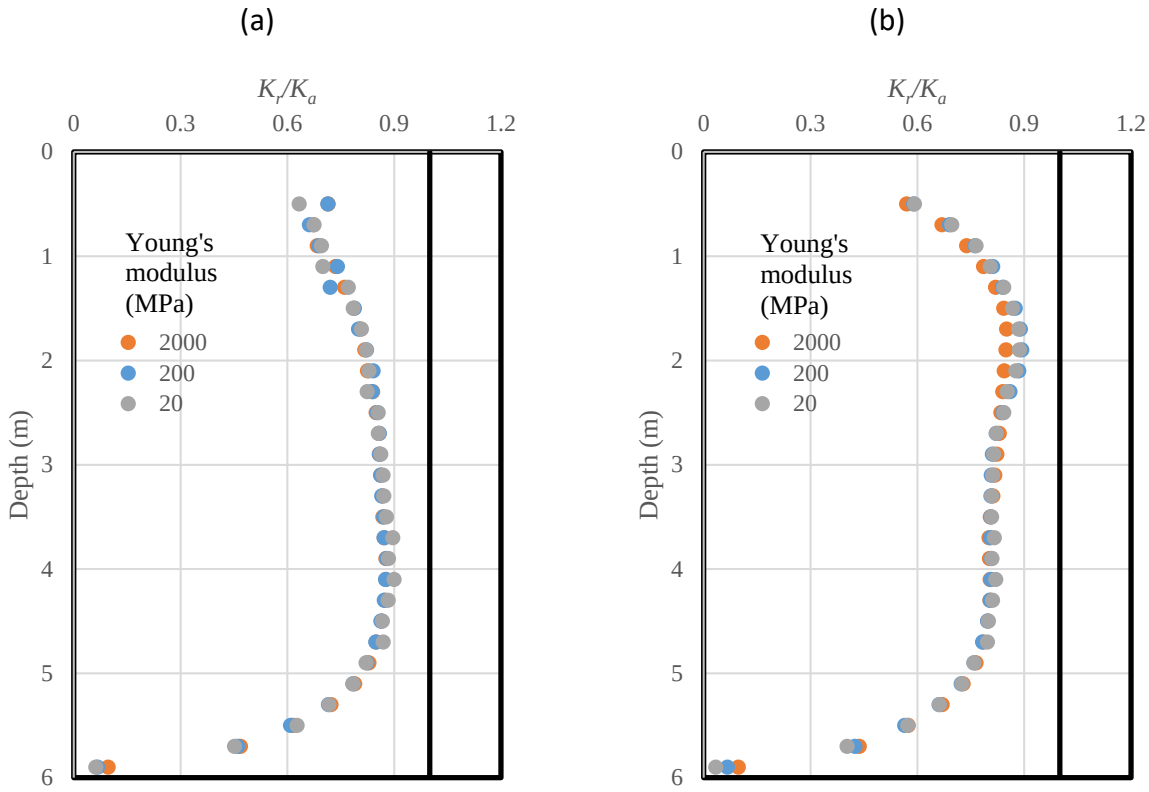

Fig. 7.4.105: Effect of the foundation compressibility on the normalized coefficient of lateral earth pressure K_r/K_a: (a) Self-weight; (b) Traffic load.

7.4.5.10 EFFECT OF BEAM SEAT WIDTH

This section discusses the effect of the beam seat width *b*. In the baseline model, the beam seat width *b* = 0.6 m (2 ft). Additional two cases with *b* of 0.9 m (3 ft) and 1.2 m (4 ft) were studied.

7.4.5.10.1 Lateral earth pressure

Figure 7.4.106 shows the effect of the beam seat width *b* on the lateral earth pressure behind the CMU facing blocks under both self-weight (i.e., Stage 2) and traffic load conditions (i.e., Stage 6). Under the self-weight, all three curves overlapped with each other, which was reasonable since the bridge slab was not placed on the top of the wall yet. The lateral earth pressure under the self-weight was close to Coulomb's active lateral earth pressure. Under the traffic load, however, the increase of the beam seat width resulted in lower lateral earth pressure behind the CMU facing blocks near the top of the wall. The larger beam seat width resulted in the bridge slab load farther away from the wall facing, thus the lower lateral earth pressure.

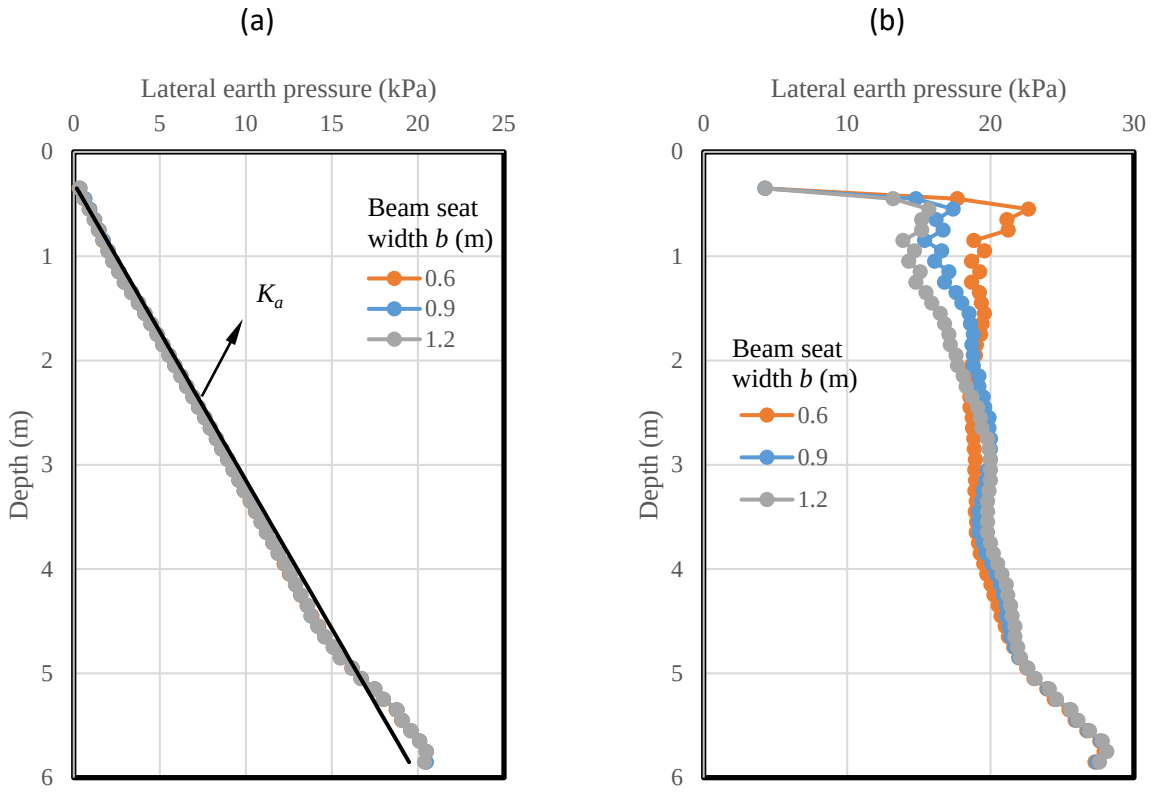

Fig. 7.4.106: Effect of the beam seat width on the lateral earth pressure behind CMU facing blocks: (a) Self-weight; (b) Traffic load.

7.4.5.10.2 Additional vertical stress induced by loading

Figure 7.4.107 shows the effect of the beam seat width b on the distribution of additional vertical stress Δp with the depth due to loading. Due to the change of the beam seat width, the location of the additional vertical stress Δp varied (i.e., the distance between the centroid of the concentrated vertical load and the back of the wall face $d = b/2 + a_b$ changed due to the change of b). The location of the Δp distribution presented in Fi.g 7.4.107 changed from 0.5 m (20 in) from the back of CMU facing blocks when b = 0.6 m (2 ft) m to 0.65 m (26 in) from the back of CMU facing blocks when b = 0.6 m (3 ft) and finally to 0.8 m (31 in) from the back of CMU facing blocks when b = 1.2 m (4 ft).

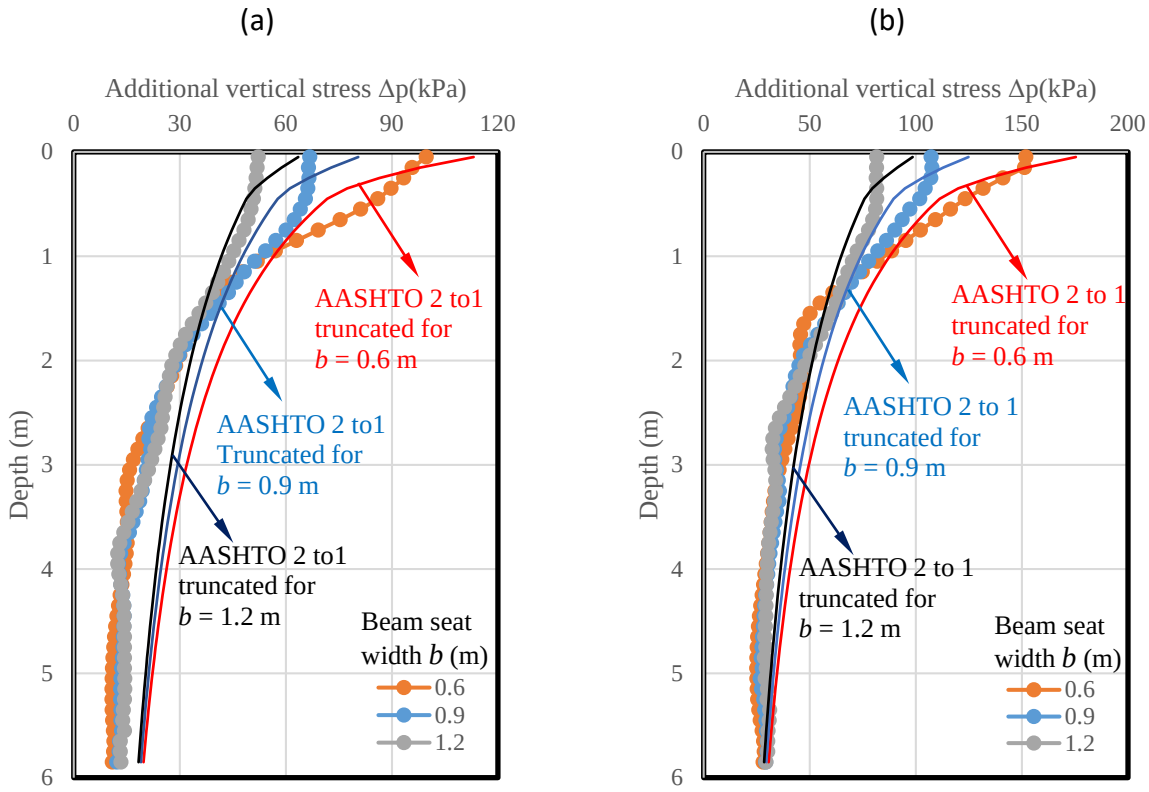

Fig. 7.4.107: Effect of the beam seat width on the additional vertical stress induced by loading: (a) Induced by the self-weight of the bridge slab; (b) Induced by the self-weight of the bridge slab and the traffic load.

Figure 7.4.107 shows that the increase of the beam seat width b significantly reduced the additional vertical stress Δp caused by loading near the top of the wall to the depth of approximately 1 m (3.3 ft). Below this depth, the change of the beam seat width did not affect the additional vertical stress distribution inside the wall since it was far away from the loading area. Figure 7.4.107 also shows the calculated additional vertical stress Δp using the AASHTO 2 to 1 truncation method using different beam seat widths b. The AASHTO 2 to 1 truncation method calculated higher Δp than the numerical results under the bridge slab (i.e., from the depth of 0 to 0.3 m (1 ft)). The existence of 0.3 m (1 ft) thick geofoam in front of the bridge seat might have resulted in lower additional stress in the numerical model under the bridge slab. From the depth of 0.3 m (1 ft) to a certain depth, the AASHTO 2 to 1 truncation method calculated lower additional vertical stresses than the numerical results. This depth varied due to the change of the beam seat width b. Below a certain depth, the AASHTO 2 to 1 truncation method calculated higher Δp than the numerical results. Salgado (2008) pointed out that the 2 to 1 approximation method underestimated the vertical stress within the depth range between 0 to 1.5b vertically below the load and overestimated it at a greater depth. The numerical results are consistent with the conclusion of Salgado (2008).

7.4.5.10.3 Lateral displacement of CMU facing blocks

Figure 7.4.108 shows the effect of the beam seat width *b* on the lateral displacement of CMU facing blocks under self-weight (i.e., Stage 2), bridge slab (i.e., Stage 4), and traffic load conditions (i.e., Stage 6). Under the self-weight, all three curves overlapped with each other since the bridge slab had not been placed on the top of the wall yet. Under the bridge slab load and traffic load, the increase of the beam seat width resulted in slightly smaller lateral displacement of CMU facing blocks near the top of the wall and slightly larger lateral displacement near the mid-height of the wall.

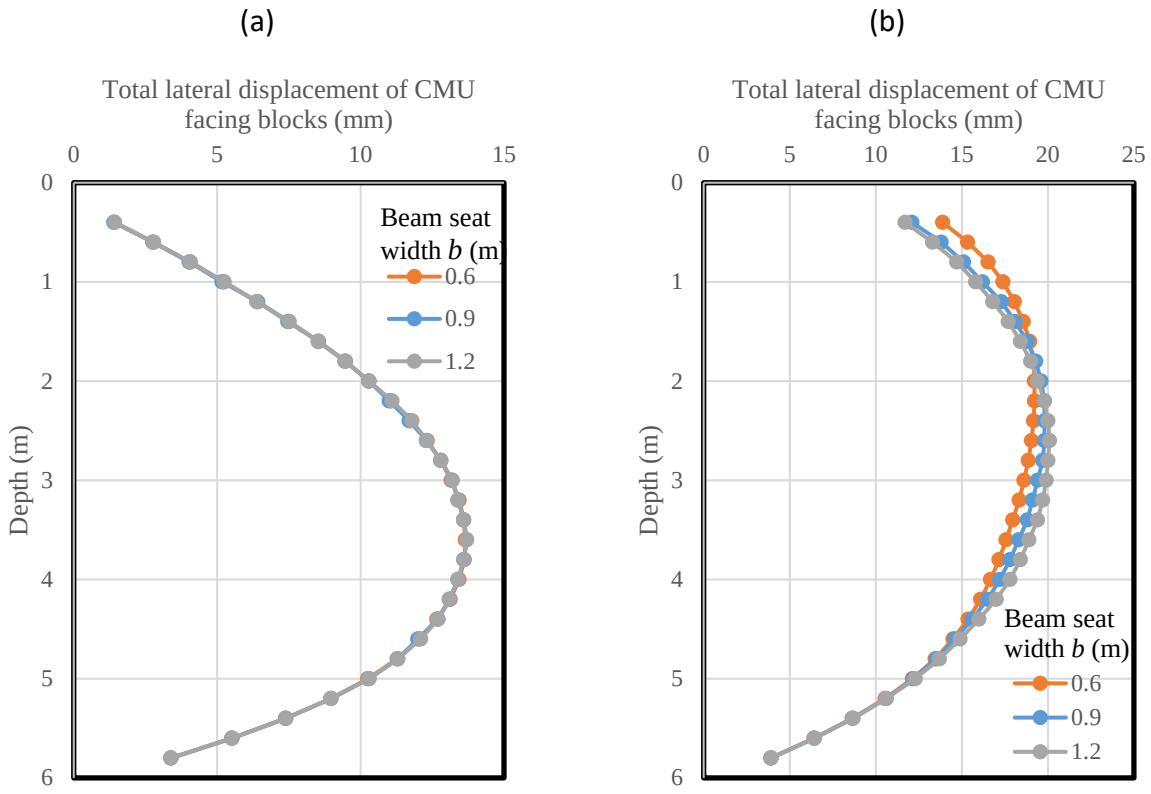

Fig. 7.4.108: Effect of the beam seat width on the lateral displacement of CMU facing blocks: (a) Self-weight; (b) Bridge slab;

(c)

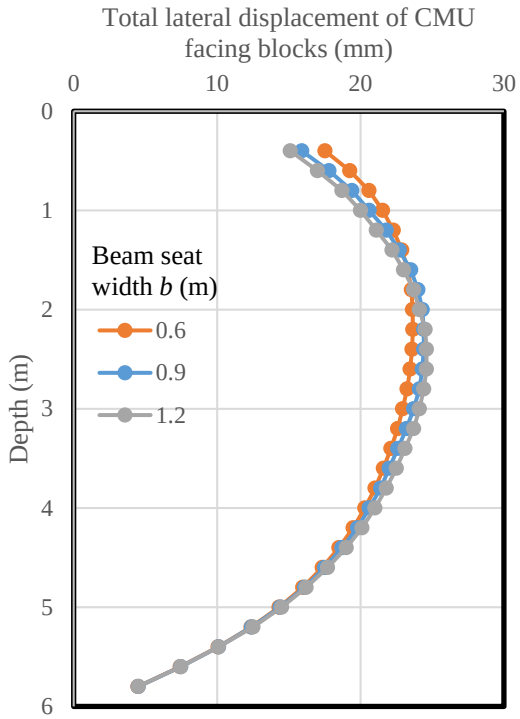

Fig. 7.4.108: Effect of the beam seat width on the lateral displacement of CMU facing blocks: (c) Traffic load (continued).

Figure 7.4.109 shows the effect of the beam seat width on the additional lateral displacement of CMU facing blocks induced by the traffic load only (i.e., the difference in the lateral displacement between Stage 6 and Stage 5). When the beam seat width increased, the total load applied on the top of the wall also increased. Therefore, the increase of the beam seat width resulted in larger additional lateral displacement of CMU facing blocks near the mid-height of the wall. However, the increase of the additional wall deflection due to the traffic load was minimum and within 1.0 mm (0.04 in). The effect of the beam seat width on the additional lateral displacement of CMU facing blocks induced by traffic load was limited to the upper portion of the wall. This was because the traffic load was applied on top of the wall and the change of beam seat width resulted in different applied pressure on top of the wall. The influence of beam seat width was expected to decrease with increasing depth away from top of the wall.

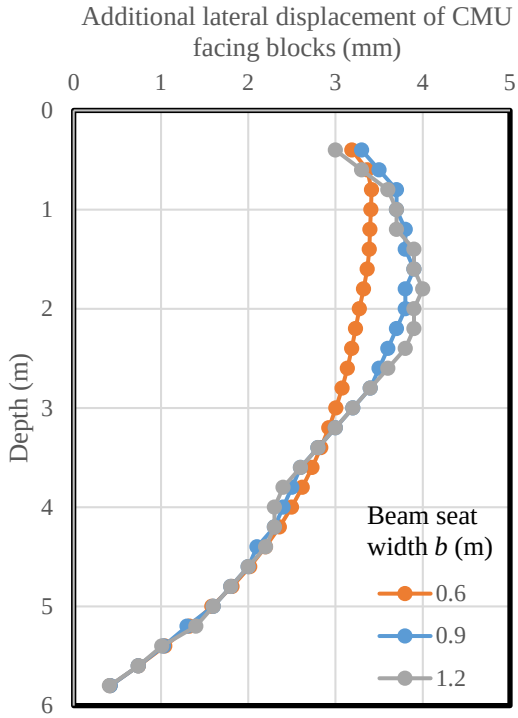

Fig. 7.4.109: Effect of the beam seat width on the additional lateral displacement of CMU facing blocks induced by traffic load

7.4.5.10.4 Settlement profile for the bridge slab and integrated approach

Figure 7.4.110 shows the effect of the beam seat width on the additional settlement on the top of the bridge slab and integrated approach induced by the traffic load (i.e., the difference in the settlement between Stage 6 and Stage 5). Figure 7.4.110 shows that the increase of the beam seat width reduced the additional settlement of both the bridge slab and the integrated approach way induced by the traffic load. In additional, the differential settlement at the end of the bridge slab also decreased with the increase of the beam seat width.

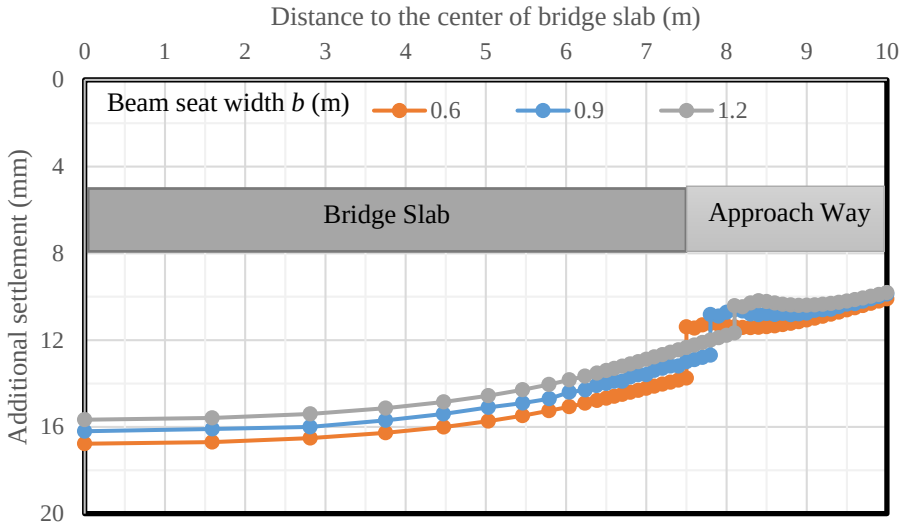

Fig. 7.4.110: Effect of the beam seat width on the additional settlement of the bridge slab and integrated approach induced by traffic load

7.4.5.10.5 Volume change of the abutment

Figure 7.4.111 shows the effect of the beam seat width on the normalized lateral volume change – normalized vertical volume change curves. Figure 7.4.111 shows that the increase of the beam seat width slightly increased the total vertical compression and lateral deflection of the abutment since the total load applied on the top of the abutment increased. However, the difference among these three cases was minimum.

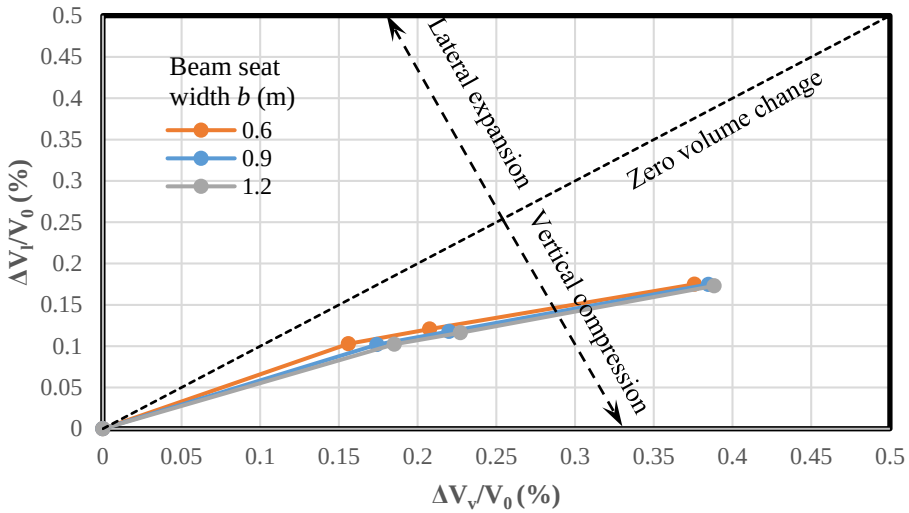

Fig. 7.4.111: Effect of the beam seat width on the volume change of the GRS-IBS abutment

Table 7.4.24 summarizes the effect of the beam seat width on the maximum vertical and lateral displacement of the abutment. It should be noted that all the displacements presented in Table 7.4.24 excluded the displacements of the abutment in Stage 3. In other words, the displacements of the abutment were initialized after the construction of the abutmentand the beam seat were finished.

Table 7.4.24: Effect of the beam seat width on the maximum vertical and lateral displacements of the abutment

Beam seat width (m)	Displacement (mm)	Construction stage		
		Stage 4 (bridge slab)	Stage 5 (integrated approach)	Stage 6 (traffic load)
0.6	$\delta_{v\text{-max}}$	35.36	37.19	51.06
	$\delta_{l\text{-max}}$	10.63	11.18	14.54
0.9	$\delta_{v\text{-max}}$	31.14	32.74	45.94
	$\delta_{l\text{-max}}$	9.11	9.72	13.42
1.2	$\delta_{v\text{-max}}$	28.46	29.96	42.66
	$\delta_{l\text{-max}}$	8.64	9.04	12.74

7.4.5.10.6 Tension in the reinforcement

Figure 7.4.112 shows the effect of the beam seat width on the maximum tensile forces of the reinforcement T_{max} under both self-weight (i.e., Stage 2) and traffic load conditions (i.e., Stage 6). Under the self-weight, all three curves overlapped with each other, which is reasonable since the bridge slab had not been placed on the top of the wall yet. Under the traffic load, the increase of the beam seat width resulted in larger maximum tensile force T_{max} in the reinforcement near the top of the wall and smaller T_{max} near the mid-height of the wall.

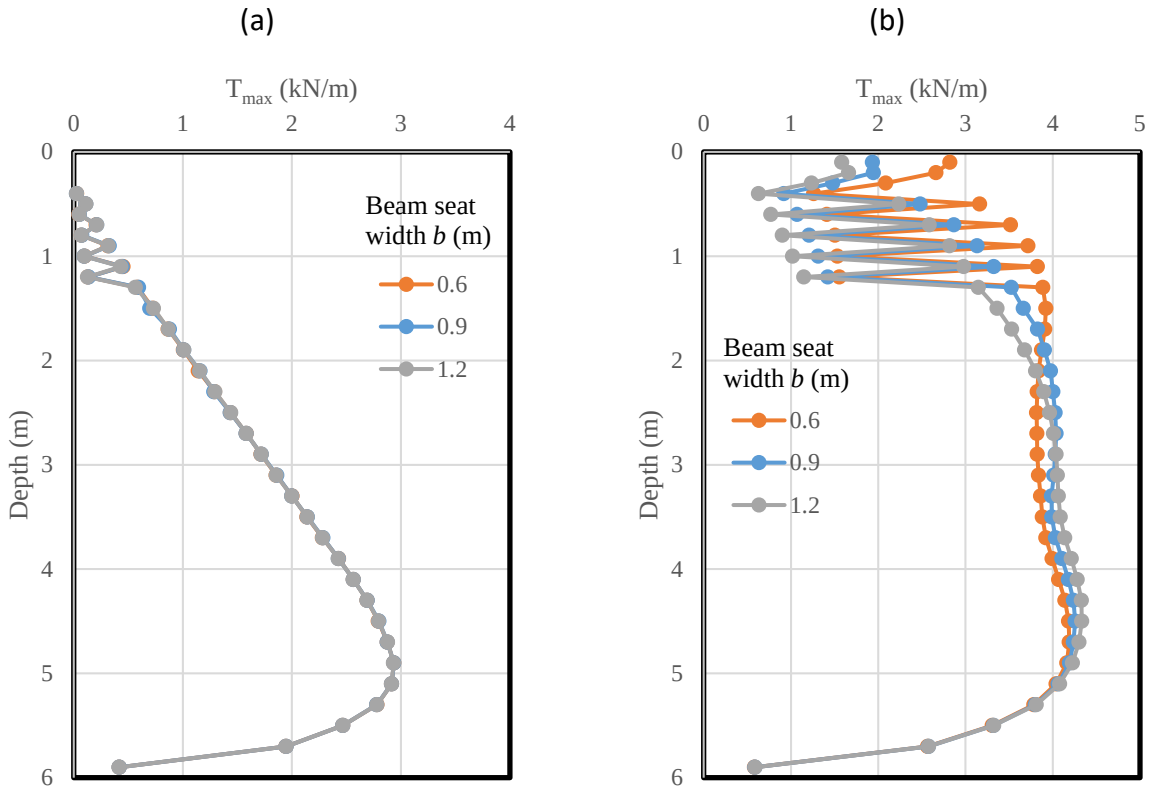

Fig. 7.4.112: Effect of the beam seat width on the maximum tensile force T_{max} in the reinforcement: (a) Self-weight; (b) Traffic load.

Figure 7.4.113 shows the effect of the beam seat width on the ratios of the connection force T_0 to the maximum tensile force T_{max} in the reinforcement under both self-weight (i.e., Stage 2) and traffic load conditions (i.e., Stage 6). Under the self-weight, all three curves overlapped with each other, which is reasonable since the bridge slab had not been placed on the top of the wall yet. Under the traffic load, however, the increase of the beam seat width resulted in lower T_0/T_{max} near the depth of approximately 2 m (6.5 ft). The larger beam seat width resulted in the center of the vertical load farther away from the wall facing connection, thus the lower T_0/T_{max}. However, this decrease was minimum.

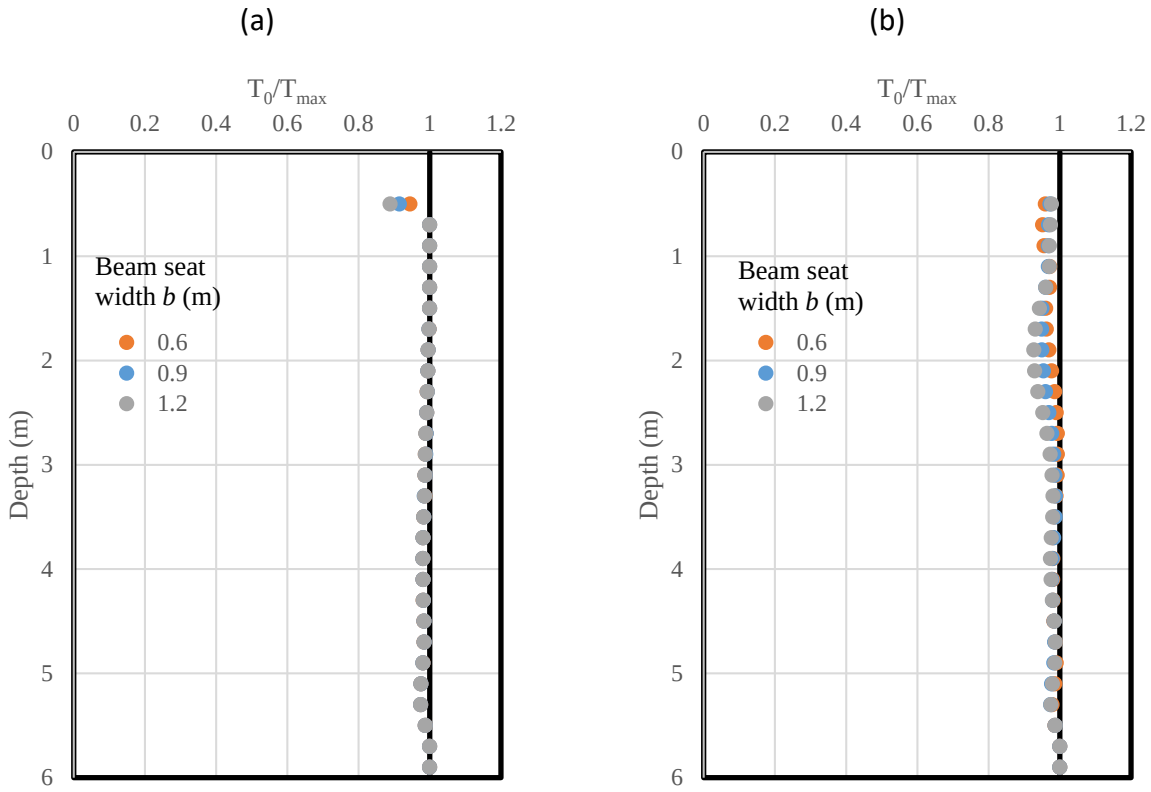

Fig. 7.4.113: Effect of the beam seat width on the ratio of connection force T_0 to the maximum tensile force T_{max} in the reinforcement: (a) Self-weight; (b) Traffic load.

Figure 7.4.114 shows the effect of the beam seat width on the normalized coefficients of lateral earth pressure K_r/K_a under both self-weight (i.e., Stage 2) and traffic load conditions (i.e., Stage 6). Under the self-weight, all three curves overlapped with each other, which is reasonable since the bridge slab had not been placed on the top of the wall yet. Under the traffic load, the increase of the beam seat width resulted in the increase of the normalized coefficient of lateral earth pressure K_r/K_a near the mid-height of the wall. The calculation of K_r/K_a under the traffic load required the additional vertical stress calculated using the AASHTO 2 to 1 truncation method as shown in Fig. 7.4.107. The AASHTO 2 to 1 truncation method calculated lower additional vertical stress with the increase of the beam seat width, thus resulting in larger K_r/K_a according to Equation (7.4.14).

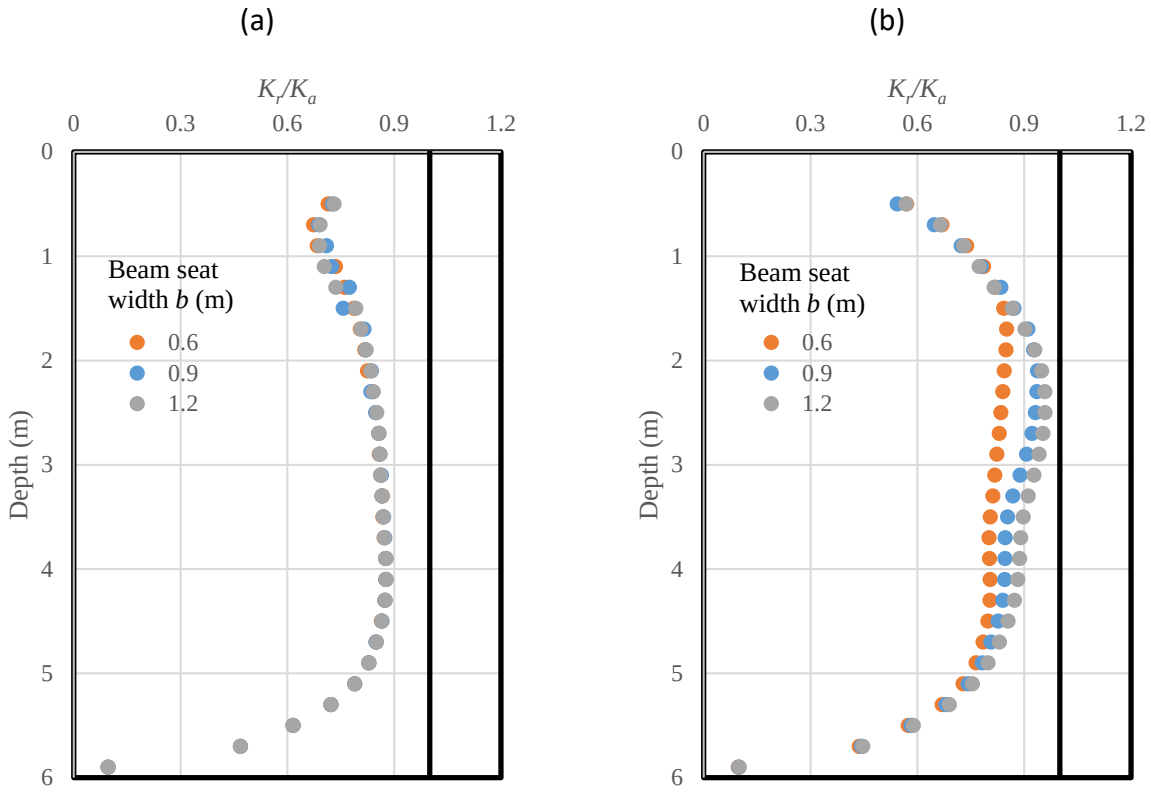

Fig. 7.4.114: Effect of the beam seat width on the normalized coefficient of lateral earth pressure K_r/K_a: (a) Self-weight; (b) Traffic load.

7.4.5.11 EFFECT OF COMPACTION STRESS

This section discusses the effect of the compaction stress. In the baseline model, no compaction stress was considered. An additional case of 8 kPa (167 psf) compaction stress was studied. A uniform vertical stress of 8 kPa (167 psf) was applied on top of each lift of the backfill soil layer and was removed before the placement of next lift to simulate the compaction effect in the field. The compaction stress was only applied to the soil in the reinforced zone. Hatami and Bathurst (2005) and Zheng and Fox (2017) have successfully used 8 kPa (167 psf) vertical compaction stress in their numerical models to study the effect of compaction.

7.4.5.11.1 Lateral earth pressure

Figure 7.4.115 shows the effect of the compaction stress on the lateral earth pressures behind the CMU facing blocks under both self-weight (i.e., Stage 2) and traffic load conditions (i.e., Stage 6). Figure 7.4.115 (a) shows that the lateral earth pressure behind wall facing from the numerical calculation was in good agreement to Coulomb's active earth pressure under the self-weight when no compaction stress was applied. When a uniform compaction stress of 8 kPa (167 psf) was applied on top of each lift and removed before the next lift, the lateral earth pressure had an almost uniform increase throughout the whole wall height. These results are consistent with those found by Filz and Duncan (1996), who reported that the permanent lateral earth pressure increased with compaction. Figure 7.4.115 (b) shows that the influence of the compaction stress

decreased under the traffic load as compared to that under the self-weight. The lateral earth pressures behind the wall facing for both cases were almost the same.

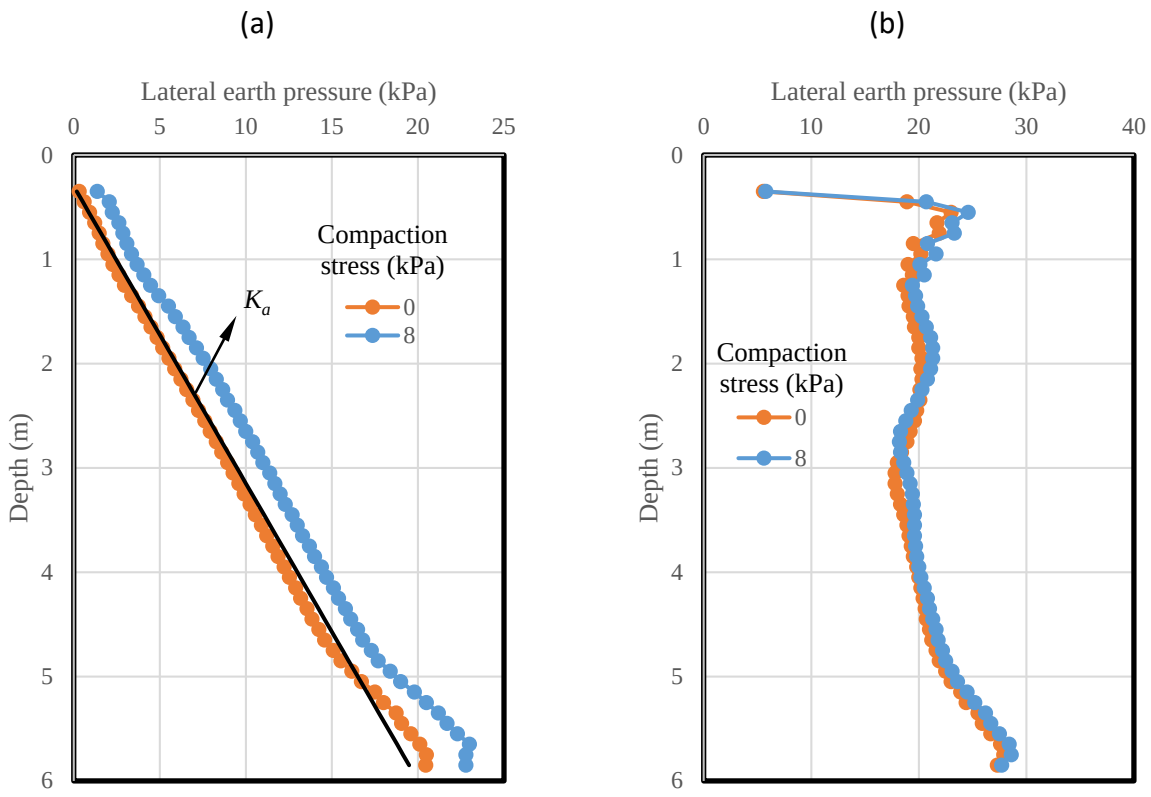

Fig. 7.4.115: Effect of the compaction stress on the lateral earth pressure behind CMU facing blocks: (a) Self-weight; (b) Traffic load.

7.4.5.11.2 Additional vertical stress induced by loading

Figure 7.4.116 shows the effect of the compaction stress on the distribution of additional vertical stress Δp at 0.5 m (20 in) from the back of CMU facing blocks with the depth due to loading. Figure 7.4.116 shows that the effect of the compaction stress on the additional vertical stress induced by loading was limited. The use of a uniform vertical compaction stress of 8 kPa (167 psf) resulted in slightly higher Δp on the top of the wall just beneath the bridge slab. The AASHTO 2 to 1 truncation method calculated the additional stresses in reasonable agreement with the numerical results.

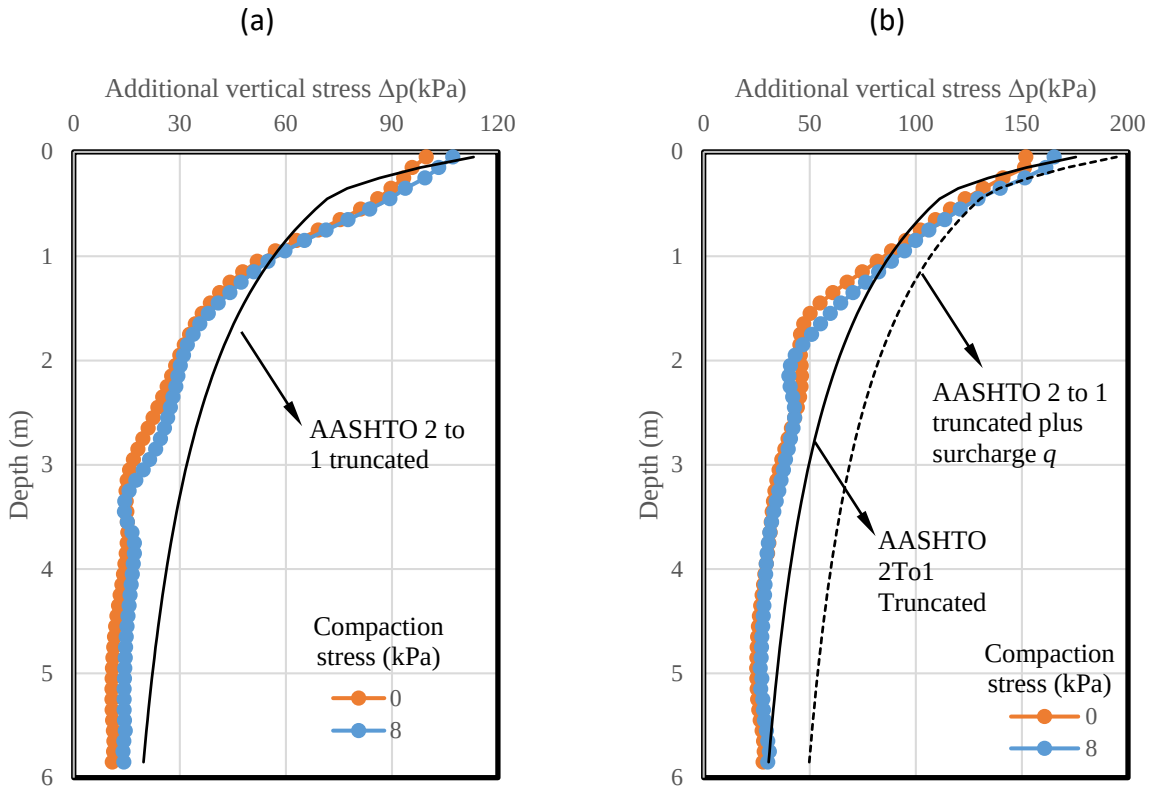

Fig. 7.4.116: Effect of the compaction stress on the additional vertical stress induced by loading: (a) Induced by the self-weight of the bridge slab; (b) Induced by the self-weight of the bridge slab and the traffic load.

7.4.5.11.3 Lateral displacement of CMU facing blocks

Figure 7.4.117 shows the effect of the compaction stress on the lateral displacements of CMU facing blocks under self-weight (i.e., Stage 2), bridge slab (i.e., Stage 4), and traffic load conditions (i.e., Stage 6). Figure 7.4.117 shows that the compaction stress of 8 kPa (167 psf) generated more lateral displacement of CMU facing blocks under the self-weight. Under both the bridge slab load and the traffic load, however, the total lateral displacement of CMU facing blocks were almost the same for both cases, indicating that the modulus of the backfill soil in the reinforced zone was increased due to compaction and the additional lateral displacement of wall facing decreased.

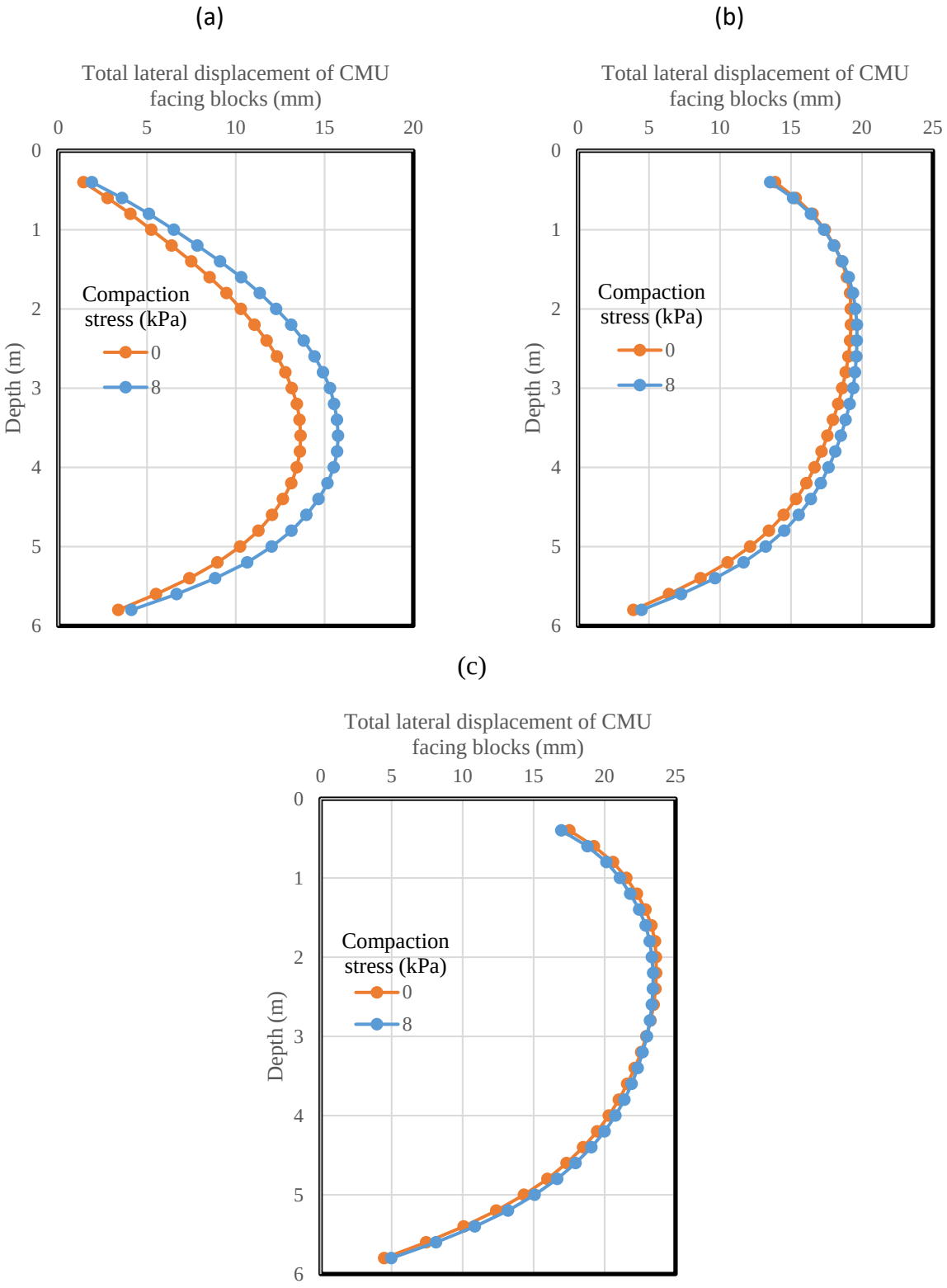

Fig. 7.4.117: Effect of the compaction stress on the lateral displacement of CMU facing blocks: (a) Self-weight; (b) Bridge slab; (c) Traffic load.

Figure 7.4.118 shows the effect of the compaction stress on the additional lateral displacement of CMU facing blocks induced by the traffic load only (i.e., the difference in the lateral displacements between Stage 6 and Stage 5). Figure 7.4.118 shows that the uniform vertical compaction stress of 8 kPa (167 psf) reduced the additional lateral displacement of CMU facing blocks induced by the traffic load. However, this reduction was minimum.

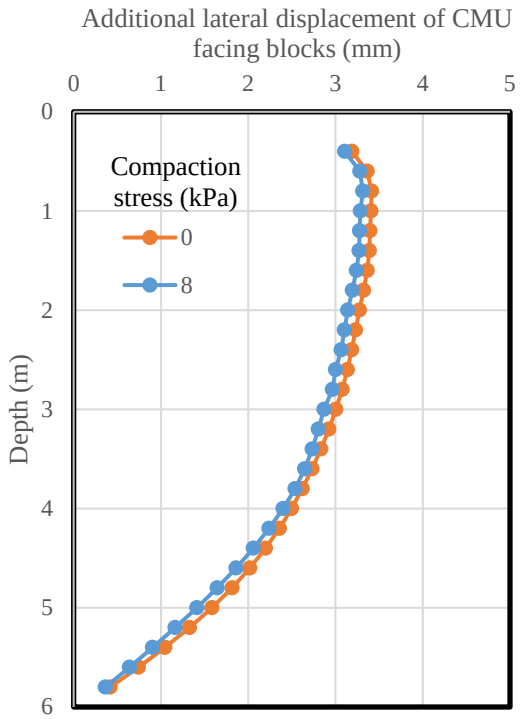

Fig. 7.4.118: Effect of the compaction stress on the additional lateral displacement of CMU facing blocks induced by traffic load

7.4.5.11.4 Settlement profile for the bridge slab and integrated approach

Figure 7.4.119 shows the effect of the compaction stress on the additional settlement on the top of the bridge slab and integrated approach induced by the traffic load (i.e., the difference in the lateral displacements between Stage 6 and Stage 5). Figure 7.4.119 shows that the compaction stress did not affect the additional settlement of the bridge slab induced by the traffic load. However, the additional settlement of the integrated approach way induced by the traffic load decreased when a uniform vertical compaction stress of 8 kPa (167 psf) was applied and removed later at each lift.

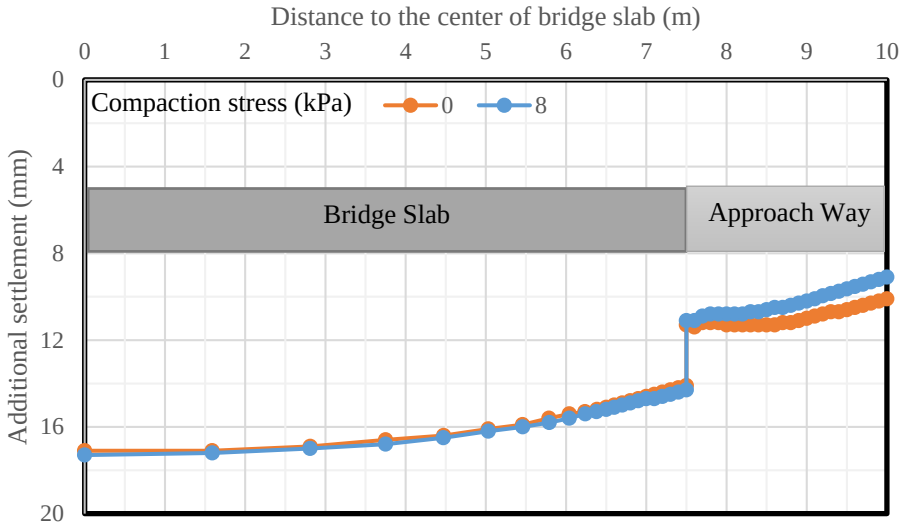

Fig. 7.4.119: Effect of the compaction stress on the additional settlement of the bridge slab and integrated approach induced by traffic load

7.4.5.11.5 Volume change of the abutment

Figure 7.4.120 shows the effect of the compaction stress on the normalized lateral volume change – normalized vertical volume change curve. The first point in Fig. 7.4.120, located at the origin, represents the condition of Stage 3 when the construction of the abutment including the placement of the bridge seat was finished and both the lateral and vertical displacements were initialized. Figure 7.4.120 shows that the case with the application and removal of the compaction stress of 8 kPa (167 psf) at each lift had smaller lateral deflection and vertical compression as compared to the case with no compaction stress. The application and removal of the uniform vertical compaction stress of 8 kPa (167 psf) at each lift increased the modulus of the backfill soil in the reinforced zone, thus reducing the additional vertical compression and lateral deflection of the abutment induced by the self-weight of the bridge slab (i.e., the second point), the self-weight of the integrated approach (i.e., the third point), and the traffic load (i.e., the fourth point).

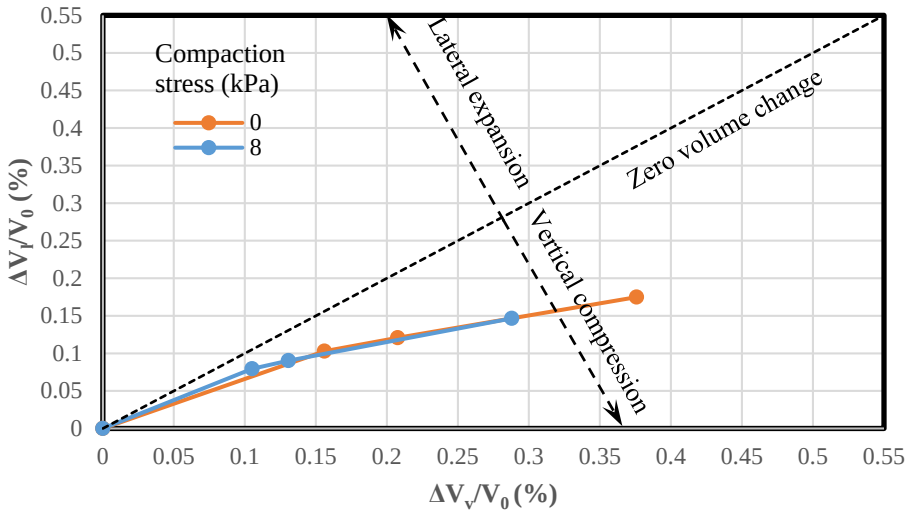

Fig. 7.4.120: Effect of the compaction stress on the volume change of the GRS-IBS abutment

Table 7.4.25 summarizes the effect of the compaction stress on the maximum vertical and lateral displacements of the abutment. It should be noted that all the displacements presented in Table 7.4.25 excluded the displacements of the abutment in Stage 3. In other words, the displacements of the abutment were initialized after the construction of the abutmentand the beam seat were finished.

Table 7.4.25: Effect of the compaction stress on the maximum vertical and lateral displacements of the abutment

Compaction stress (kPa)	Displacement (mm)	Construction stage		
		Stage 4 (bridge slab)	Stage 5 (integrated approach)	Stage 6 (traffic load)
0	$\delta_{v\text{-max}}$	35.36	37.19	51.06
	$\delta_{l\text{-max}}$	10.63	11.18	14.54
8	$\delta_{v\text{-max}}$	29.90	31.3	45.4
	$\delta_{l\text{-max}}$	9.76	10.07	13.58

7.4.5.11.6 Tension in the reinforcement

Figure 7.4.121 shows the effect of the compaction stress on the maximum tensile forces of the reinforcement T_{max} under both self-weight (i.e., Stage 2) and traffic load conditions (i.e., Stage 6). Under the self-weight, the application and removal of the uniform vertical compaction stress of

8 kPa (167 psf) at each lift resulted in an almost uniform increase of T_{max} throughout the whole wall height. The compaction stress resulted in larger lateral deformation and settlement of the backfill soil. The relative displacement between geotextile reinforcement and backfill soil was also increased, thus resulting in larger T_{max}. Under the traffic load, however, the compaction stress resulted in slightly larger T_{max} from the top of the wall to the mid-height. Below the depth of 3 m (10 ft), T_{max} in the reinforcement were almost the same for both cases.

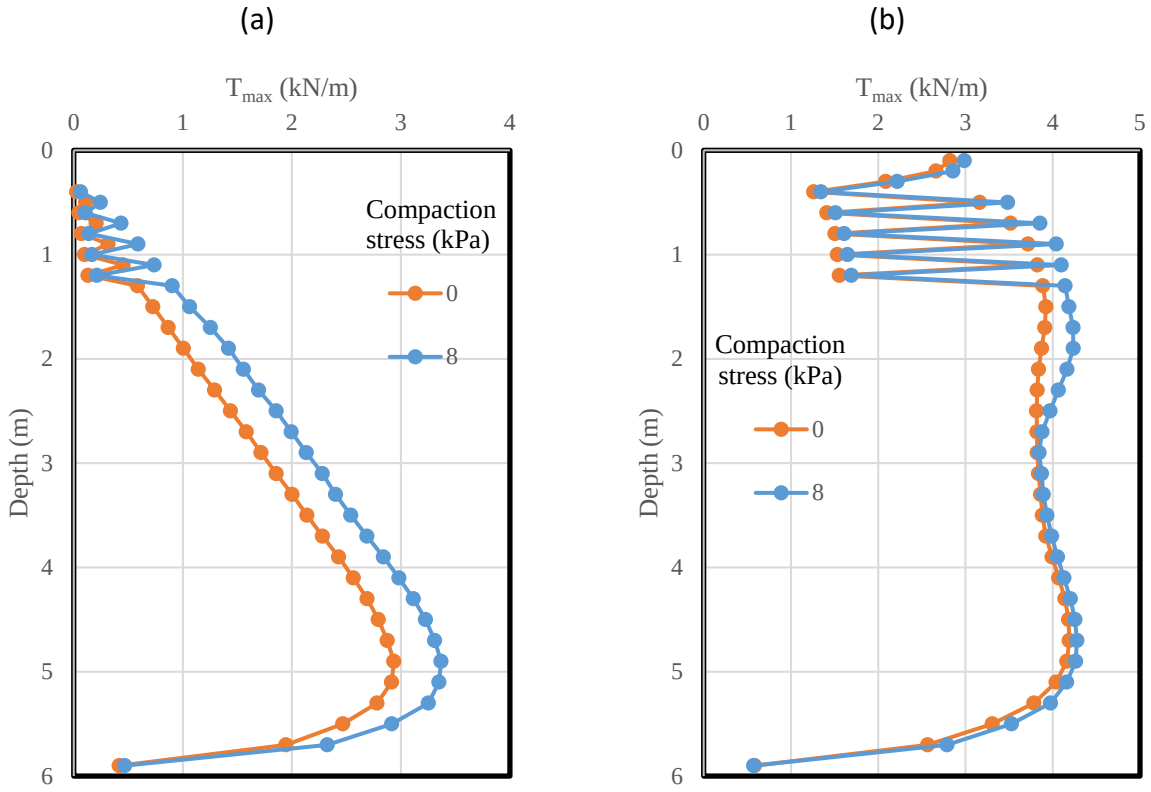

Fig. 7.4.121: Effect of the compaction stress on the maximum tensile force T_{max} in the reinforcement: (a) Self-weight; (b) Traffic load.

Figure 7.4.122 shows the effect of the compaction stress on the ratios of connection force T_0 to the maximum tensile force T_{max} in the reinforcement under both self-weight (i.e., Stage 2) and traffic load conditions (i.e., Stage 6). Figure 7.4.122 shows that the ratios T_0/T_{max} were close to 1.0 for both cases, indicating that the maximum tensile force T_{max} in the reinforcement happened near the wall facing connection. The application of the compaction stress did not change the location of T_{max}.

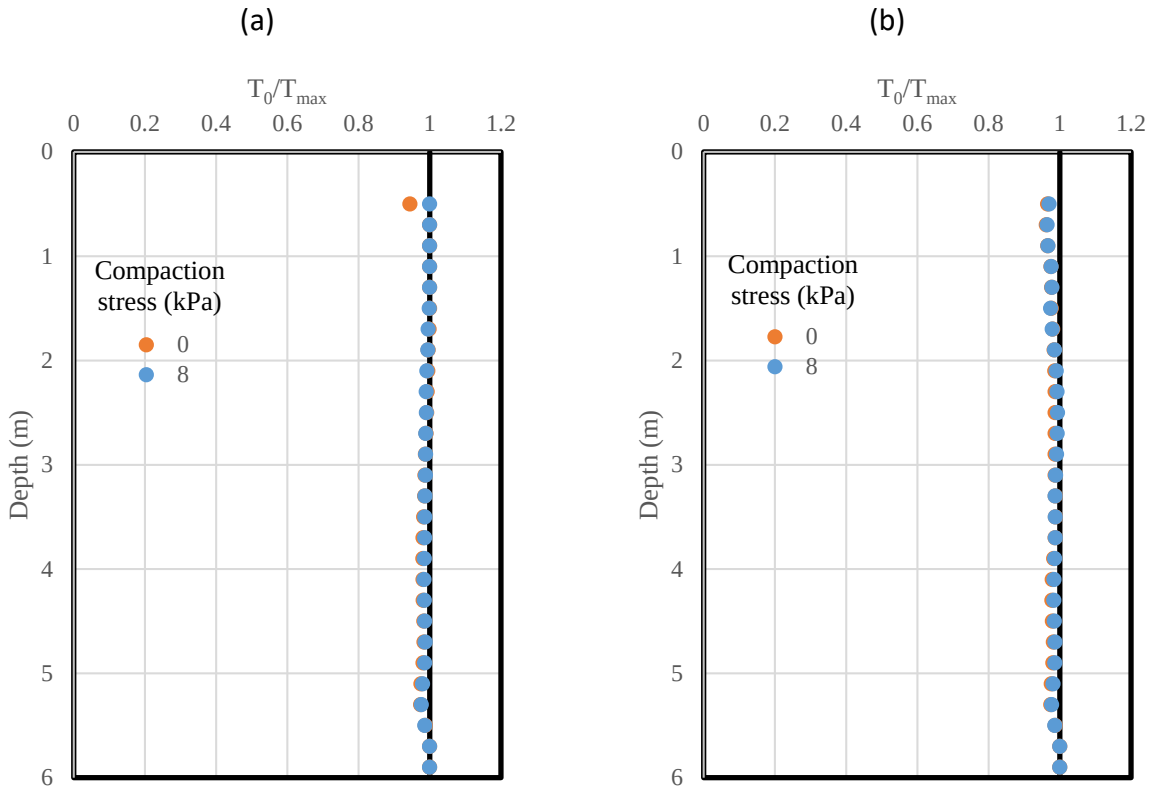

Fig. 7.4.122: Effect of the compaction stress on the ratio of connection force T_0 to the maximum tensile force T_{max} in the reinforcement: (a) Self-weight; (b) Traffic load.

Figure 7.4.123 shows the effect of the compaction stress on the normalized coefficients of lateral earth pressure K_r/K_a under both self-weight (i.e., Stage 2) and traffic load conditions (i.e., Stage 6). Since the additional vertical stress induced by loading was calculated using the AASHTO 2 to 1 method (not affected by the compaction stress), the change of K_r/K_a was due to the change of T_{max} as shown in Fig. 7.4.121. Under the self-weight, the compaction stress resulted in a significant increase of the normalized coefficient of lateral earth pressure K_r/K_a due to the increase of T_{max} as shown in 7.4.121 (a). Under the traffic load, however, the normalized coefficients of lateral earth pressure K_r/K_a were almost the same for both cases from the bottom of the wall to the mid-height. From the top of the wall to the mid-height, the compaction stress resulted in slightly larger K_r/K_a.

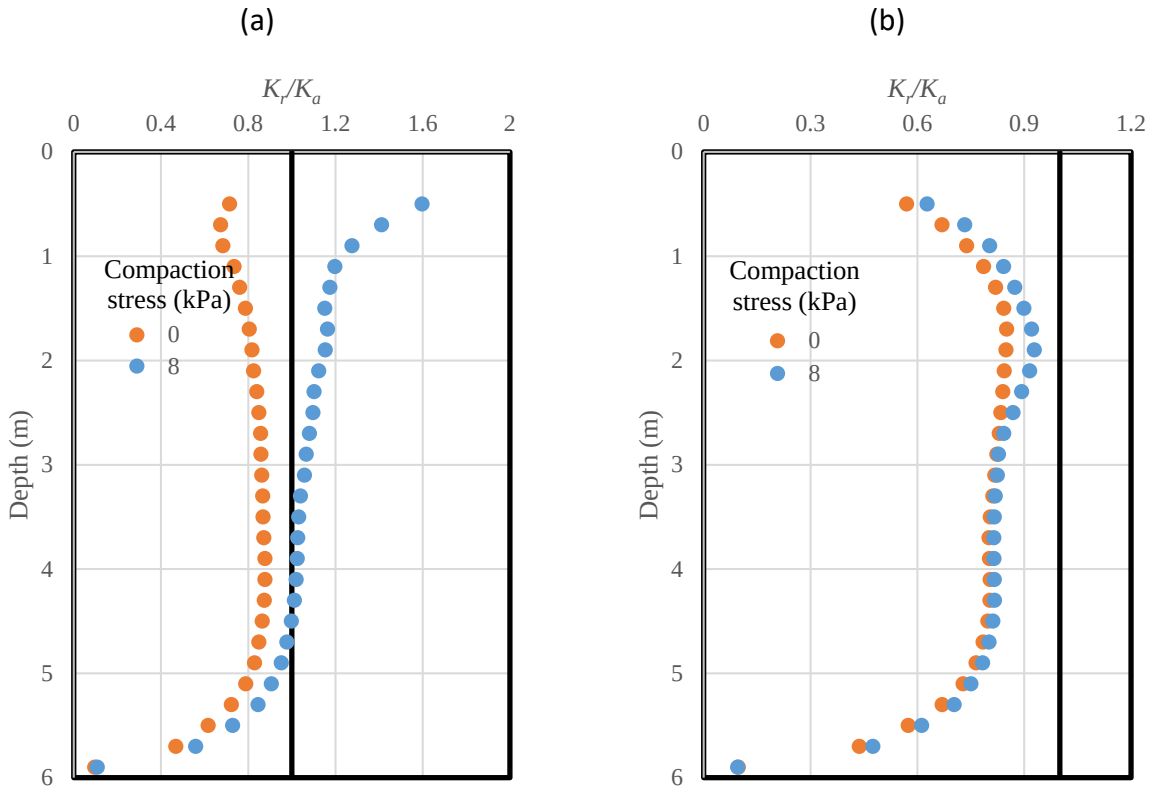

Fig. 7.4.123: Effect of the compaction stress on the normalized coefficient of lateral earth pressure K_r/K_a: (a) Self-weight; (b) Traffic load.

7.4.5.12 EFFECT OF FACING CONNECTION STRENGTH

This section discussed the effect of the facing connection strength. In the baseline model, a frictional connection was used between the geotextile reinforcement and CMU facing blocks except that the top three layers of CMU facing blocks were connected using a mechanical connection. An additional case with the mechanical connection used throughout the entire wall height was studied. The properties of the mechanical connection are shown in Table 7.4.12.

7.4.5.12.1 Lateral earth pressures

Figure 7.4.124 shows the effect of the facing connection on the lateral earth pressure behind the CMU facing blocks under both self-weight (i.e., Stage 2) and traffic load conditions (i.e., Stage 6). Figure 7.4.124 shows that under the self-weight, the facing connection had no influence on the lateral earth pressure behind wall facing. Under the traffic load, the facing connection did not affect the lateral earth pressure from the top of the wall to the depth of approximately 1.5 m (5 ft) and from the depth of 4 m (13 ft) to the bottom of the wall. From the depth of 1.5 m (5 ft) to 4 m (13 ft), the lateral earth pressure showed some differences between these two cases. The case with the mechanical connection showed a more uniform lateral earth pressure distribution with the depth as compared to the case with the frictional connection.

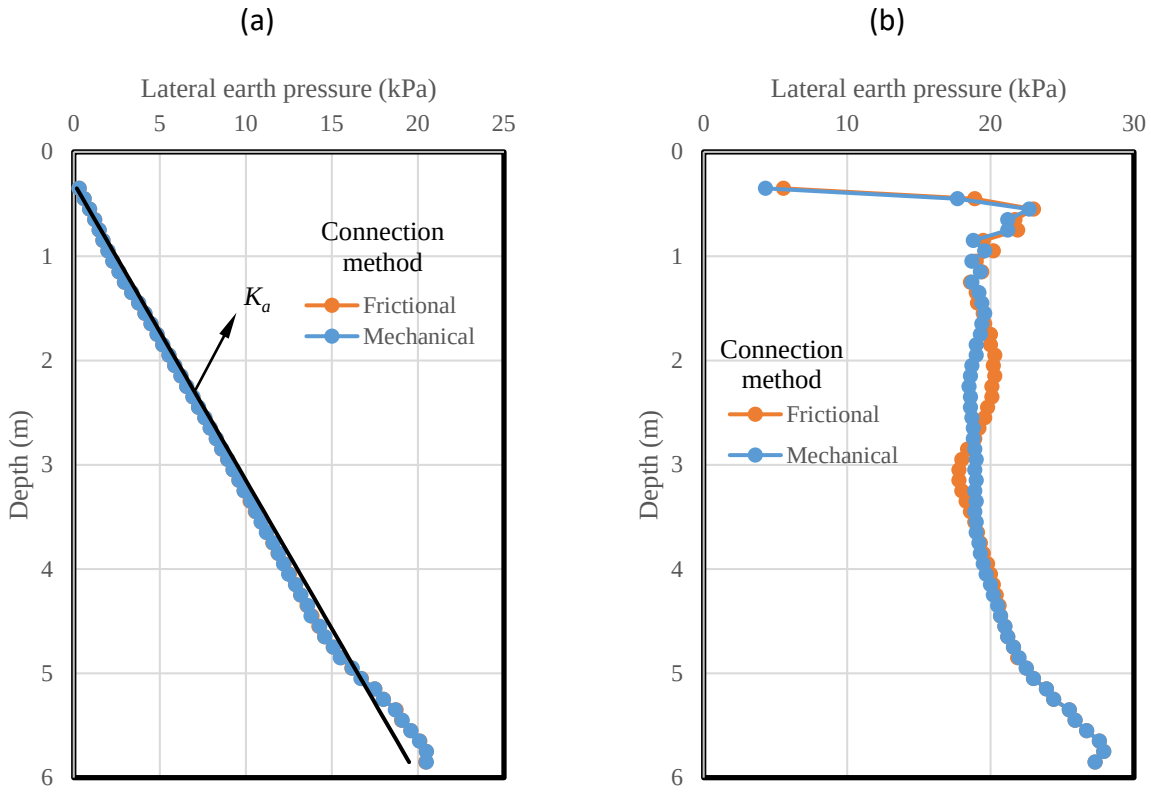

Fig. 7.4.124: Effect of the facing connection strength on the lateral earth pressure behind CMU facing blocks: (a) Self-weight; (b) Traffic load.

7.4.5.12.2 Additional vertical stress induced by loading

Figure 7.4.125 showed the effect of the facing connection on the distribution of additional vertical stress Δp at 0.5 m (20 in) from the back of CMU facing blocks with depth induced by loading. Figure 7.4.125 showed that two curves representing these two cases overlapped with each other, indicating that the facing connection had no influence on the additional vertical stress induced by loading. The AASHTO 2 to 1 truncation method calculated the additional stresses in reasonable agreement with the numerical results.

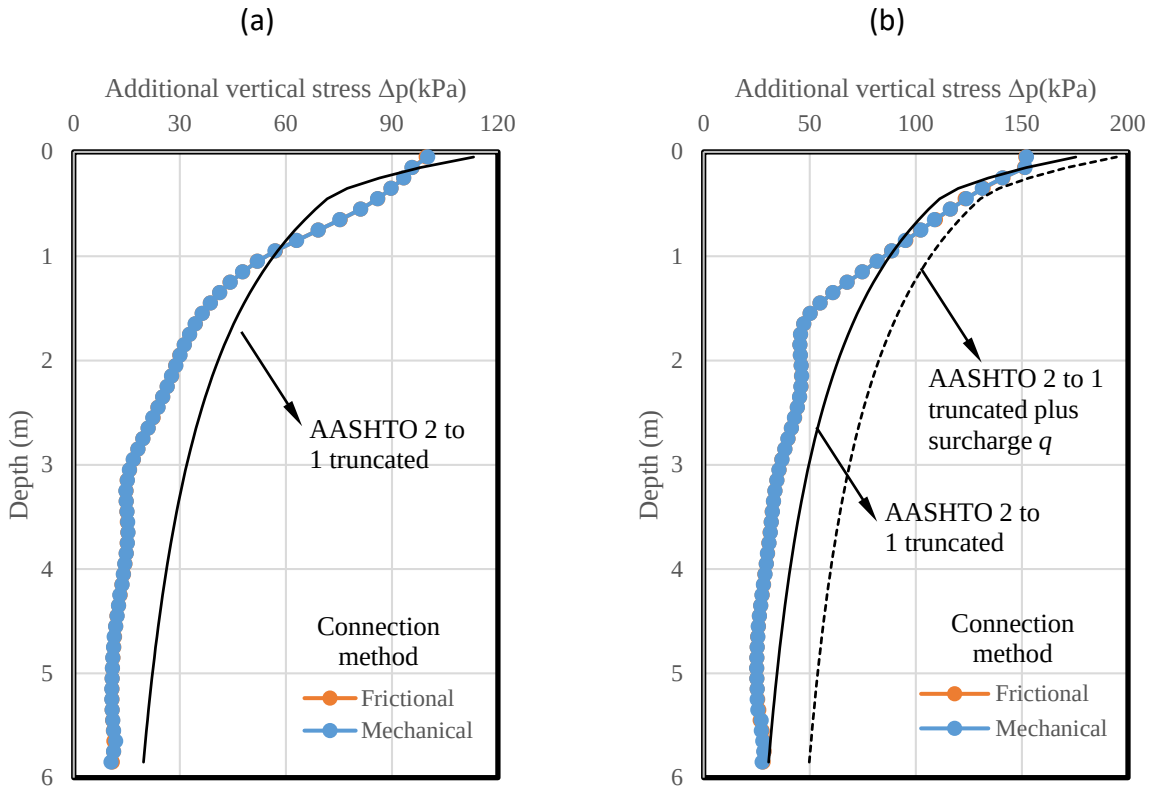

Fig. 7.4.125: Effect of the facing connection strength on the additional vertical stress induced by loading: (a) Induced by the self-weight of the bridge slab; (b) Induced by the self-weight of the bridge slab and the traffic load.

7.4.5.12.3 Lateral displacement of CMU facing blocks

Figure 7.4.126 shows the effect of the facing connection on the lateral displacements of CMU facing blocks under self-weight (i.e., Stage 2), bridge slab (i.e., Stage 4), and traffic load conditions (i.e., Stage 6). Figure 7.4.126 shows that these two cases had almost the same total lateral displacements of CMU facing blocks, indicating that the facing connection did not affect the wall facing deflection. Figure 7.4.127 shows the effect of the facing connection on the additional lateral displacement of CMU facing blocks induced by the traffic load only (i.e., the difference in the lateral displacements between Stage 6 and Stage 5). Figure 7.4.127 also confirmed that the facing connection had no influence on the additional wall facing displacement induced by the traffic load. One possible reason was that the abutment was under a working stress. The connection force provided by the frictional connection was enough. The load on the top of the abutment was not large enough to mobilize the additional connection force provided by the mechanical connection. In other words, the frictional connection provided the same connection force as the mechanical connection under the loading conditions in the numerical analysis.

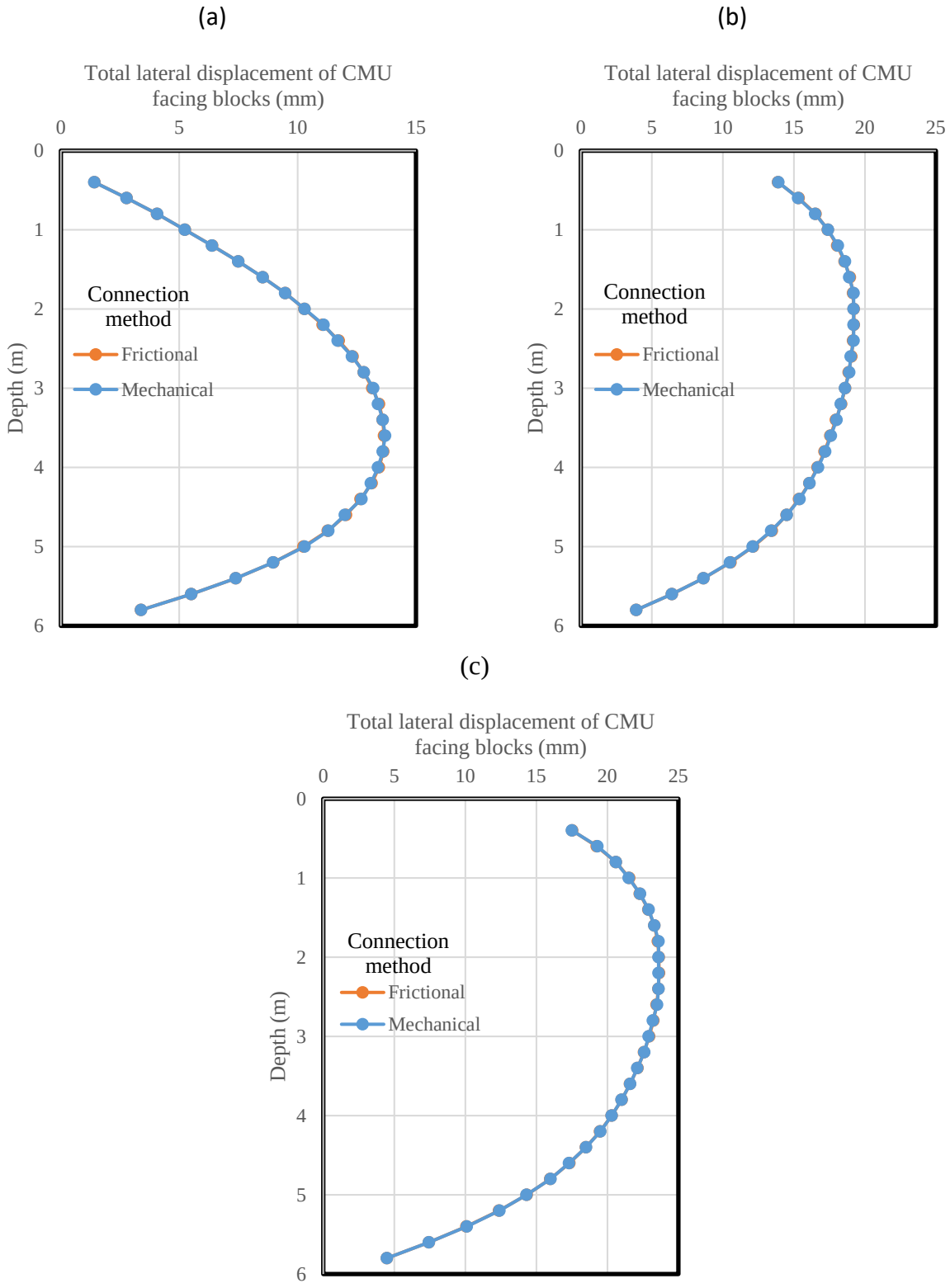

Fig. 7.4.126: Effect of the facing connection strength on the lateral displacement of CMU facing blocks: (a) Self-weight; (b) Bridge slab; (c) Traffic load.

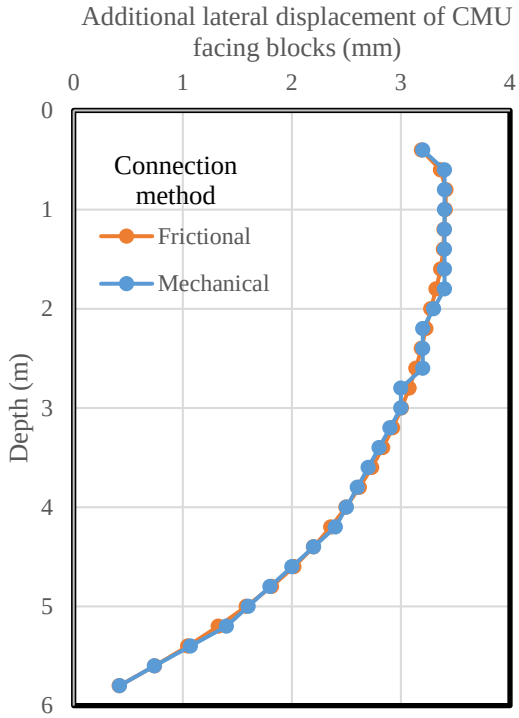

Fig. 7.4.127: Effect of the facing connection strength on the additional lateral displacement of CMU facing blocks induced by traffic load

7.4.5.12.4 Settlement profile for the bridge slab and integrated approach

Figure 7.4.128 shows the effect of the facing connection on the additional settlement on the top of the bridge slab and integrated approach induced by the traffic load (i.e., the difference in the settlement between Stage 6 and Stage 5). Similar to the lateral displacement of CMU facing blocks, the facing connection also had no influence on the additional settlement of both the bridge slab and the integrated approach way induced by the traffic load. The connection force provided by the frictional connection was enough to resist the traffic load. The additional connection force that the mechanical connection could provide was not mobilized under the traffic load in the numerical analysis.

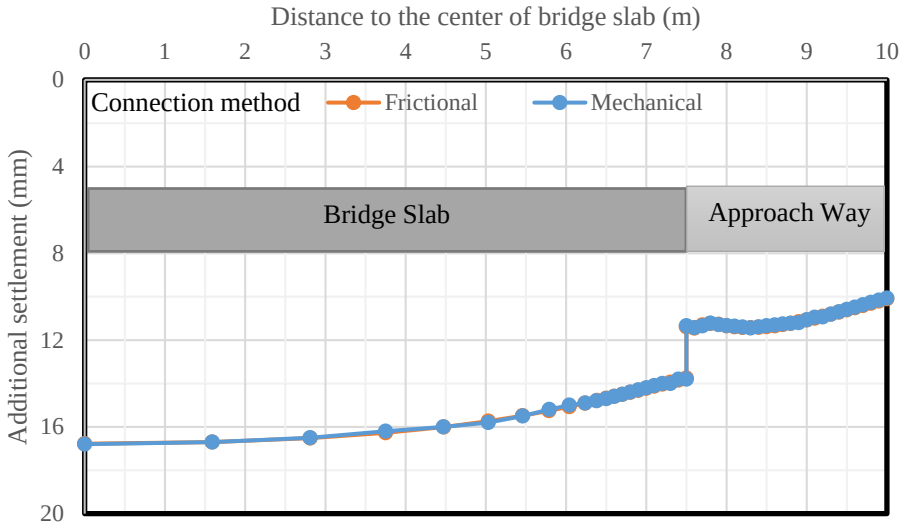

Fig. 7.4.128: Effect of the facing connection strength on the additional settlement of the bridge slab and integrated approach induced by traffic load

7.4.5.12.5 Volume change of the abutment

Figure 7.4.129 showed the effect of the facing connection on the normalized lateral volume change – normalized vertical volume change curve. Figure 7.4.129 shows that two curves overlapped with each other, indicating that facing connection did not change the volume change of the abutment under the loading conditions in the numerical analysis.

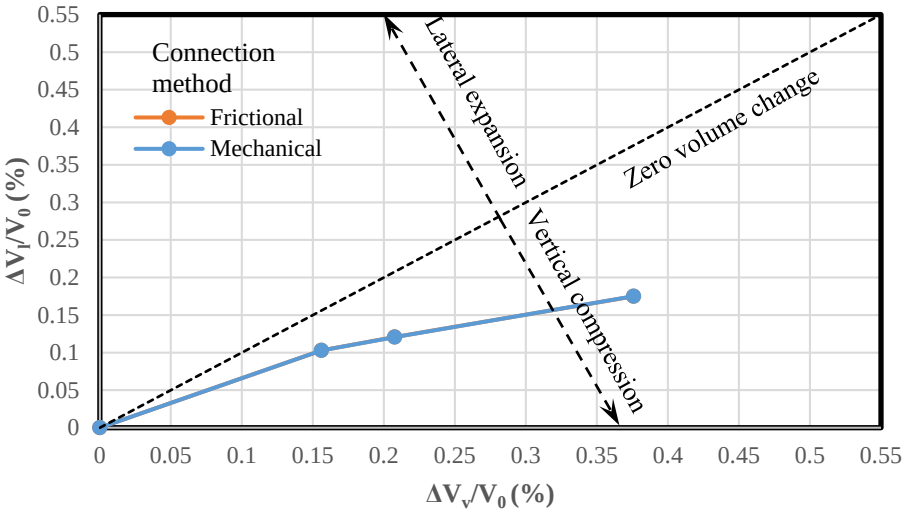

Fig. 7.4.129: Effect of the facing connection strength on the volume change of the GRS-IBS abutment

Table 7.4.26 summarizes the effect of the facing connection on the maximum vertical and lateral displacements of the abutment. It should be noted that all the displacements presented in Table 7.4.26 excluded the displacements of the abutment in Stage 3. In other words, the displacements of the abutment were initialized after the construction of the abutment and the beam seat were finished.

Table 7.4.26: Effect of the facing connection strength on the maximum vertical and lateral displacements of the abutment

Facing connection	Displacement (mm)	Construction stage		
		Stage 4 (bridge slab)	Stage 5 (integrated approach)	Stage 6 (traffic load)
Frictional	$\delta_{v\text{-max}}$	35.36	37.19	51.06
	$\delta_{l\text{-max}}$	10.63	11.18	14.54
Mechanical	$\delta_{v\text{-max}}$	35.34	37.14	51.04
	$\delta_{l\text{-max}}$	10.59	11.19	14.59

7.4.5.12.6 Tension in the reinforcement

Figure 7.4.130 shows the effect of the facing connection on the maximum tensile forces of the reinforcement T_{max} under both self-weight (i.e., Stage 2) and traffic load conditions (i.e., Stage 6). The two curves for these two cases overlapped with each other, indicating that the facing connection did not influence the T_{max} distribution with the depth. Figure 7.4.131 shows the effect of the facing connection on the ratios of the connection force T_0 to the maximum tensile force T_{max} in the reinforcement under both self-weight (i.e., Stage 2) and traffic load conditions (i.e., Stage 6). Figure 7.4.131 also shows that the T_0/T_{max} distribution with the depth was the same for both cases. Since the T_{max} distribution with the depth did not change with the change of the facing connection, Fig. 7.4.131 shows that the connection force T_0 when frictional connection was used was the same as that when mechanical connection was used. The load (e.g., the self-weight of the bridge slab and the traffic load) used in the numerical analysis was not large enough to mobilize additional connection force from the mechanical connection. In other words, the connection force provided by the frictional connection was sufficient and there was no need for the mechanical connection to provide additional resistance. Figure 7.4.132 shows the effect of the facing connection on the normalized coefficients of lateral earth pressure K_r/K_a under both self-weight (i.e., Stage 2) and traffic load conditions (i.e., Stage 6). The determination of σ_v under different loading conditions was discussed in Section 7.4.5.2.6 (i.e., using the overburden stress and the AASHTO 2 to1 truncation method without surcharge q). Again, Fig. 7.4.132 shows that the mechanical connection behaved the same as the frictional connection, thus resulting in the same K_r/K_a distribution with the depth.

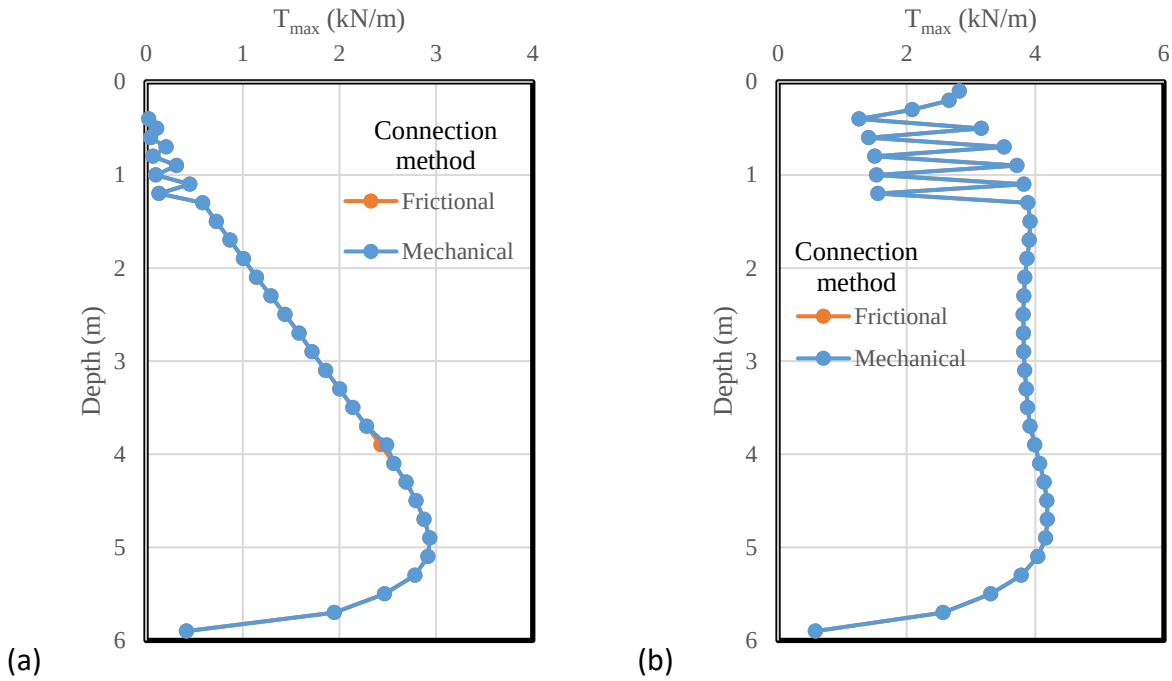

Fig. 7.4.130: Effect of the facing connection strength on the maximum tensile force T_{max} in the reinforcement: (a) Self-weight; (b) Traffic load.

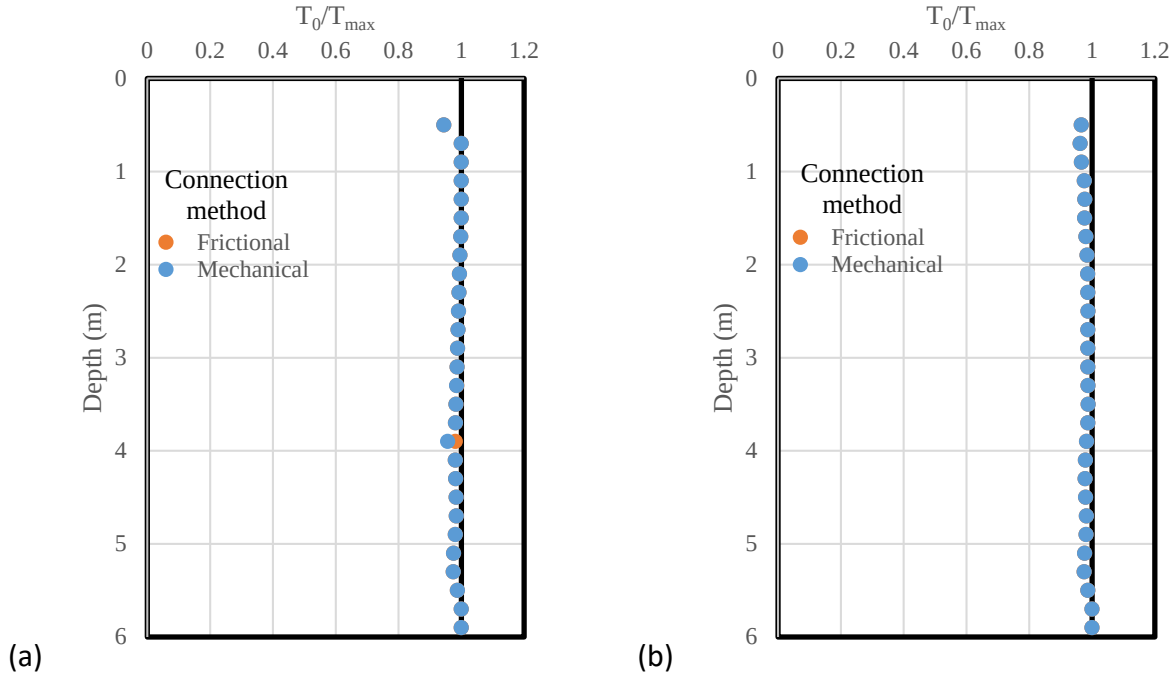

Fig. 7.4.131: Effect of the facing connection strength on the ratio of connection force T_0 to the maximum tensile force T_{max} in the reinforcement: (a) Self-weight; (b) Traffic load.

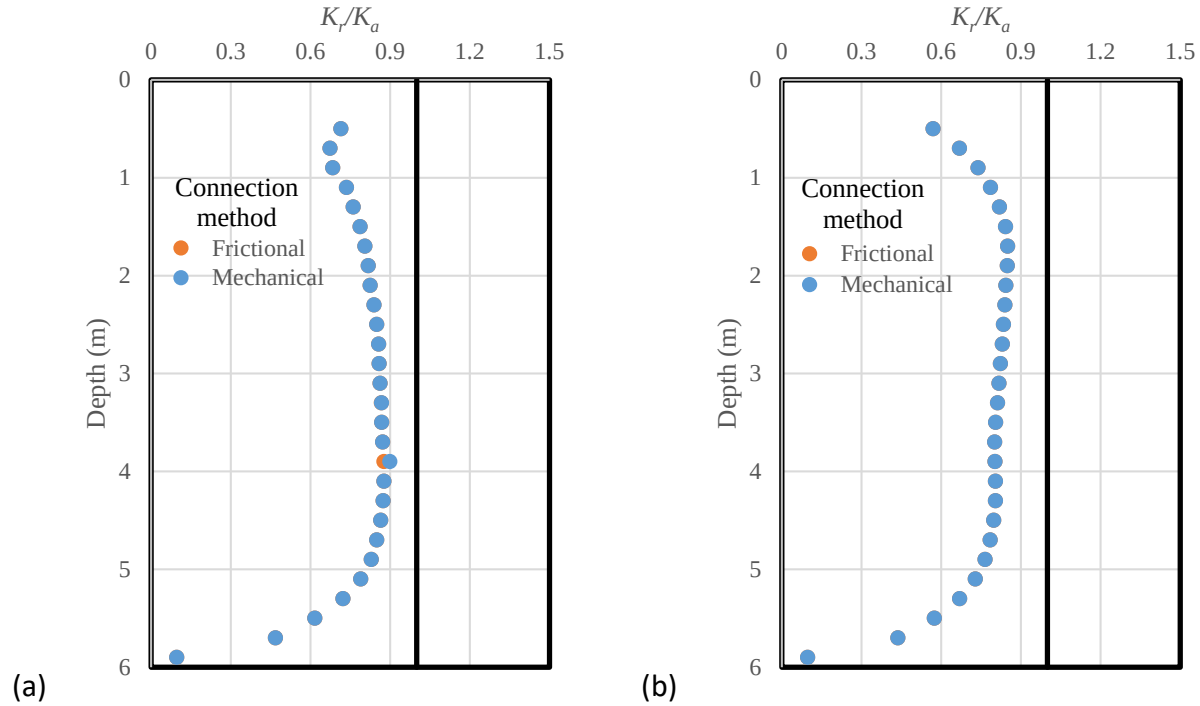

Fig. 7.4.132: Effect of the facing connection strength on the normalized coefficient of lateral earth pressure K_r/K_a: (a) Self-weight; (b) Traffic load.

Numerical results discussed in Section 7.4.5.12 indicated that the facing connection strength had no influence on the performance of the GRS-IBS under self-weight, bridge slab, and traffic load. However, parametric study of GRS piers showed that facing connection strength had a significant effect on the performance of the GRS pier under vertical load as discussed in Section 7.3.3.7. One possible reason was that the connection force provided by the frictional connection was enough in the GRS-IBS. The load on the top of the GRS-IBS (e.g., the self-weight of the bridge slab and the traffic load) was not large enough to mobilize the additional connection force provided by the mechanical connection. In other words, the connection force provided by the frictional connection was sufficient and there was no need for the mechanical connection to provide additional resistance in GRS-IBS under the loading conditions used in the numerical simulation. In the GRS pier, however, the load applied on top of the pier mobilized more connection force in the reinforcement especially within the upper portion of the pier when the mechanical connection was used as shown in Fig. 7.3.55, thus resulting in a significant effect of the connection strength on the performance of the GRS pier.

7.4.5.13 EFFECT OF FACING CONNECTION STIFFNESS

This section discusses the effect of the facing connection stiffness. In the baseline model, the facing connection stiffness values: $k_n = 1 \times 10^9$ N/m/m and $k_s = 4 \times 10^7$ N/m/m were used, which are the same as those recommended by Hatami and Bathurst (2005). An additional case

with low facing connection stiffness values: $k_n = 1 \times 10^8$ N/m/m and $k_s = 4 \times 10^6$ N/m/m, was studied.

7.4.5.13.1 Lateral earth pressure

Figure 7.4.133 shows the effect of the facing connection stiffness on the lateral earth pressure behind the CMU facing blocks under both self-weight (i.e., Stage 2) and traffic load conditions (i.e., Stage 6). Under the self-weight, the reduction of the facing connection stiffness resulted in slightly lower lateral earth pressure behind wall facing. The calculated lateral earth pressure was close to Coulomb's active lateral earth pressure when high facing connection stiffness was used. Under the traffic load, the reduction of the facing connection stiffness resulted in lower lateral earth pressure near the top and bottom of the wall and higher lateral earth pressure from the depth of 1 m (3.3 ft) to 4 m (13 ft).

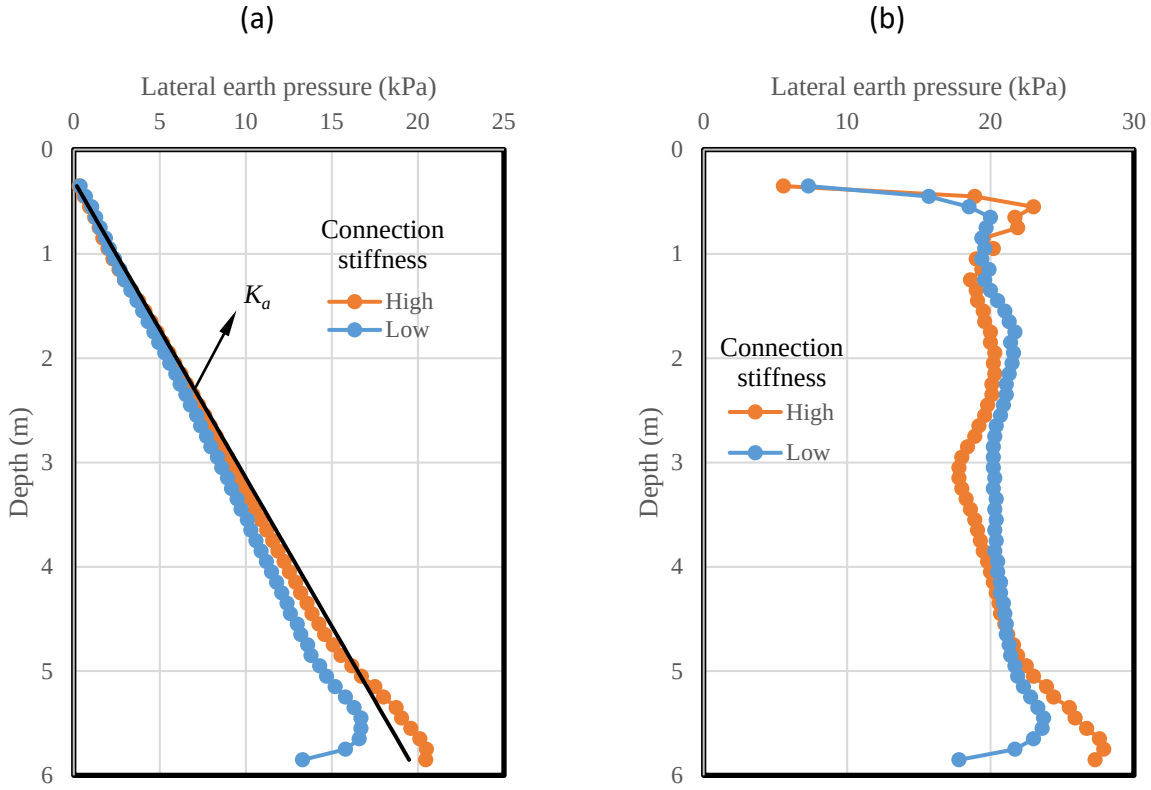

Fig. 7.4.133: Effect of the facing connection stiffness on the lateral earth pressure behind CMU facing blocks: (a) Self-weight; (b) Traffic load.

7.4.5.13.2 Additional vertical stress induced by loading

Figure 7.4.134 shows the effect of the facing connection stiffness on the distribution of additional vertical stress Δp at 0.5 m (20 in) from the back of CMU facing blocks with the depth induced by loading. Figure 7.4.134 shows that the reduction of the facing connection stiffness resulted in higher additional vertical stress inside the wall induced by loading. The AASHTO 2 to 1 truncation method underestimated Δp near the top of the wall. However, the numerical results of the case

with the low facing connection stiffness were close to those calculated by the AASHTO 2 to 1 truncation method from the depth of approximately 1 m (3.3 ft) to the bottom of the wall.

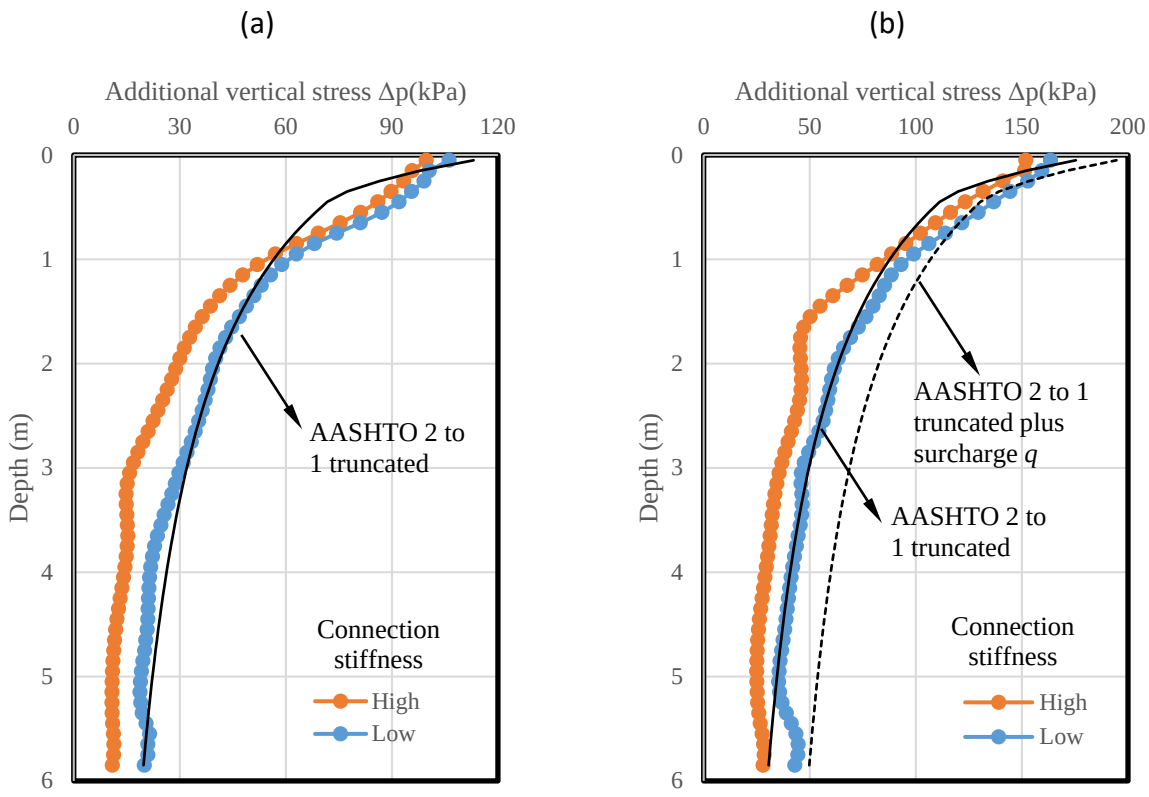

Fig. 7.4.134: Effect of the facing connection stiffness on the additional vertical stress induced by loading: (a) Induced by the self-weight of the bridge slab; (b) Induced by the self-weight of the bridge slab and the traffic load.

7.4.5.13.3 Lateral displacement of CMU facing blocks

Figure 7.4.135 shows the effect of the facing connection stiffness on the lateral displacements of CMU facing blocks under self-weight (i.e., Stage 2), bridge slab (i.e., Stage 4), and traffic load conditions (i.e., Stage 6). As expected, the reduction of the facing connection stiffness resulted in larger total lateral displacement of CMU facing blocks.

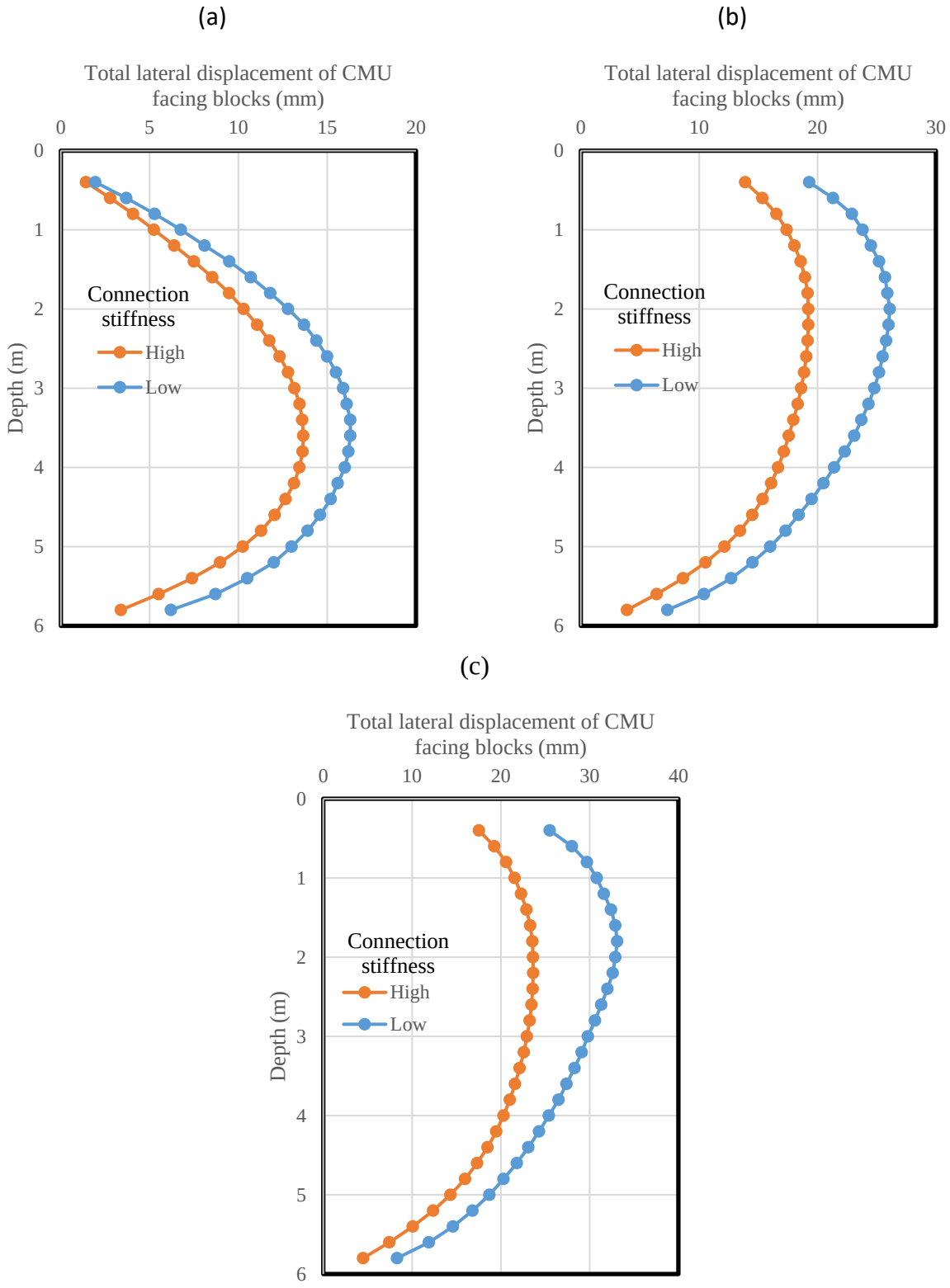

Fig. 7.4.135: Effect of the facing connection stiffness on the lateral displacement of CMU facing blocks: (a) Self-weight; (b) Bridge slab; (c) Traffic load.

Figure 7.4.136 shows the effect of the facing connection stiffness on the additional lateral displacement of CMU facing blocks induced by the traffic load only (i.e., the difference in the lateral displacements between Stage 6 and Stage 5). Figure 7.4.136 also shows that the reduction of the facing connection stiffness resulted in larger lateral displacement of CMU facing blocks. The difference in the additional lateral displacements between these two cases was small at the bottom of the wall. The increase of the additional wall facing displacement induced by the reduction of the facing connection stiffness was much larger near the top of the wall since the traffic load was applied on the top.

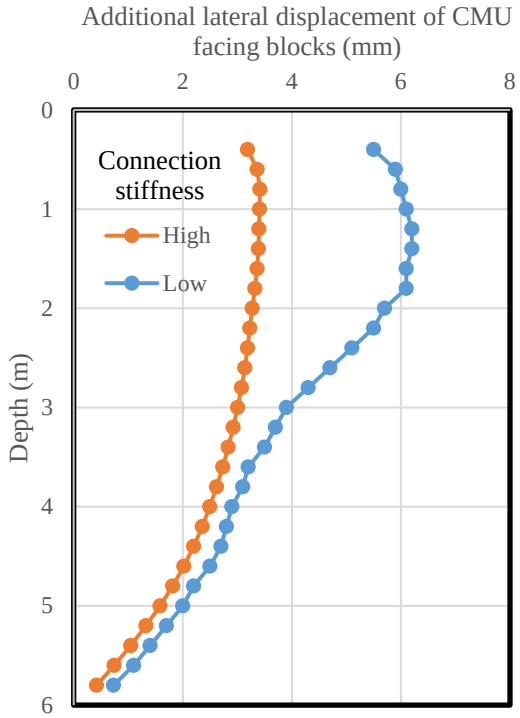

Fig. 7.4.136: Effect of the facing connection stiffness on the additional lateral displacement of CMU facing blocks induced by traffic load

7.4.5.13.4 Settlement profile for the bridge slab and integrated approach

Figure 7.4.137 shows the effect of the facing connection stiffness on the additional settlement on the top of the bridge slab and integrated approach induced by the traffic load (i.e., the difference in the settlement between Stage 6 and Stage 5). As expected, the reduction of the facing connection stiffness resulted in larger additional settlement of both the bridge slab and the integrated approach induced by the traffic load. The increase of the additional settlement of the bridge slab was much larger than that of the integrated approach way since the bridge slab was closer to the facing connection. The reduction of the facing connection stiffness also increased the differential settlement happened at the end of the bridge slab.

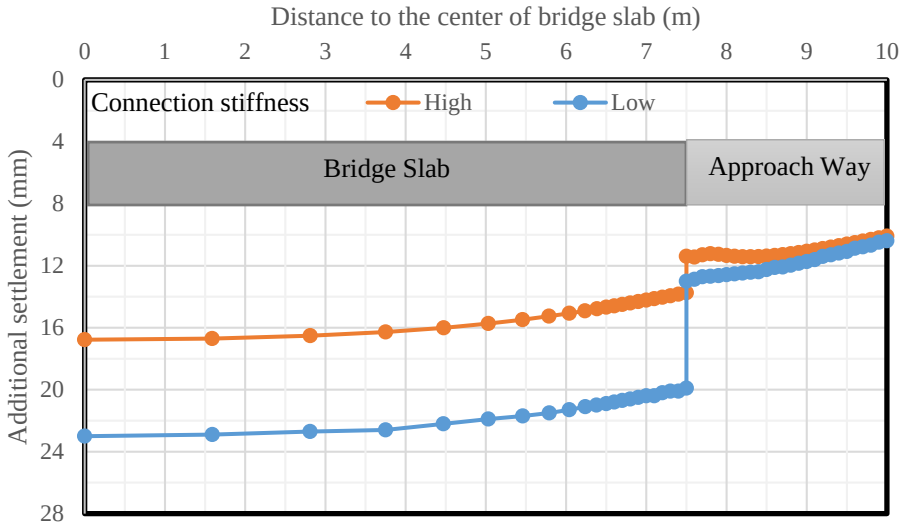

Fig. 7.4.137: Effect of the facing connection stiffness on the additional settlement of the bridge slab and integrated approach induced by traffic load

7.4.5.13.5 Volume change of the abutment

Figure 7.4.138 shows the effect of the facing connection stiffness on the normalized lateral volume change – normalized vertical volume change curve. Figure 7.4.138 shows that the reduction of the facing connection stiffness resulted in larger vertical compression and lateral deflection of the abutment. The curve for the case with the high facing connection stiffness was to the right of that for the case with the low facing connection stiffness, indicating that the contribution of the increase of the facing connection stiffness to the reduction of the lateral deflection of the abutment was more significant than that to the reduction of the vertical compression.

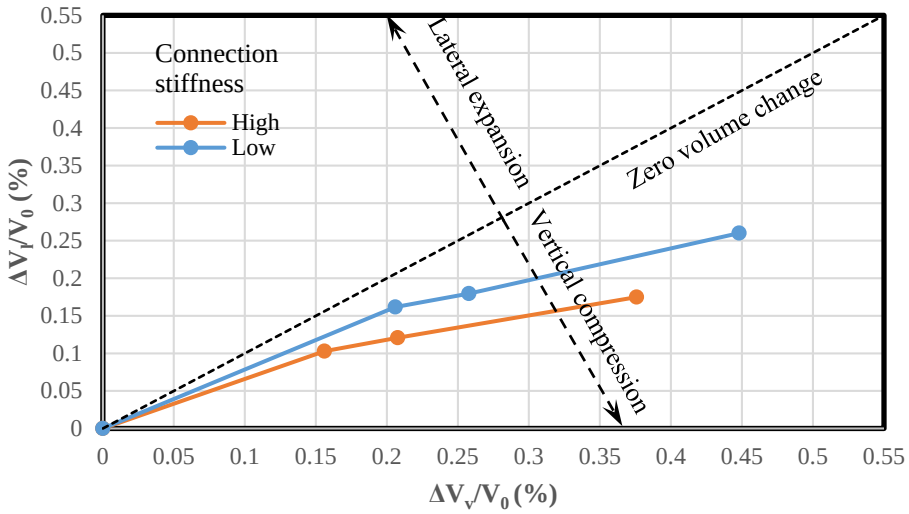

Fig. 7.4.138: Effect of the facing connection stiffness on the volume change of the GRS-IBS abutment

Table 7.4.27 summarizes the effect of the facing connection stiffness on the maximum vertical and lateral displacements of the abutment. It should be noted that all the displacements presented in Table 7.4.27 excluded the displacements of the abutment in Stage 3. In other words, the displacements of the abutment were initialized after the construction of the abutment and the beam seat were finished.

Table 4.7.27: Effect of the facing connection stiffness on the maximum vertical and lateral displacements of the abutment

Facing connection stiffness	Displacement (mm)	Construction stage		
		Stage 4 (bridge slab)	Stage 5 (integrated approach)	Stage 6 (traffic load)
High	$\delta_{v\text{-max}}$	35.36	37.19	51.06
	$\delta_{l\text{-max}}$	10.63	11.18	14.54
Low	$\delta_{v\text{-max}}$	43.79	45.99	66.09
	$\delta_{l\text{-max}}$	15.47	16.27	22.24

7.4.5.13.6 Tension in the reinforcement

Figure 7.4.139 shows the effect of the facing connection stiffness on the maximum tensile forces of the reinforcement T_{max} under both self-weight (i.e., Stage 2) and traffic load conditions (i.e.,

Stage 6). Figure 7.4.139 shows that the reduction of the facing connection stiffness resulted in larger maximum tensile force not only in the primary reinforcement but also in the bearing reinforcement layers. The reduction of the facing connection stiffness mobilized more relative movement between soil and geotextile reinforcement, thus increasing the T_{max} in the reinforcement.

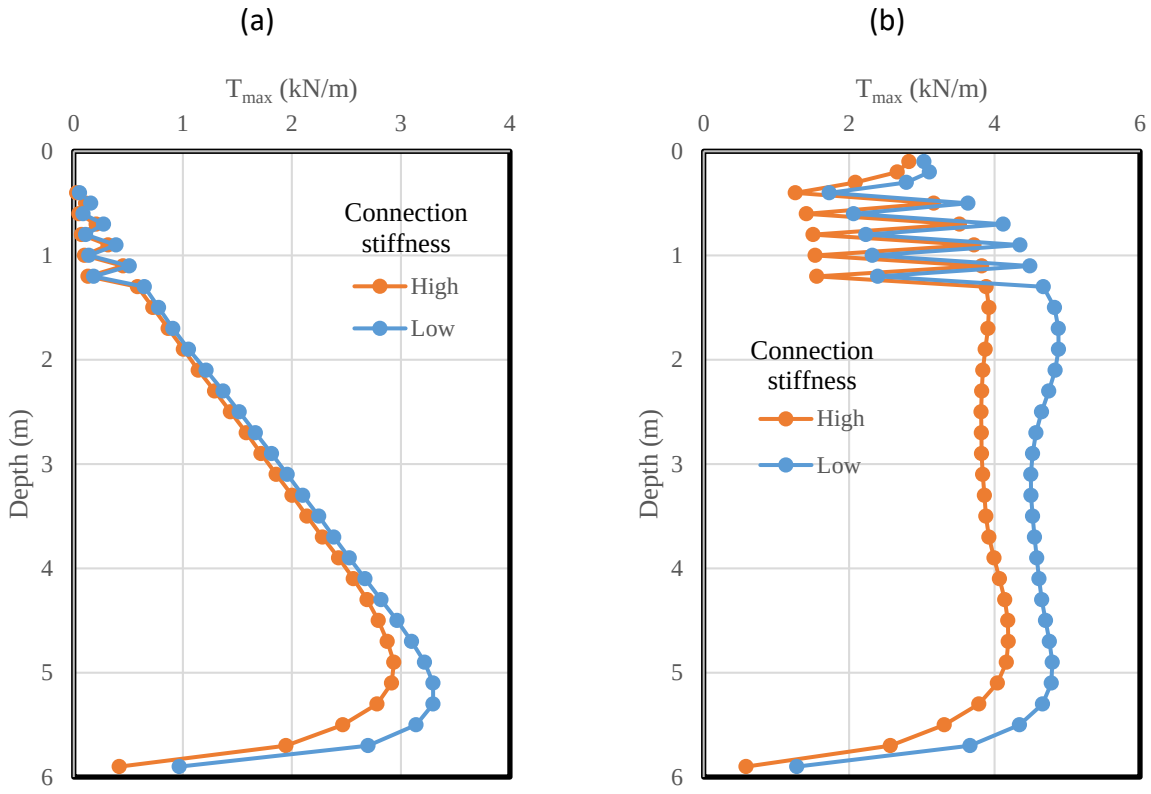

Fig. 7.4.139: Effect of the facing connection stiffness on the maximum tensile force T_{max} in the reinforcement: (a) Self-weight; (b) Traffic load.

Figure 7.4.140 shows the effect of the facing connection stiffness on the ratios of the connection force T_0 to the maximum tensile force T_{max} in the reinforcement under both self-weight (i.e., Stage 2) and traffic load conditions (i.e., Stage 6). Figure 7.4.140 shows that the reduction of the facing connection stiffness resulted in lower T_0/T_{max}. When the high facing connection stiffness was used, T_0/T_{max} was close to 1.0, indicating that T_{max} happened very close to the facing connection. When the low facing connection stiffness was used, however, the location of T_{max} moved away from the facing connection into the reinforced zone.

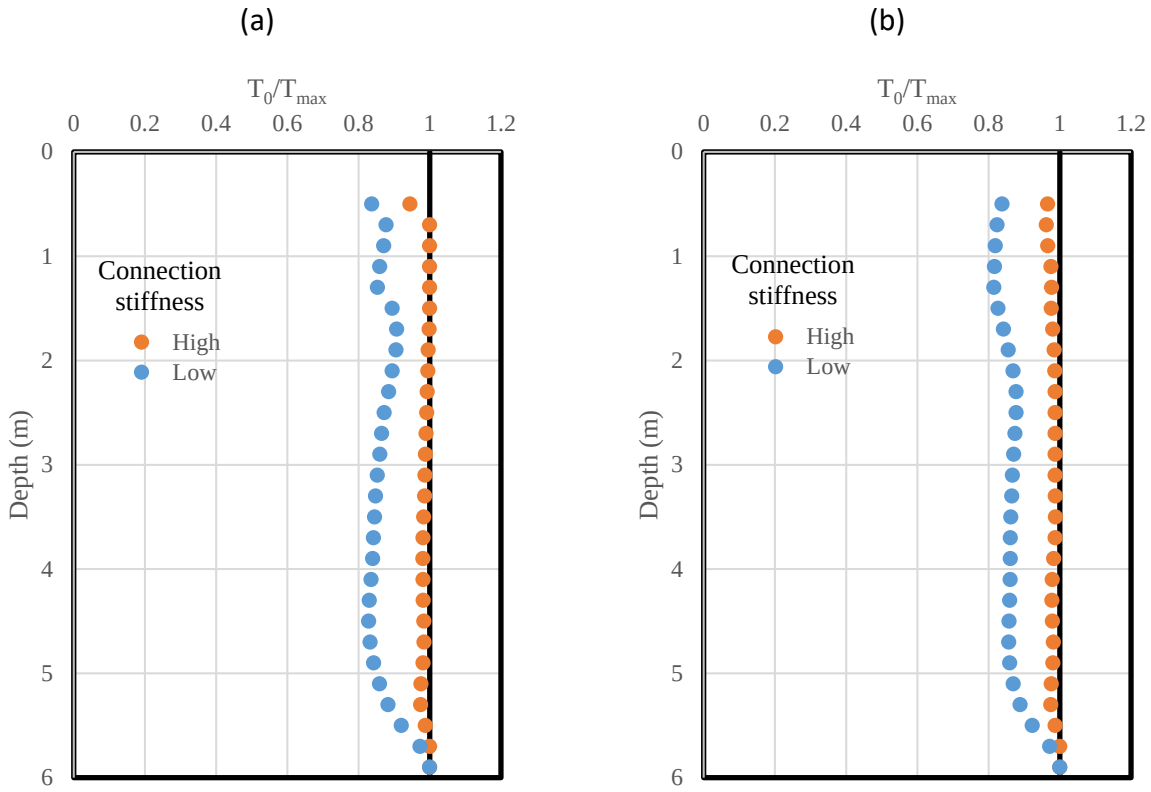

Fig. 7.4.140: Effect of the facing connection stiffness on the ratio of connection force T_0 to the maximum tensile force T_{max} in the reinforcement: (a) Self-weight; (b) Traffic load.

Figure 7.4.141 shows the effect of the facing connection stiffness on the normalized coefficients of lateral earth pressure K_r/K_a under both self-weight (i.e., Stage 2) and traffic load conditions (i.e., Stage 6). Since the additional vertical stress induced by loading was calculated using the AASHTO 2 to 1 method (not affected by the change of the facing connection stiffness), the change of K_r/K_a was due to the change of T_{max} as shown in Fig. 7.4.139. Figure 7.4.141 shows that the reduction of the facing connection stiffness resulted in larger K_r/K_a distribution with the depth.

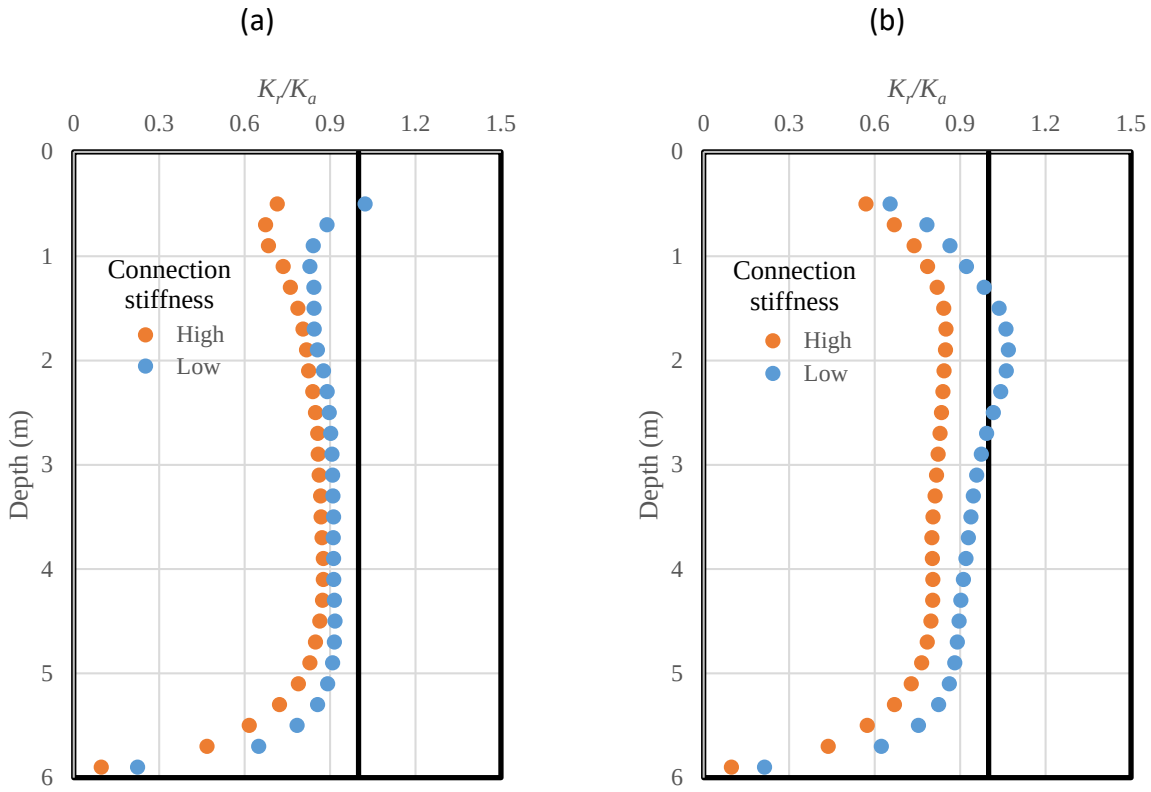

Fig. 7.4.141: Effect of the facing connection stiffness on the normalized coefficient of lateral earth pressure K_r/K_a: (a) Self-weight; (b) Traffic load.

7.4.6 CONCLUSIONS

This study was conducted using a two-dimensional finite difference method-based program, FLAC, to simulate the performance of a Geosynthetic Reinforced Soil – Integrated Bridge System (GRS-IBS) constructed by VDOT in the field. The numerical model was calibrated and validated against the field measurements (e.g., the lateral earth pressure behind wall facing, the additional vertical stress induced by loading, the lateral displacement of wall facing, and the strain of geotextile reinforcement. The comparisons between the field measurements and the numerical results showed that the numerical model was able to reasonably predict the behavior of the VDOT wall.

After the numerical model was verified, additional numerical simulations were conducted to compare the behavior of walls with different layouts of geotextile reinforcement (i.e., the trapezoidal layout and the uniform layout). The numerical results showed that these two layouts gave similar responses of the abutment under both self-weight and loading. Therefore, the uniform layout was adopted in the parametric study since AASHTO (2012) adopted the same layout.

A parametric study was then conducted using the uniform layout to investigate the influence of the following factors on the performance of the GRS-IBS: friction angle of the backfill soil, stiffness of the reinforcement J, reinforcement spacing S_v, combined effect of reinforcement stiffness and spacing J/S_v, bearing reinforcement layers, soil – reinforcement interaction coefficient C_i, primary reinforcement length L_r, foundation compressibility E, beam seat width b, compaction stress, facing connection strength, and the facing connection stiffness. The following conclusions can be drawn from this parametric study:

1 The lateral earth pressures behind wall facing from the numerical analysis were in good agreement with Coulomb's active earth pressure under the fill self-weight. Under the bridge slab and the traffic load, the lateral earth pressure increased significantly towards the top of the wall.
2 The additional vertical stress Δp induced by loading was highest at the top of the wall just below the bridge slab and then showed a decreasing trend with the depth. The Δp values calculated using the AASHTO 2 to 1 truncation method were in reasonable agreements with the numerical results.
3 Under self-weight conditions, the maximum lateral displacements of wall facing developed at the middle to lower portion of the wall. Under both the bridge slab load and the traffic load conditions, the location of the maximum lateral displacement developed at a comparatively higher elevation.
4 Differential settlements happened at the end of the bridge slab. The bridge slab settled more than the integrated approach way as a consequence of the high concentrated load applied on the beam seat.
5 Volume changes within the GRS-IBS abutment were found not to exactly follow the zero-volume change assumption proposed by Adams et al. (2002). The abutment had more vertical compression than lateral deflection when the entire reinforced zone was considered in calculating the vertical volume change.
6 The maximum tension in the reinforcement T_{max} increased with the depth under the self-weight. Under traffic loading, the maximum tensile force in the reinforcement T_{max} increased significantly at the top of the wall due to the loading. The T_{max} values in the bearing reinforcement layers were lower than those in the primary reinforcement.
7 The ratio of the connection force T_0 to the maximum tensile force T_{max} in the reinforcement was approximately 1.0, indicating that the maximum tensile force in the reinforcement T_{max} developed near the wall facing connection under both the self-weight and the traffic load.
8 The normalized coefficients of lateral earth pressure K_r/K_a from the numerical simulation were less than 1.0. In most of the cases, the normalized coefficients of lateral earth pressure $K_r/$Ka were approximately 0.8 and reasonably constant along the depth of the wall.
9 The friction angle of the backfill soil had a significant influence on the performance of the GRS-IBS. An increase in friction angle resulted in decreasing lateral earth pressures behind wall facing, smaller lateral displacement of wall facing, smaller settlement of both the bridge slab and integrated approach way, and lower maximum reinforcement tension T_{max}. The friction angle of backfill soil was found not to affect significantly the additional vertical stress behind wall facing induced by loading.

10 An increase in reinforcement stiffness resulted in slightly increased lateral earth pressures behind wall facing under the bridge slab and the traffic load, decreased lateral displacements of wall facing, decreased settlement of both the bridge slab and the integrated approach way, and increased maximum tension in the reinforcement T_{max}. The effect of the reinforcement stiffness on the additional vertical stress behind wall facing induced by loading was minor.

11 A decrease of the reinforcement spacing resulted in increased lateral earth pressures behind wall facing under the bridge slab and the traffic load, decreased lateral displacement of wall facing, decreased settlement of both the bridge slab and the integrated approach way, and decreased maximum tension in the reinforcement T_{max}. The effect of reinforcement spacing on the additional vertical stress behind wall facing induced by loading was minor.

12 This study investigated the combined effect of reinforcement stiffness J and spacing S_v on the performance of the abutment while maintaining a constant ratio of J/ S_v. One case used larger reinforcement spacing with stiffer reinforcement while the other case used smaller reinforcement spacing with less stiff reinforcement. The responses of the abutment (e.g., lateral earth pressure behind wall facing, additional vertical stress induced by loading, lateral displacement of wall facing, and settlement of the bridge slab and the integrated approach way) were similar for the two cases evaluated in this study, under self-weight, bridge slab, and traffic load conditions. The maximum reinforcement tension T_{max} was found to decrease approximately proportionally with decreasing reinforcement spacing under the same load. These two cases required almost the same total maximum tension ΣT_{max} under the self-weight and the traffic load.

13 The presence of bearing reinforcement layers was found to change the response of the upper portion of the wall where the bearing reinforcement layers were placed. The use of the bearing reinforcement layers resulted in comparatively smaller lateral displacement of wall facing in the upper portion of the wall, smaller settlement of the bridge slab, and smaller maximum tension T_{max} in the primary reinforcement.

14 Changes in soil-reinforcement interaction coefficient from 0.5 to 0.9 were found not to affect significantly the behavior of the abutment.

15 A decrease in the primary reinforcement length was found to result in increased lateral earth pressures behind the wall facing, increased lateral displacement of wall facing, larger settlement of both the bridge slab and the integrated approach way, and increased maximum tensile force in the reinforcement T_{max}. The primary reinforcement length should be at least equal or larger than half of the wall height (i.e., 0.5H) to minimize excessive wall deformations.

16 An increase in the foundation soil compressibility was found to result in increased lateral displacement of wall facing and increased settlement of both the bridge slab and the integrated approach way.

17 Changes in the beam seat width were found to significantly affect the additional vertical stress profile with depth induced by loading. Specifically, an increase in beam seat width resulted in decreased additional vertical stress under the center of the loading area, reduced additional settlement of both the bridge slab and the integrated approach way, and reduced maximum tension in both the primary reinforcement and the bearing layers in the upper portion of the wall.

18 Compaction stresses were found to affect the behavior of the abutment under the self-weight. A uniform vertical compaction stress of 8 kPa (167 psf) resulted in comparatively higher lateral earth pressures behind wall facing, larger lateral displacements of wall facing, and larger maximum tensile force in the reinforcement T_{max}. However, under the bridge slab and the traffic load, the influence of the compaction stress was found to be minor.

19 The frictional facing connection resulted in the same response of the wall as the mechanical facing connection under the different loading conditions in the numerical simulations. One possible reason was that the load on the top of the wall (e.g., the self-weight of the bridge slab and the traffic load) was not large enough to mobilize the additional connection force provided by the mechanical connection. In other words, the connection force provided by the frictional connection was sufficient and there was no need for the mechanical connection to provide additional resistance.

20 A reduction in the facing connection stiffness resulted in comparatively higher additional vertical stress induced by loading, larger lateral displacement of wall facing, larger settlement of both the bridge slab and the integrated approach way, and larger maximum reinforcement tension in the reinforcement. A comparatively low facing connection stiffness resulted in the location of T_{max} moving away from the facing connection into the reinforced zone.

7.4.7 REFERENCES

AASHTO, 2012. LRFD bridge design specifications. 6th ed., Washington, DC.

Adams, M., Lillis, C., Wu, J., Ketchart, K., 2002. Vegas mini pier experiment and postulate of zero volume change, Proceedings, Seventh International Conference on Geosynthetics, pp. 389-394.

Adams, M., Nicks, J., Stabile, T., Wu, J., Schlatter, W., Hartmann, J., 2011. Geosynthetic Reinforced Soil Integrated Bridge System, Synthesis Report.

Adams, M., Nicks, J., Stabile, T., Wu, J., Schlatter, W., Hartmann, J., 2012. Geosynthetic Reinforced Soil Integrated Bridge System, Interim Implementation Guide.

Awad, M.I., Tanyu, B.F., 2014. Laboratory evaluation of governing mechanism of frictionally connected MSEW face and implications on design. Geotextiles and Geomembranes 42, 468-478.

Berg, R.R., Christopher, B.R., Samtani, N.C., 2009. Design of Mechanically Stabilized Earth Walls and Reinforced Soil Slopes–Volume I.

Bolton, M., 1986. The strength and dilatancy of sands. Geotechnique 36, 65-78.

British Standards Institution, 2004. Eurocode 2: Design of Concrete Structures: Part 1-1: General Rules and Rules for Buildings. British Standards Institution, London.

Coduto, D.P., 2015. Foundation design: principles and practices. Pearson.

Filz, G., Duncan, J., 1996. Earth pressures due to compaction: comparison of theory with laboratory and field behavior. Transportation Research Record: Journal of the Transportation Research Board, 28-37.

Goodhue, M.J., Edil, T.B., Benson, C.H., 2001. Interaction of foundry sands with geosynthetics. Journal of geotechnical and geoenvironmental engineering 127, 353-362.

Hatami, K., Bathurst, R.J., 2005. Development and verification of a numerical model for the analysis of geosynthetic-reinforced soil segmental walls under working stress conditions. Canadian Geotechnical Journal 42, 1066-1085.

Huang, B., Bathurst, R.J., Hatami, K., 2009. Numerical study of reinforced soil segmental walls using three different constitutive soil models. Journal of Geotechnical and Geoenvironmental engineering 135, 1486-1498.

Huang, B., Bathurst, R. J., Hatami, K., Allen, T. M., 2010. Influence of toe restraint on reinforced soil segmental walls. Can. Geotech. J., 47(8), 885–904.

Itasca Consulting Group, 2008a. FLAC Example Applications. Itsca Consulting Group Inc.

Itasca Consulting Group, 2008b. FLAC Theory and Background. Itsca Consulting Group Inc.

Mitchell, J.K., Soga, K., 2005. Fundamentals of soil behavior. John Wiley & Sons, Inc.

Negussey, D., 2007. Design parameters for EPS geofoam. Soils and foundations 47, 161-170.

Pham, T.Q., 2009. Investigating Composite Behavior of Geosynthetic-Reinforced Soil (GRS) Mass. University of Colorado Denver, Colorado, USA, p. 3797p.

Saghebfar, M., Abu-Farsakh, M., Ardah, A., Chen, Q., Fernandez, B.A., 2017. Performance monitoring of Geosynthetic Reinforced Soil Integrated Bridge System (GRS-IBS) in Louisiana. Geotextiles and Geomembranes 45, 34-47.

Salgado, R., 2008. The engineering of foundations. McGraw-Hill New York.

Subramanian, N., 2008. Design of steel structures. Oxford University Press.

Tjie-Liong, G., 2014. Common mistakes on the application of plaxis 2d in analyzing excavation problems. International Journal of Applied Engineering Research 9, 8291-8311.

Wu, J.T., Yang, K.-H., Mohamed, S., Pham, T., Chen, R.-H., 2014. Suppression of soil dilation—A reinforcing mechanism of soil-geosynthetic composites. Transportation Infrastructure Geotechnology 1, 68-82.

Zheng, Y., Fox, P. J., 2016. Numerical investigation of geosynthetic-reinforced soil bridge abutments under static loading. Journal of Geotechnical and Geoenvironmental Engineering, 142(5), 04016004.

Zheng, Y., Fox, P. J., 2017. Numerical Investigation of the Geosynthetic Reinforced Soil–Integrated Bridge System under Static Loading. Journal of Geotechnical and Geoenvironmental Engineering 143, 04017008.

7.5 EFFECT OF BOUNDARY CONDITIONS ON THE PERFORMANCE OF GEOSYNTHETIC REINFORCED SOIL STRUCTURES

7.5.1 INTRODUCTION

The numerical analysis of geosynthetic reinforced soil pier tests described in Section 7.2 of this report indicated that the contribution of a decreased reinforcement spacing S_v was more significant than that of an increased reinforcement stiffness J when J/S_v was kept the same. On the other hand, the numerical analysis of the GRS-IBS as discussed in Section 7.4, indicated similar behavior of two structures simulated with the same J/S_v ratio. That is, the abutment with closely-spaced reinforcement was found to behave similarly as that with larger reinforcement vertical spacing when J/S_v was kept the same. The main difference between the GRS pier and the GRS-IBS was their boundary conditions. The GRS pier was similar to a retaining wall with limited fill space while the fill space behind the wall facing of GRS-IBS was relatively larger. In addition, the GRS pier included a footing on top of the pier and the width of the footing was equal to the width of the pier. The GRS-IBS, on the other hand, involved a bridge slab on top of the abutment and the contact area between the bridge slab and the abutment was much smaller than the width of the reinforced zone. The numerical evaluation presented in this Section of the report aims to investigate the effect of boundary conditions on the performance of GRS structures using the finite difference method-based programs FLAC2D and FLAC3D. Four different boundary conditions were studied in this research component. The behavior of the GRS structure, such as the lateral displacement of wall facing and the reinforcement tension were investigated.

7.5.2 GEOMETRY

Figure 7.5.1 presents the geometry of numerical models used in this evaluation. Four cases with different boundary conditions were analyzed. The first case, labelled as the 3D Pier (L = 0.5H), involved a three-dimensional (3D) GRS pier simulated using FLAC3D with a height of 2 m (6.6 ft) and a width of 1 m (3.3 ft). The second case, labelled as the 2D Pier (L = 0.5H), involved a two-dimensional (2D) GRS pier simulated using FLAC2D with the same height and width as those of the 3D Pier. The third case, labelled as the 2D Wall (L = 0.5H), was a 2D GRS wall with a height of 2 m (6.6 ft) and a reinforced zone width of 1 m (3.3 ft). The 2D Wall (L = 0.5H) included a retained soil mass behind the reinforced zone. The fourth case, labelled as the 2D Pier (L = 1.5H), involved a 2D GRS pier with a height of 2 m (6.6 ft) and width of 3 m (10 ft). In all four cases, ten layers of Concrete Masonry Units (CMU) were used as facing blocks. Each CMU had dimensions of 0.4 m (16 in) (long) × 0.2 m (8 in) (wide) ×0.2 m (8 in) (high). A concrete slab with dimensions of 0.2 m (8 in) wide and 0.3 m (12 in) high was applied on top of the reinforced zone in all four cases to serve as the footing for loading. Geotextile was used as reinforcement material in all four cases. The CMU blocks were frictionally connected to the geotextile reinforcement. In each case, two different reinforcement spacing S_v and reinforcement stiffness J were adopted, as shown in Fig. 7.5.1, to investigate the effect of the combination of J an S_v on the performance of the structure when the ratio of J/S_v was kept as the same. It should be note that the case with S_v = 0.2 m (8 in) provided slightly larger tension than the case with S_v = 0.4 m (16 in) (i.e., $9 \times 35 = 315$ kN/m (21584 lb/ft) $> 4 \times 70 = 280$ kN/m (19186 lb/ft)).

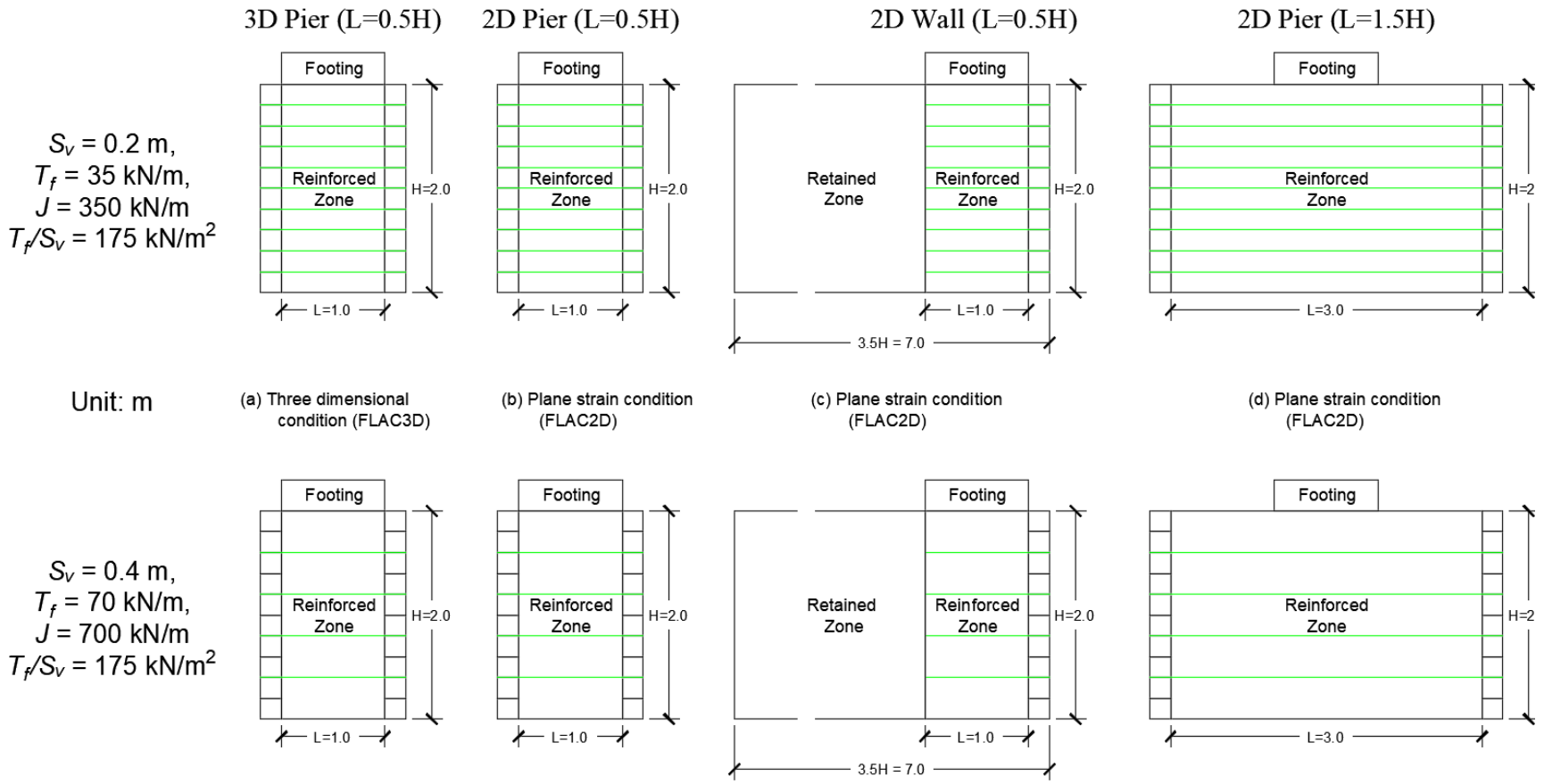

Figure 7.5.1: Geometry of the numerical model: (a) 3D Pier (L = 0.5H); (b) 2D Pier (L = 0.5H); (c) 2D Wall (L = 0.5H); (d) 2D Pier (L = 1.5H).

7.5.3 CONSTITUTIVE MODELS

Table 7.5.1 summarizes the parameters adopted in the constitutive models used in the simulations. The Mohr-Coulomb model was used to simulate the backfill soil for the reinforced zone and the retaining soil while the elastic model was used to simulate the CMU facing blocks and concrete footing.

Table 7.5.1: Constitutive model used in the numerical analysis

Model Variable		Value
Reinforced Zone	Constitutive Model	Mohr-Coulomb
	Elastic Modulus E (MPa)	25
	Poisson's Ratio ν	0.25
	Friction Angle ϕ (°)	38
	Dilation Angle ψ (°)	8
	Cohesion (kPa)	0
	Density (kg/m^3)	2000
Retained Zone （For 2D Wall (L=0.5H)）	Constitutive Model	Mohr-Coulomb
	Elastic Modulus E (MPa)	20
	Poisson's Ratio ν	0.3
	Friction Angle ϕ (°)	30
	Dilation Angle ψ (°)	0
	Cohesion (kPa)	20
	Density (kg/m^3)	1750
CMU blocks and Concrete Footing	Constitutive Model	Elastic
	Elastic Modulus E (GPa)	2
	Poisson's Ratio ν	0.15
	Density (kg/m^3)	2500 (for Concrete Slab) 1230 (for CMU blocks)

7.5.4 REINFORCEMENT AND INTERFACE

In the FLAC3D software, the geotextile reinforcement was modeled as an isotropic elastic material using "geogrid" structural elements available in the software package. The geogrid structural element is designed to resist only membrane loads. The thickness of the geotextile was assumed to be 1 mm (0.04 in) and its Poisson's ratio was assumed to be 0.33. Different tensile stiffness values were adopted for the geotextile based on the plan of numerical analysis as shown in Fig. 7.5.1. The Young's modulus of the geotextile was calculated by dividing the stiffness by the thickness. Table 7.5.2 summarizes the properties of geogrid structural elements used in FLAC3D.

Table 7.5.2: Geogrid structural element properties used in FLAC3D

Element properties	Geogrid Structural Element	
Stiffness (kN/m)	350	700
Thickness (mm)	1	1
Elastic modulus (MPa)	350	700

In the FLAC2D software, both cable structural elements and beam structural elements were used in the numerical model to simulate the geotextile reinforcement. Horizontal geotextile between CMU facing blocks was modeled using beam structural elements with zero moment of inertia (i.e., no bending stiffness) and frictional interfaces on both sides. The geotextile not sandwiched between CMU facing blocks was simulated using cable structural elements with frictional interfaces on both sides. Assuming the thickness of the geotextile to be 1 mm (0.04 in), the elastic modulus of the structural elements was calculated by dividing the stiffness by the thickness. Table 7.5.3 summarizes the properties of both beam and cable structural elements used in FLAC2D.

Table 7.5.3: Properties for beam and cable structural elements used in FLAC2D

Element properties	Cable		Beam	
Stiffness (kN/m)	350	700	350	700
Thickness (mm)	1	1	1	1
Elastic modulus (MPa)	350	700	350	700
Cross-sectional Area (m^2)	0.001	0.001	0.001	0.001
Perimeter (m)	2.002	2.002	2.002	2.002
Yield strength T_f (kN/m)	35	70	/	/
Moment of inertia (m^4)	/	/	0	0

Different types of interfaces were used in the numerical simulations. They were represented using interface elements, which involved linearly-elastic perfectly-plastic springs with the Mohr - Coulomb failure criterion. Table 7.5.4 summarizes the interface properties used in the numerical model.

Table 7.5.4: Interface properties

Interface	k_n (N/m/m)	k_s (N/m/m)	Interaction coefficient C_i	Friction angle (°)	Cohesion (kPa)
Geotextile – Backfill soil (Reinforced zone)	/	1×10^6	0.9	35.1	0
Backfill soil – CMU (Vertical interface between soil and CMU)	1×10^8	1×10^6	0.65	26.9	0
Geotextile – CMU (Frictional connection)	1×10^9	4×10^7	/	16.2	9.5
CMU – CMU (Frictional connection)	1×10^9	4×10^7	/	31.0	0
Concrete footing – Backfill soil	1×10^8	1×10^6	0.9	35.1	0

7.5.5 CONSTRUCTION SEQUENCE

Numerical model was activated layer by layer to simulate the construction process. During construction, CMU facing blocks separated by interface were used to provide lateral confinement to the GRS mass. Layers of geotextile reinforcements were placed over the backfill soil based on the reinforcement plan. Corresponding interfaces and connection were assigned. No compaction stress was applied on top of each layer of backfill soil. After the GRS structure construction was finished, a concrete slab was put on top of the structure. The displacement of the structure was initialized before loading. Vertical pressure was then applied in increments of 40 kPa (5.8 psi) on the concrete footing until it reached 200 kPa (4177 psf). The applied pressure of 200 kPa (4177 psf) was determined based on the FHWA (Adams et al., 2011) recommendation as the service pressure for the GRS structure. For the pier cases, the bottom of the numerical model was fixed in all directions and no fixity was applied to the left, right, front and back sides of the pier. For the wall case, the left boundary was fixed in the horizontal direction and was free to move in the vertical direction while the bottom boundary was fixed in both horizontal and vertical directions.

7.5.6 RESULTS AND DISCUSSION

7.5.6.1 3D PIER (L = 0.5H) VERSUS 2D PIER (L = 0.5H)

7.5.6.1.1 Applied pressure – vertical strain curve

Figure 7.5.2 shows the applied pressure versus vertical strain curves for both the 3D Pier (*L* = 0.5*H*) and the 2D Pier (*L* = 0.5*H*). The numerical results of the 3D Pier (*L* = 0.5*H*) and the 2D Pier

(L = 0.5H) show that the case with comparatively small reinforcement spacing and low stiffness (i.e., J = 350 kN/m (24 kip/ft), S_v = 0.2 m (8 in)) resulted in significantly smaller vertical strains at the applied pressure of 200 kPa (4177 psf). This response indicates that the contribution of close reinforcement spacing S_v was more significant than that of high reinforcement stiffness J when the ratio of J/S_v was kept constant same. The curves of the 2D Pier (L = 0.5H) were similar to those of the 3D Pier (L = 0.5H), indicating that the behavior of the 2D Pier under the same applied pressure could reasonably represent that of the 3D Pier. In other words, the software FLAC3D and FLAC2D did not result in significantly different applied pressure - vertical strain curves.

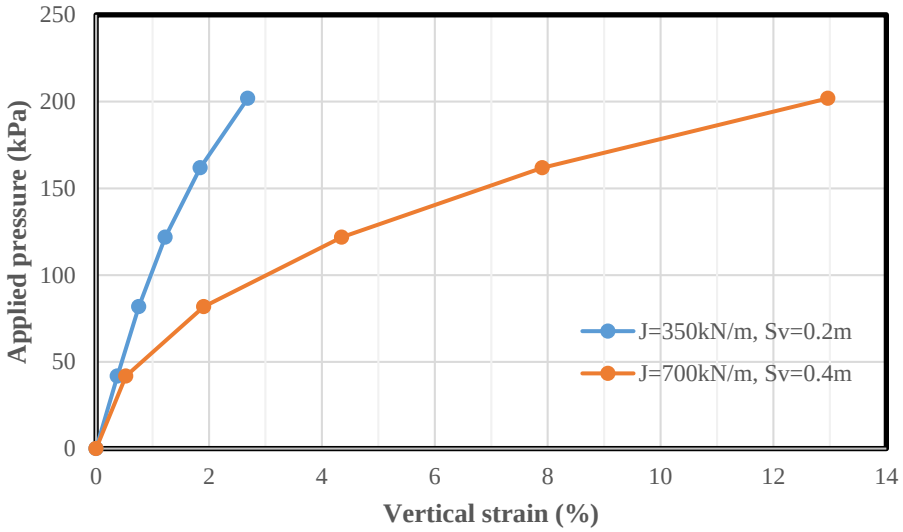

(a)

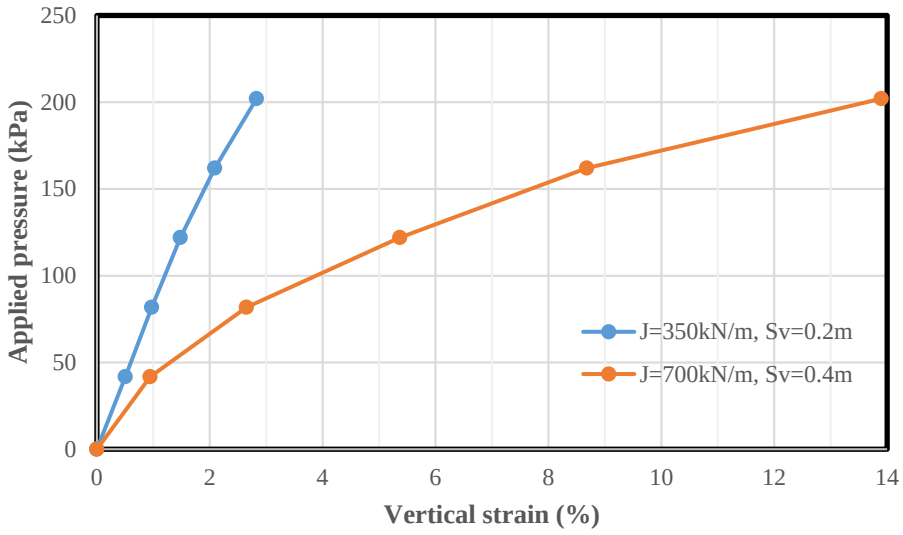

(b)

Fig. 7.5.2: Applied pressure versus vertical strain curves: (a) 3D Pier (L = 0.5H); (b) 2D Pier (L = 0.5H).

7.5.6.1.2 Lateral displacement of CMU facing blocks

Figure 7.5.3 shows the lateral displacements of CMU facing blocks under the applied pressure of 200 kPa (4177 psf) for both the 3D Pier (L = 0.5H) and the 2D Pier (L = 0.5H). The lateral displacement of wall facing of the 2D Pier was slightly larger than that of the 3D Pier. Similar to the applied pressure – vertical strain curves, the lateral displacements of CMU facing blocks showed very different results for the two cases with the same ratio of J/S_v. Specifically, the lateral displacement of wall facing was much larger for the case with large reinforcement spacing and high stiffness (i.e., J = 700 kN/m (48 kip/ft), S_v = 0.4 m (16 in)) than for the other case (i.e., J = 350 kN/m (24 kip/ft), S_v = 0.2 m (8 in)). The reason of significant differences of lateral displacements between two cases with the same J/S_v will be discussed later in Section 7.5.6.3 when the results of 2D pier (L = 0.5H) and 2D pier (L = 1.5H) are compared.

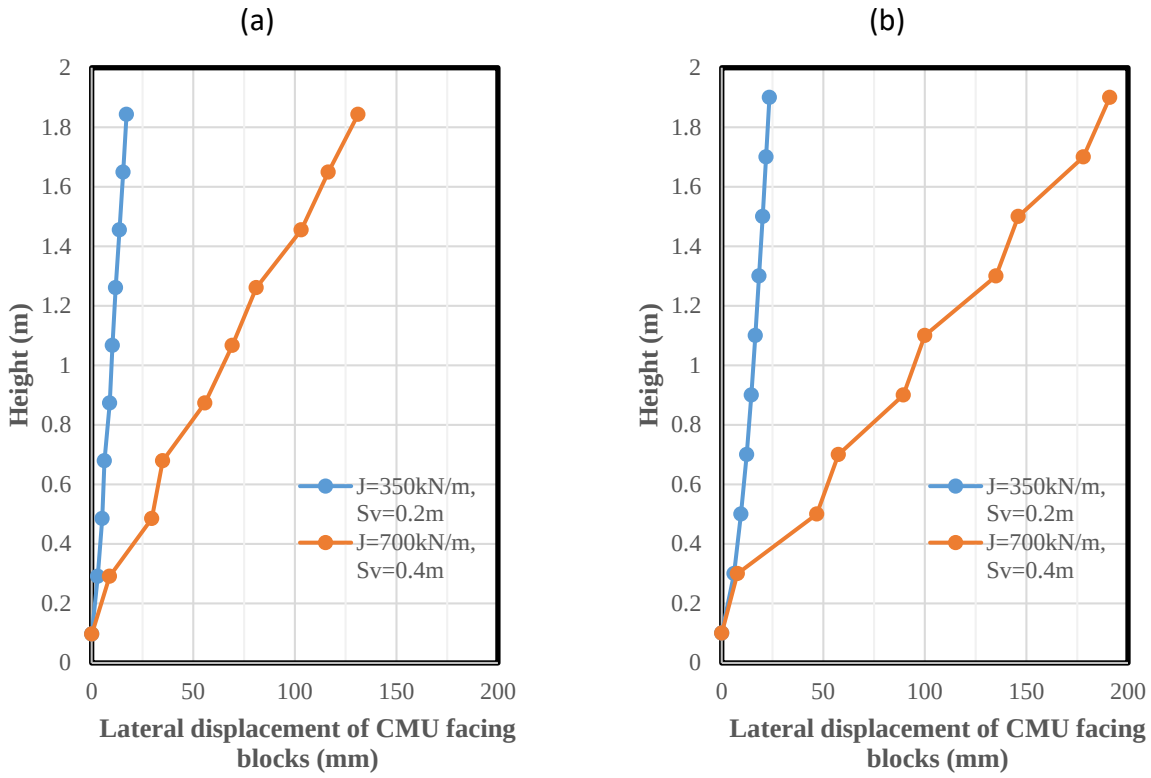

Fig. 7.5.3: Lateral displacements of CMU facing blocks under the applied pressure of 200 kPa (4177 psf): (a) 3D Pier (L = 0.5H); (b) 2D Pier (L = 0.5H).

7.5.6.1.3 Additional vertical stress induced by loading

Figure 7.5.4 shows the additional vertical stresses under the center of the footing induced by the applied pressure of 200 kPa (4177 psf) for both the 3D Pier (L = 0.5H) and the 2D Pier (L = 0.5H). Both the 3D Pier (L = 0.5H) and the 2D Pier (L = 0.5H) show that the case with small reinforcement spacing and low stiffness (i.e., J = 350 kN/m (24 kip/ft), S_v = 0.2 m (8 in)) resulted in lower additional vertical stresses under the center of the footing than the other case (i.e., J = 700 kN/m (48 kip/ft), S_v = 0.4 m (16 in)). The use of close spacing reinforcement increased the vertical load

capacity and reduced the lateral deformation by providing more lateral confinement to the pier. The additional vertical stresses under the center of footing in the 2D Pier (L = 0.5H) were slightly lower than those in the 3D Pier (L = 0.5H).

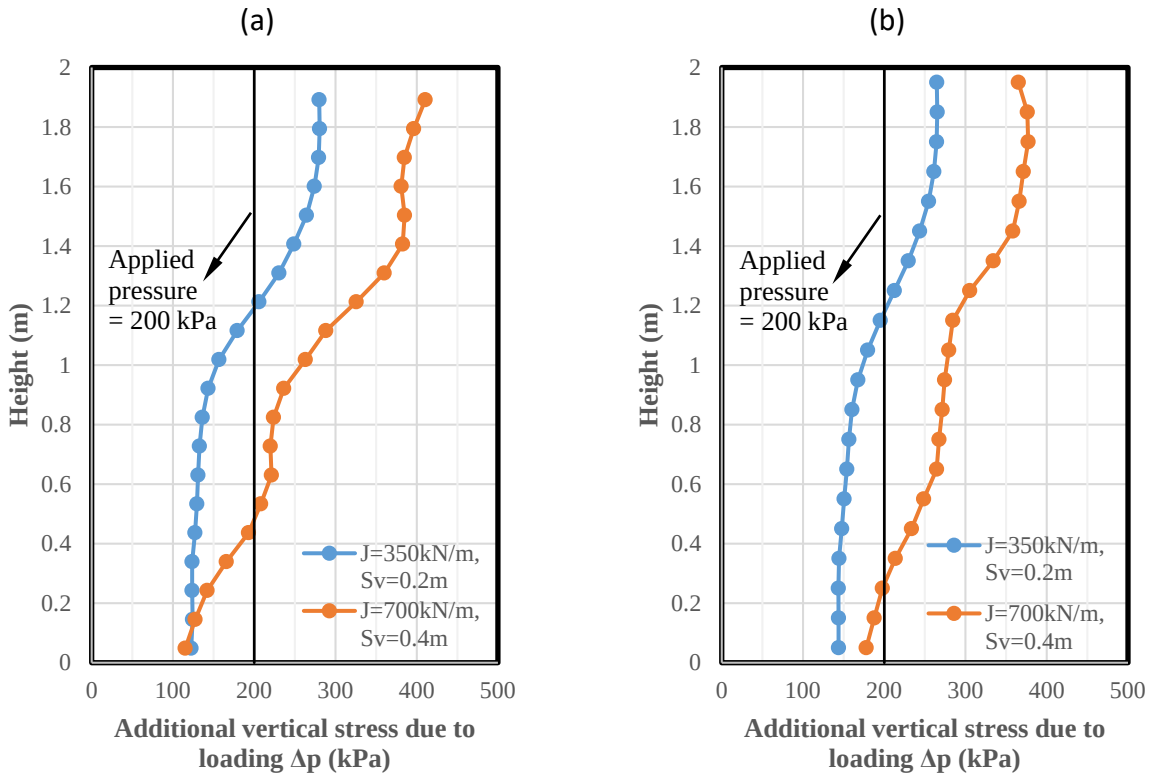

Fig. 7.5.4: Additional vertical stresses under the center of the footing induced by the applied pressures of 200 kPa (4177 psf): (a) 3D Pier (L = 0.5H); (b) 2D Pier (L = 0.5H).

7.5.6.1.4 Reinforcement tension

Figure 7.5.5 shows the maximum tension T_{max} in the reinforcement under the applied pressure of 200 kPa (4177 psf) for both the 3D Pier (L = 0.5H) and the 2D Pier (L = 0.5H). For the 3D Pier (L = 0.5H), the case with S_v = 0.4 m (16 in) required a total maximum tension ΣT_{max} = 58.1 kN/m (3981 lb/ft) while the case with S_v = 0.2 m (8 in) required a total maximum tension ΣT_{max} = 45.2 kN/m (3097 lb/ft). For the 2D Pier (L = 0.5H), the case with S_v = 0.4 m (16 in) required a total maximum tension ΣT_{max} = 86.4 kN/m (5920 lb/ft) while the case with S_v = 0.2 m (8 in) required a total maximum tension ΣT_{max} = 74.0 kN/m (5071 lb/ft). Both the 3D Pier (L=0.5H) and the 2D Pier (L = 0.5H) showed that the use of close reinforcement spacing reduced the required total maximum tension in the reinforcement. The 2D Pier (L = 0.5H) mobilized more tension in the reinforcement than the 3D Pier (L = 0.5H).

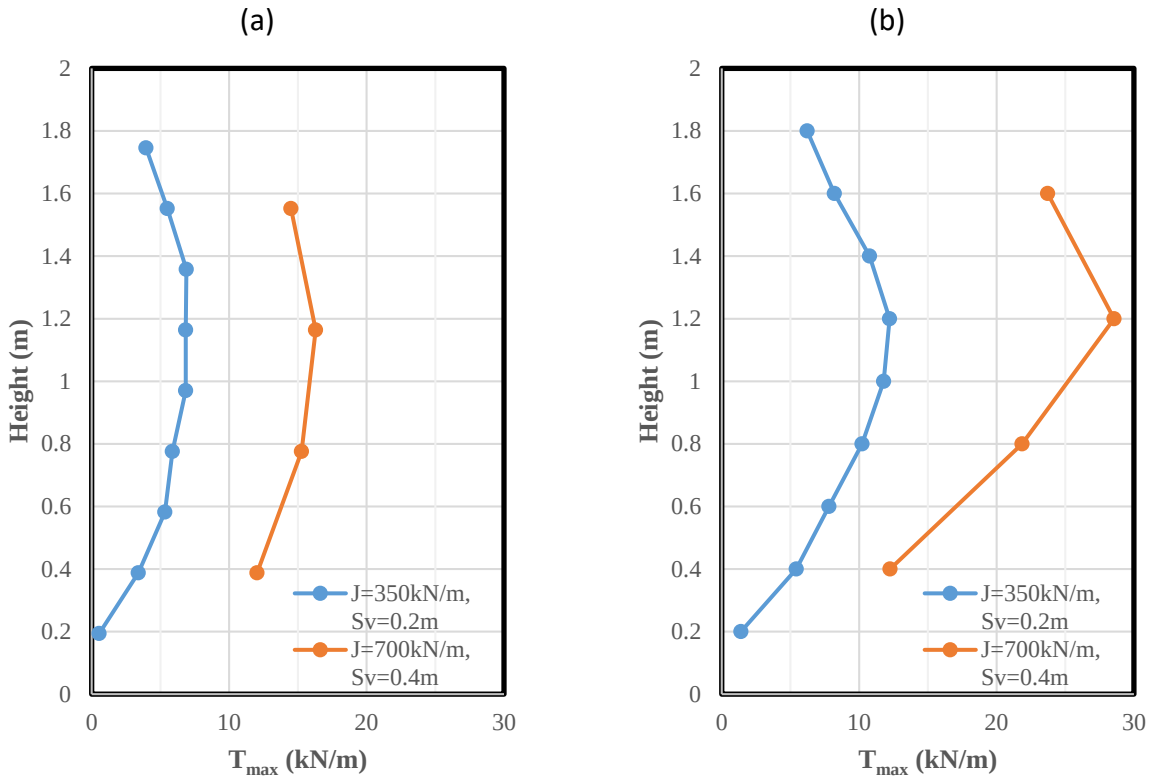

Fig. 7.5.5: Maximum tension T_{max} in the reinforcement under the applied pressure of 200 kPa (4177 psf): (a) 3D Pier (L = 0.5H); (b) 2D Pier (L = 0.5H).

Figure 7.5.6 shows the ratio of the connection force T_0 to the maximum tension T_{max} in the reinforcement under the applied pressure of 200 kPa (4177 psf) for both the 3D Pier (L = 0.5H) and the 2D Pier (L = 0.5H). Both the numerical results of the 3D Pier (L = 0.5H) and the 2D Pier (L = 0.5H) show that the ratio of T_0/T_{max} was larger for the case of S_v = 0.2 m (8 in) than that for the case of S_v = 0.4 m (16 in), indicating that the use of close reinforcement spacing resulted in more uniform distribution of tensile forces in the reinforcement.

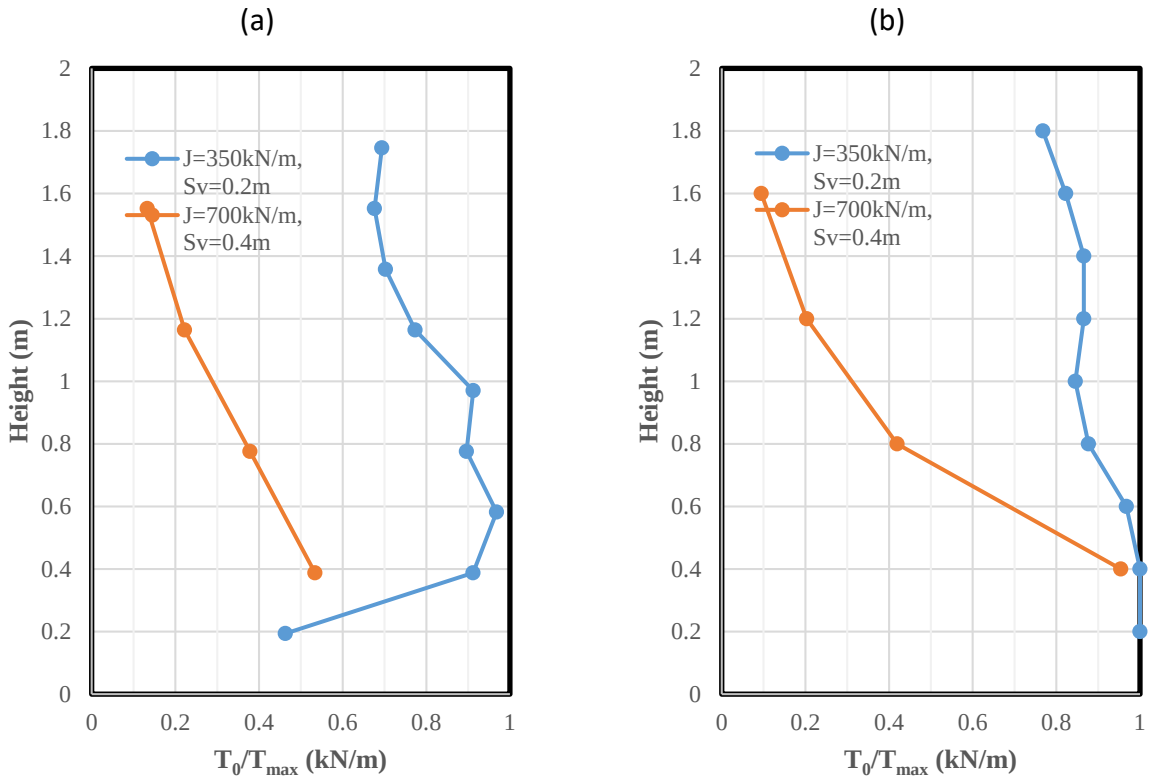

Fig. 7.5.6: The ratios of the connection force T_0 to the maximum tension T_{max} in the reinforcement under the applied pressure of 200 kPa (4177 psf): (a) 3D Pier (L = 0.5H); (b) 2D Pier (L = 0.5H).

From the previous discussion it could be concluded that the behavior of the 3D Pier (*L* = 0.5*H*) was similar to that of the 2D Pier (*L* = 0.5*H*). Under both conditions, the use of close reinforcement spacing was predicted to reduce the required total maximum reinforcement tension. In other words, the contribution of close reinforcement spacing S_v was more significant than that of high reinforcement stiffness *J* when the ratio of J/S_v was kept the same.

7.5.6.2 2D PIER (L = 0.5H) VERSUS 2D WALL (L= 0.5H)

7.5.6.2.1 Applied pressure – vertical strain curve

Figure 7.5.7 shows the applied pressure versus vertical strain curves for both the 2D Pier (*L* = 0.5*H*) and the 2D Wall (*L* = 0.5*H*). The behavior of the 2D Wall (*L* = 0.5*H*) was similar to the behavior of the 2D Pier (*L* = 0.5*H*). The 2D Wall (*L* = 0.5*H*) with small reinforcement spacing and low stiffness (i.e., *J* = 350 kN/m (24 kip/ft), S_v = 0.2 m (8 in)) had smaller vertical strains than the 2D Wall (*L* = 0.5*H*) with large reinforcement spacing and high stiffness (i.e., *J* = 700 kN/m (48 kip/ft), S_v = 0.4 m (16 in)) under applied pressure of 200 kPa (4177 psf). The 2D Wall (*L* = 0.5*H*) showed comparatively larger vertical strain than the 2D Pier (*L* = 0.5*H*) under the same applied pressure because the footing tilted towards the wall facing under loading.

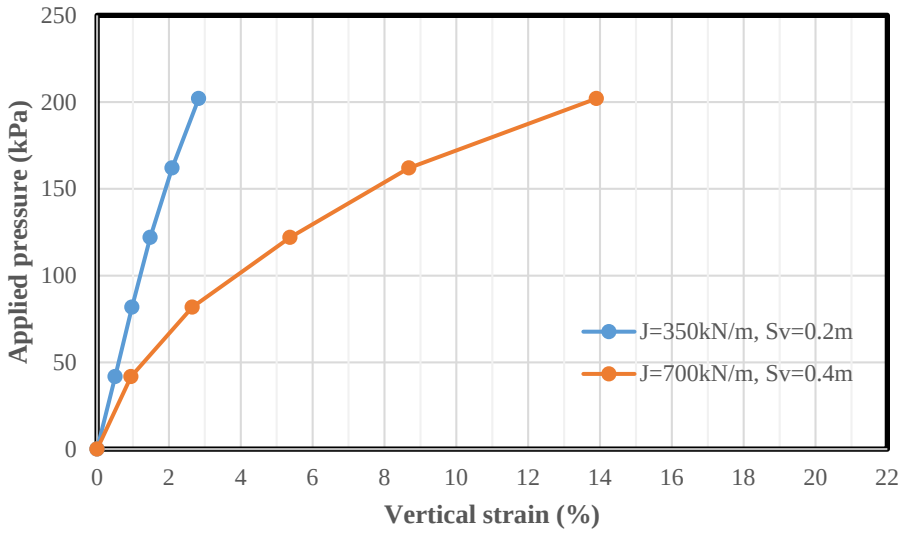

(a)

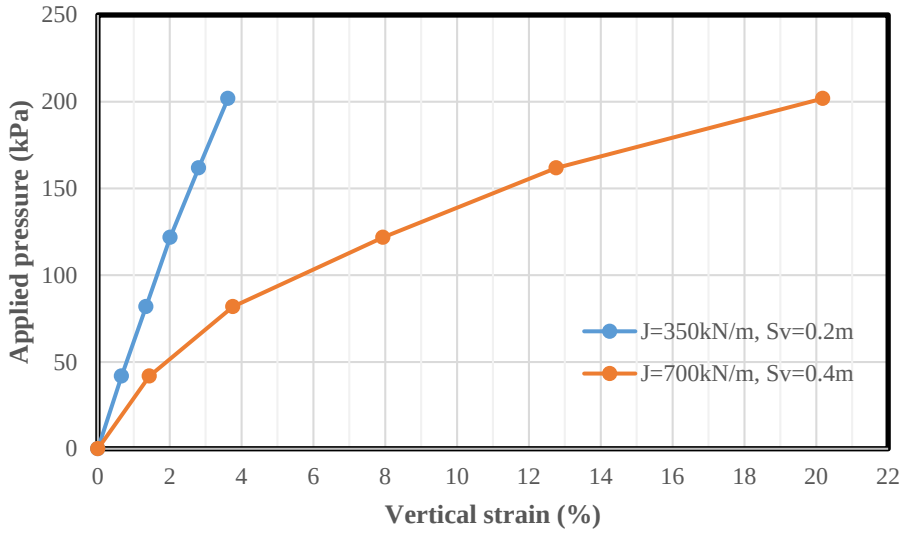

(b)

Fig. 7.5.7: Applied pressure versus vertical strain curves: (a) 2D Pier (L = 0.5H); (b) 2D Wall (L =0.5H).

7.5.6.2.2 Lateral displacement of CMU facing blocks

Figure 7.5.8 shows the lateral displacement of CMU facing blocks under the applied pressure of 200 kPa (4177 psf) for both the 2D Pier (L = 0.5H) and the 2D Wall (L = 0.5H). Consistent with the behavior of 2D Pier (L = 0.5H), the 2D Wall (L = 0.5H) had the lateral displacement of wall facing much larger for the case with large reinforcement spacing and high stiffness (i.e., J = 700 kN/m (48 kip/ft), S_v = 0.4 m (16 in)) than the other case (i.e., J = 350 kN/m (24 kip/ft), S_v = 0.2 m (8 in)). The 2D Wall ((L = 0.5H) had larger lateral displacement of CMU facing blocks than the 2D Pier (L

= 0.5*H*) because the footing tilted toward the wall facing under loading and the wall facing deflected more under the eccentric footing load.

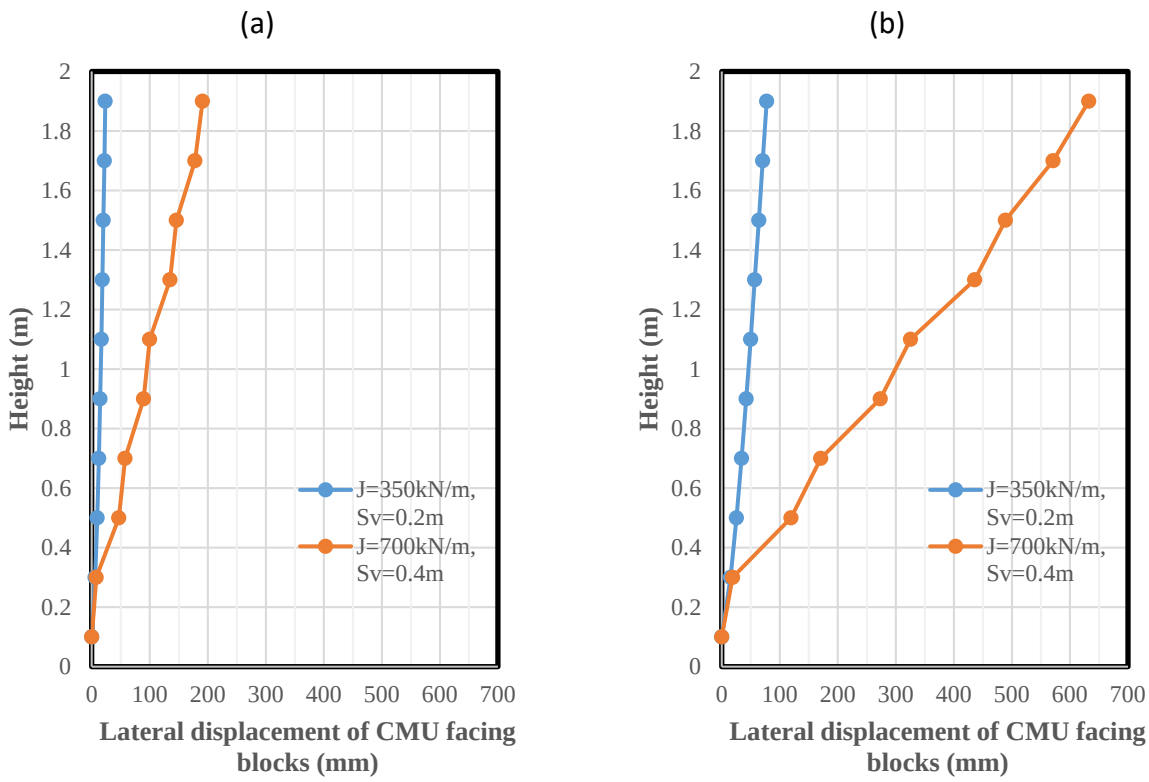

Fig. 7.5.8: Lateral displacements of CMU facing blocks under the applied pressure of 200 kPa (4177 psf): (a) 2D Pier (L = 0.5H); (b) 2D Wall (L = 0.5H).

7.5.6.2.3 Additional vertical stress induced by loading

Figure 7.5.9 shows the additional vertical stress under the center of the footing induced by the applied pressure of 200 kPa (4177 psf) for both the 2D Pier (*L* = 0.5*H*) and the 2D Wall (*L* = 0.5*H*). Consistent with the behavior of the 2D Pier (*L* = 0.5*H*), the 2D Wall (*L* = 0.5*H*) with small reinforcement spacing and low stiffness (i.e., *J* = 350 kN/m (24 kip/ft), S_v = 0.2 m (8 in)) had lower additional vertical stresses under the center of the footing than the other case (i.e., *J* = 700 kN/m (48 kip/ft), S_v = 0.4 m (16 in)). The difference of additional vertical stresses under the center of the footing between the 2D Pier (*L* = 0.5*H*) and the 2D Wall (*L* = 0.5*H*) was small.

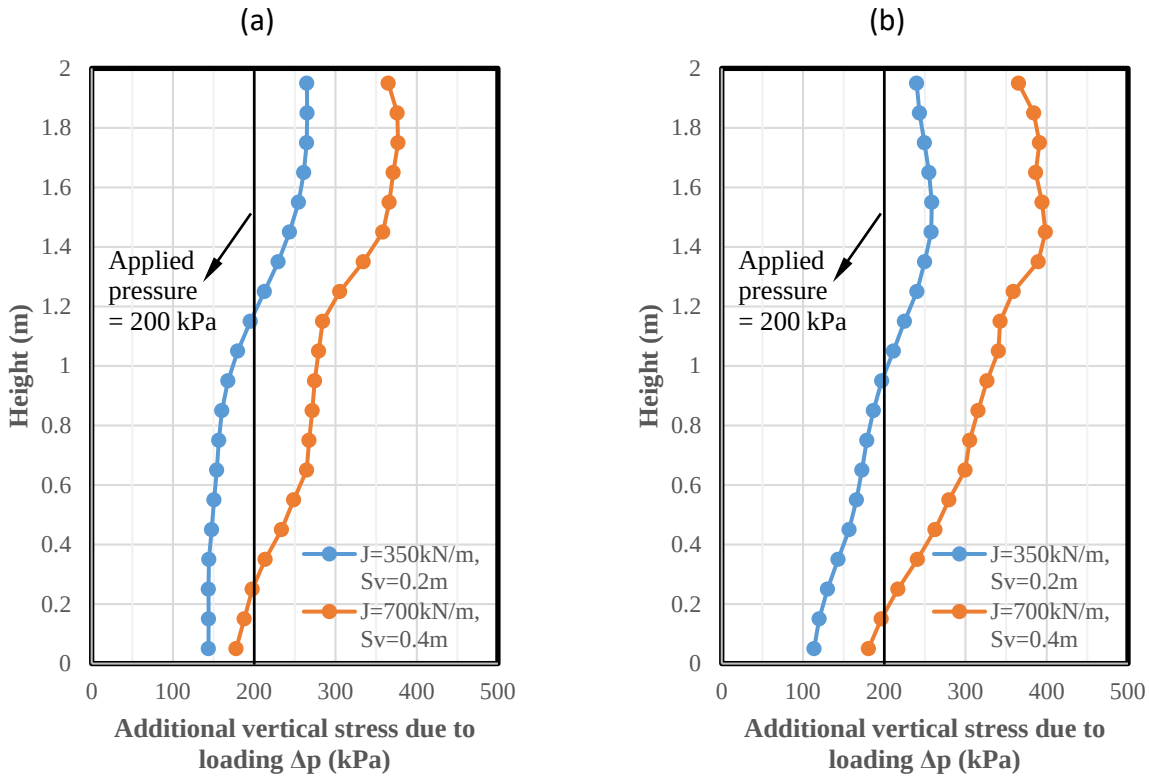

Fig. 7.5.9: Additional vertical stresses under the center of the footing induced by the applied pressures of 200 kPa (4177 psf): (a) 2D Pier (L = 0.5H); (b) 2D Wall (L = 0.5H).

7.5.6.2.4 Reinforcement tension

Figure 7.5.10 shows the maximum tension T_{max} in the reinforcement under the applied pressure of 200 kPa (4177 psf) for both the 2D Pier (L = 0.5H) and the 2D Wall (L = 0.5H). For the 2D Pier (L = 0.5H), the case with S_v = 0.4 m (16 in) required the total maximum tension ΣT_{max} = 86.4 kN/m (5920 lb/ft) while the case with S_v =0.2 m (8 in) required the total maximum tension ΣT_{max} = 74.0 kN/m (5071 lb/ft). For the 2D Wall (L = 0.5H), the case with S_v = 0.4 m (16 in) required the total maximum tension ΣT_{max} = 97.8 kN/m (6701 lb/ft) while the case with S_v =0.2 m (8 in) required the total maximum tension ΣT_{max} = 73.4 kN/m (5029 lb/ft). The numerical results of both the 2D Pier (L = 0.5H) and the 2D Wall (L = 0.5H) show that the use of close reinforcement spacing led to a reduction in the required total maximum reinforcement tension ΣT_{max}. The reduction in the total maximum tension ΣT_{max} in the reinforcement was 17% and 33% for the case of 2D Pier (L = 0.5H) and 2D Wall (L = 0.5H) respectively.The 2D Wall (L = 0.5H) mobilized more tensile force in the reinforcement than the 2D Pier (L = 0.5H) with the same S_v = 0.4 m (16 in).

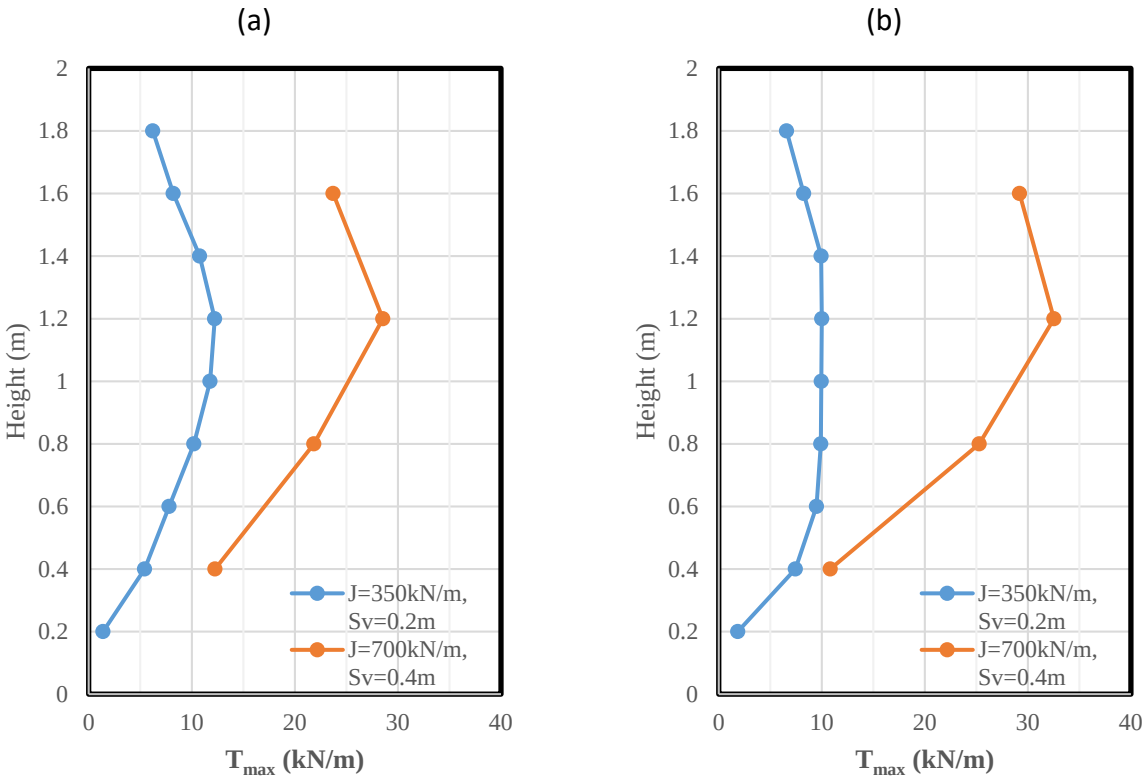

Fig. 7.5.10: Maximum tension T_{max} in the reinforcement under the applied pressure of 200 kPa (4177 psf): (a) 2D Pier (L = 0.5H); (b) 2D Wall (L = 0.5H).

Figure 7.5.11 shows the ratios of the connection force T_0 to the maximum reinforcement tension T_{max} under the applied pressure of 200 kPa (4177 psf) for both the 2D Pier (L = 0.5H) and the 2D Wall (L = 0.5H). Both the 2D Pier (L = 0.5H) and the 2D Wall (L = 0.5H) showed larger ratios of T_0/T_{max} with reinforcement spacing S_v = 0.2 m (8 in) than those with S_v = 0.4 m (16 in). For the 2D Wall (L = 0.5H), the ratio of T_0/T_{max} was close to 1 for the case with S_v = 0.2 m (8 in), indicating that the maximum tension in the reinforcement happened near facing connection when close reinforcement spacing was used.

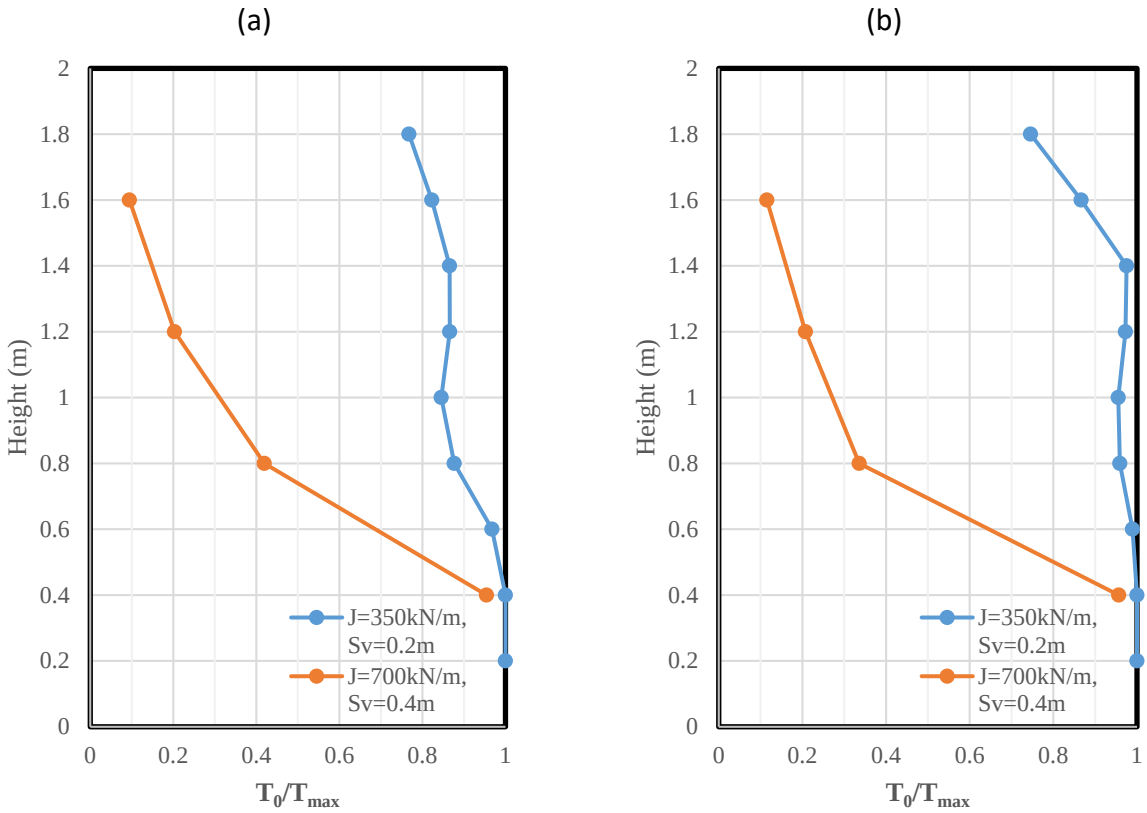

Fig. 7.5.11: The ratios of the connection force T_0 to the maximum tension T_{max} in the reinforcement under the applied pressure of 200 kPa (4177 psf): (a) 2D Pier (L = 0.5H); (b) 2D Wall (L = 0.5H).

Figure 7.5.12 shows the distributions of the tension in the reinforcement at four depths under the applied pressure of 200 kPa (4177 psf) for both the 2D Pier (L = 0.5H) and the 2D Wall (L = 0.5H). For the cases with S_v = 0.4 m (16 in), both the 2D Pier (L = 0.5H) and the 2D Wall (L = 0.5H) developed the maximum reinforcement tension under the center of footing, with the reinforcement connection forces in the reinforcement T_0 being lower than the maximum reinforcement tension T_{max} (except at the bottom reinforcement layer in the 2D Wall (L = 0.5H). Tension in the reinforcement decreased linearly with distance towards both left and right sides, indicating that pullout of the reinforcement may happen from both ends when S_v = 0.4 m (16 in). For the case with S_v = 0.2 m (8 in), however, the tensile force in the reinforcement was more uniformly distributed, resulting in larger ratio of T_0/T_{max} near CMU facing blocks as shown in Fig. 7.5.11.

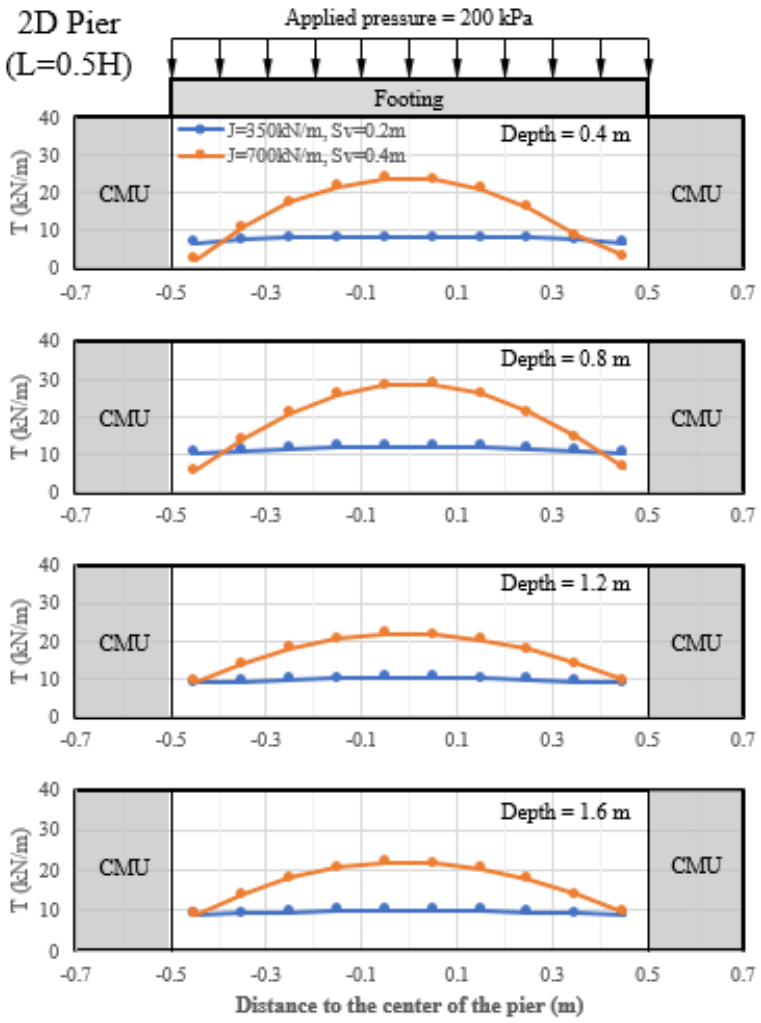

(a)

Fig. 7.5.12: Distributions of the tension in the reinforcement at four depths under the applied pressure of 200 kPa (4177 psf): (a) 2D Pier (L = 0.5H);

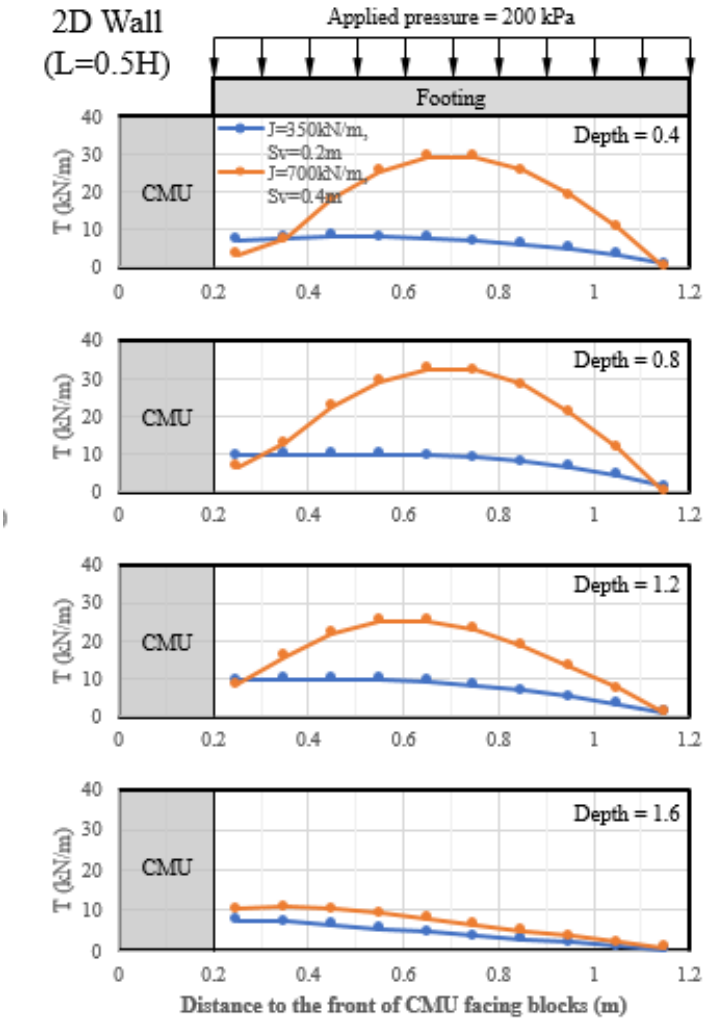

(b)

Fig. 7.5.12: Distributions of the tension in the reinforcement at four depths under the applied pressure of 200 kPa (4177 psf): (b) 2D Wall (L = 0.5H) (continued).

From the previous discussion it could be concluded that the behavior of the 2D Pier (L = 0.5H) was similar to that of the 2D Wall (L = 0.5H) except that the 2D Wall (L = 0.5H) resulted in larger deformations since the footing tilted toward the wall facing under loading. Under both conditions, the use of closely-spaced reinforcement resulted in a reduced total maximum reinforcement tension ΣT_{max}. In other words, the contribution of close reinforcement spacing S_v was more significant than that of high reinforcement stiffness J for a given J/S_v ratio. The distribution of tension in the reinforcement indicates that reinforcement pullout may happen at both ends when a large reinforcement spacing S_v = 0.4 m (16 in) was used. The use of closely-spaced reinforcement resulted in a more uniform reinforcement tension distribution.

7.5.6.3 2D PIER (L = 0.5H) VERSUS 2D PIER (L = 1.5H)

7.5.6.3.1 Applied pressure – vertical strain curve

Figure 7.5.13 shows the applied pressure versus vertical strain curves for both the 2D Pier (L = 0.5H) and the 2D Pier (L = 1.5H). Figure 7.5.13 shows that the 2D Pier (L = 0.5H) and the 2D Pier (L = 1.5H) had very different results. The numerical result for the 2D Pier (L = 0.5H) shows that a closely-spaced reinforcement resulted in significantly smaller vertical strain under the same applied pressure than a largely-spaced reinforcement. The numerical result for the 2D Pier (L = 1.5H), however, shows that the reinforcement spacing did not have a significant effect on the applied pressure – vertical strain curve, as shown in Fig. 7.5.13 (b). The change of reinforcement length resulted in different results. The reason of significant differences of the applied pressure versus vertical strain curves between the 2D Pier (L = 0.5H) and the 2D Pier (L = 1.5H) will be provided later in Section 7.5.6.3.4 when reinforcement tension is discussed.

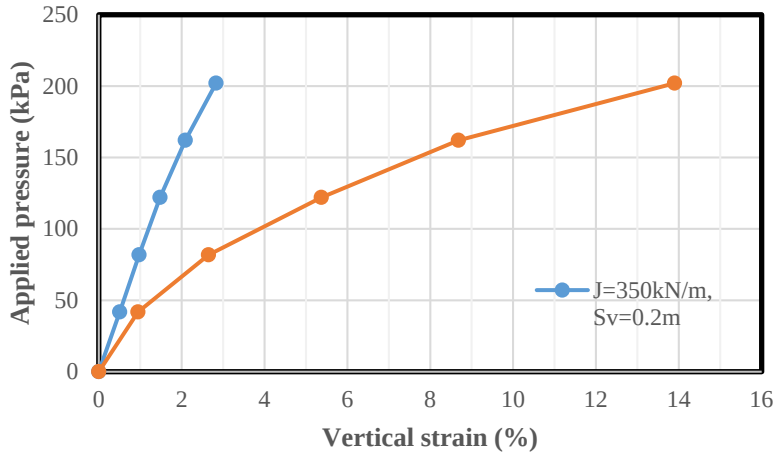

(a)

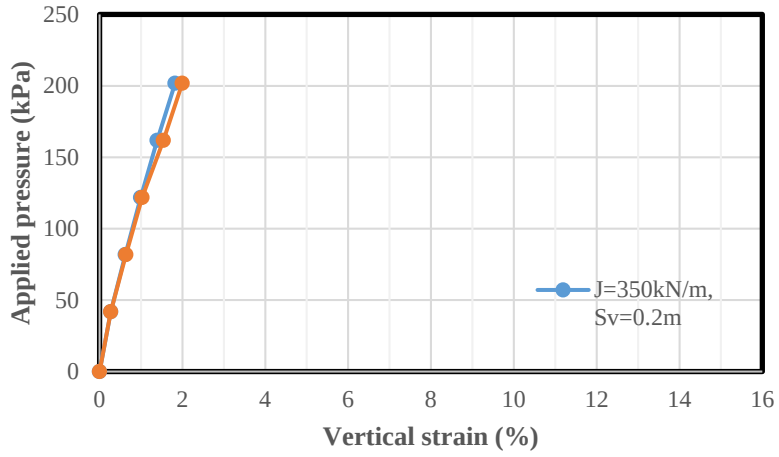

(b)

Fig. 7.5.13: Applied pressure versus vertical strain curves: (a) 2D Pier (L = 0.5H); (b) 2D Pier (L = 1.5H).

7.5.6.3.2 Lateral displacement of CMU facing blocks

Figure 7.5.14 shows the lateral displacements of CMU facing blocks under the applied pressure of 200 kPa (4177 psf) for both the 2D Pier (L = 0.5H) and the 2D Pier (L = 1.5H). Similar to the applied pressure – vertical strain curves, the 2D Pier (L = 0.5H) and the 2D Pier (L = 1.5H) had different results in terms of their lateral wall deflections. The 2D Pier (L = 0.5H) had much larger lateral displacement of CMU facing blocks for the case with reinforcement spacing S_v = 0.4 m (16 in) than that for the case with S_v = 0.2 m (8 in). The 2D Pier (L = 1.5H), however, had almost the same lateral displacements of CMU facing blocks for the two cases with different reinforcement spacing. The reason of significant differences of the lateral displacements of CMU facing blocks between the 2D Pier (L = 0.5H) and the 2D Pier (L = 1.5H) will also be provided later in Section 7.5.6.3.4 when reinforcement tension is discussed.

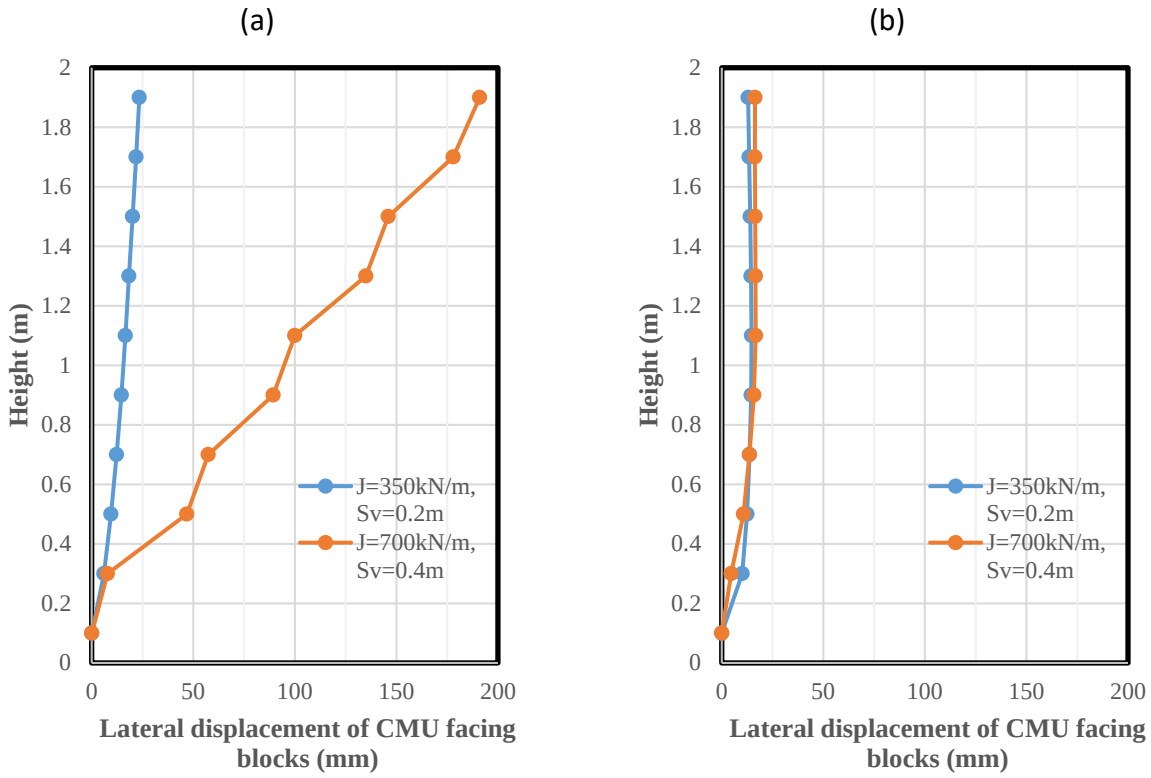

Fig. 7.5.14: Lateral displacements of CMU facing blocks under the applied pressure of 200 kPa (4177 psf): (a) 2D Pier (L = 0.5H); (b) 2D Pier (L = 1.5H).

7.5.6.3.3 Additional vertical stress induced by loading

Figure 7.5.15 shows the additional vertical stresses under the center of the footing induced by the applied pressure of 200 kPa (4177 psf) for both the 2D Pier (L = 0.5H) and the 2D Pier (L = 1.5H). The 2D Pier (L = 0.5H) with closely-spaced reinforcement had lower additional vertical stresses under the center of the footing than that with largely spaced reinforcement. The 2D Pier (L = 1.5H), however, had almost the same additional vertical stresses under the center of the footing for two cases with different reinforcement spacing.

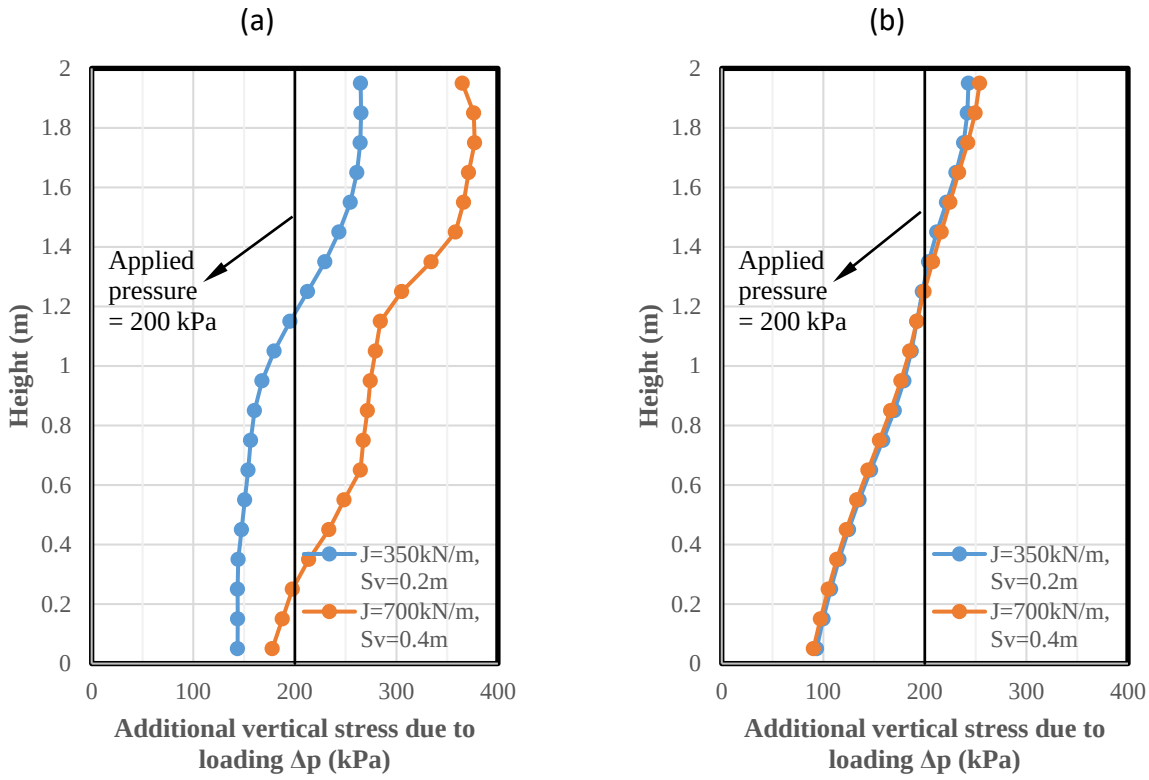

Fig. 7.5.15: Additional vertical stresses under the center of the footing induced by the applied pressures of 200 kPa (4177 psf): (a) 2D Pier (L = 0.5H); (b) 2D Pier (L = 1.5H).

7.5.6.3.4 Reinforcement tension

Figure 7.5.16 shows the maximum tension T_{max} in the reinforcement under the applied pressure of 200 kPa (4177 psf) for both the 2D Pier (L = 0.5H) and the 2D Pier (L = 1.5H). For the 2D Pier (L = 0.5H), the case with S_v = 0.4 m (16 in) required the total maximum tension ΣT_{max} = 86.4 kN/m (5920 lb/ft) while the case with S_v =0.2 m (8 in) required the total maximum tension ΣT_{max} = 74.0 kN/m (5071 lb/ft). The use of closely-spaced reinforcement reduced the required total maximum tension ΣT_{max} in the reinforcement than the use of largely-spaced reinforcement when the reinforcement length was half of the pier height. For the 2D Pier (L = 1.5H), the case with S_v = 0.4 m required the total maximum tension ΣT_{max} = 36.1 kN/m (2474 lb/ft) while the case with S_v =0.2 m required the total maximum tension ΣT_{max} = 38.8 kN/m (2659 lb/ft). These two piers required similar total maximum tension ΣT_{max} in the reinforcement when the reinforcement length was 1.5 times the pier height.

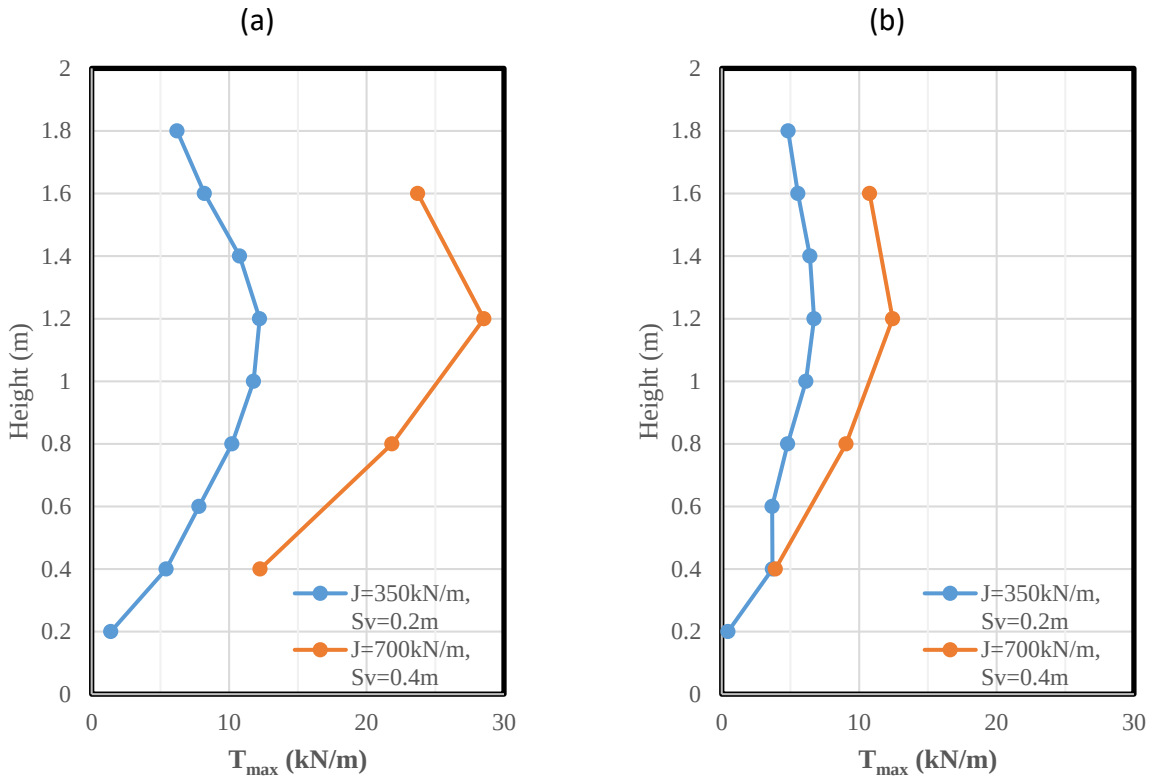

Fig. 7.5.16: Maximum tension T_{max} in the reinforcement under the applied pressure of 200 kPa (4177 psf): (a) 2D Pier (L = 0.5H); (b) 2D Pier (L = 1.5H).

Figure 7.5.17 shows the ratios of the connection force T_0 to the maximum tension T_{max} in the reinforcement under the applied pressure of 200 kPa (4177 psf) for both the 2D Pier (L = 0.5H) and the 2D Pier (L = 1.5H). The numerical result for the 2D Pier (L = 0.5H) shows that the use of closely-spaced reinforcement resulted in the connection force in the reinforcement closer to the maximum tension in the reinforcement. The numerical result for the 2D Pier (L = 1.5H), however, shows that the difference in the ratio of T_0/T_{max} between two cases with different reinforcement spacing was smaller than that for the 2D Pier (L = 0.5H), indicating that the change of reinforcement spacing did not have much effect on the ratio of T_0/T_{max} when longer reinforcement layers were used.

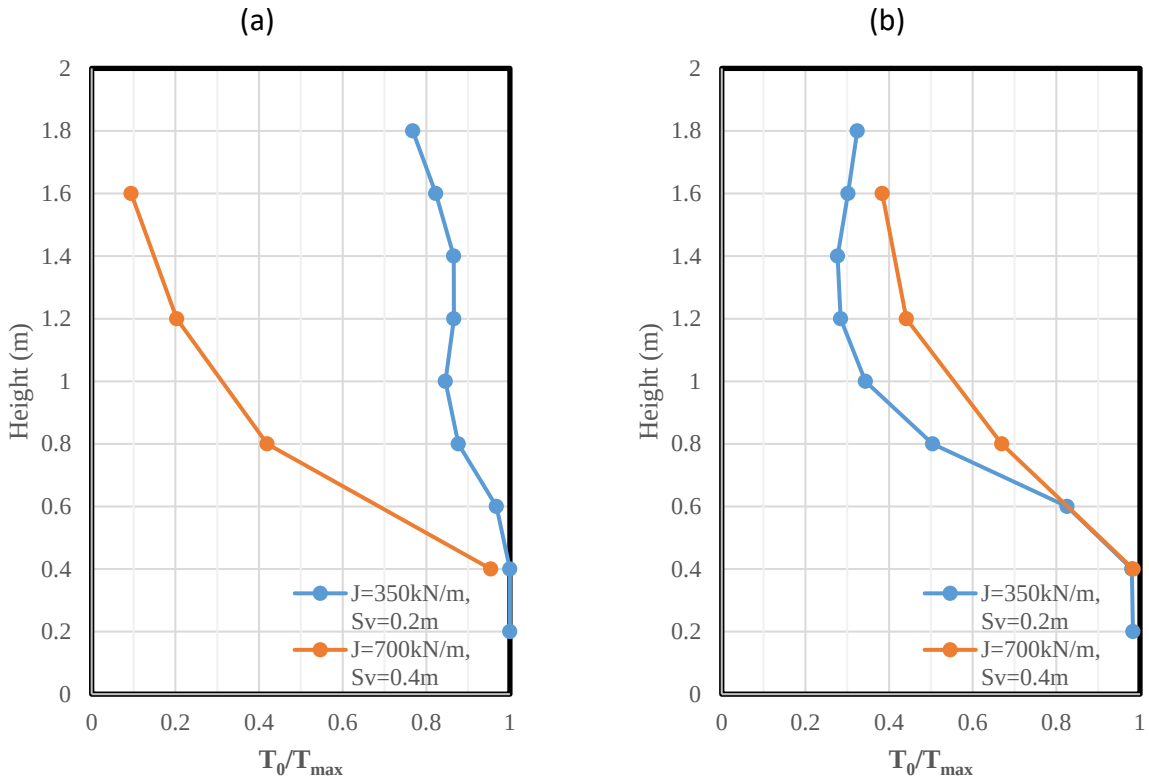

Fig. 7.5.17: The ratios of the connection force T_0 to the maximum tension T_{max} in the reinforcement under the applied pressure of 200 kPa (4177 psf): (a) 2D Pier (L = 0.5H); (b) 2D Pier (L = 1.5H).

Figure 7.5.18 shows the distributions of the tension in the reinforcement at four depths under the applied pressure of 200 kPa (4177 psf) for both the 2D Pier (L = 0.5H) and the 2D Pier (L = 1.5H). The 2D Pier (L = 0.5H) had different distributions of the tension in the reinforcement when the reinforcement spacing was changed. When S_v = 0.4 m (16 in), the tension in the reinforcement was largest under the center of the footing and decreased linearly towards CMU facing blocks at both left and right sides, indicating that pullout of the reinforcement may happen at both ends. When S_v = 0.2 m (8 in), the tension in the reinforcement was distributed more uniformly and the connection force was closer to the maximum tensile force in the reinforcement. The 2D Pier (L = 1.5H), however, had similar distributions of the tensile force in the reinforcement despite the change of reinforcement spacing. For both cases with different reinforcement spacing, the maximum tensile forces in the reinforcement happened under the center of the footing and the connection force was lower than the maximum tensile force except for the bottom layers of the reinforcement. However, no pullout of reinforcement happened since the length of the reinforcement was long enough (i.e. L = 1.5H) to provide anchorage despite the change of reinforcement spacing.

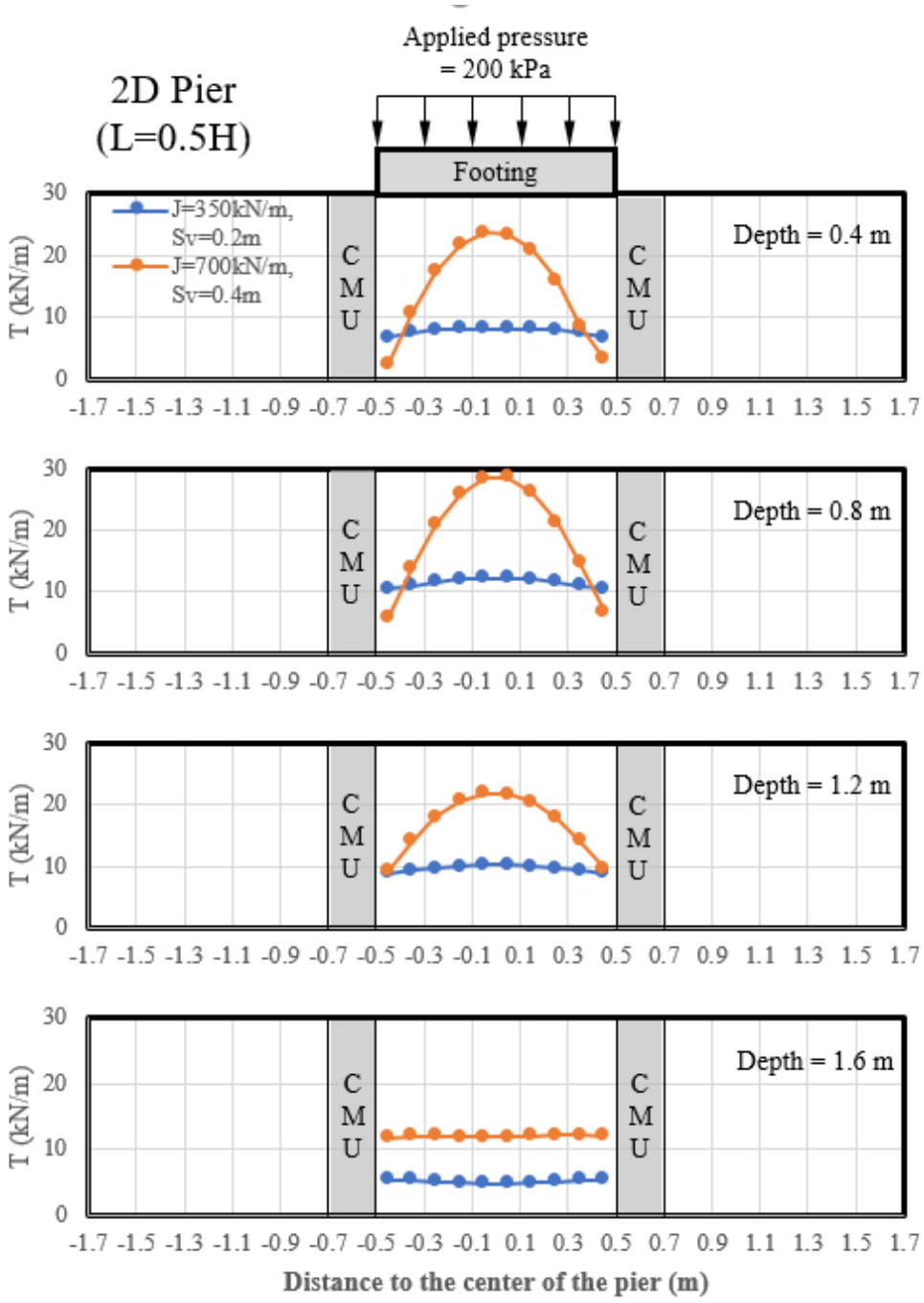

(a)

Fig. 7.5.18: Distributions of the tension in the reinforcement at four depths under the applied pressure of 200 kPa (4177 psf): (a) 2D Pier (L = 0.5H);

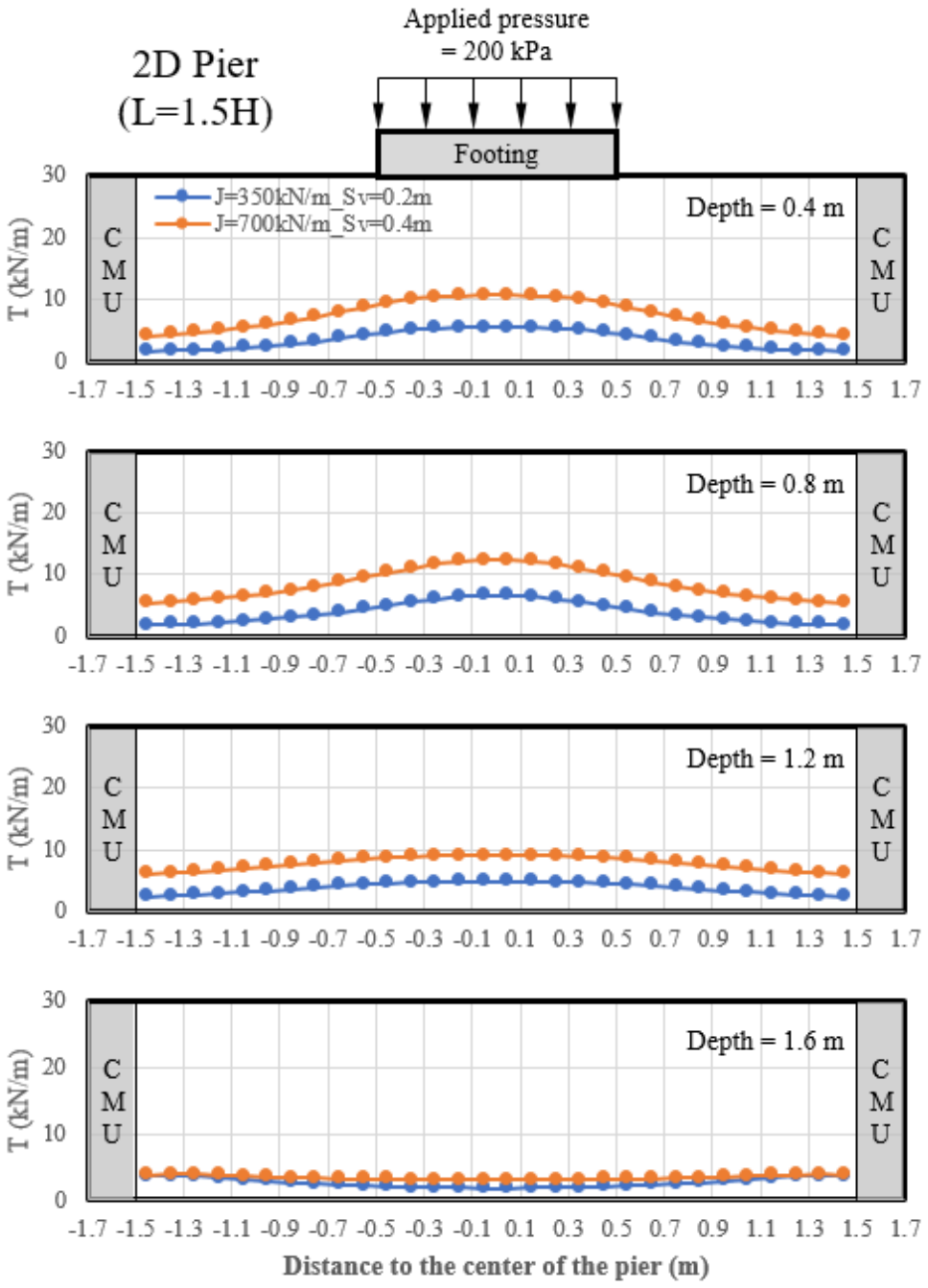

(b)

Fig. 7.5.18: Distributions of the tension in the reinforcement at four depths under the applied pressure of 200 kPa (4177 psf): (b) 2D Pier (L = 1.5H) (continued).

From the previous discussion, it can be concluded that when pullout of the reinforcement controlled the performance, the structure with close reinforcement spacing and low reinforcement stiffness showed a better performance than that with large reinforcement spacing

and high reinforcement stiffness when the ratio of J/S_v was kept the same. In other words, the contribution of close reinforcement spacing S_v was more significant than that of the high reinforcement stiffness J when the ratio of J/S_v was kept the same. This result is reasonable because the use of closely-spaced reinforcement resulted in more layers of reinforcement in the structure. More layers of reinforcement provided better lateral restraint and higher pullout resistance due to more interfaces existing in the structure. When pullout of the reinforcement did not control the performance, however, the two structures required essentially the same total maximum tension ΣT_{max} in the reinforcement and behaved almost the same despite the change of reinforcement spacing and stiffness when the ratio of J/S_v was kept the same. Therefore, the behavior of GRS structures is controlled by the mode of reinforcement failure.

7.5.7 CONCLUSIONS

This study aimed to investigate the effect of boundary conditions on the performance of Geosynthetic Reinforced Soil structures using the finite difference method-based program FLAC2D and FLAC3D. Four different boundary conditions, labelled as the 3D Pier (L = 0.5H), the 2D Pier (L = 0.5H), the 2D Wall (L = 0.5H), and the 2D Pier (L = 1.5H), were studied in this study where L represents the reinforcement length and H represents the structure height. The behavior of the GRS structure, such as the applied pressure – vertical strain curve, the lateral displacement of wall facing, additional vertical stress induced by loading, and the tension in the reinforcement, was investigated. Based on the numerical results and discussion, the following conclusions can be made:

1 The behavior of the 3D Pier (L = 0.5H H) was close to that of the 2D Pier (L = 0.5H). Both the 3D Pier (L = 0.5H H) and the 2D Pier (L = 0.5H) showed the benefits of closely-spaced reinforcement when the ratio of reinforcement stiffness J to spacing S_v was maintained the same. Under both conditions, the use of closely-spaced reinforcement reduced the required total maximum tension ΣT_{max} in the reinforcement. FLAC3D and FLAC2D obtained similar numerical results.

2 The 2D Wall (L = 0.5H) had more deformation than the 2D Pier (L = 0.5H) since the footing in the 2D Wall (L = 0.5H) tilted towards the wall facing under loading and the 2D Wall (L = 0.5H) deflected more under the eccentric footing load. Both the 2D Wall (L = 0.5H) and the 2D Pier (L = 0.5H) showed the benefits of closely-spaced reinforcement when the ratio of reinforcement stiffness J to spacing S_v was maintained the same. Under both conditions, the use of closely-spaced reinforcement reduced the required total maximum tension ΣT_{max} in the reinforcement.

3 When pullout of reinforcement controlled the performance, the structure with close reinforcement spacing S_v and low reinforcement stiffness J showed better performance than that with large reinforcement spacing S_v and high reinforcement stiffness J when the ratio of J/S_v was kept the same. When pullout of reinforcement did not control the performance, however, the two structures required almost the same total maximum tension ΣT_{max} in the reinforcement and behaved similarly despite the change of reinforcement spacing and stiffness when the ratio of J/S_v was kept the same.

7.5.8 REFERENCES

Adams, M., Nicks, J., Stabile, T., Wu, J., Schlatter, W., Hartmann, J., 2011. Geosynthetic Reinforced Soil Integrated Bridge System, Synthesis Report.

7.6 STABILITY ANALYSIS OF GEOSYNTHETIC-REINFORCED SOIL STRUCTURES

7.6.1 INTRODUCTION

The parametric study on Geosynthetic-Reinforced Soil – Integrated Bridge Systems (GRS-IBS) conducted in Section 7.4 focused on the behavior of the system under working stress conditions. The maximum reinforcement tension T_{max} from the previous parametric study did not reflect that under a limit state. Therefore, stability analysis is necessary to further assess the performance of GRS structures under a limit state. Two different methods, the continuum mechanics-based numerical method using finite the difference software FLAC2D and the limit equilibrium (LE) method using the LE software ReSSA (Leshchinsky et al., 2016), were used in this study. The shear strength reduction technique was adopted in the software FLAC2D to solve for a factor of safety suitable to assess the stability of slopes, which is compared with that from ReSSA.

7.6.2 GEOMETRY

Figure 7.6.1 shows the geometry of the model used in this study. The wall was 3 m (10 ft) high (H = 3 m (10 ft)) with 15 layers of CMU facing blocks. Each CMU facing block was 0.2 m (8 in) high and 0.2 m (8 in) wide. To eliminate the effect of boundary conditions, the foundation soil had a depth of 3 m (10 ft) (1H) and the right lateral boundary was located at 15 m (50 ft) (5H) behind the wall facing. The left boundary was located 3 m (10 ft) (1H) in front of the wall facing. Lateral boundaries were fixed in the horizontal direction and were free to move in the vertical direction while the bottom boundary was fixed in both horizontal and vertical directions. The primary reinforcement length was 4.9 m (16 ft), which was the same as that used in the baseline model of the parametric study of the VDOT wall discussesd in Section 7.4.5.1. Two values of reinforcement vertical spacing S_v, 0.2 m (8 in) and 0.6 m (24 in or 2 ft), were considered in the stability analysis to investigate the effect of reinforcement spacing on the stability of the structure. A 0.6 m (2 ft) wide footing was applied on top of the wall to simulate the bridge slab. The width of the footing was kept the same as the beam seat width b used in the baseline model of the parametric study of the VDOT wall. The offset of the footing to the back of the wall facing was set as 0.2 m (8 in), which is the same as the setback distance a_b used in the baseline model of the parametric study of the VDOT wall. Bearing reinforcement layers (i.e., secondary reinforcement) were used below the footing to carry the large concentrated load from the bridge slab and the traffic load. Bearing reinforcement layers were not connected to the facing blocks. The length of the bearing reinforcement layers was 1.6 m (5 ft)), which was the same as that used in the baseline model of the parametric study of the VDOT wall. The bearing reinforcement spacing was half of the spacing between primary reinforcement.

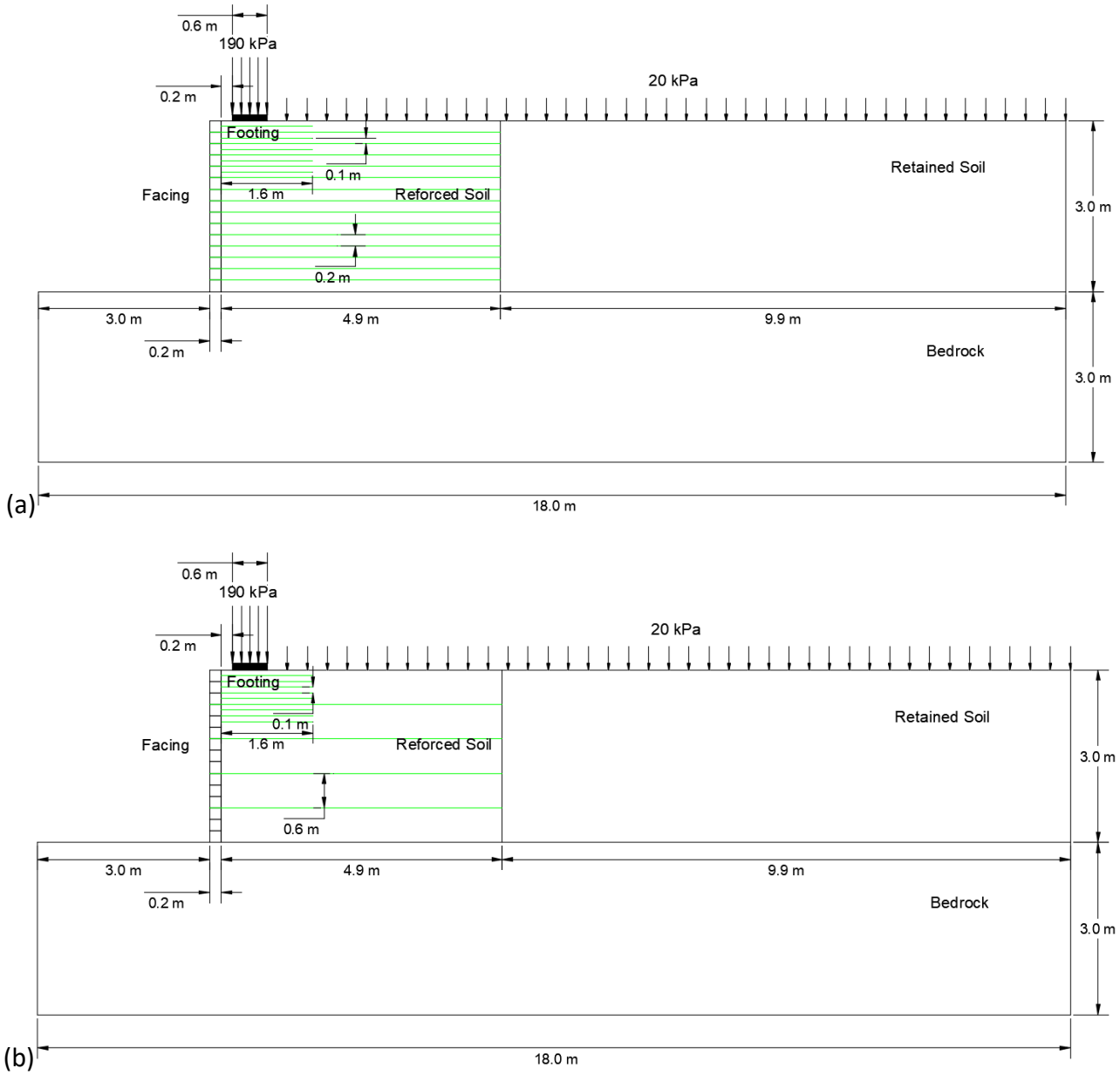

Fig. 7.6.1: Geometry of limit equilibrium and numerical analysis: (a) Reinforcement vertical spacing S_v = 0.2 m (8 in); (b) Reinforcement vertical spacing S_v = 0.6 m (24 in or 2 ft);

7.6.3 MATERIAL AND INTERFACE PROPERTIES

Since the stability analysis aimed to investigate the behavior of the structure under a limit state (i.e., verge of failure), it depends mainly on the failure criterion (i.e., Mohr-Coulomb strength parameters). In other words, the analyses are insensitive to the selected elastic parameters, Young's modulus and Poisson's ratio. Table 7.6.1 summarizes the material properties used in the analysis. Both beam and cable structural elements were used in the numerical model to simulate

the geotextile reinforcement. Horizontal geotextile layers between CMU facing blocks were modeled using beam structural elements with zero moment of inertia while horizontal geotextile layers embedded in backfill soil were modeled using cable structural elements. The elastic modulus of the structural elements is not important to stability analysis under a limit state while their yield strength is important to the analysis. Table 7.6.1 also shows the properties of structural elements used to simulate the geotextile reinforcement.

Table 7.6.1: Material properties

Materials	Properties
Facing	$\rho = 1230\,\text{kg/m}^3$, $\varphi = 0$, $c = 10\,\text{MPa}$
Reinforced soil	$\rho = 1650\ \text{kg/m}^3$, $\varphi = 38°$, $c = 0$
Retained soil	$\rho = 1750\ \text{kg/m}^3$, $\varphi = 30°$, $c = 20\ \text{kPa}$
Reinforcement	$T_f = 5.36$ kN/m for S_v = 0.2 m; $T_f = 16.66$ kN/m for S_v = 0.6 m
Bedrock	$\rho = 2000\ \text{kg/m}^3$ (Elastic model)

Different types of interfaces were used in the numerical simulations, as shown in Fig. 7.6.2. They were represented by the interface elements available in the software package, which are linearly-elastic perfectly-plastic springs with the Mohr-Coulomb failure criterion. For the properties of interfaces between backfill soil and geotextile reinforcement, an interaction coefficient C_i of 0.9 and zero cohesion were used. For the vertical interface between backfill soil and CMU facing blocks, zero friction angle and zero cohesion were used in the numerical simulations to compare the results calculated using FLAC with those obtained using ReSSA. For the interface between geotextile and CMU blocks, Awad & Tanyu (2014) conducted both direct shear tests and pullout tests to investigate the connection strength between geotextile and facing blocks. Based on their results, a friction angle δ of 16.2° and a cohesion of 9.5 kPa (1.4 psi) were assigned to the interface between CMU blocks and geotextile. When the reinforcement spacing S_v was 0.6 m (24 in or 2 ft), two CMU facing blocks were connected with each other without the geotextile reinforcement in between. In other words, interfaces between CMU facing blocks were considered. Based on the recommendation by Eurocode2 (British Standards Institution, 2004), a friction coefficient of 0.6 was assigned to the interface between CMU facing blocks in the numerical analysis. In other words, the interface friction angle between CMU blocks was equal to $\delta = \arctan(0.6) = 31.0°$. Table 7.6.2 summarizes the interface properties used in the analysis.

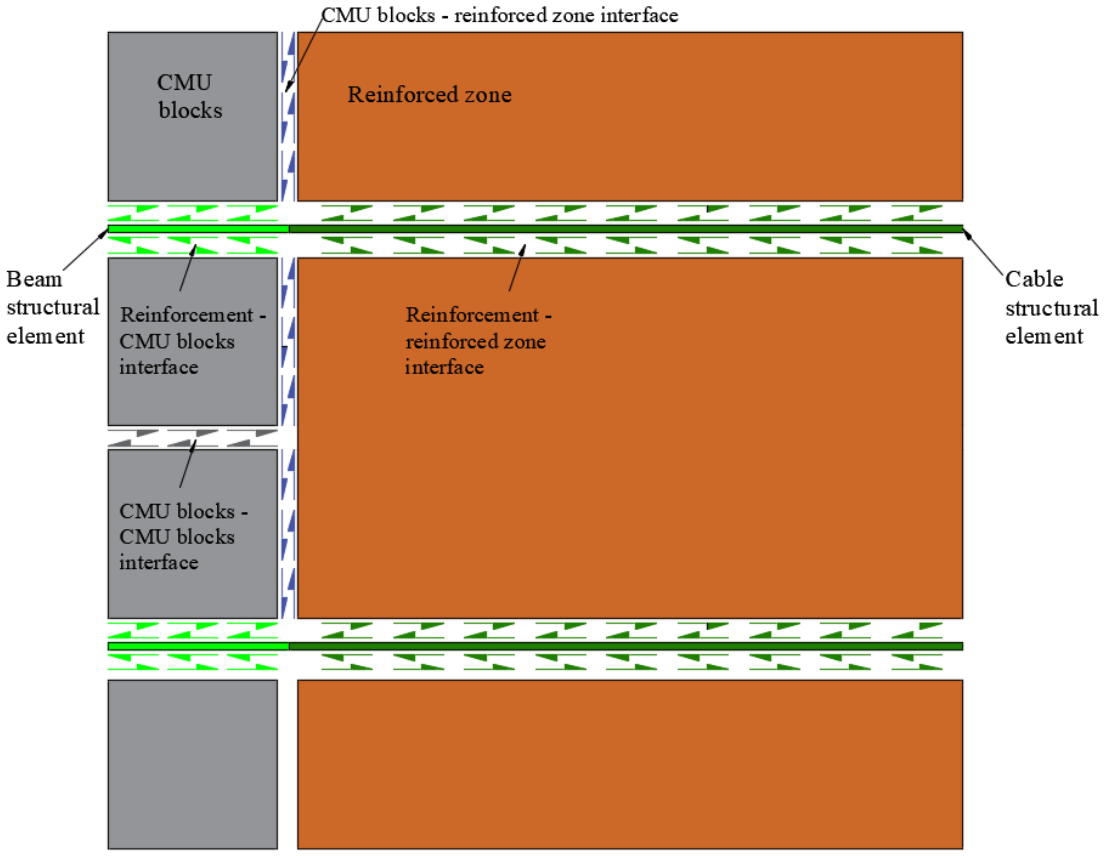

Fig. 7.6.2: Interfaces used in the numerical analysis

Table 7.6.2: Interface properties

Interfaces	Properties
Reinforcement – Reinforced Zone	$\varphi = 35.11°,\ c = 0\ \ (C_i = 0.9)$
CMU Blocks – Reinforced Zone	$\varphi = 0,\ c = 0$
Reinforcement - CMU Blocks	$\varphi = 16.2°,\ c = 9.5$ kPa
CMU Blocks – CMU Blocks	$\varphi = 30.96°,\ c = 0\ \ (\mu = 0.6)$

7.6.4 CONSTRUCTION SEQUENCE AND TRAFFIC LOAD

Construction was simulated in the numerical simulations. Before the wall construction, the bedrock reached an equilibrium under gravity. A layer of the CMU facing block, the backfill soil, the retained soil, and the geotextile reinforcement were installed until the designed wall height was reached. Corresponding interfaces and connection were assigned. No compaction stress was applied on top of the backfill soil. After the construction of the wall was finished, a footing was placed on top of the wall. Different traffic loads were then applied on top of the footing and the

wall behind the footing as shown in Fig. 7.6.1. A uniform vertical stress of 190 kPa (3968 psf) was applied on top of the footing to represent the self-weight of the bridge slab the traffic load applied on top of the bridge span. A uniform stress of 20 kPa (418 psf) was applied on top of the wall behind the footing to represent the self-weight of the approach way and the traffic load applied on the approach way.

In the numerical model, the required strength of the reinforcement T_f was determined in FLAC until the computed factor of safety of the whole system reached 1.0. When the factor of safety was 1.0, the system was at the verge of failure, which corresponded to the state of limit equilibrium. The responses of the system in FLAC under the factor of safety of 1.0 (i.e., the slip surface and the tensile force in the reinforcement) were then compared to the results calculated using ReSSA with the same material and interface properties.

7.6.5 RESULTS AND DISCUSSION

7.6.5.1 CRITICAL SLIP SURFACE

7.6.5.1.1 Reinforcement vertical spacing S_v = 0.2 m (8 in)

Figure 7.6.3 and Fig. 7.6.4 show the critical and potential slip surfaces predicted by FLAC and ReSSA for the case of reinforcement spacing S_v = 0.2 m (8 in). Both FLAC and ReSSA found that the critical slip surface started from the right of the footing and extended to the wall toe. In the numerical model, the critical slip surface started from the toe and followed the Rankine slip plane (the dashed line) up to approximately 2/3 wall height and then extended almost vertically to the right edge of the footing. In ReSSA, the shape of the critical slip surface was an arc starting from the wall toe and extending to the right edge of the footing. Both FLAC and ReSSA gave similar shapes of the slip surfaces.

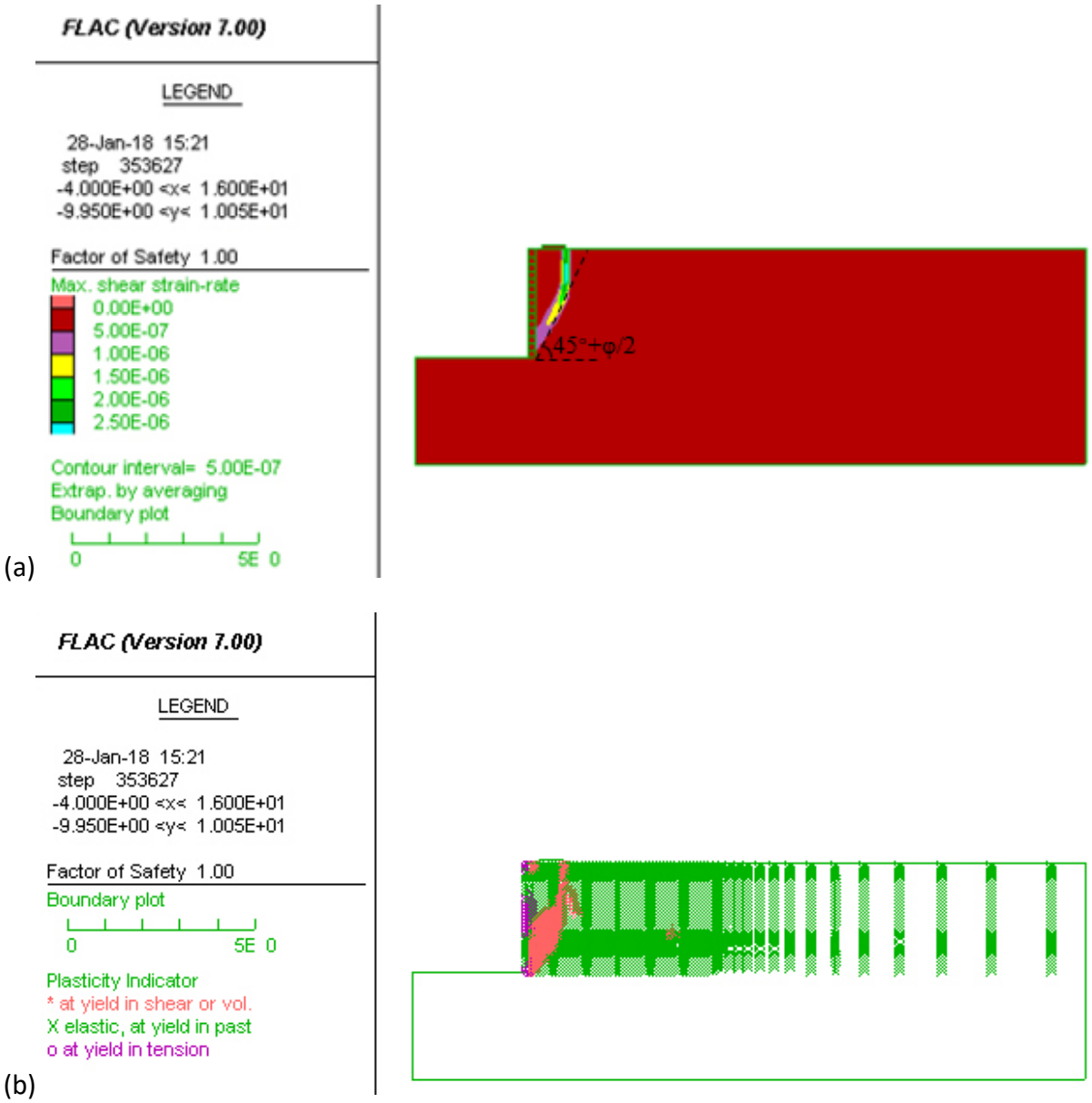

Fig. 7.6.3: Critical and potential slip surfaces predicted by FLAC for the case with reinforcement spacing S_v = 0.2 m (8 in): (a) Max shear strain rate; (b) Plasticity zone.

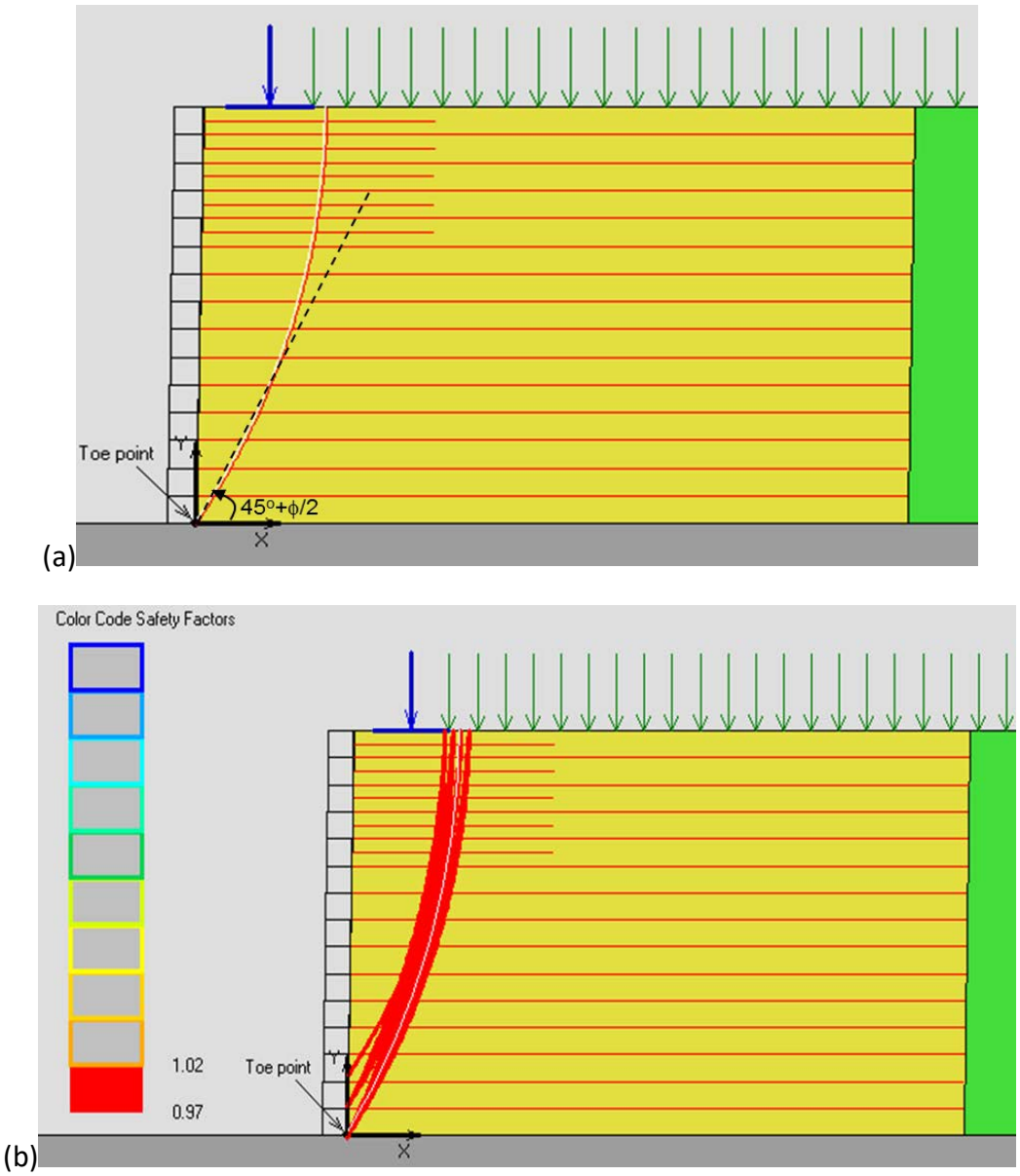

Fig. 7.6.4: Critical and potential slip surfaces predicted by ReSSA for the case with reinforcement spacing S_v = 0.2 m (8 in): (a) Critical slip surface corresponding to the factor of safety of 1.0; (b) Safety map by ReSSA.

7.6.5.1.2 Reinforcement vertical spacing S_v = 0.6 m (24 in or 2 ft)

Figure 7.6.5 and Fig. 7.6.6 show the critical and potential slip surfaces predicted by FLAC and ReSSA for the case with reinforcement spacing S_v = 0.6 m (24 in or 2 ft). The critical slip surface as shown in Fig. 7.6.6 (a) predicted by ReSSA for the case with large reinforcement spacing was similar to the case with small spacing as shown in Fig. 7.6.4 (a). The slip surface started from the wall toe and extended to the right of the footing. However, the shape of the critical slip surface predicted by FLAC as shown in Fig. 7.6.5 was different. It started from the wall toe and the slope

of the critical slip surface was a comparatively flatter than the Rankine slip plane (the dashed line). The critical slip surface extended to the end of bearing reinforcement layers, which was 1.6 m (5.2 ft) away from back of CMU facing blocks. Local failure also happened in the reinforced zone behind the bearing reinforcement layers. The plasticity zone shown in Fig. 7.6.5 also confirmed the shape of critical slip surface by indicating the locations of backfill soil at yield in shear or volume.

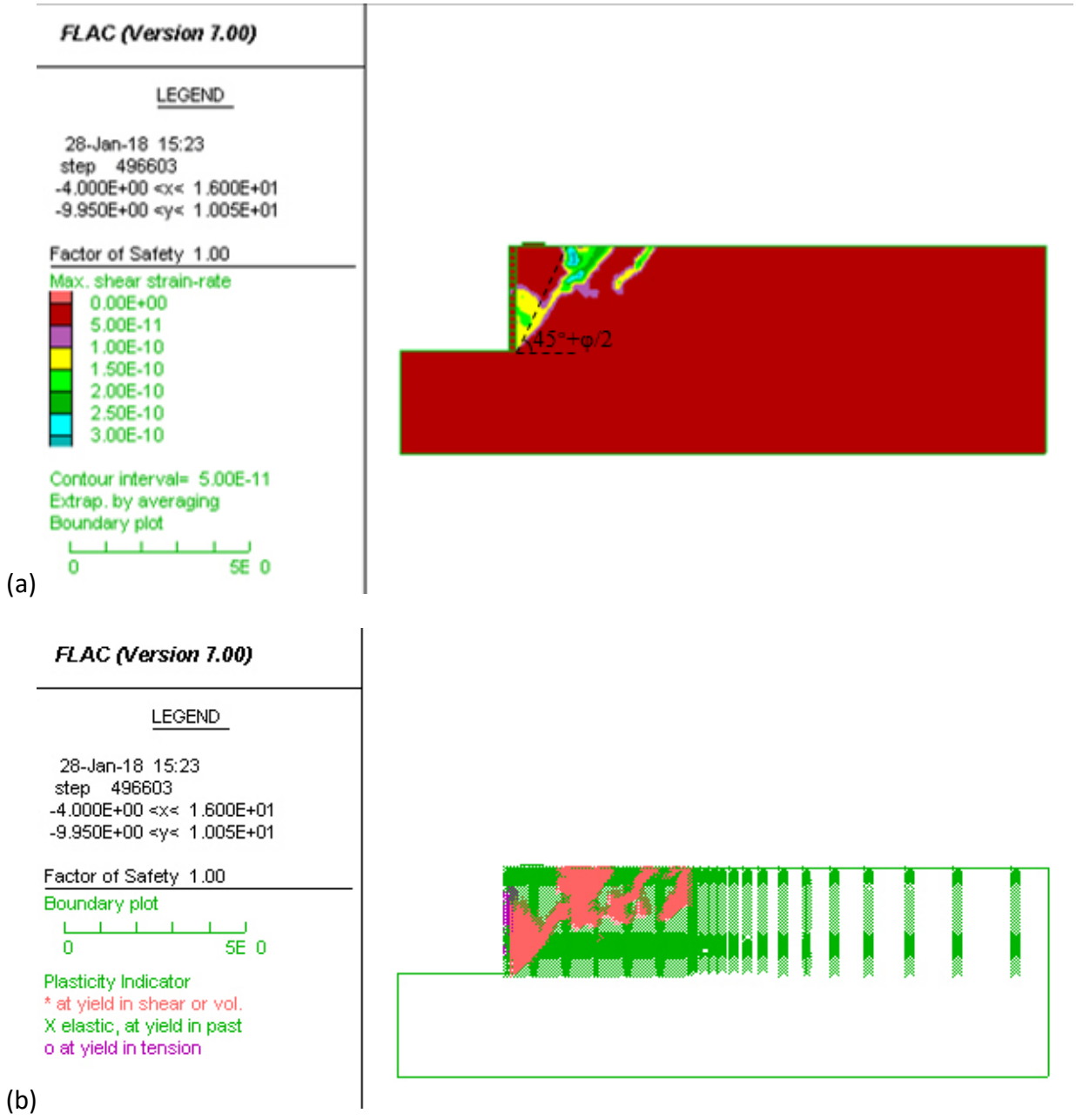

Fig. 7.6.5: Critical and potential slip surfaces predicted by FLAC for the case with reinforcement spacing S_v = 0.6 m (24 in or 2 ft): (a) Max shear strain rate; (b) Plasticity zone.

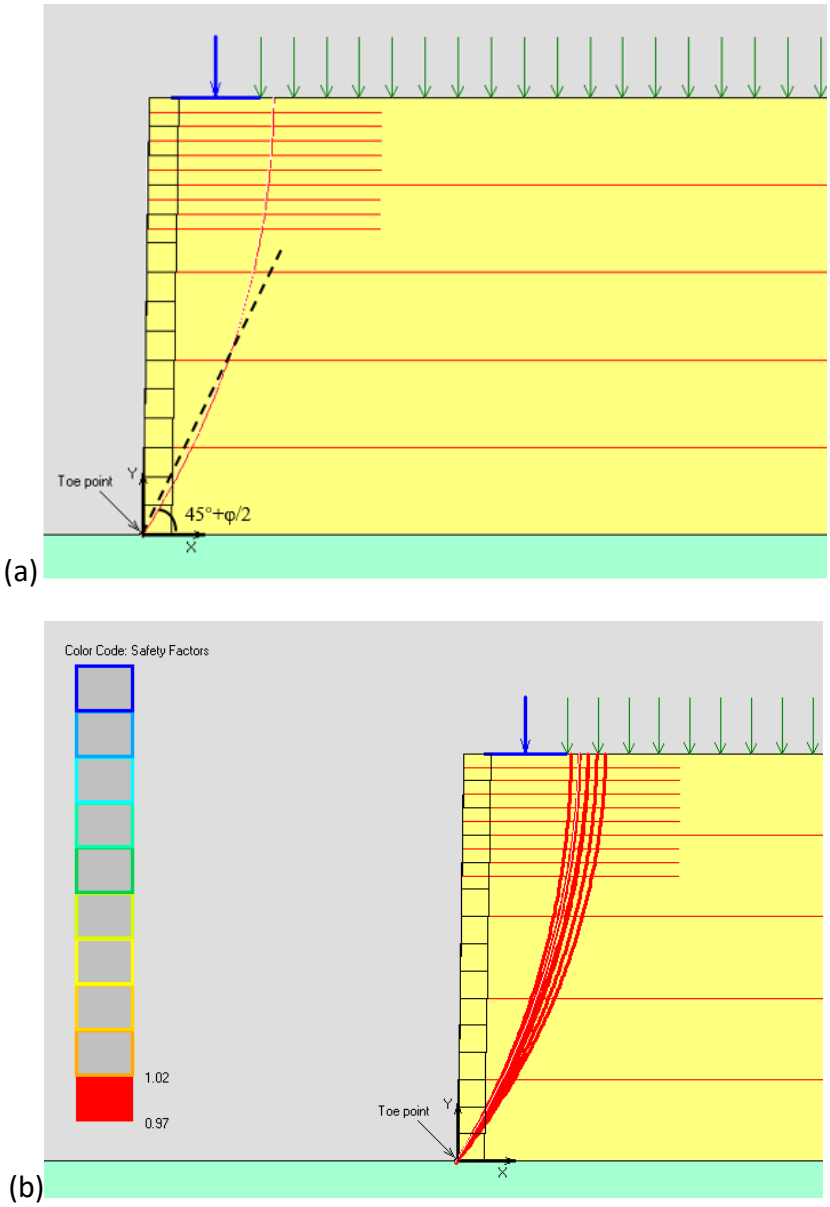

Fig. 7.6.6: Critical and potential slip surfaces predicted by ReSSA for the case with reinforcement spacing S_v = 0.6 m (24 in or 2 ft): (a) Critical slip surface corresponding to the factor of safety of 1.0; (b) Safety map by ReSSA.

7.6.5.2 REINFORCEMENT TENSION

7.6.5.2.1 Reinforcement vertical spacing Sv = 0.2 m (8 in)

Figure 7.6.7 shows the distribution of the reinforcement tension predicted by FLAC for the case with reinforcement spacing S_v = 0.2 m (8 in). The required strength of the reinforcement T_f for the numerical model to reach the factor of safety of 1.0 was 5.36 kN/m (367 lb/ft) (as shown in Table 7.6.1) for the case of reinforcement spacing S_v = 0.2 m (8 in). Figure 7.6.7 (a) shows that

the required strength of the reinforcement T_f was mobilized in both the primary reinforcement and bearing reinforcement layers except for the bottom one. The distribution of the maximum tension in the reinforcement along depth was uniform. Both Fig. 7.6.7 (b) and (c) show that the connection force T_0 in the reinforcement was close to the maximum tension T_{max} in the reinforcement except for the primary reinforcement at the top of the wall, indicating that the maximum tension in the reinforcement happened near the facing connection.

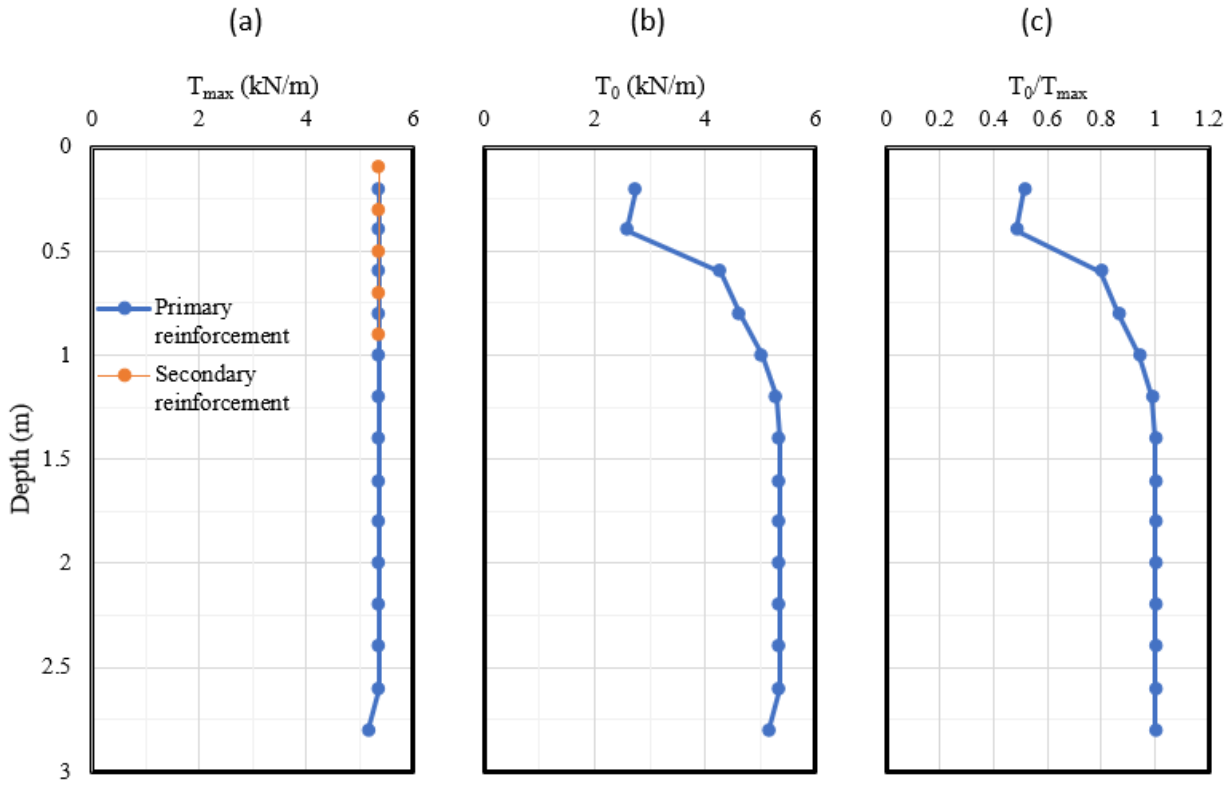

Fig. 7.6.7: Distribution of reinforcement tension along depth predicted by FLAC for the case with reinforcement spacing S_v = 0.2 m (8 in): (a) Maximum reinforcement tension T_{max}; (b) Connection force in the reinforcement T_0; (c) The ratio of connection force to the maximum tension in the reinforcement T_0/T_{max}.

Figure 7.6.8 shows the distributions of tension in the reinforcement predicted by FLAC for the case with reinforcement spacing S_v = 0.2 m (8 in). It also shows the location of the maximum tensile force T_{max} in the reinforcement corresponded to the critical slip surface as shown in Fig. 7.6.3.

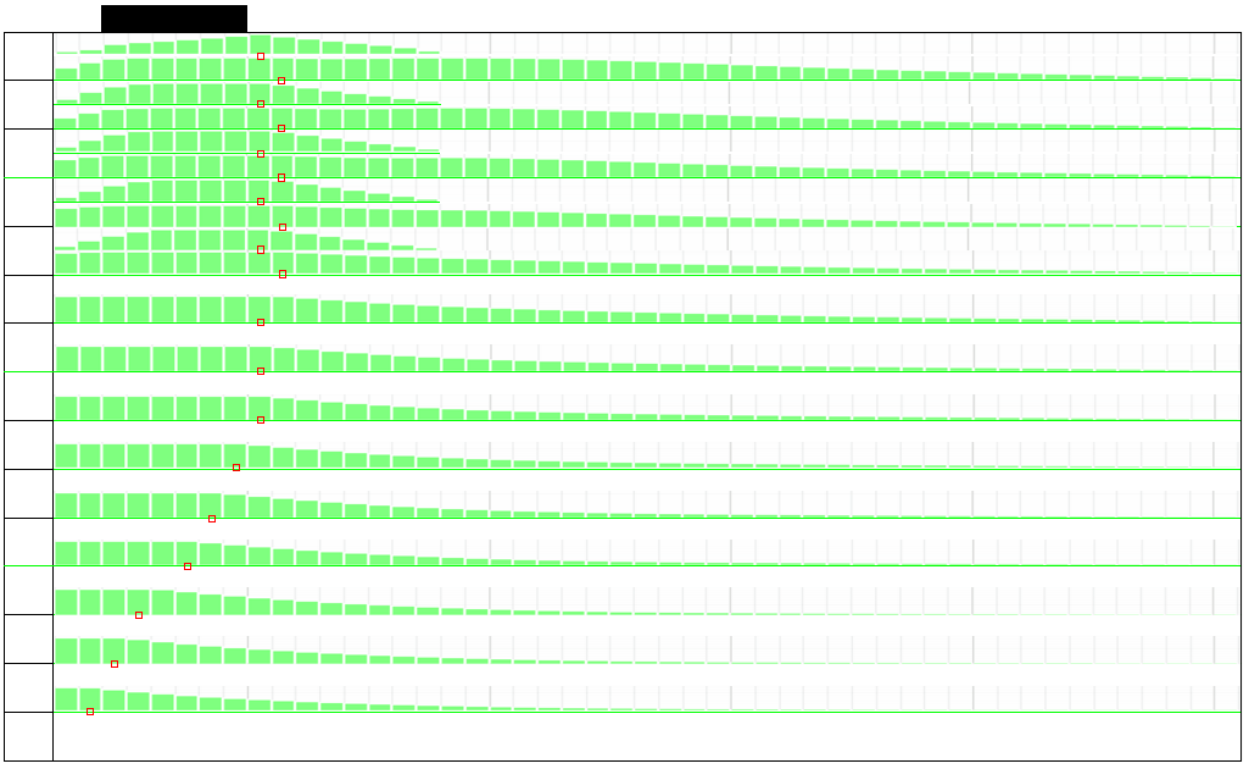

Fig. 7.6.8: Distributions of tension in the reinforcement predicted by FLAC for the case with reinforcement spacing S_v *= 0.2 m (8 in).*

Figure 7.6.9 shows the distributions of tension in the primary reinforcement at four depths predicted by FLAC for the case with reinforcement spacing S_v = 0.2 m (8 in). Figure 7.6.9 shows that the maximum reinforcement tension T_{max} developed near the wall facing and under the footing. The primary reinforcement was long enough so that no pullout failure occurred at back. The location of T_{max} in the reinforcement corresponded to the critical slip surface as shown in Fig. 7.6.3. Figure 7.6.10 shows the distribution of tension in the bearing reinforcement layers predicted by FLAC for the case with reinforcement spacing S_v = 0.2 m (8 in). Bearing reinforcement layers means the short (1.6 m) secondary reinforcement layers which were not connected to the facing blocks. In Section 7.6.2, there was a detailed introduction of bearing reinforcement layers. Figure 7.6.10 shows that the maximum tension in the bearing reinforcement layers happened under the footing except that T_{max} happened to the right of the footing for the top layer. Linear decrease of the tension happened at both the front and rear ends of the bearing reinforcement layers, indicating that pullout was mobilized from both ends.

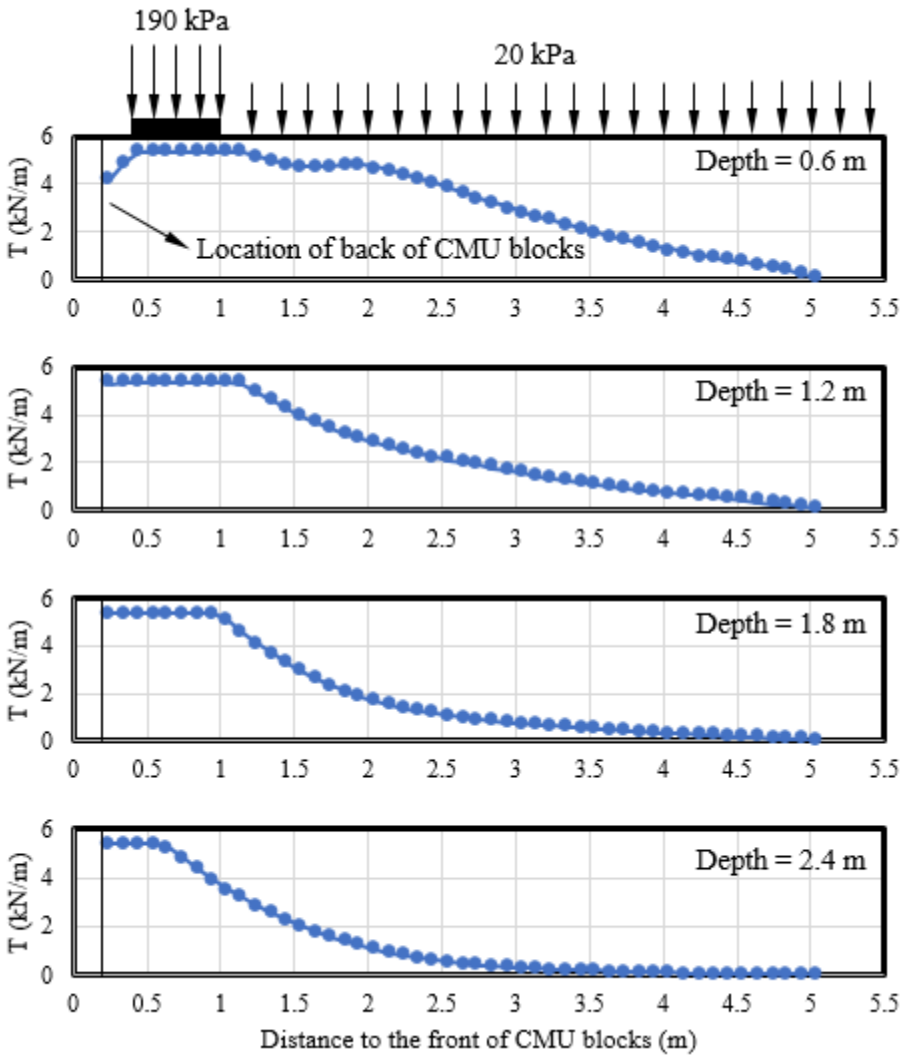

Fig. 7.6.9: Distributions of tension in the primary reinforcement at four depths predicted by FLAC for the case with reinforcement spacing S_v = 0.2 m (8 in)

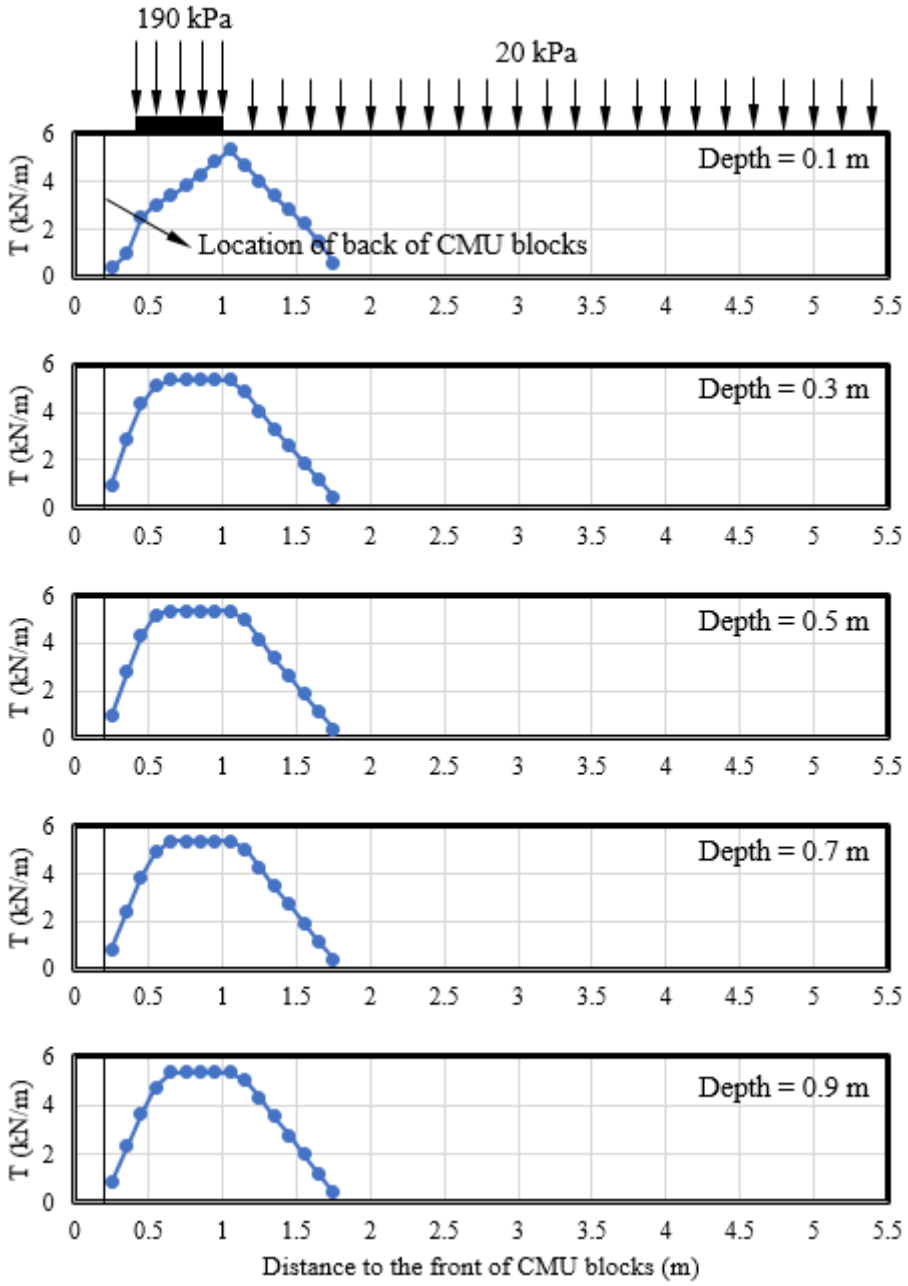

Fig. 7.6.10: Distributions of tension in the bearing reinforcement layers predicted by FLAC for the case with reinforcement spacing S_v = 0.2 m (8 in)

Figure 7.6.11 shows the distribution of the tension in the reinforcement along depth predicted by ReSSA for the case with reinforcement spacing S_v = 0.2 m (8 in). The required strength of the reinforcement T_f in ReSSA to reach the factor of safety of 1.0 was 6.3 kN/m (432 lb/ft), which was larger than T_f = 5.36 kN/m (367 lb/ft) predicted in the FLAC simulation. Figure 7.6.11 shows that that the required strength of the reinforcement T_f was mobilized in both the primary reinforcement and bearing reinforcement layers, which was also observed in the numerical

simulation conducted using FLAC as shown in Fig. 7.6.7. However, the connection force T_0 in the reinforcement in ReSSA was significantly smaller than T_{max}, which differs from the distribution of the connection forces predicted by FLAC. The small connection forces predicted by ReSSA may explain that the required strength of the reinforcement T_f predicted using ReSSA was larger than that predicted using FLAC.

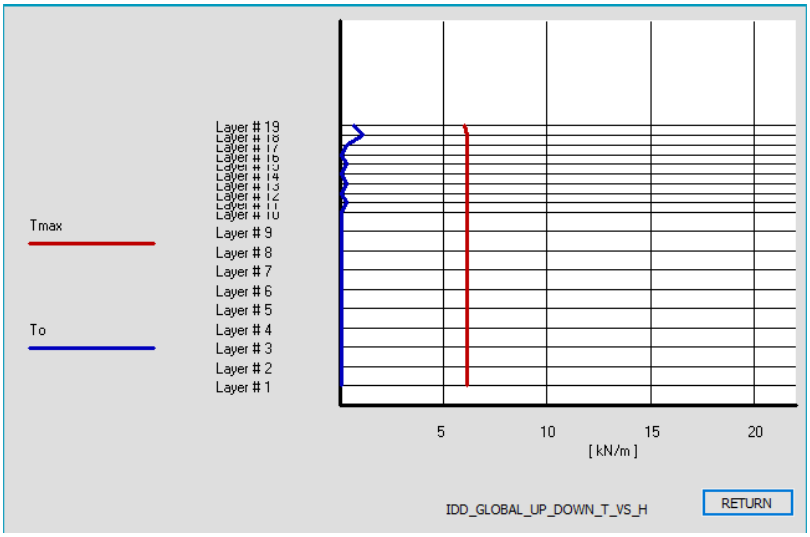

Fig. 7.6.11: Distribution of reinforcement tension along depth predicted by ReSSA for the case with reinforcement spacing S_v = 0.2 m (8 in)

Figure 7.6.12 shows the distribution of the reinforcement tension predicted by ReSSA for the case with reinforcement spacing S_v = 0.2 m (8 in). It also shows the location of the maximum tensile force T_{max} in the reinforcement corresponded to the critical slip surface as shown in Fig. 7.6.4.

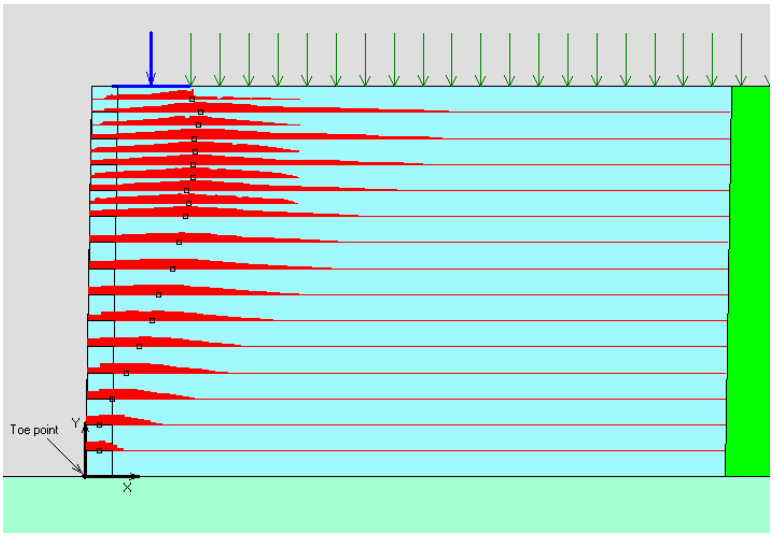

Fig. 7.6.12: Distribution of reninforcement tension and location of T_{max} predicted by ReSSA for the case with reinforcement spacing S_v = 0.2 m (8 in)

Figure 7.6.13 provides the information of the tension in all reinforcement layers predicted by ReSSA for the case with reinforcement spacing S_v = 0.2 m (8 in). Figure 7.6.13 shows that pullout resistance was reached in the bearing reinforcement layers at the rear end (Layers 11, 13, 15, 17, and 19), which was also observed in the numerical simulations conducted using FLAC as shown in Fig. 7.6.10.

Layer No.	Height from Toe	T-required			To (front end)	To/T max	T max affected by rear end pullout	Coverage Ratio, Rc	Interblock	
		T max	X	Theta		[%]			Rv	Rh
	[m]	[kN/m]	[m]	[degrees]	[kN/m]				[kN/m]	[kN/m]
1	0.20	6.14	0.10	-57.0	0.10	2	No	1.00	6.47	3.89
2	0.40	6.14	0.10	-55.0	0.10	2	No	1.00	6.08	3.67
3	0.60	6.14	0.21	-55.0	0.10	2	No	1.00	5.70	3.56
4	0.80	6.14	0.31	-55.0	0.10	2	No	1.00	5.31	3.44
5	1.00	6.14	0.41	-55.0	0.10	2	No	1.00	4.91	3.33
6	1.20	6.14	0.51	-55.0	0.10	2	No	1.00	4.50	3.21
7	1.40	6.14	0.56	-55.0	0.10	2	No	1.00	4.09	3.09
8	1.60	6.14	0.66	-55.0	0.10	2	No	1.00	3.67	2.97
9	1.80	6.14	0.72	-55.0	0.10	2	No	1.00	3.24	2.84
10	2.00	6.14	0.77	-55.0	0.10	2	No	1.00	2.80	2.71
11	2.10	6.14	0.79	-55.0	0.30	5	Yes	1.00	2.35	2.58
12	2.20	6.14	0.77	-55.0	0.10	2	No	1.00	2.12	2.52
13	2.30	6.14	0.82	-55.0	0.30	5	Yes	1.00	1.89	2.45
14	2.40	6.14	0.82	-55.0	0.10	2	No	1.00	1.66	2.38
15	2.50	6.14	0.84	-55.0	0.30	5	Yes	1.00	1.43	2.32
16	2.60	6.14	0.83	-55.0	0.10	2	No	1.00	1.19	2.25
17	2.70	6.14	0.86	-55.0	0.30	5	Yes	1.00	0.96	2.18
18	2.80	6.14	0.88	-55.0	1.10	18	No	1.00	0.72	2.11
19	2.90	6.04	0.82	-52.0	0.70	12	Yes	1.00	0.48	2.04

Fig. 7.6.13: Output of reinforcement tension from ReSSA for the case with reinforcement spacing S_v = 0.2 m (8 in)

7.6.5.2.2 Reinforcement vertical spacing Sv = 0.6 m (24 in or 2 ft)

Figure 7.6.14 shows the distribution of reinforcement tension predicted by FLAC for the case with reinforcement spacing S_v = 0.6 m (24 in or 2 ft). The required strength of the reinforcement T_f for the numerical model to reach the factor of safety of 1.0 was 16.66 kN/m (1142 lb/ft) (as shown in Table 7.6.1) for the case of reinforcement spacing S_v = 0.6 m (24 in or 2 ft). Figure 7.6.14 (a) shows that the required strength of the reinforcement T_f was mobilized in the primary reinforcement only but not in the bearing reinforcement layers. The distribution of the maximum reinforcement tension along depth was not uniform. Both Fig. 7.6.14 (b) and (c) show that the connection force T_0 in the reinforcement was significantly smaller than the maximum tension T_{max} in the reinforcement, which is a different trend than that shown in the case with reinforcement spacing S_v = 0.2 m (8 in).

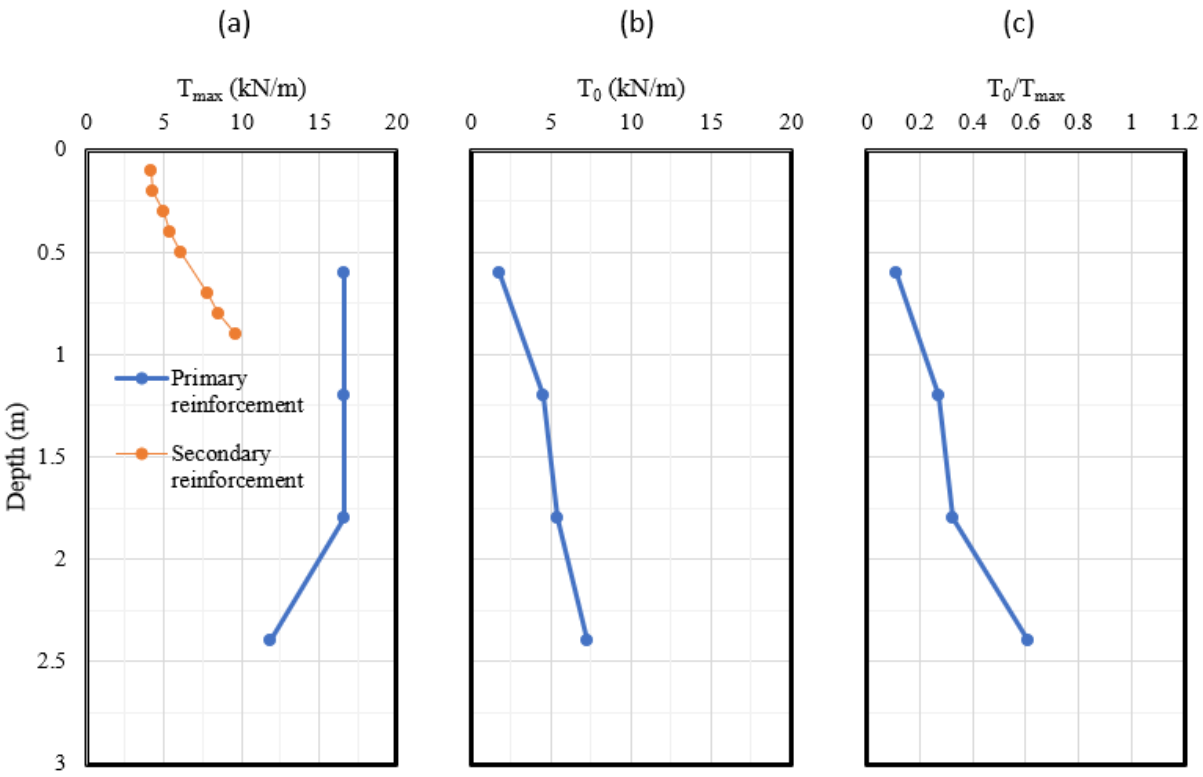

Fig. 7.6.14: Distribution of reinforcement tension along depth predicted by FLAC for the case with reinforcement spacing S_v = 0.6 m (24 in or 2 ft): (a) Maximum reinforcement tension T_{max}; (b) Connection force in the reinforcement T_0; (c) The ratio of connection force to the maximum tension in the reinforcement T_0/T_{max}.

Figure 7.6.15 shows the distributions of tension in the reinforcement predicted by FLAC for the case with reinforcement spacing S_v = 0.6 m (24 in or 2 ft). It also shows the location of the maximum tensile force T_{max} in the reinforcement corresponded to the critical slip surface as shown in Fig. 7.6.5.

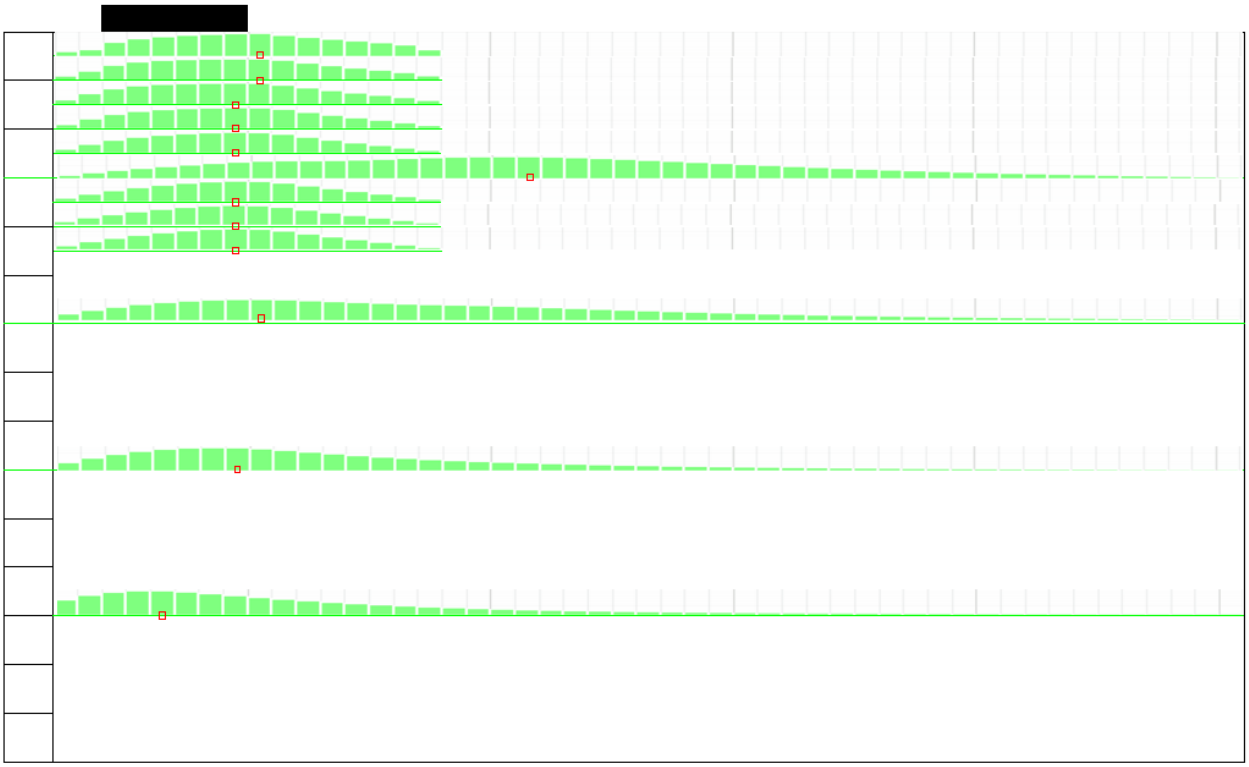

Fig. 7.6.15: Distributions of tension in the reinforcement predicted by FLAC for the case with reinforcement spacing S_v *= 0.6 m (24 in or 2 ft).*

Figure 7.6.16 shows the distributions of tension in the primary reinforcement at four depths predicted by FLAC for the case with reinforcement spacing S_v = 0.6 m (24 in or 2 ft). Figure 7.6.16 shows that the maximum tension T_{max} in the reinforcement happened under the footing except for the top layer. T_{max} happened near the end of bearing reinforcement layers for the top primary reinforcement layer, which corresponded to the location of critical slip surface as shown in Fig. 7.6.5. The primary reinforcement was long enough to prevent the pullout from happening at the rear end. However, linear decrease of the tension near the front of the primary reinforcement indicates that pullout happened from the front (i.e., pullout near facing).

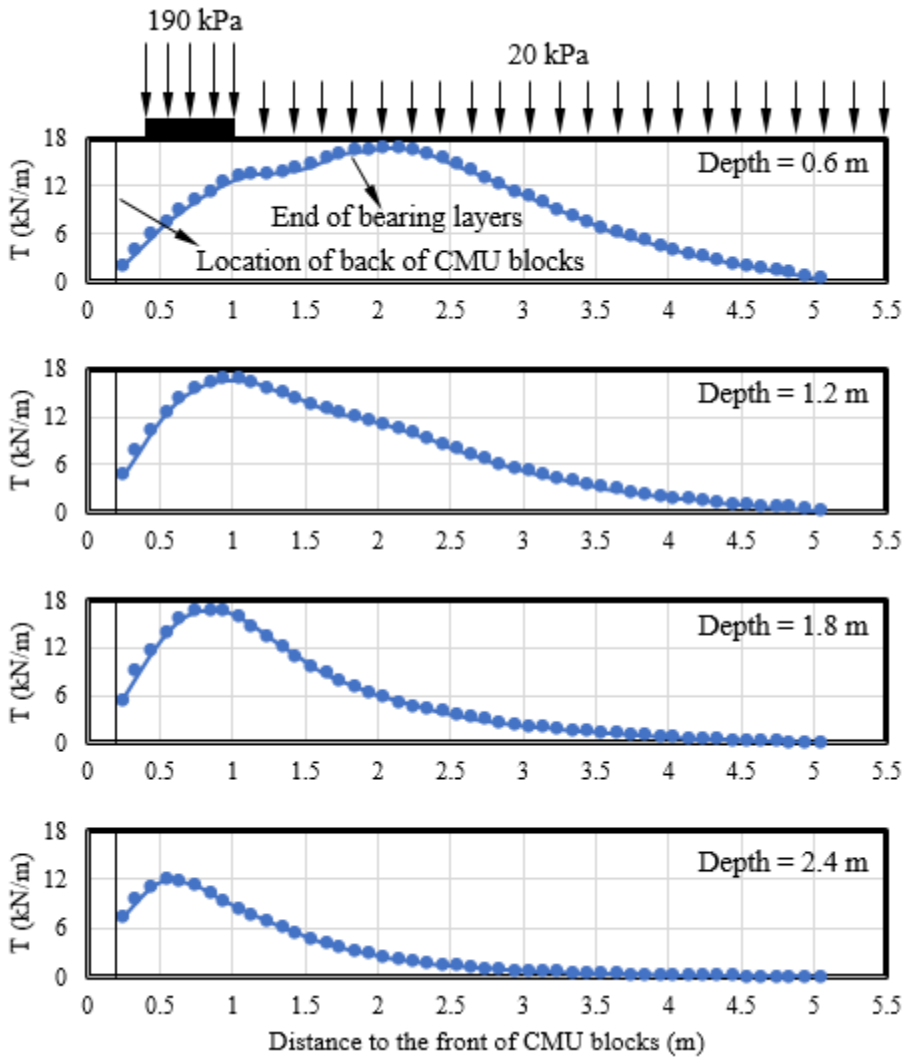

Fig. 7.6.16: Distributions of tension in the primary reinforcement at four depths predicted by FLAC for the case with reinforcement spacing S_v = 0.6 m (24 in or 2 ft)

Figure 7.6.17 shows the distributions of tension in the bearing reinforcement layers predicted by FLAC for the case with reinforcement spacing S_v = 0.6 m (24 in or 2 ft). Figure 7.6.17 shows that the maximum tension in the bearing reinforcement layers happened near the right edge of the footing (i.e., 1.0 m (3.3 ft) from front of CMU facing blocks). Linear decrease of the tension happened at both the front and rear ends of the bearing reinforcement layers, indicating that pullout happened from both ends.

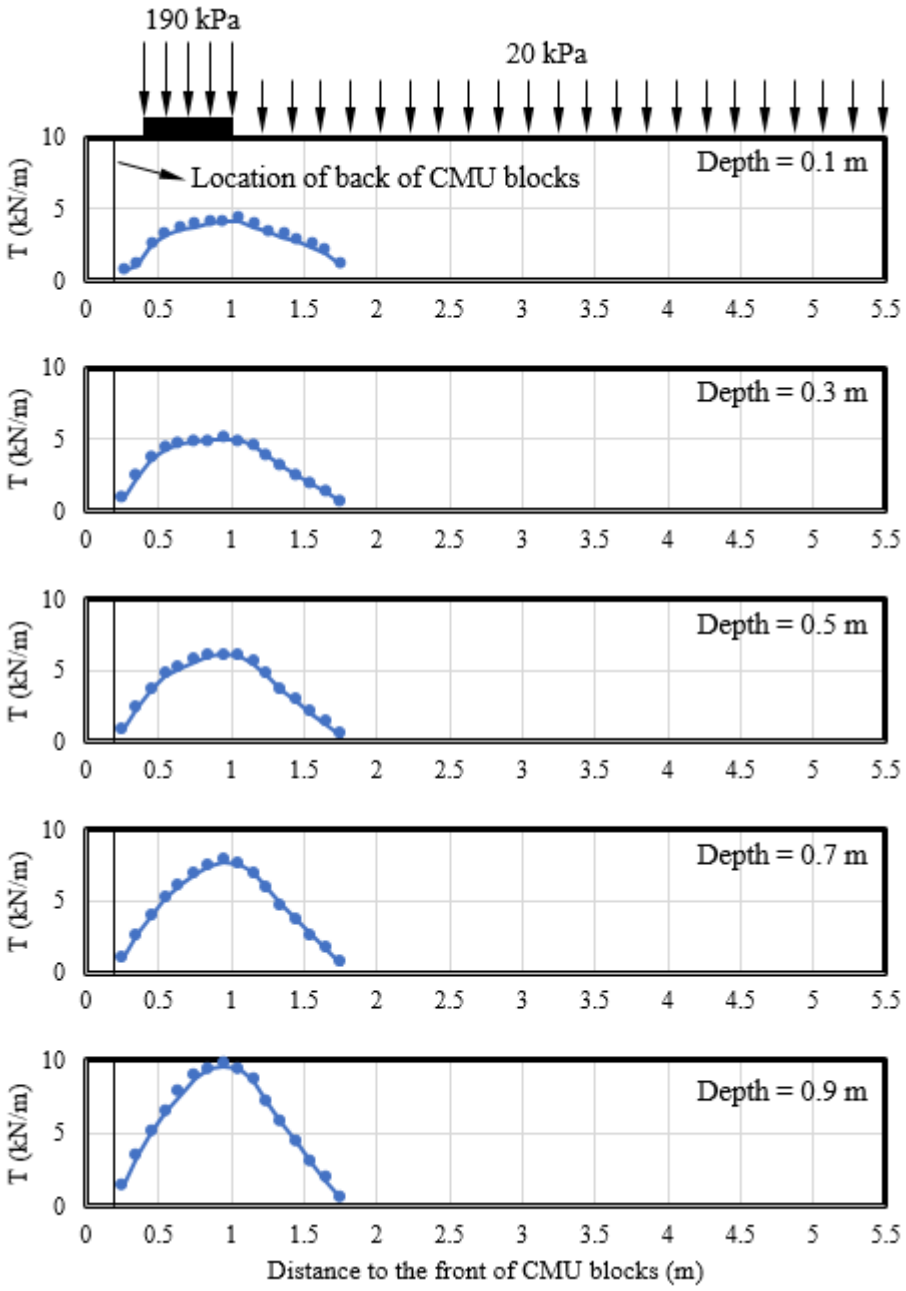

Fig. 7.6.17: Distributions of tension in the bearing reinforcement layers predicted by FLAC for the case with reinforcement spacing S_v = 0.6 m (24 in or 2 ft)

Figure 7.6.18 shows the distribution of reinforcement tension along depth predicted by ReSSA for the case with reinforcement spacing S_v = 0.6 m (24 in or 2 ft). The required strength of the reinforcement T_f in ReSSA to reach the factor of safety of 1.0 was 14.7 kN/m (1007 lb/ft), which was smaller than the T_f = 16.66 kN/m (1142 lb/ft) in FLAC. Figure 7.6.18 shows that the required strength of the reinforcement T_f was mobilized in only the primary reinforcement but not in bearing reinforcement layers, which was also observed in the numerical model in FLAC. The

connection force T_0 in the reinforcement was much smaller than the maximum tension T_{max} in the reinforcement, which is also consistent with the results from FLAC.

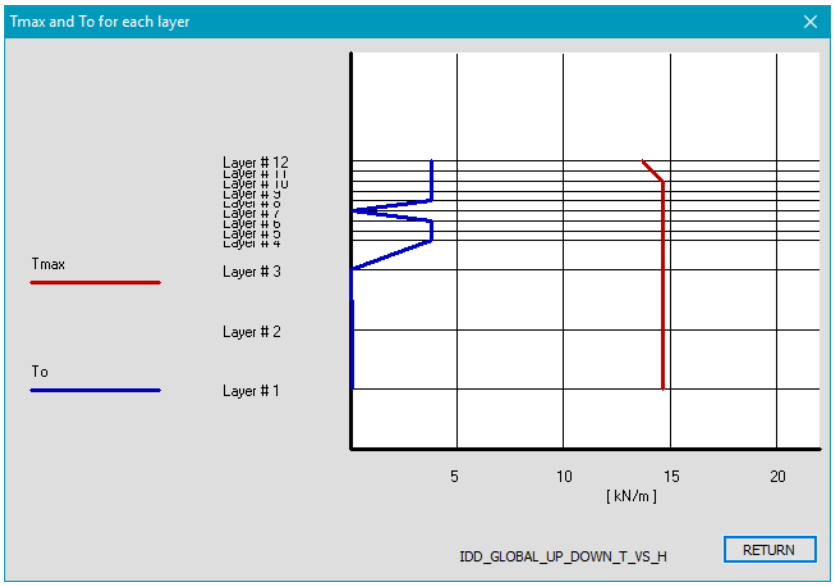

Fig. 7.6.18: Distribution of reinforcement tension along depth predicted by ReSSA for the case with reinforcement spacing S_v = 0.6 m (24 in or 2 ft)

Figure 7.6.19 shows the distribution of the tensile forces in the reinforcement predicted by ReSSA for the case with reinforcement spacing S_v = 0.6 m (24 in or 2 ft). Figure 7.6.19 also shows the location of the maximum tension T_{max} in the reinforcement corresponded to the critical slip surface as shown in Fig. 7.6.6. Note that in ReSSA the increase in vertical stress due to strip footing surcharge is based on a 2:1 pyramid stress distribution, as recommended by AASHTO. Fig. 7.6.19 reflects the impact of this distribution as seen in the locus of T_{max} as well as in the distribution of load in the reinforcements.

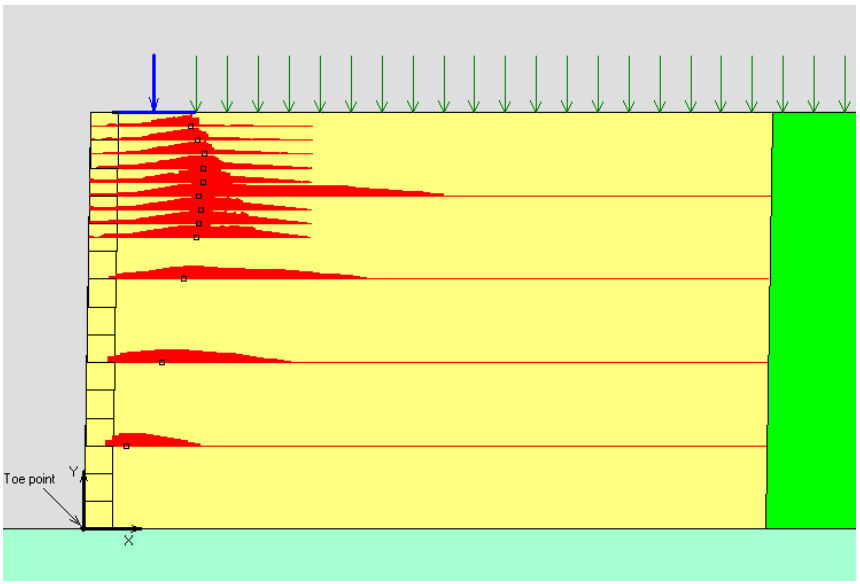

Fig. 7.6.19: Distribution of reninforcement tension and location of T_{max} predicted by ReSSA for the case with reinforcement spacing S_v = 0.6 m (24 in or 2 ft)

Figure 7.6.20 contains all the information of reinforcement tension from ReSSA for the case with reinforcement spacing S_v = 0.6 m (24 in or 2 ft). Figure 7.6.20 shows that pullout happened in the bearing reinforcement layers at the rear end (Layers 4 to 6 and Layers 8 to 12), which was also observed in the numerical model in FLAC as shown in Fig. 7.6.17.

Layer No.	Height from Toe	T-required			To (front end)	To/T max	T max affected by rear end pullout	Coverage Ratio, Rc	Interblock	
		T max	X	Theta		[%]			Rv	Rh
	[m]	[kN/m]	[m]	[degrees]	[kN/m]				[kN/m]	[kN/m]
1	0.60	14.67	0.30	-57.0	0.10	1	No	1.00	6.47	3.89
2	1.20	14.67	0.56	-57.0	0.10	1	No	1.00	5.31	3.44
3	1.80	14.67	0.72	-57.0	0.00	0	No	1.00	4.09	3.09
4	2.10	14.67	0.80	-57.0	3.80	26	Yes	1.00	2.80	2.71
5	2.20	14.67	0.82	-57.0	3.80	26	Yes	1.00	2.12	2.52
6	2.30	14.67	0.84	-57.0	3.80	26	Yes	1.00	1.89	2.45
7	2.40	14.67	0.82	-57.0	0.10	1	No	1.00	1.66	2.38
8	2.50	14.67	0.86	-57.0	3.80	26	Yes	1.00	1.43	2.32
9	2.60	14.67	0.86	-57.0	3.80	26	Yes	1.00	1.19	2.25
10	2.70	14.67	0.86	-57.0	3.80	26	Yes	1.00	0.96	2.18
11	2.80	14.17	0.81	-59.0	3.80	27	Yes	1.00	0.72	2.11
12	2.90	13.68	0.77	-61.0	3.80	28	Yes	1.00	0.48	2.04

Fig. 7.6.20: Output of reinforcement tension from ReSSA for the case with reinforcement spacing S_v = 0.6 m (24 in or 2 ft)

The results of stability analysis from FLAC show that the required strength of the reinforcement T_f for the numerical model to reach the factor of safety of 1.0 was 5.36 kN/m (367 lb/ft) and 16.66 kN/m (1142 lb/ft) for the cases with reinforcement spacing S_v = 0.2 m (8 in) and S_v = 0.6 m (24 in or 2 ft) respectively. Therefore, the numerical results show that T_f decreased almost proportionally with the decrease of reinforcement spacing under the limit state.

7.6.6 CONCLUSIONS

The evaluation summarized in this research component included stability analysis on a Geosynthetic-Reinforced Soil structure conducted to investigate its behavior under a limit state. Two different methods, the continuum mechanics-based numerical method using the finite difference software FLAC and the limit equilibrium (LE) method using the LE software ReSSA, were used. Two values of reinforcement vertical spacing S_v, 0.2 m (8 in) and 0.6 m (24 in or 2 ft), were adopted to investigate the effect of reinforcement spacing on the stability of the structure. The structure evaluated in this research component considered a footing load and a uniform surcharge to simulate the traffic loads applied on the bridge span and approach way. By comparing the results from both FLAC and ReSSA, the following conclusions can be made from this study:

(1) Results from FLAC and ReSSA were comparable when the factor of safety of the system reached 1.0. When the factor of safety was 1.0, the system was at the verge of failure, which corresponded to the state of limit equilibrium.
(2) Results from FLAC showed that the shape of critical slip surface was different for the case with reinforcement spacing S_v = 0.2 m (8 in) and the case with S_v = 0.6 m (24 in or 2 ft). When the reinforcement spacing S_v = 0.2 m (8 in), the critical slip surface started from the toe and followed the Rankine slip plane up to approximately 2/3 wall height and then almost vertically extended to the right of the footing. When the reinforcement spacing S_v = 0.6 m (24 in or 2 ft), the slip surface started from the wall toe and extended to the end of bearing reinforcement layers. Local failure also happened in the reinforced zone behind the bearing reinforcement layers.
(3) When the reinforcement spacing S_v = 0.2 m (8 in), the required tensile strength T_f of the reinforcement was mobilized in both primary reinforcement and bearing reinforcement layers. The maximum tension T_{max} in the reinforcement was essentially uniformly distributed along depth. When the reinforcement spacing S_v = 0.6 m (24 in or 2 ft), however, the required tensile strength T_f of the reinforcement was nonuniform and only mobilized in primary reinforcement and the maximum tension T_{max} in the reinforcement was higher in primary reinforcement and much lower in bearing reinforcement layers.
(4) Pullout from both ends developed in the bearing reinforcement layers independent of the vertical reinforcement spacing. When the reinforcement spacing was S_v = 0.2 m (2 in), no pullout developed in the primary reinforcement. When the reinforcement spacing S_v = 0.6 m (24 in or 2 ft), however, pullout from the wall facing also developed in the primary reinforcement.

(5) Numerical results showed that the required strength of the reinforcement T_f for the numerical model to reach the factor of safety of 1.0 decreased almost proportionally with the decrease of reinforcement spacing under the limit state.

7.6.7 REFERENCES

Awad, M. I. & Tanyu, B. F. (2014). Laboratory evaluation of governing mechanism of frictionally connected MSEW face and implications on design. Geotextiles and Geomembranes, 42(5), 468-478.

British Standard Institute (2004). Eurocode 2: Design of Concrete Structures: Part 1-1: General Rules and Rules for Buildings. London: British Standards Institution.

Leshchinsky, D., Leshchinsky, O., Zelenko, B., and Horne, J. (2016). Limit Equilibrium Design Framework for MSE Structures with Extensible Reinforcement, FHWA-HIF-17-004, Contract DTFH6114D00047-5010.

8 RECOMMENDATIONS FOR DESIGN

8.1 INTRODUCTION

An important goal of this project is to produce recommendations for refinement of design procedures and specifications that can be integrated consistently into AASHTO LRFD Bridge Design Specifications (AASHTO 2017), specifically into Section 11.10 covering reinforced soil structures. Consequently, the qualitative and quantitative outcomes of this research, stemming from laboratory testing, numerical analysis, field tests, and reinterpretation of work conducted by others, is consolidated into recommendations for revisions of current design procedures that are compatible with AASHTO LRFD. That is, the approach followed herein involves modifying existing design procedures based on the findings of the multiple components of this research.

The Research Team's initial priority was to define the boundary for composite behavior of GMSE structures. Based on the findings from the experimental research component (Chapter 5), the proposed design procedure accounts for this boundary, while being fully consistent with AASHTO LRFD. The research results from the field monitoring program (Chapter 6) and the numerical modeling study (Chapter 7) were used to reassess current approaches, including correlations established by FHWA (2018) regarding the effect of vertical spacing. This information allows for rigorous integration of the findings of this project into the LRFD framework currently in AASHTO as proposed later in this section.

Section 8.2 provides an overview of the current design procedures of geosynthetic-reinforced soil structures with closely spaced reinforcement, highlighting the discrepancies between such procedures. With this background in mind, a total of five design aspects were identified to group the design recommendations stemming from the research findings. Accordingly, Section 8.3 provides the proposed revisions to current AASHTO design procedures that would allow incorporation of the effect of S_v into the design of geosynthetic-reinforced soil structures. Finally, Section 8.4 presents the basis to support the revisions proposed in the previous section, by referencing specific outcomes of this research.

8.2 OVERVIEW OF CURRENT DESIGN PROCEDURES FOR GEOSYNTHETIC-REINFORCED SOIL STRUCTURES WITH CLOSELY-SPACED REINFORCEMENT

8.2.1 BACKGROUND ON CURRENT DESIGN PROCEDURES

The design of geosynthetic-reinforced soil structures involving closely-spaced reinforcements for transportation infrastructure in the US has been conducted using two different approaches: (1) the "GRS-IBS" approach (also identified herein as the "composite design" approach), as detailed in FHWA-HRT-11-026 (FHWA 2012) and recently in FHWA-HRT-17-080 (FHWA 2018); and, (2) the

"simplified method," also known as the "tie back wedge" approach (identified herein as the "current AASHTO" approach), as detailed in AASHTO 2017 and FHWA 2009. The GRS-IBS approach focuses on the design of a subset of load-carrying GMSE bridge abutments (i.e. GRS-IBS) that are characterized by having closely-spaced reinforcements and other prescriptive construction requirements. The current AASHTO approach, included in the AASHTO 2017 LRFD Bridge Design Specifications and the FHWA (2009) guidelines can be adopted for both closely- and comparatively widely-spaced reinforcements, but does not account for potential added benefits of the closely-spaced nature of the reinforcement layout. Both the AASHTO (2017) and FHWA (2009) documents focus on conventional GMSE structures, with specific additional considerations for the case of load-carrying GMSE bridge abutments. The primary philosophy that guided the development of AASHTO's current approach was to establish a unified design framework that allows designers to evaluate reinforced wall alternatives for different reinforcement materials (e.g. steel or geosynthetic reinforcement) systematically, based on performance and cost. This philosophy ultimately led to a significant increase in the number of reinforced walls relative to conventional systems. Using the same philosophy of establishing unified design frameworks whenever feasible, the design recommendations proposed in Chapter 8.2 aim at developing a singular design framework that allows designers to evaluate reinforced wall alternatives (including load carrying MSE bridge abutments) systematically for different reinforcement vertical spacing (e.g. closely- or widely-spaced reinforcement) based on performance and cost.

It should be noted that the current AASHTO approach was validated through research performed on full-scale structures, centrifuge models and numerical models, as part of the FHWA study documented in Volume II of FHWA Report No. FHWA-RD-89-043 (Christopher et al. 1989) and in Christopher (1993). It was acknowledged that the method was inherently conservative to ensure acceptable performance. While this conservatism results in excessive reinforcement in terms of limit state performance, it has resulted in tolerable deformations of the structure under working load conditions. That is, the resulting amount of reinforcement would enable failure loads well in excess of the predicted values. However, deformations occurring under operating conditions have proven to be adequately small. It was suggested that additional studies be performed on the influence of external loading conditions and additional consideration be given to the influence of varying reinforcement vertical spacing through changes in its layer spacing. Additional studies have also been suggested on coupling the effects of reinforcement creep with those of soil creep. Further justification, including calibration of the design approach, is provided by Allen et al. (2001). While a maximum reinforcement spacing value was established at that time to facilitate construction and control face deformations, methods were not identified to capitalize on additional advantages of closely spaced reinforcement. Much of the effort was also placed on the design of roadway walls, with only limited research conducted on bridge abutments and piers. However, this procedure has been used to safely design a number of GMSE walls supporting bridge structures (e.g. the Founders Meadows bridge abutment as reported in Section 4.5 of this report).

The GRS-IBS method was reportedly developed to take advantage of closely spaced geosynthetic reinforcement, recognizing that decreased spacing provides increased confinement, reduced

lateral deformation, suppressed dilation, and a reduction in connection stresses (e.g. FHWA 2012). An increased density of reinforcement layers also increases the inherent redundancy of the structure thus resulting in better performance. The method was specifically developed for bridge support, as these advantages would be most beneficial for this application and would also address a need for replacement of smaller bridge structures. FHWA developed both empirical and analytical design models for geosynthetic-reinforced soil structures supporting bridge loads (FHWA 2012, FHWA 2018). FHWA also calibrated the reliability of these models using performance test data, which have been correlated against results from laboratory and field monitoring programs (Nicks et al. 2013). However, the results of those studies are only deemed valid for the conditions specifically simulated in that research, as that study did not consider generic boundaries for which improved performance occurs due to closely-spaced reinforcement.

8.2.2 COMPARISON OF CURRENT DESIGN PROCEDURES

To develop the philosophy for the final design approach proposed herein, the Research Team first reviewed the fundamental differences between the currently available AASHTO approach and the existing approach developed specifically for the design of GRS-IBS structures. While there are a number of details that vary between these two methods, there is a distinct difference in the design premise used in the development of these two approaches. The GRS-IBS design method outlined by FHWA (2012, 2018) is specifically for load-carrying geosynthetic-reinforced soil abutments. The method only provides minimal design information for free standing GMSE walls (e.g. wing walls) and no design details are provided for walls supporting embankment type surcharge loads (albeit reinforcement spacing will also influence those designs). On the other hand, the current AASHTO wall design approach was essentially developed for free standing structures to which surcharge loads could be applied (e.g. footing supporting bridge, wall supporting embankment slopes). This fundamental difference of decoupling the bridge from the supporting structure in the latter case does not account for considerations such as mechanisms of load transfer immediately below the applied vertical load, the need to accurately predict vertical movements, and the restraining of lateral deformations of the bridge on the load-carrying GMSE system.

Differences between the two methods have been detailed in a number of publications, most notably the publication by Nicks et al. (2013a). The key differences between the two design methods are shown in Table 8.2.1. External stability considers the reinforced soil as a coherent mass and is largely the same in both approaches, except that the GRS-IBS design approach eliminates the requirement to calculate the eccentricity related to overturning. The changes involving internal stability are significant and attributed to closely-spaced reinforcement layers required in GRS-IBS (i.e. S_v less than or equal to 0.3 m (12 in.)) combined with high quality backfill requirements. Wu et al. (2013) documents the anticipated response, identified as composite behavior of the reinforced soil mass, and provides justification for the layer spacing requirements and proposed model to predict lateral deformations. The justification for the absence of pullout requirement is based on a composite hypothesis in which the composite mass moves as a whole due to the interaction between reinforcement and soil (Wu and Pham, 2014). Justification for the

absence of connection strength requirement and for test data to support this design requirement is provided by Iwamoto et al. (2013) and adopted in the GRS-IBS approach.

Table 8.2.1. *Comparison between GMSE and GRS-IBS design methods (adapted after Nicks et al. 2013a)*

Design Check	GMSE (AASHTO and FHWA GEC-11)	FHWA GRS-IBS Method
Required reinforcement vertical spacing, S_v	S_v ≤ 0.8 m (32 in.), but no lower limit. Can be comparatively small, but provides no benefits to adopt closely-spaced reinforcement in the design. That is, design strength is strictly linear with reinforcement vertical spacing, as follows. $T_{max} = \sigma_h S_v$	S_v ≤ 0.3 m (12 in.), with bearing bed reinforcement (minimum of 5 layers) placed beneath beam seat in between primary reinforcement at S_v ≤ ½ primary spacing. Design strength relates non-linearly with reinforcement vertical spacing, as follows: $T_{req} = \left[\frac{\sigma_h}{0.7^{\left(\frac{S_v}{6d_{max}}\right)}}\right] S_v$
Reinforced fill (range)	100% < 100 mm (4 in.) to 100% < No. 4, sand to cobles with up to 15% finer than 0.075 mm (US No. 200 sieve) and PI ≤ 6.	100% < 50 mm (2 in.), clean, open-graded crushed gravel and well-graded sandy gravel.
Reinforcement length, *B*	*B* ≥ 6.7 m (22 ft.) for bridge structures, uniform. Allows different reinforcement length values, with *0.4H* at the base with an overall average of *0.7H*.	*B* = *0.3H* or 1.8 m (6 ft.) at the base, non-uniform with a minimum of *0.7H* in upper reinforcement layers. Includes a reinforced soil foundation (RSF), which increases base width *B* to *(*B + *0.25B)*.
Vertical load capacity	Vertical load capacity is not established. However, provides allowable load for serviceability limit and strength limit state, factored bearing resistance, based on limited field performance tests and monitored structures.	Vertical load capacity is established empirically (based on performance test results) or analytically. The capacity uses the same allowable load limit from AASTHO and GEC-11, as follows: $q_{ult,an} = \left[0.7^{\left(\frac{S_v}{6d_{max}}\right)} \frac{T_f}{S_v}\right] K_{pr}$ $V_{allow,an} = \frac{q_{ult,an}}{FS_{capacity}} = \frac{q_{ult,an}}{3.5}$
Deformation	Chart provided for estimation of lateral movement during construction. Post construction deformations not available.	Empirical deformation requirements provided (based on performance test and monitored structures). - Vertical Strain, ε_v ≤ 0.5%, and - Lateral Strain, ε_L ≤ 1.0%
Reinforcement rupture	$T_{al} = \frac{T_{ult}}{RF_{CR}.RF_{ID}.RF_D}$	$T_{f,f} = \frac{0.9T_f}{2.5}$ With $T_{allow} \leq T_{@\varepsilon = 2\%}$
Reinforcement pullout	Required	No criterion provided
Connection strength	Required	No criterion provided
Friction angle	≤ 40 deg (Instrumented structures indicates that design model underestimate reinforcement loads at higher friction angles)	≥ 38 deg As defined by minimum required value reported by Adams et al. (2012)
Limiting eccentricity	Required	No criterion

Taking into account the genesis of the current design guidelines as documented in this Section 8.2, the remainder of Chapter 8 provides recommendations for incorporating the benefits of

closely-spaced reinforcement into AASHTO. Specifically, Section 8.3 provides the actual revisions into current AASHTO design procedures, while Section 8.4 documents the basis from these recommendations, pointing to specific research findings documented in Chapters 2 through 7 of this report.

8.3 PROPOSED REVISIONS TO INCORPORATE S_V INTO CURRENT AASHTO DESIGN PROCEDURES

8.3.1 OVERVIEW

The qualitative and quantitative outcomes of this research, stemming from laboratory testing, field instrumentation data, numerical analysis, and comprehensive interpretation of previous work by others, was used to develop the design recommendations proposed herein. This section summarizes these recommendations and provides guidance for modification of appropriate sections of AASHTO to recognize the benefits of using closely spaced reinforcements in both GMSE and load-carrying GMSE bridge abutments (including those currently identified as GRS-IBS structures).

The outcomes of this research study, as detailed in the previous sections of this report, led to a number of design recommendations presented herein to evaluate the effect of closely-spaced reinforcements on the design of geosynthetic-reinforced soil structures. The proposed revisions to incorporate the effect of S_v into current AASHTO design procedures are grouped into five design aspects, as follows:

1) Effect of vertical spacing S_v on T_{max} magnitude and distribution
2) Effect of vertical spacing S_v on T_o magnitude and distribution
3) Effect of vertical spacing S_v on stress distribution and the design of the bearing seat, including the design of reinforcement under bearing seat
4) Effect of vertical spacing S_v on the structure's vertical and lateral deformation
5) Effect of vertical spacing S_v on the bump at the end of the bridge

In the execution of this study, a distinct influence of closely spaced reinforcement was identified on the performance of geosynthetic-reinforced soil structures. Accordingly, the boundary vertical spacing below which such improvement is significant was identified. The major benefits of adopting a comparatively closely-spaced vertical reinforcement spacing S_v are described in the results of the research conducted as part of this project (see Sections 5 through 7 of this report) as well as in the results of research by others (see Section 4 of this report). As indicated in Section 8.1, the specific basis and research outcomes relevant to the five identified design aspects will be documented in Section 8.4.

A combination of experimental results and numerical parametric evaluations of reinforced fill materials having different shear strength properties showed little to no effect on the extent of the soil-geosynthetic interaction influence zone. On the other hand, soil-reinforcement interface

shear strength properties were found to have a significant impact on the extent of the influence zone. Specifically, increasing soil-reinforcement interface strength was found to result in larger load transfer from the reinforcement to the surrounding soil. Considering the minor influence of soil shear strength properties, a zone of influence ranging from 0.1 to 0.2 m (4 to 8 in.) on each side of the geosynthetic is recommended for cases where the coefficient of interaction exceeds 0.8 (i.e., the reinforcement pullout factor $F^* > 0.8 \tan \phi$) for free draining reinforced fill materials that currently meet AASHTO 2017 specifications. Additional testing would be required to define the extent of the zone of influence for soil-geosynthetic interfaces characterized by comparatively lower interface shear strength values.

As will be discussed throughout the rest of this Chapter, the primary structural advantages of closely-spaced reinforcement include the following:

- A uniform distribution of reinforcement unit tension with depth, which has cost-effectiveness implications for the case of structures designed using the same vertical reinforcement spacing and reinforcement design strength with depth.
- A uniform distribution of reinforcement connection load with depth, which also has cost-effectiveness implications for the case of structures designed using the same vertical reinforcement spacing and reinforcement design strength.
- Improvement of structural stiffness as it relates to comparatively decreased lateral displacements of the overall structure.
- Improved performance of the bearing seat for the case of load-carrying GMSE bridge abutments (including GRS-IBS structures)
- Decreased bump at the end of the bridge for the case of load-carrying GMSE bridge abutments (including GRS-IBS structures)
- Reduction in the potential for pullout failure, both at the back of the reinforced soil mass and at the face when using frictional connections.
- Comparatively more consistent and uniform placement and compaction of backfill soil due to enhanced distribution of compaction stresses and expected improved field quality control during construction.

The increased number of reinforcement layers was observed to decrease the lateral movement and rotation of the facing elements. As a result, the wall facing unit actually carries more load as observed through increased lateral stress measurements on facing elements that have modest interface strength between units, thereby reducing the stress in the reinforcements, especially at the facing connection T_0. Similar reductions in T_0 were also observed when using secondary reinforcements at the facing with wider spaced primary reinforcements. These improved responses appear to be especially significant for support of external surcharges such as bridge structures.

With regard to the discrepancy between design equations currently available to predict tension in the reinforcement T_{max}, a major conundrum is the reliability of the current methods of design. For stand-alone roadway walls, the current AASHTO (2017)/FHWA (2009) simplified method has been reported to over predict the required maximum T_{max} for geosynthetics based on

instrumented structures, with an overestimation often reported to be a factor of two (Allen et al. 2001, Allen et al. 2002a, Allen and Bathurst 2002b, Miyata and Bathurst 2007a, 2007b, and Bathurst et al. 2008). Such overestimation has often been explained by acknowledging that instrumentation results provide working stress conditions rather than limit state conditions. The GRS-IBS design guide (FHWA 2012, 2018) produces both a limit state design value for the failure strength T_f and a required working stress value T_{req}, somewhat related to service conditions. However, the ultimate strength value was defined based on 3D column tests, which may not have boundary conditions that are representative of walls supporting bridges (e.g., confinement of the loading plate and 3D vs 2D loading). These results have been reported to be even more conservative for roadway walls, requiring almost twice the reinforcement strength obtained using the AASHTO/FHWA design method (Phillips et al. 2015). For bridge-supported structures, the two methods have been reported to result in reasonably similar tensile capacity requirements, but are both still overly conservative based on results from instrumented structures (Phillips et al. 2015). The two new design approaches for geosynthetic reinforcements, limit equilibrium method at a limit state (Leshchinsky et al. 2016) and simplified stiffness method at working load conditions (Allen and Bathurst 2018), produce less conservative, although seemingly more accurate results based on results from instrumented structures.

As a result of the findings from the different research components conducted in this project, the most appropriate approach is to incorporate the design of structures with closely spaced reinforcements directly into the current AASHTO Section 11 (AASHTO 2017) design specifications based on the Simplified method, but adopting special considerations for the distribution of T_{max} with depth and the deformation response of GMSE systems with closely-spaced reinforcement. Accordingly, changes are proposed to Article 11.10 of the existing AASHTO code that incorporates the benefits of closely-spaced reinforcements. In addition, the method could also be incorporated directly into the newly proposed simplified stiffness method, which accounts for the stiffness of the reinforced soil mass and facing stiffness. Finally, the newly proposed limit equilibrium method (Leshchinsky et al. 2016) could also be appropriately modified based on the same approach. However, the modifiers for the design approaches other than the Simplified method would need to be method-specific due to differences in the reliability of the predictions. Additionally, modifications to the current Article 11.10.10.1, Concentrated Load Conditions, are proposed for the case of load-carrying GMSE bridge abutments in general and for the case of GRS-IBS structures in particular, due to the uniqueness of the approach and documented performance.

The selected design approach can be directly incorporated into the current AASHTO LRFD design approach using the current nominal and factored reinforcement strength requirements for internal stability as the method does not modify the global determination of strength demand. The synthesis of data generated by others, as documented in Chapters 2 to 4 of this report provide additional support to the proposed revisions in the design methodology. The use of existing resistance factors is recommended as they are inherently conservative for closely-spaced reinforcement. Although sufficient data may not be available for full calibration of the approach, the use of closely-spaced reinforcements leads to several inherent benefits that improve the overall conservatism of the structure and should balance out any uncertainties resulting from the

proposed modifications. These include increased redundancy in the system and better control of lift thickness and correspondingly compaction control. Different resistance factors could and should be developed in the future to account for these improvements in uncertainty.

In summary, adopting closely-spaced reinforcement in design was found to have significant impact on design on a number of aspects, including the distribution of maximum reinforcement tension with depth (a comparatively uniform profile was identified), as well as the magnitude of the horizontal structure deformations (a comparatively smaller magnitude), with these impacts being particularly evident after a vertical surcharge has been applied. Adoption of a uniform distribution of reinforcement tension with depth may have significant beneficial implications for the cost of structures constructed using a single reinforcement type and vertical reinforcement spacing with depth. However, the recommendation is to maintain the same overall reinforcement tensile capacity of the wall, independent of the reinforcement vertical spacing, when using reinforcements of the same modulus/strength. This is because a further reduction in the tension carried by the reinforcements that can be directly attributed to closely spaced conditions was found to be difficult to quantify. Specific revisions to account for the impact of S_v on current AASHTO design procedures are provided next, with revisions grouped according to the previously identified five design aspects.

8.3.2 EFFECT OF S_v ON T_{MAX} MAGNITUDE AND DISTRIBUTION

A number of revisions to the current AASHTO design procedures are recommended to account for the impact of reinforcement vertical spacing, S_v, and particularly the effect of closely-spaced reinforcements on the magnitude and distribution of T_{max}. The specific revisions recommended for incorporation into AASHTO are:

- For the purposes of defining T_{max}, a vertical spacing $S_{v,nc}$ = 0.4 m (16 in.) shall be adopted as the vertical spacing above which prediction of T_{max} does not account for any benefits of "closely-spaced" reinforcement when considering free draining granular materials.
- For the purposes of defining T_{max}, a vertical spacing $S_{v,c}$ = 0.2 m (8 in.) shall be adopted as the vertical spacing below which prediction of T_{max} accounts for the benefits of "closely-spaced" reinforcement when considering free draining granular materials.
- When adopting intermediate vertical spacing, ranging from $S_{v,c}$ = 0.2 m (8 in.) to $S_{v,nc}$ = 0.4 m (16 in.), determination of T_{max} partially benefits from "closely-spaced" reinforcement.
- The total tensile capacity T_s (i.e. the summation of maximum tension in the entire structure) shall be the same, independent of the reinforcement vertical spacing, and equal to that currently adopted by AASHTO for the Simplified method. That is, for surcharge-free geosynthetic-reinforced structures, the total tensile capacity remains as (see Figure 8.3.1):

$$T_s = \sum T_{max,i} = \frac{1}{2} K_a \cdot \gamma \cdot H^2 \qquad \textit{[Equation 8.3.1]}$$

The total horizontal load resulting from the increased horizontal stresses due to surcharge loads, $\Delta\sigma_H$, should be added to the total tensile capacity T_s defined using Equation 8.3.1.

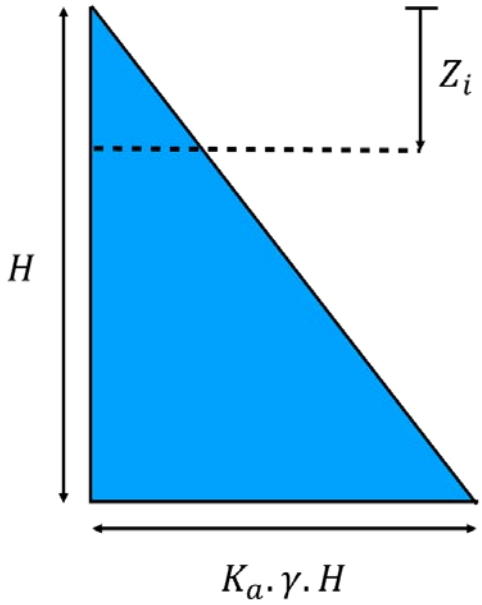

Figure 8.3.1: Total tensile capacity (shaded area) for all MSE walls, independent of the reinforcement vertical spacing, S_v

- Even though the effect of closely-spaced vertical spacing does not affect the calculated total tensile capacity, it is considered to affect the distribution with depth of $T_{max.}$ Specifically, while the distribution remains linear with depth for widely-spaced reinforcement, it should be considered uniform with depth for closely-spaced reinforcement, and should involve an intermediate distribution with depth for the case of intermediate vertical reinforcement spacing, as follows (see Figure 8.3.2):

$$T_{max,i} = K_a \cdot \gamma \cdot z_i \cdot S_v + \Delta\sigma_H \cdot S_v \qquad \text{for } S_v \geq S_{v,nc} = 16\text{"} \text{ [Equation 8.3.2]}$$

$$T_{max,i} = \frac{1}{2} K_a \cdot \gamma \cdot S_v \cdot H + \Delta\sigma_H \cdot S_v \qquad \text{for } S_v \leq S_{v,c} = 8\text{"} \text{ [Equation 8.3.3]}$$

$$T_{max,i} = K_a \cdot \gamma \cdot S_v \cdot \left[z_i + \left(\frac{S_{v,nc} - S_v}{S_{v,c}} \right) \left(\frac{H}{2} - z_i \right) \right] + \Delta\sigma_H \cdot S_v$$

$$\text{for } 8\text{"} = S_{v,c} \leq S_v \leq S_{v,nc} = 16\text{"} \text{ [Equation 8.3.4]}$$

- The resistance factors could be different (higher) for structures involving closely-spaced reinforcements than for structures involving comparatively widely-spaced reinforcements due to the inherent improved reliability of structures with closely-spaced reinforcement.
- Until sufficient data for calibration is generated, the same resistance factors shall be adopted for closely-spaced and widely-spaced reinforcements (even though use of different notations for the two resistance factors are recommended).

- The reinforcement strength and layout selected under working load conditions must also be evaluated under limit state conditions. Global stability using limit equilibrium analysis, as currently recommended by AASHTO, should confirm the adequacy of the adopted resistance factor on soil strength at a limit state of the wall. The reciprocal value of the resistance factor on soil strength is the conventional factor of safety, recommended by AASHTO as 1.3 or 1.5, depending on the criticality of the structure. The importance of such assessment is demonstrated by Leshchinsky (2009) and Leshchinsky et al. (2017).
- While the distribution of T_{max} with depth is supported by field data, it is assumed that its locus coincides with a planar slip surface inclined at $(45+\phi/2)$. Such an assumption is consistent with AASHTO for vertical walls. Subsequently, knowledge of T_{max} and its location for each layer enables assessment of the adequacy of the available pullout resistance.

Overall, and while no differences are recommended at this point regarding the calculated total tensile capacity in structures involving closely- and widely-spaced reinforcements, the distribution of T_{max} with depth for the case of closely-spaced reinforced structures under working stress conditions should be considered uniform. The practical implication is that the T_{max} for structures involving closely-spaced reinforcement will be approximately half the maximum value of T_{max} for structures with the same total tensile capacity but widely-spaced reinforcements (this is for the case in which the reinforcement is uniformly spaced and its type does not vary along the height of the wall).

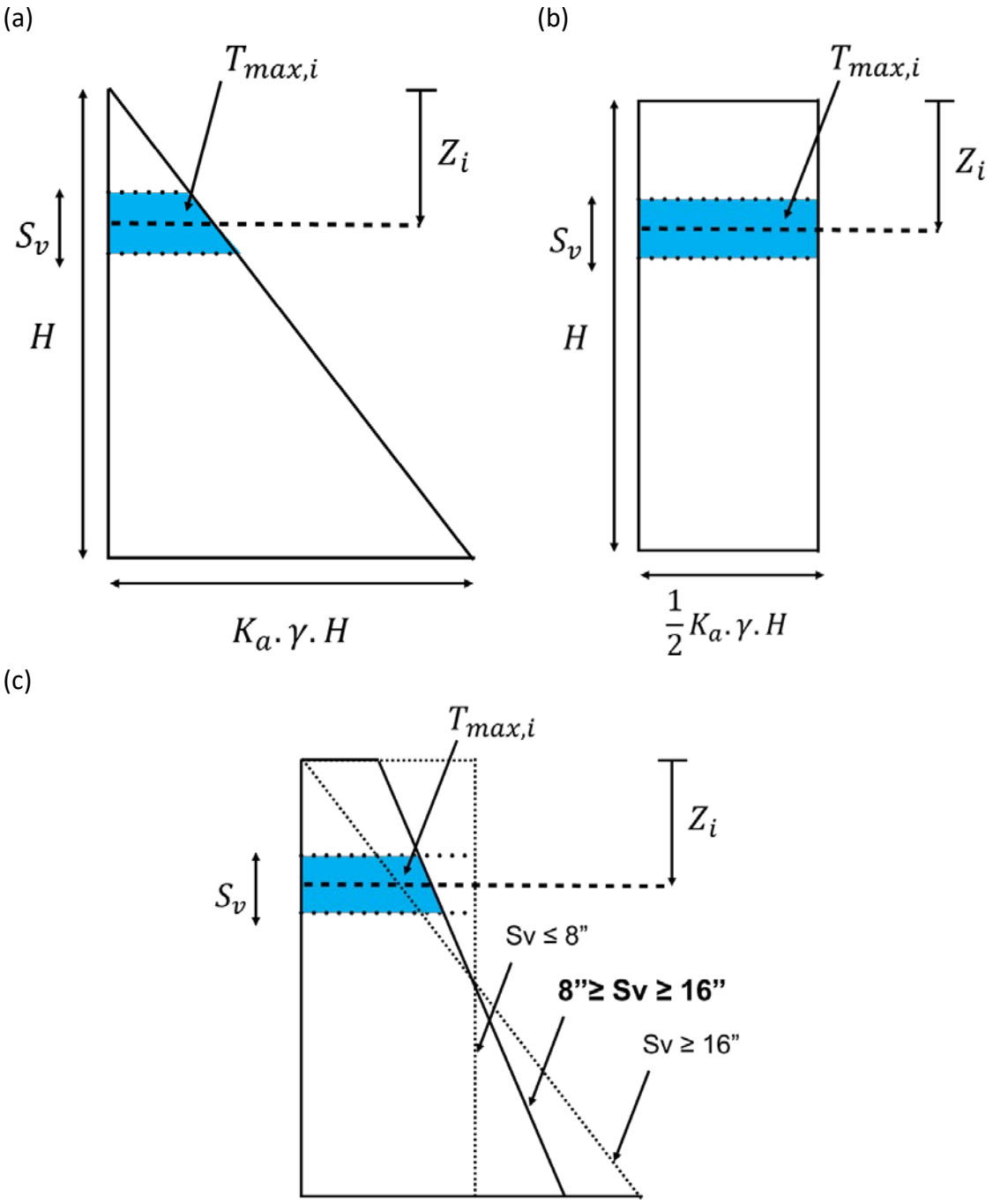

Figure 8.3.2: $T_{max,i}$ value for reinforcement layer at a depth z_i: (a) for cases involving $S_v \geq 16$"; (b) for cases involving $S_v \leq 8$"; (c) for cases involving $8" \leq S_v \leq 16"$

This study concluded that close vertical spacing in extensible geosynthetic reinforced walls, having coverage of 100%, affects the distribution of $T_{max.}$ over the depth of a wall. Specifically, while the distribution remains linear with depth for widely-spaced reinforcements, it is considered uniform with depth for closely-spaced reinforcements. Specific recommendations to

incorporate this approach into AASHTO would be in Article 11.10.6.2.1 (Maximum Reinforcement Loads), as follows:

Edit paragraph 4 of 11.10.6.2.1 as follows:

For the Simplified Method, factored horizontal stress, σ_H, at each reinforcement level shall be determined as:

$$\sigma_H = \gamma_P \left(\sigma_v k_r + \Delta\sigma_H\right) \quad (11.10.6.2.1\text{-}1)$$

where:

γ_P = the load factor for vertical earth pressure *EV* from Table 3.4.1-2

k_r = horizontal pressure coefficient (dim.)

σ_v = pressure due to gravity forces from soil self-weight within and immediately above the reinforced wall backfill, and any surcharge loads present (ksf)

$\Delta\sigma_H$ = horizontal stress at reinforcement level resulting from any applicable concentrated horizontal surcharge load as specified in Article 11.10.10.1 (ksf)

For design with geosynthetic reinforcement, the beneficial effect of closely-spaced reinforcements can be accounted for in the Simplified Method by using the following equation, instead of 11.10.6.2.1-1, when the reinforcement vertical spacing is less than or equal to 8 inches:

$$\sigma_H = \gamma_P(0.5\, k_r\, \gamma\, H + \Delta\sigma_H) \quad (11.10.6.2.1\text{-}2)$$

and the following equation, instead of 11.10.6.2.1-1, when the reinforcement vertical spacing is between 8 and 16 inches:

$$\sigma_H = \gamma_P \left[k_r \left(\sigma_v + \left(\frac{16-S_v}{8}\right)\left(\frac{\gamma\, H - 2\sigma_v}{2}\right)\right) + \Delta\sigma_H\right] \quad (11.10.6.2.1\text{-}3)$$

where:

S_v is geosynthetic reinforcement vertical spacing (inches)

Commentary: Add following to C11.10.6.2.1

NCHRP Report 24-41 found that closely-spaced vertical spaced reinforcements in walls reinforced using extensible geosynthetic reinforcements affects the distribution of T_{max} over the depth of a wall. Specifically, while the distribution remains linear with depth for structures with widely-spaced reinforcement, it is considered uniform with depth for closely-spaced reinforcement, as shown in the following figure.

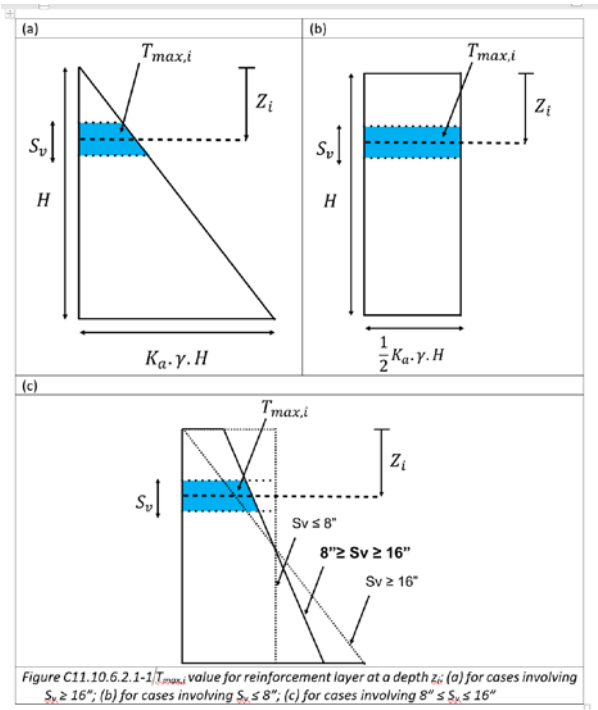

Figure C11.10.6.2.1-1 $T_{max,i}$ value for reinforcement layer at a depth z_i: (a) for cases involving $S_v \geq 16$"; (b) for cases involving $S_v \leq 8$"; (c) for cases involving $8" \leq S_v \leq 16"$

Equations 11.10.6.2.1-2 and 11.10.6.2.1-3 account for this benefit. The equations are valid for continuous geogrid and geotextile reinforcements. Research has not been performed to verify the use of these equations for the case of geosynthetic strip or inextensible steel reinforced walls.

8.3.3 EFFECT OF S_V ON T_0 MAGNITUDE AND DISTRIBUTION

A number of revisions are recommended herein to account for the impact of reinforcement vertical spacing, S_v, and the effect of closely-spaced reinforcements on the magnitude and distribution of T_0 in particular. The specific revisions recommended for incorporation into the current AASHTO design procedures are:

- Consistent with the limits defined for determining T_{max}, For the purposes of defining T_0, a vertical spacing $S_{v,nc}$ = 0.4 m (16 in.) can be adopted as the vertical spacing above which prediction of T_0 would not account for any benefits of "closely-spaced" vertical spacing when considering free draining granular materials.
- For the purposes of defining T_0, a vertical spacing $S_{v,c}$ = 0.2 m (8 in.) can be adopted as the vertical spacing below which prediction of T_0 accounts for the benefits of "closely-spaced" vertical spacing when considering free draining granular materials.
- The adoption of an intermediate vertical spacing, between $S_{v,c}$ = 0.2 m (8 in.) and $S_{v,nc}$ = 0.4 m (16 in.) would partly account for the benefits of "closely-spaced" vertical spacing in T_0 when considering free draining granular materials.
- The magnitude of the connection load, T_0 is recommended as follows:

$$T_{0,i} = \lambda \, . \, T_{max,i} \qquad \textit{[Equation 8.3.5]}$$

  where λ is the connection load coefficient (dimensionless)
  While it is anticipated that the value of λ may be a function of the vertical spacing S_v, sufficient data is not available to establish such differentiation. Consequently, no revision to the AASHTO Design Guidelines is recommended at this point on the relation between T_0 and T_{max}, which effectively implies a connection load coefficient λ = 1 for any value of S_v.
- The resistance factors should be different (higher) for structures involving closely-spaced reinforcements than for structures involving comparatively widely-spaced reinforcements.
- Until sufficient data is generated for calibration, the resistance factors for closely-spaced reinforcement shall be adopted as being equal to that for widely-spaced reinforcements (even though different notations for the two resistance factors are recommended).

Since the distribution of T_{max} with depth for the case of closely-spaced reinforced structures should be considered uniform, even the conservative assumption of T_0 = T_{max} will lead to comparatively lower requirements of T_0 for the case of closely-spaced reinforced structures.

The bulleted list of recommendations above should be incorporated into the commentary section of AASHTO to identify the effect of S_v on T_0 magnitude and distribution in Article C11.10.6.2.2, as follows:

	C11.10.6.2.2 For closely spaced geosynthetic reinforcement, T_0 will be equal to the maximum nominal reinforcement tension as calculated and the vertical spacing defined as in 11.10.6.2.2. Based on research in NCHRP 24-41 the magnitude of the connection load, T_0 is recommended as follows:

	$T_{0,i} = \lambda \, . T_{max,i}$ C11.10.2.2-1 where λ is the connection load coefficient (dimensionless) While it is anticipated that the value of λ is a function of the vertical spacing S_v and is anticipated to be < 1. However, sufficient data is not currently available to establish such differentiation. Consequently, λ = 1 for any value of S_v.

8.3.4 EFFECT OF S_v ON STRESS DISTRIBUTION AND DESIGN OF BEARING SEATS

Modest revisions are also recommended to account for the effect of geosynthetic reinforcement vertical spacing, S_v, and the effect of closely-spaced reinforcement on the bearing seat in particular. These recommendations impact the design of the reinforcement under the bearing seat. Research findings documented in Chapter 7 of this report strongly supports the use of the truncated 2:1 distribution currently in AASHTO Article 3.11.6.3 and in FHWA (2009) for stress distribution when using closely spaced reinforcement. The primary recommendation is to add commentary to Article 3.11.6.3 as well as Articles 11.10.10.1—Concentrated Dead Loads and 11.10.11-—MSE Abutments on the benefits of a bearing reinforced zone including:

- A bearing reinforced zone, involving geosynthetic reinforcements with a vertical spacing of 10 cm (4 in). is recommended for placement under the bearing seat of the bridge structure.
- Increasing the density of geosynthetic reinforcement immediately below the bearing seat or bridge wing wall is recommended, as it has a significant impact in minimizing the bump at the end of the bridge and reducing the lateral deformation of the wall.
- While the benefits of closely-spaced reinforcement may be applicable to steel reinforcements, research has not been conducted to verify the effect on the performance of steel-reinforced reinforced soil walls.

The increase in vertical stress, $\Delta\sigma_v$, due to bearing seat loading affects the lateral deformations of load-carrying GMSE walls . It is also directly incorporated in the prediction of T_{max} and T_0 at each depth. The value of $\Delta\sigma_v$ is added to the soil overburden pressure which, upon multiplication by appropriate lateral earth pressure coefficient, leads to the horizontal stress used to predict the reinforcement load. The rate at which the stress dissipates with depth in the proposed approach is defined by a 2D pyramid with side slopes of 2(v) to 1(h). This approach is consistent with AASHTO (2017) and FHWA (2001, 2009).

Extensive experience gained through the construction and operation of numerous GRS-IBS structures has indicated that very close reinforcement, spaced 0.1 m (4 in.) apart, will enhance performance when placed under the bearing seat. This bearing reinforcement zone may be

composed of primary, full length layers spaced every 0.2 m (8 in.) whereas intermediate length layers are placed mid-span between the primary layers. Consequently, a reinforced mass under the seat bed is formed at a spacing of 0.1 m (4 in.). For the purpose of enhancing the load-carrying performance, the intermediate layers should be placed to a depth equal to at least the width of seat bed and extend at least 1.5 m (5 ft.) beyond the edge of the seat.

Again, the specific commentary on the recommendations to incorporate into AASHTO regarding design of the bearing seat would be in Articles 3.11.6.3, 11.10.10, and 11.10.11 as follows:

	Commentary: Add the following to C3.11.6.3, C11.10.10, and C11.10.11 For geosynthetic reinforced MSE walls supporting strip loads (e.g., bridge structures), a bearing reinforced zone, involving geosynthetic reinforcements with a vertical spacing of 4 in. is recommended for placement under the bearing seat of the bridge structure based on research performed under NCHRP Project 24-41 and field data developed under other FHWA research studies (FHWA-HRT-17-080 Adams and Nicks, 2009). Increasing the density of geosynthetic reinforcement immediately below the bearing seat or bridge wing wall is recommended, as it has a significant impact in minimizing the bump at the end of the bridge and reducing the lateral deformation of the wall. Design guidelines for an alternate approach using geosynthetic reinforced soil walls to support bridge structures and other strip loads is provided in (FHWA-HRT-17-080 Adams and Nicks, 2009).

8.3.5 EFFECT OF S_V ON VERTICAL AND LATERAL DEFORMATIONS

The results of the parametric numerical evaluation (Chapter 7) indicated a significant influence of reinforcement vertical spacing on the lateral deformation response of GMSE structures in general, and load-carrying GMSE bridge abutments in particular. The revisions recommended in this section are those to account for the impact of reinforcement vertical spacing, S_v, and the

effect of closely-spaced reinforcement on the lateral deformations of GMSE structures in particular. While improvement could also be identified in the structure vertical response, the magnitude was minor. The specific revisions recommended for incorporation into the current AASHTO design procedures when using closely spaced reinforcement and high quality aggregates (which should always be used for load-carrying GMSE bridge abutments and other GMSE structures supporting footings) are:

- Vertical displacements in load-carrying GMSE bridge abutments should be predicted using empirical data from similar structures (i.e., based on load test or similar instrumented structures) or analytical methods such as that proposed by Schmertmann as documented in FHWA (2006).
- In cases where the vertical settlement is known, or can be accurately estimated, the maximum lateral displacement and maximum lateral strain shall be estimated in agreement with the method documented in FHWA (2018), as follows:

$$D_L = 2\ x\ b_{q,vol}\ x\ \frac{D_V}{H} \qquad \textit{[Equation 8.3.6]}$$

$$\varepsilon_L = \frac{D_L}{b_{q,vol}} = \frac{2D_V}{H} = 2\varepsilon_V \qquad \textit{[Equation 8.3.7]}$$

  where: D_L is the maximum lateral displacement,
  $b_{q,vol}$ is the width of the load along the top of the wall including the setback,
  D_V is the vertical settlement of the load, H is the height of the structure,
  ε_L is the maximum lateral strain, and
  ε_V is the vertical strain.

  The calculated lateral strain is typically limited to 2% (FHWA, 2018).
- In cases where the vertical settlement is unknown, a first order estimation of the lateral movement for free standing walls as well as walls supporting surcharge loads with closely-spaced reinforcement can predicted using a model established considering AASHTO (2017) Figure C11.10.4.2-1 / FHWA (2009), as follows:

$$\delta_R = 11.81\left(\frac{L}{H}\right)^4 - 42.25\left(\frac{L}{H}\right)^3 + 57.16\left(\frac{L}{H}\right)^2 - 35.45\left(\frac{L}{H}\right) + 9.471 \qquad \textit{[Equation 8.3.8]}$$

$$\delta_{max} = \left(\frac{\delta_R H}{50\frac{J}{S_v}\cdot\frac{1}{p_o}}\right) x\left(1 + 1.25\frac{q}{p_o}\right) \qquad (extensible\ reinforcement) \qquad \textit{[Equation 8.3.9]}$$

  where: δ_R is an empirically derived relative displacement coefficient (dim.),
  δ_{max} is the maximum displacement (units of H),
  H is the height of the wall (ft or m),
  J is the reinforcement tensile stiffness defined by the secant modulus at 2% strain,
  S_v is the reinforcement vertical spacing (units of H),
  q is the surcharge magnitude, and

p_o is atmospheric pressure introduced in the equation for normalization purposes.

Specific recommendations to incorporate into AASHTO the approach proposed herein regarding prediction of vertical and lateral deformations would be in Articles 11.10.4.1 and 11.10.4.2, and a specific commentary should be added to Article 11.10.11 outlining these approaches and referring to Article 11.10.4, as follows:

11.10.4.1 (add the following) For vertical compression within the reinforced zone in load-carrying GMSE bridge abutments shall be predicted using empirical data from similar structures (i.e., based on load test or similar instrumented structures) or analytical methods such as that proposed by Schmertmann as documented in FHWA (2006).	
11.10.4.2	C11.10.4.2- Add under Figure C11.10.4.2-1 The curve in the figure can be modeled using the following equation: $\delta_R = 11.81\left(\frac{L}{H}\right)^4 - 42.25\left(\frac{L}{H}\right)^3 + 57.16\left(\frac{L}{H}\right)^2 - 35.45\left(\frac{L}{H}\right) + 9.471$ *[Equation C11.10.4.2-1]* INSERT THE FOLLOWING AT THE END OF THE CURRENT COMMENTARY: For closely spaced reinforcement (< 16 in.) and high quality aggregates (which should always be used for load-carrying GMSE bridge abutments and other GMSE structures supporting footings), lateral wall displacement can be predicted base on one of the following two methods. Where vertical settlement is known, or can be accurately estimated using the methods in Article 11.10.4.1, [INSERT 2ND BULLET ABOVE]

	In cases where the vertical settlement is unknown, [INSERT 3RD BULLET ABOVE]
	C11.10.11 Lateral displacements shall be evaluated following the recommendations in Article 11.10.4.2. The calculated lateral strain ε_L shall be limited to 2% (FHWA-HRT-17-080 Adams and Nicks, 2018).

8.3.6 EFFECT OF S_V ON BUMP AT THE END OF THE BRIDGE

Revisions are recommended herein to account for the impact of reinforcement vertical spacing, S_v, and particularly the effect of closely-spaced reinforcements on the abutment transition (i.e. "bump at the end of the bridge") for the case of GMSE structures associated with bridge abutments (either load-carrying GMSE structures or structures with bridge loads transferred through piles to the foundation soils). The specific revisions recommended for incorporation into the current AASHTO design procedures are:

- A prediction of the total foundation settlements, $S_{t,f}$, for the abutment and embankment behind the abutment should be produced as part of the design of a GMSE bridge abutment involving the use of deep foundations to transfer the bridge loads in accordance with AASHTO Articles 10.5.2.4 and 10.6.2.4.
- A prediction of vertical reinforced fill elastic compression, $S_{e,r}$, should be produced as part of the design of a GMSE abutment (whether a load-carrying GMSE abutment or a GMSE abutment involving deep foundations) in accordance with AASHTO Article 10.6.2.4.
- The bump-at-the-end-of-the-bridge, *BEB*, for the case of a GMSE bridge abutment involving deep foundations is based on the settlement of the fill and foundation soils behind the deep foundations and shall be predicted as $BEB = S_{t,f} + S_{e,r}$.
- The bump-at-the-end-of-the-bridge, *BEB*, for the case of a load-carrying GMSE bridge abutment (including GRS-IBS walls) shall be predicted as $BEB = S_{e,r}$
- Decreasing the reinforcement vertical spacing immediately below the bearing seat or bridge wing wall is recommended, as it has a significant impact in minimizing the bump at the end of the bridge.

Specific recommendations to incorporate into AASHTO the approach proposed herein regarding prediction of the bump at the end of the bridge would include a paragraph added to Article 11.10.4.1, as follows, with commentary added to 11.11.1:

11.10.4.1 Add the following after last paragraph in current article: Differential settlement shall also be part of the analysis of abutment transitions in accordance with Article 10.5.2.4. For MSE walls with the bridge abutment supported by deep foundations, the analysis shall include the total settlement of the embankment behind the bridge including the compression of the fill following Article 10.6.2.4, as compared to the settlement of the footing supported by the deep foundation based on Articles 10.7.2.3 -10.7.2.5 for piles or Articles 10.8.2.2 – 10.8.2.4 for drilled shafts. For load-carrying MSE bridge abutments (i.e. cases in which the bridge is supported directly by the reinforced fill), the analysis shall include the compression of the reinforced fill under the bridge load following Article 10.6.2.4 and assume there is negligible compression of the fill behind the end of the bridge.	
	C11.11.1. Add the following: Differential settlement shall also include an analysis of the abutment transition in accordance with Article 10.5.2.4 and Article 11.10.4. Design guidelines for an alternate approach for mitigating differential settlement (e.g., the bump at the end of the bridge) by using closely spaced geosynthetic soil reinforcement and an integrated bridge structure is provided in (FHWA-HRT-17-080 Adams and Nicks, 2009).

8.4 RESEARCH BASIS SUPPORTING THE PROPOSED REVISIONS TO INCORPORATE S_V INTO DESIGN PROCEDURES

The outcomes from this research study that provide justification for the recommended revisions to the AASHTO Design Method presented in Section 8.3 are provided herein. Consistent with Section 8.3, the research basis supporting the proposed revisions into current AASHTO design procedures are also grouped into five design aspects. In addition, an initial discussion is provided on the identification of the magnitude of reinforcement vertical spacing that defines the 'boundary' of composite behavior.

8.4.1 BOUNDARY FOR COMPOSITE BEHAVIOR OF GEOSYNTHETIC-REINFORCED SOIL STRUCTURES

Before discussing the research basis for recommended revisions on each design aspect presented in Section 8.3, an overarching important question is "what constitutes closely-spaced reinforcement?", i.e., what is the vertical reinforcement spacing, S_v, below which the influence among adjacent reinforcement layers (i.e. composite behavior) should be considered.

As discussed in Chapter 5, Figure 8.4.1 shows a conceptual relationship for the interaction between neighboring reinforcement layers (i.e., inter-layer interaction) and the reinforcement spacing. In this figure, a vertical spacing $S_{v,c}$ (i.e. composite behavior) is indicated below which full interlayer interaction (or composite behavior) occurs. The figure also identifies a vertical spacing $S_{v,nc}$ (i.e. non-composite behavior) beyond which no interlayer interaction occurs. Varying degrees of interlayer interaction develop for vertical spacing values ranging from $S_{v,c}$ to $S_{v,nc}$.

Figure 8.4.2 shows experimental data used to quantify the interaction between neighboring reinforcement layers at various reinforcement spacings. The indicator for this interaction adopted in this evaluation is the ratio between the reinforcement displacements measured in a neighbor reinforcement, *v*, to that measured in the active reinforcement, *u*. Specifically, Figures 8.4.2 a, b, and c show the relationship for active reinforcement displacements of 2, 5, and 10 mm (0.1, 0.2 and 0.4 in), respectively (i.e. three different loading tensile levels). The results in the figure indicate that full interlayer interaction occurs for vertical spacing values below approximately 0.1 m (4 in.) ((i.e. $S_{v,c}$ = 0.1 m (4 in.)). On the other hand no composite behavior is considered for vertical spacing values above approximately 0.1 m (4 in.) ((i.e. $S_{v,nc}$ = 0.2 m (8 in.)), as beyond this distance the interaction has been significantly reduced. Consequently, according to these experimental results, the composite behavior can be observed to an average of 0.15 m (6 in.) from the soil-geosynthetic interface.

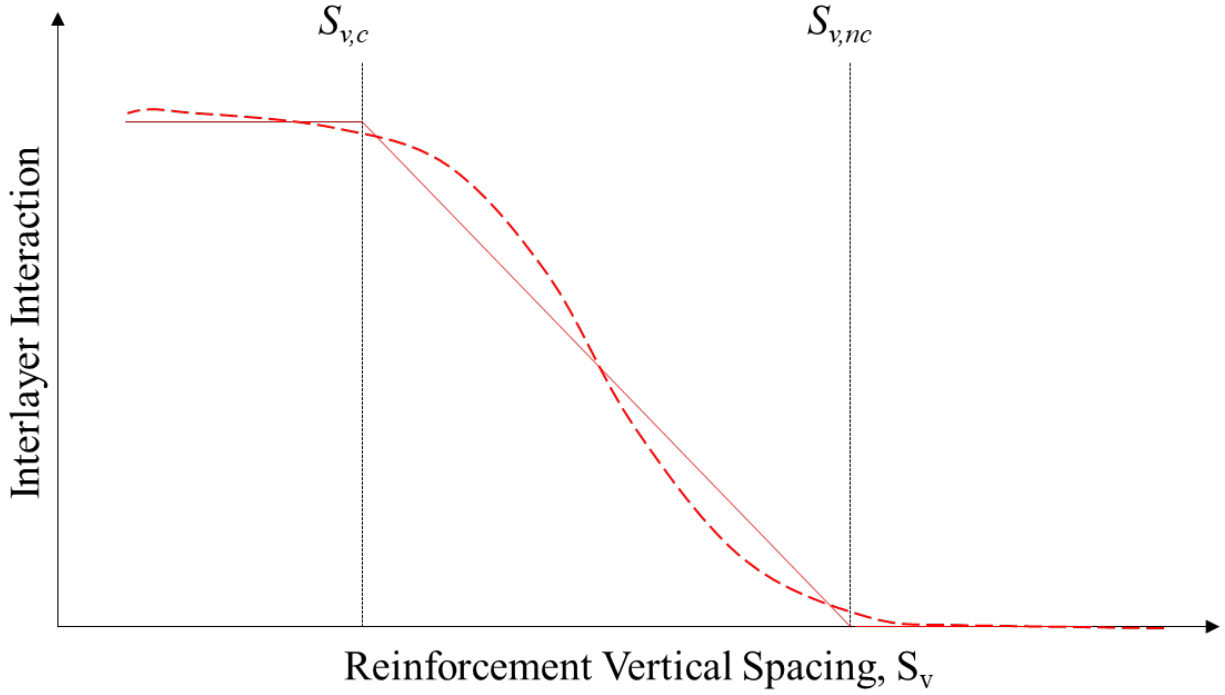

Figure 8.4.1. Conceptual relationship for the interaction between neighboring reinforcement layers (i.e., interlayer interaction) and the reinforcement spacing

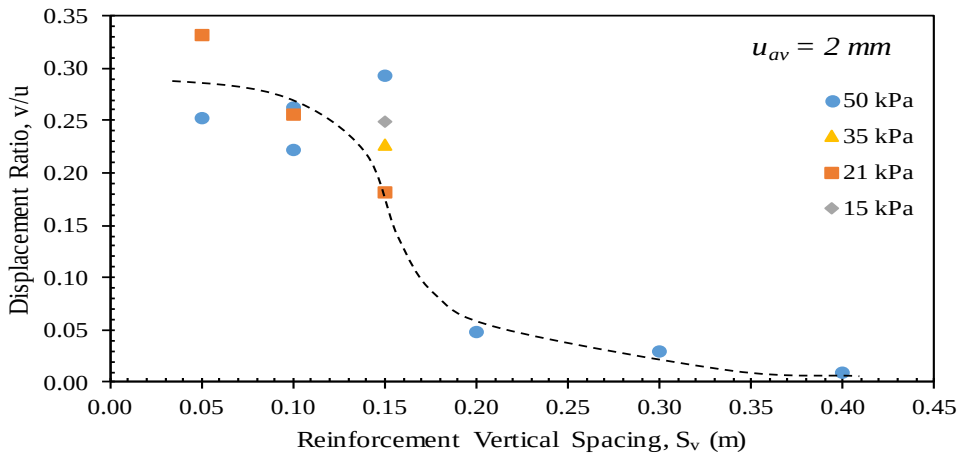

(a)

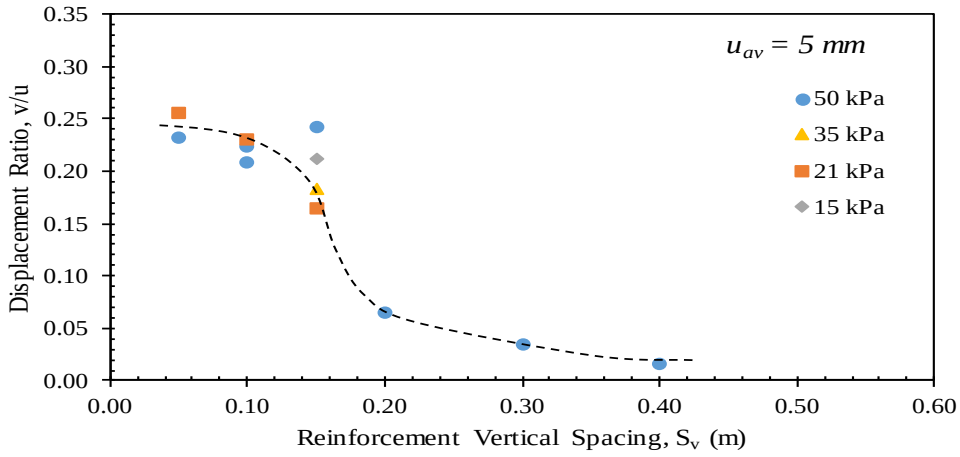

(b)

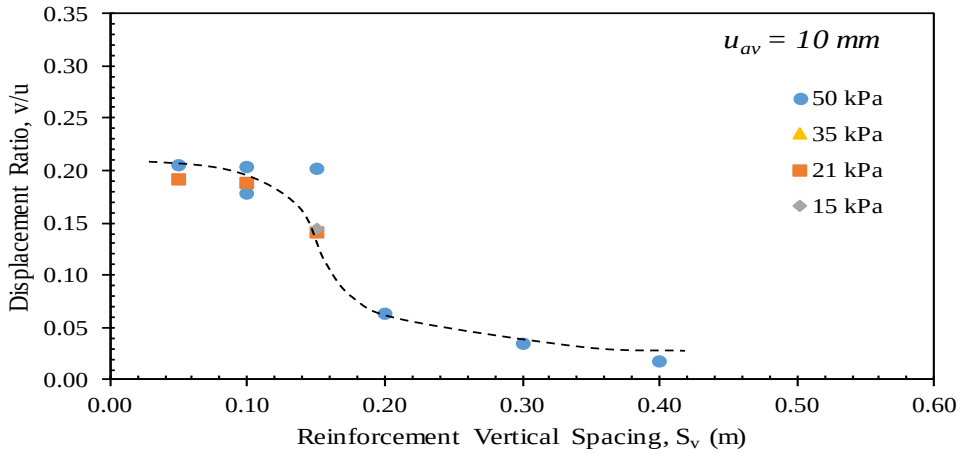

(c)

Figure 8.4.2. Displacement ratio versus reinforcement spacing at various active reinforcement displacements: (a) 2 mm (0.08 in); (b) 5 mm (0.2 in); and (c) 10 mm (0.4 in)

The reinforcement spacing in these figures at which a significant change in the interaction between contiguous reinforcements occur corresponds to the experimentally-defined boundary for composite behavior of a geosynthetic-reinforced soil mass, $S_{v,c}$. However, this value represents a lower bound, as load in the experimental testing setup was mobilized in only one of the reinforcements. In case of multiple loaded reinforcements, the soil between two contiguous reinforcements would be mobilized in shear by the two reinforcement layers. Consequently, according to these experimental results, a composite behavior would be observed for vertical spacing values having an average of 0.30 m (12 in.) for select backfill. This value is well in agreement with current limits for reinforcement spacing established by the FHWA GRS-IBS design approach, as indicated in Table 8.2.1. In order to avoid having a sharp change of response at a given vertical spacing, and consistent with the experimental data shown in Figure 8.3.2, which indicates a transition zone between the responses at widely- and closely-spaced reinforcements, a transition is proposed for the determination of T_{max} as a function of vertical spacing. Accordingly, a magnitude $S_{v,c}$ of 0.2 m (8 in.). was identified as the spacing below which a composite behavior is considered, while a magnitude $S_{v,nc}$ of 0.4 m (16 in.) was identified as the spacing above which a non-composite behavior shall be considered. A transition zone was proposed for reinforcement vertical spacing values ranging from $S_{v,c}$ and $S_{v,nc}$ (i.e. between 0.2 and 0.4 m (8 and 16 in.)).

As previously mentioned, a combination of experimental results and numerical parametric evaluations showed little to no effect of the backfill strength properties on the extent of the soil-geosynthetic interaction influence zone. Consequently, the boundary of the composite behavior of geosynthetic-reinforced soil structures is recommended for select backfill where the soil-geosynthetic coefficient of interaction exceeds 0.8 (i.e., $F^* > 0.8 \tan \phi$).

8.4.2 EFFECT OF S_V ON T_{MAX} MAGNITUDE AND DISTRIBUTION

In order to provide the basis for the recommended effect of S_v on T_{max} magnitude and distribution, as presented in Section 8.3.2, the different research outcomes, including those from experimental, field and numerical components were holistically assessed. They are summarized next.

8.4.2.1 EXPERIMENTAL RESEARCH OUTCOMES THAT SUPPORT THE PROPOSED RECOMMENDATIONS

The results from the experimental testing program documented in Chapter 5 of this report provide evidence on the existence of a relationship between the maximum reinforcement unit tension and the reinforcement vertical spacing. The impact of vertical spacing could be experimentally identified for vertical spacing values ranging from 0.10 m to 0.20 m (4 to 8 in) and being somewhat independent of the normal stress for ranges that are typical for working stress conditions (15 to 50 kPa (2.2 to 7.3 psi)). While load in the experimental testing program was mobilized in only one of the neighboring reinforcements, the thickness of the soil layer affected by the shear transfer would double for the case of load mobilized in multiple reinforcements. As discussed in Section 8.4.1, the center of the transition zone is 0.15 m (6 in) from each soil-geosynthetic interface (or 0.30 m (1 ft) for a soil layer bound by two geosynthetics). The design

recommendations proposed in Section 8.3.2 consider full interaction (i.e. composite behavior) for the reinforcement vertical spacings below 0.40 m (8 in.). Also consistent with the experimental and numerical results, a transition between composite and non-composite behaviors was recommended in the determination of T_{max} for vertical spacing values ranging from 0.40 m (8 in.) and 0.80 m (16 in.).

As discussed in Chapter 5 of this report, load shedding was observed in the experimental results for tests where the the reinforcement vertical spacing S_v was within the values recommended for implementation in AASHTO. That is, load was observed to transfer through shear bands from highly stressed geosynthetic layers to the adjacent layers that were comparatively less stressed. Ultimately, geosynthetic layers are expected to be tensioned uniformly in a reinforced soil mass, provided that the reinforcement vertical spacing is small enough to facilitate load transfer through the soil by shear. This observation implies that for conditions involving reasonably highly mobilized loads and closely-spaced reinforcements, each layer would be expected to carry a similar T_{max} (assuming that all layers are long enough).

8.4.2.2 FIELD RESEARCH OUTCOMES THAT SUPPORT THE PROPOSED RECOMMENDATIONS

Data compiled for T_{max} for the GRS-IBS bridge instrumented abutment presented in Chapter 6 was plotted along with additional data compiled for other GMSE structures of different vertical reinforcement spacings presented in Chapter 4.6. Figures 8.4.3a through 8.4.3d present measured T_{max} profiles from self-weight loading condition together with the design load distribution proposed in this study for four cases: Virginia Bridge, Louisiana Bridge, Delaware Bridge, and Founders Meadows Bridge. It can be observed that the distribution of T_{max} with depth is reasonably uniform and does not tend to either increase with depth. In addition, Figures 8.4.4a through 8.4.4d present measured T_{max} profiles from self-weight and surcharge loading condition for Virginia Bridge, Louisiana Bridge, Delaware Bridge, and Havana Yard Abutment (Wu et al. 2001 - FHWA-RD-00-038 Report). Also in this case, the distribution of T_{max} with depth is reasonably uniform and does not tend to either increase with depth.

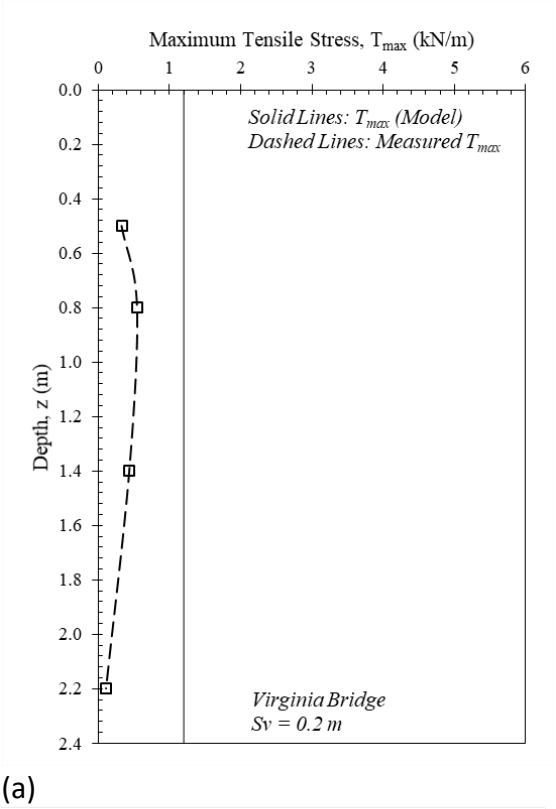

(a)

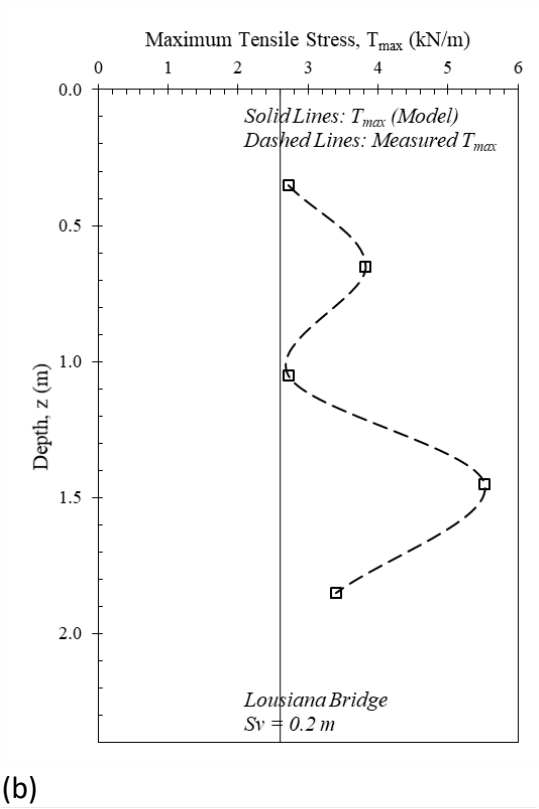

(b)

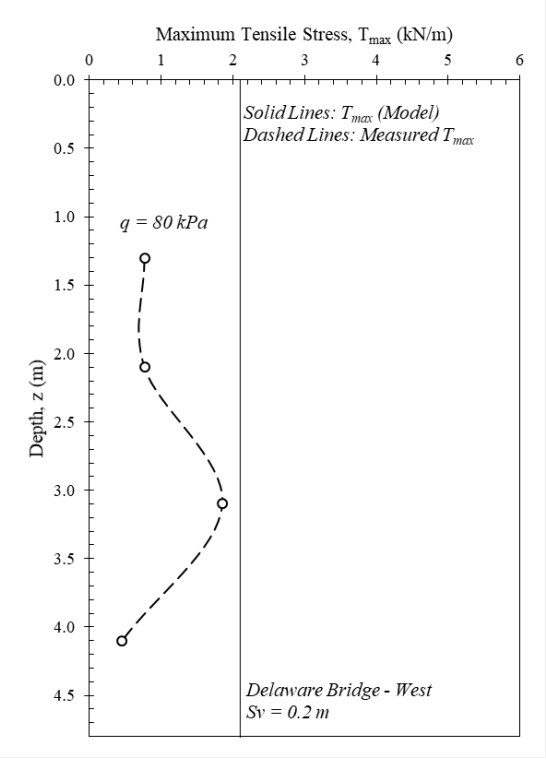

(c)

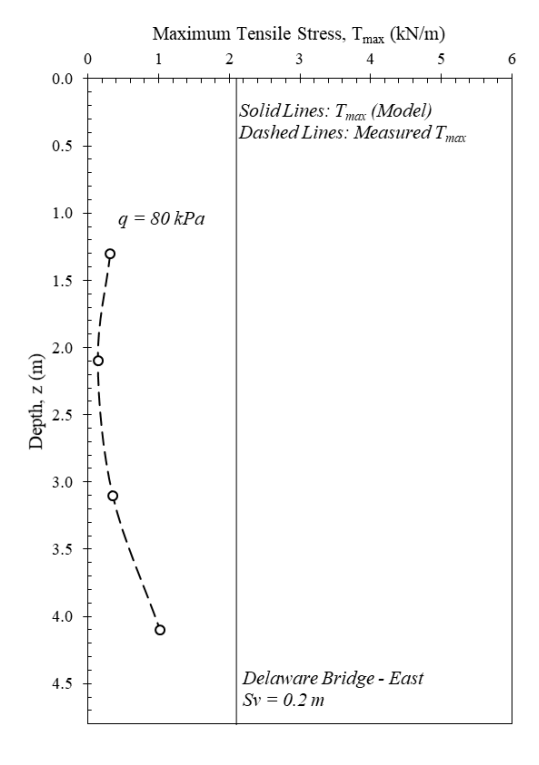

(d)

Figure 8.4.3. Measured T_{max} profiles from self-weight loading condition and proposed design envelopes: (a) Virginia Bridge; (b) Louisiana Bridge; (c) Delaware Bridge – East Abutment; and (d) Delaware Bridge – West Abutment.

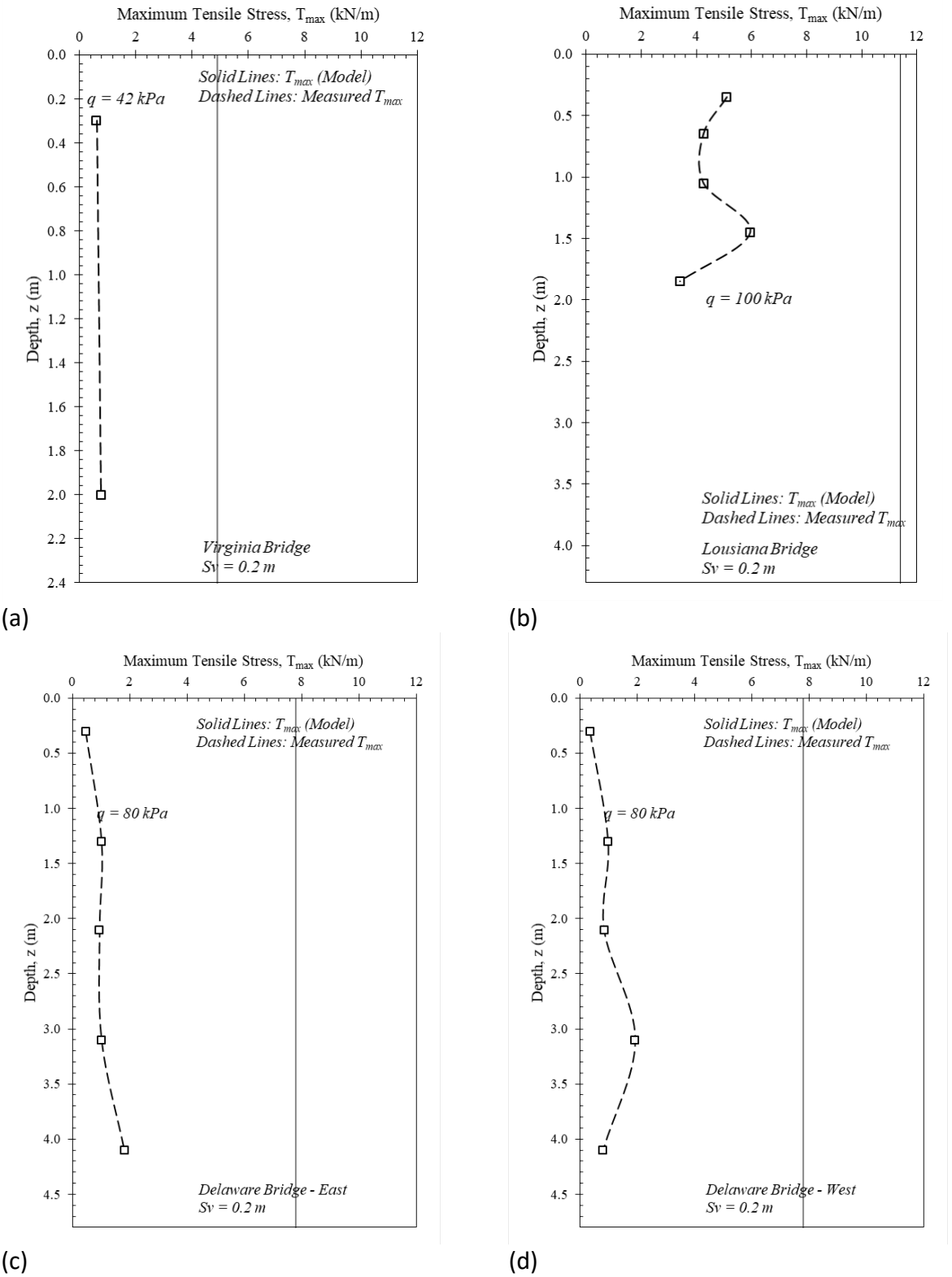

Figure 8.4.4. Measured T_{max} profiles from self-weight and surcharge loading condition and proposed design envelopes: (a) Virginia Bridge; (b) Louisiana Bridge; (c) Delaware Bridge – East Abutment; and (d) Delaware Bridge – West Abutment.

8.4.2.3 NUMERICAL SIMULATION OUTCOMES THAT SUPPORT THE PROPOSED RECOMMENDATIONS

In order to complement observations from field monitoring data, which may show significant scatter, numerical simulations were used to extend the evaluation of the effect of S_v on the magnitude and distribution of T_{max} . As discussed in detail in Chapter 7 of this report, Figure 8.4.5 shows the effect of the reinforcement spacing on T_{max} with depth, under both self-weight and traffic load conditions. It should be noted that these results represent working stress conditions as the numerical model was calibrated for structures under these conditions. The prediction of σ_v under different loading conditions was evaluated using the overburden stress and the AASHTO 2 to 1 truncation method. In Figure 8.4.5, z is the depth measured from top of the wall, normalized against the wall height H . The numerical predictions in Figure 8.4.5 shows that for self-standing walls, the numerical predictions for T_{max} could not reproduce the uniform distribution observed in field structures. However, both under traffic load and under bridge load surcharge, the predicted T_{max} was found to be reasonably uniform. It should also be noted that the predicted max(T_{max}) is smaller than the value that would have been used for the case of structures with widely spaced reinforcement.

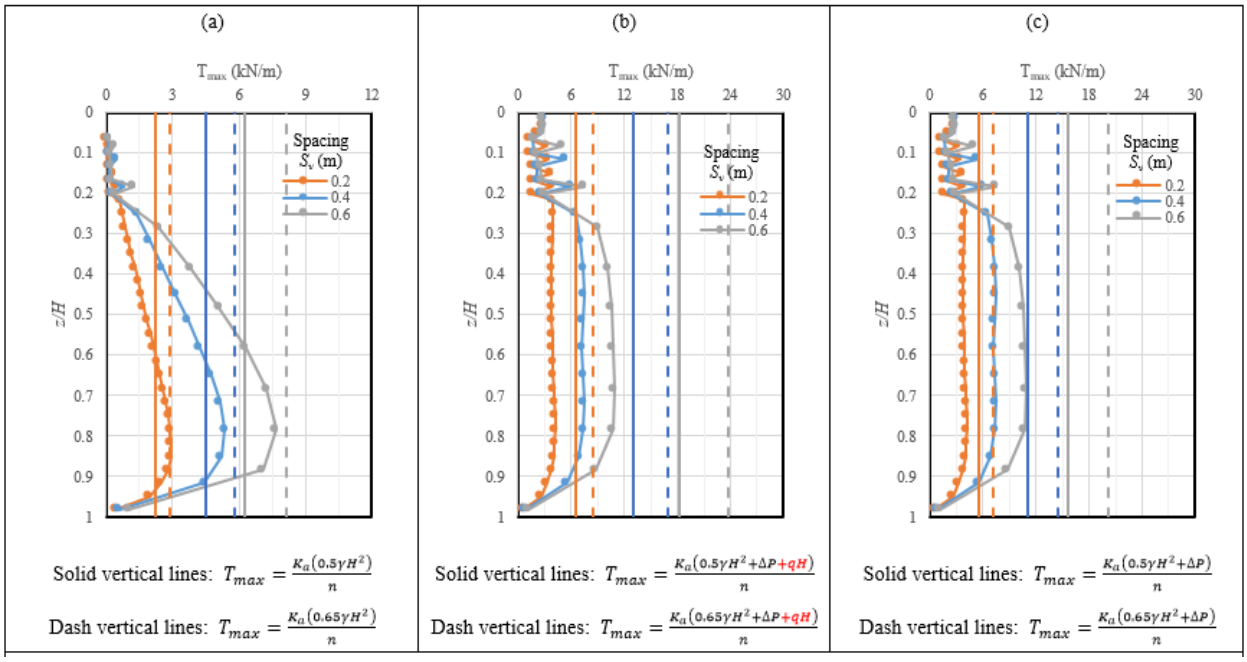

Figure 8.4.5: Effect of S_v on T_{max} vs depth for: (a) Self-weight; (b) Traffic load with consideration of surcharge q; (c) Traffic load without consideration of surcharge q

8.4.2.4 LIMIT EQUILIBRIUM RESEARCH OUTCOMES THAT SUPPORT THE PROPOSED RECOMMENDATIONS

The LE-based methodology presented in Leshchinsky et al. (2016) Report No. FHWA-HIF-17-004, utilizing program ReSSA+, shows that when the reinforcement is long enough, T_{max} amongst reinforcement layers is nearly uniformly mobilized. This finding results from examination of numerous slip surfaces, several of which yield the same T_{max} although the surfaces are different.

For example, some surfaces reflect a compound mode of failure while others are strictly internal but emerging either at or above the toe of the wall. The nearly uniform mobilization of reinforcement was demonstrated analyzing a wall with a height of 6 m (20 ft), reinforcement length of 4.2 m (14 ft), and reinforcement spacing of either 0.4 m or 0.2 m (16 in. or 8 in.). Figures 8.4.6a and 8.4.6b show T_{max} profile obtained from the LE analysis and the current AASHTO design envelope for zero surcharge and for 200-kPa (4000-psf) surcharge, respectively.

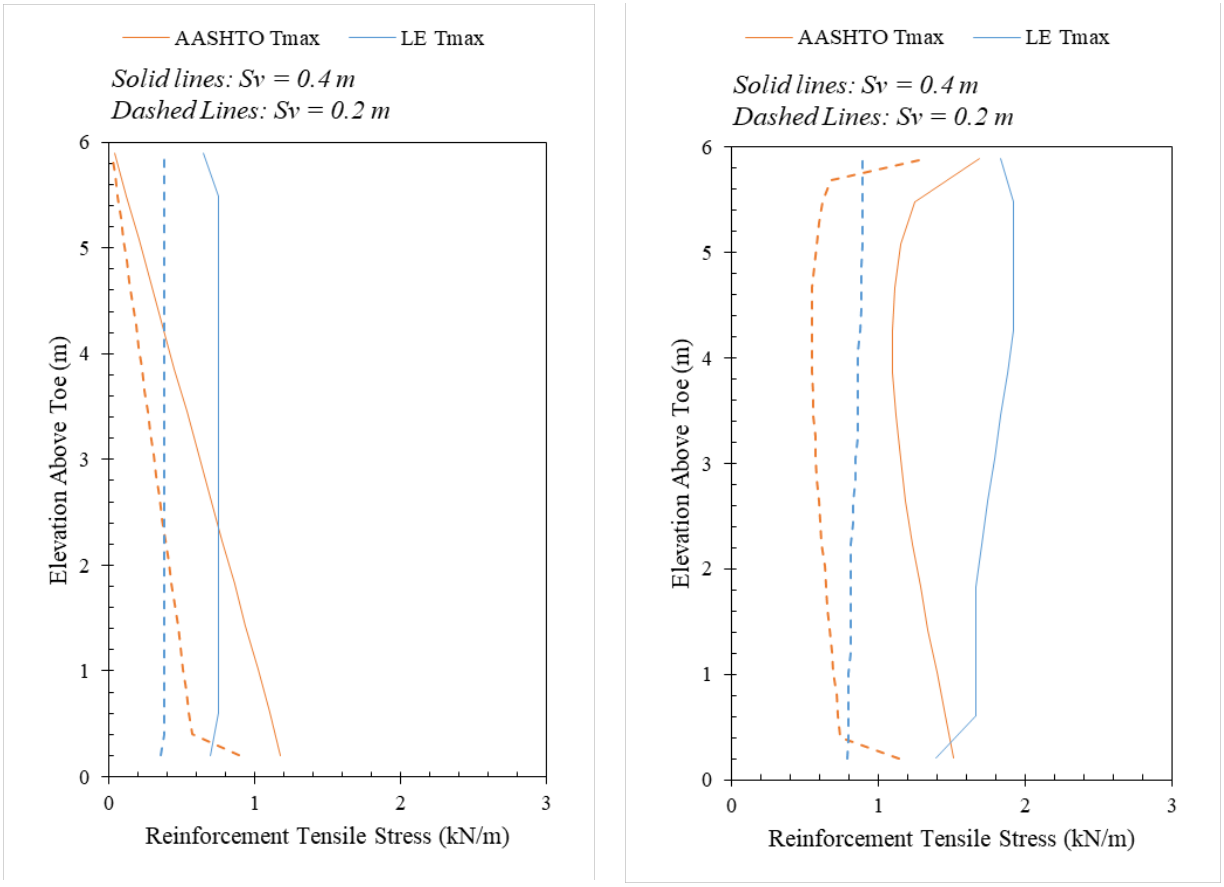

(a) (b)

Figure 8.4.6. Comparison between the limit-equilibrium computed T_{max} envelope and current AASHTO design envelope: (a) surcharge, q = 0; (b) surcharge, q = 20 kPa (430 psf)

8.4.3 EFFECT OF S_V ON T_0 MAGNITUDE AND DISTRIBUTION

In order to provide the basis for the recommended effect of S_v on the magnitude and distribution of the connection load, T_0, as presented in Section 8.3.3, the different research outcomes were holistically assessed. They are presented next.

8.4.3.1 FIELD RESEARCH OUTCOMES THAT SUPPORT THE PROPOSED RECOMMENDATIONS

The current design models for evaluating T_0 are significantly different As previously indicated in Section 8.2.2 and Table 8.2.1, current design models differ significantly on their evaluation of T_0.

Specifically, AASHTO requires $T_0 = T_{max}$, while the FHWA GRS-IBS design approach assumes that the lateral pressure on the facing is comparatively small and does not require a design. That is, friction connection is deemed to be sufficient to take on the small tensile load that the FHWA GRS-IBS approach assumes at the connection. Field data on connection loads from three different studies, as compiled by Wu and Ooi (2015) Report No. FHWA-HRT-14-094 were reassessed as part of the study in order to validate the hypothesis that the magnitude of connection loads is comparatively minor. The field data involved four piers (Mitchell 2002), the Founders Meadows load-carrying GMSE bridge abutment and two GMSE structures (Yogarajah and Andrawes 1994). Figure 8.4.7 compares the measured magnitude of the connection loads against predicted values using the approaches proposed by Wu (2001) and Soong and Koerner (1997), both of which have been reported to predict connection load values that are below those adopted by AASHTO. The reassessment of field data showed, however, that the measured connection loads were comparatively high, at least in relation to those predicted by the methodologies proposed by Wu (2001) and Soong and Koerner (1997). In addition, Figure 8.4.8 shows an increase in bias with increasing lateral earth pressure, resulting in differences of up to 15 times. This lateral pressure is expected to be larger in load-carrying GMSE bridge abutments, where a footing or bearing seat is subjected to high loads (e.g., 200 kPa (4,200 psf)), which are often expected to be near the wall facing.

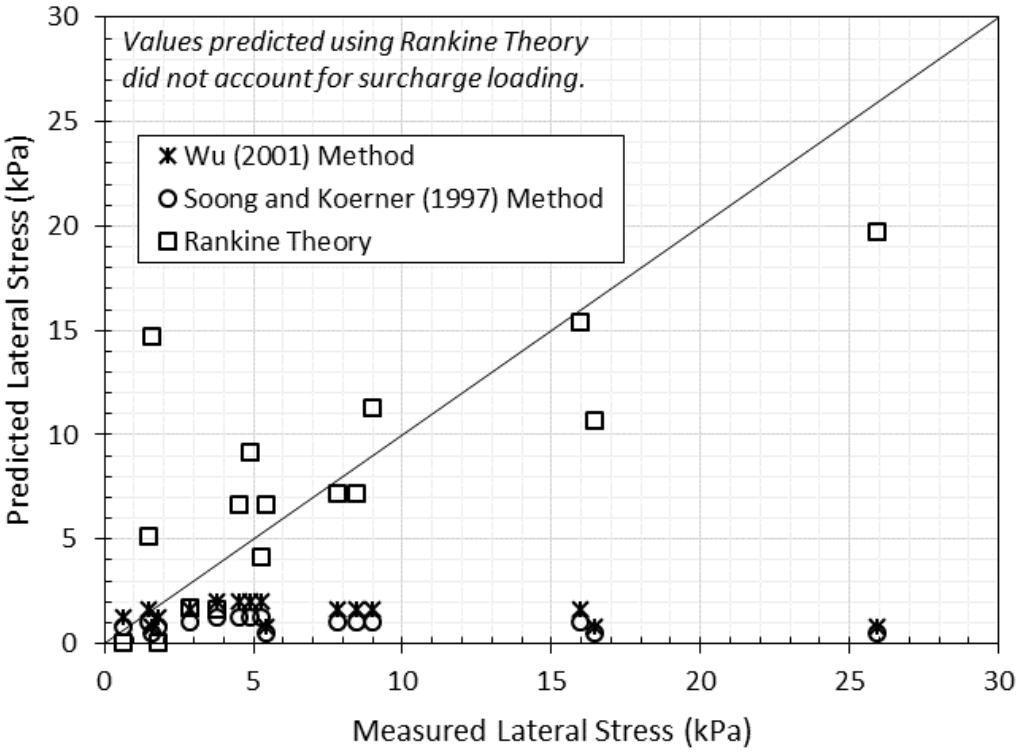

Figure 8.4.7. Predicted versus measured lateral stress against facing blocks

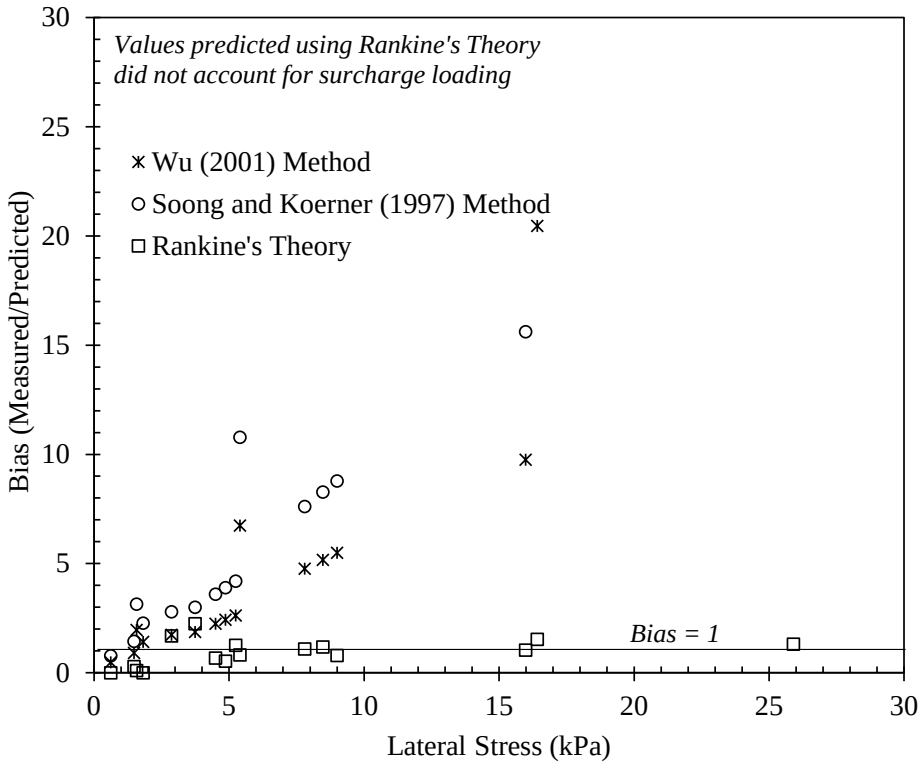

Figure 8.4.8. Bias in the lateral stress prediction models

The reason for the scatter shown in Figures 8.4.7 and 8.4.8 may be the product of a number of complicating factors in the monitored structures, including lateral movement and tilting of the facing blocks as well as parasitic loads that are often induced at the facing connection due to reinforcement downdrag. Even some mini-pier tests indicated downdrag stresses on the connection, to the point that failure of the reinforcement at the connection occurred in some tests or at least very high deformation observed at the connection during dismantling (Iwamoto, 2014). In summary, a number of mechanisms may affect the magnitude of the measured connection loads, including the development of relative movements between the facing and the reinforced soil mass, the method of instrumentation (e.g., earth pressure cells, strain gages, extensometers mounted on the reinforcements), and the location of the monitoring instruments. Consequently, and in spite of reasonable scatter in the field data, the available field measurements have indicated that the magnitude of the connection loads is not necessarily negligible, which is consistent with the recommended revisions presented in Section 8.3.3.

The distribution of connection loads with depth was also evaluated as part of this study. This involved reassessment of data collected as part of the field research component documented in Chapter 6 and field data collected by others as reported in Chapter 4.6. Even though no changes are recommended in this study regarding the magnitude of T_0 in relation to T_{max}, changes are proposed to the AASHTO design approach regarding the distribution of T_{max} with depth. These changes effectively result in a change on the distribution of T_0 with depth for the case of GMSE

walls with closely-spaced reinforcement. Specifically, from Equations 8.3.3 and 8.3.5, the connection load T_0 of a given reinforcement layer *i* can be expressed as follows:

$$T_{0,i} = \frac{1}{2} K_a \cdot \gamma \cdot S_v \cdot H + \Delta\sigma_H \cdot S_v \qquad for\ S_v \leq S_{v,c} = 8" \quad \textit{[Equation 8.4-1]}$$

Also, for reinforcement vertical spacings ranging from $S_{v,c}$ and $S_{v,nc}$ (i.e., from 0.2 to 0.4 m (8 to 16 in.)), the magnitude of $T_{0,i}$ would be defined from Equations 8.4.4 and 8.4.5, as follows:

$$T_{0,i} = K_a \cdot \gamma \cdot S_v \cdot \left[z_i + \left(\frac{S_{v,nc} - S_v}{S_{v,c}} \right) \left(\frac{H}{2} - z_i \right) \right] + \Delta\sigma_{\mathrm{H}} \cdot \mathrm{S_v}$$
$$for\ \ 8" = S_{v,c} \leq S_v \leq S_{v,nc} = 16" \ \textit{[Equation 8.4.2]}$$

Figure 8.4.9 shows the profile of normalized T_0 versus depth, defined using field data corresponding to strain gages (SG) and rectangular pressure cells (RPC) installed in the Virginia (VA) GRS-IBS structure, SG installed in the Delaware (DE) GMSE structure, earth pressure cells (EPC) installed in the Colorado (CO) GRS-IBS structure and SG installed in the Founders Meadows (FM) load-carrying GMSE abutment. The vertical reinforcement spacing (S_v) in the VA and DE structures was 0.20 m (8 in.) in the primary reinforcement zone and 0.10 m (4 in.) in the bearing seat zone. The vertical reinforcement spacing (S_v) in the Colorado GRS-IBS and Founders Meadows GMSE abutments were 0.10 and 0.40 m (4 and 16 in.), respectively.

As shown in the results presented in the figure, the profile of connection loads (or its normalized value) can be reasonably described as having a uniform distribution with depth.

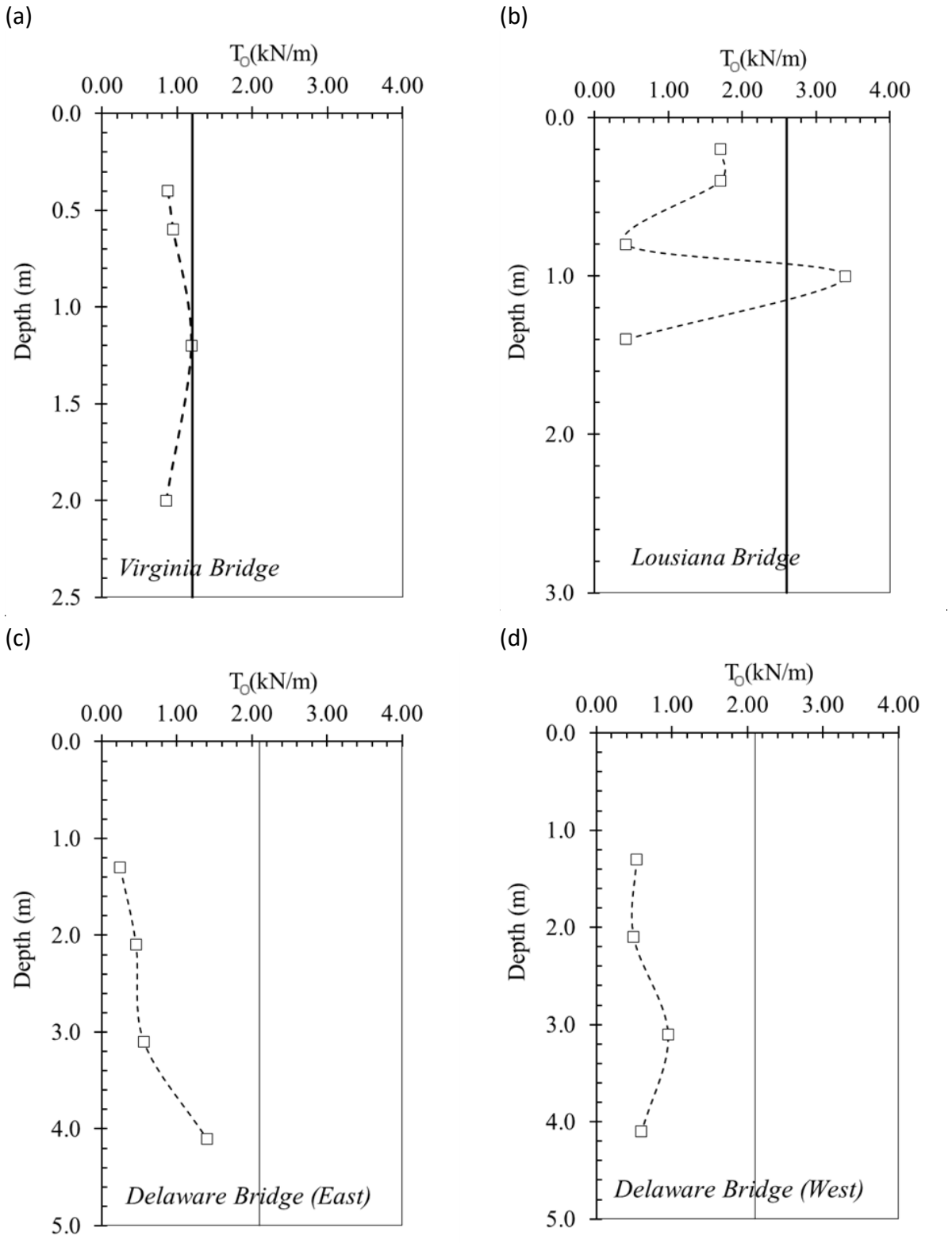

Figure 8.4.9: Profiles of connection load with depth for (a) the Virginia GRS-IBS structure, (b) the Louisiana GRS-IBS, (c) the Delaware GRS-IBS structure (East Abutment), and (d) the Delaware GRS-IBS structure (East Abutment)

Additional evidence of the appropriateness of adopting a uniform distribution with depth for the connection load, T_0, is provided by the connection loads predicted at the Founders Meadows load-carrying GMSE bridge abutment. As discussed in Chapter 4.5, the reinforcement vertical spacing for this structure was 0.40 m (16 in.), which is in the upper limit of the range recommended in Chapter 8.3 for "closely-spaced" reinforcement. Figure 8.4.10 shows the connection loads at geogrid layers 6 and 10 placed 3.05 and 1.43 m (10 and 4.7 ft) below the bridge footing, respectively. The change in connection load is provided as a function of the vertical pressure predicted along the different stages of construction of the bridge structure, including field placement, placement of the footing and placement of the bridge girders. The connection loads were obtained using measurements from strain gauges placed on the geogrids in close proximity to the facing blocks. As shown in the figures, the connection loads at the two different elevations remained approximately uniform, at T_0 = 6 kN/m (± 1 kN/m) (34.2 lb/in ± 5.7 lb/in), throughout the different stages of construction. The linear prediction that would be obtained using current AASHTO design approach would deviate significantly from the actual connection loads. Additional evidence on the proposed distribution of reinforcement connection loads with depth is provided by Leshchinsky et al. (2010) who reported observations from an exhumed geogrid-reinforced retaining wall with a vertical reinforcement spacing of 0.40 m (16 in.) constructed on highly compressible foundation soils. Forensic evaluation of the recovered geogrids allowed determination of the mobilized tensile strains in the geogrid panels along the height of the wall, which revealed a relatively uniform distribution of tension with depth.

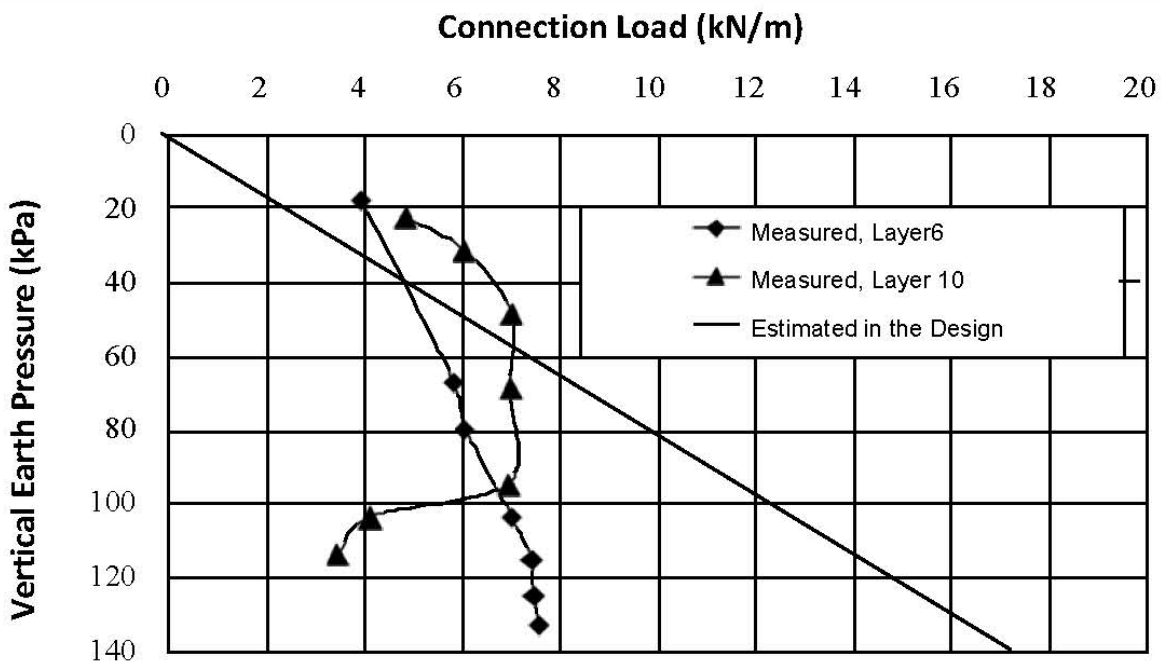

Figure 8.4.10. Measured and AASHTO-predicted connection loads in geogrid layers 6 and 10 at the Founders Meadows load-carrying GMSE bridge abutment.

8.4.3.2 NUMERICAL SIMULATION OUTCOMES THAT SUPPORT THE PROPOSED RECOMMENDATIONS

The numerical simulations conducted as part of this study (Chapter 7 of this report) provide additional justification to the revisions to AASHTO design approach presented in Section 8.3.3. They also provide insight on relevant differences between the response of GRS piers and GRS-IBS structures. Based on numerical simulations of GRS piers, the connection loads T_0 was reasonably smaller than the T_{max} values, as the geotextile reinforcements were frictionally connected to the facing blocks. The predicted T_{max} value was found to develop at the center of the pier, where the surcharge-induced vertical stresses were the highest. However, T_0 developed as a connection force at the interface between the geotextile reinforcements and the CMU blocks. In fact, the reinforcement spacing was found not to have a significant effect on the predicted connection force T_0, independent on the type of reinforcement or magnitude of reinforcement stiffness adopted in the analyses. Figure 8.4.11 illustrates this response for the case of analyses conducted with reinforcements of the same stiffness but varying vertical spacing. In addition, Figure 8.4.12 shows the distribution of connection loads predicted in mini-piers when using the same ratio of reinforcement stiffness to reinforcement vertical spacing. In both cases, a reasonably uniform connection load was predicted with depth (except for loads predicted the base of the mini-piers).

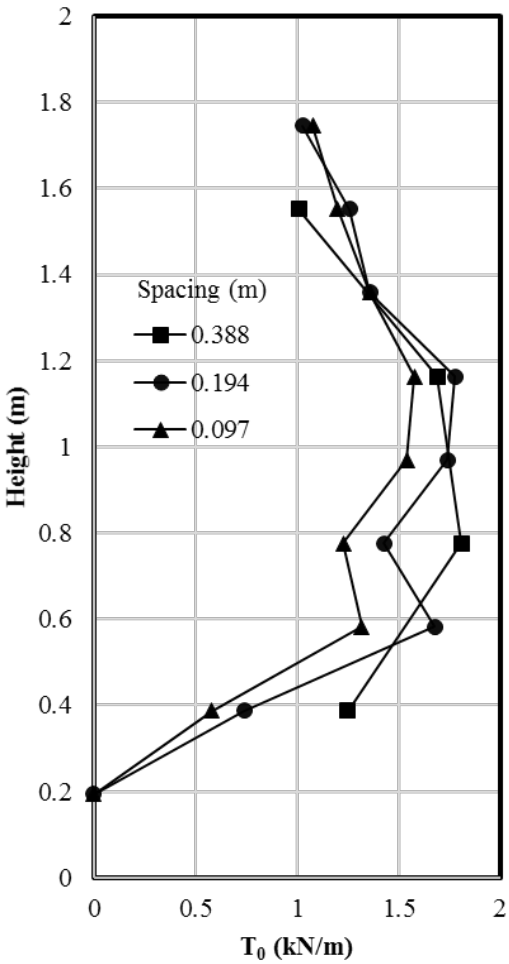

Figure 8.4.11: Distribution of connection loads predicted in mini-piers for different reinforcement vertical spacing using the same reinforcement type

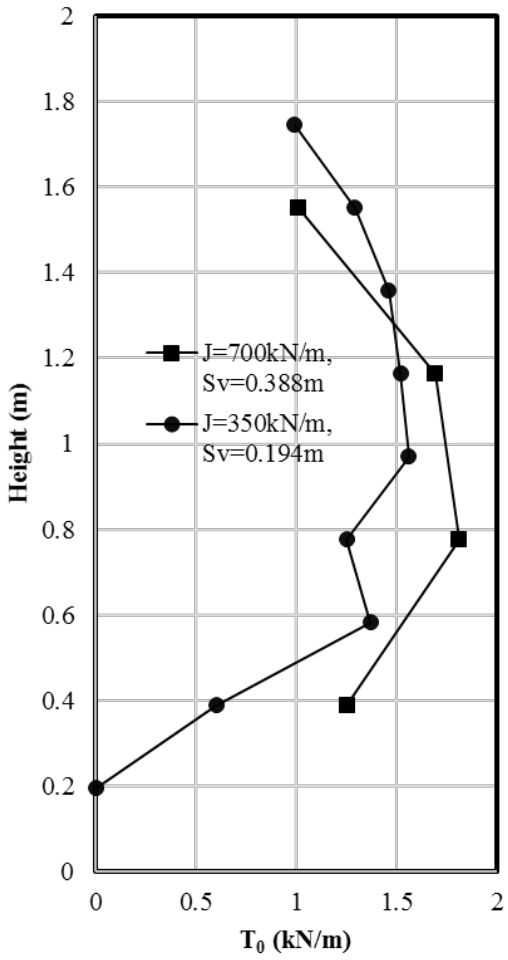

Figure 8.4.12: Distribution of connection loads predicted in mini-piers when using the same ratio of reinforcement stiffness to reinforcement vertical spacing

While the numerical simulations of mini-piers showed a significant difference between the predicted T_{max} and T_0 values, the numerical simulation of GRS-IBS showed that the location of T_{max} was very close to the connection between geotextile and CMU facing blocks. Consequently, the connection load was found to be similar to the maximum tension in the reinforcement, justifying the recommendation of adopting λ =1 in Equation 8.3.5. This is illustrated in Figure 8.4.13 for conditions corresponding to self-weight loading and of to bridge loading acting on the GRS-IBS system. Figure 8.4.14 shows a similar response but for simulations conducted using structures that involved different reinforcement vertical spacing while maintaining the same stiffness to vertical spacing ratio.

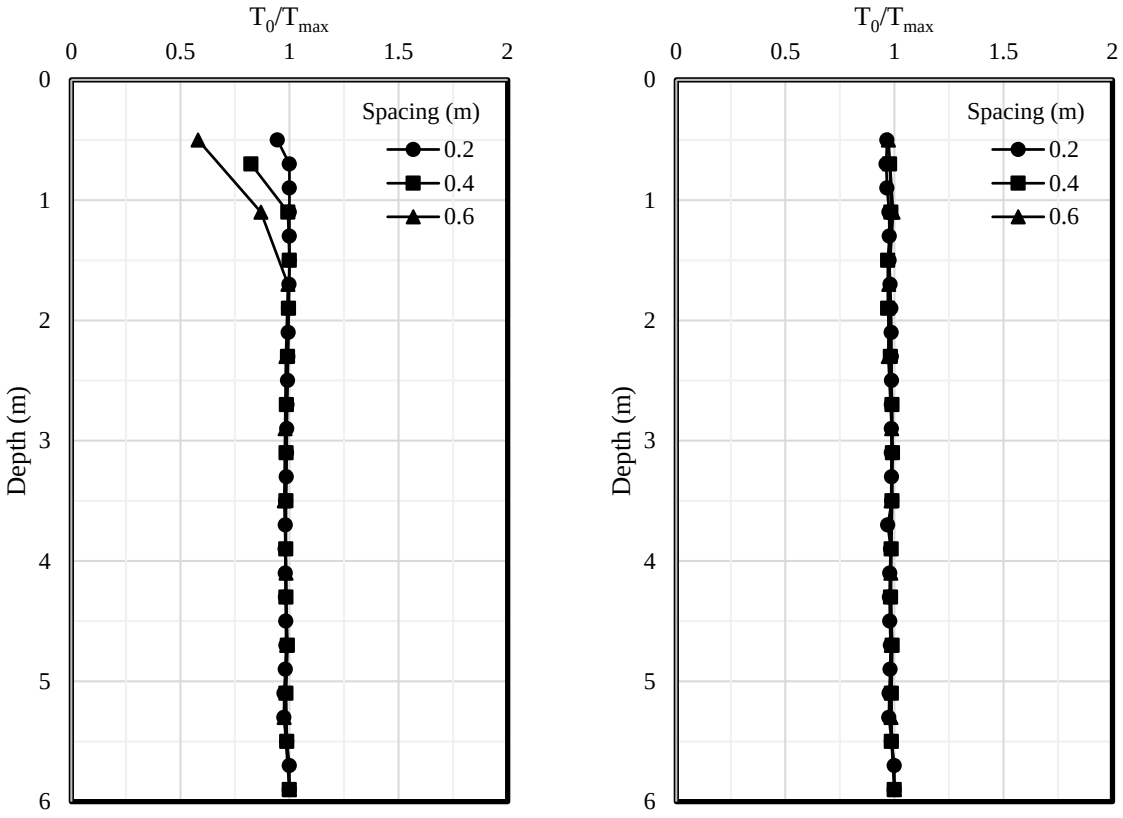

(a) Under self-weight of the wall (b) Under bridge slab and traffic load

Figure 8.4.13: Effect of reinforcement spacing on the connection force of the reinforcement: (a) Under self-weight of the wall; (b) Under bridge slab and traffic load.

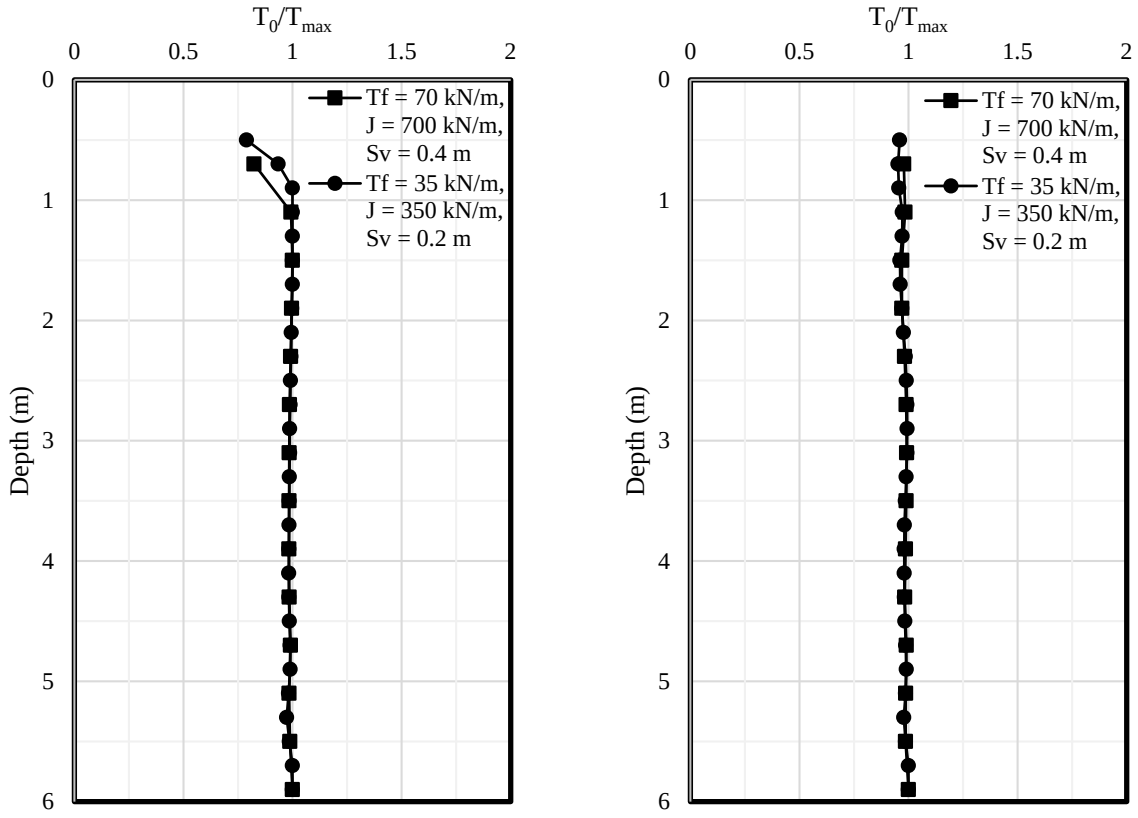

(a) Under self-weight of the wall (b) Under bridge slab and traffic load

Figure 8.4.14: Effect of combination of reinforcement stiffness and spacing on the connection force of the reinforcement: (a) Under self-weight of the wall; (b) Under bridge slab and traffic load.

8.4.4 EFFECT OF S_v ON STRESS DISTRIBUTION AND DESIGN OF BEARING SEATS

In order to provide the basis for the recommended effect of S_v on stress distribution and the design of bearing seats, as presented in Section 8.3.4, the different research outcomes from this NCHRP study were holistically assessed. They are presented next.

8.4.4.1 FIELD RESEARCH OUTCOMES THAT SUPPORT THE PROPOSED RECOMMENDATIONS

For the case of geosynthetic-reinforced soil structures with closely spaced-reinforcement, the results from field monitoring programs and numerical simulations show that the maximum vertical stress induced at various depths below the bearing seat agrees reasonably well with predictions obtained from analytical solutions such as that of Boussinesq. However, the maximum vertical stress was found to also agree well with the predictions obtained using approximate solutions such as pyramid stress distribution, especially when considering its truncation as recommended by Berg et al. (2009).

Figure 8.4.15 shows the stress distribution before and after placement of the bridge superstructure at the Founders Meadows load-carrying GMSE bridge abutment. It should be noted that the dashed lines in the figure correspond to measured values while solid lines correspond to predictions obtained using the Boussinesq approach. As illustrated in the figure, there is good agreement between measured vertical stresses and analytically predicted values.

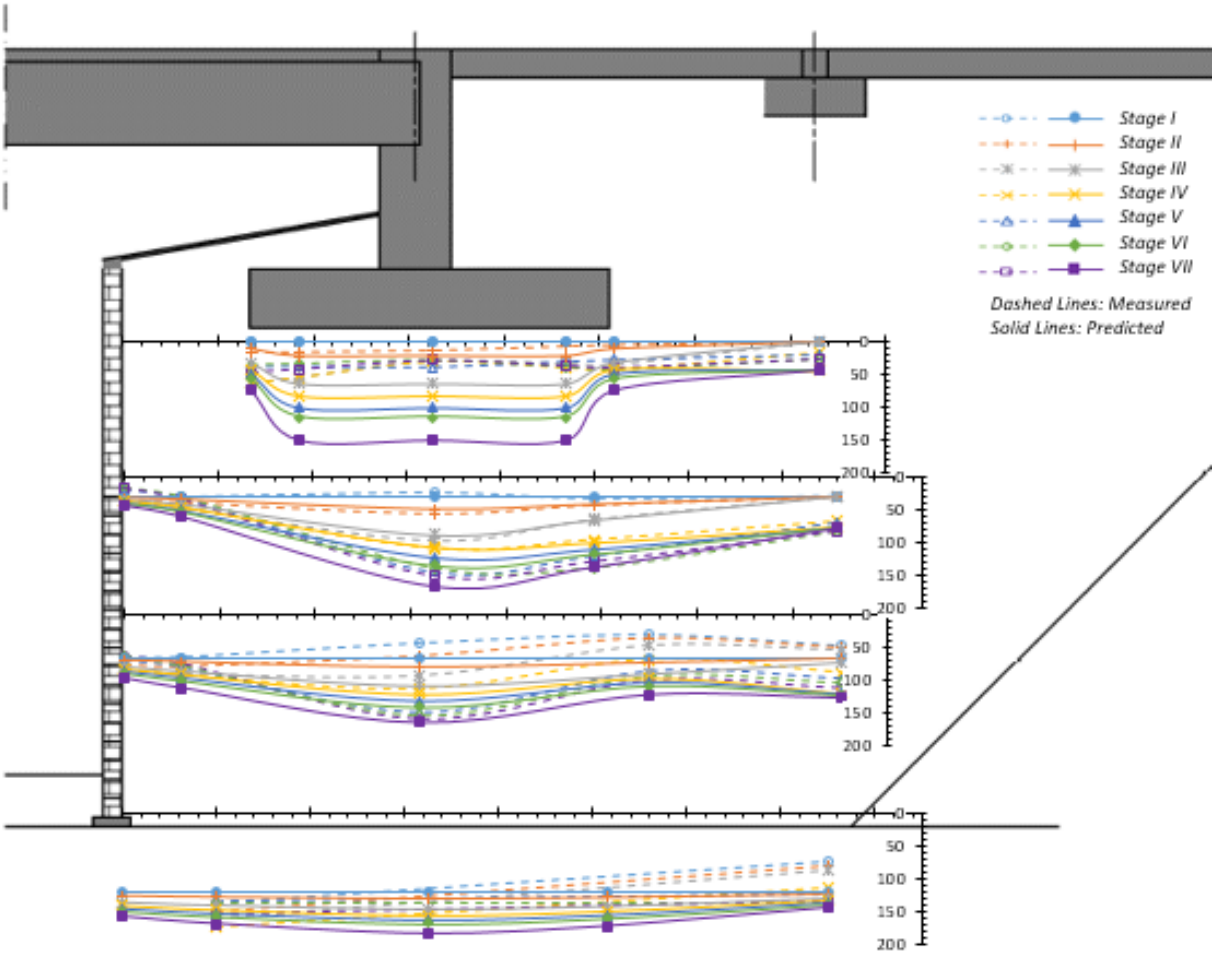

Figure 8.4.15: Stress distribution within the GMSE mass during the various construction stages of the Founders Meadows load-carrying GMSE bridge abutment (Note: stress values in kPa)

The effect of the bearing bed zone on the vertical stress distribution within the fill of the Virginia GRS-IBS structure was evaluated based on the stress distribution within the structure after placing the bridge slab load. The evaluation was conducted by comparing the field monitoring data from earth pressure cells with the stress distribution estimated using AASHTO's 2:1 approach and FHWA's recommended Boussinesq theoretical approach, as used in design of MSE wall and GRS-IBS. Figures 8.4.16 and 8.4.17 provide the results for abutments A and B, respectively, of the GRS-IBS constructed in Virginia and reported in detail in Chapter 6. Overall, the stress distribution profile obtained using field monitoring results was in agreement with the predicted stress distributions. It was observed that the load from the slab was transferred to the foundation through the bearing bed zone. The thickness of the bearing bed was the same in both

abutments, with the bearing bed proving effective in reducing the applied slab load to about half. However, this reduction was more evident in the case of Abutment A than in Abutment B. This is most likely because the vertical stresses in Abutment A (with smaller beam seat width) were higher than those in Abutment B.

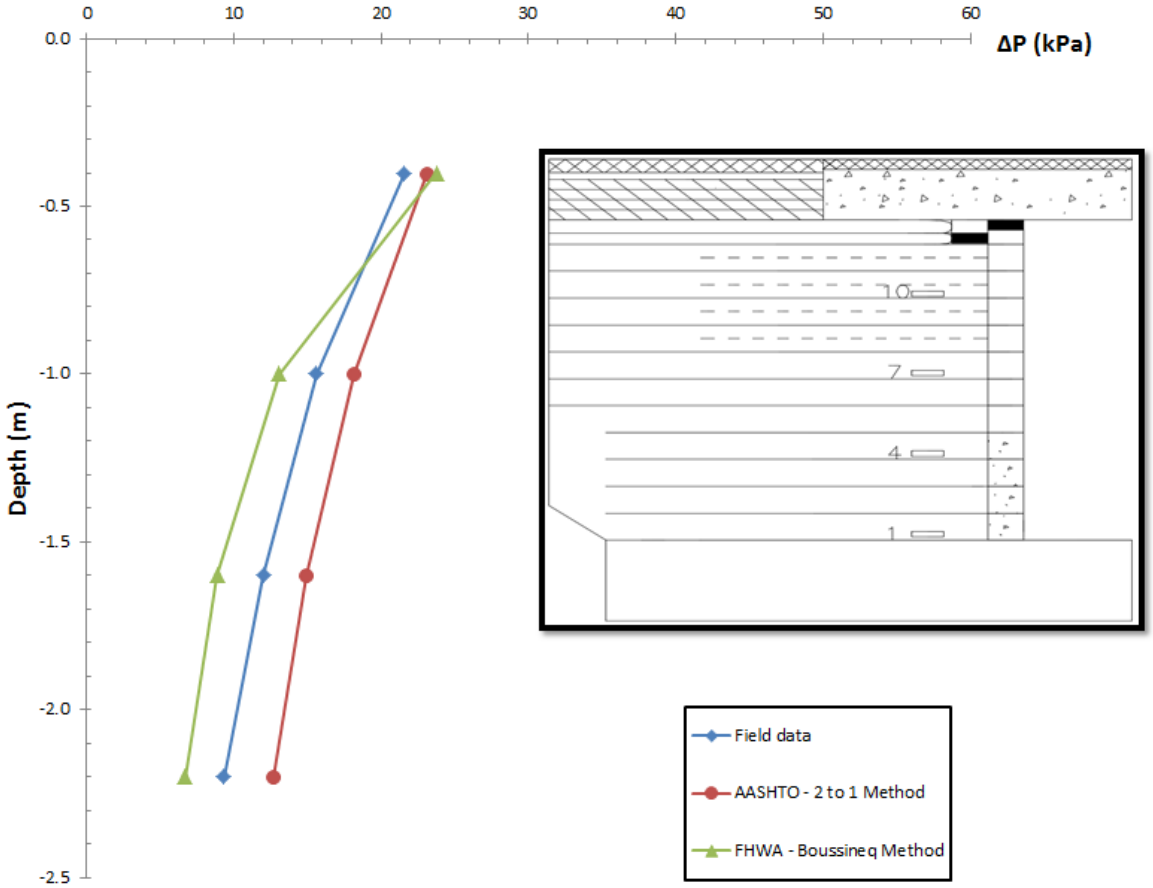

Figure 8.4.16: Vertical stress distribution due to slab load in abutment A of VDOT GRS-IBS
Note: Field data refers to pressures measured from the earth pressure cells shown in the insert of this figure (i.e. EPCs 1, 4, 7, and 10).

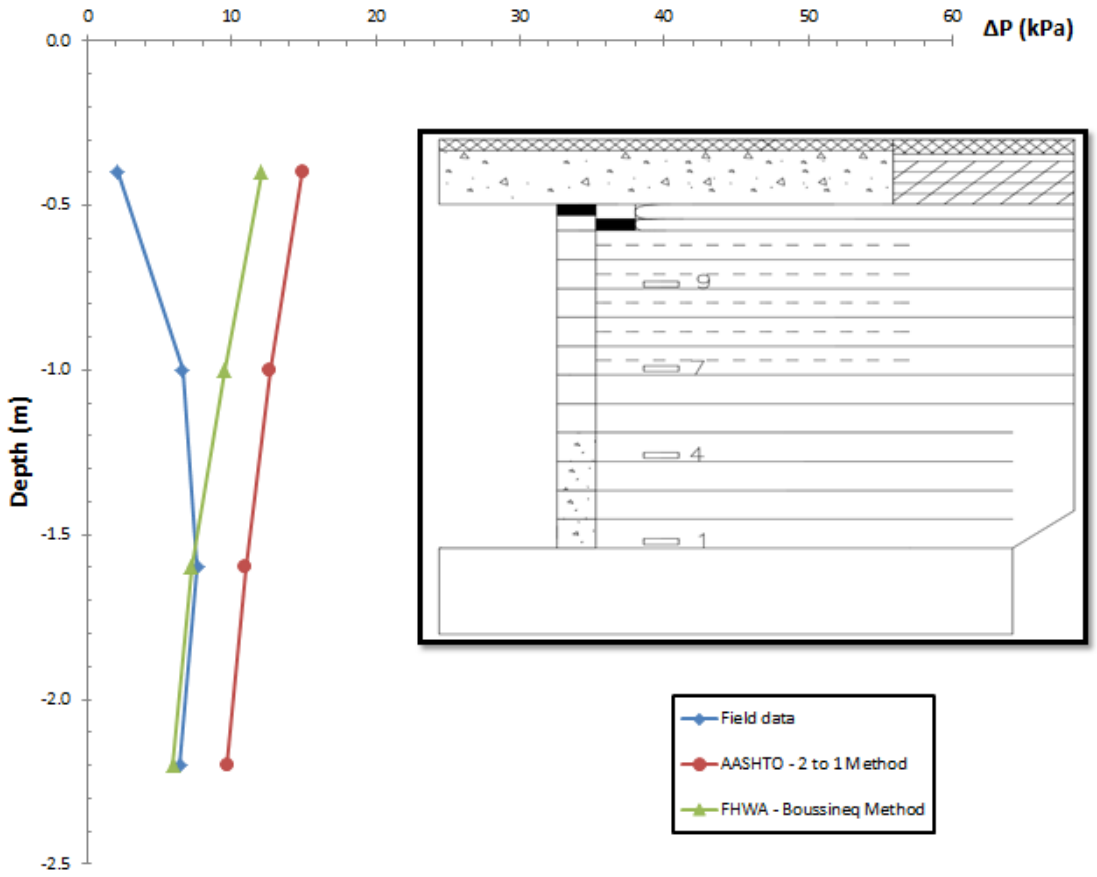

Figure 8.4.17: Vertical stress distribution due to slab load in abutment B of VDOT GRS-IBS
Note: Field data refers to pressures measured from the earth pressure cells shown in the insert of this figure (i.e. EPCs 1, 4, 7, and 9).

8.4.4.2 NUMERICAL SIMULATION OUTCOMES THAT SUPPORT THE PROPOSED RECOMMENDATIONS

The results of numerical simulations of mini-piers revealed a significant effect of the reinforcement spacing on the profile with depth of additional vertical stresses induced by surcharge loads. However, the results of numerical simulations of GRS-IBS structures showed a comparatively smaller effect. Figure 8.4.18 shows the effect of the reinforcement spacing on the distribution with depth of surcharge-induced vertical stress Δp at 0.5 m (1.6 ft) from the back of CMU facing blocks. It also shows the predicted surcharge-induced vertical stress predicted using the AASHTO 2 to 1 truncated method. The results shown in the figure illustrate that the surcharge-induced vertical stress Δp was not significantly affected by the reinforcement vertical spacing. An increasing reinforcement spacing was found to result in a slightly lower surcharge-induced vertical stress. AASHTO's 2 to 1 truncated method was found to predict the surcharge-induced stresses that were in reasonably good agreement with the numerical predictions.

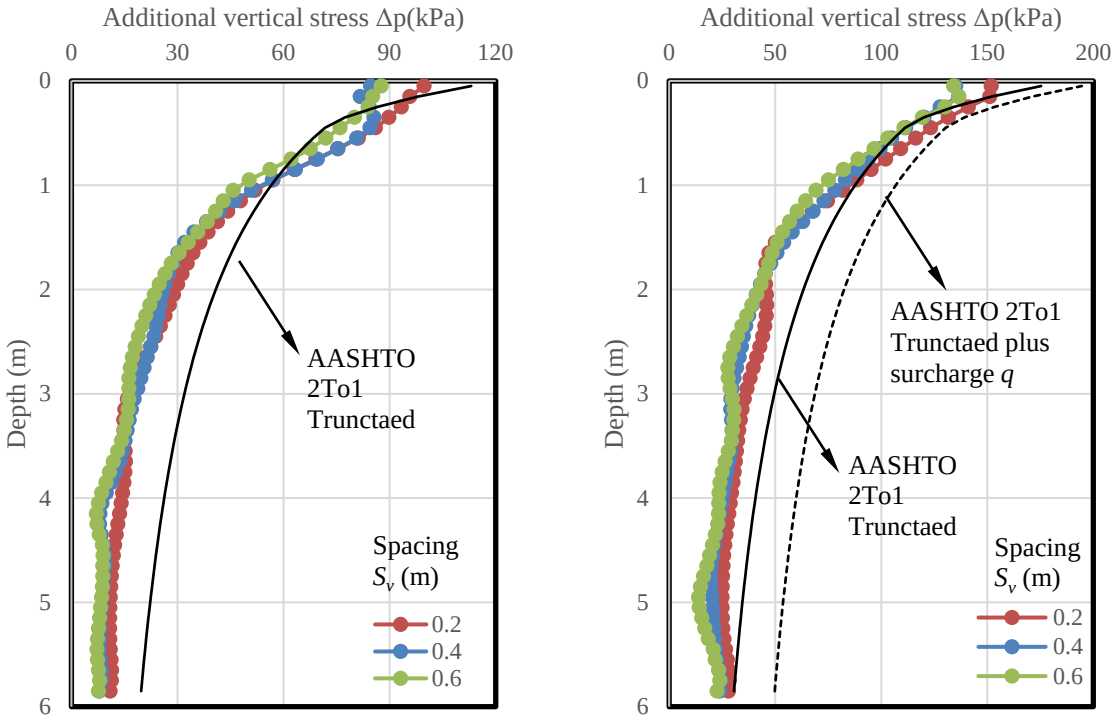

(a) Induced by bridge slab weight (b) Induced by bridge slab weight and traffic loads

Figure 8.4.18: Effect of the reinforcement spacing on the surcharge-induced vertical stresses: (a) Induced by the weight of the bridge slab; (b) Induced by the weight of the bridge slab and the traffic load.

Figure 8.4.19 shows the combined effect of reinforcement stiffness and vertical spacing on the distribution with depth of surcharge-induced vertical stress Δp applied at 0.5 m (1.6 ft) from the back of CMU facing blocks. The results show that the surcharge-induced vertical stress was similar for the two cases being compared, except for comparatively minor differences towards the top of the wall. Also in this case, AASHTO's 2 to 1 truncated method was found to lead to surcharge-induced vertical stresses that are in reasonably good agreement with the numerical results.

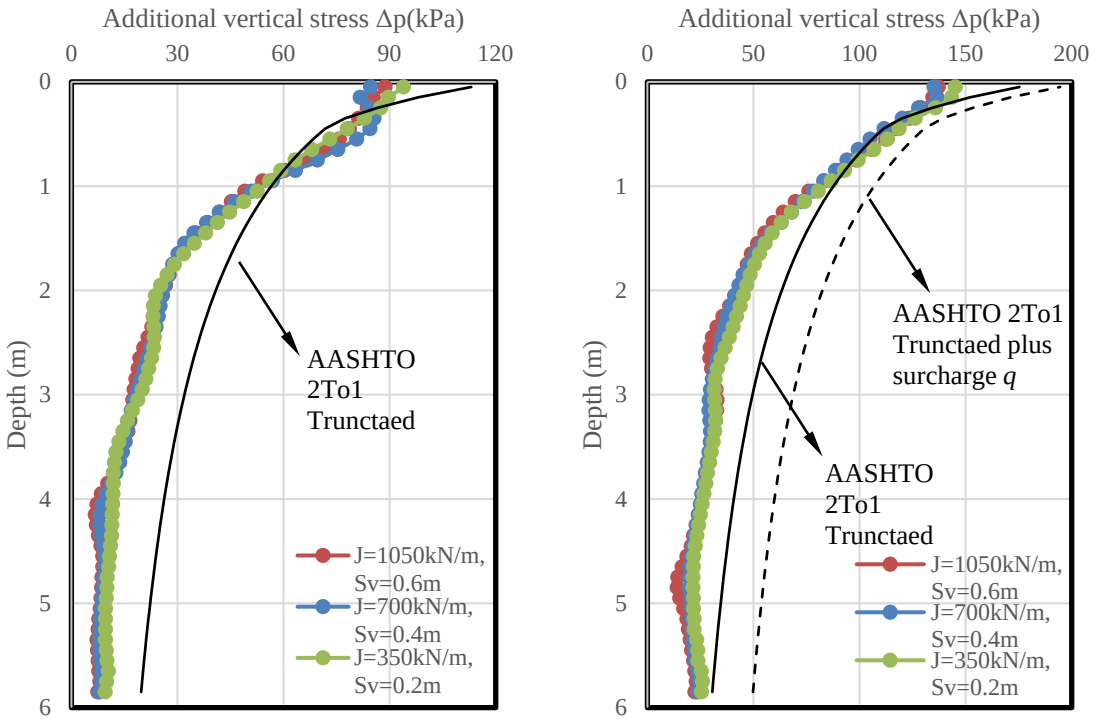

(a) Induced by bridge slab weight (b) Induced by bridge slab weight and traffic loads

Figure 8.4.19: Combined effect of reinforcement stiffness and vertical spacing on surcharge-induced vertical stresses: (a) Induced by the weight of the bridge slab; (b) Induced by the weight of the bridge slab and the traffic load.

8.4.5 EFFECT OF S_v ON VERTICAL AND LATERAL DEFORMATIONS

Reinforcement vertical spacing was found to significantly affect the vertical and lateral deformation response of GMSE structures, particularly under bridge loading. This effect was identified as a result of the parametric numerical evaluation reported in Chapter 7 of this report. The lateral deformation limits reported in the two current national design guidelines, AASHTO (2017)/FHWA 2009 (Christopher et al. 1990) for GMSE structures and FHWA (2012, 2018) for GRS-IBS were compared to these numerical predictions as well as to data from field monitoring projects reviewed in this study in order to establish recommendations for revising the AASHTO design specifications. The AASHTO (2017)/FHWA (2009) method provides a first order, empirically derived approach to evaluate maximum anticipated movement during construction. The approach uses the information presented in Figure 8.4.20 to define the reinforced soil wall deformation coefficient (δ_R) for a given reinforcement length (L) to wall height (H) ratio.

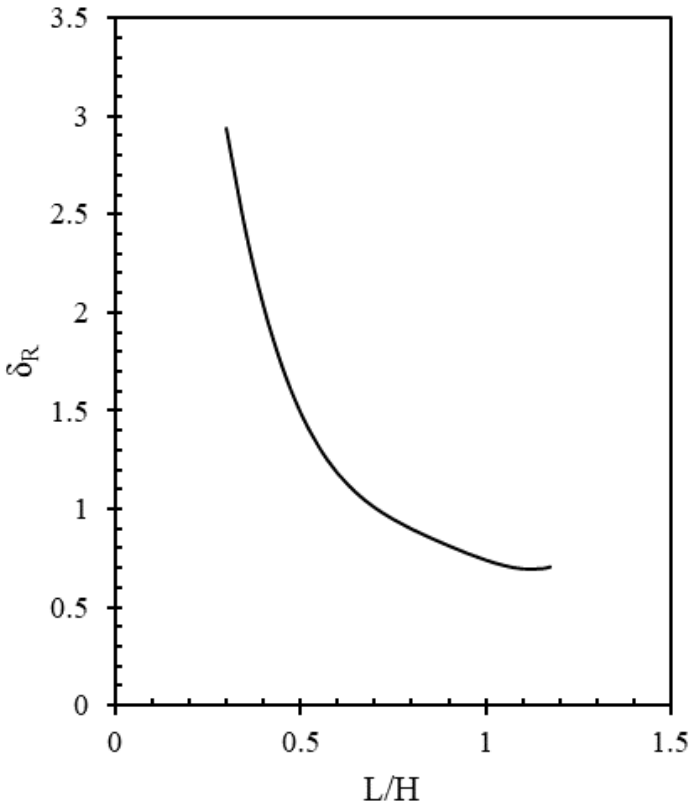

Figure 8.4.20. Variation of the reinforced soil wall deformation coefficient (δ_R) with L/H ratio

The curve in Figure 8.4.20 can also be expressed as follows:

$$\delta_R = 11.81\left(\frac{L}{H}\right)^4 - 42.25\left(\frac{L}{H}\right)^3 + 57.16\left(\frac{L}{H}\right)^2 - 35.45\left(\frac{L}{H}\right) + 9.471 \qquad \textit{[Equation 8.4.3]}$$

Using the calculated value of δ_R, the maximum lateral deformation can then be calculated for extensible geosynthetic type and inextensible steel type reinforcements, as follows:

$$\delta_{max} = \frac{\delta_R H}{75} \qquad (extensible\ reinforcement) \qquad \textit{[Equation 8.4.4]}$$

$$\delta_{max} = \frac{\delta_R H}{250} \qquad (inextensible\ reinforcement) \qquad \textit{[Equation 8.4.5]}$$

where: δ_R is a dimensionless reinforced soil wall deformation coefficient,
L is the reinforcement length (in units of *H*),
H is the wall height measured from the top of the leveling pad (in units of either ft. or m), and
δ_{max} is the maximum lateral deformation of reinforced soil wall (in units of *H*).

The basis for having two forms of the equation (i.e. for inextensible and for extensible) pertains to the global stiffness of the wall (S_r) (i.e., the average reinforcement stiffness over the wall face

area). The prediction equation uses the *L/H* ratio (ranging between 0.3 and 1.175) and the reinforcement type. It should be noted that this equation was developed to predict the maximum lateral displacement of a wall during its construction, which is rarely measured in practice. While this model does not directly predict the additional lateral displacement that can take place upon the application of surcharge loads, Christopher et al. (1990) stated that for a 6-m (20-ft) high wall, each additional 20 kPa (417 psf) of surcharge load results in a 25% increase in the relative deformation.

The FHWA (2012,2018) method of evaluating lateral deformation relies on vertical deformation data collected from mini-pier tests, and established the following approach to determine the Lateral deformation D_L:

$$D_L = 2\ x\ b_{q,vol}\ x\ \frac{D_V}{H} \qquad \textit{[Equation 8.4–6]}$$

where: D_L is the maximum lateral displacement,
$b_{q,vol}$ is the width of the load along the top of the wall including the setback, and
D_V is the vertical settlement of the load, and H is the height of the structure.

$$\varepsilon_L = \frac{D_L}{b_{q,vol}} = \frac{2D_V}{H} = 2\varepsilon_V \qquad \textit{[Equation 8.4–7]}$$

where: ε_L is the maximum lateral strain, and
ε_V is the vertical strain.

Both methods have been previously compared to field measurements along with a number of other methods proposed in the technical literature.

Bathurst et al. (2010) reviewed vertical limits established by 11 design codes as compared to a database of wall performance. In that study, they concluded that the AASHTO/FHWA method provided a reasonable upper limit in most cases for end-of-construction movements for walls constructed on firm foundations. However, both the vertical spacing of the reinforcement S_v and the facing varied considerably in the walls evaluated. The study also evaluated a careful set of full-scale wall tests that revealed that end of construction deformations are influenced by both compaction effort and global reinforcement stiffness when other factors remain unchanged. This effort is somewhat related to changing the spacing of reinforcements with the same modulus. In this case, the wall global stiffness would increase proportionally to the decreased spacing, as reviewed later in this section.

Based on a comparison of seven methods, a study by Khosrojerdi et al. (2017) the method reported in FHWA (2012) was found to be one of the best in predicting lateral deformations. Specifically, this method was only found to be slightly unconservative, as it predicted lateral deformations that were on average 88% of the actual measured values. The method was also found to have good reliability when compared to other methods with a low COV value of 0.51 obtained for the 12 structures evaluated using that method. As noted by the authors, a limitation of this method is that the magnitude of the structure's vertical settlement must be known to

predict the lateral deformations. Otherwise, estimates of vertical settlement would need to be made, which would potentially increase the uncertainty of this method.

Khosrojerdi et al. (2017) also evaluated the AASHTO/FHWA method which, although it was found to be highly conservative, it was reported as having a fair reliability. The authors noted that the AASHTO/FHWA method requires few input parameters (height of the wall, length of reinforcement) and, consequently, can be used to provide a rough estimation of the maximum lateral deformation of GMSE walls even before construction. The authors also contribute the conservatism to different design and construction conditions before 1990, upon which this method was based, however, the Bathurst results were based on some walls constructed after that period of time. The conservatism that they identified in the method is likely due to the use of highly select backfill for the test walls that were the basis for the Khorsrojerdi et al. (2017) study. As indicated in their paper, "which may lead to smaller displacements compared to typical walls in the field because of special attentions in the test wall constructions." To overcome this apparent bias in the evaluation of the AASHTO/FHWA method, experimental GMSE wall structures with reliable lateral deformation data were carefully selected as part of the work conducted in this NCHRP study to calibrate the AASHTO/FHWA prediction method. The walls include the following:

- Two walls constructed in Stockbridge, Georgia in 1994 (Ling and Leshchinsky 1996). These walls are the same structures evaluated in Section 4.3 of this report (University of Delaware Studies). These walls were constructed with an *L/H* ratio of 0.3. While this *L/H* value is much smaller than that specified in AASHTO, it is still in the L/H range for which the AASHTO/FHWA lateral deformation prediction model was developed. The lateral deformations of these walls were monitored during construction as well as after construction completion and application of fill surcharge. The vertical reinforcement spacing values in these walls were 0.4 and 0.8 m (1.3 and 2.6 ft). These structures were selected because of the availability to the authors of the displacement data collected during construction, which is deemed a rare dataset.
- One wall reported by Begnini et al. (1996). This wall was monitored after construction, so it provided data for calibration of surcharge-induced displacements only. This wall was constructed with an *L/H* ratio of 0.34 and vertical reinforcement spacing of 0.5 m (20 in.). Additional displacement readings were recorded with time in this wall under constant surcharge after the maximum load was applied. Only displacement data due to increasing surcharge load was collected. This structure was selected to account for surcharge-induced lateral displacements (i.e. post-construction lateral displacements).
- One wall reported by Bathurst et al. (1993), which was monitored after construction and, consequently, it provided data for calibration of surcharge-induced displacements only. This wall was constructed with an *L/H* ratio of 0.70 and vertical reinforcement spacing of 0.8 m (32 in.). Additional displacement readings were recorded in this wall with time and constant surcharge after maximum surcharge was reached. Only displacement data due to increasing surcharge load was collected. This structure was selected to account for surcharge-induced lateral displacements (i.e. post-construction lateral displacements).

The AASHTO/FHWA model was modified to account for the global stiffness of the structure, which was the genesis of the model development . The proposed modifications include the following: (1) Modifying the equation to become a function of the *J/Sv* ratio; and (2) Introducing a surcharge-induced component into the equation. The resulting formulation is as follows:

$$\delta_R = 11.81\left(\frac{L}{H}\right)^4 - 42.25\left(\frac{L}{H}\right)^3 + 57.16\left(\frac{L}{H}\right)^2 - 35.45\left(\frac{L}{H}\right) + 9.471 \qquad \textit{[Equation 8.4–8]}$$

$$\delta_{max} = \left(\frac{\delta_R H}{50\frac{J}{S_v}\cdot\frac{1}{p_o}}\right) x \left(1 + 1.25\frac{q}{p_o}\right) \qquad (extensible\ reinforcement) \qquad \textit{[Equation 8.4–9]}$$

where: δ_R *is an empirically derived relative displacement coefficient (dimensionless),*

H is the height of the *wall* and the units of *H* in equation 8.4.9 defines the units of the maximum estimated lateral deformation δ_{max},

J is the reinforcement tensile stiffness defined by the secant modulus at 2% strain,

S_v is the reinforcement vertical spacing (in units of *H*),

q is the surcharge magnitude, and

p_o is atmospheric pressure introduced in the equation for normalization purposes.

It should be noted that the second term (multiplier) in Equation 8.4.6 includes in turn two terms: the unity term, which corresponds the maximum lateral displacement during construction, and the surcharge term, which corresponds the maximum lateral displacement induced by surcharge only. Figure 8.4.21 presents the predicted versus measured maximum displacements for the four structures evaluated in this study. For those walls whose displacements were only measured post construction (including surcharge-induced displacements), Equation 8.4.9 was used but without the unity term.

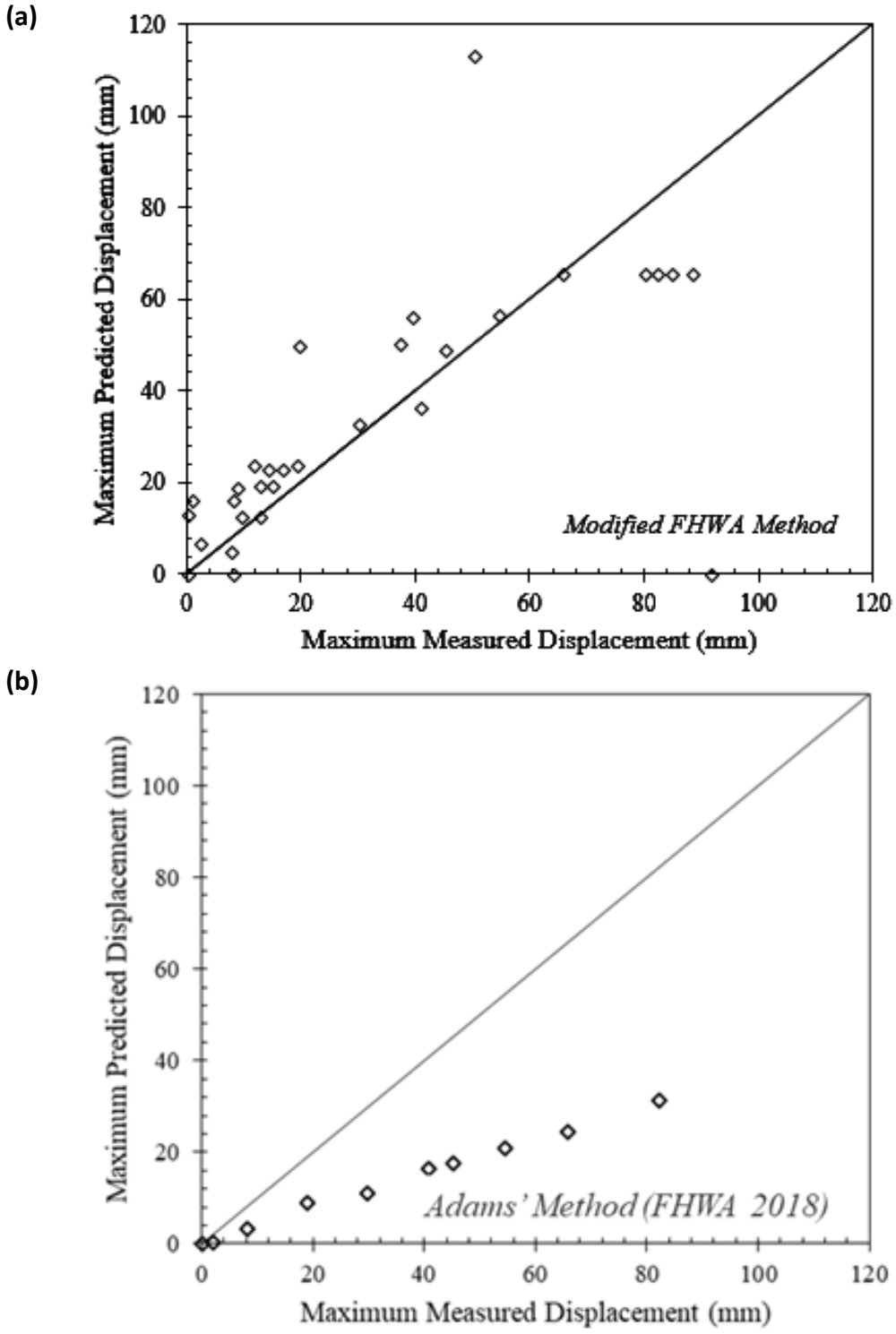

Figure 8.4.21. Predicted versus measured maximum displacements using the proposed model: (a) Modified FHWA Method; (b)FHWA 2018 Method

The comparison shown in Figure 8.4.2 reveals good agreement between the lateral displacements predicted using the proposed modified method and field displacement measurements. Consequently, the modifications proposed for the equations are deemed adequate for incorporation into AASHTO for prediction of lateral displacements in GMSE structures with closely-spaced reinforcements.

Based on these findings, it is recommended that in cases where the vertical displacements are known (can be accurately predicted) in load-carrying GMSE bridge abutments, the lateral deformation be estimated as approximately 2 times the vertical movement, which is in agreement with the method in FHWA (2018). However, in cases where vertical displacement measurements are not available, the proposed modified AASHTO approach be used for both free standing walls as load-carrying GMSE bridge abutments (or walls with generic surcharge loads). The recommended approach should only be adopted for the case of walls constructed using high quality backfill, which were the basis for calibration of the model.

8.4.6 EFFECT OF S_v ON BUMP AT THE END OF THE BRIDGE

In order to provide the basis for the recommended effect of S_v on the development of a "Bump at the End of the Bridge," as presented in Section 8.3.6, the different research outcomes from this research project were holistically assessed. The recommendations apply for the case of load-carrying GMSE bridge abutments, which as a design concept already aim at minimizing the bump at the end of the bridge. Among these structures, systems designed with closely-spaced reinforcement (e.g. GRS-IBS) were analyzed. The basis for the recommendations to the AASHTO design method are presented next.

8.4.6.1 FIELD RESEARCH OUTCOMES THAT SUPPORT THE PROPOSED RECOMMENDATIONS

The potential reduction of the bump at the end of the bridge when adopting closely-spaced reinforcement was evaluated using field data reported by others as well as site visits to three projects conducted as part of this study. The structures whose data was gathered during this study include the VDOT wall project (reported in Chapter 5), the Founders Meadows CDOT project (reported in Sections 4.5 and 4.6.4), and the MnDOT GRS-IBS project, also referred to as Rock County GRS-IBS (Reported in Section 4.6.2). At each of these sites, the existence of a bump at the bridge super-structure was monitored through visual inspections, level monitoring of the road surface during site visits, and survey data available from the relevant state DOT. The condition surveys during field visits focused mainly on the intersection of the bridge slab and the integrated approach where a potential bump is expected to be visible. At the VDOT wall project, no bump was observed at the intersection of the bridge slab and the integrated approach on the road surface, as shown in Figure 8.4.22. Abu-Hejleh et al. (2002) reported on the transition from bridge deck to approaching roadway at the Founders Meadows load-carrying GMSE abutment and reported no indication of the development of the bump at the end of the bridge. Complementing this initial reporting, the results in Figure 8.4.23 shows the results of surveys of the Founders Meadows bridge as collected during the initial 5 years after opening to traffic and as recently as 2016 (i.e. 17 years after opening to traffic). As shown in figure, the profiles reveal

no development of a “bump at the end of the bridge”. On the other hand, the visit to the MnDOT GRS-IBS project revealed that “bumps” had developed at both ends of the bridge, as shown in Figure 8.4.24. Survey data provided by MnDOT provides a direct measure of the magnitude of the bumps as shown in Figure 8.4.25. It should be noted that this structure had a significant slope and skew, which may have contributed to the occurrence of the observed nonconformities.

Figure 8.4.22: Road surface level monitoring at the intersection of bridge super-structure and integrated approach 2.5 years after construction in VDOT GRS-IBS

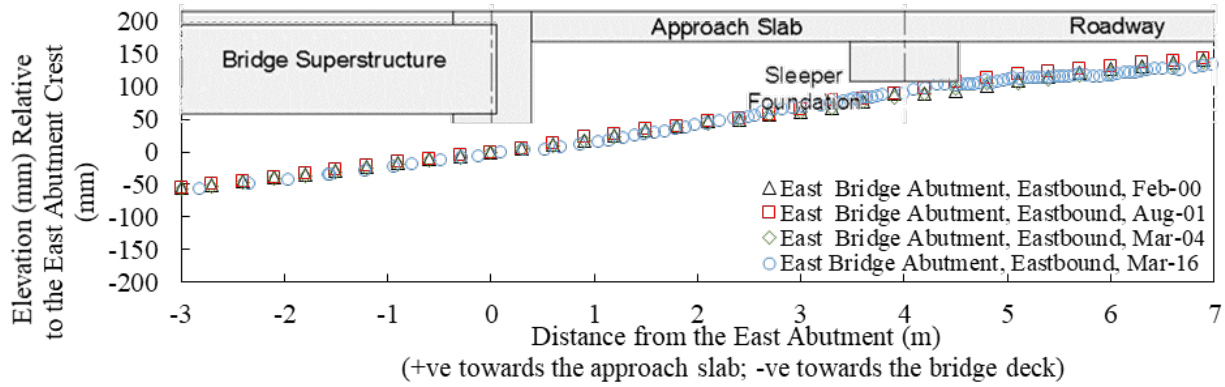

Figure 8.4.23. Profilometer measurements at the Founders/Meadows bridge abutment

a) b)

Figure 8.4.24. Settlement at the MnDOT GRS-IBS: a) North Abutment; b) South Abutment

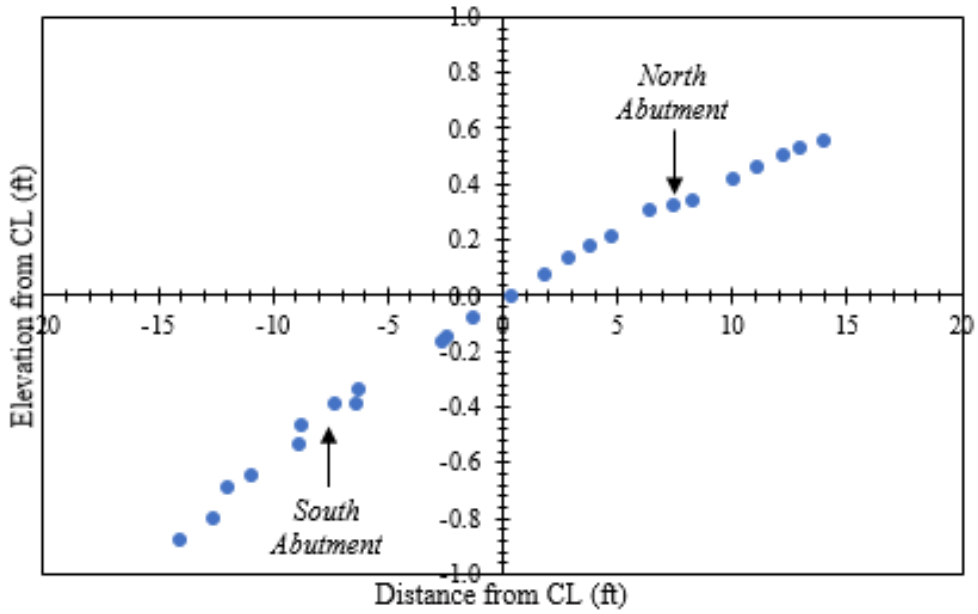

Figure 8.4.25. Longitudinal Profile at the North and South ends of the MnDOT GRS-IBS project

In addition to site visits, a report providing IRI data and surface profiles of the approaching roadways over five GRS-IBS structures constructed in St. Lawrence, New York were reviewed. The projects were constructed from 2009 to 2011. The surveys were performed several years after construction (2013) and the sites were visually observed in 2013 as part of this research project. Neither the visual observations nor the profiles showed a "bump" at the transition from the approaching roadways and any of the bridges.

8.4.6.2 NUMERICAL SIMULATION OUTCOMES THAT SUPPORT THE PROPOSED RECOMMENDATIONS

Considering the results from field observations, especially the development of a bump at the ends of the MnDOT GRS-IBS, numerical simulations were conducted to evaluate the potential occurrence of a bump. Based on the numerical predictions of a structure representing a generic

GRS-IBS, the potential for the development of differential settlements at the end of the bridge slab could be identified, as shown in Figure 8.4.26. However, a decrease in reinforcement vertical spacing was found to have a significant impact in reducing the bump at the end of the bridge slab.

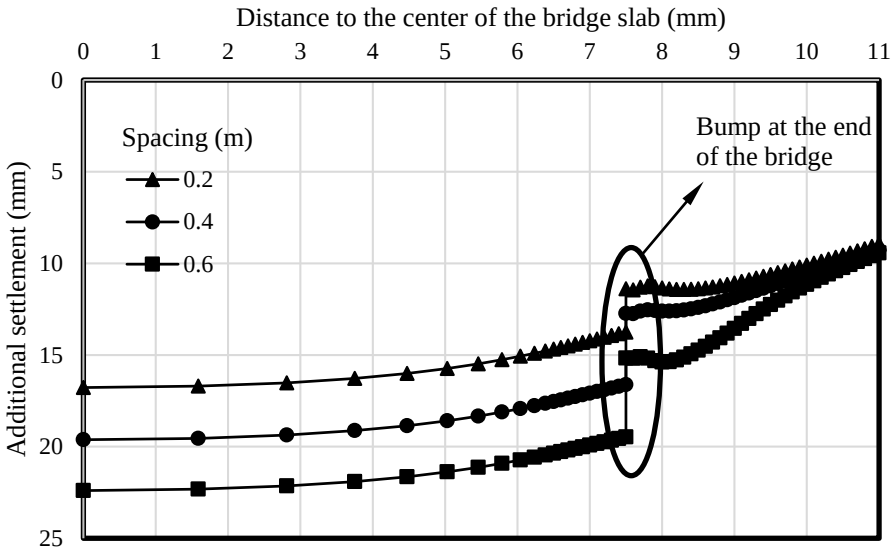

Figure 8.4.26: Effect of reinforcement spacing on the bum at the end of the bridge due to traffic load

Figure 8.4.27 shows the combined effect of reinforcement stiffness and spacing on the development, due to traffic loads, of a bump at the end of the bridge. When the same ratio J/S_v (of T_f/S_v) is maintained, the impact of reinforcement vertical spacing was found to be comparatively small. However, it should be noted that the pavement structure of the approaching roadway was not modeled in this simulation, which could be credited with reduction in the potential development of a bump (FHWA 2012, 2018). Overall, the numerical predictions indicate significant benefit of increasing the reinforcement density under the bearing seat or bridge wing walls, beyond the reinforcement required to provide the target total tensile capacity.

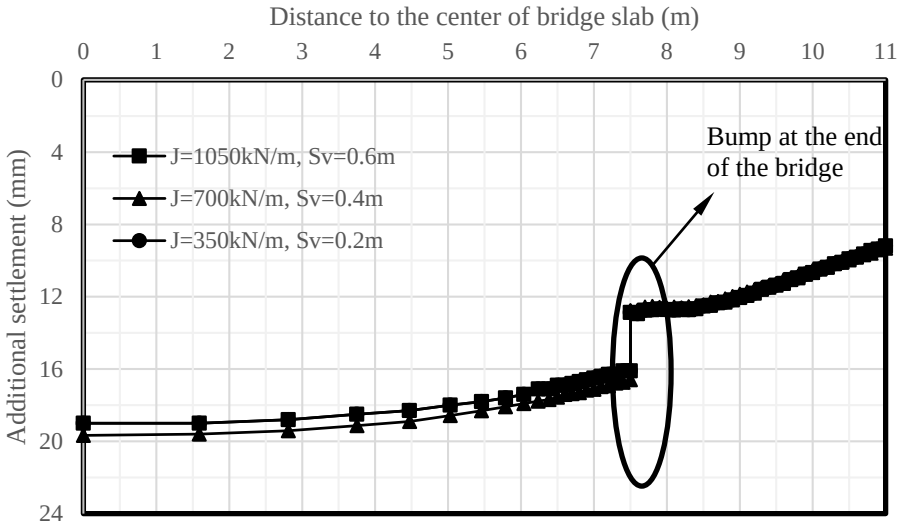

Figure 8.4.27: Combined effect of reinforcement stiffness and spacing on the bump at the end of the bridge due to traffic load.

8.5 REFERENCES

AASHTO (2017) *LRFD Bridge Design Specifications*, 8th Edition, American Association of State Highway and Transportation Officials, Washington, DC, 1,780p.

Abu-Hejleh, N., Zornberg, J.G., Wang, T., and Watcharamonthein, J. (2002). "Monitored Displacements of Unique Geosynthetic-Reinforced Soil Bridge Abutment." Geosynthetics International, Vol. 9, No. 1, pp. 71-95.

Allen, T.M. and Bathurst, R.J. (2002a). "Soil reinforcement loads in geosynthetic walls at working stress conditions," *Geosynthetics International*, 9(5-6): 525-566.

Allen, T.M. and Bathurst, R.J. (2002b). "Observed long-term performance of geosynthetic walls, and implications for design," *Geosynthetics International*, 9(5-6): 567-606.

Allen, T. M., and R. J. Bathurst. 2003. *Prediction of Reinforcement Loads in Reinforced Soil Walls*. Report WA-RD 522.2. Washington State Department of Transportation, Olympia, WA.Allen, T.M., Christopher, B.R., Elias, V., and DiMaggio, J. (2001). "Development of the Simplified Method for Internal Stability Design of Mechanically Stabilized Earth Walls." Report No. WA-RD 513.1, Washington State Department of Transportation, Olympia, Washington.

Allen, T.M., and Bathurst, R.J., 2018, "Application of the Simplified Stiffness Method to Design of Reinforced Soil Walls," *ASCE Journal of Geotechnical and Geo-environmental Engineering*, DOI: http://dx.doi.org/ 10.1061/(ASCE)GT.1943-5606.0001874, 13 pp.

Bathurst, R.J., Simac, M.R., Christopher, B.R. and Bonczkiewicz, C. (1993). "A database of results from a geosynthetic reinforced modular block soil retaining wall," Proc. *Soil Reinforcement: Full Scale Experiments of the 80's*, ISSMFE/ENPC, Paris, France, November 1993, pp. 341-365.

Bathurst, R.J., Miyata, Y., Nernheim, A. and Allen, T.M. (2008). “Refinement of K-stiffness method for geosynthetic reinforced soil walls,” *Geosynthetics International*, 15(4): 269-295.

Bathurst, R.J., Miyata, Y and Allen, T.M. (2010) “Facing Displacements in Geosynthetic Reinforced Soil Walls,” *Earth Retention Conference 3 (ER2010)*, ASCE, Geo-Institute, Bellevue, Washington, 1-4 August, 18 p.

Begnini, C., Bosco, G., Cazzuffi, D., and De Col, R. (1996). “Construction and Performance of an Experimental Large-Scale Wall Reinforced with Geosynthetics.” In Proceedings of Earth Reinforcements, Ochiai, Yasufuku & Omine (eds), 1996 Balkema, Rotterdam, pp. 315-320.

Christopher, B.R. (1989) Reinforced Soil Structures, Volume II. Summary of Research and Systems Information, U.S. Department of Transportation, Federal Highway Administration, Washington DC, Report No. FHWA-RD--89-043, Nov 1989, 158 p.

Christopher, B.R. (1993). "Deformation Response and Wall Stiffness in Relation to Reinforced Soil Wall Design." Ph.D. Dissertation, Department of Civil Engineering, Purdue University, West Lafayette, IN, 354 p.

Christopher, B.R. (2013). "Review of June 18, 2013 GRS-IBS Showcase at Clarkson University, Potsdam, New York and St. Lawrence County Wall Visits." Memorandum by Christopher, B.R.

FHWA (1990) Christopher, B.R., Gill, S.A., Giroud, J.P., Juran, I. Scholsser, F., Mitchell, J.K. and Dunnicliff, J., (1990) Reinforced Soil Structures, Volume I. Design and Construction Guidelines, U.S. Department of Transportation, Federal Highway Administration, Washington DC, Report No. FHWA-RD--89-043, Nov 1989, 287 p.

FHWA (2001) *Mechanically Stabilized Earth Walls and Reinforced Soil Slopes, Design and Construction Guidelines*, Authored by Elias, V, and Christopher, B.R. and Berg, R.R., U.S. Department of Transportation, Federal Highway Administration, Washington DC, FHWA-NHI-00-043, 2001, 418 p.

FHWA (2006) *Soils and Foundations Reference Manual - Volume 2*, Authored by Samtani, N.C. and Nowatzki, E.A., U.S. Department of Transportation, Federal Highway Administration, Washington DC, FHWA-NHI-06-089, 594 p.

FHWA (2009) *Mechanically Stabilized Earth Walls and Reinforced Soil Slopes, Design and Construction Guidelines*, Authored by Berg, R.R., Christopher, B.R. and Samtani, N., U.S. Department of Transportation, Federal Highway Administration, Washington DC, FHWA-NHI-09-083 and FHWA GEC011, 2009, 668 p.

FHWA (2012). *Geosynthetic-reinforced Soil Integrated Bridge System, Interim Implementation Guide*, Authored by Adams, M., Nicks, J., Stabile, T., Wu, J., Schlatter, W., and Hartmann, J., Report No. FHWA-HRT-11-026, Federal Highway Administration, McLean, VA.

FHWA (2018). *Design and Construction Guidelines for Geosynthetic Reinforced Abutments and Integrated Bridge Systems*. Authored by Adams, M., and Nicks, J., Report No. FHWA-HRT-17-080, Federal Highway Administration, McLean, VA.

Iwamoto, M.K., Ooi, P.S.K., Adams, M.T., and Nicks, J.E. (2013). "Composite Properties from Instrumented Load Tests on Soil Columns Reinforced with Geotextiles." Transportation Research Broad, TRB 2014 Annual Meeting.

Iwamoto, M. K. (2014). Observations from load tests on geosynthetic reinforced soil (Doctoral dissertation, [Honolulu]: [University of Hawaii at Manoa], [May 2014]).

Khosrojerdi, S., Xiao, M., Qiu, T., Nicks, J. (2017) “Evaluation of Prediction Methods for Lateral Deformation of GRS Walls and Abutments,” Technical Note, Journal *of Geotechnical and Geoenvironmental Engineering,* ASCE, 143(2).

Ling, P. and Leshchinsky, D. (1996). "Mesa Walls: Field Data Reduction, Finite Element Analysis, and Preliminary Design Recommendations." Report to Tensar Earth Technologies, Inc., Atlanta, GA, February 1.

Leshchinsky, D. (2009), “On Global Equilibrium in Design of Geosynthetic Reinforced Walls,” ASCE, *Journal of Geotechnical and Geoenvironmental Engineering*, 2009, 135(3), 309-315.

Leshchinsky, D., Imamoglu, B., and Meehan, C. (2010). “Exhumed Geogrid-reinforced Retaining Wall.” Journal of Geotechnical and Geoenvironmental Engineering, ASCE, Vol. 136, No. 10, pp. 1311-1323.

Leshchinsky, D., Leshchinsky, B., and Leshchinsky, O., (2017). “Limit State Design Framework for Geosynthetic Reinforced Soil Structures,” *Geotextiles and Geomembrane*s, 45(6), 642-652.

Leshchinsky, D., Leshchinsky, O., Zelenko, B., and Horne, J., *Limit Equilibrium Design Framework for MSE Structures with Extensible Reinforcement*, FHWA-HIF-17-004, October 2016.

Leshchinsky, D. and Vahedifard, F. (2012), "Impact of Toe Resistance in Reinforced Masonry Block Walls: Design Dilemma," *Journal of Geotechnical and Geoenvironmental Engineering,* ASCE, 138(2), 2012, 236-240.

Mitchell, J.W., Behavior of Geosynthetically Reinforced Soil Bridge Piers, M.S. Report, University of Massachusetts at Amherst, 2002.

Miyata, Y. and Bathurst, R.J. (2007a). “Development of K-stiffness Method for geosynthetic reinforced soil walls constructed with c-ϕ soils,” *Canadian Geotechnical Journal*, 44(12): 1391-1416.

Miyata, Y. and Bathurst, R.J. (2007b). “Evaluation of K-stiffness Method for vertical geosynthetic reinforced granular soil walls in Japan,” *Soils and Foundations*, 47(2): 319-335.

Nicks, J. E., Adams, M. T., Ooi, P. S. K., & Stabile, T. (2013). Geosynthetic reinforced soil performance testing—Axial load deformation relationships. Report No. FHWA-HRT-13-066, Federal Highway Administration, McLean, VA.

Phillips, E.K., Filz, G.M., Berg, R.R., Brown, M.C. (2015). "Required Ultimate Geosynthetic Reinforcement Tensile Strengths According to Four Analysis Methods for MSE and GRS Walls." Geosynthetics 2015, Feb. 15-18, Portland, Oregon.

Soong, T-Y. and Koerner, R.M. (1997). "On the Required Connection Strength of Geosynthetically Reinforced Walls." *Geotextiles and Geomembranes*, Vol. 15, pp. 377-393.

Wu, J.T.H. (2001). *Revising the AASHTO Guidelines for Design and Construction of GRS Walls*. Report No. CDOT-DTD-R-2001-16, Colorado Department of Transportation, 148 p.

Wu, J. T., & Ooi, P. S. (2015). Synthesis of geosynthetic reinforced soil design topics. Report No. FHWA-HRT-14-094, Federal Highway Administration, McLean, VA.

Wu, J.T.H. and Pham, T.Q. (2014). "Closure to “Load-Carrying Capacity and Required Reinforcement Strength of Closely Spaced Soil Geosynthetic Composites”." Journal of Geotechnical and Geoenvironmental Engineering.

Wu, J.T.H., Pham, T.Q., and Adams, M.T. (2013). "Composite Behavior of Geosynthetic Reinforced Soil Mass." Report No. FHWA-HRT-10-077, Federal Highway Administration, McLean, VA.

Wu, J.T.H., Ketchart, K., and Adams, M.T. (2001). "GRS Bridge Piers and Abutments." Report No. FHWA-RD-00-038, Federal Highway Administration, McLean, VA.

Yogarajah, I., and Andrawes, K.Z. (1994), “Modeling Construction Effects in Polymeric Grid Reinforced Soil Walls,” Proceedings, 5th International Conference on Geotextiles and Related Products, Singapore, 1, 1994, pp. 177–182.

APPENDIX A: SI CONVERSION FACTORS

SI CONVERSION FACTORS				
APPROXIMATE CONVERSIONS FROM SI UNITS				
Unit	**When you know**	**Multiply By**	**To Find**	**Unit**
LENGTH				
mm	millimeters	0.039	inches	in
m	meters	3.28	feet	ft
m	meters	1.09	yards	yd
km	kilometers	0.621	miles	mi
AREA				
mm^2	sq. millimeters	0.0016	sq. inches	in^2
m^2	sq. meters	10.764	sq. feet	ft^2
m^2	sq. meters	1.195	sq. yards	yd^2
ha	hectares	2.47	acres	ac
km^2	sq. kilometers	0.386	sq. miles	mi^2
VOLUME				
ml	milliliters	0.034	fluid ounces	fl oz
l	liters	0.264	gallons	gal
m^3	cubic meters	35.71	cubic feet	ft^3
m^3	cubic meters	1.307	cubic yards	yd^3
MASS				
g	grams	0.035	ounces	oz
kg	kilograms	2.202	pounds	lb
TEMPERATURE				
°C	Celsius	1.8C+32	Fahrenheit	°C
WEIGHT DENSITY				
kN/m^3	kilonewton/cubic m	6.36	poundforce/cubic foot	pcf
FORCE and PRESSURE or STRESS				
N	newtons	0.225	poundforce	lbf
kN	kilonewtons	225	poundforce	lbf
kPa	kilopascals	0.145	poundforce/sq in.	psi
kPa	kilopascals	20.9	poundforce/ sq ft	psf

APPENDIX B: ADDITIONAL DATA FROM FIELD COMPONENT

This appendix is specifically created to supplement Chapter 6.

It is provided to present the after construction field instrumentation data from GMU-VDOT GRS-IBS site.

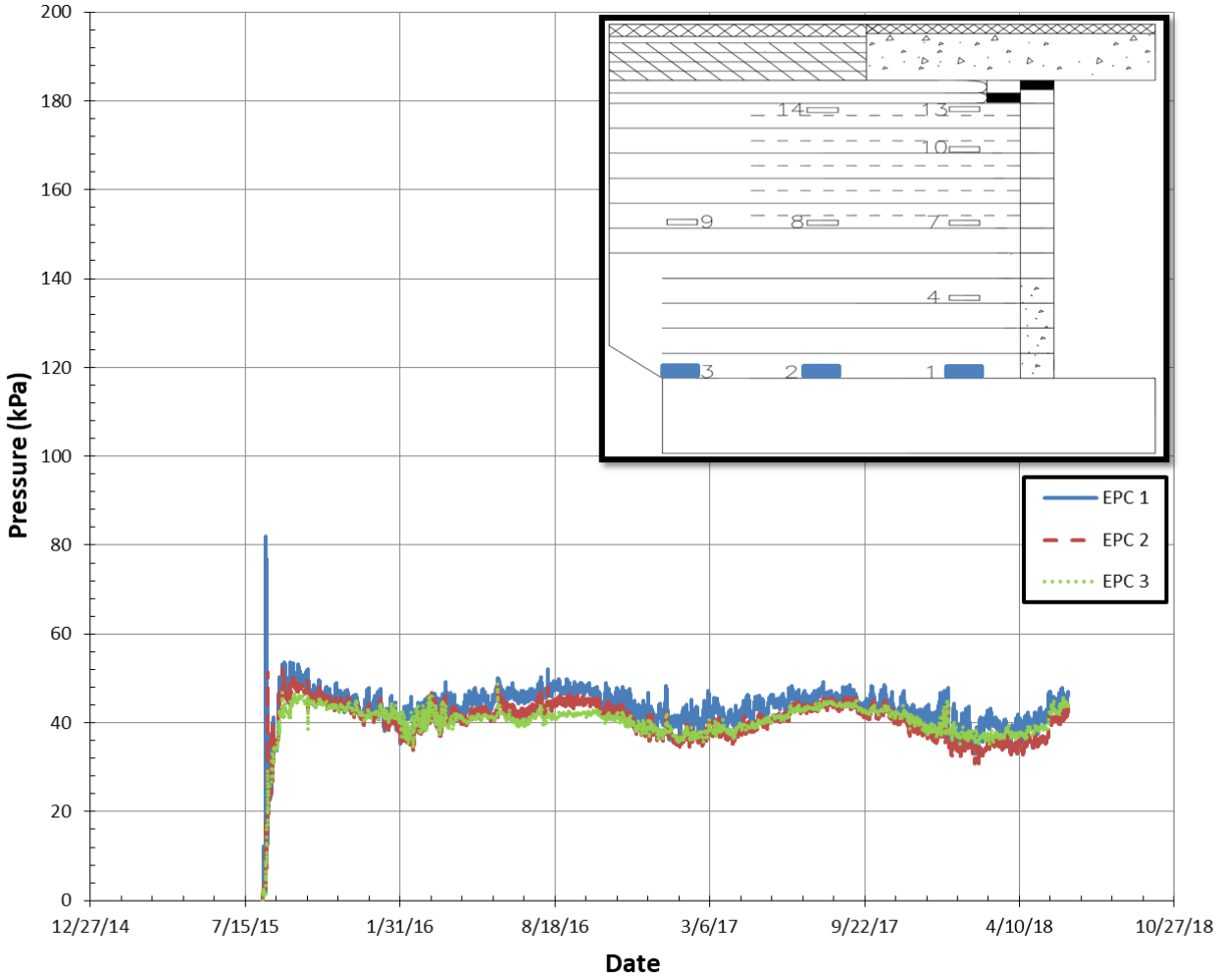

Fig. B1. Vertical stresses developed in layer 1 on Abutment A

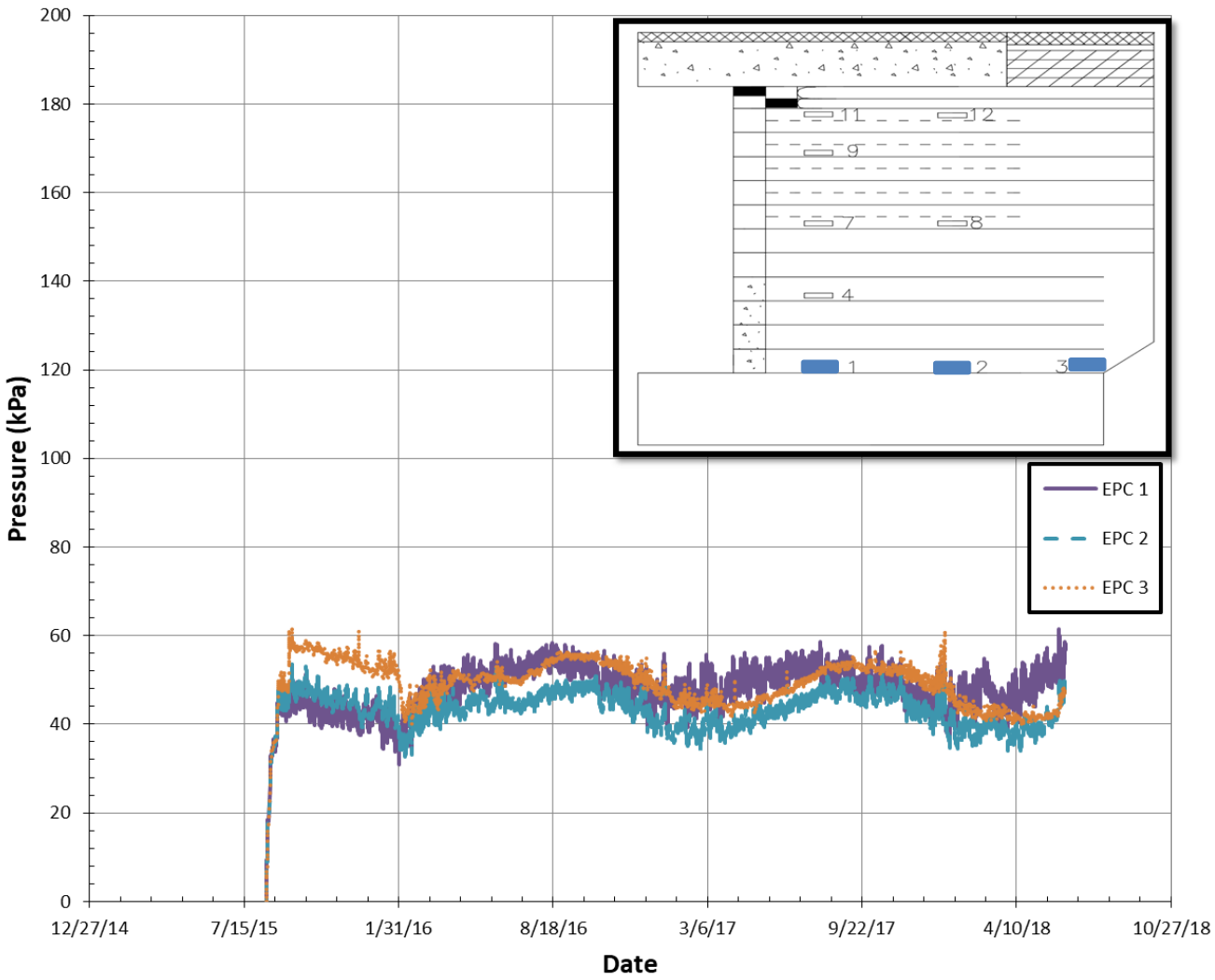

Fig. B2. Vertical stresses developed in layer 1 on Abutment B

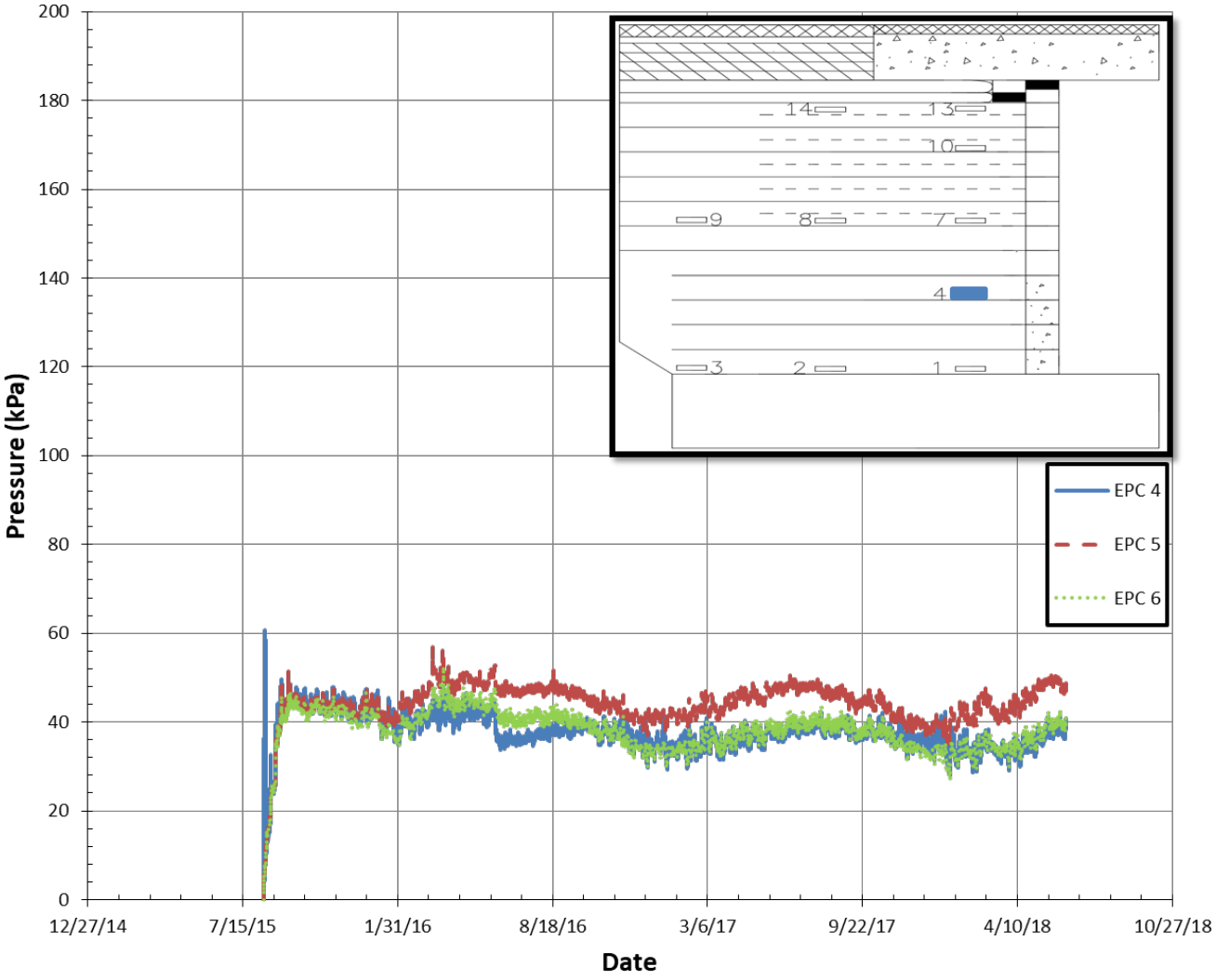

Fig. B3. Vertical stresses developed in layer 4 on Abutment A (EPC 5 and 6 are located on the North and South sides)

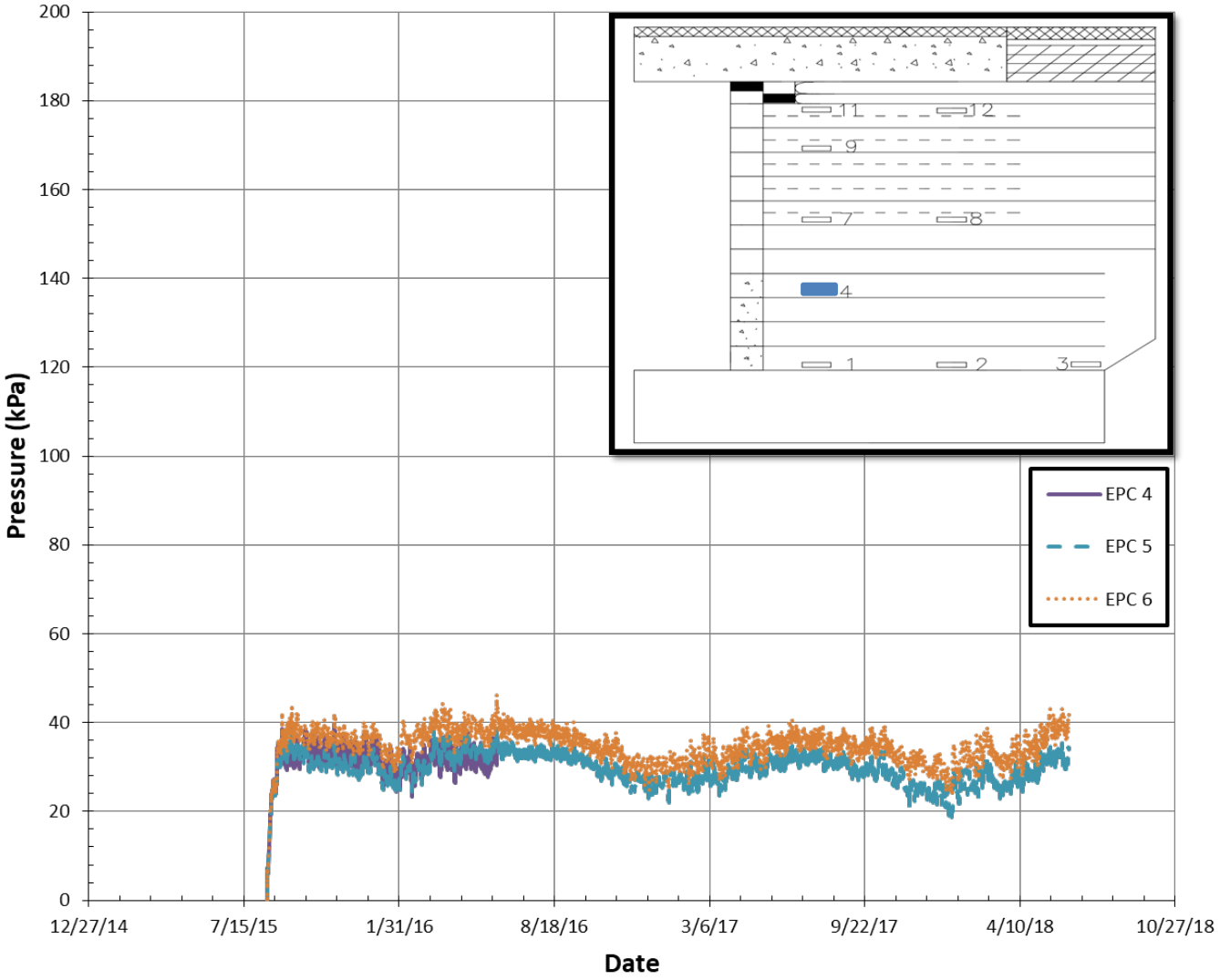

Fig. B4. Vertical stresses developed in layer 4 on Abutment B (EPC 5 and 6 are located on the North and South sides)

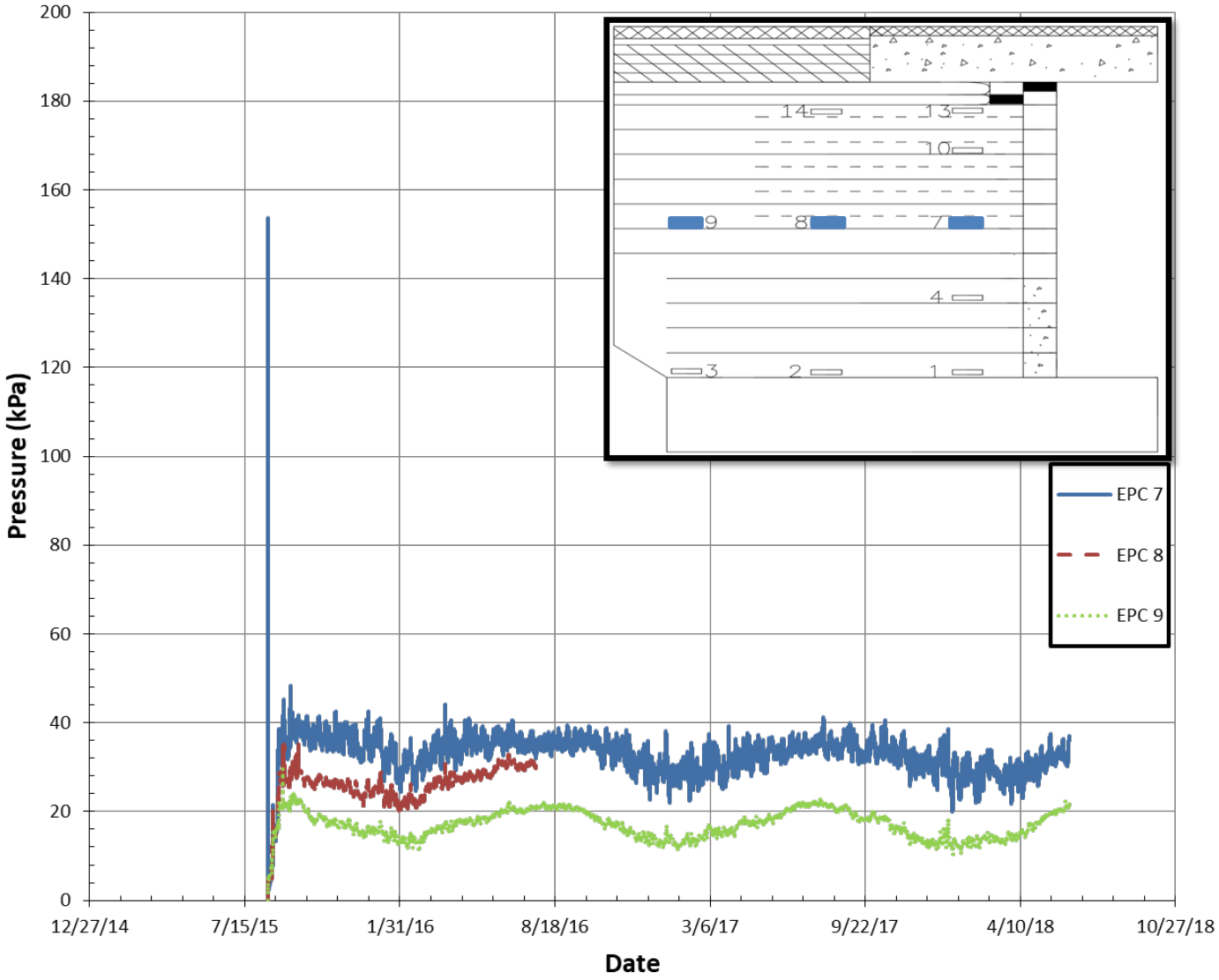

Fig. B5. Vertical stresses developed in layer 7 on Abutment A

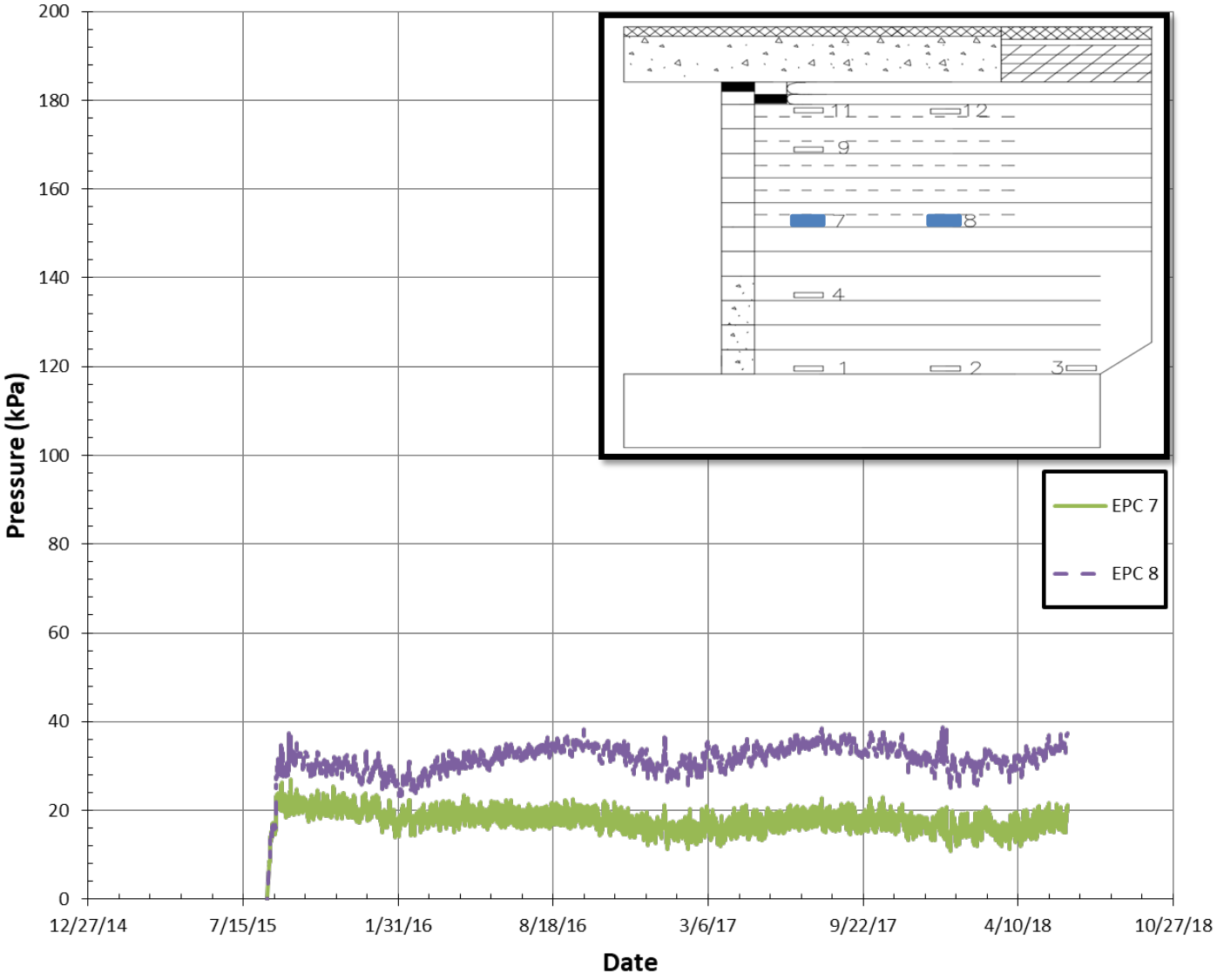

Fig. B6. Vertical stresses developed in layer 7 on Abutment B

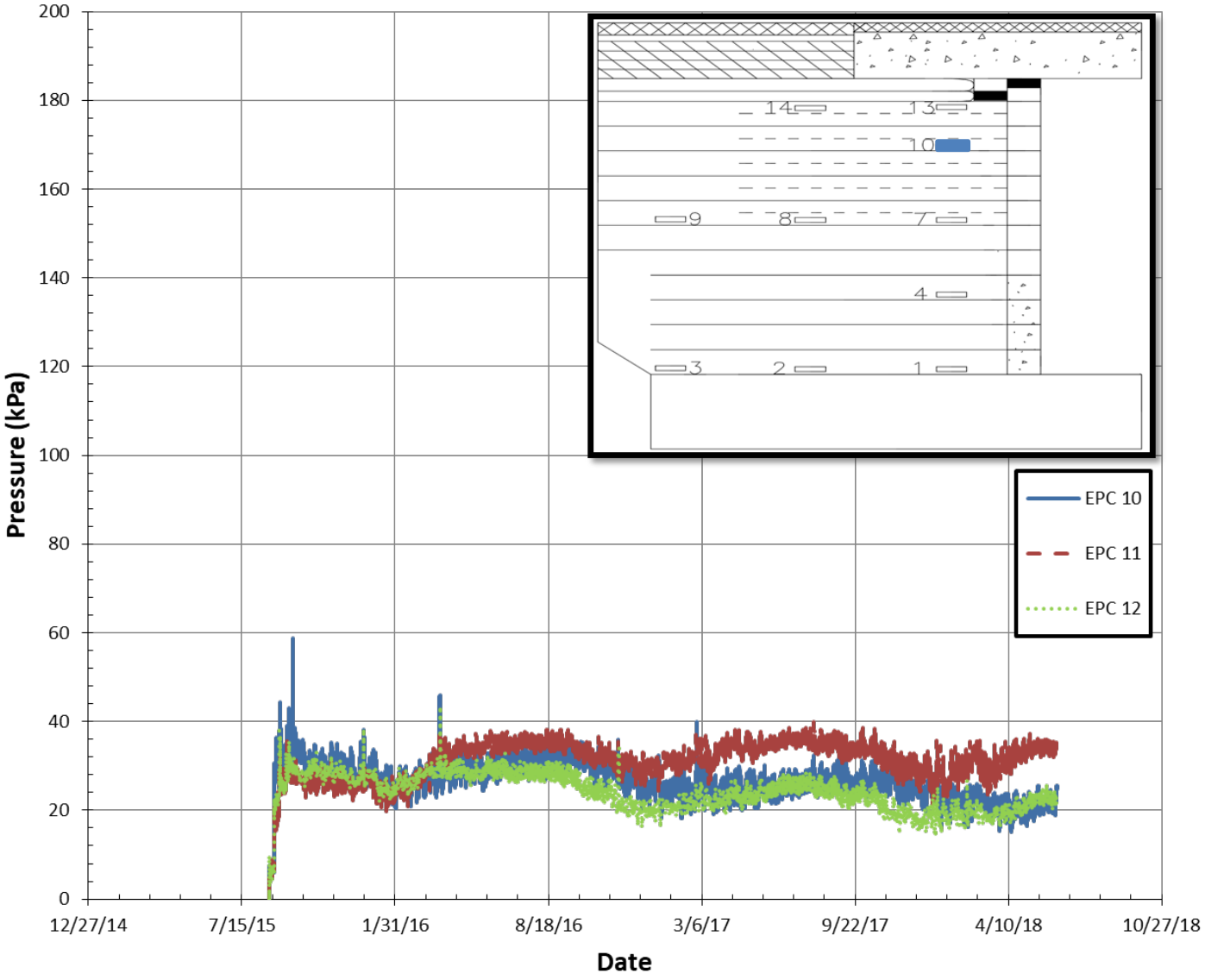

Fig. B7. Vertical stresses developed in Layer 13 on Abutment A (EPC 11 and 12 are located on the north and south sides)

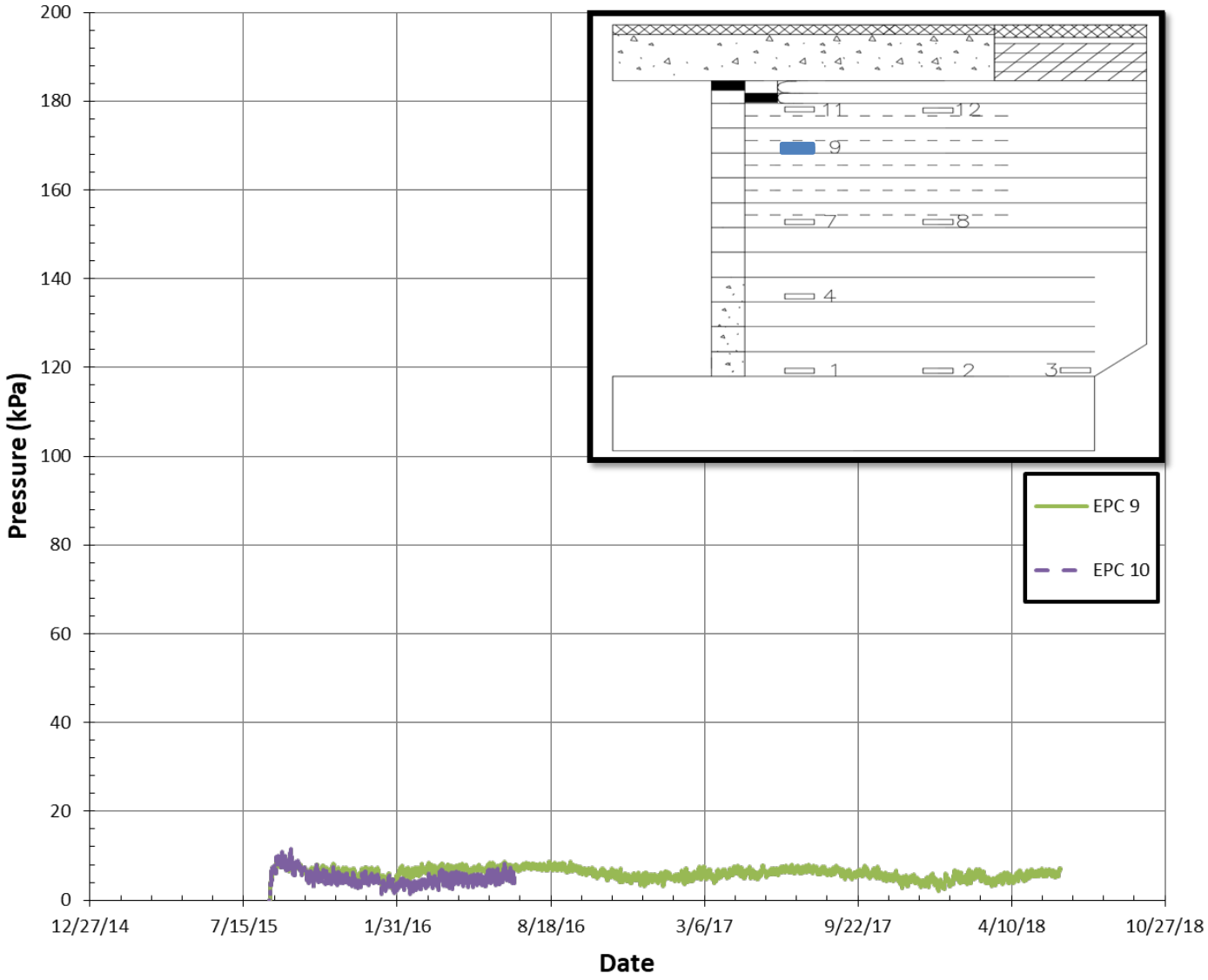

Fig. B8. Vertical stresses developed in layer 13 on Abutment B (EPC 10 is located on the North side)

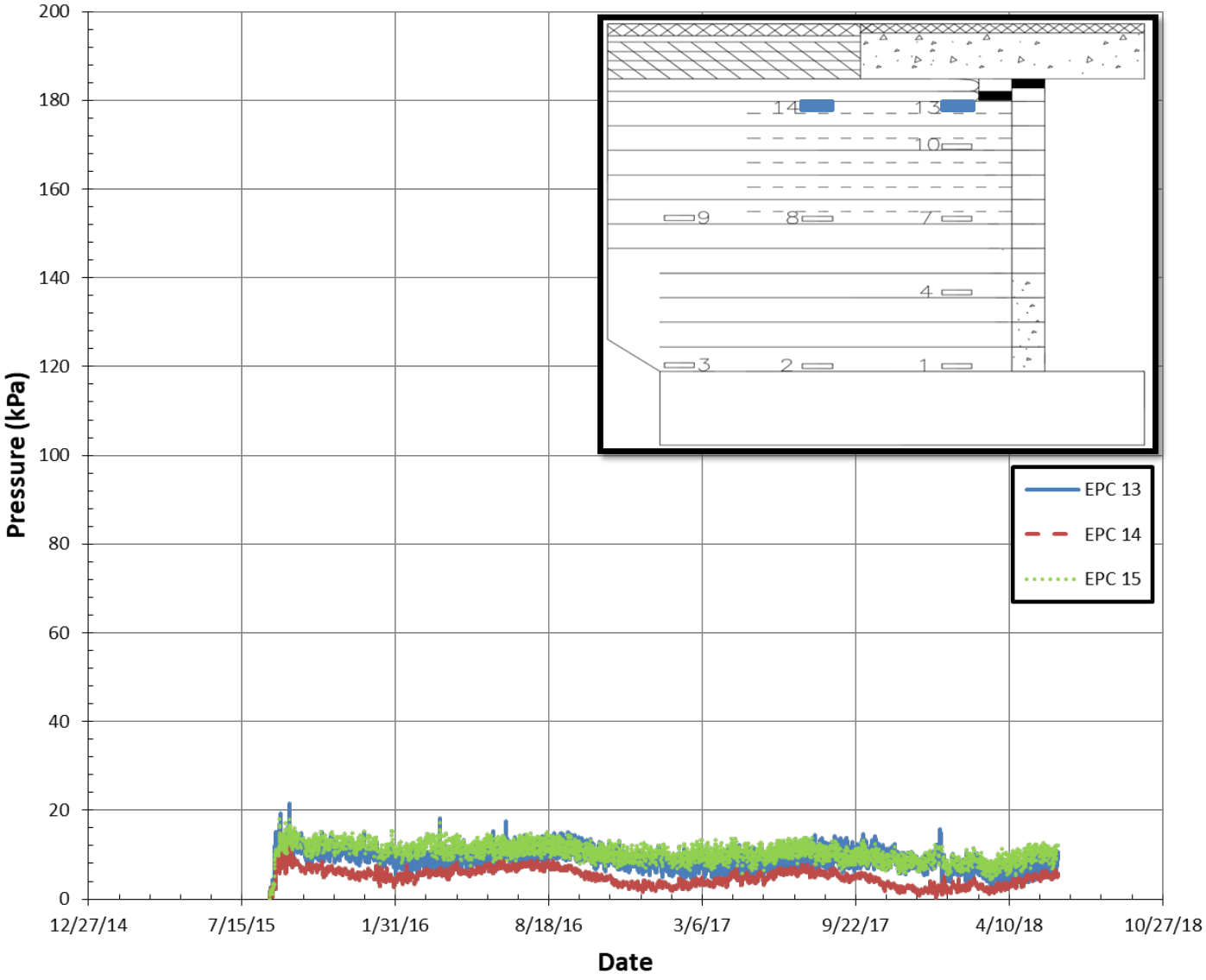

Fig. B9. Vertical stresses developed in layer 16 on Abutment A (EPC 15 is located on the North side)

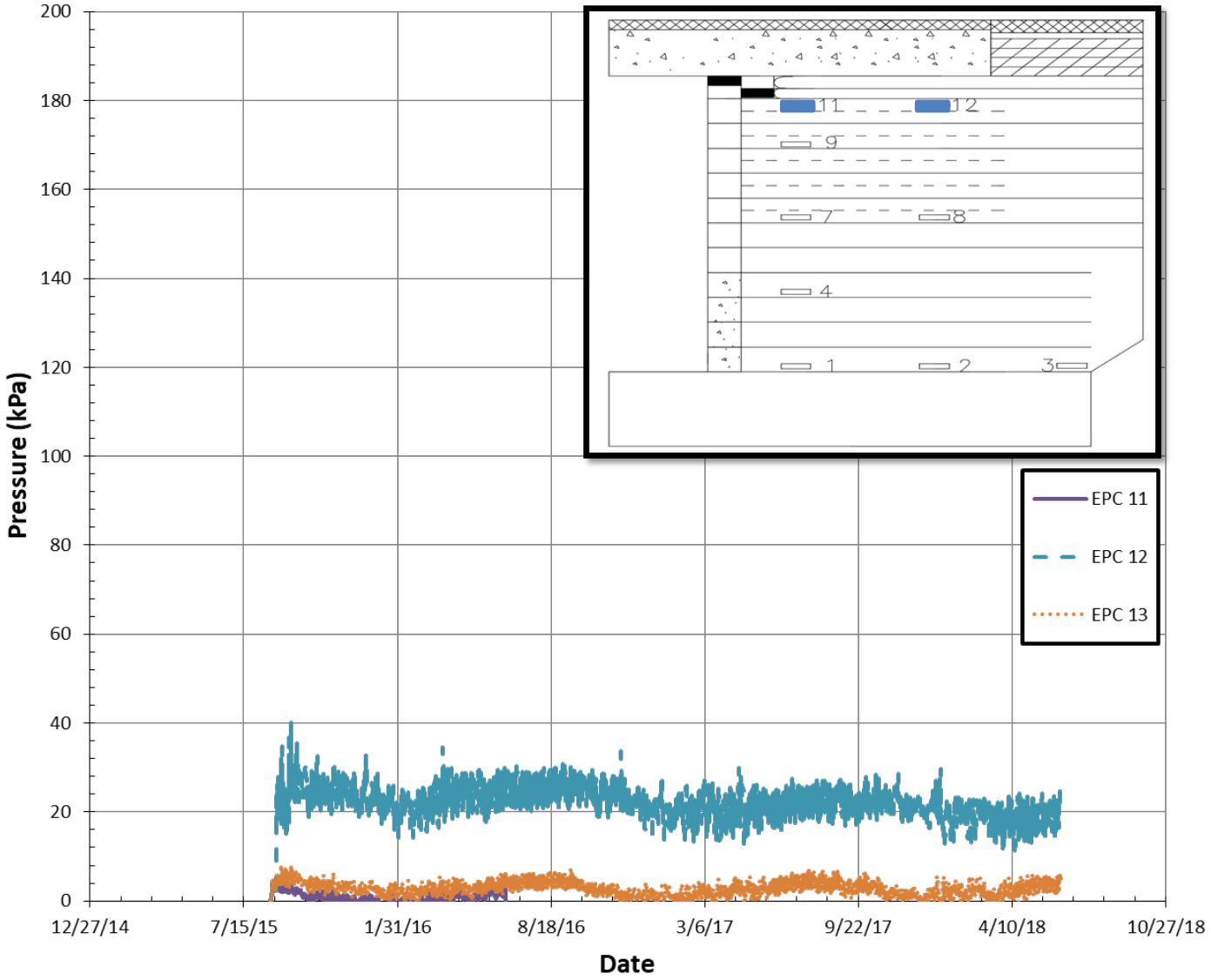

Fig. B10. Vertical stresses developed in layer 16 on Abutment B (EPC 13 is located on the South side)

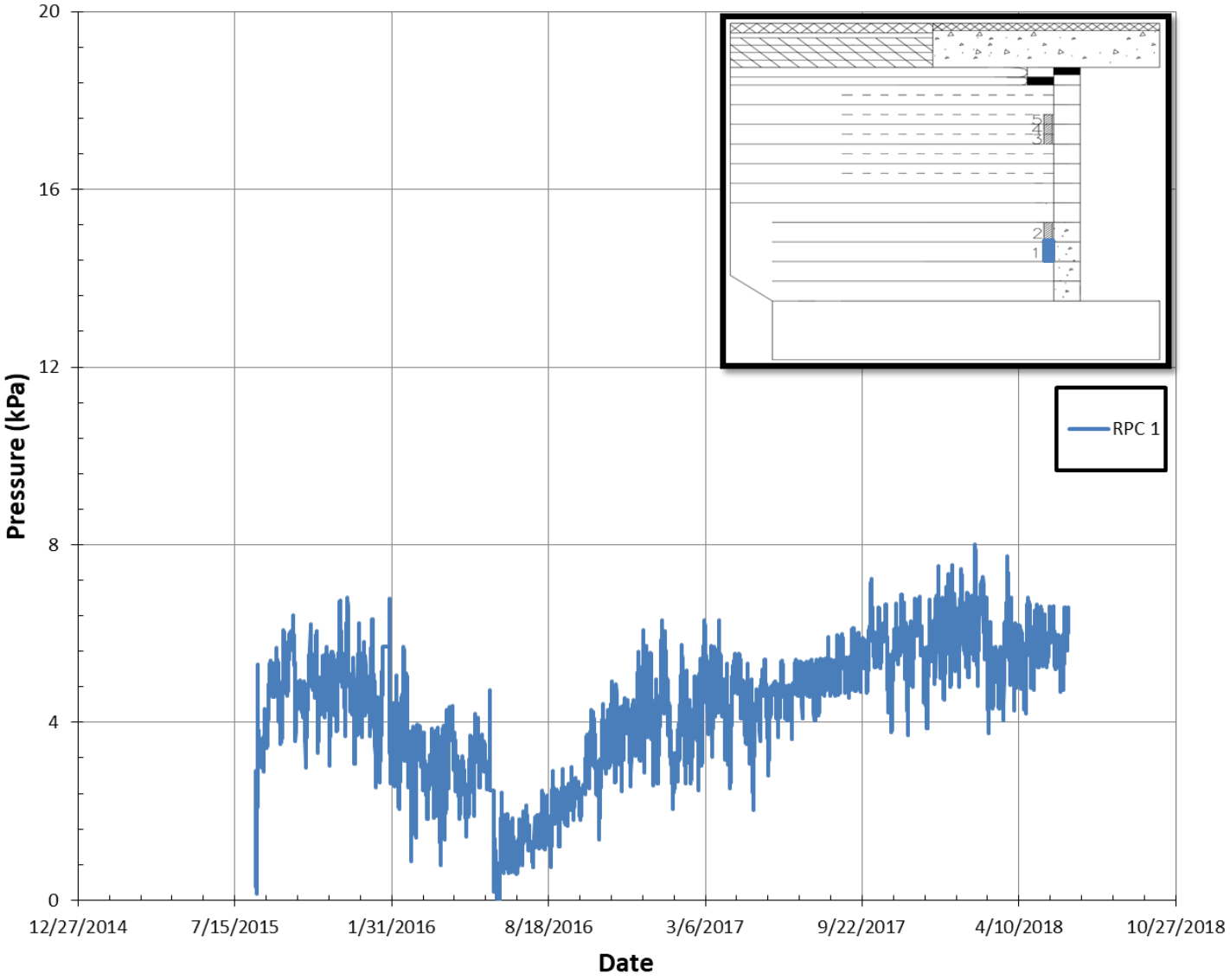

Fig. B11. Lateral stresses developed behind the facing blocks in layer 3 on Abutment A

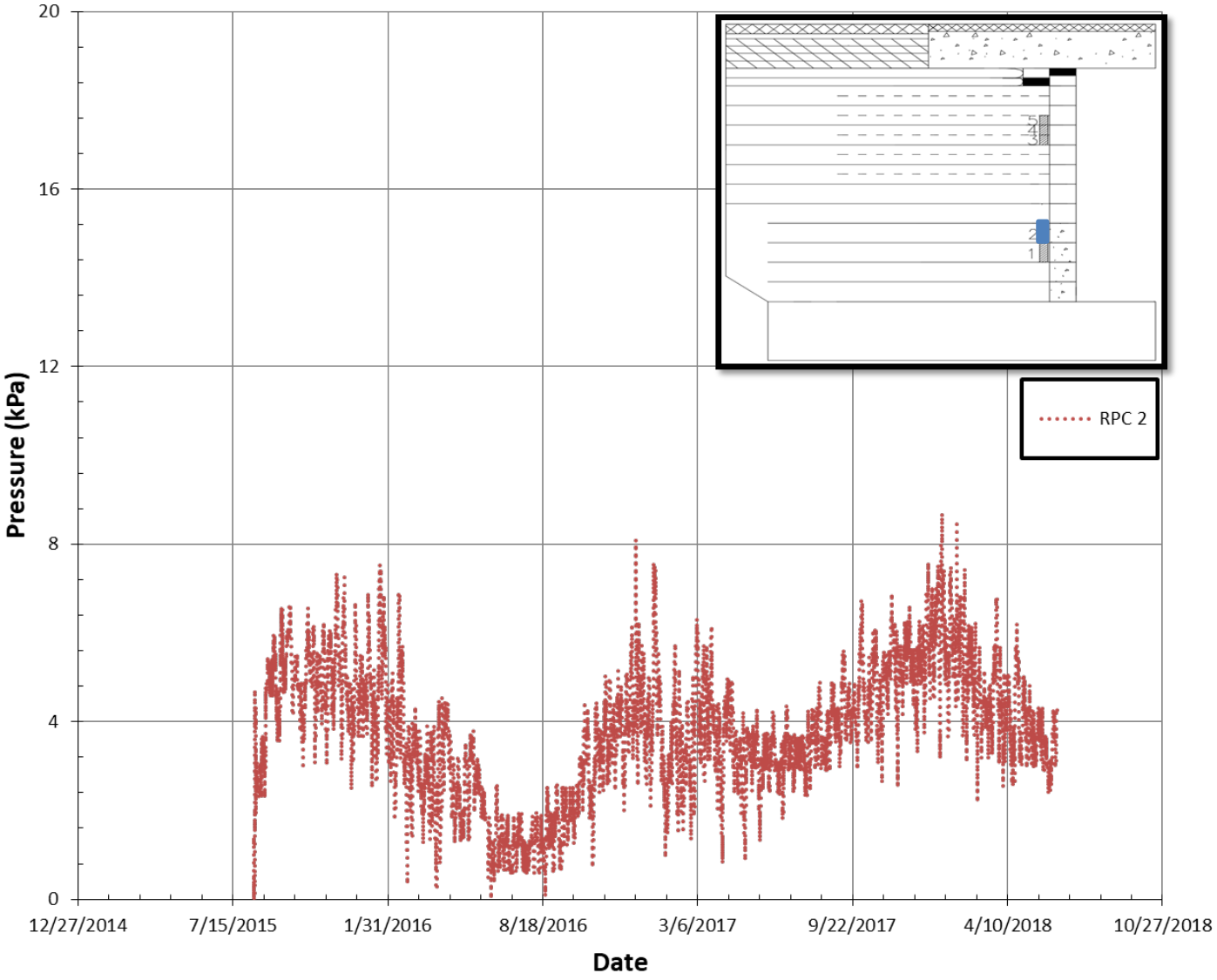

Fig. B12. Lateral stresses developed behind the facing blocks in layer 4 on Abutment A

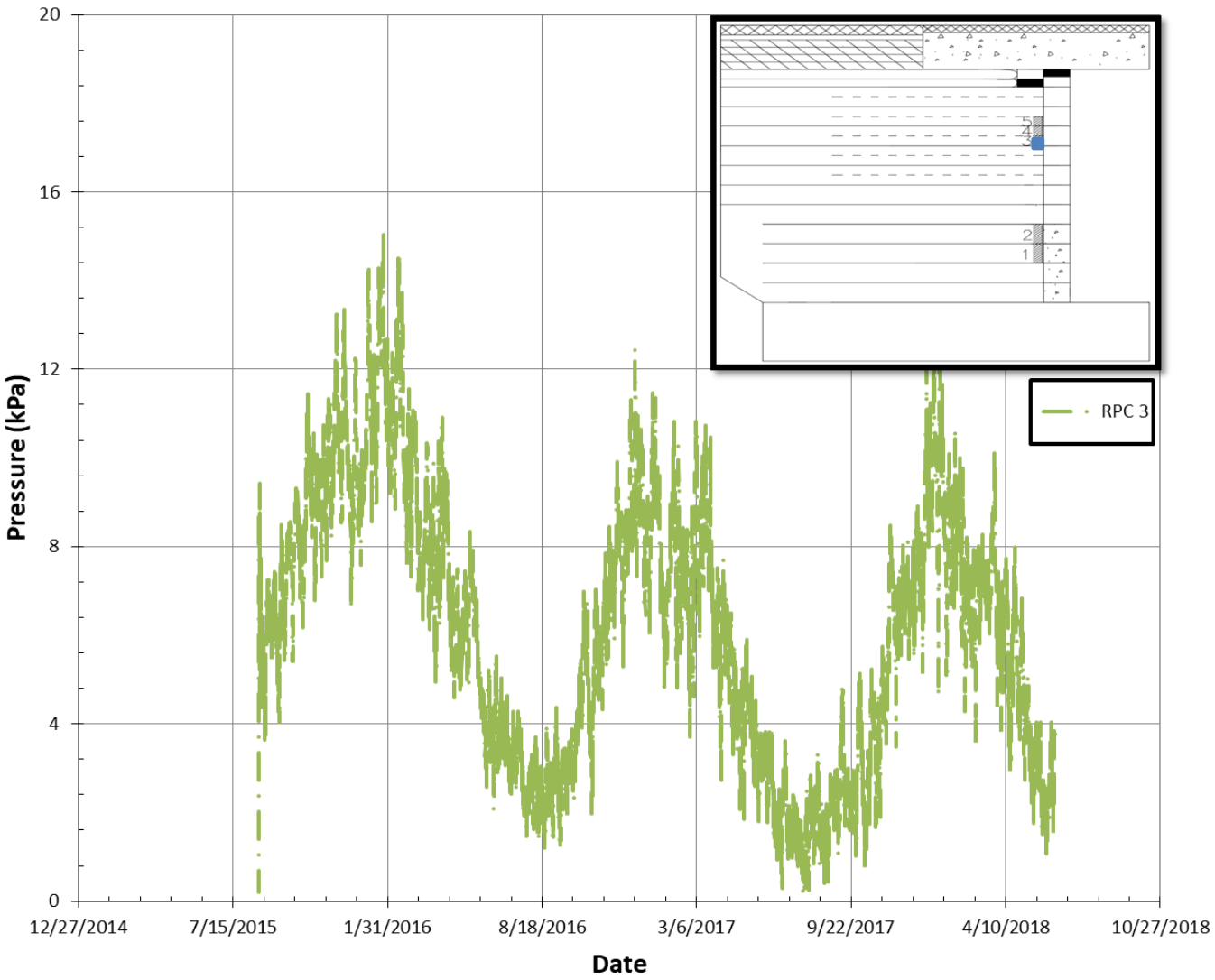

Fig. B13. Lateral stresses developed behind the facing blocks in layer 11 on Abutment A

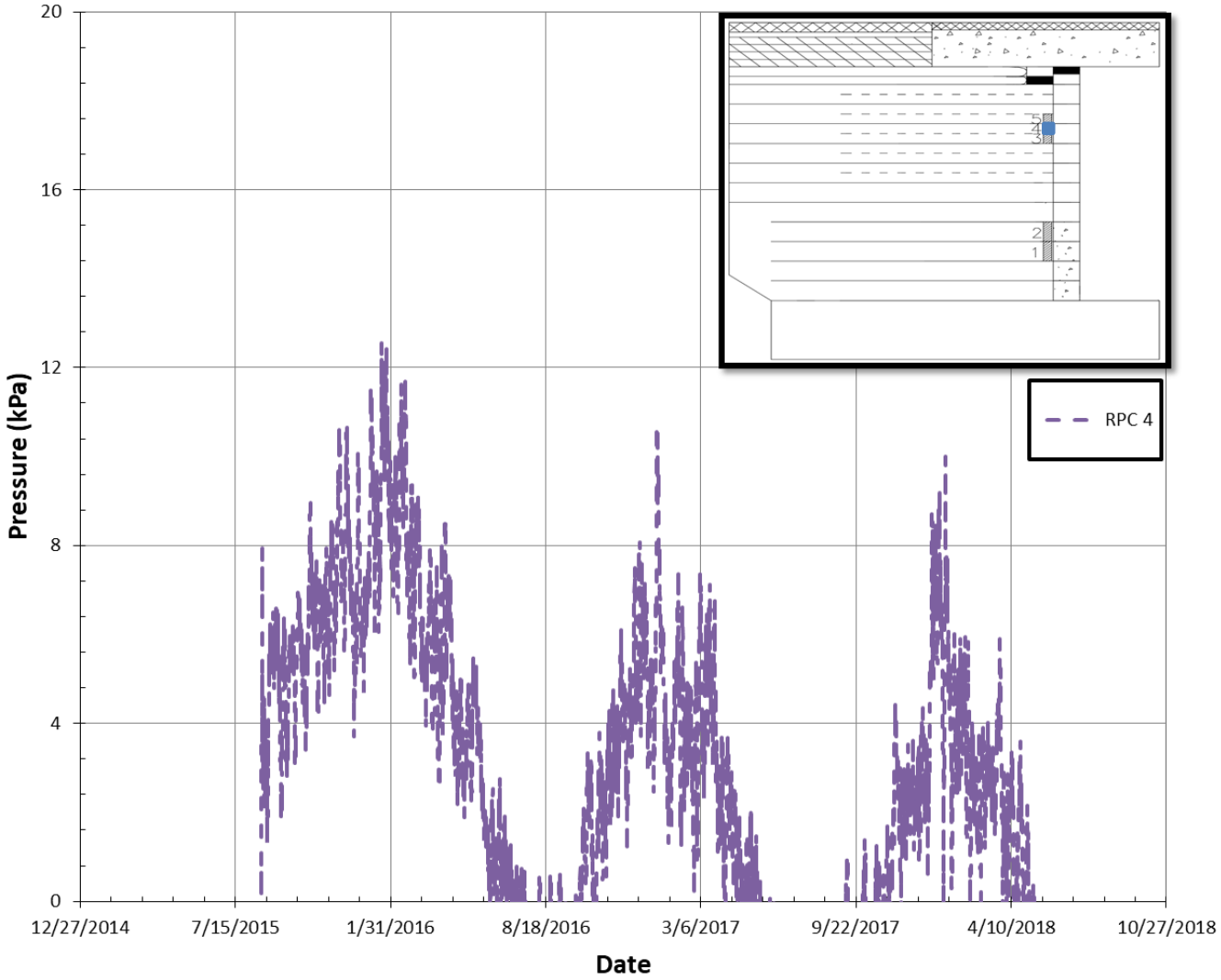

Fig. B14. Lateral stresses developed behind the facing blocks in layer 12 on Abutment A

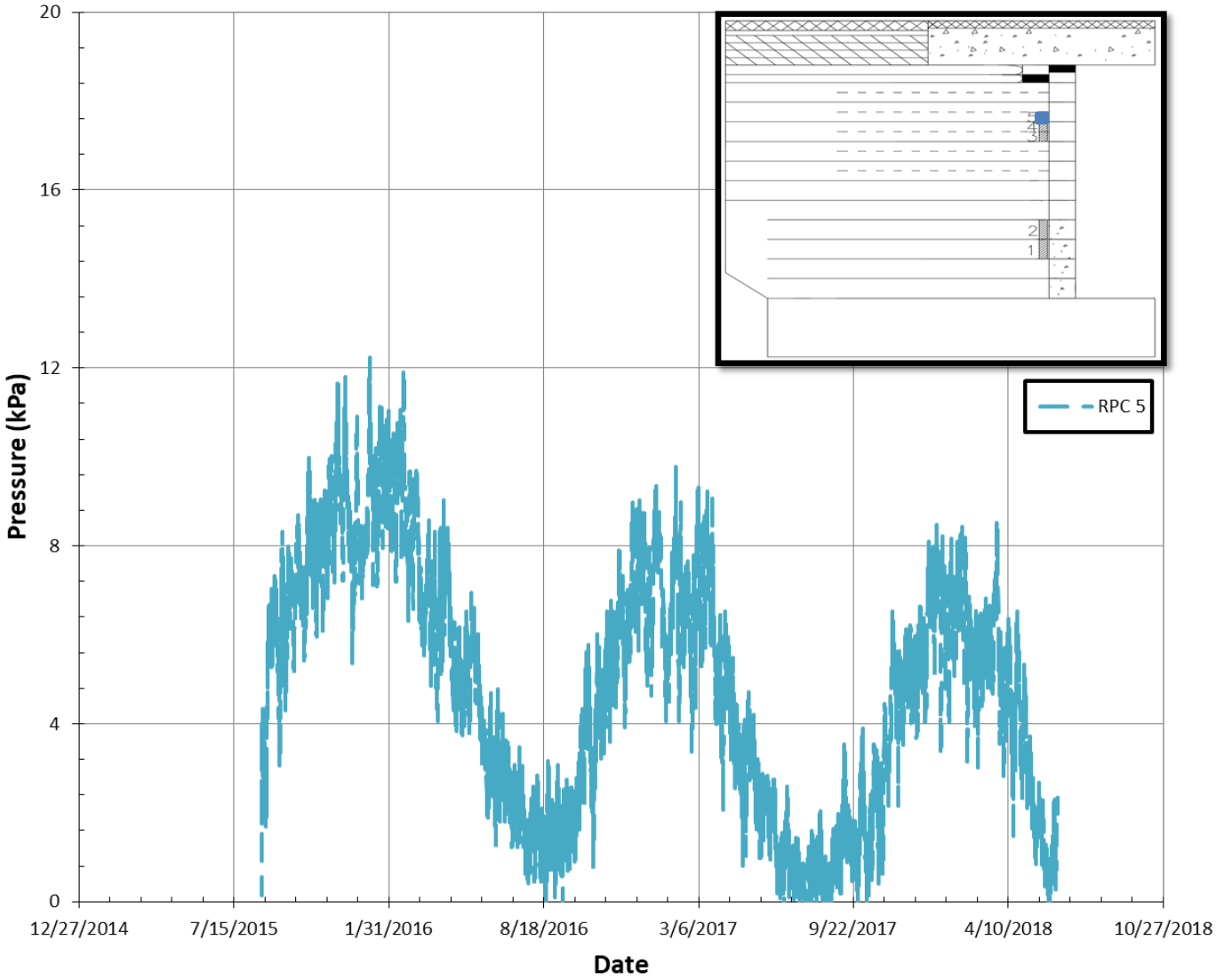

Fig. B15. Lateral stresses developed behind the facing blocks in layer 13 on Abutment A

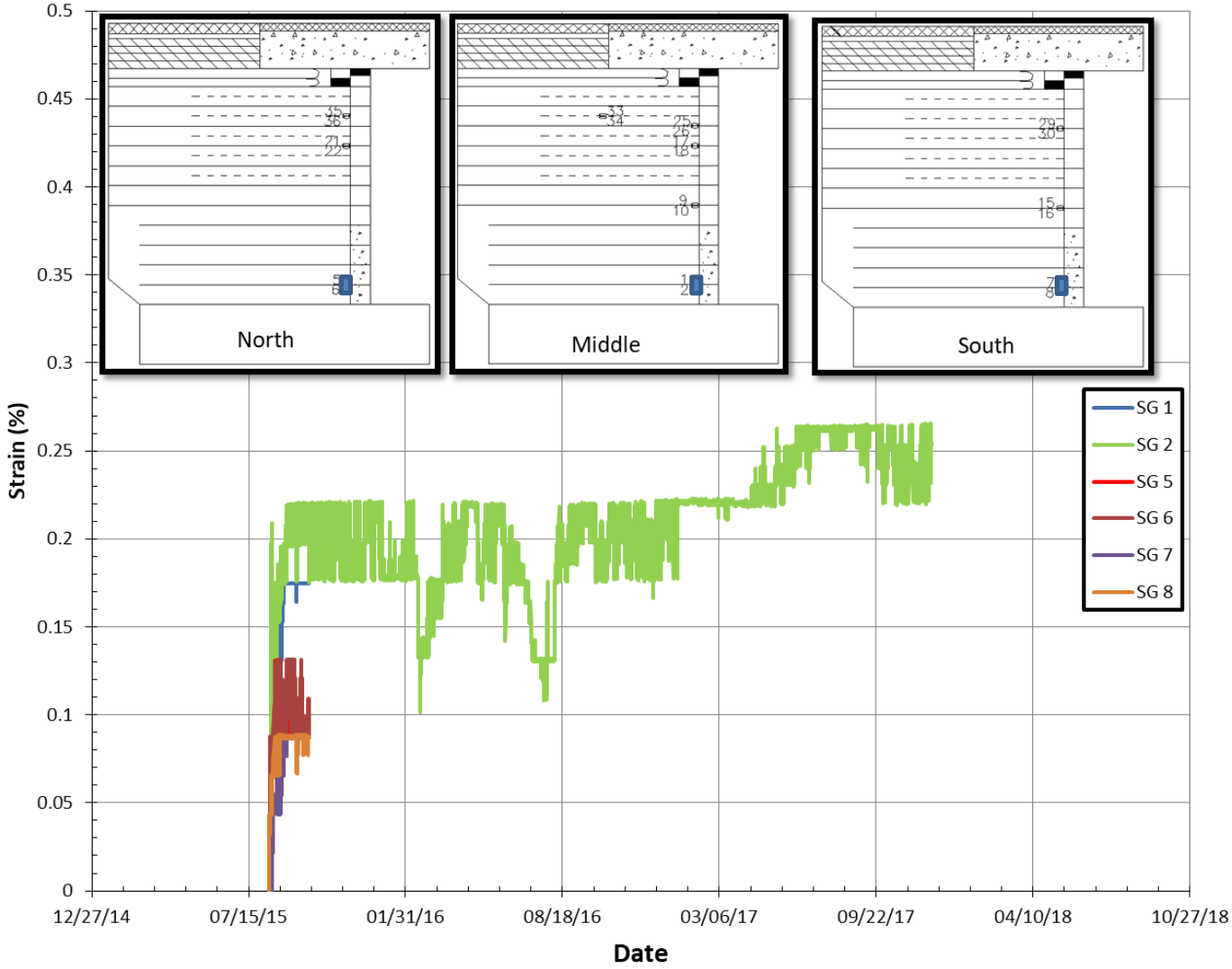

Fig. B16. Lateral geotextile strains developed in layer 2 on Abutment A

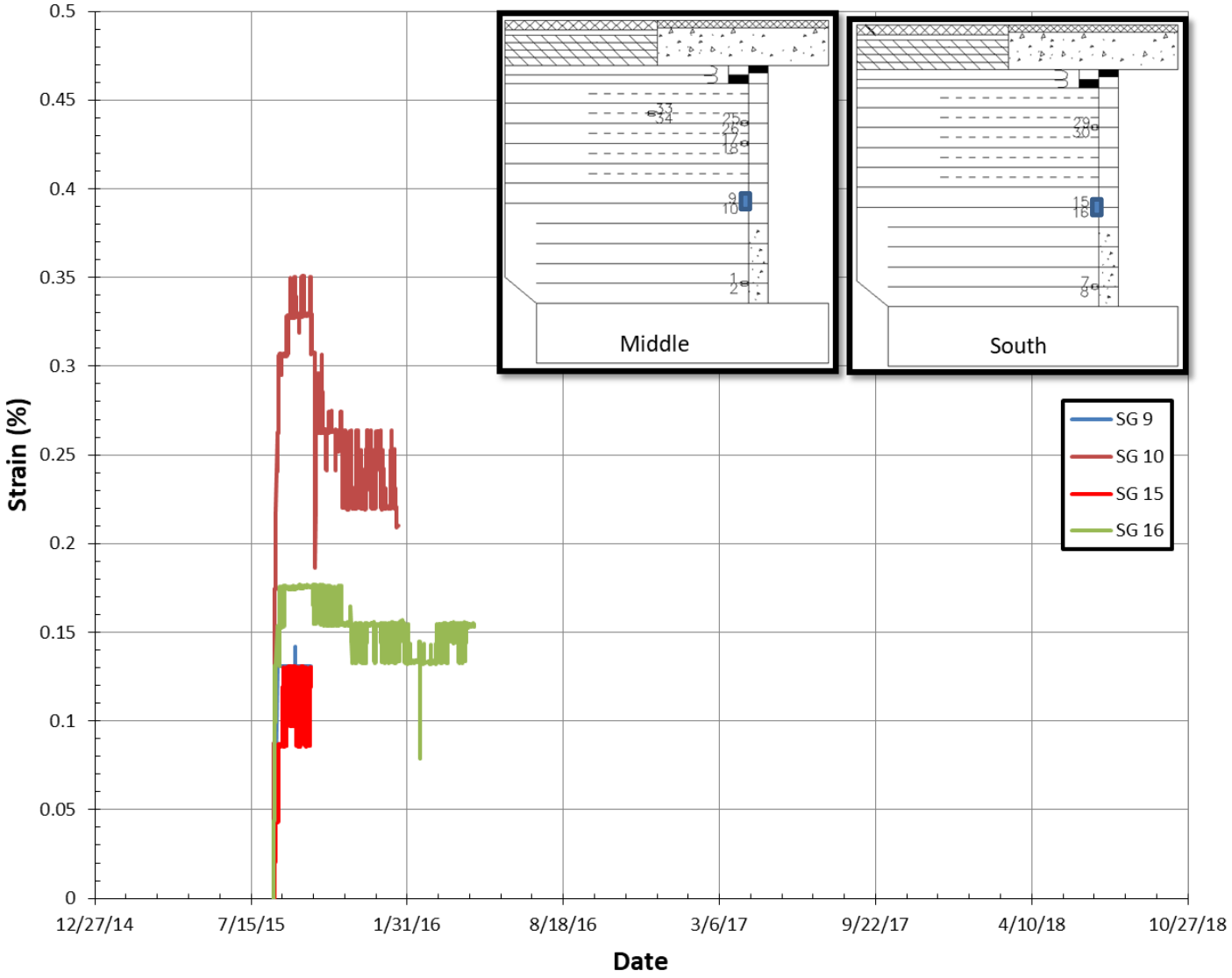

Fig. B17. Lateral geotextile strains developed in layer 6 on Abutment A

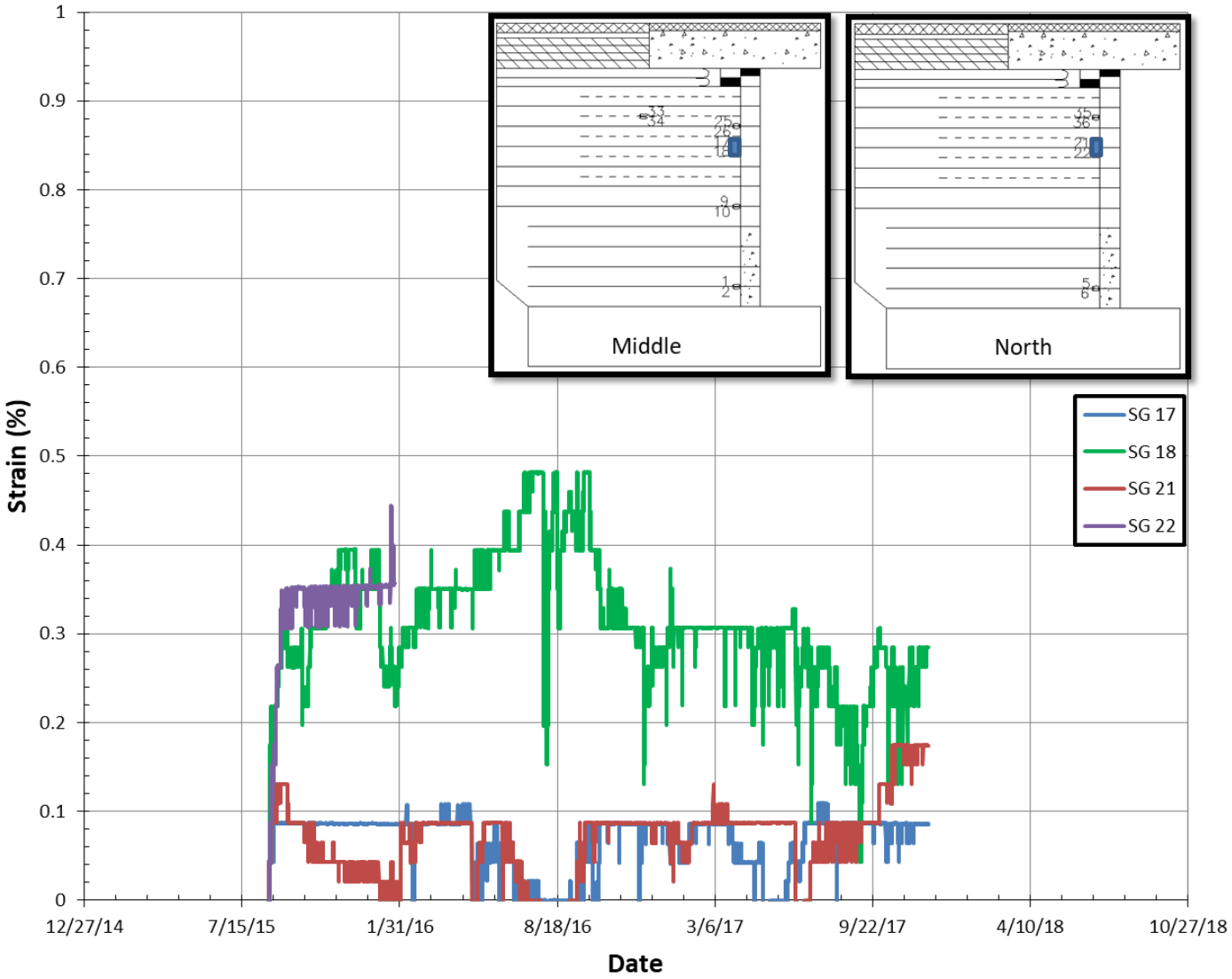

Fig. B18. Lateral geotextile strains developed in layer 11 on Abutment A

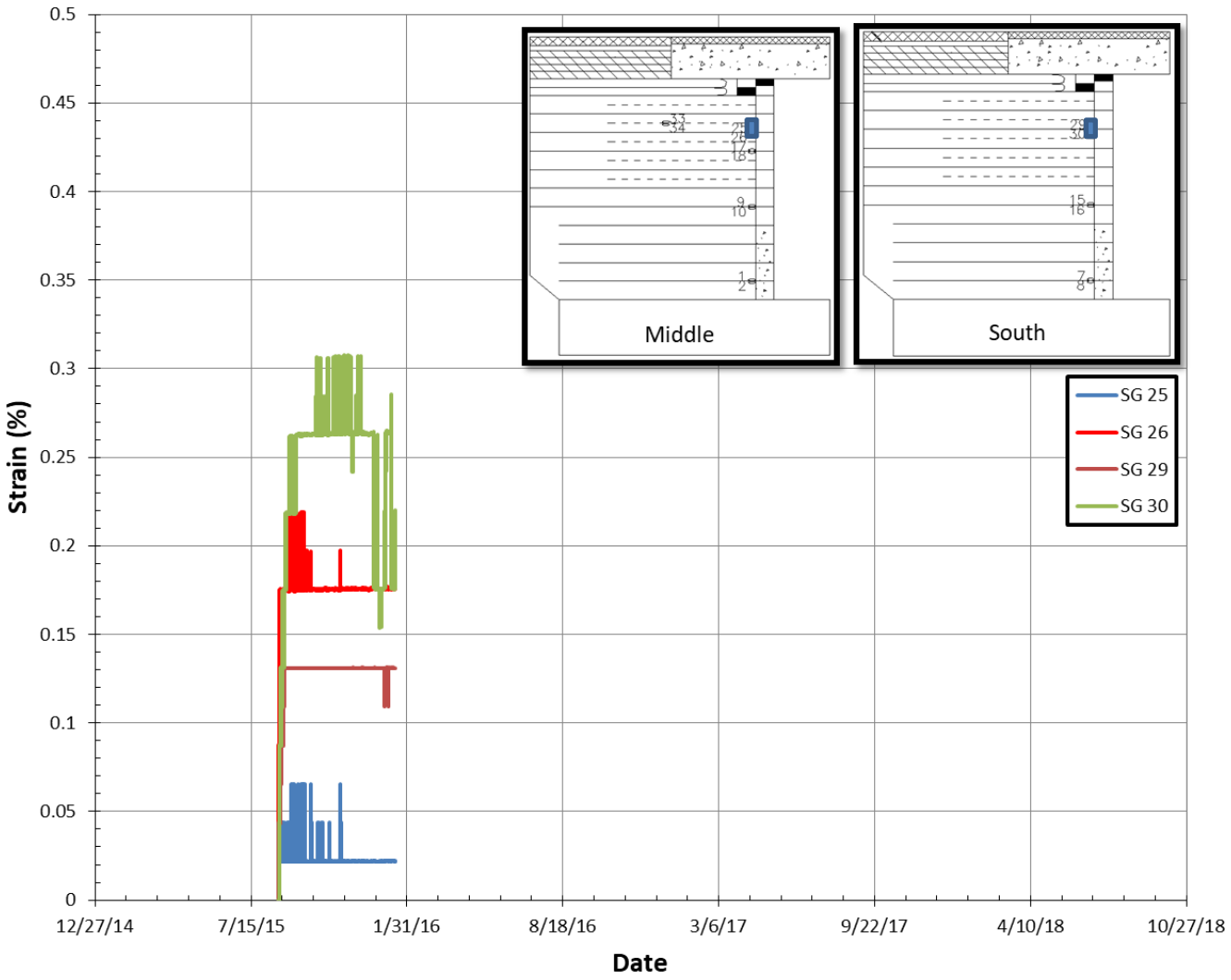

Fig. B19. Lateral geotextile strains developed in layer 13 on Abutment A

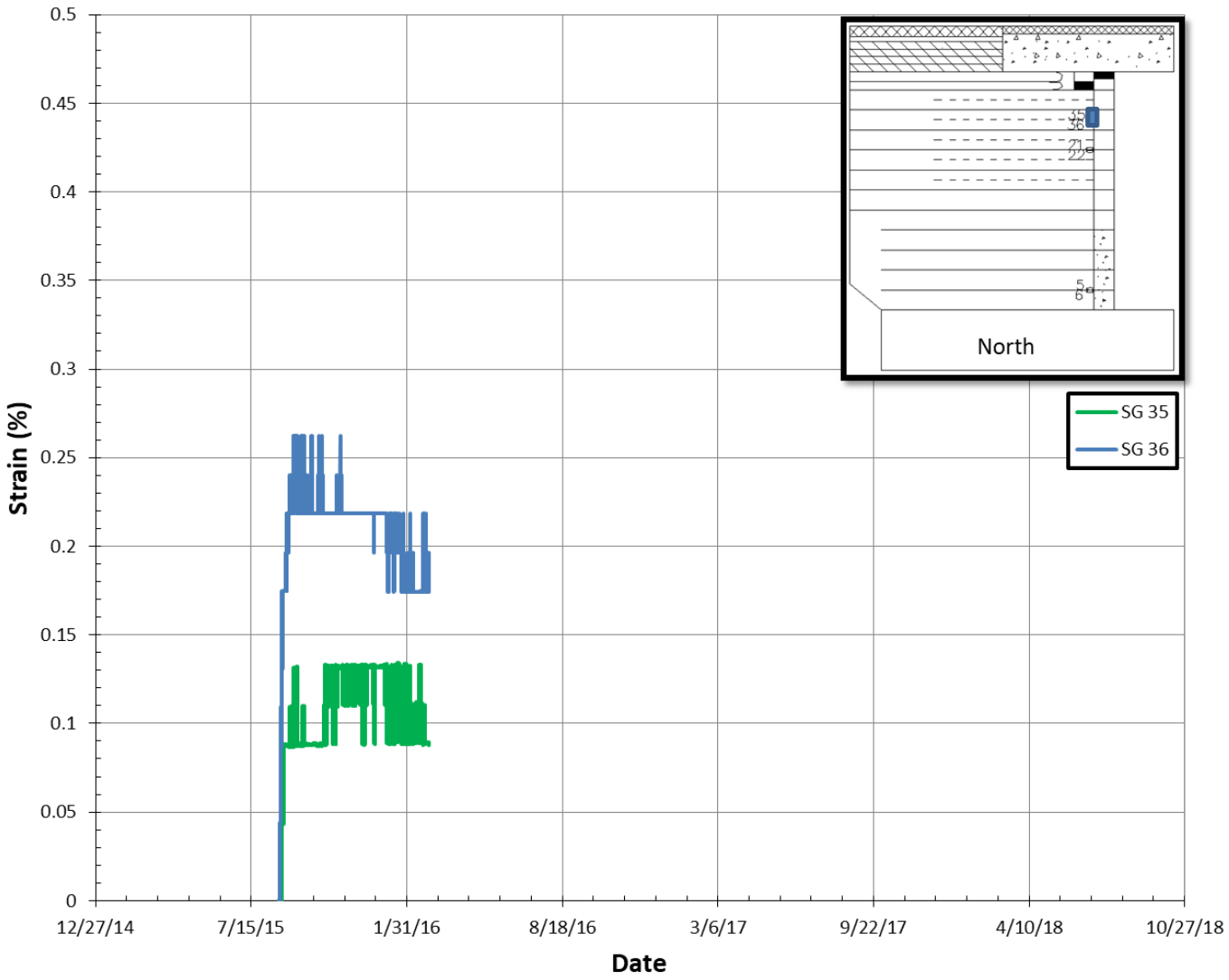

Fig. B20. Lateral geotextile strains developed in layer 14 on Abutment A

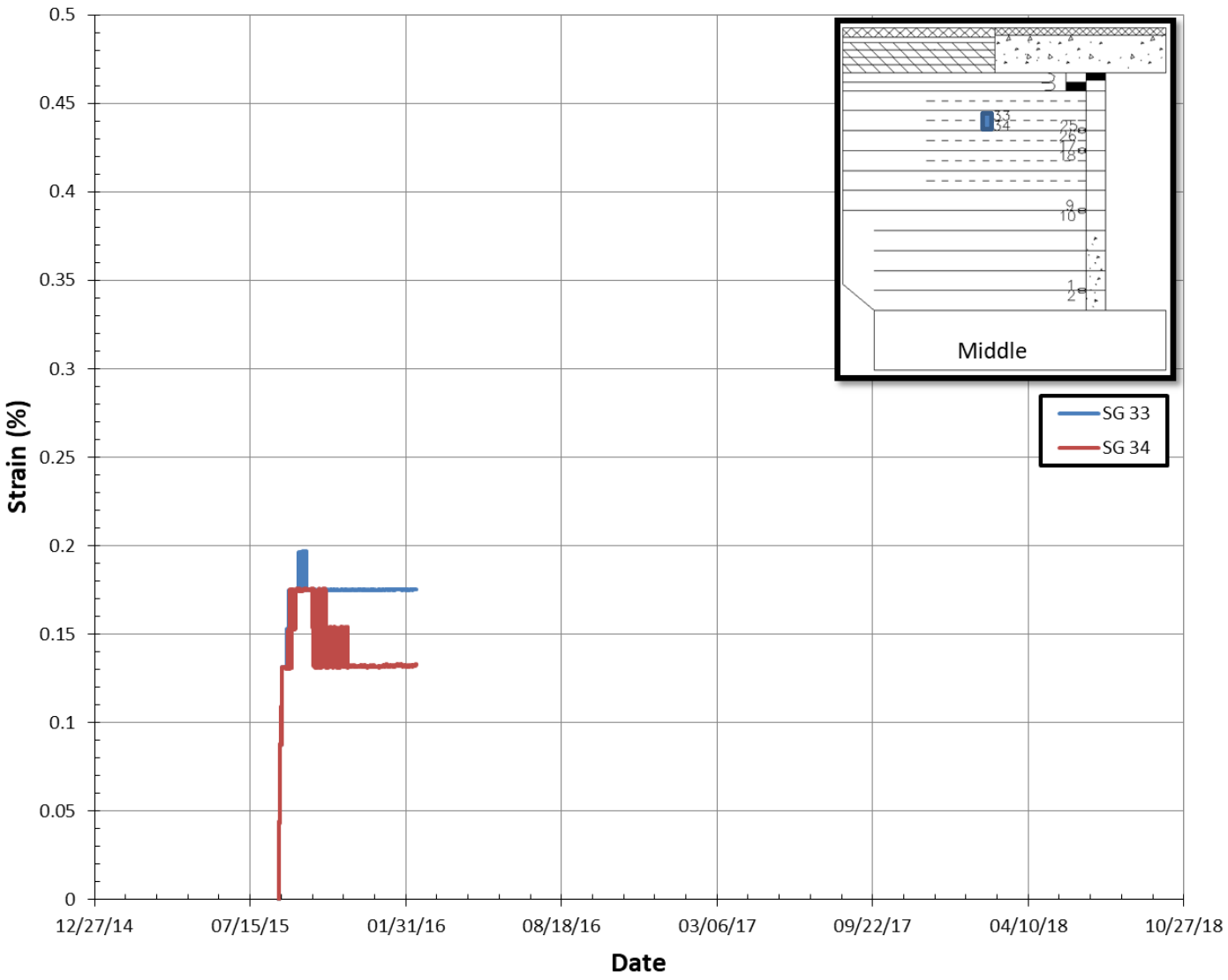

Fig. B21. Lateral geotextile strains developed in layer 14 on Abutment A

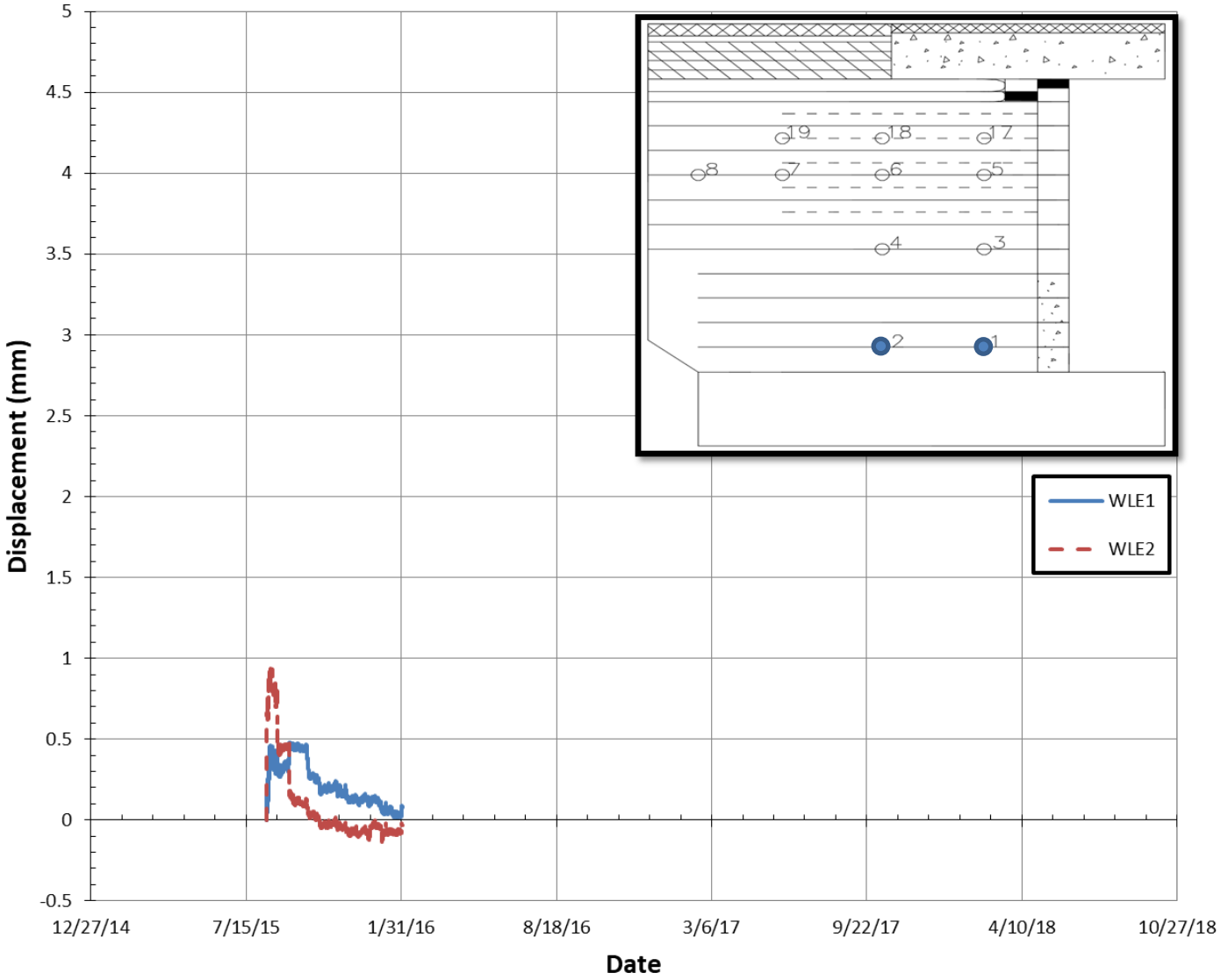

Fig. B22. Lateral geotextile displacements developed in layer 2 on Abutment A

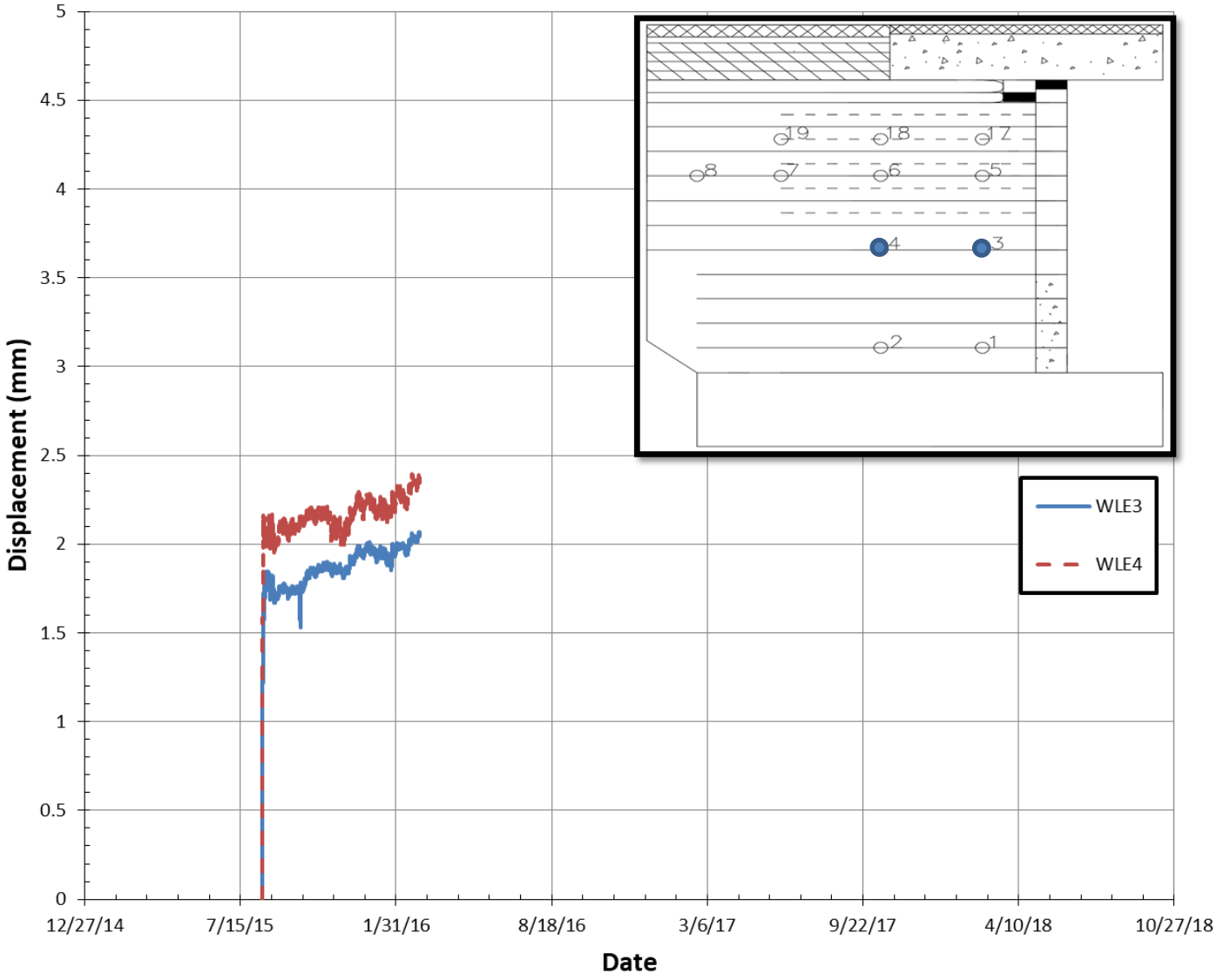

Fig. B23. Lateral geotextile displacements developed in layer 6 on Abutment A

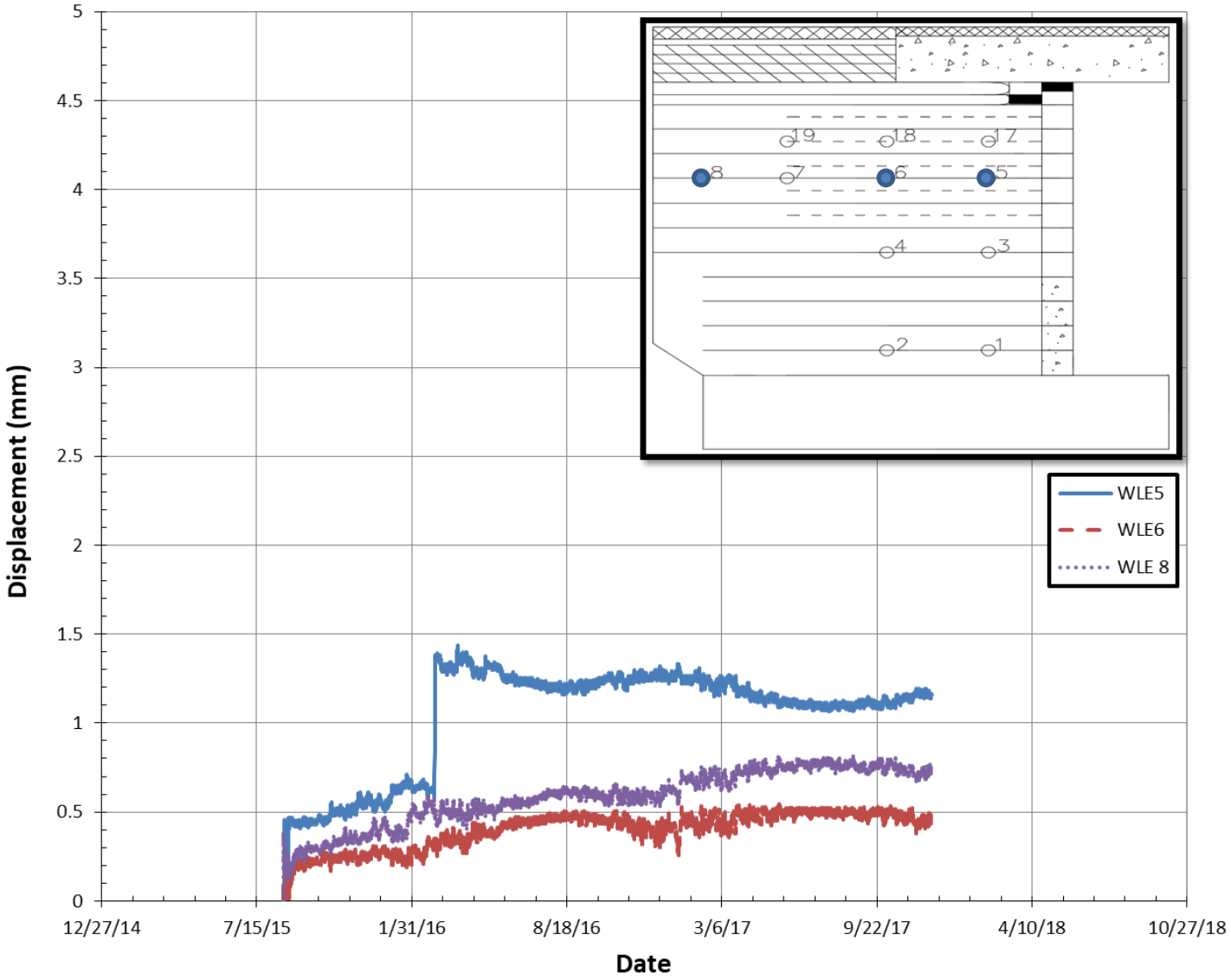

Fig. B24. Lateral geotextile displacements developed in layer 11 on Abutment A

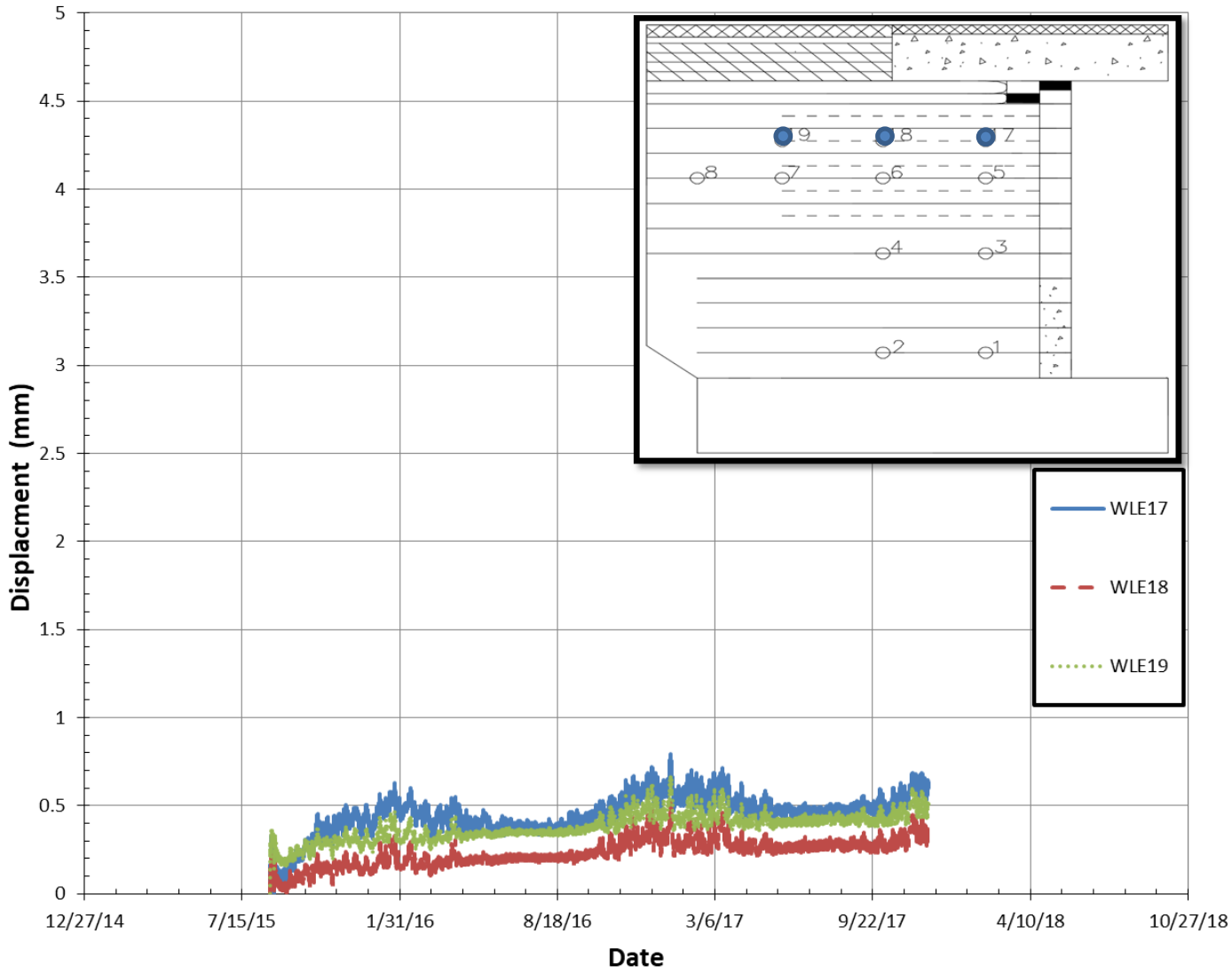

Fig. B25. Lateral geotextile displacements developed in layer 14 on Abutment A

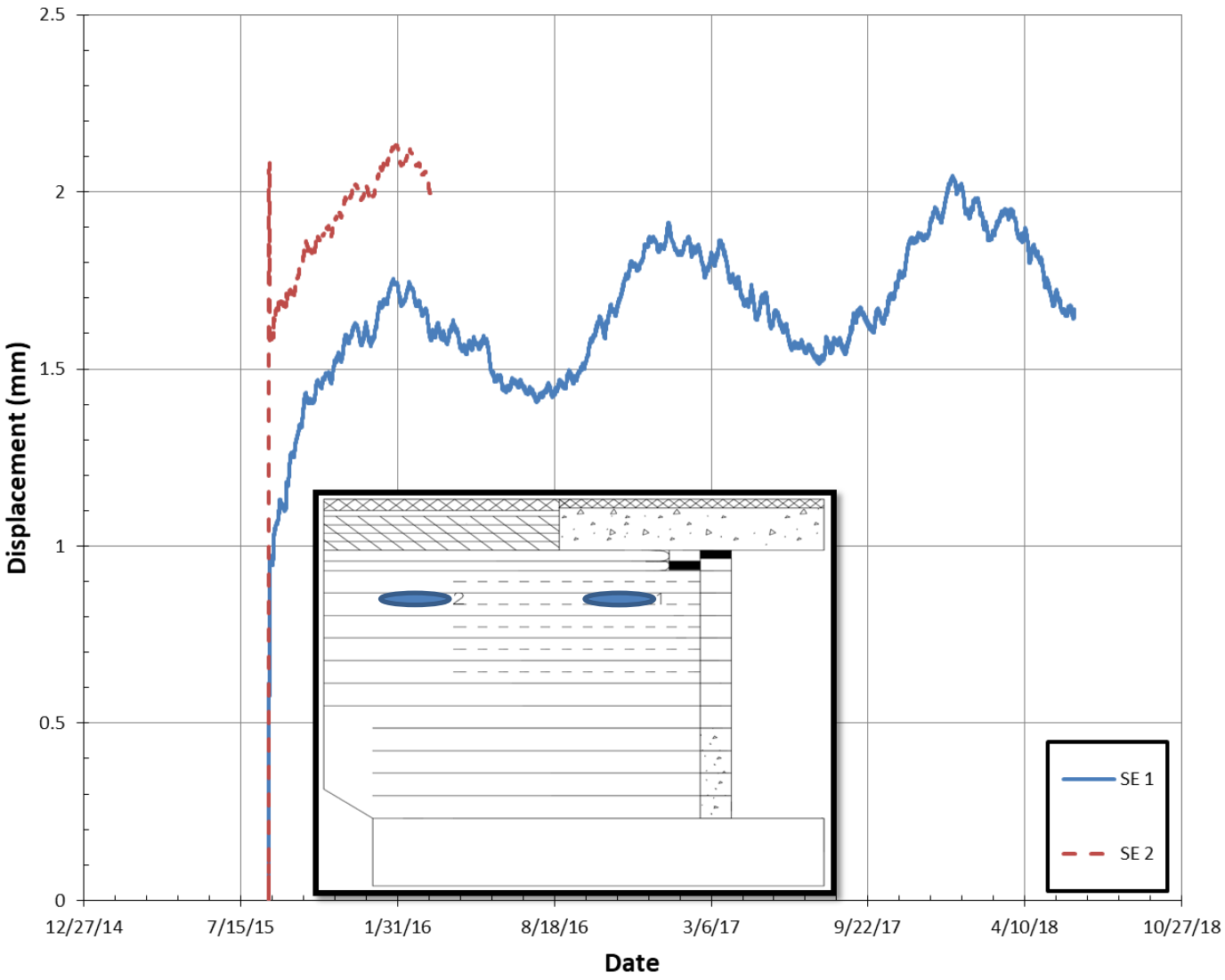

Fig. B26. Lateral backfill deformations developed in layer 14 on Abutment A